

NAM

V4 Ground-Motion Model (GMM) for Response Spectral Accelerations, Peak Ground Velocity, and Significant Durations in the Groningen Field

**Julian J Bommer¹, Bernard Dost², Benjamin Edwards¹, Pauline P Kruiver³,
Piet Meijers³, Michail Ntinalexis¹, Adrian Rodriguez-Marek¹, Elmer
Ruigrok², Jesper Spetzler², & Peter J Stafford¹**

1. Independent consultant,
2. Royal Netherlands Meteorological Institute (KNMI),
3. Deltares

Datum June 2017

Editors Jan van Elk & Dirk Doornhof

General Introduction

The hazard due to induced earthquakes is primarily presented by the ground motion to which buildings and people are subjected. The prediction of ground motion, resulting from the earthquakes in the Groningen area induced by the production of gas, is therefore critical.

This research was started in 2012 and is continuing with ever more ground motion data from Groningen earthquakes being collected. The methodology for Ground Motion Model (GMM) is therefore updated and progress documented regularly. In the Technical Addendum to Winningsplan 2013, a Ground Motion Prediction methodology based on a catalogue of tectonic earthquakes in southern Europe, was presented (Ref. 1). This methodology was inherently conservative, in the sense that it predicted ground motions which in future are in general more likely to be adjusted downwards than upwards.

In the report “Development of GMPEs for Response Spectral Accelerations and for Strong-Motion Durations (Version 1)” the status in May 2015 was documented (Ref. 2). An update of this document was issued in November 2015 and presented version 2 of the of the GMPE methodology (Ref. 3), which was an update of this Ground Motion Prediction methodology tailored to the Groningen situation (Ref. 4 to 6). In general this update led to downward adjustment of assessed ground motions for larger earthquakes, resulting in a reduction of the assessed hazard. After incorporating some adjustments, this version of the GMM was used for the hazard and risk assessment supporting Winningsplan 2016, issued in April 2016.

Originally, an update of the GMM (version 3) was planned for July 2016, in support of the hazard and risk assessment for Winningsplan 2016. However, when early 2016 the deadline of submission for the Winningsplan was brought forward from July 2016 to April 2016, version 3 of the GMM could not be ready in time to be implemented in the hazard and risk assessment for this winningsplan.

The current report describes version 4 of the Ground Motion Model (GMM), which was completed mid-2017. This version of the GMM will be incorporated in the hazard assessment in the update of the NEN-NPR to be released in July 2017.

References:

- 1 Technical Addendum to the Winningsplan Groningen 2013; Subsidence, Induced Earthquakes and Seismic Hazard Analysis in the Groningen Field, Nederlandse Aardolie Maatschappij BV (Jan van Elk and Dirk Doornhof, eds), November 2013.
- 2 Development of Version 1 GMPEs for Response Spectral Accelerations and for Strong-Motion Durations, Julian J Bommer, Peter J Stafford, Benjamin Edwards, Michail Ntinalexis, Bernard Dost and Dirk Kraaijpoel, March 2015.
- 3 Development of Version 2 GMPEs for Response Spectral Accelerations and Significant Durations for Induced Earthquakes in the Groningen field, Julian J Bommer, Bernard Dost, Benjamin Edwards, Adrian Rodriguez-Marek, Pauline P Kruiver, Piet Meijers, Michail Ntinalexis & Peter J Stafford, October 2015
- 4 Geological schematisation of the shallow subsurface of Groningen (For site response to earthquakes for the Groningen gas field) – Part I, Deltares, Pauline Kruiver and Ger de Lange.
- 5 Geological schematisation of the shallow subsurface of Groningen (For site response to earthquakes for the Groningen gas field) – Part II, Deltares, Pauline Kruiver and Ger de Lange.
- 6 Geological schematisation of the shallow subsurface of Groningen (For site response to earthquakes for the Groningen gas field) – Part III, Deltares, Pauline Kruiver and Ger de Lange.

These reports are also available at the study reports page of the website www.namplatform.nl.



NAM

Title	V4 Ground-Motion Model (GMM) for Response Spectral Accelerations, Peak Ground Velocity, and Significant Durations in the Groningen Field	Date	June 2017
		Initiator	NAM
Autor(s)	Julian J Bommer ¹ , Bernard Dost ² , Benjamin Edwards ¹ , Pauline P Kruiver ³ , Piet Meijers ³ , Michail Ntinalexis ¹ , Adrian Rodriguez-Marek ¹ , Elmer Ruigrok ² , Jesper Spetzler ² , & Peter J Stafford ¹	Editors	Jan van Elk & Dirk Doornhof
Organisation	1. Independent consultant, 2. Royal Netherlands Meteorological Institute (KNMI), 3. Deltares	Organisation	NAM
Place in the Study and Data Acquisition Plan	<u>Study Theme:</u> Ground Motion Prediction <u>Comment:</u> The prediction of Ground Motion is central to the hazard assessment. This report describes an update of the Ground Motion Prediction methodology (version 4) for the Groningen situation.		
Directly linked research	(1) Hazard Assessment. (2) Fragility assessment of buildings in the Groningen region.		
Used data	Accelerograms from the accelerometers placed in the Groningen field. P- and S-wave velocity model sub-surface Groningen. Description of the shallow geology of Groningen.		
Associated organisation	KNMI		
Assurance	External assurance team has reviewed this report. Comments have been addressed in the report or have been incorporated section Future Work, and will be addressed in GMM version 5.		

V4 Ground-Motion Model (GMM) for Response Spectral Accelerations, Peak Ground Velocity, and Significant Durations in the Groningen Field

**Julian J Bommer¹, Bernard Dost², Benjamin Edwards¹,
Pauline P Kruiver³, Piet Meijers³, Michail Ntinalexis¹,
Adrian Rodriguez-Marek¹, Elmer Ruigrok², Jesper Spetzler², & Peter J Stafford¹**

1. Independent consultant, 2. Royal Netherlands Meteorological Institute (KNMI), 3. Deltares

Version 2

3 June 2017

Table of Contents

Executive Summary	iii
Acknowledgements	xiii
1. INTRODUCTION	1
1.1. Purpose and applications of the GMM	1
1.2. Overview of Groningen GMM development process	2
1.3. GMM requirements for fragility functions and risk calculations	7
1.4. Overview of report	13
2. OVERVIEW of V4 GMM	15
2.1. Predicted and explanatory variables	15
2.2. Overview of derivation process	18
2.3. Definition of reference rock horizon	20
2.4. Spatial correlation of ground motions	24
3. GRONINGEN GROUND-MOTION DATABASES	27
3.1. Groningen ground-motion recording networks	27
3.2. Strong-motion database for Groningen	30
4. CHARACTERISATION of RECORDING STATIONS	39
4.1. Site kappa values for recording stations	39
4.2. Preliminary station profiles for site response analyses	46
4.3. Site response analyses and linear amplification factors for stations	54
5. INVERSION of GROUND MOTIONS for SOURCE, PATH and REFERENCE ROCK PARAMETERS	58
5.1. Fourier amplitude spectra at the reference rock horizon	58
5.2. Overview of inversion process for source, path and reference rock parameters	59
5.3. Alternative inversion formulations	61
5.4. Geometrical spreading function	65
5.5. Inversions for source, path and reference rock parameters	71
6. EQUATIONS for GROUND MOTIONS at REFERENCE ROCK HORIZON	78
6.1. Finite-fault stochastic simulations	78
6.2. Predicted SA and PGV at reference rock horizon	85
6.3. Functional form for reference rock GMPE	90
6.4. Regression analyses	93
6.5. Residual analyses	110
6.6. Ground-motion model for reference rock horizon	123
7. SITE RESPONSE MODEL	139
7.1. Shallow V_s profiles	139
7.2. Extension of V_s profiles to reference rock horizon	148
7.3. Layering model and layer-to-layer correlations	153
7.4. Mass densities	154
7.5. Modulus reduction and damping curves	154
7.6. Modulus reduction and damping curves for peats	160
7.7. Randomisations	165
8. SITE RESPONSE ANALYSES	171
8.1. Choice of analysis procedure	171
8.2. Input motions at reference rock horizon	195
8.3. Amplification factors and variability	199

9. ZONATION for SITE AMPLIFICATION FUNCTIONS	204
9.1. Criteria for zonation	204
9.2. Zonation of the study area	206
9.3. Zone amplification factors	208
9.4. Comparison with amplification factors for recording stations	230
10. SIGMA MODEL	236
10.1. Elements of the sigma model for surface motions	236
10.2. Component-to-component variability	241
10.3. Tau and ϕ_{ss} model	249
10.4. Site-to-site variability model	258
11. APPLICATION and EXTENSION of the GMM for $S_a(T)$	260
11.1. Model for predicting surface response spectra	260
11.2. Residual of surface motions	286
11.3. Period-to-period correlations	298
11.4. Vertical-to-horizontal ratios	299
12. GMPE for DURATION	305
12.1. Durations of Groningen ground motions	305
12.2. Simulated NS_B durations	312
12.3. GMPE for surface durations	317
12.4. Residuals and sigma model	323
12.5. Correlation of residuals of duration and amplitude	326
13. CONCLUDING REMARKS	328
REFERENCES	339
APPENDIX I Station V_s , density and damping profiles	354
APPENDIX II Transfer functions for recording stations	404
APPENDIX III Linear amplification functions for $S_a(T)$ at recording stations	415
APPENDIX IV Response spectra at surface and reference rock	455
APPENDIX V Groningen soil characteristics	486
APPENDIX VI Analysis of TNO accelerograph recordings	505

Executive Summary

Overview

The V4 Groningen ground-motion model (GGMM) predicts amplitudes and durations of ground motions due to induced and triggered earthquakes in the Groningen gas field, covering a magnitude range from M_L 2.5 to around 7. The predicted amplitude parameters are the 5%-damped pseudo-spectral accelerations, $S_a(T)$, at 23 oscillator periods, T , from 0.01 to 5 seconds, and the peak ground velocity, PGV; the value of $S_a(0.01s)$ is assumed equivalent to the peak ground acceleration, PGA. In all cases, the geometric mean of the horizontal components of $S_a(T)$ and PGV are predicted.

The V4 GGMM retains the same basic structure as previous models: equations for the prediction of accelerations at a buried reference rock horizon (NS_B) combined with frequency-dependent non-linear site amplification factors (AFs) assigned to zones defined throughout the study area (onshore gas field plus 5 km buffer). However, the equations for the rock motions are now derived from finite fault rupture-based stochastic simulations and consequently instead of epicentral distance (R_{epi}) the equations are now based on the rupture distance (R_{rup}), which is the shortest distance between the site and fault rupture. The introduction of this distance metric means that earthquakes can no longer be represented by point sources but rather by extended fault ruptures, the dimensions of which increase with earthquake magnitude. Since ruptures are assumed to initiate in the Rotliegend and to propagate laterally and downwards, the minimum value of R_{rup} is 3 km. In common with earlier models, however, the model is calibrated in terms of local magnitude M_L , which is consistent with the magnitude scale used to define the recurrence rates in the seismological model.

The basic elements of the model implementation are illustrated in Figure ES.1. The example schematically illustrates the predictions at three surface locations in two zones, for an earthquake of magnitude M_a and an event-term of $\varepsilon_{b\tau}$. For each location, the level of rock motion includes samples from the spatial (within-event) variability of the NS_B motions; in this simple example, the within-event variability is sampled without considering spatial correlation. The AFs applied in each zone to transfer the rock motions to the ground surface are obtained from the median value, conditioned on the realisation of the rock motion, together with a random sample from the site-to-site variability term.

As in earlier versions of the model, durations are predicted directly at the ground surface as a function of magnitude (M_L), distance (R_{rup}) and the time-average shear-wave velocity over the uppermost 30 metres (V_{S30}

This document summarises the basic elements of the model as required for its implementation. The coefficients and additional values (such as the site amplification zonation) are included in supplementary Excel files identified in the text.

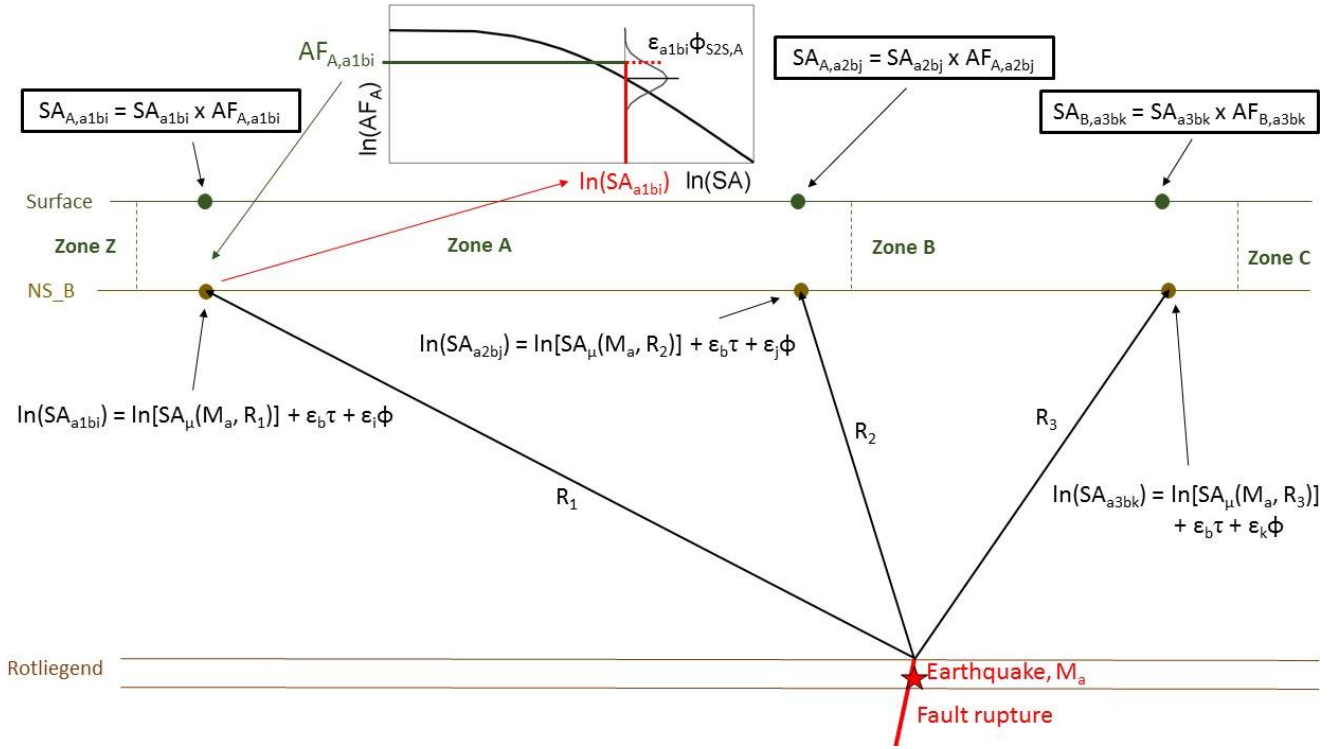


Figure ES.1. Schematic illustration of the implementation of the V4 GMM for a single earthquake scenario and three target locations at the ground surface, located in two zones

Equations for Median Motions at NS_B Rock Horizon

The equations for predicting the median ground-motion parameters at the NS_B rock horizon are a function of only local magnitude (M_L) and distance (R_{rup}); hereafter, these are specified simply as M and R , the latter measured in km. The model can be represented as comprising a source component and a path component, the latter being a function of magnitude and distance:

$$\ln(Y) = g_{source}(M) + g_{path}(R, M) \quad (ES.1)$$

where Y is either $Sa(T)$ in cm/s^2 or PGV in cm/s . The source-related terms are segmented into three ranges of magnitude:

$$g_{source}(M) = m_0 + m_1(M - 4.7) + m_2(M - 4.7)^2 \quad M \leq 4.7 \quad (ES.2a)$$

$$g_{source}(M) = m_0 + m_3(M - 4.7) \quad 4.7 < M \leq 5.45 \quad (ES.2b)$$

$$g_{source}(M) = m_0 + m_3(5.45 - 4.7) + m_4(M - 5.45) + m_5(M - 5.45)^2 \quad M > 5.45 \quad (ES.2c)$$

Similarly, the path terms are also segmented into ranges of rupture distance:

$$g_{path}(R, M) = (r_0 + r_1 M) \ln\left(\frac{R}{3}\right) \quad R < 7 \text{ km} \quad (\text{ES.3a})$$

$$g_{path}(R, M) = (r_0 + r_1 M) \ln\left(\frac{7}{3}\right) + (r_2 + r_3 M) \ln\left(\frac{R}{7}\right) \quad 7 \leq R < 12 \text{ km} \quad (\text{ES.3b})$$

$$g_{path}(R, M) = (r_0 + r_1 M) \ln\left(\frac{7}{3}\right) + (r_2 + r_3 M) \ln\left(\frac{12}{7}\right) + (r_4 + r_5 M) \ln\left(\frac{R}{12}\right) \quad R \geq 12 \text{ km} \quad (\text{ES.3c})$$

There are four versions of the median equations for Y at the NS_B horizon, as summarised in Table ES.1; these models correspond to different values of the stress parameter, $\Delta\sigma$. There are two central models, both having the same value of the stress parameter in the magnitude range of the existing Groningen data; at larger magnitudes, the stress parameters rise to a lower (Ca) and higher (Cb) values.

Table ES.1. Weights on the four branches for median predictions at NS_B.

Model	Code	Weight
Upper	U	0.3
Central – upper	Cb	0.3
Central – lower	Ca	0.3
Lower	L	0.1

The coefficients of equations (ES.2) and (ES.3) for the four individual models are presented in the Excel file [V4_GMM_Medians_NS_B.xlsx](#). The basic logic-tree structure for the estimation of SA and PGV at the NS_B horizon is shown in Figure ES.2; the variability components are explained below.

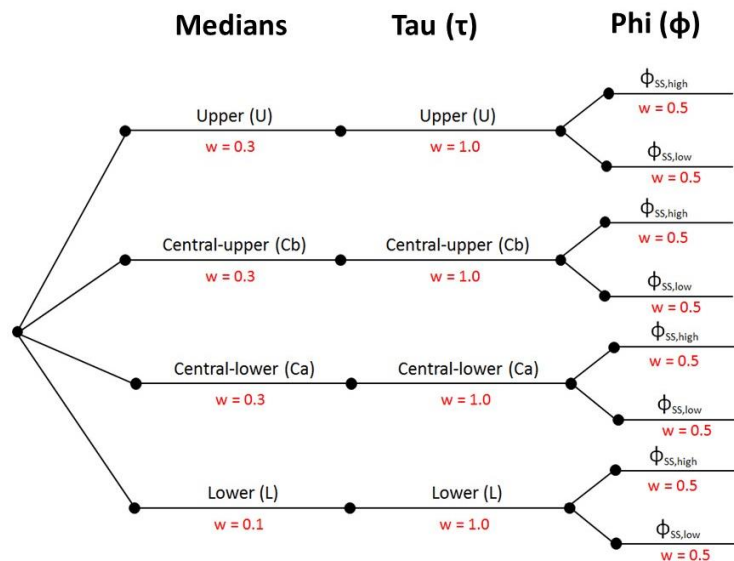


Figure ES.2. Logic-tree structure for model for motions at the NS_B horizon

Sigma Model for NS_B Rock Horizon GMPEs

The sigma model representing the aleatory variability in the values of $\ln(Y)$ from Eq.(ES.1) includes a between-earthquake component, τ , and a within-earthquake component, ϕ_{SS} . If Y_μ is the median value obtained from Eqs.(1)-(3), then two different quantities may be predicted by sampling from the components of variability: Y_{GM} , the geometric mean component (to be used for hazard mapping), and Y_{arb} , the arbitrary component (to be used in risk calculations):

$$\ln(Y_{GM}) = \ln(Y_\mu) + \varepsilon_E \tau + \varepsilon_S \phi_{SS} \quad (\text{ES.4a})$$

$$\ln(Y_{arb}) = \ln(Y_\mu) + \varepsilon_E \tau + \varepsilon_S \phi_{SS} + \varepsilon_C \sigma_{C2C} \quad (\text{ES.4b})$$

The ε values represent the number of standard deviations from the each of the standard normal distributions; σ_{C2C} is the component-to-component variability.

A unique value of between-earthquake variability is associated with each median model and there are two equally-weighted branches for the within-event variability (Figure ES.2). The sigma components are presented in the Excel file **V4_GMM_Sigmas_NS_B.xlsx**.

Field Zonation

The study area is divided into **160** zones having a common set of AFs for both $Sa(T)$ and PGV (Figure ES.3). The zones are defined by a numerical code. The Excel file **V4_GMM_Zones.xlsx** lists 140,862 voxel squares of 100 x 100 m—each identified by the RD coordinates of their centre—and the zone to which each voxel is identified.

Median Non-Linear Soil Amplification Factors

For each of the 160 zones and each ground-motion parameter (spectral acceleration at 23 periods and PGV), the amplification factors, AF , are defined as follows:

$$\ln[AF(Sa)] = f_1^* + f_2 \ln\left(\frac{Sa_{NS_B,g} + f_3}{f_3}\right) \quad (\text{ES.5a})$$

$$\ln[AF(PGV)] = f_1^* + f_2 \ln\left(\frac{PGV_{NS_B} + f_3}{f_3}\right) \quad (\text{ES.5b})$$

In Eq.(ES.5a), $Sa_{NS_B,g}$ is the spectral acceleration at the NS_B horizon, expressed in units of g (981 cm/s²); in Eq.(ES.5b), PGV_{NS_B} is the PGV value at the same reference rock horizon, in units of cm/s.

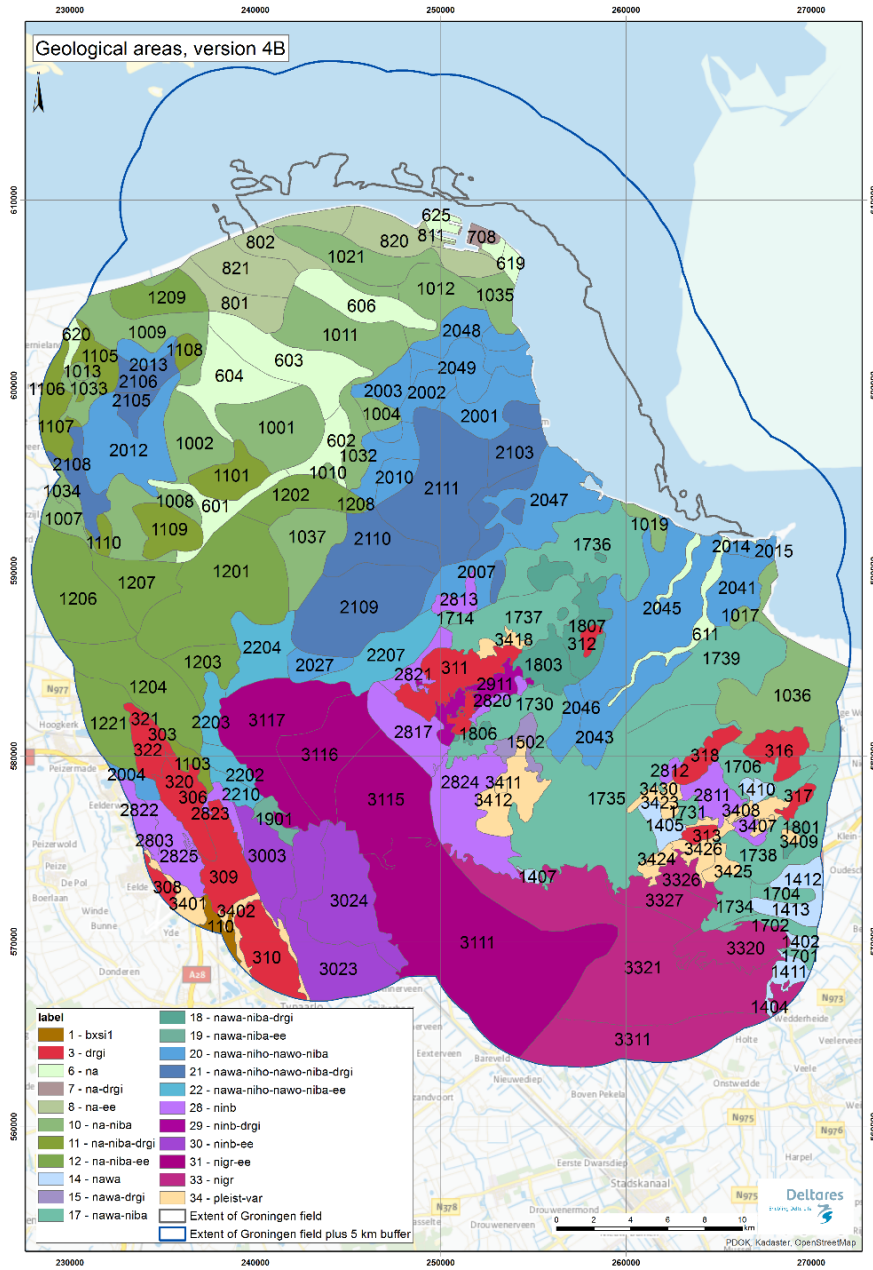


Figure ES.3. V4 zonation of the Groningen field for site amplification factors

The first term on the right-hand side of Eq.(ES.5), f_1^* , is the natural logarithm of the linear part of the amplification factors. The term is magnitude- and distance-dependent:

$$f_1^* = \ln[e^{f_1} + a_1(R^* - R_{anch}) + b_0(M^* - M_{anch})] \quad (\text{ES.6})$$

where R_{anch} is equal to 5 km, M_{anch} is equal to 4.8 and:

$$M^* = \min(M, M_{max}) \quad (\text{ES.7a})$$

$$R^* = \min(R, R_{max}) \quad (\text{ES.7b})$$

M_{\max} is equal to 5.5 for spectral acceleration, $Sa(T)$, and to 3.8 for PGV.

R_{\max} is defined as follows:

$$R_{\max} = 5 \quad \text{for } M \leq 3.8 \quad (\text{ES.8a})$$

$$R_{\max} = 5 + 10 \left(\frac{M - 3.8}{5 - 3.8} \right) \quad \text{for } 3.8 < M < 5.0 \quad (\text{ES.8b})$$

$$R_{\max} = 15 \quad \text{for } M \geq 5.0 \quad (\text{ES.8c})$$

The parameters f_1 , f_2 , and f_3 , are defined for each response period (plus PGV) and for each zone, and are listed in the Excel file **V4_GMM_AFs.xlsx**; in this table, a period of -10 is used to denote PGV. The same table indicates values of AF_{\min} and AF_{\max} , which are imposed lower and upper limits on the median value of AF. The coefficients a_1 and b_0 are zone-independent and are listed in the second sheet of the same Excel file.

Site-to-Site Variability Model

The variability in the site amplification factors within a zone is given by the standard deviation ϕ_{S2S} , which is defined as a tri-linear function as defined in the following equations (and illustrated in Figure ES.4):

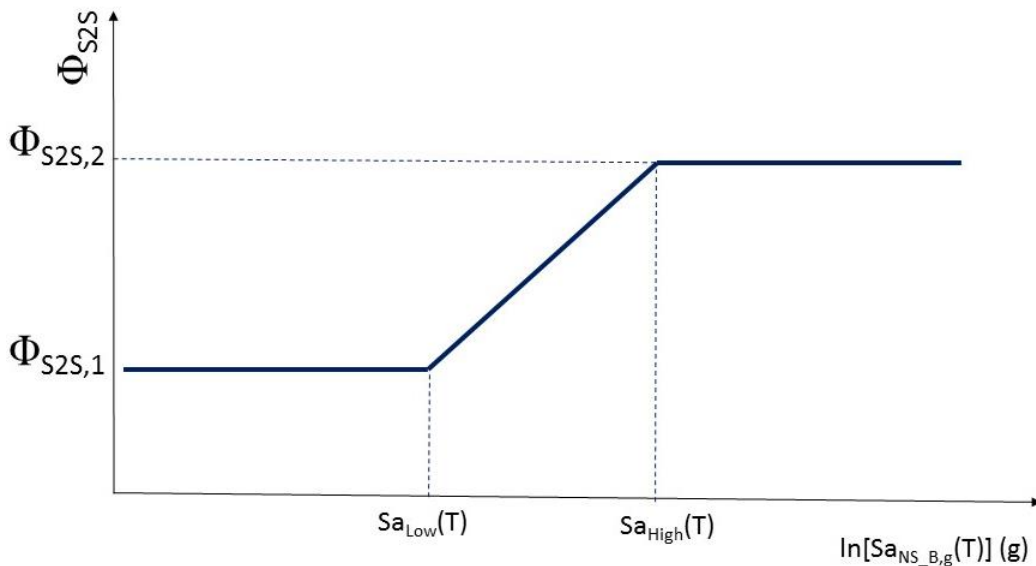


Figure ES.4. Schematic illustration of the site-to-site variability model. The values on the x-axis are the spectral acceleration at the NS_B, expressed in units of g , or the PGV value in cm/s . In either case, the value is obtained by application of Eqs.(ES.1) to (ES.4)

$$\phi_{S2S} = \phi_{S2S,1} \quad Sa_{NS_B,g} < Sa_{Low} \quad (ES.9a)$$

$$\phi_{S2S} = \phi_{S2S,1} + (\phi_{S2S,2} - \phi_{S2S,1}) \left[\frac{\ln(Sa_{NS_B,g}) - \ln(Sa_{low})}{\ln(Sa_{high}) - \ln(Sa_{low})} \right] \quad Sa_{Low} \leq Sa_{NS_B,g} \leq Sa_{High} \quad (ES.9b)$$

$$\phi_{S2S} = \phi_{S2S,2} \quad Sa_{NS_B,g} > Sa_{High} \quad (ES.9c)$$

The four parameters defining the site-to-site variability model for each zone and ground-motion parameter are listed in the Excel file **V4_GMM_AFs.xlsx**.

Period-to-Period Correlation of Residuals of Sa(T)

For the risk calculations, values of Sa(T) calculated at a given location for different periods, T, must account for the period-to-period correlations of the residuals. The correlation coefficients, to be applied to all components of variability, for Sa(T) at all 23 periods are provided in the Excel file **V4_GMM_T2T_correlations.xlsx**.

Duration Model

The model for the prediction of durations has four branches that should each be used in conjunction with the corresponding median branch on the predictions for Sa(T) and PGV. The median predictions of the duration, D_{S5-75} (significant duration based on the accumulation from 5% to 75% of the total Arias intensity), is comprised of a source component and a path component to obtain the NS_B motions, plus a site component that transforms the rock motions to the ground surface:

$$\ln(D_{S5-75}) = f_{source}(M) + f_{path}(R, M) + f_{site}(V_{S30}) \quad (ES.10)$$

The source function is defined as:

$$f_{source} = m_6 + m_7(\max[M, 3.5] - 5.45) \quad M \leq 5.45 \quad (ES.11a)$$

$$f_{source} = m_6 + m_8(M - 5.45) + m_9(M - 5.45)^2 \quad M > 5.45 \quad (ES.11b)$$

The path function is dependent on both distance and magnitude:

$$f_{path} = (r_6 + r_7 M') \left[\ln\left(\frac{R}{3}\right) \right]^{r_8} \quad R \leq 12 \quad (ES.12a)$$

$$f_{path} = (r_6 + r_7 M') \left[\ln\left(\frac{12}{3}\right) \right]^{r_8} + (r_9 + r_{10} M') \ln\left(\frac{R}{12}\right) \quad R > 12 \quad (\text{ES.12b})$$

where, $M' = \min[\max(M, 3.5), 6.0]$ (ES.12c)

The site term is very simple:

$$f_{site}(V_{S30}) = -0.2246 \ln\left(\frac{\min(V_{S30}, 600)}{600}\right) \quad (\text{ES.13})$$

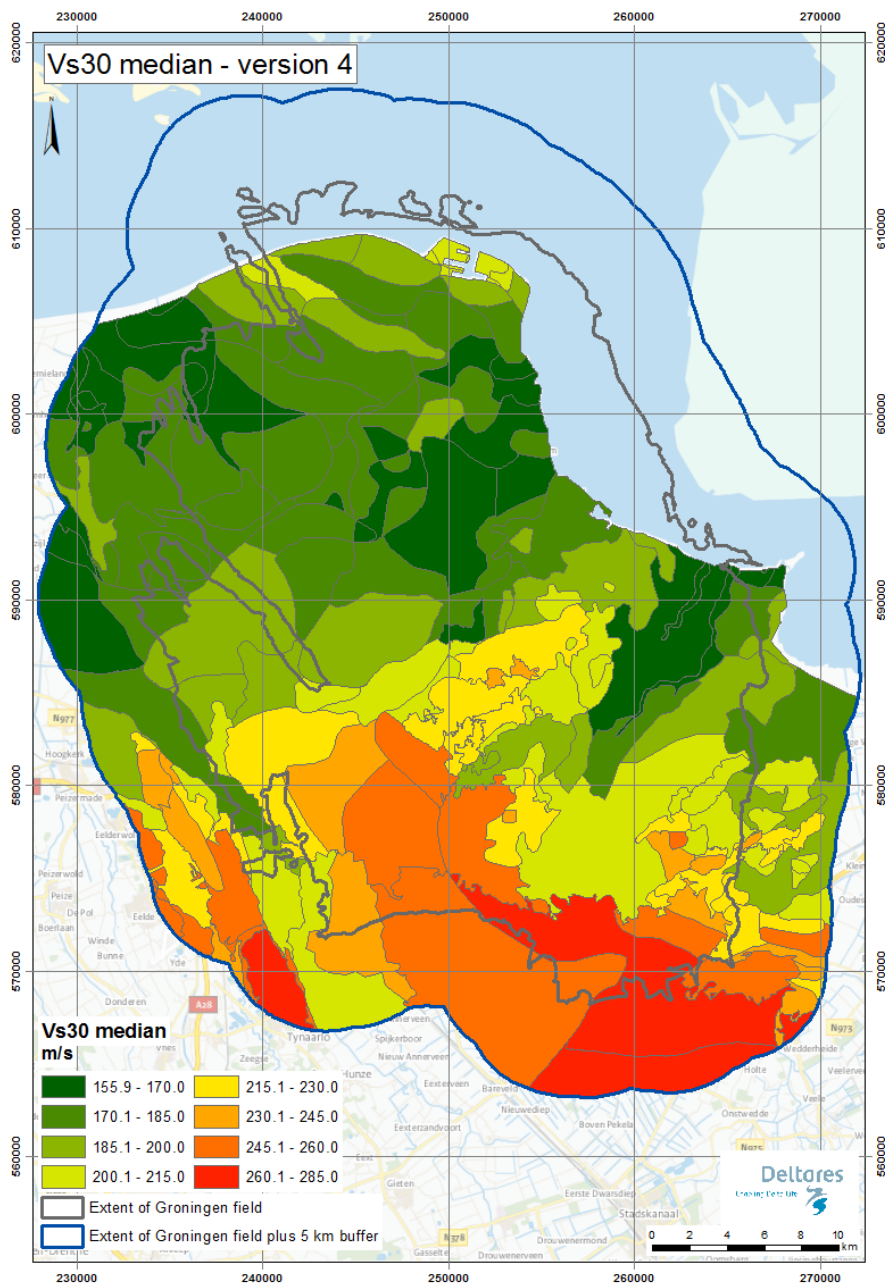


Figure ES.5. Median V_{S30} values of each zone

The duration model requires V_{S30} as an input parameter. The median V_{S30} value for each of the 160 zones is listed in the Excel file **V4_GMM_Zones.xlsx**. A map showing these median V_{S30} values is presented in Figure ES.5.

The coefficients of Eqs.(ES.11) and (ES.12) are all listed, for all four branches, in the Excel file **V4_GMM_Durations.xlsx**. The total variability in the duration predictions is given by the sigma values in Table ES.2; this variability is sampled conditioned on the residual of the amplitude-based parameter, using the correlation coefficients in Table ES.3. The four duration branches are to be implemented in combination individually with the corresponding median branch for spectral accelerations and PGV.

Table ES.2. Total sigma values for $\ln(D_{S5-75})$

Model	Lower	Central-lower	Central-upper	Upper
$\sigma[\ln(D_{S5-75})]$	0.637	0.636	0.631	0.637

Table ES.3. Correlation coefficients for total residuals of duration and $S_a(T)$ or PGV

T [s]	0.01	0.025	0.05	0.075	0.1	0.125	0.15	0.175	0.2	0.25	0.3	0.4
ρ	-0.45	-0.45	-0.45	-0.45	-0.39	-0.39	-0.39	-0.39	-0.39	-0.39	-0.39	-0.33
T [s]	0.5	0.6	0.7	0.85	1	1.5	2	2.5	3	4	5	PGV
ρ	-0.28	-0.24	-0.21	-0.17	-0.13	-0.05	-0.01	0.02	0.05	0.09	0.12	-0.26

Summary List of Electronic Appendices

As noted in the preceding text, the numerical parameter values are summarised in a set of six Excel files (with a total of 14 sheets) distributed together with the document. For ease of reference, the full list of these Excel files and the contents on each sheet is given here:

1. **V4_GMM_Medians_NS_B.xlsx**
 - a. Coefficients for lower median (L) model
 - b. Coefficients for central-lower (Ca) model
 - c. Coefficients for central-upper (Cb) model
 - d. Coefficients for upper (U) model
2. **V4_GMM_Sigmas_NS_B.xlsx**
 - a. Tau (between-event sigma) values for four models
 - b. PhiSS (within-event sigma) values for two branches
 - c. Component-to-component variability for spectral accelerations
3. **V4_GMM_Zones.xlsx**
 - a. Zone designation for each 100 m x 100 m voxel (140,862 voxels)
 - b. Median V_{S30} value for each zone (160 values)
4. **V4_GMM_AFs.xlsx**
 - a. Zone-dependent parameters
 - b. Zone-independent parameters
5. **V4_GMM_T2T_correlations.xlsx**
 - a. Period-to-period residual correlations for spectral accelerations
6. **V4_GMM_Durations.xlsx**
 - a. Median coefficients and sigmas for four models
 - b. Correlation coefficients for residuals of duration and S_a/PGV

All of the Excel files are provided in a single zipped file: **V4 GMM Coefficients.zip**.

A second zipped file—**V4 GMM Coefficients CSV.zip**—contains the same information but as CSV files, with filenames in the following format: **gmpe_description_date_V4.csv**. In these files, the model branches are numbered from the lower branches upwards.

Acknowledgements

First and foremost, our thanks to Jan van Elk who, with assistance from Dirk Doornhof, has provided clear leadership, helpful guidance and continuous support for the work presented herein. Jan provided the conditions that enabled this study to be carried out in a timely fashion by a multi-disciplinary team distributed over several locations. Assistance provided by Jeroen Uilenreef at NAM has also been very useful in several situations.

We are also indebted to Helen Crowley, who is leading the development of the fragility functions for the Groningen risk study, for her very helpful inputs and clear communication regarding the required ground motion and hazard inputs for the fragility derivation and the risk calculations. Similarly, we have benefited from feedback, questions and checks from Stephen Bourne and Steve Oates, who implement the ground-motion and fragility models into their hazard and risk calculation engines. Discussions with Helen, Stephen and Steve, and also with Rui Pinho (the fifth member of the core Hazard & Risk Assessment Team, together with the lead author of this report) from the very beginning of the project have always been constructive, stimulating and informative, and these exchanges of ideas have added great value to the work. The plots produced by Stephen at each phase of model implementation have always been very informative and the identification of inconsistencies and incompleteness in the documentation of the models, particularly by Steve, has been of great value as well. Barbara Polidoro provided valuable assistance with the database development and the derivation of the duration GMPEs during the V2 phase.

We also wish to express thanks to Pourya Omid and Tomas Storck of ALTEN, who are now developing the hazard and risk engine and performing cross-validation checks. We have enjoyed interactions with Pourya and Tomas, and we are also grateful for the greater flexibility offered by the considerably faster calculation times that they have achieved.

A very sincere expression of gratitude is due to Tom Piesold of Shell who, with the support of Steve Oates, processes for us recordings from the new borehole instruments operated by KNMI, making available a very valuable part of the V3/V4 database at a critical moment in the model development. Jodri Domingo Ballesta of KNMI was also very helpful in regard to access to these recordings and identification of the instrument characteristics, and his help is also noted with gratitude. We also acknowledge helpful contributions from Jelena Tomic.

A note of gratitude is due to Dr Emil Seyhan for providing the NGA-West2 data used to explore the magnitude- and distance-dependence of the component-to-component variability of horizontal ground motions.

In the development of the GMM, a significant development has been the incorporation of a field-wide model for non-linear site response and many individuals have contributed significantly to this work. Specific mention is due to members of the team at Deltares: Marco de Kleine for descriptions of the surface geology at the recording stations and for leading the work to conduct *in situ* V_s measurements at the recording stations; Ger de Lange and

Renée de Bruijn for information regarding the field geology and advice on appropriate geotechnical properties for the Groningen soils; Pim Witlox, Bruno Zuada Coelho, Jonathan Nuttal and Tommer Vermaas for programming STRATA and for running enormous numbers of site response analyses; and Veronique Marges for generating maps and for numerous GIS operations. The Deltares team members also express thanks to Mandy Korff for her role as the liaison with NAM. In terms of the *in situ* V_s measurements at the KNMI accelerograph stations, the support of Eddie Siemerink from NAM is gratefully acknowledged, as is the assistance of all those who worked with Marco de Kleine to perform the field measurements. Antonio DiMatteo from Shell was very helpful in advising on the design of the MASW arrays and he also worked extensively, together with Rik Noorlandt from Deltares, on the interpretation of the MASW measurements.

A great deal of assistance with the site response modelling and analyses was also provided by Ashly Cabas of North Carolina State University, and Julia Baaklini, Bernardo Castellanos, and Mahdi Bahrampouri of Virginia Tech. We also gratefully acknowledge the helpful responses from Albert Kottke to various queries regarding STRATA and the helpful discussions with Ellen Rathje at an early stage of the model development. The development of the site response models for the Groningen field also benefited from several discussions with Russell Green at Virginia Tech.

Ewoud van Dedem also played a key role in building the sub-surface velocity model for the field together with Remco Romijn from NAM whose contributions on the deeper velocity model were of critical importance. Remco also played a central role in the selection of the base of the Upper North Sea formation as the reference rock horizon for the site response calculations.

The GMM development work has also benefited from waveform modelling results provided by Ewoud van Dedem of Shell, supported by Sara Minisini and Alexander Droujinine and building on earlier work by Diego di Lazzari, also all at Shell. The ongoing interactions with Ewoud and Sara regarding the influence of the velocity structure of the field on the propagation of seismic waves from the reservoir to the ground surface continue to be valuable and to provide valuable insights. In this regard we have also benefited from discussions with colleagues at ExxonMobil who are performing their own waveform simulations for the Groningen field and the mutual exchange of results with the ExxonMobil Upstream Research team—including Erika Biediger, Will Burnett, Grant Gist, Paul Hector, Darren Pais, Joe Reilly, Pablo Sanz Rehermann, Ward Turner and Brian Zureck—as well as their earthquake engineering consultant Ron Hamburger, has proven helpful.

A very special note of gratitude is due to members of the independent review panel established for the development of the Groningen GMM and site response model. Constructive and useful feedback on the V1 model and the proposed approach for the development of the V2 models was provided by Hilmar Bungum, John Douglas, Jonathan Stewart and Ivan Wong. We are also grateful to Trevor Allen and Bob Darragh for very helpful feedback on the V1 model that they provided in their capacity as peer reviewers for the *Bulletin of the Seismological Society of America*. Our thanks also to Jonathan Stewart

for making available the draft version of his new duration prediction equation. John Douglas also sent detailed review comments on the first draft of this report that helped us to improve the presentation and correct several errors.

The full review panel (Gail Atkinson, Hilmar Bungum, Fabrice Cotton, John Douglas, Jonathan Stewart, Ivan Wong and Bob Youngs) participated in a workshop held in London on 27-28 October 2015 to discuss the V2 GMM and provide potential improvements. The open and constructive discussions at that meeting, and the many suggestions, insights and recommendations made by the panel members during that meeting have greatly enriched our ideas for improving the model.

We also need to acknowledge the very valuable input received at another review workshop, held in London in July 2016, jointly with URC researchers, to discuss the incorporation of finite fault simulations in the ground-motion model building. Participants in this meeting including Dr Luis Angel Dalguer, from SwissNuclear, Dr Bob Youngs of AMEC Foster Wheeler, and Dr Norm Abrahamson of the University of California at Berkeley. Dr Christine Goulet from the Southern California Earthquake Center (SCEC) also provided very valuable contributions, which were presented by Drs Abrahamson and Youngs when it became impossible for her attend in person. The insights, feedback and suggestions provided at the workshop were extremely useful in relation to key decisions taken for the V4 model development.

Finally, we need to acknowledge the international review panel that was convened once again in April and May 2017, coordinated by Professor Jonathan Stewart and comprising Dr Norm Abrahamson, Professor Gail Atkinson, Dr Hilmar Bungum, Professor Fabrice Cotton, Dr John Douglas, Ivan Wong and Dr Bob Youngs, to review in detail an earlier version of this report on the V4 GMM. Their valuable feedback, provided in a timely and extremely well organised manner, led to a number of improvements in this report and provided valuable ideas to be considered in the ongoing development and refinement of the ground-motion model for the Groningen field. Many of the ideas presented by the review panel are recorded in Chapter 13, which outlines potential future modifications and refinements to the model.

1. INTRODUCTION

Gas production in the Groningen field in the northern Netherlands is inducing earthquakes, the largest of which to date was the magnitude M_L 3.6 (**M** 3.4) Huizinge event of August 2012. In response to the induced seismicity, NAM is developing a comprehensive seismic hazard and risk model for the region—which comprises the entire gas field plus a 5 km buffer zone onshore—in order to ascertain the threat to local inhabitants and to design, where necessary, appropriate remedial measures to reduce the risk to acceptable levels.

1.1. Purpose and applications of the GMM

The primary objective of the NAM study is currently the development of a risk model that characterises the threat from induced earthquakes to the exposed population in terms of the probabilities of earthquake-induced damage to buildings leading to injury or death. This requires comprehensive modelling of the sequence of steps from production-induced compaction of the gas reservoir through to estimated damage levels in the exposed buildings and the consequent effects on their inhabitants. In broad terms, the risk model, spanning the entire process from production scenarios to casualty estimates, may be viewed as illustrated in Figure 1.1. The first part of the model predicts possible seismicity patterns in terms of the expected numbers and locations of earthquakes of different magnitudes in a given production period. The impact of these potential earthquakes on people is estimated via a model that combines the exposure model (in effect, a database of the building stock), fragility functions for each building type that define the probability of reaching or exceeding a defined damage state under different levels of shaking, and casualty functions that specify the probability of injury to inhabitants within a building experiencing that damage state. The seismicity model is linked to the fragility-casualty models via a ground-motion model (GMM), which predicts distributions of specified ground-motion parameters as a function of parameters such as earthquake magnitude, the distance from the earthquake source to the site, and the dynamic characteristics of the site itself. The GMM links the seismicity and fragility models in the calculation of risk by providing estimates at the location of each exposure element as a result of each earthquake simulated by the seismicity model.

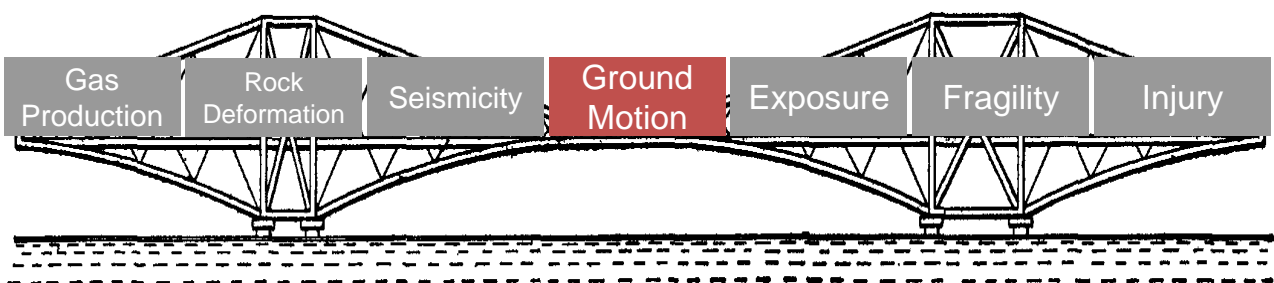


Figure 1.1. Schematic illustration of the full risk calculation process from gas production causing compaction of the field to building damage leading to casualties (*image courtesy of Jan van Elk*)

As the link between the two models, the GMM must be consistent and compatible with the parameterisation of the seismicity model, which is discussed in Section 2.1. Similarly, the GMM needs to provide outputs that are consistent with the definitions of the fragility functions, as discussed below in Section 1.3.

The primary purpose of the GMM is therefore to serve as the linking element between the seismicity and fragility models in the calculation of risk in the Groningen field. However, the GMM will also be used in combination with the seismicity model to generate estimates of the seismic hazard in terms of ground-motion parameters with a specified annual probability of exceedance (for a given production period). Such hazard estimates can be displayed in the form of contour maps for a given ground-motion parameter—such as peak ground acceleration (PGA)—or as acceleration response spectra at specified locations. Such representations of the ground shaking hazard may be useful for the purpose of calibration of seismic design codes such as the draft NPR 9998 (NEN, 2015) which has been produced to guide earthquake-resistant design for structures in the Groningen region. In general, representations of the seismic hazard may be useful for defining seismic actions to be considered in the design of new constructions or the retrofit of existing buildings, although it is more logical to base these directly on risk calculations (*e.g.*, Bommer *et al.*, 2005; Crowley *et al.*, 2012). Such considerations are implicit in the derivation of the seismic design loads and performance requirements in the NPR 9998 document, but in the long-run it is expected that the seismic risk model will allow iterative modelling to determine directly appropriate strengthening levels for existing buildings. In summary, the hazard outputs are viewed as a beneficial by-product of the seismic risk model, but the primary focus—which therefore dictates the requirements of the GMPEs—is the calculation of risk.

1.2. Overview of the Groningen GMM development process

The GMMs presented in this report are developed for the V4 seismic hazard and risk model. The development of seismic hazard models for the Groningen field began following the 2012 Huizinge earthquake and a preliminary model was produced for the Winningsplan submitted in late 2013 (Bourne *et al.*, 2014; Bourne *et al.*, 2015). One of the outcomes of that application for a continued gas production license was the development of a comprehensive probabilistic risk assessment as part of the Winningsplan due for submission in 2016. The work on extending the initial seismic hazard model to a full probabilistic risk model began in April 2014 with snapshots of the model presented for review and evaluation at six-monthly intervals. The first complete risk model—dubbed Version 0, or V0—was presented in October 2014, and this was superseded in April 2015 by the V1 model. This was followed by a new update for the V2 seismic risk model that was issued in October 2015 (Bommer *et al.*, 2015d). The current work is focused on the V3 seismic risk model, which was presented on 1st June 2016; originally, the V3 model was expected to be the basis for the 2016 Winningsplan but movement of the deadline for the application for the gas production plan to 1st April 2016 meant that the V2 model became the basis of the Winningsplan. The changes and improvements in the models from V0 to V1 were substantial and even greater modifications were implemented in the V2 model. Refinements to the V2 model were made between November 2015 and March 2016, in the light of feedback and sensitivity analyses, leading

to the V3 model, which was not made public but rather treated as an internal development phase. The V4 model presented herein was produced in the period from April 2016 to January 2017.

V0 GMM

For the 2013 Winningsplan, a GMM was developed for the prediction of PGA and peak ground velocity (PGV) as a result of induced earthquakes in the Groningen field. The equations were modified versions of the GMPEs (ground-motion prediction equations) derived using strong-motion data from Europe, the Mediterranean and the Middle East by Akkar *et al.* (2014a), hereafter ASB14. The equations using hypocentral distance, R_{hyp} , were selected, and applied with an assumed field-wide time-averaged shear-wave velocity in the top 30 metres, V_{S30} , of 200 m/s and the assumption of normal faulting. The coefficients of the equations were modified below a certain magnitude—**M4.2** for PGA, **M3.8** for PGV—to fit the peak motions from 40 accelerograms obtained from 8 earthquakes by the KNMI network. The aleatory variability for the small-magnitude extension, represented by the standard deviation (sigma) of the residuals, was assumed to be the same as that associated with the original equations. This preliminary GMM is described as part of the 2013 hazard model in Bourne *et al.* (2015). For the Version 0 hazard and risk model, an additional 14 records were available from the **M3.0** Leermens earthquake of February 2014. A very simple residual analysis suggested that the additional data did not warrant a modification of the 2013 GMM, for which reason it was decided to retain those PGA and PGV equations for the Version 0 hazard and risk models (Bommer & Dost, 2014). The residual analyses did show, however, that the models did not fit the data well at short epicentral distances, which was concluded to be a consequence of the functional form of the ASB14 equation and specifically the use of a fixed value for the near-source saturation term at all magnitudes. The addition of the Leermens records expanded the available dataset but not sufficiently to allow direct calculation of the aleatory variability.

The V0 GMM was calibrated to local recordings of ground motion in the small-magnitude range and followed patterns inferred from recordings of tectonic earthquakes in the larger magnitude range, without any confirmation of the applicability of the latter to Groningen. Moreover, the equations were only developed for PGA and PGV, and were associated with the large sigma values obtained from regression analysis using a heterogeneous database from Europe and the Middle East. One potential merit of the V0 GMM was the inclusion of site amplification terms based on V_{S30} and the inclusion of non-linear soil response in these terms. However, the equations were applied with a constant value of V_{S30} (200 m/s) over the entire field, which therefore ignored any spatial variation in the ground conditions; although subsequent work has suggested that 200 m/s was a good estimate of the average value for the study area although the actual values vary considerably (Kruiver *et al.*, 2015). In addition to these shortcomings, the non-linear site amplification functions were empirically derived from ground-motion recordings in Japan and Europe (Sandikkaya *et al.*, 2013) without any calibration to Groningen conditions. Another important feature of the V0 GMM was that it did not represent the range of epistemic uncertainty in the ground-motion predictions, which will inevitably be large for magnitudes above the largest recorded event of M_L 3.6 (**M 3.4**). Rather than providing best estimate predictions accompanied by alternative models to capture the

range of uncertainty, single equations were produced for PGA and PGV. Consequently, these tended towards being conservative estimates—both in terms of median predictions and sigma values—by adopting models derived from recordings of tectonic earthquakes.

V1 GMM

The V1 GMM addressed several of the shortcomings in the V0 equations, while consciously leaving one specific feature (the site amplification functions) to be improved in the V2 development stage when the required field information would become available. The most fundamental difference with regards to the V0 model was that rather than extrapolate a GMPE derived from tectonic earthquakes to match local recordings in the small-magnitude range, a model calibrated to the Groningen database—which was expanded relative to that used in adjusting the V0 equations—was extrapolated to larger magnitudes. The Groningen database was used to constrain both the median predictions and estimates of the sigma model, and three alternative models were generated to capture the epistemic uncertainty, which grows with increasing earthquake magnitude and hence greater extrapolation from the data (Figure 1.2). The V1 GMM was produced for PGA and for response spectral ordinates at four oscillator periods (0.2, 0.5, 1.0 and 2.0 seconds) as required for the fragility functions. While a positive development, the limited number of response periods for which the full GMM was developed imposed two limitations on the development of the V1 fragility functions, the first being that all building typologies needed to be represented by one of the five selected periods (with PGA assumed equal to the spectral acceleration at 0.01 seconds; see Figure 1.3), which in some cases represented a poor approximation to the dynamic characteristics of the buildings. The second limitation, directly related to the first, was that response spectral shape became an important parameter, requiring formulation of the fragility functions to include magnitude as a surrogate for this feature of the ground motions. This in turn precluded the explicit modelling of the influence of duration on the structural response, even though it is expected to be an important factor in the damage experienced by unreinforced masonry buildings (e.g., Bommer *et al.*, 2004). The V1 GMM is documented in detail in Bommer *et al.* (2015a) and summarised in Bommer *et al.* (2016a).

The most important weakness of the V1 GMM relates to the modelling of site response. Rather than using an assumed value of a proxy such as V_{S30} and imported site amplification functions, a network-average site amplification term was derived from the recordings and then used in forward modelling to generate the predictive equations. One shortcoming of this approach is that it assumes that the sampling of the dynamic characteristics at the recording station locations is a reasonable approximation to the average amplification functions across the entire field. To some extent this is likely to be a conservative assumption since most of the records were obtained by instruments located in the north of the gas field where softer soils are encountered than in the south. However, the model was considered to be limited in so far as it did not reflect the spatial variation of ground conditions and their effect on the surface motions. The most serious deficiency in the model, however, is the failure to account for non-linear site response. Given the weak levels of motion recorded to date, it is likely that the inferred amplification function is a reasonable estimate of the average linear site response term across the recording network. However, when extrapolated to larger magnitudes, the soils would be expected to respond non-linearly to the higher amplitudes of

acceleration propagating upwards from the underlying rock, leading to reduced surface accelerations. Consequently, it can be assumed with confidence that the V1 GMM is potentially conservative when applied for larger magnitudes and short distances, especially the upper branch (Figure 1.2).

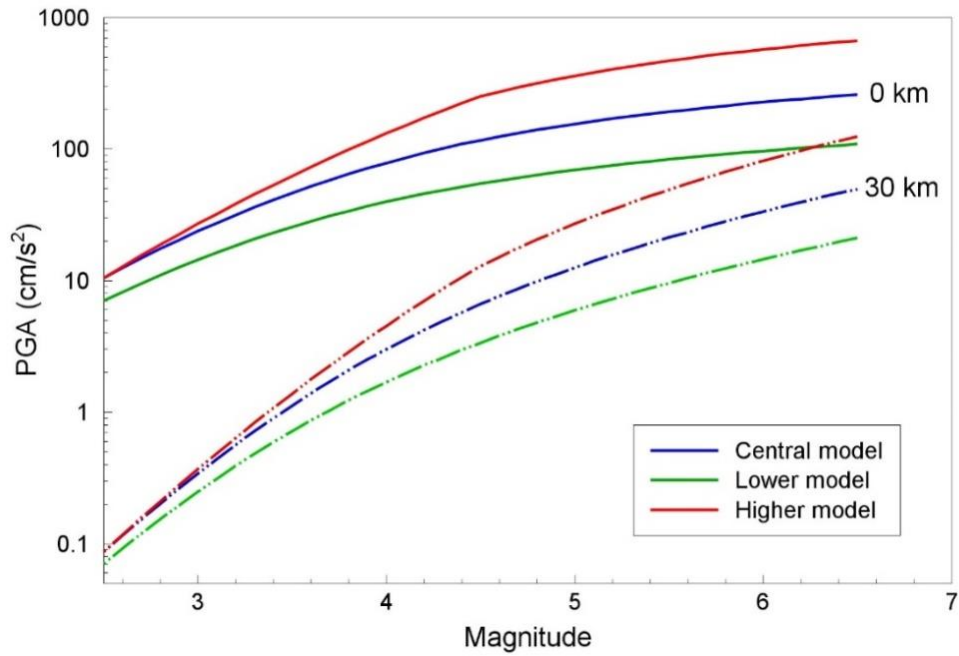


Figure 1.2. Median PGA predictions from V1 GMM as a function of magnitude at two distances

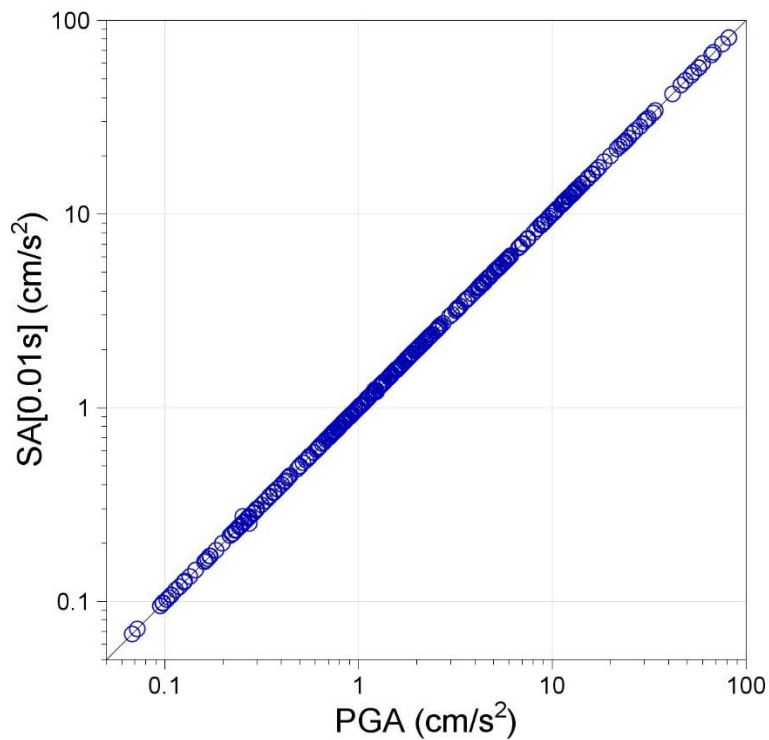


Figure 1.3. Correlation between PGA and Sa(0.01s) for all individual horizontal components in the Groningen ground motion database (see Section 3.2)

V2 GMM

The single most important feature of the V2 GMM development with respect to the V1 equations was the explicit inclusion of field-specific non-linear site amplification functions. Other improvements embodied in the V2 GMM include the generation of predictive equations for a much larger number of response periods. Table 1.1 summarises the developmental stages with regards to the GMM for horizontal amplitudes of the ground motion. As can be appreciated from Table 1.1, the V2 GMM really represented a major step forward in terms of developing a Groningen-specific model for ground-motion prediction from induced earthquakes (Bommer *et al.*, 2015d). The implementation of the model was fundamentally different from both the V0 and V1 models in so much that rather than directly predicting the ground motions at the surface, the hazard calculations now involved a two-step implementation: calculation of motions at a selected reference rock horizon, and then convolution of this rock hazard with the non-linear amplification factors. Within the Monte Carlo framework adopted for the Groningen seismic hazard and risk model, the convolution is performed directly, multiplying the rock motion by the corresponding non-linear amplification factor. One advantage of this implementation is that the non-linear site amplification factor is conditioned on the actual realisation of the rock motion rather than just the median spectral acceleration for the magnitude and distance defining each earthquake scenario.

Table 1.1. Key features of the four phases of Groningen GMM development; NU_B and NS_B refer to the base of the Upper North Sea and base of the North Sea formations, respectively

GMM Feature	V1	V2	V3	V4
Predicted parameters	Sa(T) for 5 periods	Sa(T) for 16 periods	Sa(T) for 23 periods	Sa(T) for 23 periods, PGV
Distance metric	R _{epi}	R _{epi}	R _{epi}	R _{rup}
Epistemic uncertainty	Three alternatives (coupled μ and σ)	Three alternatives (coupled μ and σ)	Three alternatives (coupled μ and σ)	Eight alternatives (four μ and two σ)
Target horizons	Surface	NU_B and surface	NS_B and surface	NS_B and surface
Site classification	Field-wide constant (<i>i.e.</i> , single zone); network average	Zonation based on amplification factors (167 zones)	Zonation based on amplification factors (161 zones)	Zonation based on amplification factors (160 zones)
Site amplification	Network average, linear extrapolation	Zone-specific, non-linear frequency-dependent AFs	Zone-specific, non-linear frequency-dependent AFs	Zone-specific, non-linear frequency-dependent AFs; M-R dependence at short periods
Period-to-period correlations	Used Akkar <i>et al.</i> (2014b)	Uses Akkar <i>et al.</i> (2014b)	Baker & Jayaram (2008)	Baker & Jayaram (2008)

V3 and V4 GMMs

The most significant change from the V2 to V3 GMM was to move the reference rock horizon from NU_B to NS_B (see Section 2.3), the latter representing a much clearer and more pronounced impedance contrast. In most other regards, the framework for the GMM was essentially the same. One other change was to add seven more target response periods, all which were at the lower end of the spectrum (from 0.025 to 0.25 seconds); the sole purpose

of these additional spectral ordinates was to facilitate the generation of more realistic vertical spectra when V/H ratios are applied to the horizontal spectra.

The V3 model was documented in considerable detail in the report by Bommer *et al.* (2016b) and also summarised in a journal paper (Bommer *et al.*, 2017). The V3 report was not widely distributed for the simple reason that it was viewed as a 'staging post' in the ongoing evolution of the Groningen ground-motion models. As can be appreciated from Table 1.1, the V4 GMM shares many aspects in common with the V3 model. One new feature is the inclusion of PGV as predictor variable, for reasons explained below in Section 1.3.

The most significant change from V3 to V4, however, is adoption of extended source ruptures to represent earthquake sources rather than points (hypocentres). While the latter may be appropriate for the small-magnitude earthquakes that have occurred in the field to date, it is not a realistic representation for larger events. Although it was demonstrated that the use of point source representations, in conjunction with GMMs using epicentral distance, is conservative in terms of risk calculations (Bommer *et al.*, 2015d), it is more consistent with the physics of earthquake generation to explicitly account for the extension of fault ruptures in the model rather than use approximations to these effects (*e.g.*, Yenier & Atkinson, 2014).

One other important development from V3 to V4 is the expansion of the GMM logic-tree from three to eight branches. The limitation of three branches in earlier models, in which the higher median model was coupled with the higher sigma model and so on, was simply a compromise to render the calculations more efficient. In the meantime, the hazard and risk engine has been made considerably faster and there is consequently less onus to simplify the model. The eight branches now included better capture the centre, the body and the range of the distribution of possible ground motions from future earthquakes in the Groningen field.

1.3. GMM requirements for fragility functions and risk calculations

Structural sensitivity analyses conducted for the early development of the V2 fragility functions explored which intensity measures (IMs) would be efficient predictors of the maximum displacement experienced by typical structures in the Groningen field, a response parameter that in turn can be related to damage. The spectral acceleration at the fundamental vibration period of the structure was found to be an efficient IM, in terms of being able to predict the maximum displacement of the structures with low dispersion. Additional analyses were conducted to establish whether this IM was also sufficient with respect to magnitude, distance and a measure of ground-motion duration; sufficiency would imply that including additional parameters would have no effect in terms of reducing the dispersion in the predictions. The spectral acceleration, $S_a(T)$, was found to be sufficient with respect to magnitude but not with respect to distance or duration, the latter being measured using the significant duration definition and the interval of 5-75% of the total Arias intensity, I_A , which is referred to hereafter as D_{S5-75} . Consequently, the fragility functions will be based on $S_a(T)$ with the possibility of slightly improved constraint by extending this to a vector prediction of $S_a(T)$ and D_{S5-75} .

For the primary IM of $S_a(T)$, there are two decisions to be made. The first regards the appropriate range of response periods to be covered by the equations and an appropriate sampling within this range, the second the component definition. Regarding the first issue, whereas the greatest flexibility for the development and application of the fragility functions would be provided by generating the GMPEs for $S_a(T)$ at a large number of response periods, there are issues of computational effort—with regards to the GMPE derivation and to the execution of the risk calculations—that make it advantageous to limit the numbers of response periods explicitly modelled. Figure 1.4 shows a histogram of periods of vibration for the Groningen building typologies in the current risk model. The total number of periods shown exceeds the number of building typologies (56 in the V3 model) because some have distinct periods in the two orthogonal directions—especially terraced houses—and there are also the periods used in local rocking mechanisms that apply to about 20 typologies. The final range of target oscillator periods needs to account for the fact that at some stage it may be desirable to estimate risk in terms of lower (pre-collapse) damage states, which would point to shorter response periods, and the fact that those implied in the final fragility functions might be slightly larger than these yield periods (to account for period elongation after damage).

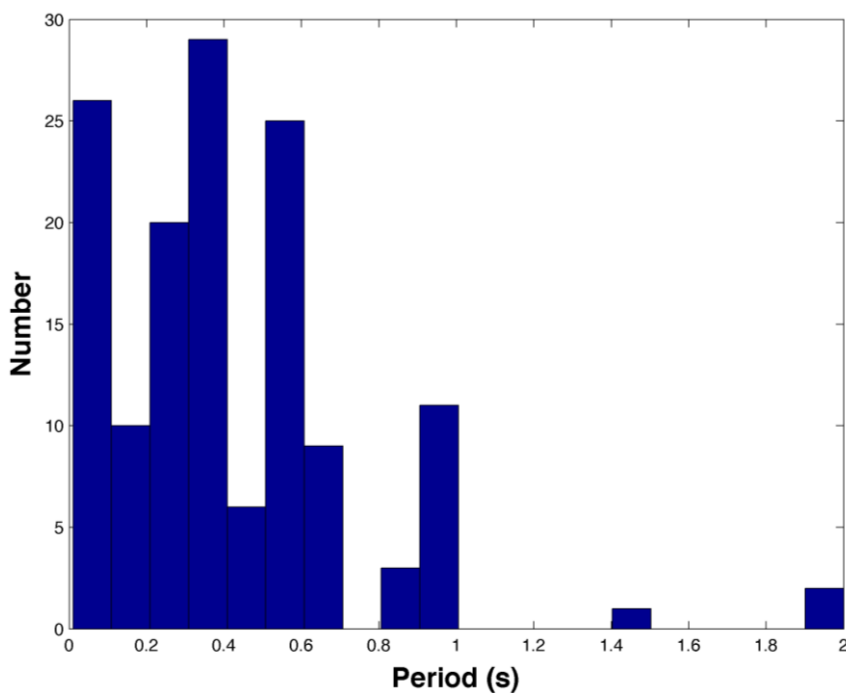


Figure 1.4. Histogram of main vibration periods for the building typologies defined for the Groningen exposure database (*image courtesy of Helen Crowley*)

The motivation for increasing the number of oscillator periods is primarily to provide greater flexibility for the derivation of the fragility functions but also to allow generation of complete response spectral shapes. For the latter, GMPEs often provide coefficients and sigmas at a large number of response periods—often sampled at regular intervals in log-space—to provide smooth spectral shapes; for example, Akkar *et al.* (2014a) provided equations at 62 oscillator periods between 0.01 and 4.0 seconds (in the electronic supplement; a subset of 18 of these were presented in the paper itself). The sampling of periods in log-space tends

to be particularly dense at shorter periods, which allows for clear definition of the spectral peak and the shape of the spectra at high oscillator frequencies. For the Groningen risk model, we do not necessarily require such dense sampling for two reasons: one is that short periods (< 0.15 s) are of little relevance to the structural response of buildings in the Groningen region, and the second is that the very soft soil conditions across most of the field lead to spectral shapes that peak at longer periods (> 0.2 s).

There are, however, other considerations when selecting target response periods for the models. In addition to the final surface predictions that will be used to link the hazard model to the fragility functions, there is the intermediate step of the reference rock motions, which correspond to a much stiffer horizon at which the spectral peak is likely to occur at much shorter periods (where the influence of the kappa parameter—which is effectively a high-frequency filter, as explained in Sections 4.1 and 5.2—is most pronounced). Moreover, if vertical spectra are required, these will be obtained by multiplication of the horizontal spectral ordinates by V/H spectral ratios, which tend to peak at very short periods. In order to obtain a well-defined vertical spectrum, therefore, it is necessary to define the short-period horizontal spectrum with high resolution. This last issue, in particular, motivated the addition of 7 extra response periods for the V3 model, all at periods of less than 0.3 seconds; these are retained in the V4 model. The list of target periods is presented in Table 1.2.

Table 1.2. Target response periods the V4 GMM

Period (s)	Frequency (Hz)	Period (s)	Frequency (Hz)
0.01	100.00	0.5	2.000
0.025	40.00	0.6	1.667
0.05	20.00	0.7	1.429
0.075	13.33	0.85	1.176
0.10	10.00	1.0	1.000
0.125	8.00	1.5	0.667
0.15	6.67	2.0	0.500
0.175	5.71	2.5	0.400
0.20	5.00	3.0	0.333
0.25	4.00	4.0	0.250
0.30	3.33	5.0	0.200
0.40	2.50		

The second key decision required with respect to the modelling of the horizontal response spectral acceleration is the component definition to be employed. For the V1 GMM, the definition used was simply the geometric mean of the two horizontal components, which is the most widely-used definition, although there are several subtle variations of this definition (Boore *et al.*, 2006; Boore, 2010). For derivation of the V3 fragility functions, however, there were advantages in adopting the arbitrary component of motion. This issue has been considered in detail by Dr Helen Crowley—who leads the fragility development work—and discussed with the GMM development team; in the following text we briefly summarise these considerations and the final decisions in this regard. The reader should note that at the time of producing the V4 GMM, the V3 fragility functions have not yet been replaced since that work is undergoing a longer development cycle.

The first point to note is that, provided consistent definitions are used for the hazard and fragility, the probabilistic risk assessment should be the same regardless of the definition of spectral acceleration, with an increased dispersion either being estimated on the side of the hazard (when the arbitrary component definition is used) or on the side of the fragility (when the geometric mean is used). The drawback of the latter is that more dynamic analyses are required to predict the dispersion with a given level of confidence, although this should not necessarily restrict the choice of spectral acceleration to the arbitrary component, given the simplicity of the structural models currently being used. The V3 fragility models for the building typologies in Groningen will be developed through non-linear dynamic analyses of equivalent single-degree-of-freedom (SDOF) systems. Given that a number of the typologies have very different stiffness and strength in their two orthogonal axes, SDOF systems for each direction will be calibrated, and fragility functions in each direction of the building will be developed.

In order to develop the V3 fragility functions in terms of the geometric mean spectral acceleration at a given period of vibration, it would be necessary to associate the nonlinear response of the SDOF (e.g., drift) obtained from a single component of the ground motion against the geometric mean spectral acceleration of the two components of ground motion. As noted above, this will result in higher dispersion in the response, given the spectral acceleration at the selected period of vibration (which is the selected IM), as the response will be plotted using the geometric mean response spectrum of the two components, rather than the IM from the response spectrum of the component used in the analysis. In this case, the risk engine would need to estimate the geometric mean significant duration and the geometric mean spectral acceleration for the period of vibration defined in each direction of the building using period-to-period correlation of the geometric mean residuals, and the probability of collapse would be defined by the direction with the highest probability of collapse.

Figure 1.5 shows an example of typical response spectra of two components of ground motion, and the geometric mean response spectrum. As can be seen in this figure, the spectra of the two horizontal components cross at various periods across the spectrum. The recordings from the Groningen field to date, however, show a strong polarization, as shown in Figure 1.6. In order to ensure that this polarization is accounted for when modelling the response of the SDOF systems, modifications to the records selected for the dynamic analyses would probably need to be made, to ensure that the component-to-component ratios are consistent with those found in the Groningen field. In order to develop the V3 fragility functions in terms of the arbitrary component of hazard, the nonlinear response of the SDOF (e.g., drift) obtained from a single component of the ground motion would be plotted against the spectral acceleration at the given period of vibration for that component. The risk engine would need to estimate the arbitrary component spectral acceleration for the period of vibration defined in each direction of the building, as well as the arbitrary component significant duration, and the probability of collapse (for the structure) would be defined by the direction with the highest probability of collapse. The period-to-period correlation of the residuals of the two horizontal components of ground motion would be needed to estimate the demand in each direction of the building (e.g., Baker & Cornell, 2006a).

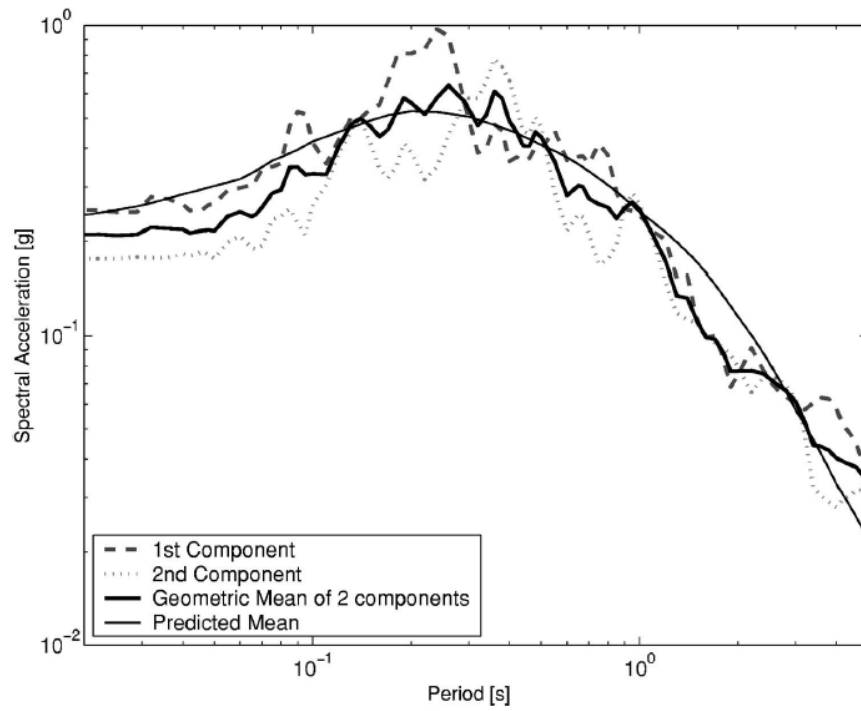


Figure 1.5. Response spectra for two horizontal components of ground motion (*dashed and dotted line*), the geometric mean of the response spectra (*bold line*) and the predicted mean from a GMPE (*thin line*) (Baker & Cornell, 2006a)

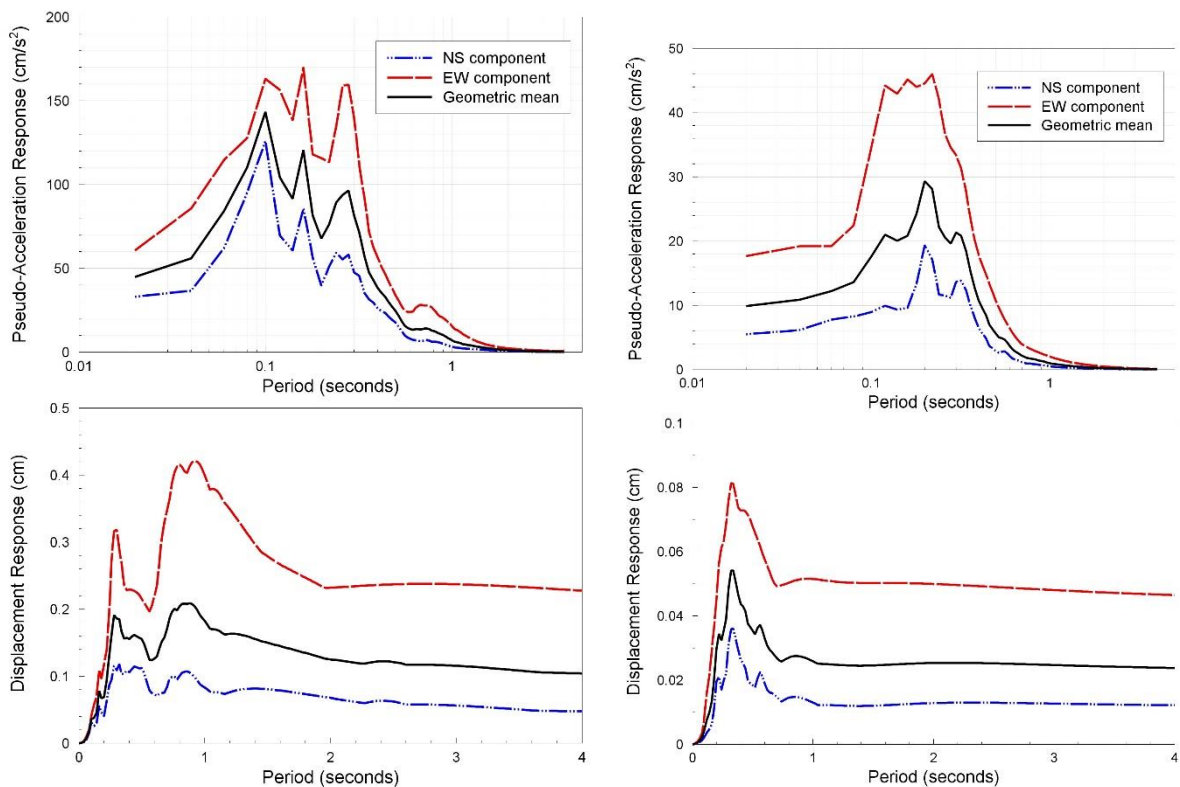


Figure 1.6. Example response spectra from the Groningen field, illustrating the strong polarisation in the horizontal components. *Upper*: pseudo-acceleration response spectra; *lower*: displacement response spectra

Defining the V4 hazard in terms of the geometric mean component would have the advantage that estimates of the hazard for the Groningen field would be directly comparable with previous models. However, the records used for the development of fragility functions may need modification to ensure that their component-to-component ratios are consistent with those found in the Groningen field. Furthermore, the physical meaning of the geometric mean significant duration is unclear. The use of an arbitrary component GMM for the V3 hazard assessment would appear to lead to higher levels of hazard as compared to previous models (V0 and V1), due to the increased aleatory variability in the GMM. Although comparison of the models would not be valid, as the component of spectral acceleration would have changed from V0/V1 to V2 and V3, such comparisons would undoubtedly be made nonetheless without attention to appropriate caveats. For this reason it would be prudent to continue to develop a GMM in terms of the geometric mean spectral acceleration, for the hazard assessment. All of these arguments continue to apply at the V4 development stage.

For the development of fragility functions, the use of the arbitrary component spectral acceleration has the advantage that fewer non-linear dynamic analyses are needed to predict the dispersion with a given level of confidence. Furthermore, the component-to-component ratios would not need to be explicitly considered when selecting the records.

Hence, for the V3 hazard and risk assessment it was decided that a GMM for geometric mean spectral acceleration would be developed for the hazard model, whilst GMMs for arbitrary component spectral acceleration, together with a model of the correlation of the residuals between two horizontal components in perpendicular directions, would be developed for the risk model. In essence, the only difference between the geometric mean and the arbitrary components is in the sigma values, with the median predictions expected to be identical. This still holds for the V4 model and therefore, in developing the sigma model, the component-to-component variability is also required.

Although it is not envisaged that the vertical components of motion will be explicitly included in the fragility functions or the risk calculations, it is believed that some of the structural typologies encountered in the Groningen field may be sensitive to vertical motions. For this reason, structural modelling may require definition of the vertical response spectrum and to this end a Groningen-specific model for the vertical-to-horizontal response spectral ratios is developed.

As noted previously, the fragility functions are now defined in terms of both spectral acceleration, $S_a(T)$, and the significant duration, D_{S5-75} , for some building typologies. This then requires the vector prediction of these two parameters. In essence, this means developing a model for the prediction of durations conditional on the predictions of $S_a(T)$, which is also addressed in this report.

Until recently, all of the work in developing seismic risk estimates for the Groningen field were focused almost exclusively on levels of structural damage sufficiently severe to present a threat to life and limb of the occupants. More recently, attention has begun to shift to lower levels of damage, which do not threaten structural stability or the safety of building inhabitants. The fragility team will consequently develop functions not only for damage states

D4 and D5 but also lower levels. These are most likely to also be defined in terms of $S_a(T)$, possibly in conjunction with duration in some case, for consistency with the higher damage states (Helen Crowley, *personal communication*, 2017). However, it has been decided to also include peak ground velocity, PGV, as an additional predicted parameter for the V4 model, since even if not used directly for the fragility functions it may still prove useful since most published guidelines on tolerable levels of ground vibration due to anthropogenic sources (such as blasting, pile driving and traffic) define thresholds of PGV that lead to unacceptable disturbance or damage, whether cosmetic or more serious (see, for example, Bommer *et al.*, 2006). For the seismic assessment of some lifelines, such as buried pipelines, PGV is often used in conjunction with wave propagation velocities to determine strains (e.g., Scandella & Paolucci, 2010). There are several other common application of PGV in earthquake engineering practice (Bommer & Alarcón, 2006) that make it a useful parameter.

1.4. Overview of the report

From the discussions in the previous sections it may be concluded that the basic requirement for the V4 hazard and risk model is a suite of equations and site amplification factors for the prediction of both the geometric mean and arbitrary component of 5%-damped response spectral acceleration at 23 oscillator periods (Table 1.2), the geometric mean component of PGV, and the significant duration of shaking. The GMM should be well calibrated to the seismological, geological and geotechnical conditions encountered in the Groningen field, and most specifically they should reflect the non-linear dynamic response of near-surface layers across the study area. An overview of how the basic models are developed is given in Chapter 2, which focuses in particular on the scheme for predicting motions at a reference rock horizon and then transferring these rock motions to the ground surface via non-linear site amplification factors. Chapter 2 also includes a brief discussion of the issue of spatial correlation of ground motions.

Chapter 3 then describes the characteristics of the Groningen ground-motion databases used in the derivation of the V4 GMM. Chapter 4 discusses the dynamic characterisation of the recording station sites and the development of linear site amplification factors that are used to translate the surface motions to the reference rock horizon. Chapter 5 describes the inversion of the motions at the rock horizon to estimate source and path parameters for Groningen, together with a field-wide amplification factor for the reference rock elevation. In Chapter 6, the parameters obtained from the inversions are applied in simulations to generate spectral accelerations at the rock horizon, to which functional forms are fitted in order to obtain parametric GMPEs for the median motions at this level. The residuals of the recorded motions deconvolved to the reference rock horizon are calculated to inform the development of the sigma model (Chapter 10).

Chapters 7 to 9 are focused on the development of the non-linear site amplification factors that are applied in conjunction with the rock GMPEs to obtain median ground-motion predictions at the surface. Chapter 7 describes the development of layer models for the profiles from the reference rock horizon to the ground surface across the entire field, and Chapter 8 describes the site response analyses performed using these profiles. Chapter 9

explains the aggregation of the calculated site amplification factors into zones for which a single representative site amplification function may be adopted.

Chapter 10 explains the development of the sigma model for the GMM at the ground surface, for both the geometric mean and arbitrary components of motion. Chapter 11 then summarises the current models and its practical application. The performance of the model with respect to the existing Groningen ground-motion database is also presented, and potential refinements discussed in the light of these analyses. Chapter 11 also discusses additional features required for various applications, including period-to-period correlation functions and vertical-to-horizontal response spectral ratios.

Chapter 12 describes the derivation of improved GMPE for the significant duration of ground shaking in the field. Through the identification of a correlation function between the residuals of duration and of spectral accelerations, a vector model is developed through which the duration conditioned on the spectral acceleration is predicted.

Chapter 13 closes the report with a discussion of the potential refinements and improvements to be applied to the V4 GMM, both in the short-term (*i.e.*, the next development stage up to V5, due in Q3 2017) and the longer term.

In addition to the 13 chapters presenting the derivation of the V4 GMM for response spectral accelerations, PGV and durations, there are several appendices, most of which contain plots related to different elements of the model development process. In order to avoid an excessively large report, detailed documentation on various aspects of the work is provided in supplementary reports that are referenced in this report. Additionally, there are a number of electronic supplements containing the coefficients of equations and coordinates of the field zonation required for the full implementation of the model. These electronic supplements are identified in the Executive Summary.

2. OVERVIEW of V4 GMM

This Chapter provides a general overview of the V4 GMM for response spectral accelerations and PGV, including the form of the equations and the procedure established for their derivation, details of which are provided in subsequent chapters. The chapter closes with a brief discussion of the choice not to model spatial correlations in the current phase of development of the hazard and risk models.

2.1. Predicted and explanatory variables

As discussed in Section 1.2, the V4 GMM predicts horizontal 5%-damped pseudo-spectral accelerations at 23 oscillator periods from 0.01 to 5.0 seconds and the horizontal component of peak ground velocity. For all of these parameters, the geometric mean of the two horizontal components of each record is adopted as the definition for both Sa(T) and PGV. However, the provision of the component-to-component variability also allows the arbitrary horizontal component to be estimated. The adopted definition of the ground-motion duration is the significant duration defined as the interval over which 5% to 75% of the total Arias intensity, DS_{5-75} is accumulated. The explanatory variables of the duration prediction model are discussed in Chapter 12.

The models for Sa(T) and PGV predict motions at the NS_B rock horizon through a GMPE and then convolve these rock motions with non-linear site amplification factors. The rock GMPEs are a function only of magnitude and distance. There was no motivation to include any other terms in the equations since none of the other parameters commonly used in modern GMPEs could be defined in a way that would be expected to refine the predictions. In terms of style-of-faulting, for example, it is known that ruptures in the Groningen field may be pure normal, strike-slip or an oblique combination of these mechanisms, but fault plane solutions are not available for most of the earthquakes in the database. Including a parameter such as depth-to-top-rupture, Z_{TOR} , would not improve the predictive power of the model since all earthquakes are assumed to occur within the gas reservoir at a depth of about 3 km (although it must be recognised that there is no clear model regarding the expected geometry and vertical extent of the fault ruptures associated with larger earthquakes).

The final form and parameterisation of the reference rock GMPE is presented in Section 6.3. If we designated the predicted spectral acceleration at a given period as Sa(T) and the corresponding median value at the reference rock horizon as $Sa_{ref}(T)$, then the general form of the GMPE can be written as follows:

$$\ln[Sa(T)] = \{\ln[Sa_{ref}(T)] + \delta B + \delta WS\} + \ln[AF_j(T)] + \delta S2S_j \quad (2.1)$$

where $AF_j(T)$ is the median amplification function for the spectral acceleration at period T for the j^{th} zone, and $\delta S2S_j$ is the variability of the zone-specific amplification function. In terms of the variability in the predictions, the term δB is the earthquake-to-earthquake residual (*i.e.*, a

random sample from the distribution of between-event variability) and δWS is randomly sampled from the distribution of single-station within-event variability.

In Eq.(2.1) both δB and δWS are assumed to be zero-mean Gaussian random variables with standard deviation τ and Φ_{ss} , respectively. These two components of variability will have distributions that are constant across the field. The term $\delta S_2 S_j$ is the randomly sampled residual from the site-to-site variability for zone j , which is assumed to be a zero-mean Gaussian random variable with standard deviation $\Phi_{S_2 S_j}$; for more background on these terms and the decomposition of the ground-motion variability, see Al Atik *et al.* (2010) and Rodriguez-Marek *et al.* (2014).

As in the V1, V2 and V3 models, the magnitudes associated with the ground-motion database are local magnitudes (M_L) as determined by KNMI. The same magnitudes are used for the earthquake catalogue and hence to define the seismological model, hence the seismic hazard model remains internally consistent. Previously, the assumption was made that these local magnitudes could be assumed equal to moment magnitudes, \mathbf{M} . Since the V2 model was completed, new work led by KNMI has looked again into the relationship between these two magnitude scales in the Groningen field (Figure 2.1). The conclusion of this study (Dost *et al.*, 2016) is that for magnitudes above 2.5, moment magnitude is, on average, 0.2 units smaller than moment magnitude, *i.e.*, $\mathbf{M} = M_L - 0.2$ (Figure 2.2). We note, however, that work on the estimation of seismic moments for Groningen earthquakes is ongoing and consequently the relationship between \mathbf{M} and M_L in the field may be updated.

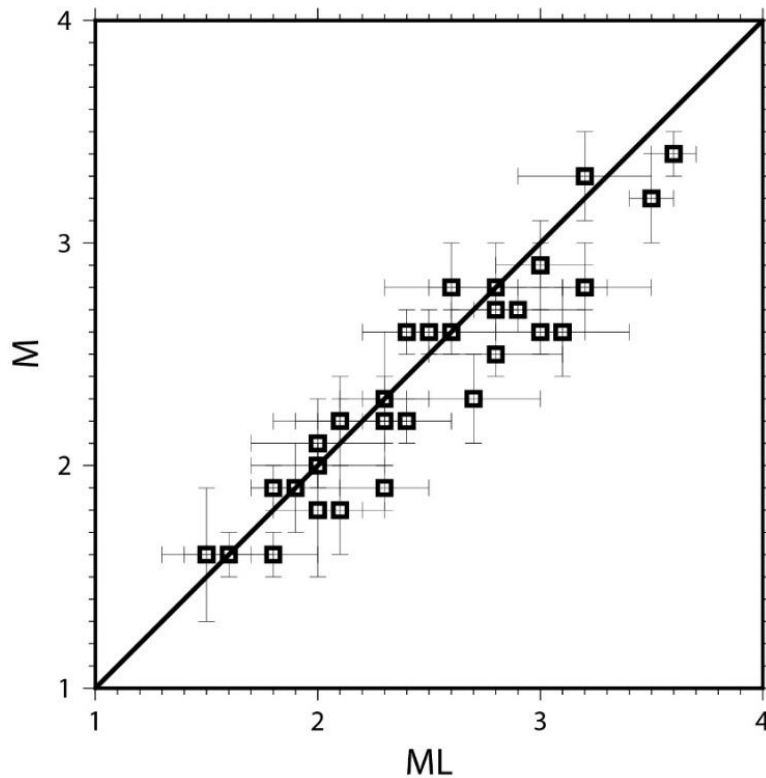


Figure 2.1. Moment magnitude \mathbf{M} as a function of local magnitude M_L

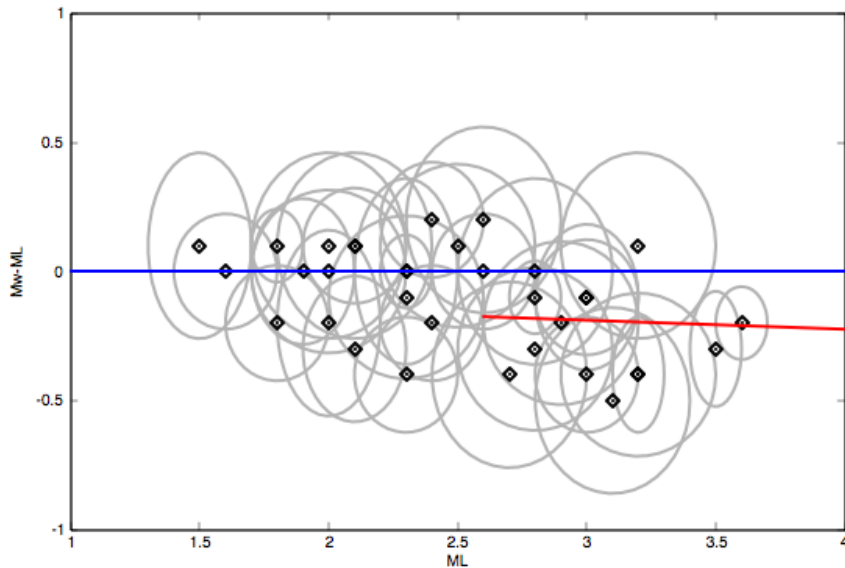


Figure 2.2. $M_w - M_L$ as a function of M_L for Groningen events. Uncertainties are shown as ellipses. A linear regression for $M_L > 2.5$, taking into account uncertainties in both parameters, is shown in red (Dost *et al.*, 2016)

The relationship between M_L and M has minimal impact on the development of the GMPE and the seismic hazard model for the reason stated above, namely that both the seismicity and ground-motion models continue to be defined on a common scale (M_L). However, there are important implications of the relationship, the most fundamental being that the proportionality between the two scales is constant (*i.e.*, the gradient of the relationship is unity). This is important because the use of stochastic simulations is predicated on the assumption of linear scaling with seismic moment, and this is not contradicted by the relationship that has been found between the two scales. Similarly, any comparisons of the V4 predictions with other GMPEs—apart from the V1, V2 and V3 models for Groningen—needs to take into account the differences in the magnitude scales since nearly all modern equations are based on moment magnitude.

As previously noted, in the V4 GMM development an important enhancement with respect to earlier models is the use of a distance metric defined relative to extended fault ruptures rather than to point sources. The main choices available are the rupture distance, R_{rup} , and the Joyner-Boore distance, R_{JB} . The former is simply the distance from the site to the closest point on the fault rupture plane, whereas the latter is the horizontal distance to the closest point on the projection of the fault rupture plane onto the ground surface. For vertically-dipping faults that rupture to the ground surface, the two metrics are equivalent; for other situations, R_{rup} will be equal to or greater than R_{JB} . The key difference between the two metrics is that the Joyner-Boore distance does not account for the depth of the fault rupture within the crust. In view of the shallow depth at which Groningen earthquakes initiate, the rupture distance was considered a more appropriate metric, especially if comparisons are to be made with other predictive models (for R_{JB} -based GMPEs, this would involve the implicit assumption of comparable depth distributions in both regions). The focal depths are all taken as 3 km (Spetzler & Dost, 2017) and ruptures are assumed to propagate down-dip and along strike.

As noted previously, the ultimate objective is to develop GMPEs that include non-linear site amplification functions for the Groningen field. The aim is to condition the functions at each response period on the spectral acceleration at the same period in the underlying reference rock, which is preferable to the more widely-used approach of conditioning the non-linear response on PGA, as recommended by Bazzurro & Cornell (2004a) and implemented by Chiou & Youngs (2008). While it is tempting to integrate fully probabilistic site response into the hazard and risk calculations following the method of Bazzurro & Cornell (2004b), especially in view of the relatively simple (but computationally intense) implementation of this approach within a Monte Carlo framework, this is more appropriate for site-specific studies (e.g., Rodriguez-Marek *et al.*, 2014). It may also be noted in Eq.(2.1) that the intention is to condition the non-linear site response not on the median prediction of the $S_{a,ref}(T)$ but on the actual predicted value resulting from the sampling of the between-event variability and the single-station within-event variability.

The formulation in Eq.(2.1) requires the study region to be divided into a number of zones, within each of which a unique set of non-linear site amplification functions—for the 23 selected response periods—is assumed to be representative. The definition of these zones is described in Chapter 9. The degree of variation of the site amplification functions across an individual zone is reflected in the assigned value of the term $\delta S_2 S_j$.

2.2. Overview of derivation process

Figure 2.3 provides an overview of the process followed to define the V4 GMM in the form of a flowchart superimposed on a cross-section of the Groningen field. This figure applies to the models for $S_a(T)$ and PGV; the derivation of the duration model is similar and uses the same simulated ground motions at the reference rock horizon, but it also has important differences, as explained in Chapter 12.

The process begins with the recordings of earthquake ground-motions from Groningen (see Section 3.2). These records are used to infer site kappa values at the recording station locations. Chapter 4 describes the development of linear site amplification functions for the recording stations using available V_s information and assigning damping values that are consistent with a reasonable estimate of the kappa value in the underlying reference rock. Linear amplification factors suffice at this stage because the surface recordings to which they will be applied to deconvolve the motions to the rock horizon are rather weak (the highest recorded PGA value is 0.08g). Amplification factors are derived both in terms of Fourier amplitude spectra (FAS), $S_a(T)$ and PGV. The former are applied to the surface motions to obtain acceleration FAS at the reference rock horizon, which—as described in Chapter 5—are inverted to obtain estimates of source, path and site parameters for the Groningen earthquakes. The source parameters include the Brune stress parameter and the seismic moment. The path parameters are the geometric spreading model—which will be at least partially constrained by finite difference simulations, as discussed in Chapter 5—and the attenuation parameter Q . The site terms are a site kappa value for the reference rock and a field-wide amplification factor.

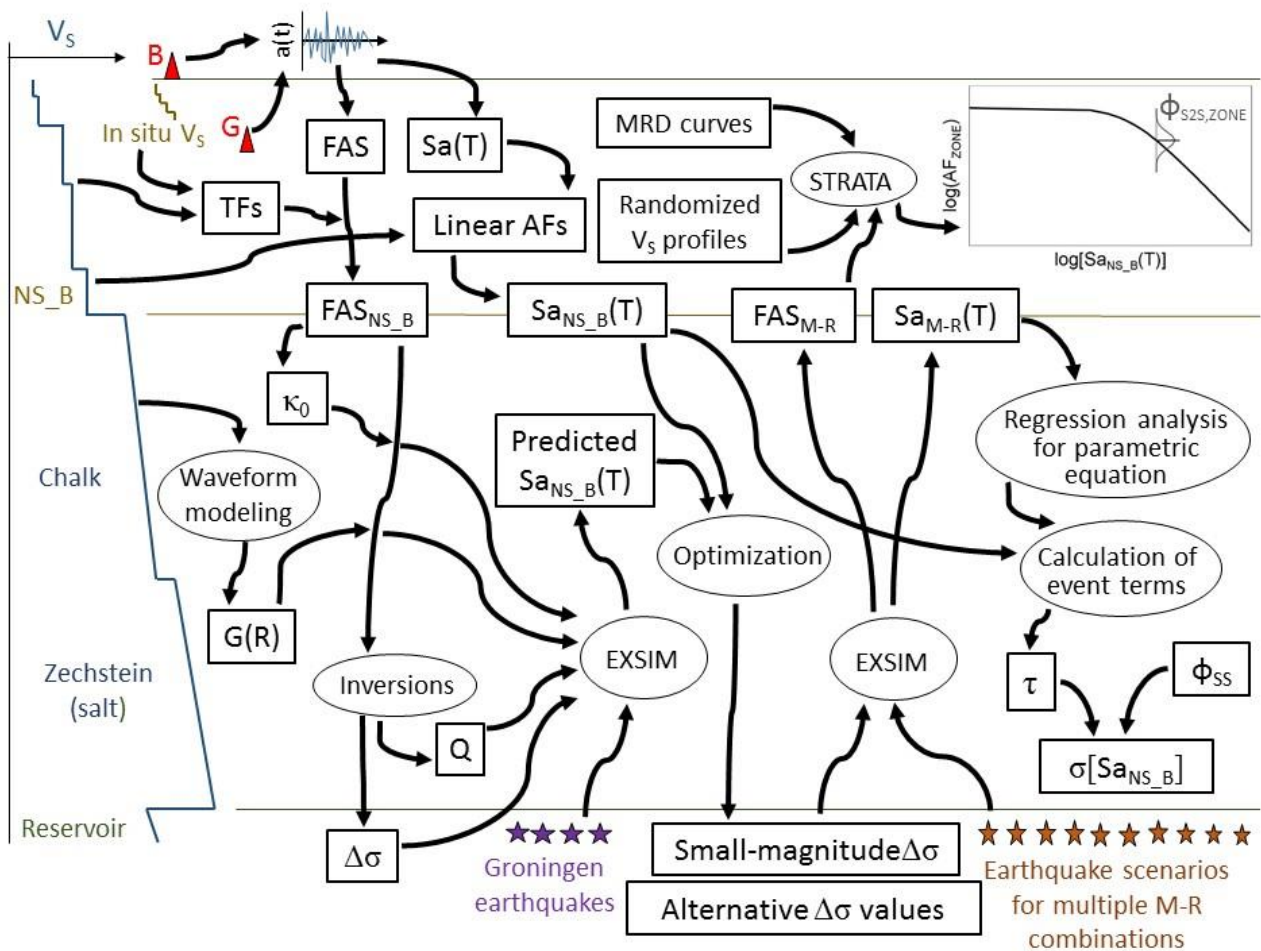


Figure 2.3. Schematic illustration of the derivation of the Groningen ground-motion model for response spectral accelerations at the surface, with quantities in rectangles and processes in ellipses. B and G refer to the surface and borehole stations, respectively (Section 3.1) and NS_B is the reference rock horizon; TF is transfer function; AF is amplification factor; FAS is Fourier amplitude spectra, Sa(T) is response spectral acceleration at period T; G(R) is the shape of the geometric spreading function; EXSIM is the software used for the simulations (Motazedian & Atkinson, 2005, as modified by Boore, 2009); STRATA is the site response program by Kottke & Rathje (2008) used to conduct RVT-based 1D equivalent linear response analyses. MRD refers to modulus reduction and damping in the site response; M-R refers to magnitude-distance pairs, and the suffix ZONE refers to the zonation of the field for site amplification factors. The elements of the total aleatory variability at the rock horizon (σ) are the between-event (τ) and single-station within-event (ϕ_{SS}) standard deviations; the additional variability in the site amplification factors is the site-to-site standard deviation (ϕ_{S2S}). Adapted from Bommer *et al.* (2017).

The full velocity model for the Groningen field is described in Chapter 7 and also in the paper by Kruiver *et al.* (2017). An important consideration is that for the B-station accelerographs (surface), there are now *in situ* measurements of the near-surface V_s profiles, so the TFs and AFs at these sites can be calculated with high confidence, especially since the uppermost 30-50 m exert such a strong influence on the surface motions. At G-stations (boreholes), there have not yet been any *in situ* V_s measurements, for which reason there is lower confidence in the near-surface velocity profiles. To avoid introducing additional uncertainty into the model derivation, the records from the 200 m geophones at these

locations are deconvolved to the NS_B, thus minimising the influence of the near-surface layers.

Optimal values of inverted parameters are then used to perform stochastic simulations of the motions, expressed in terms of both FAS of acceleration and response spectra, at the reference rock horizon. For the response spectra simulations estimates of the signal duration are also required. As for previous GMMs, multiple values of the Brune stress parameter will be applied in these forward simulations to generate multiple models in order to capture the inevitable epistemic uncertainty associated with the predictions at larger magnitudes. The simulations for response spectral accelerations and the fitting of suitable functional forms to these values to obtain the median GMPEs for the reference rock horizon are described in Chapter 6.

The two parallel activities of building a site response model (Chapter 7) and developing GMPEs for the reference rock horizon (Chapter 3 to 6) come together in Chapter 8, which corresponds to the bottom right-hand side of the figure. The site response analyses are performed using an RVT-based implementation of the 1D equivalent linear approach, for reasons that are explained in detail in Section 8.1. One of the advantages that this approach provides is that the input rock motions can be directly generated in the form of FAS that are also used in the stochastic simulations (Section 8.2). These analyses result in non-linear site amplification functions, which are coalesced into zones to which a representative function is assigned; this aggregation procedure is described in Chapter 9. The remainder of the figure corresponds to calculating the variability terms, from both the residuals of recorded surface motions and from the site amplification factors, which are used to construct the sigma models (Chapter 10).

2.3. Definition of the reference rock horizon

The first step in developing a model as described by Eq.(2.1) is to define the reference rock horizon that will be treated as the top of the elastic half-space for the site response calculations. The general geological profile across the field is illustrated in Figure 2.4. The gas reservoir is comprised of the Rotliegend sandstone layer which has a thickness varying from about 130 to 300 m, underlain by hard Carboniferous rock. Immediately above the reservoir is the Zechstein salt layer, with a very high-velocity basal anhydrite (Tenboer). The Zechstein is overlain by a layer of Cretaceous chalk. The uppermost part of the field is comprised of Cenozoic and younger deposits, including the North Sea formation that is mainly claystone.

In general, the criteria for selecting a reference rock horizon are related to the required properties corresponding to the assumption of an elastic half-space below that horizon. The key criteria are that the layer should be sufficiently stiff to behave linearly under the envisaged levels of acceleration and also that it should be an absorbing boundary, which means that downward propagating waves (reflected from the free surface) are not reflected back up towards the surface. There are also practical considerations for this particular application, for which some degree of simplification is desirable in view of the large numbers of site response calculations that are required to obtain amplification functions over the entire study area

(which extends for about 50 km in the north-south direction and 35 km in the east-west direction). A reference rock horizon is sought that is therefore sufficiently deep to capture the most important site response effects, and below which there is limited lateral structural variability, while avoiding the need to conduct site response analyses for very deep profiles.

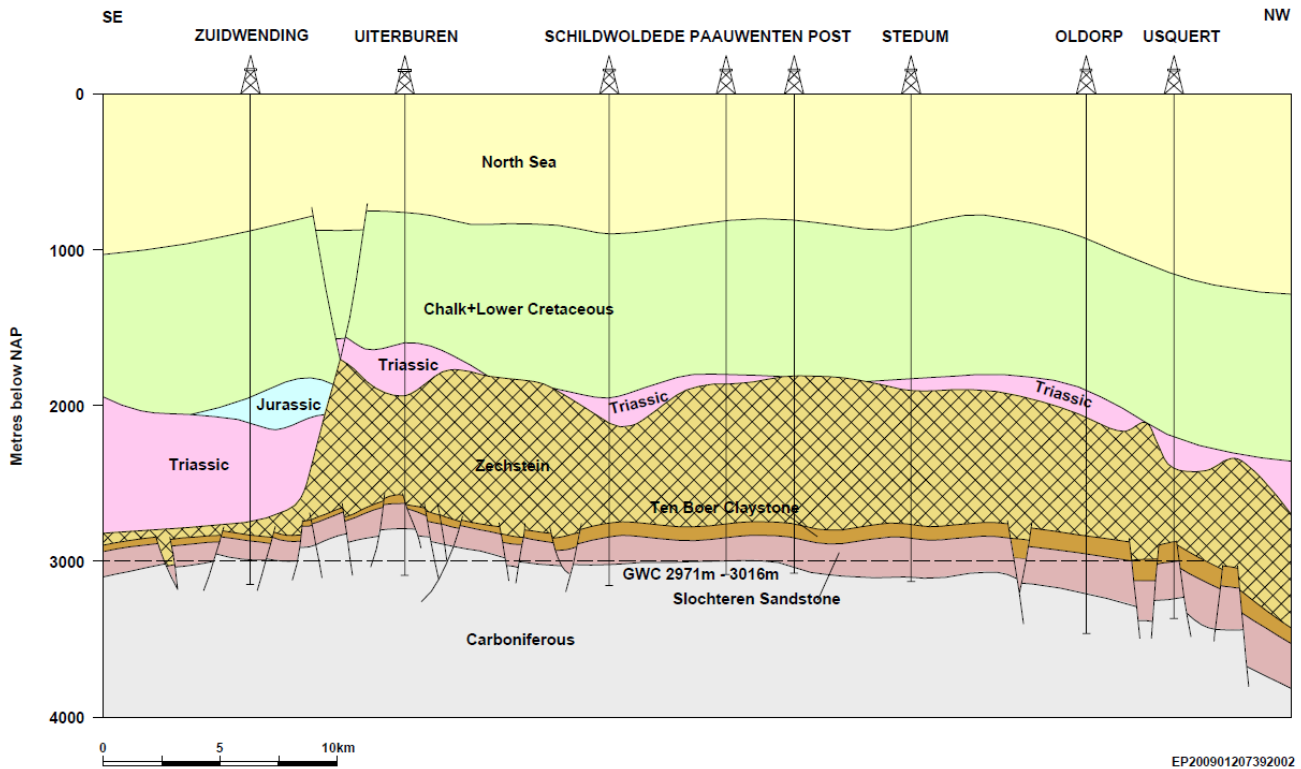


Figure 2.4. Simplified geological profile of the Groningen field (Source: NAM). The lowest coloured layer (above the light grey of the Carboniferous) is the Rotliegend sandstone that holds the gas reservoir.

To inform the final decision, V_s profiles extending down to the reservoir from the surface, obtained from two deep boreholes, were examined (Figure 2.5) as well as the field-wide deep velocity model developed by NAM. Two horizons are indicated on the figure, the base of the North Sea Supergroup Formation (NS_B) and the base of the Upper North Sea Formation (NU_B), located at depths of about 800 m and 350 m, respectively. The NS_B horizon is a very clear impedance contrast and it would therefore appear to be a logical choice for the top of the elastic half-space. However, it is also the case that the profile across the entire gas field between the NU_B and NS_B horizons is fairly uniform, which means that an additional ~400 m would be included in the site response analyses that might not produce significant differences in the resulting surface motions from one location to another. In view of this, the NU_B horizon was preferred for the V2 model. However, this choice has been subsequently re-visited and re-evaluated. In Figure 2.5, it may be noted that there is an apparent impedance contrast approximately 100 m below the NU_B horizon, which corresponds to the Brussels Sands, and at the time NU_B was chosen as the reference rock horizon there was some confusion regarding the two elevations. Moreover, based on the experience of a site-specific hazard assessment for the Groninger Forum site in the city of Groningen (Bommer

et al., 2015b), it was known that the NS_B impedance contrast creates a strong amplification in the 2-3 second range. In the V2 model, this was added to rock motions through modelling—since it occurs beyond the upper limit of useable periods from the recordings—but this required some adjustments to be compatible with the field-wide amplification factor for the NU_B level across the field (Bommer *et al.*, 2015d). To circumvent this issue and to define the top of the elastic half-space to be coincident with the most marked impedance contrast, the V3 and V4 models have adopted the NS_B horizon as the reference rock elevation. This is one of the single most significant differences between the V2 and subsequent models. The NS_B horizon is very well constrained throughout the entire study area (Figure 2.6).

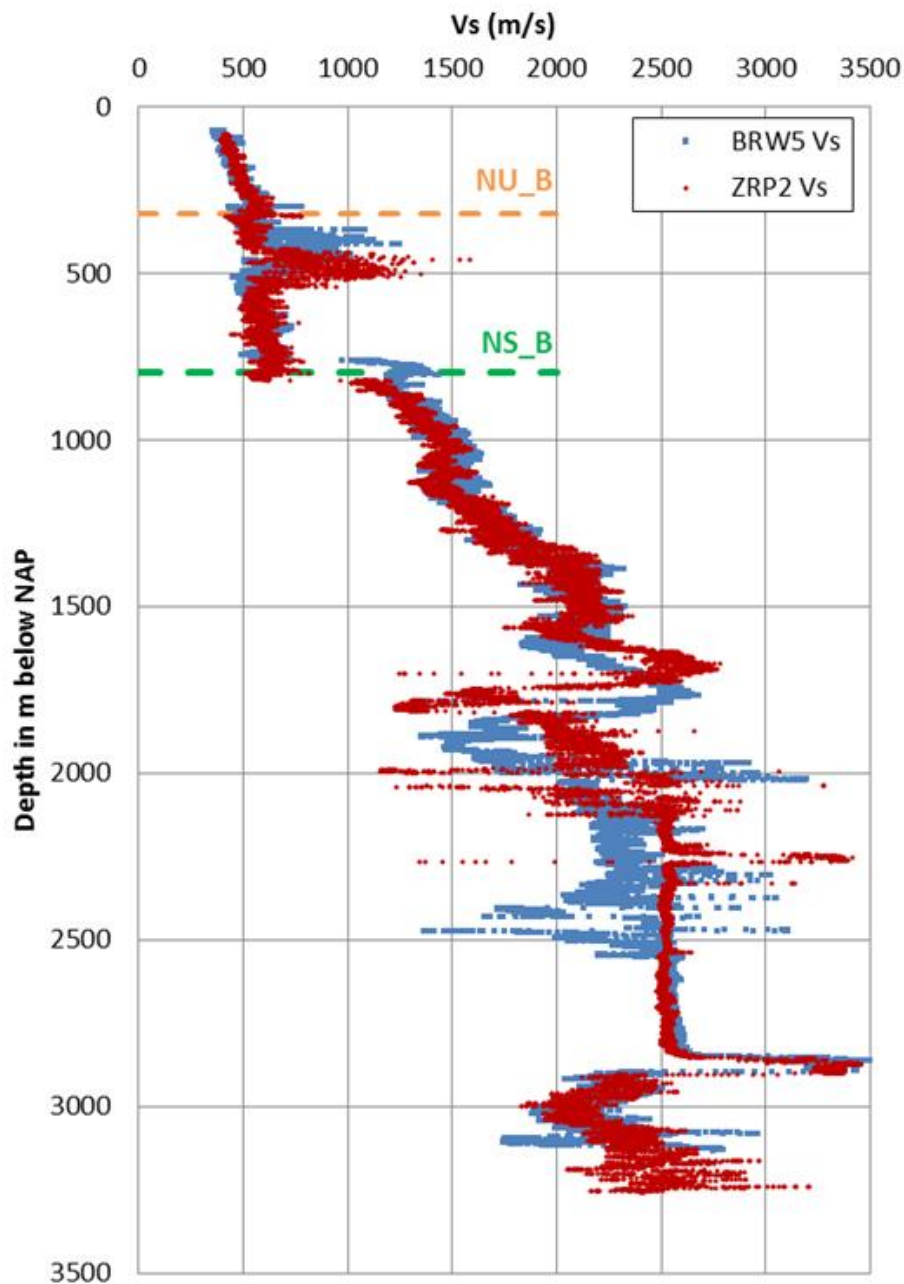


Figure 2.5. Shear-wave velocity profiles from two deep borehole logs, indicating the location of the base of both the North Sea Supergroup Formation (NS_B) and the Upper North Sea Formation (NU_B) formations (Source: NAM database)

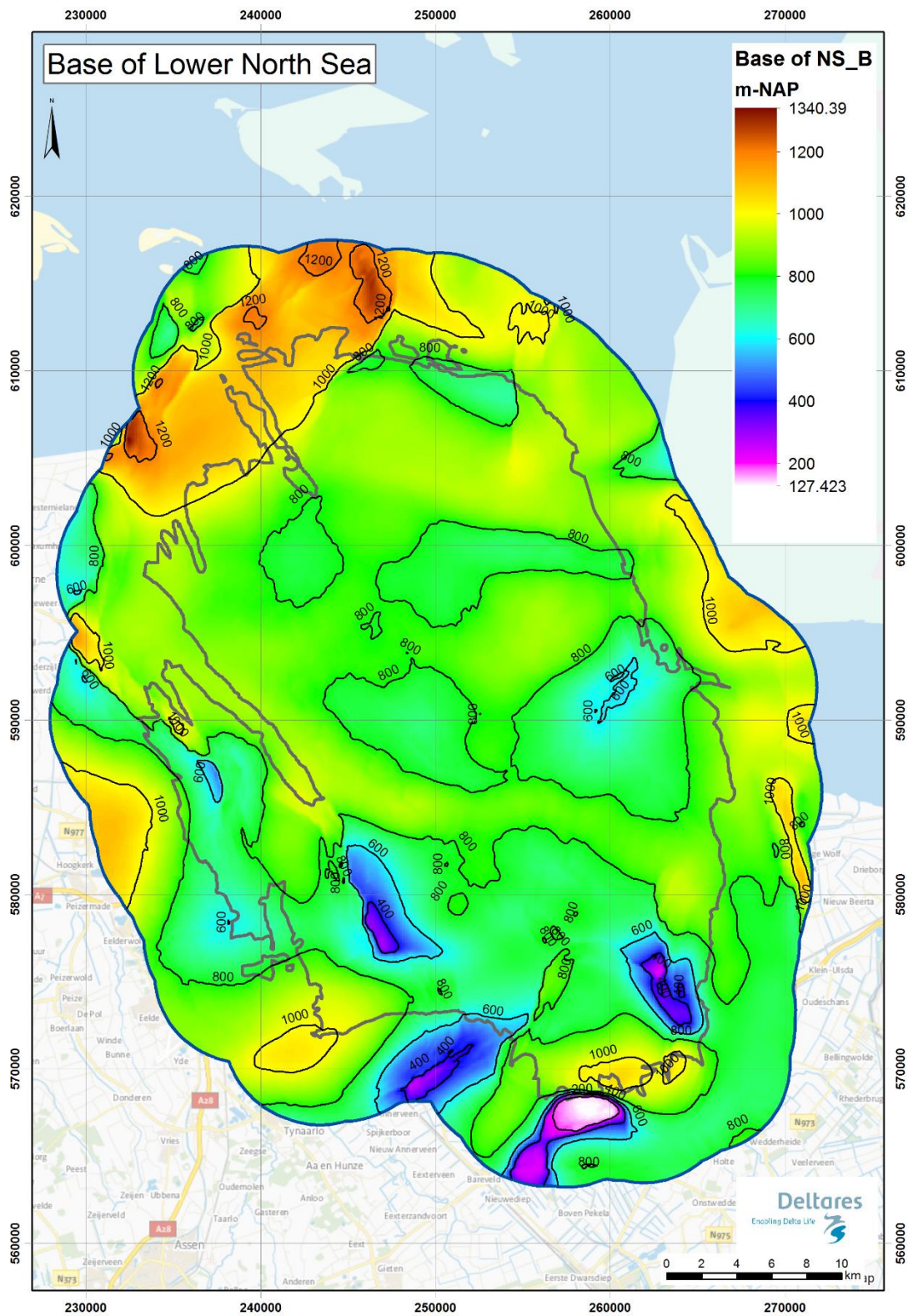


Figure 2.6. Maps of the study area showing the depth to the NS_B horizon (*figure prepared by Deltares using data from NAM database*). The extent of the field is shown by the bold grey line and the Groningen field plus the buffer zone that define the study area by the bold blue line. For clarity, in addition to the colour scale, 200 m contours are also plotted.

Over most of the field the NS_B horizon is encountered at a depth of about 800 m; it is at appreciably greater depths to the northwest of the area, but since some of these areas are

offshore (as are the slightly deeper areas to the north and east of the study area) they are of little consequence. To the south there are small areas in which the NS_B horizon is much closer to the surface but these areas are a very small proportion of the entire study region. An important point to emphasise is that selection of the NS_B horizon as the reference rock level does not mean that the influence of deeper impedance contrasts is being entirely ignored. The inversions of the recorded motions are expected to capture such effects if they are sufficiently influential to manifest in the surface motions. Where these contrasts are persistent across the entire field—or at least across the area covered by the recording networks—they will manifest in the average field-wide NS_B amplification factor obtained from the inversions. Where deep impedance contrasts may be more localised, they would be expected to influence the estimation of sigma, although it is noted that this will not account for such local variations that are outside the area covered by the recording network.

The dynamic properties assigned to the elastic half-space include a shear-wave velocity, V_s , of 1,400 m/s, mass density of 22 kN/m³, and a damping (which exerts very little influence on the outcome of site response analyses) of 0.3%, having been chosen to be consistent with the Q value (Q=150) determined from accelerograph data and used for the V1 GMM simulations. The half-space V_s is derived in chapter 7.2 For the calculation of the linear amplification factors at the recording stations used to deconvolve the recordings to the NS_B horizon (Section 4.3), values of 21 kN/m³ for density and 0.5% for damping were adopted, but these differences will have had a negligible effect on the results.

2.4. Spatial correlation of ground motions

The preceding sections of this chapter, together with Section 1.3, have provided an overview of all the elements that are included in the V4 GMM. To close these introductory chapters, we briefly explain why a choice was made not to include a function for the spatial correlations of ground motions for implementation of the risk calculations at the current time.

Several studies have noted that the variability of ground-motion amplitudes at closely-spaced accelerograph stations is lower than that expected from empirical GMPEs, indicating that there is a degree of spatial correlation in the seismic shaking (*e.g.*, Boore *et al.*, 2003; Wang & Takada, 2005; Jayaram & Baker, 2009; Goda & Atkinson, 2010; Esposito & Iervolino, 2011). Examples of spatial correlation functions for PGA are shown in Figure 2.7.

The considerable variation among these models suggest that there is still a degree of uncertainty regarding the spatial correlation lengths or that these lengths are influenced by local factors; the latter interpretation would lead us to conclude that a Groningen-specific correlation model would be needed rather than simply adopting one or more of the existing relationships. Regardless of the specific model for the variation of the correlation coefficient with separation distance, the effect of the spatial correlation of ground motions is to produce pockets of higher and lower motions rather than simply random variations that would result from simply sampling the within-event variability of the GMPE. In terms of group risk (GR), these spatial concentrations of elevated ground motion can result in higher estimates of losses in risk modelling for geographically-distributed exposure when these coincide with

concentrations of weak buildings (e.g., Crowley *et al.*, 2008). However, local personal risk (LPR), which reflects the risk at a single location, should not be significantly affected by spatial correlations of ground motions. Since the primary risk metric being considered for the Groningen field is LPR, the decision to not model spatial correlation is relatively unimportant. However, since there is also an interest in GR estimates, it will need to be borne in mind that the absence of a spatial correlation model may lead to some underestimation of this metric.

While it has been stated that spatial correlations can play an important role within the assessment of GR, in some cases they can also impact upon LPR estimates. The reason for this is not necessarily obvious, but relates to the manner in which the variance components of the ground-motion model are calibrated. In the case that the variance components are constrained using local observations (as is the case in this study) then if these observations are recorded on instruments with small separation distances the observed variance may underestimate the true marginal variance. When multiple instruments are located in a region of relatively similar levels of motions resulting from the spatial correlation then the variability of observations over these instruments will reflect the variation in amplitudes given the correlations in the ground motion field. For the prediction of LPR, what is really desired is the true marginal variation for any given location.

For this reason, spatial correlations were taken into consideration when partitioning the variance components. The specific approach taken is outlined in detail within Section 6.5 of this report. The effect of accounting for the spatial correlation is to obtain slightly larger estimates of the variance components than would have been obtained by ignoring the spatial correlations

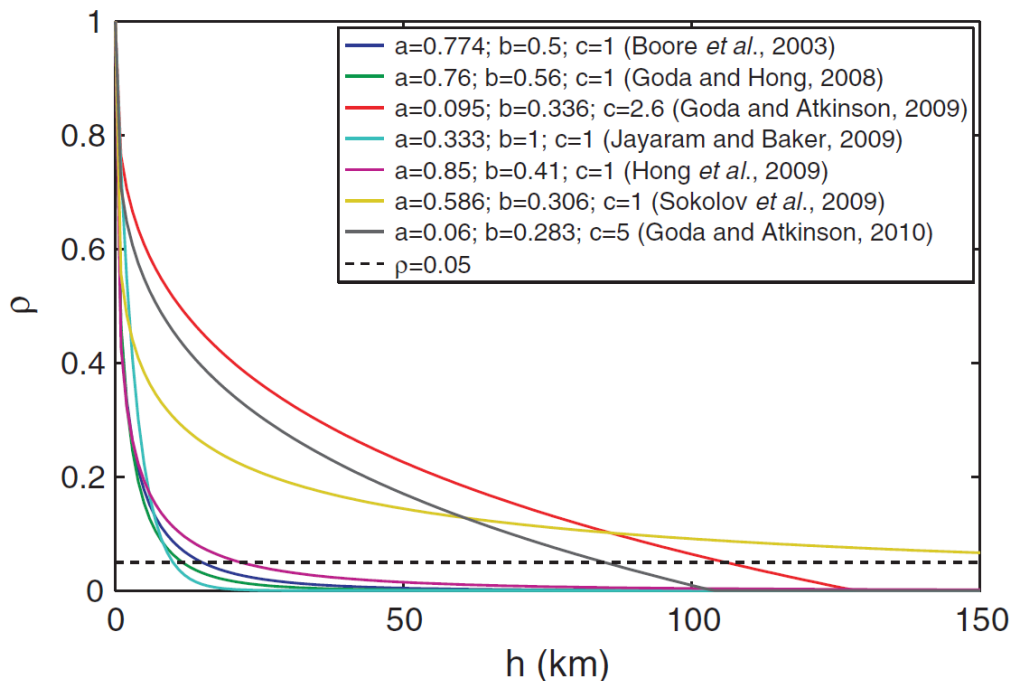


Figure 2.7. Comparison of published correlation functions for PGA as a function of separation distance, h ; the dashed black line represents the correlation coefficient of 0.05, which may be considered as the level at which all correlation is effectively lost (Esposito & Iervolino, 2011)

In the Version 0 and Version 1 risk models, the exposure is grouped into 3 x 3 km squares and the ground-motion amplitudes calculated at the centre of each square applied to all buildings within the grid cell. This is a computational convenience, since sensitivity analyses showed that using a smaller grid size (such as 1 x 1 km) resulted in a tremendous computational penalty, while the coarser grid does not result in great loss of accuracy, consistent with findings from other studies (e.g., Bal *et al.*, 2010). The assumption of uniform motions across each grid cell also conveniently serves as a surrogate for including spatial correlation. However, it must be recognised that the correlation lengths vary with spectral response period (e.g., Esposito & Iervolino, 2012), so the approximation becomes even cruder when spectral ordinates at multiple oscillator frequencies are being considered. From the V3 model onwards, different approaches to the spatial discretisation of the ground-motion field have been implemented, starting with the site amplification zones (see Section 9.2) with larger zones sub-divided, and subsequently moving towards finer grids after new programming efforts increased the efficiency of the calculations. Any assumptions regarding the approximation of a true spatial correlation model will obviously depend on the spatial discretisation of the final implementation. The final decision about whether to include a more explicit model for spatial variation will depend primarily on whether or not spatially aggregated risk metrics are required. Nonetheless, to pre-empt such a need, work is beginning to develop a spatial correlation model for the Groningen field, as discussed in Chapter 13, informed by the consideration of spatial correlation considered in the regression analyses described in Section 6.4.

3. GRONINGEN GROUND-MOTION DATABASES

The most valuable resource used for the derivation of GMPEs for a given region is a database of accelerograph recordings from local networks. The Groningen seismic hazard and risk modelling project is in a privileged position in this regard, with excellent networks now in operation in the gas field and a growing database of ground-motion records. In this chapter we provide a brief overview of the existing and forthcoming networks of recording instruments, identifying those from which records are being used in the derivation of the V3 equations. The characteristics of the current database are then summarised, followed by an overview of the additional recordings from smaller-magnitude events that were added for inversions to estimate source, path and site parameters.

3.1. Strong-motion networks in the Groningen field

The existing and planned strong-motion recording networks in the Groningen field were discussed in the V1 GMPE report (Bommer *et al.*, 2015a). The network that has provided the majority of the recordings in the current database are the digital accelerographs that have been operated by KNMI in the field for many years. The network was expanded and upgraded between 2013 and 2014, and now consists of 18 instruments, all installed at the ground surface (Figure 3.1).

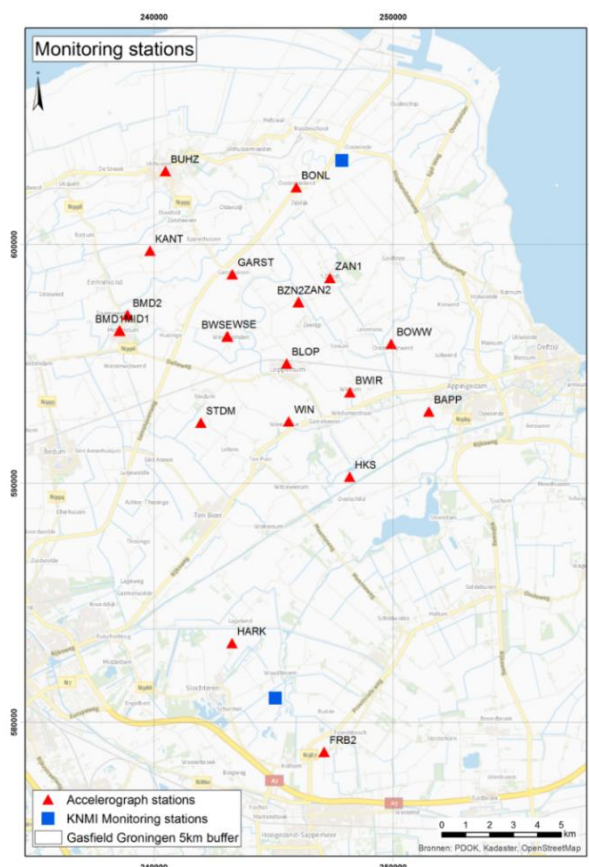


Figure 3.1. Locations of KNMI accelerographs (*red triangles*) and seismographs (*blue squares*) in the Groningen field.

of the combined networks means that all earthquakes of interest to the GMPE derivation (*i.e.*, $M_L \geq 2.5$) are likely to yield large numbers of recordings: as explained in the following section, the largest earthquake in the field to date—the M_L 3.6 Huizinge event of August 2012—yielded 7 useable accelerograms, whereas the M_L 3.1 Hellum earthquake of 30 September 2015 contributed 42 records to the database. Taking into account that the new borehole network was not fully installed at the time of the Hellum earthquake, the outlook for a very rich database of recordings—at least in terms of distance and azimuth distribution, if not magnitude—is very promising.

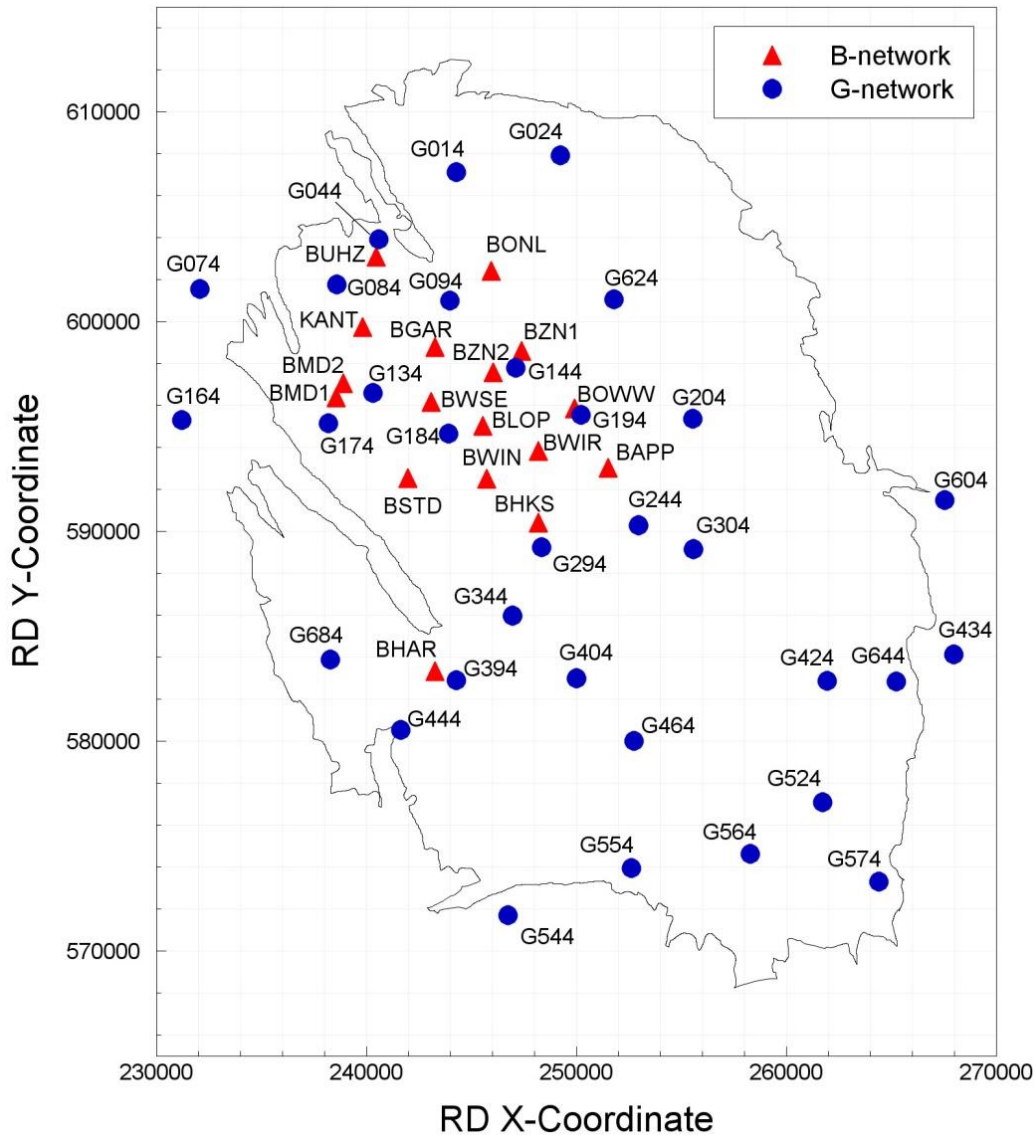


Figure 3.3. Locations of KNMI accelerographs (B-stations) and new boreholes with geophones and surface accelerographs (G-stations)

There are two other accelerograph networks operating in the Groningen field. An additional 66 accelerographs have been installed (in clusters of three instruments at each of 22 locations) on the key facilities of the NAM gas production network in the field. The purpose

of the NAM accelerograph is to allow safe shut-down of the facilities if accelerations in excess of specific thresholds are exceeded, but the records obtained by these instruments may also be made available and are likely to be added to database used for derivation of the GMM, provided that the records are not excessively contaminated by the influence of the gas production plant and equipment at the sites. The records obtained to date are being evaluated—and compared to those from the other networks during the same events—with a view to their subsequent incorporation into the database. If the records are judged to be usable for ground-motion prediction purposes, it will be necessary to expand the current programme of field measurements conducted by Deltares (Section 4.2) to also incorporate these recording locations.

A fourth network consists of some ~300 accelerographs that have been installed by TNO, under contract to NAM, in some public buildings and private homes. The latter instruments were installed in homes selected by requests made in response to an open invitation by NAM. The spread and density of this network is such that it could provide invaluable information for the refinement of the ground-motion model. To date the records obtained from these instruments have not been incorporated into the database because of concerns regarding their installation. The digital accelerographs have been mounted on small steel brackets (weighing 5 kg) and in many instances the brackets have then been affixed to walls several centimetres above the floor, which means that contamination of the records by the building response is likely. The TNO network is also operated differently from the other field networks of accelerographs, applying a trigger level for retrieval of data. A summary of the ongoing explorations of these recordings, with a view to including them in the project database for refinement of the GMM, is presented in Appendix VI.

3.2. Strong-motion database for Groningen

For the V1 GMM, records were selected from events of magnitude 2.5 and greater for which the accelerograms were judged, on the basis of visual inspection, to have acceptably high signal-to-noise ratios. The records were adjusted using linear or polynomial baselines, as needed, after truncation of the pre-event memory, and used to generate response spectral ordinates at periods up to 2 seconds. The total dataset consisted of 85 recordings from 12 earthquakes. For the V2 GMM, the database was expanded but the additional recordings included several from earthquakes of magnitude smaller than 2.5, which were subsequently excluded. Moreover, some corrections were made to magnitude values used in the V1 database, with the corrected magnitudes sometimes being below the threshold of M_L 2.5. The final database therefore still consisted of 12 earthquakes—although not exactly the same events as in the V1 database—yielding a total of 106 records, representing only a modest increase with respect to V1.

For the V3 and V4 models, an appreciably larger database of ground-motion recordings became available. Considering only earthquakes with magnitude of M_L 2.5 or greater, recordings are now available from a total of 22 earthquakes (Table 3.1.). Some of these are older events from which the records from the KNMI network had not previously been

incorporated into the database; such events are identified by blanks in the second column of Table 3.1.

Table 3.1. Earthquakes in the V3/V4 ground-motion database

EQ ID	V2 EQ ID	Date			Time		M	WGS84		RD Coordinates		Name
		Y	M	D	H	M		N°	E°	X (m)	Y (m)	
01	01	2006	VIII	8	05	04	3.5	53.350	6.697	242,159	596,659	Westeremden
02		2006	VIII	8	09	49	2.5	53.350	6.707	242,826	596,579	Westeremden
03	02	2008	X	30	05	54	3.2	53.337	6.720	243,740	595,168	Westeremden
04		2009	IV	14	21	05	2.6	53.342	6.678	240,955	595,673	Huizinge
05	03	2009	V	8	05	23	3.0	53.354	6.762	246,479	597,129	Zeerjip
06		2010	VIII	14	07	43	2.5	53.403	6.703	242,496	602,509	Uithuizermeeden
07	05	2011	VI	27	15	48	3.2	53.303	6.787	248,253	591,487	Garrelsweer
08		2011	VIII	31	06	23	2.5	53.444	6.687	241,305	607,070	Uithuizen
09		2011	IX	VI	21	48	2.5	53.338	6.805	249,399	595,368	Ooosterwijterd
10	06	2012	VIII	16	20	30	3.6	53.345	6.672	240,504	596,073	Huizinge
11		2013	II	7	22	31	2.7	53.375	6.667	240,112	599,405	Zandeweer
12	08	2013	II	7	23	19	3.2	53.389	6.667	240,085	600,945	Zandeweer
13		2013	II	9	05	26	2.7	53.366	6.758	246,230	598,516	t Zandt'
14		2013	VII	02	23	03	3.0	53.294	6.785	248,163	590,446	Garrelsweer
15		2013	IX	04	01	33	2.8	53.344	6.772	247,166	596,048	Zeerjip
16	09	2014	II	13	02	13	3.0	53.357	6.782	247,804	597,489	Leermens
17	10	2014	IX	1	07	17	2.6	53.194	6.787	248,489	579,359	Froombosch
18	11	2014	IX	30	11	42	2.8	53.258	6.655	239,565	586,336	Garmerwolde
19	12	2014	XI	5	1	12	2.9	53.374	6.678	240,890	599,307	Zandeweer
20	13	2014	XII	30	2	37	2.8	53.208	6.728	244,561	580,898	Woudbloem
21	14	2015	I	6	6	55	2.7	53.324	6.678	246,987	593,800	Wirdum
22		2015	IX	30	18	05	3.1	53.258	6.800	251,603	584,016	Hellum

The numbers of records from each earthquake and the key features of the recordings are listed in Table 3.2. The largest peak acceleration recorded to date remains the 0.084g on the NS component of the MID1 (now BMD1) accelerogram of the August 2012 Huizinge earthquake. The largest PGV value of 3.51 cm/s corresponds to this same record; the record processing procedures are discussed below. Comparing Tables 3.1 and 3.2 it can be seen that the additional records from 8 pre-2014 earthquakes did not expand the database very much, with an average of only 2.5 records per event. The growth of the database in terms of the number of records owes more to the expansion of the recording networks, with the five most recent events all contributing at least 12 records, and the most recent event a total of 42 recordings. The V3/V4 database now consists of 178 accelerograms from 22 earthquakes. Full details of the V3/V4 database and the characteristics of the records and their response spectra are provided in Ntinalexis *et al.* (2016). The magnitude-distance distribution of the database is illustrated in Figure 3.4.

The locations of the earthquake epicentres are shown in Figure 3.5. As for the V2 database, recordings from the FRB2/BFB2 station have been excluded because of a strong high-frequency content throughout the entire signal (Bommer *et al.*, 2015a). The most likely cause of this noise in the record is the nearby gas production well.

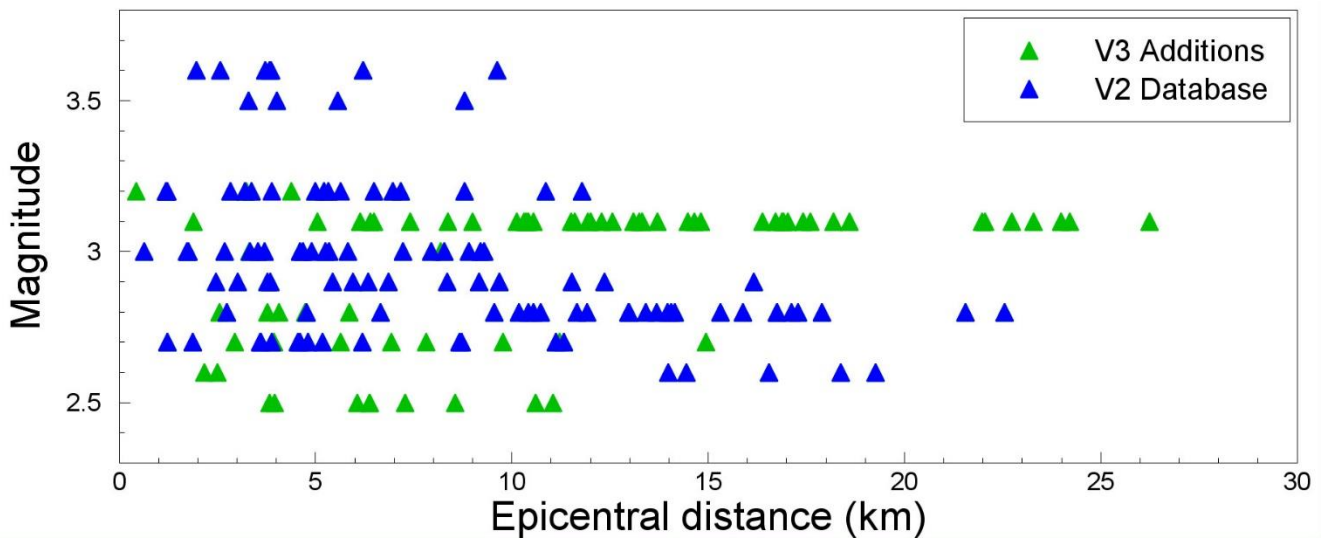


Figure 3.4. Magnitude-distance distribution of the V3 database. The symbols distinguish the data from the 12 earthquakes in the V2 database (*blue triangles*) and the additional recordings added to the V3 database (*green triangles*)

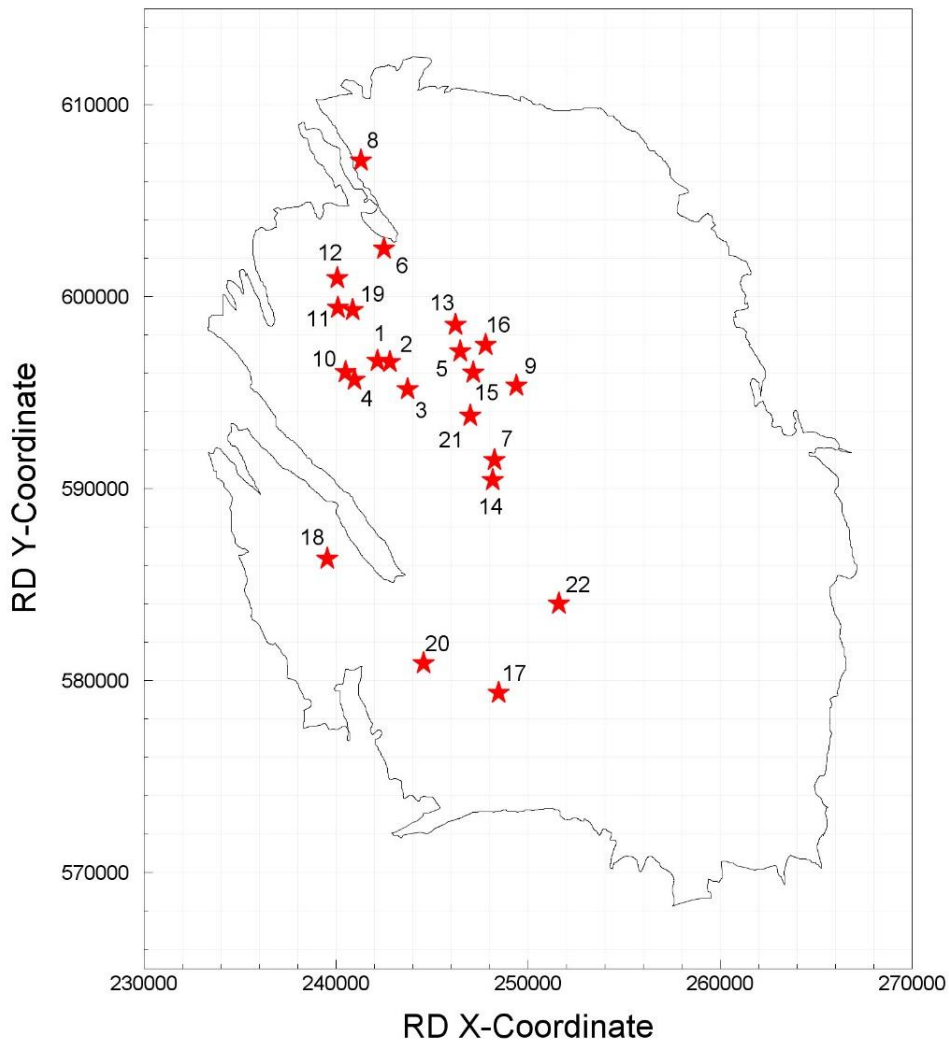


Figure 3.5. Location of the epicentres of the earthquakes in the current database; earthquake ID numbers as in Table 3.1

Table 3.2. Numbers and features of records from each earthquake

EQ ID	M	Recs	Tot	Min. R_{epi} (km)	Max. R_{epi} (km)	Max. PGA (g)	Max. PGV (cm/s)
01	3.5	4	4	3.30	8.79	0.050	1.25
02	2.5	1	5	3.97	3.97	0.005	0.13
03	3.2	6	11	1.20	5.32	0.035	1.44
04	2.6	3	14	2.18	2.50	0.014	0.44
05	3.0	5	19	0.63	7.95	0.023	0.62
06	2.5	5	24	3.84	7.28	0.014	0.28
07	3.2	8	32	1.21	11.78	0.027	1.21
08	2.5	3	35	8.55	11.05	0.006	0.12
09	2.5	1	36	6.37	6.37	0.001	0.02
10	3.6	7	43	1.97	18.54	0.082	3.51
11	2.7	3	46	0.43	4.39	0.019	0.55
12	3.2	3	49	1.23	5.64	0.031	1.44
13	2.7	2	51	2.95	3.94	0.009	0.36
14	3.0	2	53	3.31	8.19	0.014	0.55
15	2.8	5	58	2.56	5.87	0.013	0.48
16	3.0	14	72	1.75	9.29	0.070	1.62
17	2.6	5	77	13.98	19.26	0.0003	0.02
18	2.8	12	89	4.78	17.29	0.002	0.11
19	2.9	14	103	2.46	16.16	0.077	1.78
20	2.8	14	117	2.74	22.54	0.017	0.35
21	2.7	19	136	1.22	15.04	0.013	0.43
22	3.1	42	178	1.90	26.24	0.005	0.25

In order to provide an indication of how the expansion of the recording networks has improved capture of the ground-motion field during induced earthquakes in the Groningen field, Figure 3.6 shows the epicentral locations and the accelerographs producing records from the 2012 Huizinge and 2015 Hellum earthquakes.

Epicentral distances are calculated using the station coordinates and epicentral locations provided by KNMI; all focal depths are assumed to be equal to 3 km (*i.e.*, all earthquakes are assumed to be located within the gas reservoir). As for the earlier GMPEs, the event size is based on the local magnitudes calculated by KNMI but, as explained in Section 2.1, we no longer make the assumption that these are equivalent to moment magnitudes (*i.e.*, $M_L = M$), since it has been found that there is a consistent average difference of 0.2 between the two scales in the magnitude range of interest.

the criteria that Bommer *et al.* (2010) put forward for basic acceptability of empirical GMPEs was the specification that the database should include at least 10 earthquakes for each unit of magnitude covered and 100 records per 100 km of distance covered. In the magnitude range from M_L 2.5 to 3.6, the database now includes 18.3 earthquakes per magnitude unit, which is therefore acceptable (although, of course, this does not allow for extrapolation to larger magnitudes if this were done empirically). In terms of distance, the criterion proposed by Bommer *et al.* (2010) is satisfied and exceeded by a factor of more than 6. Since some of the coefficients of the model are constrained by direct empirical regression (see Chapter 6), these indicators are useful although it is clear that the constraint on earthquake-to-earthquake variability may not be as robust as would be desired.

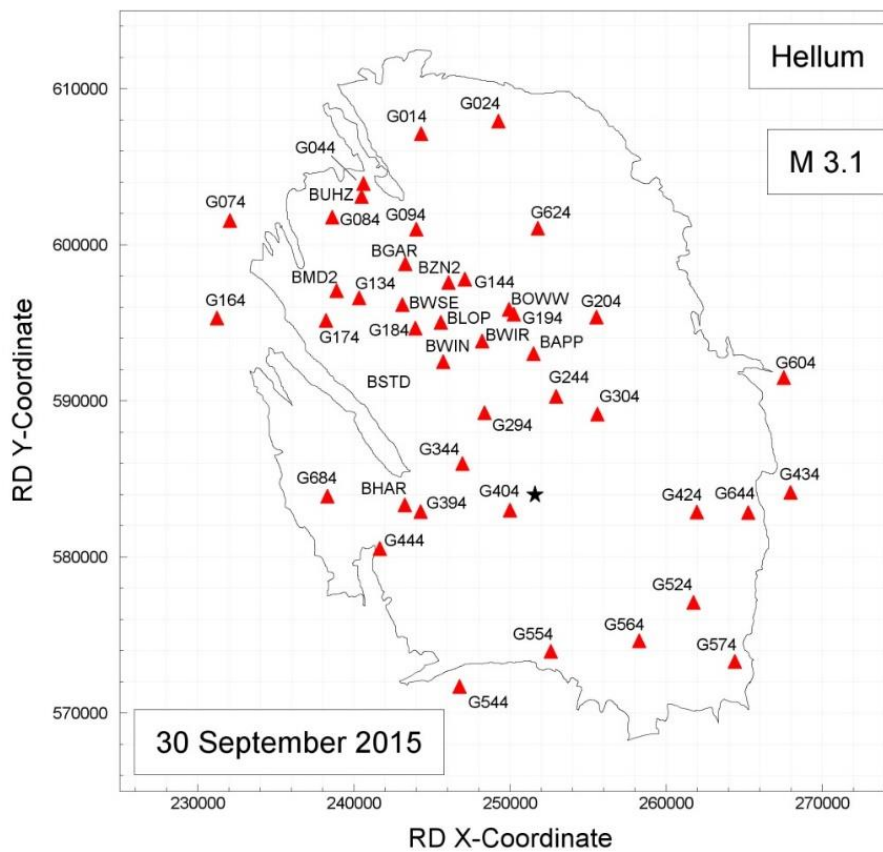
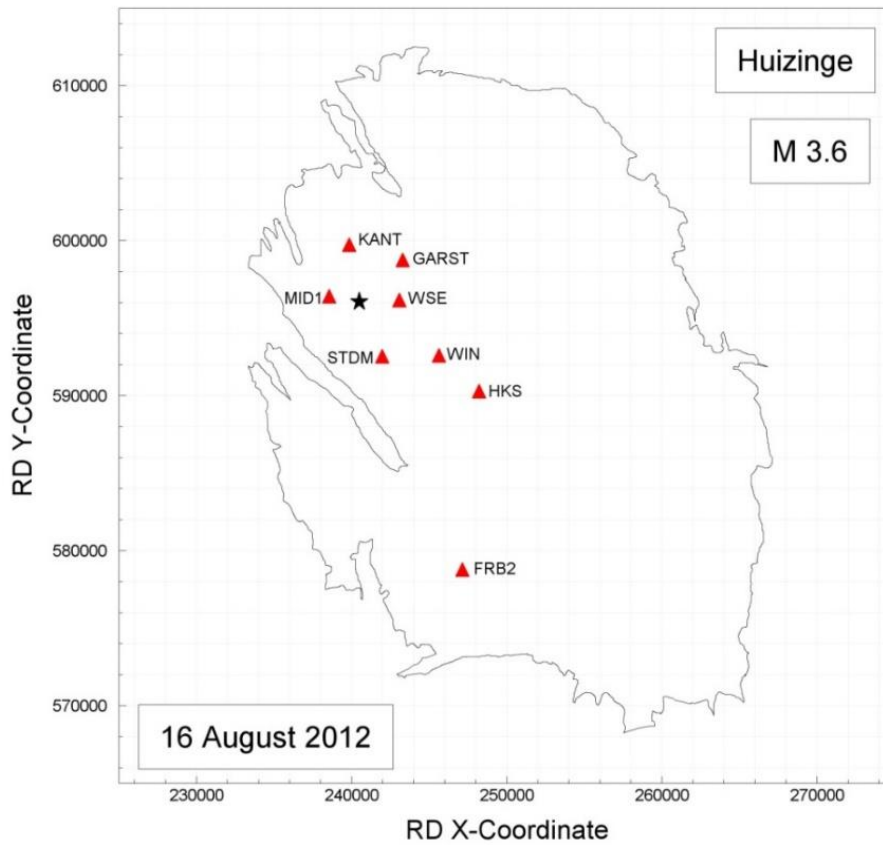


Figure 3.6. Location of the epicentres and recording stations for the largest earthquake in the database (*upper*) and the most recent earthquake in the database (*lower*); in each plot, the black triangle is the earthquake epicentre and the red triangles the recording stations.

A very important improvement of the V2 database with regard to that used to derive the V1 GMPEs was that the records have been uniformly processed with individually selected high-pass filter parameters to remove long-period noise. Full details of the record processing is presented in a separate report (Ntinalexis *et al.*, 2015) and the filter parameters are summarised in the database report (Ntinalexis *et al.*, 2016) but a brief summary is given below for completeness.

The records were processed using an 8-order acausal Butterworth filter with the cut-off selected on the basis of deviation of Fourier amplitude spectrum (FAS) of acceleration of the record from an ideal f^2 trend. Signal-to-noise ratios from the FAS were also explored using the pre-event memory as the noise model but the very low amplitude of many of the records made it very difficult to clearly distinguish a pre-event memory from the signal. The same filter was applied to both horizontal components on each recording to allow for the possibility of vector resolution and other such operations on the processed accelerograms (Boore & Bommer, 2005). The maximum usable period was then defined as 0.9 of the long-period cut-off, confirmed as appropriate by comparison between the acceleration response spectra of filtered and unfiltered records, and also consistent with the recommendations of Akkar & Bommer (2006) for digital accelerograms. The filter cut-offs that were applied were less severe than might be expected for such small-magnitude recordings, suggesting that the recording are of very high quality (see Fig. 2 of Akkar & Bommer, 2006). A point worthy of note in this context is that the geophones record velocity, which is converted to acceleration by differentiation, facilitated by the sampling frequency of 200 Hz, which corresponds to a Nyquist frequency of 200 Hz. Very similar low-cut filter frequencies were found to be suitable for the surface accelerograms and for the acceleration time-series obtained from the velocity recordings at all depths. The transfer function of the geophones transducer, with a natural frequency of 10 Hz, is shown in Figure 3.7.

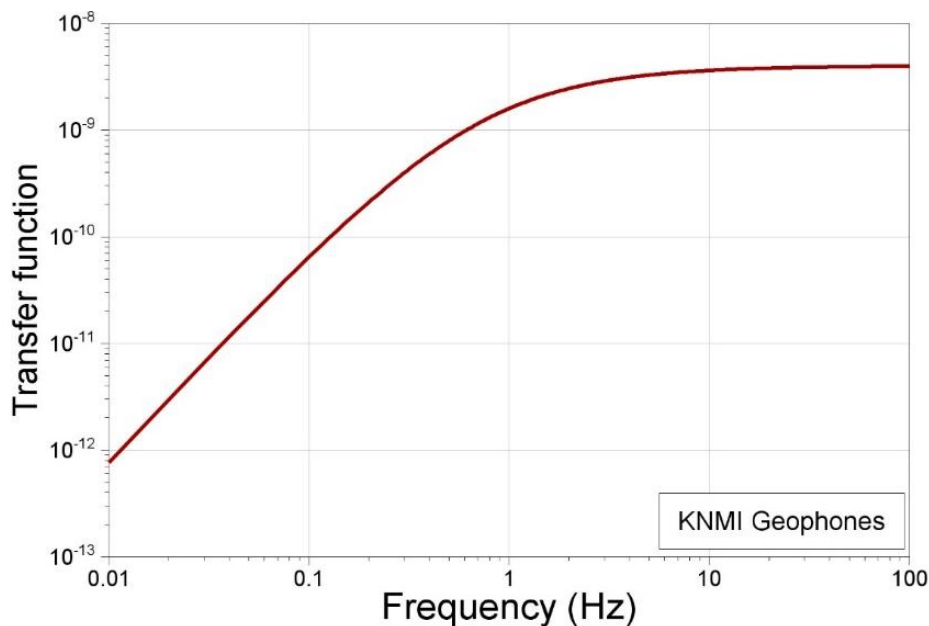


Figure 3.7. Transfer function of the KNMI borehole geophones

A very important feature of the V3 database is the fact that it was possible to account much more accurately for local site effects at the recording stations producing the records. For recordings from the KNMI permanent accelerograph stations (B-stations in Figure 3.3), as mentioned previously, this added accuracy in the characterisation of the site amplification effects was obtained through *in situ* measurements of the near-surface V_s profiles (see Section 4.2). For recordings obtained at the new instrumented boreholes (G-stations in Figure 3.3), we made use of the geophone recordings from 200 m depth. The advantage of using these borehole recordings is that for deconvolution of the motions to the reference rock horizon (Section 4.3), the influence of the uppermost 200 metres—which has a pronounced effect on the motions—was largely circumvented. Since no *in situ* measurements are available as yet from these locations, the use of the deeper recordings avoided considerable uncertainty that would result from using inferred V_s profiles for the near-surface layers. These records were differentiated to obtain acceleration traces and thereafter treated in the same way as the surface accelerograms in terms of filtering, as noted previously.

The consequence of the filtering is that the number of spectral accelerations available for analyses decreases with increasing oscillator period (Figures 3.8 and 3.9). Up to 0.5 seconds, the full dataset is retained and even up to 0.85 seconds only 8 records (4.5% of the data) drop out because of the usable period range. Thereafter, however, the rate of attrition increases sharply and at 1 second only 85% of the records are retained and at 1.5 seconds this is reduced to 47%. For response periods of 3 seconds and greater there are almost no usable records at all (Figure 3.8). For response periods beyond 1 second, the data are unlikely to be sufficient to serve as a basis for constraining the aleatory variability (σ) and other features of the ground-motion model, which means that there will be additional uncertainty associated with the predictions for longer periods.

The geometric mean values of PGA of the entire database of surface motions—from both B- and G-stations—are plotted against distance in Figure 3.10. General trends of increasing acceleration with increasing magnitude and decreasing distance can be observed, as would be expected although there is also clearly considerable variability in the data as well since there is appreciable mixing of the two groups. A noteworthy observation is that a rather small number of the recordings have geometric mean PGA values greater than $0.01g$. Similar plots are shown for response spectral accelerations at different oscillator periods in Figure 3.11 but without any grouping by magnitude range. However, in those plots the surface values are shown for accelerograms from the B-stations and spectral accelerations from the 200 m-deep recordings from the G-stations, since these are the actual records used as input to the V4 GMPE derivation. As would be expected, the surface recordings display larger amplitudes by virtue of the amplifying effect of the uppermost 200 metres of soft soils.

An important point to note herein is that the recordings in the database are all of very low amplitudes. While this creates a challenge in extrapolating to predictions of motions from much larger earthquakes, it does allow the assumption to be made with some confidence that the site response embedded in these recordings is linear, which allows the relatively simple deconvolution to the reference rock horizon (see Figure 2.3), which is an essential step in the model-building procedure designed for the Groningen GMM.

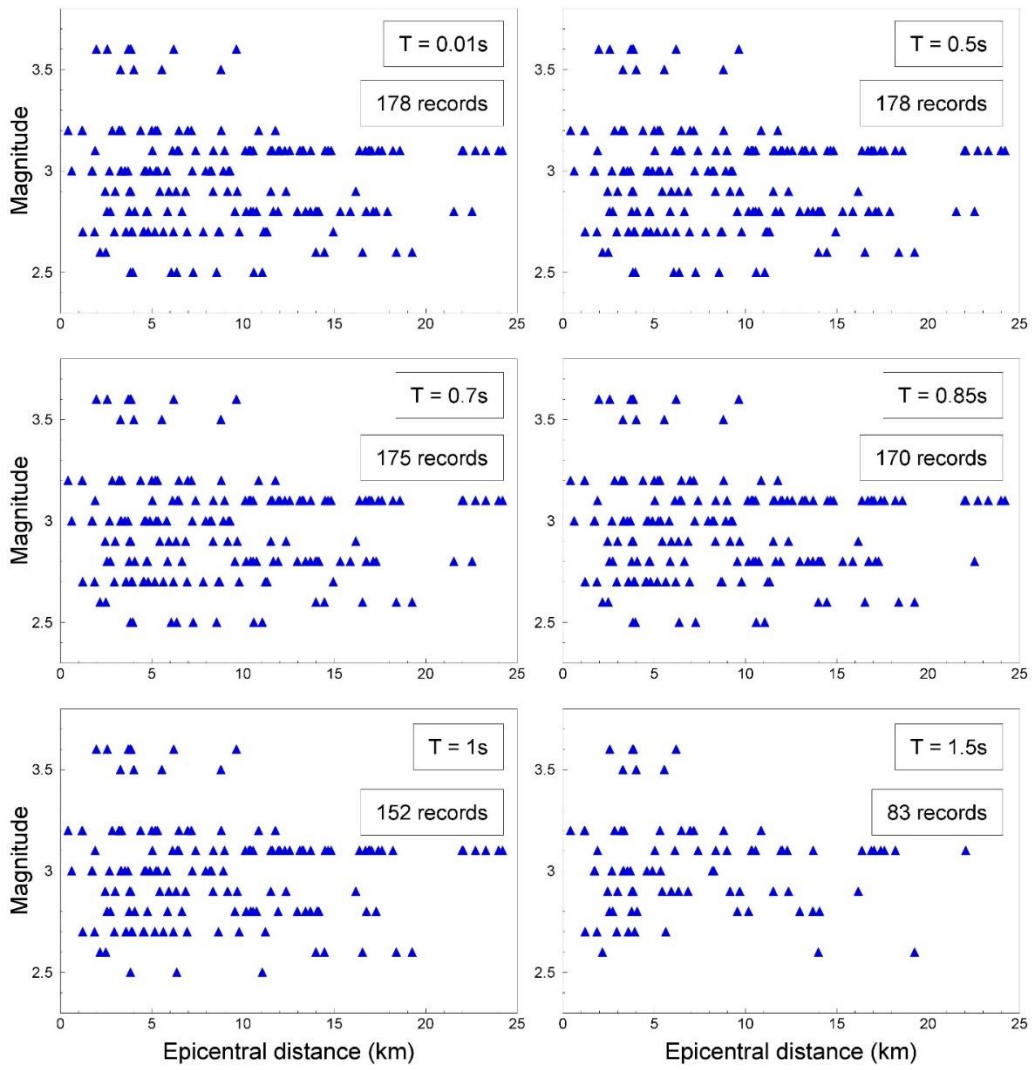


Figure 3.8. Magnitude-distance distribution of the spectral acceleration as a function of oscillator period as a result of the application of high-pass filters to the recordings

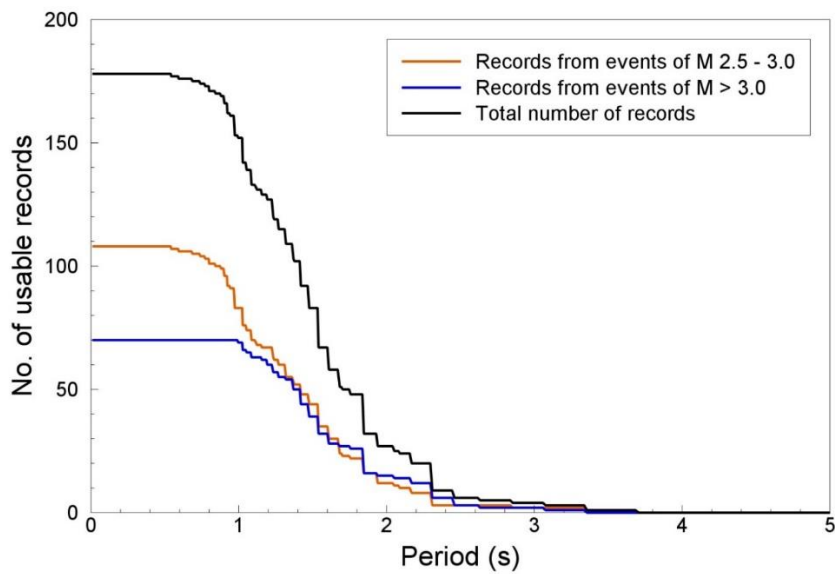


Figure 3.9. Number of usable records as a function of oscillator period, showing the total number and those corresponding to different earthquake magnitude ranges

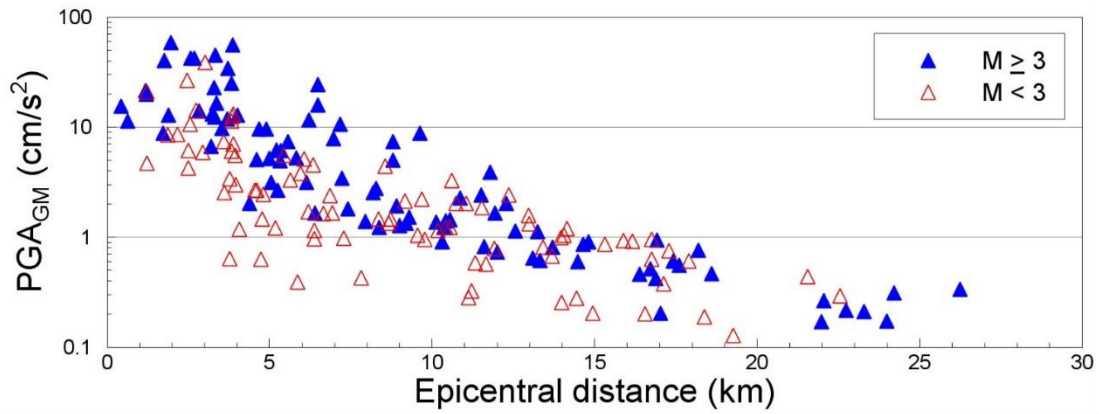


Figure 3.10. Geometric mean values of PGA against epicentral distance

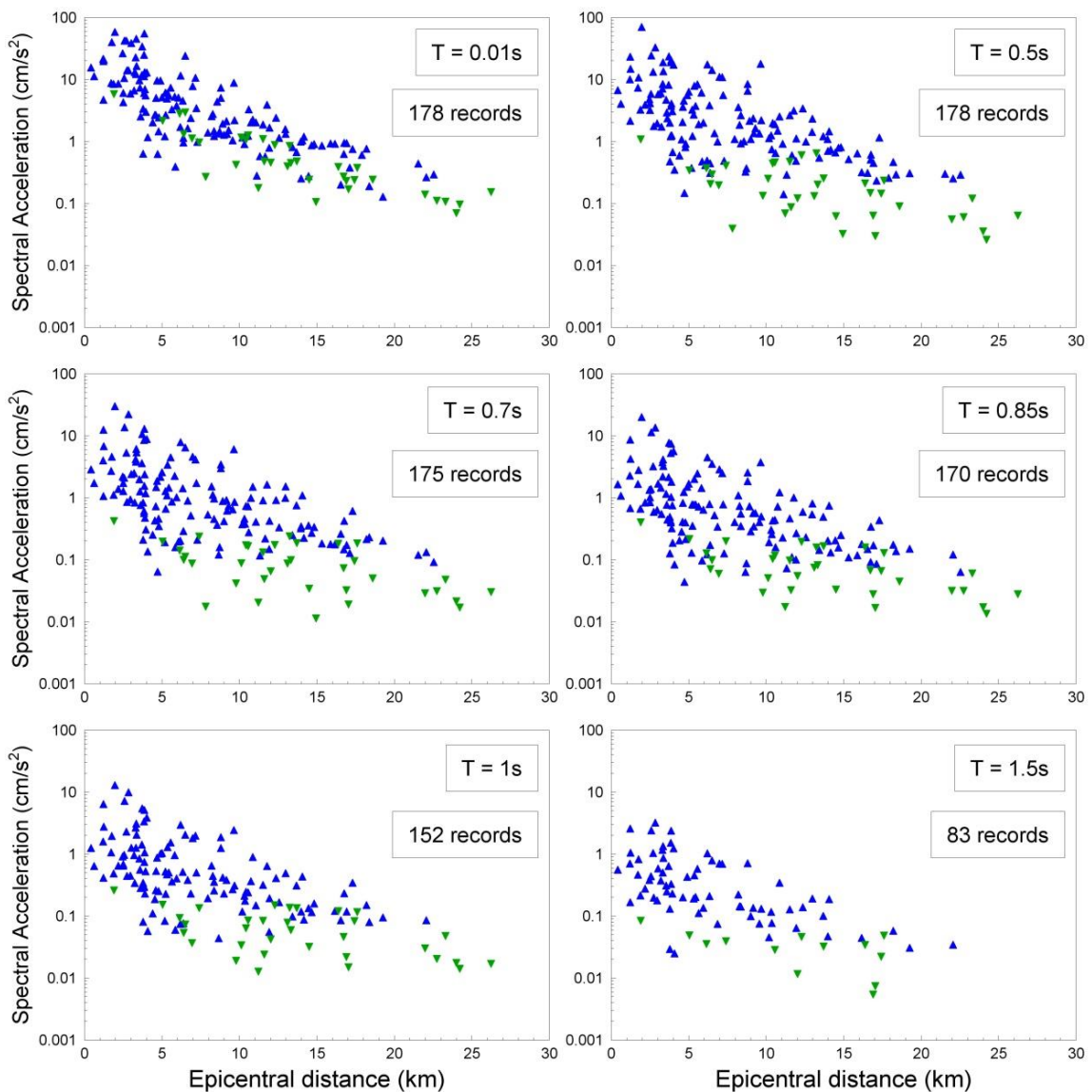


Figure 3.11. Geometric mean values of spectral accelerations at different oscillator periods plotted against epicentral distance; only the usable records are plotted at each period. The blue triangles correspond to surface recordings from the KNMI permanent accelerograph stations, and the green triangles to recordings obtained from geophones at a depth of 200 metres in the newly-installed borehole array

4. CHARACTERISATION of RECORDING STATIONS

In accordance with the decision to develop ground-motion predictions at the NS_B horizon and to then combine these with site amplification factors, the first stage of the work is to transform the surface recordings to the NS_B horizon. For this purpose, transfer functions at each of the recording stations, defined relative to the NS_B horizon, are required.

4.1. Site kappa values for recording stations

Surface stations

In order to guide the choice of damping models for site response analysis, initial estimates of damping at each site were calculated. This ensures that the ground-motion data, when deconvolved with the full NS_B-surface response, will not exhibit unphysical spectral shapes at high frequency (*i.e.*, negative κ). One method to estimate this damping at each station is to calculate site-specific κ_0 , and is addressed in the following paragraphs. It should be noted that the κ_0 values calculated in this section are first-order estimates of damping through the entire rock and soil column. They are therefore only used for guiding the selection of damping used in the site response analyses. The κ_0 value used for the simulation of ground motion at the NS_B is calculated later in this report, after the data have been deconvolved to the NS_B reference rock horizon.

Following the approach of Anderson & Hough (1984), the slope of the high-frequency decay ($-\pi\kappa$) of log-Fourier amplitude spectra of acceleration (FAS) is determined for each of the recordings in the V4 database with a sufficient signal-to-noise ratio (SNR). κ is measured directly from the recorded FAS by fitting a line with gradient equal to $-\pi\kappa$ to the high-frequency part of the log-FAS. The frequency range over which the slope is measured is from f_1 (lying above the source corner frequency) to f_2 , which is below the frequency at which the noise floor begins (Figure 4.1).

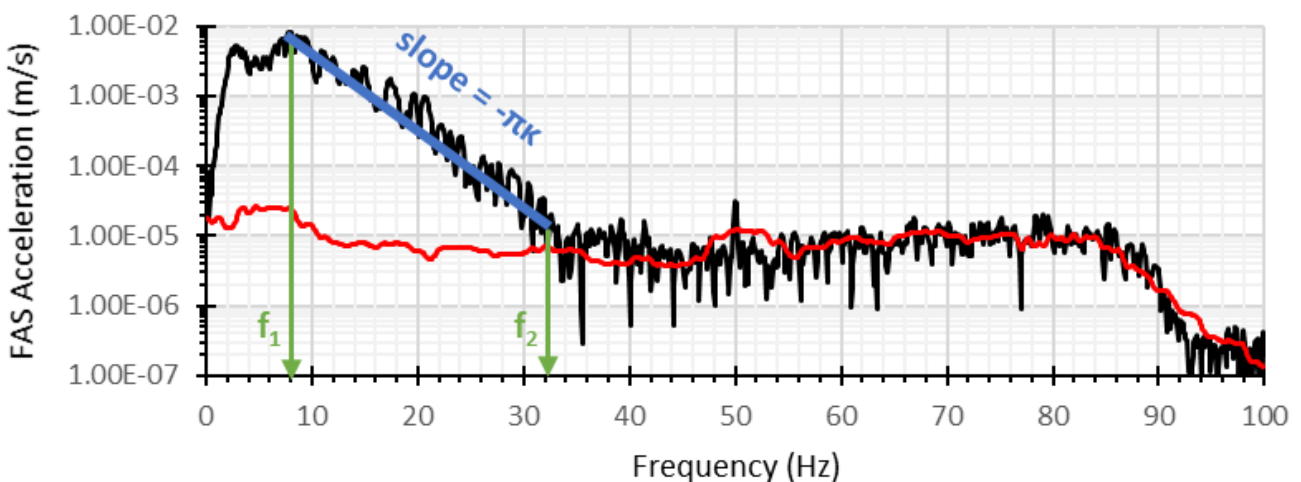


Figure 4.1. Example of κ measured from FAS recorded in the Groningen gas field. The black line indicates the earthquake signal, red the noise and blue the fitted slope in the frequency range $f_1 - f_2$.

The frequency f_1 was based on estimates for the source corner frequency in two magnitude ranges (M_L 2.5-2.7 and 2.8-3.6). Spectra were visually inspected to ensure that there were no significant resonant peaks in this range. However, due to the low velocity of the sites it is likely that these estimates are influenced by amplification effects (See Appendix II). As mentioned the κ_0 values calculated at the surface were simply used to test the selection of damping profiles to ensure that, upon deconvolution to the NS_B, that unphysical negative κ_0 was avoided.

The decay of the high frequency FAS, as characterised by κ , has, in the past, been attributed to both source, path and site effects. However, the majority of studies find dominant effects related to the path and site, with measured κ increasing with distance from the source. This has been interpreted as being related to Q , where attenuation acting along the whole path length contributes to the loss of high frequency energy, such that:

$$\kappa = \int_{r=0}^R \frac{1}{\beta(r)Q(r)} dr \quad (4.1)$$

where $\beta(r)$ and $Q(r)$ are the shear wave velocity and Q at given points along the propagation path, respectively. From borehole analyses (e.g., Abercrombie & Leary, 1993) it is apparent that the bulk of this observed high-frequency decay is due to attenuation (characterized by Q) in the uppermost layers of rock and soil. Since the near surface is (i) significantly more heterogeneous than the deeper layers and (ii) the time that the seismic waves spend in the near surface is significantly shorter it is common to separate path and site components in Eq. (4.1):

$$\kappa = \frac{R}{\bar{\beta}Q} + \kappa_0 \quad (4.2)$$

where $\bar{\beta}$ and Q are the average shear wave velocity and attenuation along the path (excluding the uppermost layers) and κ_0 is the path-independent site specific attenuation attributed to the uppermost layers. Conceptually this defines a layer-over-half-space, with the layer depth not explicitly defined. The component of κ that increases with distance from the source is attributed to Q in the half-space, while the 'zero-distance' part κ_0 is attributed to propagation in the upper layers, where body wave paths are almost vertical due to the velocity reduction. Consistent with its implementation in forward simulations (SMSIM: Boore, 2005a; EXSIM: Motazedian & Atkinson, 2005; Boore, 2009), and Eqs. (4.1) and (4.2) for short path lengths, the distance metric used in Eq. (4.2) is hypocentral distance. This is different from the distance metric used by Anderson & Hough (1984), which was epicentral distance. The minimum frequency used to measure the slope of the FAS of acceleration (f_1) was calculated based on the expected source-corner frequency for a $\Delta\sigma = 5$ MPa earthquake according to the model of Brune (1970) (see Section 5). f_1 is set to 10 Hz for earthquakes with $M_L \geq 2.7$, and 15 Hz for smaller events with $2.5 \leq M_L < 2.7$. The upper frequency (f_2) is record-specific and is defined as the highest frequency at which the signal-plus-noise-to-

noise ratio exceeds 2.5 [equivalent to a signal-to noise (SNR) of 1.5]; the identification of this upper frequency is performed automatically. An example of the κ fits is shown in Figure 4.2.

After measuring κ for all records with suitable SNR, κ_0 values for each station are determined by separating the path (Q) and site-specific components (κ_0) in Eq. (4.2). Different approaches can be used to effectively decouple the path and site components. In Anderson & Hough (1984) this was performed individually for each station, providing a unique slope of measured κ versus distance (or Q) for each station (although they did not state Q explicitly). As a field-wide average Q will subsequently be used in the simulations for response spectral ordinates at the NS_B, we therefore require damping, and hence κ_0 , values consistent with this field-wide average Q . Two approaches are used here, the first is to use an iterative approach—where we can take advantage of an outlier-resistant technique (minimisation of the misfit modulus, L1)—with an initial regression using all stations for a common Q and record-average κ_0 . Subsequent station-by-station regressions are performed using this Q as fixed, searching only for the best fitting site-specific κ_0 . The second approach is to solve simultaneously for Q and site specific κ_0 using a least-squares minimisation. The latter (matrix) approach avoids issues related to uneven data sampling.

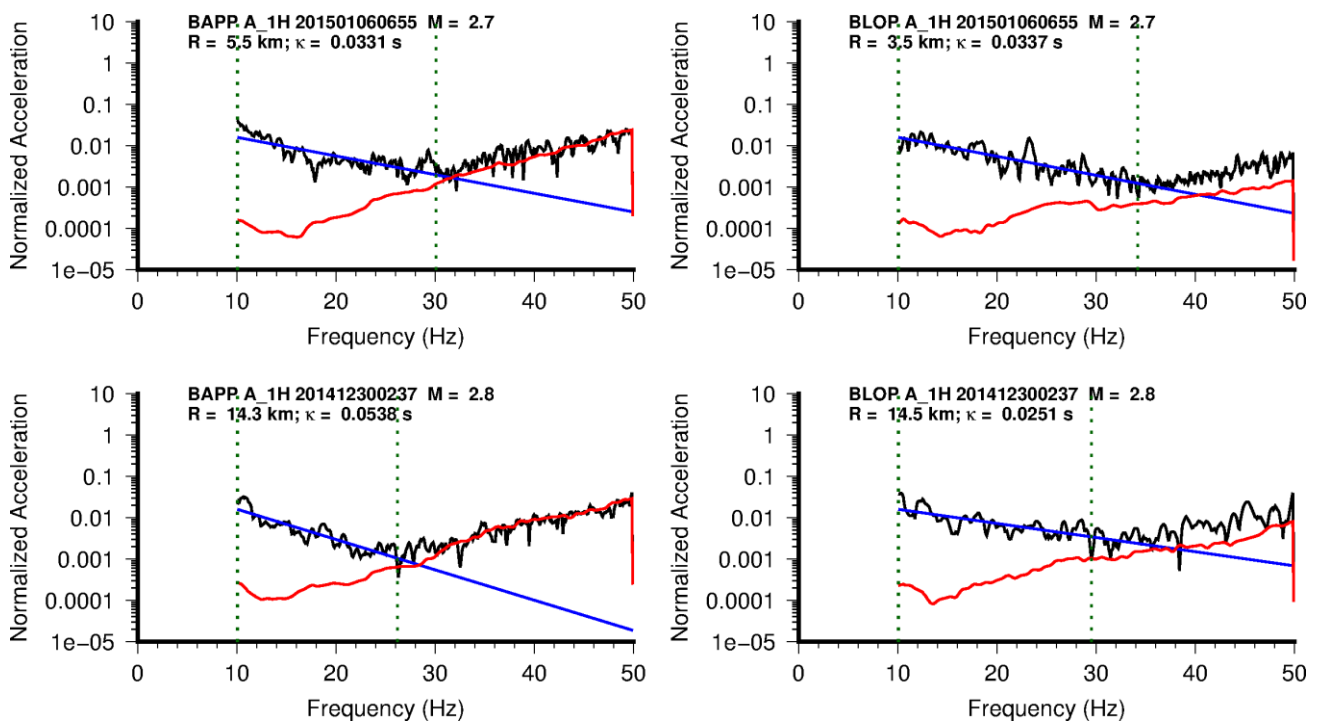


Figure 4.2. Example of $-\pi\kappa$ fits (blue) to the surface FAS of acceleration (black) for stations BAPP and BLOP. Noise FAS estimates are shown in red, with the fitting limits f_1 and f_2 indicated by dotted vertical lines.

Using all available data, the L1 solution for Q was 441 using an average shear-wave velocity of $\bar{\beta} = 2.6$ km/s. The value of $\bar{\beta} = 2.6$ km/s is the ‘average’ shear-wave velocity between the reservoir and surface for typical travel paths ($R_{\text{epi}} < 25$ km) as determined from NAM’s 3D V_s model. This value was used for all calculations (simulations and inversions) where an average path V_s was

required. A bug in EXSIM_dmb was corrected for (reported to and confirmed by Dr David M Boore) that initially did not use the path β appropriately to calculate damping in the simulations. For the purpose of comparison, the apparent Q was 328 using a more common average crustal shear-wave velocity of 3.5 km/s. A bootstrapping procedure was used to estimate the uncertainty, resampling the data 1000 times with random selection (with repetition) in each sub-sample. The resulting Q values have a mean value of 401 with lower and upper limits of the standard-deviation 262 and 846 respectively. Using the matrix approach, a Q value of 392 was found, with standard-error spanning limits 338 to 467. The mean values are higher than found in previous analyses performed in Groningen and in the wider region by KNMI. As concluded previously, the approach of Anderson & Hough (1984) is not suitable for robustly determining Q in Groningen due to the limited number of recordings that can be used (due to bandwidth and SNR limitations). The impact on the κ_0 values is nevertheless expected to be relatively small considering the large variability of measured κ (i.e., approximately 0.01 s at 20 km, and less for closer recordings). κ_0 values were obtained for 46 stations using (a) the mean Q value from the bootstrap analyses ($Q = 401$), (b) the matrix solution Q ($Q = 392$) and (c) $Q = 200$, which was used for ground motion simulations in the V3 model (Figure 4.3, Table 4.1).

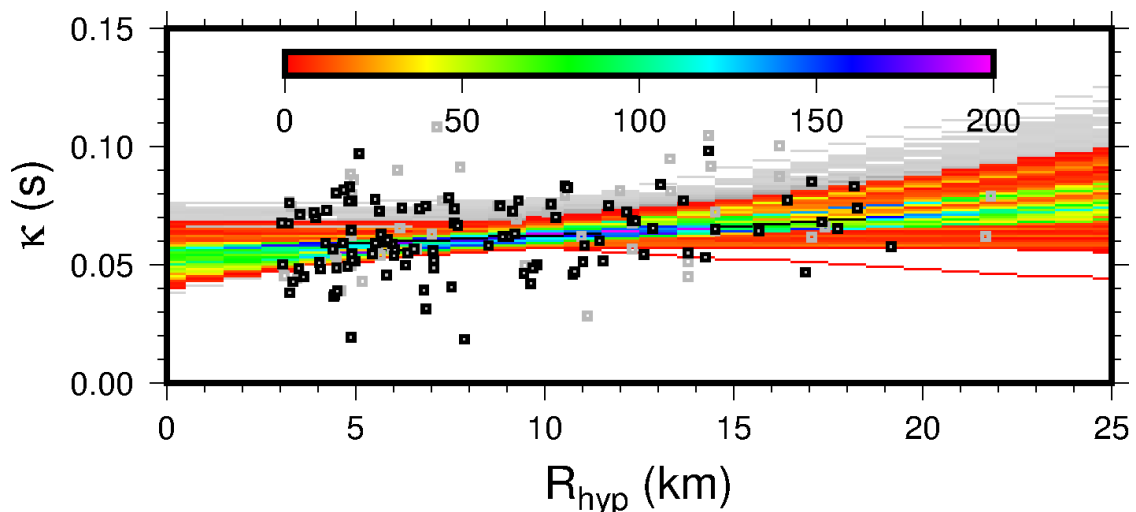


Figure 4.3. Bootstrap results of fitting Q and record-average κ_0 . Grey symbols and lines are from V2, black symbols and coloured lines are from the V3/V4 database. Colour indicates the density of solutions overlapping. Note that the data availability changed between V2 and V3/V4 due to (a) reclassification of magnitudes – and subsequent removal of $M_L < 2.5$; (b) inclusion of new events.

A comparison between the κ_0 values found for the current database (V4) and those values shown in the V2 GMPE report (Bommer *et al.*, 2015d) is shown in Figure 4.4 (note that the V3 database of surface recordings was identical to V4). On average, the κ_0 values are similar despite the differences in Q used to correct measured κ values for path effects. This indicates that the values are robust within the reported uncertainties, and is helped by the fact that the recordings are abundant at short distances, where path effects are small. The scatter between the V2 and V4 values nevertheless highlights the uncertainty of their determination, which is also consistent with the reported standard error (error bars, Figure 4.4). It is again

emphasised that the computations at this stage are for guidance of site response analyses only and are not directly used in the future simulations.

Table 4.1. Estimates of K_0 for Groningen accelerograph stations. Column headings in square brackets indicate the method (iterative or matrix: see text for description) and Q used.

	κ_0 (s) [iterative Q = 401]	Std. Deviation (s)	κ_0 (s) [matrix Q = 392]	Std. Error (s)	κ_0 (s) [matrix Q = 200]	Std. Error (s)	# Recs	V2 κ_0 (s) [matrix Q = 273]	Std. Error (s)
BAPP	0.0712	0.0148	0.0689	0.0058	0.0606	0.0060	3	0.0660	0.0091
BLOP	0.0530	0.0135	0.0510	0.0058	0.0440	0.0060	3	0.0455	0.0064
BMD2	0.0554	0.0124	0.0534	0.0058	0.0462	0.0060	3	0.0483	0.0077
BONL	0.0624	0.0073	0.0605	0.0058	0.0536	0.0060	3	0.0536	0.0079
BOWW	0.0631	0.0151	0.0620	0.0071	0.0579	0.0073	2	0.0638	0.0067
BUHZ	0.0416	0.0000	0.0391	0.0100	0.0300	0.0103	1	0.0583	0.0088
BWIR	0.0403	0.0045	0.0380	0.0045	0.0301	0.0046	5	0.0334	0.0078
BWSE	0.0632	0.0175	0.0611	0.0050	0.0536	0.0052	4	0.0469	0.0092
BZN1	0.0589	0.0000	0.0574	0.0100	0.0521	0.0103	1	N/A	N/A
BZN2	0.0592	0.0122	0.0571	0.0050	0.0497	0.0052	4	0.0542	0.0066
BMD1	0.0429	0.0000	0.0403	0.0100	0.0311	0.0103	1	N/A	N/A
GARST	0.0599	0.0100	0.0597	0.0035	0.0541	0.0036	8	0.0607	0.0063
KANT	0.0635	0.0140	0.0581	0.0045	0.0535	0.0046	5	0.0712	0.0085
STDM	0.0145	0.0000	0.0108	0.0100	0.0034	0.0103	1	0.0648	0.0086
WIN	0.0795	0.0000	0.0782	0.0100	0.0737	0.0103	1	0.071	0.012
WSE	0.0373	0.0108	0.0359	0.0050	0.0309	0.0052	4	0.0436	0.0062
MID3	0.0491	0.0100	0.0498	0.0038	0.0440	0.0039	7	0.0578	0.0085
ZAN1	0.0573	0.0142	0.0569	0.0058	0.0520	0.0060	3	0.0662	0.0071
ZAN2	0.0513	0.0113	0.0499	0.0058	0.0448	0.0060	3	0.0495	0.0063
BGAR	0.0402	0.0084	0.0411	0.0050	0.0351	0.0052	4	0.0621	0.0071
BHAR	0.0698	0.0003	0.0673	0.0058	0.0582	0.0060	3	0.0650	0.0075
BHKS	0.0524	0.0089	0.0497	0.0050	0.0401	0.0052	4	0.0477	0.0075
BSTD	0.0757	0.0000	0.0730	0.0100	0.0631	0.0103	1	0.0646	0.0124
BWIN	0.0625	0.0078	0.0602	0.0058	0.0521	0.0060	3	0.0561	0.0068
G094	0.0509	0.0127	0.0478	0.0071	0.0371	0.0073	2	0.0591	0.0091
G134	0.0439	0.0000	0.0389	0.0100	0.0209	0.0103	1	N/A	N/A
G184	0.0557	0.0000	0.0512	0.0100	0.0348	0.0103	1	N/A	N/A
G194	0.0673	0.0000	0.0637	0.0100	0.0509	0.0103	1	N/A	N/A
G204	0.0596	0.0000	0.0564	0.0100	0.0447	0.0103	1	N/A	N/A
G244	0.0562	0.0000	0.0528	0.0100	0.0407	0.0103	1	N/A	N/A
G294	0.0517	0.0165	0.0497	0.0071	0.0426	0.0073	2	N/A	N/A
G304	0.0467	0.0000	0.0448	0.0100	0.0382	0.0103	1	N/A	N/A
G344	0.0624	0.0003	0.0601	0.0071	0.0516	0.0073	2	N/A	N/A
G394	0.0542	0.0022	0.0523	0.0071	0.0456	0.0073	2	N/A	N/A
G404	0.0611	0.0000	0.0591	0.0100	0.0518	0.0103	1	N/A	N/A
G424	0.0404	0.0000	0.0395	0.0100	0.0364	0.0103	1	N/A	N/A
G434	0.0502	0.0000	0.0473	0.0100	0.0369	0.0103	1	N/A	N/A
G444	0.0347	0.0000	0.0303	0.0100	0.0143	0.0103	1	N/A	N/A
G524	0.0750	0.0000	0.0722	0.0100	0.0623	0.0103	1	N/A	N/A
G544	0.0454	0.0000	0.0421	0.0100	0.0302	0.0103	1	N/A	N/A
G554	0.0745	0.0000	0.0711	0.0100	0.0588	0.0103	1	N/A	N/A
G564	0.0684	0.0000	0.0657	0.0100	0.0562	0.0103	1	N/A	N/A
G604	0.0667	0.0000	0.0636	0.0100	0.0526	0.0103	1	N/A	N/A
G624	0.0608	0.0000	0.0560	0.0100	0.0388	0.0103	1	N/A	N/A

G644	0.0525	0.0000	0.0478	0.0100	0.0311	0.0103	1	N/A	N/A
------	--------	--------	--------	--------	--------	--------	---	-----	-----

From this analysis we can see that the surface κ_0 range between approximately 0.03 and 0.08 s (Figure 4.4). The field-wide average appears to be around 0.05-0.06 s (Figure 4.2). This indicates a high degree of damping that can be attributed to site-specific effects. It is consistent with the expectation for a typical site with $V_{S30} \sim 200$ m/s, where loose unconsolidated material or peats lead to significant damping of the incident seismic wave-field.

Borehole Stations

In the V4 database a number of records are at newly installed accelerograph stations, which have co-located borehole sensors available (station prefix G). For these stations we can perform additional analysis to estimate the damping due to the upper 200 m, *i.e.*, the material between the lowest sensor and the surface. Two approaches were used to do this:

1. Measure the slope (κ) of individual recordings at both the surface and 200 m borehole instruments individually. The difference between the two ($\Delta\kappa = \kappa_{\text{surface}} - \kappa_{\text{borehole}}$) amounts to an estimate of damping in the upper 200 m.
2. Take the ratio of the surface and borehole FAS and directly fit $\Delta\kappa$ that accounts for the propagation through the upper 200m (using (a) full FAS and (b) just FAS > 10 Hz). We also force $\Delta\kappa$ to be positive in this case.

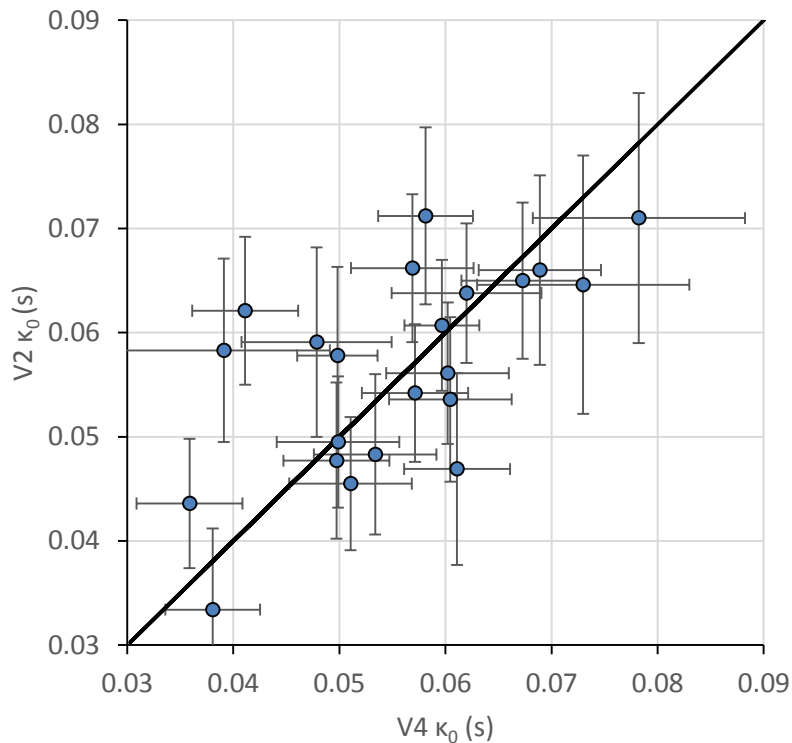


Figure 4.4. Comparison of κ_0 obtained for the expanded V2 dataset compared to the values found for the current Version 4 GMM dataset; error bars indicate standard errors.

Both methods aim to resolve the same phenomenon – the damping in the upper 200 m. The ratio method (no. 2, above) is, in principal, more insensitive to source effects (which are cancelled by taking the ratio) and choice of fitting bandwidth. However, in this analysis we did not account for the fact that:

- a. amplification is different in downhole and surface records;
- b. down-going (reflected) waves are present in the borehole record (κ in the borehole record is affected by both material above and below the sensor). Since the damping above the borehole is likely to be strong, the effect of the reflected waves is rapidly diminished for high-frequencies (e.g., $f > 10\text{Hz}$) leading to an apparent increase in κ in the borehole record. This means that any measurement of $\Delta\kappa$ will likely be a lower bound on the possible damping in the upper 200 m.

Figure 4.5 shows the results only (a) using the Hellum ($M_L = 3.1$) event, and (b) using all events with $M > 2$.

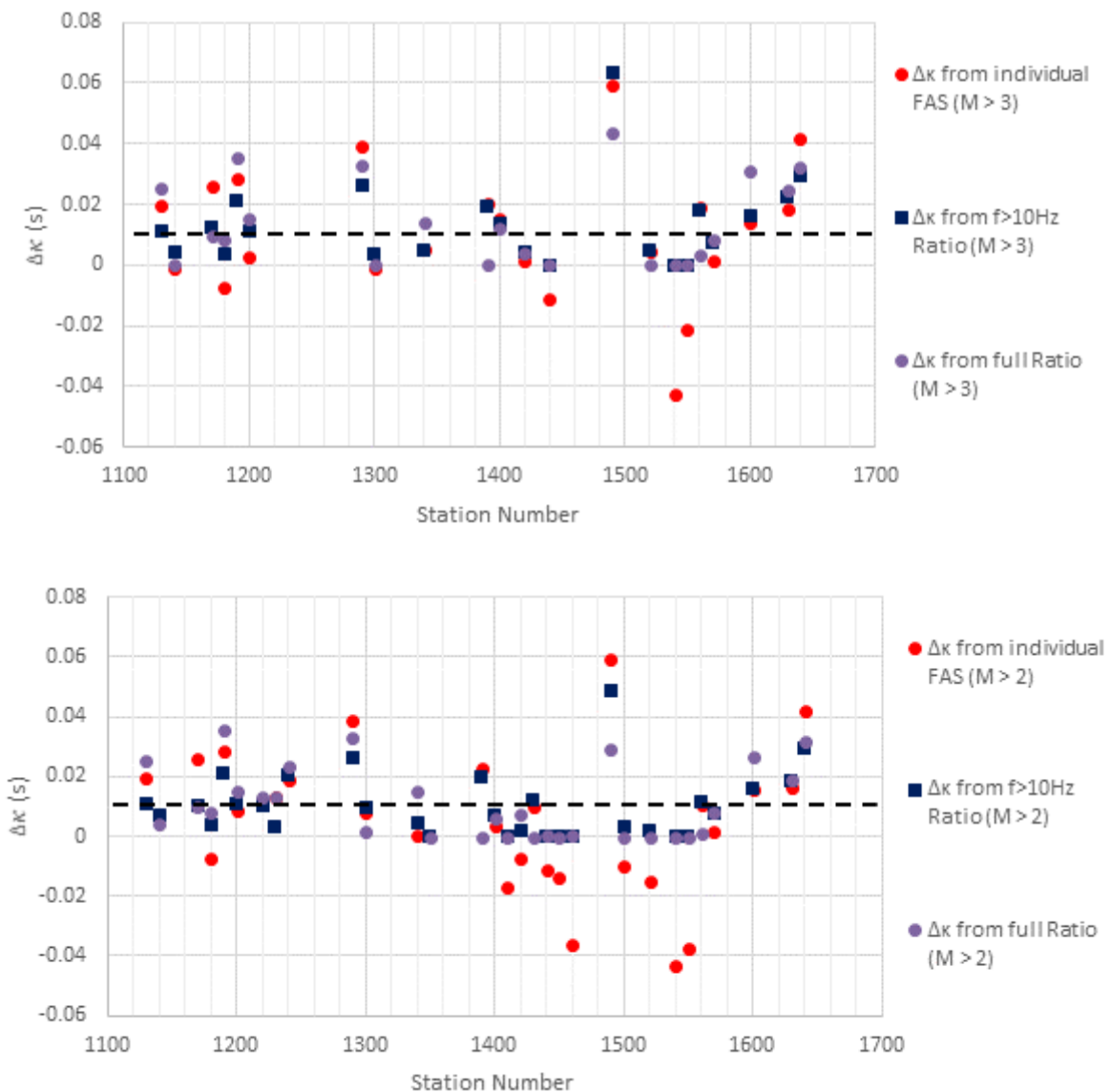


Figure 4.5. $\Delta\kappa$ ($\kappa_{\text{surface}} - \kappa_{\text{borehole}}$) determined for the available co-located surface/borehole instruments. Top: only data from the Hellum event ($M_L = 3.1$); bottom: all data $M_L > 2$. Note this data is outside the V3 database and was explicitly collected for the purpose of this task. The dashed line indicates the average $\Delta\kappa = 0.01$ s for the upper 200m.

The average value of $\Delta\kappa$ over all available stations was 0.01 s. However, individual stations did indicate stronger damping (up to 0.06 s). Others indicated less damping apparent at the surface than in the borehole. This is clearly an artefact and is probably due to the fact that amplification and surface reflection effects are not taken into consideration. Limiting the analysis to stations where $\Delta\kappa$ is consistent (*i.e.*, the standard deviation of observed $\Delta\kappa < 0.0065$ s), and where $\Delta\kappa$ is positive (13 sites), the average damping, assuming an average V_s of 350 m/s in the upper 200 m, is 1.2 % (only the Hellum data) or 1.3 % (all data $M_L > 2$), with individual values ranging from 0.5 % to 3%. The calculation of the damping values—using Eq.(4.3)—is discussed in the next section. As noted previously, due to the fact that reflections from the surface are incident on the borehole, these values should be considered as lower bounds. The range of κ_0 values determined for the surface ($V_{S30} \sim 200$ m/s), in addition to the -200 m borehole level ($V_{S30} \sim 500$ m/s) and at the NS_B are consistent with other data derived globally, and to various $\kappa_0 - V_{S30}$ relationships (Figure 4.6).

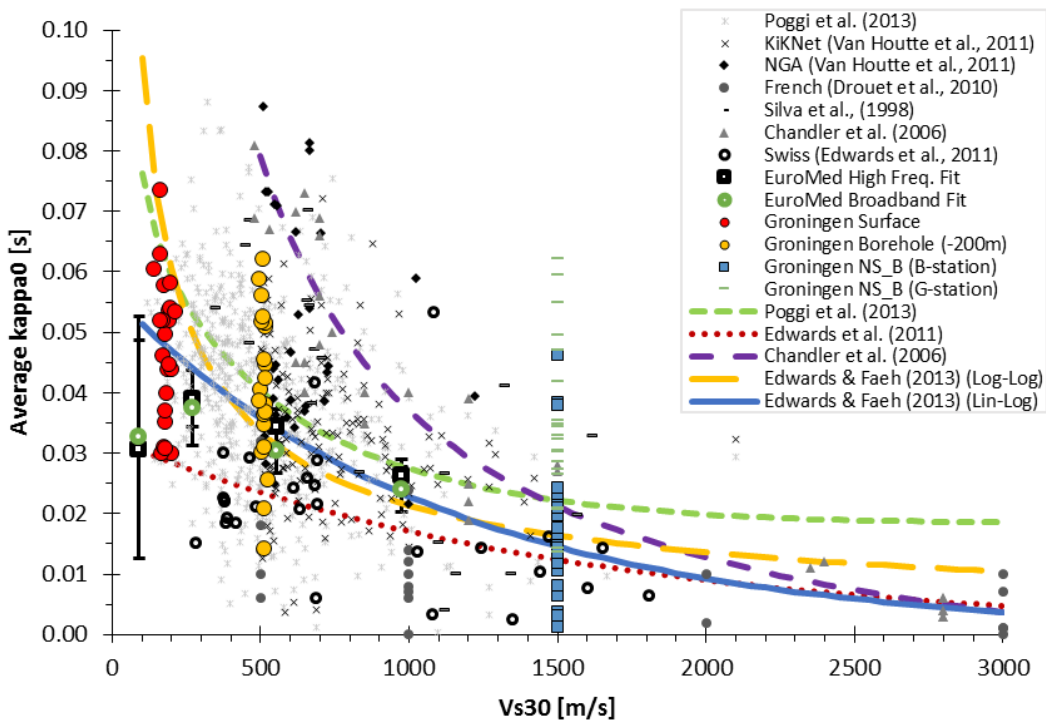


Figure 4.6 V_{S30} versus κ_0 for Groningen surface data (*red circles*) compared to data from other regions and existing $V_{S30} - \kappa_0$ relationships. The Edwards & Faeh (2013) log-log and linear-log fits indicated show the fit to all data in the plot (excluding Groningen). Figure modified after Edwards & Faeh (2013).

4.2. Station profiles for site response analyses

In order to deconvolve the motions recorded at the surface down to the NS_B horizon, it was necessary to calculate the transfer functions at the location of each recording station. In order to develop a GMPE including field-specific site response characteristics it is clearly very important to have the best possible dynamic characterisation of the locations at which the ground-motion recordings have been obtained. To this end a fieldwork campaign has been conducted by Deltares in August and September 2015 to determine representative V_s profiles at the locations of the KNMI accelerograph stations (stations with code B, Figure 3.3) to a depth of ~30 m. This fieldwork had a view to extend these measurements subsequently to the new accelerographs being co-located with the 200-m geophone boreholes (stations with code G, Figure 3.3).

Apart from profiles of V_s , profiles of density and damping at each of the locations are also required for the deconvolution of the motions recorded at the surface. Since only linear response is expected for the motions in the current database, modulus reduction and damping curves (against shear strain) are not required. The profiles developed for all of the station sites are presented in Appendix I, each plot showing the full profile down to the NS_B horizon and also the uppermost 50 m on separate plots in order to allow the near-surface details to be appreciated. The profiles from all the sites over the full depth are shown together in Figure 4.7. The plots confirm the consistency of the profile at greater depths, apart from the depth at which the NS_B is encountered (see Figure 2.5), and also the considerably variability of the near-surface profiles. The latter feature justifies the need for location-specific site amplification factors. Moreover, these profiles indicate that there is likely to be even greater lateral variation over the entire study area, which further reinforces the need to model the site amplification functions at different locations.

The profiles were developed by Deltares using a combination of field measurements of V_s (de Kleine *et al.*, 2016) and the field-wide models that have been developed as part of the Groningen seismic hazard and risk assessment project. Brief explanations regarding the sources of information for the three sets of profiles are given below. Greater details regarding many aspects of the profile construction are provided in Chapter 7, where the development of such profiles for non-linear site response analyses over the entire field is described.

Shear-wave velocity, V_s

The campaign of *in situ* measurements consisted of applying a wide range of techniques at the first few stations in order to test and calibrate the different approaches and to select those most suitable for general application across the networks. The multiple measurement approach was also designed to provide insight into the inherent uncertainty in the resulting V_s profiles and, to some extent, the degree of lateral heterogeneity at each site. The techniques used included seismic CPT (cone penetration testing), with differing offsets, active MASW (with multiple sources), passive multi-channel analysis of surface waves (MASW), cross-hole measurements and PS suspension logging. The full range of measurement techniques has been applied at pilot stations BAPP, BWSE and BUHZ. At the remaining “B” stations (*i.e.*, stations of the KNMI surface accelerograph network), only seismic CPT (SCPT) and MASW were applied.

Different techniques sample the V_s over different volumes of soil. The SCPT is a detailed, but very local determination of V_s (average V_s over ~ 1 m vertical distance, within ~ 1 m horizontal distance of the cone), whereas MASW averages V_s over much larger spatial scales (tens to hundreds of m, depending on the frequency of measurement). There are still unresolved issues regarding how representative a measured V_s profile (with a given method) is with respect to lateral heterogeneity and sampling volume. For the purpose of constructing V_s profiles that serve as input for the GMPE, the pragmatic choice was to use the V_s profile from the SCPT that was closest to the station. Only in case of unreliable results (in the top 1-4 m at 4 SCPT locations), the V_s was replaced by the MASW value. The intended maximum depth penetration of the SCPTs was 30 m below the surface. When the maximum cone pressure has been reached (15 ton), the sounding stops in order to avoid damage to the instrument. As a result, the maximum depth for seven SCPTs is considerably less than 30 m (21-27 m).

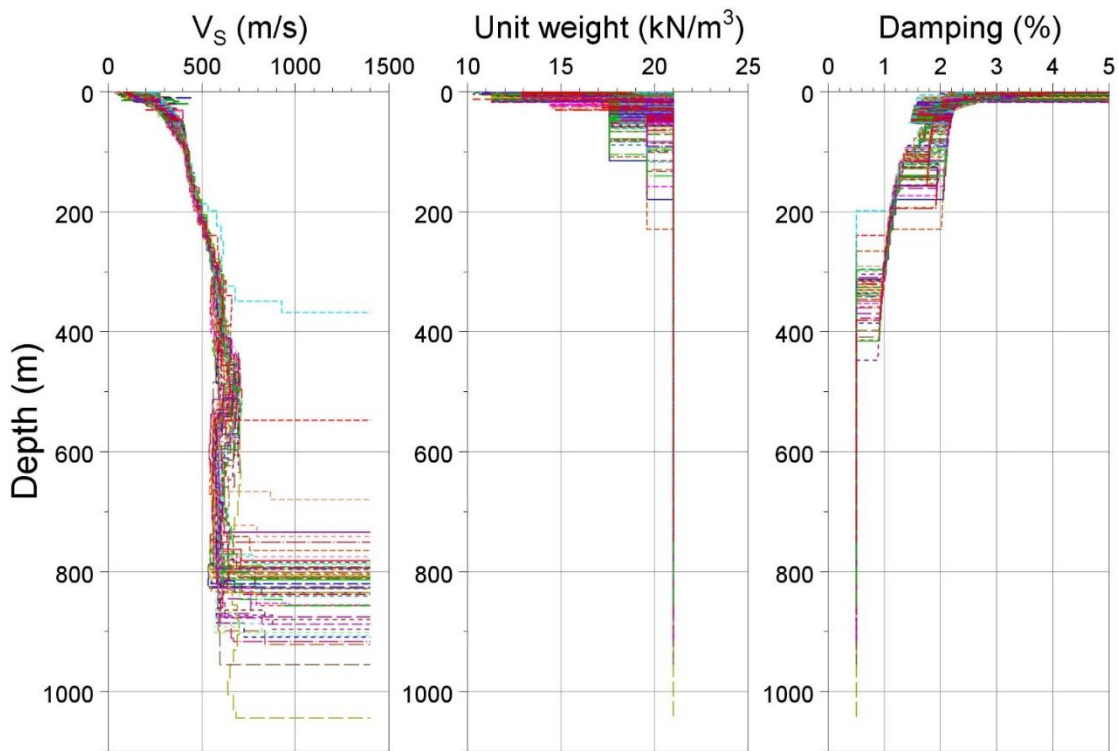


Figure 4.7. Profiles of shear-wave velocity, unit weight and density at the KNMI accelerograph stations; for the plots at individual stations see Appendix I

The measured V_s profiles in the top ~ 30 m for the B stations are included in Figure 4.7. No choice could be made for station BOWW. The two near-by measured SCPTs are very different in V_s profile and geology and have the same distance to the station. Therefore, both V_s profiles were included. The final choice was made with considerations of the results of inversion of ground motions (Chapter 5).

The full V_s profiles are a combination of measurements of V_s to a maximum depth of 30 m and three models of V_s of varying depth ranges. The V_s model is described in Kruiver *et al.*

(2017) and included in Sections 7.1 and 7.2. The shallow depth range from the surface to a maximum depth of 30 m consists of measured V_s profiles for the B stations. The next depth range, from the maximum depth of the SCPT to NAP-50 m (NAP is Normaal Amsterdams Peil, the Dutch Ordnance Datum) consists of V_s values assigned to vertical sections through the GeoTOP model of stratigraphic units and lithological class (Section 7.1). The V_s values are based on the average V_s measured in the Groningen SCPT dataset for each combination of stratigraphical unit and lithological class. The intermediate depth range, from NAP-50 m to approximately NAP-120 m, is based on the reinterpretation of the ground-roll (surface wave) signal from Shell's legacy data of land seismic surveys (Section 7.2). Between a depth of approximately NAP-70 m and the reference baserock horizon NS_B, the V_s is based on the Pre-Stack Depth Migration velocity model from the seismic imaging of the reservoir which is converted to a V_s model (Section 7.2).

Density and Unit Weight

The assignment of unit weight is based on representative values for lithostratigraphical units derived from CPTs using Lunne *et al.* (1997). For the Formations of Oosterhout and Breda, present at deeper depth ranges, the density is taken to be constant, consistent with the borehole logs from two NAM boreholes BRW5 and ZRP2 (see Section 7.4).

Damping

The values of small-strain damping are based on estimates from the quality factor Q measured at two borehole arrays of the old KNMI monitoring network at the edges of the Groningen field. The quality factor can be converted into the low strain damping:

$$D_{min} = \frac{1}{2Q} \quad (4.3)$$

De Crook and Wassing (1996) measured Q -values for KNMI borehole FSW, located at the eastern rim of the study area (Figure 3.2), at depths between 75 and 300 m. This borehole was the first experimental borehole deployed in 1991 and is equipped with four levels of geophones at 75 m spacing. In addition, a near-surface geophone was deployed for some time at 2.5m depth. Following Hauksson *et al.* (1987), using a simple spectral ratio technique, damping was measured and the average Q factor between 75 and 300 m was found to be $Q=40$, or its equivalent in terms of a damping factor 0.013 (1.3%). Attenuation in the upper 75 m could not be determined.

In a follow-up of this study, de Crook & Wassing (2001) measured damping in the upper 25m near the borehole ZLV (Zuidlaarderveen, at the southern rim of the study area, Figure 3.2). This borehole is equipped with two strings with 50m spacing between the geophone levels. Strings are co-located but at a vertical offset of 25m, resulting in a 25m spacing between the geophone levels. Using a seismic vibrator and recording the signal in a cone at depth intervals of 1 m, average damping in the upper 25 m was calculated, again using Hauksson *et al.* (1987). From the comparison between the modelled and the measured damping values, the results indicate a damping factor of 2-3%. The best estimated field-wide estimate of the

low-strain damping D_{\min} is shown in Figure 4.8. This damping profile, however, does not distinguish between soil types, and it is known from laboratory tests that the characteristics of the soil affect the values of D_{\min} (Darendeli, 2001; Menq, 2003). Hence, we adopt a hybrid approach whereas the laboratory-based damping values of Darendeli (2001) and Menq (2003) are scaled so that on average they match the profile shown in Figure 4.8. This approach is discussed in detail in Section 7.5. In addition, a model of D_{\min} for peats is developed for this study (see Section 7.6). Damping profiles for all the KNMI accelerograph stations are shown in Figure 4.7. Damping profiles for all the stations are given in Appendix I.

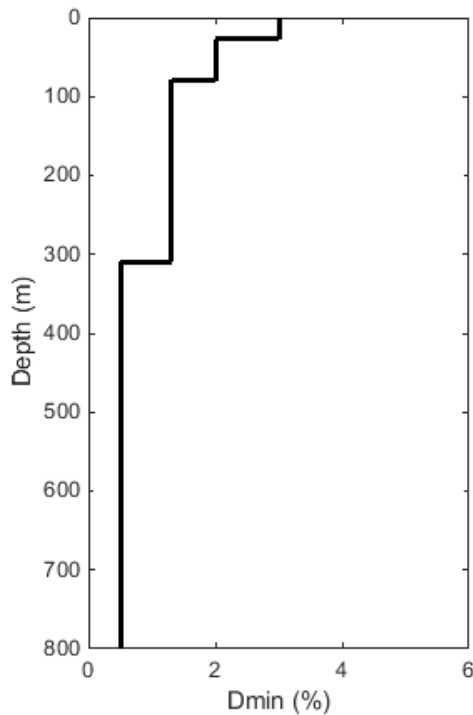


Figure 4.8. Low strain damping (D_{\min}) profile with depth obtained from Q measurements at downhole arrays near the Groningen field.

Surface Geology and V_{S30} at the Stations

Figure 4.9 shows the locations of the recording stations superimposed on the general geological map of the Groningen field from Kruiver *et al.* (2015). Table 4.2 summarises the surface geology and V_{S30} values at each B station. In general, the stations with lower V_{S30} values are found in the north of the field, where Holocene deposits of clays and peats are encountered, whereas the higher V_{S30} values are encountered to the south where Pleistocene deposits—mainly sands—predominate. Over the network of stations, the V_{S30} values measured at the stations range from 138 m/s to 251 m/s, with an average value of 179 m/s, standard deviation of 24 m/s and median value of 176 m/s. These values are broadly consistent with those determined for the entire field (Section 9.3). There are two important conclusions that can be drawn from these results, the first being that although the range of V_{S30} values may only be ~ 100 m/s, in terms of relative changes from one location to another the spatial variation is appreciable. Secondly, in most site classification schemes the entire study area would be denoted as ‘soft soil’ and therefore significant site effects may be expected.

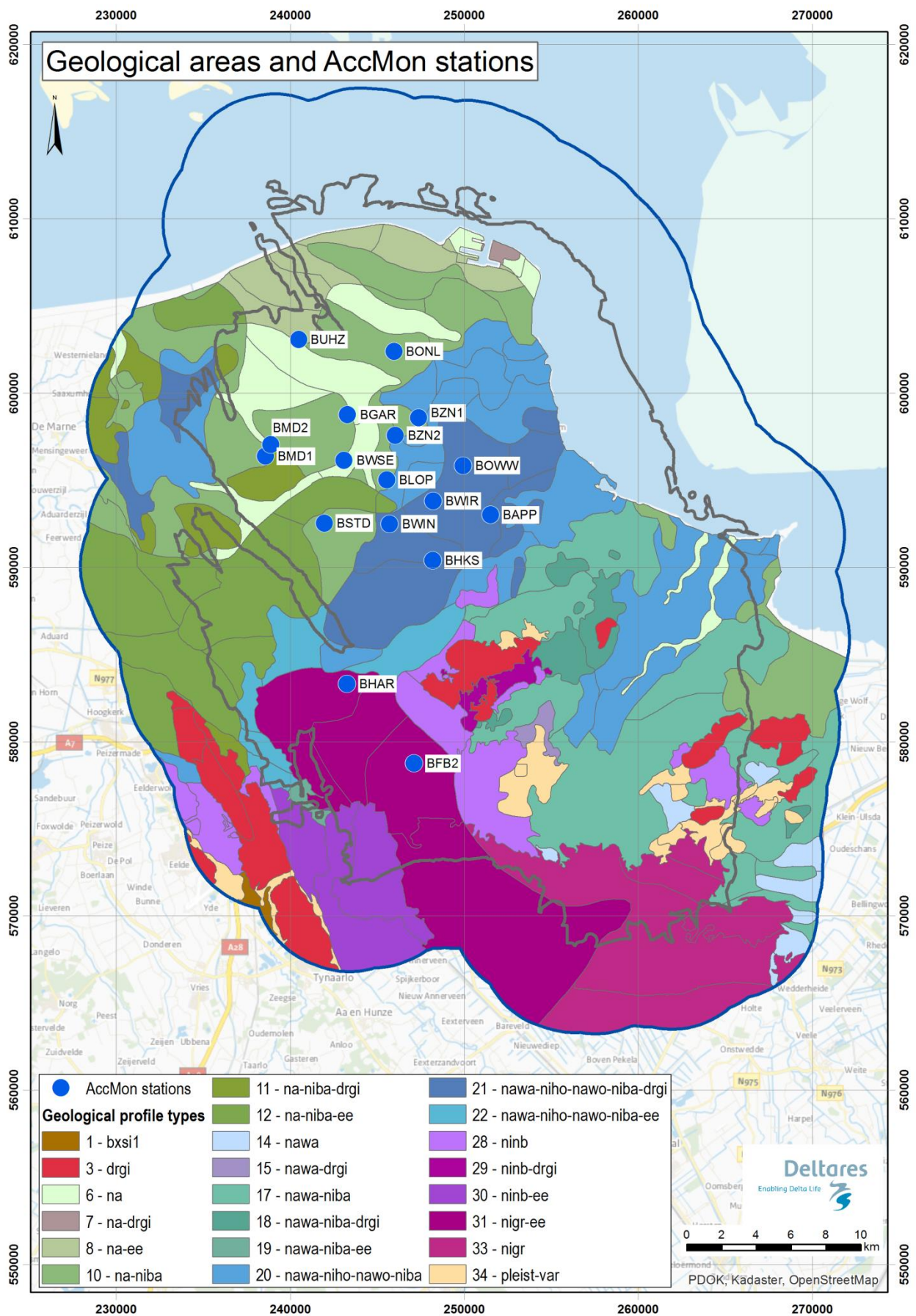


Figure 4.9. Geological map of the Groningen area from Kruiver *et al.* (2015) and Kruiver & Wiersma (2016) showing the locations of surface accelerograph (B-stations).

Table 4.2. Geological descriptions and measured V_{S30} values of B-station locations.

Station Code	V_{S30} (m/s)	Geological description of near-surface profile at station
BAPP	138	The location is situated in a non-erosive area. The Holocene deposits consist of clay with a peat layer in between at a depth of 1 metre. The basal peat is present in this area. Top of the Pleistocene is found at a depth of ~5 metres with a slope to the east to 6 metres. Glacial till is present. The location is situated in the middle of a Peelo valley at a depth of 180 metres.
BMD1	172	The location is situated in a non-erosive area bordering a small erosive valley in the north at a distance of 700 metres at a depth up to 15 metres. Pleistocene is covered by Holocene deposits with a thickness of ~10 metres. The deposits can be divided in a coverage layer of clay with a thickness of ~3 metres on a sandy layer. The basal peat and older clay has remained untouched and present.
BOWW	147-172 (two very different SCPTs)	The location is situated in a non-erosive area. The top of the Pleistocene is situated at a depth of 8 to 10 metres. The Holocene deposits consist of a clay layer with a peat layer in between at a depth of ~2.5 metres. Basal peat is present in this area. To the east at a distance of 500 metres is a small erosive valley with clay on top of boulder clay from the formation of Drente. The top of the boulder clay is found at a depth of 10 metres. The location is situated on the bottom of a Peelo valley at a depth of 100 metres.
BONL	192	The location is situated on a NW-SE running ridge with a width of 1500 metres and sided with Holocene erosion valleys at a depth up to ~25 metres. The Pleistocene is covered with ~14 metres of Holocene deposits mostly consisting of sand with clay layers. The base of the Holocene consists of basal peat or humid clay and therefore the top of the Pleistocene is not eroded.
BZN2	178	The location is situated in a non-erosive area bordering an erosive valley in the West. The Pleistocene is covered with Holocene deposits consisting mostly of sand that is part of an erosive system but at the base older clay and basic peat has remained untouched. Thickness of the Holocene is up to ~12 metres. The location is situated outside the Peelo valleys.
BZN1	192	The location is situated in a non-erosive area. The Pleistocene is covered with Holocene deposits consisting mostly of sand that is part of an erosive system but at the base older clay and the basal peat has remained untouched. Thickness of the Holocene is up to ~12 metres. The location is situated outside the Peelo valleys.
BGAR	193	The location is situated on the edge of a non-erosive area bordering an erosive valley in the east. The Pleistocene is covered with ~14 metres of Holocene deposits consisting of sands and clay. The base of the Holocene consists of Basic peat or humid clay and therefore the top of the Pleistocene is not eroded.
BWSE	198	The location is situated in a narrow Holocene erosive valley with a width of ~800 metres. The depth of the valley is 12 metres southwest of the location and deepening up to ~20 metres to the northeast. The Holocene fill of the valley is in the southwest in majority clay and to the northeast a mix of sand and clay. In the non-erosive surrounding area, the basal peat is found on the top of the Pleistocene. The accelerograph is positioned either within or just outside this Holocene valley. The site is position outside of the Peelo valley.
KANT	213	The location is situated in an erosive area within distance of 750 metres from a non-erosive area in the southeast. The Holocene deposit consist of clay with an erosive sand base on top of a thin Pleistocene sand layer. Underneath 'Pot clay' (Peelo formation) can be found. The location is situated in an erosive area within distance of 750 metres from a non-erosive area in the southeast. The Holocene deposit consists of clay with an erosive sand base on top of a thin Pleistocene sand layer. Underneath 'Pot clay' (Peelo formation) can be found. Top of the Pleistocene at the location is found at a depth of ~20 metres. In the southeast the top Pleistocene depth is ~10 metres with a slope to the north and the northeast to 25 metres.
BMD2	168	The location is situated in a non-erosive area bordering a small erosive valley in the West at a distance of 100 metres at a depth up to 15 metres. Pleistocene is covered by Holocene deposits with a thickness of ~10 metres. The deposits can be divided in a coverage layer of clay with a thickness of ~3 metres on a sandy layer. The basal peat and older clay has remained untouched and present.

Table 4.2. *Continued.*

Station Code	V _{S30} (m/s)	Geological description of near-surface profile at station
BWIN	176	The location is situated in a non-erosive area. The top of the Pleistocene is situated at a depth of 6 to 7 metres. The Holocene deposits consist of a clay layer with a peat layer in between, at a depth of ~3 metres. The basal peat is present in this area as is the glacial till. The location is situated on the bottom of a Peelo valley at a depth of 135 metres.
BSTD	162	The location is situated in a non-erosive area. The top of the Pleistocene is situated at a depth of ~9 metres. The Holocene deposits are clay layers. The basal peat is present in this area. Possibly part of the survey line is positioned on a small erosive channel. The location is situated on the declining slope of a Peelo valley that reaches from 40 metres at the location up to the maximum depth of 136 metres in the centre over a distance of 2.5 kilometres to the east.
BLOP	187	The location is situated in an erosive area with clay on top of the Pleistocene. The top of the Pleistocene is situated at a depth of ~10 metres. The Holocene deposits consist mainly of clay. To the south east at a distance of 500 metres a thin layer of basic peat covers the Pleistocene. The location is situated on a declining slope of a Peelo valley that reaches from 70 metres at the location up to the maximum depth of 115 metres in the centre over a distance of 2 kilometres to the southeast.
BWIR	163	The location is situated in a non-erosive area. The top of the Pleistocene is situated at a depth of 6 to 7 metres. The Holocene deposits consist of a clay layer with a peat layer in between at a depth of ~3 metres. The basal peat is present in this area as is the glacial till. The location is situated on a declining slope of a Peelo valley that reaches from 109 metres at the location up to the maximum depth of 115 metres in the centre over a distance of 0.5 kilometre to the northwest.
BUHZ	200	The location is situated in an erosional valley bordered in the east by a non-erosive area. Eem deposits (sand) are present. Pleistocene is covered with erosive Holocene deposits consisting of fine sand. Thickness of the Holocene differs from 14 metres in the east of the line up to 30 metres to the west in the centre of the erosive channel. The site is position outside of the Peelo valley.
BHKS	159	The location is situated in a non-erosive area. The Holocene deposit consists of clay with a peat layer in between at the depth of 0.5 metre. Basic peat is present in this area. Top of the Pleistocene is found at a depth of ~5 metres. Eem deposits (sands) are present. Glacial Till (Boulder clay) is present. At a distance of 1 kilometre to the west of the line an erosive valley at a depth of ~ 8 metre can be found oriented towards the northeast. Here the Holocene clay layer is present on the Pleistocene that consists of boulder clay or cover sand. The location is situated on a flat part of a Peelo valley between two deeper valleys, the base of the valley varies from 63 metres at the accelerograph station up to the maximum depth of 174 metres in the centre of the valley over a distance of 1.5 kilometre to the southwest.
BHAR	184	The location is situated in a non-erosive area. The Holocene clay has not been deposited only a peat layer is found on top of the Pleistocene. The peat layer has a thickness of 40 cm. To the north the peat layers thickens up to 1 metre. Eem deposits (sand) are present. The location is situated on the end of a declining slope of a Peelo valley that reaches from 70 metres at the location up to the maximum depth of 106 metres in the centre over a distance of 1.3 kilometres to the northwest.
BFB2	251	The location is situated in an area with cover sand (Boxtel Formation) at the surface. There are no Holocene deposits present. Locally some thin peat layers can be found at or near the surface. Eem deposits (sand and clay) are present. The location is situated on a declining slope of a Peelo valley that reaches from 78 metres at the location up to a maximum depth of 100 metres in the centre of the valley, over a distance of 1 kilometre to the southwest.

4.3. Site response analyses and linear amplification factors for stations

In order to apply the procedure illustrated in Figure 2.3 to develop the GMPE for rock motions at the NS_B horizon, it is necessary to transform the recordings to that level. For different elements of the model-building process, both the Fourier amplitude spectra (FAS) of acceleration and acceleration response spectra are required at the NS_B horizon, so amplification factors are required in both domains. The amplification factors are derived from the surface to NS_B (for all surface stations), and for the borehole level (-200 m) to NS_B for the borehole stations (G stations). The methodology applied to calculate these amplification factors is 1D linear analysis using the random vibration theory (RVT) approach as implemented in the program STRATA (see Section 8.1). As noted in the previous section, due to the low amplitudes of the recorded motions only linear response is expected hence the only input needed are the profiles described in Section 4.2, together with the properties of the elastic half-space starting at the NS_B horizon (*i.e.*, $V_s = 1400$ m/s, unit weight = 21 kN/m³).

The input motions at the NS_B horizon, which are required for the computation of the amplification functions for response spectra, are obtained from point-source simulations using the central model from the V3 GMM (Bommer *et al.*, 2016b; Bommer *et al.*, 2017). The motions are generated for a range of scenarios reflecting the ranges covered by the recordings: M_L 2.5 to 3.6, and distances from 0 to 20 km.

The analytical transfer functions computed with STRATA are smoothed using a Konno-Ohmachi filter (Konno & Ohmachi, 1998) with the b -parameter set equal to 40. The computed and smoothed FAS amplification factors, or transfer functions, are shown in Appendix II. The computed FAS are unique for all the input ground motion scenarios because of the linearity of site response. However, the response spectra amplification factors (AF) are scenario-dependent, in particular for short oscillator periods. The scenario dependence results from the interaction of the corner frequency of the input motions with the effects of the small-strain damping in the soil column. This phenomenon is explained in detail in Stafford *et al.* (2017). The AFs for station BAPP are shown in Figure 4.10 for all the input motions. The response spectra amplification factors for all the stations are shown in Appendix III.

The scenario-dependence of the AFs is illustrated in Figure 4.11 for selected periods. The AFs shown are only for station BAPP, but the same trends are observed at all stations. Figure 4.11 includes linear AFs for magnitudes up to M_L 6.0. Observe that the AFs are dependent both on magnitude and distance. For magnitudes in the range of the recorded earthquakes at Groningen ($M_L \leq 3.6$), the magnitude dependence of the AFs is nearly linear. To capture the distance dependence of the AFs, Figure 4.12 shows the AFs for $M_L = 3.0$, as well as the slope of the AFs versus magnitude (*i.e.*, the slope of the linear portion of the AFs shown in Figure 4.11). Observe that the distance scaling is close to linear, but there is a strong deviation from linearity at $R=7$ km, most likely related to the discontinuity of the geometrical spreading caused by the high-velocity Zechstein layer. Figures 4.10 and 4.11 plot AFs from the surface to NS_B, but a similar, although milder, dependence is seen for borehole to NS_B ratios.

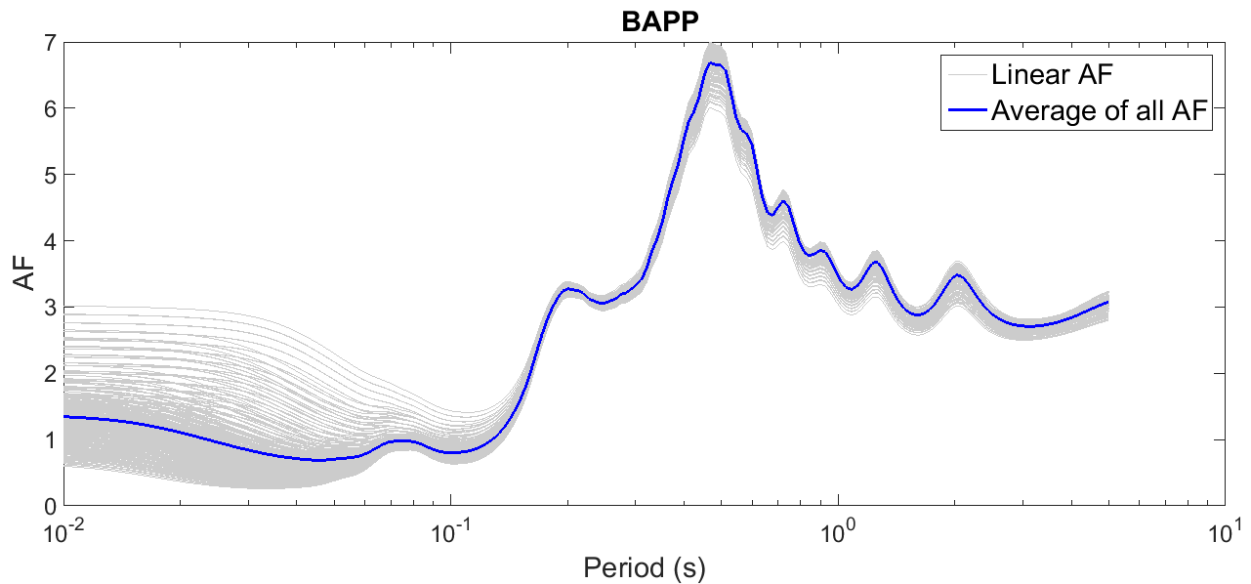


Figure 4.10. Spectral amplification factors (AF) for station BAPP. The thick lines are the AFs for all scenarios in consideration (M_L 2.5 to 3.6 and $R=0$ km to 20 km). The blue line is the average for all of the scenarios.

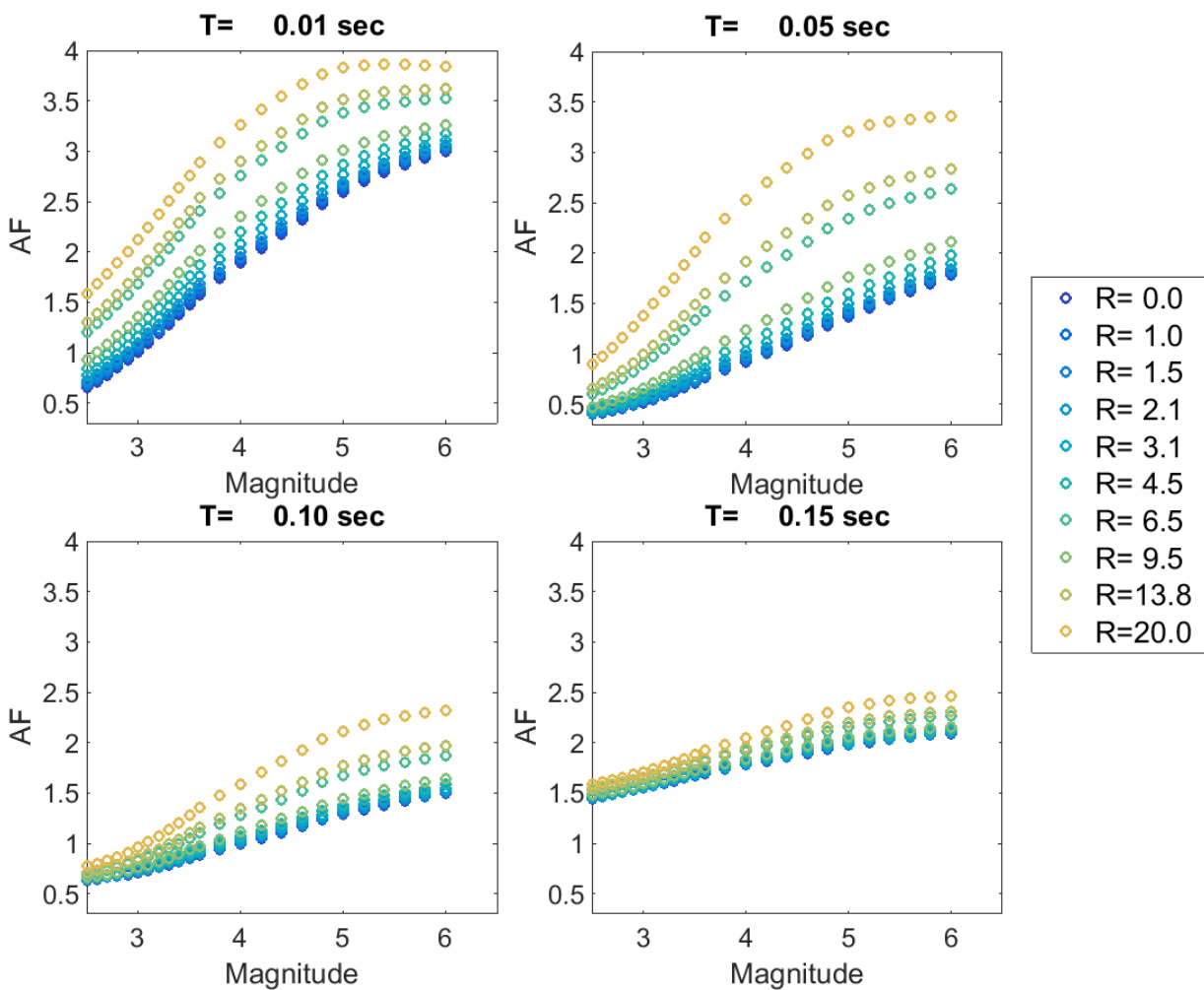


Figure 4.11. Spectral amplification factors (AF) for station BAPP and selected periods. Each AF is computed using linear site response for an input motion with a given magnitude and distance.

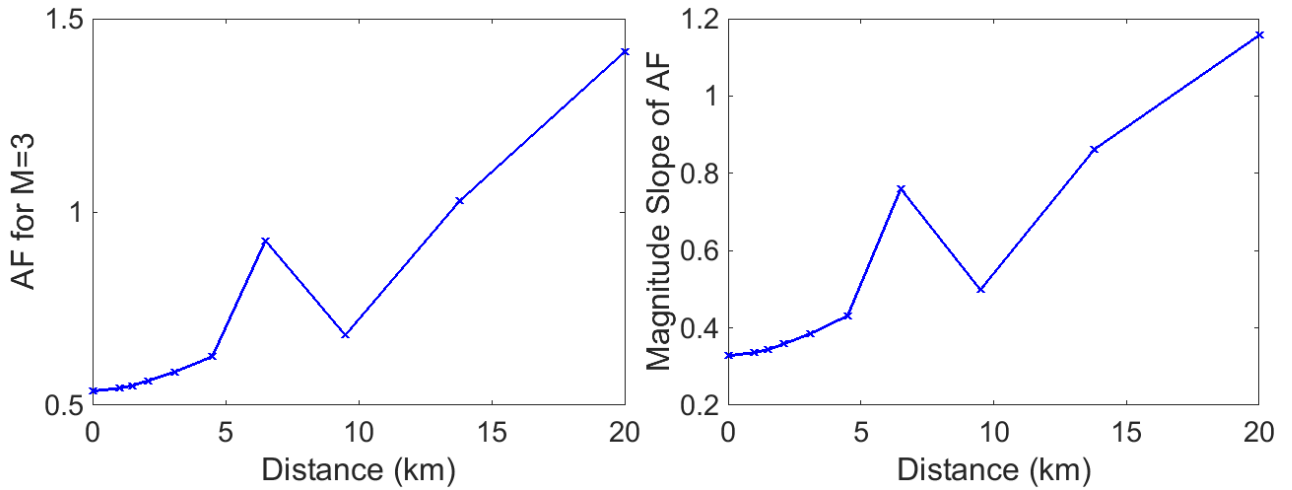


Figure 4.12. *Left.* Computed spectral amplification factors (AF) for station BAPP, $T=0.05$ sec, and $M_L=3.0$. *Right.* Slope of the magnitude dependency of AFs (*i.e.*, the slope of the linear portion in Figure 4.10) plotted as a function of epicentral distance.

In order to model the magnitude and distance dependence of the AFs at the station we make the simplifying assumption that the magnitude dependence is linear, and that the slope of AF versus magnitude has a linear dependence on distance. Hence, the following model defines the linear amplification factors for stations:

$$AF = (a_0 + a_1R) + (b_0 + b_1R)M_L \quad (4.4)$$

where a_0, a_1, b_0 , and b_1 are period dependent coefficients, R is epicentral distance in km and M_L is local magnitude. These parameters are computed for surface to NS_B ratios for the surface stations, and for the ratio of within motion at a depth -200 m to outcrop NS_B for the borehole stations. The model is only applicable for $M_L \leq 3.6$ and $R \leq 20$ km. The fit of the model in Eq.(4.4) to the computed AF at the BAPP station are shown in Figure 4.13.

The scaling with magnitude and distance is strongly site-dependent. This is illustrated in Figure 4.14 by a histogram of the slope of the AF versus magnitude for all of the B-stations. Note that for very short oscillator periods ($T \lesssim 0.1$ s) these slopes vary significantly from station-to-station. The same degree of station-to-station variability in the magnitude scaling of the site terms was observed in an analysis of ground motion data from KiK-net array sites (Stafford *et al.*, 2017). In this study, stronger magnitude scaling was observed at sites with lower V_{s30} , which is consistent with the explanation that the scenario dependence of AFs is related to small strain damping. As the oscillator period increases, magnitude dependence of the AF becomes milder (Figure 4.11). Stafford *et al.* (2017) also observed that scenario dependence of site-terms derived from KiK-net array ground motion data is only observed for oscillator periods lower than about 0.2 s.

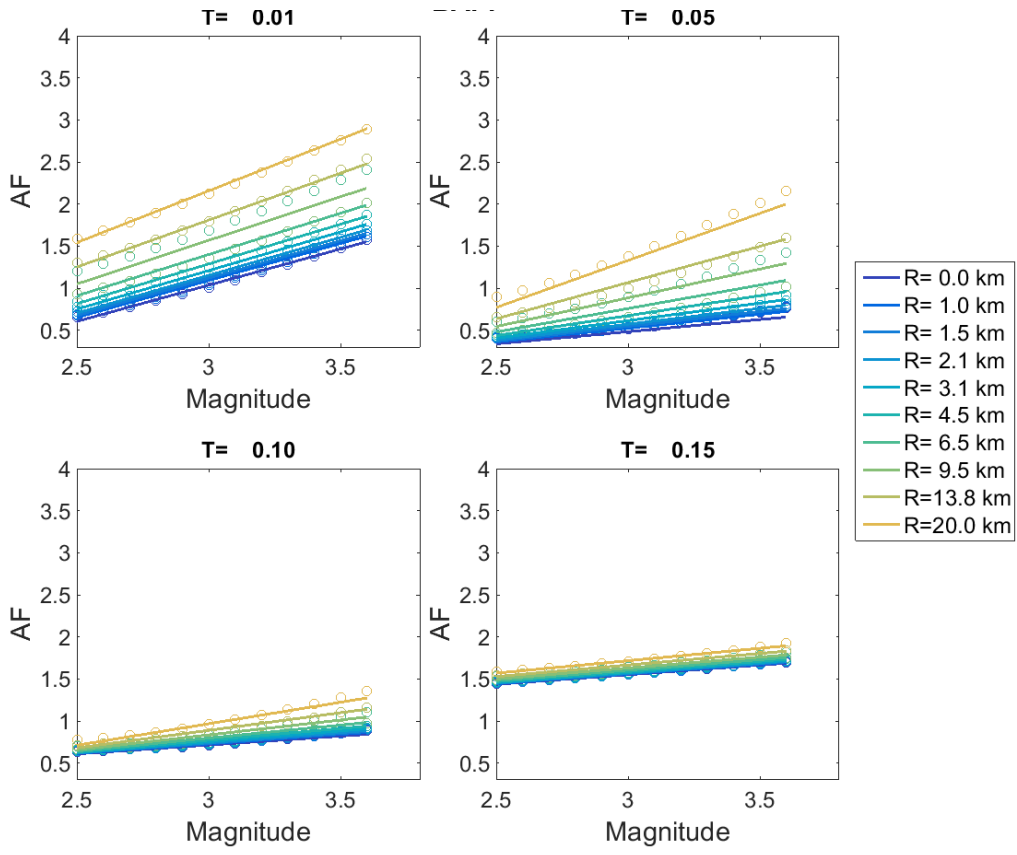


Figure 4.13. Spectral amplification factors (AF) for station BAPP and selected periods (circles) and the model of Eq.(4.4).

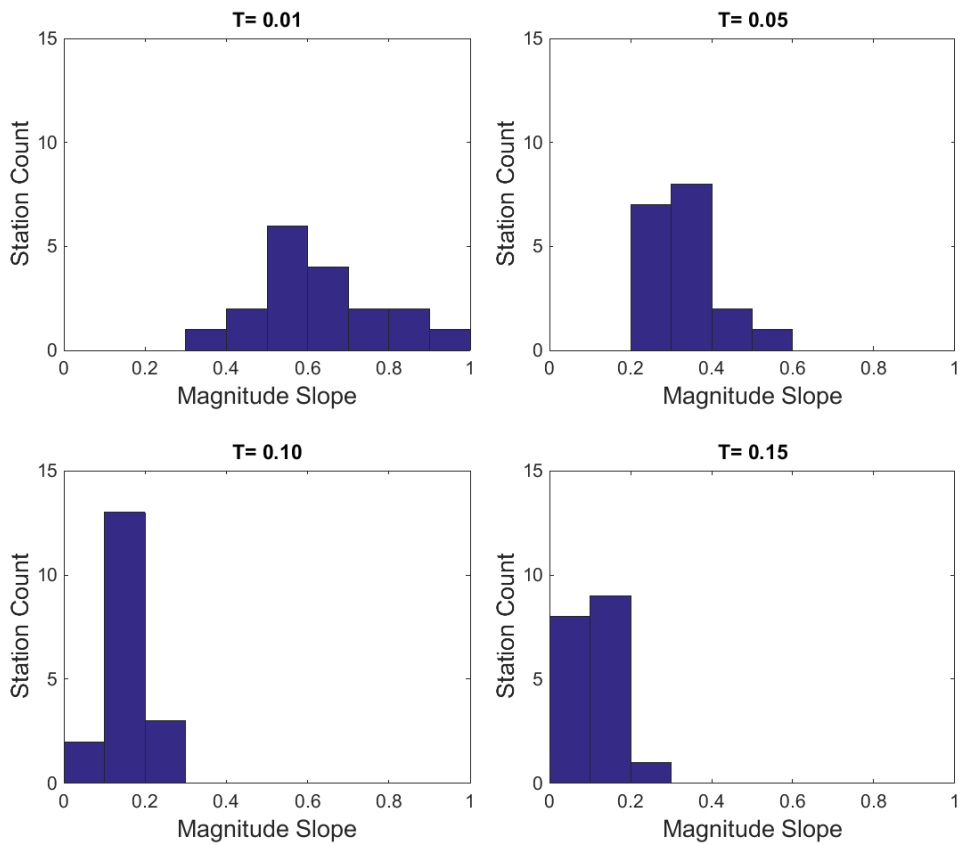


Figure 4.14. Histogram of the slope of AF versus M_L for all of the B-stations.

5. INVERSIONS of GROUND MOTIONS for SOURCE, PATH and REFERENCE ROCK PARAMETERS

In view of the limited magnitude range of the earthquakes currently represented in the Groningen ground-motion database—with an upper limit of M_L 3.6—one of the key challenges in developing the GMPEs for the hazard and risk models is the extrapolation to the largest magnitude currently considered, M 7.25. For previous (V1-3) GMPEs, this extrapolation was performed using point-source simulations based on seismological theory, with finite-fault effects accounted for using an empirical model. In the V4 model, ground-motions are calculated using finite-fault, stochastic simulations. The method used is based on a discretised rupture model with dynamic corner-frequency (EXSIM: Motazedian & Atkinson, 2005; EXSIM_dmb: Boore, 2009). Each of the distributed sub-faults in this technique is assumed to be a point source (effectively a small magnitude earthquake), and can be characterised using the seismological parameters observed in events recorded in the Groningen gas field. More specifically, the seismological characteristics required for modelling ground motion using EXSIM are estimates of the source, path and site parameters that define the Fourier amplitude spectra (FAS) and duration of the motion throughout the Groningen Field. This chapter presents the inversion of the FAS of the Groningen ground-motion recordings to obtain estimates of these parameters.

5.1. Fourier amplitude spectra at the reference rock horizon

In order to develop a finite-fault stochastic ground-motion simulation model at the reference rock horizon (the base of the Lower North Sea group, NS_B; Section 2.3) we require source, path and reference rock parameters valid at the horizon. The recorded surface motions are therefore first deconvolved with the response of the overlying material in order to obtain FAS as if they had been recorded as outcrop motions at the NS_B (Figure 5.1).

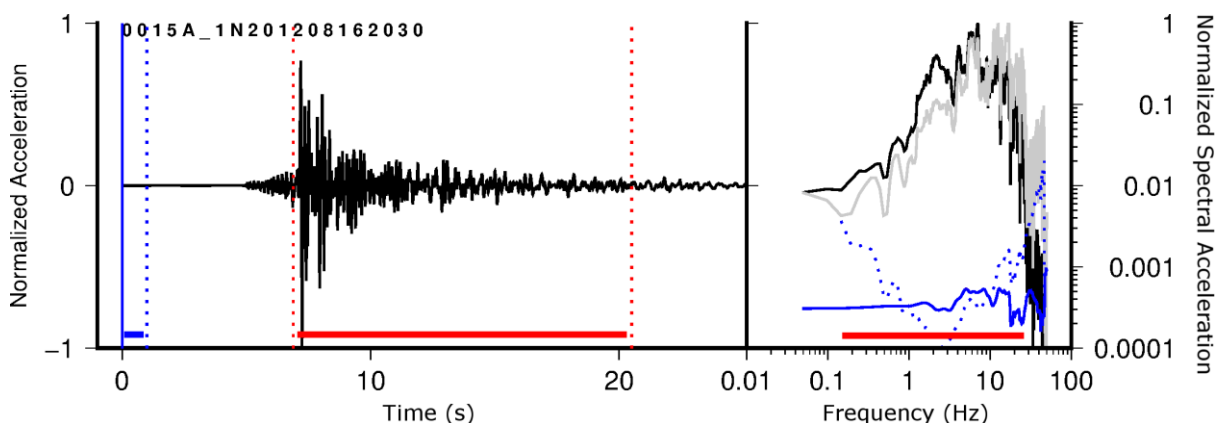


Figure 5.1. *Left*: example acceleration time series of the 2012 M_L 3.6 Huizinge earthquake recorded at station 15 (GARST), 14 km from the epicentre. The period highlighted in red indicates the S-wave signal and in blue the noise. *Right*: Fourier amplitude spectrum of the acceleration time series. Black: as recorded at the surface; grey: deconvolved to the NS_B; solid blue: recorded noise; dotted blue: noise after deconvolution to the NS_B and low frequency adjustment; the frequency range highlighted in red shows the FAS used in inversions (SNR > 2)

Fitting source, path and site parameters for developing a stochastic simulation model requires only the amplitude spectra. Therefore, the phase information is not required and the deconvolution simply involves dividing the FAS of recordings at the surface—calculated using a (5π -prolate) multi-taper Fast Fourier Transform—by the FAS transfer functions. Since the recordings are all weak-motion—and therefore not expected to exhibit non-linear amplification effects—we use linear site transfer functions to achieve this (as presented in Section 4.3, Appendix II). For sites where 200 m borehole instruments were used, the FAS deconvolution was performed using the ‘within rock’ transfer functions such that the effect of surface reflections, incident on the borehole instrument, was removed. This deconvolution provides a fully consistent approach as the same amplification functions (albeit with non-linear effects at high ground-motion levels) are used to transform the reference horizon GMPE back to the surface during hazard calculations.

5.2. Overview of inversion process for source, path and reference rock parameters

The FAS of recordings from 22 Groningen earthquakes (Section 3.2), deconvolved to the NS_B horizon, are used to determine the source, path and reference rock parameters. Initially the FAS are fit in the log-linear acceleration-frequency domain to estimate the slope of the high-frequency decay: κ (Anderson & Hough, 1984). κ values were previously measured (at the surface, rather than at the NS_B) using only the high frequency information ($f > 10$ Hz) from a limited number of records (as described in Section 4.1). However, it is not possible to use this approach for band-limited or noisy recordings, and those of smaller earthquakes (which still constitute a significant portion of the V4 database). Record-specific κ values at the NS_B were therefore estimated for all horizontal FAS using a broadband method to extend the usable frequency range to lower frequencies (e.g., Scherbaum, 1990). The approach we are using is detailed in Edwards *et al.* (2011) and fits the FAS with an earthquake far-field point-source model [e.g., Brune (1970, 1971)], defined by its source-corner frequency (f_{0i}) and long-period spectral displacement plateau (related to the seismic moment, M_0), along with the κ parameter to account for attenuation. The FAS for an acceleration recording is given by:

$$\Omega_{ij}(f) = 4\pi^2 f^2 \hat{\Omega}_{ij} E_i(f, f_{0i}) B_{ij}(f, \kappa) T_j(f) \quad (5.1)$$

where f is the frequency and i and j represent the i^{th} source and j^{th} station respectively. $\hat{\Omega}_{ij}$, the far-field spectral displacement plateau, is a frequency independent parameter that is dependent on the seismic moment (M_0), average amplification, geometrical spreading, shear wave velocity and density at the source, and radiation pattern effects. $E_i(f, f_{0i})$ is the normalised (i.e., unit amplitude at long-periods) Brune (1970, 1971) source model with a defining corner-frequency f_{0i} :

$$E_i(f, f_{0i}) = \frac{1}{\left(1 + \left(\frac{f}{f_{0i}}\right)^2\right)} \quad (5.2)$$

$B_{ij}(f, \kappa)$ is the attenuation along the whole path from source to station:

$$B_{ij}(f, \kappa) = e^{-\pi f \kappa} \quad (5.3)$$

The site amplification function, $T_j(f)$, reflects the amplification between the source and, in this case, the NS_B horizon, in addition to any effects not fully accounted for through the deconvolution described in Section 5.1.

Frequencies up to 45 Hz are considered in the fitting, with the bandwidth of individual spectra defined based on the measured signal exceeding the pre-event noise by a factor 3 (*i.e.*, signal-plus-noise to noise ratio > 3, or SNR > 2). A least-squares minimisation is performed to find the best fitting event-specific f_{0i} (using a grid-search at 5% resolution) and record specific $\hat{\Omega}_{ij}$ and path-specific κ_{ij} values (using Powell's conjugate direction method) for FAS in the lin-log space. Then, using the high-frequency decay term, κ_{ij} , defined in the previous step the FAS are refit in log-log space (with the same least-squares minimisation, this time fixing κ_{ij}) to more robustly determine the record-specific $\hat{\Omega}_{ij}$ and the event-specific f_{0i} .

The stress parameter, $\Delta\sigma$, is obtained from the source corner frequency and the seismic moment using the Brune (1970, 1971) and Eshelby (1957) models:

$$\Delta\sigma = f_0^3 M_0 / (0.4906\beta)^3. \quad (5.4)$$

Where M_0 (in SI units) is given by (Hanks & Kanamori, 1979):

$$M_0 = 10^{1.5M+9.05}. \quad (5.5)$$

The shear-wave velocity at the source, $\beta = 2.0$ km/s (Remco Romijn, *personal communication*); this differs from the path average $\bar{\beta} = 2.6$ km/s, and is taken with a high degree of certainty from NAM's 3D Vs model. The moment magnitudes are provided by KNMI, given that $\mathbf{M} = M_L - 0.2$. The far-field spectral displacement plateau, $\hat{\Omega}_{ij}$, is next decomposed into average site amplification and geometrical decay as a function of distance using the approach detailed in Edwards *et al.* (2008). The far-field long period spectral amplitude is defined as:

$$\hat{\Omega}_{ij} = \Omega_{0i} A_j S_{ij}(r, r_{0\dots n-1}, \lambda_{1\dots n}). \quad (5.6)$$

where $S_{ij}(r, r_{0\dots n-1}, \lambda_{1\dots n})$ is the amplitude decay with distance or ‘apparent geometrical spreading’, given by:

$$S_{ij}(r, r_{0\dots n-1}, \lambda_{1\dots n}) = \begin{cases} \left(\frac{r_0}{r}\right)^{\lambda_1} & r \leq r_1 \\ S(r_1) \left(\frac{r_1}{r}\right)^{\lambda_2} & r_1 \leq r \leq r_2 \\ \vdots & \vdots \\ S(r_n) \left(\frac{r_n}{r}\right)^{\lambda_n} & r \geq r_n \end{cases} \quad (5.7)$$

with r the hypocentral distance, $r_{n>0}$ are distances at which the rate of decay changes from λ_n to λ_{n+1} , and r_0 is the rupture radius. A_j is the site amplification parameter independent of frequency, and Ω_{0i} is the effective long period plateau value at the source location:

$$\Omega_{0i} = \frac{M_{0i} F \Theta_{\lambda\Phi}}{\beta^3 \rho r_0 4\pi}, \quad (5.8)$$

Brune (1970). F is the free surface amplification ($F = 2.0$ for normally incident SH waves and a good approximation for SV) and ρ is the crustal density ($\rho = 2600 \text{ kgm}^{-3}$). Due to the definition of Equations 5.6 to 5.8 the rupture radius (r_0) cancels out and does not need to be explicitly determined. Furthermore, since \mathbf{M} , and therefore M_0 are pre-defined, and we assume a constant radiation pattern coefficient of $\Theta_{\lambda\Phi} = 0.55$ (Boore & Boatwright, 1984), the only remaining terms to determine are (i) average site amplification, A_j , and (ii) variables related to the geometrical decay (Equation 5.7).

5.3. Alternative inversion formulations

Source Models

The use of Brune’s theoretical far-field earthquake source model (Brune, 1970) in previous versions of the GMPE (V1-3) was based on the fact that it has been frequently used in the literature for modelling earthquake FAS, and was found to provide a good fit to the Groningen earthquake data. However, alternative source model formulations are available. The most common used for point source simulations is Boatwright’s (1978) model. Boatwright presented a generalised model:

$$E_i(f, f_{0i}) = \frac{1}{\left(1 + \left(\frac{f}{f_{0i}}\right)^{2\gamma}\right)^{0.5}} \quad (5.9)$$

Such that the displacement FAS is flat (horizontal) at low frequencies ($f \ll f_{0i}$), and decay proportional to ω^γ at high frequency ($f \gg f_{0i}$). For $\gamma=2.0$, this is similar to Brune's model but with a sharper corner. As with Brune's model, the shape of Boatwright's source model is defined solely by its corner-frequency, f_{0i} . In order to test the suitability of Boatwright's model, we have implemented it in the inversion by replacing the Brune formulation of $E_i(f, f_{0i})$ in Equation 5.1 with that of Equation 5.9, using $\gamma=2.0$. Other source models, such as double corner-frequency models are also plausible, especially considering the possibility of elongated faults at larger magnitudes (*i.e.*, a large fault area contained within the reservoir). However, this should be accommodated to some extent through the finite-fault modelling of larger ruptures: while the Brune formulation is used to model small earthquakes here (and later to characterise sub-faults of the finite fault simulation), the final spectral shape is controlled by the full finite-fault simulation and is not conditioned to be Brune (or Boatwright) type at large magnitude, but rather will reflect the fault geometry and kinematics.

Testing Boatwright's Source Model

An inversion of the log-log space FAS in the V2 database was performed directly for the three spectral shape parameters (κ , $\hat{\Omega}$ and event-specific f_0) using (a) the Brune (1970) and (b) the Boatwright (1978) model with $\gamma=2.0$. In this test we skipped the initial measurement of κ_{ij} . An overall FAS specific misfit is calculated:

$$misfit = \frac{1}{N} \sum_{k=1}^N \frac{[\ln(\Omega_{ijk}^{data}) - \ln(\Omega_{ijk}^{model})]^2}{f_k} \quad (5.10)$$

with f_k the k th frequency and N the number of samples in the FAS. An event specific misfit is then computed as the average over all used FAS for that event. In the Figure 5.2 the ratio of event misfit using the Boatwright and Brune models is shown (Boatwright/Brune misfit). Values greater than unity indicate that the Brune model is better, and vice versa. In terms of judging the 'better model', either can arguably be selected. However, for the larger events, the Brune model seems to have better performance, with four events with $\mathbf{M} > 3$ exhibiting up to 10% better fit. On the other hand, for lower magnitude events the Boatwright model performs better. This may be due to the emergence of a smoother transition between the displacement plateau and ω^2 decay as rupture kinematics becomes apparent for larger events (*e.g.*, Madariaga, 1976).

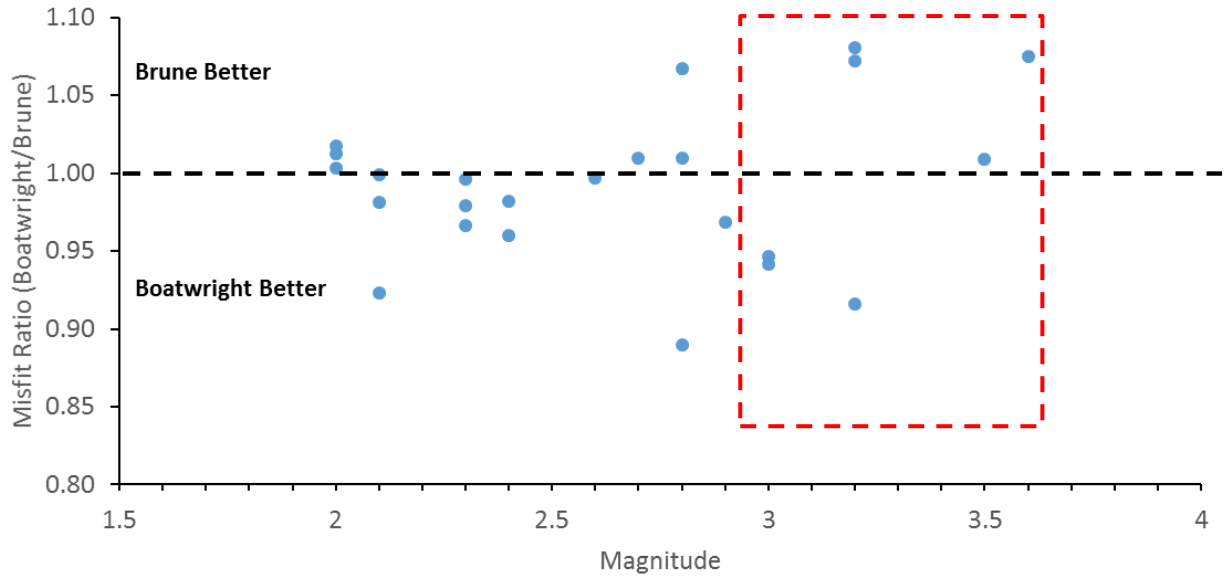


Figure 5.2. Comparison of goodness of fit for the different source models using the V2 database

Attenuation

An additional formulation of the inversion model is the frequency dependence of attenuation. These have been considered by modifying the anelastic attenuation (Equation 5.3), to instead use:

$$B_{ij}(f, \kappa) = \exp(-\pi f^{1-\alpha} \kappa) \quad (5.11)$$

with α determining the frequency dependence of Q :

$$Q(f) = Q_0 f^\alpha \quad (5.12)$$

and implicitly assuming that κ is due to the anelastic attenuation (defined by Equation 5.12) along the path. Alternatively, we can assume that there exist two components to the anelastic path attenuation, frequency dependent path and frequency independent site (κ_0).

$$B_{ij}(f, \kappa) = \exp(-\pi f(\kappa_r r f^{-\alpha} + \kappa_0)) \quad (5.13)$$

Each of these was tested in early inversions (and discussed subsequently). While in some cases the fit to the empirical data was improved using these alternate formulations, this comes at a cost of increased model complexity, degrees-of-freedom, and therefore uncertainty. It was, therefore, decided for the final simulations used to construct the finite fault model using the Brune source model (Equation 5.2) for sub-faults and to use frequency independent anelastic attenuation (Equation 5.3).

In order to test the suitability of using a frequency dependent Q model we implemented two formulations (Equation 5.11 and 5.13). The former assumes that along the path between the

source and NS_B the wavefield undergoes attenuation that is completely frequency dependent (according to Equation 5.12). In the latter, we assume that there are two components, the first attributed to the majority of the travel-path, which is frequency dependent (Equation 5.12) and a site-specific component that is frequency independent (*i.e.*, using κ_0). Both cases result in a small decrease in misfit over the ensemble of recordings (Figure 5.3) with best-fitting models at $\alpha=0.14$ or $\alpha=0.21$ (using κ_0) depending on the model formulation.

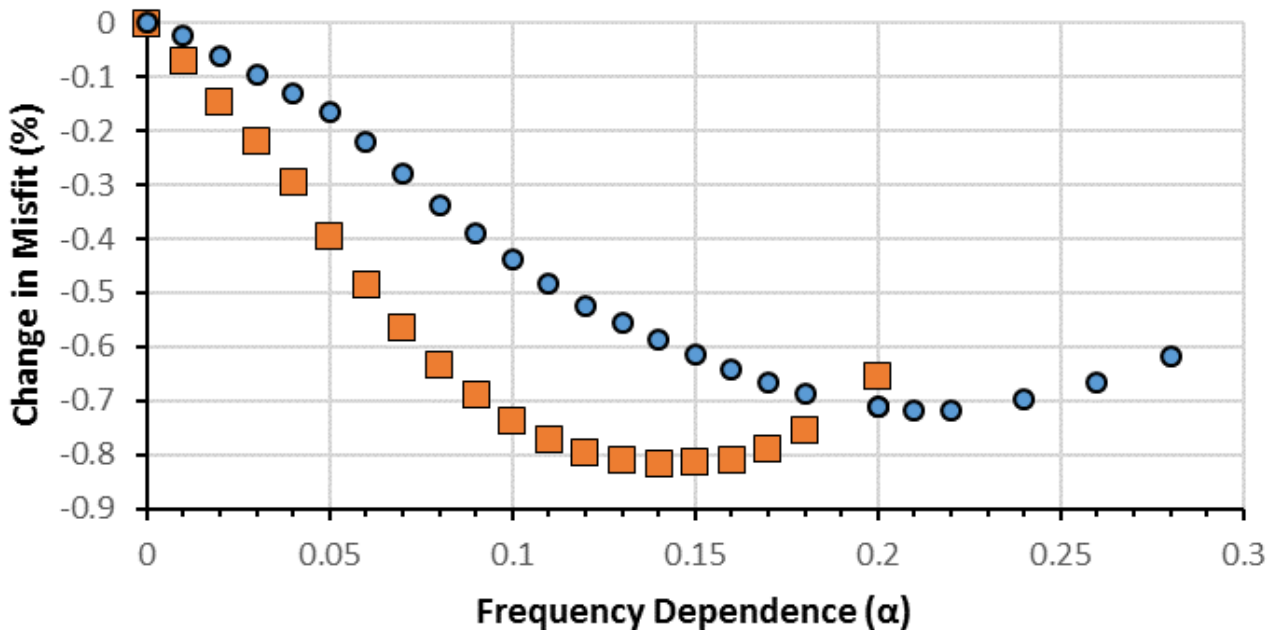


Figure 5.3. Misfit reduction as a result of introducing frequency-dependent Q, with formulation in Equation 5.11 (*squares*) and 5.13 (*circles*)

However, the improvement in the fit is below 1%, a level at which basic statistical tests indicate it is not possible to reject the null hypothesis of frequency-independent Q. Furthermore, while the influence of Q and its frequency dependence may be an issue at regional scales, the short path lengths relevant to the seismic risk of the field do not justify trying to constrain a more complex functional form for Q. This is highlighted in Figure 5.4, where the effect of damping due to Q is shown for the frequency independent model adopted, and for a corresponding frequency dependent model. Frequencies up to 10 Hz are shown as above these frequencies S_a is controlled by increasingly lower-frequency ground motion. The differences shown are significantly below the uncertainties of other parameters (such as stress-drop). Therefore, while we accept that frequency-dependent Q is a likely phenomenon, it is not possible to robustly determine (and will result in even less robust measures of Q_0). Since the influence of Q, unlike other model parameters such as stress parameter, near-source geometrical decay, *etc.*, is limited to greater distances—which are of little relevance to the hazard and risk estimates—we believe the frequency-independent model for Q is a suitable choice.

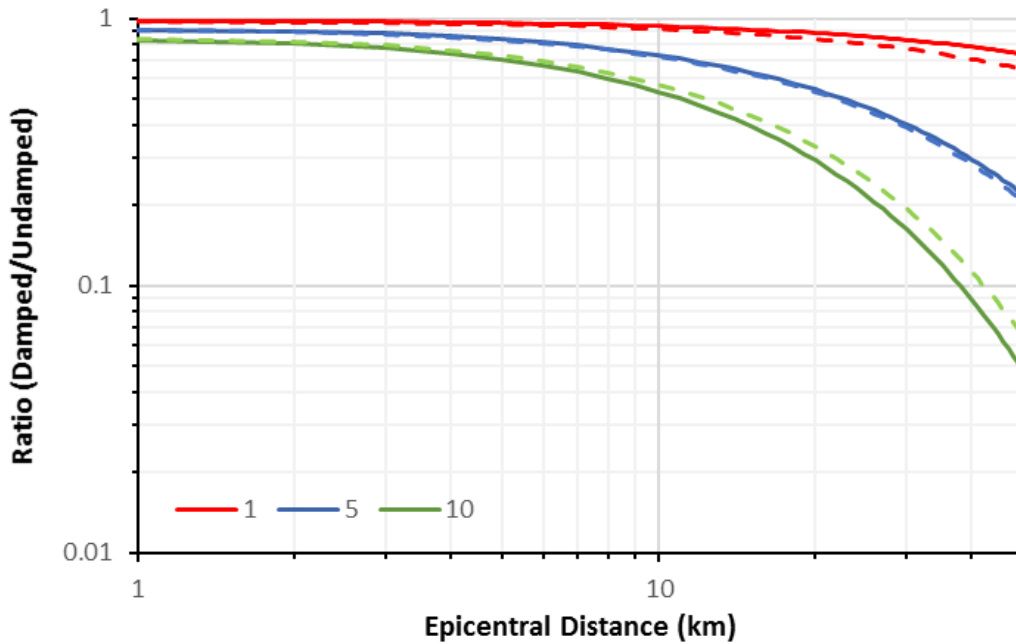


Figure 5.4. Effect of damping due to crustal Q. Solid lines indicate a frequency-independent Q (equal to 200), as used in simulations; dashed lines are for $Q(f) = 140f^{0.2}$. Note that data are available to ~ 25 km.

5.4. Geometrical spreading function

Early in the project it was observed that the residual misfit of the modelled data to the V1 GMPE followed a characteristic pattern with distance, suggesting changes in the rate of decay. Such behaviour has previously been observed at regional scales, and is attributed to the Moho bounce effect: strong reflections from the Mohorovičić discontinuity leading to increased amplitudes (and an apparent decrease in the rate of decay) somewhere between 50 and 120 km from the source. In order to explore if this effect—albeit on a smaller scale—was present in Groningen, full waveform simulations were undertaken at Shell and results compared with measurements from recorded accelerations at the surface. These simulations have the potential to inform the inversion for source, path and site parameters. Since such inversions (Section 5.2) are known to suffer from parameter trade-offs, gaining insight into the geometrical behaviour of the wavefield has the potential to guide the subsequent inversions and lead to more reliable results.

A range of simulations have been performed using the Shell WFD simulation code with progressively more complex velocity models, and using a variety of source mechanisms and distributions. For the source model, a wavelet was created that is consistent with the seismological model described in the previous section—termed the Brune wavelet—a time-domain wavelet with frequency characteristics of the Brune earthquake source model (Equation 5.2). Three characteristic wavelets were used: $f_0=0.4$ Hz (equivalent to **M** 5.0 for a stress drop of $\Delta\sigma = 30$ bars, and $\beta=2$ km/s), $f_0=2.3$ Hz (**M** 3.5) and $f_0=4$ Hz (**M** 3.0). From initial testing in layered media, with velocities similar to those seen in the field, it was obvious that a change in the rate of geometrical decay may occur with increasing distance from the source (consistent with the residual analysis of the early GMPEs). In order to define a model

for this behaviour, the most complex—and realistic— 3D simulations were performed over a duration of 16 s for the full 3D model and 32 s for an extended 1D model (over greater dimensions) at 16 ms intervals. Virtual recordings were made at the NS_B interface at 500 m intervals in the horizontal x and y directions. Two velocity models were used: (1) the full 3D Groningen velocity model (Figures 5.5 and 5.6), which includes an update of the near-surface velocities that was implemented between the development of the V2 and V3 ground motion models; and (2) a 1D representation of the 3D model (taken at $X=590000\text{m}$, $Y=245000\text{m}$), specifically for long offset simulations. The boundary conditions are absorbing apart from at the surface, which is treated as a free surface. Source mechanisms were averaged over a range of strikes (130° to 150° and 310° to 350° , in 10° steps), dips (60° to 90° in 10° steps) and rakes (-100° to -80° in 10° steps). While it was shown that the source location made a small difference to the observed ground-motion, it was decided to place the source in the centre of the field to maximise the observed distances and range of azimuths. The simulation does not take damping into account, focussing purely on geometrical and scattering effects.

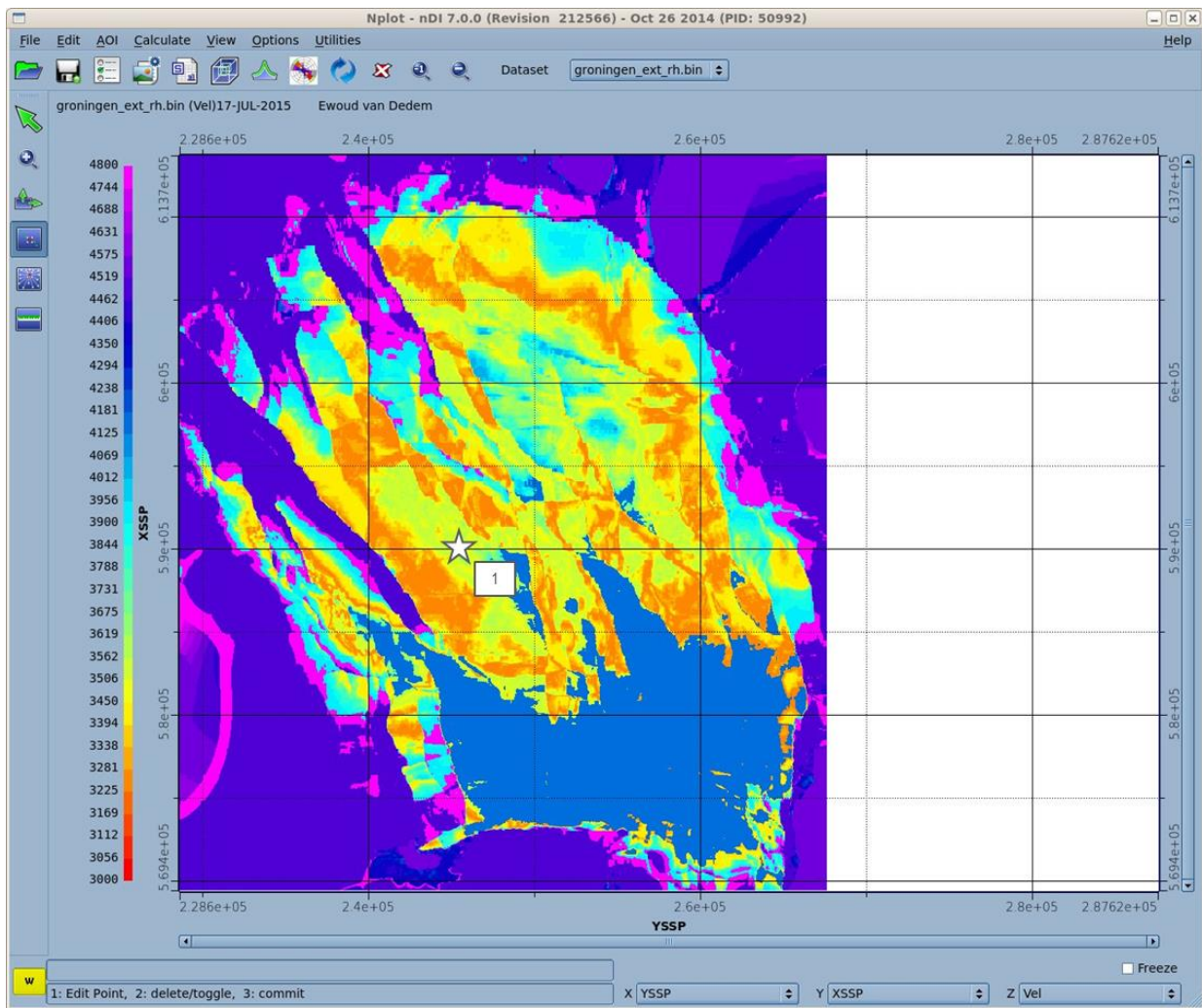


Figure 5.5. Screenshot of velocity model and source location used in full waveform simulations (Courtesy of Ewoud van Dedem, Shell)

For each set of simulations (with unique wavelet), the average ground-motion field in terms of geometrical mean (i) horizontal PGV, normalised to the maximum PGV (over all virtual recordings); and (ii) horizontal FAS at discrete frequencies, normalised to the corresponding peak FAS (over all virtual recordings), was plotted against hypocentral distance (Figures 5.7 and 5.8). It was clear that a three-segment geometrical decay function, with constant rates of decay over each segment, was appropriate and this was fit to the simulated data for each source mechanism. The rates of decay were found to be dependent on the selected hinge-points, particularly for the smaller magnitudes (higher frequency) wavelets. Consequently, the hinge-distances and the decay rates must be taken as a coupled model. While significant variations were observed depending on source mechanism, the developed GMPE is independent of source mechanism (with earthquakes represented as hypocentres), it is therefore necessary to provide a model, as above, averaged over a realistic range of possible sources. It is interesting to note that for the 1D simulations (Figure 5.8) the change in the rate of decay is much stronger than for the 3D simulations. This indicates that the uneven stratigraphy (Figure 5.6) smooths out the geometrical and scattering effects to an extent. An additional useful insight from the 1D simulation, which were performed in an extended model space (up to ~ 65 km in each direction), is that beyond 12 km the decay rate is similar to a homogeneous half space (1/R).

Based on the observations over numerous simulations, distances of 3, 7 and 12 km were selected as the hinge-points for Equation 5.7. Averaging the rates of decay (from the results using different wavelets) between those distances, the values in Table 5.1 were determined. The 1D simulations were only performed for one wavelet type ($f_0=4$ Hz), so no standard deviation is provided for PGV. The values most relevant for the FAS analysis are the average values over the individual simulations 1-11 Hz (in 1 Hz spacing, labelled Avg. 1-11 Hz in Table 5.1).

Table 5.1. Summary of geometrical decay values from the full waveform simulations. The maximum distance for the 3D case was 25 km and 65 km for the 1D case.

Simulation	Slope 2.5-7 km	Slope 7-12 km	Slope 12-[25/65] km	Slope 2.5-[25/65] km
3D PGV	-2.16 +/- 0.06	0.90 +/- 0.12	-1.17 +/- 0.03	-1.40 +/- 0.03
3D Avg. 1 - 11 Hz	-1.95 +/- 0.20	0.50 +/- 0.41	-0.86 +/- 0.19	-1.08 +/- 0.05
1D PGV	-2.4635	1.337	-1.1628	-1.6111
1D Avg. 1 - 11 Hz	-2.17 +/- 0.65	1.21 +/- 0.76	-1.05 +/- 0.08	-1.35 +/- 0.42

A frequency dependence of the apparent geometrical decay is evident in Figures 5.7 and 5.8. The ‘shoulder’ in the distance-amplitude function is only apparent at moderate and high frequencies ($f > \sim 2$ Hz) and is most pronounced at ~ 5 Hz in the 3D velocity model and ~ 10 Hz in the 1D model. To test if this is also observed in the real recordings we fitted the Groningen FAS, deconvolved to the NS_B and corrected for Q and site specific κ_0 . A best fitting (frequency independent) 3-segment geometrical spreading model, with hinges at 3, 7 and 12 km is determined and the residual misfit at discrete frequencies is calculated. In the case that clear differences in geometrical spreading at different frequencies would be

apparent (e.g., Figures 5.7 and 5.8), this should manifest in deviations away from the unit fractional residual line, particularly around 10 km. This is, however, not observed in the empirical Groningen data (Figure 5.9). The reason for this may be indicated by the fact that the feature is ‘smoothed out’ when going from 1D (Figure 5.8) to 3D simulations (Figure 5.7). In reality, an even more heterogeneous velocity structure than is accounted for in the 3D model may result in further smoothing of the effect. Nevertheless, the full waveform simulations provide a useful insight into the expected geometrical behavior of the wavefield. The features observed, namely the defined hinge-points, strong initial decay with a shoulder at ~ 10 km and $1/R$ decay at greater distances, are taken into account in developing the empirical model in the following section. Frequency-independent geometrical spreading (in terms of FAS) was used in the simulations.

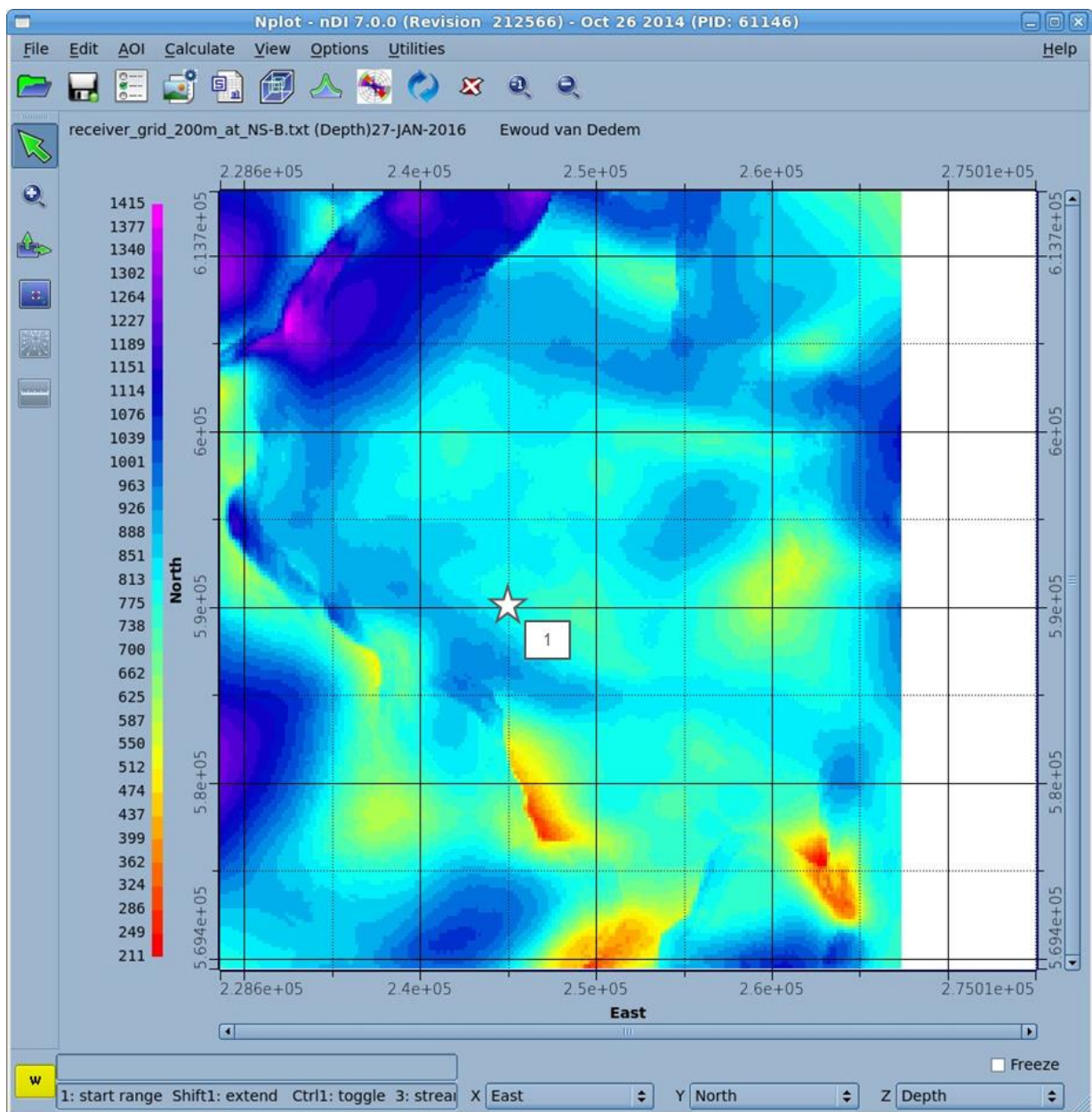


Figure 5.6. Screenshot of NS_B (virtual recording) depth model and source location used in full waveform simulations (Courtesy of Ewoud van Dedem, Shell)

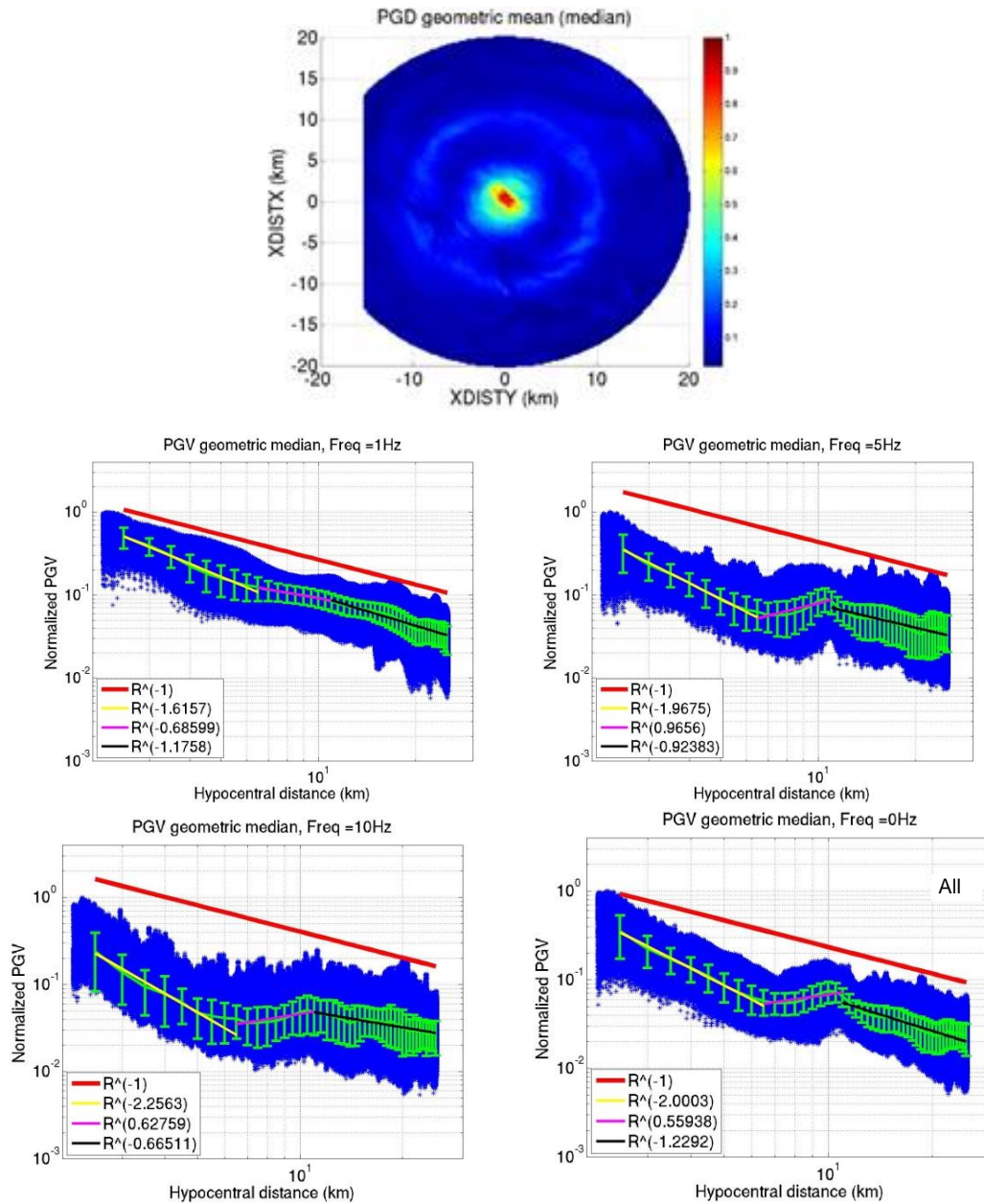


Figure 5.7. *Top*: Example of normalised ground-motion field for the full 3D simulations; *Bottom*: PGV values (narrow-band limited at the respective frequencies) plotted against hypocentral distance with binned mean values every 500m. $1/R$ decay (*red line*) is indicated for reference; a 3-segment geometrical spreading model is fit to the binned data (*Courtesy of Ewoud van Dedem, Shell*)

In Figures 5.7 and 5.8, the PGV value are narrow-band limited ground velocities; the frequency indicates the central frequency. In addition to the simulation results, geometrical spreading was also initially measured from the distance dependence of the far field spectral displacement plateau (Ω_0 , Equation 5.8), obtained from preliminary inversions of the FAS. Although there is a strong trade-off between corner frequency and damping in the inversions, inversion results for $\hat{\Omega}_{ij}$ are more stable. For comparison between events, $\log(\hat{\Omega}_{ij})$ values are normalised by division by $\log(M_0)$. Figure 5.10 shows results with a linear fit to the data with a slope of -1.89 ($R^2=0.72$), which corroborates the findings from the simulations.

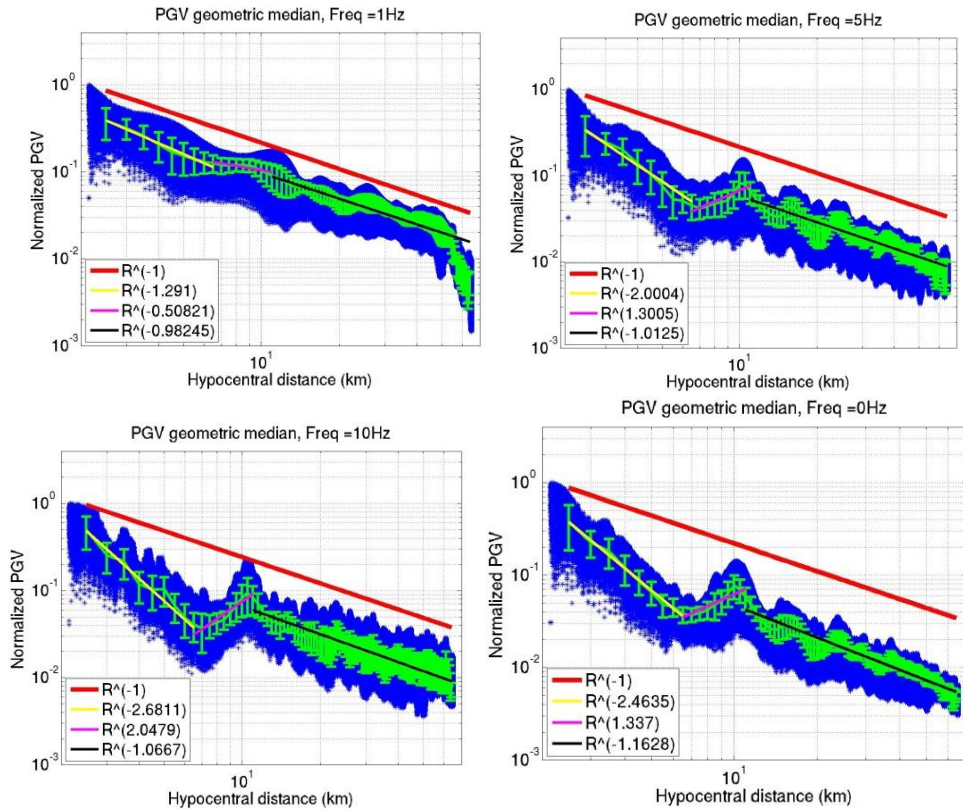


Figure 5.7. Example of normalised ground-motions for the ‘extended distance’ 1D simulations. PGV values (at different frequencies) plotted against hypocentral distance with binned mean values every 500m. $1/R$ decay (red line) is indicated for reference; a 3-segment geometrical spreading model is fit to the binned data (Courtesy of Ewoud van Dedem, Shell)

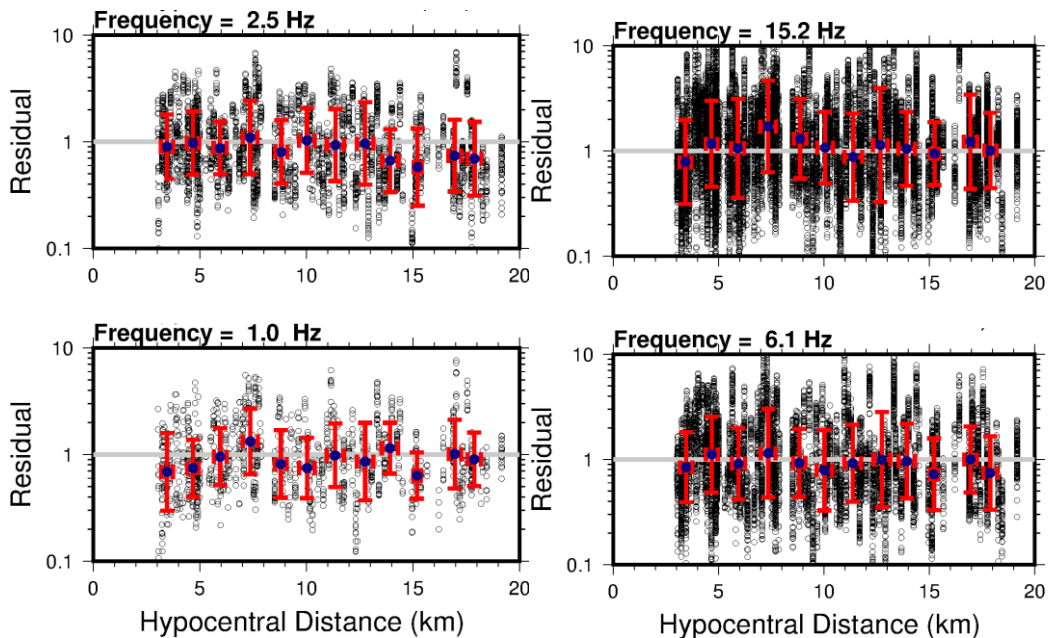


Figure 5.9. Evidence against a frequency dependent geometrical decay (as observed in simulations): residual misfit of the Groningen FAS, deconvolved to the NS_B and corrected for $Q = 130$ ($\bar{\beta} = 2.6$ km/s) and site specific κ_0 , to a (frequency independent) 3-segment geometrical spreading model, with hinges at 3, 7 and 12 km. Note that site specific NS_B amplification is not considered; the Q value is discussed below in Section 5.5.

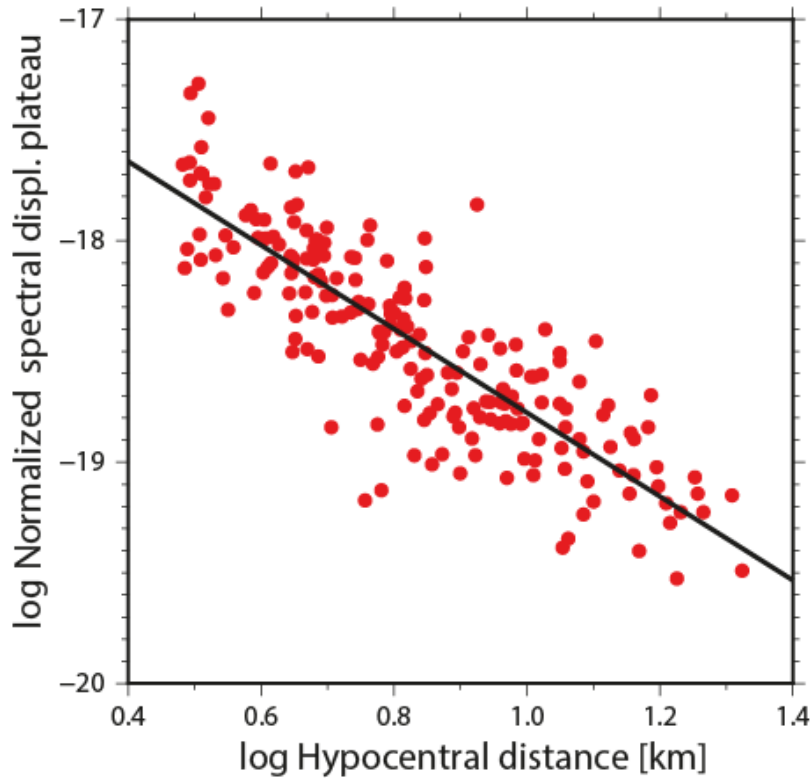


Figure 5.10. Measured $\hat{\Omega}_{ij}$, normalised with respect to M_0 , for Groningen events. The linear fit to the data has a slope of -1.89

5.5. Inversions for source, path and reference rock parameters

The Groningen FAS, deconvolved to the NS_B horizon using the linear transfer functions (Section 4.3), are inverted for source, path and reference rock parameters. The FAS were then processed according to the methodology described in Section 5.2. Initial estimates of path κ values at the NS_B were determined using the FAS in the lin-log domain (Figure 5.11).

As seen in Section 4.1 (Figure 4.2) there is a large uncertainty in the Q value obtained from the record-specific κ terms. In this broadband analysis a Q value of 130 is obtained for an average shear-wave velocity of 2.6 km/s. This is lower than the value used for simulation in the V3 model (Q=200), but is higher than determined from the high-frequency analysis in Section 4.1, Q ~ 400). Testing the Q value used in V3 model (Q = 200 at 2.6 km/s), we can see no discernible trend in the residual misfit (Figure 5.12), so there is no strong reason to change this value based on the new data—but it is clear that this parameter is still uncertain (with values anywhere between ~ 100 and 400 depending on data subset and method) due to the limited distance range of the data used. As seen in Figure 5.13, the κ_0 values computed at the NS_B (allowing for the field-wide average Q) are, as expected, lower than those calculated at the surface (Section 4.1). The average difference between surface and NS_B horizon κ_0 is 0.028 s., which is consistent with the average damping profile calculated for the field (Figure 4.8).

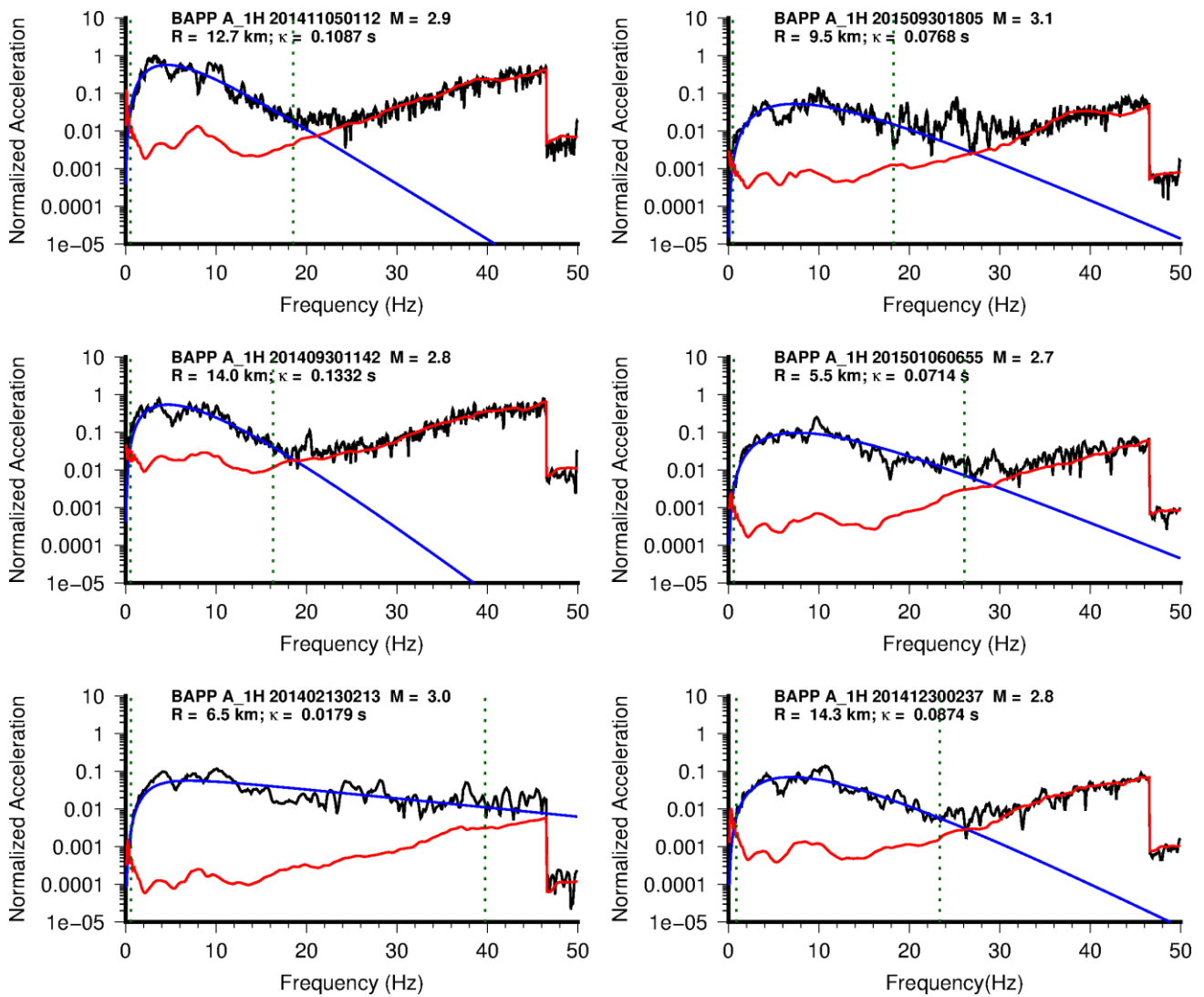


Figure 5.11. Broadband acceleration FAS at station BAPP deconvolved to the NS_B (black: S-waves; red: noise) and the modelled FAS. The fitting bandwidth (where SNR > 2) is indicated by the dashed vertical lines. Note that data at $f > 45$ Hz has not been NS_B corrected

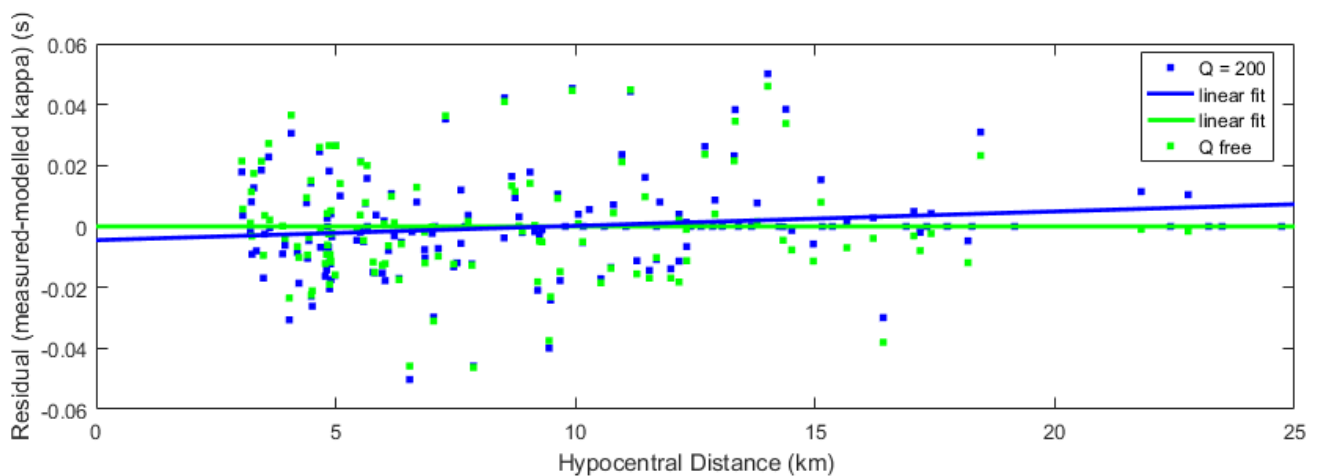


Figure 5.12. Residual misfit of the κ values as a function of distance using the V3 Q model ($Q = 200$, average velocity 2.6 km/s) and with a free Q determined as part of the inversion; the residuals obtained with $Q = 200$ are zero-centred, by definition, but show a very small trend with distance that is not considered to be important

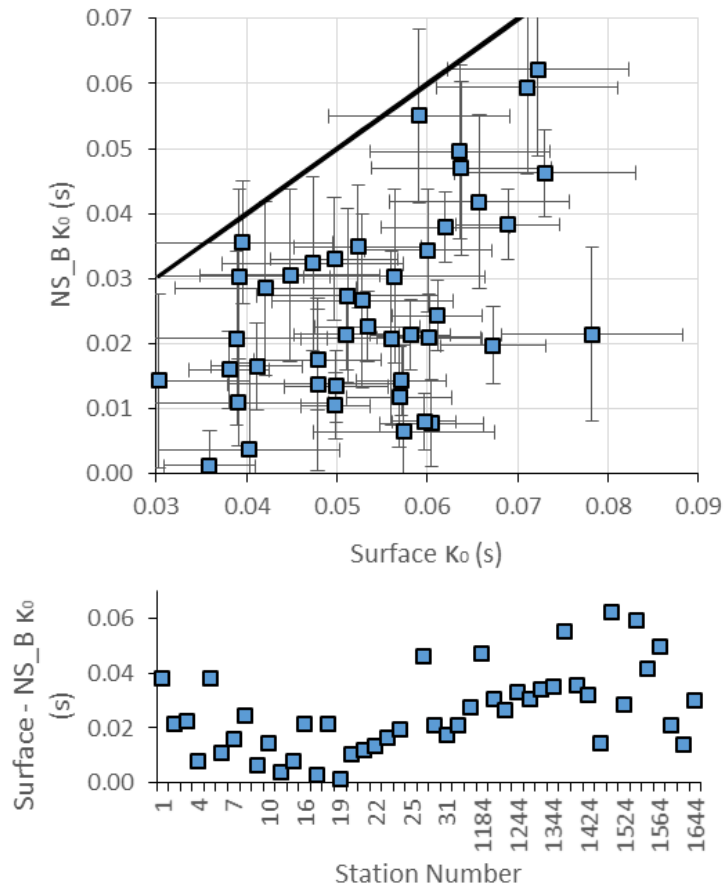


Figure 5.13. Comparison of κ_0 values computed at the surface (Section 4.1) and κ_0 values computed at the NS_B horizon. Physically realistic values should fall below the solid black line. Bottom: difference (surface - NS_B κ_0) vs. station number

Figure 5.14 shows typical surface FAS fits using the record specific long-period displacement plateau; event-specific source corner frequency and site-specific amplification computed using the NS_B corrected FAS, and applying the NS_B to surface transfer function (Section 4.3).

Using the long-period displacement plateau of the NS_B-corrected FAS, the geometrical decay function was inverted for along with average site amplification (Equation 5.6), fixing the moment magnitudes as in the V3 database. The hinge points of the geometrical spreading function (Equation 5.7) were selected to coincide with the distances observed during the full waveform simulations (Section 5.4): 7 km and 12 km. We assume that below 3 km (the minimum observed hypocentral distance), the decay is the same as between 3 to 7 km. The shape of the decay observed (Figure 5.15) is similar (although less pronounced) to that seen during the simulations (Figure 5.7), indicating that the velocity structure has a strong impact on the recorded amplitudes as a function of distance. The decay rates observed were: $R^{-1.17}$ up to 7 km, $R^{0.39 \pm 0.23}$ from 7 to 12 km, and $R^{-1.50 \pm 0.43}$ from 12 to 25 km. There is no error assigned to the first rate of decay, as it is conditioned on the selected \mathbf{M} values (and segmentation distances). Although there are no data beyond around 25 km we assume R^{-1} , as indicated by the full waveform analyses (Table 5.1, Figure 5.7). It is noted that the initial rate of decay is strongly dependant on the \mathbf{M} values used in the inversion. In the V3 model, we used higher values of \mathbf{M} (*i.e.*, assuming $\mathbf{M} = M_L$ rather than $\mathbf{M} = M_L - 0.2$,

and therefore with seismic moments ~ 2 times larger). This led to a much higher rate of decay in the first 7 km of $R^{-1.7}$ in the V3 model. The reason for this is that the moment magnitude (and therefore seismic moment) sets the initial (source) amplitude, while the first observations occur at ~ 3 -7km. The reduction ($\times 0.5$) of seismic moment in the current model means that the initial rate of decay must also reduce (to $\sim R^{-1.2}$) to match the observed amplitudes between 3 and 7 km.

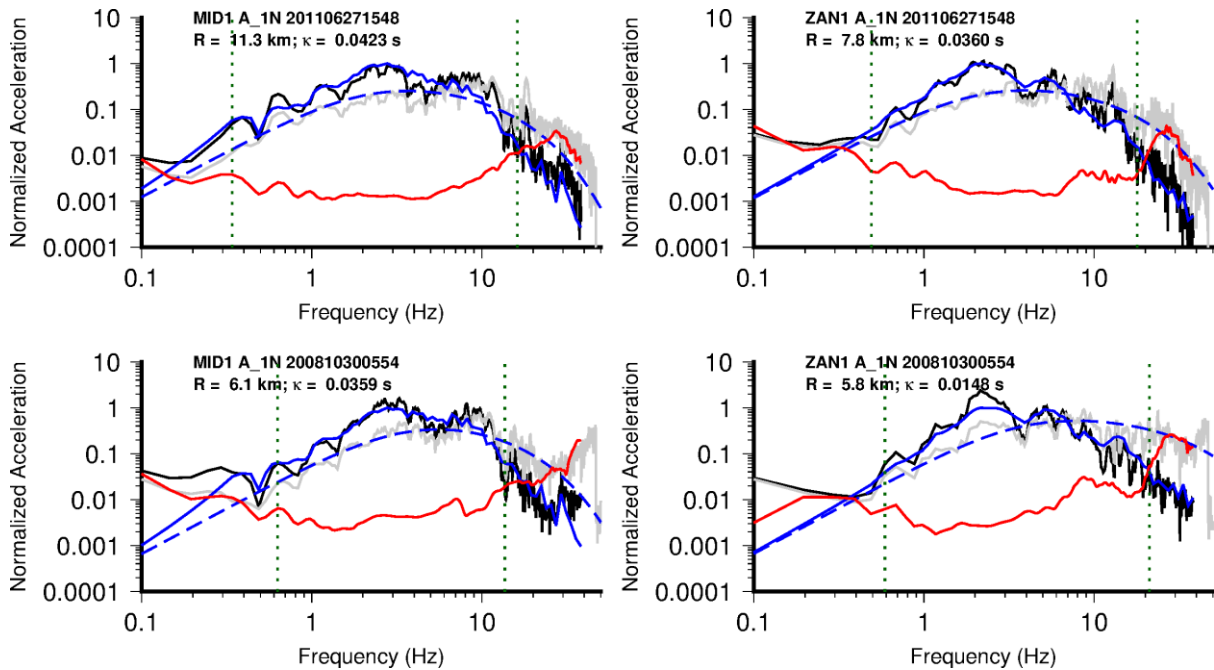


Figure 5.14. Comparison of observed (surface recordings at MID1 and ZAN1 accelerometers) and modelled FAS for two $M_L = 3.2$ events: top – 2011 Garrelsweer event ($f_0 = 2.1$ Hz); bottom – 2008 Westeremden event ($f_0 = 3.7$ Hz). Note absolute amplitudes are normalized such that only spectral shape is fit. Black line: surface acceleration FAS; red: surface noise FAS; grey: FAS deconvolved to NS_B using site transfer function; blue: modelled FAS (dashed: at NS_B; and solid: at surface).

Comparing the empirically derived amplification at the surface [the inverted source to NS_B amplification multiplied by the theoretical NS_B to surface amplification (Section 4.3)] with the NS_B to surface amplification alone (Figure 5.16) we see a good match in most cases, indicating that almost all amplification occurs above the NS_B, and that the transfer functions are representative of the true amplification observed at the stations. This is a significant improvement on previous models (V2 and earlier). Differences observed between empirical and theoretical amplification in the V2 model, which previously used an estimate of the sites' Vs profiles (as opposed to the directly measured profiles in this version), are not present.

In order to define a field average amplification at the NS_B level, the (geometric) average amplification (source to NS_B) of all sites was computed. The amplification was found to be broadly frequency independent between ~ 1 and 20 Hz and around unity (albeit with a large standard deviation), suggesting that the effect of the velocity structure between the source (the reservoir) and the NS_B interface (Figure 5.18) results, overall, in no significant amplification. The change in velocity between ~ 2 km/s at the reservoir and ~ 1.3 km/s at the

NS_B can also be considered to lead to only a small overall amplification (according to quarter-wavelength theory a factor of ~ 1.4 is possible based on the V_s and density profile in Figure 5.18).

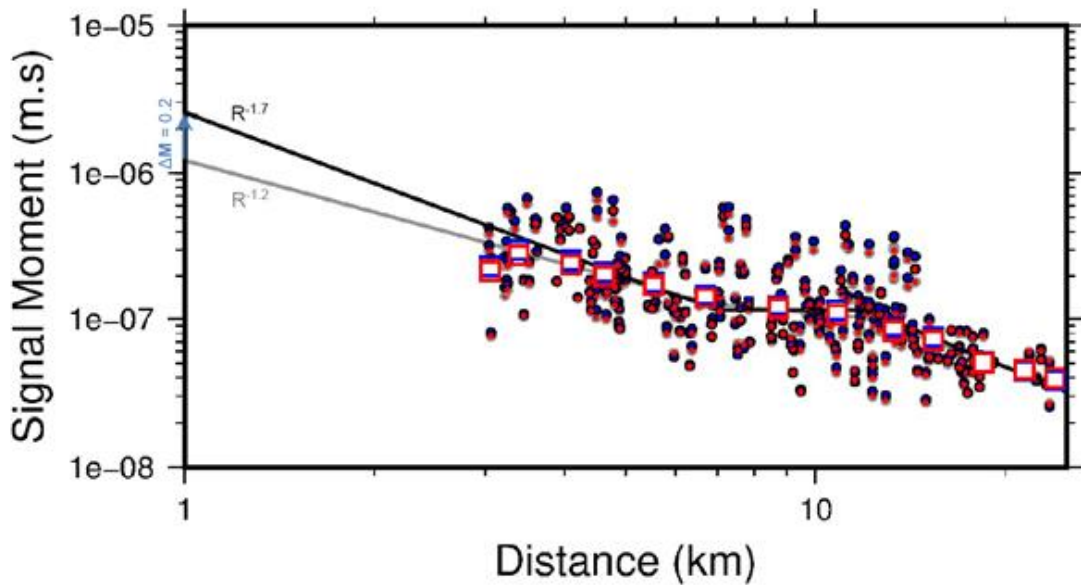


Figure 5.15. Normalised signal moment (long-period spectral plateau for a M 3 event) for V3 (blue) and V4 (red) plotted against distance and the best fitting geometrical spreading model for V3 (black line) and V4 (grey line)

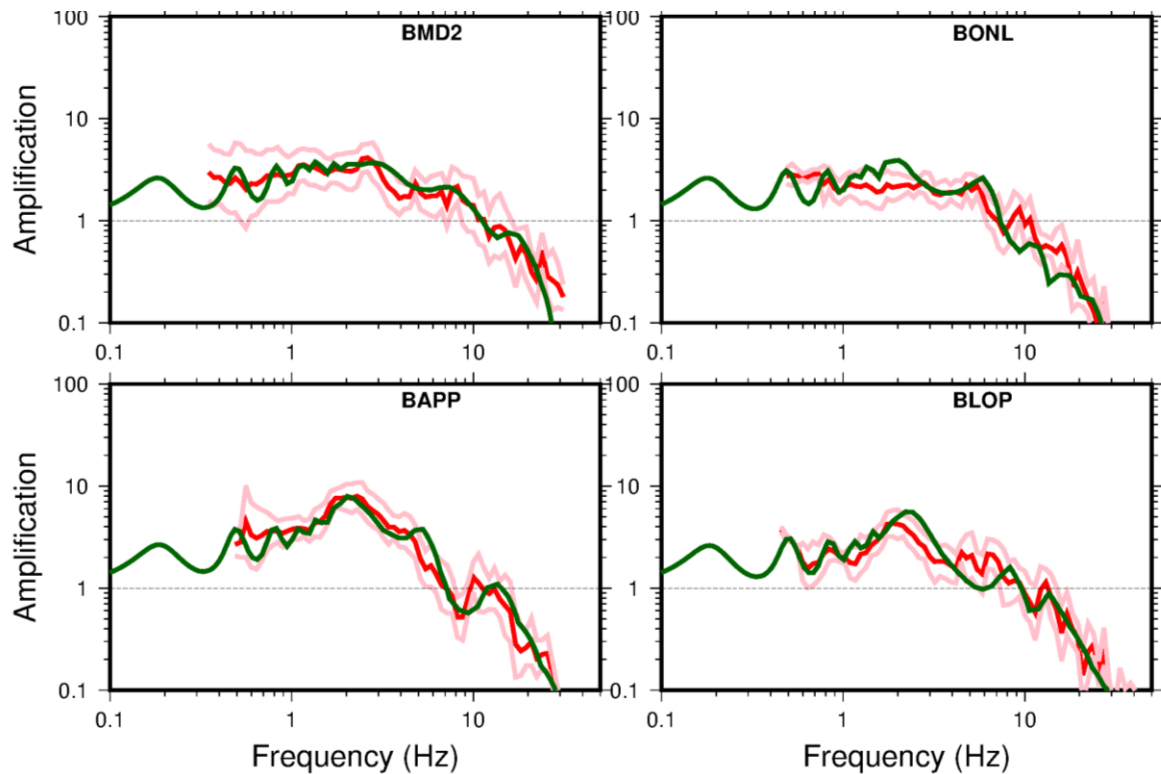


Figure 5.16. Comparison of total amplification (inverted source to NS_B amplification \times 1D-SH NS_B to surface amplification) (red) and standard deviation (pink) along with the 1D-SH NS_B to surface amplification (green) as presented in Section 4.3

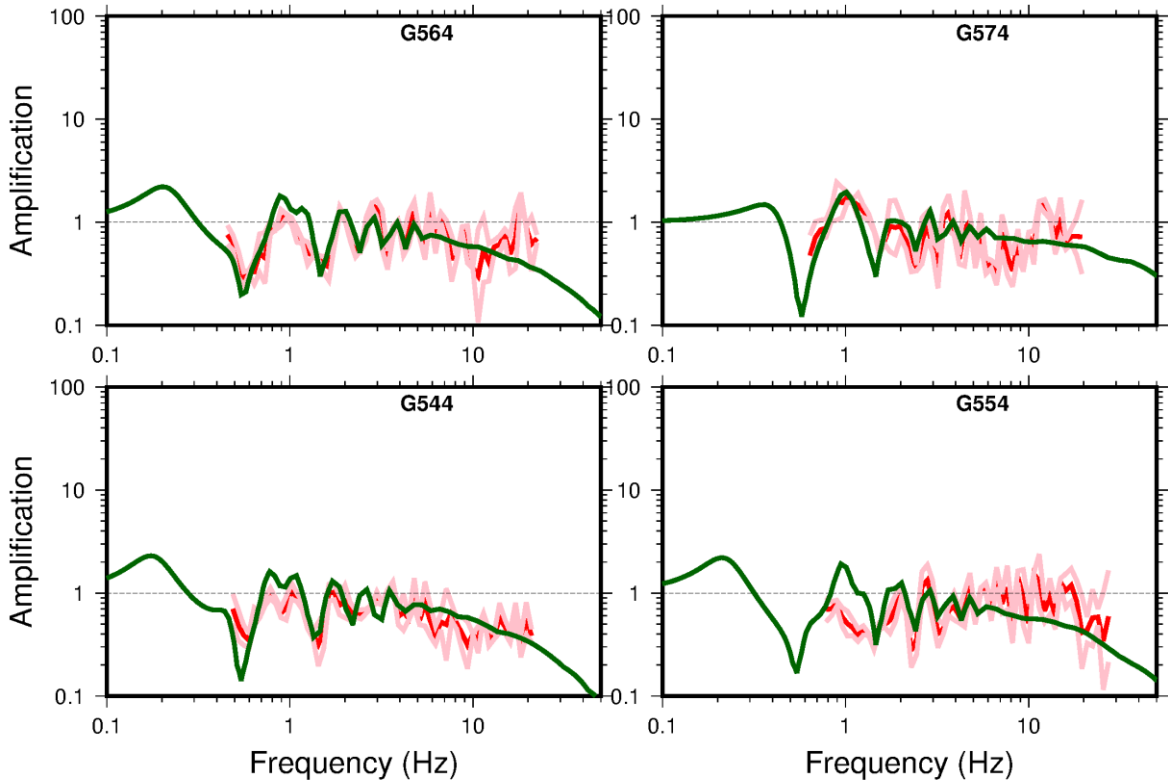


Figure 5.17. As Figure 5.16, but showing the source to 200 m depth amplification (red) and NS_B to 200 m depth (within rock) 1D-SH amplification for four 200m borehole sites.

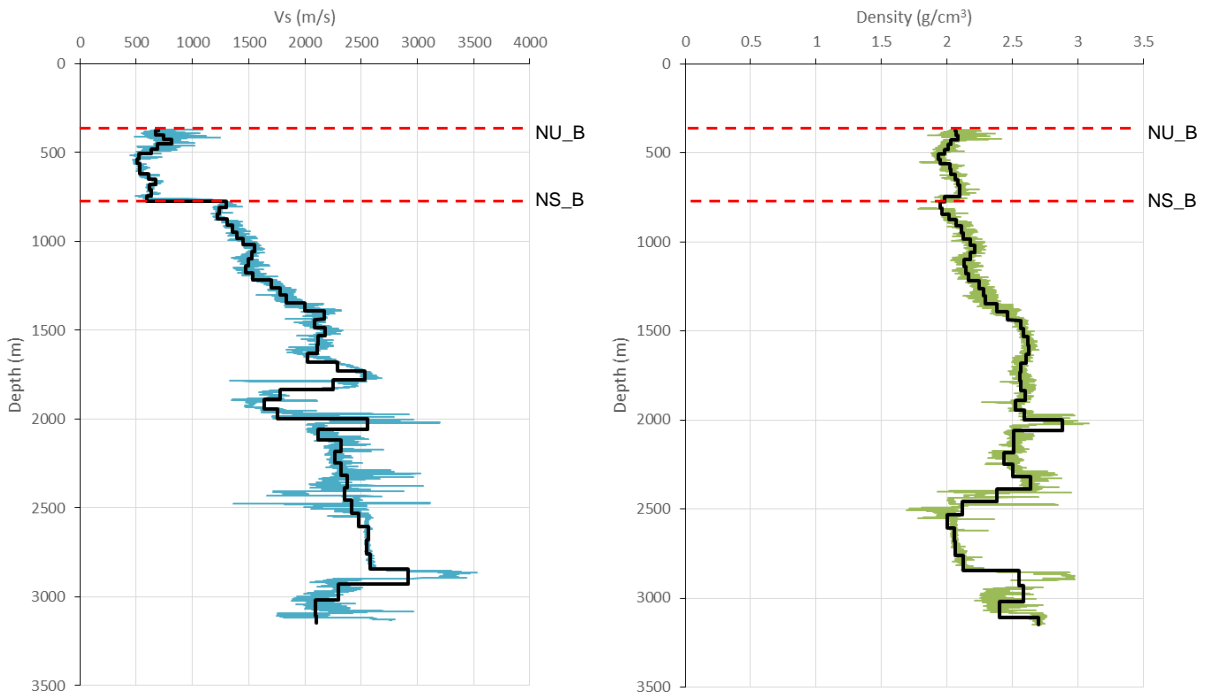


Figure 5.18. Measured velocity (*left*) and density (*right*) profiles from the BRW5 log; the stepped black lines show the layer model developed for the simulation of the motions in the Groningen Forum site-specific study

Due to the change in M in the V4 database, the spectral fitting of Groningen FAS, corrected to the NS_B, led to estimates of the stress parameter that were lower than those determined for the V3 GMPEs (Figure 5.19). As in V3, the weak magnitude dependence in the relationship between stress parameter and magnitude, observed for the V2 data, is not apparent (Figure 5.20). The average stress parameter determined from the 22 Groningen events was 36 bar (with \log_{10} standard error 0.16), based only on corner frequency f_0 . Discounting four events with the largest stress parameters (which could not be fully resolved to within $\pm 5\%$ misfit), the average was 20 bar (with \log_{10} standard deviation 0.14); however, excluding these larger stress parameter estimates naturally introduces a low bias.

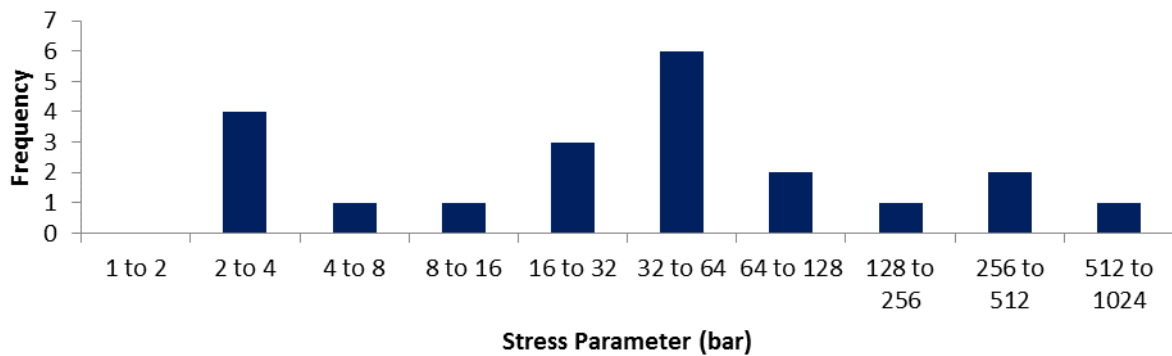


Figure 5.19. Comparison of stress parameters computed for the V4 data

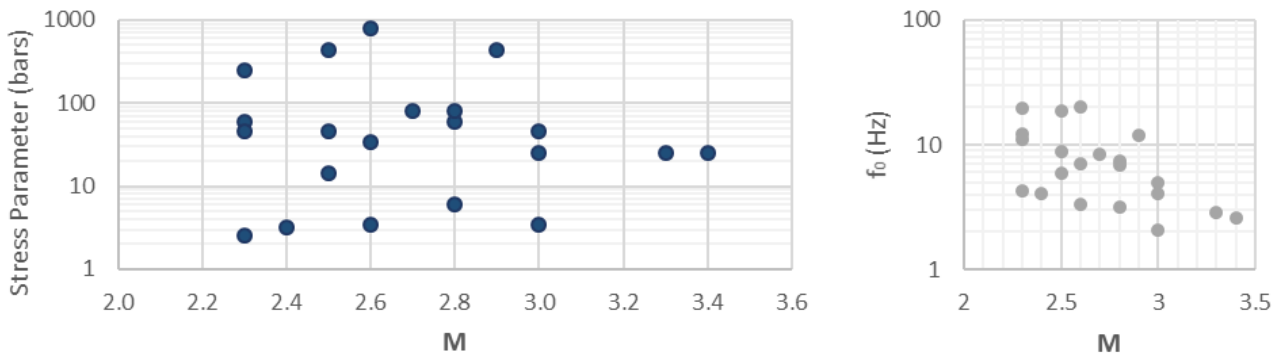


Figure 5.20. Best-fitting stress parameter for Groningen earthquakes (*left*). Plot of source corner frequency (f_0) versus moment magnitude (*right*).

6. EQUATIONS for GROUND MOTIONS at REFERENCE ROCK HORIZON

This chapter describes the derivation of the basic equations for predicting response spectral accelerations at the NS_B horizon, which is the first part of the V4 GMPE as defined in Eq.(2.1). The median motions are obtained primarily from simulations using the results of the inversions described in the previous chapter, as summarised in Section 6.1. The results of the simulations are described briefly in Section 6.2, after which the appropriate functional form for the parametric GMPEs is discussed in Section 6.3. The results of regression analyses on the simulations to fit the functional form are presented in Section 6.4. Section 6.5 is concerned with the calculation of the 'residuals' using the recordings, including their transformation to the NS_B horizon in order to estimate variability components. Section 6.6 summarises the equations for prediction of the rock motions at NS_B.

6.1. Finite-fault stochastic simulations

In the V4 Groningen ground motion model input ground motions are calculated using a finite-fault stochastic simulation methodology (EXSIM_dmb [version date: 17/10/2016]: Boore, 2009, based on EXSIM: Motazedian & Atkinson, 2005). Similar to the point source simulation technique used in V3, this approach produces full time-histories (and corresponding spectral-ordinates) by specifying a simplified seismological model (earthquake source, propagation and site effects). The advantage of the finite-fault approach adopted for V4 is that, rather than relying on an extrapolated empirical model, the transition from small to large magnitude events is controlled by properties of the seismicity and geological structure of the Groningen field.

Finite-fault stochastic simulation essentially combines numerous small earthquakes (sub-faults) into a larger rupture. Seismicity observed in the field is used to produce a model for determining ground motion from each sub-fault, with all sub-faults combined by invoking a hypocentre and slip model (defining the time-delay of successive sub-faults slipping). As a result of the increased model complexity, additional parameters must be specified (such as fault dimensions, hypocentre location, slip velocity), but the methodology to determine the ground motion for each sub-fault (individually behaving as a small earthquake, or point-source) remains the same as the V3 model.

For the simulations we assume normal faulting, with rupture dimensions given by Wells & Coppersmith (1994). This particular scaling relationship was chosen for simplicity; we could equally have used Leonard (2014) or Stafford (2014), but since none of the relationships is known to be applicable to Groningen earthquakes, we opted for the simplest among them. Variability in fault size is accommodated through a zero-mean log-normal distribution with standard deviation 0.15 (natural log units). Fault length and width are negatively correlated to ensure that the total fault area ($L \times W$) is maintained. All hypocentres are located in the reservoir, at a depth of 3 km, but occur randomly along strike. Ruptures grow downwards (i.e., $Z_{top} = 3$ km), limited by the seismogenic depth (13 km). This depth is inferred from two sources of information: Cacace (2008) developed rheological models that identified

increasing crustal strength down to about 10 km followed by weakening due to elevated temperatures, which might indicate a seismogenic depth on the order of 10 km. Yudistira (2015) estimated crustal velocity profiles from ambient noise measurements, and from the profiles developed a seismogenic depth of 10-13 km would be inferred; at 13 km, there is a marked velocity contrast, with V_s increasing from 3.1 to 4.0 km/s.

Fault dip is set at 75 degrees based on faults in the field exhibiting dips between 60 and 90 degrees. Simulated ruptures that reach the maximum accommodated width (10.4 km for a 75 degree dipping fault) are adjusted in length to ensure that the rupture area is maintained; the maximum aspect ratio of ruptures is 9.5. Slip velocity is given by 0.8β , with β the average shear-wave velocity over the fault plane. For events with $M \leq 4$ this is $\beta = 2.0$ km/s (the reservoir velocity). For events with $M \geq 5.5$, $\beta = 3.5$ km/s (velocity of the Carboniferous), with linear interpolation in the range $4.5 < M < 5.5$.

Sub-fault properties: calibration to Groningen seismicity

The duration model developed for the V3 Groningen ground motion model is used to define the shaking duration of individual sub-fault waveforms. This model has been calibrated to observed durations in the Groningen field, and therefore provides durations for low-magnitude events consistent with local seismicity. It also includes a V_{s30} adjustment that allows predictions to be made at the higher-velocity NS_B. Note that this does not condition the durations of larger events (constructed from numerous sub-faults) to be the same as the V3 duration model, as the duration of these larger events is determined based on the summation of signals from the individual sub-faults. The total duration is therefore a function of the duration of sub-fault signals (*i.e.*, small earthquakes), the slip velocity and the fault dimensions. The input duration for subfault motions in EXSIM_dmb (*TEXSIM*) is not equal to $T_{5,75}$ (as provided by the V3 duration model). Therefore, an initial calibration step is undertaken to ensure that the output duration of simulated waveforms (at small magnitude) is consistent with the V3 $T_{5,75}$ duration model. The calibration showed that $TEXSIM = T_{5,75} / 0.383$ ($R^2 = 0.98$). The input duration for subfault motions in EXSIM was therefore defined as: $T_{5,75}(R, M=3, VS30=1500 \text{ m/s}) / 0.383$, with $T_{5,75}$ given by the V3 Groningen duration model. The V3 duration model provides durations ($T_{5,75}$) that are consistent with Groningen seismicity and considered valid at $M=3$. Since we need only define the shaking duration for sub-faults (small ruptures, $M \sim 3$) this is sufficient (no extrapolation is needed or performed). The simulation then computes the total duration through summation of the contributions from individual sub-faults.

The inversions discussed in Section 5.5 yield a range of possible combinations of source, path and site parameters that are consistent with the recorded data (after its translation from the surface to the NS_B horizon using the transfer functions from Section 4.3). While there is therefore an estimate of the mean value of each of the parameters obtained from the inversion, what is sought is the combination that when used in stochastic simulations yields predicted spectral ordinates that best reproduce the recordings. The objective was to perform a grid search in order to identify the optimal values to be used in the simulations for the median motions. Based on the initial observations (Section 5.5) and spanning a broad range

of the model space, we defined 216 parameter combinations based on: κ_0 values of 0.001, 0.005, 0.010, 0.015, 0.020 and 0.025 s; Brune stress parameter, $\Delta\sigma$, of 10, 30, 50, 60, 70, 80, 90, 100, 120, 150, 200 and 300 bar and Q values of 130, 200 and 300. All simulations used the geometrical spreading model determined in Section 5.5, which was based on the segmentation distances from full waveform modelling. Source to NS_B amplification, computed using the quarter-wavelength approach and modified for the network-average, was relatively small ($< \sim 1.5$), but non-negligible. The simulations were compared to the individual horizontal component response spectra at the NS_B horizon for all 20 spectral periods for which recorded data were available (0.01 to 2.5 s). Initial testing indicated that there was limited resolution in the path attenuation (Q) parameter (as found in the spectral analyses, Sections 4.3 and 5.5) since recordings are only present within ~ 25 km. Therefore, the Q = 200 model was chosen as a compromise between the range of values possible from the different analyses (approximately 100 to 400), given that $1/Q$ is normally distributed. This value is also consistent with values proposed by KNMI in earlier work using borehole data.

In order to assess the fit of each model the inter-event terms are calculated at each of the 20 periods. The random-effect terms are calculated using:

$$\eta_i = \frac{\tau^2 \sum_{j=1}^{n_i} y_{ij} - \mu_i}{n_i \tau^2 + \phi^2} \quad (6.1)$$

(Abrahamson and Youngs, 1992) with arbitrary starting values of the intra-event term $\phi=0.5$ and inter-event term $\tau=0.5$ (\log_{10}) and iterating until convergence. n_i is the number of records for the i th event (y_{ij} , which are $\log_{10}[\text{PSa}]$) and μ_i is the mean value of y_{ij} for the i th event. From the inter-event terms (Eq. 6.1) the average model bias, b , (at individual periods, T) is measured from the N events:

$$b(T) = \frac{1}{N} \sum_{i=1}^N \eta_i(T) \quad (6.2)$$

The average RMS (root-mean-square, or modulus) bias, $\overline{|b|}$ [hereinafter termed ‘RMS bias’], over all $M=23$ periods is defined as:

$$\overline{|b|} = \frac{1}{M} \sum_{k=1}^M |b(T_k)| \quad (6.3)$$

and standard deviation of the period-to-period RMS bias, $\sigma_{|b|}$ [termed ‘sigma(RMS bias)’], is calculated as:

$$\sigma_{|b|} = \sqrt{\frac{1}{(M-1)} \sum_{k=1}^M (|b(T_k)| - \overline{|b|})^2} \quad (6.4)$$

to provide a simulation specific (period independent) measure of model bias and period-to-period variance. Note that the model RMS bias $\overline{|b|}$ will only be 0 in the case that the model is perfectly unbiased at all periods since both underestimation and overestimation lead to

positive $|b|$. Low $\sigma_{|b|}$ indicates that the residual misfit is consistently biased (or unbiased), high values indicate period-to period differences are present.

EXSIM performs time-domain simulation, and is significantly slower than SMSIM, which can use random-vibration theory to speed up the process when only peak-amplitude ordinates (e.g., PSA) are required. For small magnitude events, EXSIM_dmb has been shown to produce the same results as SMSIM (Boore, 2009). This has been verified by comparing simulations using the V3 seismological model (without empirical scaling adjustment), to those using EXSIM (Figure 6.1). This comparison confirmed that for the small magnitude events, SMSIM could be used to quickly evaluate the fit of seismological parameters for use in EXSIM simulations, significantly reducing the computational time. The grid-search of seismological parameters was therefore undertaken with SMSIM.

The results in terms of mean and sigma of the RMS bias are shown in Figures 6.2 and 6.3 versus stress parameter and κ_0 ; these simulations are performed only for the range of magnitudes in the current Groningen database. These contour plots clearly show the trade-off between the source and site terms, with increasing stress-parameter being accompanied by increased κ_0 to provide similar bias. The best fitting model for the motions at the NS_B horizon is found to have the following parameter combination based on the smallest RMS average misfit (bias) and sigma: $\Delta\sigma = 60$ bar; $\kappa_0 = 0.015$ s (RMS bias = 0.070 ± 0.073). The stress parameter value is slightly lower than determined for the V3 central model (70 bars). The decrease however, is within the median standard error of this parameter from spectral analyses (equivalent to ~ 50 to 70 bars) and may be related to changes in other parameters, such as the new magnitude ($M = M_L - 0.2$) and consequent changes in geometric spreading. The value determined from the response spectra is higher than the average of ~ 40 bars determined from spectral analysis. It is reiterated, however, the approach here is to determine a full set of simplified parameters that reproduce the observed PSA, rather than replicating the mean observed for the individual events.

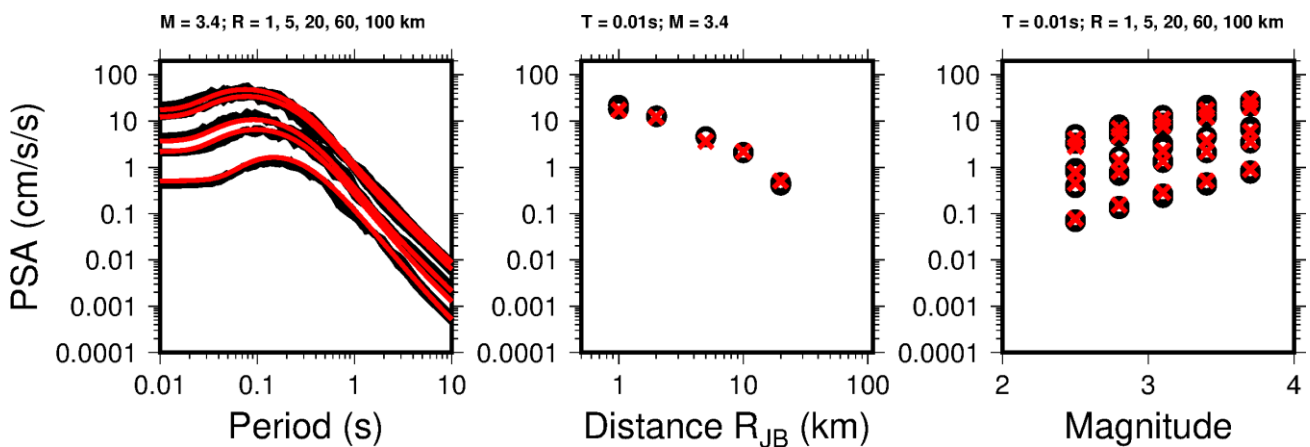


Figure 6.1. Comparison between EXSIM_dmb and SMSIM (RVT implementation) for an identical seismological model. Black: EXSIM_dmb; red: SMSIM (RVT). *Left*: PSA vs. period. *Middle*: PSA vs. distance. *Right*: PSA vs. magnitude. All for scenarios indicated above panels.

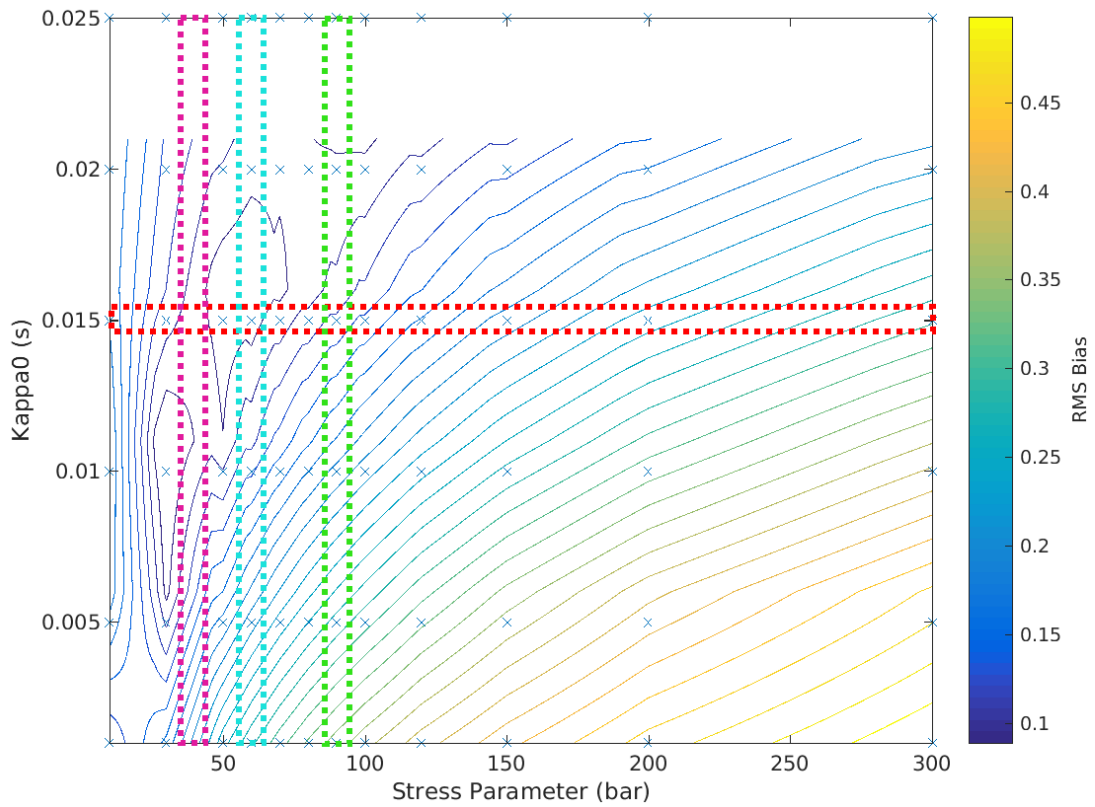


Figure 6.2. RMS bias (Eq.6.3) contoured against stress parameter and κ_0 for $Q=200$. Dashed lines indicate the selected central (blue), lower (purple) and upper (green) model parameters for $\mathbf{M} \leq 3.4$.

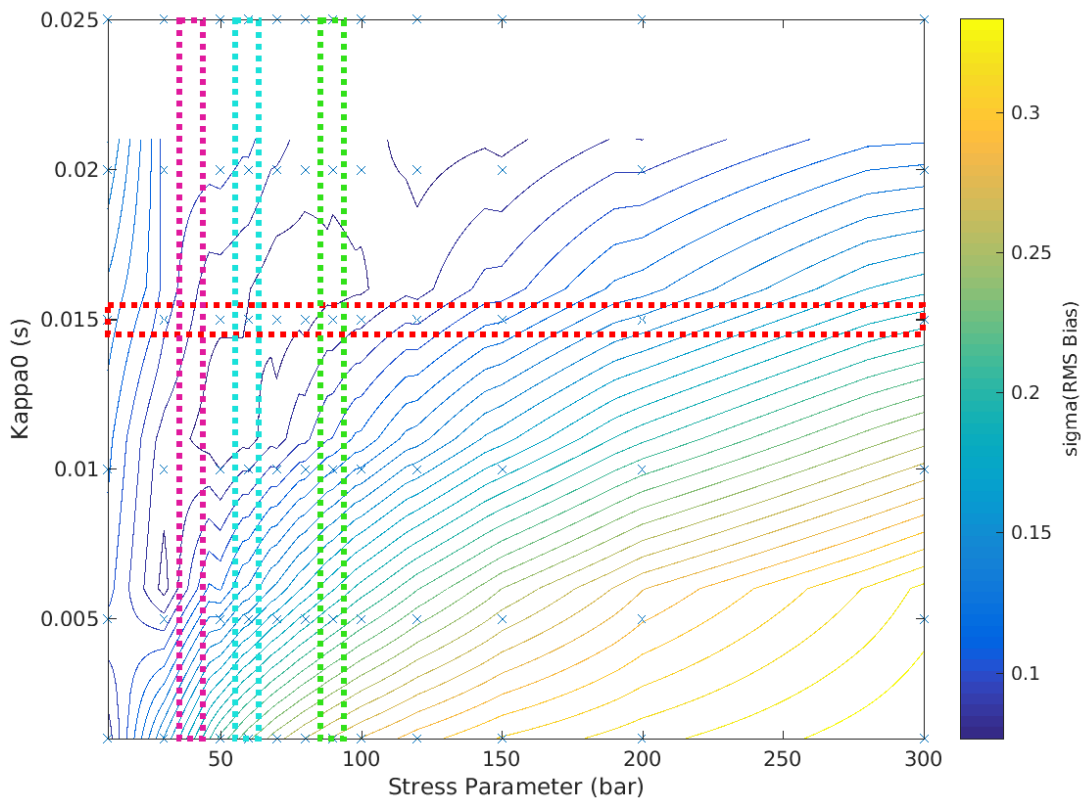


Figure 6.3. Sigma of RMS bias (Eq.6.4) contoured against stress parameter and κ_0 for $Q=200$. Dashed lines indicate the selected central (blue), lower (purple) and upper (green) model parameters for $\mathbf{M} \leq 3.4$.

Calibration to global GMPEs

The aim of the highest (upper) branch Groningen ground motion model is to reflect ground motions observed for small M events in the gas field, while producing ground motions comparable with global tectonic seismicity when extrapolating to larger M . In order to calibrate the model at large magnitude we have performed a similar process to that described above for matching models with locally observed events. However, we now set the target as the PSA at 6 spectral periods (PGA, 0.1, 0.2, 0.3, 1 and 2 s) at magnitudes $M = 5, 6$ and 7, for logarithmically spaced distances of 0, 2.5, 5, 10 and 20 km and with $V_{S30} = 1500$ m/s. Normal faulting is assumed, with a dip of 75 degrees. The log-average of three representative NGA-W2 models (BSSA14: Boore *et al.*, 2014; CY14: Chiou & Youngs, 2014; CB2014: Campbell & Bozognia, 2014) was used as the target PSA at each combination of parameters. Due to the larger stress-drops expected, the grid-search was expanded to include 20 values between 50 and 1600 bars. For the BSSA14 model, which uses the R_{JB} distance metric, this was converted to R_{rup} simply by assuming the latter is the hypotenuse of the former and the depth of 3 km. Based on the work of Boore (2009), who compared SMSIM against EXSIM_dmb, and the comparisons undertaken here, SMSIM (with the R_{EFF} distance metric used for finite-fault approximation) was again used for the calibration since the implementation differences were generally small (see Figure 6.4).

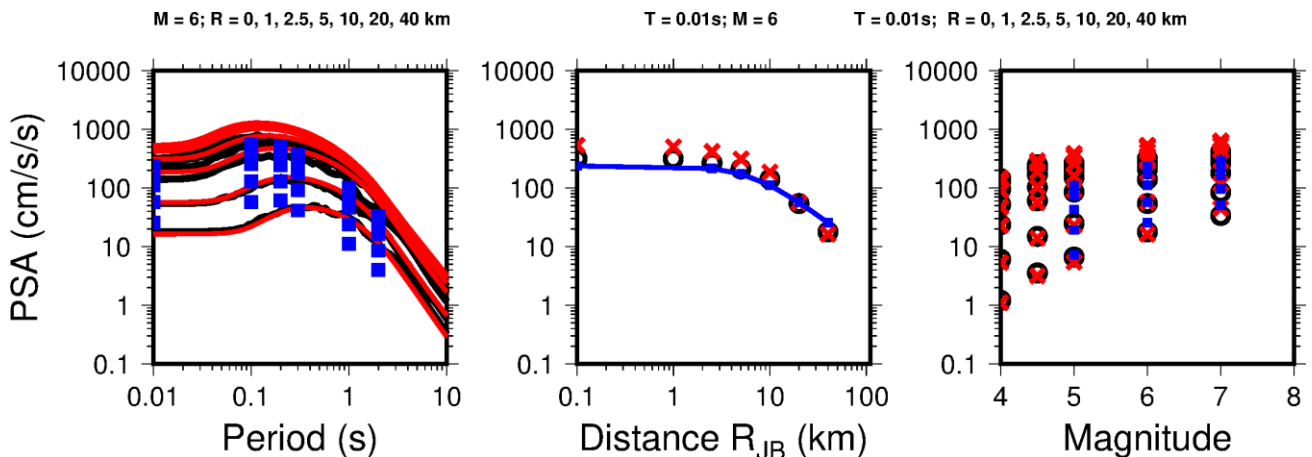


Figure 6.4. Comparison of simulations (upper model) using EXSIM_dmb (black); SMSIM RVT (R_{eff} version) (red) and the average of three NGA-W2 GMPEs (blue). *Left:* PSA vs. period. *Middle:* PSA vs. distance. *Right:* PSA vs. magnitude. All for scenarios indicated above panels.

Models with low bias (over the range of κ_0) and period-to-period variability in bias $\sigma(\text{RMS bias})$ use 100 – 400 bars (Figure 6.5). Assessing the fit was somewhat subjective due to the strong attenuation in the Groningen model, which was not exhibited in the NGA-W2 models and leads to a greater spread of PSA at moderate and short periods with distance (Figure 6.4). The $\sigma(\text{RMS bias})$ suggests a lower stress-drop value reduces the period-to period variability in misfit. However, to be conservative, a model with 300 bars was selected after inspection of the residual misfit plots to ensure that predicted motions for the upper model are consistent with (or, if necessary, exceed) tectonic seismicity across the range of periods.

Effectively this means accepting a small positive model bias (*i.e.*, overestimation of long-period ground-motion) in order not to underestimate the short period motions. A comparison of the simulated ground motions in terms of period, distance and magnitude is shown in Figure 6.4 for the selected 300 bar model.

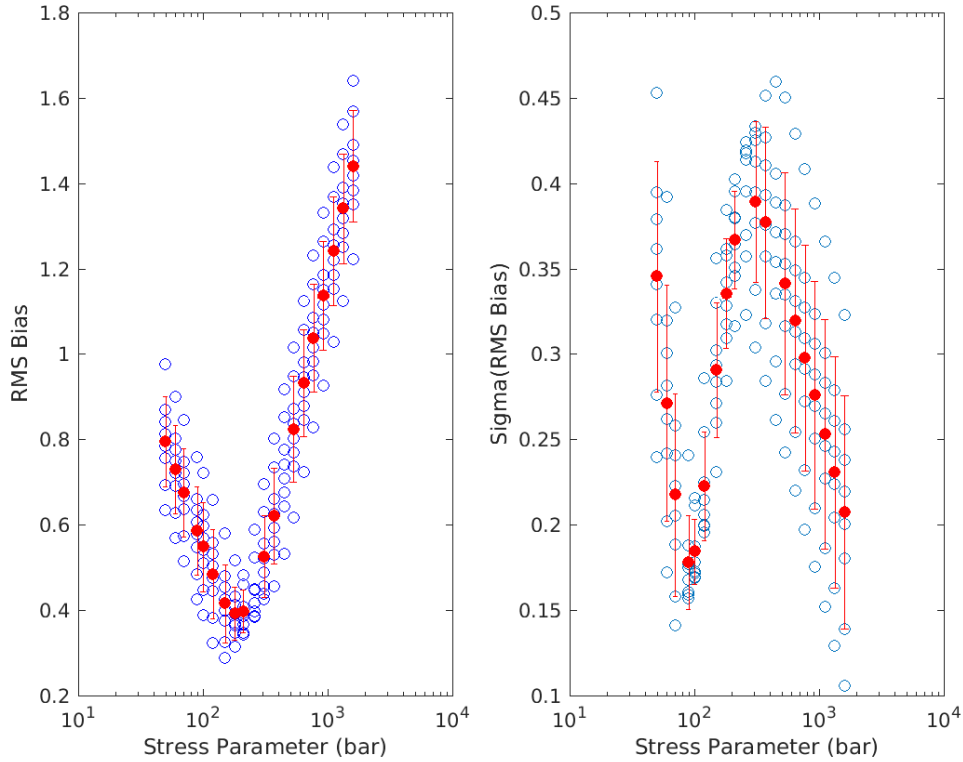


Figure 6.5. RMS bias (*left*, Eq.6.3) and Sigma of RMS bias (*right*, Eq.6.4) against stress parameter for the GMPE target PSA.

Selection of lower, central and upper models

As in the V1-3 models, for the forward simulations it was decided to use alternative values of the stress parameter to reflect the considerable epistemic uncertainty associated with extrapolation to much larger magnitudes. In a change from V3, the V4 model now uses four branches to capture this uncertainty. In the magnitude range covered by data ($M \leq 3.4$) the two central branches have a stress parameter of 60 bars (the best-fit model to local data, no bias), the lower branch 40 bars [with median bias to local data at moderate to short periods (0 to 0.2 s) $\sim -0.5\tau t_0 - \tau$] and—reflecting the possibility of the motions being similar to those from normal tectonic earthquakes—the upper branch has 90 bars [median bias to local data at short periods $\sim +0.5\tau t_0 + \tau$]. All models exhibit an increase of stress-parameter with magnitude, reflecting the belief that for larger events, increasingly sampling greater depths of the crust, the low $\Delta\sigma$ values observed in the reservoir at low M are unrealistic. For the two central models (central *a* and central *b*), $\Delta\sigma$ rises to 120 bars and 190 bars at M 5, respectively, then remains constant. Similarly, the lower and upper models rise to 75 bars and 300 bars, respectively (Figure 6.6). The latter is designed to produce motions, given the Groningen-specific attenuation and site characteristics, which are similar to those observed

globally. The lower model, with stress drops increasing to 75 bars for $M \geq 5$, is designed to reflect that we do not believe that median stress drops at moderate and large magnitude could be as low as those observed for local seismicity in the reservoir.

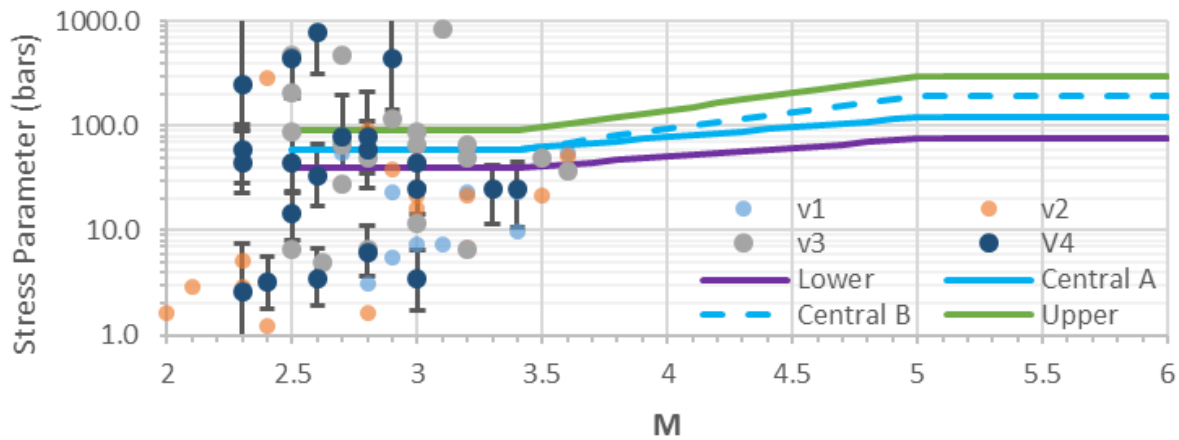


Figure 6.6. Estimates of stress drop together with confidence intervals as a function of magnitude, together with the three median models adopted for the simulations.

Table 6.1 summarises the full set of inputs to the simulations used to generate the motions at the NS_B reference for the derivation of the median GMPEs. For each of the model branches (lower, central a/b, and upper), response spectra were simulated using EXSIM_dmb for 2100 scenario events with $M = 2.0$ to 7.0 in steps of 0.25 . For each scenario event a random epsilon was selected to define the length and width of the rupture. Recording locations were placed radially above the centre of the fault's top edge at 0 km and then 25 distances logarithmically spaced between 1.0 and 79.5 km. For each distance 8 sites were located, at 0 to 315 degrees (in 45 degree steps). In total 1.75 million response spectra were calculated, with 436,800 spectra computed for each of the model branches.

6.2. Predicted accelerations at reference rock horizon

Using the parameter suites summarised in Table 6.1, extended-source stochastic simulations were performed for spectral accelerations at the target oscillator periods using EXSIM_dmb (Boore, 2009). For each oscillator period and for each stress parameter, simulations were performed for a wide range of magnitudes and distances, as summarised above. The patterns displayed by these simulated spectral accelerations concord with expectations in terms of the scaling with magnitude and stress drop, and especially the divergence among the four models with increasing magnitude that correctly reflects the greater epistemic uncertainty with increasing separation from the range covered by the data. Figures 6.7 to 6.12 show the predicted $S_a(T)$ at different oscillator periods from the four models as a function of magnitude, for sites at two rupture distances, the shorter corresponding to the epicentre. Figure 6.13 shows the same information but for PGV. The search is focused on values for the prediction of median ground motions; the associated variability is obtained through separate analyses (see Section 6.5).

Table 6.1. EXSIM_dmb parameter values used in simulations for NS_B motions

Parameter	Symbol (units)	Value(s)	Notes
Density	ρ (g/cm ³)	2.6	
Shear-wave velocity at the source	β (km/s)	2 3.5	M \leq 4.5 (in reservoir) M \geq 5.5 (Carboniferous)
Average shear-wave velocity from the gas reservoir to the NS_B horizon	$\bar{\beta}$ (km/s)	2.6	Applicable for short epicentral distances (< 25 km)
Horizontal partition		0.707	
Radiation coefficient	θ	0.55	
Free surface	F	2	
Sub-fault source type		Brune ω^{-2}	
Top of rupture depth	Z_{top} (km)	3	
Seismogenic depth	Z_{seis} (km)	13	
Fault dip	Dip (degrees)	75	Average of observed 60 – 90 degrees.
Fault mechanism		Normal	
Fault width	W (km)	$\min(W(W\&C'94), [Z_{seis}-3]/\sin(\text{dip})]$	W(W&C'94): Width from Wells & Coppersmith (1994)
Fault length	L (km)	$L(W\&C'94)*(W/W\&C'94)$	L(W&C'94): Length from Wells & Coppersmith (1994) Conserve area of fault A given by $L \times W$ in case limited by Z_{seis}
Hypocentre location	H(ΔL , ΔW) (km, km)	Random, 0	Located randomly along strike, at 3 km depth (top of fault).
Slip velocity	V_{slip} (km/s)	0.8β	
Stress parameter (Lower, Central, Upper)	$\Delta\sigma$ [M \leq 3.4] (bars)	40, 60, 60, 90	Linear interpolation of $\log(\Delta\sigma)$ with M
	$\Delta\sigma$ [M \geq 5.0] (bars)	75, 120, 190, 300	
Geometrical spreading distances (R_{hyp})	R1, R2, R3 (km)	7, 12, 25	
Geometrical decay rates	$\lambda_1, \lambda_2, \lambda_3, \lambda_4$	-1.17, -0.39, -1.50, -1.00	
Path attenuation	Q	200	
Site attenuation	κ_0 (s)	0.015	
Source duration	T_s (s)	$1/0.4906\beta(\Delta\sigma/M_0)^{1/3}$	SI units
Path duration for sub-fault signals	T_p [R (km)]	$T_{5,75}/0.383$	V3 Groningen $T_{5,75}$ model for M = 3.0, V_{S30} =1500.
Rise time	T_s (s)	$1/f_0$	
Site amplification	A(f)	Network average NS_B + Quarter Wavelength	
Dynamic, pulsing percentage		50%	
Sub-fault averaging		RMS	
Scaling		(Acceleration FAS) ²	

The patterns remain rather consistent across the period range, with weaker magnitude scaling at shorter distances and shorter response periods. The greater spread in the simulated values at larger magnitudes reflects the different ray paths associated with a single rupture distance from each extended fault source.

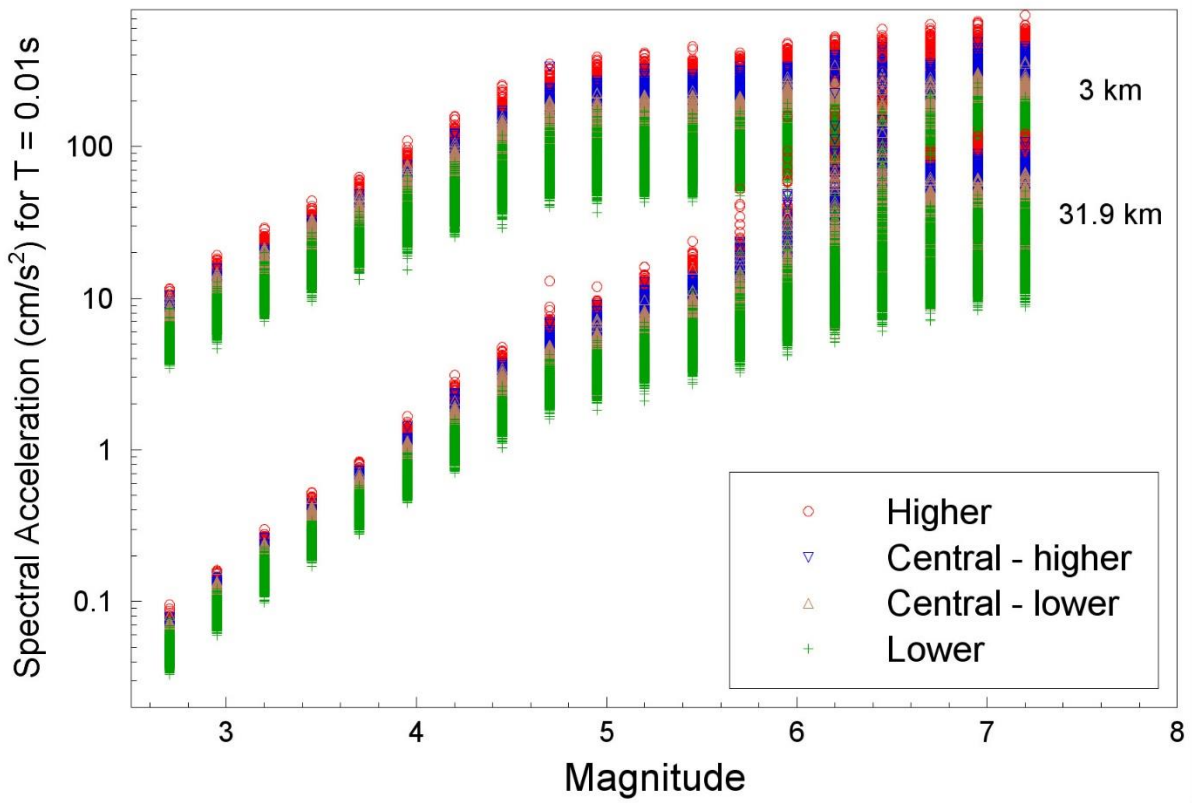


Figure 6.7. Spectral accelerations at 0.01 s from finite-source stochastic simulations for the four stress parameter models at rupture distances of 3 and 32 km as a function of magnitude

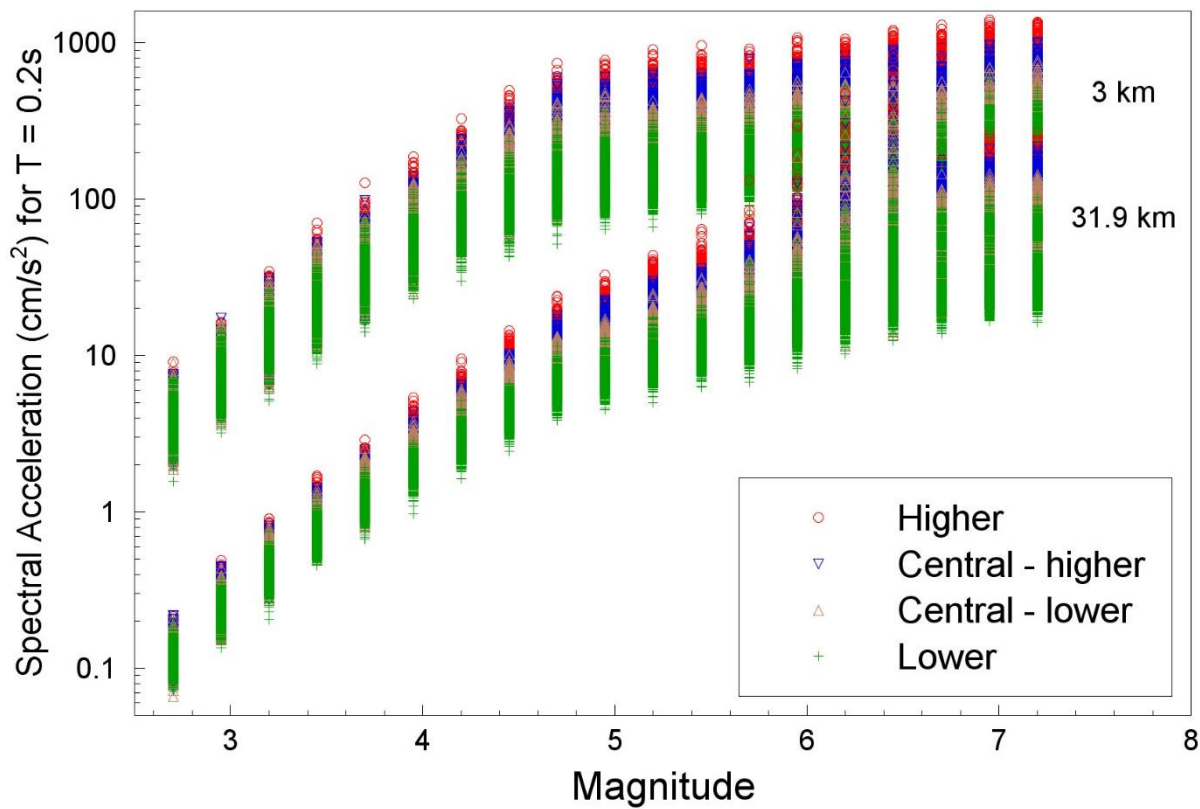


Figure 6.8. Spectral accelerations at 0.2 s from finite-source stochastic simulations for the four stress parameter models at rupture distances of 3 and 32 km as a function of magnitude

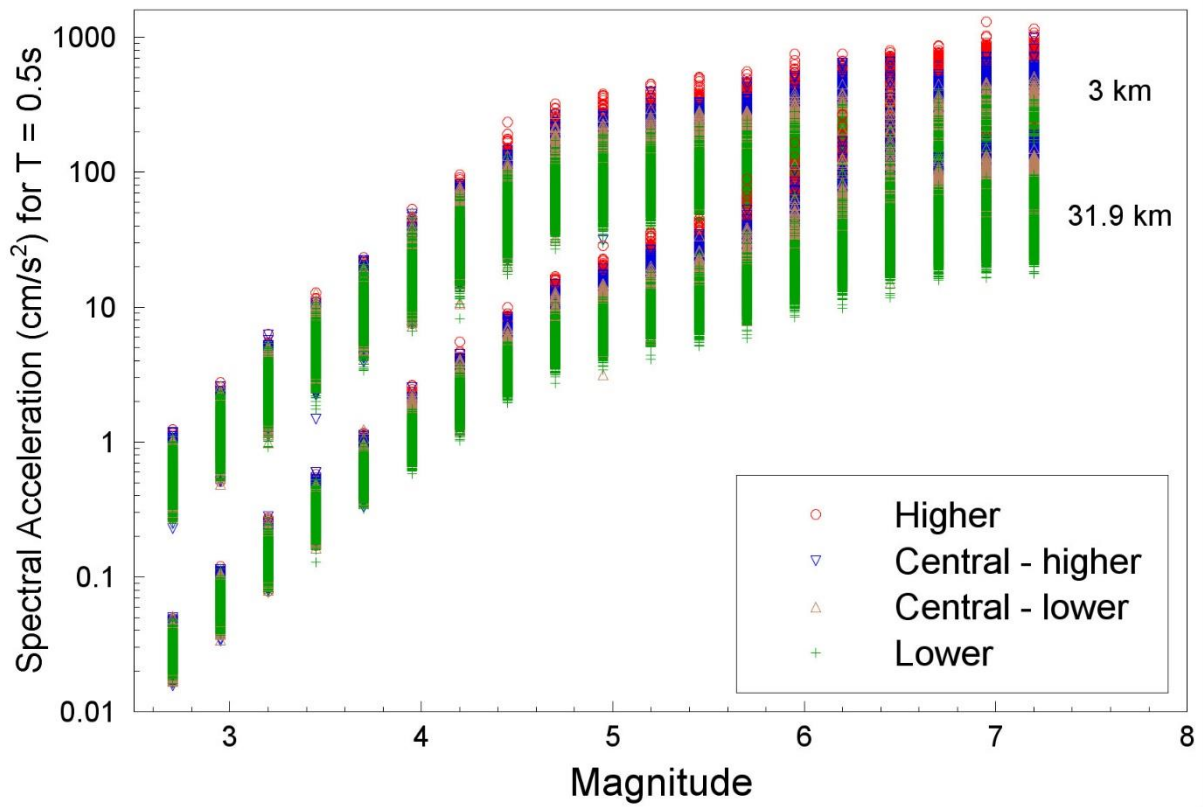


Figure 6.9. Spectral accelerations at 0.5 s from finite-source stochastic simulations for the four stress parameter models at rupture distances of 3 and 32 km as a function of magnitude

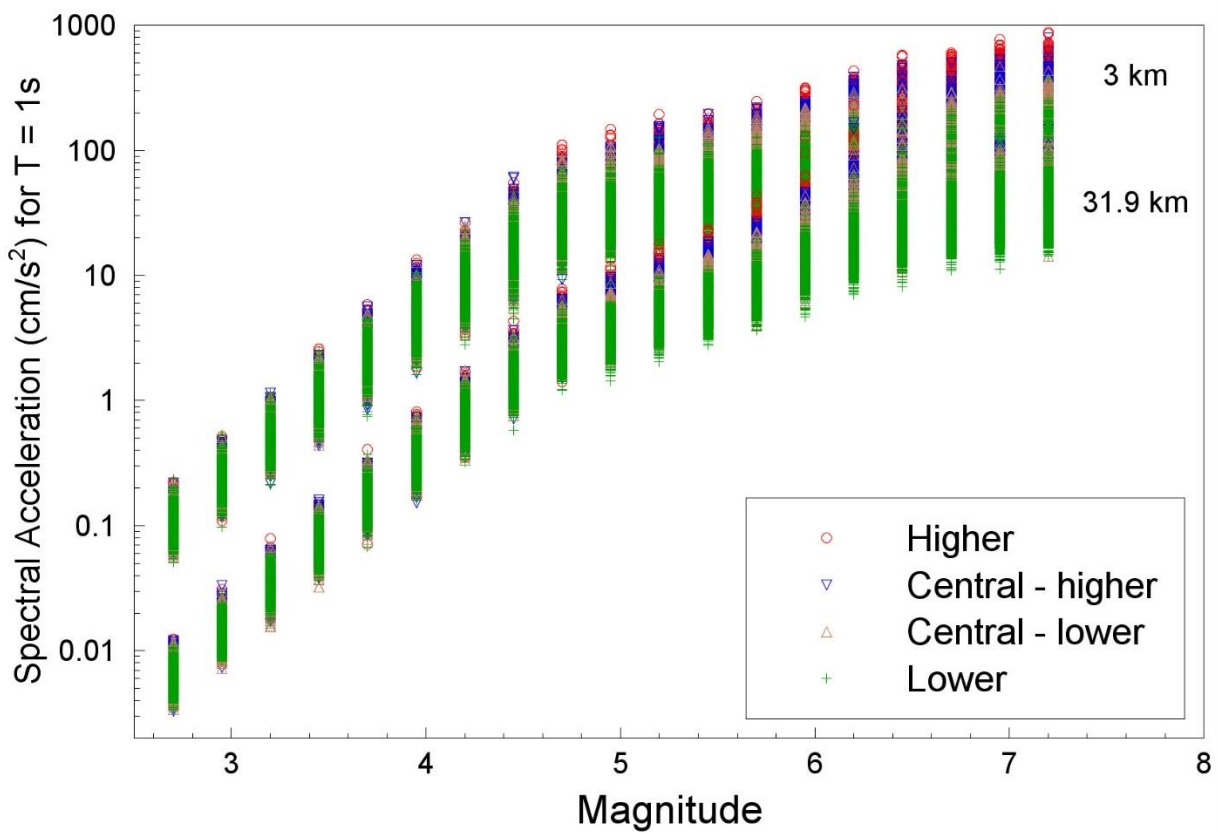


Figure 6.10. Spectral accelerations at 1.0 s from finite-source stochastic simulations for the four stress parameter models at rupture distances of 3 and 32 km as a function of magnitude

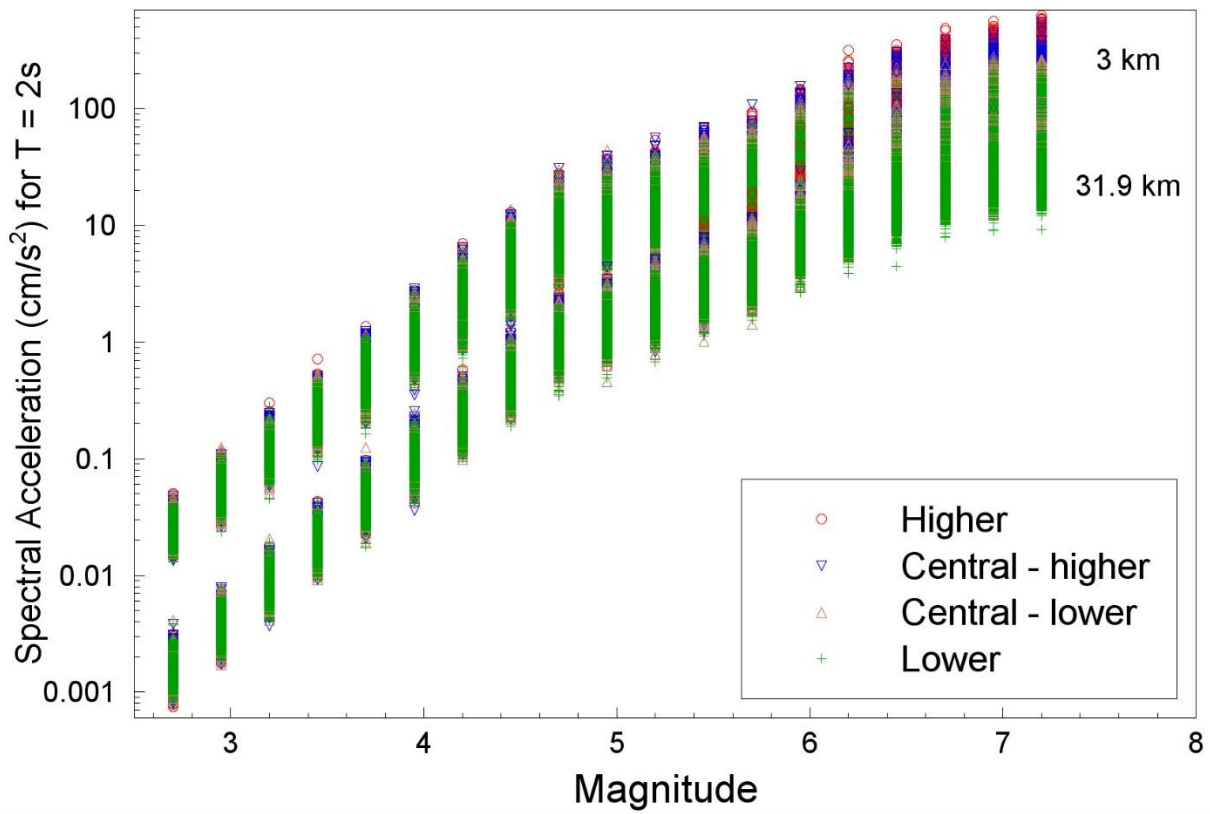


Figure 6.11. Spectral accelerations at 2.0 s from finite-source stochastic simulations for the four stress parameter models at rupture distances of 3 and 32 km as a function of magnitude

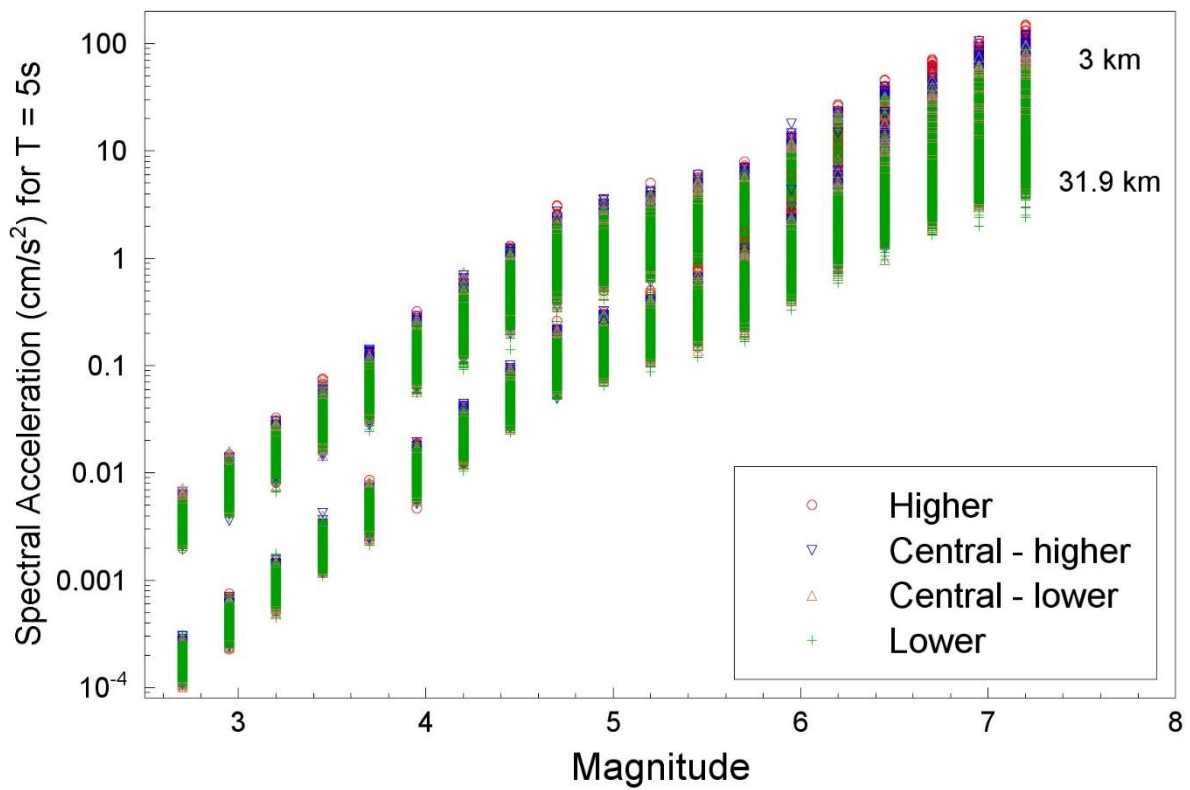


Figure 6.12. Spectral accelerations at 5.0 s from finite-source stochastic simulations for the four stress parameter models at rupture distances of 3 and 32 km as a function of magnitude

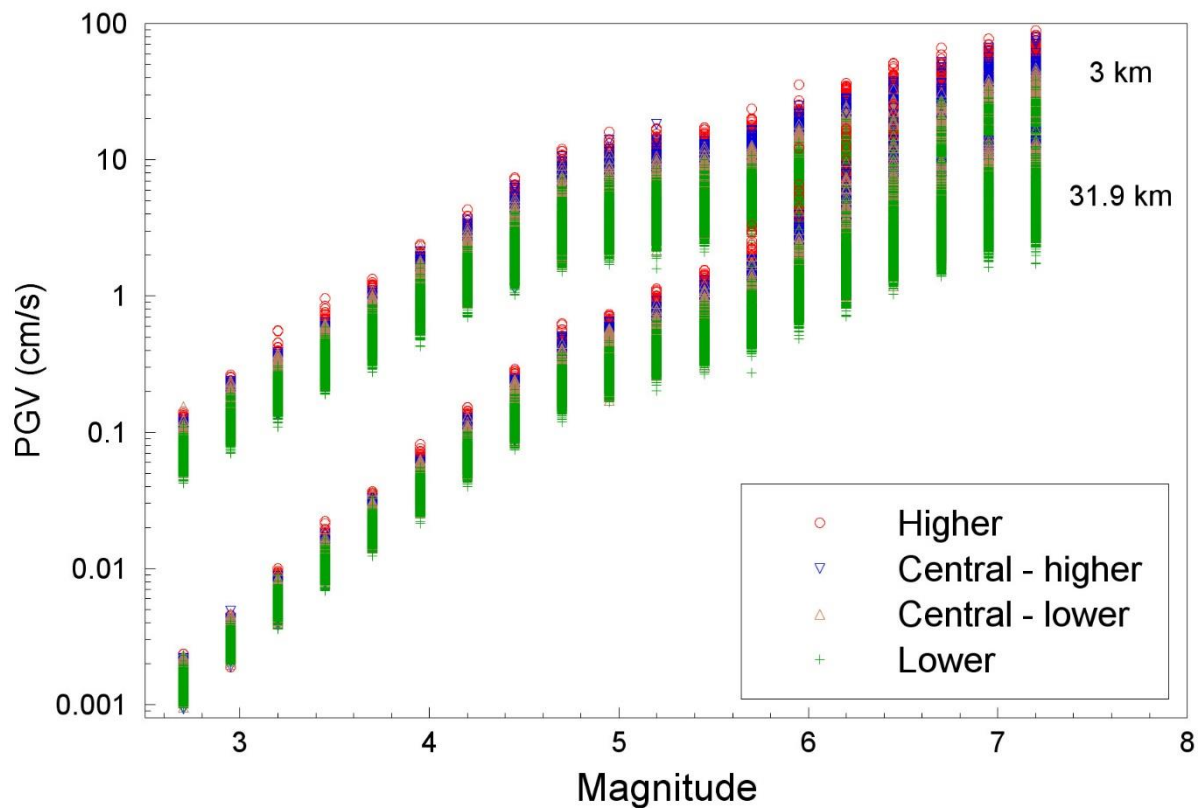


Figure 6.13. Spectral accelerations at PGV from finite-source stochastic simulations for the four stress parameter models at rupture distances of 3 and 32 km as a function of magnitude

6.3. Functional form for reference rock GMPE

For the V1 and V2 GMPEs, a functional form was chosen that was able to provide a good fit to the simulations over the range of magnitudes from M_L 2.5 to M_L 6.5. There was a conscious decision not to develop equations applicable to smaller magnitudes since this would have required an additional break in magnitude scaling to capture the influence of kappa (e.g., Douglas & Jousset, 2011; Baltay & Hanks, 2014). Given the null contributions of smaller earthquakes to all relevant estimates of both hazard and risk, the lower magnitude limit is maintained. Whereas the V3 GMPE model was constrained for large magnitude events using point-source stochastic simulations, the use of finite-fault stochastic simulations (with EXSIM) for the V4 model leads to more realistic predictions of motions from large events. For the EXSIM simulations, moment magnitudes spanning the range $M \in [2,7]$ were considered. The assessment of the model with respect to the field observations for V4 is still based upon motions from events of at least M 2.3, but the upper range of applicability now exceeds the M 6.5 level suggested for the V3 model and realistic predictions will be recovered for events as large as M 7. The range of applicability therefore covers the range of M_{max} values for the hazard and risk model.

The functional form for the V4 GMPE differs slightly from the generic form adopted for V1-3 in that the magnitude scaling is now partitioned into three distinct regions as opposed to two. These three regions were required for the V4 GMPE in order to reflect the more sophisticated manner in which the scaling from small to large events was accounted for. In particular, as

the largest considered events are assumed to have significant portions of their ruptures propagating into the higher-velocity material below the reservoir, the typical rupture velocity for these larger events is assumed to reflect this deeper material. In addition, the scaling of stress drop in the EXSIM analyses was set to transition from values representative of the field at low magnitudes, to values representative of triggered or tectonic events at larger magnitudes. Finally, the modelled size of ruptures had different constraints imposed for the small and large events.

Collectively, these three transitions result in the scaling of spectral accelerations changing with magnitude. For the smallest events the scaling is very much calibrated to be consistent with the field observations, while for the largest events considered within the hazard and risk model the constraints are imposed from using analogies with triggered or tectonic events in other seismic regions. Two of the scaling regimes reflect these small ($M \leq 4.7$) and large ($M \geq 5.45$) events, while the third regime represents the transition between the small and large events. In Figures 6.14-6.29 the locations of these breaks in scaling are shown by vertical dashed grey lines. The stress drop scaling that transitions from the lowest stress drop values at moment magnitudes of 3.4 up to their highest values at magnitude 5.0 do not actually contribute particularly strongly to the breaks in scaling. On the other hand, the combined effect of changing the rupture velocity from a value of 2.0 km/s for events below magnitude 4.5 up to a value of 3.5 km/s for events of magnitude greater than 5, as well as moving from Eshelby/Brune source size scaling for events below magnitude 5.25 to Wells & Coppersmith (1994) scaling above this point contributes strongly to the changes in magnitude scaling. For a given magnitude, these rupture velocity and rupture size changes effectively map across into a change in the corner frequency and hence effect the nature of the magnitude scaling."

The functional form can generically be written as a combination of source, g_{src} , and path, g_{path} , contributions:

$$\ln[Sa_{\mu}(T)] = g_{src}(M) + g_{path}(R_{rup}, M) \quad (6.5)$$

where $Sa_{\mu}(T)$ is the spectral acceleration in units of cm/s^2 . The magnitude scale is M_L , the local magnitude as calculated by KNMI and as used in the characterisation of the seismicity model. This local magnitude is related to the moment magnitude via $M = M_L - 0.2$, as in the V3 model. Whereas the distance used within the V3 model was an effective distance based upon the use of epicentral distance and some magnitude-dependent term to account for near-source effects, the use of the finite-fault simulations through EXSIM allow the distance to now be defined directly in terms of the closest distance the earthquake rupture, R_{rup} , given in kilometres.

The three distinct scaling regimes are reflected in the source components as:

$$g_{src}(M) = \begin{cases} m_0 + m_1(M - 4.7) + m_2(M - 4.7)^2 & \text{for } M \leq 4.7 \\ m_0 + m_3(M - 4.7) & 4.7 \leq M < 5.45 \\ m_0 + m_3(5.45 - 4.7) + m_4(M - 5.45) + m_5(M - 5.45)^2 & \text{for } M \geq 5.45 \end{cases} \quad (6.6)$$

For the V1-V3 GMPEs a point-source distance (epicentral distance) was employed that required an effective distance to be used to obtain realistic motions from larger events. This effective distance was obtained by combining the epicentral distance with a magnitude-dependent near-source saturation term. Various proposals for this near-source saturation term have appeared in the literature in recent years (Yenier & Atkinson, 2014; Atkinson, 2015), but there is still a significant degree of uncertainty related to how these saturation effects scale over the full range of magnitudes required in the hazard and risk model.

The advantage of using the finite-fault simulations within EXSIM is that the effects of motions originating from distinct patches of the rupture are directly accounted for and this circumvents the need for an effective distance to be used. The path component of Eq.(6.3) is therefore defined directly in terms of the rupture distance and the magnitude-dependent saturation term is dropped from the developed GMPE.

The path scaling for the V4 GMPE is again comprised of three distinct scaling regimes that are informed by the numerical waveform modelling conducted for the field. Since the numerical waveform modelling was conducted using point sources, the boundaries of the three different scaling regimes are strictly defined in terms of R_{hyp} . Therefore, to impose these constraints it is assumed that the hypocentral distance is equivalent to the rupture distance. This is reasonable under the working assumption that the peak motions are ultimately controlled by a small portion of the fault rupture that is closest to the site.

All three path scaling regimes have geometric spreading coefficients that are magnitude-dependent. In the V3 model comparable magnitude dependent scaling was only used for the largest considered distances. However, the V3 model implicitly contained magnitude dependence for shorter distances through the near-source saturation term.

The overall path scaling function is provided in Eq.(6.7), in which the distance ranges are defined in kilometres:

$$g_{path}(R_{rup}, M) = \begin{cases} (r_0 + r_1 M) \ln\left(\frac{R_{rup}}{3}\right) & \text{for } R_{rup} < 7 \\ (r_0 + r_1 M) \ln\left(\frac{7}{3}\right) + (r_2 + r_3 M) \ln\left(\frac{R_{rup}}{7}\right) & 7 \leq R_{rup} < 12 \\ (r_0 + r_1 M) \ln\left(\frac{7}{3}\right) + (r_2 + r_3 M) \ln\left(\frac{12}{7}\right) + (r_4 + r_5 M) \ln\left(\frac{R_{rup}}{12}\right) & \text{for } R_{rup} \geq 12 \end{cases} \quad (6.7)$$

As for the V3 model, there is still insufficient data from events at large distances to allow explicit terms for anelastic attenuation to be considered. Such terms would only have a pronounced influence at longer distances ($\gg 30$ km) and all hazard and risk disaggregation results to date have indicated that contributions from such distant scenarios are very small. Moreover, there are no data available at such distances and the simulations for distances beyond 25 km are based on an assumed decay rate. A term could be added to the GMPE to explicitly reflect the influence of the low Q used in the simulations, but it would not serve to necessarily make the model more realistic. The absence of an explicit term to capture the

effect of Q does not, of course, mean that anelastic attenuation is omitted from the parameterised equations since the effect will influence the coefficients on the geometric spreading terms. In the V1 model, using a single geometric spreading term over all distances, resulted in slight over-prediction of the simulated motions at greater distances but some mild under-prediction at intermediate distances. This feature would tend to motivate the inclusion of an explicit anelastic term but since segmented models for geometric spreading have been included in more recent GMPES, the same effect is not expected to occur.

6.4. Regression analyses

As for the GMPEs developed for V1-V3, the regression analyses were performed to estimate the values of the coefficients of Eqs.(6.5), (6.6) and (6.7) by fitting the functional form to the outputs from the stochastic simulations using the parameter combinations summarised in Table 6.1. The coefficients for the four models that correspond to the four different representations of the stress parameter are presented in Tables 6.2 to 6.9. The coefficients for the source components are presented in Tables 6.2, 6.4, 6.6 and 6.8, while the coefficients for the path scaling components are given in Tables 6.3, 6.5, 6.7 and 6.9.

Figures 6.14 to 6.29 show comparisons of the median predictions at six response periods with simulations as a function of magnitude for four different rupture distances, all of which confirm the good fit of the regressions to the simulated motions. For the purposes of creating these plots only a subset of the simulations were included. The total number of EXSIM simulations that were used to constrain the parameters of the regression equations was 436,800. For plotting purposes, a random sample of 10,000 of these simulations was used. Naturally, this is still a very large number of simulations and the general agreement that is observed in the figures shown here also reflects the performance of the model with respect to the full dataset.

Figures 6.30 to 6.37 show the response spectral simulations and predictions for a number of different magnitude and distance scenarios, as well as for each of the four models. The spectral shapes that are presented in these figures match the simulation data very well. In addition, the general shape of the spectra are more consistent with expectations from other regions worldwide than was the case for the V3 model.

When making similar comparisons for the V3 model differences between the simulated motions and the model predictions were more readily discernible because for each magnitude and distance scenario there was only one point-source. However, with the V4 model employing EXSIM each of these magnitude and distance scenarios has a number of different rupture geometries and source-to-site orientations associated with it. For this reason the plots in Figures 6.14-6.37 indicate a degree of dispersion in the simulation results. The regression model does a very good job of reflecting the centre of these simulations, but clearly no attempt is made to match every simulation. This variability arising from the simple characterisation of the source and path effects using just magnitude and rupture distance is captured by the sigma model.

Table 6.2. Coefficients of the source scaling component of the lower model (L)

T (s)	m_0	m_1	m_2	m_3	m_4	m_5
PGV	1.41157	1.48710	-0.14778	0.30622	1.00237	-0.19078
0.01	4.64820	0.84445	-0.18303	0.01366	0.34210	-0.12947
0.025	5.02566	0.78709	-0.14323	-0.07581	0.24818	-0.11914
0.05	5.46356	0.78193	-0.14929	-0.02236	0.25327	-0.11449
0.075	5.52701	0.76427	-0.19502	0.06297	0.29762	-0.11363
0.1	5.40488	0.73548	-0.25359	0.12912	0.33547	-0.11398
0.125	5.30361	0.72534	-0.30722	0.17166	0.37163	-0.11866
0.15	5.23959	0.73574	-0.34859	0.20232	0.40060	-0.12200
0.175	5.15860	0.76848	-0.37642	0.21796	0.42387	-0.12503
0.2	5.06582	0.81427	-0.39552	0.22475	0.44958	-0.13034
0.25	4.90718	0.92931	-0.41331	0.24017	0.49489	-0.14117
0.3	4.79019	1.06079	-0.41495	0.25658	0.54070	-0.15276
0.4	4.60174	1.32440	-0.38940	0.28820	0.62271	-0.17322
0.5	4.40823	1.55304	-0.35215	0.32029	0.70316	-0.19427
0.6	4.19998	1.74957	-0.31115	0.35785	0.78698	-0.21947
0.7	4.05275	1.91921	-0.27547	0.40944	0.86915	-0.24050
0.85	3.77073	2.09896	-0.23059	0.47476	0.98955	-0.27552
1	3.50694	2.23415	-0.19367	0.53800	1.10912	-0.31005
1.5	3.01040	2.56985	-0.11318	0.73693	1.50511	-0.41388
2	2.38273	2.64004	-0.08369	0.81065	1.74269	-0.46409
2.5	1.82603	2.63601	-0.07201	0.82949	1.92138	-0.48760
3	1.37302	2.61141	-0.06951	0.83171	2.04475	-0.49156
4	0.66813	2.55031	-0.07410	0.81412	2.15914	-0.45389
5	0.13756	2.49774	-0.08090	0.78473	2.17401	-0.39201

Table 6.3. Coefficients of the path scaling component of the lower model (L)

T (s)	r_0	r_1	r_2	r_3	r_4	r_5
PGV	-2.77848	0.36824	-1.55684	0.14671	-3.18999	0.31084
0.01	-3.04031	0.37558	-1.78292	0.14511	-3.91050	0.36508
0.025	-3.35437	0.39764	-2.51640	0.24674	-4.06456	0.38674
0.05	-2.88397	0.31924	-1.88328	0.08256	-4.65117	0.45303
0.075	-2.74547	0.31557	-0.89303	-0.04903	-4.55814	0.40426
0.1	-2.64618	0.31066	-0.68180	-0.04222	-4.10392	0.32351
0.125	-2.54421	0.30137	-0.68187	-0.01557	-3.68660	0.25875
0.15	-2.46703	0.29403	-0.72110	0.00654	-3.36088	0.21260
0.175	-2.41131	0.28896	-0.75949	0.02092	-3.13155	0.18632
0.2	-2.37895	0.28800	-0.77674	0.02702	-2.96064	0.17018
0.25	-2.31971	0.28302	-0.83457	0.04056	-2.71963	0.15093
0.3	-2.25002	0.27617	-0.88036	0.04874	-2.55072	0.13865
0.4	-2.16619	0.26759	-0.91063	0.05412	-2.35080	0.12707
0.5	-2.13228	0.26555	-0.89946	0.05174	-2.24245	0.12349
0.6	-2.12414	0.26626	-0.91649	0.05420	-2.18373	0.12433
0.7	-2.10240	0.26458	-0.90387	0.05228	-2.11446	0.12126
0.85	-2.10134	0.26591	-0.92490	0.05521	-2.07497	0.12302
1	-2.12086	0.27032	-0.94238	0.05762	-2.05600	0.12660
1.5	-2.05447	0.26298	-0.89238	0.05190	-1.92007	0.11964
2	-2.11144	0.27385	-0.93650	0.05820	-1.92865	0.12619
2.5	-2.17530	0.28438	-1.01931	0.07171	-1.97619	0.13782
3	-2.22173	0.29176	-1.08889	0.08299	-2.01993	0.14782
4	-2.28052	0.30009	-1.18605	0.10012	-2.10186	0.16408
5	-2.33177	0.30851	-1.22575	0.10671	-2.16799	0.17570

Table 6.4. Coefficients of the source scaling component of the lower central model (Ca)

T (s)	m_0	m_1	m_2	m_3	m_4	m_5
PGV	1.63537	1.51378	-0.15266	0.32261	1.03364	-0.18753
0.01	4.95792	0.88466	-0.18939	0.03644	0.35056	-0.12502
0.025	5.34472	0.82354	-0.14576	-0.05793	0.25434	-0.11525
0.05	5.77618	0.80858	-0.16071	0.00858	0.25498	-0.10737
0.075	5.83569	0.78496	-0.21513	0.0992	0.30095	-0.10748
0.1	5.71629	0.76497	-0.27633	0.15648	0.34234	-0.10869
0.125	5.61401	0.76941	-0.32792	0.19851	0.3756	-0.11107
0.15	5.55005	0.79763	-0.36487	0.22825	0.40289	-0.1137
0.175	5.46831	0.8491	-0.38719	0.23978	0.43288	-0.12012
0.2	5.37184	0.90949	-0.40136	0.25173	0.45846	-0.1254
0.25	5.20551	1.05279	-0.4082	0.26569	0.51297	-0.1396
0.3	5.08366	1.20526	-0.39951	0.28363	0.56168	-0.1522
0.4	4.87951	1.48643	-0.36309	0.31702	0.66	-0.17873
0.5	4.66303	1.7188	-0.32005	0.36042	0.757	-0.20524
0.6	4.43001	1.90843	-0.27745	0.41318	0.85022	-0.23167
0.7	4.26135	2.06788	-0.2419	0.47091	0.95533	-0.26235
0.85	3.95395	2.2266	-0.20037	0.54237	1.09063	-0.30063
1	3.66997	2.34501	-0.16632	0.6081	1.2231	-0.33707
1.5	3.12011	2.6333	-0.09641	0.79509	1.65172	-0.44199
2	2.47573	2.6811	-0.07292	0.84844	1.88886	-0.48332
2.5	1.91159	2.66065	-0.06648	0.85542	2.05216	-0.49485
3	1.45713	2.62954	-0.06607	0.84761	2.15249	-0.48514
4	0.75726	2.56559	-0.07208	0.81773	2.21582	-0.42511
5	0.2317	2.5132	-0.07962	0.78818	2.19093	-0.34876

Table 6.5. Coefficients of the path scaling component of the lower central model (Ca)

T (s)	r_0	r_1	r_2	r_3	r_4	r_5
PGV	-2.83256	0.37576	-1.59548	0.15044	-3.25318	0.31749
0.01	-3.08471	0.38101	-1.80281	0.14564	-3.99541	0.37476
0.025	-3.40242	0.40334	-2.57522	0.25324	-4.16503	0.39904
0.05	-2.90821	0.32224	-1.83569	0.07113	-4.76192	0.46616
0.075	-2.76959	0.31832	-0.83487	-0.0598	-4.6256	0.40979
0.1	-2.66947	0.31292	-0.6457	-0.04848	-4.13775	0.32398
0.125	-2.56729	0.30378	-0.66404	-0.01862	-3.69893	0.25628
0.15	-2.48959	0.29635	-0.69997	0.00236	-3.37045	0.21064
0.175	-2.42868	0.29085	-0.74684	0.01748	-3.13606	0.18402
0.2	-2.38485	0.28749	-0.79401	0.02873	-2.95802	0.16715
0.25	-2.32358	0.2829	-0.84443	0.04023	-2.71927	0.14875
0.3	-2.27511	0.27892	-0.88012	0.04733	-2.55225	0.13726
0.4	-2.21644	0.27477	-0.88768	0.04823	-2.36	0.12739
0.5	-2.18174	0.27227	-0.89136	0.04897	-2.24837	0.12344
0.6	-2.16751	0.2721	-0.92487	0.05423	-2.18667	0.12377
0.7	-2.14706	0.27059	-0.91698	0.05311	-2.11878	0.12131
0.85	-2.15302	0.27334	-0.95061	0.05868	-2.07854	0.12271
1	-2.16671	0.27697	-0.97928	0.06264	-2.06455	0.12686
1.5	-2.11054	0.27212	-0.92321	0.05551	-1.9252	0.11959
2	-2.16161	0.28144	-0.96583	0.06282	-1.94874	0.12854
2.5	-2.22002	0.2907	-1.06454	0.07876	-1.99818	0.14045
3	-2.26751	0.29818	-1.13587	0.09051	-2.04017	0.14979
4	-2.34072	0.30971	-1.22304	0.10525	-2.11845	0.16482
5	-2.39055	0.31781	-1.25133	0.10893	-2.18918	0.17744

Table 6.6. Coefficients of the source scaling component of the upper central model (Cb)

T (s)	m_0	m_1	m_2	m_3	m_4	m_5
PGV	1.76522	1.66951	-0.11087	0.42596	1.06975	-0.18152
0.01	5.15084	1.11182	-0.12851	0.17563	0.36345	-0.11662
0.025	5.54228	1.05571	-0.08367	0.086	0.26171	-0.10463
0.05	5.97708	1.04457	-0.09717	0.15257	0.26006	-0.09693
0.075	6.03826	1.02292	-0.15159	0.24225	0.30292	-0.09595
0.1	5.91737	1.00568	-0.21131	0.29954	0.34709	-0.10021
0.125	5.81406	1.00701	-0.26389	0.3436	0.37819	-0.1025
0.15	5.74579	1.0306	-0.30256	0.37464	0.40818	-0.10624
0.175	5.66032	1.07729	-0.3259	0.39227	0.43366	-0.1104
0.2	5.56122	1.13803	-0.33919	0.4029	0.46511	-0.11877
0.25	5.38802	1.27669	-0.34637	0.41693	0.52592	-0.13496
0.3	5.2587	1.42546	-0.3387	0.43204	0.58836	-0.15272
0.4	5.03325	1.6873	-0.30724	0.47601	0.70034	-0.18381
0.5	4.79929	1.90011	-0.26931	0.52284	0.81341	-0.21544
0.6	4.55049	2.0714	-0.23181	0.56979	0.92842	-0.24829
0.7	4.36841	2.21576	-0.20008	0.62289	1.04893	-0.28335
0.85	4.04504	2.35731	-0.16311	0.6821	1.20988	-0.32979
1	3.74681	2.45696	-0.13443	0.73275	1.36294	-0.36941
1.5	3.16811	2.70299	-0.07723	0.8842	1.82114	-0.47562
2	2.51371	2.73668	-0.05793	0.91764	2.04747	-0.50543
2.5	1.94719	2.71045	-0.05307	0.91107	2.18	-0.49817
3	1.49329	2.67812	-0.05309	0.89649	2.24639	-0.47108
4	0.79588	2.6163	-0.05873	0.86138	2.26438	-0.39218
5	0.27336	2.56708	-0.06548	0.83652	2.21394	-0.31137

Table 6.7. Coefficients of the path scaling component of the upper central model (Cb)

T (s)	r_0	r_1	r_2	r_3	r_4	r_5
PGV	-2.80446	0.36995	-1.59931	0.15164	-3.24664	0.31324
0.01	-3.06049	0.37522	-1.79786	0.14659	-3.98545	0.3693
0.025	-3.37536	0.39641	-2.56535	0.25321	-4.15576	0.39355
0.05	-2.8881	0.31793	-1.82312	0.06991	-4.75083	0.45978
0.075	-2.74602	0.3134	-0.83979	-0.05614	-4.60985	0.40242
0.1	-2.64173	0.30781	-0.65855	-0.04358	-4.12087	0.31696
0.125	-2.54192	0.29876	-0.68304	-0.01259	-3.6848	0.25055
0.15	-2.46871	0.2923	-0.71422	0.00791	-3.35326	0.20485
0.175	-2.41758	0.28869	-0.74343	0.01869	-3.125	0.18005
0.2	-2.37375	0.2854	-0.78796	0.02947	-2.9493	0.16395
0.25	-2.30618	0.27958	-0.85772	0.04489	-2.70928	0.14574
0.3	-2.25139	0.27492	-0.875	0.04778	-2.55202	0.13621
0.4	-2.17925	0.26845	-0.89683	0.05156	-2.35679	0.12595
0.5	-2.14694	0.26675	-0.90569	0.05251	-2.2397	0.12117
0.6	-2.14181	0.26864	-0.92335	0.05389	-2.18117	0.1223
0.7	-2.12516	0.26806	-0.9122	0.05251	-2.11589	0.12021
0.85	-2.13313	0.27117	-0.93082	0.05487	-2.07769	0.12215
1	-2.15046	0.27507	-0.9671	0.06052	-2.06144	0.12607
1.5	-2.08833	0.26782	-0.91984	0.05584	-1.93187	0.12088
2	-2.13787	0.27694	-0.97804	0.06664	-1.94785	0.12786
2.5	-2.209	0.28856	-1.06035	0.07958	-1.99952	0.13993
3	-2.26307	0.29758	-1.11476	0.08722	-2.04852	0.15053
4	-2.33338	0.30889	-1.19184	0.0987	-2.12985	0.16628
5	-2.37716	0.31517	-1.24039	0.10703	-2.19128	0.17662

Table 6.8. Coefficients of the source scaling component of the upper model (U)

T (s)	m_0	m_1	m_2	m_3	m_4	m_5
PGV	1.98714	1.69414	-0.1169	0.42055	1.06242	-0.16172
0.01	5.45214	1.14403	-0.13717	0.18381	0.3368	-0.09735
0.025	5.85483	1.08263	-0.08962	0.08975	0.236	-0.08735
0.05	6.28809	1.06248	-0.1127	0.16545	0.23599	-0.07956
0.075	6.34229	1.03919	-0.17488	0.25984	0.28222	-0.07953
0.1	6.21984	1.03328	-0.23573	0.31667	0.32152	-0.08146
0.125	6.11477	1.05476	-0.28371	0.359	0.35203	-0.08292
0.15	6.0472	1.10357	-0.3149	0.38381	0.38914	-0.09032
0.175	5.95903	1.16685	-0.33216	0.39891	0.42269	-0.09837
0.2	5.85592	1.24012	-0.34055	0.41102	0.45511	-0.10673
0.25	5.67251	1.39572	-0.33928	0.43488	0.51437	-0.12199
0.3	5.53259	1.55802	-0.32399	0.45489	0.58499	-0.14249
0.4	5.28298	1.83027	-0.28325	0.50325	0.72118	-0.18249
0.5	5.02246	2.04009	-0.24177	0.56068	0.85528	-0.2209
0.6	4.74886	2.20135	-0.20369	0.61355	0.98648	-0.25783
0.7	4.5444	2.33358	-0.17335	0.67252	1.12228	-0.29547
0.85	4.19748	2.45373	-0.14117	0.72811	1.30497	-0.34545
1	3.88087	2.53608	-0.11626	0.77082	1.47579	-0.38788
1.5	3.26057	2.75405	-0.0631	0.90046	1.95745	-0.49085
2	2.59226	2.7604	-0.0519	0.92211	2.16556	-0.50726
2.5	2.02625	2.72698	-0.04977	0.90682	2.26348	-0.48308
3	1.57467	2.68938	-0.05232	0.88817	2.29338	-0.43754
4	0.88457	2.6271	-0.05904	0.84961	2.26934	-0.34399
5	0.36861	2.58207	-0.06501	0.82082	2.20018	-0.2622

Table 6.9. Coefficients of the path scaling component of the upper model (U)

T (s)	r_0	r_1	r_2	r_3	r_4	r_5
PGV	-2.8662	0.37806	-1.64791	0.15761	-3.30718	0.31948
0.01	-3.12048	0.38365	-1.84036	0.15115	-4.06705	0.37826
0.025	-3.43062	0.40332	-2.64997	0.26396	-4.25559	0.40555
0.05	-2.92509	0.32202	-1.78992	0.06201	-4.86134	0.47243
0.075	-2.76795	0.31551	-0.81557	-0.06001	-4.67105	0.40635
0.1	-2.68286	0.31347	-0.62483	-0.04845	-4.14988	0.31635
0.125	-2.58943	0.30564	-0.64409	-0.01816	-3.6972	0.24817
0.15	-2.48577	0.29433	-0.71961	0.00853	-3.36285	0.20314
0.175	-2.43383	0.29035	-0.76219	0.02238	-3.129	0.17777
0.2	-2.39532	0.28779	-0.80024	0.03173	-2.95398	0.16239
0.25	-2.35215	0.28616	-0.83982	0.04083	-2.71846	0.14558
0.3	-2.29588	0.28108	-0.88233	0.04813	-2.55565	0.13533
0.4	-2.2403	0.27742	-0.90262	0.05155	-2.3612	0.12571
0.5	-2.1954	0.27387	-0.93143	0.05525	-2.25166	0.12253
0.6	-2.18945	0.2755	-0.96025	0.05943	-2.18951	0.12319
0.7	-2.16579	0.27361	-0.95479	0.05894	-2.12298	0.12111
0.85	-2.16079	0.2743	-0.98364	0.06359	-2.09363	0.12424
1	-2.17485	0.27747	-1.02264	0.07021	-2.07674	0.12778
1.5	-2.11935	0.27201	-0.9837	0.06542	-1.93667	0.12108
2	-2.18707	0.28426	-1.0379	0.07446	-1.95289	0.12841
2.5	-2.25469	0.29542	-1.12647	0.08847	-2.01001	0.14106
3	-2.30232	0.30233	-1.18761	0.09864	-2.06156	0.15167
4	-2.37268	0.31298	-1.25437	0.10836	-2.14846	0.16806
5	-2.42237	0.32111	-1.28849	0.11264	-2.21346	0.17895

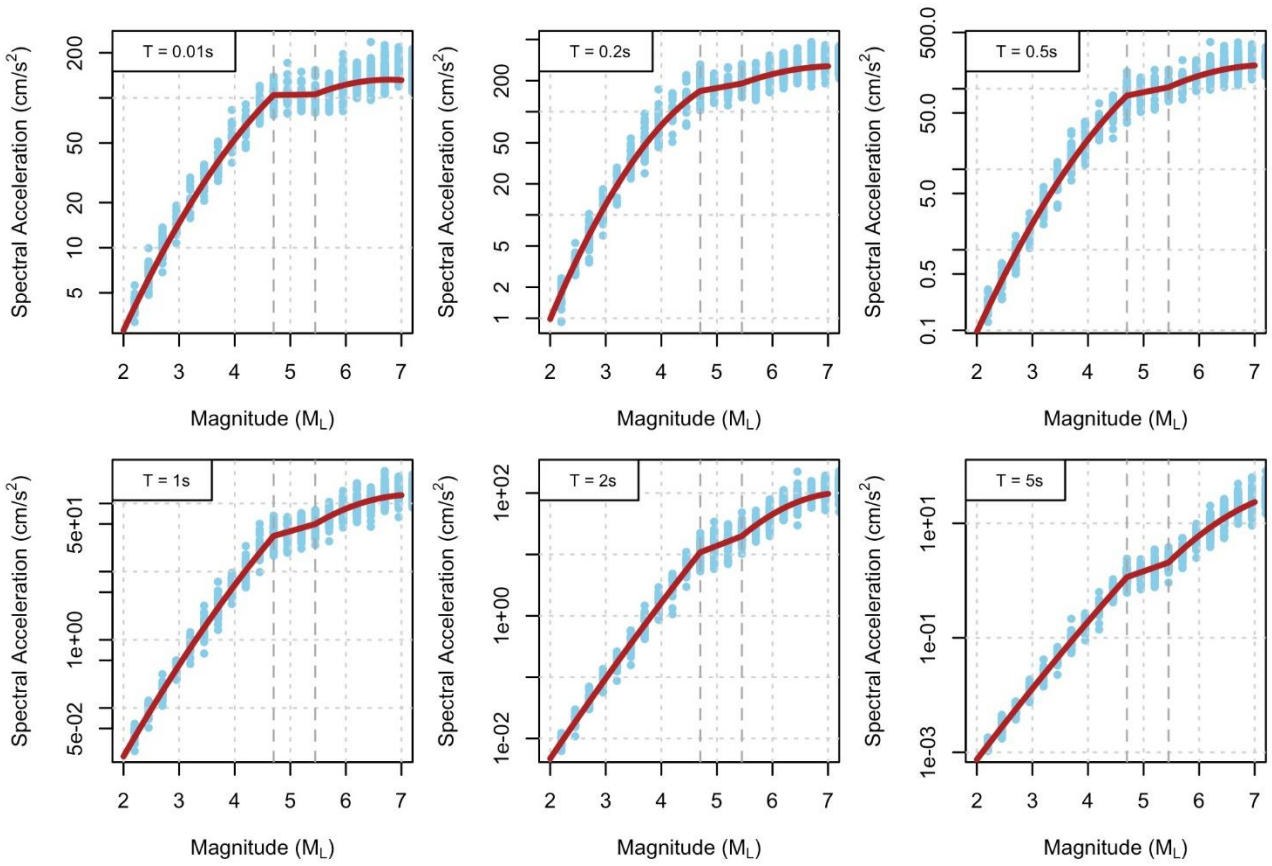


Figure 6.14. Comparison of simulations and median predictions from the equation for the lower model (L) for 6 response periods at 3 km rupture distance

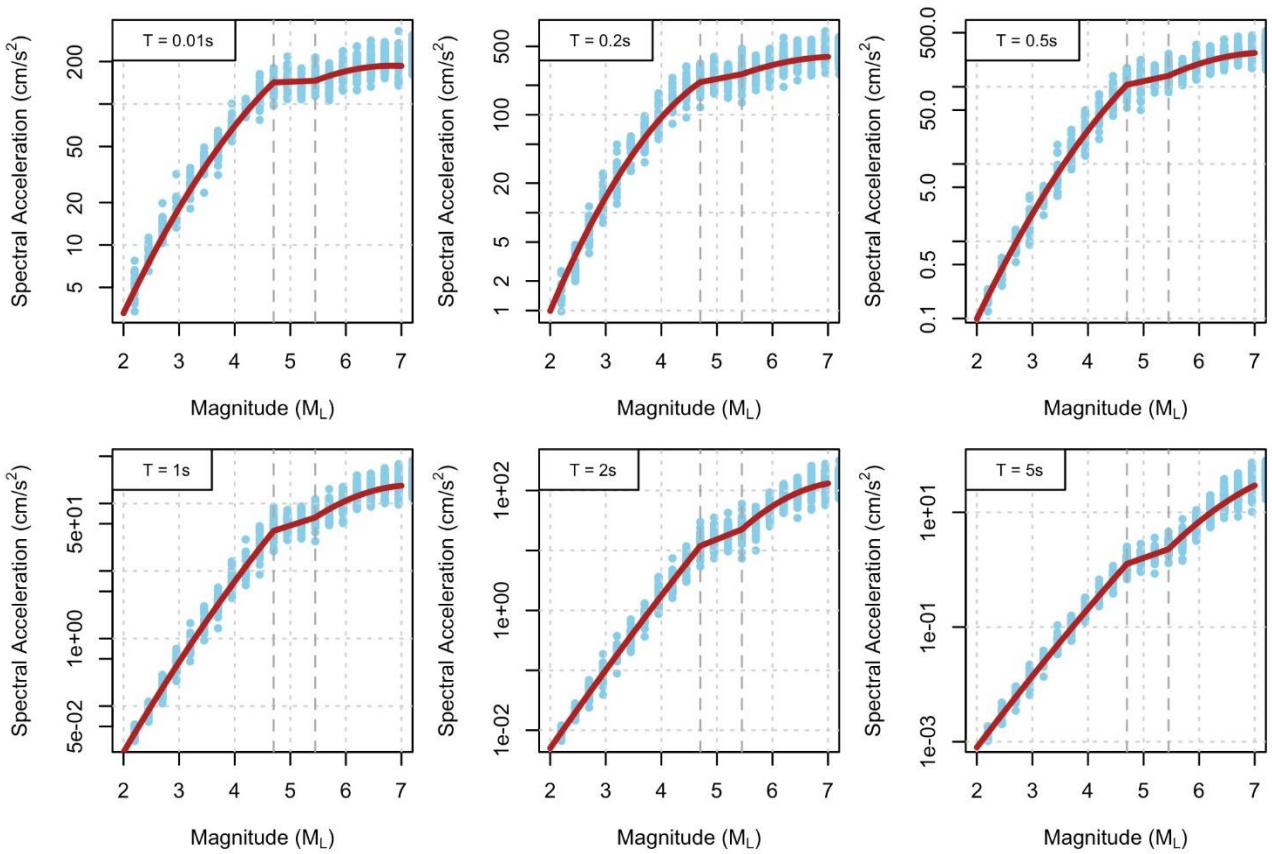


Figure 6.15. Comparison of simulations and median predictions from the equation for the lower-central model (Ca) for 6 response periods at 3 km rupture distance

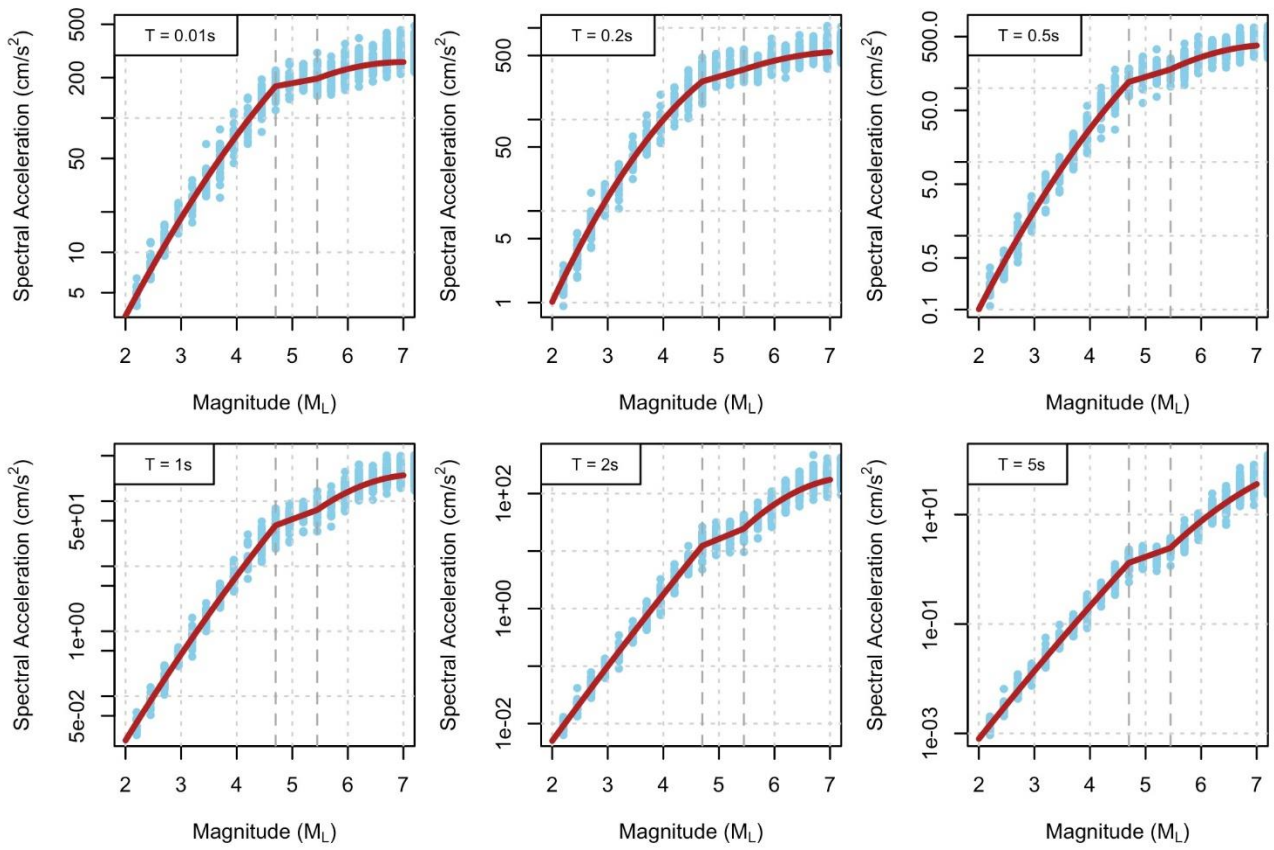


Figure 6.16. Comparison of simulations and median predictions from the equation for the upper-central model (Cb) for 6 response periods at 3 km rupture distance

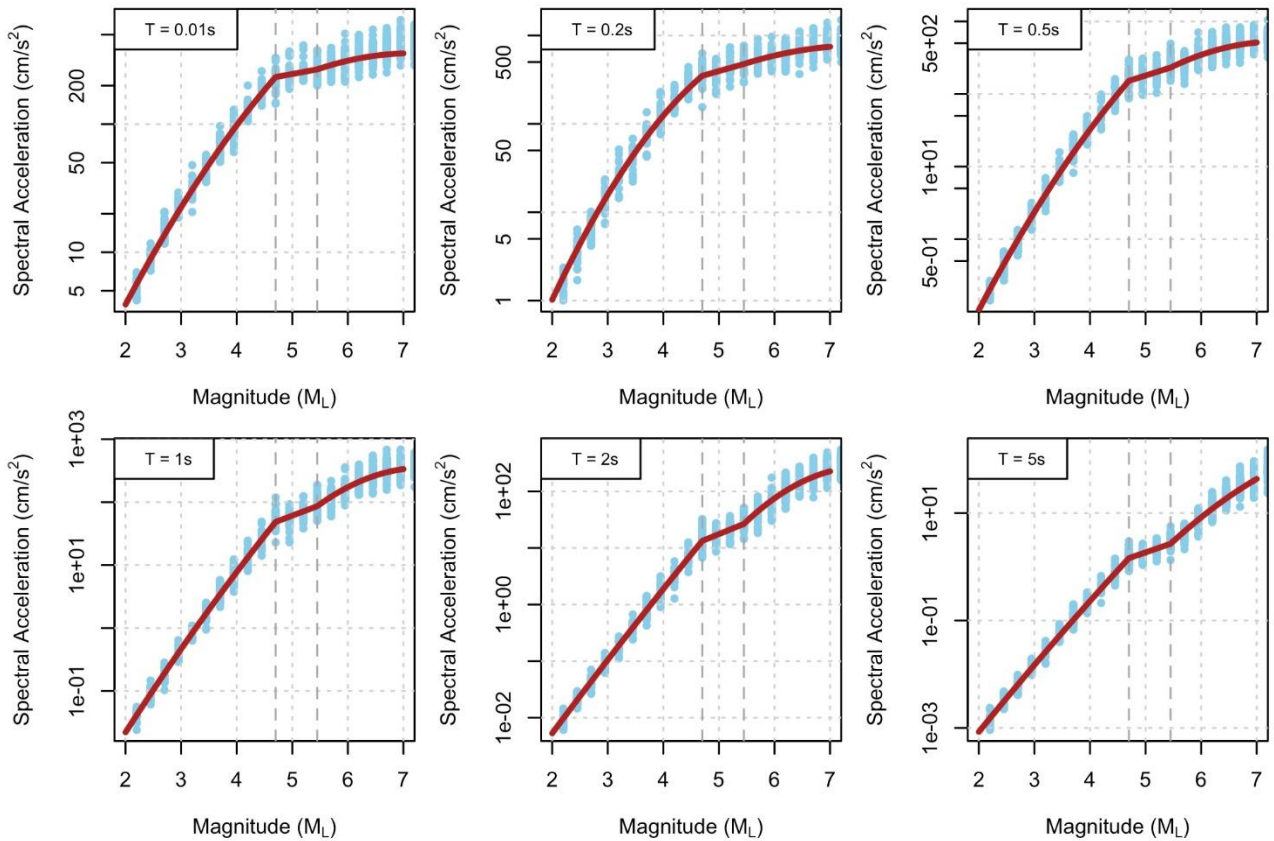


Figure 6.17. Comparison of simulations and median predictions from the equation for the upper model (U) for 6 response periods at 3 km rupture distance

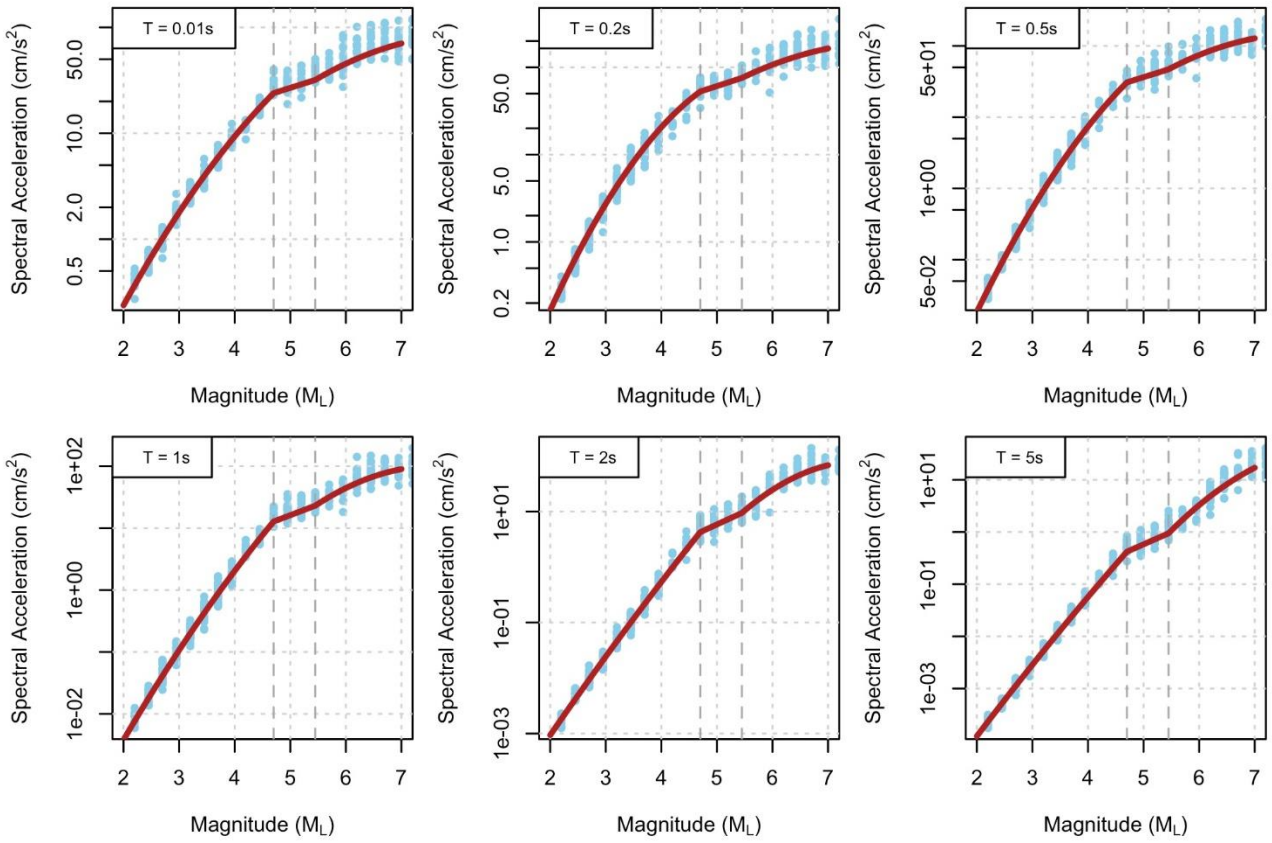


Figure 6.18. Comparison of simulations and median predictions from the equation for the lower model (L) for 6 response periods at 10 km rupture distance

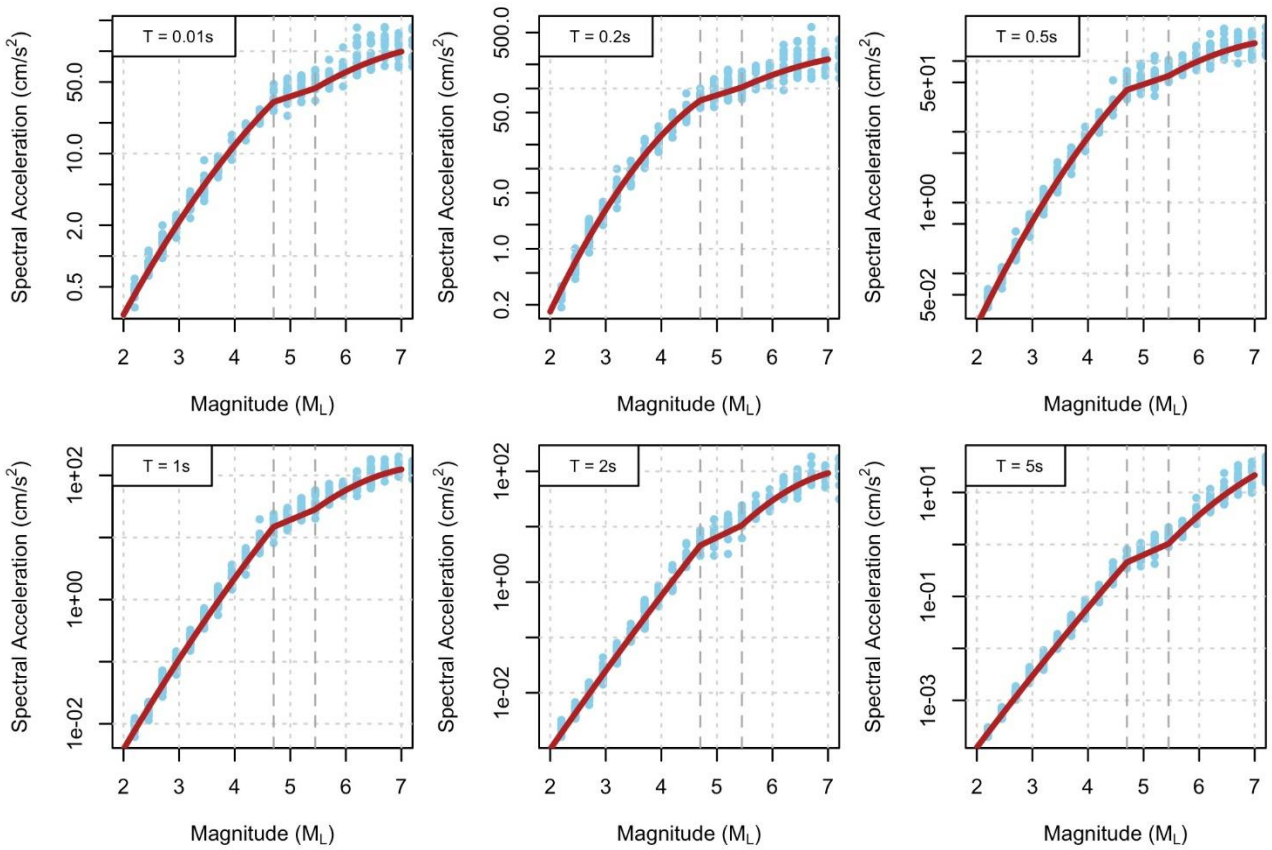


Figure 6.19. Comparison of simulations and median predictions from the equation for the lower-central model (Ca) for 6 response periods at 10 km rupture distance

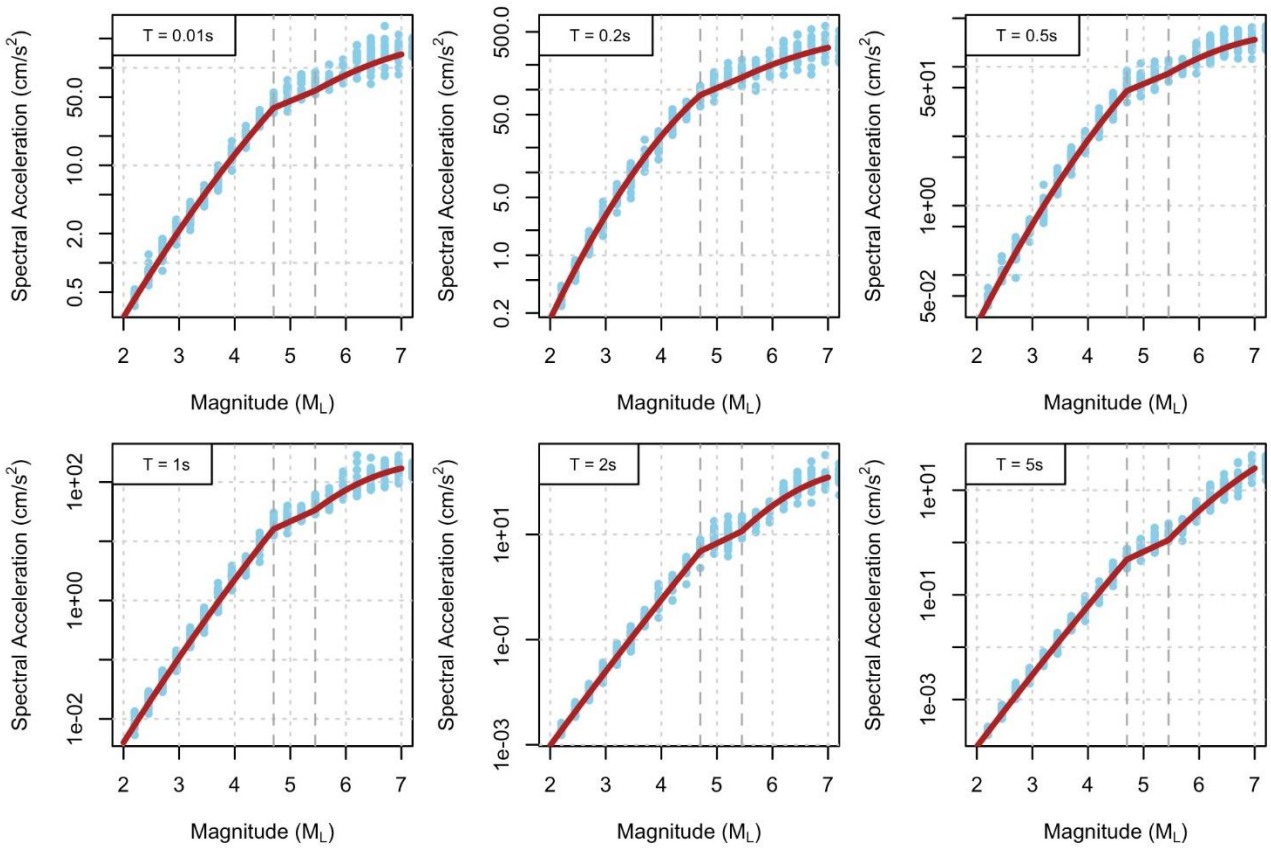


Figure 6.20. Comparison of simulations and median predictions from the equation for the upper-central model (Cb) for 6 response periods at 10 km rupture distance

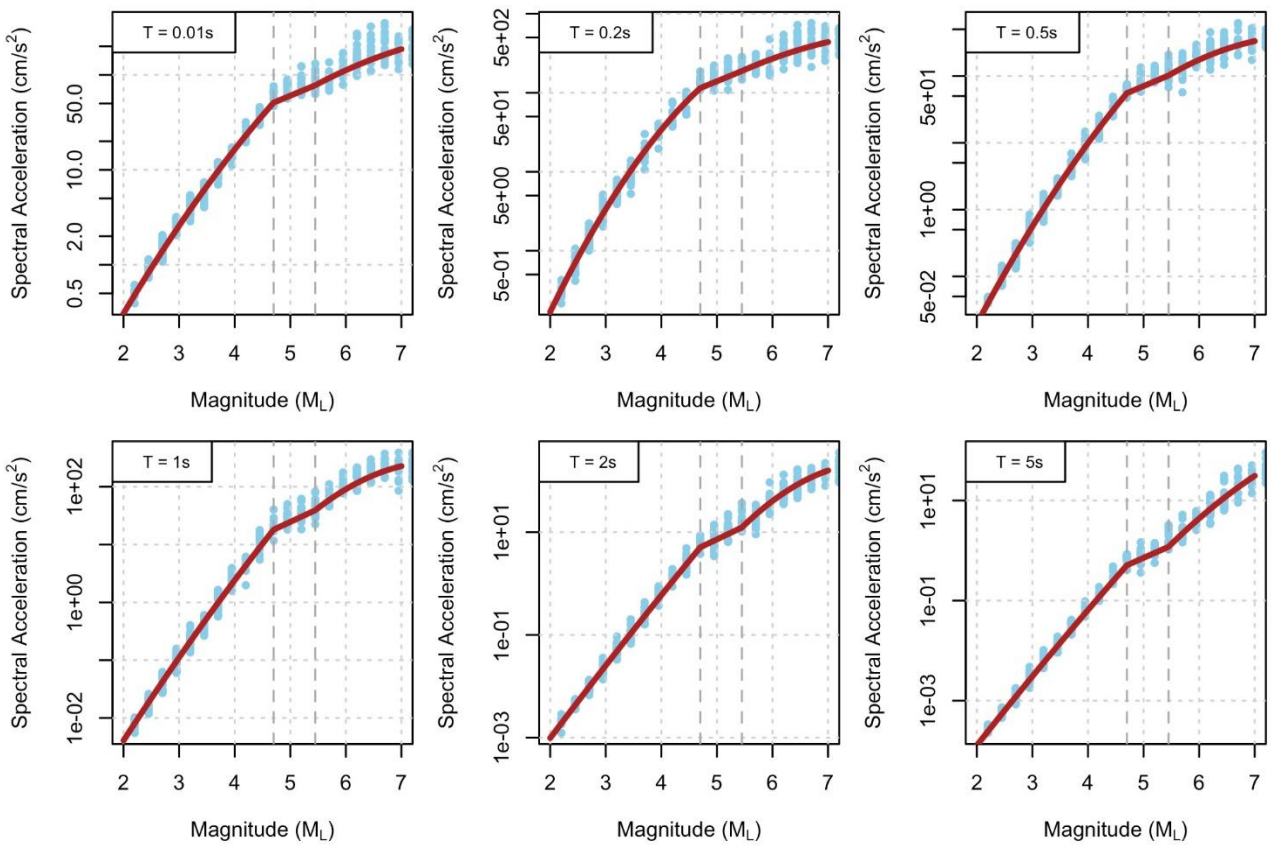


Figure 6.21. Comparison of simulations and median predictions from the equation for the upper model (U) for 6 response periods at 10 km rupture distance

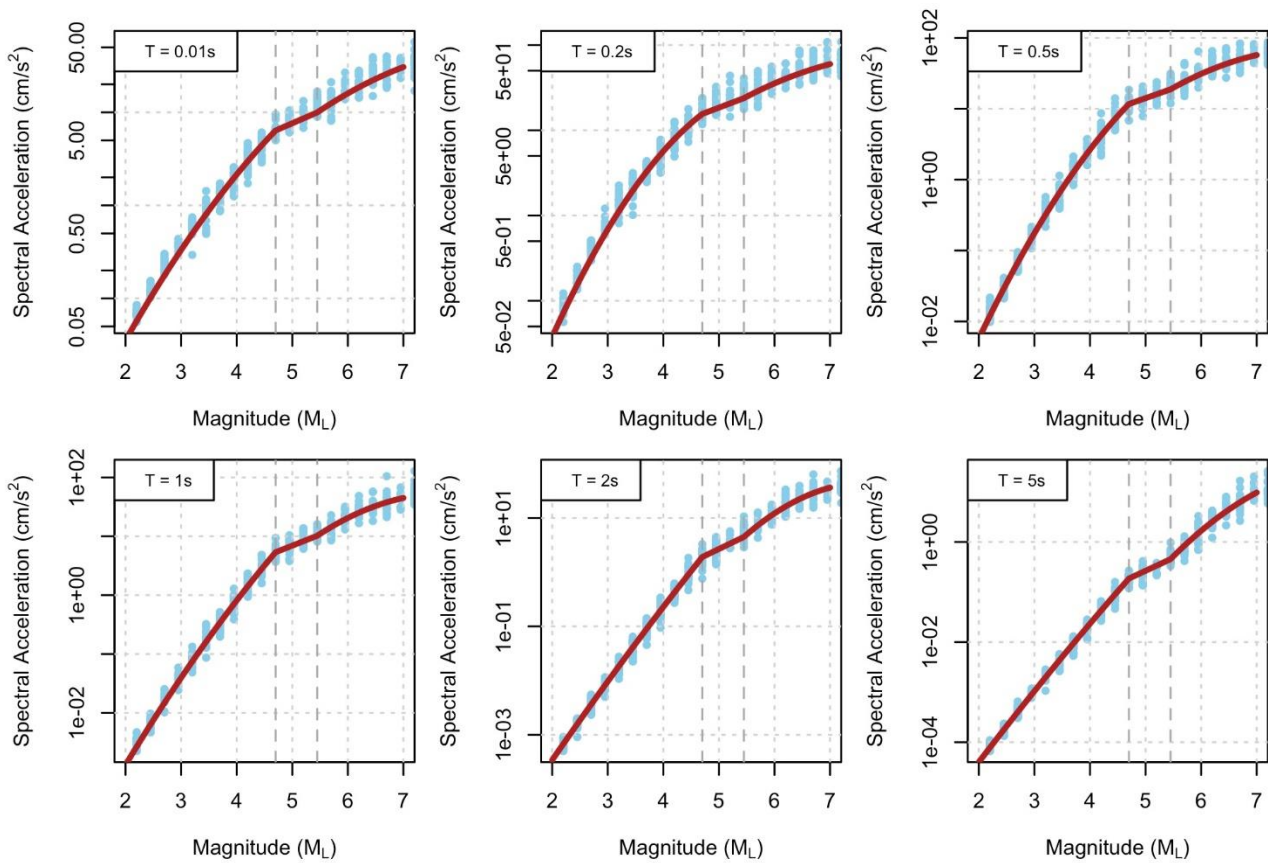


Figure 6.22. Comparison of simulations and median predictions from the equation for the lower model (L) for 6 response periods at 20 km rupture distance

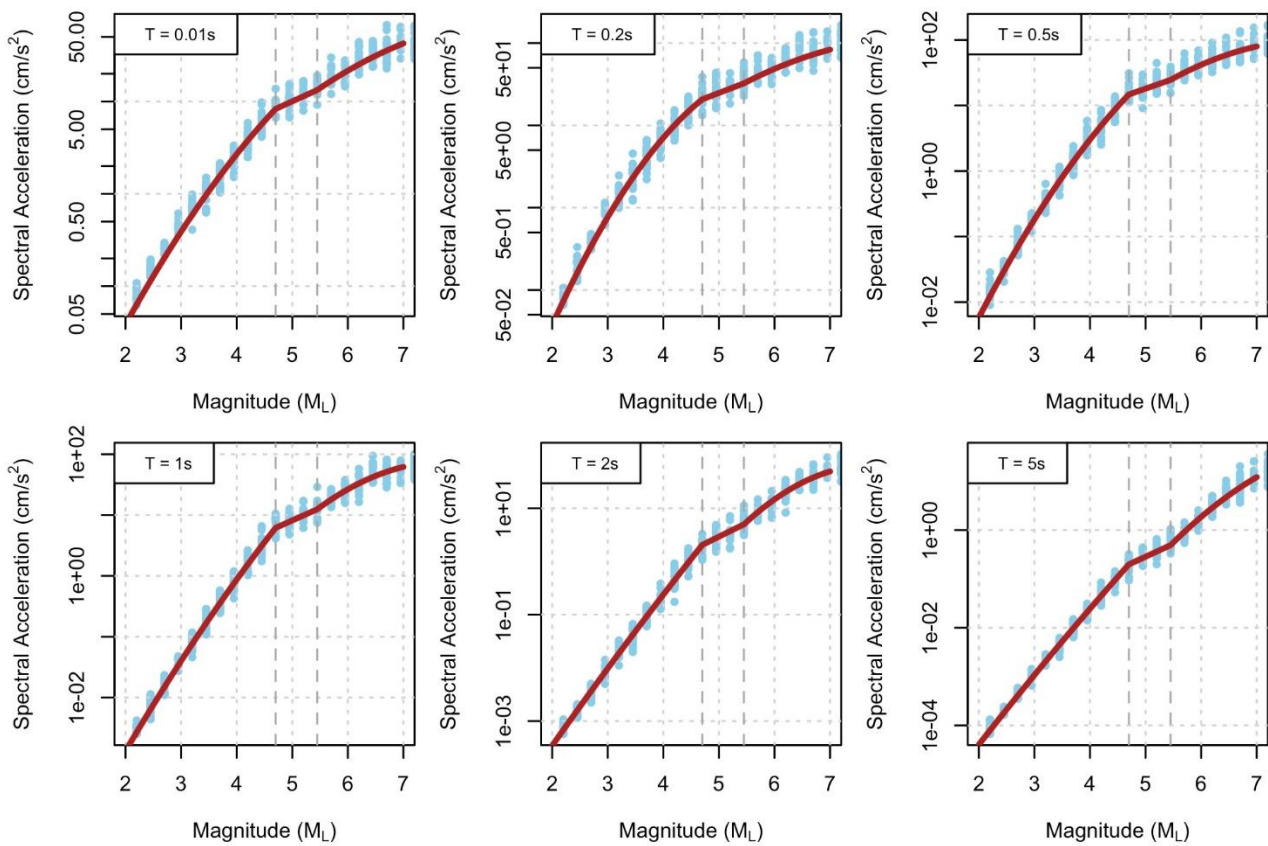


Figure 6.23. Comparison of simulations and median predictions from the equation for the lower-central model (Ca) for 6 response periods at 20 km rupture distance

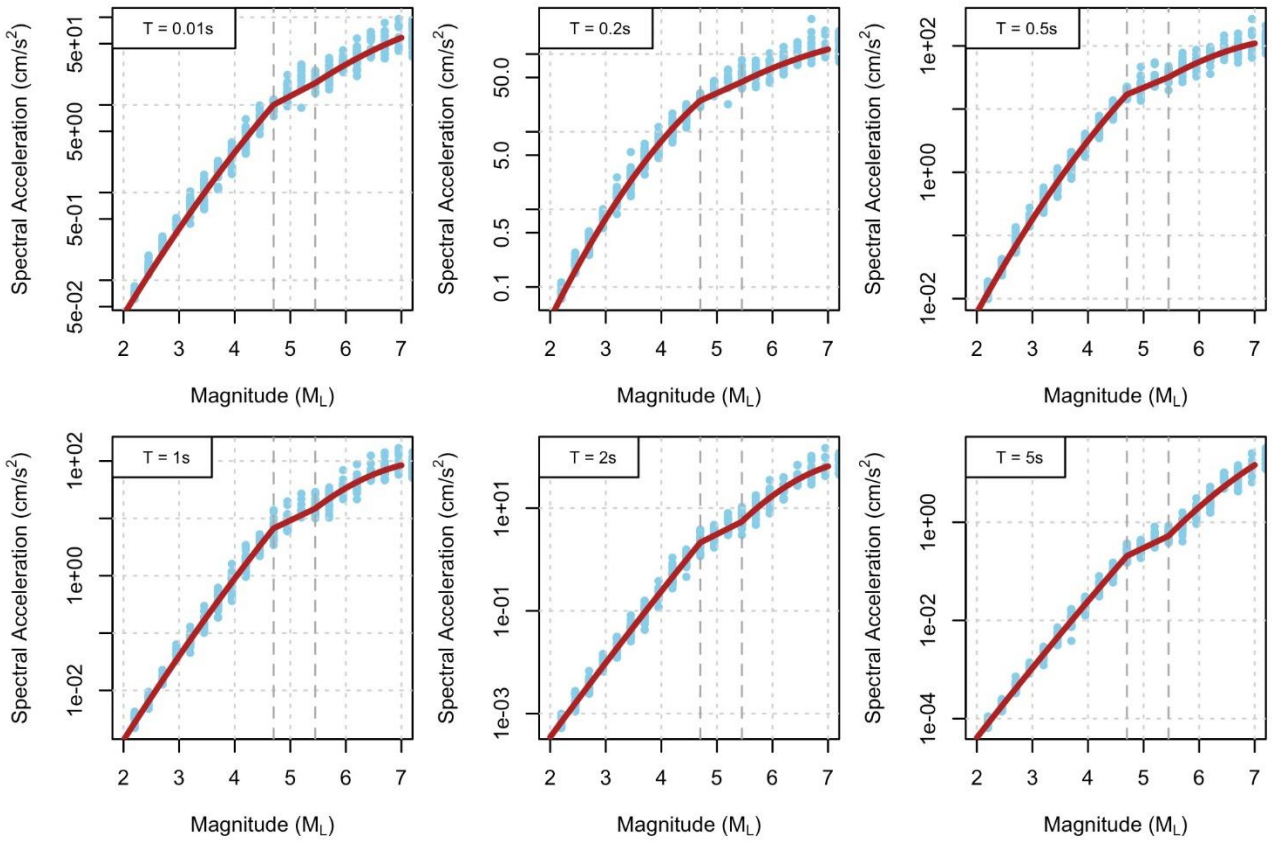


Figure 6.24. Comparison of simulations and median predictions from the equation for the upper-central model (Cb) for 6 response periods at 20 km rupture distance

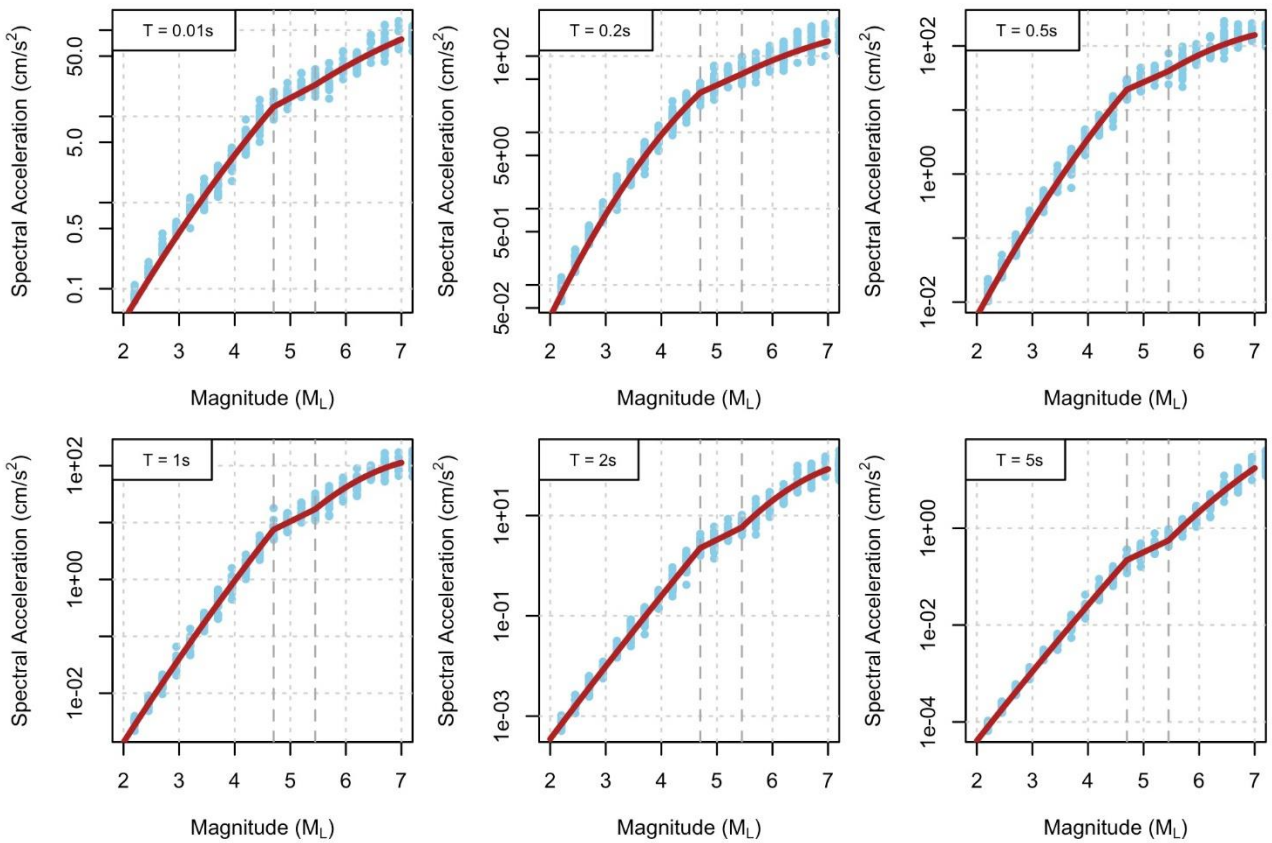


Figure 6.25. Comparison of simulations and median predictions from the equation for the upper model (U) for 6 response periods at 20 km rupture distance

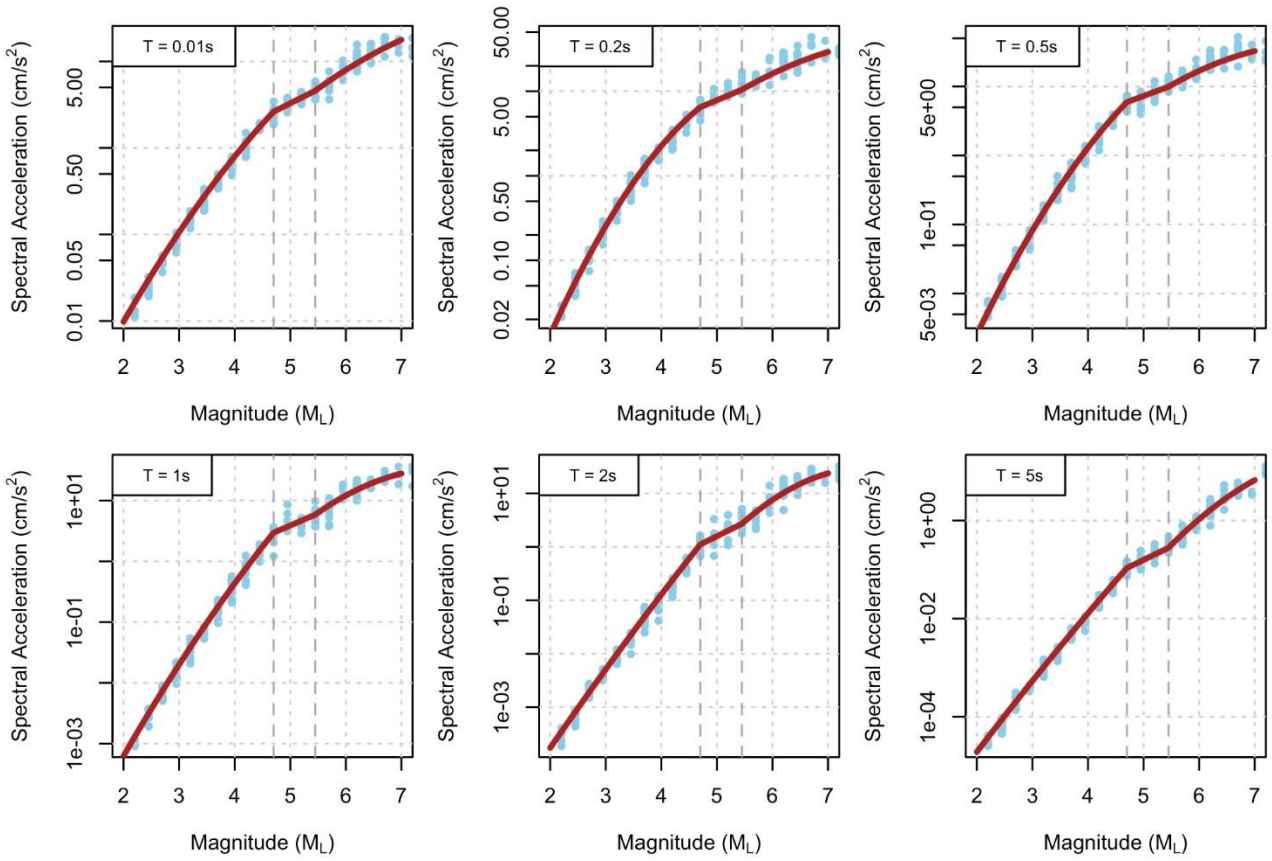


Figure 6.26. Comparison of simulations and median predictions from the equation for the lower model (L) for 6 response periods at 30 km rupture distance

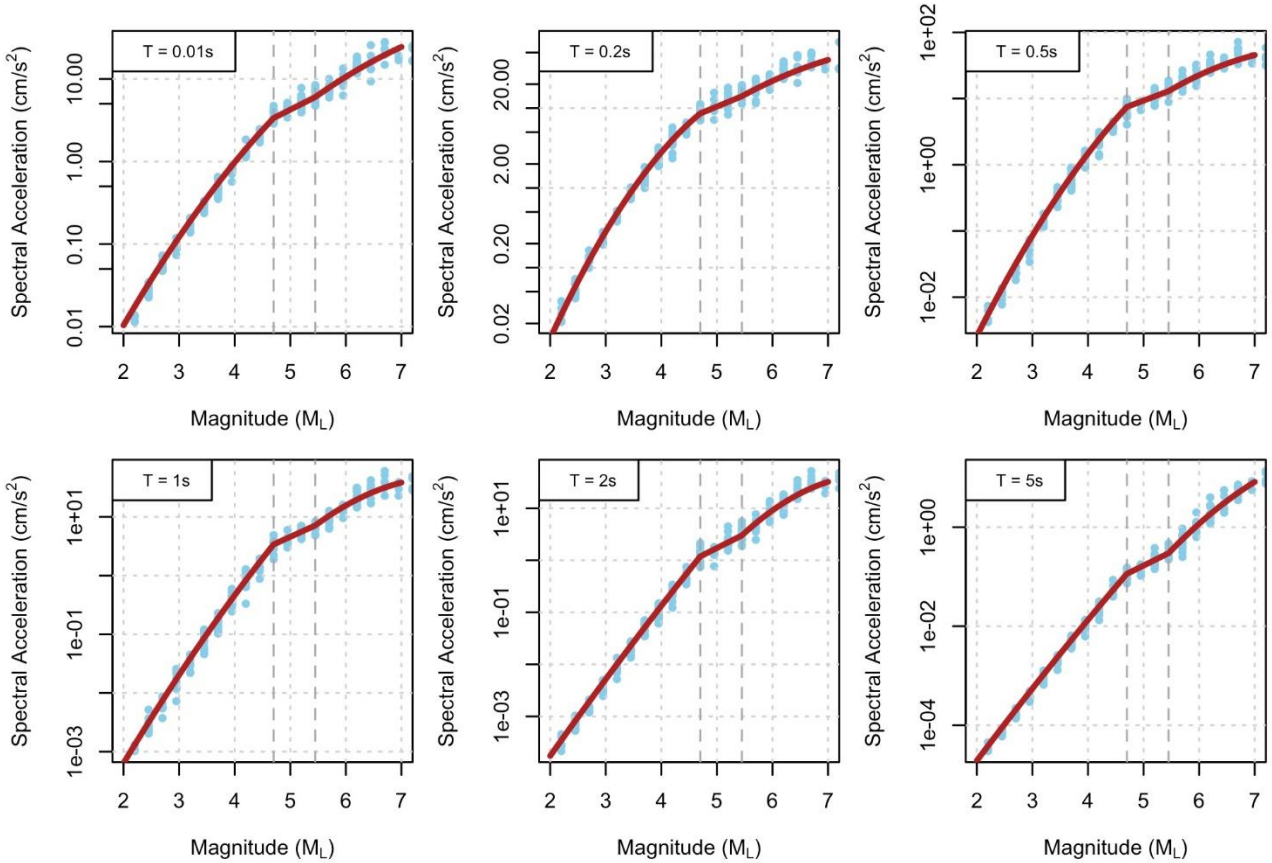


Figure 6.27. Comparison of simulations and median predictions from the equation for the lower-central model (Ca) for 6 response periods at 30 km rupture distance

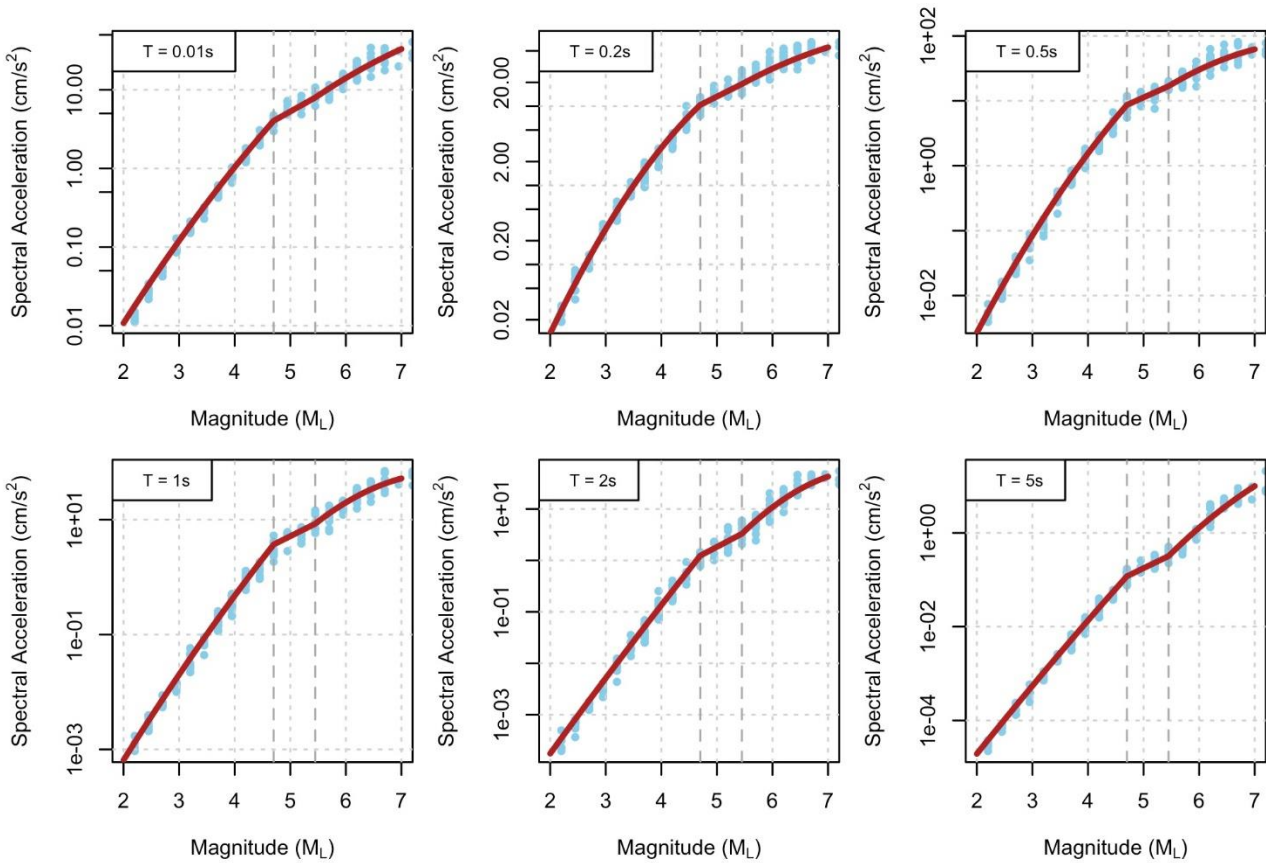


Figure 6.28. Comparison of simulations and median predictions from the equation for the upper-central model (Cb) for 6 response periods at 30 km rupture distance

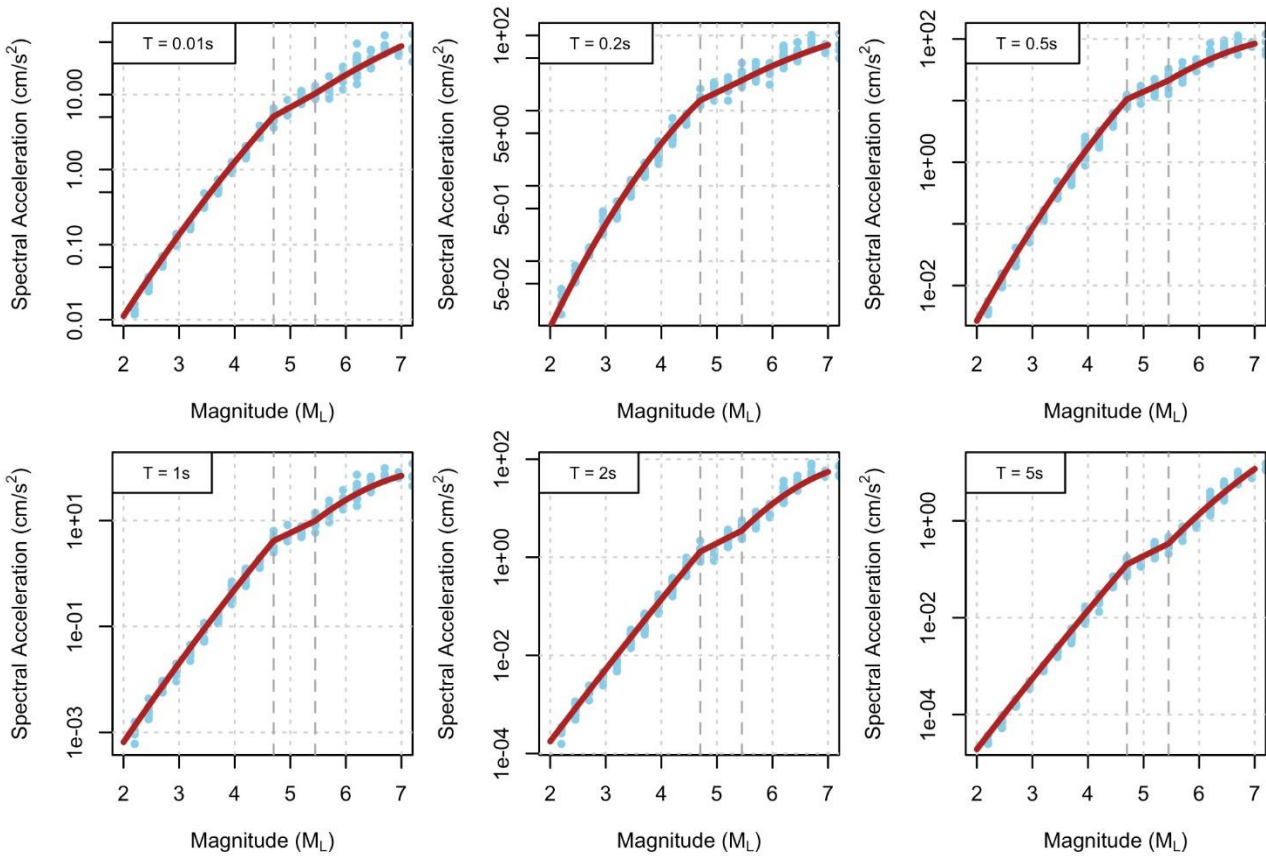


Figure 6.29. Comparison of simulations and median predictions from the equation for the upper model (U) for 6 response periods at 30 km rupture distance

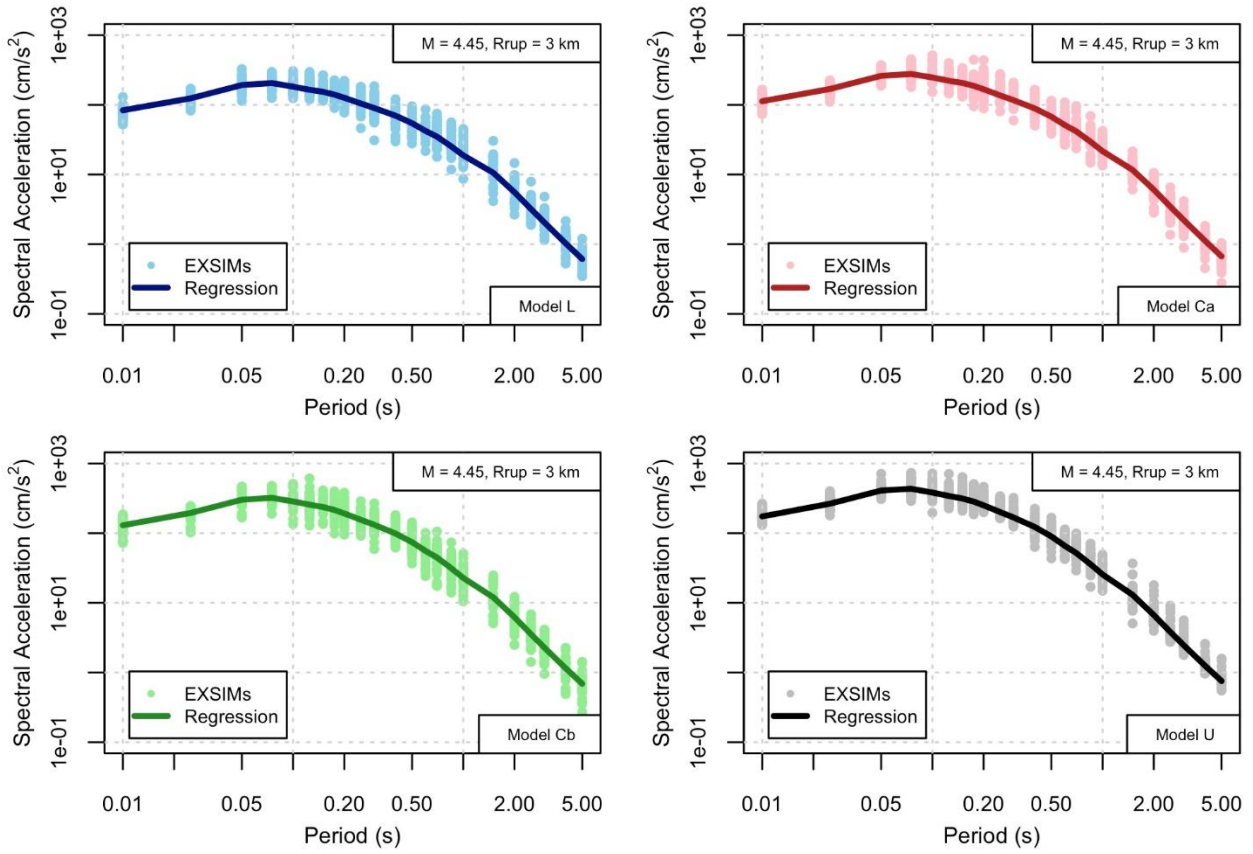


Figure 6.30. Comparison of simulated and predicted response spectra at NS_B due to a magnitude M_L 4.45 earthquake at a rupture distance of 3 km

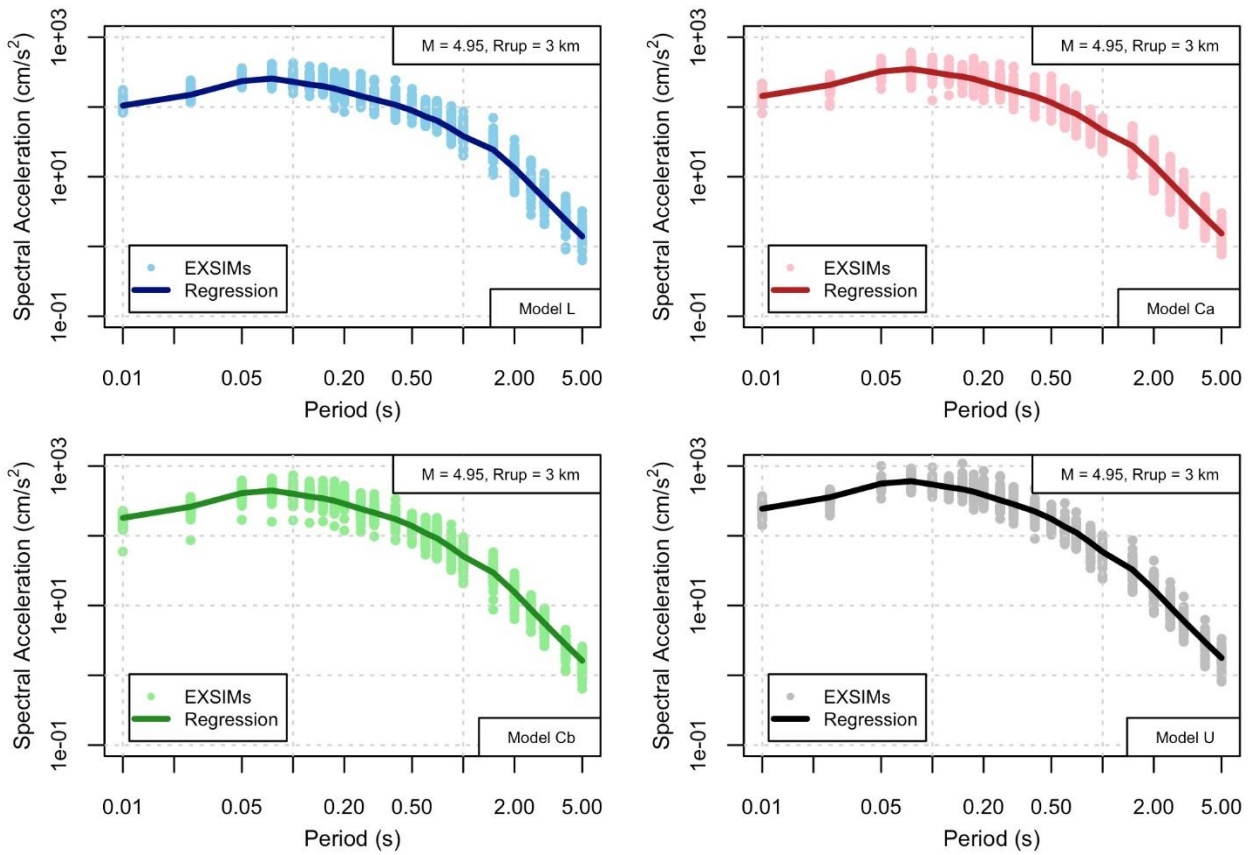


Figure 6.31. Comparison of simulated and predicted response spectra at NS_B due to a magnitude M_L 4.95 earthquake at a rupture distance of 3 km

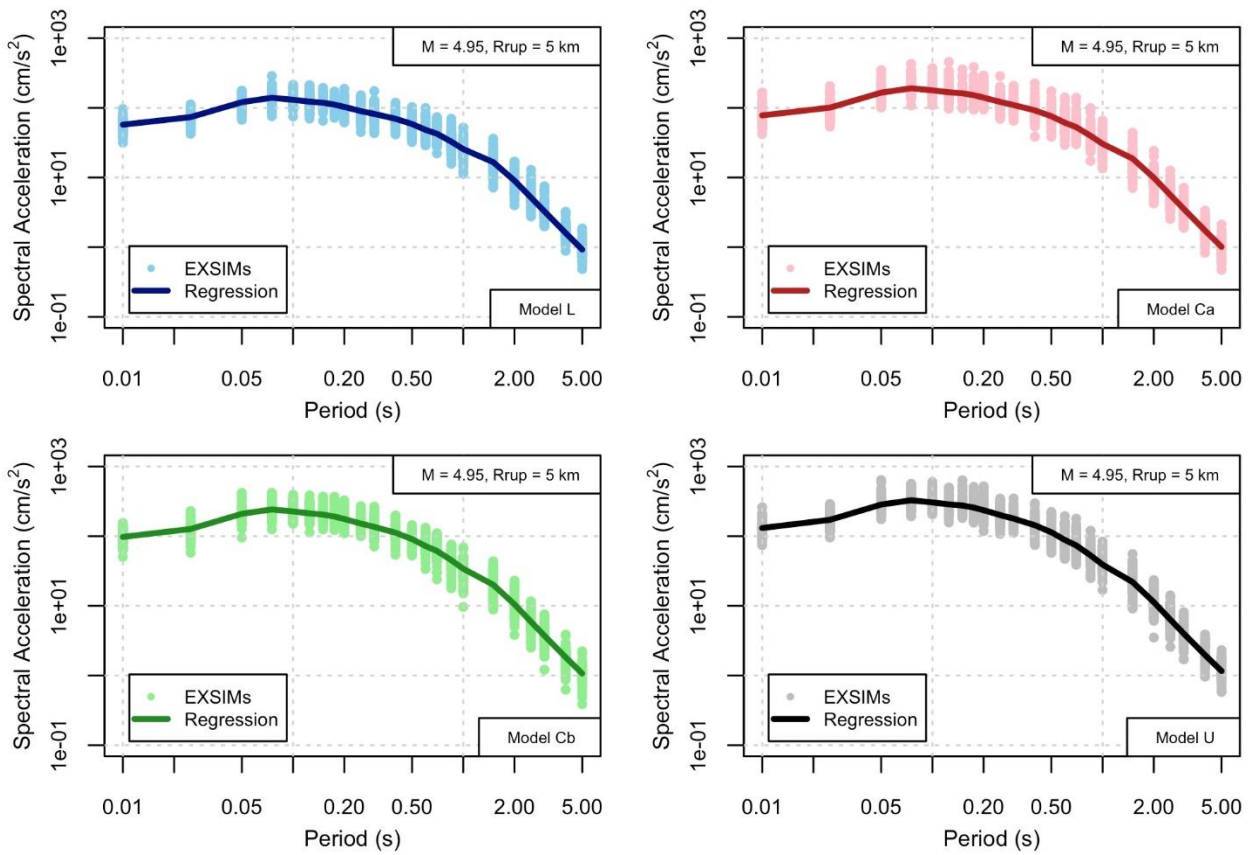


Figure 6.32. Comparison of simulated and predicted response spectra at NS_B due to a magnitude M_L 4.95 earthquake at a rupture distance of 5 km

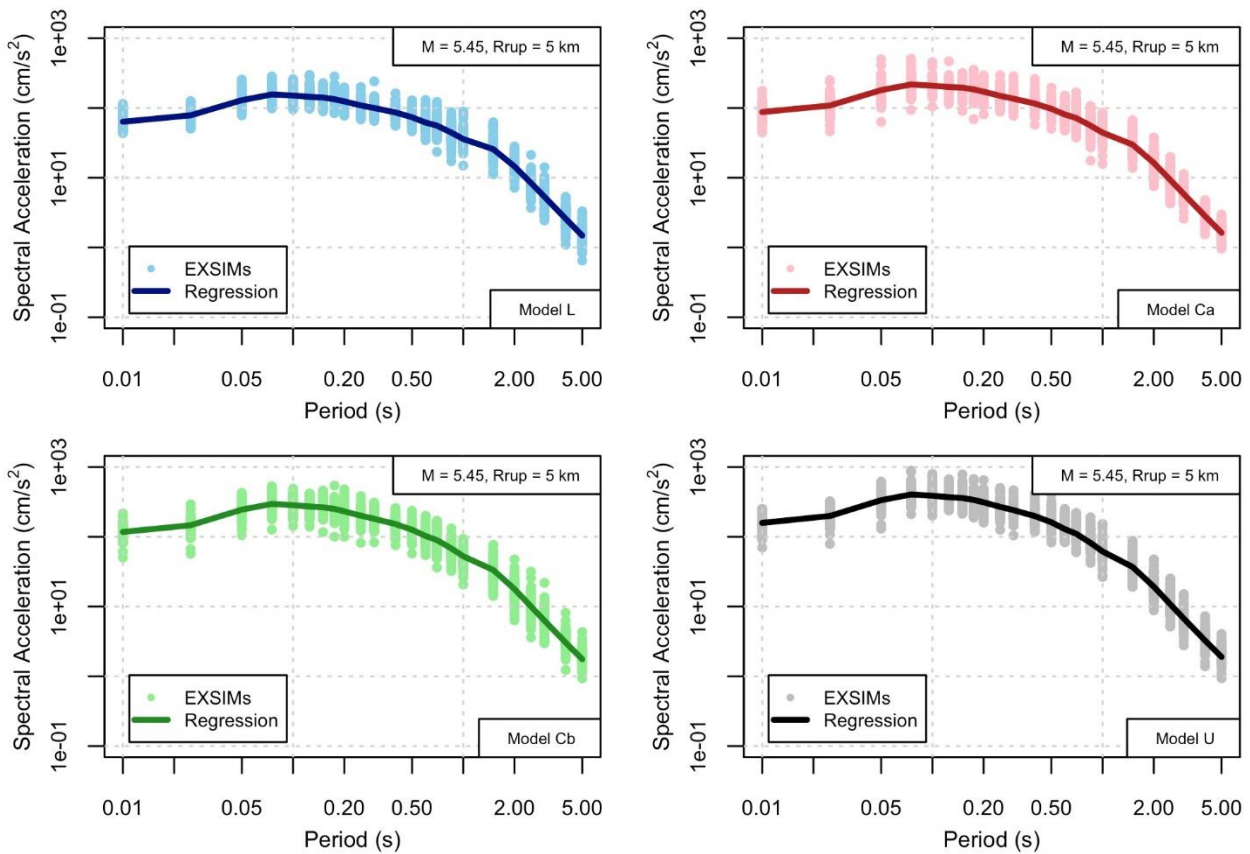


Figure 6.33. Comparison of simulated and predicted response spectra at NS_B due to a magnitude M_L 5.45 earthquake at a rupture distance of 5 km

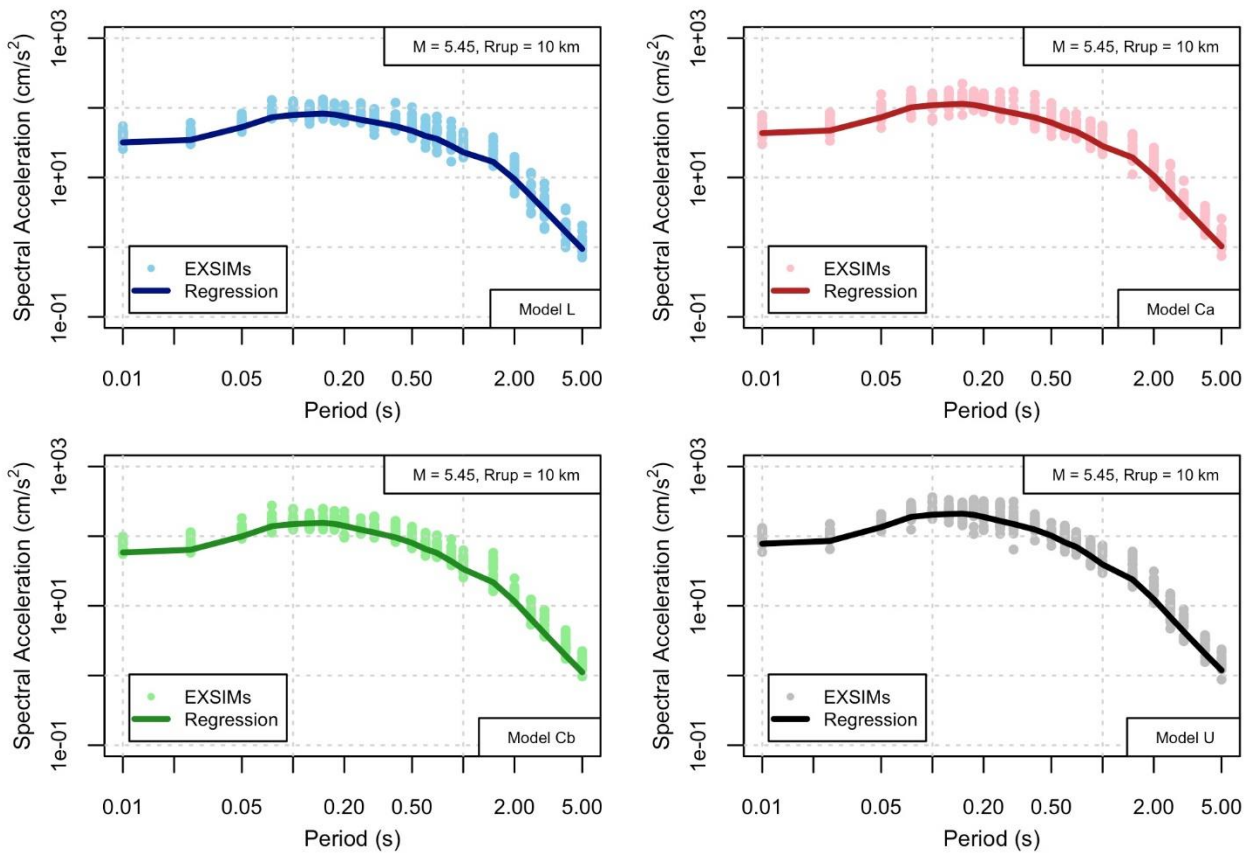


Figure 6.34. Comparison of simulated and predicted response spectra at NS_B due to a magnitude M_L 5.45 earthquake at a rupture distance of 10 km

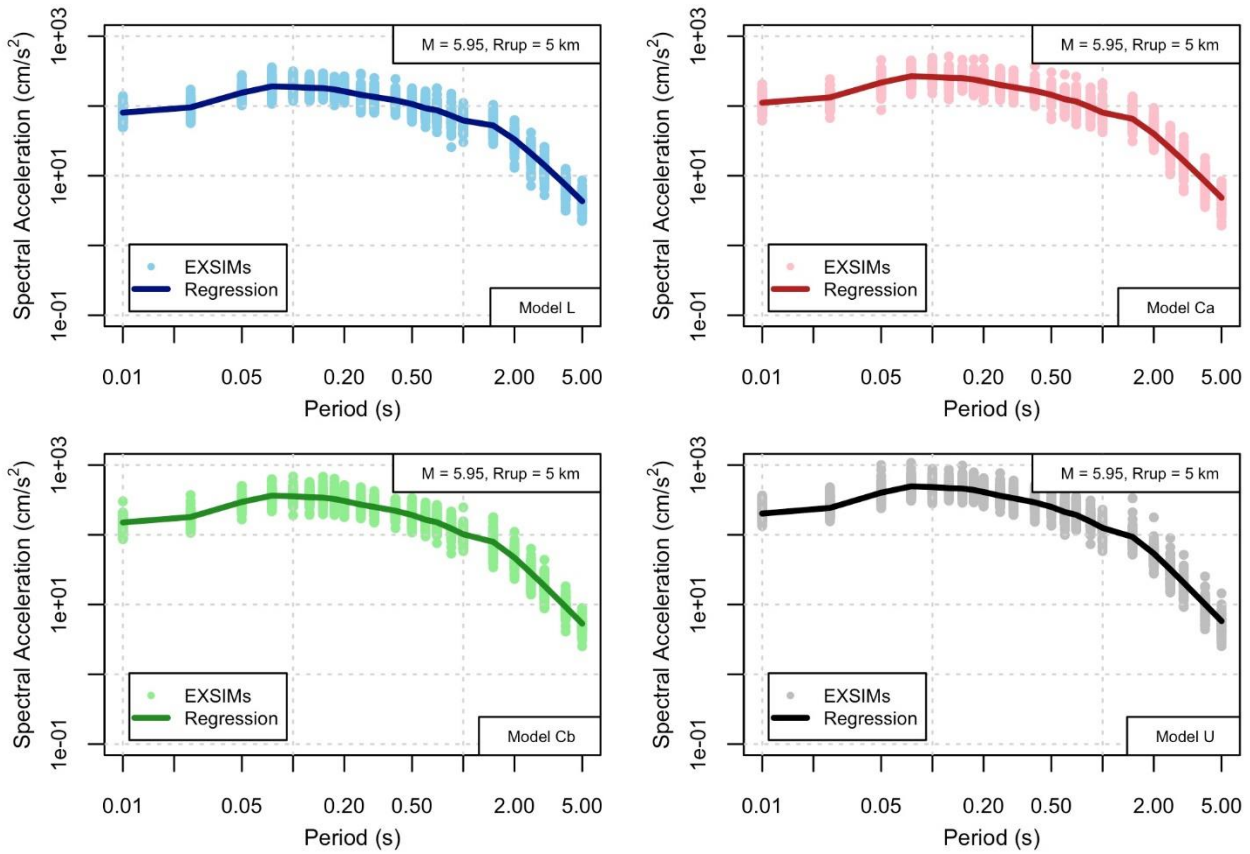


Figure 6.35. Comparison of simulated and predicted response spectra at NS_B due to a magnitude M_L 5.95 earthquake at a rupture distance of 5 km

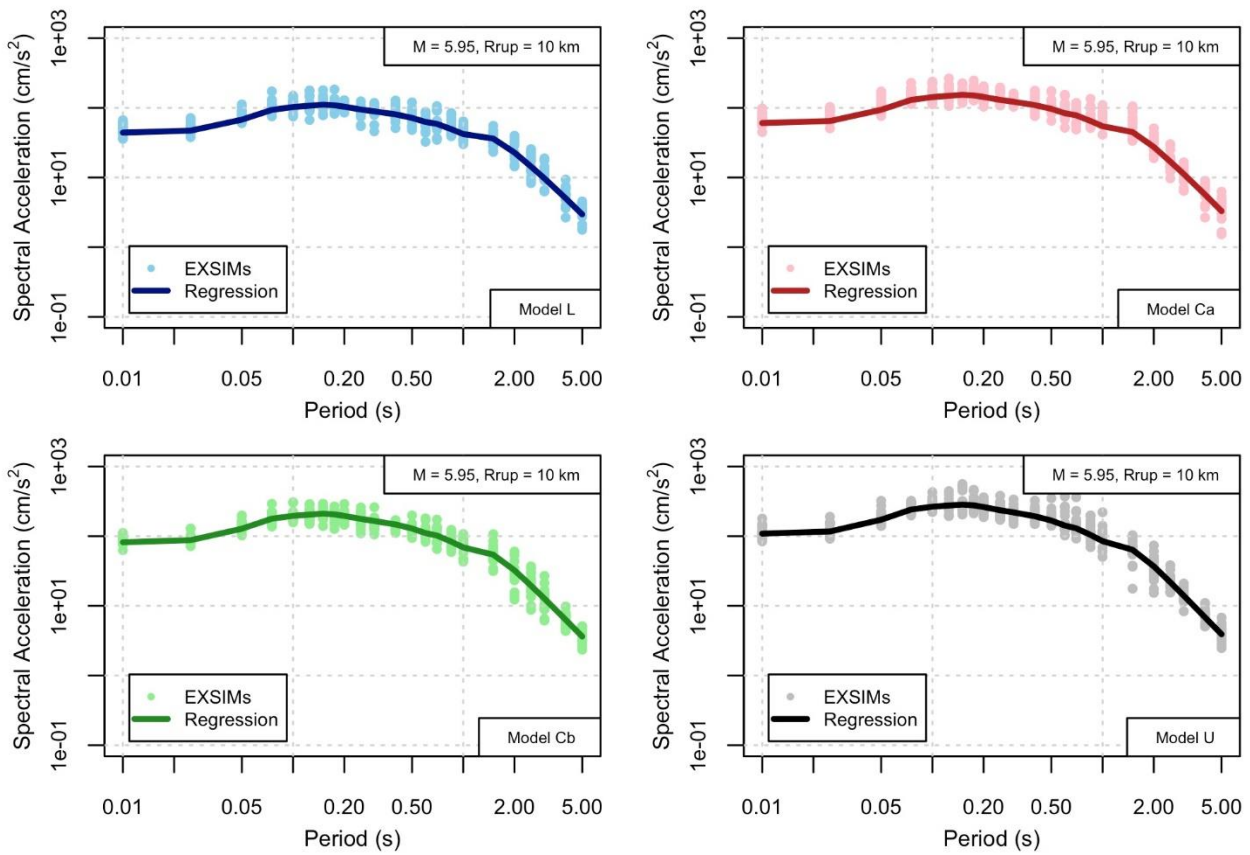


Figure 6.36. Comparison of simulated and predicted response spectra at NS_B due to a magnitude M_L 5.95 earthquake at a rupture distance of 10 km

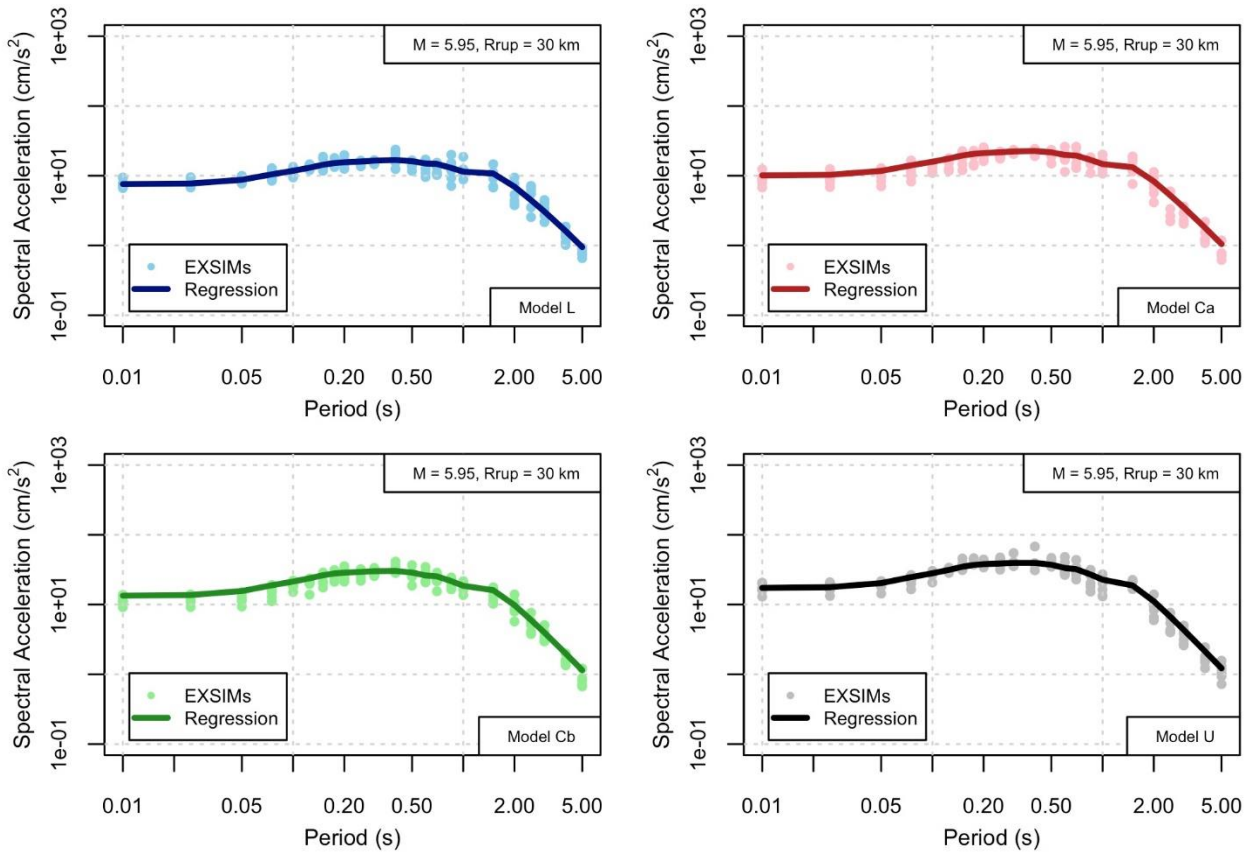


Figure 6.37. Comparison of simulated and predicted response spectra at NS_B due to a magnitude M_L 5.95 earthquake at a rupture distance of 30 km

We believe that the final models represent a good balance between replicating the simulations in a simple functional form that is amenable to implementation the seismic hazard and risk calculations, and the accuracy with which the simulations are reproduced by the equations. An alternative approach, which would avoid any deviation from the precise values obtained from the simulations, would be to replace the functional forms with look-up tables of median spectral accelerations for a wide range of magnitude-distance combinations. However, such an approach would be significantly less flexible, both for the hazard and risk model as well as for other applications, and would very probably result in significantly slower run times. For a hazard and risk model covering the geographical scale of the Groningen region, computational efficiency is an important consideration. Moreover, it is perhaps misleading to focus excessively on how exactly the regressions fit the simulations since the output from EXSIM are estimated values rather than data. As discussed in the next section, an equally important consideration is how well the equations reproduce the actual recordings of ground motion from the field, albeit in the limited magnitude range of the contributing earthquakes.

6.5. Residual analyses

The V3 model for spectral accelerations had inter-event variance components that were much larger than typically expected in spectral ground motion models. This was a very unusual feature of this model given the field specific nature of the model should have meant less between event variability than more ergodic models. In order to investigate this issue for the development of the V4 model a number of considerations were made that resulted in significant reductions being obtained. The present section outlines the investigations, with a particular emphasis upon the advanced regression approaches that were employed in order to obtain estimates of the variance components for the spectral ground motion model.

The inter-event standard deviations for the V3 ground-motion model were obtained by first fitting a functional form to the stochastically generated motions over a large magnitude and distance range, and then using this fitted model to compute residuals with respect to Groningen data where this was available. This same process has been followed for the development of the V4 model, but using EXSIM rather than SMSIM for the stochastic simulations. The total residuals (logarithmic observed amplitudes minus the logarithmic predictions) were then partitioned into between-event and within-event components using a traditional random effects formulation.

This approach, which is standard practice for ground-motion model development, involves some implicit assumptions that are often not strictly correct. These assumptions include:

- Residual error components are independently and identically distributed (*i.i.d.*);
- Site-terms δ_{S2S} can be ignored; and,
- All independent variables are known exactly (and hence any uncertainties in these variables can be ignored).

One of the reasons why these effects are routinely ignored, or are assumed to have negligible influence, is that it is non-trivial to properly account for these effects within a regression framework. However, in some cases ignoring the fact that these assumptions are being made can lead to inflated estimates of the variance components of the model. For this reason, more advanced regression approaches were employed in order to see if these assumptions were contributing to the large inter-event standard deviations that were obtained in the V3 model.

In order to relax the assumption of *i.i.d.* residual errors the impact of potential spatial correlations among observations was considered. In order to account for these correlations, the coordinates of the stations and events needed to be added to the flatfile used for the regression analysis. In addition, to account for uncertainties in the earthquake magnitude, estimates of the magnitude uncertainties also needed to be added to the flatfile. During the process of exploring the updated flatfile a minor error in the meta data was identified in which the magnitude values that had been assigned to two poorly recorded events had been swapped. Because these events were poorly recorded this error did not have a significant impact upon the general scaling of the models that were developed. However, it did play a significant role in explaining why the inter-event variability was apparently inflated.

The actual changes to the magnitude values are shown in Figure 6.38. In this figure we see two clear outliers when the old and new magnitude values are plotted against each other in the left panel. In the right panel of the figure we see that these outliers involve events 11 and 12 whose magnitudes have both changed by 0.5 units.

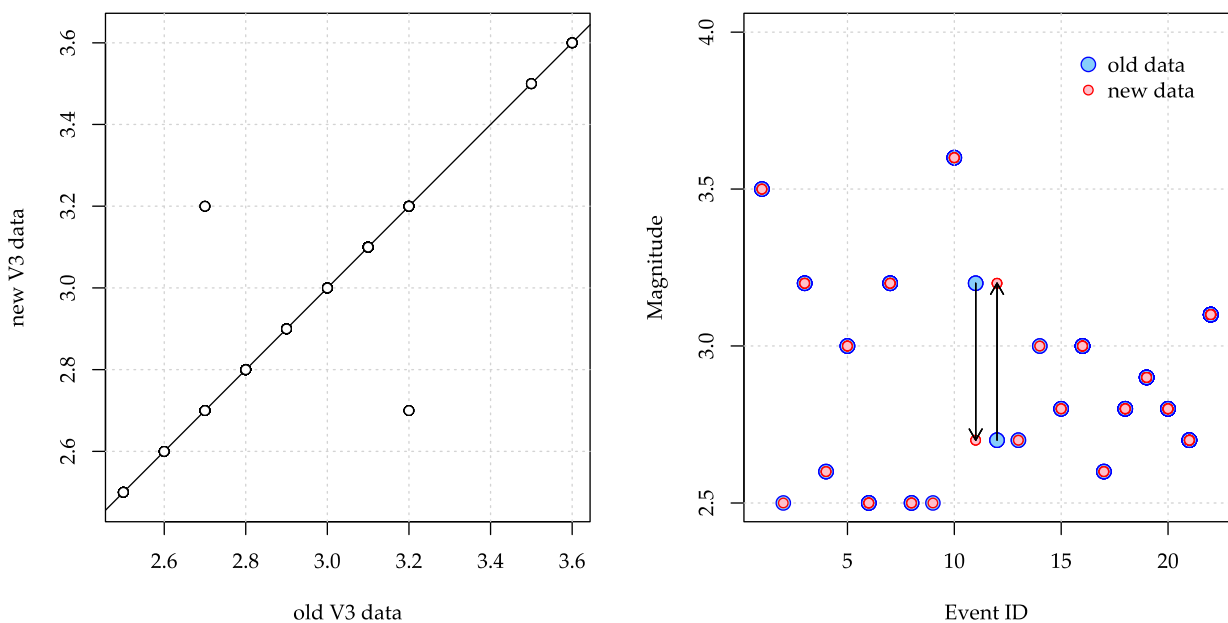


Figure 6.38. Differences in magnitude values identified in revising the V3 flatfile

The impact of just these changes to the magnitudes for these two events can be seen in Figure 6.39 where the inter-event standard deviations computed using a traditional random effects formulation are compared for the original and updated V3 datasets (the corrections

made in the updated V3 dataset were incorporated within the V4 dataset). While this correction only influenced two poorly recorded events, when computing inter-event variance, every event contributes and the reduction observed at intermediate-to-long periods is significant.

While this data correction accounted for an important portion of the inflated inter-event standard deviation, a more significant improvement can be made by using advanced regression procedures.

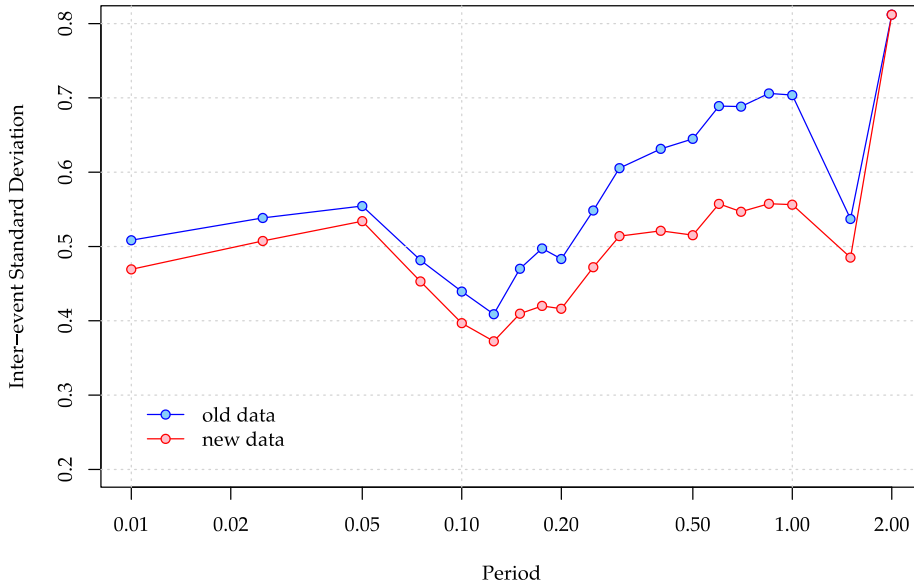


Figure 6.39. Impact of the changes to magnitude values for events 11 and 12 in terms of the resulting inter-event standard deviations computed as a function of period.

Rather than provide explicit details about how each of the assumptions outlined above were removed, the present section simply describes the structure of the covariance matrix, \mathbf{C} , that is used in each type of analysis. This covariance matrix is central to a mixed effects formulation as the variance components are those that maximise the logarithmic likelihood function - which depends strongly upon the covariance matrix.

The same generic likelihood function can be written in all cases as:

$$\ln \mathcal{L} = -\frac{N}{2} \ln(2\pi) - \frac{1}{2} \ln(|\mathbf{C}|) - \frac{1}{2} (\mathbf{y} - \boldsymbol{\mu})^T \mathbf{C}^{-1} (\mathbf{y} - \boldsymbol{\mu}) \quad (6.8)$$

in which \mathbf{y} is normally a vector of observed quantities, $\boldsymbol{\mu}$ is a vector of model predictions, and we also require computation of the determinant of the covariance matrix $|\mathbf{C}|$ and its inverse \mathbf{C}^{-1} . The covariance matrix \mathbf{C} represents the covariance among the observations in \mathbf{y} (at least for the population from which the observations are drawn).

For all of the regression cases outlined hereafter, the observed quantities \mathbf{y} are the total residuals obtained from using the V4 ground-motion model at the NS_B horizon along with

the surface and borehole records transformed down to this horizon. The ‘model’ μ in this case is actually just a single constant parameter that represents the average bias in the V4 model when compared to the V4 dataset at NS-B. This bias is denoted β_0 and is computed in natural logarithmic units, i.e., in the same scale as y and μ . While the model is simply a scalar constant, within the framework of Eq.(6.6), μ is simply $\beta_0 \mathbf{1}_{N \times 1}$ with $\mathbf{1}_{N \times 1}$ being an $N \times 1$ vector of ones and N being the total number of records in the dataset.

In each of the following subsections the structure of the covariance matrix is described for each of the regression approaches considered herein. It is also worth noting that the log-likelihood function is never maximised directly. Rather, various different approaches are used to obtain the optimal variance components, and these are noted in each section.

Traditional random effects

The first case considered is simply the traditional random effects formulation of Abrahamson & Youngs (1992). The $N \times N$ global covariance matrix in this case is:

$$\mathbf{C} = \bigoplus_{i=1}^M \mathbf{C}_i \quad (6.9)$$

where \mathbf{C}_i is the covariance matrix for event i (out of a total of M events) and is defined as:

$$\mathbf{C}_i = \tau^2 \mathbf{1}_{n_i \times 1} \otimes \mathbf{1}_{n_i \times 1} + \phi^2 \mathbf{I}_{n_i \times n_i} \quad (6.10)$$

In the above equations \bigoplus is the direct sum operator used to construct block diagonal matrices and \otimes is the Kronecker product.

The global covariance matrix is essentially a block diagonal matrix with blocks for each earthquake event. Each block has off-diagonal elements equal to τ^2 (the inter-event variance) and diagonal elements equal to $\tau^2 + \phi^2$ (where ϕ is the intra-event standard deviation). The number of records for each earthquake is defined by n_i and $N = \sum_i^M n_i$. In this study the solutions to this problem were obtained using the *R* package *nlme*.

Random effects accounting for spatial correlation

One of the reasons why residual error components may not be *i.i.d.* is that there may be within-event correlations that arise from spatial proximity of the recording stations and recordings sharing common source-to-site travel paths. To account for this effect we explicitly model spatial correlations within the covariance matrix.

The global covariance matrix given by Eq.(6.9) is still applicable in this case, but the individual covariance matrices for each event are modified from Eq.(6.10) to:

$$\mathbf{C}_i = \tau^2 \mathbf{1}_{n_i \times 1} \otimes \mathbf{1}_{n_i \times 1} + \phi^2 \mathbf{\Lambda}_i \quad (6.11)$$

In Eq.(6.11) the only difference is the new $n_i \times n_i$ matrix $\mathbf{\Lambda}_i$ that replaces the identity matrix. The matrix $\mathbf{\Lambda}_i$ is the correlation matrix that links observations from the same event to each other through their separation distance. For two sites j and k located at positions x_j and x_k ,

that both recorded a given event, their correlation, and the relevant entry within Λ_i is defined as:

$$\Lambda_{i,jk} = \rho(\mathbf{x}_j, \mathbf{x}_k) = \exp\left(-\frac{|\mathbf{x}_j - \mathbf{x}_k|}{r_c}\right) = \exp\left(-\frac{r_{jk}}{r_c}\right) \quad (6.12)$$

where r_c is the correlation length, and r_{jk} is the distance between the two recording sites. Note that in this case the correlation length is estimated as part of the analysis.

The usual effect of including spatial correlation is to inflate the intra-event variance above what would be obtained by ignoring the spatial correlations. However, as the total observed variance is maintained, increasing the intra-event variance leads to a reduction in the inter-event variance. The extent of the reduction depends upon how large the correlation length r_c is in comparison with the typical separation of recording stations. Spatial correlation was accounted for by again using the *R* package *nlme*.

Random effects for both event and site

Variations in the crustal properties near the NS_B horizon can lead to particular locations having average levels of motion that deviate from the field-wide average. While these effects tend to be more common for surface recordings, they can also be observed at depth. These site terms are represented by δ_{S2S} and the variability of these terms is represented by the standard deviation ϕ_{S2S} . While values of ϕ_{S2S} are not usually computed within a regression analysis, they can be through the use of *crossed* random effects.

For this case, the global covariance matrix loses its clean block-diagonal form and complicates the regression analysis quite considerably. The blocks for each earthquake event are initially given by:

$$\mathbf{C}_i = \tau^2 \mathbf{1}_{n_i \times 1} \otimes \mathbf{1}_{n_i \times 1} + \phi^2 \mathbf{I}_{n_i \times n_i} \quad (6.13)$$

as was previously the case in Eq.(6.10). However, the global covariance matrix is adjusted to become:

$$\mathbf{C} = \bigoplus_{i=1}^M \mathbf{C}_i + \mathbf{C}_s \quad (6.14)$$

where \mathbf{C}_s is a new matrix that links observations made for different earthquakes at the same site.

If \mathbf{s} is an $N \times 1$ vector containing a site identifier for each recording station then element (j, k) of matrix \mathbf{C}_s is defined by:

$$\mathbf{C}_{s,jk} = \begin{cases} \phi_{S2S}^2 & \text{for } \mathbf{s}_j = \mathbf{s}_k \\ 0 & \text{for } \mathbf{s}_j \neq \mathbf{s}_k \end{cases} \quad (6.15)$$

Therefore, every diagonal element of \mathbf{C} now includes a ϕ_{S2S}^2 contribution, and some off-diagonal elements outside of the event blocks will also contain entries. To obtain the variance components for this case the R package *lme4* was employed.

Random effects considering magnitude uncertainties

For the traditional random effects formulation we can write the regression equation for each earthquake as:

$$\mathbf{y}_i = \boldsymbol{\mu}_i + \mathbf{Z}_i \mathbf{b}_i + \boldsymbol{\varepsilon}_i \quad (6.16)$$

For the model of Abrahamson & Youngs (1992) $\mathbf{Z}_i = \mathbf{1}_{n_i \times 1}$ and $\mathbf{b}_i = b$ is simply a constant equal to the inter-event residual (or the random effect for event i). The variance of \mathbf{b}_i in this case is simply τ^2 .

The covariance for the records from this event is given by:

$$\mathbf{C}_i = \mathbf{Z}_i \boldsymbol{\Psi} \mathbf{Z}_i^T + \phi^2 \mathbf{I}_{n_i \times n_i} \quad (6.17)$$

This general formulation can be extended for the case in which magnitude uncertainties are considered. In that context, we assume that we have two independent random effects: one replicating the traditional event term; and one representing some systematic deviation away from the true event magnitude. We can then define a vector of random effects as $\mathbf{b}_i = [b_{\sigma_m} \quad b_\tau]^T$ and the covariance of the random effects is:

$$\boldsymbol{\Psi} = \begin{bmatrix} \sigma_{m,i}^2 & 0 \\ 0 & \tau^2 \end{bmatrix} \quad (6.18)$$

and the matrix \mathbf{Z}_i becomes:

$$\mathbf{Z}_i = \begin{bmatrix} \frac{\partial y_i}{\partial m} & \mathbf{1}_{n_i \times 1} \end{bmatrix} \quad (6.19)$$

Here the partial derivative $\partial y / \partial m$ reflects the sensitivity of the response to variations in magnitude. Note also that in this case the $\sigma_{m,i}$ values are not estimated during the analysis, but are assumed to be known inputs to the problem.

The same expression as in Eq.(6.9) is again used to construct the global covariance matrix. This formulation can be shown to be equivalent to that presented by Rhoades (1997) - although he considered a much simpler case where the partial derivatives were simply constant values for all observations. To obtain the optimal parameter estimates in this case, custom code was developed.

Random effects considering all of the above

In the previous subsections a single layer of complexity beyond the traditional random effects approach of Abrahamson & Youngs (1992) was added to the regression formulation. This

was done to examine which aspect has the greatest power to reduce the apparent variability reflected by τ .

In the present subsection, all of the above features are now included within a single framework. The global covariance matrix in this case can be written as:

$$\mathbf{C} = \bigoplus_{i=1}^M \mathbf{C}_i + \mathbf{C}_s \quad (6.20)$$

where \mathbf{C}_s is again represented by:

$$\mathbf{C}_{s,jk} = \begin{cases} \phi_{S2S}^2 & \text{for } \mathbf{s}_j = \mathbf{s}_k \\ 0 & \text{for } \mathbf{s}_j \neq \mathbf{s}_k \end{cases} \quad (6.21)$$

Note that without explicitly representing this in an equation, the above formulation is equivalent to including a random effect for each site. We then also need two other random effects for each earthquake, one to represent the magnitude uncertainty and one to reflect the between event variability. As these random effects operate at the level of individual earthquakes we can still write a covariance matrix for the event, but we now also want to include spatial correlation effects here. The covariance matrix for a given event is therefore:

$$\mathbf{C}_i = \mathbf{Z}_i \boldsymbol{\Psi} \mathbf{Z}_i^T + \phi^2 \boldsymbol{\Lambda}_i \quad (6.22)$$

This formulation represents a very complicated covariance matrix structure. To visualise this complexity, Figure 6.40 shows images of the covariance matrices for each regression case considered.

In order to determine the optimal estimates of the variance components for this most elaborate case, a Bayesian hierarchical model analysed with Markov-chain Monte Carlo (MCMC) sampling was utilised.

With the structure of the covariance matrices for each case considered above defined, the log-likelihood functions can be maximised in order to determine the bias of the V4 spectral models with respect to the small magnitude Groningen data as well as the variance components relevant for each case.

To compare the actual regression results we first present the bias estimates using each approach. We should not expect drastic differences in the estimate of the bias, but the various approaches do act to weight different observations in a distinct manner and so the bias estimate is influenced.

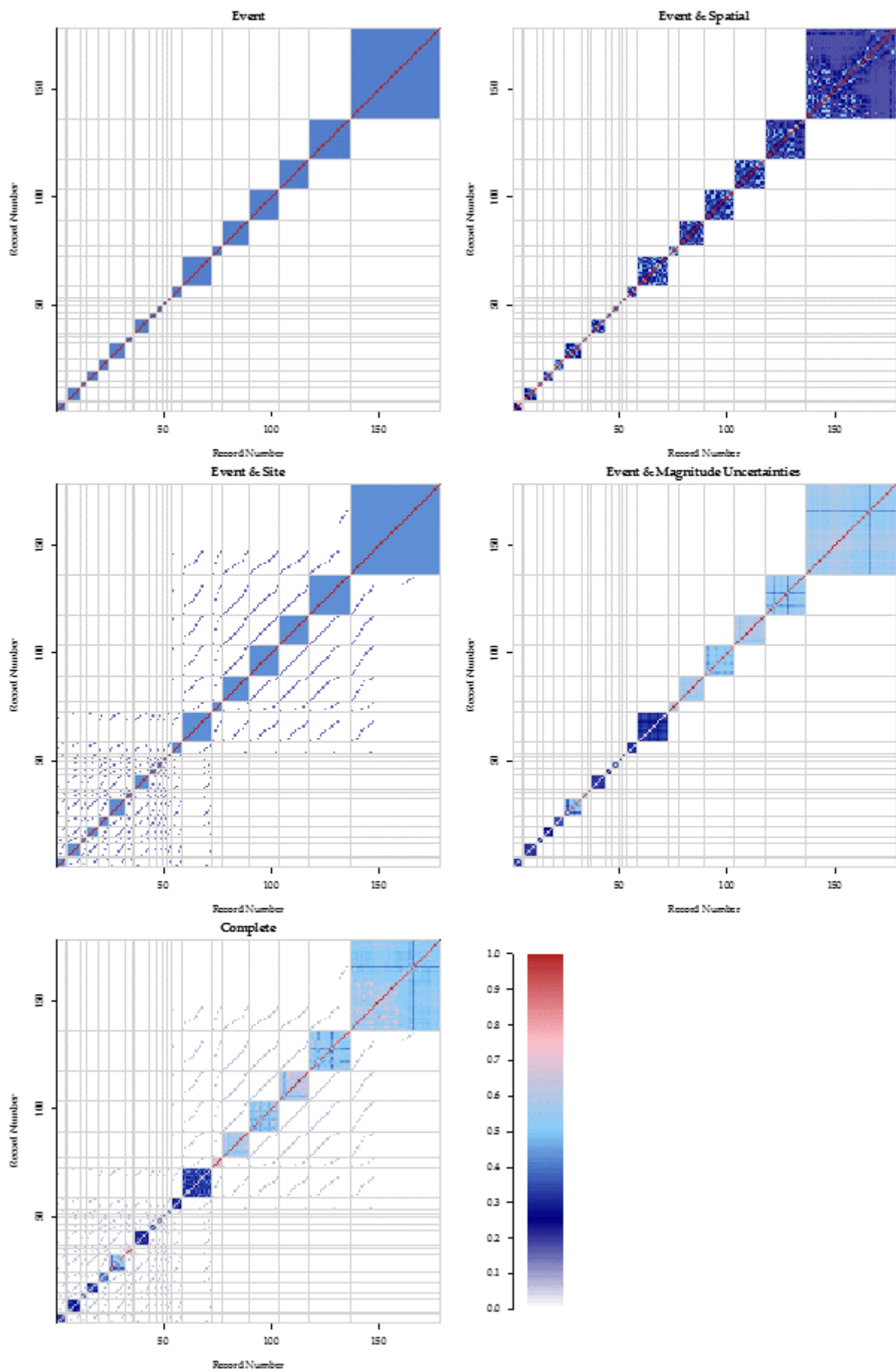


Figure 6.40. Visualisation of the structure of the covariance matrices for each of the regression analyses performed. All matrices are normalized such that their maximum element is equal to 1.0

Figure 6.41 shows these bias estimates as well as approximate 95% confidence intervals for each case. Note that as the regression approaches differ the actual method used to estimate these intervals varies. In particular, the intervals for the 'Complete' case aren't actually 95% confidence intervals, but instead reflect the stability of the bias estimates against random sampling.

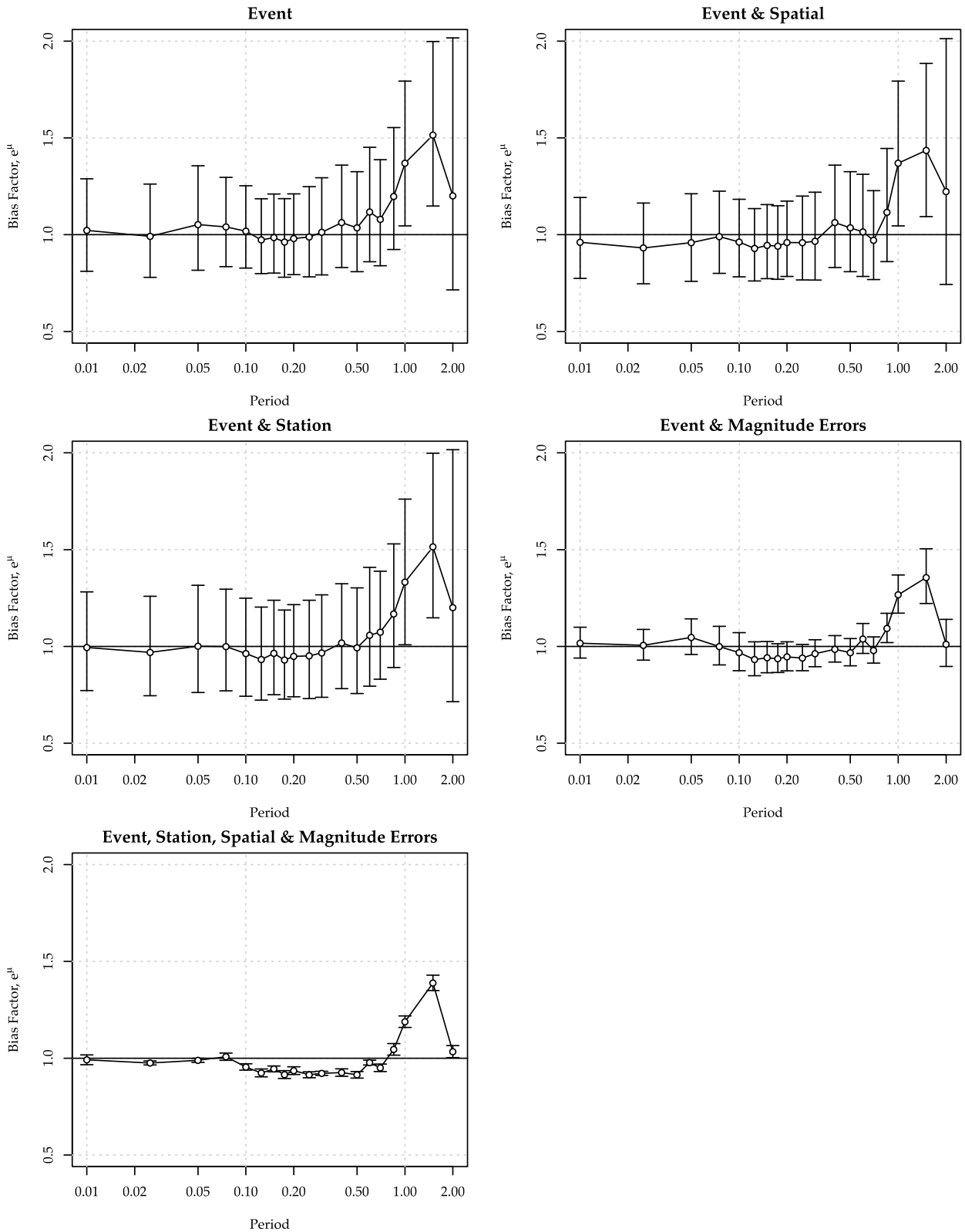


Figure 6.41. Bias factors computed with respect to the lower central model using the five different regression approaches discussed in Section 6.4.

For the MCMC sampling approach 5 parallel chains of sampling are run and the intervals shown here indicate how much the results from each parallel chain differed. This representation gives an indication for how stable the MCMC sampling is. The small intervals indicate that the number of samples that has been used is resulting in a good degree of stability in the results for this parameter.

Figure 6.41 demonstrates that the central lower branch of the V4 model results in predictions that match the centre of the Groningen data very well. In this figure, a bias factor $\exp(\beta_0)$ will be equal to 1.0 when there is no bias, *i.e.*, $\beta_0 = 0$. This situation of effectively unbiased predictions is valid for the vast majority of periods, but breaks down at longer periods above approximately 1 second where we have far fewer records in the empirical dataset. For example, the number of earthquakes that provide records at 2 seconds is less than half the number providing records at 1 second, while the actual number of records at 2 seconds is less than 20% of the number available at shorter periods. Therefore, the departures from a bias factor of 1.0 at these longer periods should be interpreted with caution.

The bias factors obtained using the most complete regression formulation are shown in Figure 6.42 for each of the four stress parameter models. This figure shows that the central models both result in unbiased predictions while the lower and upper branches provide factors of about 1.2-1.25 above and below this level.

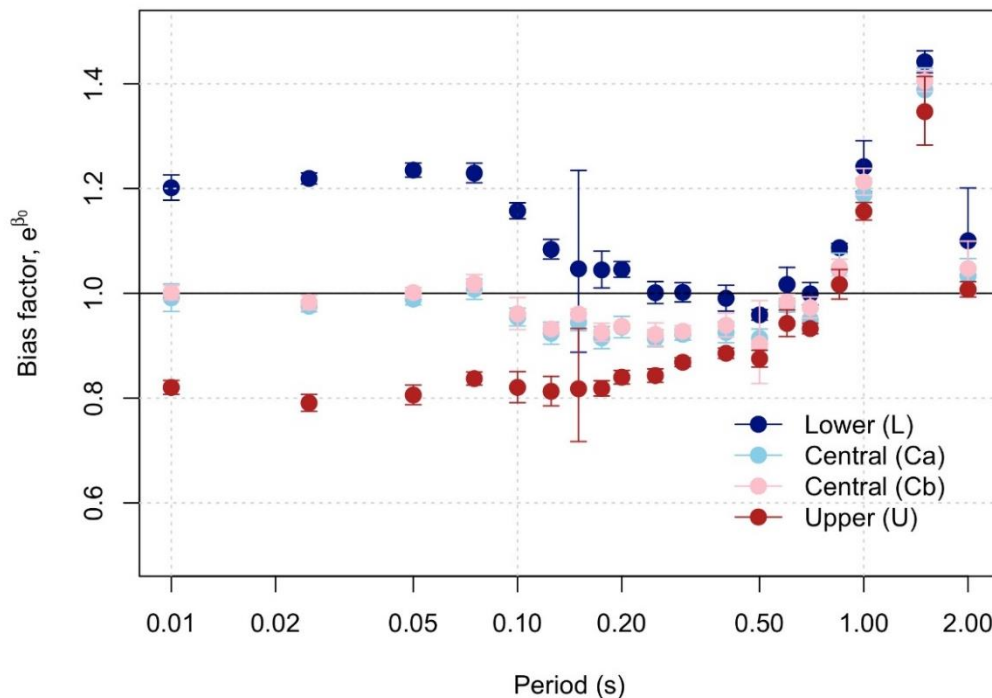


Figure 6.42. Comparison of the bias factors associated with each of the four stress drop branches.

The agreement between the central branches in this figure is to be expected given that the main difference between these central branches is related to how they extrapolate stress parameter estimates for larger magnitude events not contained within the Groningen data. The bias factors for all branches converge to a roughly unbiased state at the longer periods

(when the poorly constrained values beyond ~ 1 second are disregarded). The values of the variance components obtained for the complete regression in which magnitude uncertainties, spatial correlations, and site terms are considered are presented for each branch in Tables 6.10 to 6.13.

Table 6.10. Variance components estimated for the Lower V4 branch

Period (s)	Bias, β_0	Std. Error σ_{β_0}	τ	ϕ_{S2S}	ϕ	σ	Range, r_c	Num. Eqs	Num. Recs
PGV	0.2257	0.007	0.266	0.1977	0.5171	0.6142	4.045	22	178
0.01	0.1836	0.0097	0.2198	0.2625	0.5515	0.6491	4.3805	22	178
0.025	0.1982	0.0042	0.2884	0.2468	0.5603	0.6767	4.5873	22	178
0.05	0.2112	0.0051	0.2567	0.2552	0.6243	0.7216	5.31	22	178
0.075	0.2066	0.0073	0.2085	0.3388	0.6317	0.7465	4.2878	22	178
0.1	0.1462	0.0063	0.2165	0.399	0.6138	0.7634	4.4111	22	178
0.125	0.0805	0.0083	0.2128	0.3568	0.5871	0.7193	4.5418	22	178
0.15	0.0457	0.0794	0.1618	0.3241	0.5315	0.6432	4.5803	22	178
0.175	0.0437	0.0162	0.2056	0.3079	0.5063	0.6272	4.048	22	178
0.2	0.0446	0.0069	0.2266	0.3097	0.5136	0.6411	4.3435	22	178
0.25	0.0011	0.01	0.2582	0.2684	0.4959	0.6202	4.6651	22	178
0.3	0.0017	0.0087	0.2551	0.2563	0.5252	0.6377	5.1058	22	178
0.4	-0.0095	0.0119	0.2557	0.2412	0.512	0.6211	4.6687	22	178
0.5	-0.0421	0.005	0.2674	0.2419	0.5528	0.66	5.3255	22	178
0.6	0.0169	0.0151	0.283	0.2316	0.5597	0.6686	5.4515	22	176
0.7	-0.001	0.0103	0.248	0.1084	0.582	0.6419	6.9534	22	175
0.85	0.0835	0.0035	0.2817	0.1828	0.5462	0.6411	5.8965	22	170
1	0.2166	0.0187	0.2448	0.2384	0.545	0.6432	4.3144	21	152
1.5	0.3659	0.007	0.2452	0.1544	0.5751	0.644	4.0851	18	83
2	0.0956	0.0421	0.7071	0.1426	0.4685	0.8601	6.2545	10	27

Table 6.11. Variance components estimated for the lower Central V4 branch

Period (s)	Bias, β_0	Std. Error σ_{β_0}	τ	ϕ_{S2S}	ϕ	σ	Range, r_c	Num. Eqs	Num. Recs
PGV	0.0782	0.0075	0.2842	0.1969	0.5132	0.6188	3.9865	22	178
0.01	-0.0086	0.0128	0.2648	0.2449	0.547	0.6552	4.5162	22	178
0.025	-0.025	0.0052	0.2975	0.2481	0.5543	0.6762	4.495	22	178
0.05	-0.0112	0.0054	0.2667	0.2561	0.6268	0.7278	5.3624	22	178
0.075	0.0077	0.0093	0.2072	0.3403	0.6328	0.7478	4.3082	22	178
0.1	-0.0467	0.0086	0.1947	0.3995	0.6156	0.7592	4.4036	22	178
0.125	-0.0793	0.0109	0.215	0.356	0.5879	0.7201	4.5649	22	178
0.15	-0.057	0.008	0.1976	0.3303	0.5326	0.6571	4.5248	22	178
0.175	-0.0887	0.0112	0.2336	0.309	0.5063	0.6375	4.1304	22	178
0.2	-0.0667	0.0106	0.2463	0.3092	0.5132	0.6478	4.3372	22	178
0.25	-0.0898	0.0085	0.2894	0.2708	0.4938	0.6332	4.605	22	178
0.3	-0.0816	0.0057	0.2585	0.2549	0.5236	0.6371	5.1025	22	178
0.4	-0.0774	0.0104	0.2807	0.2411	0.5075	0.6281	4.5726	22	178
0.5	-0.0898	0.0092	0.2694	0.2399	0.5561	0.6629	5.4544	22	178
0.6	-0.0231	0.0063	0.2804	0.2337	0.5568	0.6658	5.4355	22	176
0.7	-0.0511	0.0101	0.2461	0.1172	0.5784	0.6394	6.9828	22	175
0.85	0.0443	0.0142	0.2619	0.1901	0.5444	0.6334	5.9689	22	170
1	0.1723	0.0125	0.2566	0.2421	0.5422	0.6469	4.3299	21	152
1.5	0.3282	0.0143	0.2541	0.1423	0.5754	0.6449	4.0759	18	83
2	0.0331	0.0151	0.6559	0.1529	0.4695	0.821	6.7911	10	27

Table 6.12. Variance components estimated for the upper Central V4 branch

Period (s)	Bias, β_0	Std. Error σ_{β_0}	τ	ϕ_{S2S}	ϕ	σ	Range, r_c	Num. Eqs	Num. Recs
PGV	0.0793	0.0081	0.264	0.1976	0.5162	0.6125	4.0566	22	178
0.01	0.0012	0.0065	0.2878	0.2465	0.5473	0.6657	4.4819	22	178
0.025	-0.0175	0.0066	0.2995	0.2478	0.5565	0.6789	4.539	22	178
0.05	0.0014	0.0047	0.2394	0.2557	0.6282	0.7193	5.3717	22	178
0.075	0.0187	0.0079	0.2052	0.3425	0.6339	0.7492	4.3236	22	178
0.1	-0.0398	0.0153	0.1721	0.3954	0.6137	0.7501	4.3966	22	178
0.125	-0.0705	0.0047	0.1846	0.3559	0.587	0.7109	4.5307	22	178
0.15	-0.0406	0.0049	0.2079	0.3324	0.5347	0.663	4.5903	22	178
0.175	-0.0774	0.0089	0.2146	0.308	0.5083	0.6319	4.1676	22	178
0.2	-0.065	0.0021	0.2358	0.3091	0.5149	0.6451	4.3383	22	178
0.25	-0.0817	0.0114	0.2599	0.2702	0.4937	0.6199	4.5736	22	178
0.3	-0.0753	0.0055	0.2547	0.2556	0.5273	0.639	5.1841	22	178
0.4	-0.063	0.0116	0.299	0.2436	0.5057	0.636	4.4796	22	178
0.5	-0.1015	0.0421	0.2432	0.2343	0.555	0.6497	5.2549	22	178
0.6	-0.0175	0.0075	0.2817	0.2341	0.5613	0.6703	5.5263	22	176
0.7	-0.0277	0.0098	0.2603	0.1098	0.5782	0.6436	6.8694	22	175
0.85	0.0477	0.0074	0.2614	0.1799	0.5462	0.6317	5.8795	22	170
1	0.1927	0.0101	0.2554	0.2411	0.5423	0.6461	4.2805	21	152
1.5	0.3402	0.0069	0.2622	0.155	0.5743	0.65	4.0741	18	83
2	0.0462	0.0234	0.6997	0.1634	0.4643	0.8554	6.6824	10	27

Table 6.13. Variance components estimated for the Upper V4 branch

Period (s)	Bias, β_0	Std. Error σ_{β_0}	τ	ϕ_{S2S}	ϕ	σ	Range, r_c	Num. Eqs	Num. Recs
PGV	-0.059	0.0036	0.2704	0.201	0.5095	0.6108	3.9712	22	178
0.01	-0.198	0.0078	0.2548	0.2442	0.5448	0.6491	4.4914	22	178
0.025	-0.2348	0.0098	0.3286	0.2491	0.5476	0.6855	4.4125	22	178
0.05	-0.2158	0.0112	0.2687	0.2584	0.6258	0.7284	5.3978	22	178
0.075	-0.1777	0.0072	0.2227	0.3432	0.6316	0.7525	4.2716	22	178
0.1	-0.1979	0.0174	0.1802	0.4021	0.6176	0.7587	4.5121	22	178
0.125	-0.2071	0.0166	0.2105	0.3565	0.5866	0.718	4.5528	22	178
0.15	-0.2011	0.0632	0.1686	0.3273	0.5313	0.6464	4.7404	22	178
0.175	-0.2003	0.0086	0.2238	0.3111	0.5064	0.635	4.114	22	178
0.2	-0.1746	0.0075	0.2453	0.3093	0.516	0.6497	4.4093	22	178
0.25	-0.1708	0.0074	0.2975	0.2712	0.4944	0.6375	4.6264	22	178
0.3	-0.1411	0.0046	0.2464	0.2543	0.5237	0.6321	5.0586	22	178
0.4	-0.1215	0.0054	0.2829	0.2419	0.5049	0.6273	4.5054	22	178
0.5	-0.1333	0.0088	0.2751	0.2428	0.5491	0.6604	5.2955	22	178
0.6	-0.0592	0.013	0.2557	0.2339	0.555	0.6543	5.453	22	176
0.7	-0.0697	0.0052	0.2553	0.1099	0.5804	0.6435	6.9879	22	175
0.85	0.0167	0.0134	0.2403	0.1865	0.551	0.6293	6.1595	22	170
1	0.1453	0.007	0.2477	0.2446	0.5405	0.6429	4.3513	21	152
1.5	0.2977	0.0234	0.2675	0.1415	0.5763	0.6509	4.0198	18	83
2	0.0073	0.007	0.6992	0.1588	0.4615	0.8527	6.3085	10	27

These tabulated values reinforce the statements made earlier that the V4 model is either unbiased for the central models, or is deliberately biased for the lower and upper branches. Again, it should be noted that the primary role of the four branches is to provide sensible measures of epistemic uncertainty for the larger scenarios, but the robust performance with respect to the small magnitude Groningen data is also comforting.

Figure 6.43 demonstrates that the net effect of undertaking more advanced regression procedures and correcting the error in magnitude assignments, is to reduce the estimated inter-event standard deviation in a very significant way. Whereas the V3 spectral GMPE had unusually large values of the standard deviation, the advanced regression analyses and particularly the impact of accounting for magnitude uncertainties, has allowed this variance component to be reduced significantly for the V4 model. The largest reduction occurs at intermediate to long periods where Figure 6.43 shows factors of 2-3 reduction in the inter-event standard deviation.

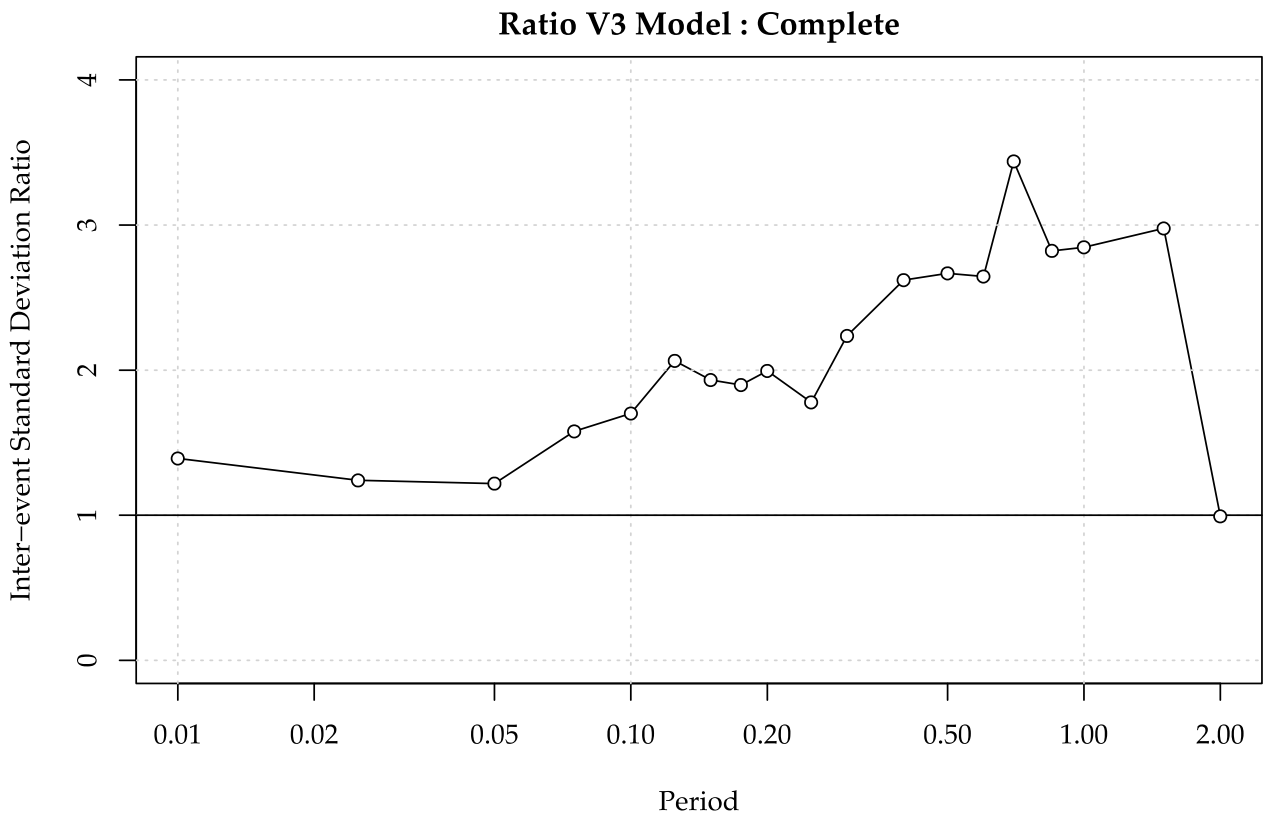


Figure 6.43. Ratio of the inter-event standard deviation in the V3 model and the inter-event standard deviations estimated in the V4 model.

The complete model for the variance components is discussed in detail in Chapter 10, and particularly in Section 10.3 where the model for the inter-event variability is presented. This model has been informed by the results obtained using these advanced regression approaches.

6.6. Ground-motion model for reference rock horizon

The ground-motion model for predicting median spectral accelerations at the NS_B horizon at the 23 selected target oscillator periods and PGV is fully defined equations and coefficients provided in the previous two sub-sections. Figures 6.44 to 6.47 show the predicted median values of $Sa(T)$ and PGV as a function of distance for various magnitudes obtained with the four branches of the GMPE.

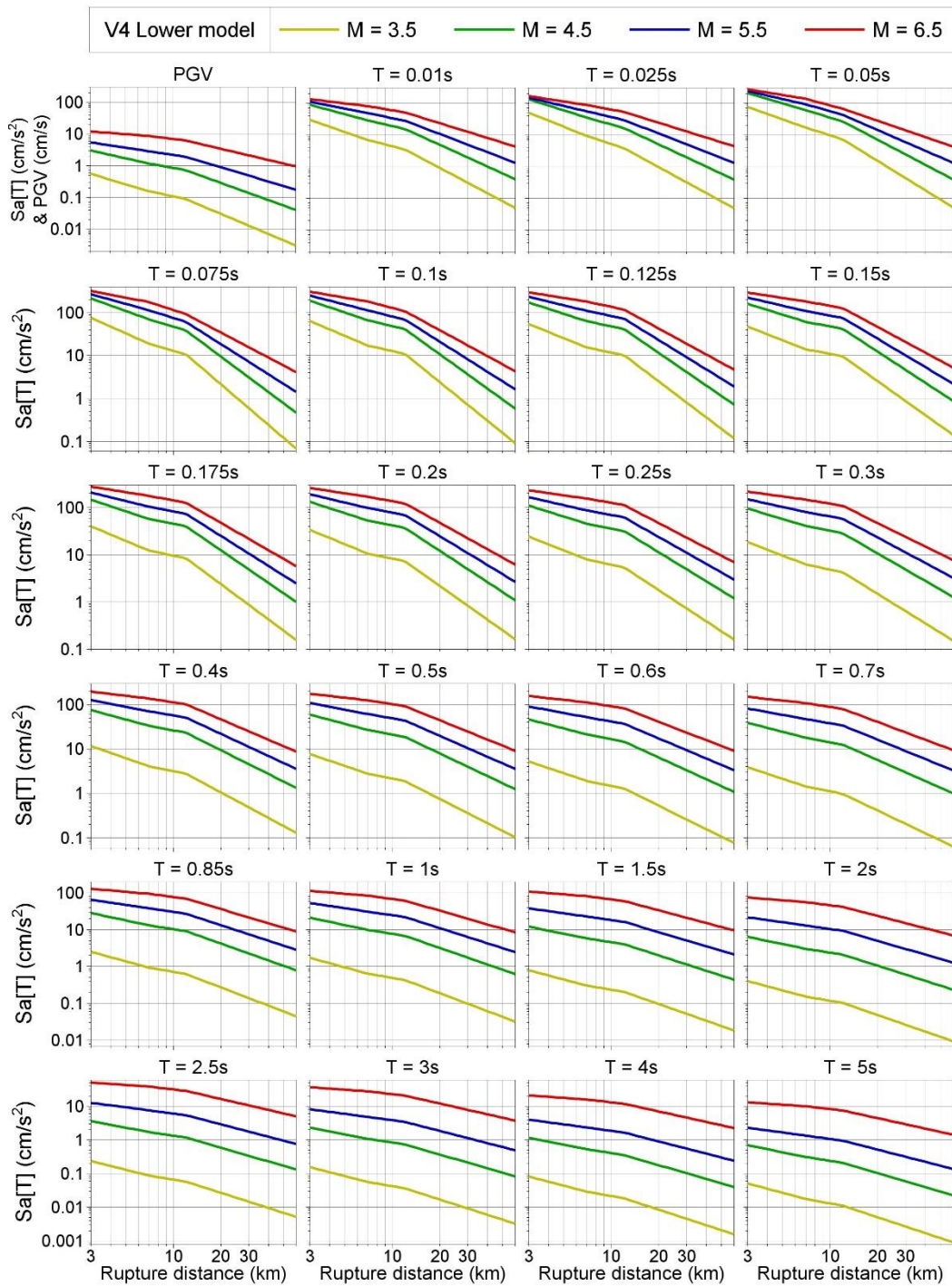


Figure 6.44. Median predictions of PGV and $Sa(T)$ from the Lower model for the NS_B reference rock horizon as a function of epicentral distance for a range of magnitudes

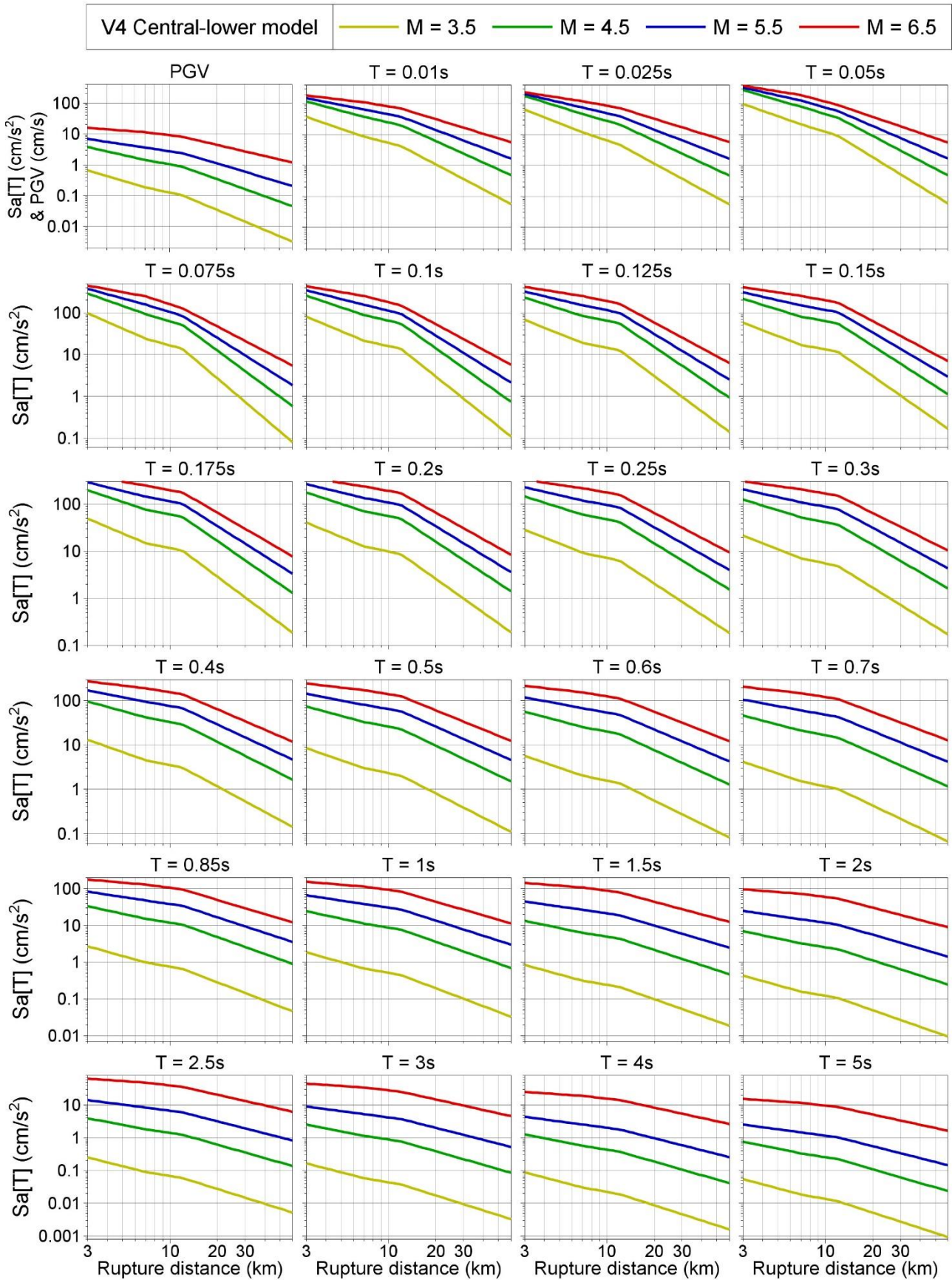


Figure 6.45. Median predictions of PGV and Sa(T) from the Central-lower model for the NS_B reference rock horizon as a function of distance for a range of magnitudes

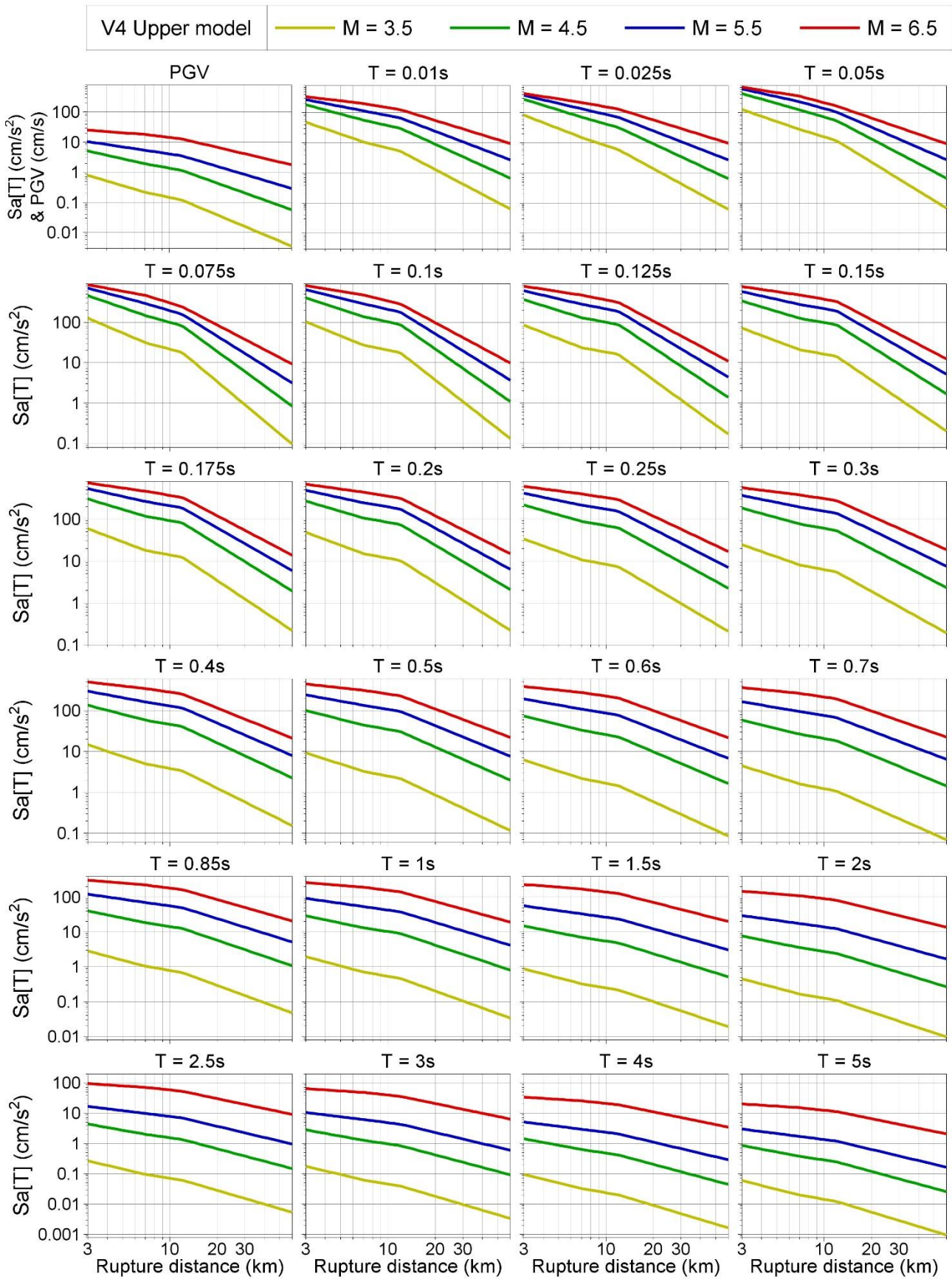


Figure 6.47. Median predictions of PGV and Sa(T) from the Upper model for the NS_B reference rock horizon as a function of distance for a range of magnitudes

In order to provide additional insight into the nature of the V4 model for predictions of spectral accelerations at the reference rock horizon, Figures 6.48 to 6.53 show median predictions from the four models (lower, central-lower, central-upper, and upper) for six response periods as a function of magnitude at different distances. Figures 6.54 to 6.59 display median response spectra from the four V4 models for four different magnitudes and a range of rupture distances.

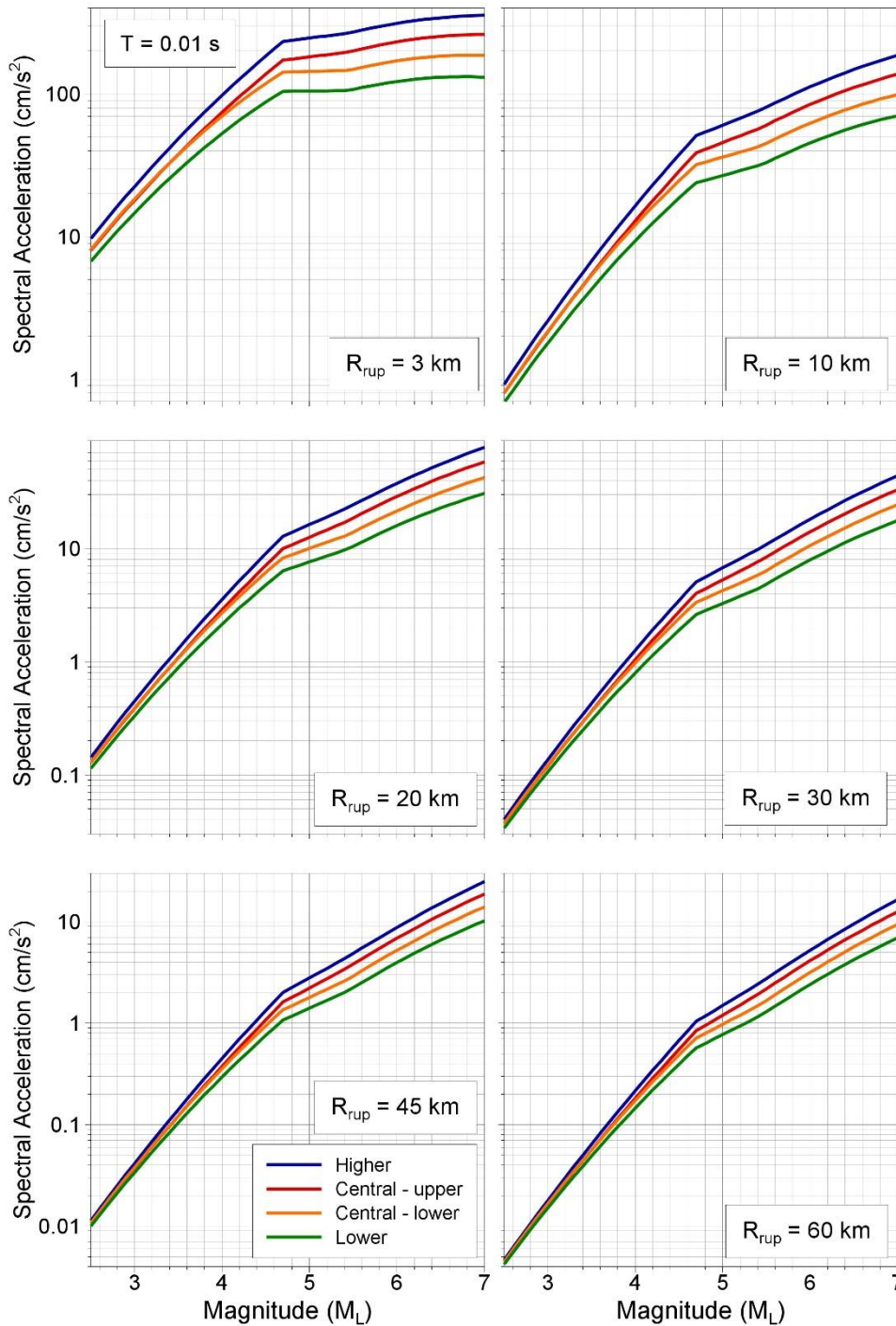


Figure 6.48. Median predictions of spectral accelerations from the V4 models for spectral accelerations at 0.01 s at the NS_B reference rock horizon as a function of magnitude for different rupture distances

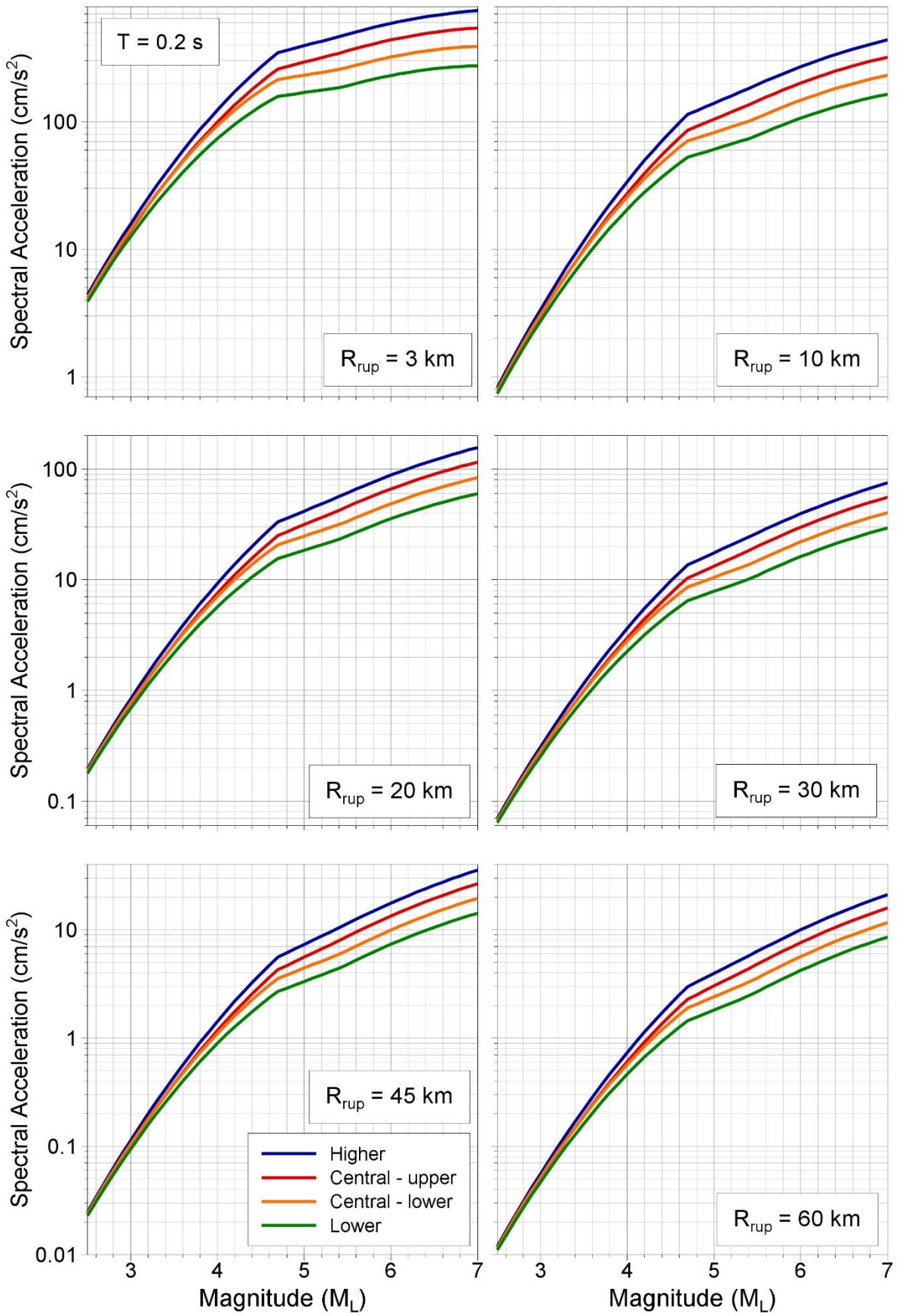


Figure 6.49. Median predictions of spectral accelerations from the V4 models for spectral accelerations at 0.2 s at the NS_B reference rock horizon as a function of magnitude for different rupture distances

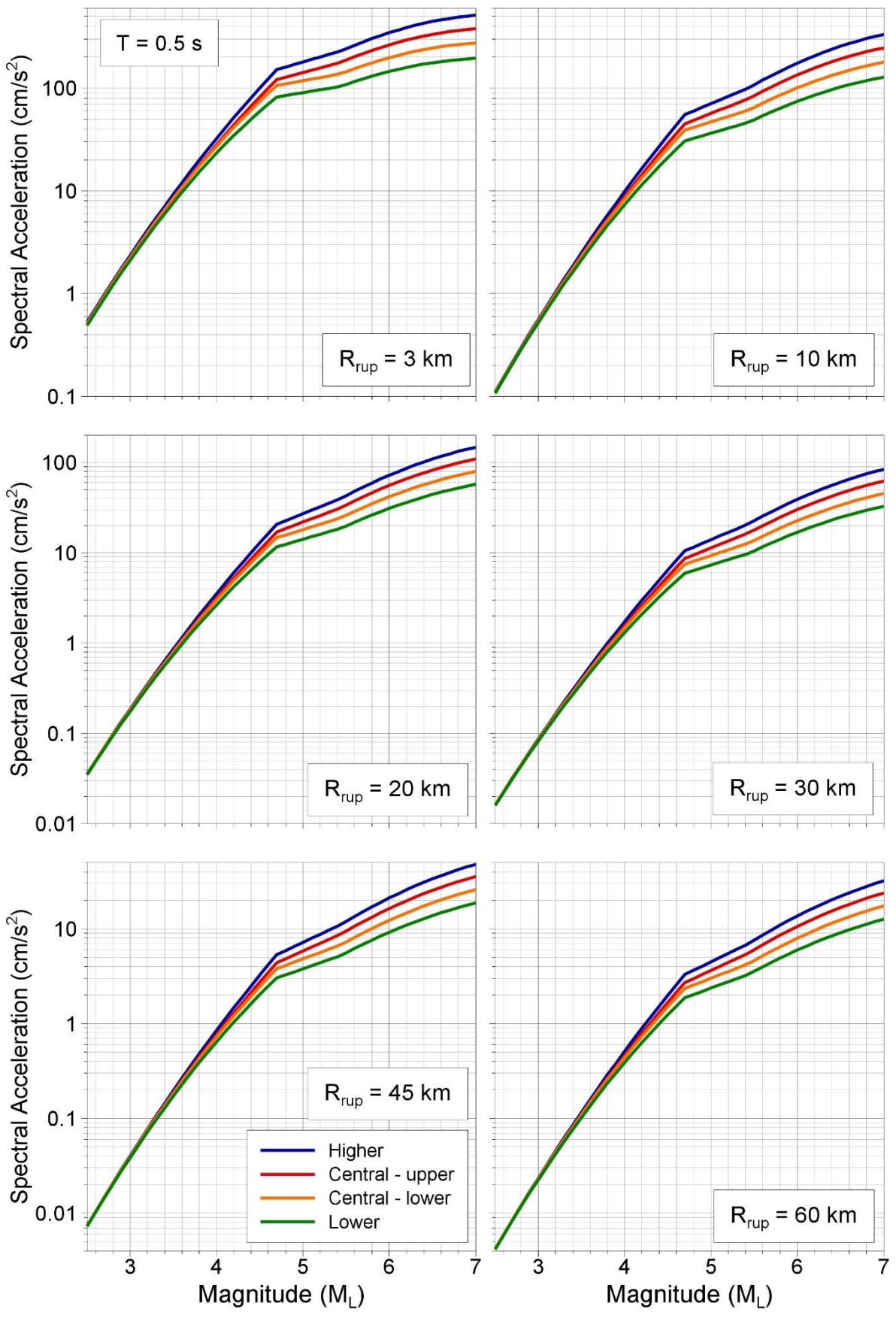


Figure 6.50. Median predictions of spectral accelerations from the V4 models for spectral accelerations at 0.5 s at the NS_B reference rock horizon as a function of magnitude for different rupture distances

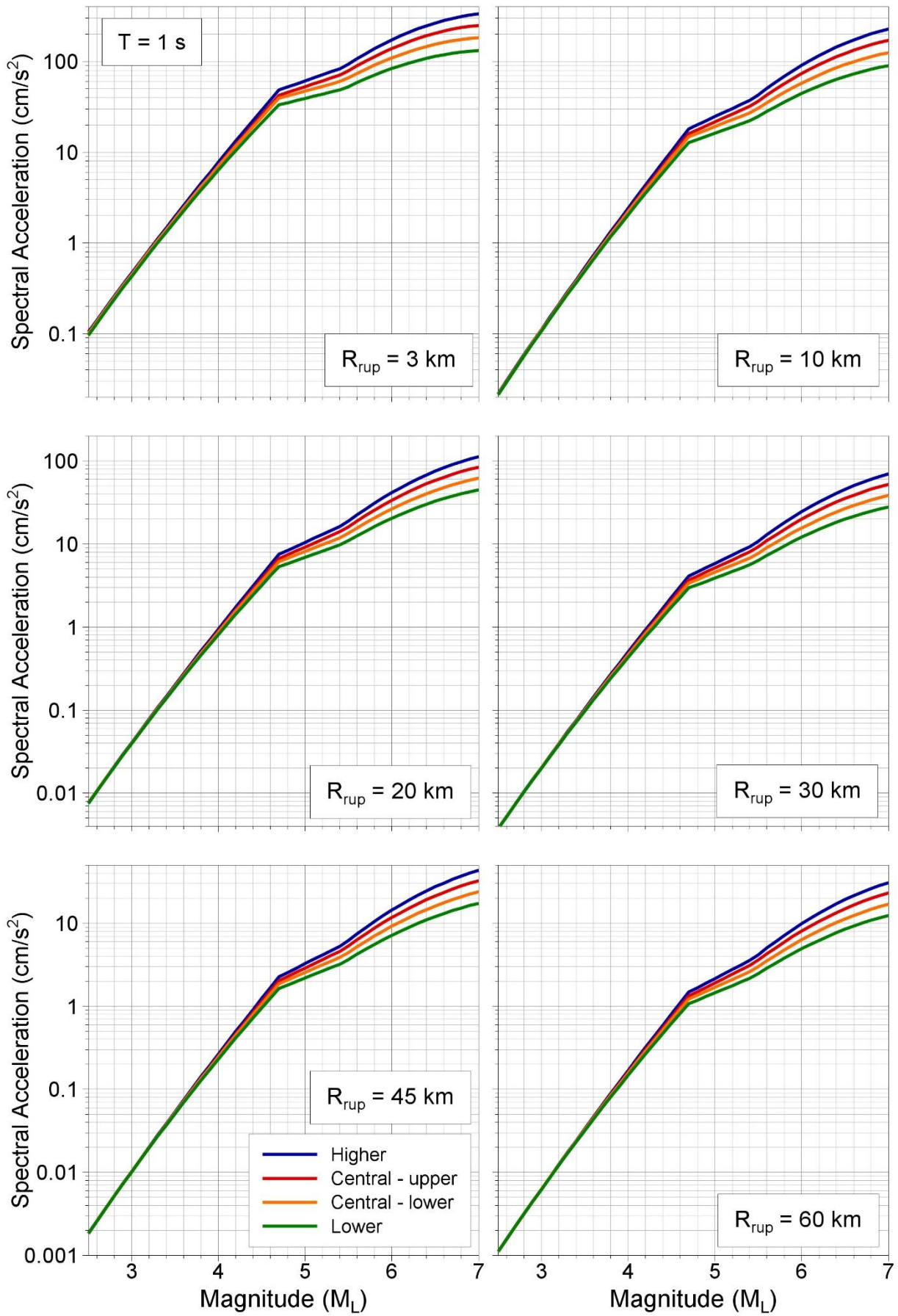


Figure 6.51. Median predictions of spectral accelerations from the V4 models for spectral accelerations at 1.0 s at the NS_B reference rock horizon as a function of magnitude for different rupture distances

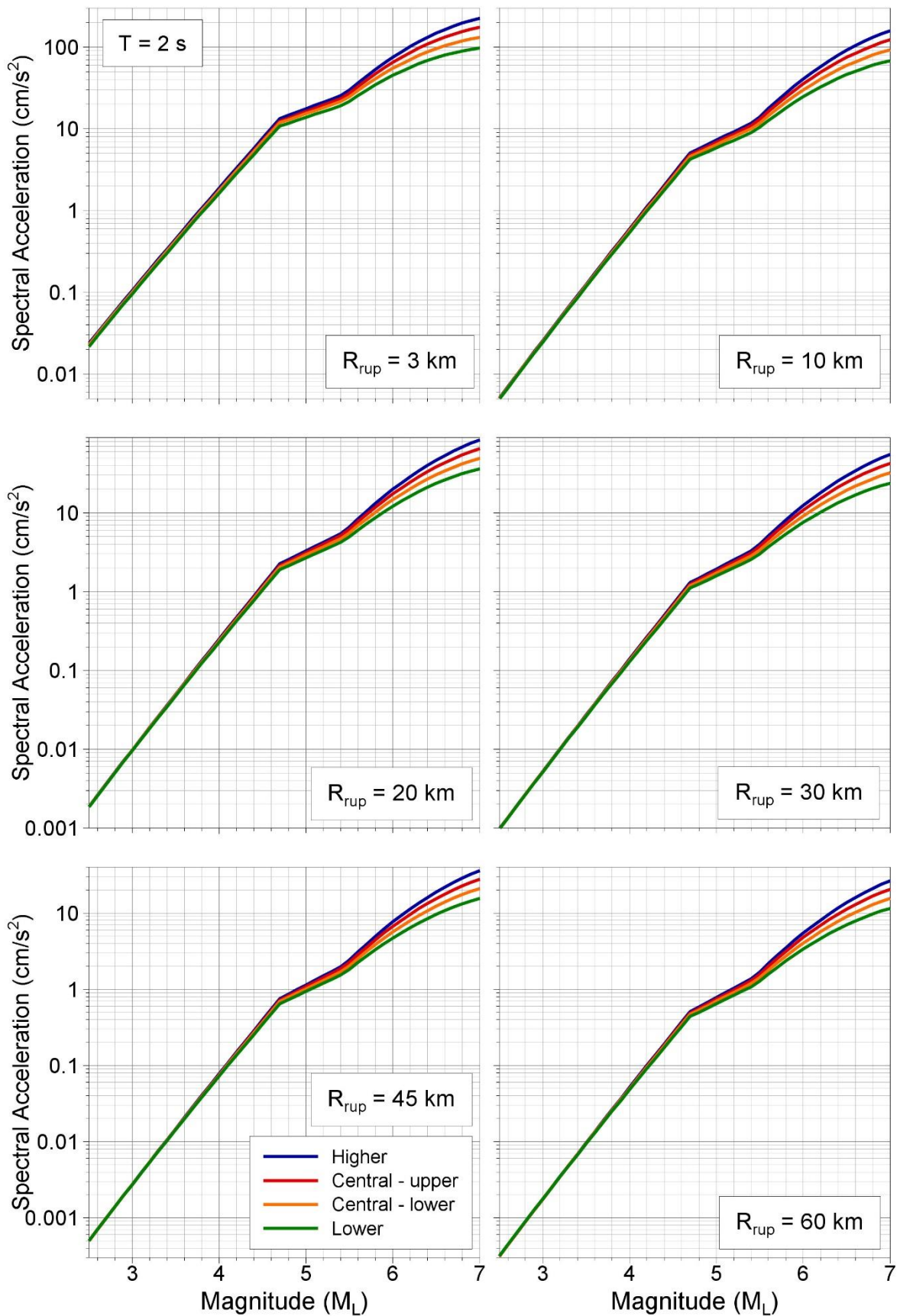


Figure 6.52. Median predictions of spectral accelerations from the V4 models for spectral accelerations at 2 s at the NS_B reference rock horizon as a function of magnitude for different rupture distances

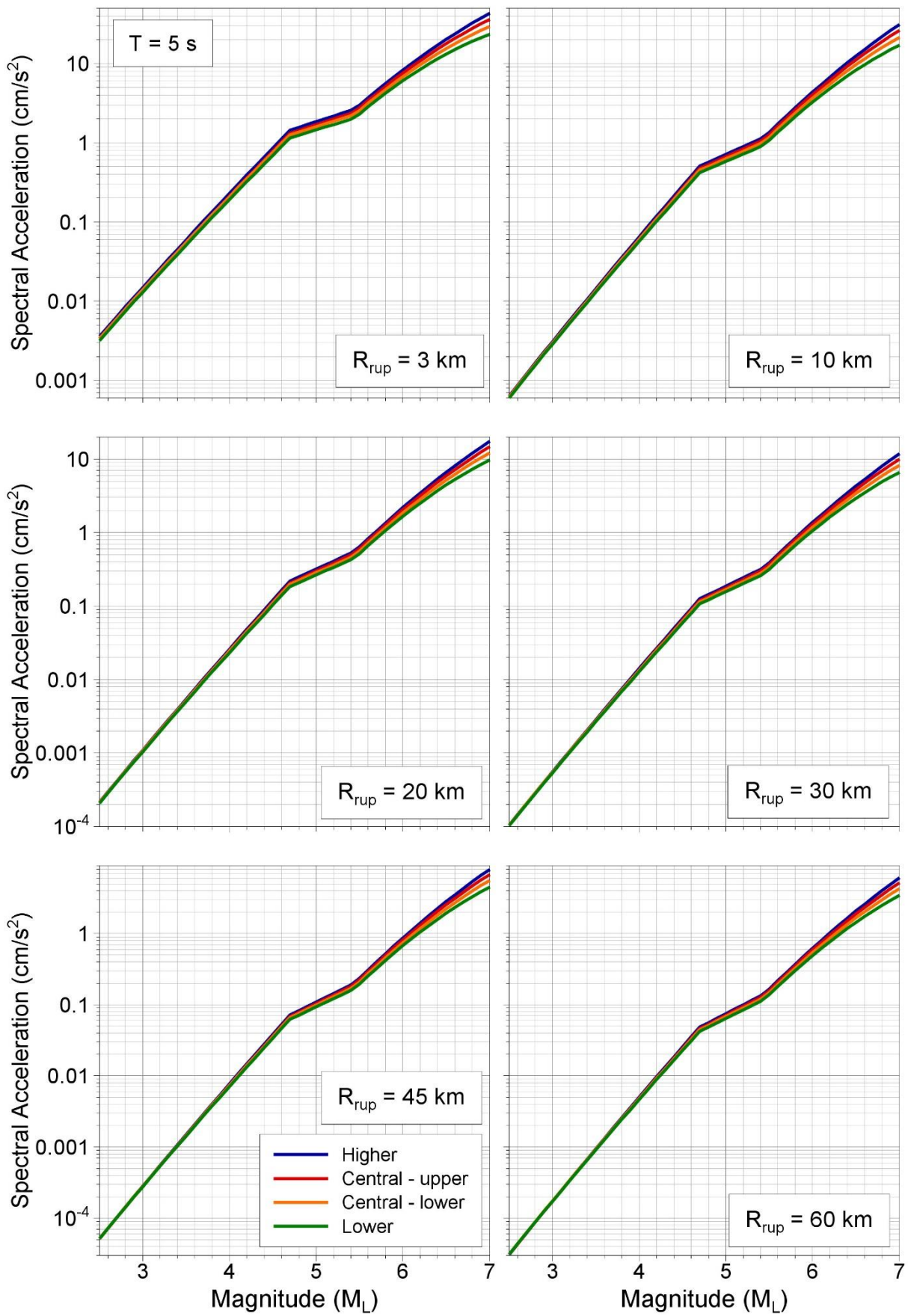


Figure 6.53. Median predictions of spectral accelerations from the V4 models for spectral accelerations at 5 s at the NS_B reference rock horizon as a function of magnitude for different rupture distances

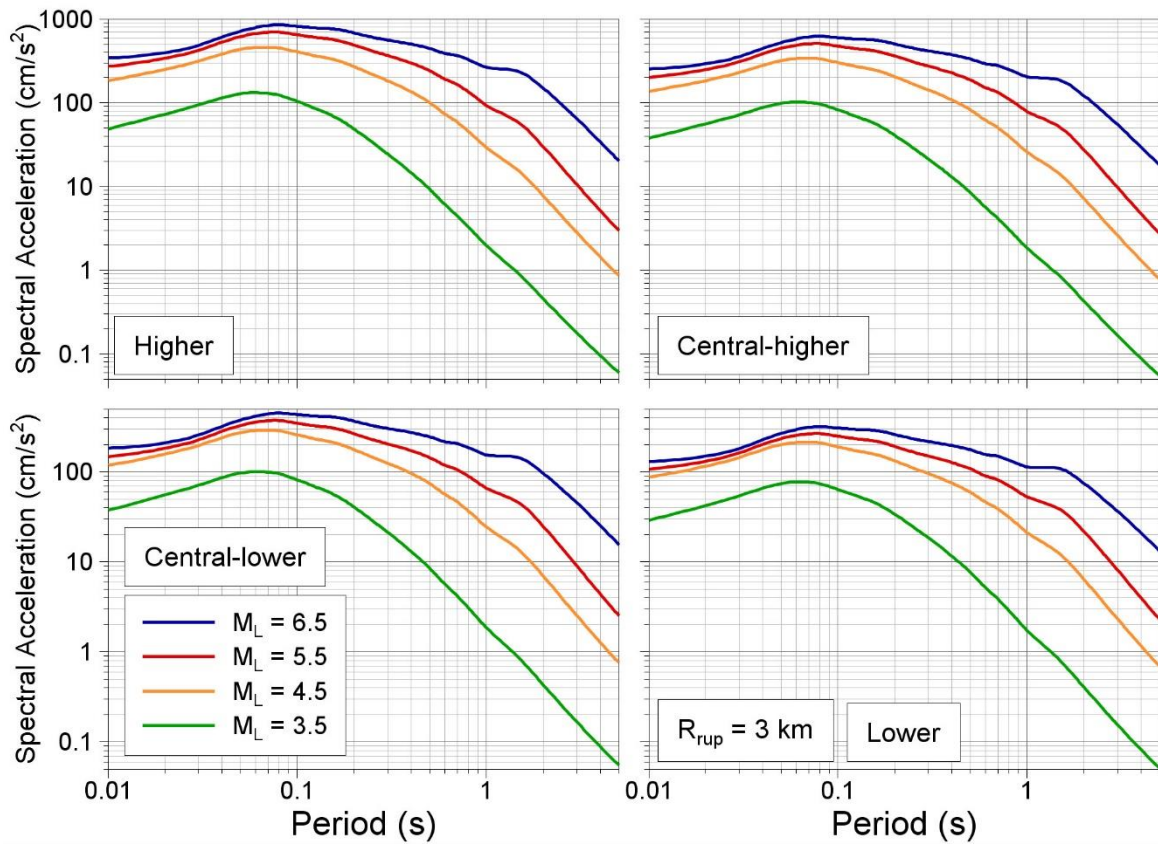


Figure 6.54. Median acceleration response spectra at the NS_B horizon from the V4 models for earthquakes four magnitudes at 3 km rupture distance

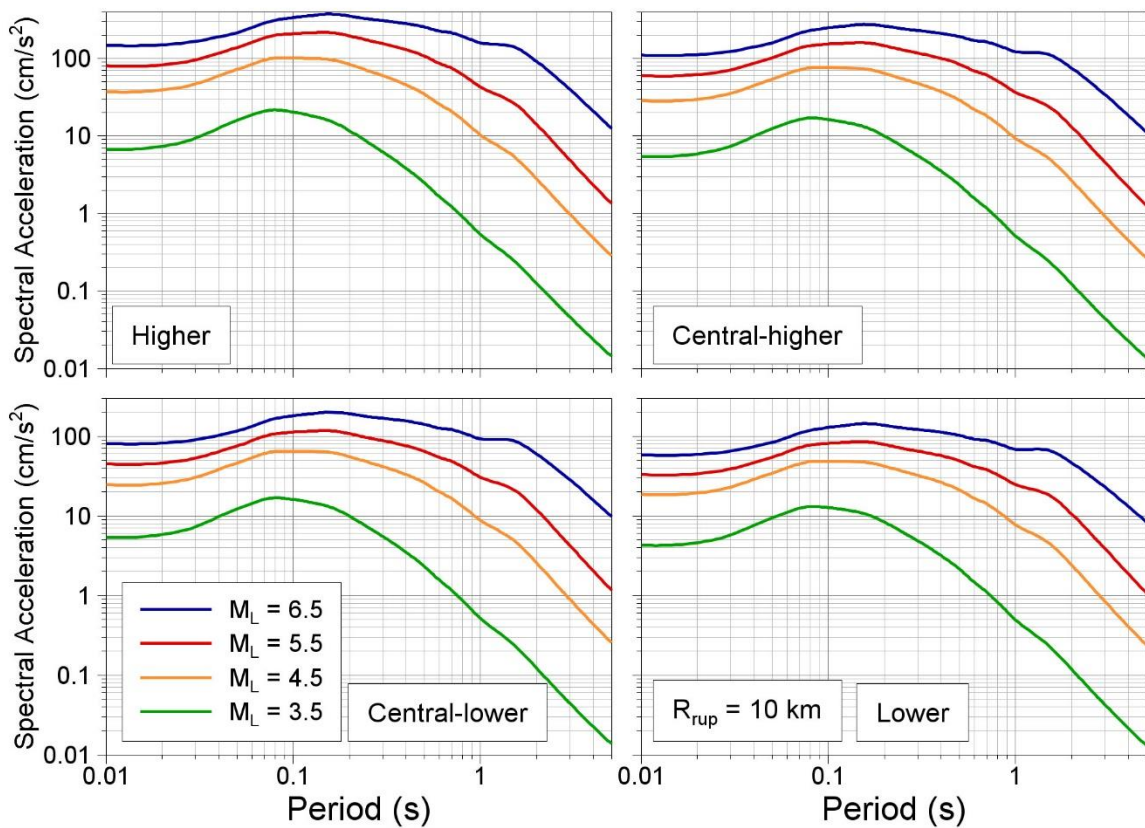


Figure 6.55. Median acceleration response spectra at the NS_B horizon from the V4 models for earthquakes four magnitudes at 10 km rupture distance

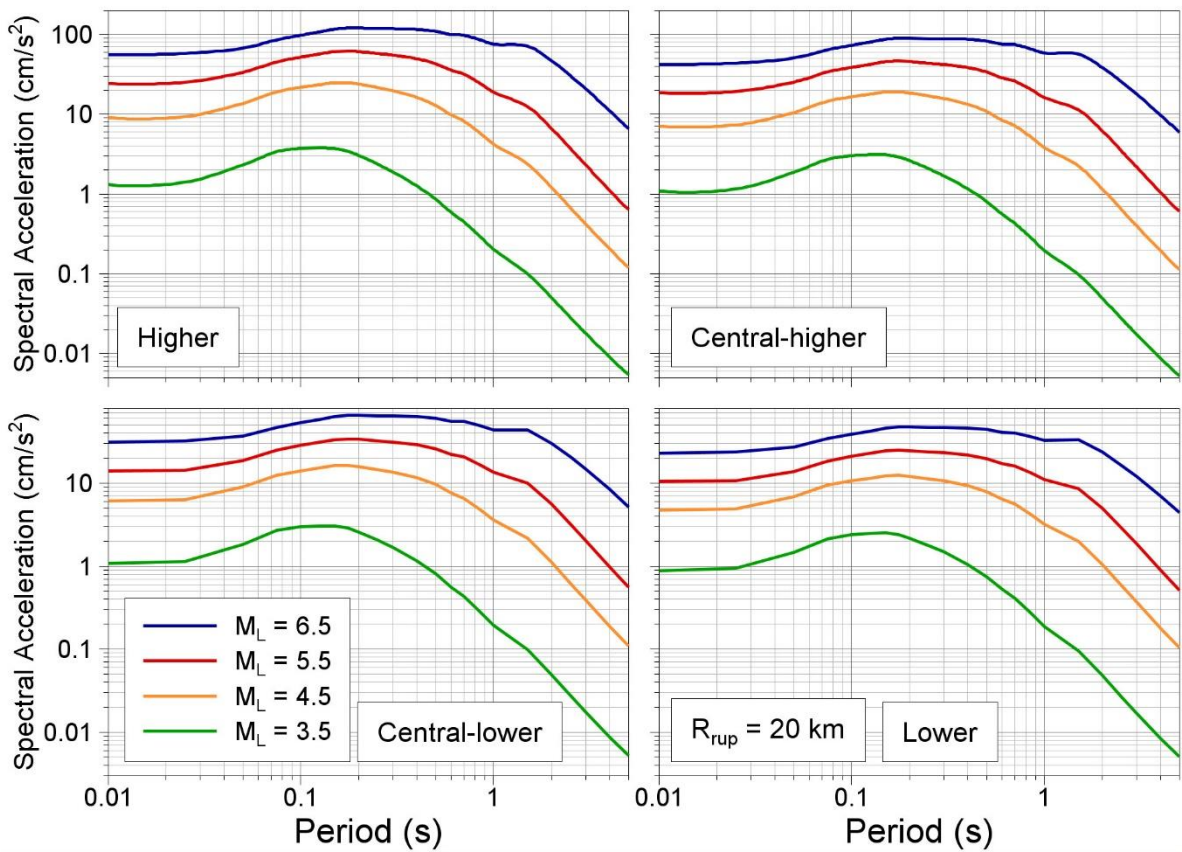


Figure 6.56. Median acceleration response spectra at the NS_B horizon from the V4 models for earthquakes four magnitudes at 20 km rupture distance

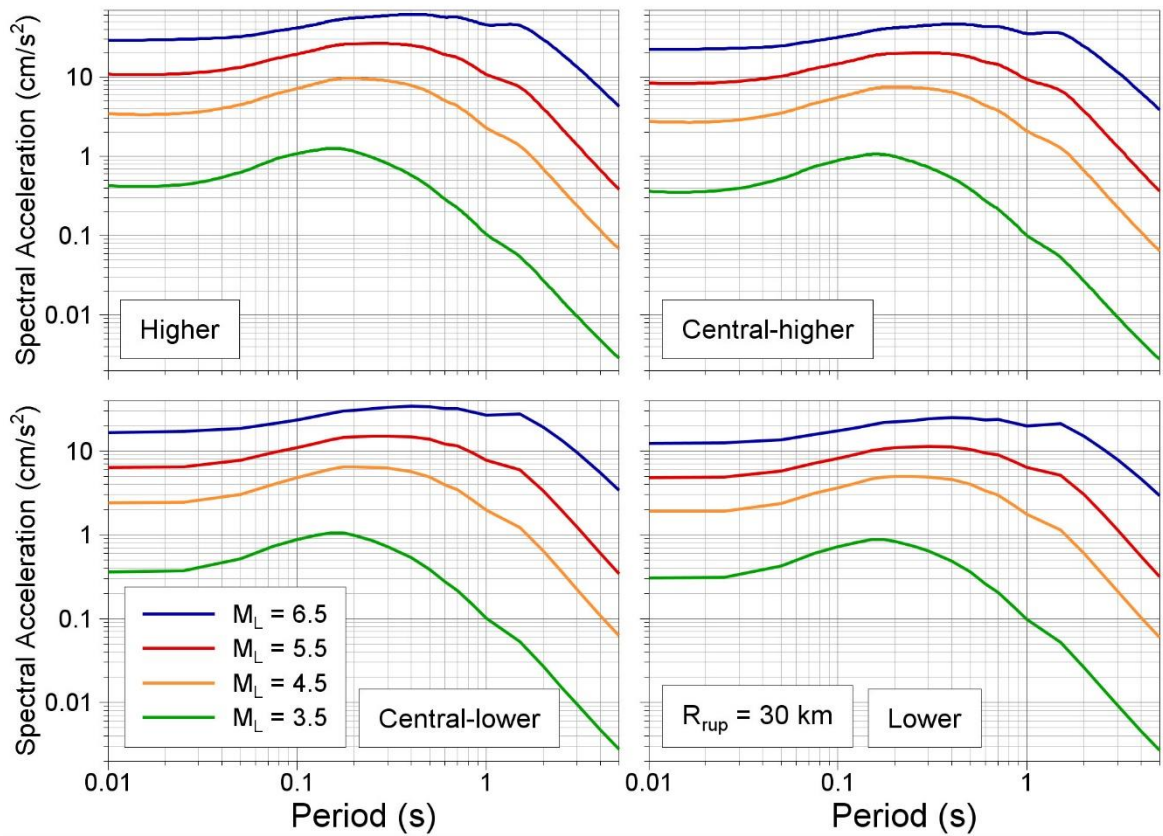


Figure 6.57. Median acceleration response spectra at the NS_B horizon from the V4 models for earthquakes four magnitudes at 30 km rupture distance

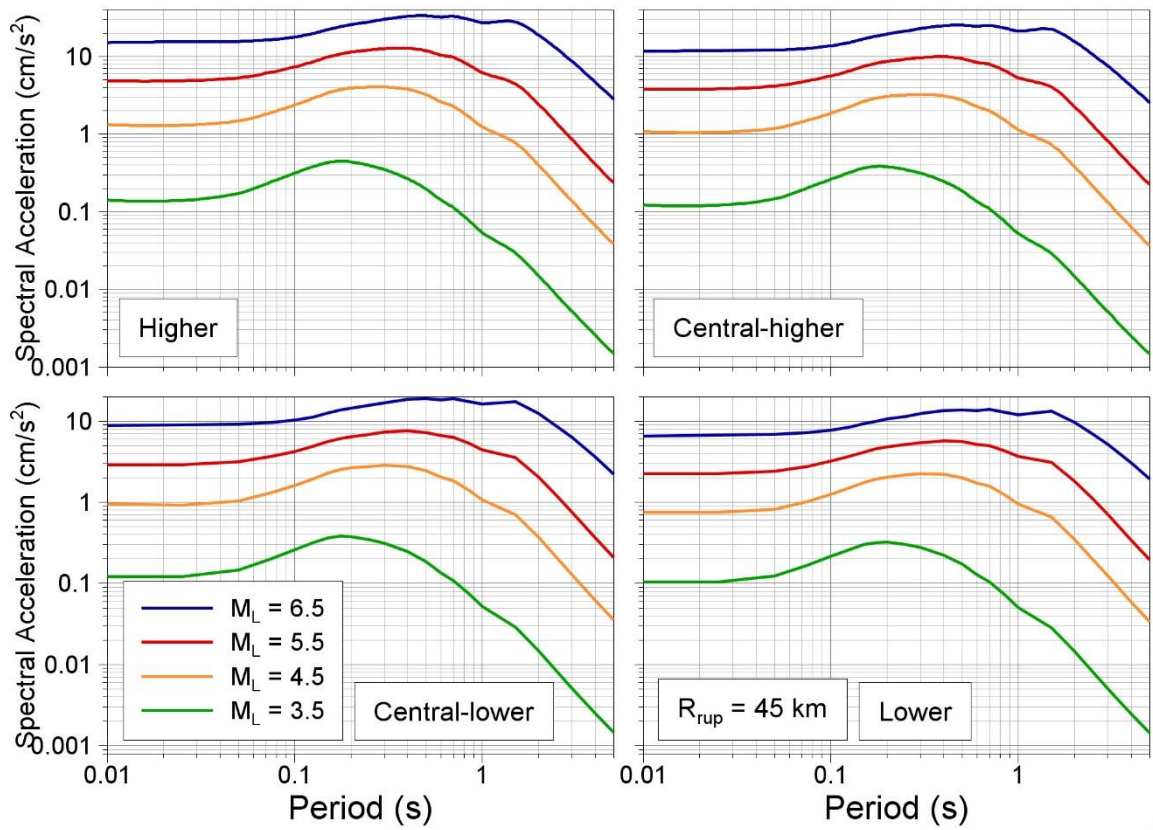


Figure 6.58. Median acceleration response spectra at the NS_B horizon from the V4 models for earthquakes four magnitudes at 45 km rupture distance

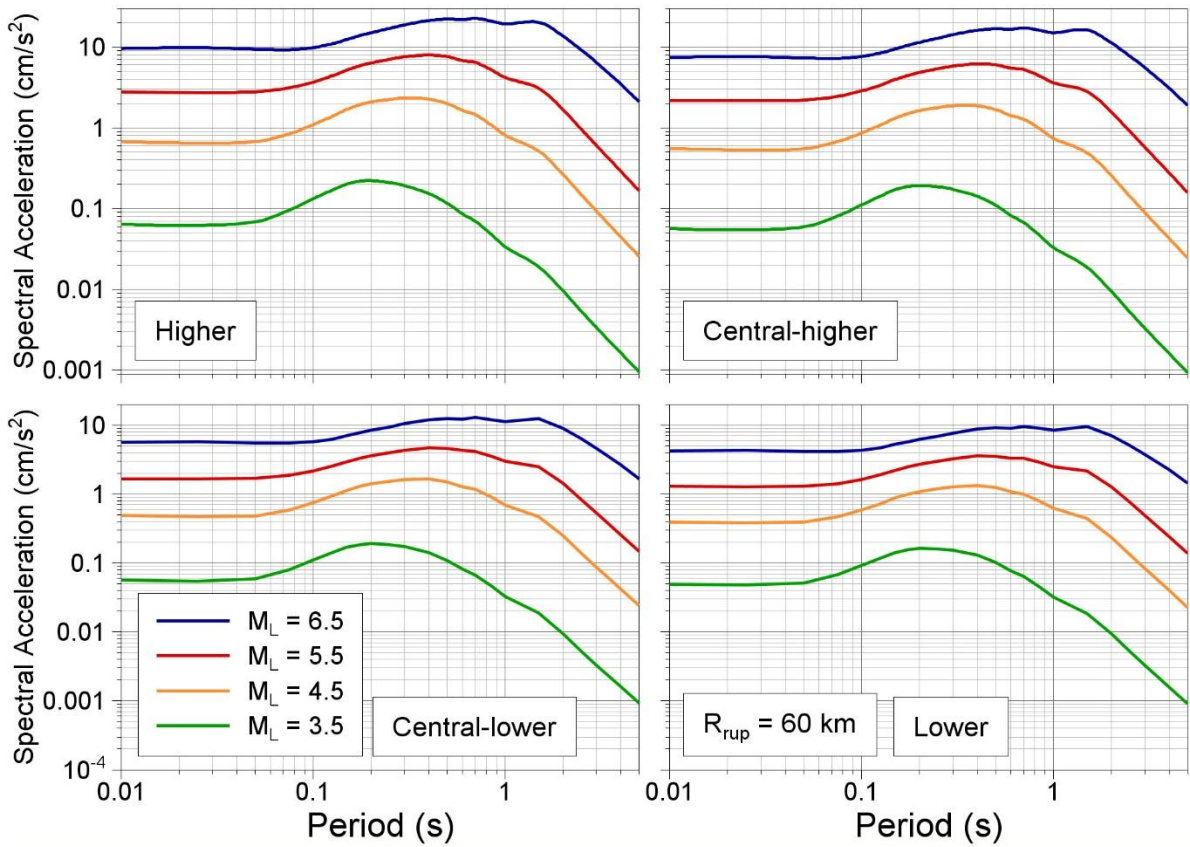


Figure 6.59. Median acceleration response spectra at the NS_B horizon from the V4 models for earthquakes four magnitudes at 60 km rupture distance

The plots in Figure 6.54 to 6.59 clearly show how the amplitude of the spectra change from model to model, and also how the smooth spectral shapes vary with magnitude. In particular, the movement of the spectral peak to longer periods with increasing magnitude and the proportionally much higher ordinates at longer periods are prominent features that coincide with what would be expected from seismological theory. One observation that can be made on these plots is that there is a distinct bump in the spectra at about 1.5 seconds, which actually reflects a peak in the residuals (Figure 6.42) that was not initially given importance since it was interpreted as being unreliable due to the small number of useable records at this response period. However, the clear persistence of this feature in the predictions warrants investigation (see Chapter 13).

The complete model requires the terms defining the variability associated with these median predictions, informed by the values inferred from the residuals presented in the previous section. The sigma model is discussed in Chapter 10.

The final step is then to assign weights to these branches. In the V1 and V2 models, we chose branch weights of 0.2 on the lower branch, 0.5 on the central branch, and 0.3 on the upper branch. This could be considered somewhat conservative, especially given the coupling of high medians with large sigmas and in view of the growing body of evidence to support lower stress drops for shallow earthquakes (Bommer *et al.*, 2015a,b; Bommer *et al.*, 2016). At the same time, it is important that motions from larger earthquakes—which may be similar to those from tectonic earthquakes, as represented by the upper model—are adequately captured. For these reasons, the weights were changed in the V3 model as follows: Lower model (0.2), Central model (0.4) and Upper model (0.4). In the V4 model, the reasoning is similar but now there are four branches. We assign a low weight of just 0.1 to the lower model and then equal weights to the other three branches (Figure 6.60).

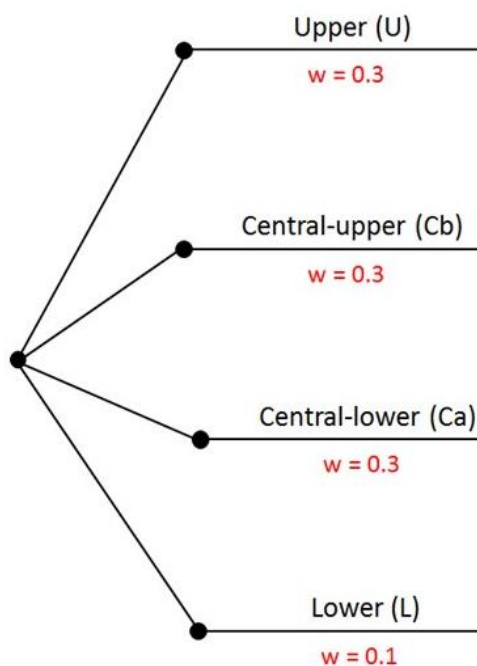


Figure 6.60. Logic-tree for median ground-motion predictions

To close this section, we briefly compare the median predictions from the V4 GMPEs for rock motions with those from other GMPEs. We do not see great value in making the comparisons with equations derived for tectonic earthquakes since the depth distributions for such events would be markedly different from the shallow foci of the Groningen earthquakes; without an appropriate adjustment for scaling of stress drop with depth, such comparisons could be misleading. We therefore prefer to limit the comparisons with other GMPEs derived for shallow-focus, moderate-magnitude induced seismicity, which are currently very few in number. One candidate model for this purpose would be the GMPEs of Douglas *et al.* (2013), but these are derived for a V_{S30} of 1,100 m/s and are not intended for application beyond **M5**. We conclude that a more appropriate model for these comparisons is that published by Atkinson (2015), notwithstanding that it was derived from recordings of tectonic earthquakes without making any adjustment for the depth-dependence of stress drop, which means that it is probably somewhat conservative for shallow earthquakes. The comparisons are also close to meaningless at larger magnitudes given that the Atkinson (2015) GMPEs use hypocentral distance and therefore model the earthquake source as a point whereas the V4 model uses rupture distance. Nonetheless, the comparisons are included for completeness because the Atkinson (2015) model has become a standard point of reference for ground motions from induced earthquakes.

The equations of Atkinson (2015) are calibrated to a V_{S30} value of 760 m/s but the predictions are adjusted to the NS_B velocity of 1,500 m/s using the site amplification factors of Boore *et al.* (2014), as recommended by Atkinson (2015). In making the comparisons, we also account for the difference of 0.2 between the moment magnitudes used by Atkinson (2015) and the local magnitudes used for the V4 model (see Section 2.1). Figure 6.61 compares the response spectra from the four V4 equations with those obtained from the two Atkinson (2015) models, which correspond to two different near-source saturation terms. No adjustment is made for the systematic differences between hypocentral and rupture distances; however, it should be borne in mind that all other factors being equal, the use of point-source-based distance metrics will always lead to higher predicted amplitudes than when using distance metrics based on extended ruptures (Bommer & Akkar, 2012). For this reason, not too much attention should be paid to the comparisons for magnitude 6 in the bottom row of the figure.

The comparisons at magnitudes 4 and 5 are probably the most relevant to the Groningen hazard and risk calculations. At magnitude 4, the Groningen equation is generally higher than the Atkinson (2015) model, except at longer distances, which are of much less significance for the hazard and risk estimates. At magnitude 5 the same observations hold for the alternative model of Atkinson (2015) with a larger near-source saturation term. Atkinson (2015) acknowledges that neither saturation model is well constrained by her data and the alternative model was previously observed to be very similar to the empirical Groningen model used in the V1, V2 and V3 models.

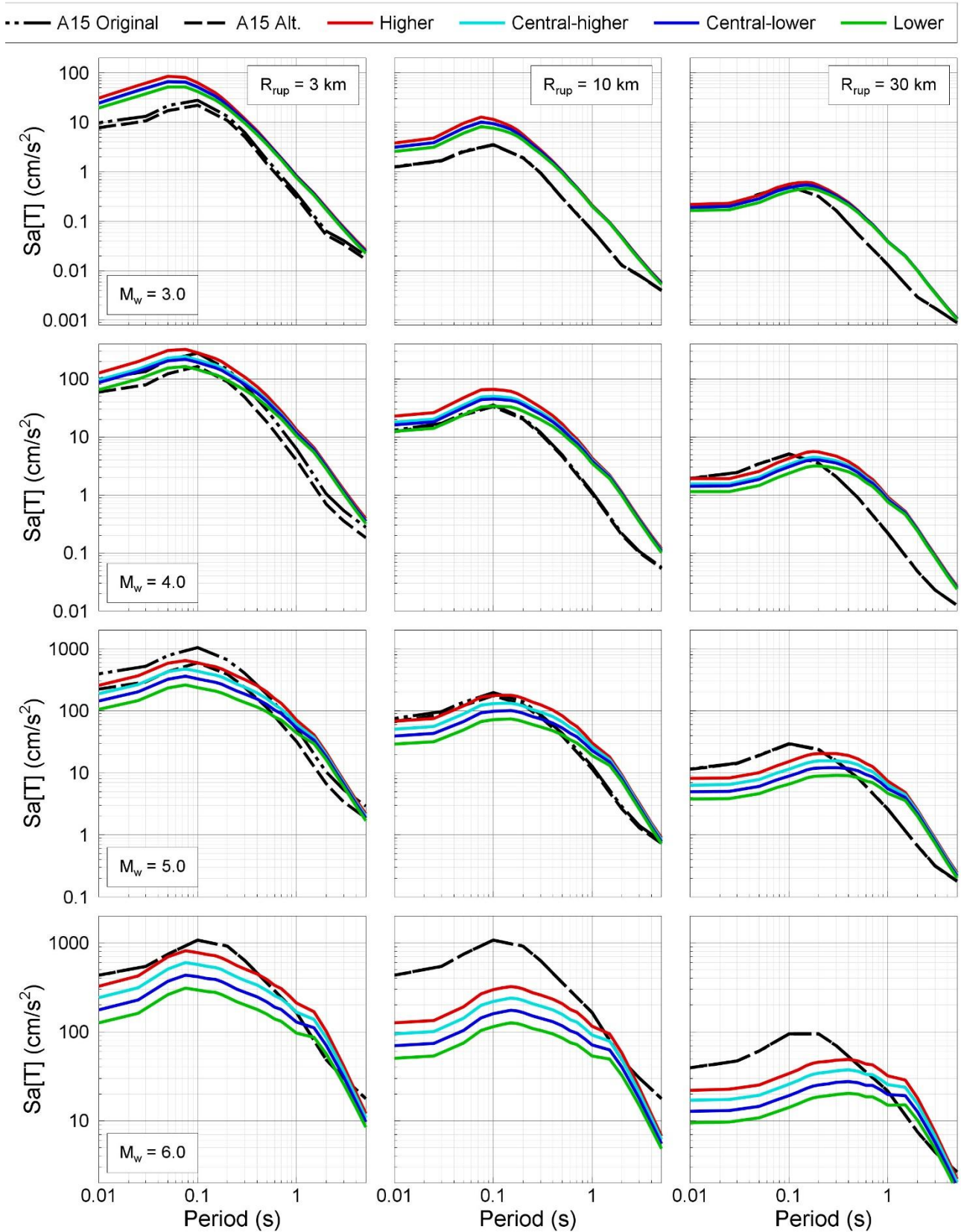


Figure 6.61. Median acceleration response spectra at the NS_B horizon from the V4 equations and the two GMPEs of Atkinson (2015) for 12 different combinations of magnitude and rupture (or hypocentral) distance

7. SITE RESPONSE MODEL

This chapter presents the development of the site response model to be used in site response analyses. The model includes the definition of shear-wave velocity (V_s) and mass density profiles for the Groningen site, and the modulus reduction and damping versus shear strain (MRD) for the soil types found at the Groningen site. The site response analyses are described in Chapter 8.

7.1. Shallow V_s profiles

The shallow V_s profiles were built from the combination of the GeoTOP model described in Kruiver *et al.* (2015) and Kruiver & Wiersma (2016) and the V_s relationships for the Groningen region. The V_s model is described in Kruiver *et al.* (2017) and summarised in Sections 7.1 and 7.2. The V_s model provides distributions of V_s defined by mean $\ln(V_s)$ and standard deviations of $\ln(V_s)$. Mean V_s profiles were used in the analysis of linear amplification factors for stations (Sections 4.2 and 4.3). The site response calculations, however, require randomised V_s profiles. The randomisation scheme is described in Section 7.7.

The GeoTOP model assigns a lithostratigraphical unit and a lithological class to each voxel in the Groningen area. Different V_s relationships were derived for each of the stratigraphic and lithological combinations that are found in the Groningen field. In the following, the combination of stratigraphy and lithology is referred to as "unit". The data set consists of 88 SCPTs in the Groningen region. This includes the new SCPTs for the V_s measurements described in Section 4.2. All V_s observations were classified in terms of stratigraphy and lithology. For each unit, the V_s observations were gathered and analysed.

Generally, V_s increases with confining stress, which implies an increase of V_s with depth (e.g., Hardin, 1978; Jamiolkowski *et al.*, 1991; Yamada *et al.*, 2008). Therefore, we checked for depth dependence within each stratigraphy-lithological unit in the SCPT V_s data set. A typical model for V_s dependence on confining stress is:

$$\ln V_s = \ln V_{s_1} + n \ln \left(\frac{\sigma'_o}{p_a} \right) \quad (7.1)$$

where σ'_o is the mean confining stress, p_a is atmospheric pressure, $\ln V_{s_1}$ is a parameter that represents the shear-wave velocity at a mean confining stress equal to one atmosphere, and n is a slope that defines confining stress dependence (Sykora 1987).

Three types of V_s relationships were defined. The selection of each of the types depends on the availability of the data per unit:

1. Depth dependence according to Eq. (7.1) based on data: when the SCPT V_s data set was sufficiently large, the parameters n and $\ln V_{s_1}$ and their statistics were determined from the data.
2. No depth dependence for V_s : Either based on the SCPT V_s data or inferred from the geological depositional environment of the unit.

3. Depth dependence according to Eq. (7.1) based on literature and expert judgement: when the SCPT V_s dataset was too small for a particular unit to define n and $\ln V_{s1}$.

An example of a depth dependent V_s relationship, for clay of the Peelo Formation, is shown in Figure 7.1, left panel. The V_s relationship is defined by the slope, the intercept and the uncertainty band in a plot of V_s versus the mean effective stress (which depends on the depth and the material). An example of V_s that is independent of depth is shown in Figure 7.1, right panel. The slope is close to 0 ($n = 0.07$). In some cases, the slope is even slightly negative. For units with negative or nearly zero slope, no depth dependence was imposed.

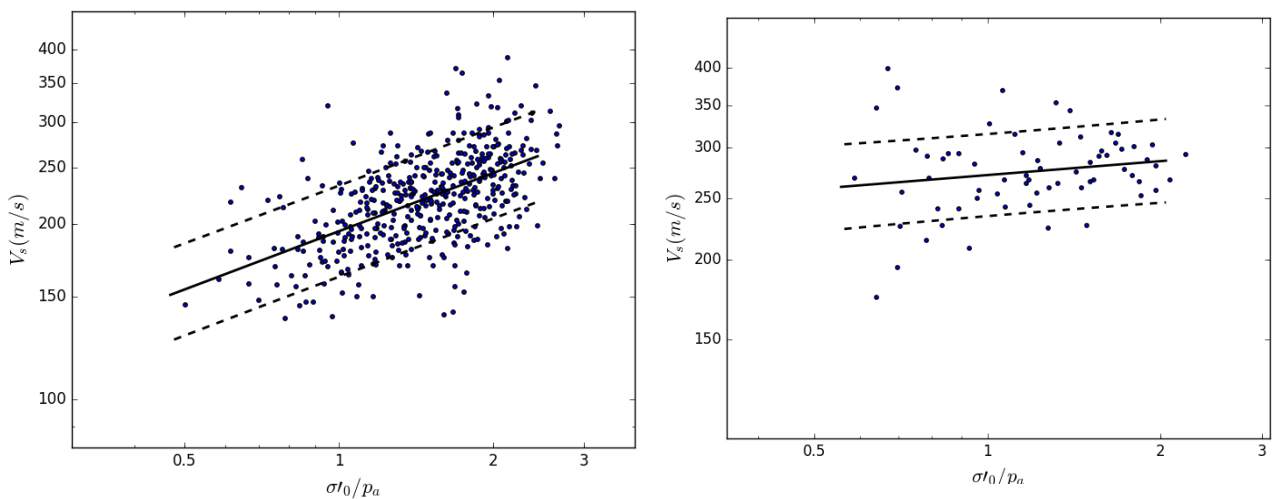


Figure 7.1. Examples of V_s observations from the SCPT data set. The solid line represents the mean V_s relationship, the dashed lines indicates the standard deviation. Left panel: for clays of the Peelo Formation showing a clear dependence. Right panel: for medium sand of the Bostel Formation, showing a slope close to 0.

The third type of V_s depth dependence applies to units where depth dependence is to be expected, but the data is insufficient to define the slope, intercept and statistics. For those units, we estimate n from literature. We use $n=0.25$ for clay, Nieuwkoop basal peat and Pleistocene peats following Hardin (1978), Jamiolkowski et al. (1991) and Yamada et al. (2008). For sand, we use $n = 0.25$ to 0.29 based on the measured coefficient of uniformity C_u following Menq (2003). Average V_s estimates were inferred from Wassing et al. (2003) and expert judgement. The intercept $\ln V_{s1}$ was determined such that the estimate of V_s occurs at the average depth of occurrence in the region and is consistent with the slope n .

In general, a minimum standard deviation of 0.27 (for the natural logarithm of V_s) was defined for peats and a minimum of 0.2 for other lithologies. The lookup table of Groningen specific V_s relationships are included in Appendix V. For units that are not included in the data set, a comparable unit is selected. For example, all Holocene Formations with peat lithology are represented by the relationship for Nieuwkoop Holland peat and all older peats by Nieuwkoop Basal peat.

An alternative to using the measured SCPTs to obtain the distribution parameters for Groningen soil types would be to use generic relations between cone resistance q_c from CPT and V_s (e.g., Andrus *et al.*, 2007 and references therein). The large database of SCPTs and CPTs for Groningen also offers the opportunity to derive Groningen-specific relations between q_c , V_s and lithology. Derivation of V_s relations based on both SCPTs and CPTs will be undertaken in future updates of the model.

The plots of the modelled V_s profiles for the locations of the B recording stations are included in Figure 7.2 and 7.3. These are sites with measured V_s profiles (Section 4.2), and the measured V_s profiles are also included in the plots. Generally, the modelled V_s agrees well with the measured V_s . In most cases, differences can be attributed to differences between the geological model and the actually encountered lithology.

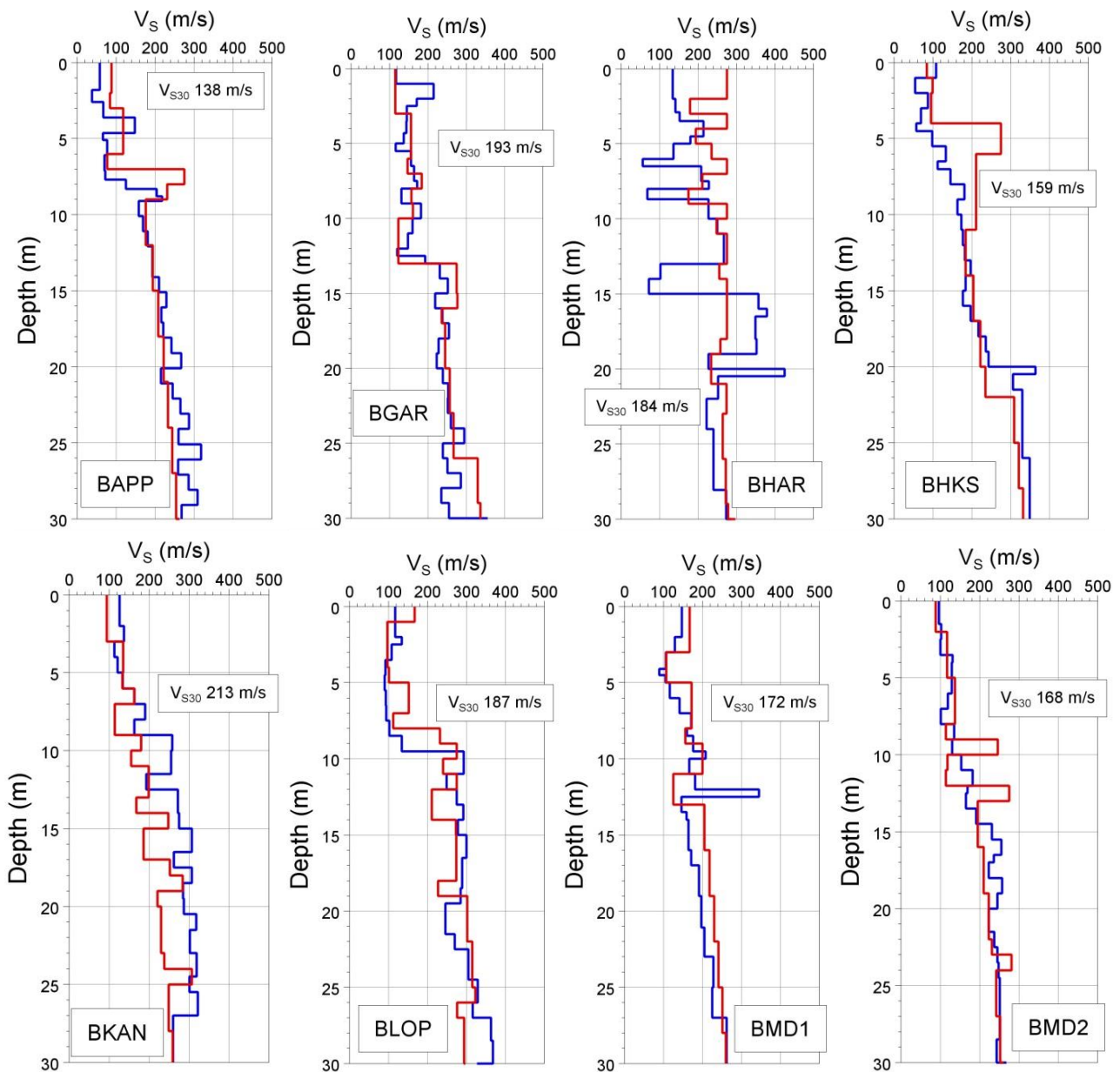


Figure 7.2. V_s profiles for B stations BAPP – BMD2. The mean modelled V_s profile is indicated by the red line, the measured V_s profile is shown in blue. The V_{s30} indicated in the graph refers to the measured V_{s30} value.

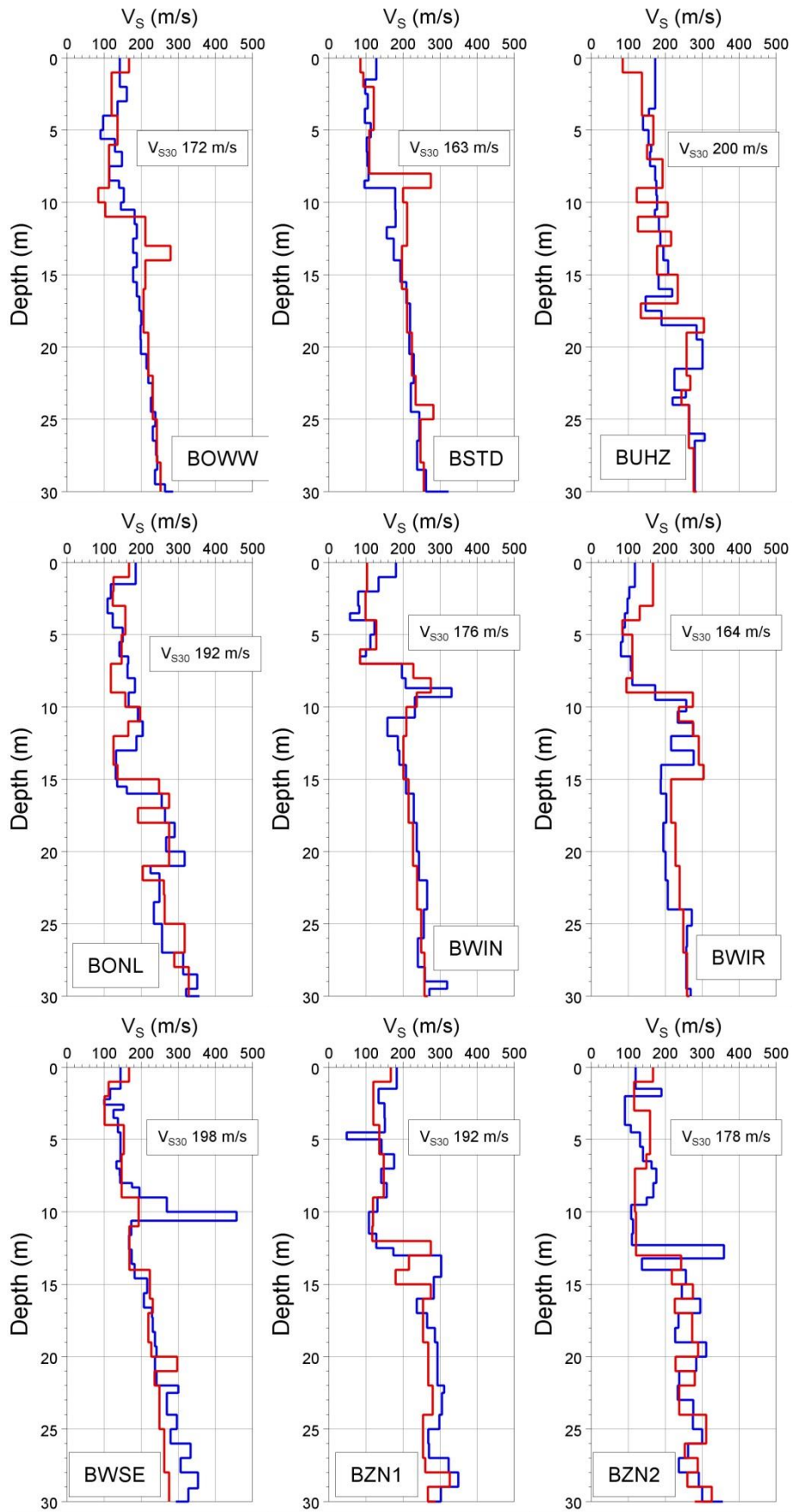


Figure 7.3. V_S profiles for B stations BOWW – BZN2. The mean modelled V_S profile is indicated by the red line, the measured V_S profile is shown in blue. The mean modelled V_S profile is indicated by the red line, the measured V_S is shown in blue. The V_{S30} indicated in the graph refers to the measured V_{S30} value.

The G recording stations consist of an accelerometer at the Earth's surface and geophones at 4 depth levels, mostly corresponding to 50, 100, 150 and 200 m depth. KNMI used local events to estimate interval velocities between different geophone / accelerometer levels applying borehole seismic interferometry (Hofman *et al.*, 2017).

The modelled V_s is compared to interval V_s determined by borehole seismic interferometry at the vertical seismic arrays at the G stations. The results are shown in Figures 7.4 to 7.9. The modelled V_s (grey lines) have a sampling interval that varies with depth, ranging from 1 m to 25 m. The KNMI V_s profiles (dark blue lines) contain average velocities over 50 meter intervals. The dashed blue lines show the modelled V_s that was harmonically averaged over 50 meter intervals to facilitate easy comparison between the modelled V_s and the interval V_s derived from seismic interferometry. The plots show that the V_s profiles of both methods generally agree well. At some sites (e.g. G29, G57, G60, and G62), the interval velocity of the top 50 m is much lower than the modelled V_s . Since the seismic interferometry data were interpreted with high confidence, this suggests that there are more low V_s layers present at the sites than is predicted by the GeoTOP model. Local measurements of V_s will improve the site characterisation at those stations, as was demonstrated at the accelerograph stations (B codes).

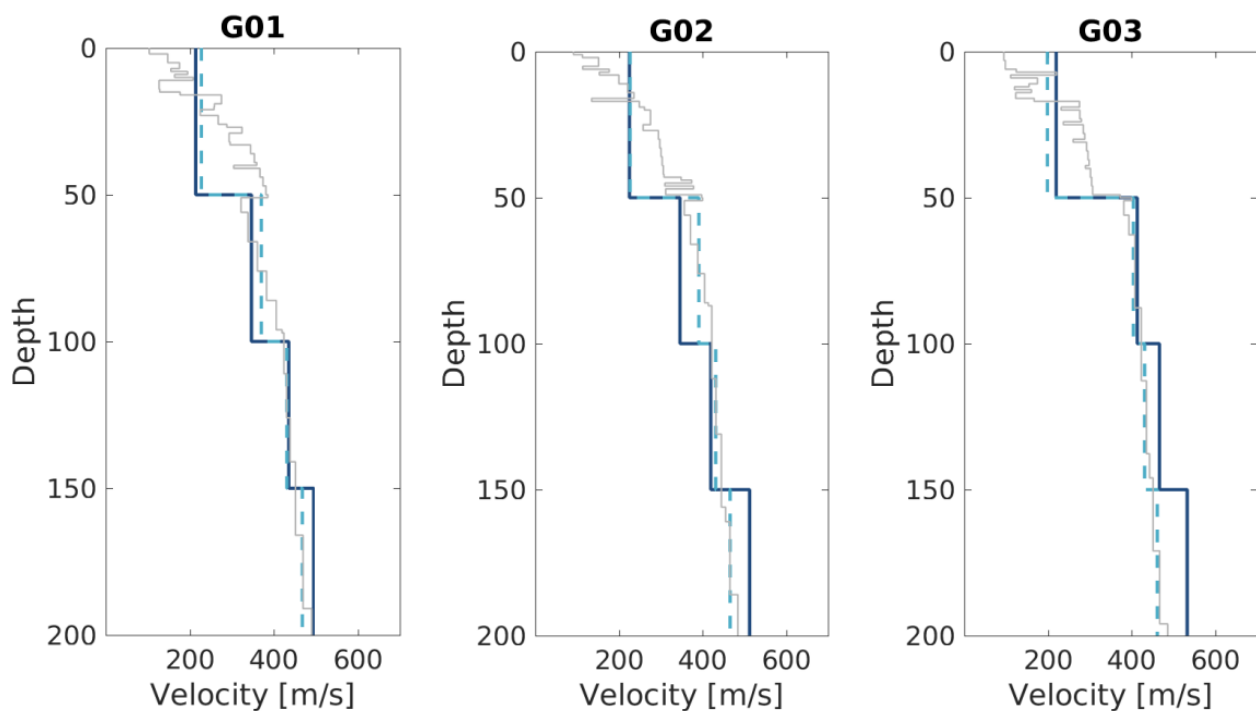


Figure 7.4. V_s profiles for G stations G01 – G03. Grey line is the modelled V_s , dashed blue line is the harmonically averaged modelled V_s over 50 m intervals, the solid blue line is the interval V_s from seismic interferometry.

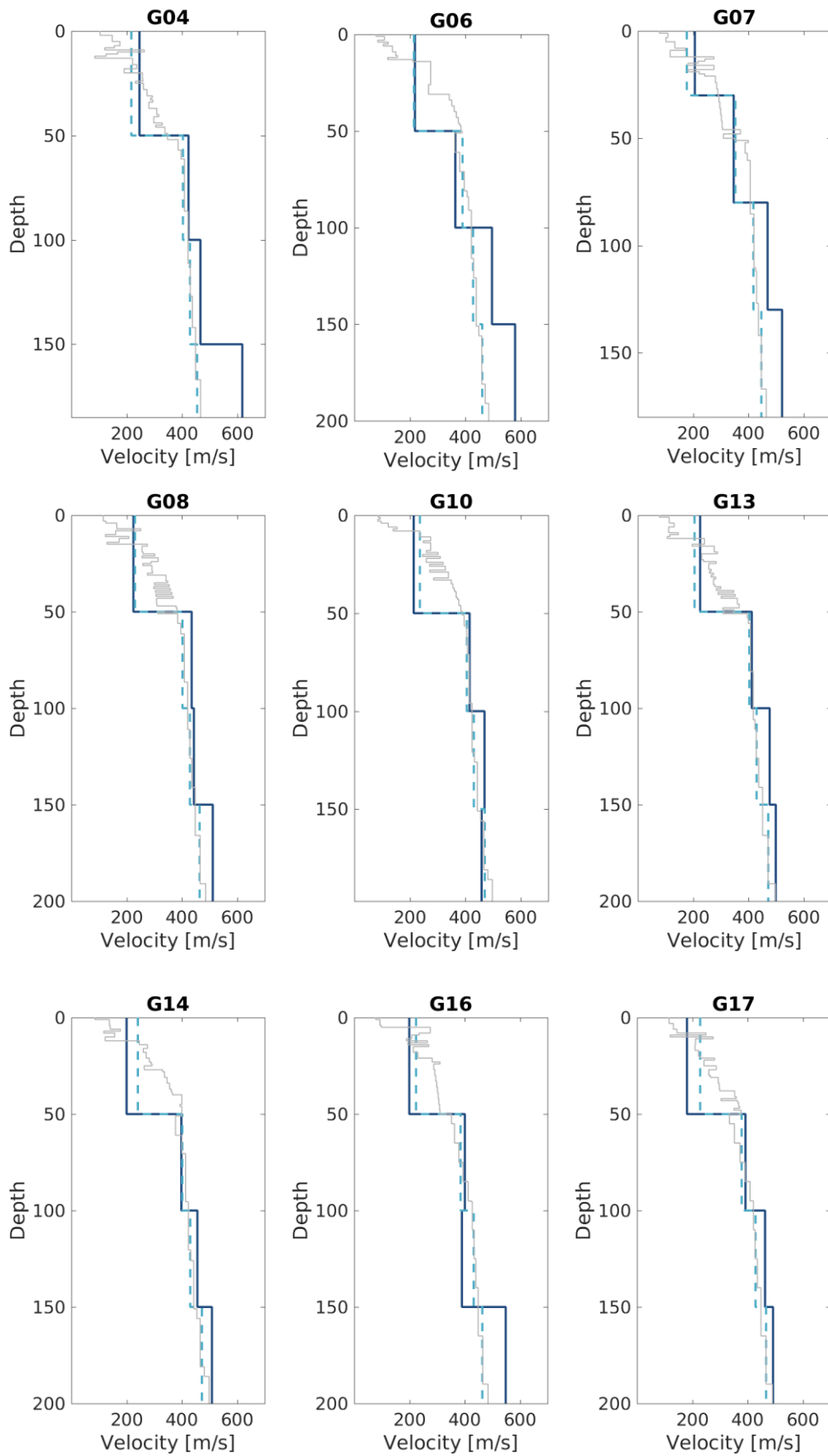


Figure 7.5. V_S profiles for G stations G04 – G17. Grey line is the modelled V_S , dashed blue line is the harmonically averaged modelled V_S over 50 m intervals, the solid blue line is the interval V_S from seismic interferometry.

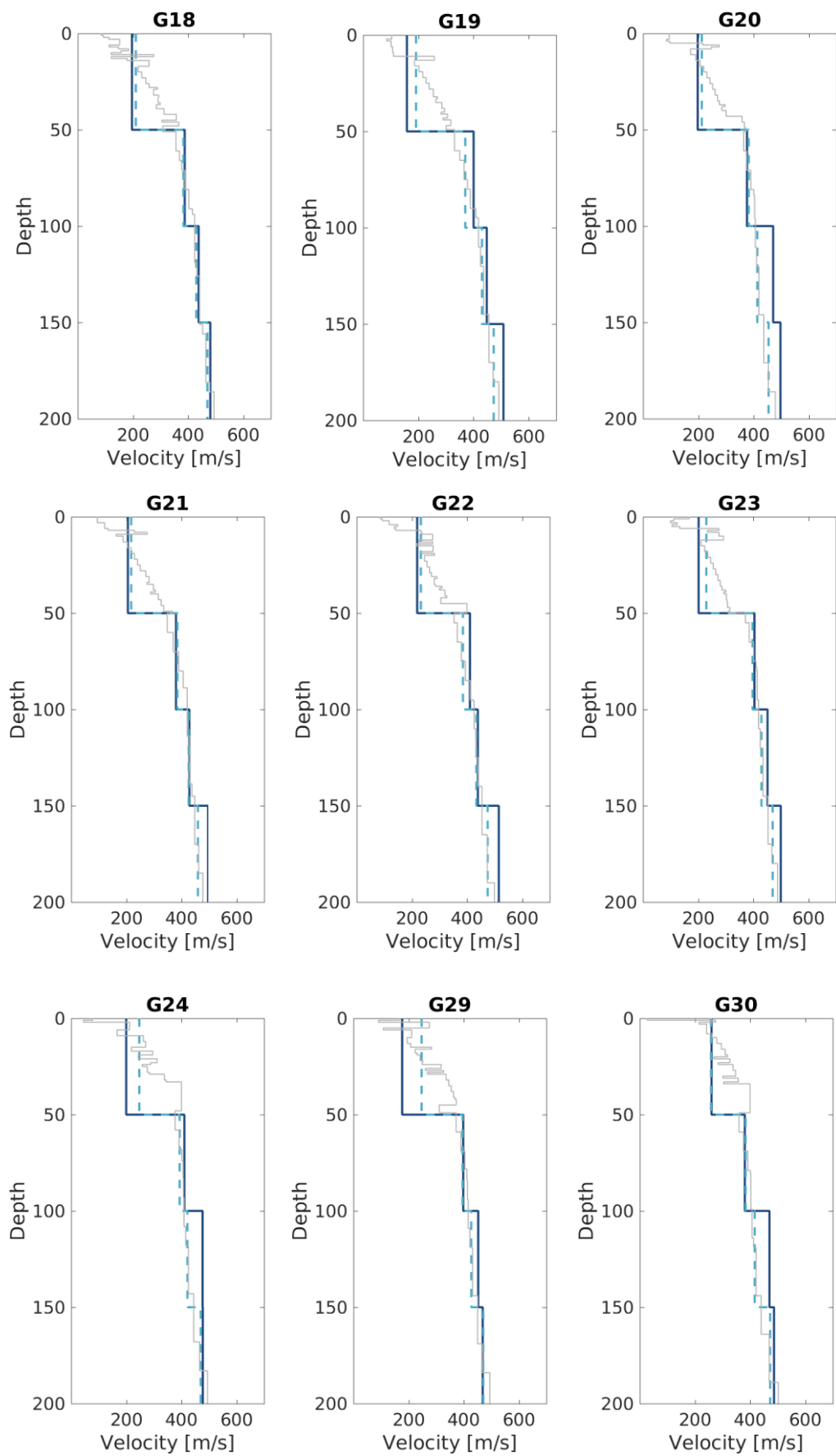


Figure 7.6. V_s profiles for G stations G18 – G30. Grey line is the modelled V_s , dashed blue line is the harmonically averaged modelled V_s over 50 m intervals, the solid blue line is the interval V_s from seismic interferometry.

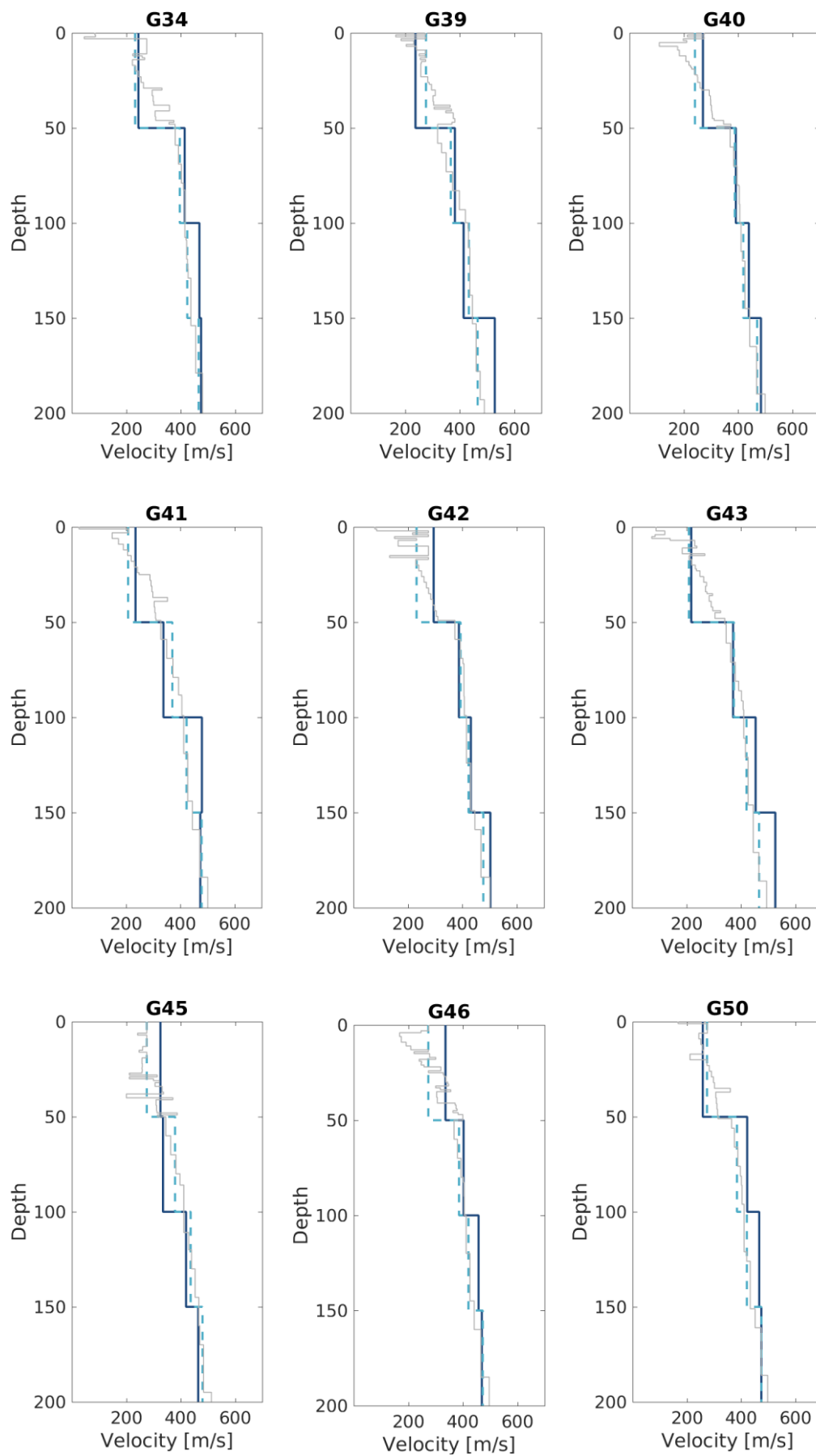


Figure 7.7. V_s profiles for G stations G34 – G50. Grey line is the modelled V_s , dashed blue line is the harmonically averaged modelled V_s over 50 m intervals, the solid blue line is the interval V_s from seismic interferometry.

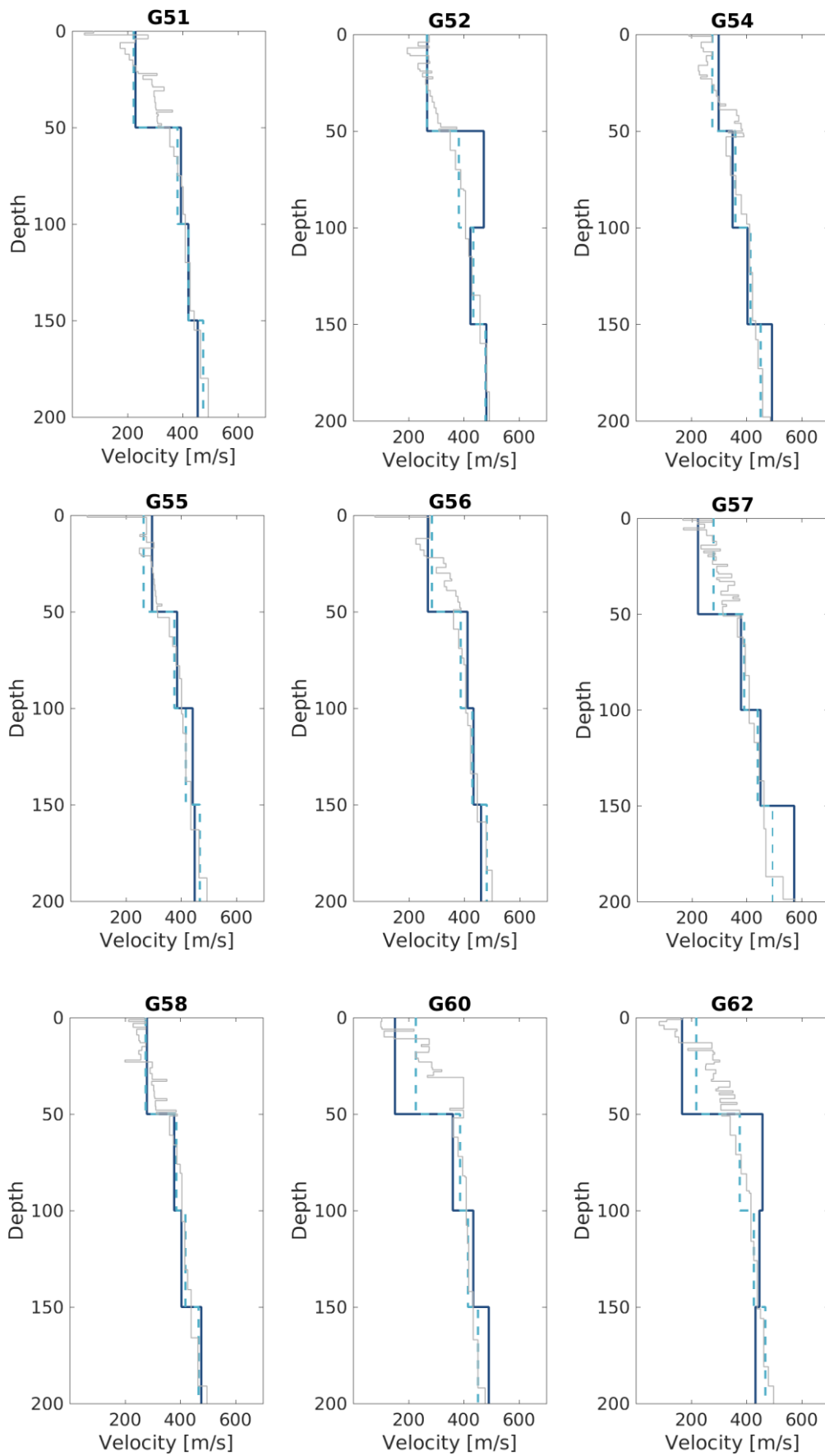


Figure 7.8. V_s profiles for G stations G51 – G62. Grey line is the modelled V_s , dashed blue line is the harmonically averaged modelled V_s over 50 m intervals, the solid blue line is the interval V_s from seismic interferometry.

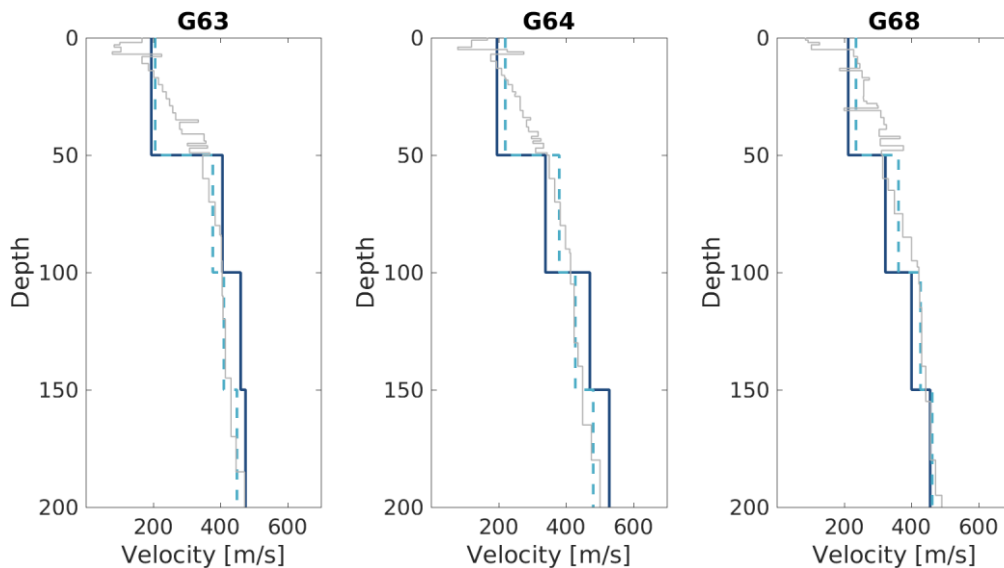


Figure 7.9. V_s profiles for G stations G63 – G68. Grey line is the modelled V_s , dashed blue line is the harmonically averaged modelled V_s over 50 m intervals, the solid blue line is the interval V_s from seismic interferometry.

7.2. Extension of V_s profiles to reference rock horizon

Information on the V_s distribution at depths larger than the range of direct measurements using SCPT comes from indirect measurements. Large seismic survey campaigns were conducted by NAM/Shell around 1988 for imaging purposes. Two legacy datasets were reinterpreted to extend the V_s distributions to depths beyond those measured by the SCPT: ground roll data (MEI) and the Pre-Stack Depth Migration velocity model combined with sonic log data (sonic V_s model). These models are summarised in this section.

MEI near surface V_s model

Ground roll refers to surface waves present in seismic records from reflection seismic geophysical surveys. For the imaging of deep reflectors associated with the reservoir, the ground roll is normally regarded as noise and removed from the data. For other purposes, this ground roll can be useful data. For the Groningen project, Ewoud van Dedem from Shell has reprocessed the ground roll (surface waves) and guided waves in the data to derive V_s and V_P values using the Modal Elastic Inversion method (MEI). MEI is an approximate elastic full waveform inversion method in which the elastic wavefield is approximated by focusing on waves that propagate laterally through the shallow surface (*i.e.*, the ground roll), its higher modes, and guided waves. A limited number of horizontally propagating modes, characterized by lateral propagation properties and depth dependent amplitude properties, are taken into account to represent the near-surface elastic wavefield (see also Ernst, 2013).

The seismic data acquisition was designed for deep imaging of the Groningen reservoir and therefore receiver arrays were used to attenuate undesired noise, such as the ground roll. The receiver arrays were designed to distort and attenuate ground roll with wavelengths

smaller than 80 m, effectively restricting the temporal frequency bandwidth that can be used for the inversion. Because of the acquisition setup and the frequencies present in the data, the depth range for which the near surface model obtained from the MEI inversions is considered to be reliable is from approximately 30 to 120 m below the surface. Additionally, there are several areas of limited size with large misfits between the ground roll data and the final V_s model. These misfits are due to different seismic sources being used in cities (vibroseis) and lakes (air guns) from the other regions (mostly buried dynamite sources).

The V_s model from the inversion of the ground roll yielded depth slices of V_s at 10 m depth intervals. An example of a depth slice is shown in Figure 7.10, in this case for NAP-65 m.

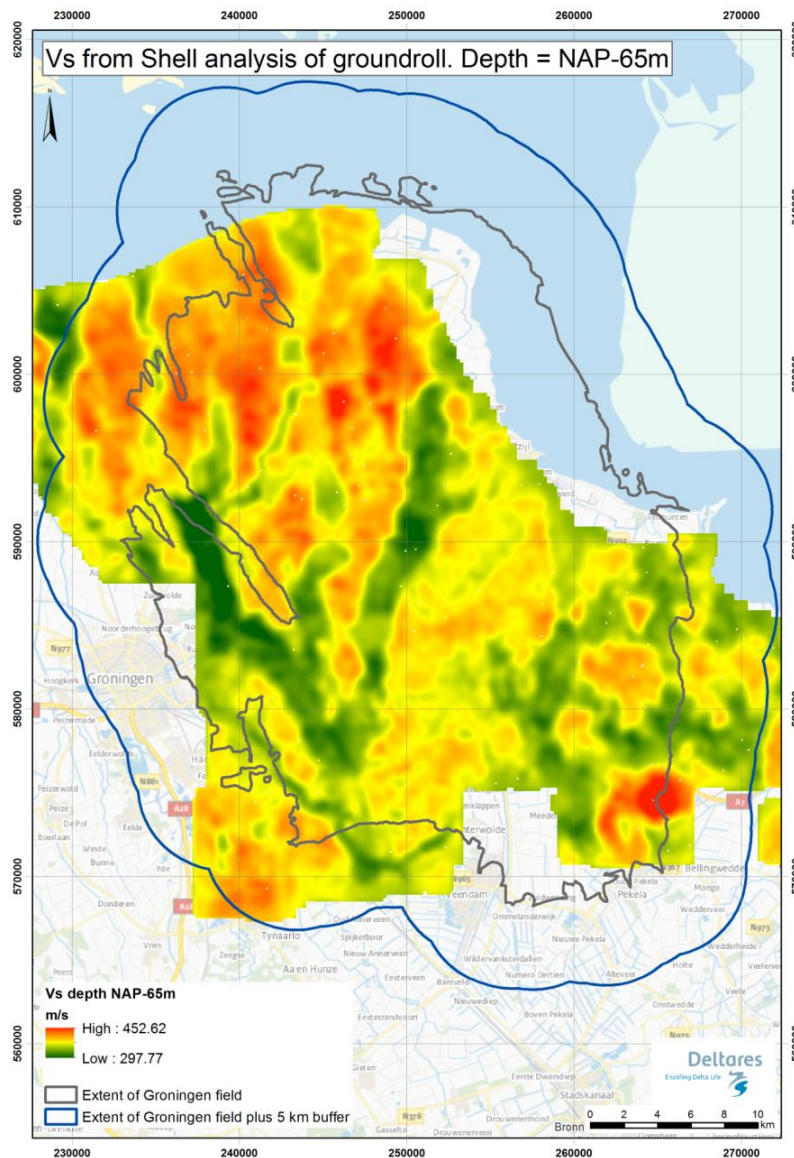


Figure 7.10. Depth slice at NAP-65 m through the MEI V_s model.
(data from Shell, courtesy Ewoud van Dedem)

Figure 7.10 shows distinct zones of relatively high and relatively low V_s values in patterns that resemble geological features, such as buried channels. Estimates of the uncertainty in phase velocities in the dispersion of the ground-roll data are on the order of 8-15%. However,

the phase velocities are not directly equivalent to shear-wave velocities. Another estimate of uncertainty in V_S has been derived from using different starting models in the MEI procedure. The different starting models produced similar results in terms of V_S models, with variations of up to 10%. Moreover, the MEI V_S model is consistent with the interval velocities at the G-stations (Figures 7.4-7.9). The MEI V_S model has a slightly smaller geographical extent than the entire area of interest (Figure 7.10). Outside of the extent of the MEI model, the average V_S value is used for each depth interval.

Sonic V_S model

Shell has a seismic model developed to image the Groningen reservoir, updated in the 2012 Groningen Field Review (GFR). For one of the processing steps, a velocity model is required, the so-called Pre Stack Depth Migration Velocity model (PSDM velocity model). Sonic logs of compressional wave velocity (V_P) and well markers for key horizons were used to construct a depth-calibrated, high-resolution P-wave (V_P) model over the entire field. There is sufficient coverage of sonic logs for depths larger than 200 m, but for shallower depths, the accuracy of the V_P model is reduced. In only two wells, both V_P and V_S were measured over the full North Sea Supergroup. The ratios between V_P and V_S (Figure 7.11) were used to convert the V_P model to a V_S model, by Remco Romijn of NAM.

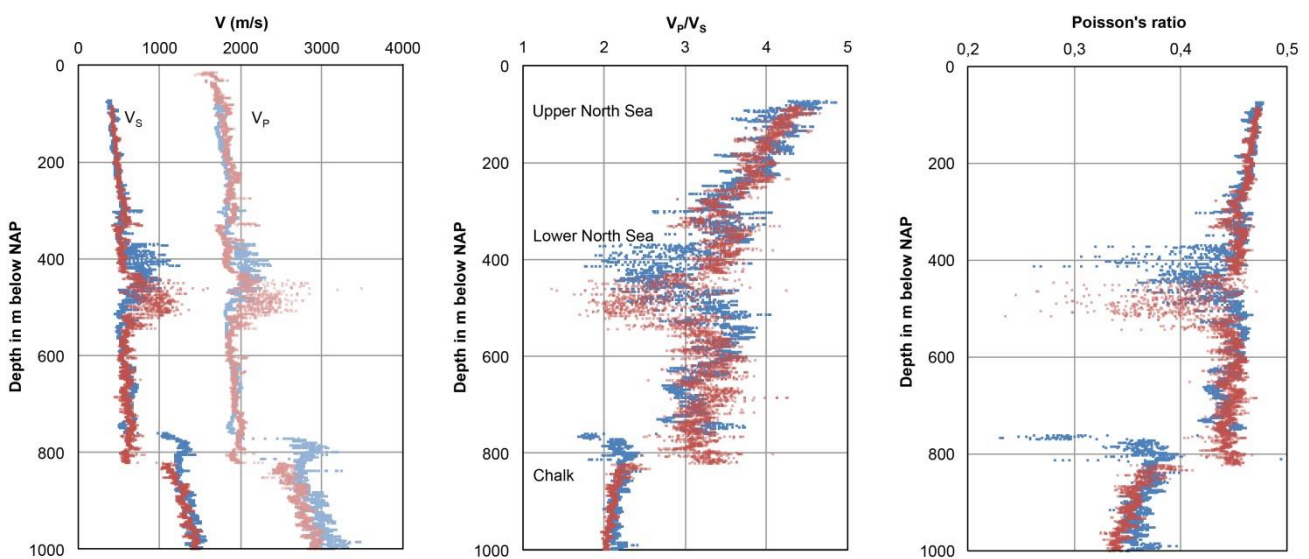


Figure 7.11. V_P and V_S profiles (*left*) and the V_P/V_S ratio (*middle*) and Poisson's ratio (*right*) for two deep wells in the Groningen field. BRW-5 in blue symbols, ZRP-2 in red symbols.

The conversion was done using a linear relation of V_P/V_S with depth for the Upper North Sea Group (see middle panel of Figure 7.11):

$$V_S = \frac{V_P}{(4.7819 - 0.0047 * Z)} \quad (7.2)$$

where Z is the depth in meters. The Poisson's ratio in the Upper North Sea Group generally varies between 0.45 and 0.47.

In the Lower North Sea Group, V_P/V_S is more or less constant, apart from the Brussels sand (high velocity layer, see Figure 7.11 and 7.12). This level, however, is not mapped by markers across the entire field. Therefore, a constant V_P/V_S is assumed for the Lower North Sea Group, given by:

$$V_S = \frac{V_P}{3.2} \quad (7.3)$$

This corresponds to a Poisson's ratio of 0.446. These values appear to be quite high, which is due to the unconsolidated nature of the sediments; similar Poisson's ratios are reported elsewhere (e.g., Bala *et al.*, 2006).

The Sonic V_S model was discretised in layers of 25 m thickness and on a grid identical to the 100 m x 100 m cells of the GeoTOP model. A cross section of the sonic V_S model through the centre of the field is shown in Figure 7.12. The V_S inversion which is present in the Lower North Sea Group at depths of ~ 500 m is caused by the Brussels sand. Locally, this sand is cemented, leading to high V_S .

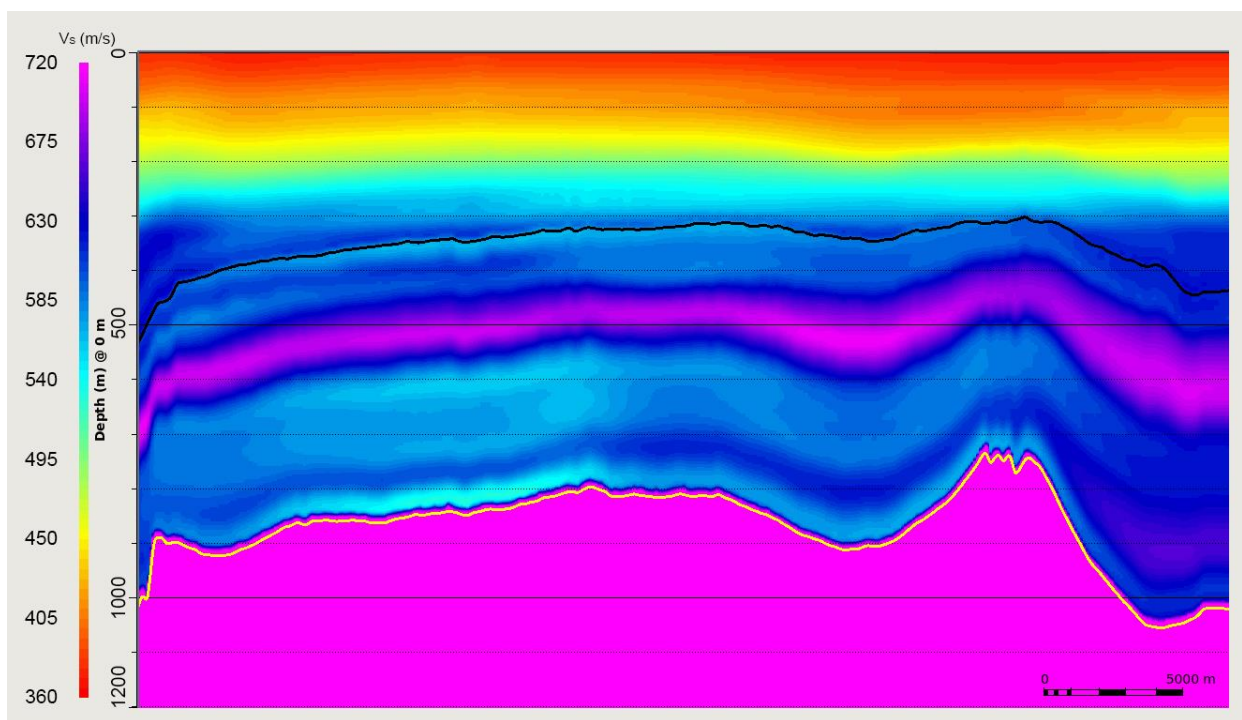


Figure 7.12. Cross section through the Sonic V_S model, from west to east at the centre of the field. The vertical scale is exaggerated. The base of the Upper North Sea Group is indicated by the black line; the base of the Lower North Sea Group by the thin yellow line.

The V_S of the reference bedrock horizon has been derived from the sonic V_S model across the field. The NS_B level cuts through the V_S model that is discretised with depth intervals of 25 m. The statistics of all voxels across the field at different levels with respect to the NS_B level are summarised in Table 7.2 and visualised in Figure 7.13. The jump in V_S at the NS_B is from 587 to 1374 m/s on average. The V_S values in one voxel above the NS_B represent

the V_S just above the NS_B. The voxels that contain the NS_B show a bimodal distribution, because they contain voxels with Lower North Sea V_S (above NS_B) and Chalk V_S (below NS_B). At 1 voxel and 2 voxels below NS_B, the voxels only contain Chalk V_S values. We defined the reference bedrock velocity as the field-wide average V_S of the two voxels below the NS_B level (Figure 7.13f) and used a value of 1400 m/s in the STRATA calculations.

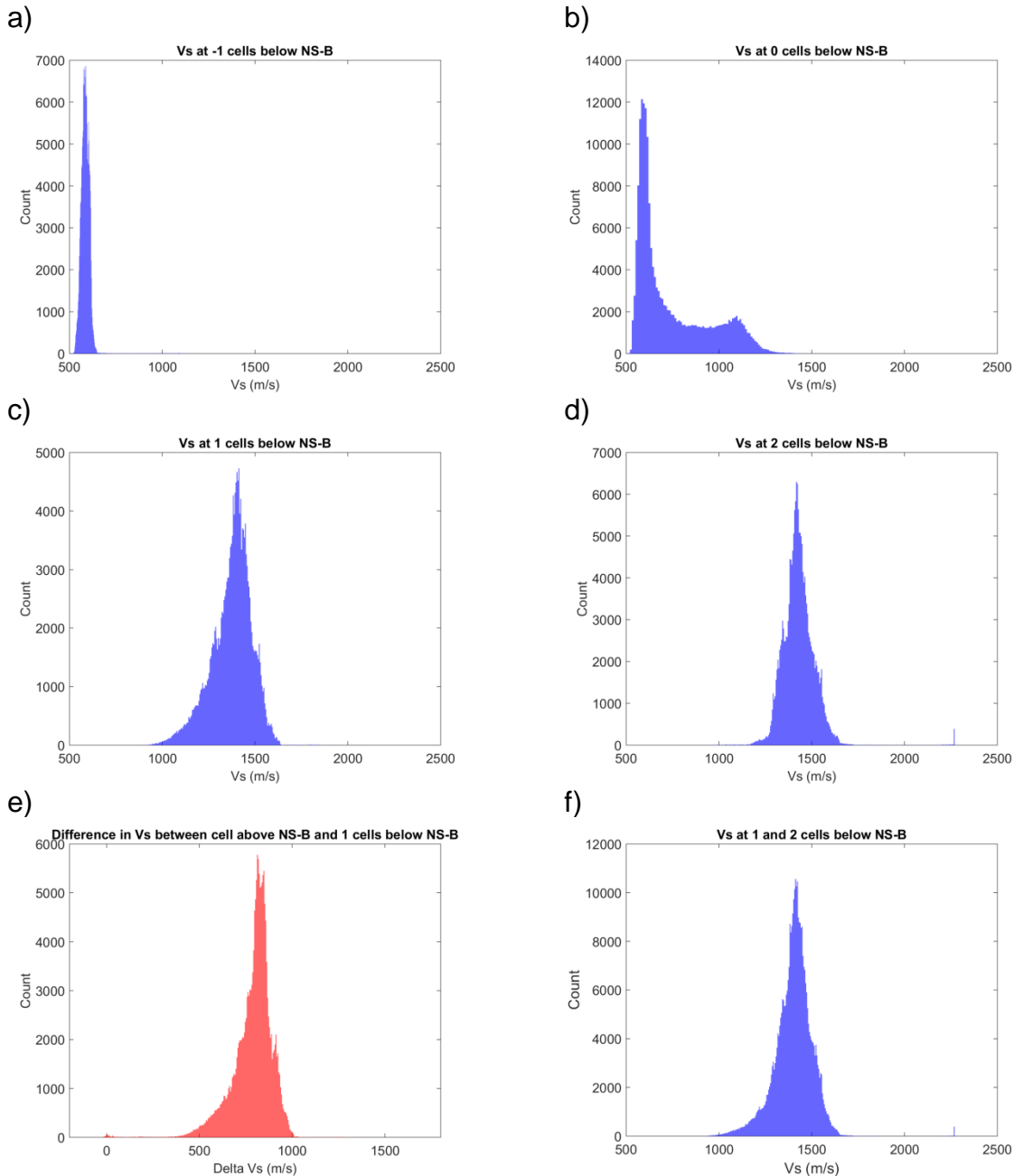


Figure 7.12. Histograms of the V_S values from the sonic V_S model around the NS_B level. (a) one voxel above the NS_B level; (b) voxel stacks containing NS_B showing a bimodal distribution of above and below V_S values; (c) one voxel below the NS_B level; (d) two voxels below the NS_B level; (e) the difference in V_S defined as $V_{S \text{ one voxel below NS}_B} - V_{S \text{ one voxel above NS}_B}$ for each voxel stack; (f) one and two voxels below the NS_B level combined leading to our choice of $V_{S \text{ bedrock}}$ of 1400 m/s.

Table 7.2. Statistics of V_s of the sonic model around NS_B

Voxels below NS_B	Average V_s (m/s)	Standard deviation of V_s (m/s)	Average difference in V_s (m/s)	Standard deviation of difference in V_s (m/s)	Remark
-1	587	36	0	0	Voxels really above NS_B
0	744	196	157	194	Voxels with V_s mixed from above and below NS_B
1	1374	109	787	110	Voxels really below NS_B
1&2	1402	105	815	104	1st and 2nd layer of voxels below NS_B combined
2	1430	92	843	90	

7.3. Layering model and layer-to-layer correlations

The main input data for the STRATA calculations are the thickness, mass density, and V_s of each layer. The V_s and density values are assumed to be constant for each layer. In addition, for each soil type modulus reduction and damping versus strain curves must be defined (Sections 7.4 and 7.5).

The thickness and the depth of the layers are based on the geological model (Kruiver *et al.*, 2015). The voxel stacks of the GeoTOP model define the vertical succession in terms of lithostratigraphy and lithoclass for each x-y coordinate to a depth of NAP-50 m. The layering in terms of lithostratigraphy and lithoclass for each x-y coordinate for the depth range below NAP-50 m is defined by the simulations for the subsurface geological zone (Figure 6.8 of Kruiver *et al.*, 2015). For each subsurface geological zone, the simulations are randomly distributed over the coordinates in that zone such that they are in agreement with the probabilities of encountering the scenarios. For example, for one subsurface geological zone with two scenarios with probabilities 0.6 and 0.4, 60% of the voxel stacks receive the layering from the first simulation and 40% of the voxel stacks receive the layering of the second simulation. The maximum thickness for each layer is 10 m for the depth range of the MEI model and 25 m for the sonic V_s model. For example, a layer between 65 and 100 m of the Urk Formation in the MEI depth range will be split into 4 layers: three layers of 10 m and one layer of 5 m. A layer between 200 and 244 m of the Oosterhout Formation in the sonic V_s depth range will be split into two layers: one of 25 m and one of 19 m.

To obtain the full stack at one x-y coordinate, the GeoTOP voxel stack layers are combined with the scenario-based layers based on that coordinate. For the GeoTOP depth range, each layer is assigned a random value from the V_s distribution based on the lithostratigraphical unit and lithoclass of the voxel and the Groningen specific V_s relationships. The randomisation of V_s profiles is described in Section 7.7. For the depth range below NAP-50 m, V_s profiles are defined by the MEI and the sonic V_s models. The transition between the MEI and the sonic V_s model is taken at a depth such that no velocity reversal occurs (*i.e.*, no decrease of V_s as depth increases). In some cases, the sonic V_s model is extrapolated to

depths shallower than NAP-70 m, although the sonic V_s model is not necessarily valid at these depths.

7.4. Mass densities

One of the parameters in STRATA is unit weight. For the shallow depth range down to approximately 30 m below the surface, the unit weights were estimated from a subset of 31 CPTs that were classified in terms of lithostratigraphical unit and lithological class. All cone tip resistance values from the CPTs from one combination of lithostratigraphical unit and lithoclass were assembled and converted to unit weight using Lunne *et al.*, (1997). The average unit weight was calculated. For units that were not represented in the CPTs, a value for unit weight from a comparable geological unit was taken. Depth dependency of unit weight has been investigated for the shallow depth range. The data were inconclusive to derive a depth relation. Therefore, no depth dependency was implemented for unit weight. For the deeper geological units, a constant value of 21 kN/m³ was determined for unit weight. This is slightly higher than the average density measured in the well logs ZRP2 and BRW5 (Figure 7.14), but corresponds with the normative values used for the densest sediments encountered in geotechnical projects in the Netherlands, based on laboratory and in-situ tests (NEN, 2006).

7.5. Modulus reduction and damping curves

A modified version of the shear modulus reduction and damping (MRD) versus strain curves of Darendeli (2001) and Menq (2003) were used to model the nonlinear behaviour of Groningen soils; the former were used for clays while the latter were used for sands. These curves are based on large numbers of measurements for both sands and clays of varying plasticity and over-consolidation ratios. These curves are widely used in equivalent site response analyses.

The general form of the Darendeli (2001) and Menq (2003) curves is described below. The shear modulus reduction curve is a hyperbolic model given by:

$$\frac{G}{G_{\max}} = \frac{1}{1 + (\gamma/\gamma_r)^a} \quad (7.4)$$

where γ is the shear strain amplitude, γ_r is the reference shear strain amplitude (shear strain amplitude at which the value of $G/G_{\max} = 0.5$) and a is a parameter describing the curvature of the shear modulus reduction curve. The damping values, D , are given by:

$$D = F \times D_{\text{Masing}} + D_{\min} \quad (7.5)$$

where F is a multiplication factor (defined below) that is used to modulate the Masing damping at large strains to prevent overdamping, D_{Masing} is the damping that results from applying the Masing rule, and D_{min} is the damping at small shear strain amplitudes.

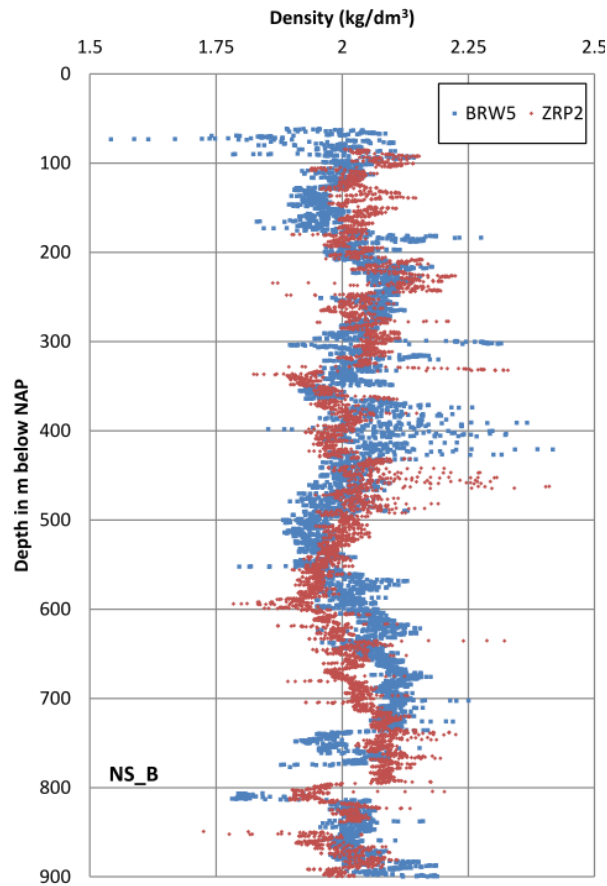


Figure 7.14. Density profiles from two deep borehole logs (Source: NAM database)

D_{Masing} is given by:

$$D_{Masing} = c_1 D_{Masing,a=1} + c_2 D_{Masing,a=1}^2 + c_3 D_{Masing,a=1}^3 \quad (7.6)$$

where the parameters c_1 , c_2 and c_3 are fit parameters and $D_{Masing,a=1}$ is the value of D_{Masing} when the parameter a is equal to 1. Darendeli (2001) derives equations for the coefficients c_1 , c_2 and c_3 as a function of the parameter a :

$$\begin{aligned} c_1 &= -1.1143a^2 + 1.8618a + 0.2523 \\ c_2 &= 0.0805a^2 - 0.071a - 0.0095 \\ c_3 &= -0.0005a^2 + 0.0002a + 0.0003 \end{aligned} \quad (7.7)$$

The parameter $D_{Masing,a=1}$ has a closed form solution that is given by:

$$D_{masing,a=1} = \frac{100}{\pi} \left[4 \frac{\gamma - \gamma_r \ln\left(\frac{\gamma + \gamma_r}{\gamma_r}\right)}{\frac{\gamma^2}{\gamma + \gamma_r}} - 2 \right] \quad (7.8)$$

The multiplication factor F in Eq. (7.5) model is given by:

$$F = b \left(\frac{G}{G_{max}} \right)^p \quad (7.9)$$

where b and p are parameters that control the shape of the function. To simplify the model a fixed value of $p=0.1$ is used by Darendeli (2001) and Menq (2003).

Equations 7.4 through 7.9 result in a 5-parameter model (G_{max} , γ_r , a , b , and D_{min}). The linear shear modulus (G_{max}) is computed from the shear-wave velocity profiles presented in Sections 7.1 and 7.2 ($G_{max} = \rho V_s^2$). The remaining parameters are computed from relationships developed by Darendeli (2001) from a large number of laboratory tests. These relationships correlate the model parameters to the mean effective stress (σ') normalized by the atmospheric pressure ($p_a = 100$ kPa), plasticity index (I_p), over-consolidation ratio (OCR), number of cycles of loading (N) and loading frequency f . The resulting expressions are given by:

$$\gamma_r = (0.0352 + 0.001 I_p OCR^{0.32463}) (\sigma' / p_a)^{0.34834} \quad (7.10)$$

$$a = 0.919 \quad (7.11)$$

$$D_{min} = (0.8005 + 0.0129 I_p OCR^{-0.1069}) (\sigma' / p_a)^{-0.2889} (1 + 0.2919 \ln(f)) \quad (7.12)$$

$$b = 0.6329 - 0.0057 \ln(N) \quad (7.13)$$

Default values recommended by Darendeli (2001) for N ($N=10$) and f ($f=1$ Hz) were used.

No laboratory tests for OCR and I_p were available at the time of starting the site response calculations. Therefore, representative values for geological units were derived in a manner similar to the derivation of unit weights (*i.e.*, based on a subset of geologically classified CPTs). For OCR, the dataset of 88 CPTs corresponding to the SCPTs was used. The OCR was estimated for clay from the normalized total cone resistance following Robertson & Cabal (2015), using the relationship suggested by Kulhawy & Mayne (1990), adjusted for Robertson's Soil Behaviour Index I_c :

$$OCR = k \left(\frac{q_t - \sigma_{v0}}{\sigma'_{v0}} \right) \quad (7.14)$$

where σ_{v0} and σ'_{v0} are the total and the effective vertical stresses, respectively, and k is a parameter that is set to 0.33. If a sufficiently large number of OCR values was available for a unit, then the linear relation between effective vertical stress and OCR was derived;

otherwise, a constant OCR value was assumed. An example of OCR from CPT data is given in Figure 7.15 for Peelo clay. In this case, the data were not extrapolated outside the data range. This means that a minimum OCR of 4 and a maximum OCR of 6 was assumed. Formations deeper/older than the Peelo Formation were not represented in the CPTs. The OCR value for the Peelo Formation at 30 m depth was assumed for these formations.

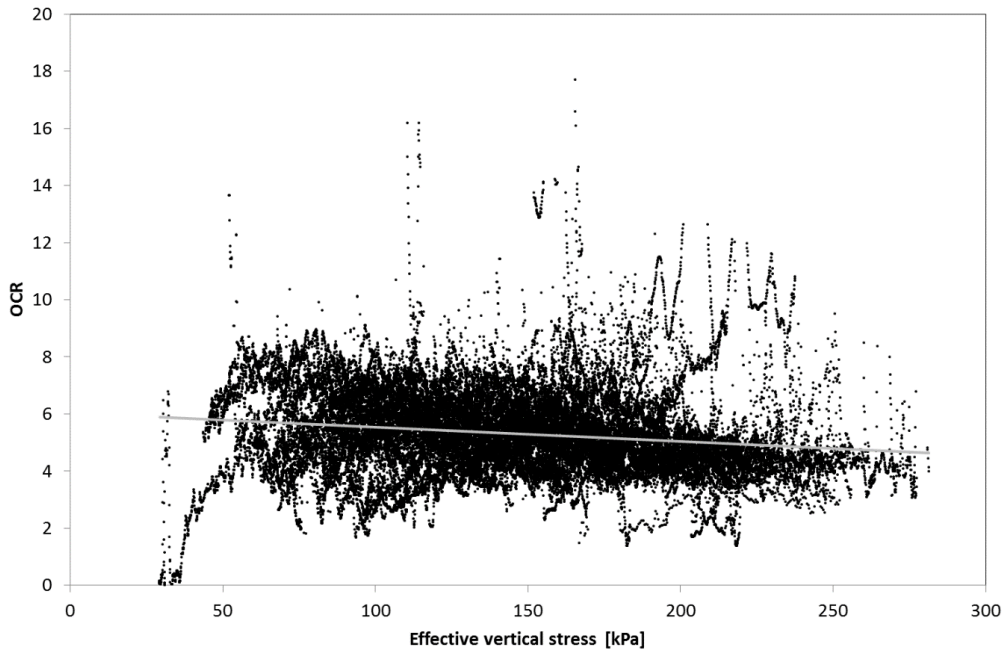


Figure 7.15. OCR for Peelo clay, derived from CPT data and related to effective vertical stress. The black dots are data points, the grey line is the linear regression line.

The plasticity index I_p was estimated from measured values at the field, using representative values from Sorensen & Okkels (2013), or from expert judgment (Appendix V) and estimated from the relationship between I_p and the undrained shear strength to overburden stress ratio from Skempton in Grace *et al.* (1957).

For sands, the model parameters (D_{min} , γ_r , a and b) were obtained by Menq (2003) from laboratory tests of sands and gravels. These parameters are given by:

$$\gamma_r = 0.12 C_u^{-0.6} \left(\frac{\sigma'_o}{p_a} \right)^{0.5 C_u^{-0.15}} \quad (7.15)$$

$$a = 0.86 + 0.1 \log \left(\frac{\sigma'_o}{p_a} \right) \quad (7.16)$$

$$b = 0.6329 = 0.0057 \ln(N) \quad (7.17)$$

$$D_{min} = 0.55 C_u^{0.1} D_{50}^{-0.3} \left(\frac{\sigma'_o}{p_a} \right)^{-0.05} \quad (7.18)$$

where C_u is the coefficient of uniformity and D_{50} is the mean grain size diameter. The values of C_u and D_{50} were obtained either from values measured for stratigraphic-lithological units in the field, or else from measured parameters for other units deemed to be representative (Appendix V). Note that the exponent of the normalized effective confining stress in Eq. (7.18) is different from that presented in Menq (2003). The value of -0.05 was recommended for application by Menq (*Personal communication*).

Recent work by Afshari & Stewart (2015) and Zalachoris & Rathje (2015) has also shown that laboratory-based MRD curves tend to underestimate the low-strain damping inferred from recordings in downhole arrays. To correct the low-strain damping values assigned to Groningen soils, we used estimates of the quality factor Q measured at two borehole arrays, at the east and south edges of the Groningen field, by De Crook & Wassing (1996, 2001). These measurements were made for depths below 75 m at the FSW station using the spectral ratio technique of Hauksson *et al.* (1987), and at shallower depths at the ZLV borehole array using a seismic vibrator and depth recordings at depth intervals of 1 m (De Crook & Wassing, 2001). The quality factor can be converted into the low strain damping D_{min} using:

$$D_{min} = \frac{1}{2Q} \quad (7.19)$$

The best estimated field-wide estimate of the low-strain damping D_{min} is shown in Figure 4.5. The Q values can also be used to estimate the amount that the material damping contributes to the high-frequency attenuation parameter κ (Anderson & Hough, 1984). This contribution, termed $\Delta\kappa$, is given by Campbell (2009):

$$\Delta\kappa = \int_0^{z_{rock}} \frac{1}{Q(z)V_S(z)} dz \quad (7.20)$$

where z_{rock} is the depth of the elastic half space.

The damping values obtained from the methodology explained in the previous paragraph are consistent with Groningen site conditions and are higher than the D_{min} from laboratory-based curves of Darendeli (2001) and Menq (2003). However, the Menq and Darendeli curves have the advantage of capturing the dependence of D_{min} on soil type and soil properties. Hence, we used a hybrid approach where laboratory-based D_{min} values are modified to match the $\Delta\kappa$ measured at the borehole sites. Using the V_S profiles at the recording stations, we computed a factor to modify the low-strain damping values from Menq (2003) and Darendeli (2001) such that the equivalent $\Delta\kappa$ is equal to that measured at the downhole array (Figure 7.16). An average factor of 2.11 was obtained from all the recording stations. The D_{min} values of Menq and Darendeli was then multiplied by this factor, with an upper limit of 5% set for this parameter, in order to constrain damping to reasonable values. In effect, this resulted in a shift of the damping curves at all strain levels. The damping for the Lower North Sea Group, which is encountered at depths larger than about 350 m, was set to 0.5%. The Lower North Sea Group mainly consists of unconsolidated sediments consisting of sands, marls and

clays. The consistency is mainly dense glauconitic sand, and hard clay. In the upper part cementation is present in the form of thin sandstone layers.

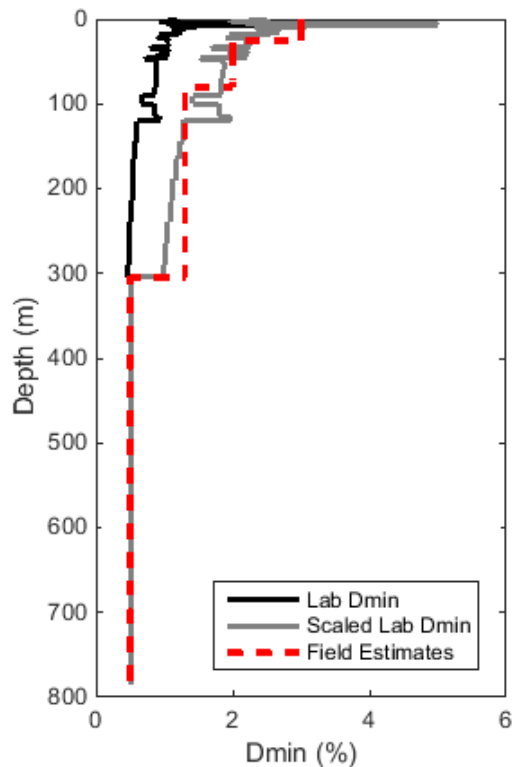


Figure 7.16 Low strain damping (D_{min}) profile with depth showing laboratory estimates (Darendeli, 2001; Menq, 2003) and field estimates, along with the Field-Wide estimated values. The damping curves used in this study are the scaled lab curves. The curve shown is for the location of the G40 borehole array.

The hyperbolic model used by the Darendeli (2001) and Menq (2003) models implies a large stress-strain behaviour that is not necessarily compatible with the shear strength of the soil. For this reason, a model to impose a limiting shear strength at large strains was implemented for clays. The undrained strength was computed from CPT tip resistance values q_c using (Lunne *et al.*, 1997):

$$s_u = \frac{q_c - \sigma_{v0}}{N_k} \quad (7.21)$$

where $N_k = 14$ as recommended by Lunne *et al.* (1997). N_k is reported to vary (e.g., Kjekstad *et al.*, 1978; Kleven, 1981). The value of $N_k = 14$ is at the lower end of the shown variation, possibly leading to high S_u values. This is a conservative choice, because a soil with higher S_u values will have lower shear modulus reduction at large strains and hence will allow for higher amplifications at the periods of interest. Uncertainty in S_u is accounted for in the MRD curve analysis in Section 9.3. The Groningen specific N_k will be investigated for future GMM versions based on the available data from CPTs and laboratory tests of S_u on samples from the Groningen region.

Using the dataset of 88 CPT/SCPTs depth dependence of s_u was determined as a function of the effective vertical stress σ'_{v0} . The peat layers were not well sampled in the original SCPT dataset used in V2. A sampling scheme dedicated to obtain representative parameter values for both Holland peat and Basal peat was applied at the SCPTs of the accelerograph stations (De Kleine *et al.*, 2016). The new CPT/SCPT data set allows for the determination of possible depth dependence of s_u for both types of peat. The s_u values from the laboratory tests of Groningen peat (Zwanenburg *et al.*, 2017) were compared to s_u from the CPTs with an adjusted value for N_k of 17 for peat and the function of $s_u = k \sigma'_{v0}$ with k varying between 0.4 and 0.6. For Holland peat, no significant relation between σ'_{v0} and s_u was present. Therefore, a constant value of $s_u = 12.5$ kPa was assumed. For basal peat, a relation between s_u and σ'_{v0} was derived based on the adjusted s_u using $N_k = 17$, resulting in $s_u = 0.25 \sigma'_{v0} + 13$.

We used the Yee *et al.* (2013) model with a parameter γ_l equal to 0.3% to modify the G/Gmax curve such that is compatible with the undrained strength. Additionally, the undrained shear strength s_u estimated from Eq. (7.21) was increased by 30% to account for rate effects (Lefebvre & LeBoeuf, 1987; Stewart *et al.*, 2014). Limiting shear strengths were implemented for clay, clayey sand and sandy clay and for peat. No limiting strength was used for sand layers because of the higher strengths for sand and the lower strains typically observed in the analyses.

7.6. Modulus reduction and damping curves for peats

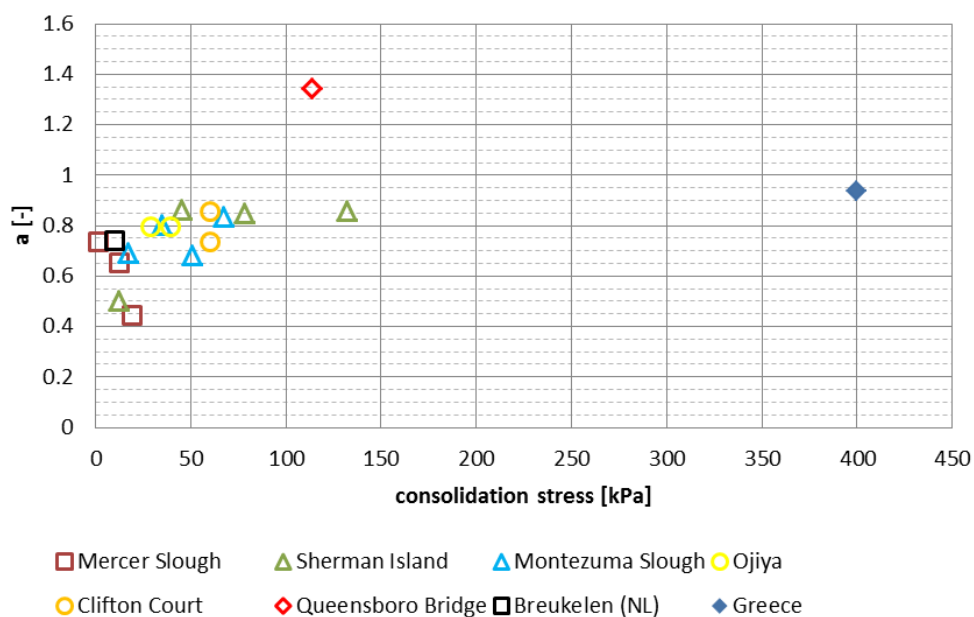
Empirical modulus reduction and damping curves specifically derived for peat are rather limited in the literature. However, preliminary studies indicated that peats have a strong influence on site response, as expected due to their low stiffness. For this reason, a particular effort was directed at obtaining representative MRD curves for peat. In the absence of curves derived from tests on Groningen peats, which are planned for the near future, we developed a model based on published worldwide data. In order to be consistent with the sand and clay curves, we adopt a formulation similar to the Darendeli (2001) model.

The available test data on peat in the literature are summarised in Table 7.3. Because of the lack of data, only confining stress dependency was modelled. The influence of overconsolidation ratio (OCR), number of cycle (N), frequency of loading (f) and organic content (OC) was ignored. There are four parameters that need to be determined to constrain the Darendeli (2001) MRD curves (γ_r , a , b , and D_{min}) model. The parameter a determines the curvature of the shear modulus reduction curve. For sands and clays, Darendeli (2001) used a constant value of 0.919. For peats, the parameter a is estimated from reported modulus reduction curves in the references listed in Table 7.3. The resulting values for a are shown in Figure 7.17. The data point from the Queensboro bridge peat is outside the range of the other soils and it is considered to be an outlier. For the other data points, the correlation between a and consolidation stress is weak, hence we conclude that the stress dependency of the parameter a is negligible. The average value of a for the peats that were studied is 0.776. This value is adopted for our model.

Table 7.3. Summary of available data for constraining the peat MRD model

Reference	Location	Consolidation stress [kPa]	Organic content [%] ^(a)	Ash content [%] ^(a)	Density [ton/m ³] ^(b)	Remarks
Seed & Idriss (1970)	Union Bay [USA]	Unknown	Unknown	Unknown	1.003 – 1.058	Damping curve not measured. Index properties from Kramer (1996)
Kramer (1996, 2000)	Mercer Slough [USA]	1,5		19.7 – 27.4	1.0 – 1.04	
		12,5		19.7 – 27.4		
		19		19.7 – 27.4		
Stokoe <i>et al.</i> (1994)	Queensboro bridge [USA]	114		37-65		Data from Kramer (2000) and Boulanger <i>et al.</i> , 1997)
Boulanger <i>et al.</i> (1997)	Sherman Island [USA]	132/200		36-65	11.1 – 11.8	
Wehling <i>et al.</i> (2001)	Sherman Island [USA]	78		48-68	1.06 – 1.23	
		45				
		12				
Kishida <i>et al.</i> (2009a)	Montezuma Slough [USA]	17	42		1.06 – 1.33	
		35	44			
		51	23			
		67	15			
Kishida <i>et al.</i> (2009a)	Clifton Court [USA]	55 - 69	14-35		1.19-1.46	
Zwanenburg (2005)	Breukelen [Netherlands]	10 30/55		44.7	1.04	damping curve not measured
Tokimatsu & Sekiguchi (2006a,b and 2007)	Ojiya P-1 [Japan], Ojiya P-2	Not reported	Not reported	Not reported	Not reported	
Kallioglou <i>et al.</i> (2009)	Greece	370/400		38 / 52	1.33/1.43	Peat from two locations in Greece, sampling depth 35 m 85 m

Notes: (a) Either the organic content or the ash content is reported in this table, depending on the parameter used in the original publication; (b) Either the mass or the density is reported in this table, depending on the parameter used in the original publication.



For the reference shear strain amplitude γ_r , we use the power function proposed by Darendeli (2001):

$$\gamma_r = a'(\sigma' / p_a)^{b'} \quad (7.22)$$

where a' and b' are model parameters, and σ' is the mean effective stress. Figure 7.18 shows the relation between γ_r and consolidation stress for all data points.

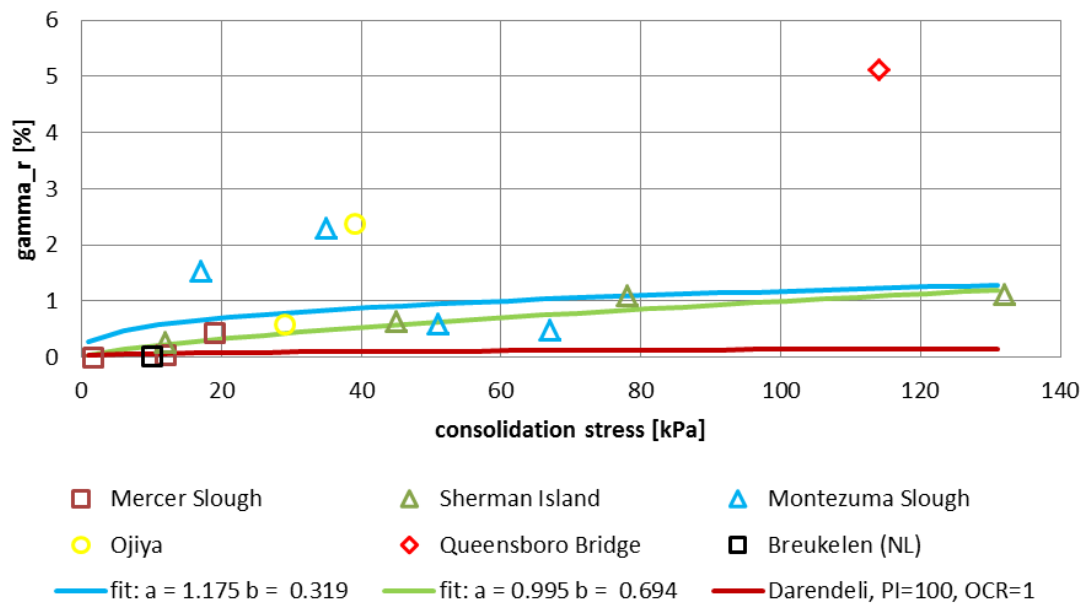


Figure 7.18. Results for curve fitting for γ_r . *Blue curve*: all data points except Queensboro Bridge; *green curve*: all data points, except the four outliers; *red curve*: Darendeli (2001) with $PI=100$ and $OCR = 1$ (shown for comparison)

Again, the data from the Queensboro Bridge soils seems to be an outlier. Moreover, one data point from Ojiya and two from Montezuma Slough seem to be outside the general trend. The data were fitted for a' and b' using a non-linear least square method for two options. The resulting values are:

- Considering all data points, except Queensboro Bridge: $a' = 1.175$ % and $b' = 0.319$.
- Ignoring all points with $\gamma_r > 1.5$ (excluding 4 data points): $a' = 0.995$ % and $b' = 0.674$

The Darendeli (2001) curve with $PI = 100$ and $OCR = 1$ is often selected as an alternative curve for peats. For comparison, this curve is also shown in Figure 7.18. It is clear that the Darendeli (2001) curve is not suitable to describe the behaviour of peat. Ignoring the four possible outliers gives a better overall fit of the data points, especially at lower consolidation stresses. Therefore, the expression for the reference strain γ_r and the consolidation stress results in:

$$\gamma_r = 0.995(\sigma' / p_a)^{0.694} \quad (7.23)$$

The damping at small shear strains, D_{min} , for the soils in Table 7.2 varies with the consolidation stress (Figure 7.19). Since the Darendeli (2001) curve for D_{min} for $I_p = 100$ and an OCR of 1 fits the data points well, we adopt for D_{min} the Darendeli (2001) formulation:

$$D_{min} = 2.512 \left(\frac{\sigma'_o}{p_a} \right)^{-0.2889} \quad (7.24)$$

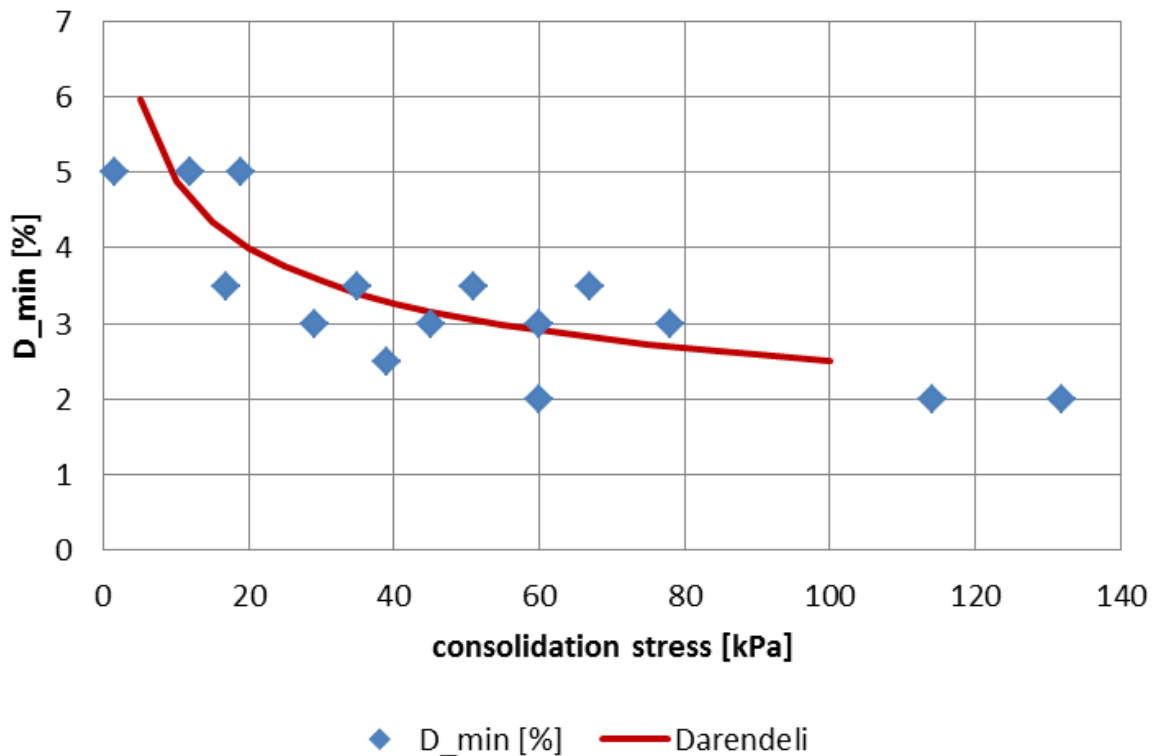


Figure 7.19. Minimum damping D_{min} as function of the consolidation stress for the soils in Table 7.2 (blue symbols). The Darendeli curve for $I_p = 100$ and OCR =1 is shown in red

Two other parameters that describe the damping curves according to Darendeli (2001) are the multiplication factor F , which is a function of parameters b and p (Eq. 7.9). Darendeli (2001) used a value of $p=0.1$, which is also adopted for the peat model. Figure 7.20 shows the values of b as a function of consolidation stress. The Queensboro Bridge data point is again considered to be an outlier. In the Darendeli formulation, parameter b is a constant, which is independent of consolidation stress. The average value for b for the literature data set, excluding the Queensboro Bridge data point, is 0.712 with a standard deviation of 0.216.

The computation of the mean effective stress requires an assumption on the value of the coefficient of earth pressure at rest. Den Haan & Kruse (2007) give a correlation between bulk density and K_o for Dutch peats. Using typical values of unit weights of peat (Appendix V), the K_o values computed using Den Haan & Kruse (2007) vary between 0.3 and 0.4. An average value of $K_o=0.35$ is used for the entire field.

For peat layers near the surface, where stresses levels are low, there is a larger uncertainty with respect to the existing stress levels. Above the water table the peat may be partly saturated and effective stresses may be higher due to capillary stresses. Moreover, influence of the weather and the resulting drying and wetting cycles may influence the peat behaviour. In particular, these cycles may create an apparent preconsolidation stress. Experience from consolidation tests on Dutch peats suggests that this apparent preconsolidation stress is in the order of 10 to 20 kPa. For this reason, a lower bound for the effective vertical stress of 15 kPa is used.

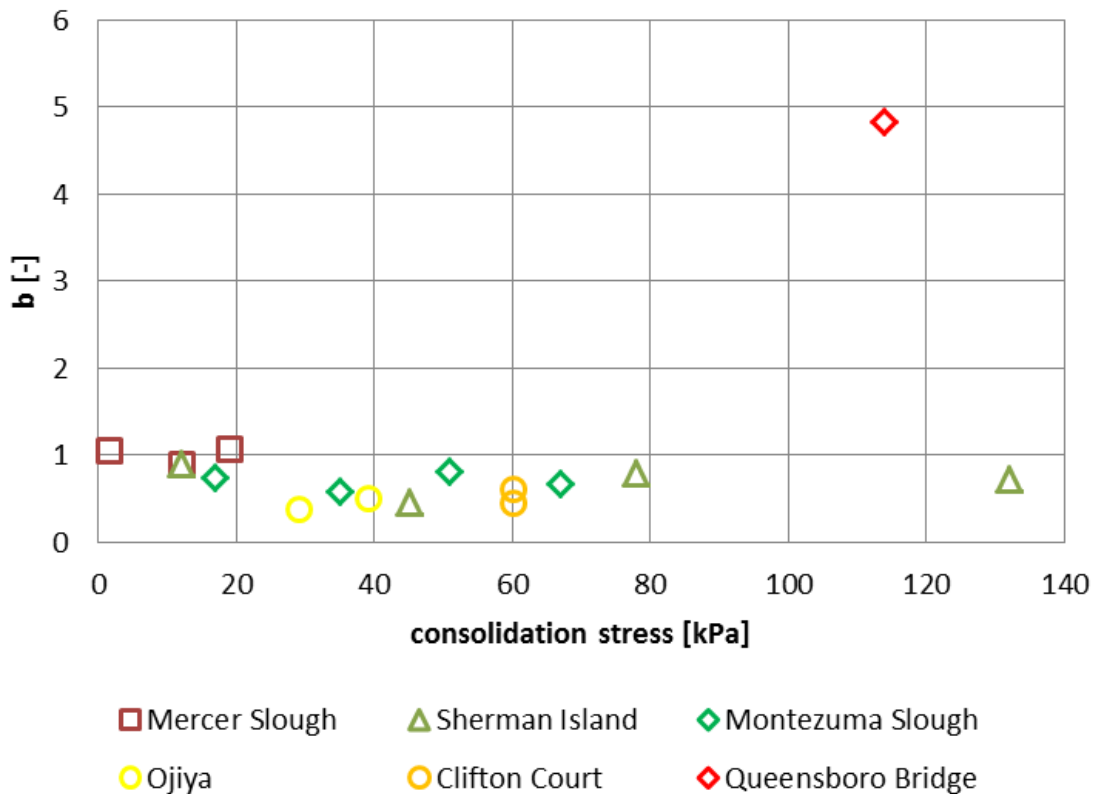


Figure 7.20. Value of b as function of the consolidation stress for the literature data set

Kishida *et al.* (2009b) published a model for the MRD curves for peats in the Sacramento River delta. A comparison of the proposed MRD curves for Peat with those of Kishida *et al.* (2009b) are shown in Figure 7.21. Note that the model proposed for this study has a stronger dependence on confining stress. This dependence was noted by various other studies (e.g., Kramer, 2000). On the other hand, the proposed model does not have dependency on organic content.

Laboratory measurements on Holland peat sampled in Groningen were conducted during the development of V4 (Zwanenburg *et al.*, 2017). The aim of these tests is to derive Groningen specific modulus reduction and damping curves for Groningen peat. The results were not yet included in V4.

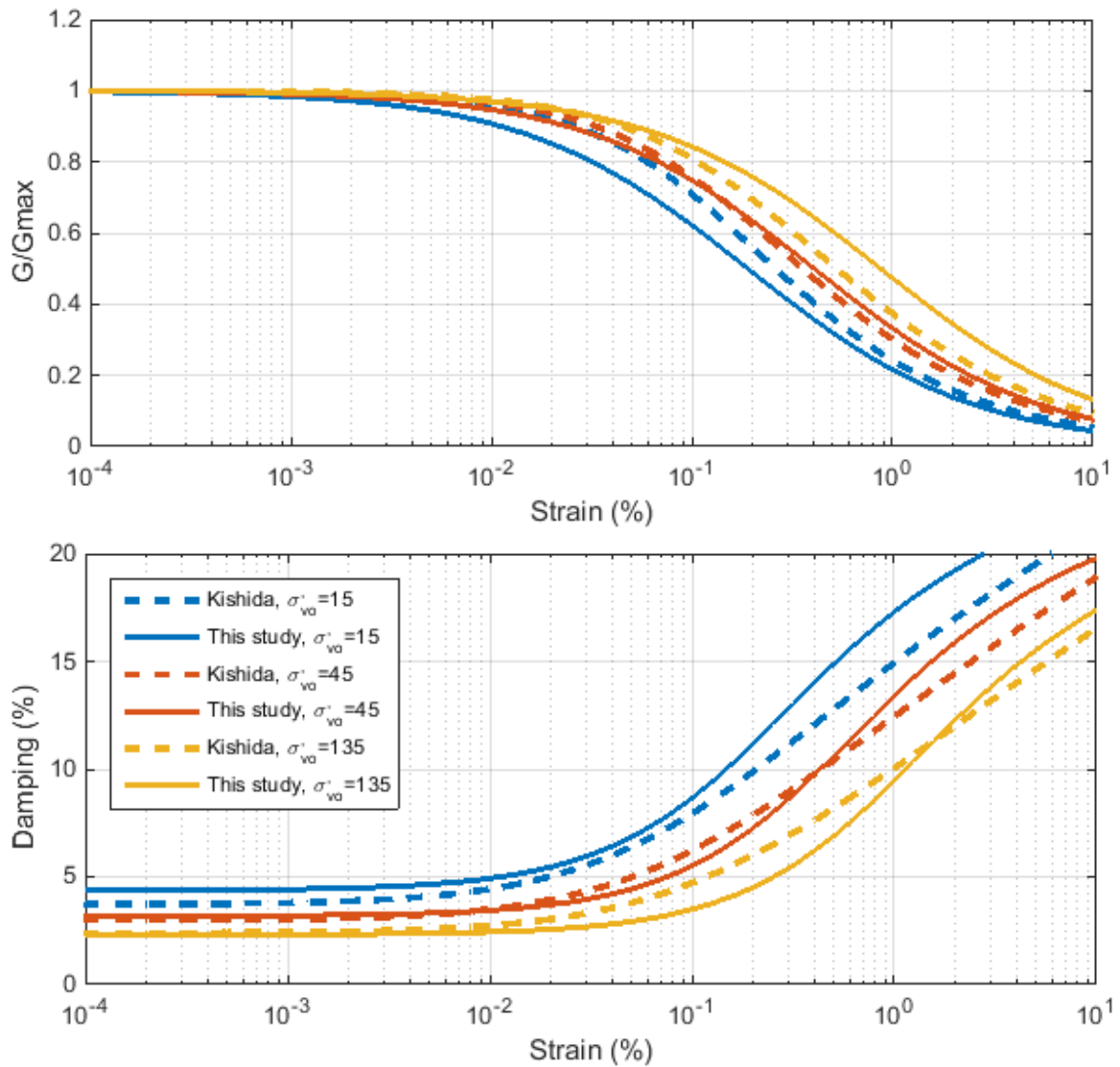


Figure 7.21. Comparison of MRD curves obtained from the proposed model and the model by Kishida *et al.* (2009b) for different vertical effective stresses. Curves for Kishida *et al.* (2009b) are shown for an organic content of 15%

7.7. Randomisations

Potentially, all variables that are input to the site response calculations can be randomized. However, for each added parameter to a randomisation process, the calculation time increases exponentially. Therefore, the parameters chosen for randomisation need to be selected carefully. Moreover, the amount of information on the variability of the parameter dictates the possibility to randomize the parameter. Figure 7.22 illustrates how the general level of knowledge varies with depth.

The following randomisations were implemented in the site response calculations:

- The variability of lithostratigraphy and lithoclass is represented by the distribution of voxel stacks of GeoTOP within one geological zone for depth range from the surface to NAP-50 m.

- The variability of lithostratigraphy in the depth range between NAP-50 m and NS_B is taken into account by the probabilities of the scenarios.
- Randomisation of V_s is applied only for the GeoTOP depth range, using the V_s distributions described in Section 7.1. The randomisation of shallow V_s profiles is described below. Below NAP-50 m, the MEI and Sonic velocities are taken as provided by NAM and Shell. No uncertainties were implemented in this depth range.
- Randomisation of input signals: The input motions were ranked according to their PGA and split into 5 classes of increasing PGA. For each layer file, one input signal was randomly selected from each class.

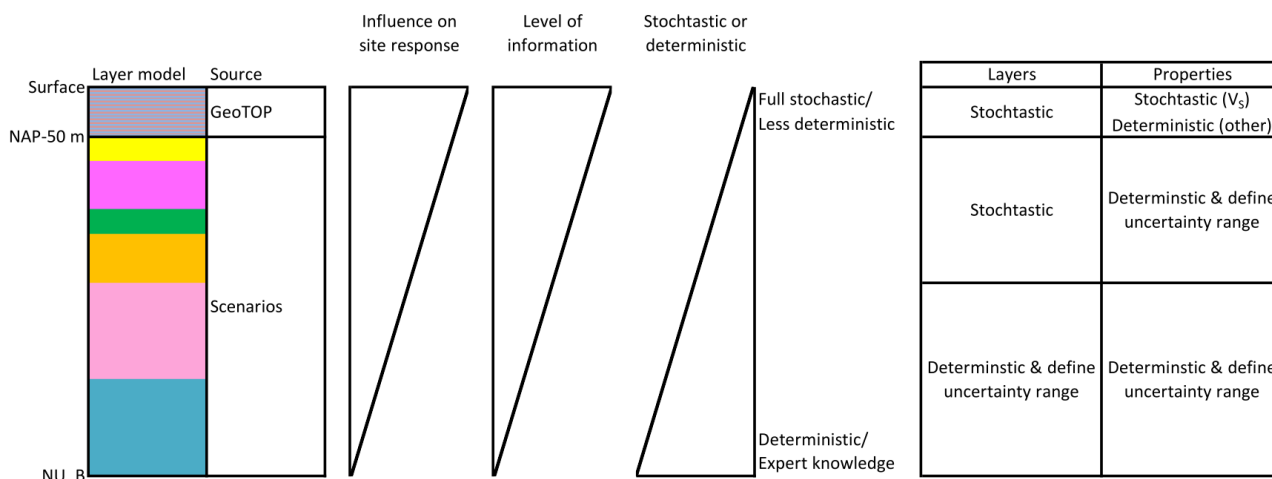


Figure 7.22. Site layer and property model with the coupling of depth ranges of the geological models (GeoTOP and scenarios, Kruiver *et al.*, 2015) to the reference baserock horizon (NS_B). The level of information decreases with depth, as does the influence of the deeper layers on the site response

No randomisation was applied to unit weight, OCR and I_p . For these parameters, average values were used for each combination of lithostratigraphy and lithoclass. Uncertainty in the MRD curves was also not taken into account in the site response analyses. Uncertainty in MRD curves is, however, taken into account in the proposed model for uncertainty of the amplification factors (Chapter 9).

Randomisation of shallow V_s profiles

The V_s profiles in the GeoTOP range were randomised in order to capture the effect of the variability in V_s in the site response. The randomisation is described in Kruiver *et al.* (2017) and repeated here. The GeoTOP voxel stack with stratigraphy and lithology attributes and the V_s relationships from Section 7.1 and Appendix V formed the basis of the randomisation. The flowchart for randomised V_s profiles is included in Figure 7.23. A sensitivity study indicated that the 0.5 m layering of GeoTOP voxel stack created unrealistic site response results. Therefore, the GeoTOP layers were resampled to a minimum thickness of 1.0 using a random scheme: a unit of only 0.5 m thickness was randomly combined with the unit above or below it. Within units, a maximum thickness of 3.0 m was imposed to preserve the depth

dependence of V_s . Additionally, the following layer to layer relations were assumed (Section 7.3):

1. Full correlation within units.
2. Correlation with a coefficient of $\rho = 0.5$ between units.

A correlated sampling approach was implemented largely following Toro (1995). The V_s distributions (Appendix V) were standardized in order to be able to sample in a correlated way between units having different V_s distributions (different average and standard deviation of $\ln V_s$). Additionally, the V_s distributions were truncated at two standard deviations to avoid extremely high or low V_s values. This follows common practice in site response analyses of nuclear facilities (EPRI, 2013). To compensate for the truncation, the V_s values were sampled from a distribution with a standard deviation that is increased by 16%. Truncation was implemented as follows:

1. Draw a random sample $\ln(V_{S_{sample}})$ from a normal distribution with

$$\mu = \ln(V_{S_{mean}}) \quad \text{and} \quad \sigma^* = 1.16 \sigma_{\ln V_s} \quad (7.25)$$

2. Standardise to a distribution with $\mu=0$ using

$$\ln(V_{S_{sample_{standardized}}}) = \frac{(\ln(V_{S_{sample}}) - \mu)}{\sigma^*} \quad (7.26)$$

3. Repeat steps 1 and 2 until

$$\left| \ln(V_{S_{sample_{standardized}}}) \right| < 2.0 \quad (7.27)$$

The random sample for each unit is taken at the average depth of occurrence of this unit in the voxel-stack. For the confining stress-dependent V_s relations in Table 1 the standard deviation is related to the distance to average $\ln\left(\frac{\sigma'_o}{p_a}\right)$. In order to avoid sampling in the confining stress range either outside the range defined by the data, or always at the tails of the distribution which might result in relatively large standard deviation, the random sample $\ln(V_{S_{sample}})$ is taken at the average depth of occurrence of the particular unit, assuming that this is comparable to the average confining stress.

When moving to the next unit in the voxel-stack, correlated sampling is applied, again at the average depth of occurrence of the next unit. The correlated sampling is implemented as follows:

1. Draw an auxiliary variable b (needed for standardized and truncated distribution) from a normal distribution with $\mu = 0$ and $\sigma = 1.16$.

2. Repeat step 1 until $|b| < 2.0$.

3. Calculate $\ln(V_{S_{sample_standardized}})$ correlated to the previous layer using the correlation coefficient ρ and auxiliary variable b using:

$$\ln(V_{S_{sample_standardized}}) = \rho \ln(V_{S_{previous\ layer_standardized}}) + b\sqrt{(1 - \rho^2)} \quad (7.28)$$

4. Transform $\ln(V_{S_{sample_standardized}})$ to $\ln(V_{S_{sample}})$ using:

$$\ln(V_{S_{sample}}) = \mu + \sigma^* \ln(V_{S_{sample_standardized}}) \quad (7.29)$$

where μ is the mean V_s value at that depth.

5. Use $\ln(V_{S_{sample_standardized}})$ as $\ln(V_{S_{previous\ layer_standardized}})$ in Eq. (7.28) in the calculation of the next unit.

Using the above described procedure, the truncated and correlated $\ln V_s$ is sampled for each unit at one depth per unit. In order to determine the shear-wave velocities at other depths of this unit in the voxel stack, the updated intercept $\ln V_{s_2}$ is determined using the slope n of the corresponding distribution and $\ln(V_{S_{sample}})$ from Eq. (7.29) for this unit using:

$$\ln V_{s_2} = \ln V_{S_{sample}} - \left(n \ln \left(\frac{\sigma'_o}{p_a} \right)_{at\ average\ depth} \right) \quad (7.30)$$

Finally, the $\ln V_s$ values at all other depths (and thus confining stresses) within this voxel-stack of this unit are calculated using:

$$\ln V_s = \ln V_{s_2} + n \ln \left(\frac{\sigma'_o}{p_a} \right) \quad (7.31)$$

In effect this means that only $\ln V_{s_1}$ and not the slope n is randomized in Eq. (7.1).

Examples of mean and sampled V_s profiles are shown in Figure 7.24. The left panel of Figure 7.24 is an example of a thick Peelo clay unit below 8 m depth. The depth dependence of V_s is clear within this unit. The middle and right panel of Figure 7.24 include examples of profiles with many more units of stratigraphy and lithology. Because of the partial correlation between units, the sampled V_s profile lies both above and below the mean V_s profile within one profile. The resulting V_s profiles, however, represent likely representatives of actual V_s profiles in the region.

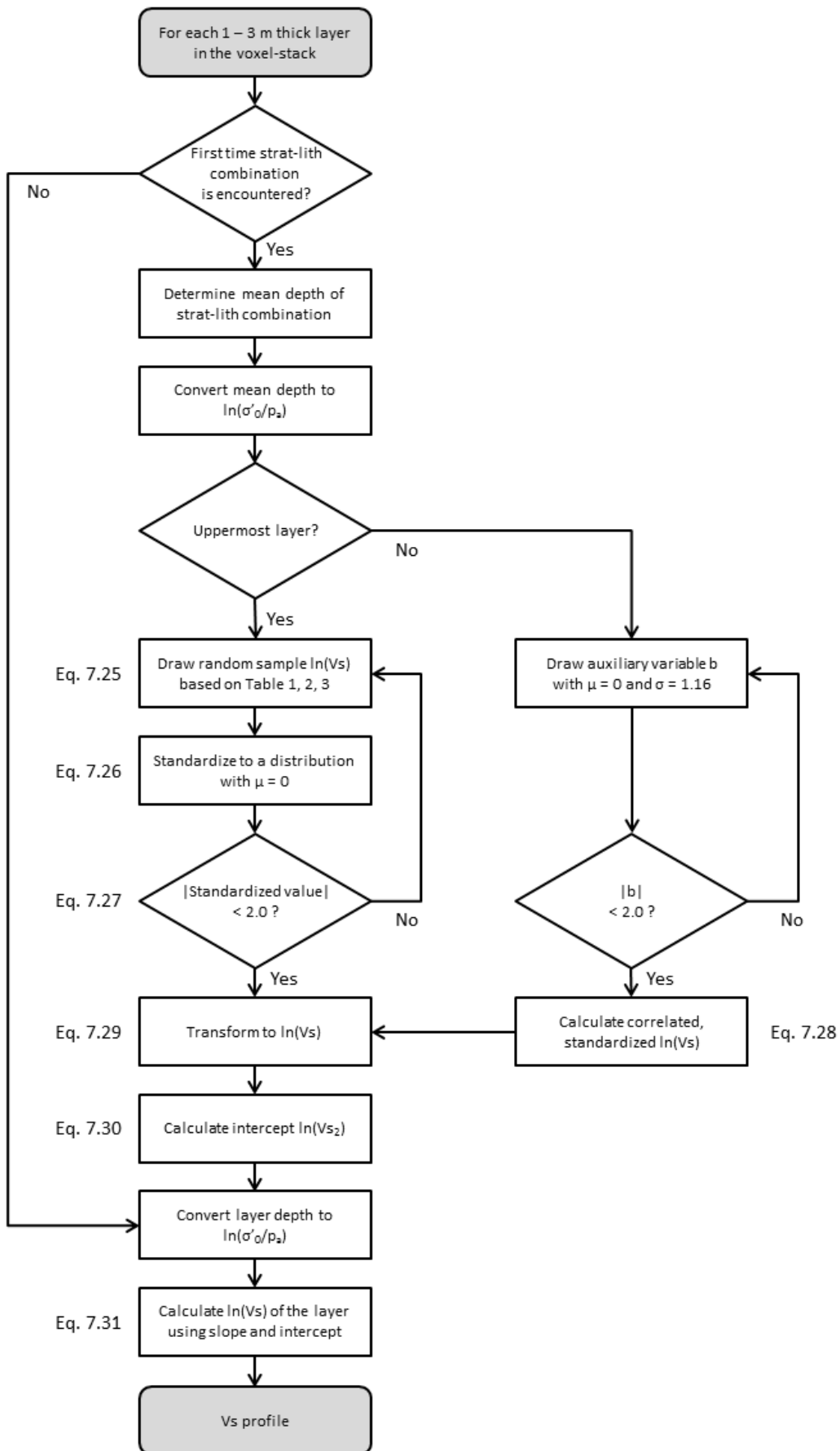


Figure 7.23. Scheme for sampling of V_s .

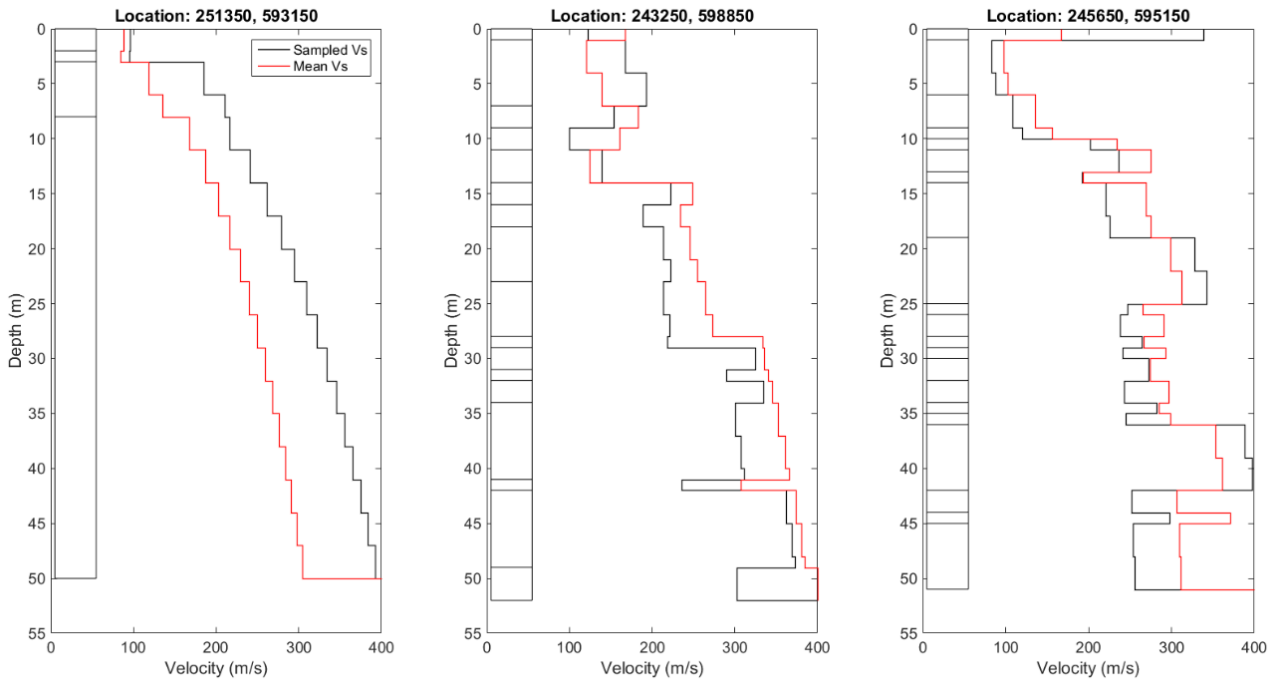


Figure 7.24. Three examples of randomized (*black line*) and mean (*red line*) shear-wave velocities. The column at the left of each graph indicates the units in the voxel stack. *Left:* example of homogeneous profile with only 4 units of stratigraphy-lithology. *Middle and right:* examples of more heterogeneous stacks.

8. SITE RESPONSE ANALYSES

This chapter follows directly from the construction of the site profile models developed for site response analyses presented in Chapter 7, and focuses on how the site response analyses have been conducted to obtain the site amplification functions for the Groningen field. The chapter begins with a discussion of the choices that were made for how the site response analyses were to be performed in terms of methodological approach. The next section describes the generation of the dynamic inputs at the elastic half-space used in the analyses, and the final section then discusses the interpretation of the site response analysis results in the form of non-linear amplification factors and their associated variability.

8.1. Choice of analysis procedure

The site response analyses for the Groningen project were conducted assuming one-dimensional (1-D) wave propagation. Non-linear soil behaviour will be modelled using an equivalent linear approach (EQL). In the EQL approach a single strain level for each soil layer is used to select strain-compatible values of shear-moduli and damping. These strains are proportional to the maximum strains, which in turn depend on the input motion. Generally, multiple input motions are necessary to capture the potential variability of maximum strain. Alternatively, Random Vibration Theory (RVT) can be used to obtain statistical estimates of maximum strains (Rathje & Ozbey, 2006). An additional advantage of RVT is that it can also be used to estimate peak time domain parameters from the predicted Fourier amplitude spectra at the surface. For these reasons, a much smaller set of input motions is needed to fully capture the effects of input motion variability on the variability of site amplification.

For the Groningen project, site response analyses will be conducted using the software STRATA (Kottke & Rathje, 2008) with the RVT option. The remainder of this section presents a review of relevant literature aimed at justifying this choice and at evaluating the possible bias resulting from this choice.

Comparison of EQL and fully non-linear analyses

EQL methods use a constant value of soil properties (shear moduli and damping) in each soil layer. This constant value is obtained by assuming a level of strain for each layer and is used in a closed-form solution of the 1-D wave propagation equation in elastic media. An iterative procedure using the soil's Modulus Reduction and Damping (MRD) curves is applied until the computed strains are equal to the assumed strains. On the other hand, non-linear (NL) site response analyses solves for the wave propagation equation using time-stepping methods where the soil properties vary with time. The soil properties can modulate with time as the severity of shaking changes (Stewart *et al.*, 2014). This approach allows for more realistic modelling of the non-linear response of the soil, especially for high-intensity input motions (Kottke, 2010).

The EQL approach is easy to use and implement and is computationally inexpensive, but it involves a larger set of approximation to soil behaviour than non-linear analyses (Hashash & Park, 2002). Discrepancies between NL and EQL site response analyses (SRA) are typically associated with large shear strains over some depth interval in the profile (Stewart *et al.*, 2014). Some authors have found that NL analyses are required when shear strains exceed 0.5-1.0% (Stewart *et al.*, 2014) while other studies suggest a smaller threshold: 0.1-0.4% (Kaklamanos *et al.*, 2013). In addition to its computational efficiency, an additional advantage of EQL is that the input parameters are generally easier to develop than those needed for NL analyses. For this reason, an issue that is commonly faced during SRA is whether EQL analyses are sufficient or whether more costly NL analyses are required (Stewart *et al.*, 2014).

Validation studies using vertical array data have shown general consistency between EQL and NL predictions of site response (*e.g.*, Stewart *et al.*, 2008; Kwok *et al.*, 2008; Assimaki & Li, 2012; Kaklamanos *et al.*, 2013). Stewart *et al.* (2014), in an extensive review article, indicate that a limitation of these studies is that they involve relatively modest levels of shear strain. Stewart *et al.* (2014) propose that more meaningful insight into the differences between EQL and NL ground motion predictions can be made when the analyses are performed for relatively strong shaking levels that induce large strains. However, care must be taken when comparing model assumptions to make sure errors in the specification of soil properties do not obscure the results.

Other researchers have also provided insights on the relationships between EQL and NL SRA by comparing NL, EQL, and linear numerical evaluations of site responses with linear empirical evaluations. For instance, Assimaki & Li (2012) found that the intensity of non-linear effects at a given site during a specific ground motion is a function of the time-average shear-wave velocity in the upper 30 m of the site (V_{s30}) and the amplitude at the fundamental resonance, and the characteristics of the incident-motion parameter. Régnier *et al.* (2013), using empirical data from the Kiban-Kyoshin (KiK-net) Japanese database and a statistical analysis showed that, regardless of the site, the probability that there is a significant departure from linear site response is greater than 20% for PGA values recorded at the downhole station between 30 to 75 cm/s².

The differences in predictions between EQL and NL analyses are primarily due to overdamping in EQL and to an overprediction of amplification at resonant frequencies due to the assumed linearity in the EQL computations. Overdamping occurs in soft soils subjected to high intensity motions because the damping levels used in the EQL analyses are those that are compatible with strain levels that occur only during a short time interval in the strain time history, yet the same damping level applies for the entire duration of the time history (Stewart *et al.*, 2014). Because damping affects more the high frequencies, this effect can cause an under-prediction of high frequency motions in EQL. On the other hand, EQL analyses may over-predict the amplitude of site response at resonance frequencies. This occurs because the EQL analyses assume time-invariant soil properties, which results in the constructive interference of trapped waves that leads to resonance. The change of soil properties with time that occurs in NL prevents the constructive interference from fully developing (Rathje & Kottke, 2011).

Another common source of discrepancies between EQL and NL analyses are due to the difference in predicted soil behaviour between the two types of analyses. The NL approach relies on a backbone shear stress-shear strain curve and Masing unloading/reloading rules to define the hysteretic response of the soil under cyclic loading. A common backbone curve is the MKZ model (Matasovic & Vucetic, 1993), which is a modified hyperbola. To relate a non-linear stress-strain model to measured modulus reduction and damping curves, a non-linear backbone curve and its associated hysteresis loops at different strain levels are converted into equivalent G/G_{max} and D curves. The non-linear fitting parameters are selected such that the equivalent modulus reduction and damping curves from the non-linear model match those specified for the soil (Kottke, 2010). Figure 8.1 shows a comparison of damping curves from the empirical model of Darendeli (2001) with those from the MKZ model. While the MKZ curves show favourable agreement at smaller strains, they deviate from the empirical curves at larger strains, with the NL model implying larger damping levels. This issue is common with NL models and is caused by the shape of the modified hyperbolic stress-strain curve at large strains and the use of the Masing rules to generate the hysteresis loops (Kottke, 2010). Improvements to these formulations have been proposed by Phillips & Hashash (2009).

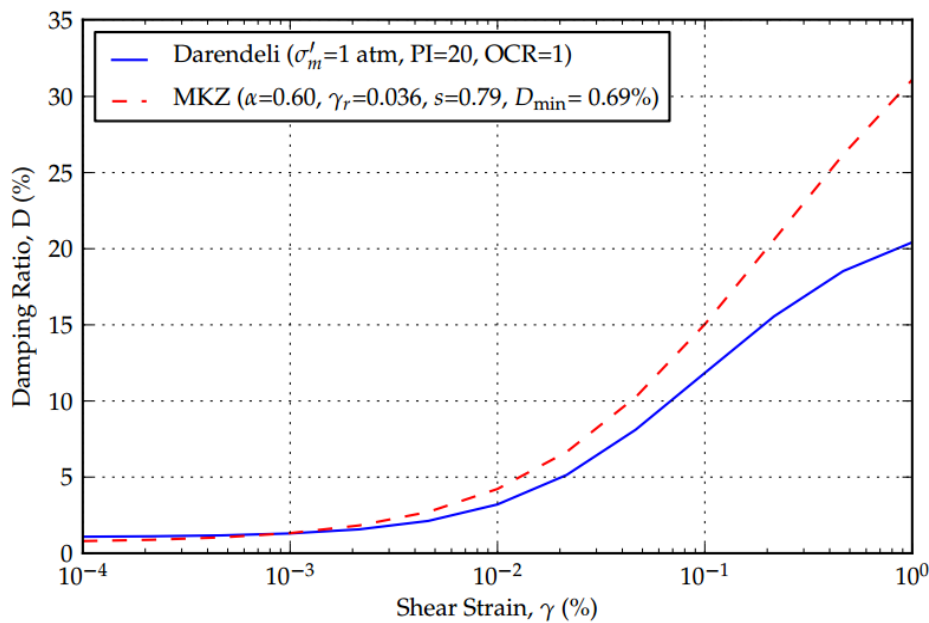


Figure 8.1. Differences in damping curves as obtained from the Darendeli (2001) and MKZ models (Kottke, 2010).

Additional differences between EQL and NL analyses can result from the numerical integration schemes implemented in NL analyses. DEEPSOIL, which is a site response program capable of conducting NL SRA, solves the equation of motion by means of the Newmark β method in time domain (Hashash *et al.*, 2015). The model assumes that the acceleration within a time step is a constant, mean value. This time stepping method is unconditionally stable (Chopra, 2007), which is beneficial for multi-degree-of-freedom

systems. However, numerical errors can produce inaccuracy in the solution in particular for the high-frequency response (Hashash *et al.*, 2015). These errors can cause frequency shortening and amplitude decay (Chopra, 2007; Kottke, 2010).

Kottke (2010) investigates these errors by considering linear-elastic (with frequency-independent damping) and NL site response results presented as the ratio of the Fourier amplitude spectrum (FAS) of the surface motion to the FAS of the input motion, which represents the equivalent transfer function for the selected sites. The amplitude of the transfer functions corresponding to the Sylmar County Hospital (SCH) parking lot site (located in San Fernando, CA) and the Calvert Cliffs (CC) site (in Maryland) for the closed form solution in the frequency domain and for three different motions used in the “linear-elastic”, time-domain analysis are shown in Figure 8.2. For the time-domain analyses, the peaks at high frequencies shift towards lower frequencies, which represents frequency shortening, and the amplitudes of the peaks decrease, which represents amplitude decay. The frequency shortening and amplitude decay are more significant for motions with larger time steps (Δt).

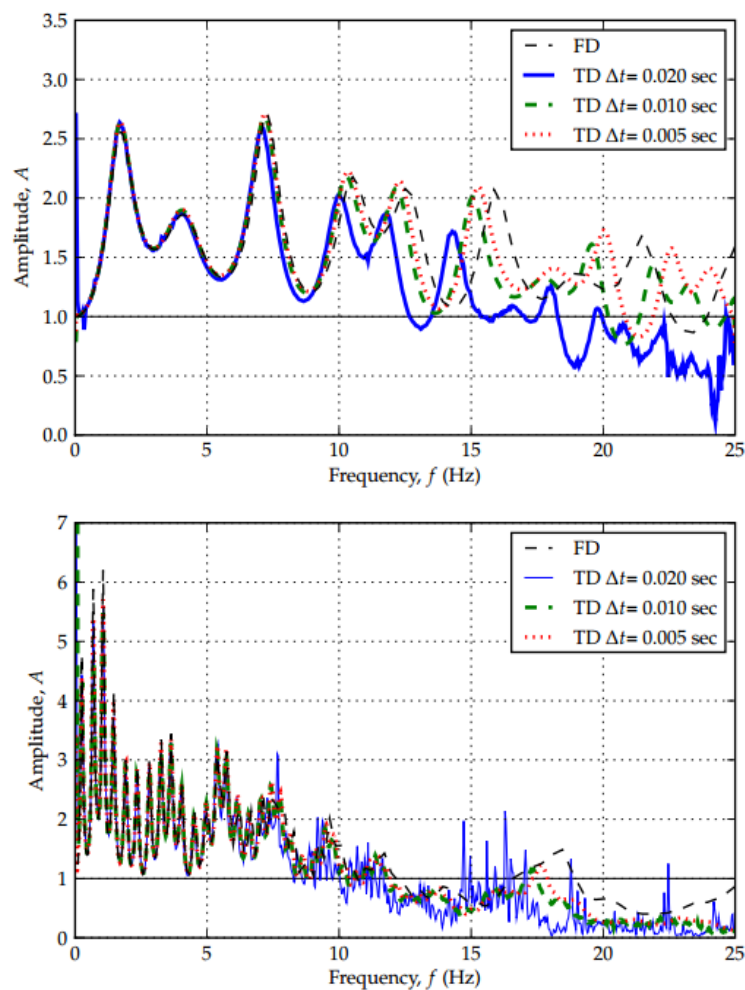


Figure 8.2. Amplitude of the transfer function computed for the SCH and CC sites using Linear Elastic time-domain (TD) and frequency-domain (FD) methods (Kottke, 2010)

The frequency shortening and amplitude decay shown in Figure 8.2 was found to affect spectral ratios at high frequencies (Kottke, 2010). For both sites investigated by Kottke (2010), the spectral ratios from the time domain analysis with frequency independent damping are 5 to 15% smaller than the frequency domain results at frequencies above 10 Hz.

Kottke (2010) investigation focused on linear-elastic time-domain analyses versus EQL SRA elucidated two important effects that cause an underestimation of the site response at high frequencies for time domain methods. First, frequency-dependent viscous damping in NL formulations can significantly underestimate the site response at high frequencies. The frequency-independent Rayleigh damping formulation of Phillips & Hashash (2009) has been found to reduce this underestimation (Hashash *et al.*, 2010), but at the expense of computational effort. Additionally, numerical errors introduced by the time-stepping integration used in time-domain analysis influence the site response at frequencies greater than about 10 Hz as shown in Figure 8.2 (Kottke, 2010).

Results from a survey conducted by Matasovic & Hashash (NCHRP, 2012) showed that there was a consensus amongst practitioners that a NL SRA is to be used when computed shear strain exceeds 1%, although this threshold was deemed as too high. These authors also indicated that only considering ground motion intensity measures cannot be sufficient to assess soil non-linearity given that strain levels in soft soil deposits can be quite high even when subjected to low intensity ground motions (Kim *et al.*, 2013).

Kaklamanos *et al.* (2013) identified critical parameters that most significantly contribute to uncertainty in estimations of site response by performing linear and equivalent linear SRA using the KiK-Net downhole array data in Japan. Thresholds for selecting among linear, EQL and NL SRA were provided with respect to the maximum shear strain in the soil profile, the observed peak ground acceleration at the ground surface, and the predominant spectral period of the surface ground motion. The aforementioned parameters were found to be the best predictors of conditions where the evaluated site response models become inaccurate (Kaklamanos *et al.*, 2013). The peak shear strains beyond which linear analyses become inaccurate in predicting surface pseudo-spectral accelerations are a function of vibration period and are between 0.01% and 0.1% for periods <0.5 s, whereas EQL SRA were found to become inaccurate at peak strains of ~0.4% over the aforementioned period range.

The proposed thresholds at which linear and EQL models should be used are presented in Figure 8.3. According to Kaklamanos *et al.* (2013), by using the statistically significant data set of 3720 ground motions at 100 sites, the breakpoint in the slope of the intra-site residuals versus the maximum shear strain (γ_{\max}) or observed peak ground acceleration (PGA_{obs}) can be used to quantify the critical values of γ_{\max} at which the linear and EQL site response estimates are no longer reliable.

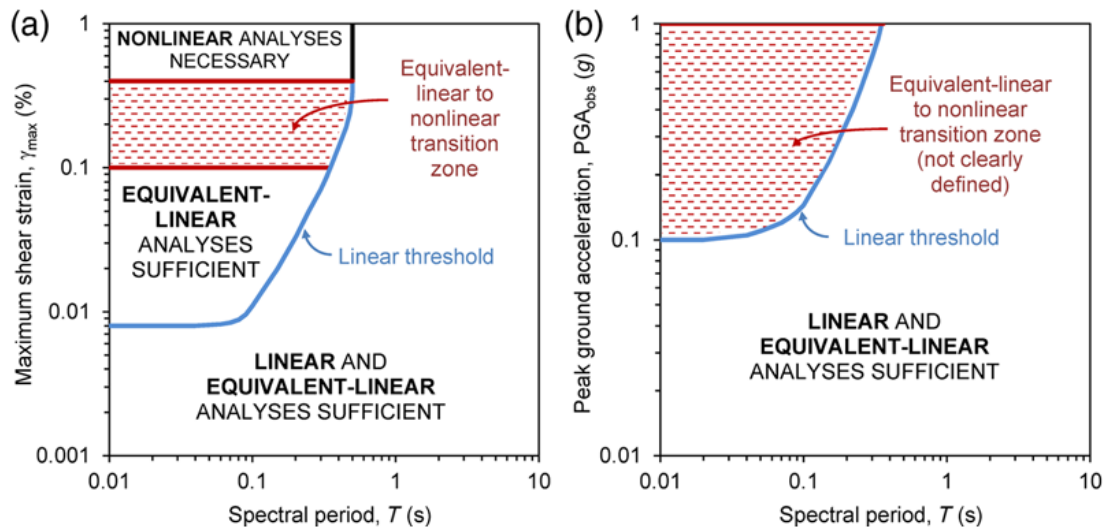


Figure 8.3. Approximate ranges of applicability of linear, EQL and NL site response analyses (Kaklamanos *et al.*, 2013).

Carlton & Tokimatsu (2016) compared EQL and NL analyses using 189 ground motions and 16 sites using the code DEEPSOIL (Hashash *et al.*, 2015). The comparisons indicated that on average, EQL analysis predicts higher spectral accelerations than NL analyses. However, around spectral periods of 0.1 s to 0.3 s, the standard deviation of the ratio of EQL to NL analysis is large, hence for some combinations of input motions and profiles NL analyses may give larger response than EQL analyses.

A comparison of EQL and NL analyses was conducted on two shallow profiles from the Groningen field by Pruiksmá (2016). The first profile was representative of soft soil (V_{S30} of 156 m/s) with an 8-m thick top layer of clay. The second profile was representative of stiffer sand (V_{S30} of 245 m/s). Only the top 30 m of these profiles were used in the analyses, hence the input motions were applied over at a depth of 30 m where an elastic half space was assumed to exist. Note that the artificial half-space at a shallow depth implies that these profiles are different than those of the Groningen field used in this study. Input signals consisted of 11 time histories. Pruiksmá (2016) finds that the differences between the two methods are significant for short spectral periods, especially for PGA. In general, EQL analyses give higher values of amplification than NL analyses. The differences between the two methods increase for higher levels of input motions. Differences between EQL and NL become significant for input motions stronger than 0.05 g for the softer profile and 0.1 g for the stiffer profile. The differences are smaller at larger spectral periods (1 to 2 s). At these longer periods, differences become significant for input motions larger than 0.2g and 0.5g for soft and stiff profile, respectively. Pruiksmá (2016) concludes that the EQL method generally leads to conservative estimates of spectral accelerations, with a few exceptions between periods of 0.05 s and 0.08 s for the chosen profiles.

Kim *et al.* (2013) computed the ratio of amplification factors resulting from EQL and NL SRA (what they refer to as Sa^{EL}/Sa^{NL}) to develop a model for quantifying the differences between both approaches. Site response simulations were conducted for 510 incident motions and 24 sites. Then, regressions of Sa^{EL}/Sa^{NL} against several ground motion and site parameters

were conducted to test their predictive capabilities. The estimated strain (γ_{est}), defined as the ratio of the peak ground velocity (PGV) and V_{s30} was found to correlate the best with relative differences between Sa^{EL} and Sa^{NL} (Kim *et al.*, 2013). A similar framework to the one previously presented by Kaklamanos *et al.* 2013 (shown in Figure 8.3) was then developed to more clearly identify the conditions leading to different site estimates from EQL and NL SRA. Values of Sa^{EL}/Sa^{NL} equal to 0.7, 0.8, and 0.9 are presented in Figure 8.4 where γ_{est} and period are set up as the y- and x-axes respectively.

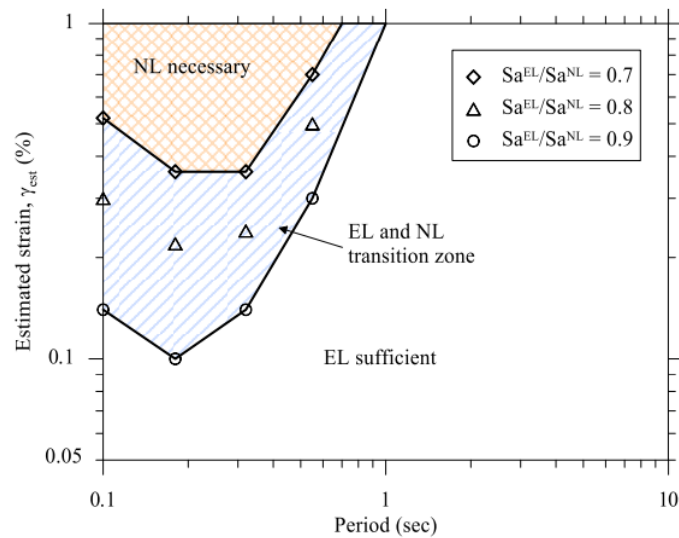


Figure 8.4. Guideline for a threshold between equivalent-linear (EL) and non-linear (NL) site response analysis in terms of estimated strain, γ_{est} , and period (after Kim *et al.*, 2013).

A more recent study (Kim *et al.*, 2016) has expanded the work of Kim *et al.* (2013) using preferred analysis protocols regarding the input motion selection process and specification of non-linear soil properties (Stewart *et al.*, 2014). Site profiles and recorded ground motions from Western US (WUS) and Central and Eastern US (EUS) were used by Kim *et al.* (2016) to conduct 13,296 site response analyses using EQL and NL models as implemented in the site response program DEEPSOIL (Hashash *et al.*, 2015).

Sa^{EL}/Sa^{NL} values were computed and plotted against the shear strain index, I_γ (*i.e.*, same as the estimated strain, γ_{est} , defined by Kim *et al.*, 2013) to investigate trends in the observed mismatch between EQL and NL SRA. Results for the WUS in terms of response spectra and FAS are presented in Figure 8.5.

EQL analyses seem to provide higher predictions of spectral accelerations at the frequencies considered for most of the I_γ values. At lower I_γ values, the Sa^{EL}/Sa^{NL} and Fa^{EL}/Fa^{NL} ratios are close to the unity for all frequencies but deviate from it for $I_\gamma > 0.1\%$. According to Kim *et al.* (2016), the decrease of Fa^{EL}/Fa^{NL} at higher frequencies (*i.e.*, $f \geq 2$ Hz) responds to the over-damping from EQL analyses and its decrease as I_γ values increase is caused by increasingly smaller strains as frequency increases. Results corresponding to the CEUS are generally similar to the ones presented in Figure 8.5. Kim *et al.* (2016) summarised their

findings in Figure 8.6, which compares trends of mean values of the aforementioned ratios against the I_γ for both WUS and CEUS.

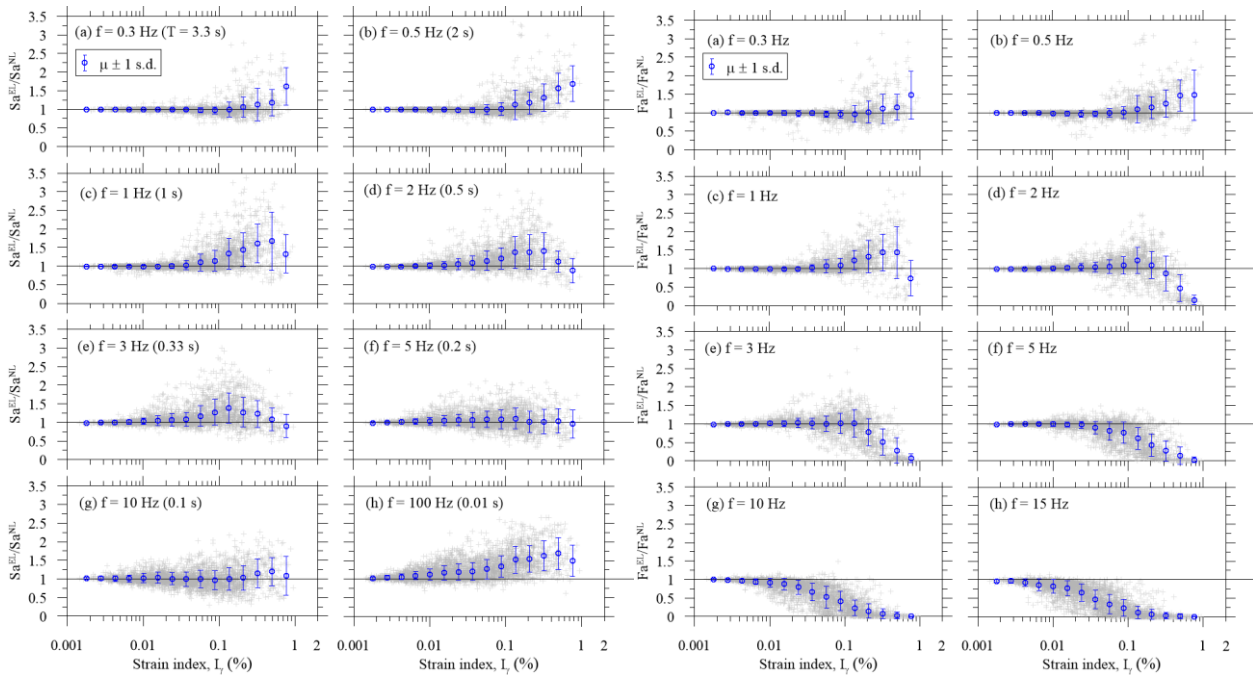


Figure 8.5. Ratio of Sa^{EL}/Sa^{NL} (left) and Fa^{EL}/Fa^{NL} (right) for WUS in terms of I_γ (Kim *et al.*, 2016)

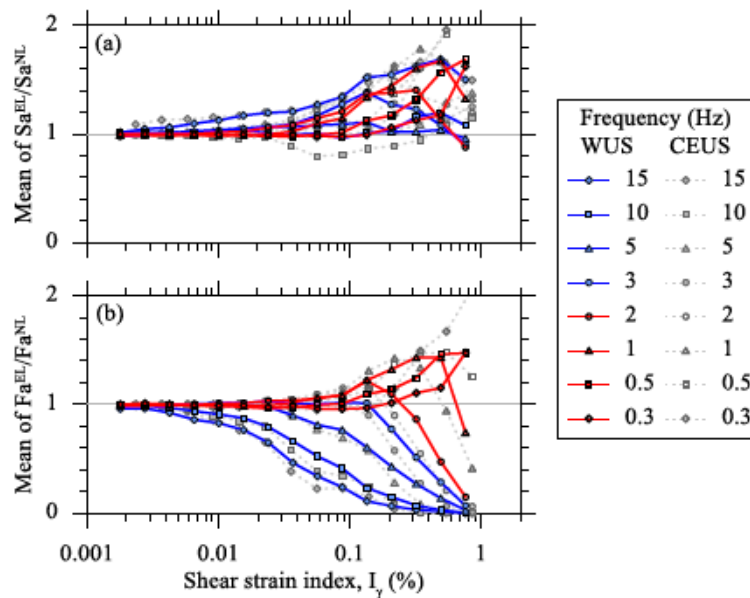


Figure 8.6. Comparison of Sa^{EL}/Sa^{NL} and Fa^{EL}/Fa^{NL} for WUS and CEUS versus I_γ (Kim *et al.*, 2016).

Mean values of Sa^{EL}/Sa^{NL} for the WUS and CEUS are generally similar (within a range of 1 to 2) although there are some differences. Likewise, for both the WUS and CEUS cases, the mean values of Fa^{EL}/Fa^{NL} start to deviate from unity at I_γ of around 0.1 %, but for frequencies greater than 5 Hz, they start to deviate from unity at lower values of I_γ (Kim *et al.* 2016).

Considering this similarity in trends for WUS and CEUS conditions, Kim *et al.* (2016) proposed frequency-dependent threshold values of I_γ to identify conditions where EQL and NL SRA differ by amounts exceeding 20% (Figure 8.7):

$$I_\gamma = 0.12f^{-0.6} \tag{8.1}$$

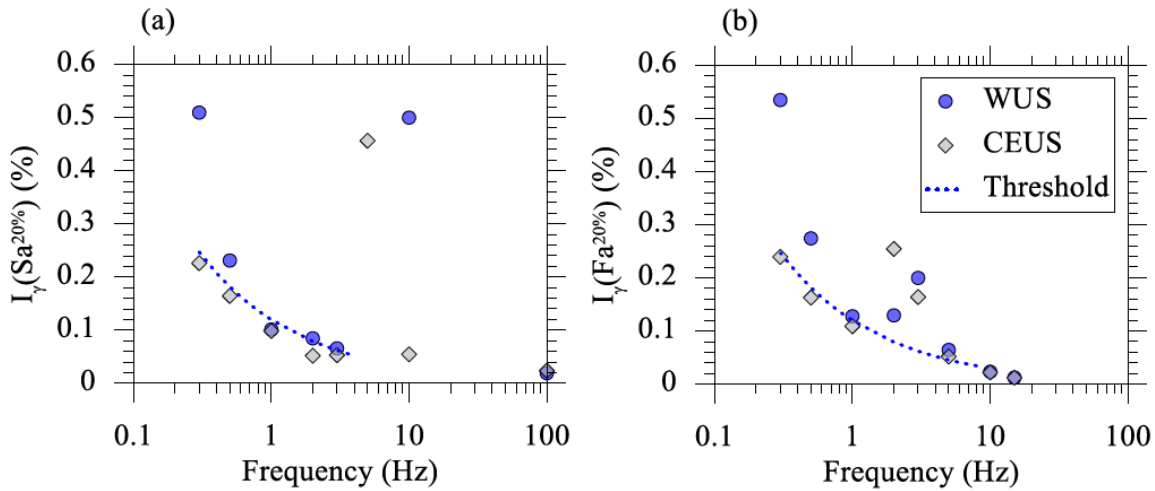


Figure 8.7. Shear strain index, I_γ , at which the EL response differs than the NL response by 20% for (A) Spectral accelerations and (B) Fourier amplitudes (Kim *et al.*, 2016).

Finally, an important contribution from this study is presented in Figure 8.8 where recommendations from previous studies for thresholds at which EQL SRA are no longer reliable are compared. The idea was to provide recommendations to identify “a priori” those conditions for which EQL and NL differ significantly.

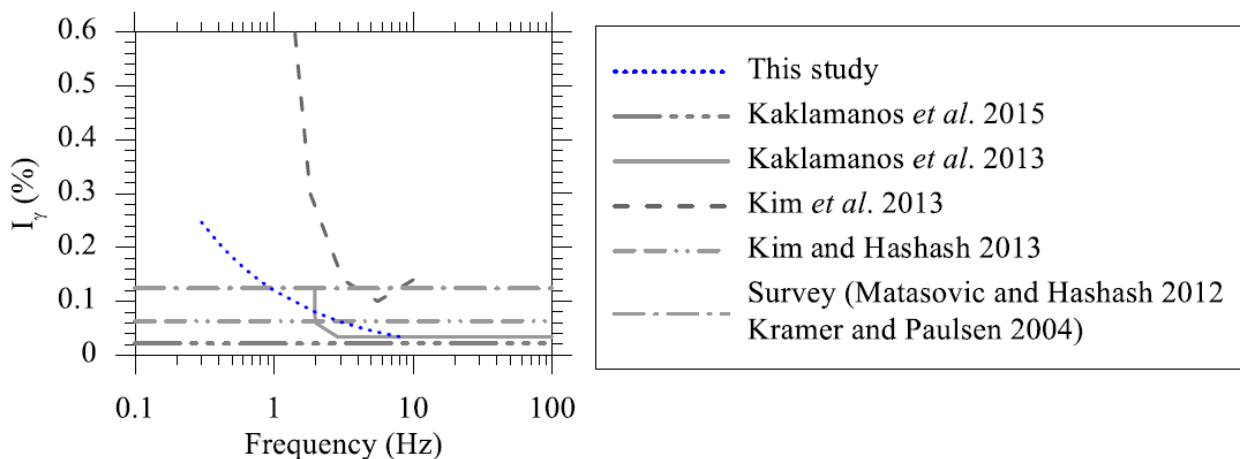


Figure 8.8. Comparison of threshold values of I_γ with those by Kim *et al.* (2013) and those converted from maximum shear strains (Kramer & Paulsen, 2004; Matasovic & Hashash, 2012; Kaklamanos *et al.*, 2013; Kim & Hashash, 2013; Kaklamanos *et al.*, 2015).

The most relevant conclusions to the Groningen project of the Kim *et al.* (2016) study are:

- Near the resonant site frequency, EQL ordinates exceed NL due to EQL forming a more strongly resonant response that is associated with the time-invariant soil properties.
- At high frequencies, EQL ordinates are lower than NL due to EQL over-damping. These differences are more distinct for Fourier amplitudes ratios than for spectral acceleration ratios.

Based on these conclusions (e.g., Figures 8.5 and 8.6), it is clear that when using response spectra, EQL analyses predict on average higher response than NL analyses at all frequencies, despite the fact that in some cases EQL results in over-damping at high frequencies (Stewart *et al.*, 2014; Kwok *et al.*, 2008). While this is true of the average response, in particular cases the amplification factors at intermediate periods (approximately between 0.1 and 0.6 seconds) might be larger for NL than for EQL analyses (Stewart & Kwok, 2008; Kottke, 2010). A similar conclusion was reached by a separate study by Tsai and Chen (2016). These authors indicate that EQL generally provide an upper bound to site response analyses, in particular if the damping levels used are high. A reason why EQL analyses are higher than NL analyses for high frequency could be due to the phase incoherence that is introduced at high frequencies (Kottke, 2010), or to the fact that softened soil properties are used throughout the entire time history in EQL analyses. An alternative explanation is that the spectral acceleration values at high oscillator frequencies are controlled by Fourier Amplitudes at much lower frequencies. At these lower frequencies, EQL analyses are not affected as much by over-damping effects.

Various other studies have looked at the bias of EQL and NL analyses with respect to recorded data. Kaklamanos *et al.* (2015) used various site response analyses methods on six KiK-net array sites. They concluded that there is a large improvement in going from linear to EQL methods, but only a slight improvement at strains above 0.05% when going from EQL to NL analyses. Kwok *et al.* (2008) did blind predictions of site response at the Turkey Flat vertical array in California using six different site response codes: SHAKE04 (Youngs, 2004); D-MOD_2 (Matasovic, 2006); DEEPSOIL (Hashash *et al.*, 2015); TESS (Pyke, 2000); OpenSees (McKenna & Fenves, 2001); and SUMDES (Li *et al.*, 1992). Acceleration response spectra and comparisons with observed data (released after the predictions were made) are presented in Figure 8.9. Kwok *et al.* (2008) indicated that at periods well beyond the elongated site period at the site (*i.e.*, 0.19-0.2 s), the predictions match the surface recordings well and are very similar to each other (which is expected considering that the computed site effect at such periods is negligible because of nearly rigid body motion. At shorter periods, the simulations generally under-predict the surface recorded motions (especially in the EW direction) and the simulation results demonstrate significant code-to-code variability. Predictions from the EQL analysis resulted in the lowest residuals. Theoretical amplification factors and observed amplification factors from recordings were also provided as a function of base motion acceleration (PGA_r) in Figure 8.10 for comparison purposes. Even though for most events the site amplification is under-predicted by the models, EQL analyses seem to provide more conservative predictions than DEEPSOIL.

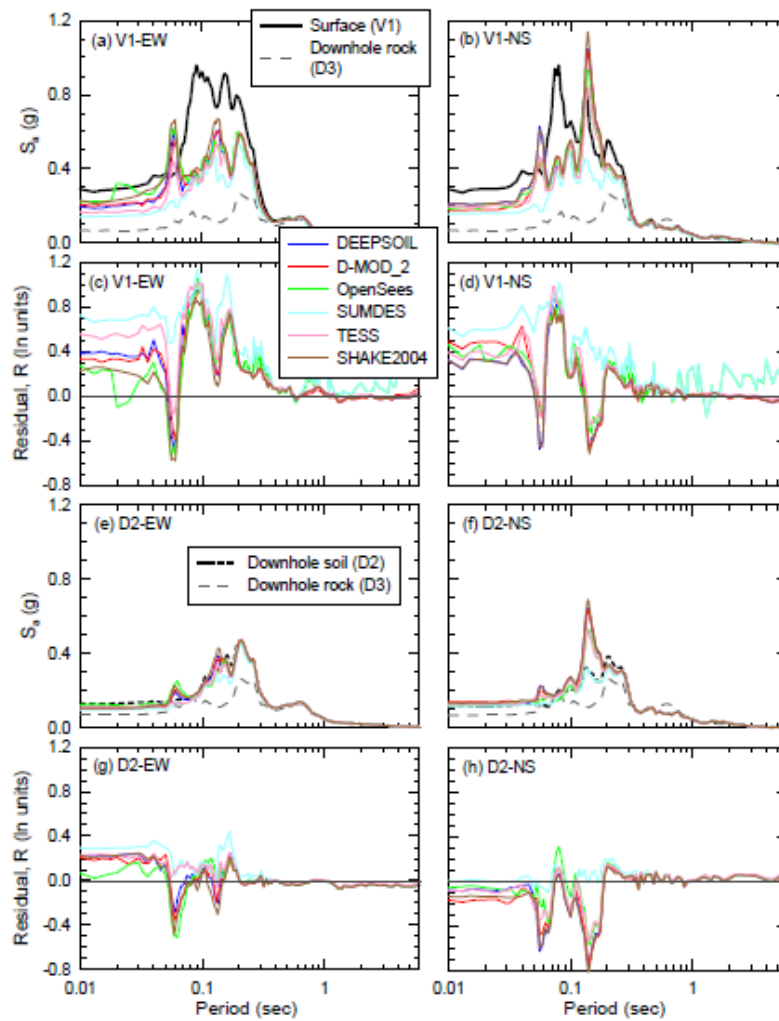


Figure 8.9. Acceleration response spectra for data and simulation results for two horizontal directions and two elevations (V1 = ground surface; D2 = 10 m depth) (Kwok *et al.*, 2008).

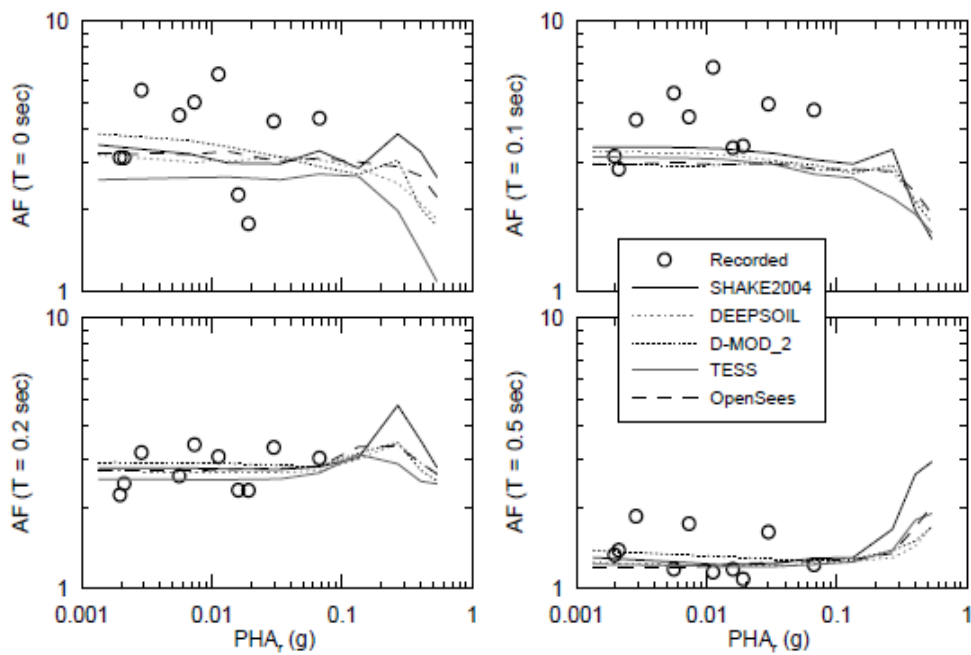


Figure 8.10. Theoretical and observed AFs at Turkey Flat site (Kwok *et al.*, 2008)

Zalachoris & Rathje (2015) compared various site response analyses methods with observed data using eleven instrumented arrays that recorded over 650 ground motions. Their comparison showed that EQL analyses may under predict observed amplification factors over the same range of spectral periods and maximum shear strains as that indicated by Kaklamanos *et al.* (2013; see Figure 8.3). However, their results also show that for large strains, the errors in site response prediction are similar for EQL and NL analyses. Zalachoris & Rathje (2015) also indicate that predictions of both EQL and NL methods improve considerably when the undrained strength of soil layers is taken into account. Zalachoris & Rathje (2015) also evaluate the predictions of an equivalent linear method with frequency dependent properties (Assimaki & Kausel, 2002). This is a phenomenological approach to account for the non-stationary nature of strain time histories. The use of this method results in over predictions of site response over a wide range of spectral periods.

The impact of EQL and NL SRA on AF was also studied by Papaspiliou *et al.* (2012) in the context of investigating the sensitivity of hazard estimates to site response. The site program SHAKE91 was used to conduct EQL SRA while NL analyses were performed by means of DMOD2000. A sandy and a clayey site with similar V_{S30} values were used for this study. The median site amplification functions for all sets of analyses considered by Papaspiliou *et al.* (2012) for the sandy site, SCH (*i.e.*, Sylmar County Hospital) are shown in Figure 8.11. EQL SRA seem to provide a conservative estimation of AF for short periods. Similar results were obtained for the clayey site. Details on the different assumptions (*i.e.*, parameter selection) behind each EQL and NL analysis performed can be found in Table 1 in Papaspiliou *et al.* (2012).

It is important to note that the NL analyses presented in this literature review were all conducted using different NL analyses methods. In a recent study (Régner *et al.*, 2016) various EQL and NL codes were compared using simple profiles. While the results of the EQL codes showed little scatter, a comparison of 20 different NL codes showed a large degree of variability in the results. This variability results from differences in the numerical integration methods used to solve the nonlinear wave propagation problem and on the assumed non-linear stress-strain behaviour of the soils. The authors of this study recommend that, given the scatter in the nonlinear results, NL analyses should always be conducted with more than one code to ensure that the epistemic uncertainty is properly captured.

Differences between Time-series EQL and RVT analyses

Kottke & Rathje (2013) compared site amplification values resulting from time series and RVT site response analyses by using the site response program STRATA (Kottke & Rathje, 2008). Stochastic simulations were used in order to ensure consistency between the ground motions needed for the time series (TS) type of analysis and the Fourier amplitude spectrum (FAS) required for the RVT approach. The program SMSIM (Boore, 2005) was used to generate a FAS based on a seismological model which was then used to generate 100 input-time series for TS site-response analysis and the FAS required as input into RVT site-response analysis (Kottke & Rathje, 2013). The parameter α_{AF} introduced by Kottke & Rathje

(2013) to quantify the differences between the RVT and TS results is defined as the ratio of the AF ($S_{a,surface} / S_{a,rock}$) from RVT (*i.e.*, AF_{RVT}) to the median TS AF (*i.e.*, AF_{TS}).

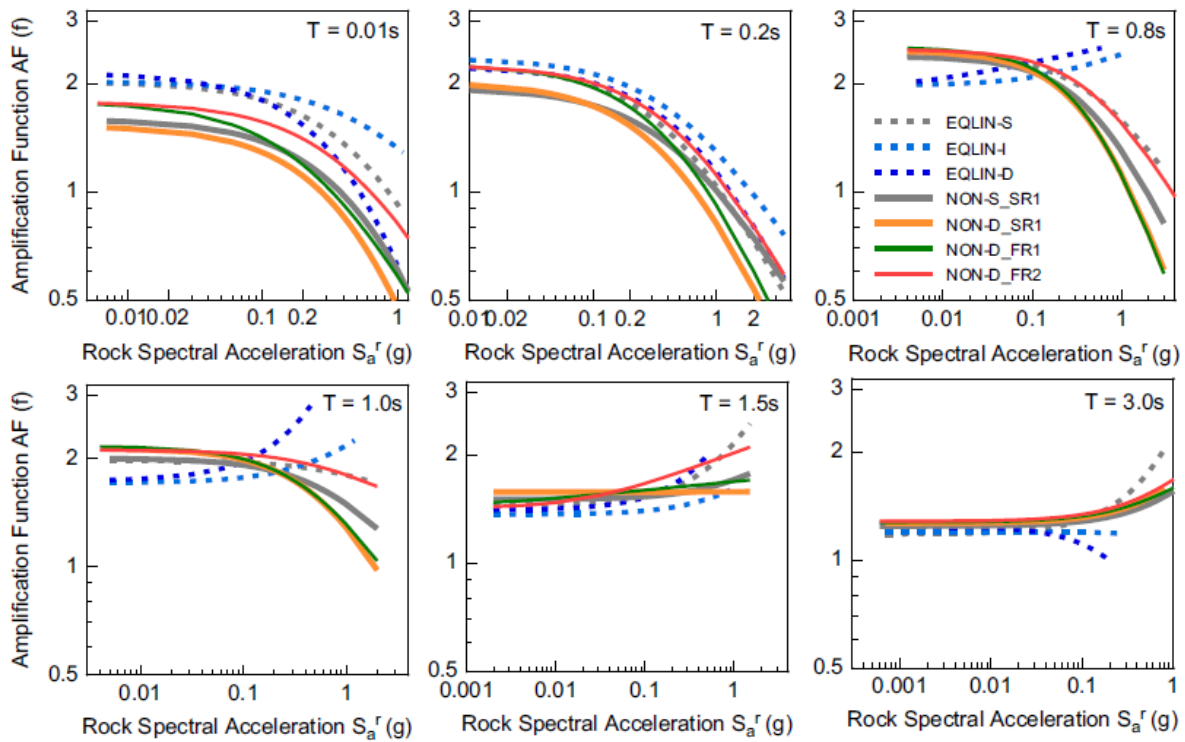


Figure 8.11. Median amplification functions for Sylmar County Hospital (SCH) (Papaspiliou *et al.*, 2012).

First, comparisons were conducted for linear-elastic conditions. TS and RVT amplification factors (AF) for one of the sites under study (*i.e.*, Sylmar County Hospital, SCH) turned out to be very similar. The value of α_{AF} varied between 0.95 and 1.1 across frequencies, with the maximum taking place at the fundamental frequency of the site (*i.e.*, 1.7 Hz). Analogously, AF were computed for a second site (the Calvert Cliffs, CC) and the corresponding results for both sites are presented in Figure 8.12. Unlike SCH, CC did show significant differences between the median TS and RVT results, especially at the site's fundamental frequency (*i.e.*, 0.25 Hz).

These findings demonstrated a site-dependency for the compatibility between TS and RVT results. A parametric study to further investigate this issue revealed that “*the maximum α_{AF} always occurs at the site frequency and that it increases as the site frequency decreases (i.e., soil thickness, H_{soil} , increases and/or V_S decreases) and as $V_{S,rock}$ increases*” (Kottke & Rathje, 2013). AF computed using RVT were found to be 20-50% larger than the AF resulting from TS analyses, while the potential under prediction can reach between 10% and 20%. The variation of the duration of the time series due to the response of the site was identified as a potential cause for the observed disagreement, given that the RVT site response does not account for it (*i.e.*, the duration of the input ground motion is the one used in RVT calculations for surface response spectrum computation).

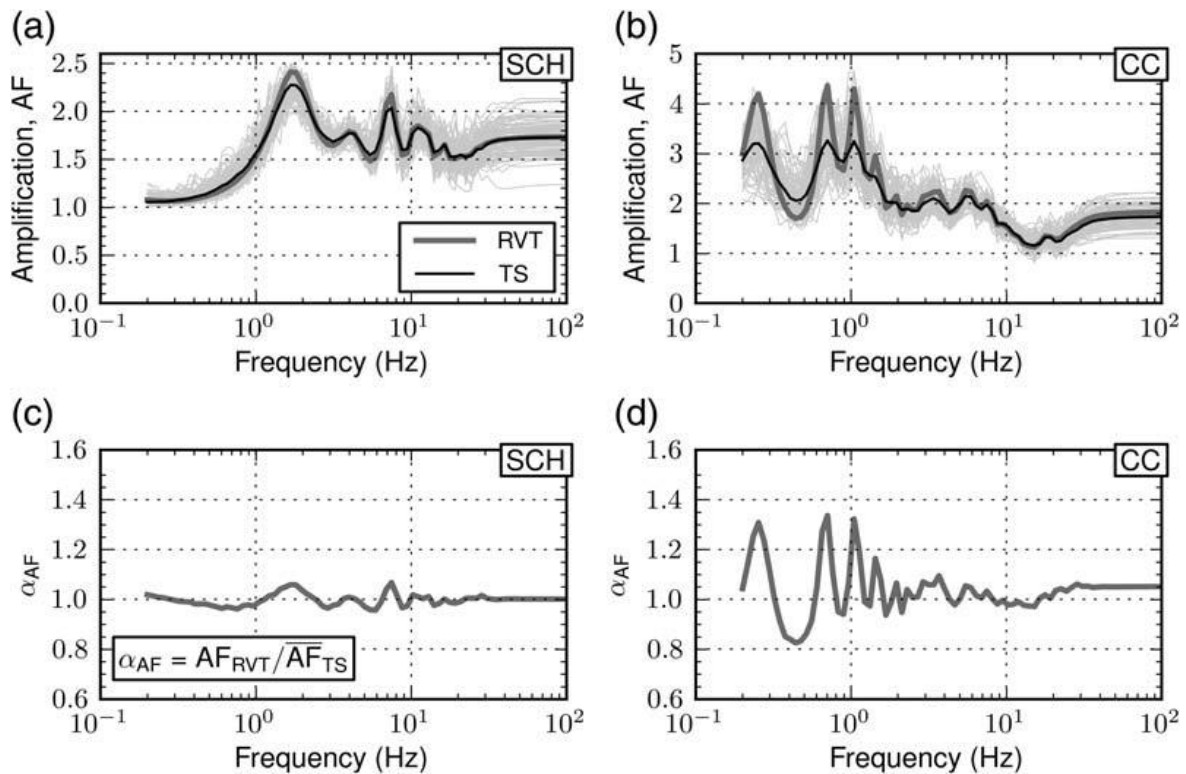


Figure 8.12. Amplification factors for TS and RVT analyses and α_{AF} for SCH and CC sites (Kottke & Rathje, 2013).

The influence of site property variations on RVT versus TS comparisons was also tested. It is well-known that introducing variability on the V_s profiles reduces the peaks in the average site amplification transfer function. This effect proved to be even more significant for RVT analyses conducted using the site response program Strata and its built-in Monte Carlo simulations as shown in Figure 8.13. For the CC site, the over prediction by RVT analyses (linear-elastic with no duration correction) at the first-mode frequency is reduced from 30% to 15% (for 100 V_s -profiles realizations with a $\sigma_{\ln V_s}=0.2$). Consequently, a better agreement between TS and RVT analyses can be achieved if velocity variations are modelled in the site response analyses; and the agreement improves with increasing levels of variability. Nevertheless, even including variability leads to differences as large as 10-20% between RVT and TS methods (Kottke & Rathje, 2013).

Furthermore, Kottke & Rathje (2013) indicate that varying V_s -profiles introduces more variability in RVT-based AF than the ones obtained by TS analyses that also account for variability in V_s : “If one is considering only the median-site amplification, then this difference in variability is not important and using Monte Carlo simulations to improve the performance of RVT site-response analysis may be a viable option. However, the increase in variability in the RVT amplification factors will influence a soil-specific seismic-hazard curve that incorporates site-specific site amplification and its variability” (Kottke & Rathje, 2013; Pehlivan *et al.*, 2012).

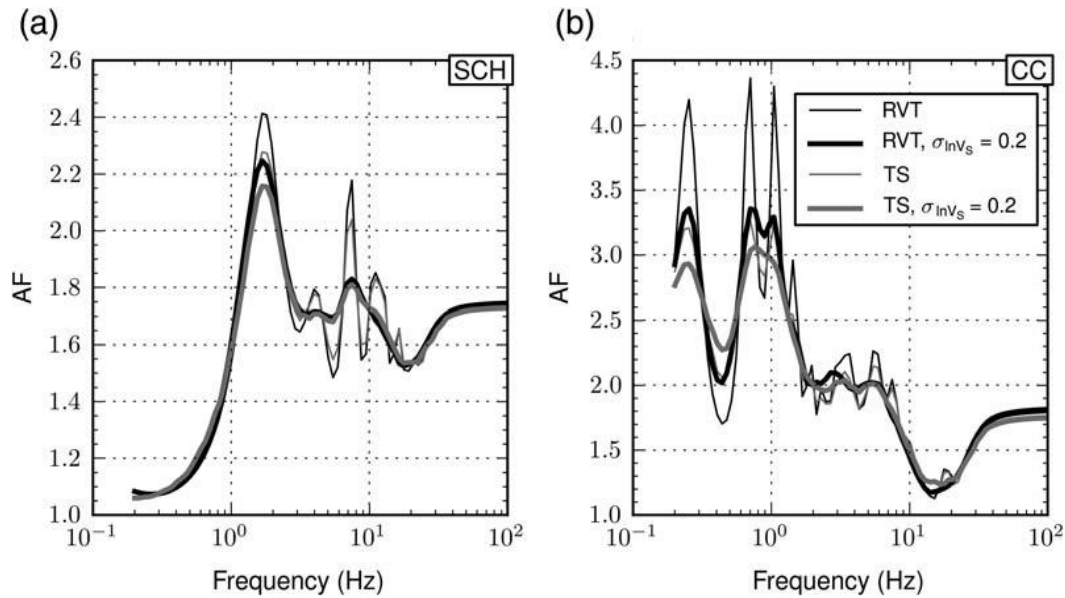


Figure 8.13. Influence of V_S variability on the site amplification predicted by RVT and TS site-response analysis (Kottke & Rathje, 2013).

Kottke (2010) also used stochastically simulated ground motions and propagated them through the Turkey Flat site in California to compare RVT and TS linear-elastic (LE) analyses (Figure 8.14). The relative differences of the spectral accelerations (δ_{Sa}) and spectral ratios (δ_{SR}) were estimated as follows:

$$\delta_{Sa} = \frac{S_{a,RVT} - \tilde{S}_{a,TS}}{\tilde{S}_{a,TS}} \quad (8.2a)$$

$$\delta_{SR} = \frac{SR_{RVT} - \tilde{SR}_{TS}}{\tilde{SR}_{TS}} \quad (8.2b)$$

where $S_{a,TS}$ and SR_{TS} are the median spectral acceleration and median spectral ratio of the time series simulations. The relative difference in the surface response spectrum was as large as 10% while it only reached 5% in terms of relative difference in spectral ratios (Figure 8.14). Kottke (2010) attributed the difference on the surface response spectrum to the relative difference observed in the input response spectrum for the stochastic input motions (Figure 8.15).

Kottke (2010) also explained that due to RVT's smooth variations in the input FAS and lack of valleys or peaks within the width of the peak of the site's transfer function, it propagates the full strength of the transfer function to the surface and predicts a larger spectral ratio. Typical input ground motions for TS analyses will have some irregularities in the FAS across the peak in the transfer function (Figure 8.16). Hence, the median spectral ratio from a suite of time-series analyses will never be as large as calculated by RVT analyses.

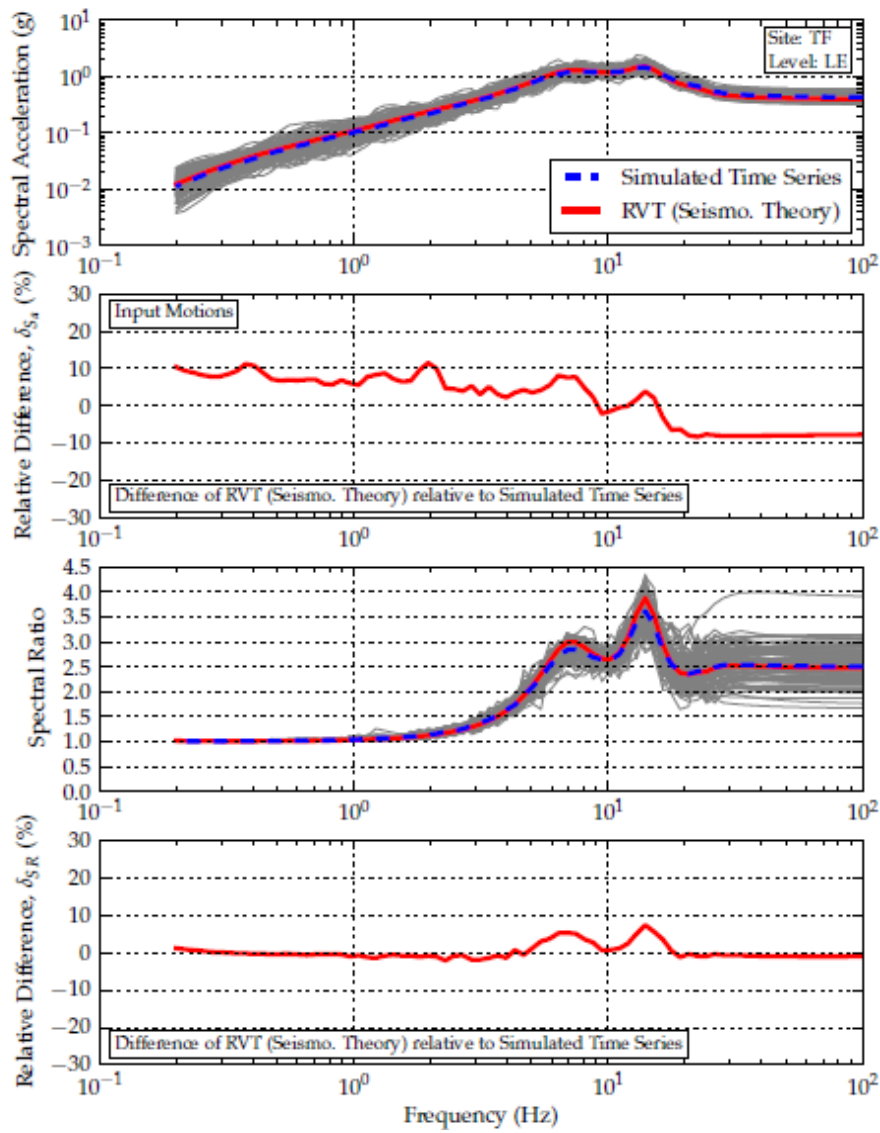


Figure 8.14. The response spectrum, spectral ratio, and relative difference for the Turkey Flat site computed with LE site response using simulated TS and an RVT motion defined by seismological theory (Kottke, 2010).

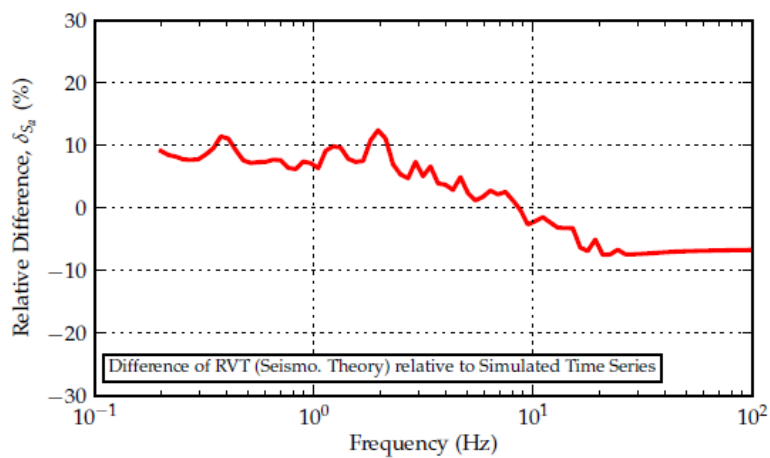


Figure 8.15. Relative difference of the input response spectrum for the stochastic input motions (Kottke 2010).

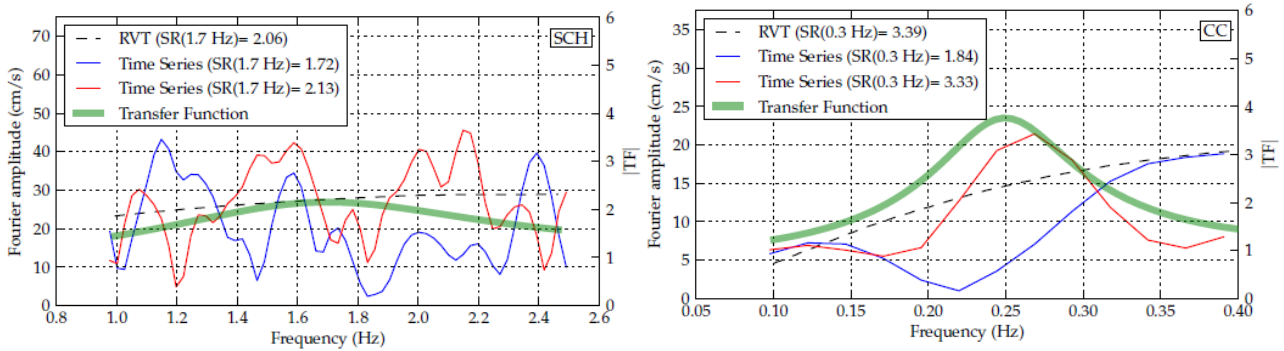


Figure 8.16. The input FAS for the time series with the largest and smallest spectral ratios for the SCH (*left*) and CC (*right*) site, along with the input FAS of the RVT analysis and the LE transfer function.

EQL site response analyses were also conducted to investigate the influence of input motion intensity and induced shear strains on the agreement between TS and RVT analyses. Input motions with median PGA of 0.17g and 0.4g were used. The comparison is presented in Figure 8.17 in terms of the parameter α_{AF} , however RVT results were not corrected for duration given that such correction was developed (and only applicable) to LE analyses (Kottke & Rathje, 2013).

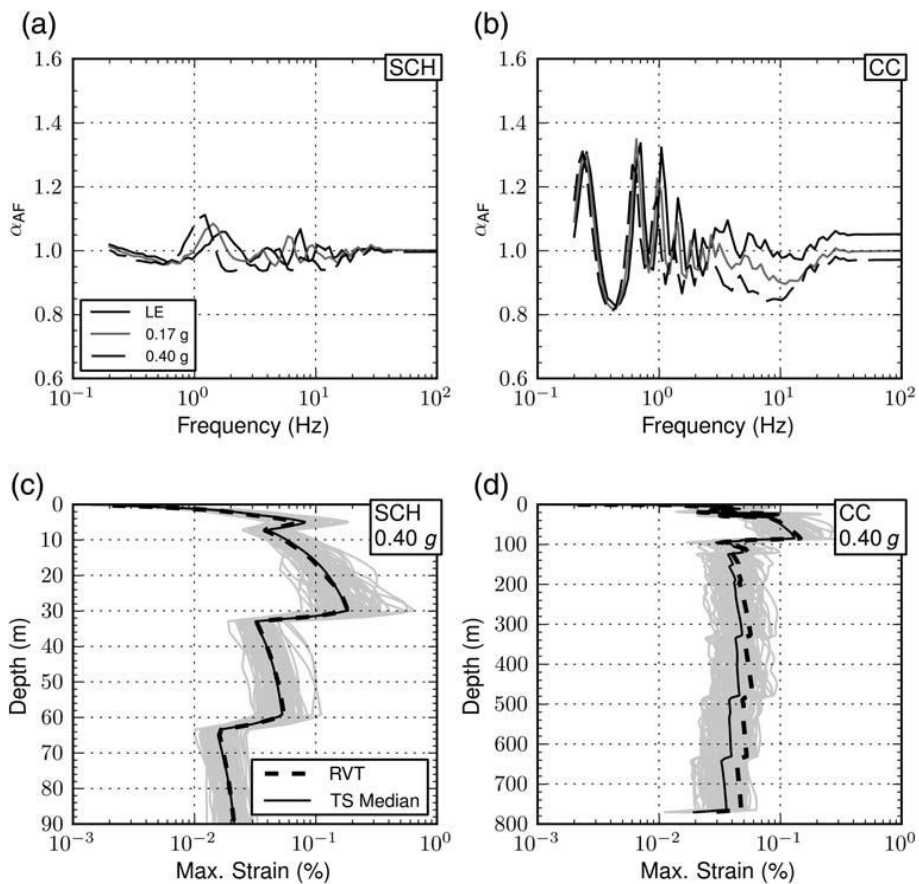


Figure 8.17. The influence of input motion intensity on α_{AF} (*a, b*); peak shear-strain profiles from RVT and TS analyses and an input PGA of 0.4g (*c, d*) (Kottke & Rathje, 2013).

Softening of strain-compatible properties at the SCH as the intensity of the input motion increases causes the site frequency to decrease and the peak α_{AF} to shift to lower frequencies. The resulting shear strains from both approaches at this site are very similar. In contrast, no significant changes in α_{AF} are observed at the CC site; probably because the large depth of the site controls the site frequency. However, the mismatch that takes place at frequencies higher than 3 Hz might be related to the larger shear strains predicted by the RVT EQL analyses. According to Kottke & Rathje (2013) “*while the levels of damping associated with the moderately larger strains are not significantly greater, when integrated over a very deep site they result in the smaller amplification factors at higher frequencies from RVT analysis*”.

Kottke (2010) conducted similar analyses and found that differences in EQL site response as computed by means of RVT and TS analyses are influenced by both the site properties and the characteristics of the input ground motion. The major findings of his work are summarized below:

- The smooth shape of the RVT input FAS is more sensitive to the site transfer function than the irregular FAS of a time series, which results in larger amplification at the frequencies associated with peaks in the transfer function and less amplification at frequencies associated with troughs in the transfer function for RVT analyses. These differences are more important for sites with low natural frequencies and larger bedrock V_s (relative differences can be as high as 30%).
- The relative difference of RVT at the site frequency increases with increasing intensity because the RVT analysis does not take into account how individual motions strain a site differently (Figure 8.18).
- Sites in which RVT predicts significantly larger spectral ratios at the site frequency may induce larger strains that lead to smaller spectral ratio values for RVT at high frequencies (*i.e.*, RVT predicts larger strains and associated damping than the time-series analysis).

Pehlivan (2013) studied the effects of varying the V_s profiles on AF resulting from RVT and TS analyses. Figure 8.19 shows how much more significant incorporating V_s variability can be for RVT results in comparison with TS analyses. A comparison of AF obtained from TS and RVT analyses is shown in Figure 8.20, where as shown before, incorporating V_s variability improves the agreement between both approaches.

Analogously to the results presented in Figure 8.19, Pehlivan (2013) investigated the comparison between TS and RVT EQL site response analyses at a deep soil site—the previously mentioned CC site, also used by Kottke (2010) and Kottke & Rathje (2013)—but this time just for three periods (*i.e.*, PGA, 0.4 s and 1.6 s). Her findings are shown in Figure 8.21. The significantly larger AF from RVT-based analysis at the CC site for some periods has been reported previously by Kottke (2010) and Kottke & Rathje (2013). These authors suggested that the difference responds to changes in ground motion duration that are ignored in current implementations of RVT site response analysis. As also indicated by previous studies, an improved agreement can be achieved by incorporating V_s profile

variability into the site response analyses. In the example presented in Figure 10, the peak observed in the RVT analysis with $\sigma_{\ln V_s}=0.2$ is comparable with the peak observed in the TS analysis with $\sigma_{\ln V_s}=0.0$ (Pehlivan, 2013). As noted by Pehlivan (2013), not only the peak of the RVT results is reduced; as V_s variability is incorporated in TS, the peak in AF also diminishes. However, the reduction caused in RVT results is more pronounced, which leads to an improved match with TS AF.

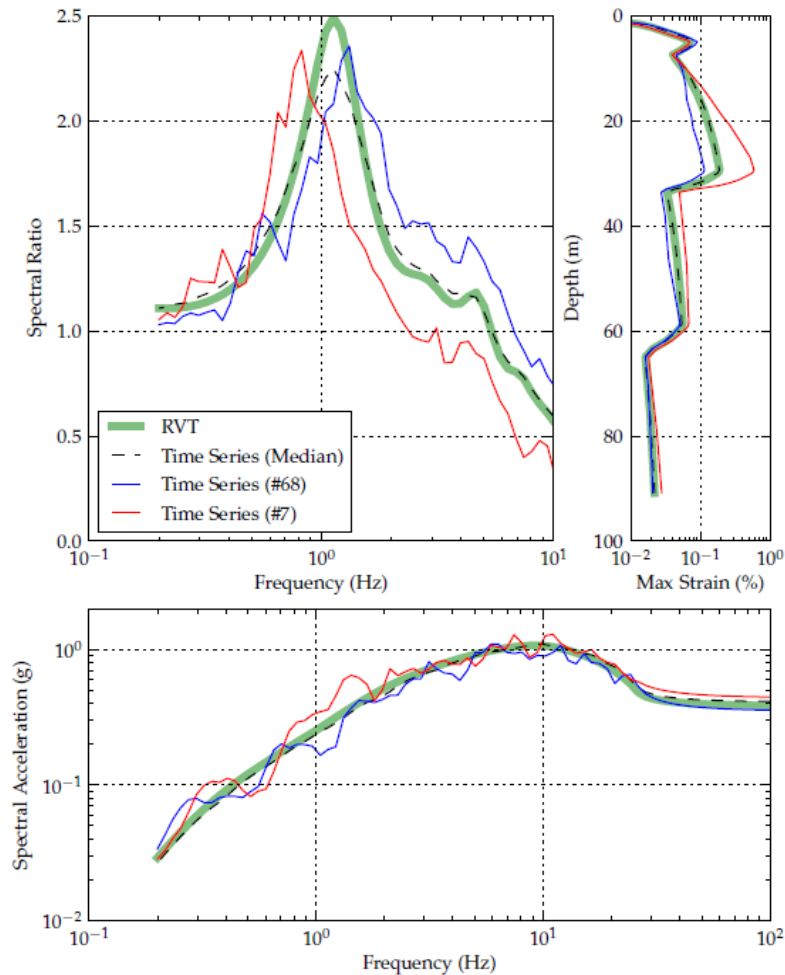


Figure 8.18. The spectral ratio and maximum strain profiles for selected motions propagated through the SCH site with an input PGA of 0.40g (Kottke, 2010).

An important reason for the differences in RVT and TS analyses is the effect of duration. An increase in duration for a given FAS results in a reduction in the root mean square acceleration (a_{rms}) as calculated by the RVT method (Kottke & Rathje, 2013):

$$a_{rms} = \sqrt{\frac{2}{D_{rms}} \int_0^{\infty} |A(f)|^2 df} = \sqrt{\frac{m_0}{D_{rms}}} \quad (8.3)$$

where $A(f)$ is the Fourier amplitude at frequency f , m_0 is the zero-th moment of the FAS, and D_{rms} is taken as the ground motion duration (D_{gm}) when using RVT to compute PGA. An increase in a_{rms} leads to smaller PGA values and spectral acceleration that ultimately would

translate into smaller AF from RVT analyses. However, the impossibility of RVT analyses accounting for the increased duration of the time-series due to the response of the site has been found to be a potential cause for RVT-based AF being larger than TS-based AF (Kottke & Rathje, 2013).

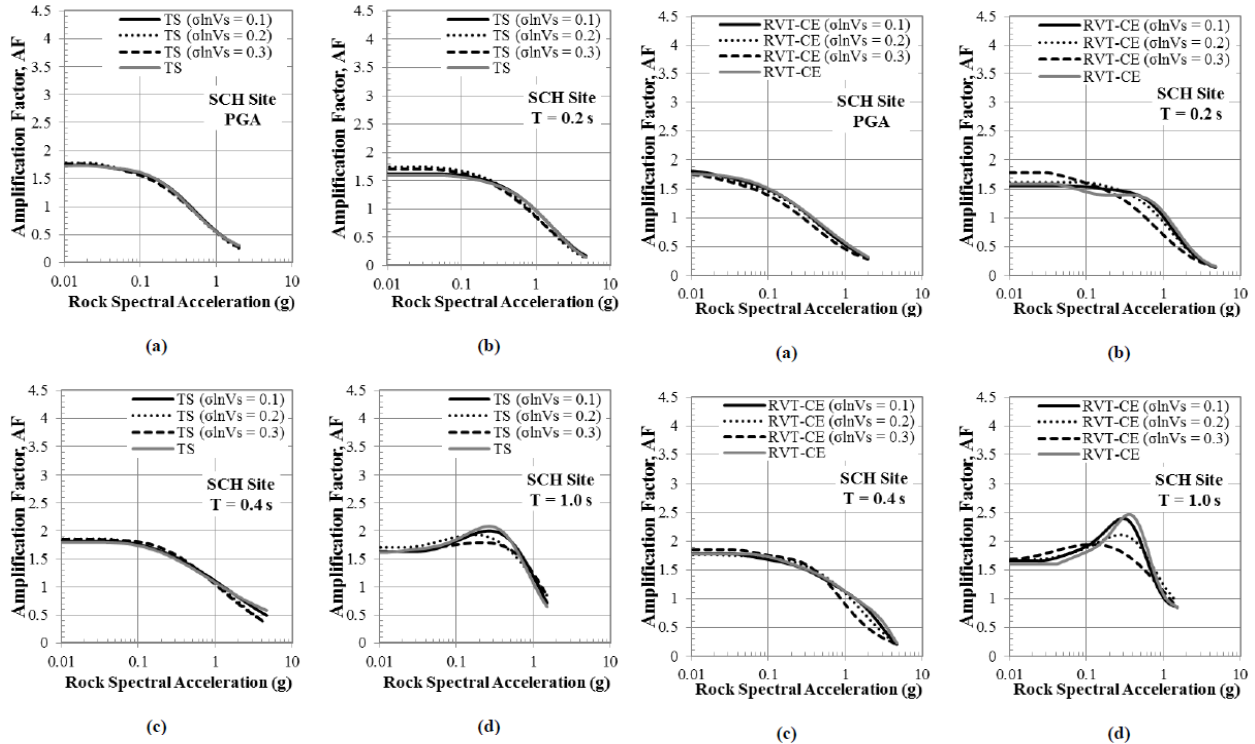


Figure 8.19. Comparison of functions of TS analyses (*left*) and RVT-CE (controlled earthquake, see Pehlivan, 2013) analyses (*right*) performed with sigmas of 0.1, 0.2, and 0.3, respectively at different periods: (a) PGA, (b) 0.2 s, (c) 0.4 s, and (d) 1.0 s (Pehlivan, 2013)

The significant duration of input and surface motions (defined as the time interval between the occurrence of 5% and 75% of the Arias intensity of the acceleration time history) was computed for different site conditions and the resulting ratio is shown in Figure 8.22 versus oscillator frequency for comparison purposes. It was found that as the natural frequency of a site decreases, differences in duration of surface and input motions increase. However, the most significant variation in duration was observed when the bedrock V_s is larger because of the multi-reflections in the soil column due to stronger impedance contrasts (Kottke & Rathje, 2013). Moreover, similar shapes of the ratios provided in Figure 8.12, led the authors to suggest that it is the changes in duration that causes the over-prediction of RVT-based AF. A simple correction proposed by Kottke & Rathje (2013) to account for the variation in duration (*i.e.*, dividing AF by the square root of the duration ratio) has proved to reduce the resulting differences between TS and RVT analyses as seen in Figure 8.23.

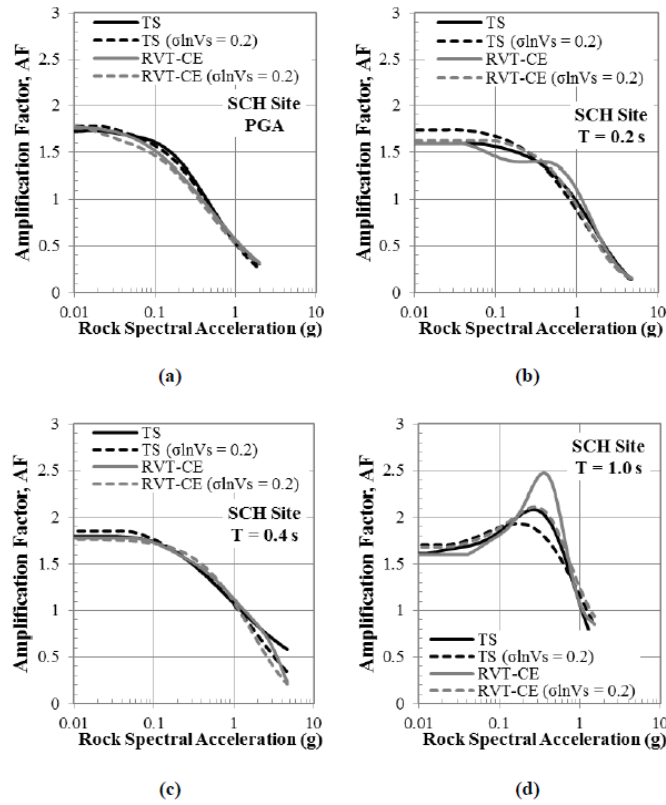


Figure 8.20. Comparison of functions predictions of TS and RVT-CE analyses performed with and without spatially varied V_s profiles (Pehlivan, 2013).

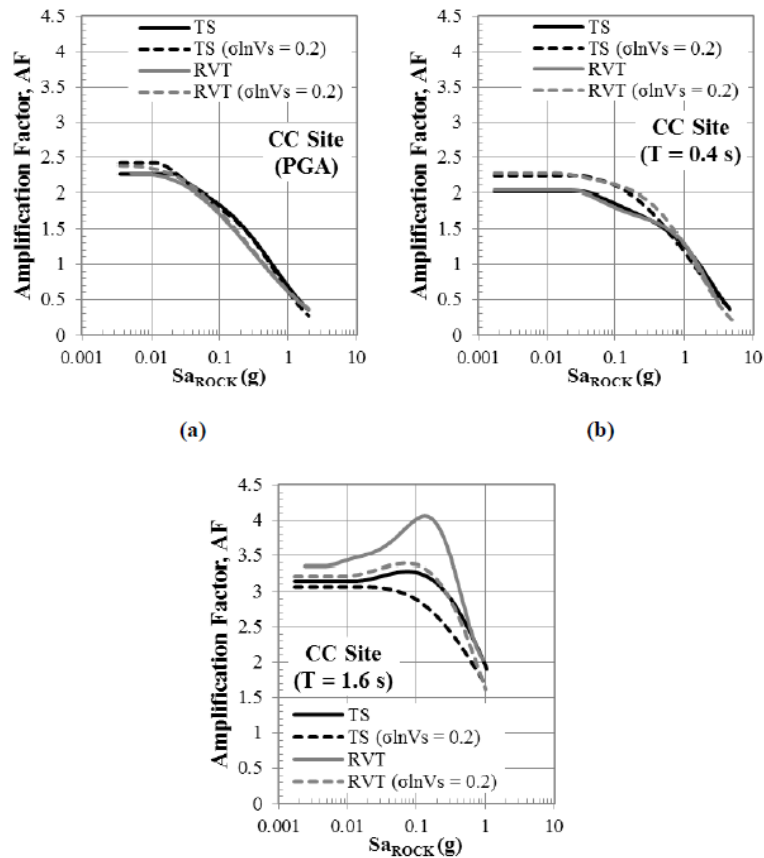


Figure 8.21. Comparison of functions predictions of TS and RVT analyses at the CC site (Pehlivan, 2013).

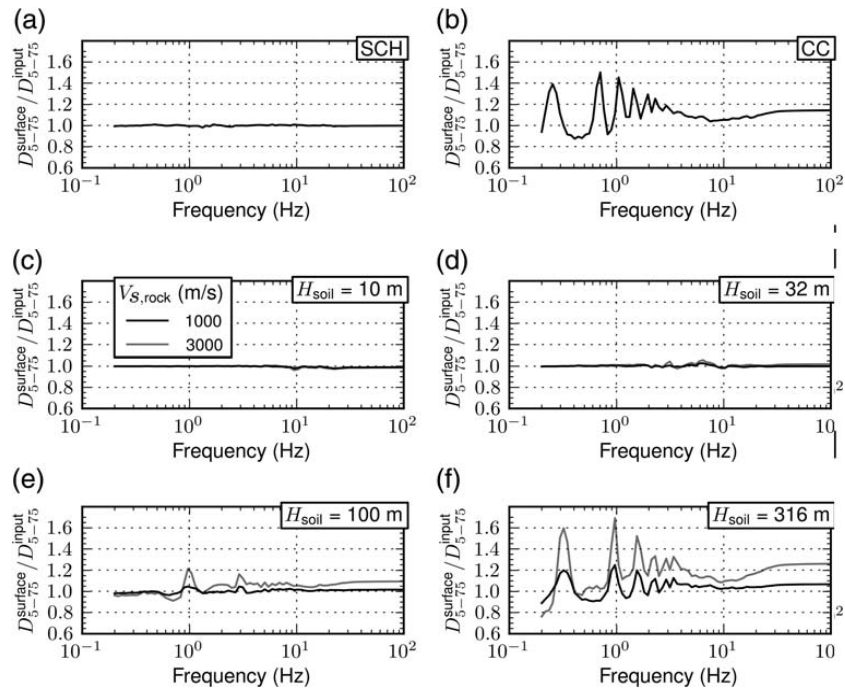


Figure 8.22. Ratio of the duration of the oscillator response of the surface motion to the duration of the oscillator response of the input motion (Kottke & Rathje, 2013).

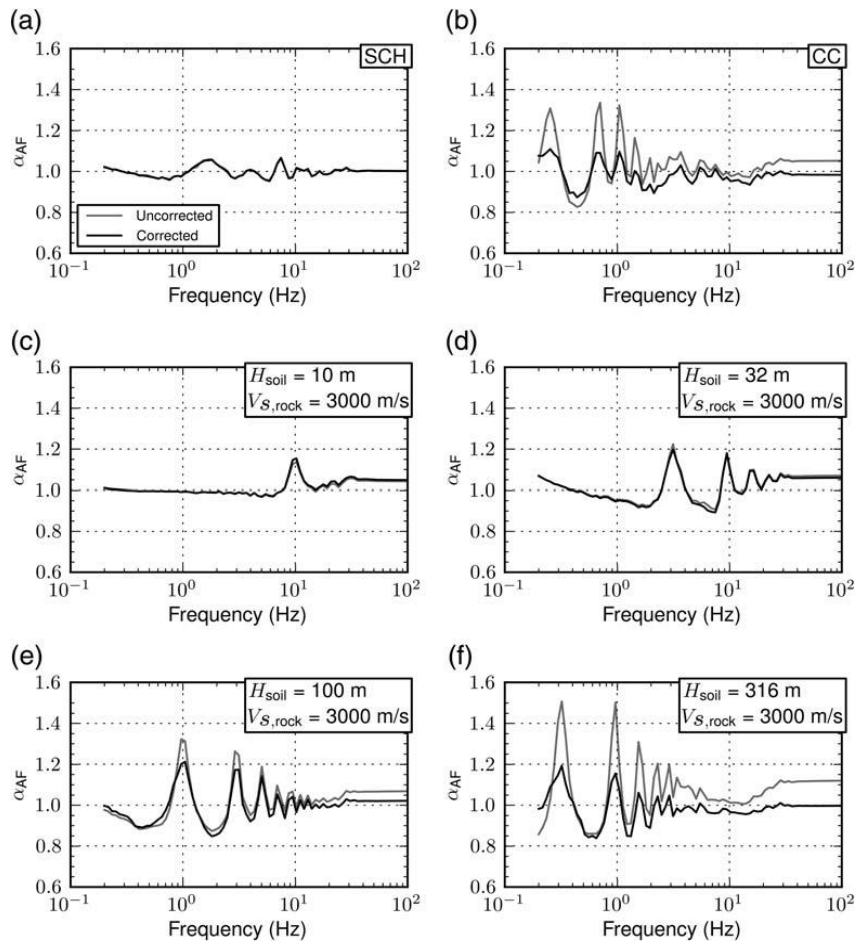


Figure 8.23. α_{AF} computed with the uncorrected RVT results and duration-corrected RVT results for each site analyzed (Kottke & Rathje, 2013).

It is important to note that the correction proposed by Kottke & Rathje (2013) is only theoretically applicable to linear-elastic conditions and it is based on duration estimates from TS analyses. However, these authors cite previous studies (e.g., Boore & Joyner, 1984; Liu & Pezeshk, 1999; Boore & Thompson, 2012) that have developed similar correction factors but in terms of spectral amplitudes computed directly from RVT and TS analyses.

The increase in duration due to the single-degree-of-freedom oscillator response must be included in the RVT calculations to obtain response spectra. Details on how to make this correction are provided in Kottke & Rathje (2013). Boore & Joyner (1984) investigated this phenomenon first when assessing RVT for use in stochastic ground-motion simulations. They noted that the increase in the duration of shaking due to the oscillator response must be taken into account in the rms calculation. They also showed that if this effect is considered RVT ground-motion simulations do not match time-domain ground-motion simulations (Rathje & Kottke, 2014).

The effect of the duration of shaking on the dynamic response of soils has been identified in other studies (e.g., Bommer *et al.* 2009). Rathje & Kottke (2014) used data from Grazier (2014) to show that the significant duration of recordings at the bedrock and at the surface differ and they show that this has an effect on comparisons between TS and RVT analyses (Figures 8.24 and 8.25). This change in duration is missing in current implementations of RVT analysis. This duration has an impact not only on the computation of the a_{rms} (Eq.8.3), but also on the estimate of peak strains. As Rathje & Kottke (2014) explain: “*The integral in Equation (1) essentially represents the energy associated with the FAS, and D_{rms} represents the duration over which that energy is distributed. Thus, a signal with the same energy and a shorter duration will generate a larger value of a_{rms}* ”.

Even though the input FAS are exactly the same for TS and RVT analyses, the response spectra differ because the duration for the RVT analysis is assigned independently of the FAS. The RVT surface-response spectrum was computed using the duration of the input ground motion and as seen in Figure 8.24c the RVT surface-response spectrum is larger than the TS surface-response spectrum at most periods. Particularly, RVT-based AF are 10-25% larger than TS-based AF at short periods, and 2 to 2.5 times larger than TS results at the fundamental modes of the site (Rathje & Kottke, 2014).

If D_{gm} is prescribed as 2.3 s (which is the significant duration of the surface motion according to TS analysis) for the RVT calculation of the surface-response spectrum, the agreement between RVT and TS surface-response spectra improves at periods less than about 0.15 s (Figure 8.25). Across all periods, the RVT response spectrum is reduced, on average, by 20% when the increased duration is used (Rathje & Kottke, 2014). Remaining differences at longer periods are most likely due to “the RVT oscillator duration correction not accurately modelling the increase in duration at oscillator frequencies associated with peaks in the FAS. The oscillator duration corrections that have been proposed in the literature (e.g., Boore & Joyner, 1984; Liu & Pezeshk, 1999; Boore & Thompson, 2012) are all based on ground-motion simulations that use smooth, seismological FAS with no local site amplification” (Rathje & Kottke, 2014).

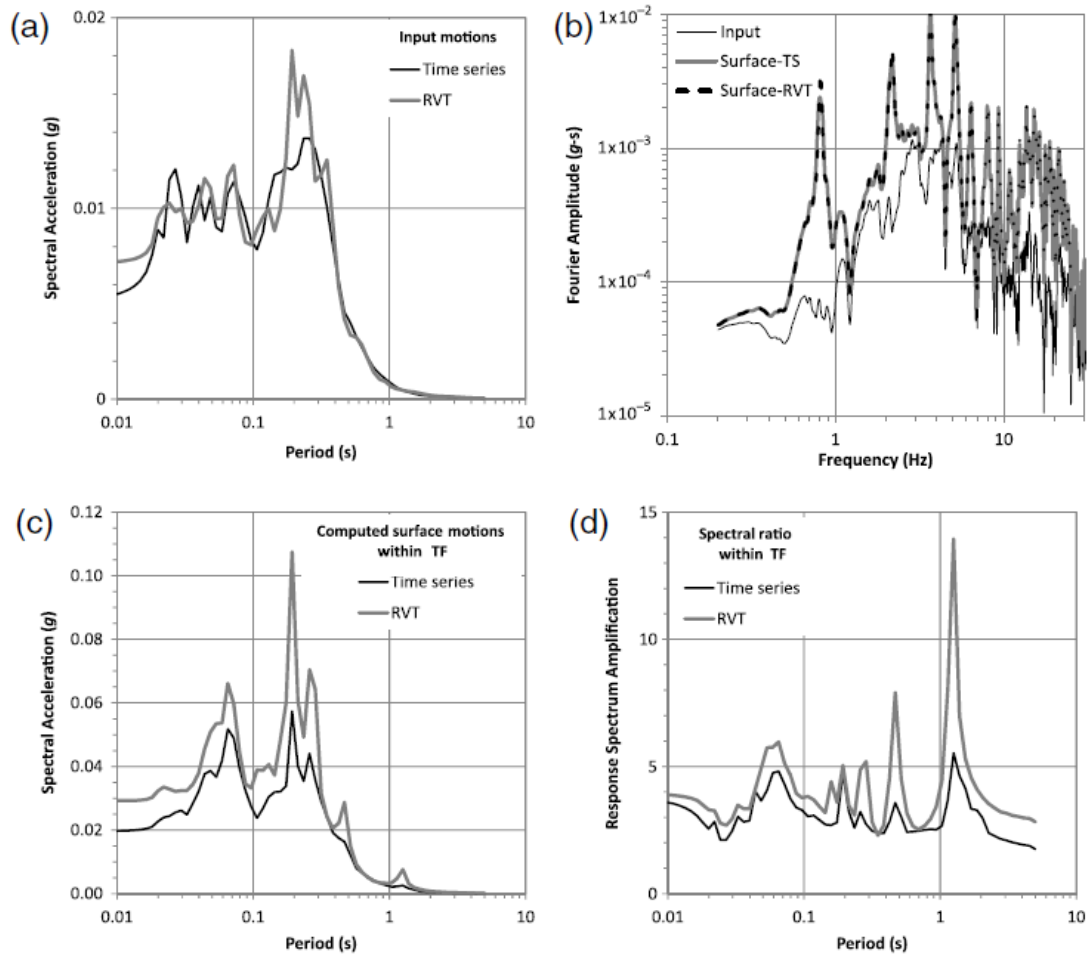


Figure 8.24. (a) Input-response spectra, (b) Fourier amplitude spectra, (c) surface-response spectra, and (d) response-spectrum amplification computed by TS and RVT site-response analyses for the Treasure Island downhole array (Rathje & Kottke, 2014).

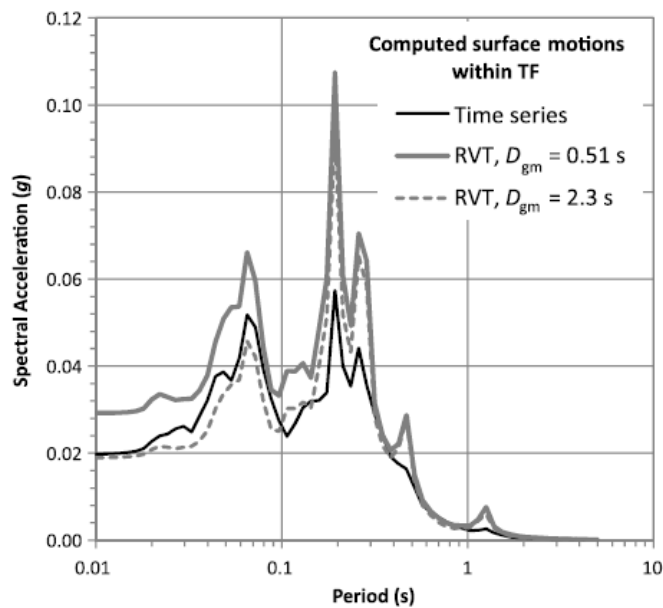


Figure 8.25. Influence of the duration of the input ground motion on computed surface-response spectrum from RVT (Rathje & Kottke, 2014).

Summary of Observations

The literature review presented in this section indicates that the choice of RVT-based EQL is justified insofar as it produces overall similar results to more elaborate non-linear time-domain analyses. An important consideration when selecting an analysis method is the possibility of model bias. The papers reviewed indicate that in general the selected analyses methods are likely to lead to positive biases in the prediction of amplification factors: RVT-based analyses are shown to consistently predict higher AFs than time series analyses, and the study of Kim *et al.* (2016) indicates that for spectral accelerations, EQL predictions of the AF are generally larger than those of NL. While other studies indicate that this is not the case in an intermediate period range, the possible under-predictions in this intermediate period range are balanced by the over-predictions due to the choice of RVT-based analyses.

8.2. Input motions at reference rock

Since the site response calculations were performed using the RVT approach in the STRATA software, the dynamic inputs at the elastic half-space need to be defined in the form of Fourier amplitude spectra (FAS) of acceleration. The STRATA program includes the facility to generate the FAS from a response spectra defined at the reference rock horizon. However, since the ground-motions at the NS_B horizon in this application are being predicted using stochastic simulations (Section 6.2), it was much more efficient to simply generate the required inputs directly as FAS using the same source, path and site simulation parameters as used for the derivation of the reference rock GMPE (Section 6.1). As for the generation of response spectral ordinates for the derivation of the GMPEs, the simulations were performed using the EXSIM software (Motazdeian & Atkinson, 2005; Boore, 2009).

A large number of reference rock motions was generated in order to capture the range of potential input motions to the layers above the NS_B horizon that could be expected from potential earthquakes in the Groningen field. The same three stress drop values that defined the lower, central and upper models for the reference rock motions—namely 50, 150 and 300 bar for magnitudes of M_L 4.5 and greater—were adopted, and for each stress parameter value the FAS were generated for 36 different combinations of magnitude and distance. Three magnitudes were considered (M_L 4, 5 and 6) that represent the main contributors to the hazard and risk estimates in the field. For each stress parameter and magnitude combination, the FAS were estimated at the epicentre and at an additional 11 log-spaced distances from 1 km to 57.7 km. The resulting 108 FAS were then ranked in terms of their intensity (based on the spectral amplitudes at 0.01 second) from the weakest to the strongest and then grouped into five sets of 21 or 22 spectra each (Figure 8.26). The purpose of this grouping was to ensure an adequate range of intensity in the reference rock motions used for each site response analysis in order to estimate both the linear and non-linear amplification factors. This was achieved by using five dynamic inputs for each site response analysis, each randomly chosen from one of the groups (Figure 8.27).

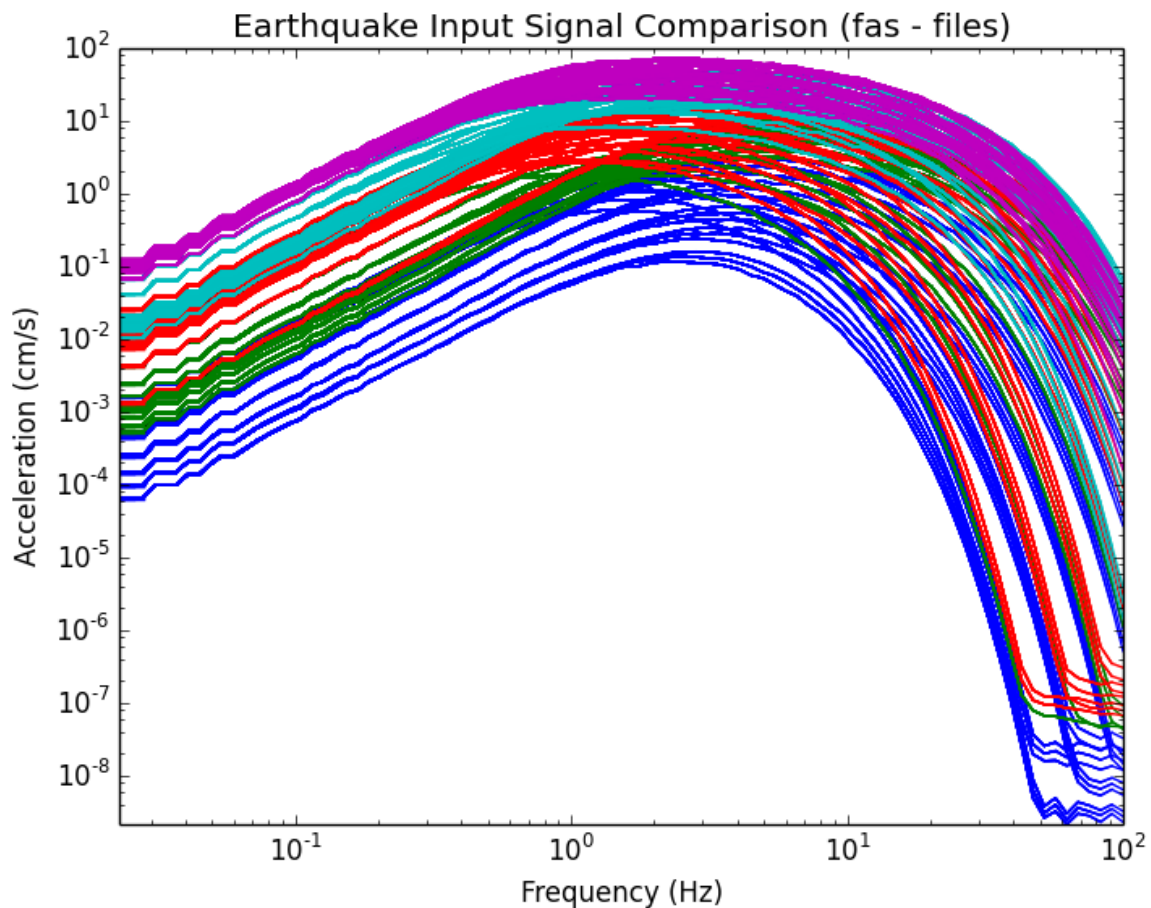


Figure 8.26. FAS generated at the NS_B horizon for use in RVT-based site response analyses

Checks were made that the sampling of the input motions had been sufficiently random to include all of the motions rather than repeatedly using the same FAS in any given site response analysis. This was considered to be important since apart from magnitude, stress parameter and distance, all other parameters used in the stochastic simulations were held constant in all cases. The overall sampling was very uniform with each of the signals used approximately the same number of times over the entire field (Figure 8.28). Checks were also made for the sampling in individual geological zones: Figure 8.29 shows the sampling in four different zones. Zones 1402 and 2002 are examples of small zones. In zone 2002, the signals were sampled approximately evenly with an average use of each one of 23 times and a standard deviation of 6. For zone 1402, the sampling was less even due to the small size of the zone: each signal was sampled on averaged only 5 times with a standard deviation of 2. Zones 1206 and 3115 are examples of large zones. In 1206, the signals were sampled evenly, with an average use of each one 104 times and a standard deviation of 11. In zone 3115 the sampling was with an average of 117 ± 10 . Based on these checks it was concluded that the selection of the NS_B motions for input to the site response analyses was sufficiently random.

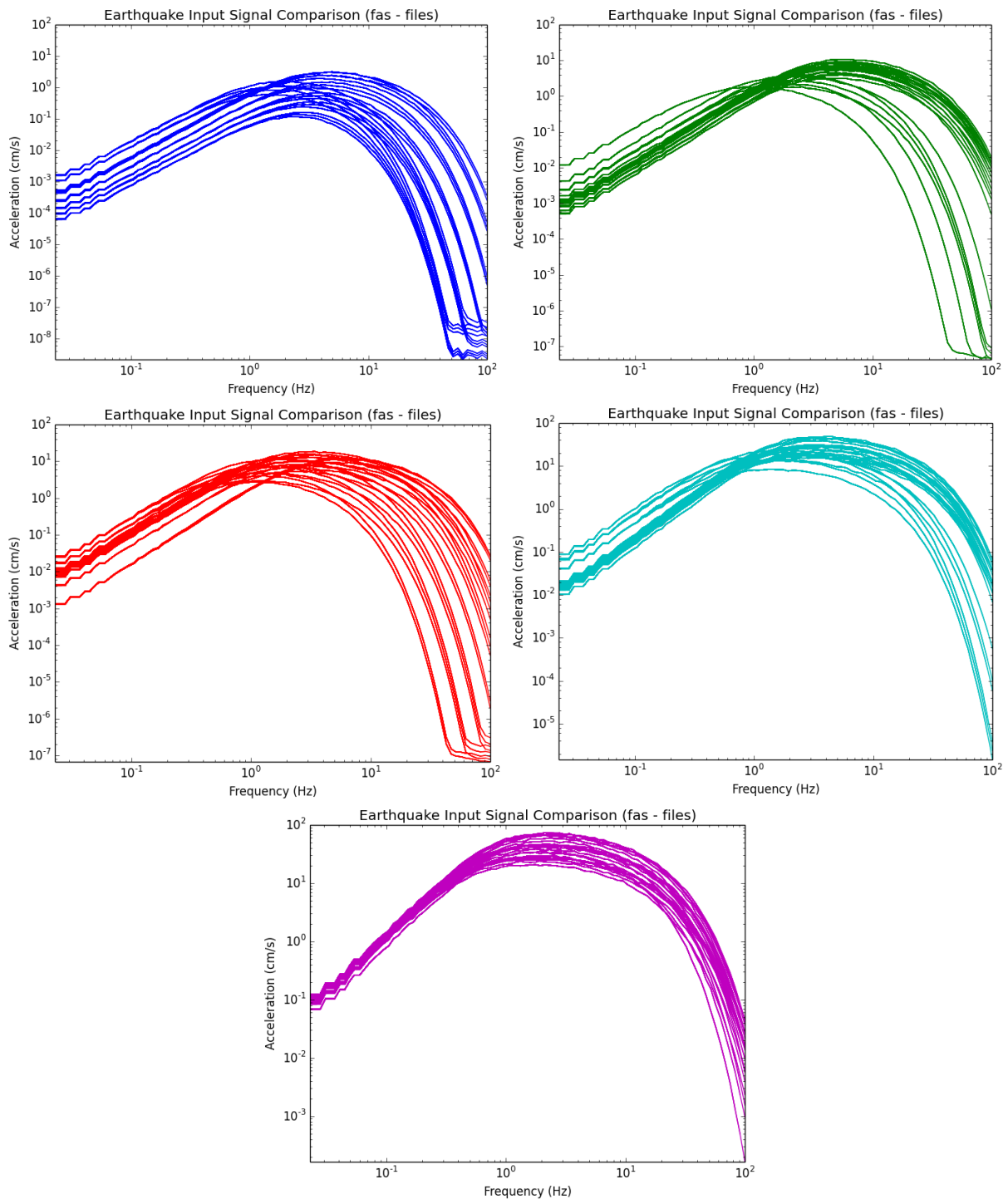


Figure 8.27. FAS generated at the NS_B horizon for use in RVT-based site response analyses shown in groups based on amplitude

The required inputs to the STRATA analyses are both an FAS and an estimate of the duration, for which the significant duration corresponding to 5-75% of the total Arias intensity is used. The durations are calculated by using the V3 duration model (calibrated to the small **M** Groningen data) as input for the sub-fault duration in EXSIM, with the average reported over 500 time-histories randomly generated for each FAS.

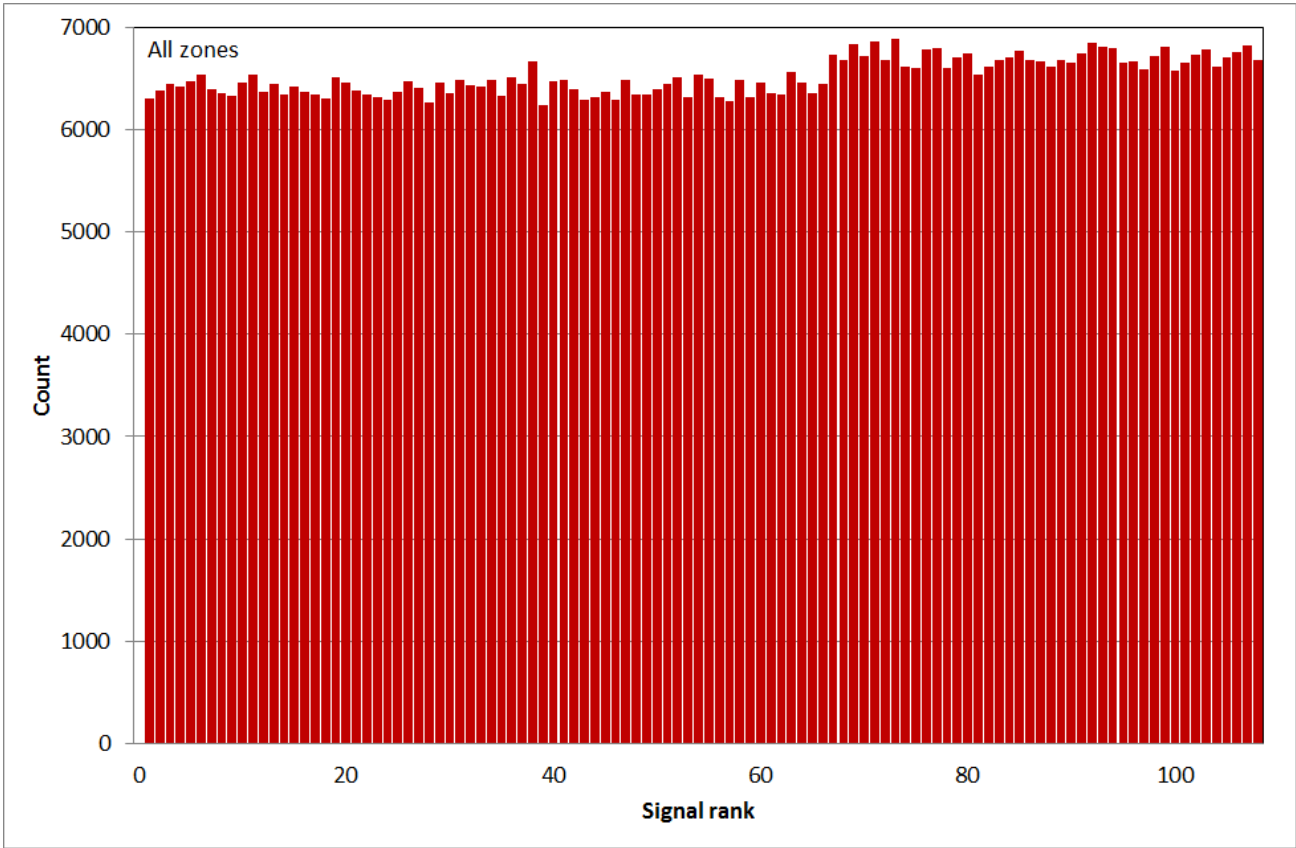


Figure 8.28. Sampling of the 108 NS_B FAS in the site response analyses over the whole field

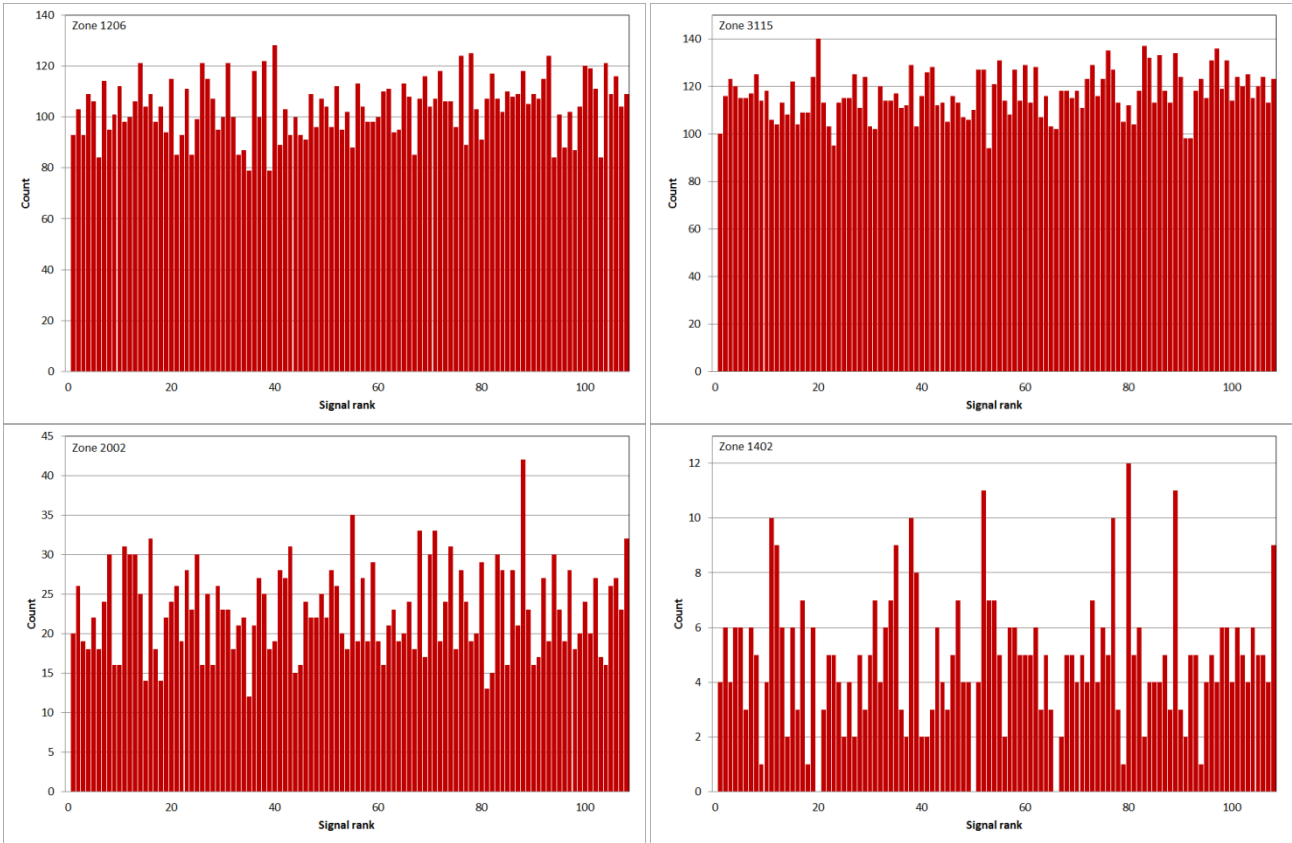


Figure 8.29. Sampling of the 108 NS_B FAS in the site response analyses for four of the geological zones

8.3. Amplification factors and variability

The spectral amplification functions (AF) were calculated using STRATA with the RVT option. Both motions at NS_B and at the surface are defined as outcrop motions (option 2A in STRATA). The input motions are entered into STRATA as Fourier Amplitude Spectra with a corresponding duration, as explained in the previous section. The spectral accelerations and PGV were computed for each input signal at NS_B and are denoted as S_{aNS_B} and PGV_{NS_B} , respectively. Five randomised input signals are used for each layer file, hence rendering five AF data points per period and layer file (input file). For each zone, all AF values were plotted versus S_{aNS_B} for each of the 23 required periods. Similarly, amplification factors were computed for PGV and were plotted versus PGV_{NS_B} . A sample of these plots for a selected zone are shown in Figure 8.31. The amplification functions (AF) were found to be strongly nonlinear, as would be expected for soft soil profiles.

For each zone and each response period (and PGV), the amplification factor is given by the following equation (Stewart *et al.*, 2014):

$$\ln(AF) = f_1^* + f_2 \ln\left(\frac{S_{aNS_B,g} + f_3}{f_3}\right) + \varepsilon \sigma_{\ln AF} \quad (8.4)$$

where f_2 , and f_3 are parameters, $S_{aNS_B,g}$ is the baserock acceleration at the NS_B horizon (in units of g), ε is a standard normal random variable, $\sigma_{\ln AF}$ is a parameter that represents the standard deviation of the data with respect to the median prediction of the model, and f_1^* is a parameter that depends on magnitude and distance as is explained below. The standard deviation $\sigma_{\ln AF}$ is allowed to vary with S_{aNS_B} (*i.e.*, a heteroskedastic model) in a manner that will be described later in this section. When the equation is applied to PGV, $S_{aNS_B,g}$ is replaced by PGV_{NS_B} in units of cm/s. The parameter f_1^* is magnitude- and distance-dependent and is given by:

$$f_1^* = \ln(\exp(f_1) + a_1(R^* - R_{anch}) + b_o(M^* - M_{anch})) \quad (8.5)$$

where f_1 , a_1 , and b_o are regression parameters, and M^* and R^* are given by

$$M^* = \min(M, M_{max}) \quad (8.6a)$$

$$R^* = \min(R, R_{max}) \quad (8.6b)$$

where M is magnitude, R is closest distance in kilometres, R_{anch} and M_{anch} are zone and period independent and are given by $R_{anch} = 10$ and $M_{anch} = 4.8$, and M_{max} and R_{max} are given by:

$$M_{max} = \begin{cases} 5.5 & \text{for Spectral Accelerations} \\ 3.8 & \text{for PGV} \end{cases} \quad (8.7a)$$

$$R_{max} = \begin{cases} 5 & \text{for } M \leq 3.8 \\ 5 + 10 \left(\frac{M-3.8}{5-3.8} \right) & \text{for } 3.8 < M < 5 \\ 15 & M \geq 5 \end{cases} \quad (8.7b)$$

Equations 8.5 to 8.7 capture the magnitude and distance dependence of the amplification factors. As discussed in Section 4.3, the magnitude and distance dependency observed in the linear amplification factors for the recording stations was observed to be approximately linear with respect to magnitude and distance, with a magnitude slope that changed with distance (the term with coefficient b_1 in Eq. 4.4). The magnitude and distance dependence for the zones could not be fully captured because the sampling of magnitude and distance of the input motions (Section 8.2) was not sufficiently broad. For this reason, the parameters a_1 and b_o in Eq. (8.5) were obtained from a single regression analyses of all of the station amplification factors shifted to a common reference point, for the stations with V_s measurements (*i.e.*, the “B” stations). For simplicity, the b_1 coefficient (see Eq. 4.3) was set to zero. The limits on magnitude and distance (Equations 8.6 and 8.7) were set by approximately matching the magnitude and distance dependency for a few representative zones. This approximate match was achieved by minimizing the average uncertainty (σ_{lnAF}) for the zones. As a result, the parameters a_1 , b_o , M_{max} , and R_{max} are period-dependent but zone-independent. The remaining parameters in Eqs.(8.5) to (8.7) (f_1 , f_2 , and f_3) are zone and period dependent. The first two parameters (f_1 and f_2) are obtained for each zone and each period through regression analyses using Maximum Likelihood regression (Benjamin & Cornell, 1970). Analogous to previous studies in the Groningen region (*e.g.*, Bommer *et al.*, 2015b), the parameter f_3 was fixed based on initial analyses of selected zones.

The choice to limit the magnitude dependence of the PGV amplification factors to a magnitude of 3.8 was made because the magnitude dependence of PGV varied significantly from zone to zone and could not be captured correctly by a single, zone-independent magnitude scaling. This aspect of the model will be modified in future versions.

An example of the AF values and the fit for zone 1208 is provided in Figure 8.30 for selected periods. Each point represents one STRATA calculation. For zone 1208, approximately 520 calculations were performed. The median fit through the data points for each period is represented by the solid lines. For simplicity, these lines are shown only for three selected magnitudes (3.8, 4.8, and 5.8) and one distance (5 km). From the example it is clear that the AFs are highly non-linear. There is a marked transition in the effects of non-linearity at periods around 1.0 to 1.5 s. The parameter f_2 is almost always negative for periods smaller or equal to 1.0 s, which implies that for larger $S_{a_{rock}}$, the AF values decrease. For periods of 1.5 s, f_2 is either positive or negative. For periods equal or larger than 2.0 s, f_2 is generally positive, indicating that soil non-linearity leads to an increase in AF at larger $S_{a_{NSB}}$.

In order to avoid unrealistic AF values outside the range of $S_{a_{NSB}}$ represented by the input motions, for each zone and each period a minimum and a maximum median AF is imposed. The minimum AF is equal to 0.25. This value is also a conservative choice that limits the reduction in ground motions resulting from the extreme nonlinear behaviour in soil layers that yield under the applied loading. The minimum AF is relevant for periods less than 1.0 s (*e.g.*,

periods of 0.05 to 0.2 s in Figure 8.30). The maximum AF is set to the predicted median AF at the maximum S_{aNS_B} according to Eq.(8.4). The maximum AF applies to cases when non-linear behavior results in an increase in predicted median AFs with increasing spectral input spectral acceleration (S_{aNS_B}), which implies a positive value of parameter f_2 (this can be seen for $T=3$ s in Figure 8.31). Positive values of f_2 occur in some cases for long periods ($T \geq 1.5$ s), and are observed because soil-nonlinearity pushes the soil into resonance at these long periods. However, this increase occurs only for a narrow range of strains (*i.e.*, for a limited range of S_{aNS_B}), hence an extrapolation of an upward trend in the median AF into higher values of S_{aNS_B} is not warranted. Hence, the limit on AF is set to prevent this unwarranted extrapolation of the model in Eq.(8.4).

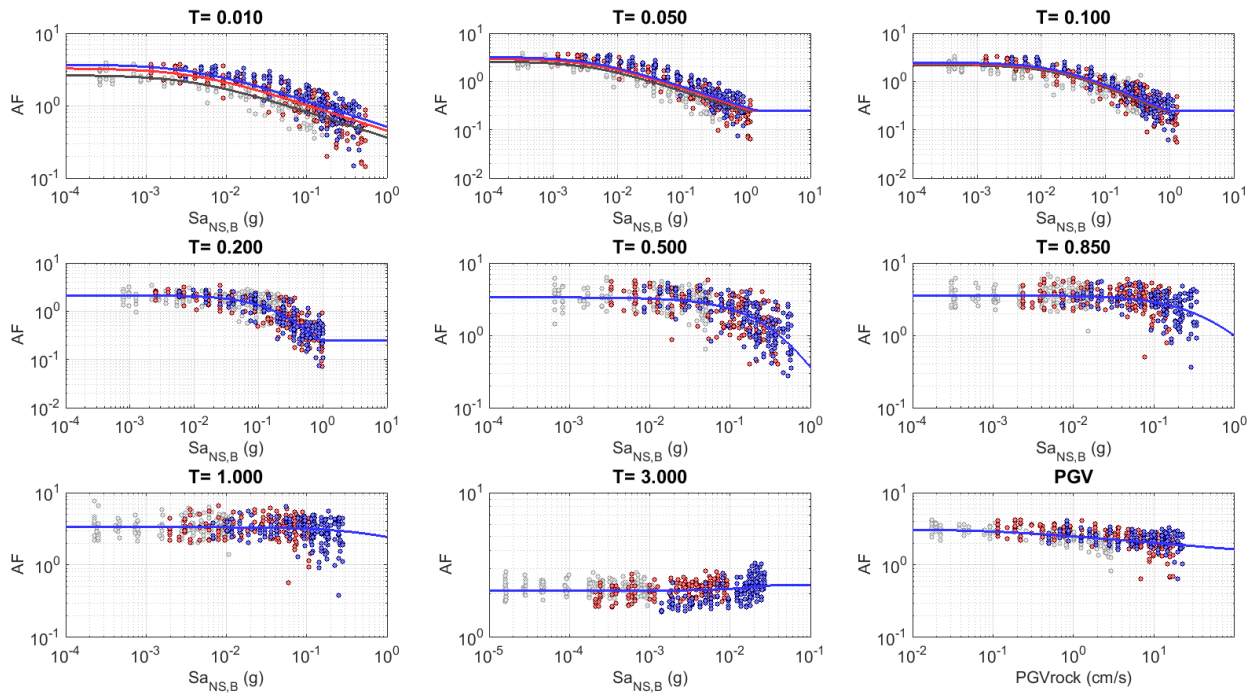


Figure 8.30. Amplification factors (AF) for zone 1208 for selected periods. The colours represent $M=3.8$ (black), 4.8 (red) and 5.8 (blue). The fit through the data is represented by the solid line, the fit line is computed for a single distance ($R=5$ km). S_{aNS_B} has units of g .

The residuals between the computed AF values and the median values predicted by Eq.(8.4) are shown in Figure 8.31. The plus/minus one standard deviation ($\sigma_{\ln AF}$) are shown by the dashed lines. Especially at smaller periods, the standard deviation varies with S_{aNS_B} (*i.e.*, an heteroskedastic model). The variation of $\sigma_{\ln AF}$ with S_{aNS_B} was modelled by a tri-linear function: a constant value σ_1 below $S_{aNS_B,low}$, a constant value σ_2 above $S_{aNS_B,high}$ and a linear increase in between these two S_{aNS_B} cut-off points (see Section 10.4).

The standard deviations obtained from Eq.(8.4) represent the uncertainty in the soil profile model at each voxel stack (Chapter 7) and the spatial variability across a zone. In addition, these standard deviations also include the effects of motion-to-motion variability because the AF were fit using a set of 100 input motions. The standard deviations, however, do not include

the effects of the variability of modulus reduction and damping (MRD). The effects of MRD uncertainty on the AF were obtained from a review of relevant literature and a study of the effect of MRD for a set of selected zones. The final uncertainty model is presented in Section 9.3.

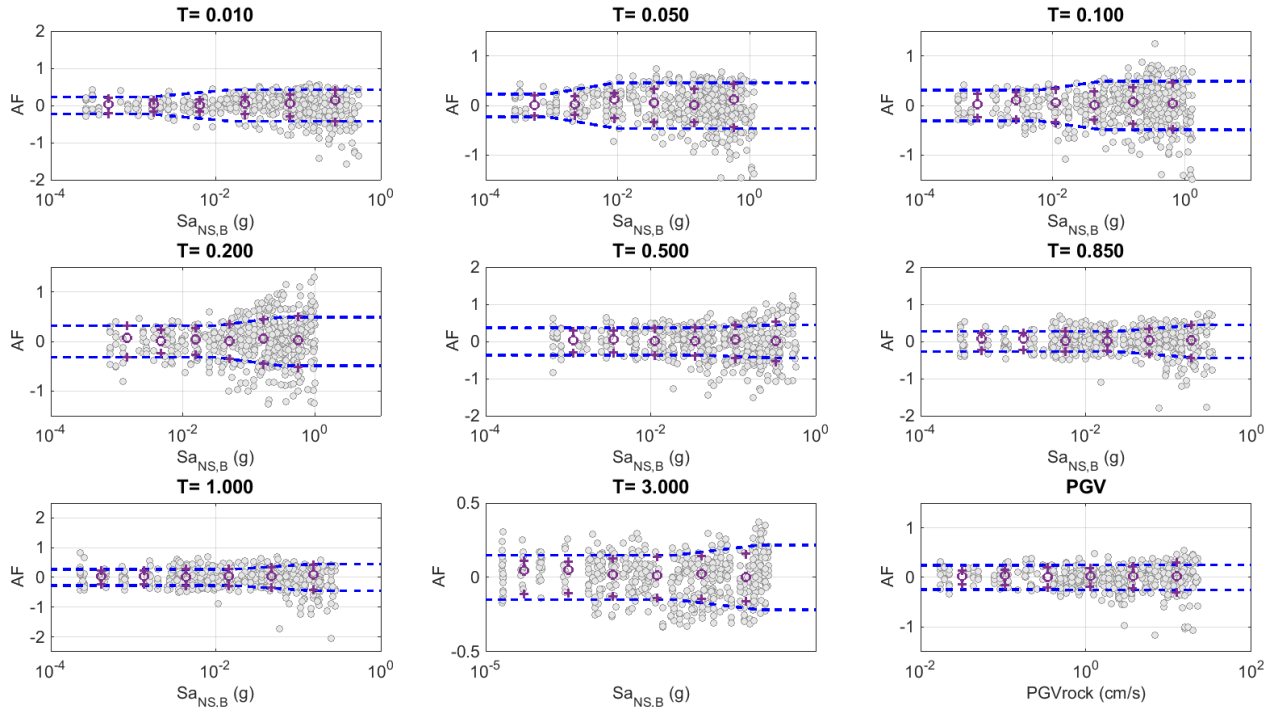


Figure 8.31. Residuals for the amplification factors for zone 1208 for selected response periods; the standard deviation is heteroskedastic; $S_{a_{NS,B}}$ has units of g . The circles and crosses represent mean and standard deviation, respectively, for binned residuals.

A notable aspect of the AFs shown in Figure 8.30 is that the nonlinearity for very short oscillator periods is initiated at very low input motions. This occurs due to two primary reasons. First, we note that the input motions in the x-axis refer to motions that are applied at a depth of about 800 m. These motions amplify prior to reaching the surface layers where nonlinearity is triggered. Another reason for this apparent initiation of nonlinearity at low input motions is the magnitude and distance dependence of amplification factors discussed in Section 4.3. In particular, the distance dependence implies that the linear AF increase in value as the distance increase, which implies that for a given magnitude the AFs would increase in value for lower values of input motions. The net effect give the appearance of nonlinearity. This is clearly seen in Figures 8.32 and 8.33. Figure 8.32 plots the AF for a selected zone and an oscillator period of 0.05 s, both using linear site response analyses and equivalent linear (EQL) site response analyses. In both cases, the observed AFs appear to be intensity dependent. When the same exercise is repeated for longer oscillator periods (where scenario-dependence is not expected), the linear AF behave as expected (Figure 8.33).

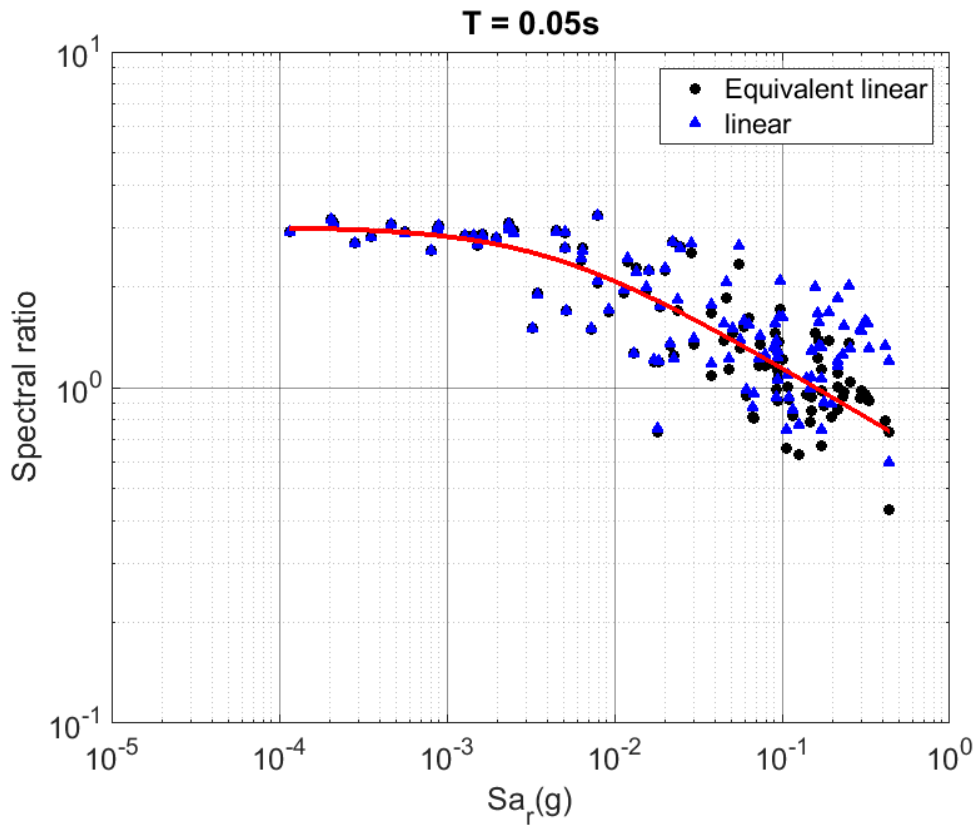


Figure 8.32. Amplification factors for a selected zone for an oscillator period of 0.05 s, using both Linear and Equivalent linear site response analyses.

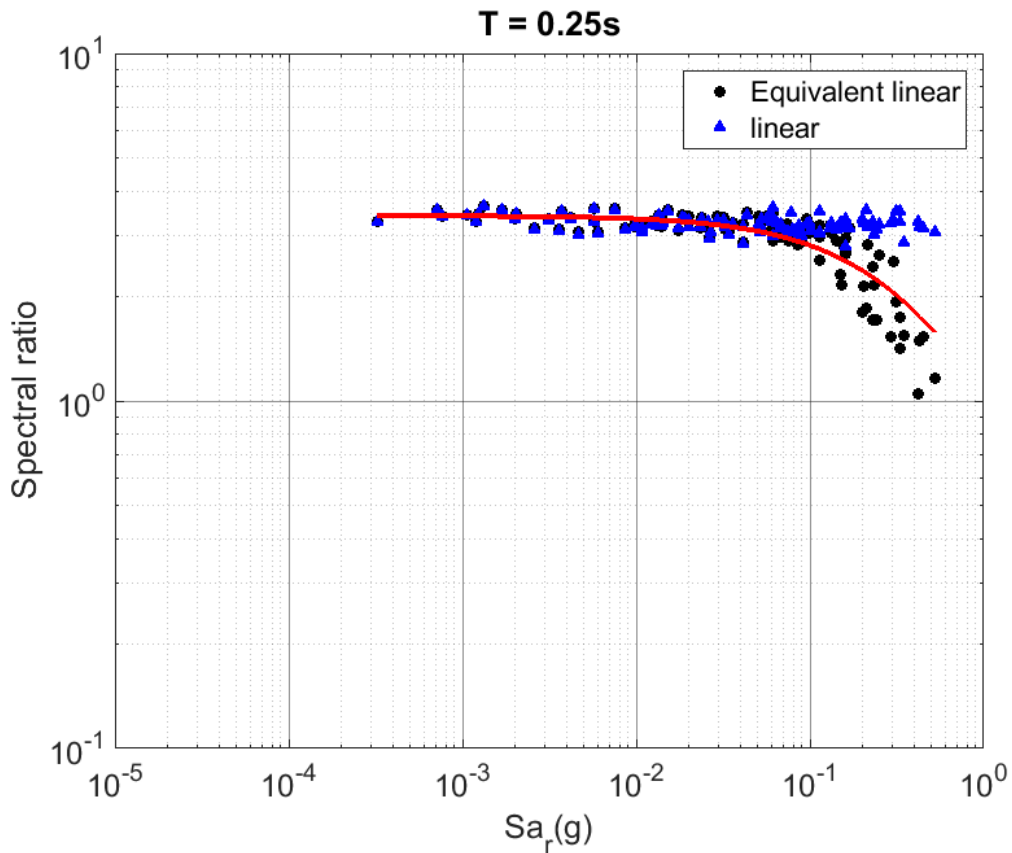


Figure 8.33. Amplification factors for a selected zone for an oscillator period of 0.25 s, using both Linear and Equivalent linear site response analyses.

9. ZONATION for SITE AMPLIFICATION FUNCTIONS

Site response in the Groningen field is accounted for through site-specific non-linear amplification factors (AF). This approach requires the development of GMPEs to predict motions at the NS_B reference rock horizon, which were broadly similar in their functional form to the V3 equations (Chapter 6). To develop a model of field-wide AFs to transfer these rock motions to the ground surface first required the development of layer models of velocity, density and damping, in addition to the selection of appropriate modulus reductions and damping curves for the different layers (Chapter 7). The model for the reference rock motions was then used to generate dynamic inputs at the NS_B horizon and these were used to run very large numbers of site response analyses for profiles covering the entire field. The output from these analyses was used to derive equations for non-linear AFs for the spectral acceleration at each of the 23 target periods (Chapter 8).

In this chapter, the zonation of the field is described whereby areas to which a common suite of AFs can be assigned are grouped into a single zone. The chapter begins with a description of the criteria adopted for grouping individual locations into zones (Section 9.1). The application of these criteria to the site response analyses results, leading to the definition of 160 zones across the study area, is described in Section 9.2. The final zone AF and their uncertainty are described in Section 9.3. Finally, Section 9.4 compares the computed AFs with the AF used at the stations for the inversion analyses, and also presents the V_{S30} characteristics of each of the zones.

9.1. Criteria for zonation

The starting point for the zonation for site response analyses is the geological model for the shallow depth range from Kruiver *et al.* (2015) and the recent update as a result of the release of the official GeoTOP model (Kruiver & Wiersma, 2016) (Figure 9.1). The Groningen field, including a 5 km buffer, but excluding the Wadden Sea, was divided into 156 geological zones. A geological zone is defined as a zone with distinct mappable geology as expressed by one or several characteristic sequence of deposits. The mappability depends on the quality and distribution of subsurface information and the associated uncertainties in the composition of each geological unit. Therefore, in some cases, a geological zone is homogeneous and contains one main characteristic sequence of deposits. In some other cases, however, the subsurface is more heterogeneous and the geological zone contains several characteristic sequences of deposits. For heterogeneous zones, smaller subdivisions were not feasible, because there is either lack of data to support a higher level of detail, or the geological zones would become too small to be of use in the hazard and risk analysis.

The geological zones were based on various sources of data including GeoTOP (version 1.3), drillings and CPTs from the Dino database, additional CPTs from two companies (Fugro and Wiertsema and Partners), the digital elevation model AHN, the Digital Geological Model (DGM), the REgional Geohydrological Information System (REGIS II), and

paleogeographical maps. The geological model of Kruiver *et al.* (2015) and Kruiver & Wiersma (2016) consists of two depth ranges: from the surface to NAP-50 m corresponds to the GeoTOP range (Figure 9.1, left) and the depth range from NAP-50 m to NS_B is covered by a separate geological model shown (Figure 9.1, right). The shallow depth range model (surface to NAP-50 m) has been used as a basis for the zonation for site amplification because soft layers in the shallow subsurface have the largest effect on site response.

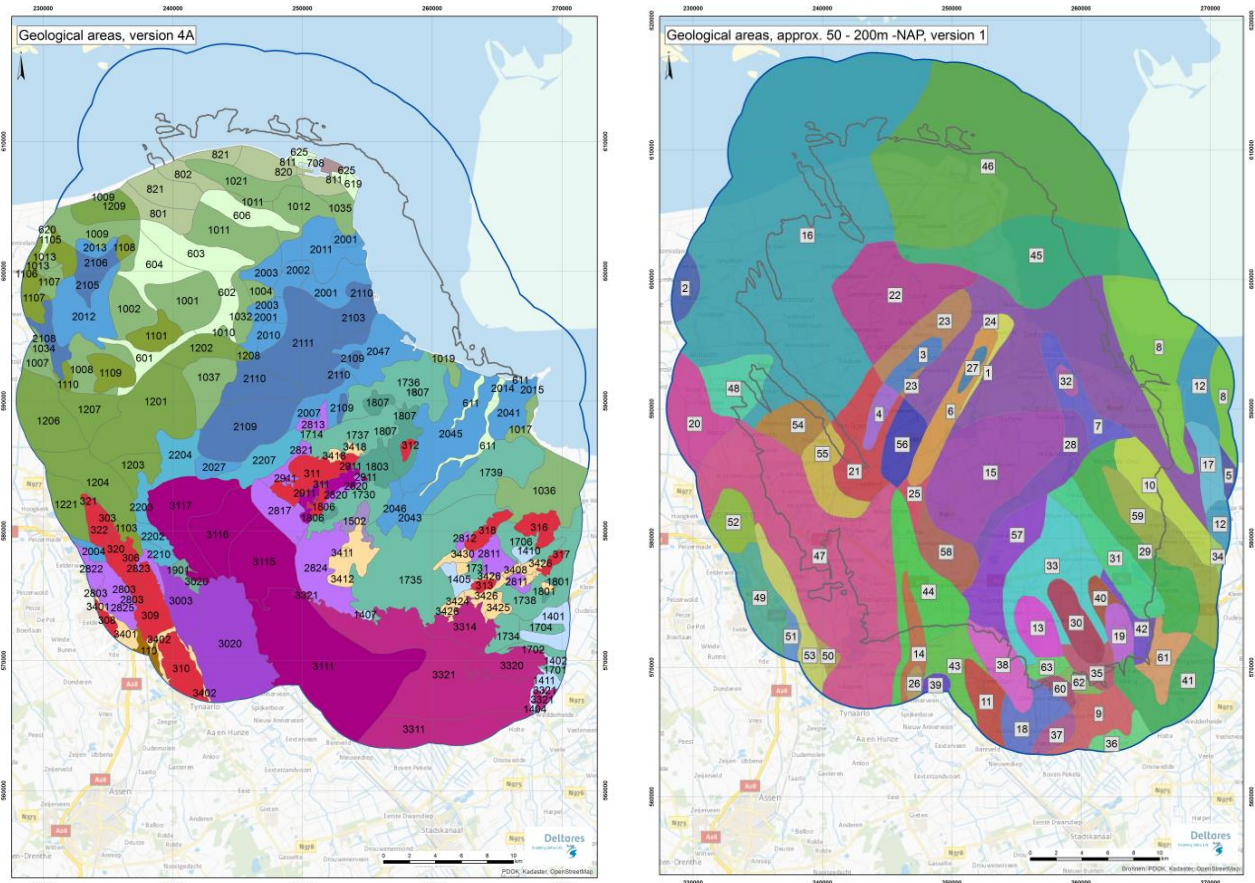


Figure 9.1. Starting point of geological zones of the geological model for site response for Groningen (Kruiver *et al.*, 2015) and Kruiver & Wiersma (2016). *Left*: depth range from surface to NAP-50 m; for legend see Figure 4.6. *Right*: for depth range below NAP-50 m, arbitrary colours

Several modifications to the original zonation of the geological model were made. These modifications were based on the AFs that were calculated from the median V_s profiles for all the voxel stacks within a zone, and an inspection of patterns of AFs for selected oscillator periods ($T=0.01, 0.1, 0.2, 0.3, 0.5$ and 1.0 s). If there were distinct zones of anomalous AFs within one zone that were consistent over various oscillator periods, then the boundaries of the zones were adjusted. This usually meant that a zone was split in two parts, based on the computed AFs for the voxels within the zone. This zonation approach is described in the next section.

9.2. Zonation of the study area

Inspection of the AF results of individual voxel stacks shows that, in general, the patterns of high and low AFs are well reflected by the geological zonation model. Figure 9.2 zooms in on the southern part of the Groningen field and shows the AF for the weakest motions (motions ranked 1-22, see Section 8.2) for an oscillator period of 0.1 s. The use of the weakest motions implies that the computed AFs are in the linear range. In total, 4 zones were split into two parts to reflect the variation of AF within the zone: three zones in the south (Figure 9.2) and one zone in the north.

Although there appear to be more zone boundaries in Figure 9.2 that seem inconsistent with the AFs, this is only the case for the oscillator period that is shown. For shorter or longer periods, the adjustment of the boundary between zones would be different. In these cases, the original zonation has been preserved and no adjustments were made.

The final zonation is shown in Figure 9.3. There are 160 zones defined in the V4 zonation of the field. A table in digital format is provided containing the zone assigned to each coordinate (see Executive Summary).

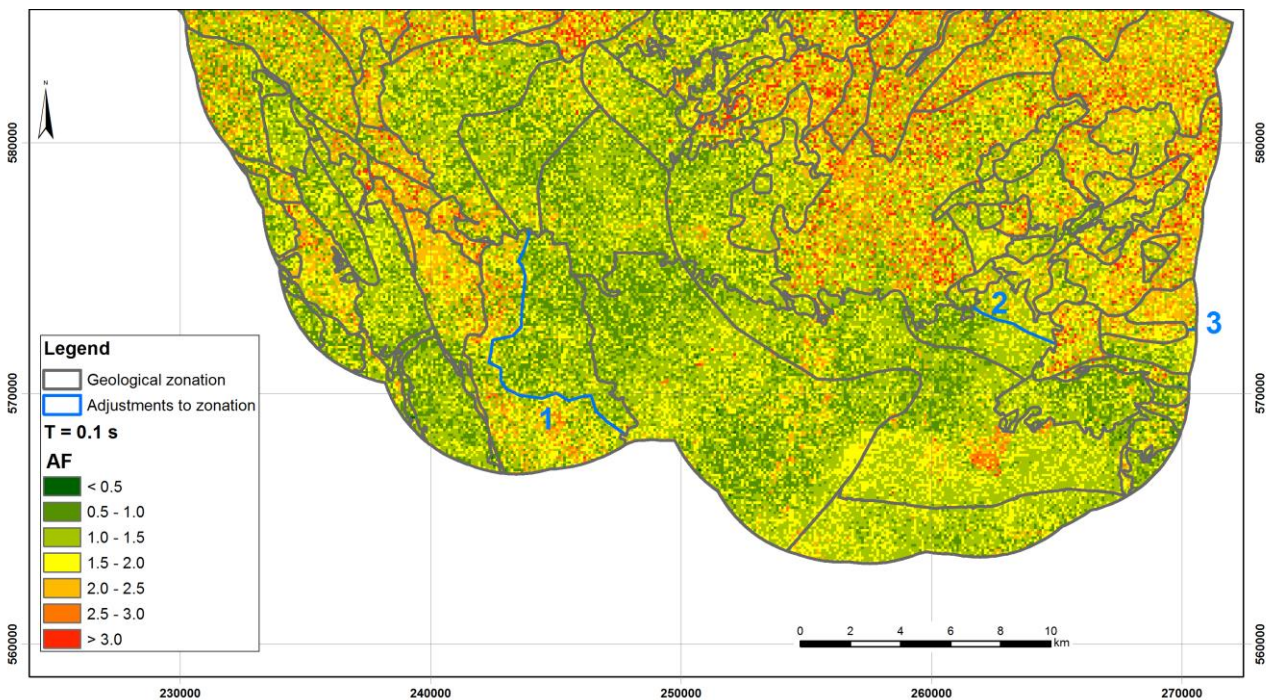


Figure 9.2. AF from the STRATA calculations, plotted for each voxel stack for the weak motions (rank 1-22) for oscillator period $T = 0.1$ s. With zonation from Figure 9.1 in grey and 4 adjustments based on AF results in purple (numbered 1 to 3, no. 4 is in north)

In GMPE V2, the Wadden Sea was excluded from the AF analysis. The inland surface waters were still included. In GMPE V3 and V4, the GeoTOP grid cells that are completely covered with water were excluded as well. These grid cells are shown in yellow in Figure 9.4. The AFs corresponding to these grid cells were not taken into consideration when computing the

amplification functions for the zone. Grid cells that are partially covered with water were included in the fit (blue in Figure 9.4). There are two exceptions: the outlines of zones 2813 and 3411 correspond to the outlines of the lake. For these lakes, the AF was calculated as if no water covered the zone. This was done simply for computational reasons (e.g., to avoid deriving amplification functions with too little or no data). For these zones, the risk is negligible because of the absence of surface structures.

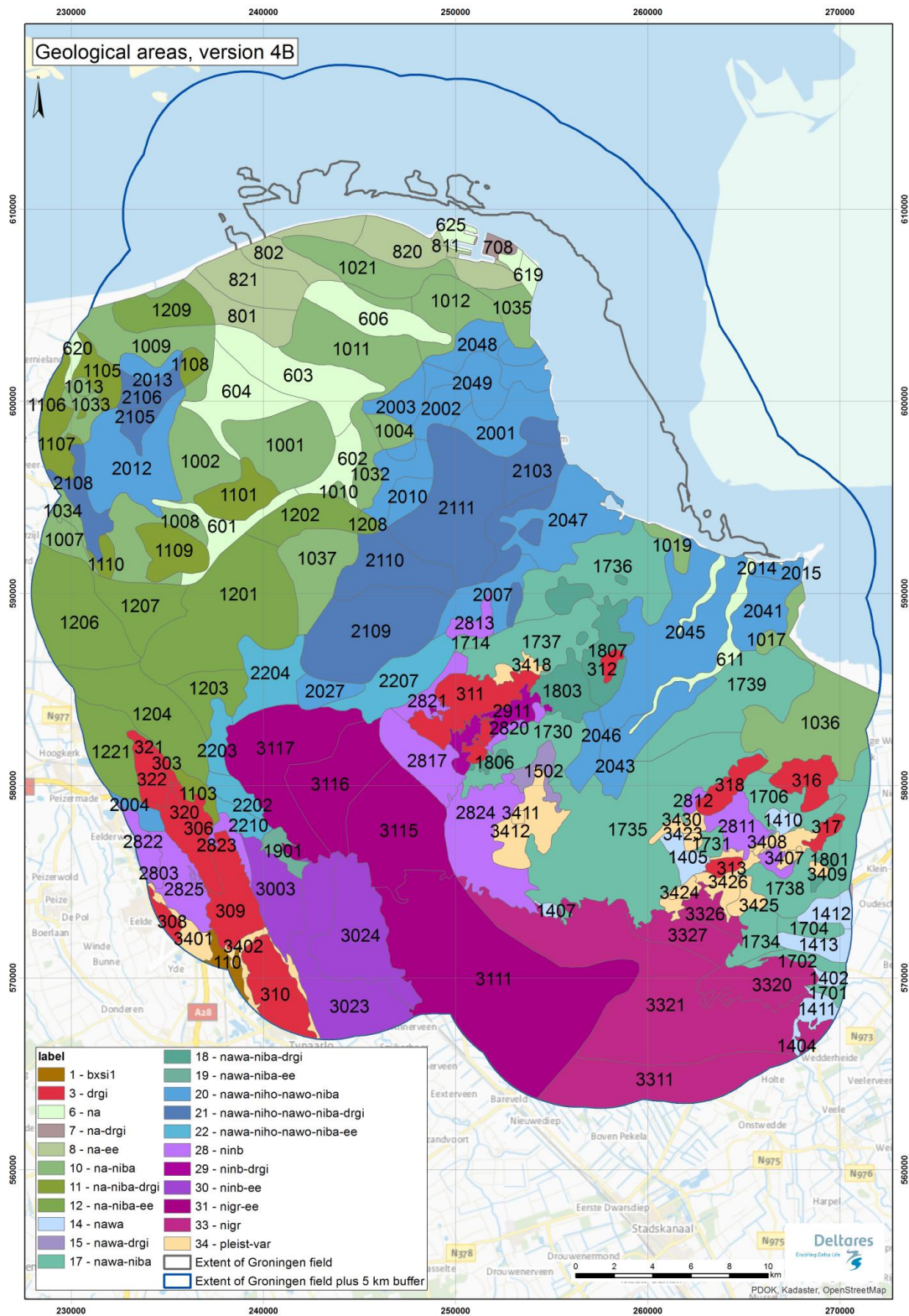


Figure 9.3. Final zonation, used for the site amplification functions in GMPE V4.

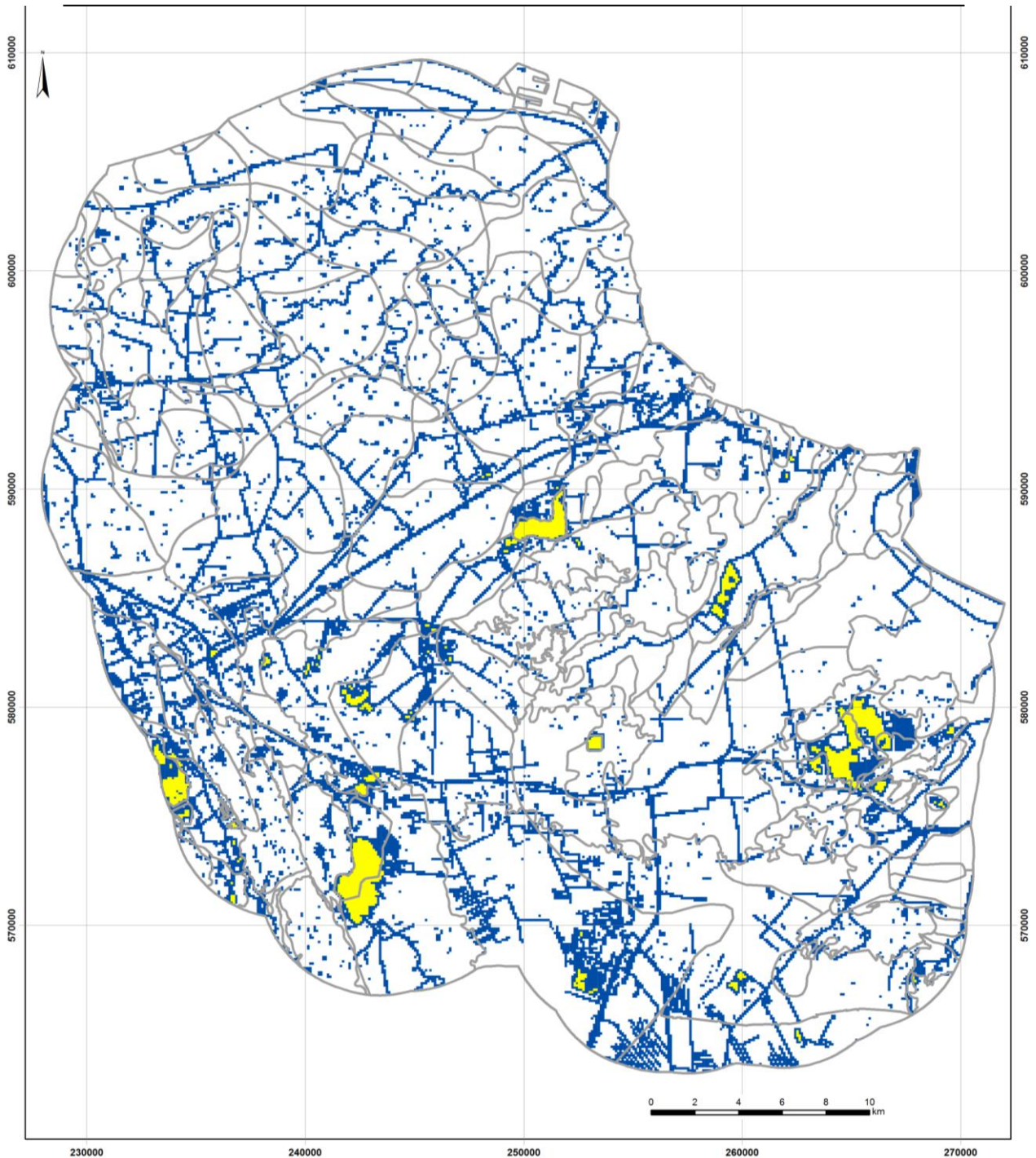


Figure 9.4. Surface water. Yellow parts contain GeoTOP grid cells that are completely covered with water. Blue parts are only partially covered with water. The grey lines show the outlines of the zonation from Figure 9.3.

9.3. Zone amplification factors

The amplification factors for the zones were computed from the site response analyses described in Section 8.3. The V_S profile for each voxel stack was randomized using the model described in Chapter 7. A single randomisation per voxel stack was used, and all the voxel stacks within a zone were grouped to compute the amplification factors for the zone. The approach was adopted because the medians and the standard deviations of V_S profiles

across a zone are relatively uniform, and the alternative (*i.e.*, to generate multiple randomization for each voxel-stack within a zone) resulted in similar results but at a much larger computational cost. The computed AF at each period were fit using Eq.(8.4), and maximum and minimum limits on the AF were imposed, as described in Section 8.3. The zone amplification functions for the entire study area are shown in Figure 9.5. Observe that these functions are highly non-linear. For the Groningen profiles, the nonlinearity implies a reduction in AF for shorter periods but an increase in the AFs at longer periods. This increase is expected as the resonant period of the sites shifts to longer periods as the soil softens.

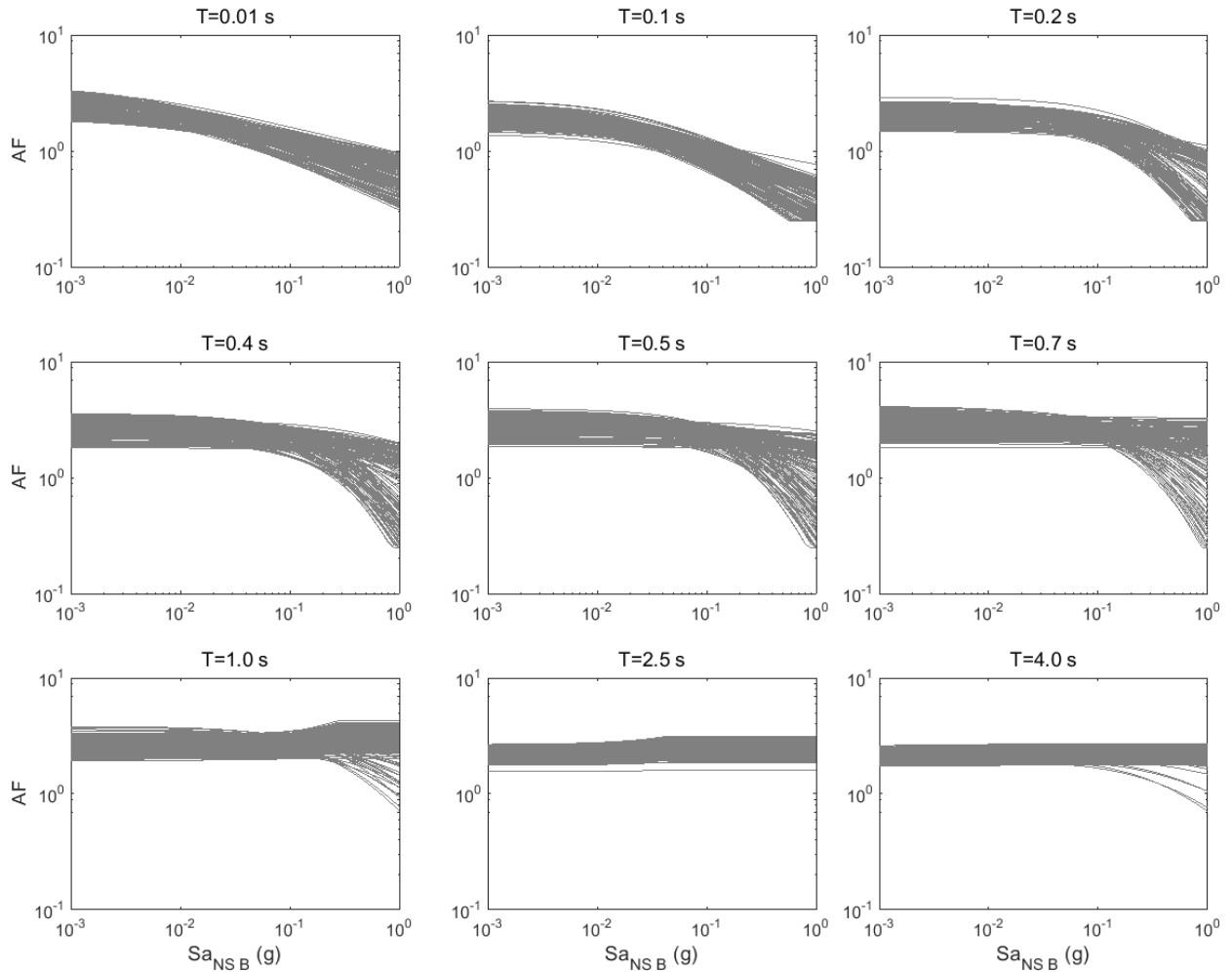


Figure 9.5. Fitted AF functions for all zones for selected periods (for M=4.5 and R=5 km).

The standard deviations of the amplification factors obtained from Eq. (8.4) (*i.e.*, $\sigma_{\ln AF}$) were fitted to a heteroskedastic tri-linear model given by:

$$\sigma_{\ln AF} = \begin{cases} \sigma_{\ln AF,1} & \text{for } Sa_{NS_B} < Sa_{rock,low} \\ \sigma_{\ln AF,1} + (\sigma_{\ln AF,2} - \sigma_{\ln AF,1}) \frac{\ln\left(\frac{Sa_{NS_B}}{Sa_{rock,low}}\right)}{\ln\left(\frac{Sa_{rock,high}}{Sa_{rock,low}}\right)} & \text{for } Sa_{rock,low} \leq Sa_{NS_B} \leq Sa_{rock,high} \\ \sigma_{\ln AF,2} & \text{for } Sa_{NS_B} > Sa_{rock,high} \end{cases} \quad (9.1)$$

where $\sigma_{\ln AF,1}$, $\sigma_{\ln AF,2}$, $Sa_{rock,low}$ and $Sa_{rock,high}$ are model parameters, and Sa_{NS_B} is the predicted spectral acceleration at the reference rock (Section 6.6). The period dependence of all the parameters in Eq.(9.1) was omitted for clarity. The parameters for Eq.(8.4), including the uncertainty parameters $\sigma_{\ln AF,1}$, $\sigma_{\ln AF,2}$ in Eq. (9.1), were computed using Maximum Likelihood regression. However, $Sa_{rock,high}$ and $Sa_{rock,low}$ could not be constrained in the regression and were determined from visual inspection for a few selected zones. The same values were applied to the entire field..

As indicated in Section 8.3, the standard deviations obtained from Eq.(8.4) and given in Eq.(9.1) represent the effect of uncertainty in the soil profile model at each voxel stack (Chapter 7) and the spatial variability across voxel stacks in a zone. In addition, the $\sigma_{\ln AF}$ also includes the effects of motion-to-motion variability. These standard deviations are the basis for the uncertainty in the site response within a zone, ϕ_{S2S} . The subscript ‘‘S2S’’ implies that this uncertainty component represents the ‘‘site-to-site’’ variability for all sites within a given zone. The following issues, which were not taken into account in $\sigma_{\ln AF}$, were considered when modifying these values to obtain the ϕ_{S2S} model:

- Contribution to uncertainty in AF due to MRD uncertainty
- Modelling error and empirical bounds

The additional uncertainty in the AF needed to account for the epistemic uncertainty in MRD was obtained through a modeling exercise at 19 selected zones. The zones were selected to represent a distribution of profile types as characterized by both the V_{S30} values and the presence of soft layers of clays and peats. The contribution of MRD uncertainty to the total uncertainty in AF was computed as follows. For each zone, a set of runs were conducted using the randomization scheme described in Chapter 7 (*i.e.*, randomizing input motions and shear wave velocity, but keeping MRD fixed at mean values). A second set of runs were conducted by also randomizing MRD curves. The contribution of MRD uncertainty (labelled $\sigma_{\ln AF,MRD}$) was then computed using:

$$\sigma_{\ln AF,MRD} = \begin{cases} \sqrt{\sigma_{\ln AF1}^2 - \sigma_{\ln AF2}^2} & \text{for } \sigma_{\ln AF1} - \sigma_{\ln AF2} \geq 0 \\ 0 & \text{for } \sigma_{\ln AF1} - \sigma_{\ln AF2} < 0 \end{cases} \quad (9.2)$$

where $\sigma_{\ln AF1}$ is the uncertainty in AF resulting from a full randomization, and $\sigma_{\ln AF2}$ is the uncertainty in AF resulting from randomizing only input motions and shear wave velocity (as described in Chapter 7). This approach implies that $\sigma_{\ln AF,MRD}$ implicitly takes into account for the correlation of the effects of shear wave velocity, input motion, and MRD effects. Equation (9.2) was applied separately for low-intensity input motions ($Sa < Sa_{rock,low}$) and high-intensity input motions ($Sa > Sa_{rock,high}$). Once the values of $\sigma_{\ln AF,MRD}$ were computed, these values were correlated to zone properties in order to extrapolate the results to other zones in the Groningen field. Additional details of this methodology are described below.

The measurement uncertainty of MRD curves was obtained from Darendeli (2001). The model proposed by Darendeli was modified to render zero uncertainty below the elastic threshold strain, because for these levels of strain the uncertainty in shear modulus is captured by the uncertainty in shear wave velocity. In the Groningen study, in addition to measurement uncertainty there is an uncertainty that results from the use of estimated soil parameters to compute the MRD curves. Namely, the curves for clays are computed from an estimated value of the plasticity index (PI) of the soil. In order to account for this uncertainty, a standard deviation for the PI was assumed to be 15, and a first order approximation (Ang & Tang, 2007) was used to propagate this uncertainty to the uncertainty in MRD curves. The uncertainty computed in this fashion was applied to the MRD curves for all materials.

An additional uncertainty on the MRD curves for clays results from the value of the undrained strength of the soil. As indicated in Chapter 7, the methodology of Yee *et al.* (2013) was used to modify the MRD curves such that its larger strain behavior is compatible with the dynamic shear strength of the soil. The same approach was used in this exercise. The standard deviation of the undrained strength of the soil was assumed to be 0.5 (in natural log units). Such a high value is warranted because of the lack of measurements of undrained strength in Groningen soils. The undrained strength was assumed to be fully correlated to the modulus reduction curve (*i.e.*, if the modulus reduction curve was higher than the median, the undrained strength was also assumed to be higher than the median).

Since modulus reduction and damping curves are applied simultaneously for a single layer, and both curves are needed for each individual soil layer, correlations are needed between the modulus reduction and the damping curves, and for MRD curves between layers. Modulus reduction and damping curves were assumed to be negatively correlated with a correlation coefficient of -0.5, following the recommendation of Kottke & Rathje (2008). A preliminary study was conducted to evaluate the effects of inter-layer correlation. For two zones, one set of runs were conducted assuming the same interlayer correlation used for shear wave velocity (Chapter 7), and another run was done for full layer-to-layer correlation. The results of these two runs were similar, with the full correlation being somewhat more conservative. For simplicity, full layer-to-layer correlation was assumed.

A final consideration is related to computational time. Performing full randomization for shear wave velocity, MRD curves, and input motions implies a very large computational time. To reduce this, we use a discrete representation of the 2D Gaussian distribution for modulus reduction and damping following Cool & Rabinowitz (1993). This implies that only 9 MRD curves are needed to fully capture the effects of MRD uncertainty. The use of the discrete sampling was validated in the preliminary exercise.

The resulting $\sigma_{\ln AF, MRD}$ for the 19 selected zones are shown in Figures 9.6 and 9.7 for the low intensity and high intensity models, respectively. As expected, the effects of MRD uncertainty are much lower for low-intensity motions than for high-intensity motions. Somewhat surprisingly, there is a very large degree of variability between zones. This partly explains the large degree of differences between previous studies that considered this phenomenon (e.g., Kwok *et al.*, 2008; Li & Assimaki, 2011; Rathje *et al.*, 2010).

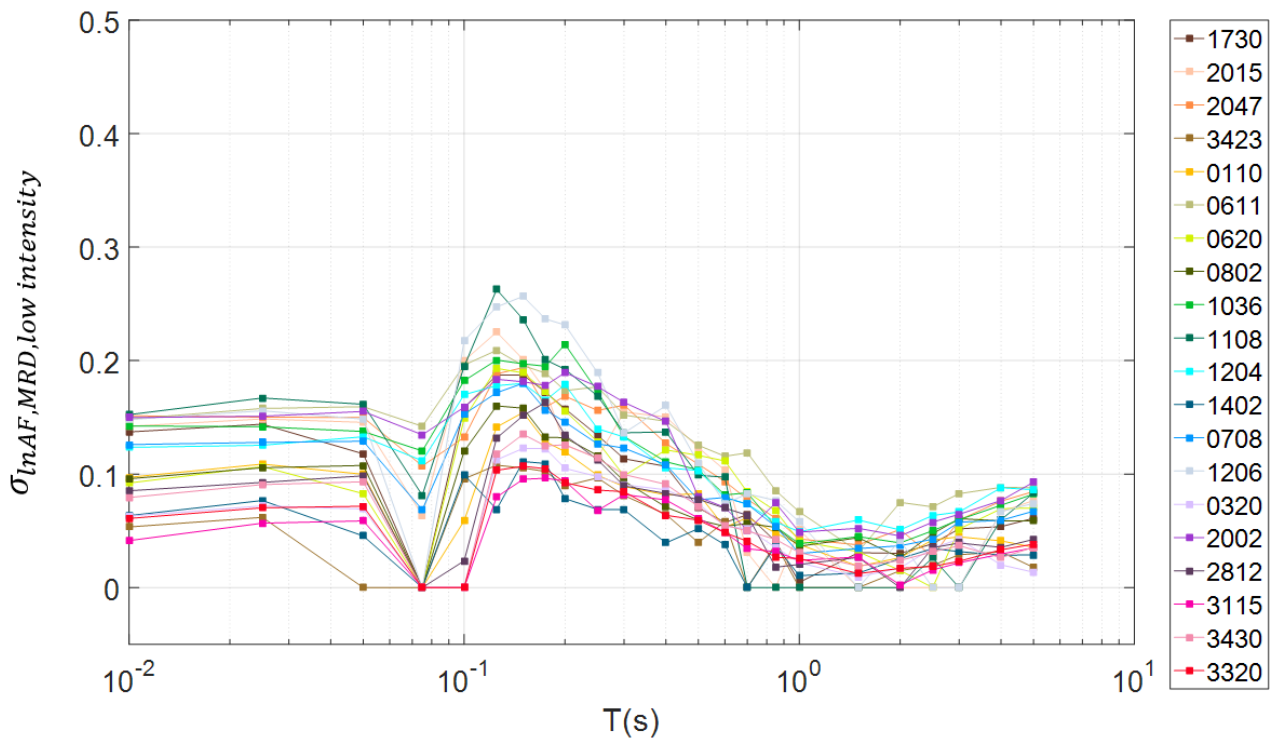


Figure 9.6. Contribution of MRD uncertainty to the total uncertainty for 19 selected zones and for low intensity input motions

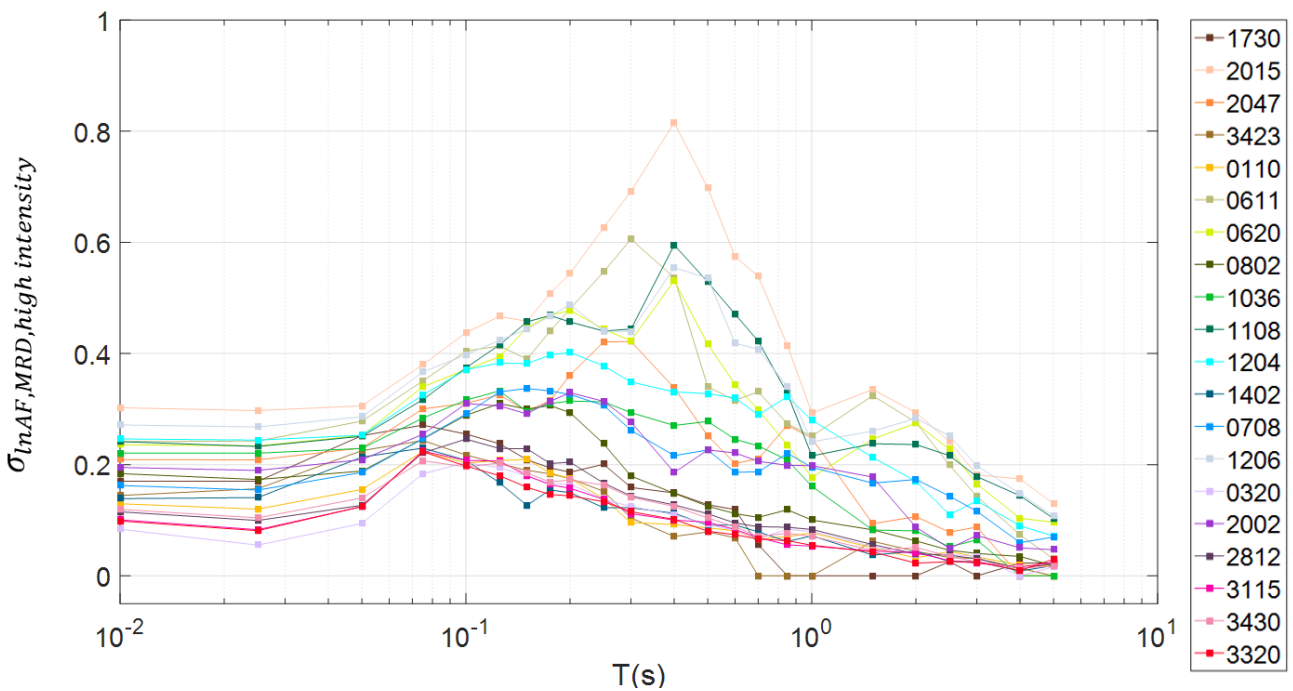


Figure 9.7. Contribution of MRD uncertainty to the total uncertainty for 19 selected zones and for high intensity input motions

In order to generalize the results shown in Figures 9.6 and 9.7 to the entire Groningen field, a model for the shape of the $\sigma_{InAF,MRD}$ contribution was first built for low and high-intensity motions (Figure 9.8). The parameters of the model were then plotted versus various zone properties (e.g., V_{s30} , V_{s10} , cumulated thickness of layers with $V_s < 100$ m/s, linear site

amplification parameters). Of all of these parameters, the best correlation was with the maximum value of the linear site amplification across all oscillator periods. We label this parameter $f_{1,max}$, where f_1 is the linear amplification parameter from Eq. (8.5). These correlations are shown in Figure 9.9. Observe that the correlations are well defined for nearly all the parameters, except maybe for θ_2 . However, since the values of this parameters are low, their impact on the uncertainty model will be small.

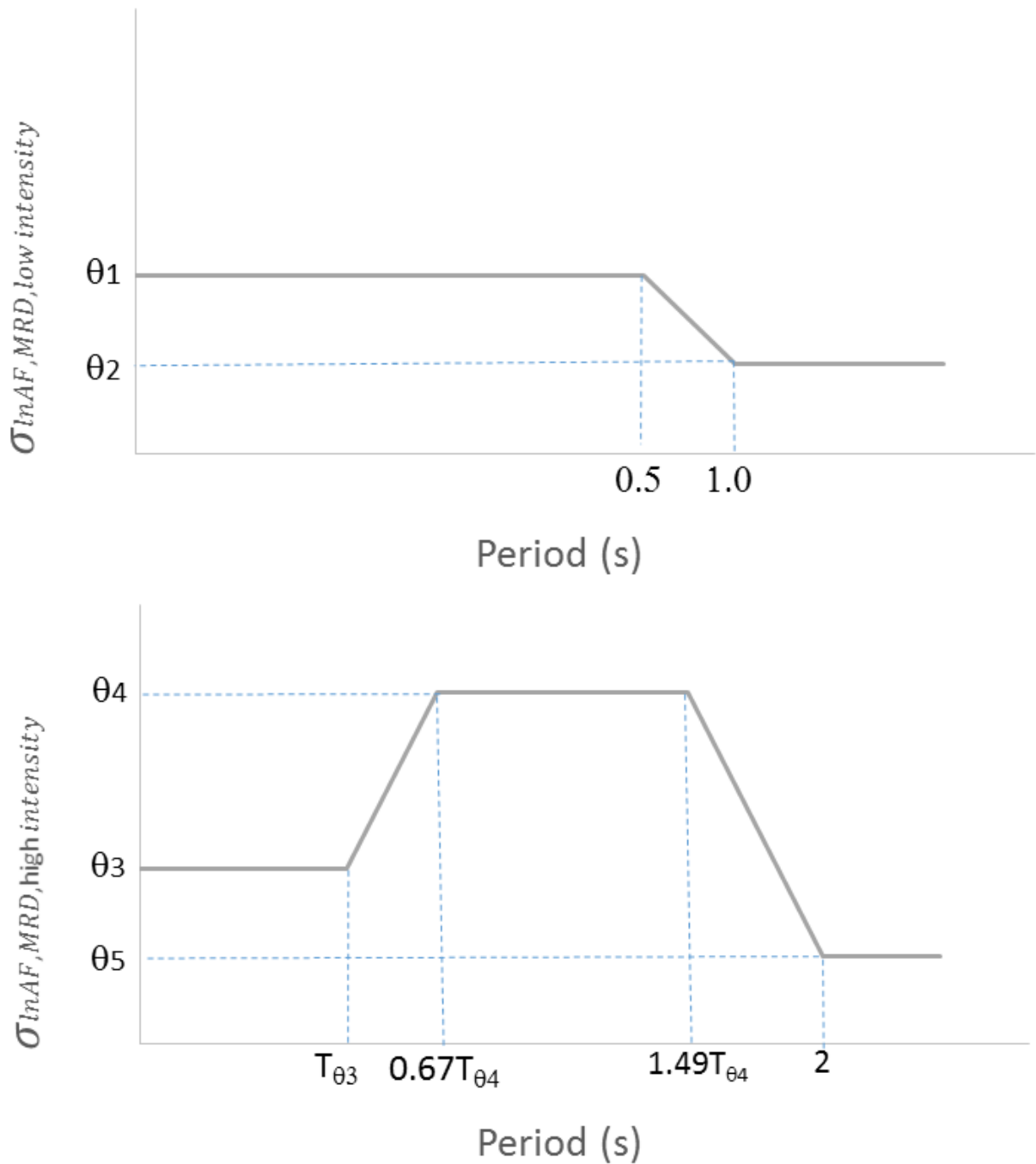


Figure 9.8. Model for the contribution of MRD uncertainty to the total uncertainty in AF. *Upper*: low intensity model, *Lower*: high intensity model. The parameters of the model are given in Eq. (9.3)

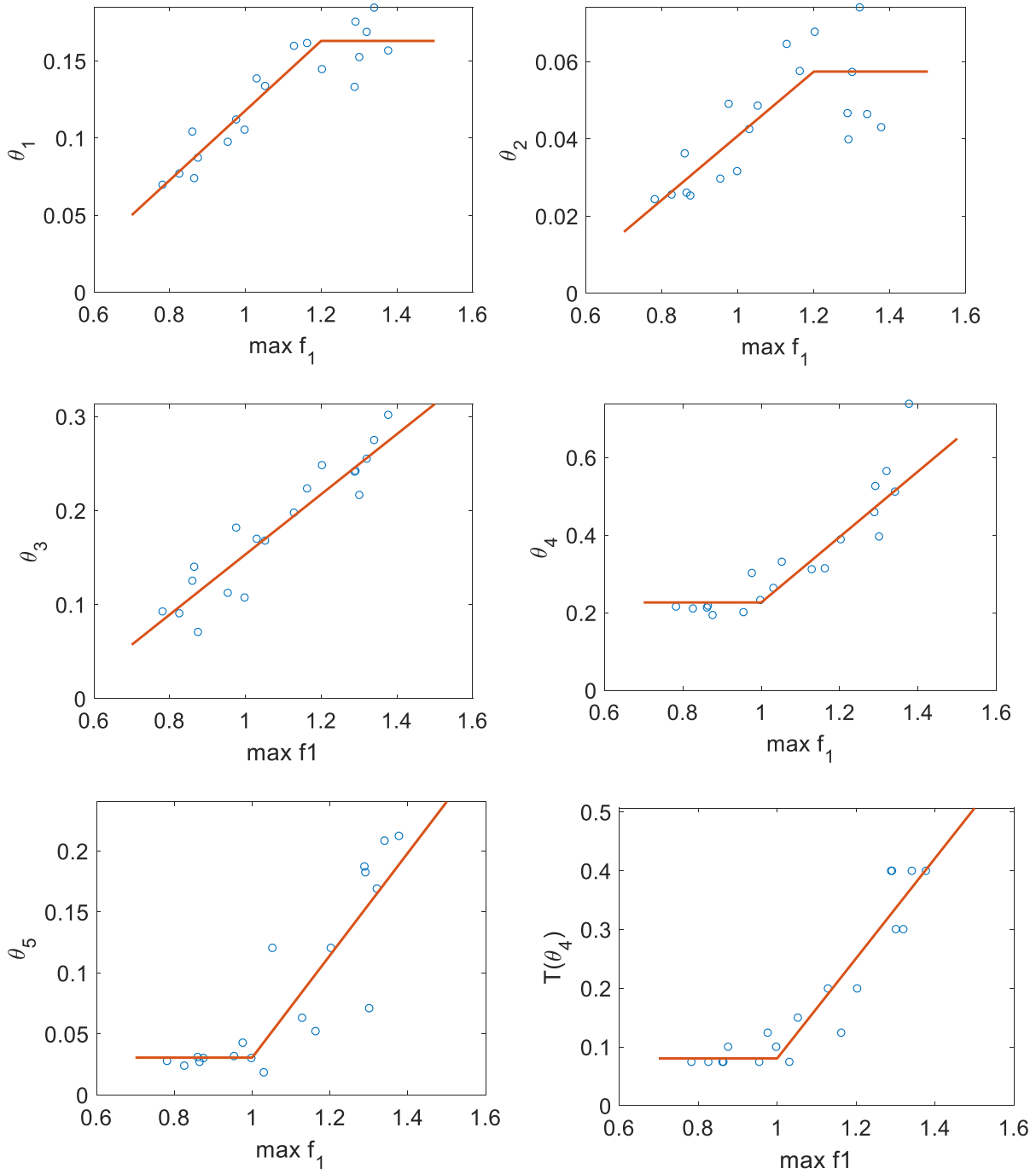


Figure 9.9. Correlation between the parameters of the $\sigma_{InAF,MRD}$ model (Figure 9.8) and the maximum linear site response across all periods

The equations for the parameters that define the models in Figure 9.8 are:

$$\theta_1 = \begin{cases} -0.106 + 0.2235 f_{1,max} & \text{for } f_{1,max} < 1.2 \\ -0.106 + 0.2235 * 1.2 & \text{for } f_{1,max} \geq 1.2 \end{cases} \quad (9.3a)$$

$$\theta_2 = \begin{cases} -0.0375 + 0.0778 f_{1,max} & \text{for } f_{1,max} < 1.2 \\ -0.0375 + 0.0778 * 1.2 & \text{for } f_{1,max} \geq 1.2 \end{cases} \quad (9.3b)$$

$$\theta_3 = -0.1778 + 0.3315 f_{1,max} \quad (9.3c)$$

$$\theta_4 = \begin{cases} -0.6183 + 0.8446 & \text{for } f_{1,max} < 1 \\ -0.6183 + 0.8446 f_{1,max} & \text{for } 1 \leq f_{1,max} \leq 1.324 \\ 0.5 & \text{for } f_{1,max} > 1.324 \end{cases} \quad (9.3d)$$

$$\theta_5 = \begin{cases} -0.4048 + 0.4345 & \text{for } f_{1,max} < 1 \\ -0.4048 + 0.4345 f_{1,max} & \text{for } f_{1,max} \geq 1 \end{cases} \quad (9.3e)$$

$$T_{\theta_4} = \begin{cases} -0.7703 + 0.8507 & \text{for } f_{1,max} < 1 \\ -0.7703 + 0.8507 f_{1,max} & \text{for } f_{1,max} \geq 1 \end{cases} \quad (9.3f)$$

Finally, T_{θ_3} is defined as 0.05 s if $0.67T_{\theta_4}$ is bigger than 0.08 s and 0.025 s otherwise. A sample of the fit of the $\sigma_{lnAF,MRD}$ model to one zone is shown in Figure 9.10. The values for $T=0.7$ s were used for PGV because the site response for this oscillator period correlated best with PGV site response.

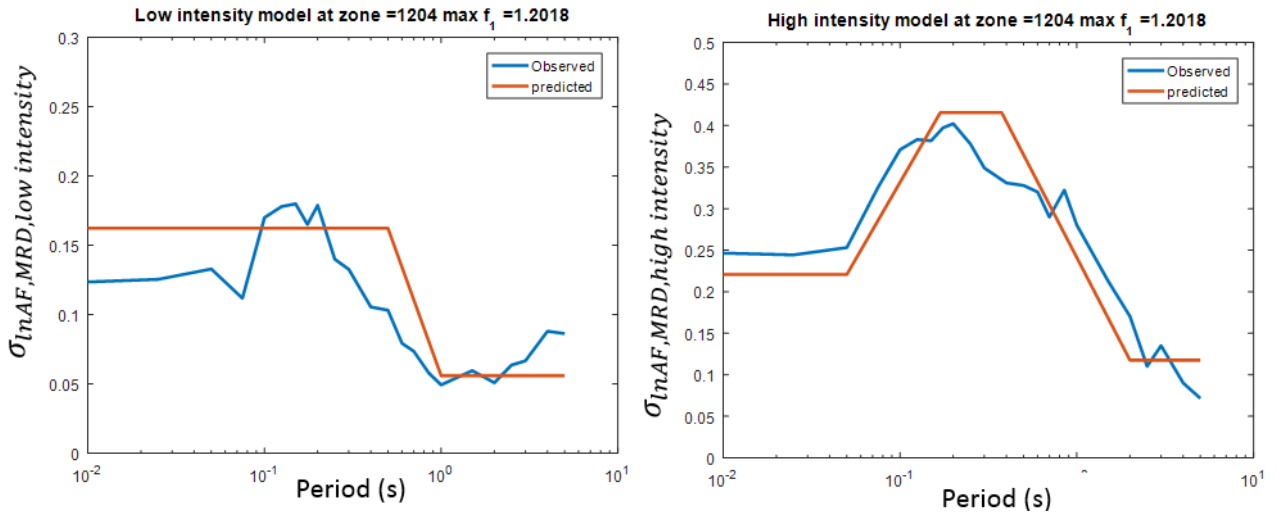


Figure 9.10. Computed and predicted values of the contribution to total uncertainty that results from MRD uncertainty. The left plot shows is for low-intensity motions, the right for high-intensity motions

The final model for the site-to-site variability in the amplification factors is then given by:

$$\phi_{S2S} = \begin{cases} \phi_{S2S,1} & \text{for } Sa_{NS,B} < Sa_{rock,low} \\ \phi_{S2S,1} + (\phi_{S2S,2} - \phi_{S2S,1}) \frac{\log\left(\frac{Sa_{NS,B}}{Sa_{rock,low}}\right)}{\log\left(\frac{Sa_{rock,high}}{Sa_{rock,low}}\right)} & \text{for } Sa_{rock,low} \leq Sa_{NS,B} \leq Sa_{rock,high} \\ \phi_{S2S,2} & \text{for } Sa_{NS,B} > Sa_{rock,high} \end{cases} \quad (9.4)$$

where $Sa_{rock,low}$ and $Sa_{rock,high}$ are model parameters and

$$\begin{aligned}\phi_{S2S,1} &= \sqrt{(\sigma_{lnAF,1})^2 + (\sigma_{lnAF,MRD,low\ intensity})^2} \\ \phi_{S2S,2} &= \sqrt{(\sigma_{lnAF,1})^2 + (\sigma_{lnAF,MRD,high\ intensity})^2}\end{aligned}\tag{9.5}$$

where $\sigma_{lnAF,MRD}$ is the additional uncertainty due to MRD for low and high intensity given by Figure 9.8 and Eq. (9.3), and σ_{lnAF} are obtained from Maximum Likelihood regression of Eq.(8.4) along with the uncertainty model in Eq.(9.1). In addition, a minimum and maximum bound to the ϕ_{S2S} values is imposed as discussed below. The minimum value accounts for modelling error, and the maximum value is an empirical bound. These bounds are discussed below.

As indicated before, the ϕ_{S2S} model represents the site-to-site variability of amplification factors within a zone. This model, however, did not include any consideration for modelling error. Modelling error can result from limitations of the adopted site response procedure. If the modelling procedure is likely to produce a bias in the results, this bias needs to be accounted for. One possible approach is to inflate the σ_{lnAF} to account for the bias. The literature review presented in Section 8.1 indicated that, in general, the EQL procedure has positive bias in computed spectral accelerations with respect to more accurate NL procedures. Similarly, the RVT procedure also produces positive bias with respect to time series analyses. For these reasons, it was considered that the selected RVT based EQL analyses results in conservative biases and σ_{lnAF} was not inflated to account for model error related to the choice of 1D analysis procedure. On the other hand, the potential biases in one-dimensional site response analyses can be used to set minimum levels of epistemic uncertainty.

In a recent study, Afshari & Stewart (2015, 2016c) evaluated site response at 12 vertical instrumental arrays in California and compared the surface-to-borehole estimates obtained from one-dimensional linear site response analyses with measured surface-to-borehole ratios at the instrumented arrays. Linear behaviour was assumed due to the low input motions recorded at the arrays. Small strain damping values were obtained from Q estimates for California (Campbell, 2009). The residuals were analysed using random effects regression to separate the motion-to-motion variability from a global bias and the average bias for each site. The standard deviation of the average bias for each site across all sites represents the model error associated with one-dimensional site response predictions. This estimate is shown in Figure 9.11. This figure also includes an estimate of model error obtained from over 100 KiK-net array sites by Kaklamanos *et al.* (2013). In this study, site response analyses were computed using equivalent linear analysis using Shake (Schnabel *et al.*, 1972). Small strain damping values were obtained by optimizing the value of Q that fits the recorded data. Similarly to Afshari & Stewart (2016c), they computed an estimate of the epistemic uncertainty in site response by obtaining the standard deviation of the bias at

each site. Note that the estimates from Kaklamanos *et al.* (2013) and Afshari & Stewart (2016c) are similar in amplitude, with only a period shift on the location of maximum error.

The model error presented in Figure 9.11 also includes potential contributions from measurement errors at the sites under analyses, as well as potential deviations from 1D conditions that may exist at these sites. For these reasons, it is not considered appropriate to add these bias to the uncertainty in site amplification factors. Instead, the computed biases shown in Figure 9.11 are used to build a model for the minimum level of epistemic uncertainty that is expected from the site response analyses. In considerations of the observations in Section 8.1 (*i.e.*, that the RVT equivalent linear analyses tends to have a positive bias with respect to other methods), and the fact that the Groningen site consists mainly of horizontal layering and hence is a good candidate for 1D site amplification, the *minimum epistemic uncertainty* model is built by creating a lower bound envelop to the model error in Figure 9.11. Hence, the minimum epistemic uncertainty is given by:

$$\phi_{S2S,min} = \begin{cases} 0.2 & \text{for } T \leq 0.05 \text{ s} \\ 0.2 + 0.1 \frac{\ln T - \ln 0.05}{\ln 0.1 - \ln 0.05} & \text{for } 0.05 \text{ s} < T \leq 0.1 \text{ s} \\ 0.3 & \text{for } 0.1 \text{ s} < T \leq 0.7 \text{ s} \\ 0.3 - 0.15 \frac{\ln T - \ln 0.7}{\ln 2 - \ln 0.7} & \text{for } 0.7 \text{ s} < T \leq 2 \text{ s} \\ 0.15 & \text{for } T > 2 \text{ s} \end{cases} \quad (9.6)$$

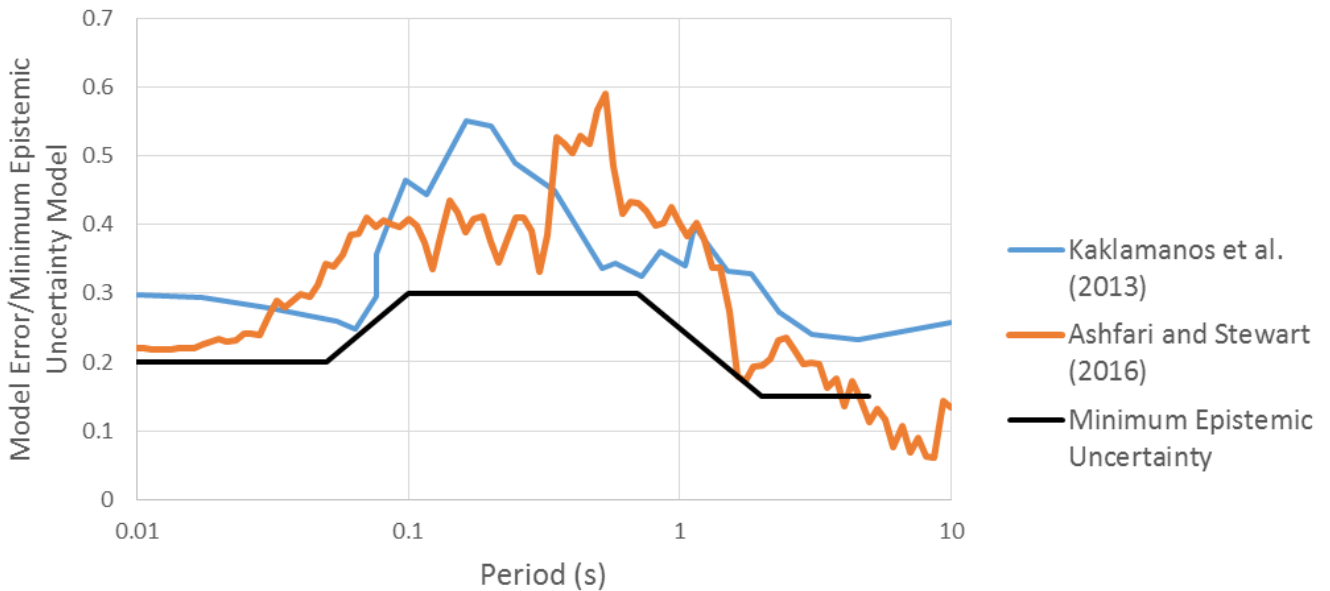


Figure 9.11. Model error computed by Afshari & Stewart (2016c) and Kaklamanos *et al.* (2013), and model for minimum epistemic uncertainty ($\phi_{S2S,min}$)

In addition to the lower bound, an upper bound to the ϕ_{S2S} values is also imposed. This upper bound is obtained by taking into consideration the site-to-site variability in recent GMPEs derived as part of the NGA-West2 project (Abrahamson *et al.*, 2014; Campbell & Bozorgnia,

2014; Chiou & Youngs, 2014; Boore *et al.*, 2014). The reasoning is that the site-to-site variability in these GMPEs, which have data from multiple regions across the world and use a simple two-parameter model for characterizing the site response cannot be larger than the site-to-site variability within one of the selected zones in Groningen, in particular when site response is characterized by a full site response analyses. For this reason, the ϕ_{S2S} model is bound by an envelope to the ϕ_{S2S} model of the NGA W2 GMPEs (Figure 9.12).

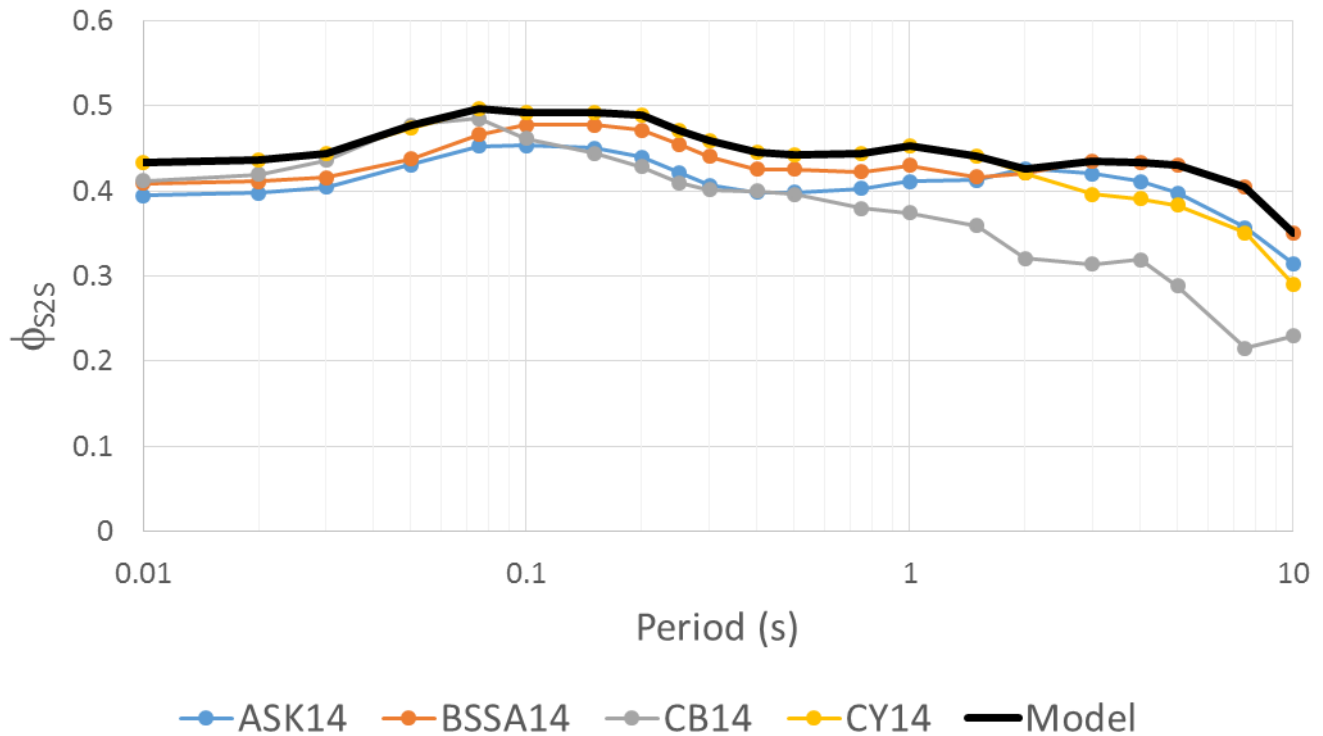


Figure 9.12. Model for the upper bound to ϕ_{S2S} . The values of ϕ_{S2S} for the NGA W2 models were provided by Linda Al Atik (*personal communication*).

An example of the model fit for one individual zone (1208) was shown in Figure 8.31. The resulting values for the fit for the median model (f_1 , f_2 , f_3) and for the standard deviation model ($\phi_{S2S,1}$, $\phi_{S2S,2}$, $S_{a,rock,low}$, and $S_{a,rock,high}$) are listed in Table 9.1 for Zone 1208. The parameters for the magnitude dependency of f_1 are given in the Executive Summary. The model for ϕ_{S2S} for this zone is shown in Figure 9.13 along with the residuals of the computed AFs. A table in digital format is provided to the hazard and risk team containing the fit parameters for all 160 geological zones of version V4 for all 23 periods and PGV (see Executive Summary).

Some more examples of the AF for various zones that have different levels of AF values are shown in Figures 9.14 through 9.16. Figure 9.14 shows the AF for Zone 309, which generally has low AF values. This region is located in the south and has a relatively high median V_{S30} (251 m/s). Figure 9.15 shows the results for Zone 601, which generally has intermediate AF values and also has an intermediate V_{S30} value (171 m/s). Figure 9.16 shows the results for Zone 1009 which has generally high AF values. The V_{S30} for this zone is 168 m/s.

Table 9.1. Example of the fit parameters and ϕ_{S2S} for zone 1208

Zone	T (s)	f ₁	f ₂	f ₃	AF _{min}	AF _{max}	$\phi_{S2S,1}$	$\phi_{S2S,2}$	Sa _{rock,low}	Sa _{rock,high}
1208	0.01	1.1875	-0.3594	0.004	0.25	3.639	0.224	0.4227	0.0015	0.015
1208	0.025	1.1769	-0.3943	0.004	0.25	3.56	0.2245	0.4257	0.0013	0.0133
1208	0.05	1.0901	-0.4355	0.004	0.25	3.141	0.2327	0.4614	0.0009	0.0095
1208	0.075	1.1771	-0.4814	0.004	0.25	3.283	0.3168	0.4967	0.0018	0.0176
1208	0.1	0.8651	-0.5894	0.0188	0.25	2.456	0.3074	0.4927	0.0058	0.0577
1208	0.125	0.6822	-0.7504	0.0625	0.25	2.04	0.3092	0.4922	0.0118	0.1178
1208	0.15	0.6819	-0.9195	0.108	0.25	2.013	0.3168	0.4918	0.0177	0.1767
1208	0.175	0.6932	-1.1167	0.1715	0.25	2.012	0.3126	0.4906	0.0242	0.2419
1208	0.2	0.7625	-1.4557	0.256	0.25	2.134	0.315	0.4895	0.0309	0.3086
1208	0.25	0.7862	-1.8423	0.5	0.25	2.188	0.3183	0.4712	0.0359	0.3589
1208	0.3	0.9106	-2.0098	0.5	0.25	2.477	0.3371	0.4596	0.0384	0.3837
1208	0.4	1.0724	-2.039	0.5	0.25	2.913	0.3837	0.4449	0.0368	0.3679
1208	0.5	1.2072	-2.0229	0.5	0.25	3.335	0.3635	0.4426	0.0314	0.3142
1208	0.6	1.2346	-1.8734	0.5	0.25	3.43	0.3226	0.4429	0.0279	0.2786
1208	0.7	1.2594	-1.5843	0.5	0.25	3.518	0.3	0.4432	0.0274	0.2739
1208	0.85	1.2716	-1.1687	0.5	0.25	3.564	0.2723	0.4475	0.0235	0.235
1208	1	1.2075	-0.2863	0.5	0.25	3.345	0.2712	0.453	0.0159	0.1594
1208	1.5	0.9402	1.0215	0.5	0.25	3.228	0.2095	0.4308	0.0092	0.0924
1208	2	1.1467	1.8432	0.5	0.25	3.993	0.15	0.282	0.0053	0.0531
1208	2.5	0.8602	1.9493	0.5	0.25	2.766	0.15	0.2634	0.0033	0.0329
1208	3	0.7409	1.6371	0.5	0.25	2.284	0.15	0.2165	0.002	0.0201
1208	4	0.7994	0.9268	0.5	0.25	2.282	0.15	0.1821	0.0013	0.0126
1208	5	0.9358	0.2396	0.5	0.25	2.56	0.15	0.1713	0.0009	0.0088
1208	PGV	1.3859	-0.0913	0.1	0.25	3.047	0.2414	0.2533	0.1	1

The geographical distribution of the linear part of the fitted AFs ($=e^{f_1}$) and the $\phi_{S2S,1}$ for each zone are plotted in Figure 9.17 for PGV and in Figures 9.18 and 9.19 for four selected periods (0.01, 0.2, 0.6 and 1.0 s). The AFs show a clear geographical variability, that is different for each period.

Most modern GMPEs as well as building codes use V_{S30} as a proxy for the site response characteristics of any given location, the reason for which is primarily related to the relative ease to obtain this parameter (30 metres being the depth to which a borehole could be drilled in one day) rather than any compelling geophysical significance. For the spectral acceleration predictions, for which transportability has not been a consideration, the use of this rather crude parameter has been circumvented through the site response zonation. However, as is explained in Chapter 12, the duration GMPE—derived in a completely different way and defined directly at the ground surface rather than at the NS_B horizon for application of the AFs in each zone—does include this simplified parameter. Therefore, the implementation of the model requires a map of V_{S30} across the field, for which the preferred solution was to assign representative V_{S30} values to each of the site amplification zones.

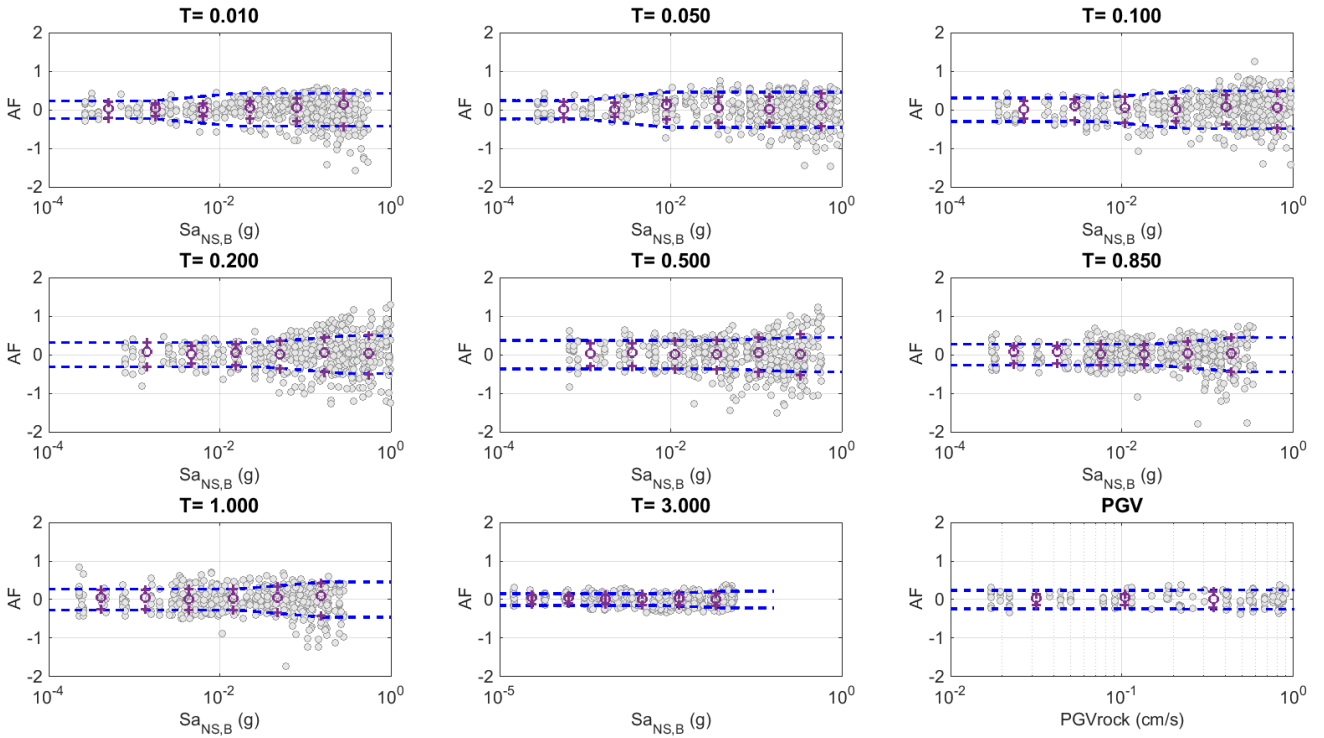


Figure 9.13. Residuals for the amplification factors for zone 1208 for selected periods. The standard deviation is heteroskedastic

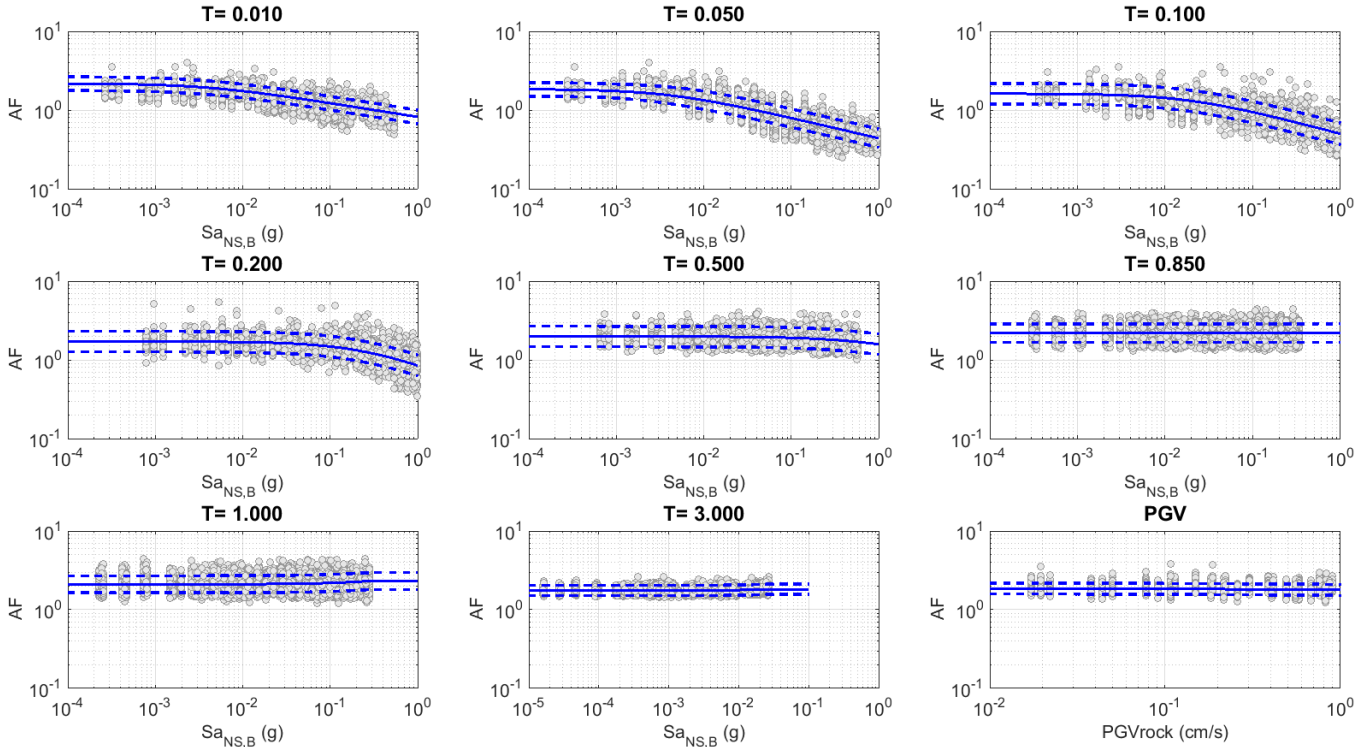


Figure 9.14. AF for Zone 309 ($V_{s30} = 251$ m/s), located in the south

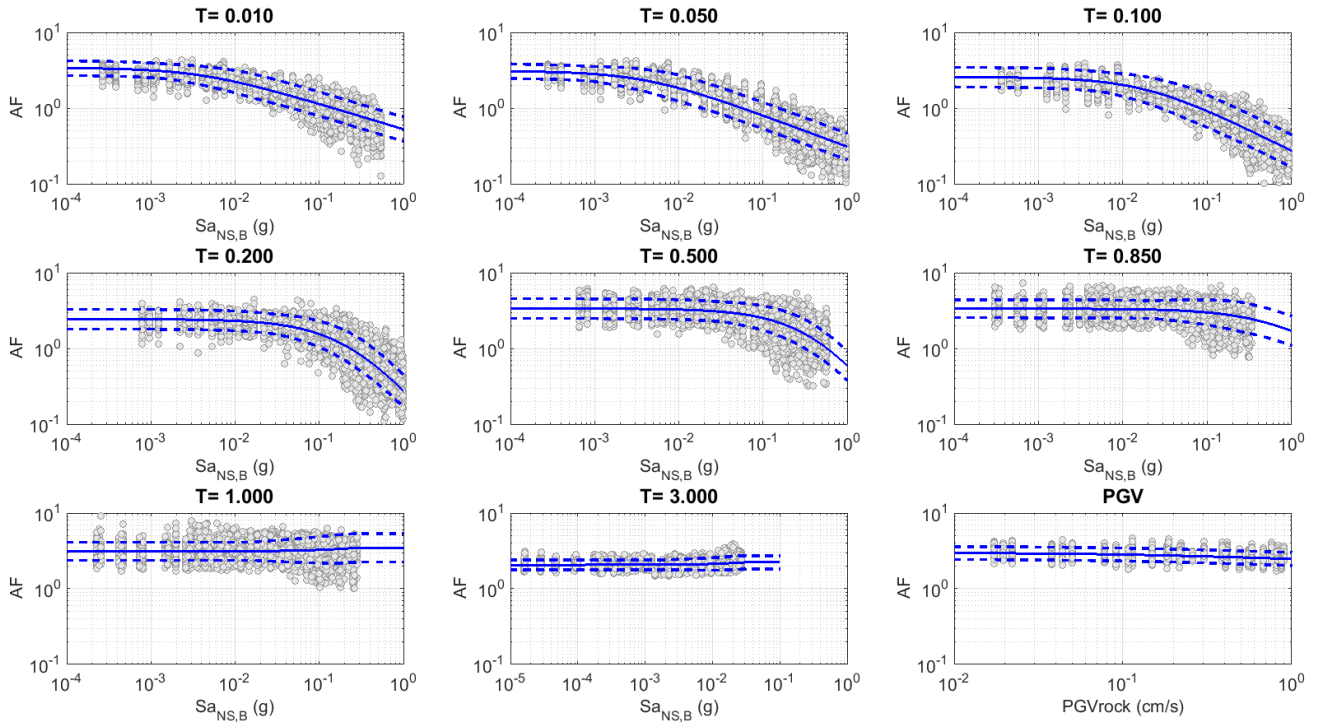


Figure 9.15. AF for Zone 601 ($V_{S30} = 171$ m/s), located in the centre

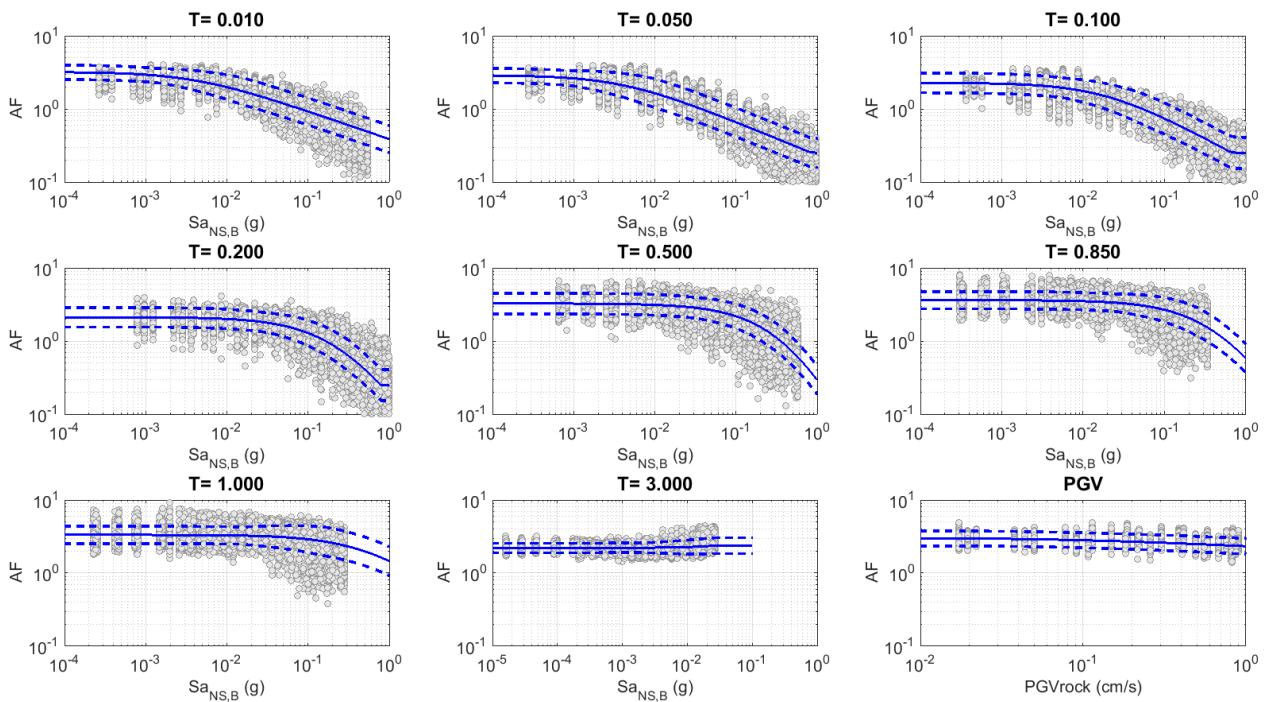


Figure 9.16. AF for Zone 1009 ($V_{S30} = 168$ m/s), located in the north-west

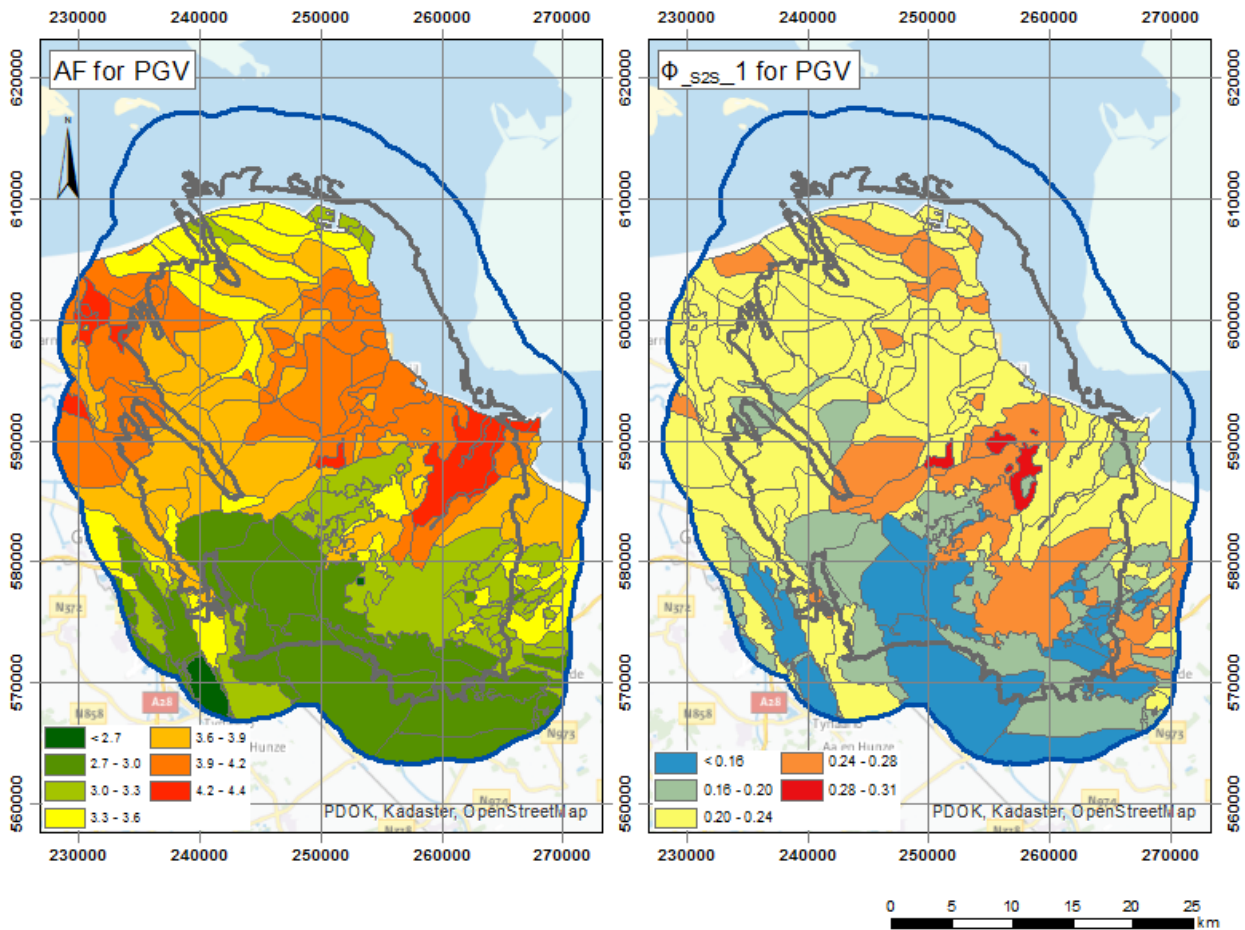


Figure 9.17. PGV fit for the zones in the Groningen region. Left: weak motion $AF(=e^{f1})$ for PGV; right: $\phi_{s2s,1}$ for PGV

For completeness, the V_{S30} values at the recording stations are reported in Table 9.2. Two V_{S30} values are reported: one set based on the zone where each station is located, and the other set calculated from the V_s profile at the station as inferred from the field measurements of V_s . The latter values were originally reported in Table 4.2 in Chapter 4. The difference between the median and the average V_s is small (not only for the zones listed in the table). This means that the values of V_{S30} are normally distributed for all zones. Additionally, the ratio of modelled over median V_{S30} for the zones housing the recording stations show consistent values. This suggests that the quality of the V_s distributions of the V_s model is similar for all zones in the table.

Based on the zonation proposed in Section 9.2 (Figure 9.3), median, average and standard deviations of V_{S30} for each zone were determined. The V_s profile for each of GeoTOP voxel stacks with 0.5 m thick layers was sampled 100 times using the approach described in Section 7.7. Next, the 100 V_{S30} values for each voxel stack were calculated. All V_{S30} values were aggregated per zone for the calculation of mean, median and standard deviation. The resulting V_{S30} maps are shown in Figures 9.20 (median V_{S30}), 9.21 (average V_{S30}) and 9.22 (standard deviation of V_{S30}). These maps may also prove useful for prioritisation schemes for building strengthening and improvements to the definition of seismic loads in the NEN-NPR draft seismic design code for the Groningen region (NEN, 2015).

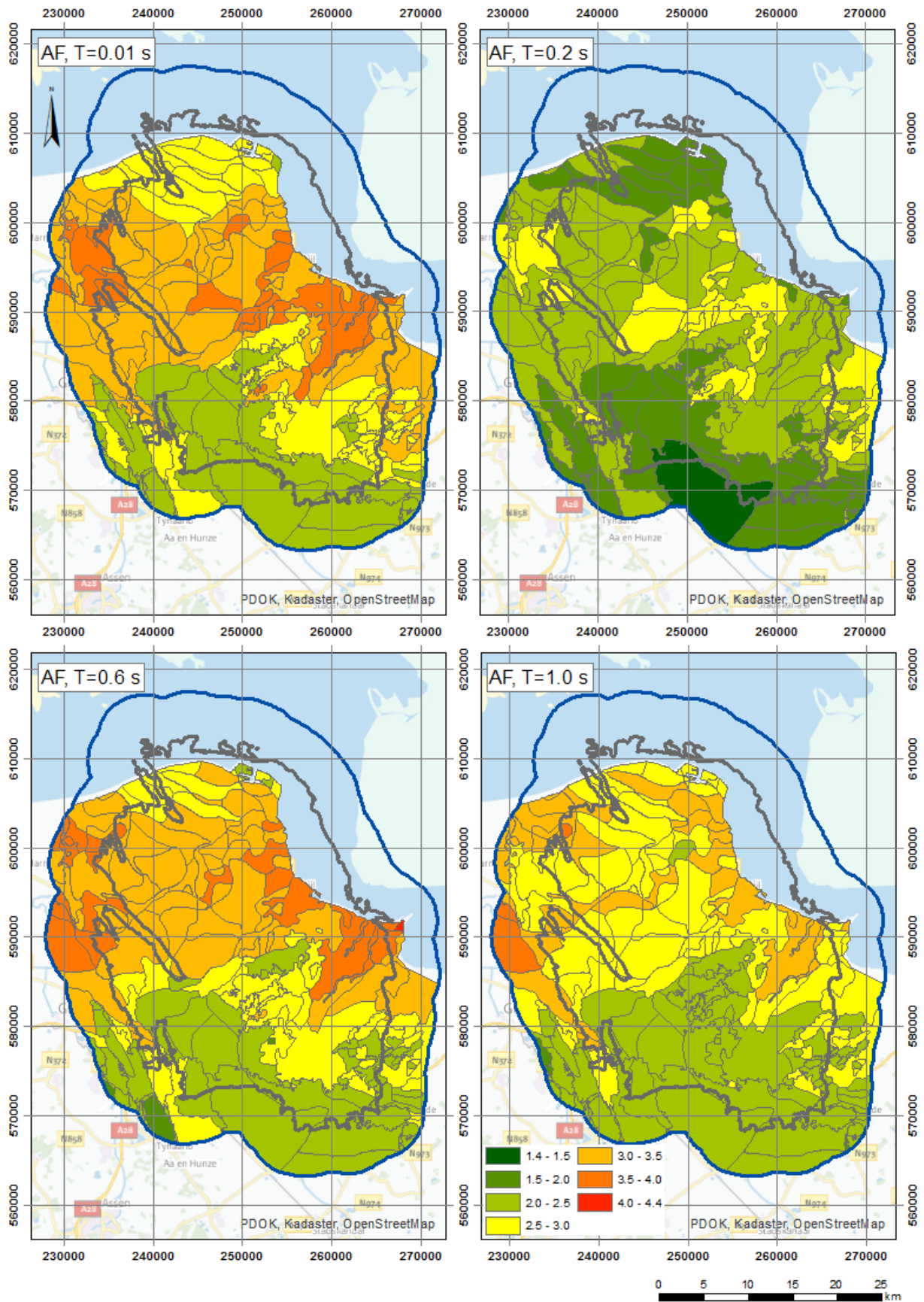


Figure 9.18. Weak motion fitted AF ($=e^{f1}$) for the zones in the Groningen region for selected periods

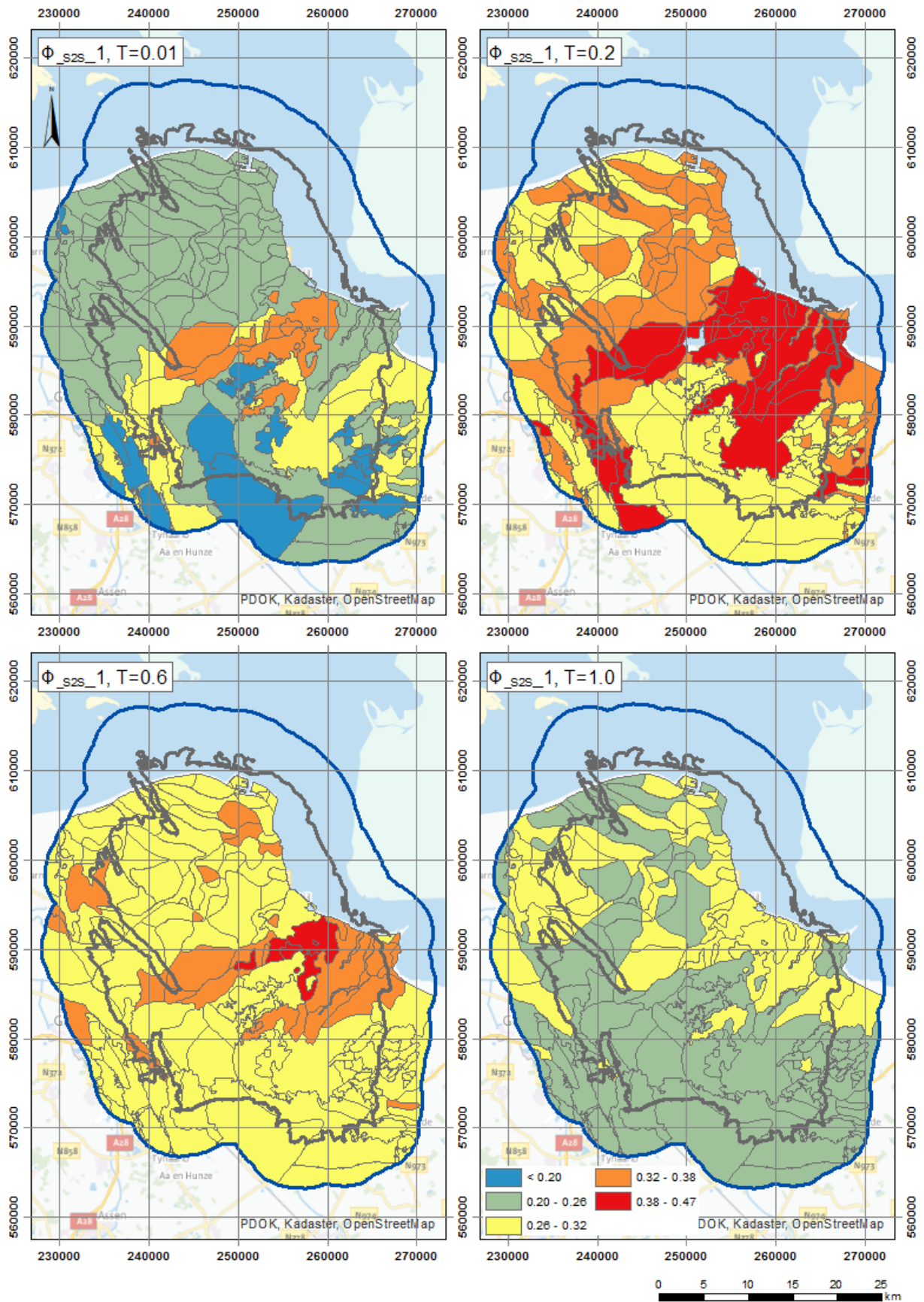


Figure 9.19. ϕ_{s2s_1} for the zones in the Groningen region resulting from the fit of AFs, for selected periods

Table 9.2. V_{S30} values at the recording stations.

Station	X (RD) of GeoTOP voxel stack	Y (RD) of GeoTOP voxel stack	Zone V4	Average V_{S30} from zone (m/s)	Median V_{S30} from zone (m/s)	Standard deviation of V_{S30} from zone (m/s)	Ratio of modelled standard deviation and median V_{S30} (zone)	V_{S30} calculated from measured V_s profile (cm/s)
BAPP	251450	593050	2111	171.5	169.5	27.5	0.16	138.4
BFB2	247050	578850	3115	256.2	254.2	40.0	0.16	250.9
BGAR	243350	598750	1001	177.7	175.9	28.4	0.16	193.1
BHAR	243250	583250	3117	231.4	229.6	34.7	0.15	183.8
BHKS	248250	590450	2110	177.0	175.0	29.1	0.17	159.1
BKAN	239850	599750	604	167.8	166.1	33.3	0.20	213.0
BLOP	245550	595050	1032	175.2	173.4	28.5	0.16	187.1
BMD1	238550	596350	1002	175.5	173.8	29.2	0.17	171.8
BMD2	238850	597050	1001	177.7	175.9	28.4	0.16	168.2
BONL	245950	602350	1011	183.7	181.4	31.3	0.17	192.4
BOWW - SCPT10	249850	595850	2111	171.5	169.5	27.5	0.16	171.6
BSTD	241950	592550	1037	181.9	180.2	29.1	0.16	162.5
BUHZ	240550	603050	801	184.9	181.5	36.1	0.16	199.9
BWIN	245650	592450	2110	177.0	175.0	29.1	0.20	176.4
BWIR	248250	593850	2111	171.5	169.5	27.5	0.17	163.6
BWSE	243050	596050	602	183.5	180.8	31.8	0.16	198.4
BZN1	247350	598650	1004	170.7	169.4	26.4	0.18	191.8
BZN2	246050	597550	1032	175.2	173.4	28.5	0.16	177.5

There is a distinct pattern in the distribution of V_{S30} , showing lower V_{S30} values in the north and higher V_{S30} values in the south. In the southern part, the high V_{S30} values reflect the presence of Pleistocene sediments at or near the surface. The Hondrug is clearly recognisable as a high V_{S30} zone in the southwest (zones 303, 306, 309, 310, 320, 322 and 3402), situated between the outline of the field and the 5 km buffer. East of the Hondrug there is a channel infill with tidal deposits, resulting in a relatively low V_{S30} value (zones 1901, 2210 and 3003). There is a sharp contrast in V_{S30} between the Hondrug and the adjacent tidal deposits. This sharp contrast is expected because of depositional environment of a tidal zone next to a ridge structure. One large channel, with clayey infill, giving rise to low V_{S30} values is present in the east (geological area 2045). In the north and west, two sandier channel infills (geological area 802 and 2108) with higher V_{S30} than the more clayey environment can be discerned.

The resulting V_{S30} value is an interplay between the lithological infill and thickness of the Naaldwijk Formation, and the presence or absence and the thickness of peat layers. Generally, the Naaldwijk Formation is expected to be more sandy and consisting of a thicker layer to the north. Both aspects have counteracting effects on V_{S30} . Locally, the occurrence of shallow Pleistocene soils also increase the V_{S30} . In general, the difference between the median and the average V_{S30} is small.

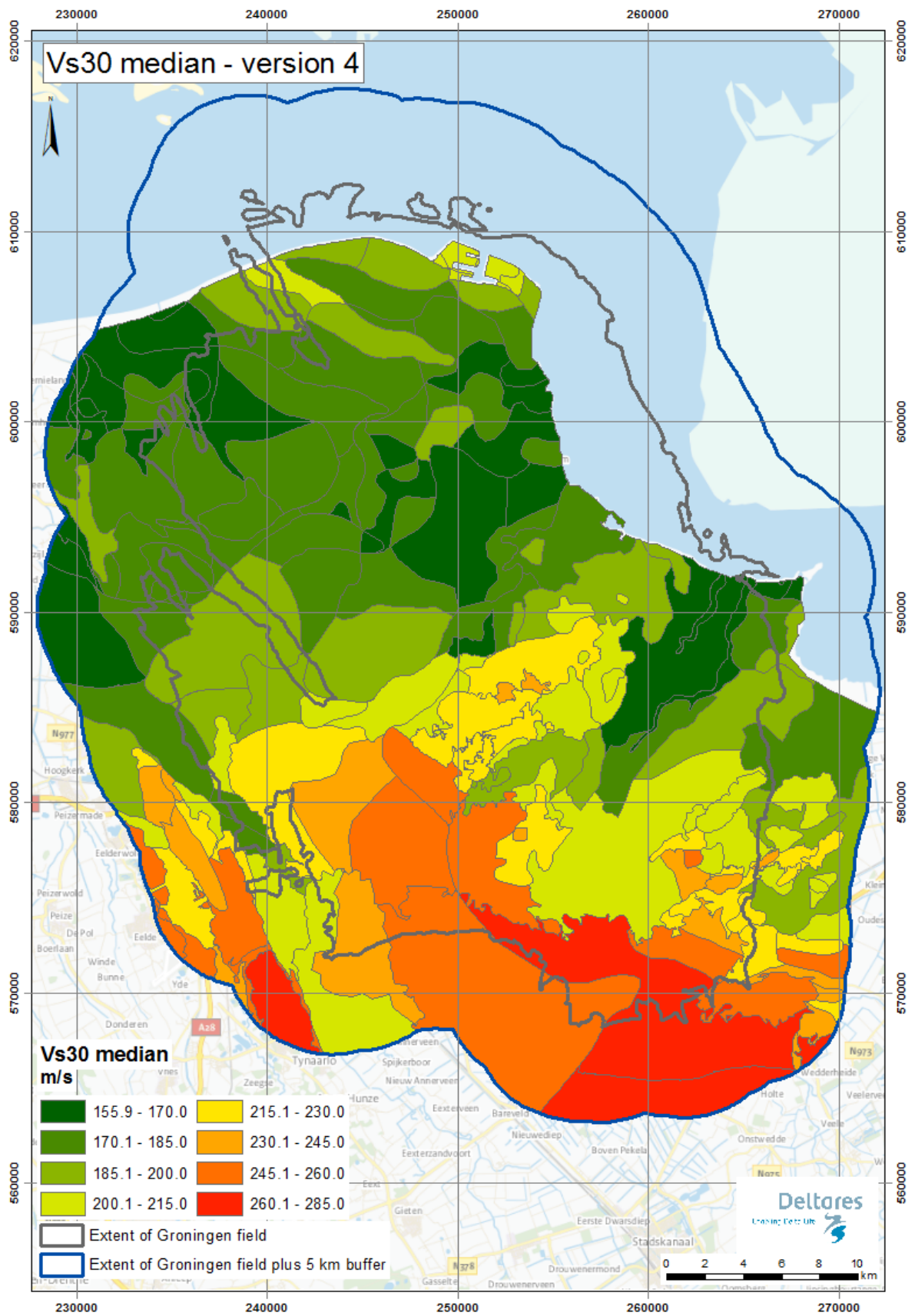


Figure 9.20. Median V_{s30} for GMPE V4

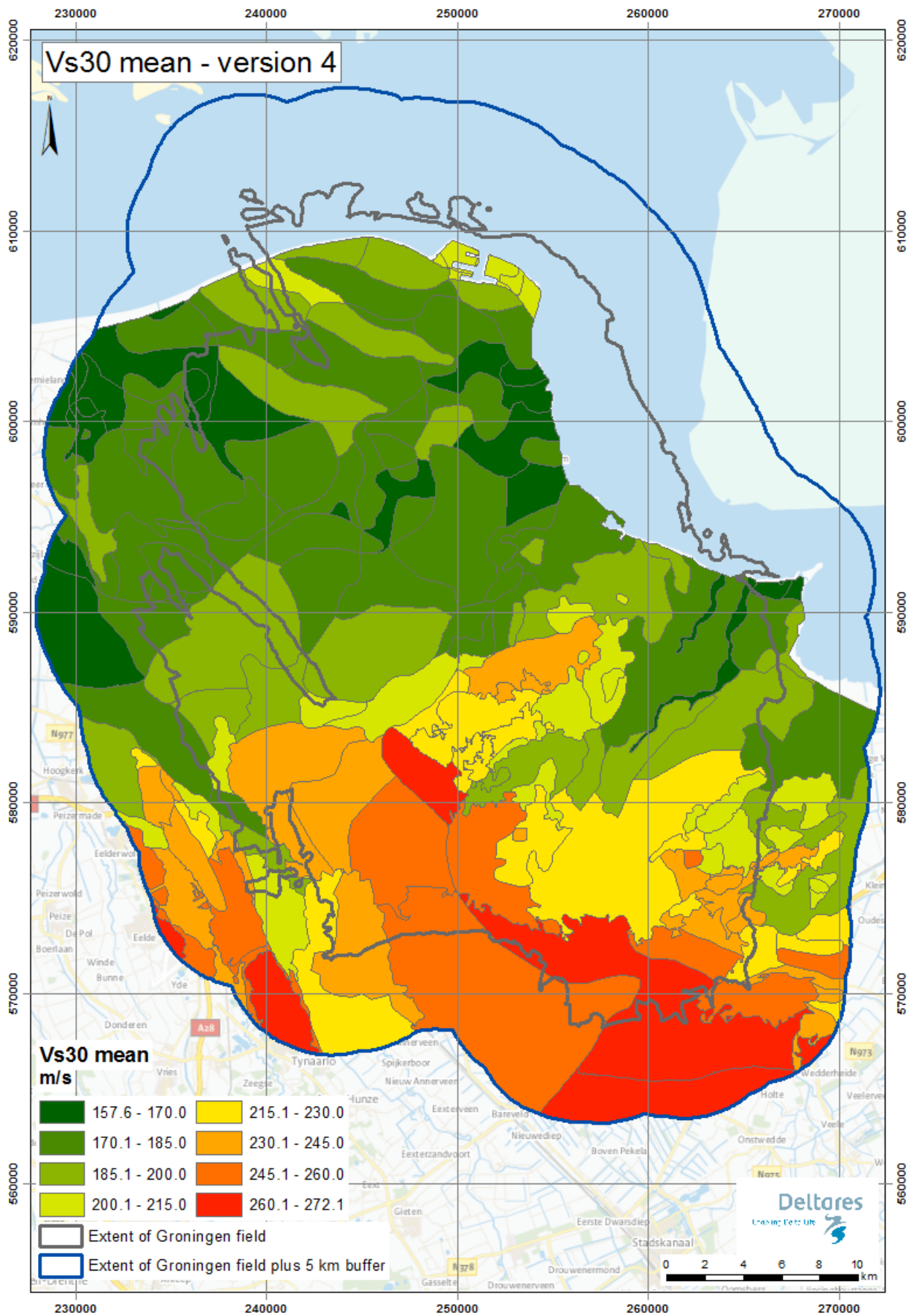


Figure 9.21. Mean V_{s30} for GMPE V4

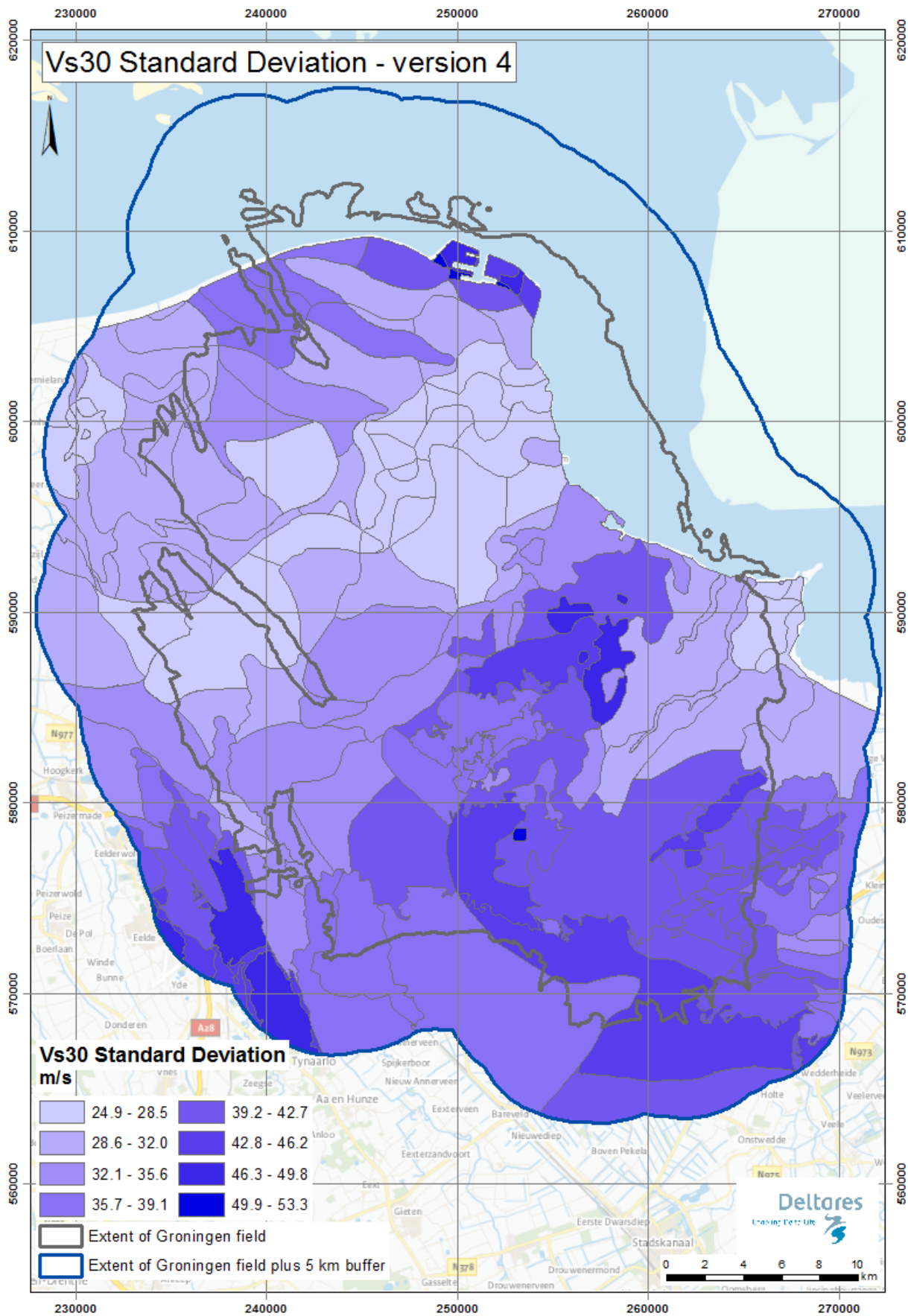


Figure 9.22. Standard deviation of V_{s30} for GMPE V4

Figure 9.23 shows the linear amplification function plotted as a function of the median V_{S30} for each zone. As expected, there is a strong correlation between linear amplification and V_{S30} . Similar observations have led to the adoption of V_{S30} as a proxy for site conditions in building codes (Borcherdt, 1994). The correlation is likely to be stronger if V_S is averaged over a depth equivalent to the quarter of the wavelength corresponding to each period (Joyner *et al.*, 1981). For example, for $T=0.2$ s, and assuming an average V_S between 120 m/s to 180 m/s for the near surface deposits, the quarter wavelength would be between 6 to 9 m. This may explain why the correlation between linear amplification and V_{S30} is not as strong for some oscillator periods. The use of the full profiles to compute amplification functions obviates the need to find site parameters proxies to compute the amplification factors. Figure 9.24 shows that the parameter f_2 plotted versus median V_{S30} for each zone. The parameter f_2 controls the nonlinear behaviour of the profiles. Figure 9.24 illustrates that the nonlinear behavior of the soils at Groningen also correlates well with V_{S30} .

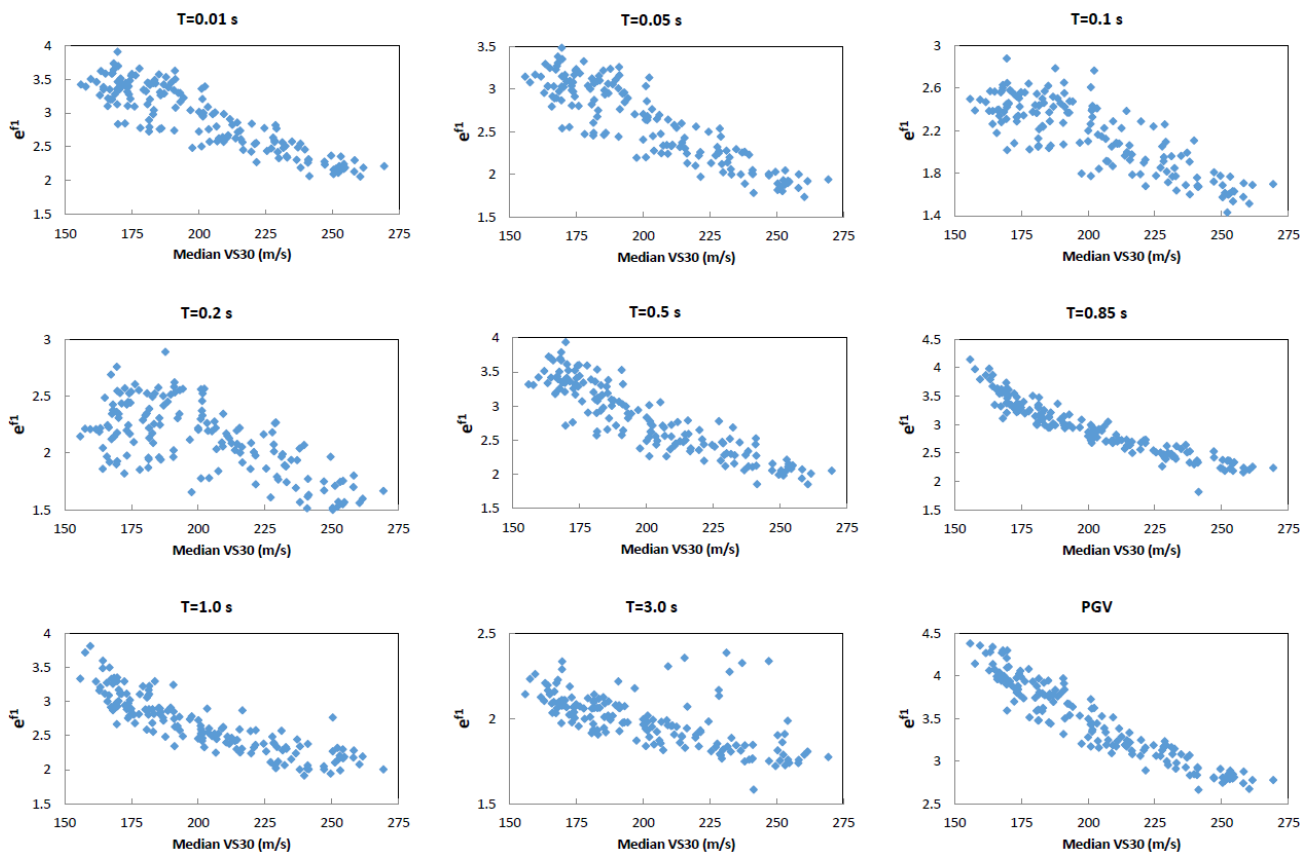


Figure 9.23. Linear amplification factors as a function of median V_{S30} for the zone

In Figure 9.24 it may be observed that there is often a plateau of f_2 at higher V_{S30} values. This simply indicates that the non-linear behaviour is not sensitive to changes in V_{S30} beyond a certain point, which does not undermine the assertion that f_2 and V_{S30} are correlated, at least at short and intermediate oscillator periods.

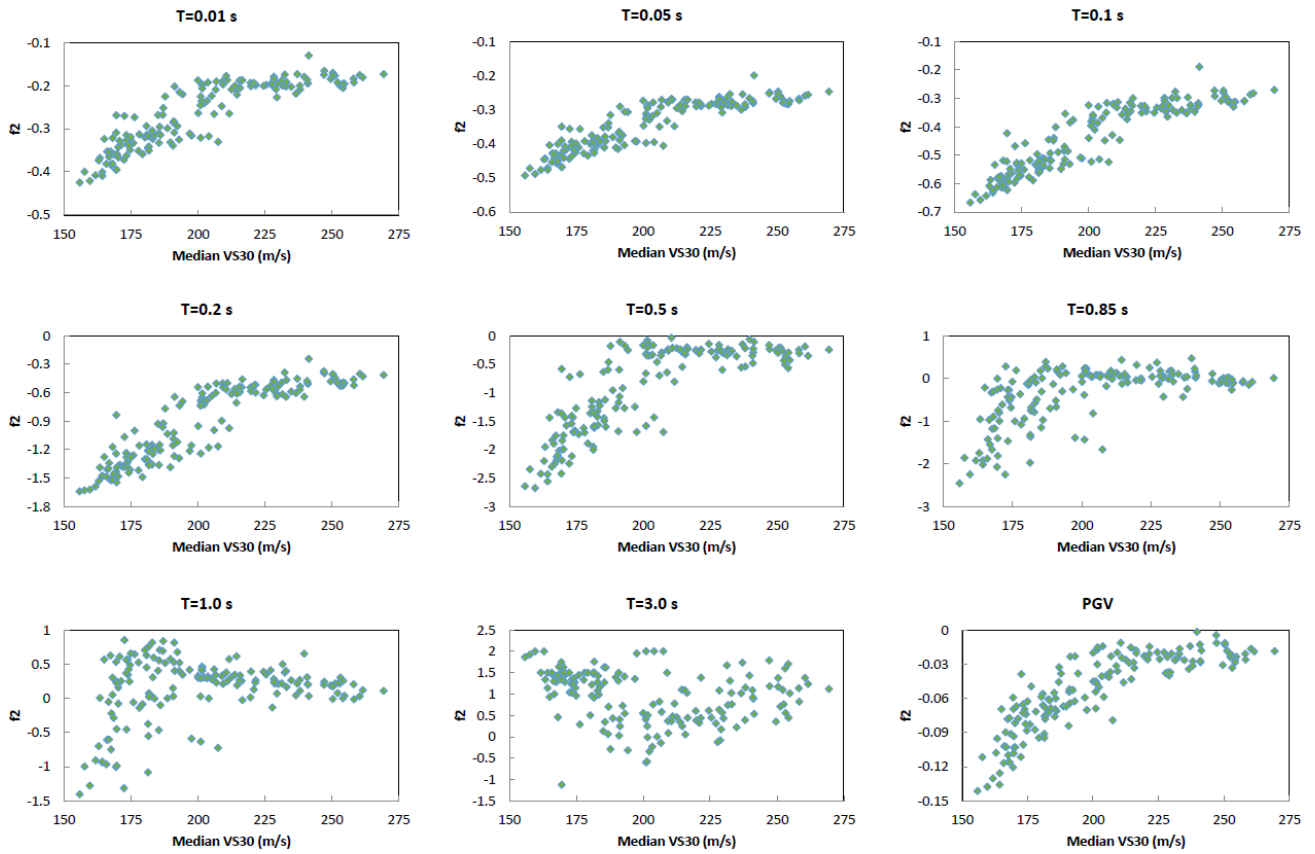


Figure 9.24. Coefficients f_2 as a function of median V_{S30} for the zone

9.4. Comparison with amplification factors for recording stations

In this section we compare the amplification factors computed for the recording stations with the zone amplification factors developed in this chapter. In Section 4.3 the linear spectral amplifications for the recording stations were computed for use in the seismological inversions. The ratios between the two sets of amplification factors were computed using the zone corresponding to the location of each ground motion station. The ratios were computed for the magnitude and distance scenarios that correspond to the recorded events at each of the stations (Chapter 3). These ratios are shown in Figures 9.25 to 9.29 for all the B stations.

Observe that the ratios approach unity for periods longer than about 0.2 seconds. A perfect match (*i.e.*, a ratio of unity) is not expected because the profile at the station location represents a single realization of the multiple profiles at the zones. However, for periods longer than about 0.2 seconds, the value of the ratio for all the stations generally oscillates between 0.8 and 1.2, which is within the range of the site to site variability (ϕ_{S2S}). At short periods, however, there is a systematic bias that is observed for all the stations. This bias is strongly magnitude dependent. In fact, a close examination of Figures 9.25 to 9.29 shows that the ratio is close to one for earthquakes with magnitude greater than 3.5. The bias for low magnitudes resulted from a mismatch between the magnitude-dependency of the amplification factors computed for the stations and those computed for the zones. Future iterations of the ground motion model will address this issue.

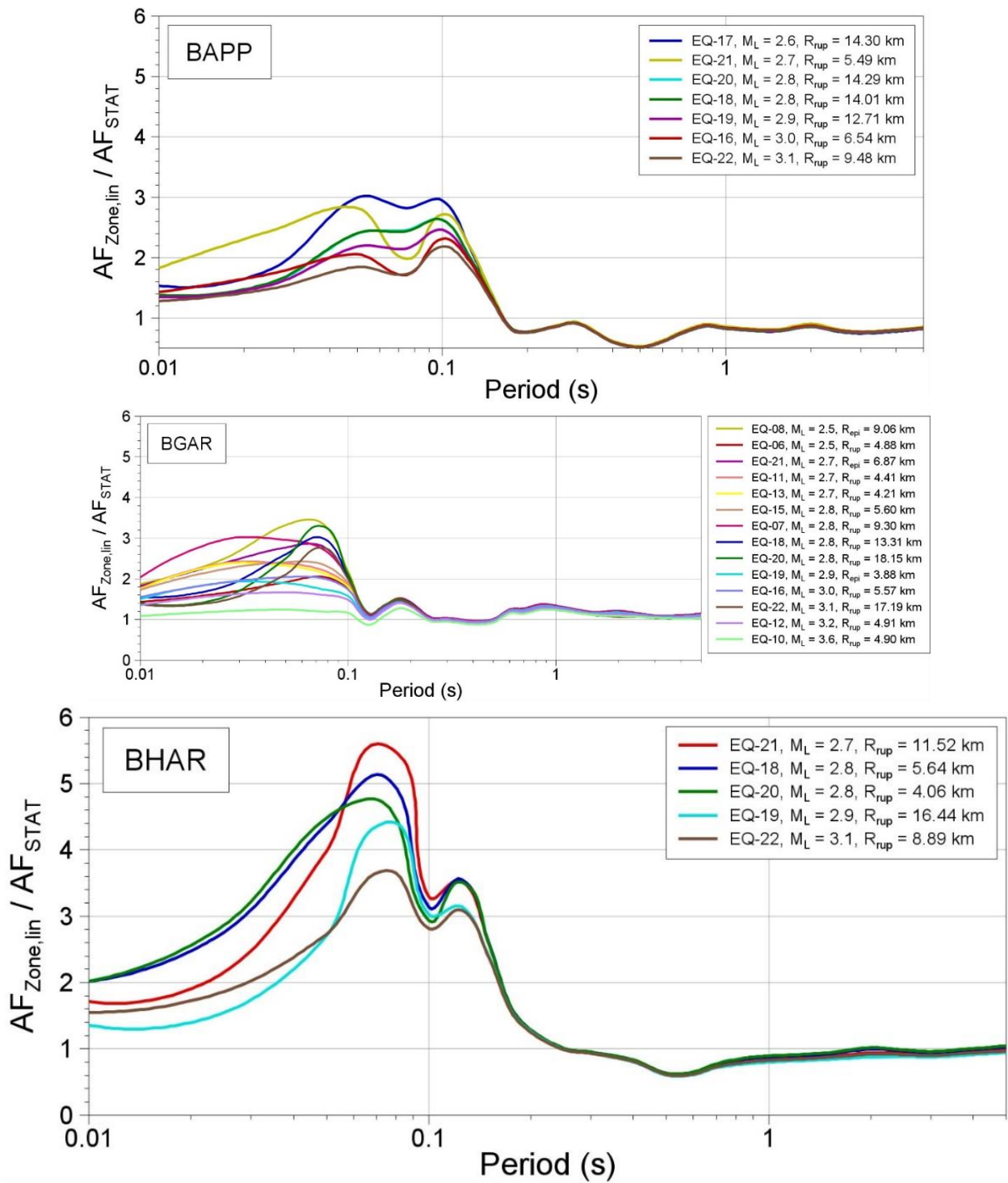


Figure 9.25. Ratios of the linear AF computed for the zone and the linear AF computed for the stations BAPP (Zone 2111), BGAR (Zone 1001), and BHAR (Zone 3118)

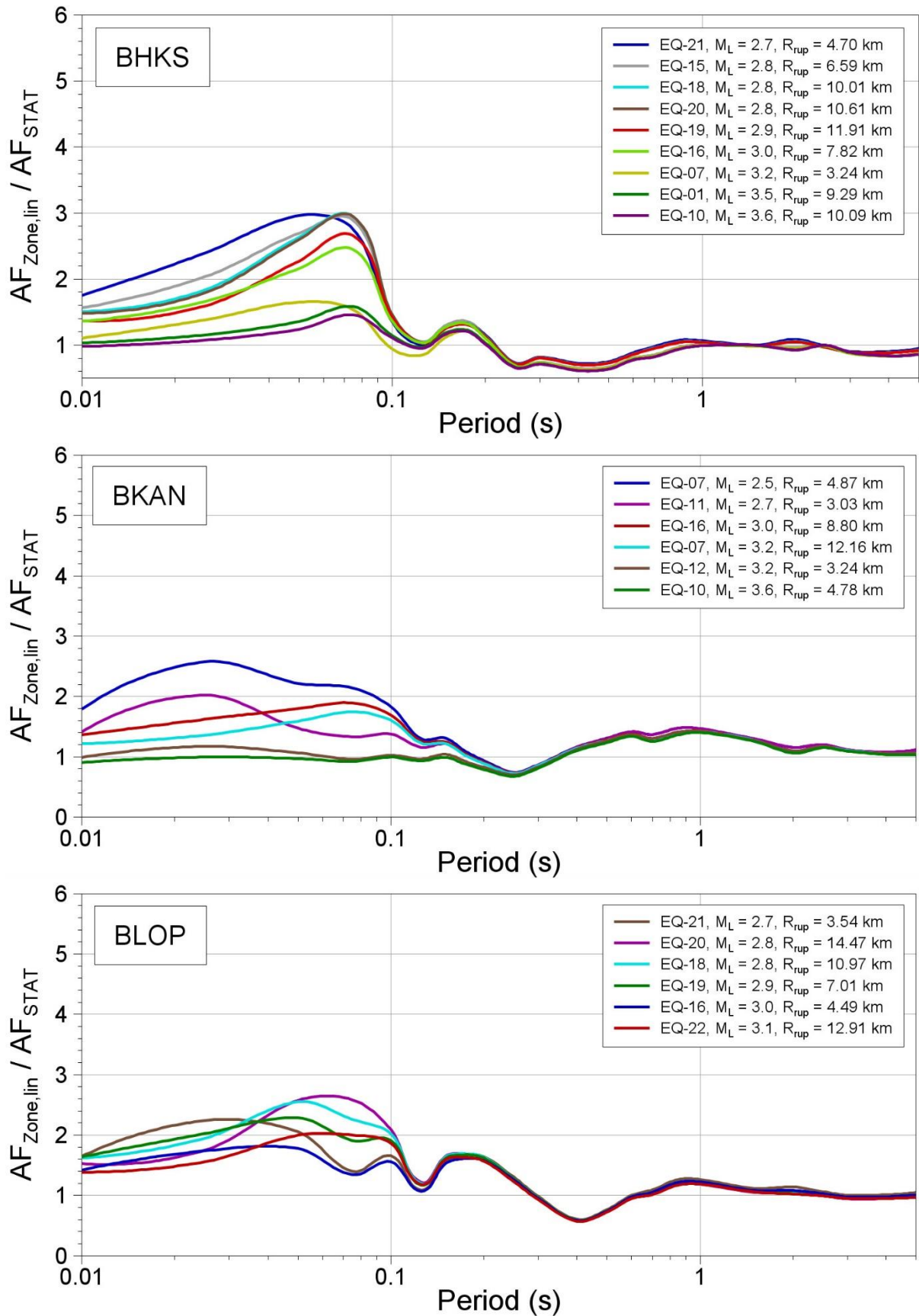


Figure 9.26. Ratios of the linear AF computed for the zone and the linear AF computed for the stations BHKS (Zone 2110), BKAN (Zone 604), and BLOP (Zone 1032)

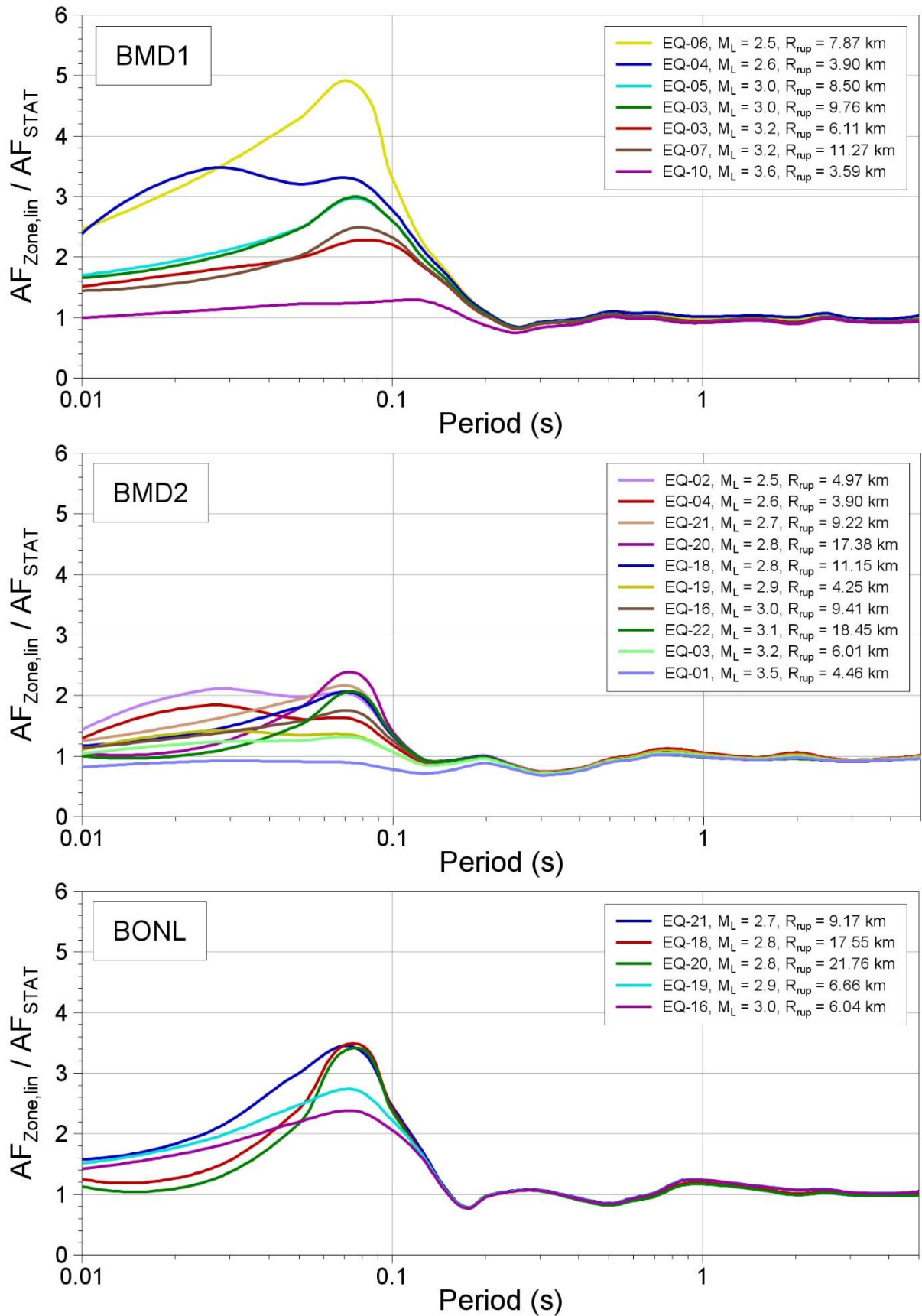


Figure 9.27. Ratios of the linear AF computed for the zone and the linear AF computed for the stations BMD1 (Zone 1002), BMD2 (Zone 1001), and BONL (Zone 1011)

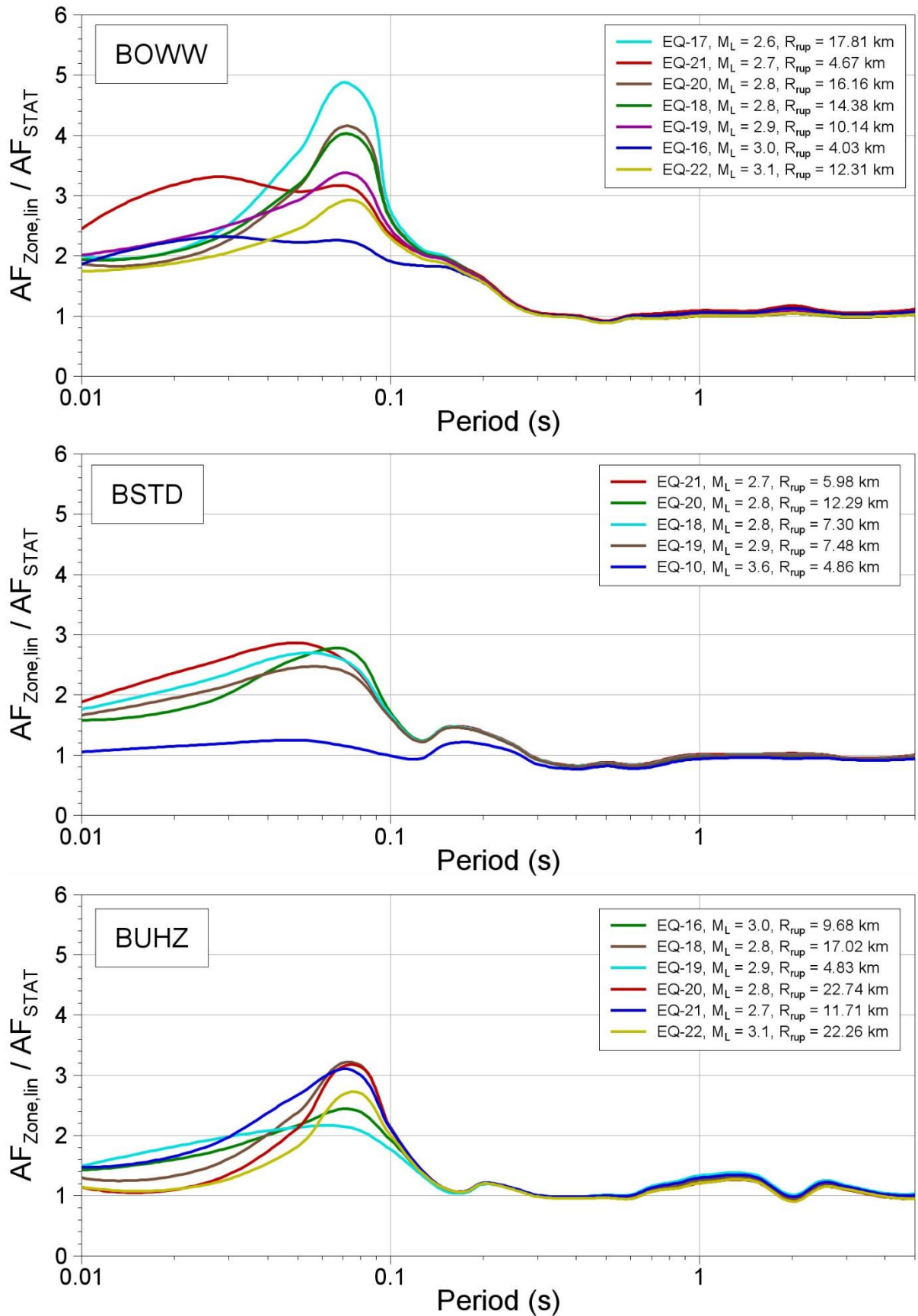


Figure 9.28. Ratios of the linear AF computed for the zone and the linear AF computed for the stations BOWW (Zone 2111), BSTD (Zone 1037), and BUHZ (Zone 801)

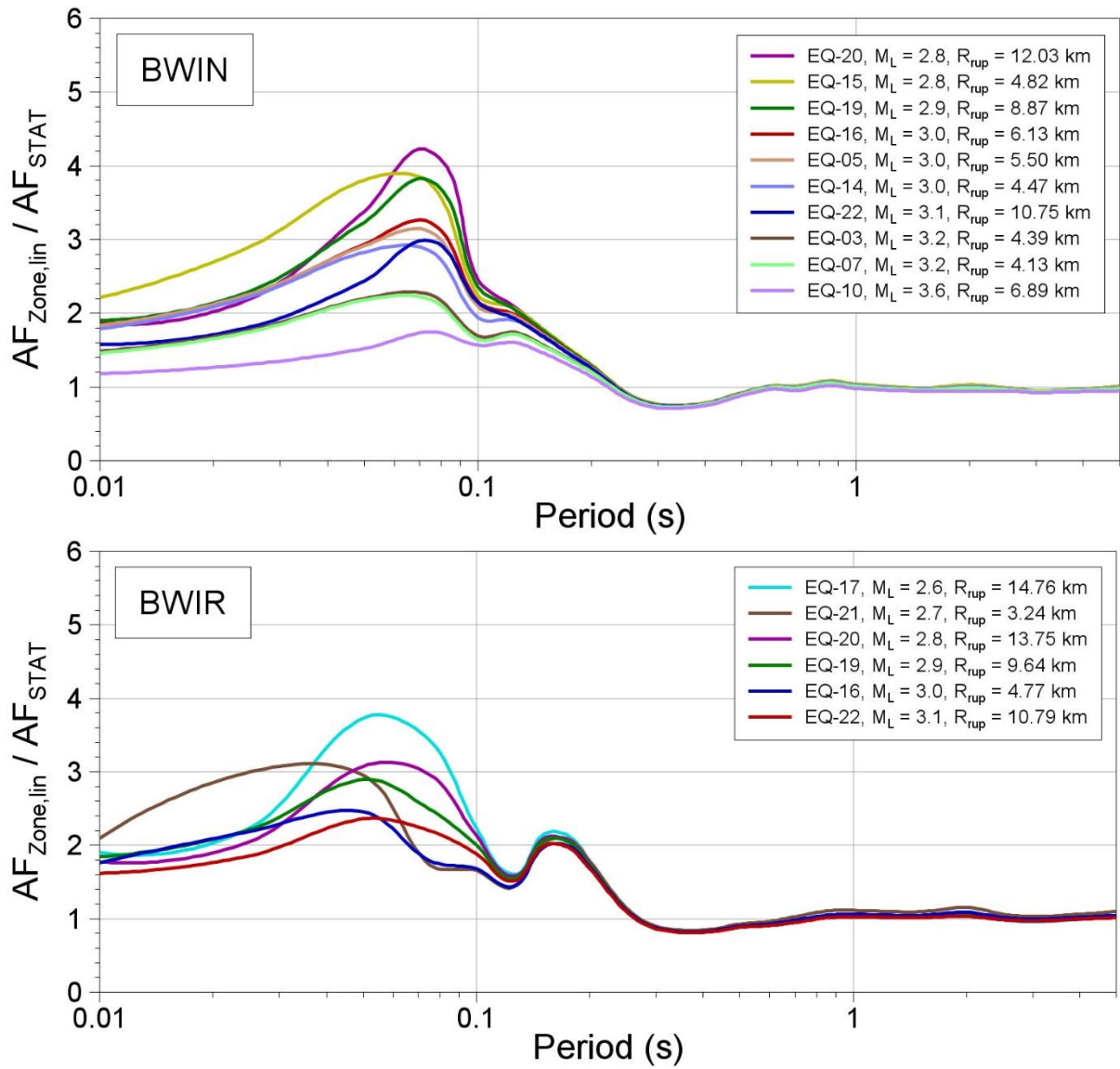


Figure 9.29. Ratios of the linear AF computed for the zone and the linear AF computed for the stations BWIN (Zone 2110) and BWIR (Zone 2111)

10. SIGMA MODEL

Ground-motion prediction equations (GMPEs) define distributions of the values of a specified ground-motion parameter for a given combination of magnitude, distance and site response. Since the residuals of the logarithmic values of ground-motion parameters with respect to the median predictions from GMPEs are generally found to follow to a Gaussian distribution, the distribution is defined by the standard deviation, sigma (σ). The value of sigma is just as important as the coefficients that define the median predictions and it can exert a very strong influence on estimates of seismic hazard and risk. This chapter describes the development of the complete sigma model for the V4 GMM, building on the calculated residuals of the recorded motions (Section 6.5) and the variability associated with the site amplification functions (Sections 8.3 and 9.3).

The chapter begins with an overview of all the components of ground-motion variability applicable to the Groningen ground-motion model for surface motions and a summary of the structure of the proposed sigma model. This is followed by a description of the derivation of an additional component of the variability that is required for the Groningen ground-motion model, namely the component-to-component variability for the horizontal ground motions, which is required in order to be able to transform predictions for the geometric mean component to the arbitrary horizontal component. This transformation is needed for the risk calculations, in order to be consistent with the treatment of the horizontal components of motion of the accelerograms used in the derivation of the fragility functions. The final two sections define the basic elements of the variability in the predicted motions at the reference rock horizon and the additional variability that is added at the ground surface to account for the site response. Since the site-to-site variability is explicitly accounted for in the surface predictions, the within-event variability in the reference rock horizons is necessarily single-station sigma.

Consistent with the functional form of the GMM as defined in Chapter 6 and of the AFs defined in Sections 8.3 and 9.3, all elements of sigma are defined in natural logarithms.

10.1. Elements of sigma model for surface motions

The variability in ground-motion prediction equations is generally represented by a normal distribution of the logarithmic residuals, which can be represented by the standard deviation, σ (sigma). As was already manifest in the calculation of residuals at the NS_B horizon (Section 6.5) there is considerable scatter observed in the data with respect to the predictions of ground motions at the reference rock, which must be incorporated into the model. In order to develop the model for the variability associated with the predictions of the spectral accelerations at the ground surface, it is helpful to explore in a little detail the nature of this variability and its different components.

Residuals of ground-motion parameters are calculated as the logarithm of the recorded value minus the logarithm of the predicted median value, which can also be interpreted as the

logarithm of the ratio of the observed to the predicted motion. A positive residual therefore means that the median GMPE is under-estimating the observed amplitude of motion and a negative residual means that the motions are being over-predicted. The large scatter invariably observed in the residuals of ground motions is generally attributed to the fact that the GMPEs are very simple models to represent complex physical phenomena: even the most complex models in current use contain no parameters to model the influence of the heterogeneity of the fault rupture process in space and time, for example. Consequently, there is scatter in the residuals due to the effect of factors that are not included in the model; if this interpretation is valid then it might be more appropriate to refer to ‘apparent randomness’. Some have argued that there may also be a genuinely random component of the ground-motion field generated by an earthquake, which could therefore never be removed regardless of the complexity of the predictive equations. The two arguments are, of course, not mutually exclusive and could both explain the origin of different parts of the variability.

Regardless of the exact nature of the variability, improvements in ground-motion modelling over the least two to three decades, in terms of expanded databases, greater numbers of explanatory variables and more sophisticated functional forms, have not led to any major reduction in the aleatory variability associated with ground-motion predictions (Strasser *et al.*, 2009). Several studies have confirmed that the residuals are generally very well represented by a log-normal distribution, so for GMPEs predicting logarithmic values of spectral acceleration, the distribution of the residuals can be fully represented by the standard normal distribution with mean of zero and a standard deviation of sigma (σ). For a given suite of predictor variables, any ground-motion amplitude can be expressed as a combination of the median value and a normalised number of standard deviations, represented by epsilon (ϵ).

For the classification of residuals, we follow the notation of Al Atik *et al.* (2010). Total residuals (Δ_{es}) are defined as the difference between recorded ground motions and the values predicted by a GMPE (in natural log units). Total residuals are separated into a between-event term (δB_e) and a within event term (δW_{es}):

$$\Delta_{es} = \delta B_e + \delta W_{es} \quad (10.1)$$

where the subscripts denote an observation for event e at station s (Figure 10.1). The between-event and the within-event residuals have standard deviations τ and ϕ , respectively, and are assumed to be uncorrelated. Therefore, the total standard deviation is given by:

$$\sigma = \sqrt{\tau^2 + \phi^2} \quad (10.2)$$

If we assume that the variability is primarily due to the influence of factors that are either not included in the GMPE or else are crudely represented by the parameters in the equation, then the between-event variability may be assumed to be due to factors such as a stress drop as well as details of the rupture propagation (and in the case of Groningen, the

mechanism of rupture), although it has been found that stress drop variability is much larger than inter-event variability (Cotton *et al.*, 2013). The within-event variability may be influenced by azimuthal variations, crustal heterogeneities, the deeper geological structure at the recording stations, and details of the near-surface velocity profiles not captured by V_{S30} .

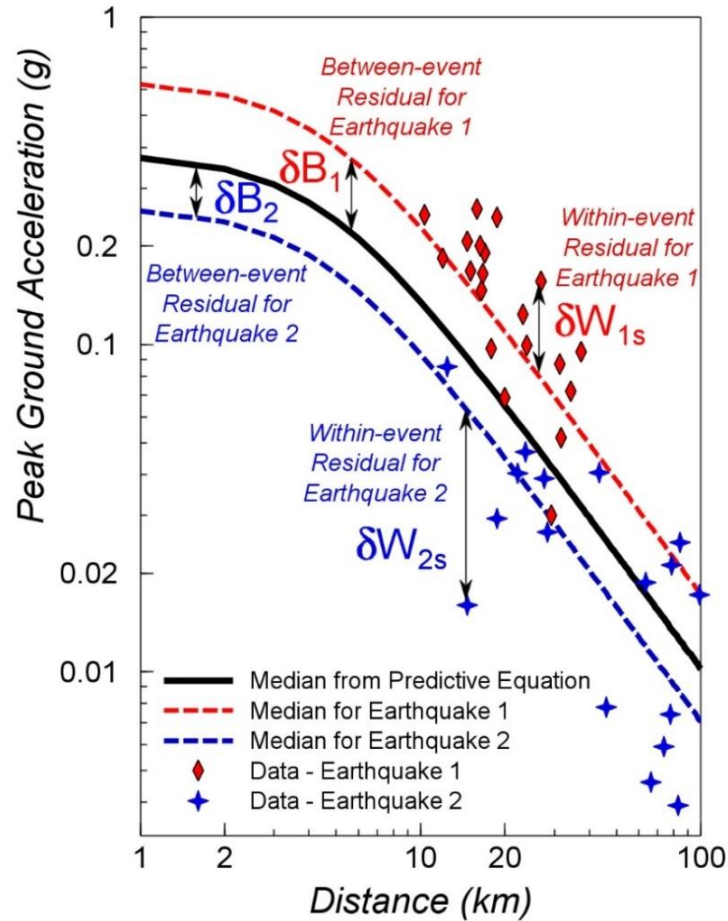


Figure 10.1. Illustration of the concepts of between-event and within-event residuals. The black curve represents the median predictions for an earthquake of magnitude M , whereas the blue and red dashed curves represent the median curves corresponding to two specific events of the same magnitude (Al Atik *et al.*, 2010)

The within-event (or intra-event) residuals, which effectively represent the spatial variability of the ground motions, can in turn be separated into:

$$\delta W_{es} = \delta S2S_s + \delta WS_{es} \quad (10.3)$$

where $\delta S2S_s$ represents the systematic deviation of the observed ground motion at site s (e.g., the ‘site term’) from the median event-corrected ground motion predicted by the GMPE, and δWS_{es} is the site- and event-corrected residual. The standard deviation of the $\delta S2S_s$ and δWS_{es} terms are denoted by ϕ_{S2S} and ϕ_{SS} , respectively. Table 10.1 lists the components of the total residual, their respective standard deviations, and the terminology used for each standard deviation component.

Table 10.1. Terminology used for residual components and their standard deviations. $SD(\cdot)$ denotes the standard deviation operator

Residual Component	Residual Notation	Standard Deviation component	Definition of standard deviation component
Total residual	Δ_{es}	Total or ergodic standard deviation	$\sigma_{ergodic} = SD(\Delta_{es})$
Event term	δB_e	Between-event (or inter-event) standard deviation (tau)	$\tau = SD(\delta B_e)$
Event-corrected residual	δW_{es}	Within-event (or intra-event) standard deviation (phi)	$\phi = SD(\delta W_{es})$
Site term	$\delta S_2 S_s$	Site-to-site variability	$\phi_{S_2 S_s} = SD(\delta S_2 S_s)$
Site- and event-corrected residual	$\delta W S_{es}$	Event-corrected single-station standard deviation (single-station phi)	$\phi_{ss} = SD(\delta W S_{es})$

The recognition of a repeatable site term—which is not random—being part of the model for the aleatory variability in the predictions challenges the ergodic assumption that is implicit in the derivation of empirical GMPEs. In applying a GMPE to the assessment of seismic hazard at a specific location, the interest is in the variation of motions at this site due to different earthquakes that could occur over time. Since it is rare to have recordings from the location under study, and even in the few cases where such recordings exist they will cover at most a few decades, PSHA generally invokes what is referred to as the ergodic assumption (Anderson & Brune, 1999). The ergodic assumption essentially states that variability over space can be used as a substitute for variation of time, and it is invoked in practice since the sigma values calculated from regression analyses to develop GMPEs represent the variability across many different sites (and sometimes many regions). Where there are multiple recordings from individual sites, they display lower variability than indicated by the sigma values of GMPEs (e.g., Atkinson, 2006), the reason being that there are components of the behaviour at an individual site that are repeated in all cases and therefore do not contribute to variability. The effect is even more pronounced when there are multiple recordings from a single site of earthquakes associated with a single seismogenic source because in that case there are repeatable effects of both the path and the site.

If the repeatable contributions to the seismic motion at the site of interest can be modelled through an appropriate adjustment to the median predictions, then the sigma value can be reduced—to a value referred to as ‘single-station sigma’ (Atkinson, 2006)—by an amount that reflects the variability of the site term. The ergodic assumption effectively folds the epistemic uncertainty regarding individual site terms into the sigma value of the GMPE, representing it as aleatory variability:

$$\sigma_{ergodic} = \sqrt{\tau^2 + \phi_{ss}^2 + \phi_{S_2 S_s}^2} \quad (10.4)$$

If the site term is modelled explicitly and therefore the site-to-site component of the ground-motion variability is accounted for in the implementation of the GMPE into hazard calculations, a partially non-ergodic approach (also called a *single-station sigma* approach) may be invoked with a reduced variability. In this case, the standard deviation is known as the *single-station standard deviation* (Figure 10.2) and is given by:

$$\sigma_{ss} = \sqrt{\tau^2 + \phi_{ss}^2} \quad (10.5)$$

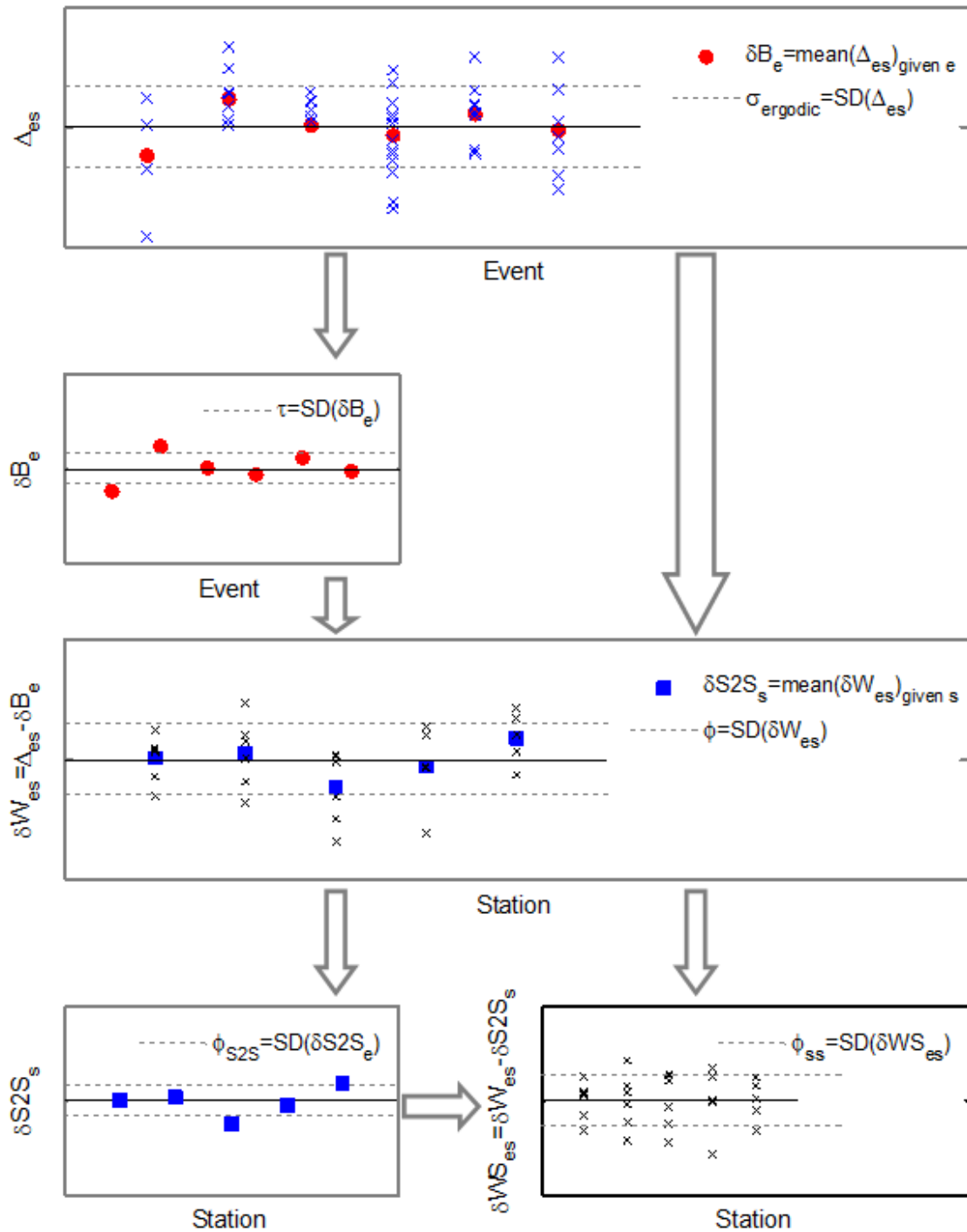


Figure 10.2. Schematic representation of the breakdown of residuals leading to the single-station ϕ (ϕ_{ss})

As is clear from the discussions of the non-linear site amplification factors and their associated variability in Section 8.3, and the zonation of the Groningen field with regard to site amplification effects presented in Chapter 9, the site-to-site variability in the estimation of surface motions in the Groningen field are being fully accounted for in the chosen formulation for the ground-motion prediction model. Therefore, it is essential to remove the site-to-site variability from the predictions of spectral accelerations at the reference rock horizon, since otherwise this element of the variability would be accounted for twice in the estimation of surface motions. This means that the within-event variability of the NS_B motions must be based on an estimate of ϕ_{SS} . In Section 10.3, the selection of the appropriate values for this parameter is discussed, together with the accompanying estimates of the between-event variability, τ . The specific model for ϕ_{S2S} is described in Section 10.4.

Before discussing these key elements of the variability in the ground-motion predictions at the reference rock horizon and at the ground surface, two other elements of the ground-motion variability are presented. The first is the component-to-component variability, required to transform the predictions of the geometric mean of the horizontal motions to the arbitrary component of horizontal motion, as required for the risk calculations (Section 1.3). The component-to-component variability is discussed in Section 10.2. The complete sigma model for the V4 GMM for Groningen is presented in Section 11.1 in the context of the complete ground-motion model and the detailed guidance on its implementation.

10.2. Component-to-component variability

Consistent with the current global practice in seismic hazard modelling, the GMPEs have been derived in terms of the geometric mean of the two horizontal components. However, for the risk calculations, it is necessary to predict spectral accelerations corresponding to an arbitrarily-selected horizontal component, for consistency with the way the fragility functions have been derived (see Section 1.3). In terms of median predictions, no adjustment to the geometric mean component is required to transform these to the arbitrary component, an adjustment is needed to the sigma value in order to account for the component-to-component variability that is lost in the calculation of the geometric mean of each pair of horizontal components. The component-to-component variance is given by the following equation (Boore, 2005b):

$$\sigma_{C2C}^2 = \frac{1}{4N} \sum_{j=1}^N [\ln(Y_{1j}) - \ln(Y_{2j})]^2 \quad (10.6)$$

where Y_1 and Y_2 are the spectral accelerations at period T from the two horizontal components of the j^{th} accelerogram, and N is the total number of records. Figure 10.3 shows the calculated values of the component-to-component variance for the Groningen ground-motion database, and also compares them with the values reported by Boore (2005b) and by Campbell & Bozorgnia (2007). The first observation that can be made from this figure is that the component-to-component variability of the Groningen recordings seems to be

exceptionally large, which is not particularly surprising given that it is known the recordings from the field show a very high degree of polarisation (see, for example, Figure 1.5). Another important observation is the erratic nature of the calculated values of component-to-component variability for the Groningen recordings at longer periods. The values above 2.0 seconds may be unreliable since the number of usable records at this period is too small to allow a stable estimate although the trends are consistent. As the number of usable records decreases with increasing period, the proportion of stronger motions increases and since the polarisation is observed to be strongest for the higher-amplitude recordings (e.g., Ntinalexis *et al.*, 2016), this may be the explanation for the increase in component-to-component variability observed at longer periods.

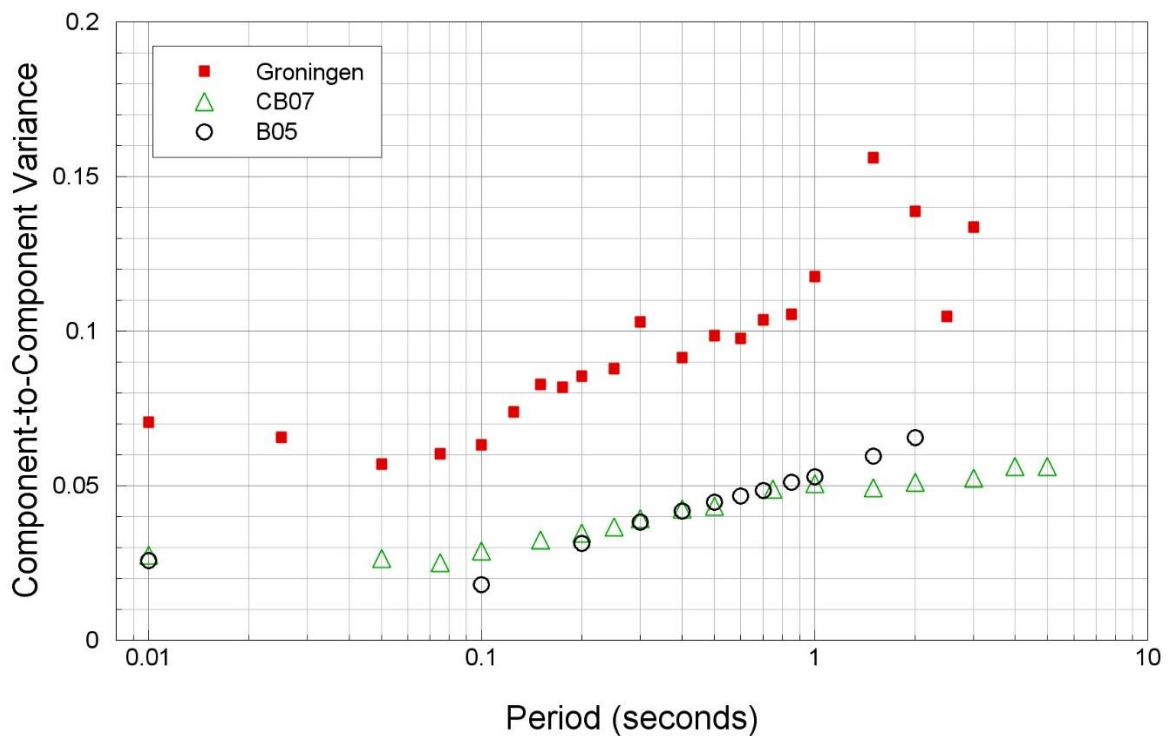


Figure 10.3. Component-to-component variance calculated for Groningen records and comparison with values from Boore (2005b) and from Campbell & Bozorgnia (2007)

The contrast between the component-to-component variances for the Groningen data and those derived from databases of tectonic earthquake recordings is striking, and immediately begs the question of whether this arises because of features specific to the Groningen earthquakes or whether this is simply a characteristics of the motions from smaller magnitude earthquakes. In order to explore this question, three databases of recordings of tectonic earthquakes were obtained, these being the European database used by Akkar *et al.* (2014a), together with additional recordings from smaller magnitude earthquakes (Bommer *et al.*, 2015a), the NGA-West2 database (Ancheta *et al.*, 2014), and the KiK-net data (Dawood *et al.*, 2016). The magnitude-distance distribution of these datasets is shown in Figure 10.4.

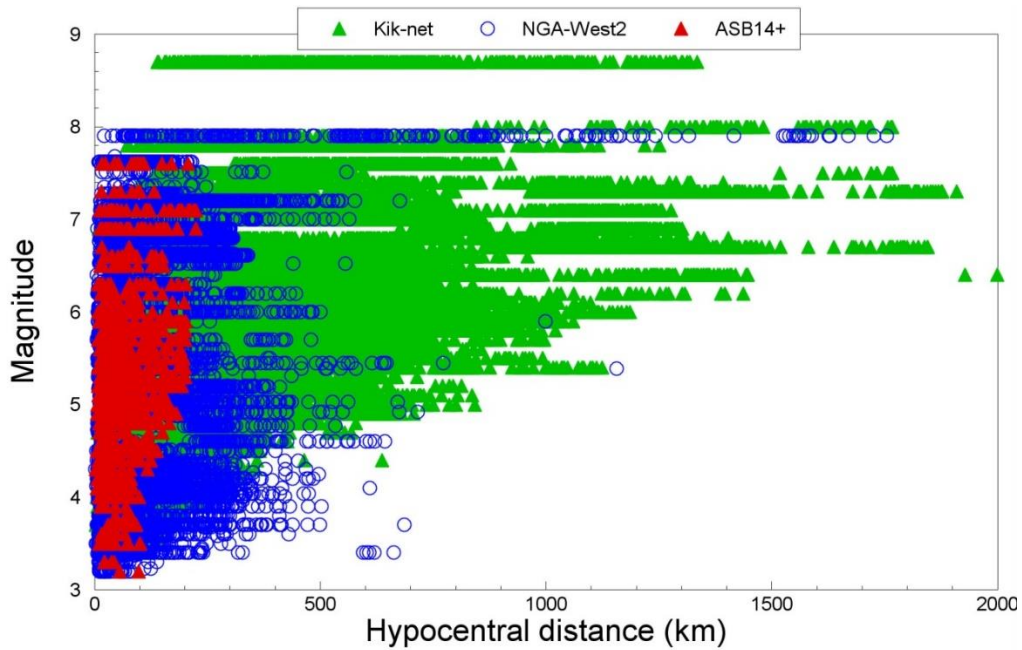


Figure 10.4. Magnitude-distance distribution of the tectonic earthquake recordings from the KiK-net, NGA-West2 and European databases

In order to reduce the number of variables being compared, a subset of these recordings was selected to represent only accelerograms from soft soil sites (defined by $V_{S30} \leq 400$ m/s) since the Groningen motions are all from soft soil sites. The magnitude-distance distribution of the resulting data, shown only for distances up to 60 km, is illustrated in Figure 10.5.

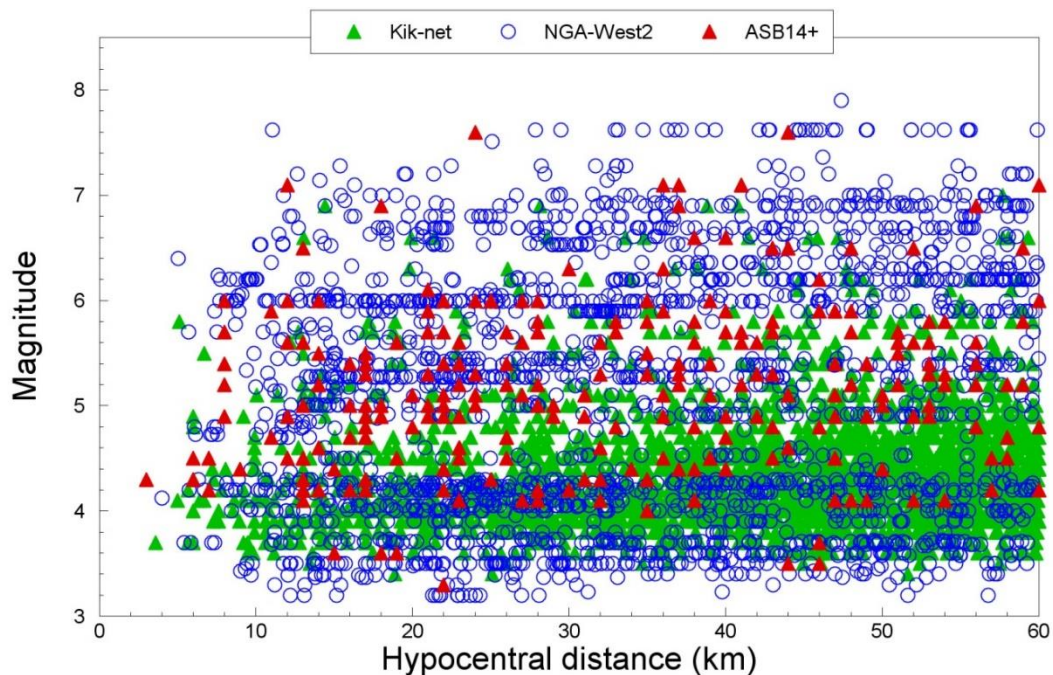


Figure 10.5. Detail of the magnitude-distance distribution of the records from stations with a V_{S30} limited to a maximum of 400 m/s from the three tectonic ground-motion databases selected for this study for hypocentral distances limited to 60 km.

The component-to-component variances of the tectonic-earthquake recordings were then calculated in exactly the same way as for the Groningen database—using Eq.(10.6)—and these are compared in Figure 10.6. For the tectonic databases, the variances were calculated for the entire database and then for the data grouped in magnitude bins; ample records were available in all bins to provide stable estimates of the component-to-component variability. As can be immediately appreciated from the figure, while there is some apparent sensitivity to magnitude, with the variances for smaller magnitudes having higher values, even for the smallest magnitude bin the values remain considerably below those obtained for the Groningen data.

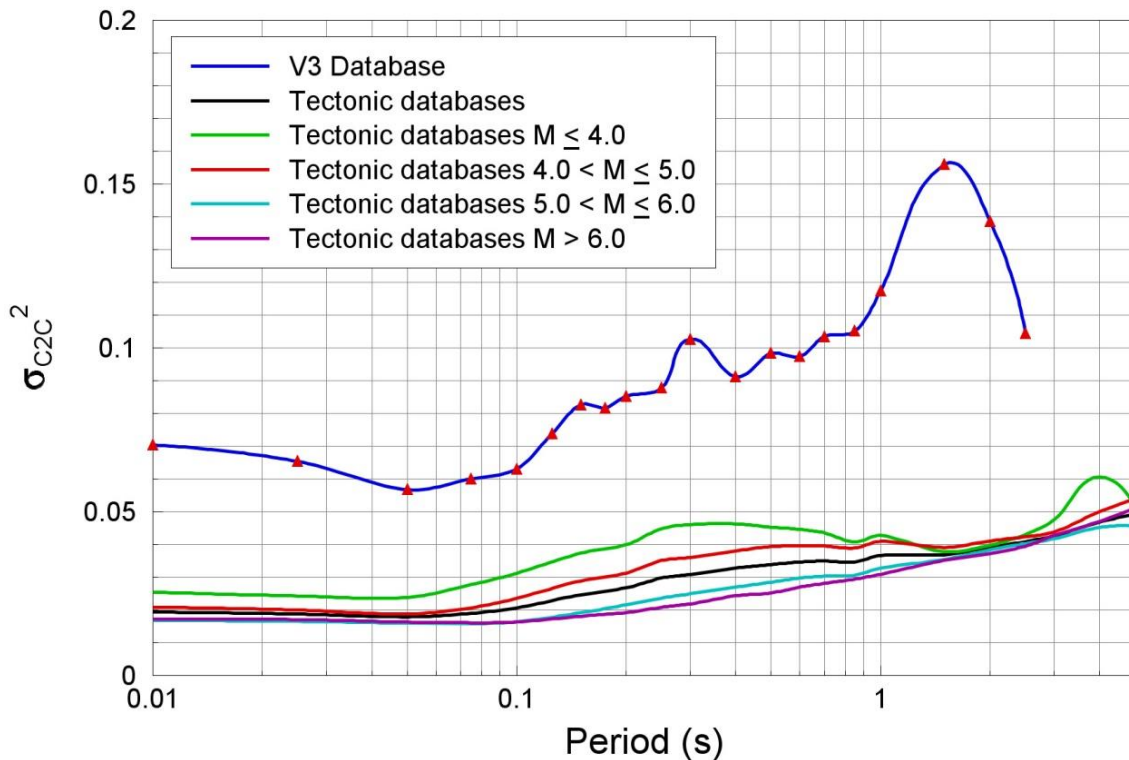


Figure 10.6. The component-to-component variance at each period for the V3 database and the combined tectonic database for a V_{S30} of 400 m/s and less.

In view of the relatively modest influence of magnitude alone, it was decided to explore whether in fact distance might also be an influencing factor on the high component-to-component variances obtained for the Groningen recordings. This was considered in particular given the greater density of recordings obtained at short distances in the Groningen database (Figure 10.7) compared to the tectonic earthquake databases, for which the numbers of recordings at hypocentral distances of less than 10 km is rather small (Figure 10.5), no doubt because of the greater average focal depths of such events. Figure 10.8 shows results similar to those depicted in Figure 10.6 but obtained limiting the tectonic data to maximum distances of 60 km and 30 km; the numbers of available records from the tectonic databases continue to be sufficient to allow stable estimates of the component-to-component variances.

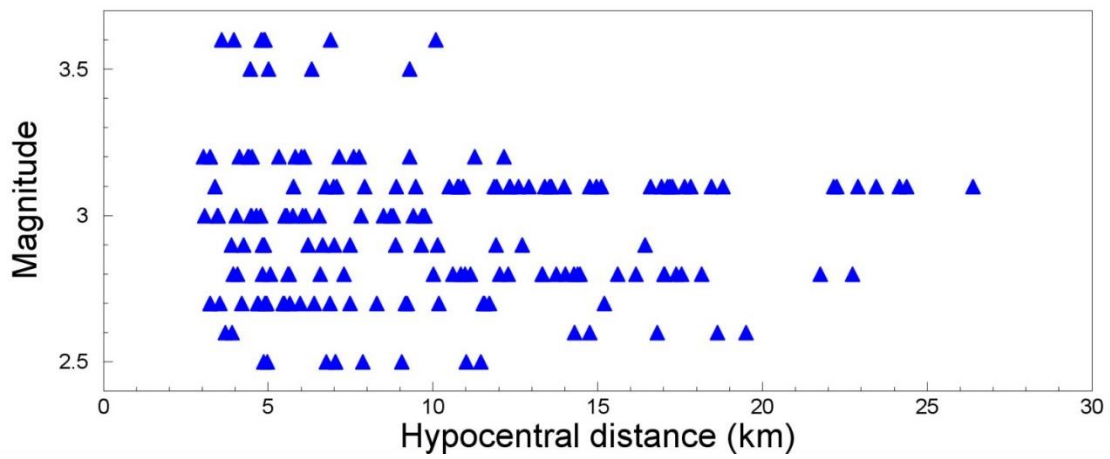


Figure 10.7. The component-to-component variance at each period for the V3 database and the combined tectonic database for a V_{S30} of 400 m

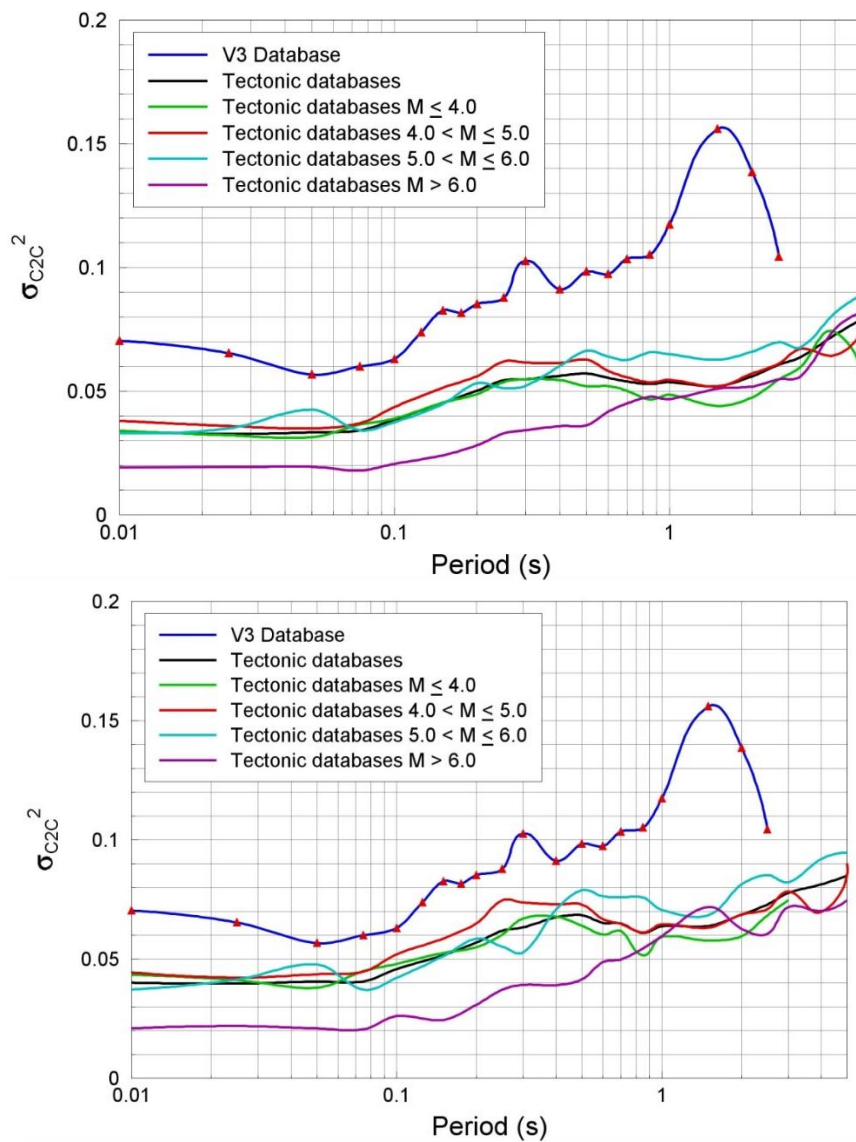


Figure 10.8. The component-to-component variance at each period for the tectonic databases below a hypocentral distance of 30 km and the V3 database, with the former limited to distances of 60 km (*upper*) and 30 km (*lower*)

Several interesting observations can be made on Figure 10.8. Firstly, when considering only recordings from shorter distances, the magnitude-dependence seems to only be strong for larger earthquakes ($M > 6$); for smaller magnitude, the patterns are less consistent and arguably not present at all. However, comparing the lower and upper plots in Figure 10.8 it is clear that the greater restriction on distance leads to an increase in the component-to-component variability. Indeed, considering only records from events of less than magnitude 6 and distances no greater than 30 km, the variances begin to tend towards those obtained from the Groningen data. Therefore, it would appear that distance may exert a greater influence on the component-to-component variability than the magnitude. This conclusion is confirmed in Figure 10.9 in which the component-to-component variances have been calculated from the tectonic databases, using only records from magnitudes below 6 and progressively imposing greater restrictions on the distance. To obtain these estimates, it was necessary to remove the restriction on V_{S30} in order to retain sufficient data in the smaller distance bins.

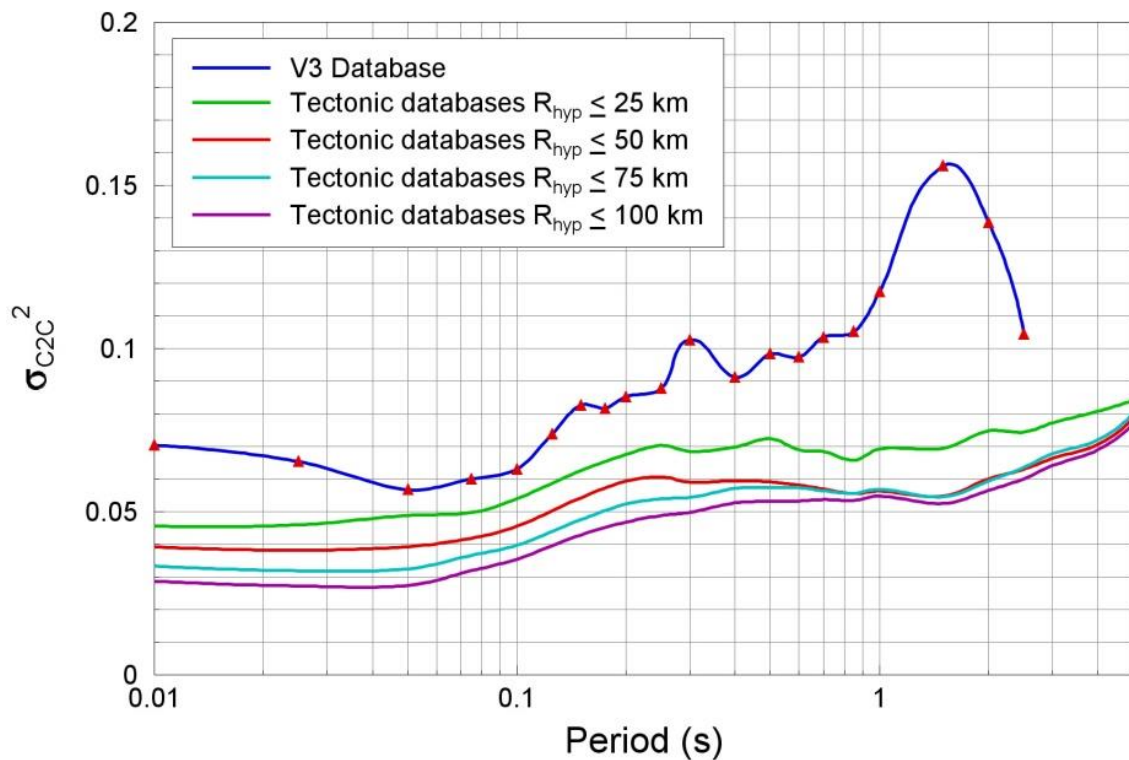


Figure 10.9. The component-to-component variance at each period for the tectonic databases for earthquakes of $M < 6$ and with data restricted to different maximum distances, compared to the V3 database (no restriction on V_{S30})

Figure 10.9 suggests that for small-to-moderate earthquakes, the component-to-component variability has a clear dependence on distance. At shorter distances, the records appear to show greater degrees of polarisation, probably as a result of the radiation pattern from the source. The degree of polarisation observed in the Groningen recordings may, therefore, result from the proximity of the source to the accelerograph stations, as a result of the shallow focal depth and the relatively short epicentral distances, leading to preservation of polarity in

the shear-wave radiation pattern. Now that the network density has been increased and large numbers of recordings are being obtained from individual earthquakes, this is something that can be investigated, as discussed in Chapter 13. For now, the question arises as to whether the strong polarisation observed at small magnitudes would persist for larger earthquakes. Within the assumptions of the current model—and specifically the focus of all earthquakes at 3 km depth within the gas reservoir—it would seem reasonable to conclude that at least up to magnitude 6, rather high levels of polarisation may be expected. Therefore, in the absence of an alternative model for such shallow events, it is conservatively assumed that the trends observed in the current Groningen database represent an appropriate model for the component-to-component variability of the motions. What is less clear is the exact trend at longer periods, where the number of available records is reduced and the signal from such small events may be rather weak. Therefore, to develop a model for the entire period range of relevance, we scale the values obtained by Campbell & Bozorgnia (2007) to approximately match the Groningen data at short periods, which requires a factor of 2.25 (Figure 10.10). Since the resulting variance values display an approximately tri-linear behaviour with respect to period, a simple linear fit is used to represent the general trend of the values without erratic period-to-period variations, as shown in Figure 10.10. The final values of the component-to-component variability, σ_{C2C} , estimated in this way are listed in Table 10.2.

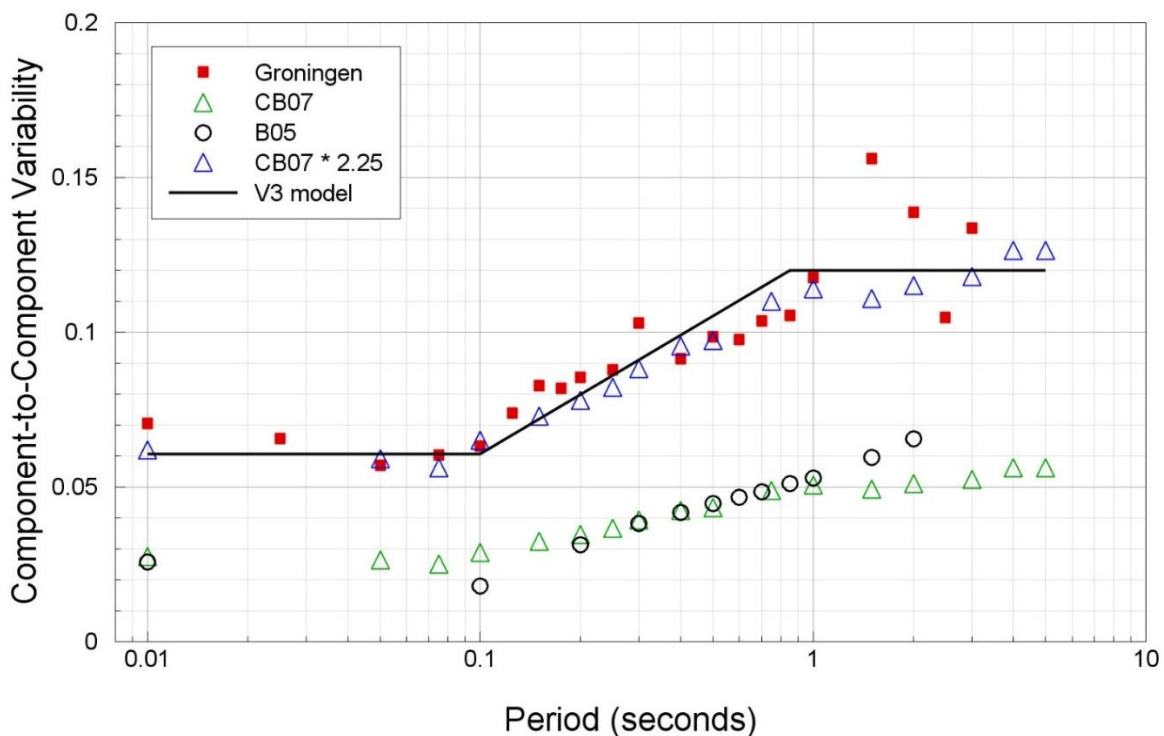


Figure 10.10. The component-to-component variances of the Groningen data (red squares) and their approximation by the scaled values from Campbell & Bozorgnia (2007), simplified by a tri-linear trend

The standard deviation of the component-to-component variability of horizontal components of PGV is calculated as 0.307. The corresponding value from Campbell & Bozorgnia (2007) is 0.190 and application of the same factor of 2.25 yields a final value of 0.297. As can be

noted from Table 10.2, this is very close to the value obtained for Sa(0.25s), which is consistent with the excellent correlation observed between PGV and Sa at periods in the range from 0.2 to 0.3 s (Figure 10.11).

Table 10.2. Component-to-component variability for Groningen V3 model

Period (seconds)	σ_{C2C}
0.01	0.246
0.025	0.246
0.05	0.246
0.075	0.246
0.1	0.246
0.125	0.267
0.15	0.274
0.175	0.280
0.2	0.290
0.25	0.298
0.3	0.310
0.4	0.320
0.5	0.327
0.6	0.333
0.7	0.340
0.85	0.346
1.0	0.346
1.5	0.346
2.0	0.346
2.5	0.346
3.0	0.346
4.0	0.346
5.0	0.346
PGV	0.297

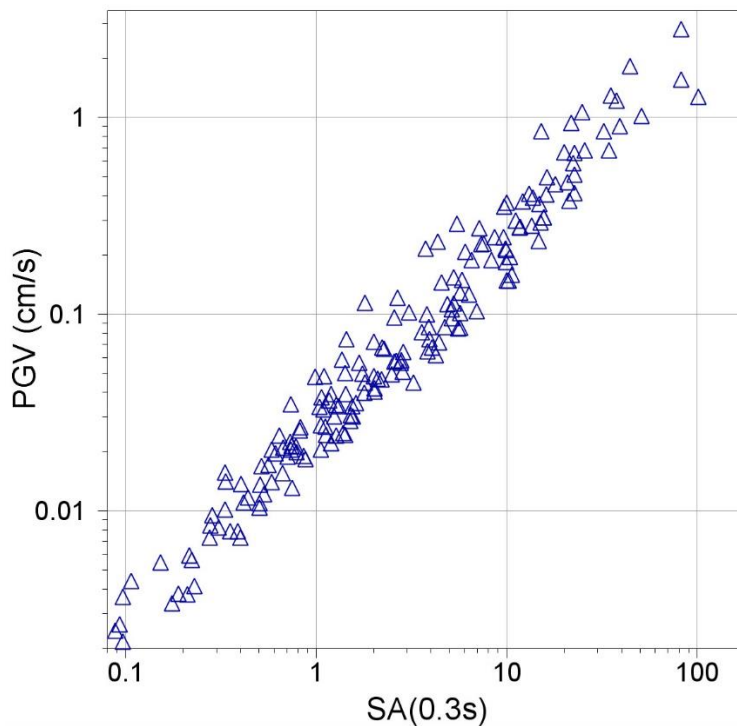


Figure 10.11. Correlations between PGV and Sa(0.3s) values for Groningen motions

10.3. Tau and Φ_{SS} model

As explained in Section 10.1, the variability in the ground-motion predictions at the NS_B reference rock horizon must be expressed as single-station sigma, which was given in Eq.(10.5) and is repeated here for completeness and ease of reference:

$$\sigma_{SS} = \sqrt{\tau^2 + \phi_{SS}^2} \quad (10.7)$$

The two elements required therefore are the between-event (earthquake-to-earthquake) variability and the single-station within-event variability.

Starting with the single-station within-event variability, one option is to estimate this from multiple recordings at individual recording locations. This option will be explored in the future refinements of the GMPE when larger numbers of recordings are available for from multiple stations; to date, relatively few stations have multiple recordings to date. Moreover, while a locally-calibrated model might generally be preferred, it has been found from detailed analysis of datasets from various different regions that estimates of ϕ_{SS} are remarkably stable around the globe (e.g., Rodriguez-Marek *et al.*, 2013). Therefore, it is defensible to adopt values estimated from such global datasets and for this purpose in the V2 model development we decided to use the homoscedastic model—in other words, the model in which the value of this variability does not vary with magnitude—as defined in the PSHA project for the Thyspunt nuclear site in South Africa (Bommer *et al.*, 2015c). The best estimate value for ϕ_{SS} is 0.45 with the epistemic uncertainty represented by upper and lower limits of 0.522 and 0.378 respectively (Rodriguez-Marek *et al.*, 2014). In the Thyspunt project, these alternative estimates were assigned weights of 0.2, while a weight of 0.6 was placed on the central value.

In the V3 model these values were modified based on recent work conducted for the NGA-East ground-motion modelling project in the United States. Figure 10.12 shows the global heteroskedastic single-station within-earthquake variability model proposed by Al Atik (2015), which displays a rather strong dependence on magnitude for the value of ϕ_{SS} at higher frequencies. As can be appreciated from this figure, for smaller magnitudes (**M** 5) the value at higher frequencies are closer to the upper branch of the V2 model than to the best estimate value. In view of the dominant influence of earthquakes in this magnitude range on the Groningen seismic hazard and risk estimates, this would therefore appear to be a more appropriate best estimate value. This conclusion is supported by Figure 10.13, which shows the constant (and homoscedastic with respect to magnitude) model proposed by Al Atik (2015) for central and eastern North America (CENA), which assumes a value of 0.513 (although the data suggest smaller values may be applicable at lower frequencies).

In view of this new information—and in the absence of evidence or analyses at this stage that would challenge its applicability to the Groningen case—we decided to modify the ϕ_{SS} model for the V3 ground motion model, and specifically to allow for larger values at high

response frequencies (*i.e.*, short oscillator periods). The V2 model was retained at longer periods (> 1 seconds) with log-linear transition introduced so that the central model approximately matches the NGA-East model for periods of 0.1 second and lower (Figure 10.14).

The proposed models for ϕ_{SS} are distance-independent, which is consistent with models used in various other hazard studies (*e.g.*, Rodriguez-Marek *et al.*, 2014; Al Atik, 2015). However, the simulations results shown in Figures 6.7 to 6.13, as well as the residuals for the ground motion model proposed in this study (see Section 11.2) indicate larger within-event standard deviations at shorter distances (below approximately 10 km). However, as indicated before the Groningen data is not sufficient to constrain a model for ϕ_{SS} . For this reason, we selected to maintain a distance independent model for ϕ_{SS} , consistent with past practice. A distance-dependent model for ϕ_{SS} could be considered in the future when more data becomes available.

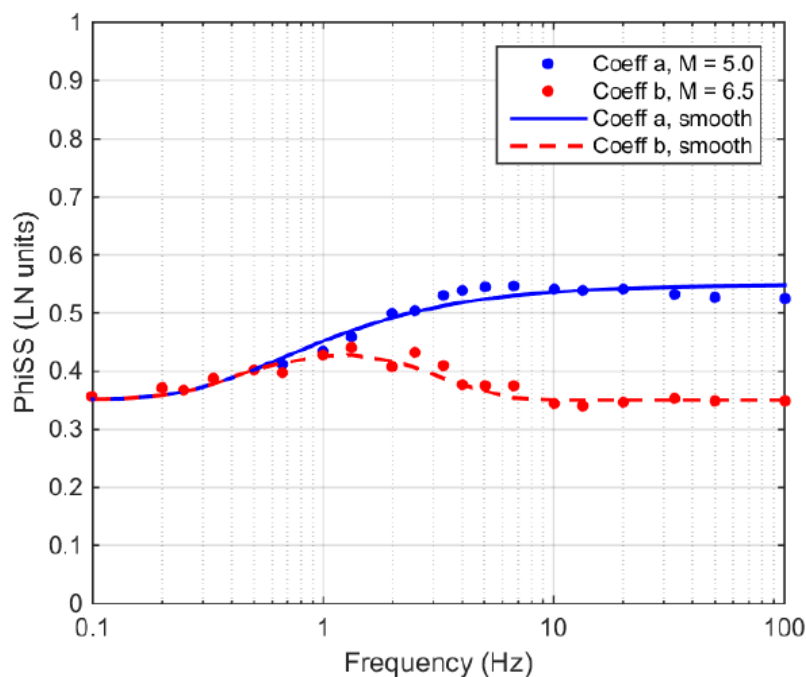


Figure 10.12. Global heteroskedastic model for ϕ_{SS} from the NGA-East project (Al Atik, 2015)

In the development of V3 model, and those that preceded it, computational efficiency was a consideration in view of the long run times for the hazard and risk calculations. This led to the decision to define three median branches and to couple these with three branches on sigma, to limit the GMM logic-tree to just three branches. With recent improvements in the computational speeds of the hazard and risk engine, there is less onus to keep the GMM logic-tree so lean, for which reason four median branches have now been defined, as described in Chapter 6. The decision was taken to use two branches to capture the uncertainty in the sigma model, and to allow all combinations of medians and sigmas, with the consequence of the final logic-tree having a total of eight branches. The three values of ϕ_{SS} in the V3 model are therefore replaced with two equally-weighted branches in the V4

model. In order to reduce the branches of the within-event variability model to two branches, we followed these principles:

1. The uncertainty of the variance standard deviation should follow a chi-squared distribution (this has been used in a number of SSHAC Level 3 PSHA and GMM projects including the Hanford PSHA and the SWUS and NGA-East projects)
2. Use previously computed values of the coefficient of variation of ϕ_{SS} (These values were computed as 0.1 for the PEGASOS Refinement Project and as 0.12 for the SWUS project).
3. A normal distribution can be approximated by a two point distribution by branches with weights of 0.5 each and each branch corresponding to $\mu + \sigma$ and $\mu - \sigma$, respectively.

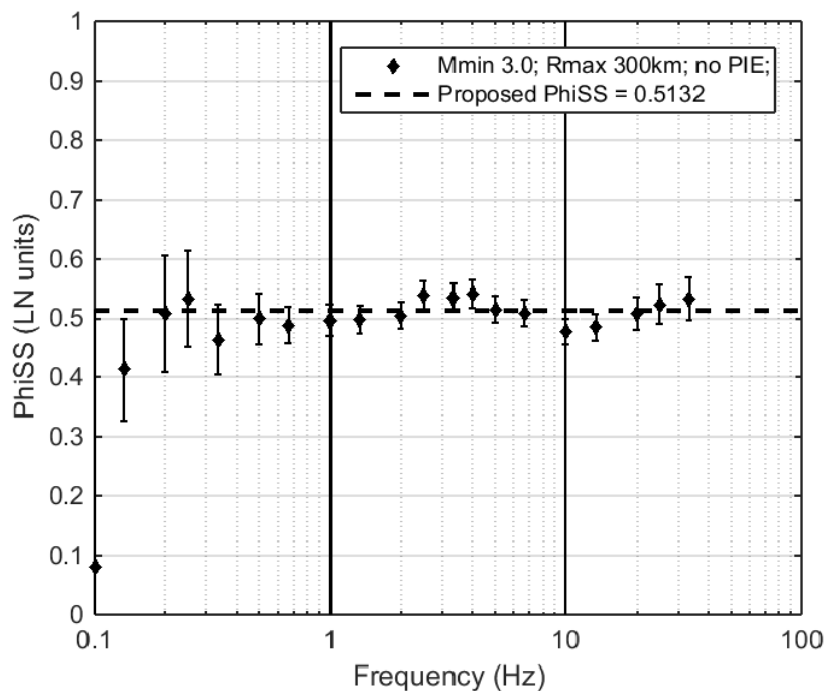


Figure 10.13. Homoskedastic model for ϕ_{SS} in central and eastern North America proposed in the NGA-East project (Al Atik, 2015)

If we follow these principles, then the standard deviation of ϕ_{SS}^2 is given by:

$$SD(\phi_{SS}^2) = 2COV\phi_{SS}^2 \tag{10.8}$$

and the branches are obtained by first computing the percentiles of a scaled Chi-square distribution with mean ϕ_{SS}^2 and standard deviation $SD(\phi_{SS}^2)$, and then taking the square root of these values. The selected percentiles are the 84.1 and 15.9 percentiles for the Low and High models, respectively (corresponding to the branches in item no. 3 above). This is expressed mathematically as follows:

$$\phi_{ss,High} = \sqrt{c \chi_{2,k}^{-1}(0.841)}$$

$$\phi_{ss,Low} = \sqrt{c \chi_{2,k}^{-1}(0.159)}$$
(10.9)

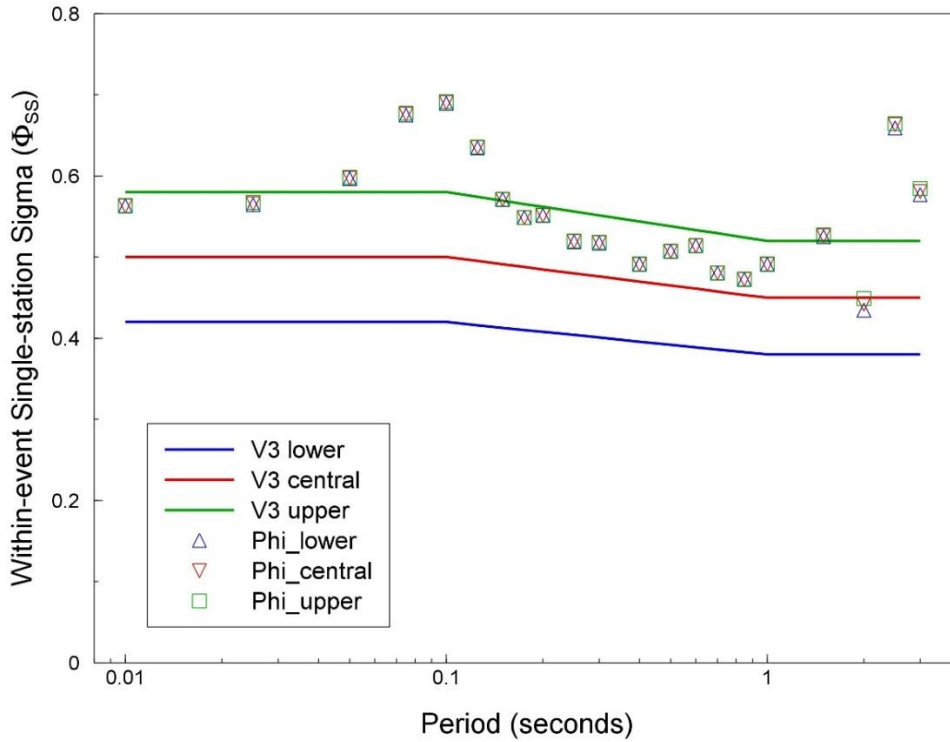


Figure 10.14. V3 model for ϕ_{ss} compared with measured values of within-event variability

where $\chi_{2,k}^{-1}(x)$ is the inverse of the Chi-square distribution with k degrees of freedom and c is a scaling parameter; k and c are given by:

$$c = \frac{(SD(\phi_{ss}^2))^2}{2\phi_{ss}^2}$$

$$k = \frac{2\phi_{ss}^4}{(SD(\phi_{ss}^2))^2}$$
(10.10)

The resulting model is shown (and compared to V3) in the Figure 10.15, both for COV = 0.1 and COV = 0.12). The final selected model uses COV = 0.12, selected on the basis of yielding slightly more conservative results.

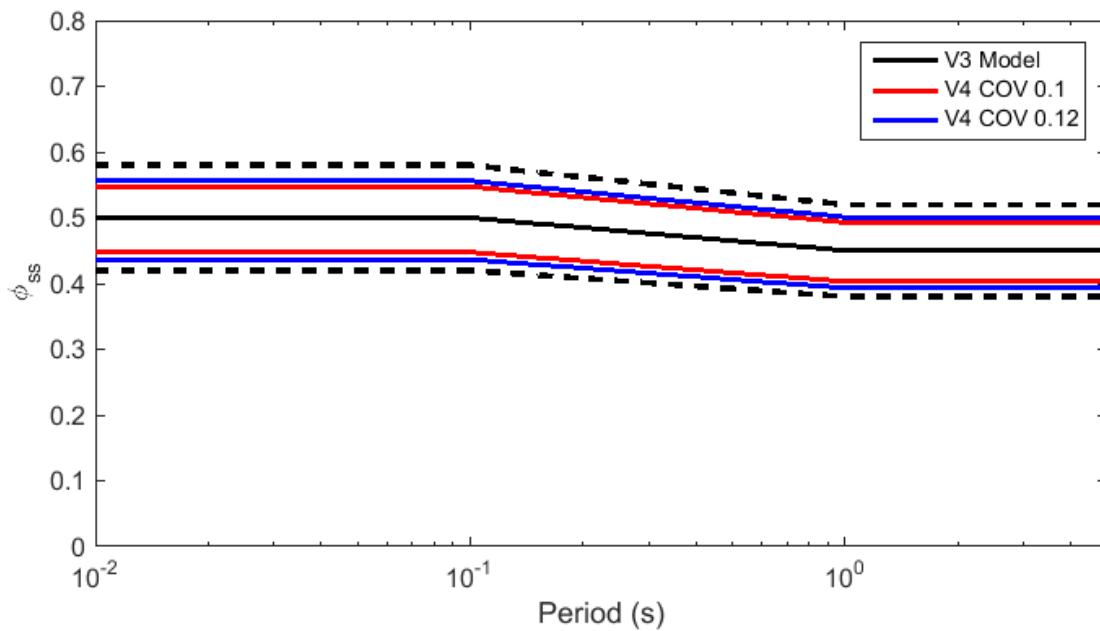


Figure 10.15. Comparison of V3 and V4 models for within-event variability, with three and two branches respectively.

Figure 10.16 compares the two branches of the V4 model with the individual within-station components of variability calculated from the regressions described in Chapter 6. The values of within-event variability are listed in Table 10.3. The value for PGV are selected to be equal to those for $S_a(0.7s)$ in light of the correlation between PGV and spectral accelerations in the period range 0.5-1.0 second for larger magnitudes (Bommer & Alarcón, 2006).

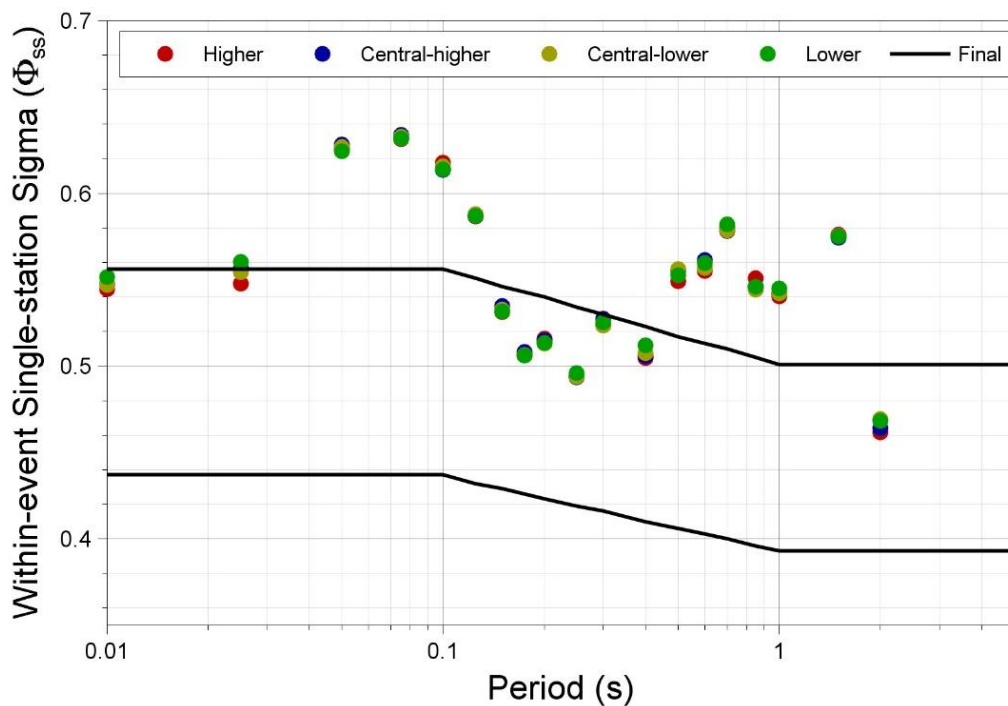


Figure 10.16. Calculated within-event variability values compared with the two branches of the V4 model

Table 10.3. Within-event standard deviations for the V4 GMPE in rock

Period (s)	Lower	Upper
0.01	0.437	0.556
0.025	0.437	0.556
0.05	0.437	0.556
0.075	0.437	0.556
0.1	0.437	0.556
0.125	0.432	0.551
0.15	0.429	0.546
0.175	0.426	0.543
0.2	0.423	0.540
0.25	0.419	0.534
0.3	0.416	0.530
0.4	0.410	0.523
0.5	0.406	0.517
0.6	0.403	0.513
0.7	0.400	0.510
0.85	0.396	0.505
1.0	0.393	0.501
1.5	0.393	0.501
2.0	0.393	0.501
2.5	0.393	0.501
3.0	0.393	0.501
4.0	0.393	0.501
5.0	0.393	0.501
PGV	0.400	0.510

Turning now to the between-event variability, the between-event variability was estimated from the bias-adjusted residuals (see Section 6.5) for the four median models. In all cases, the value of τ was found to display a consistent pattern of relatively constant values at short periods and at longer periods, with a dip in the region of 0.1 seconds (Figure 10.17). Up to a period of 0.85 seconds, all 22 earthquakes remained in the analyses (taking account of the usable period range of each record) and even at 1.0 second, 21 of the earthquakes remain with 152 of the 178 records. However, these numbers rapidly dropped off at longer periods such that at 1.5 seconds only 83 (less than half of the total number) records are still useable; the values associated with longer periods are not useable in view of how few records are used in their determination. A functional form was fitted to the inter-event standard deviations to avoid the small period-to-period fluctuations:

$$\tau(T) = \sqrt{\tau_0^2 + [g(T)\tau_1]^2 + g(T)\tau_1\tau_3} \quad (10.11a)$$

$$g(T) = \frac{2}{3} \left[\frac{1}{1 + (\tau_1 / \tau_2)^2} \right] \quad (10.11b)$$

The fitting is performed on the values at periods between 0.01 and 1.5 seconds. The coefficients of Eq.(10.11) from the four models are presented in Table 10.4 and the resulting values of τ at the 23 target periods in Table 10.5, including extrapolations to the periods beyond 1.5 seconds. The values for PGV are reported as calculated from the regressions, without smoothing.

The inter-event sigmas are coupled with the corresponding median branches and then the within-event variability branches are combined with each median- τ combination. The complete logic-tree structure for the GMPEs for the prediction of ground-motion amplitudes at the NS_B horizon is illustrated in Figure 10.18. The model has a total of eight branches that capture the full range of epistemic uncertainty in the ground-motion predictions but without the former conservatism that resulted from combining high median predictions with the largest estimates of the variability components. An implicit assumption in the current model is that the inter-event variability would be similar for larger magnitude earthquakes, including both larger induced events (up to M 5) and even larger triggered earthquakes. However, since the values in Table 10.5 are comparable to those from GMPEs derived from recordings of tectonic earthquakes, this is a reasonable and defensible assumption.

Table 10.4. Coefficients of Eq.(10.11) for the three models

Coefficient	Lower	Central-lower	Central-higher	Upper
τ_0	0.2747	0.2747	0.2747	0.2747
τ_1	0.5700	0.5935	0.6816	0.6538
τ_2	0.0944	0.0824	0.0824	0.0720
τ_3	-1.3783	-1.3014	-1.4650	-1.3495

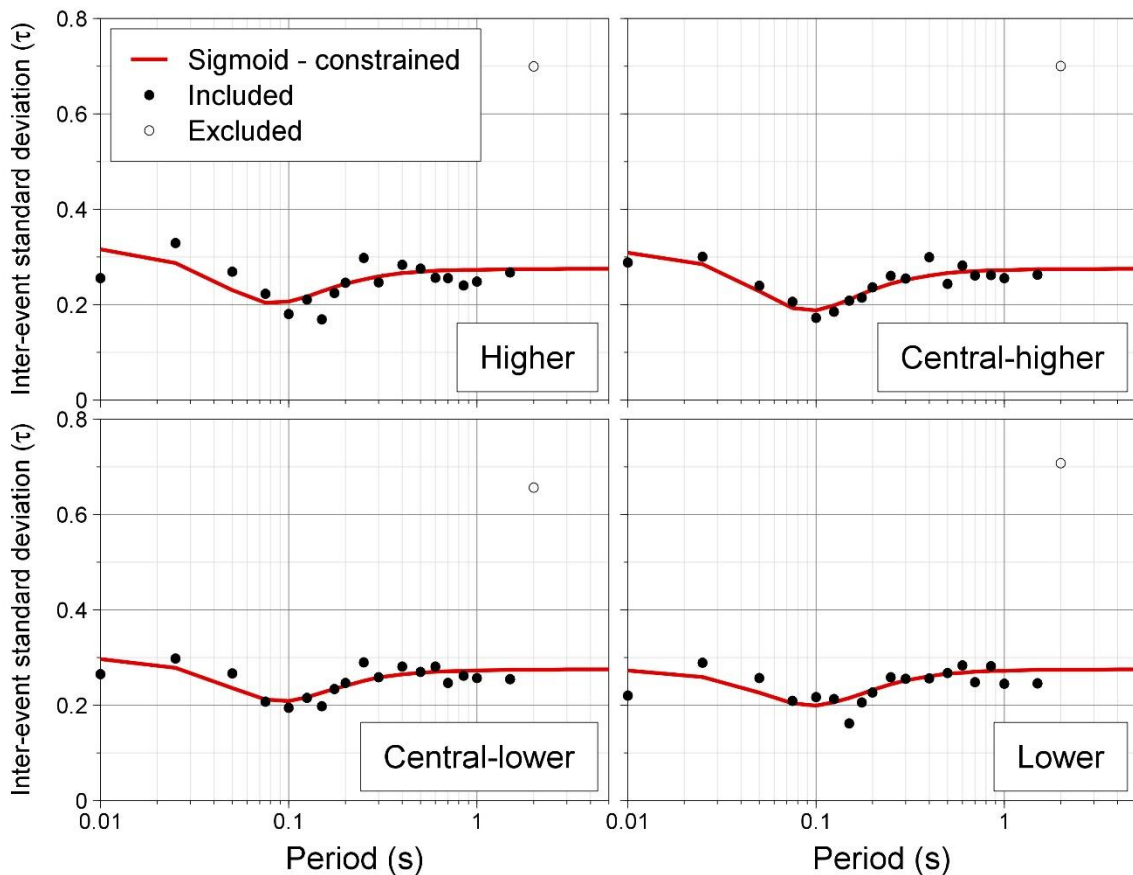


Figure 10.17. Calculated between-event standard deviations from the four median models after removal of the bias, and fitting of Eq.(10.11) to provide smoothed values at all target periods

Table 10.7. Between-event standard deviations

Period (seconds)	τ			
	Lower	Central-a	Central-b	Upper
0.01	0.273	0.297	0.309	0.316
0.025	0.259	0.278	0.285	0.287
0.05	0.226	0.236	0.228	0.230
0.075	0.204	0.212	0.193	0.204
0.1	0.199	0.209	0.188	0.206
0.125	0.206	0.217	0.198	0.217
0.15	0.215	0.226	0.210	0.228
0.175	0.224	0.234	0.222	0.237
0.2	0.232	0.241	0.231	0.244
0.25	0.244	0.251	0.244	0.253
0.3	0.252	0.258	0.252	0.259
0.4	0.261	0.265	0.261	0.266
0.5	0.266	0.268	0.266	0.269
0.6	0.268	0.270	0.269	0.271
0.7	0.270	0.271	0.270	0.272
0.85	0.272	0.272	0.272	0.273
1.0	0.272	0.273	0.272	0.273
1.5	0.274	0.274	0.274	0.274
2.0	0.274	0.274	0.274	0.274
2.5	0.274	0.274	0.274	0.274
3.0	0.274	0.275	0.274	0.275
4.0	0.275	0.275	0.275	0.275
5.0	0.275	0.275	0.275	0.275
PGV	0.266	0.284	0.264	0.270

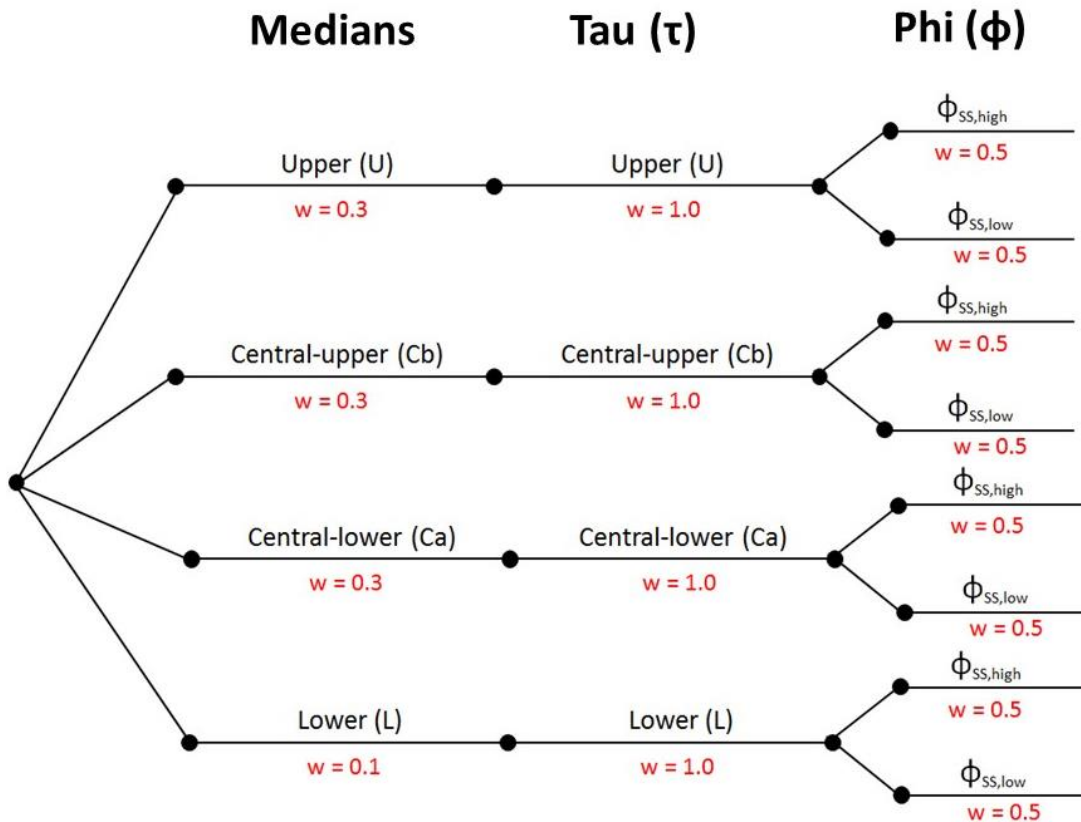


Figure 10.18. Calculated between-event standard deviations

Figure 10.19 compares the elements of the V4 sigma model in rock with those from the V2 model, which is chosen since it was the basis for the 2016 Winningsplan. The figure shows four frames, the most important being the bottom right-hand plot displaying the total sigmas. From this plot it can be appreciated that at periods greater than about 0.5 seconds, the total sigmas of the V4 model are smaller than those of the V2 model, largely due to the reduction of the between-event variability components (top left-hand plot). This reduction has been brought about by more sophisticated regression analyses, including explicitly accounting for the uncertainty in magnitude estimates, as explained in Section 6.5. At shorter response periods, the total sigmas are fractionally higher in the V4 model than in the V2 model, partly because the between-event variability is not reduced in this range, and also because of the decision to increase the within-event variability (single-station sigma) model at shorter periods, as depicted in the upper right-hand plot. Overall, the final sigma values compare favourably with those from GMPEs derived for tectonic earthquakes, presumably a consequence of the Groningen model applying to a single region whereas most tectonic GMPEs combine data from several regions. At the same time, it must be borne in mind that the full variability in the ground-motion predictions necessarily includes the site-to-site variability term as well, as described in the next section.

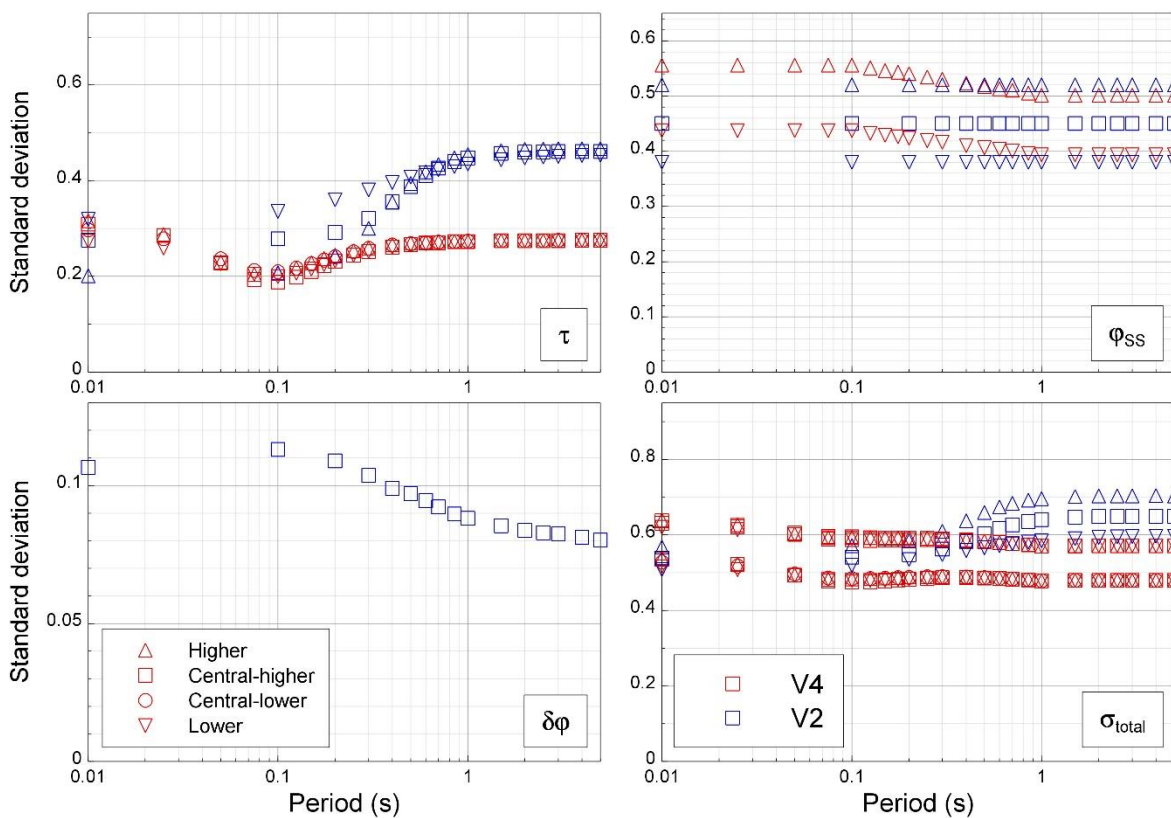


Figure 10.19. Comparison of V2 and V4 sigma components

The lower left-hand frame of Figure 10.19 shows the variability component added to previous versions of the GMM to compensate for the use of point-source representations of the earthquake sources at larger magnitudes; the example shown here is for magnitude 5 and an epicentral distance of 10 km. With the adoption of finite rupture-based distance metric in the V4 model, this term has become redundant.

10.4. Site-to-site variability model

The final component of the sigma model is the site-to-site variability, which was discussed in Section 8.3. Examples of this variability in the calculated site amplification factors for each zone were presented in Section 9.3. The variability is found to vary with the amplitude of the shaking in the reference rock, reflecting the greater variability invoked when the soil response becomes more non-linear. The variation of ϕ_{S2S} with reference rock acceleration is represented by the simple model illustrated in Figure 10.20. The model is defined by an upper and lower level of ϕ_{S2S} and the acceleration levels defining the transition from one level to another. In the very small number of cases where the results indicate a reduction of ϕ_{S2S} with increasing acceleration, ϕ_{S2SH} was simply set equal to ϕ_{S2SL} .

Figure 10.21 illustrates the ϕ_{S2S} model at six response periods for one of the 160 site amplification zones (802), from which the heteroskedastic nature of the variability can be appreciated. In this example, the minimum value is imposed over the entire range of reference rock accelerations for the response period of 5 seconds. The basis of the minimum values on ϕ_{S2S} , and the limiting values on AF as well, have all been described in detail in Section 9.3.

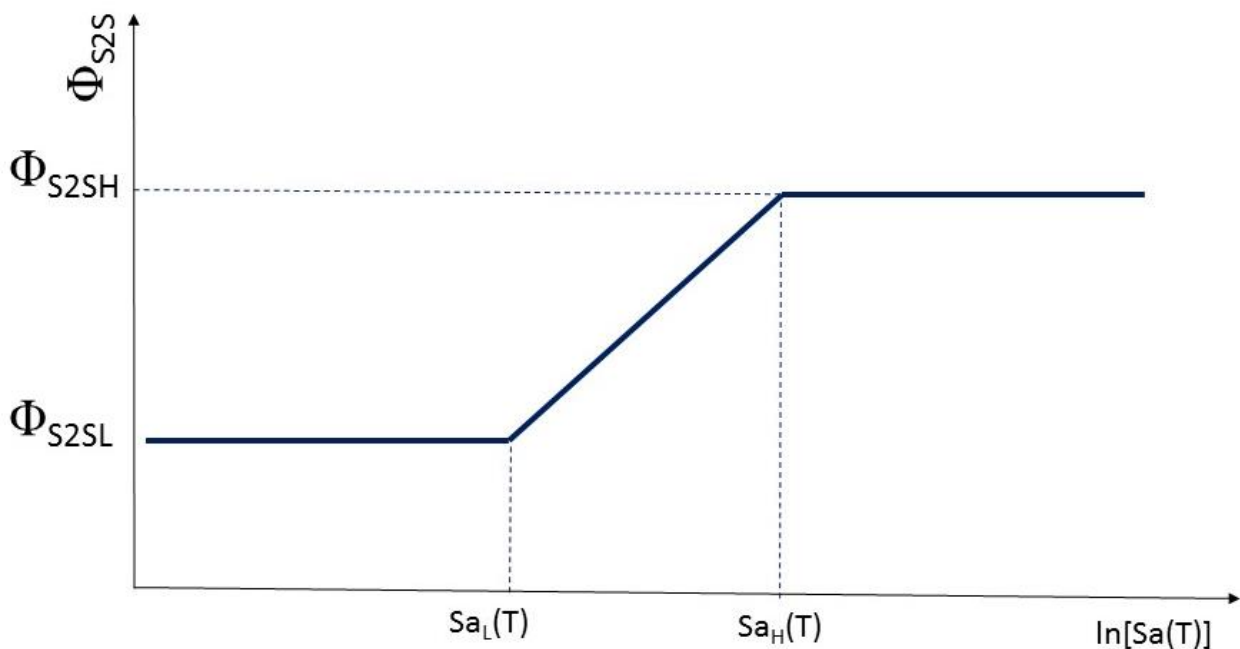


Figure 10.20. Schematic illustration of the parameters defining ϕ_{S2S} , in which the subscript L and H indicate the low and high values; the acceleration on the x-axis is the spectral acceleration at the NS_B horizon

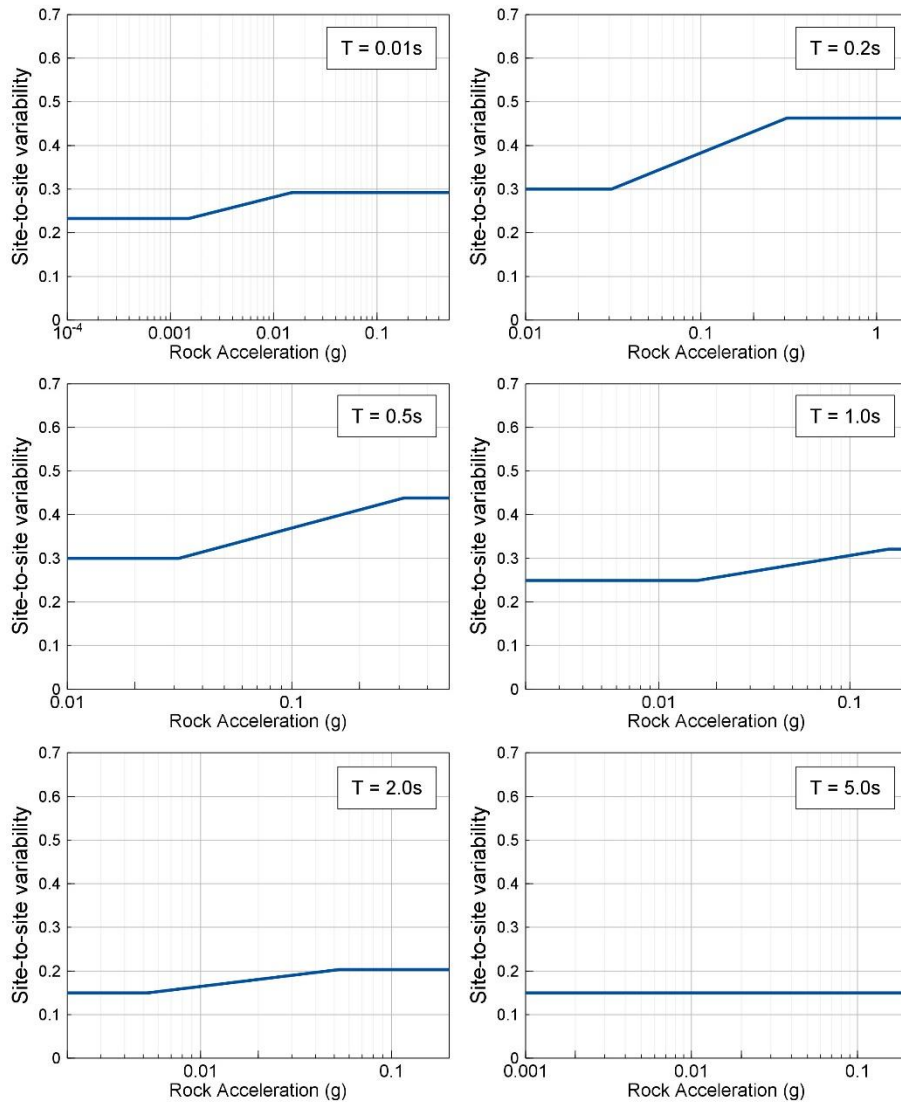


Figure 10.21. Values of ϕ_{S2S} at six response periods in Zone 802

11. APPLICATION and EXTENSION of the GMM for Sa(T)

This chapter summarises the final V4 GMM for spectral accelerations at the ground surface across the field, including additional elements required for its application in the risk calculations and in structural analyses. The first section of the chapter describes the implementation of the basic model for predicting spectral accelerations at the ground surface. The second section then examines the residuals at the ground surface. The third section summarises the adopted model for period-to-period correlations of residuals of spectral accelerations and the final section discusses suitable models for the ratio of vertical-to-horizontal spectral accelerations.

11.1. Model for predicting surface response spectra

The final model for estimating the spectral acceleration at any one of the 23 target oscillator periods at a specified location within the Groningen field as a result of a given earthquake—defined by its magnitude, M_L , and its distance from the site, R_{rup} —is in reality rather simple since it is a function of only three variables: magnitude, distance and site response zone. However, the implementation of the model is a little complex because of the multiple components of variability included in the formulation of the model. The formulation of the model was expressed in the following way in Chapter 2:

$$\ln[Sa(T)] = \{\ln[Sa_{ref}(T)] + \delta B + \delta WS\} + \ln[AF_j(T)] + \delta S2S_j \quad (11.1)$$

The calculation of the median value of the spectral acceleration at the NS_B reference rock horizon, $Sa_{ref}(T)$, for a given M_L - R_{rup} combination is performed using the equations and coefficients presented in Section 6.4. The actual spectral acceleration at the NS_B, however, used to obtain the non-linear amplification factor and to which this amplification factor is applied, requires both the median value of $Sa_{ref}(T)$ and an appropriate sampling of the associated variability (and in this regard a significant advantage of the Monte Carlo approach can be appreciated since it avoids the simplification of only conditioning the non-linear response on the median amplitudes of motion in the reference rock). The full formulation can therefore be expressed as a combination of the elements of the variability and random samples of these distributions; since every element of the model applies to a specific period, T , in order to make the equation simpler the specification (T) is removed:

$$\ln(Sa) = \{\ln(Sa_{ref}) + \varepsilon_E \tau + \varepsilon_S \phi_{SS} + \varepsilon_C \sigma_{C2C}\} + \ln(AF_j) + \varepsilon_Z \phi_{S2S_j} \quad (11.2)$$

Each of these variability terms is now briefly discussed, and the full procedure for the implementation is illustrated in Figure 11.1, which in effect illustrates the innermost of multiple loops for earthquakes within each catalogue and sites at which motions are calculated as a result of each earthquake.

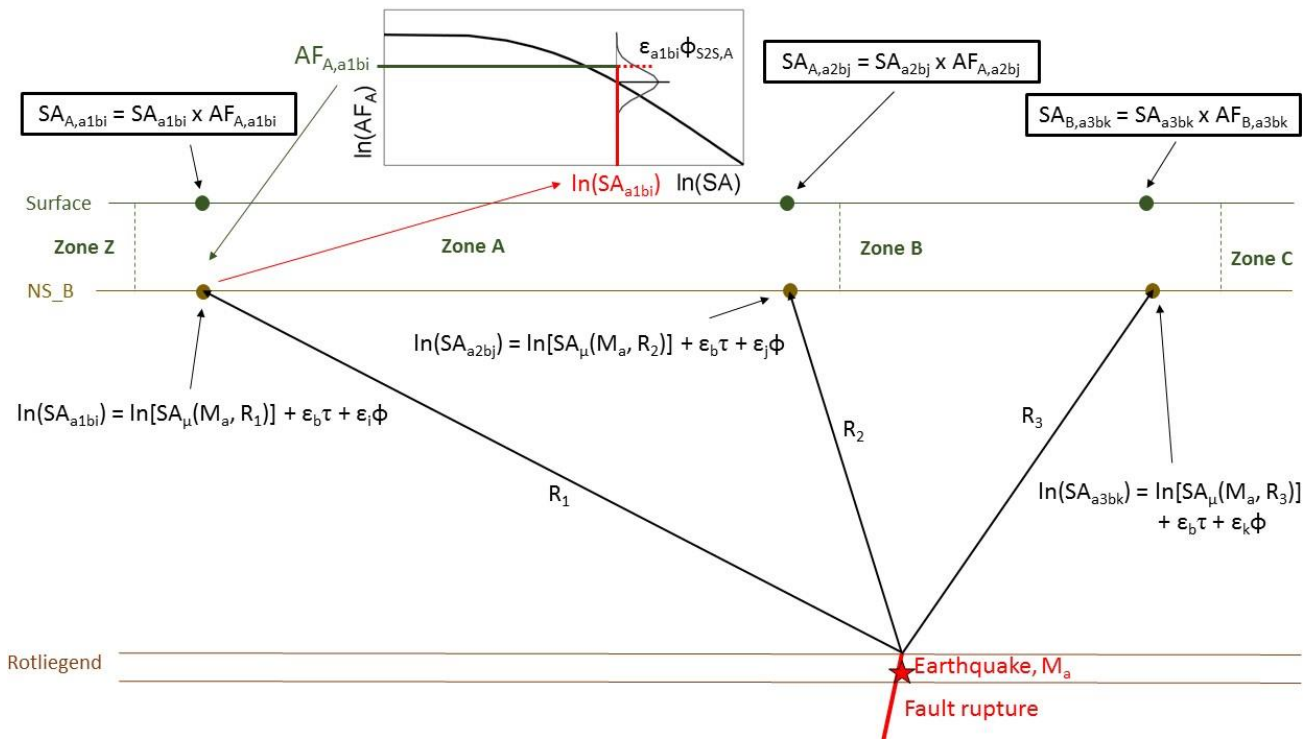


Figure 11.1. Schematic illustration of the implementation of the V4 GMM in the hazard calculations. Specifically, the figure depicts the calculation of S_a at three surface points, in two zones, for an earthquake of magnitude M_a and an event-term of $\epsilon_b\tau$; in this simple example, the within-event variability is sampled without considering spatial correlation

$S_{a_{ref}}$ is the median spectral acceleration predicted at the NS_B horizon following the formulation presented in Chapter 6.

The next term $\epsilon_E\tau$ is the between-event or inter-event residual, sampled for each earthquake in the synthetic catalogues and held constant for all sites for a given earthquake. The values of τ are given in Section 10.3.

The next term is another log-normal distribution which is sampled using the random variable ϵ_S at each location at which the hazard is calculated. ϕ_{SS} is single-station sigma and takes the values listed in Section 10.3.

The next term is another log-normal distribution sampled randomly at each location by ϵ_C ; the standard deviation σ_{C2C} represents the component-to-component variability, and the values are provided in Section 10.2. This term is included when calculating risk but should be set to zero when calculating the hazard, as explained in Section 1.3.

The three components of variability considered so far (ϵ_E , ϵ_S and ϵ_C) are assumed to be completely uncorrelated. Adding the sampled values of the standard deviations of these three components of variability to the median spectral acceleration yields the actual baserock

acceleration for each earthquake-site combination considered in the Monte Carlo simulations.

The coordinates at which the calculations are being performed automatically define which of the 160 site amplification zones the site is located within. The coefficients of the equation for the median amplification factor, AF, can then be retrieved, and the amplification factor calculated for the spectral acceleration (expressed in units of g) at the NS_B horizon. A check must then be performed that AF is neither smaller than 0.25 nor larger than the specified value of AF_{max} ; if either condition is violated, AF is set to either AF_{min} or AF_{max} . The final value of AF is then multiplied by the spectral acceleration at the NS_B horizon. The final step is then to sample randomly (ε_z) from one more log-normal distribution with standard deviation ϕ_{s2s} , which represents the site-to-site variability within the zone; $\phi_{s2s} \geq 0.2$. This variability term varies with the value of NS_B acceleration, as explained in Section 10.4. The product of the NS_B spectral acceleration and AF is then multiplied by the exponent of the value of $\varepsilon_z \phi_{s2s}$ to obtain the final surface acceleration at that period. The calculation of the surface accelerations at other response periods at the same site needs to take account of the period-to-period correlation model in Section 11.3.

For those fragility functions defined in terms of spectral acceleration and duration, the median duration should be estimated using the model in Section 12.3 and the variability (Section 12.4) sampled conditional on the total ε sampled for the acceleration, using the correlation coefficients presented in Section 12.5.

Figure 11.1 inevitably is unable to illustrate the full complexity of the calculations, which are conducted at each site for 23 oscillator periods for one of the four branches of the ground-motion logic-tree. In practice, the calculations are performed using the coefficients and sigma models for all eight branches and the weighted mean of the resulting motions (for hazard) or the weighted mean of the resulting damage levels (for risk) calculated using the assigned branch weights. For each earthquake, a large number (several hundred) of sites across the study area are considered, and then for each catalogue the calculations are repeated for all of the earthquakes. However, the diagram does serve to illustrate the key steps of the implementation and the sampling of the different components of the variability, as well as the correlations that are currently considered between these random samples.

In order to illustrate the implementation of the model, Figures 11.2 to 11.46 show the median surface response spectra for several combinations of magnitude (M_L 4, 5 and 6) and distance (R_{rup} 3, 10 and 20 km). In each case, the plots show the response spectra at the NS_B rock horizon and at the surface; in order to illustrate the influence of the soil non-linearity, the plots also show the surface response spectra that would be obtained if only linear site response were considered in the model. These plots are shown for five zones, two having high AFs (1206 and 2002), another two relatively low AFs (1402 and 3115), and one intermediate zone (802). For magnitude 4 only, the plots also show the surface predictions from the V1, V2 and V3 models. For larger earthquakes, the differences between the Repi and Rrup distance metrics would render such comparisons difficult to interpret meaningfully.

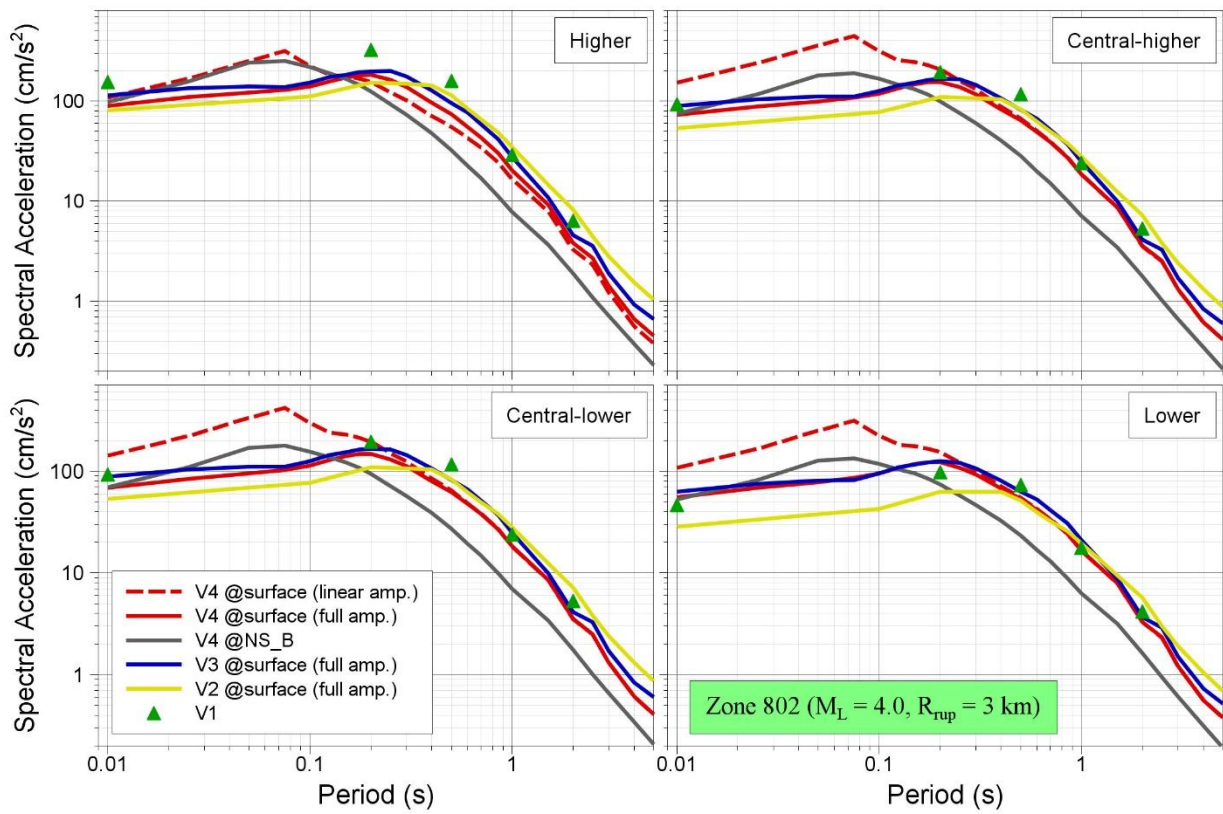


Figure 11.2. Median predicted response spectra in Zone 802 due to a magnitude M_L 4 earthquake at a rupture distance of 3 km

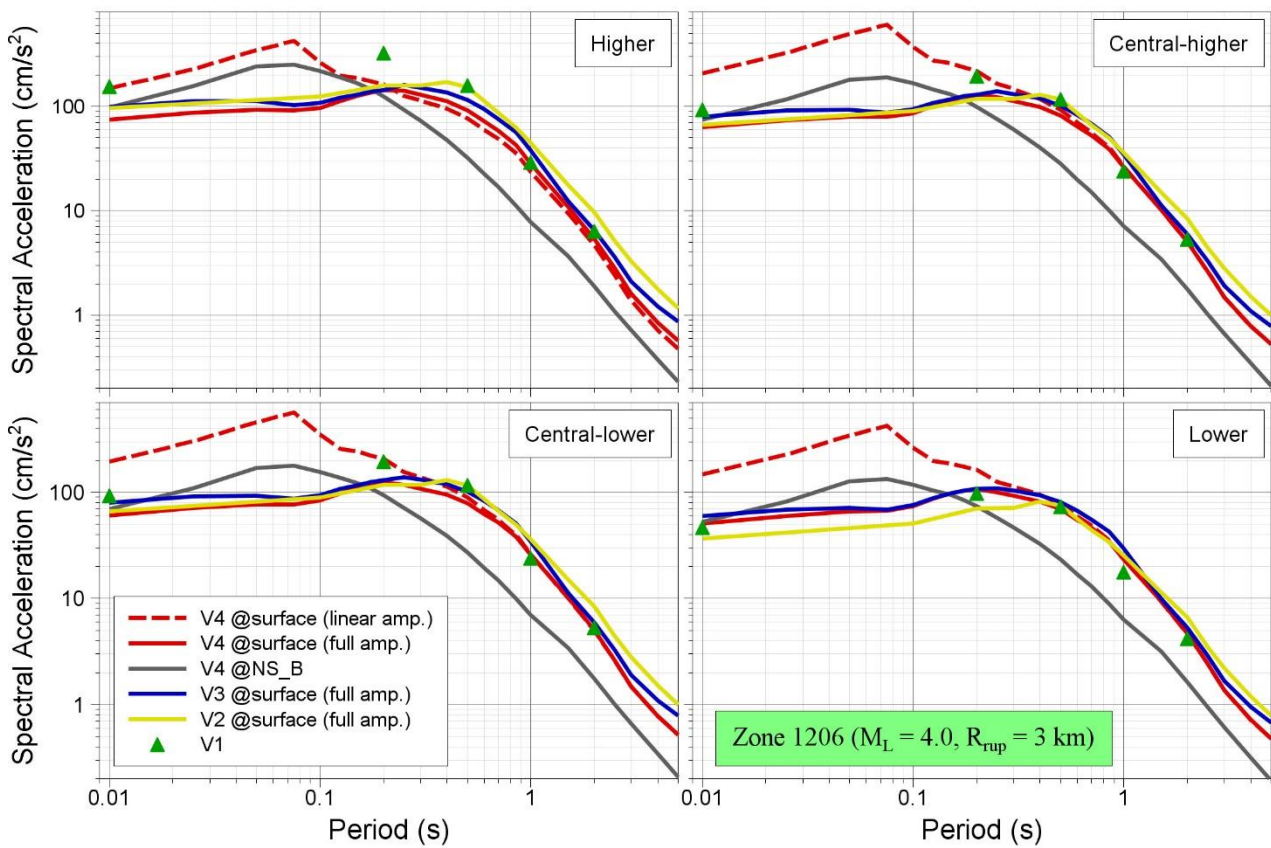


Figure 11.3. Median predicted response spectra in Zone 1206 due to a magnitude M_L 4 earthquake at a rupture distance of 3 km

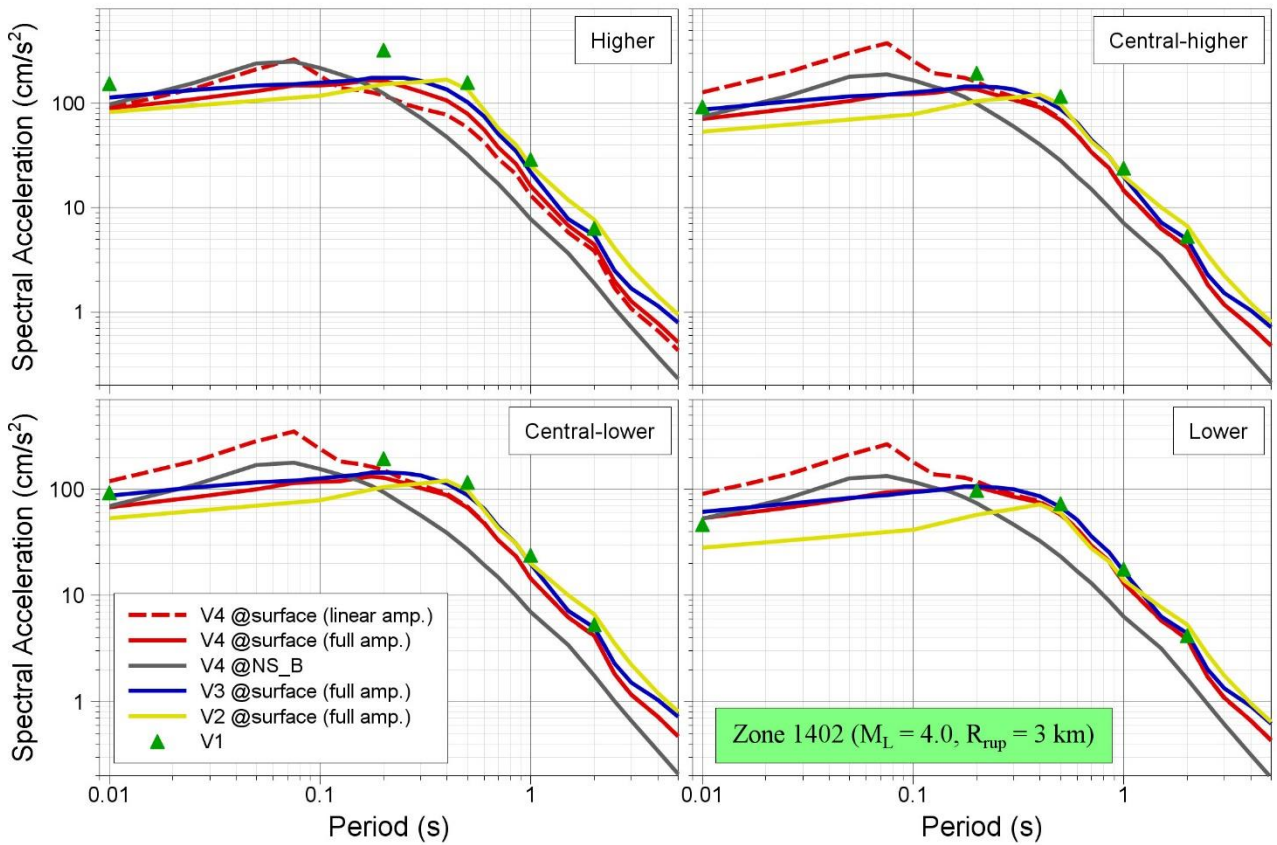


Figure 11.4. Median predicted response spectra in Zone 1402 due to a magnitude M_L 4 earthquake at a rupture distance of 3 km

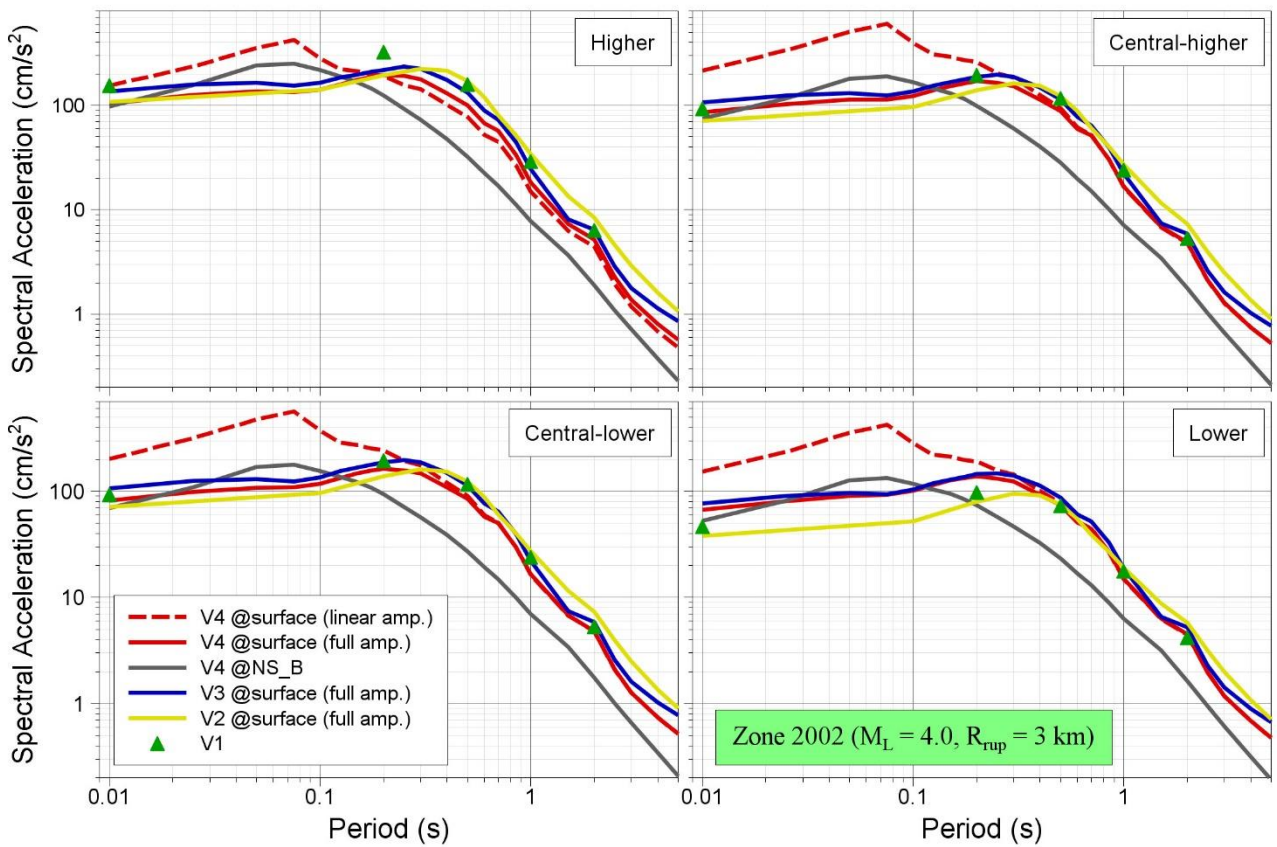


Figure 11.5. Median predicted response spectra in Zone 2002 due to a magnitude M_L 4 earthquake at a rupture distance of 3 km

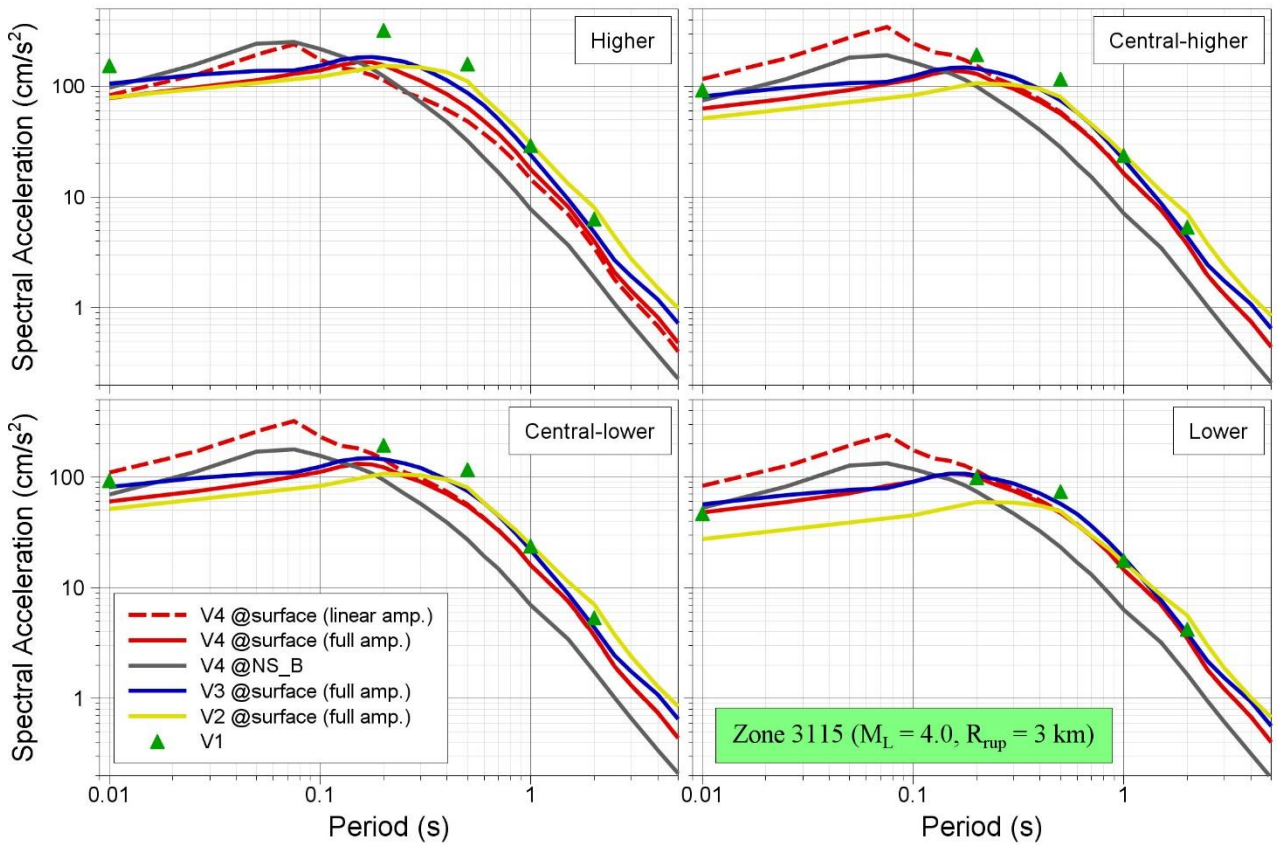


Figure 11.6. Median predicted response spectra in Zone 3115 due to a magnitude M_L 4 earthquake at a rupture distance of 3 km

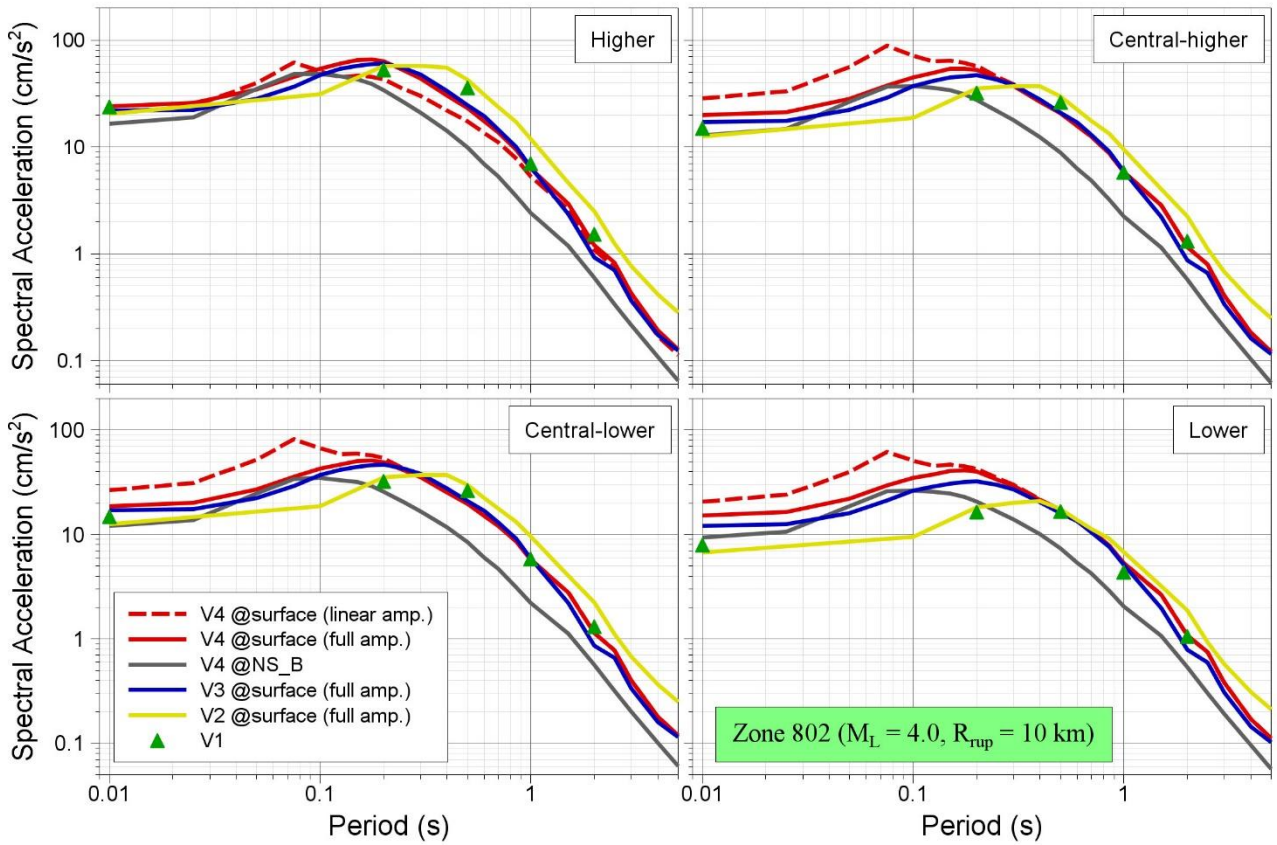


Figure 11.7. Median predicted response spectra in Zone 802 due to a magnitude M_L 4 earthquake at a rupture distance of 10 km

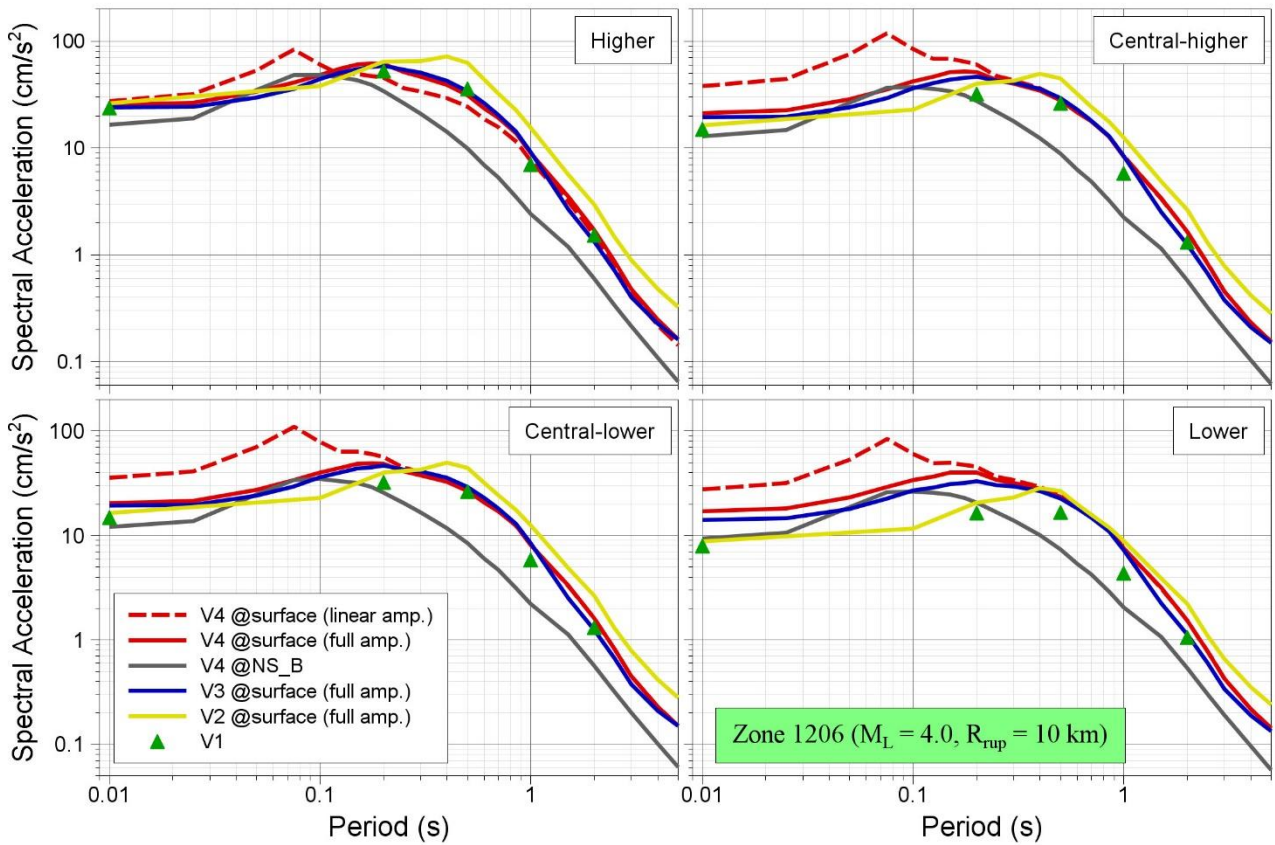


Figure 11.8. Median predicted response spectra in Zone 1206 due to a magnitude M_L 4 earthquake at a rupture distance of 10 km

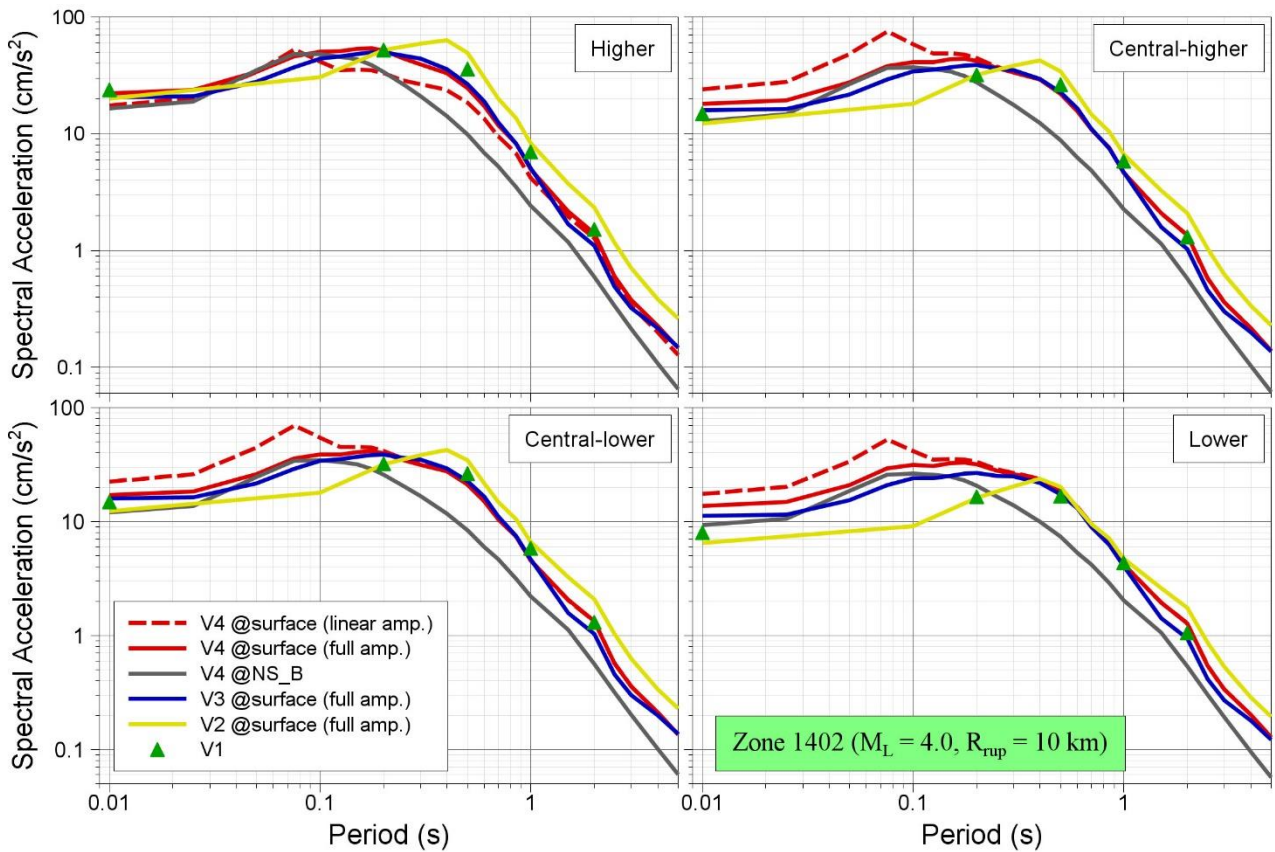


Figure 11.9. Median predicted response spectra in Zone 1402 due to a magnitude M_L 4 earthquake at a rupture distance of 10 km

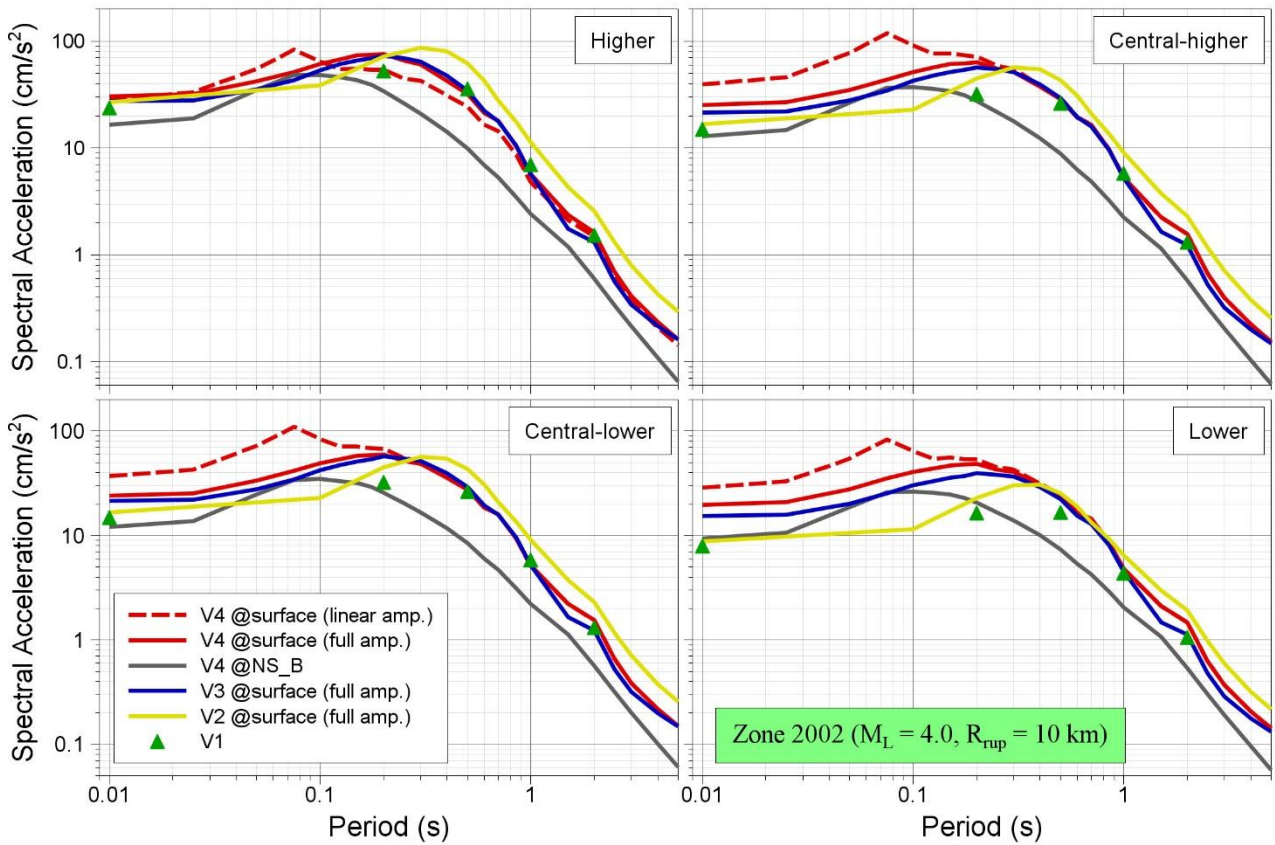


Figure 11.10. Median predicted response spectra in Zone 2002 due to a magnitude M_L 4 earthquake at a rupture distance of 10 km

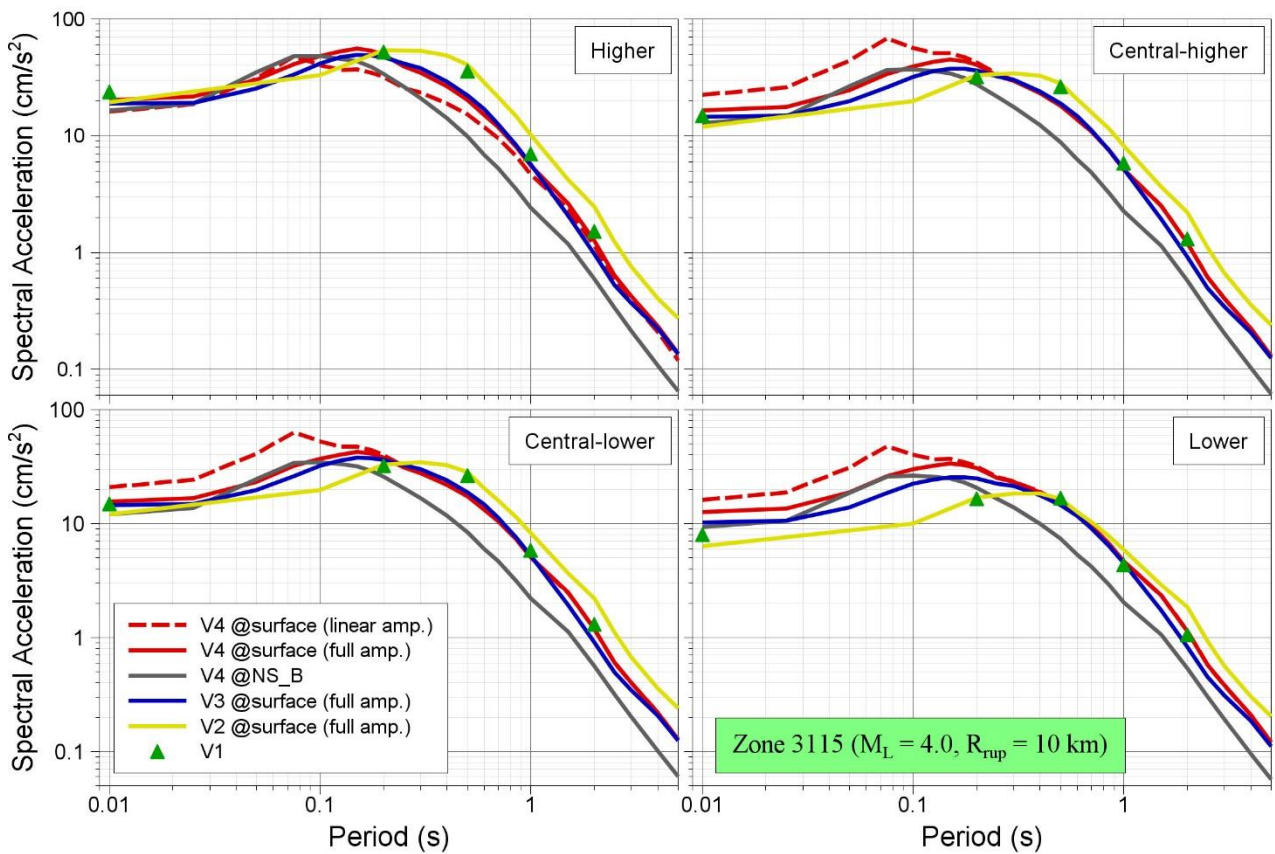


Figure 11.11. Median predicted response spectra in Zone 3115 due to a magnitude M_L 4 earthquake at a rupture distance of 10 km

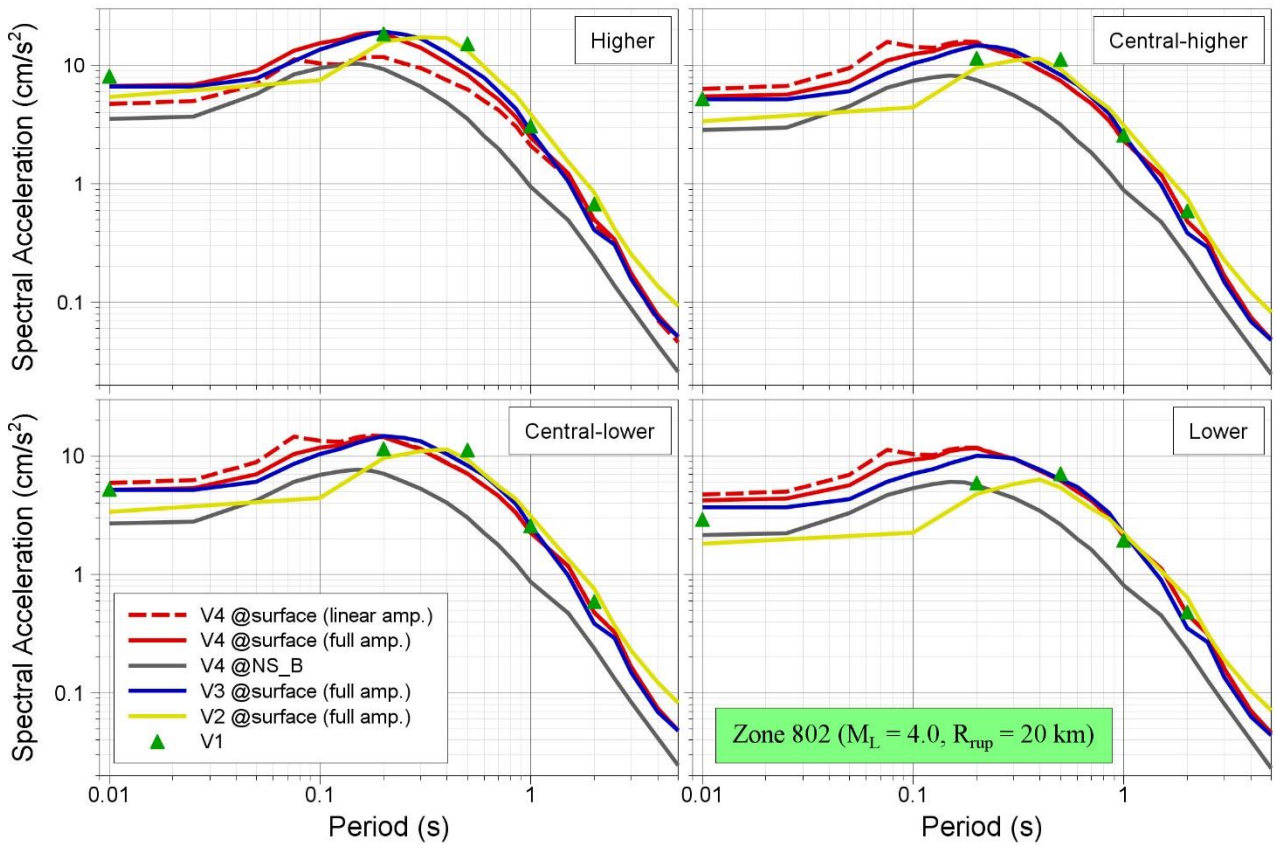


Figure 11.12. Median predicted response spectra in Zone 802 due to a magnitude M_L 4 earthquake at a rupture distance of 20 km

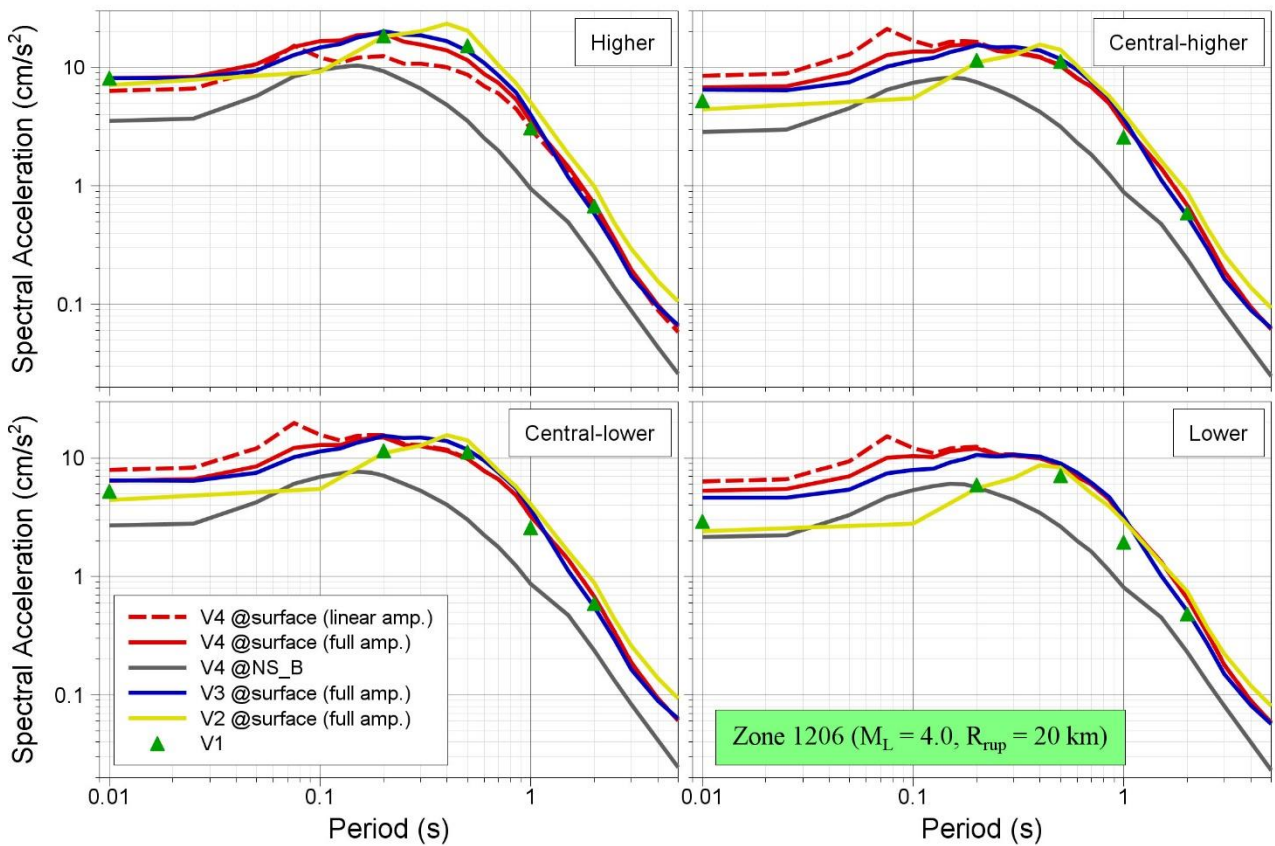


Figure 11.13. Median predicted response spectra in Zone 1206 due to a magnitude M_L 4 earthquake at a rupture distance of 20 km

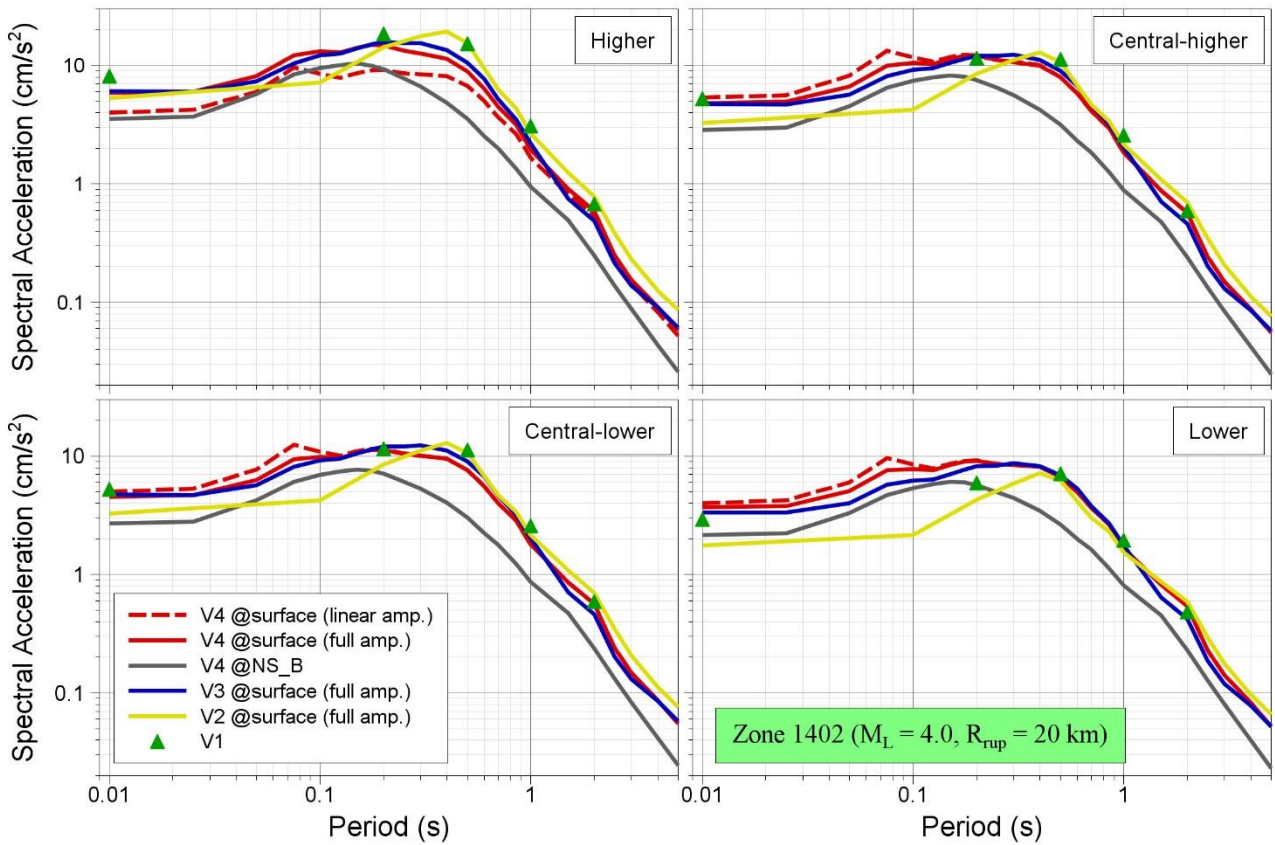


Figure 11.14. Median predicted response spectra in Zone 1402 due to a magnitude M_L 4 earthquake at a rupture distance of 20 km

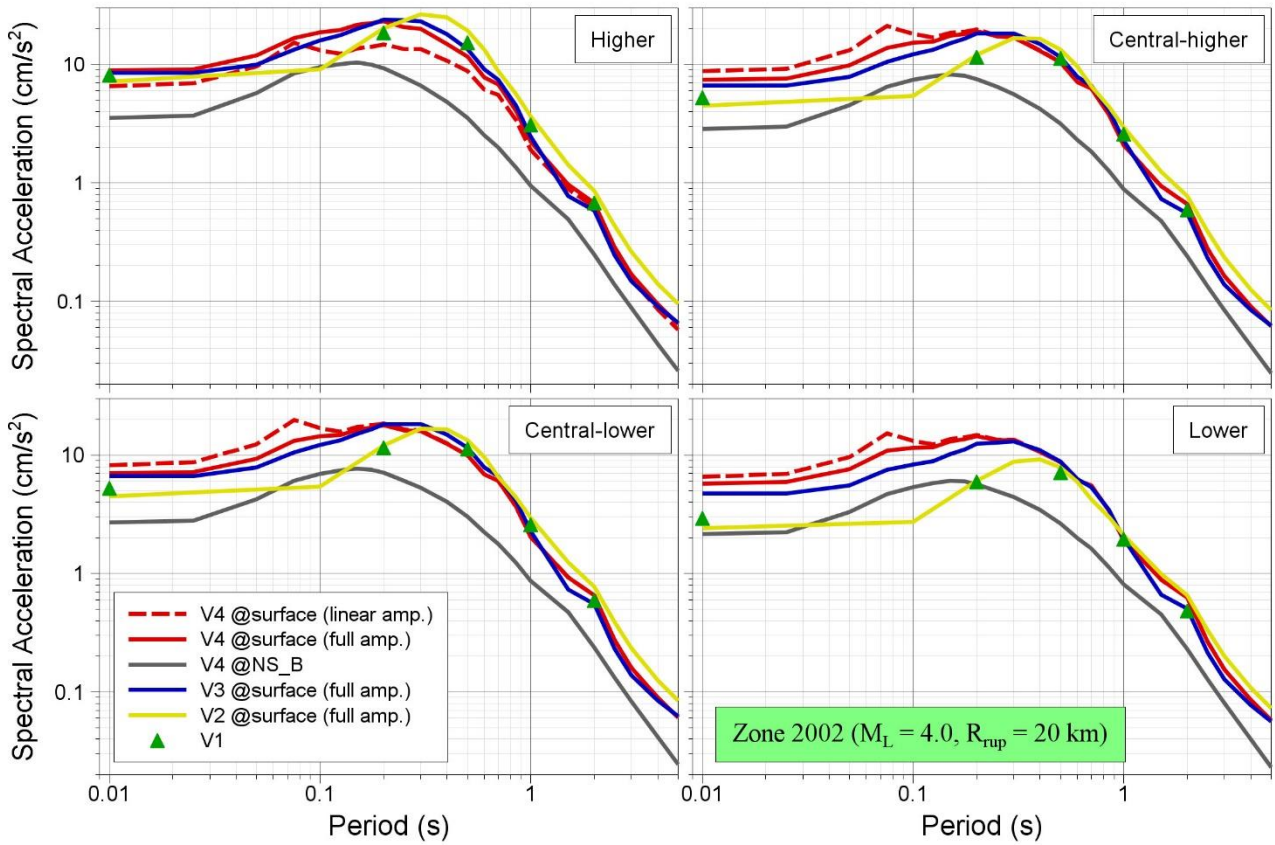


Figure 11.15. Median predicted response spectra in Zone 2002 due to a magnitude M_L 4 earthquake at a rupture distance of 20 km

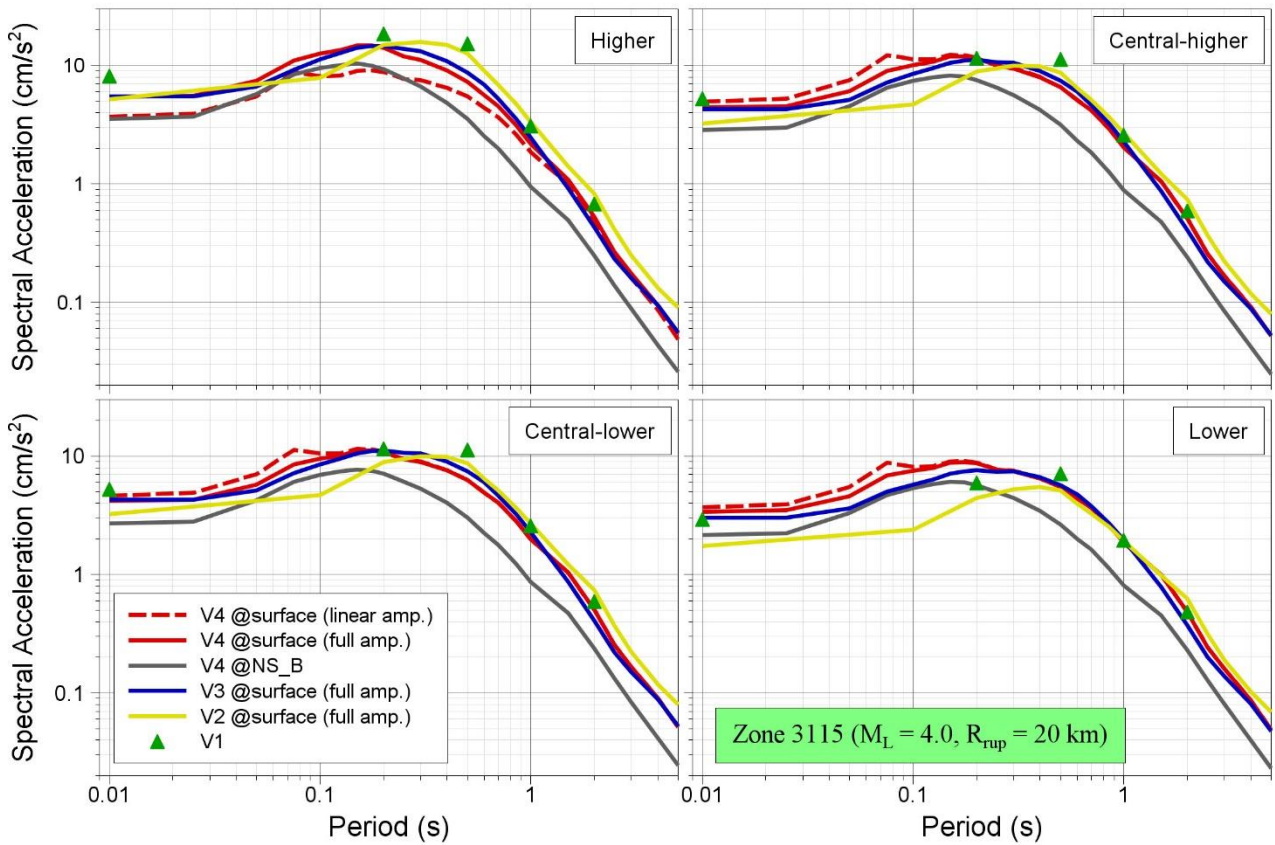


Figure 11.16. Median predicted response spectra in Zone 3115 due to a magnitude M_L 4 earthquake at a rupture distance of 20 km

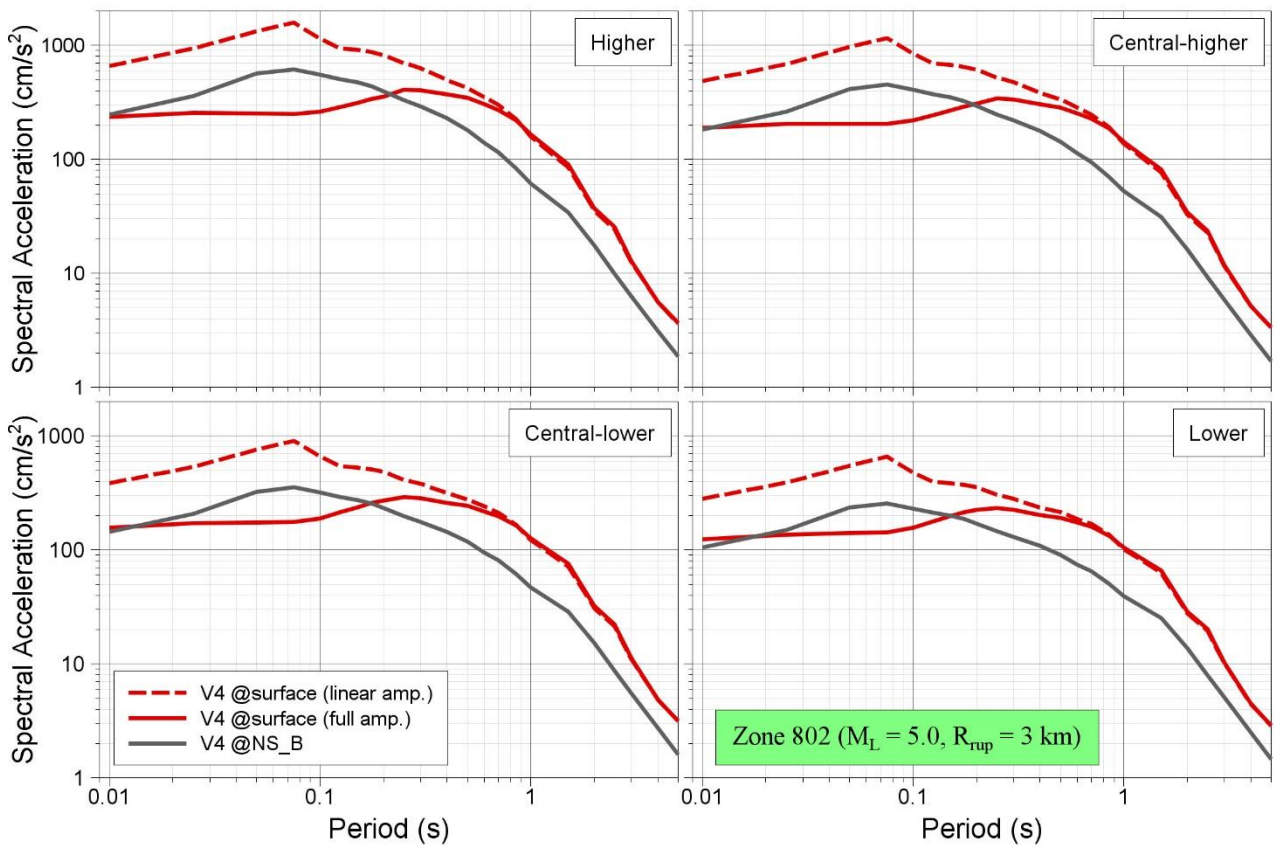


Figure 11.17. Median predicted response spectra in Zone 802 due to a magnitude M_L 5 earthquake at a rupture distance of 3 km

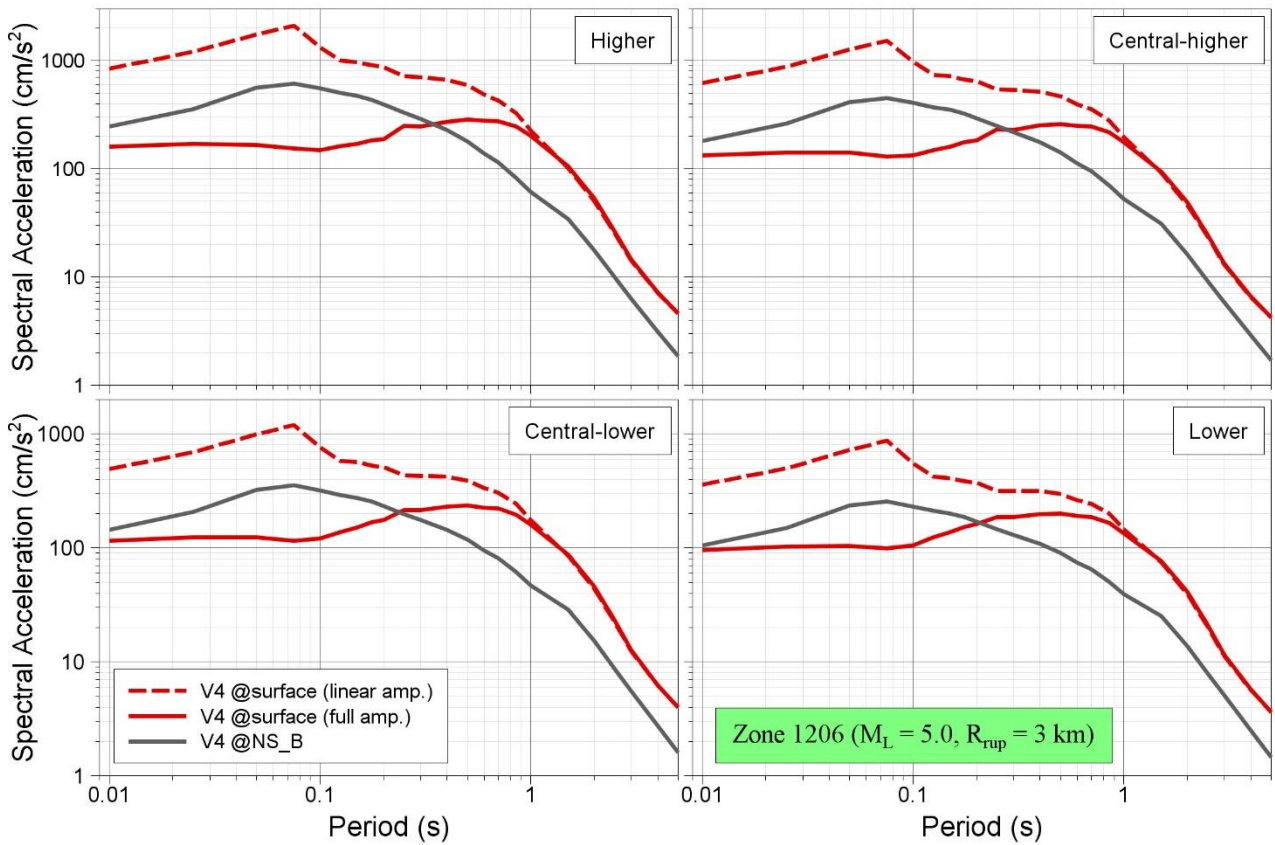


Figure 11.18. Median predicted response spectra in Zone 1206 due to a magnitude M_L 5 earthquake at a rupture distance of 3 km

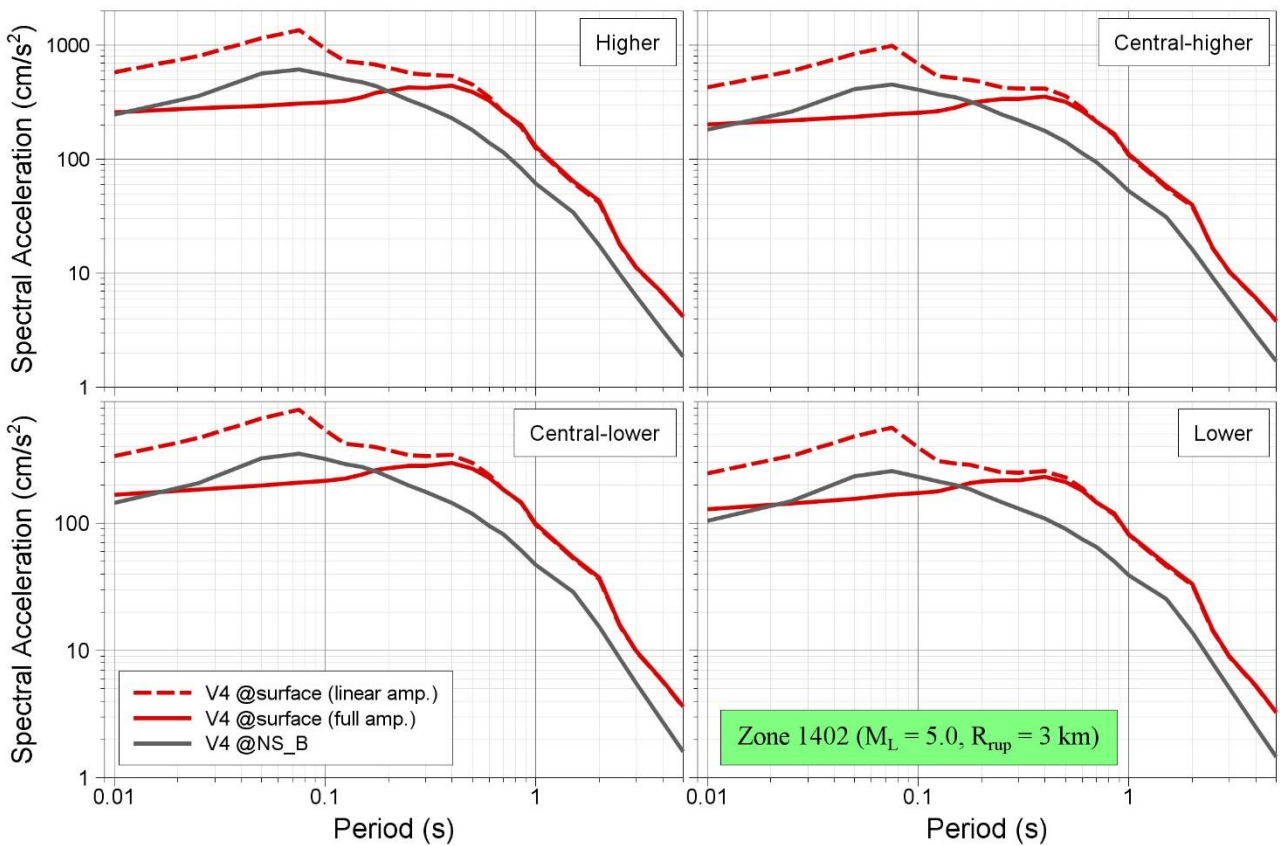


Figure 11.19. Median predicted response spectra in Zone 1402 due to a magnitude M_L 5 earthquake at a rupture distance of 3 km

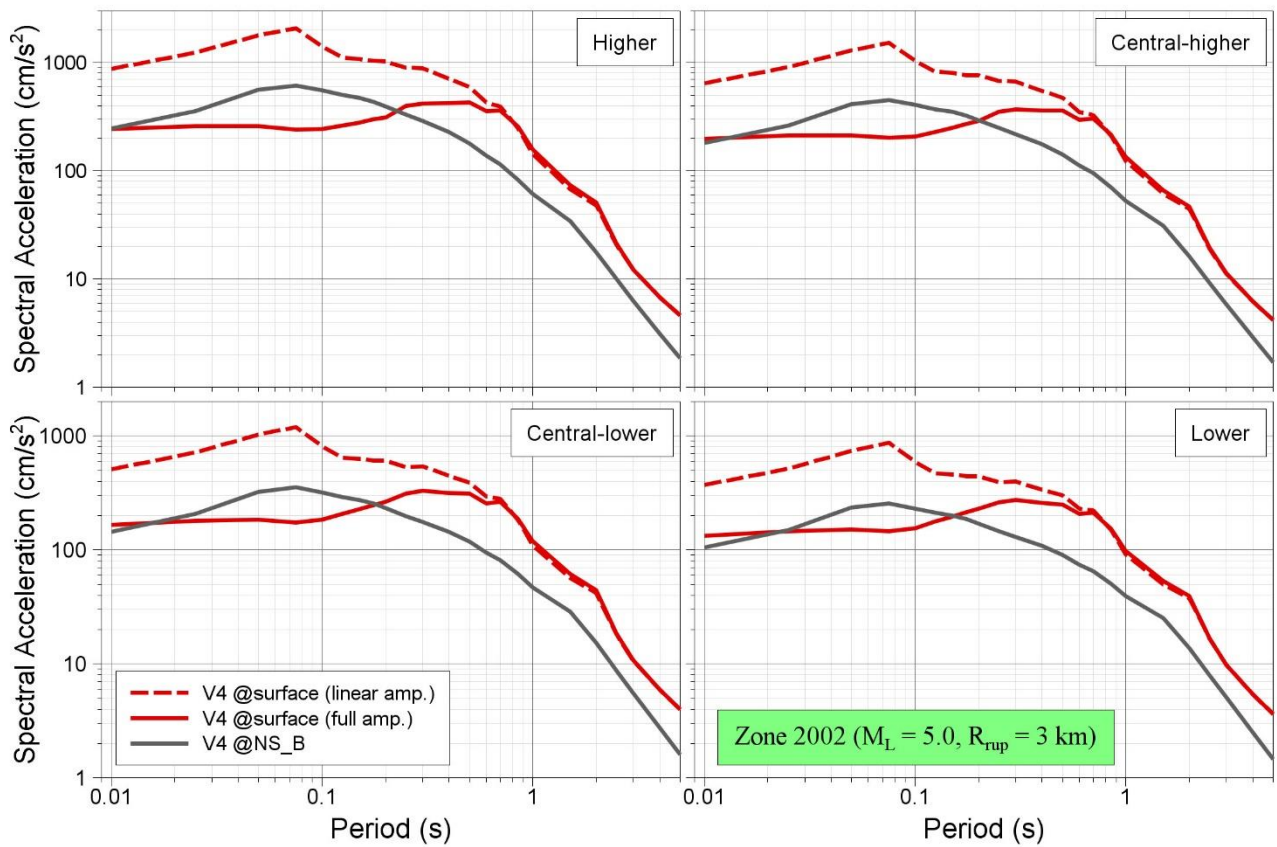


Figure 11.20. Median predicted response spectra in Zone 2002 due to a magnitude M_L 5 earthquake at a rupture distance of 3 km

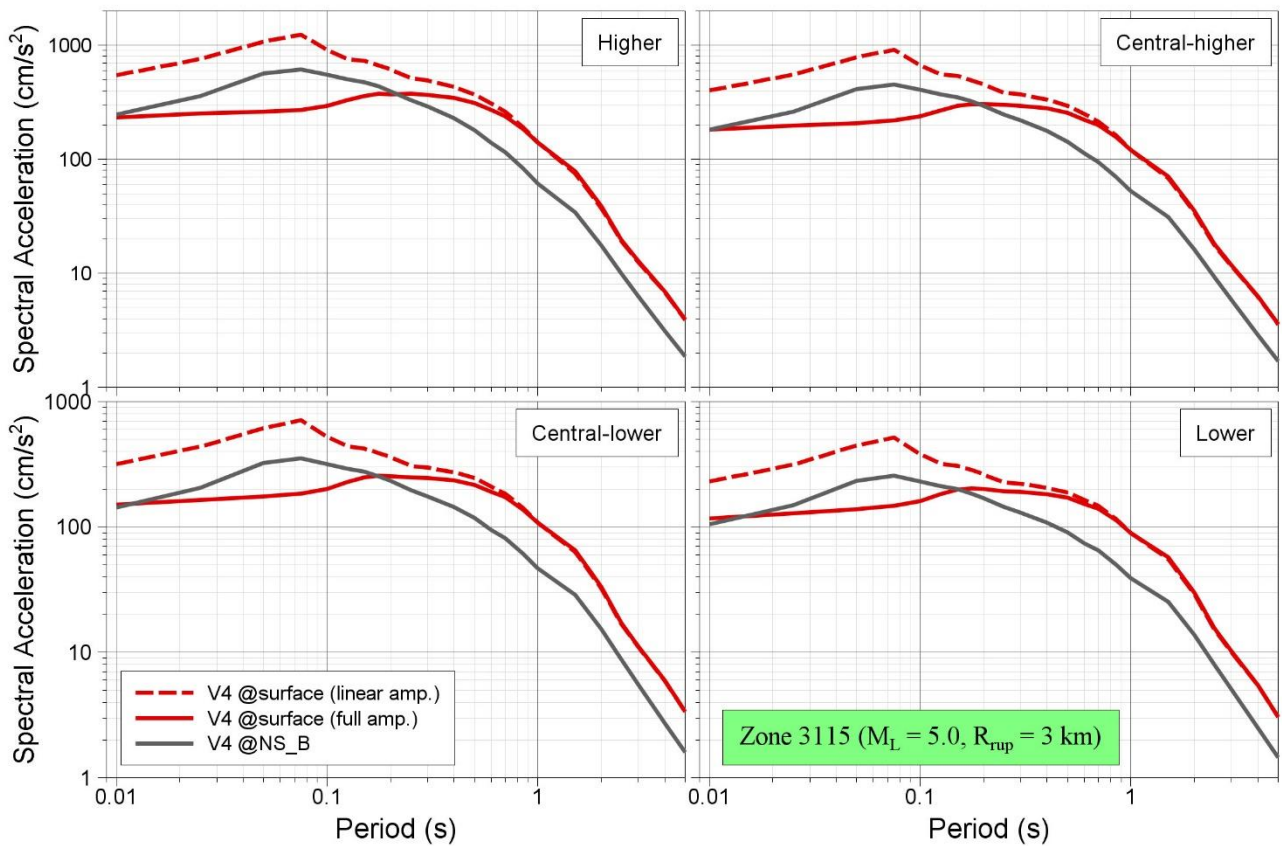


Figure 11.21. Median predicted response spectra in Zone 3115 due to a magnitude M_L 5 earthquake at a rupture distance of 3 km

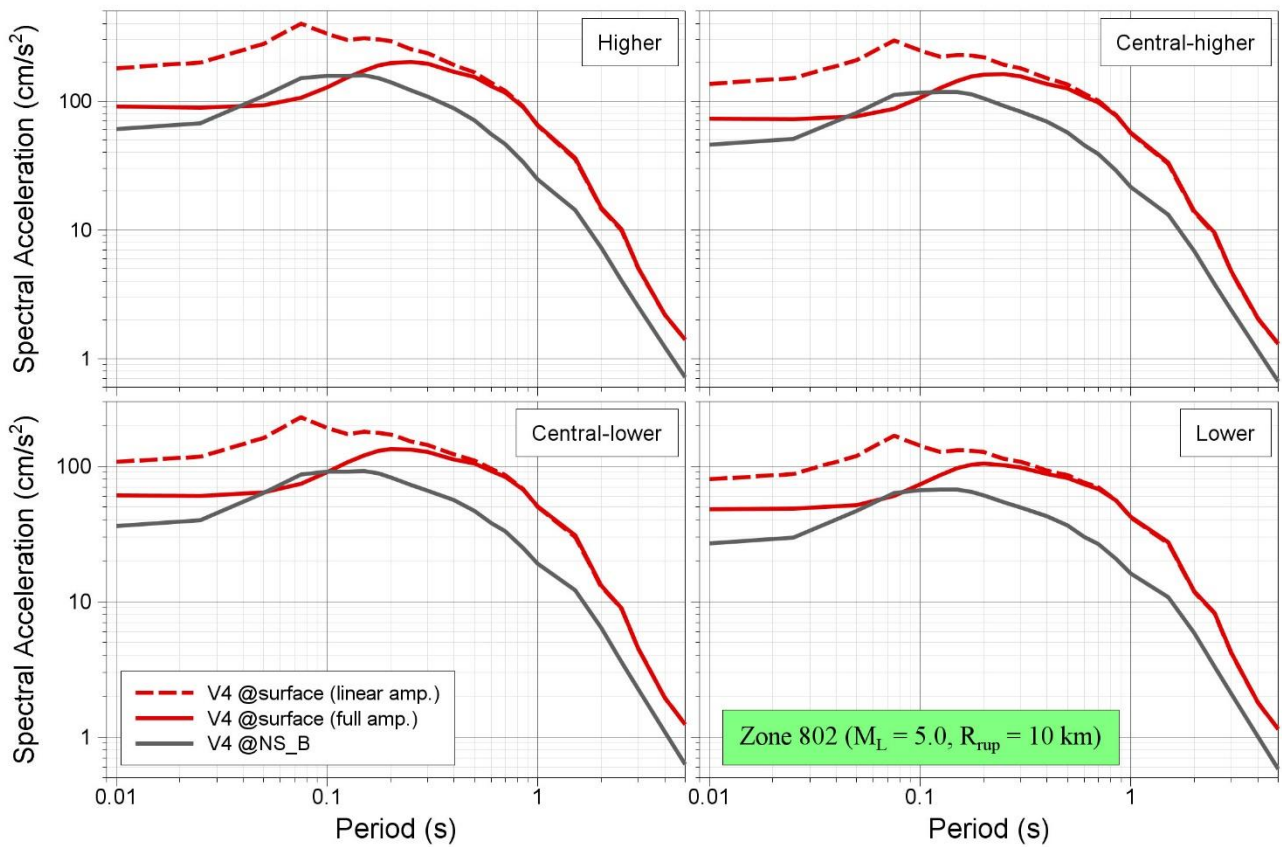


Figure 11.22. Median predicted response spectra in Zone 802 due to a magnitude M_L 5 earthquake at a rupture distance of 10 km

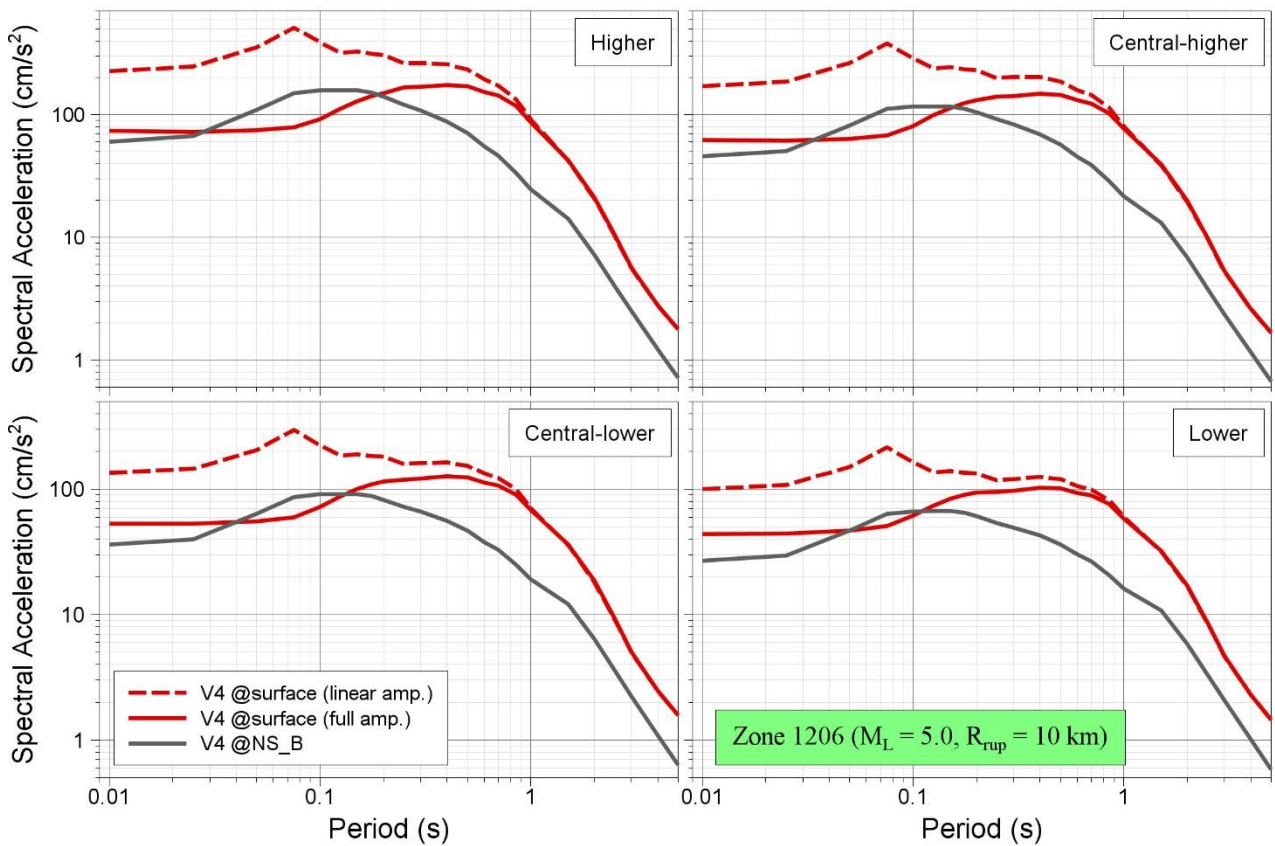


Figure 11.23. Median predicted response spectra in Zone 1206 due to a magnitude M_L 5 earthquake at a rupture distance of 10 km

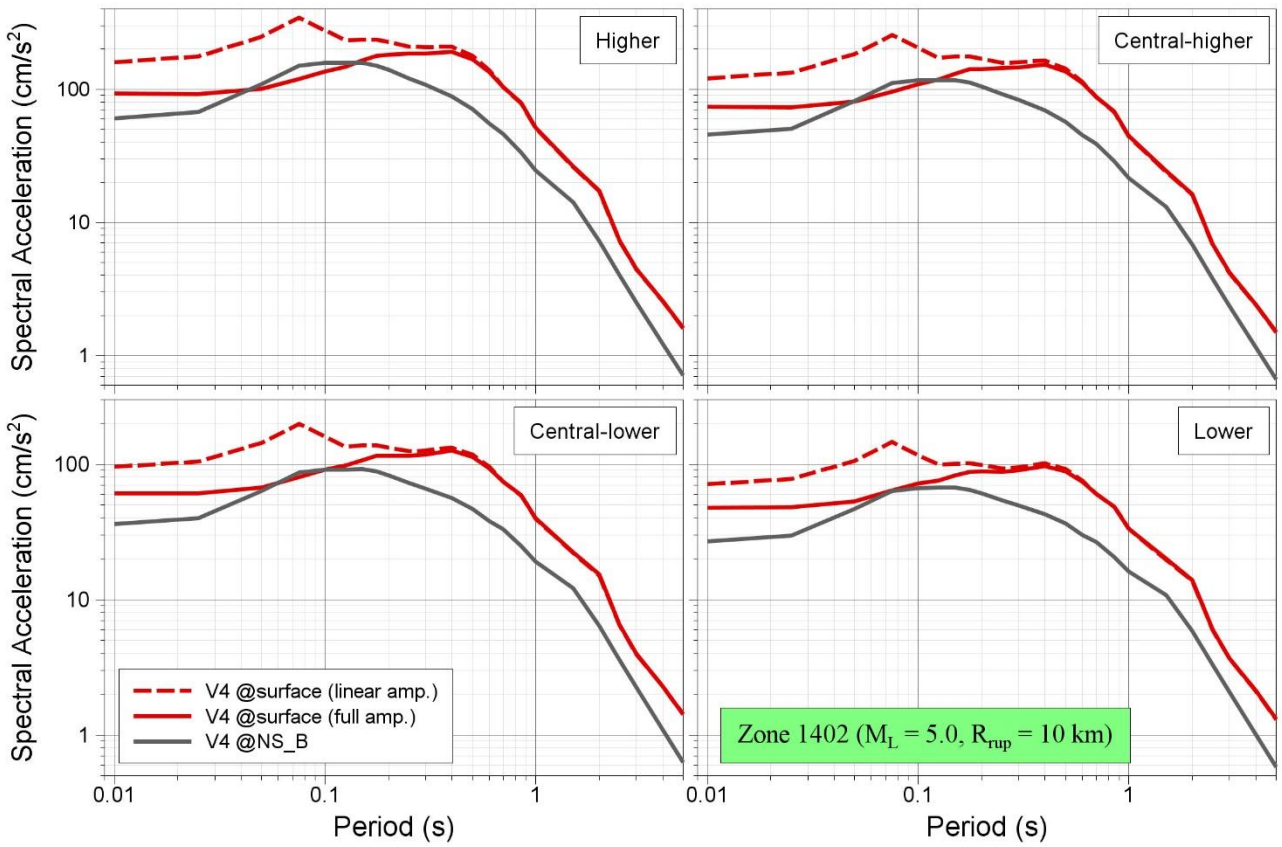


Figure 11.24. Median predicted response spectra in Zone 1402 due to a magnitude M_L 5 earthquake at a rupture distance of 10 km

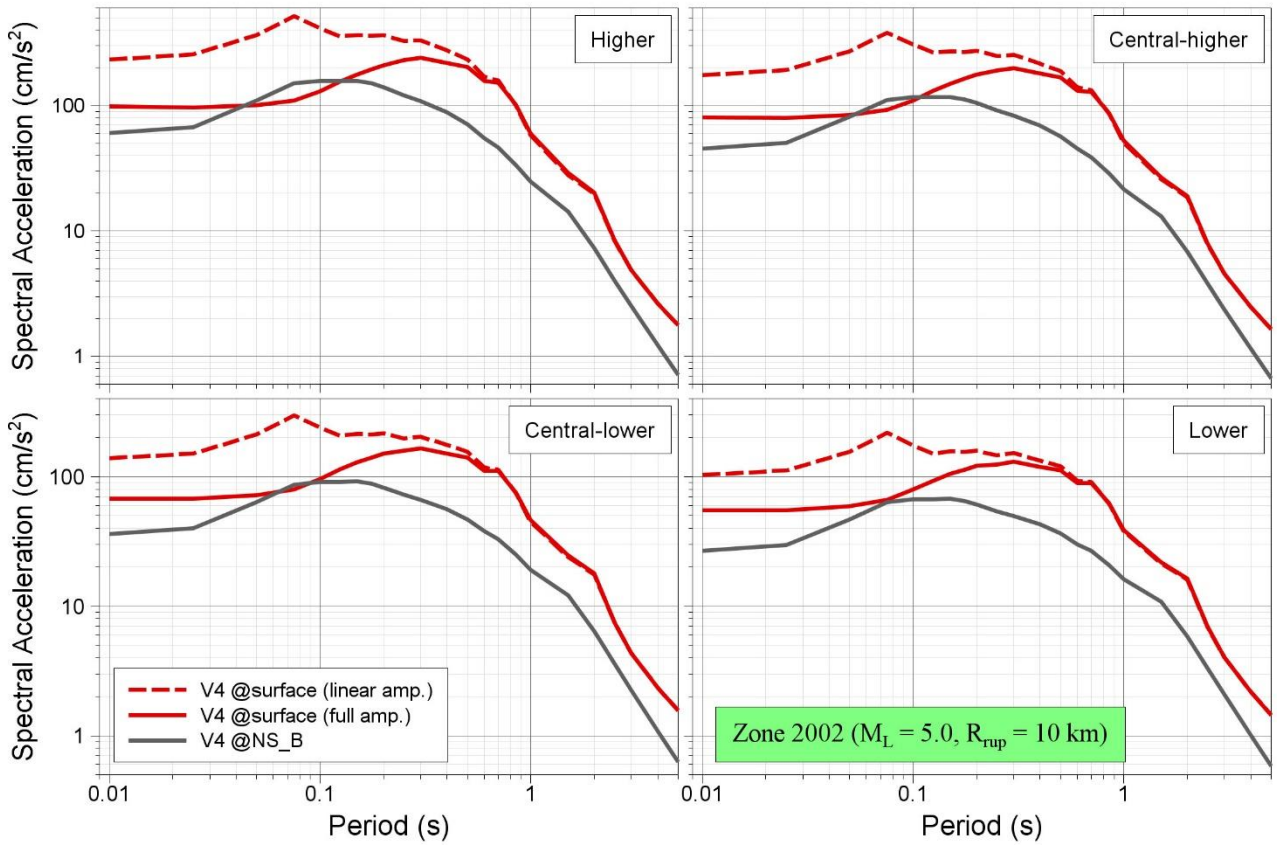


Figure 11.25. Median predicted response spectra in Zone 2002 due to a magnitude M_L 5 earthquake at a rupture distance of 10 km

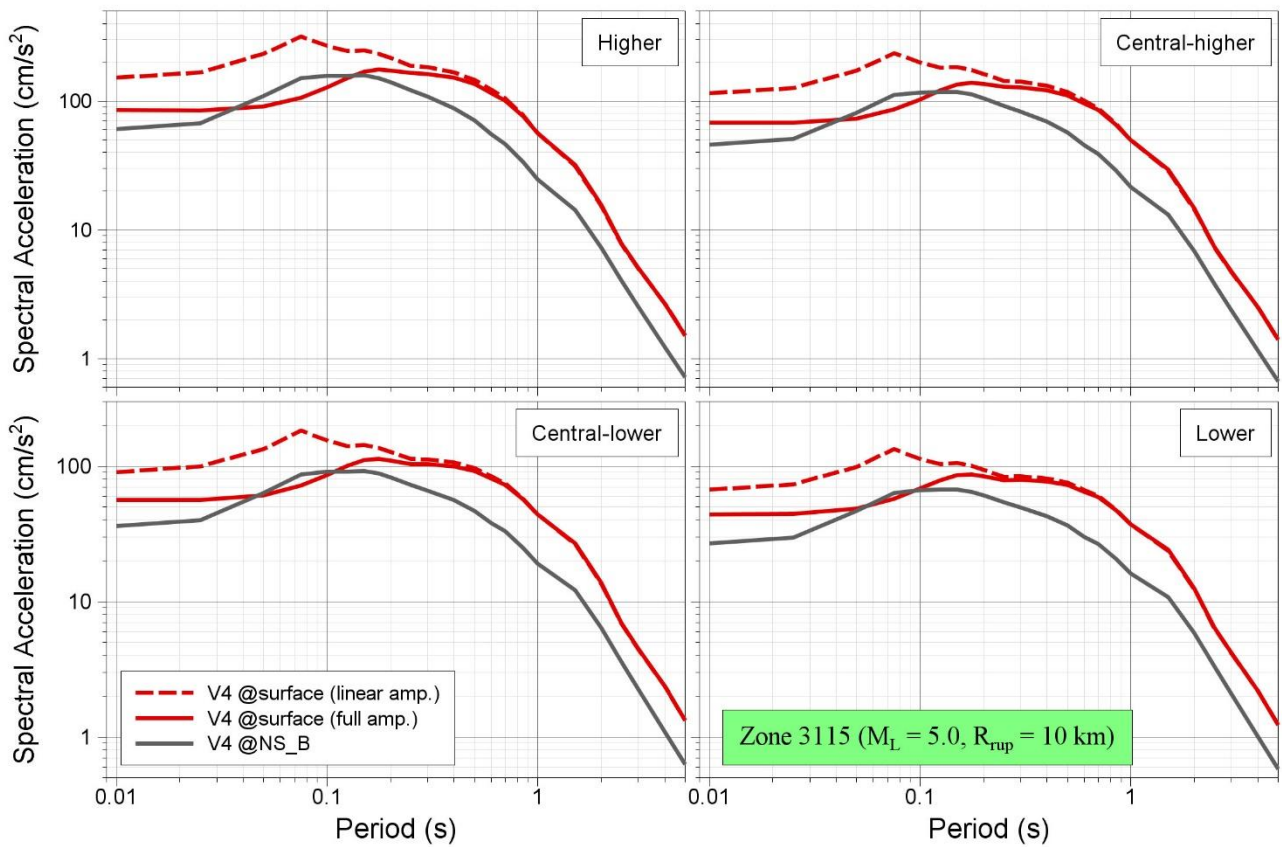


Figure 11.26. Median predicted response spectra in Zone 3115 due to a magnitude M_L 5 earthquake at a rupture distance of 10 km

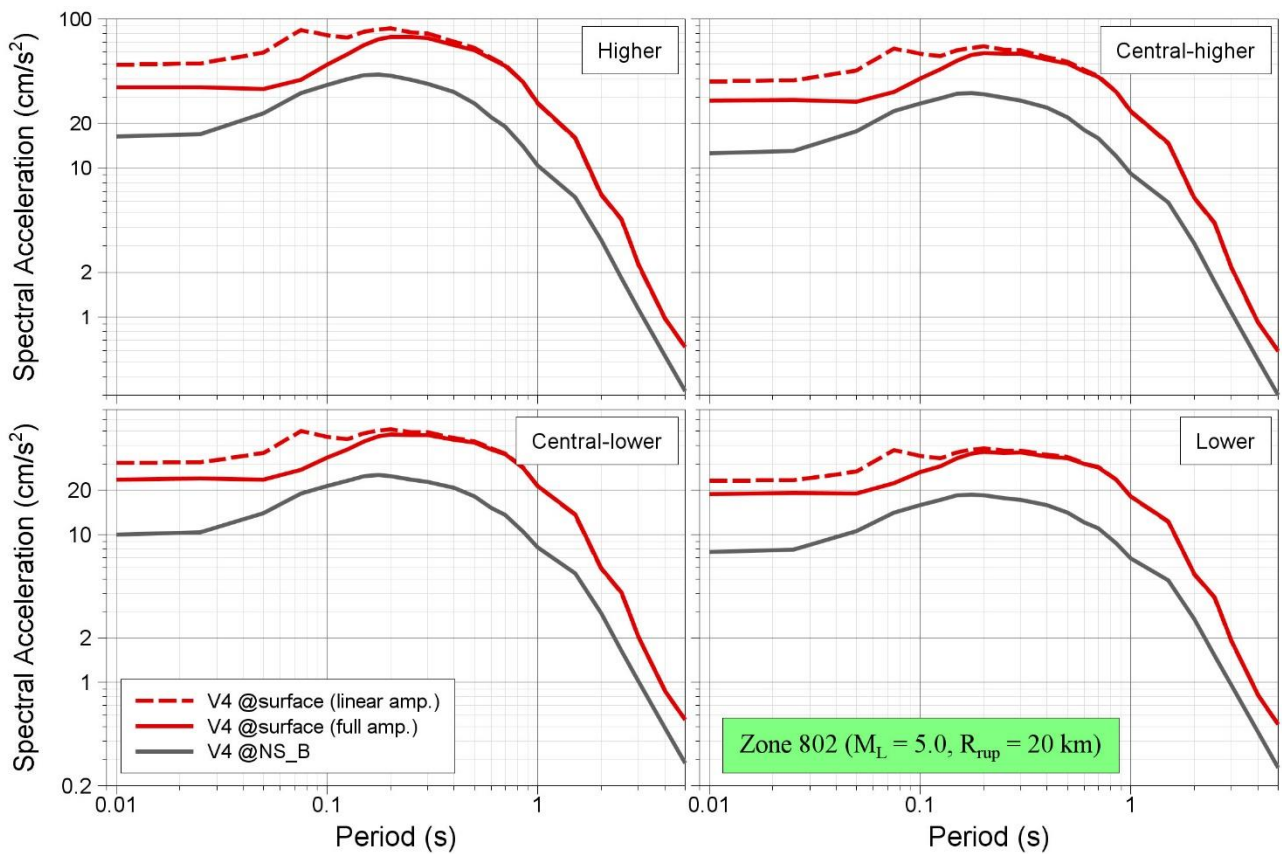


Figure 11.27. Median predicted response spectra in Zone 802 due to a magnitude M_L 5 earthquake at a rupture distance of 20 km

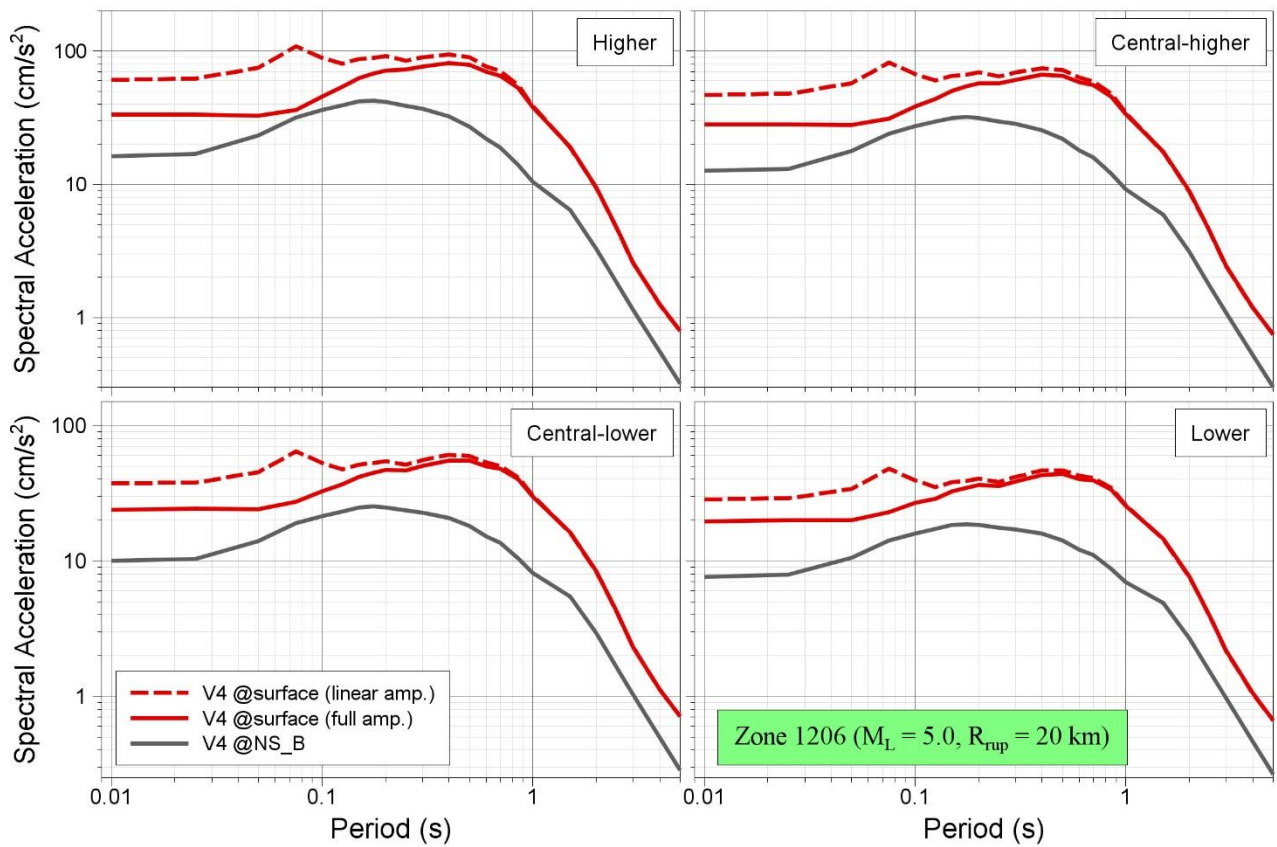


Figure 11.28. Median predicted response spectra in Zone 1206 due to a magnitude M_L 5 earthquake at a rupture distance of 20 km

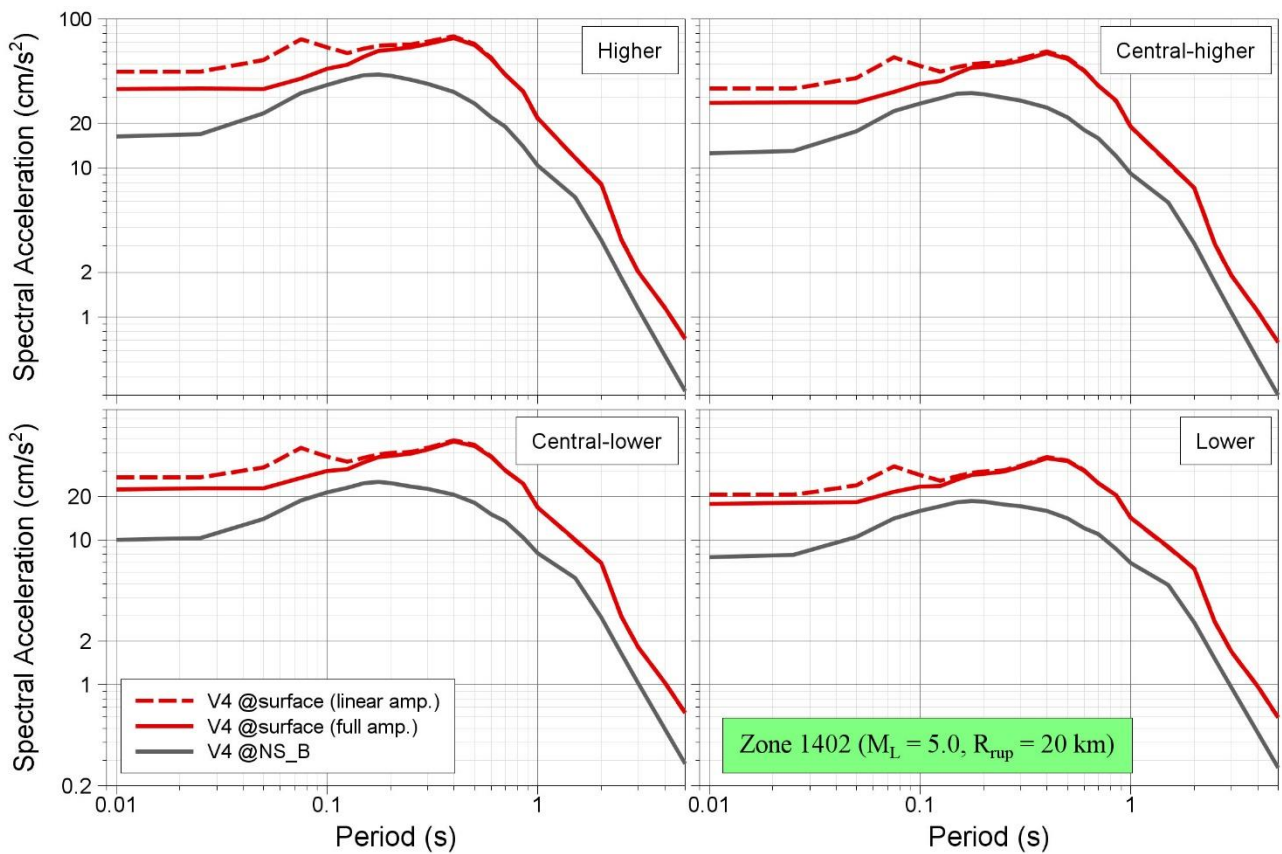


Figure 11.29. Median predicted response spectra in Zone 1402 due to a magnitude M_L 5 earthquake at a rupture distance of 20 km

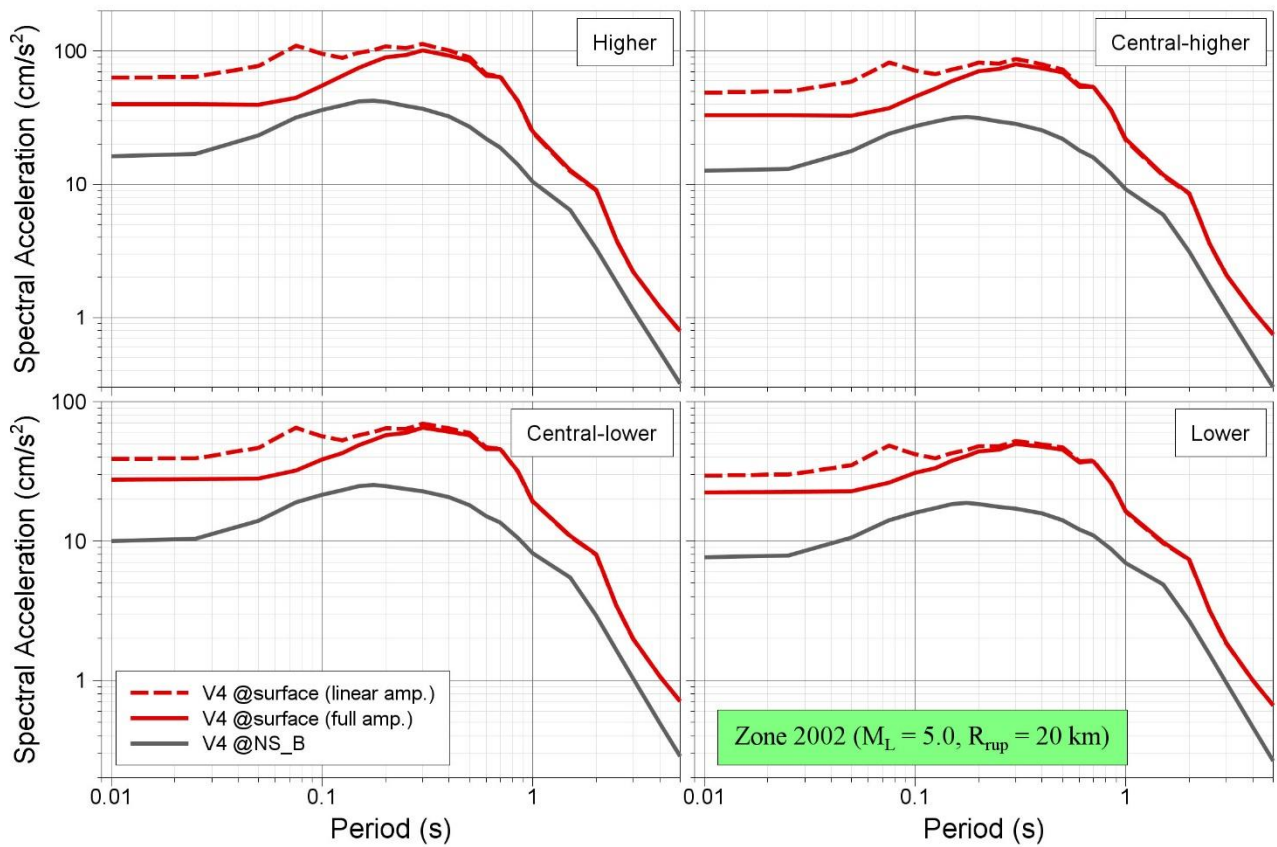


Figure 11.30. Median predicted response spectra in Zone 2002 due to a magnitude M_L 5 earthquake at a rupture distance of 20 km

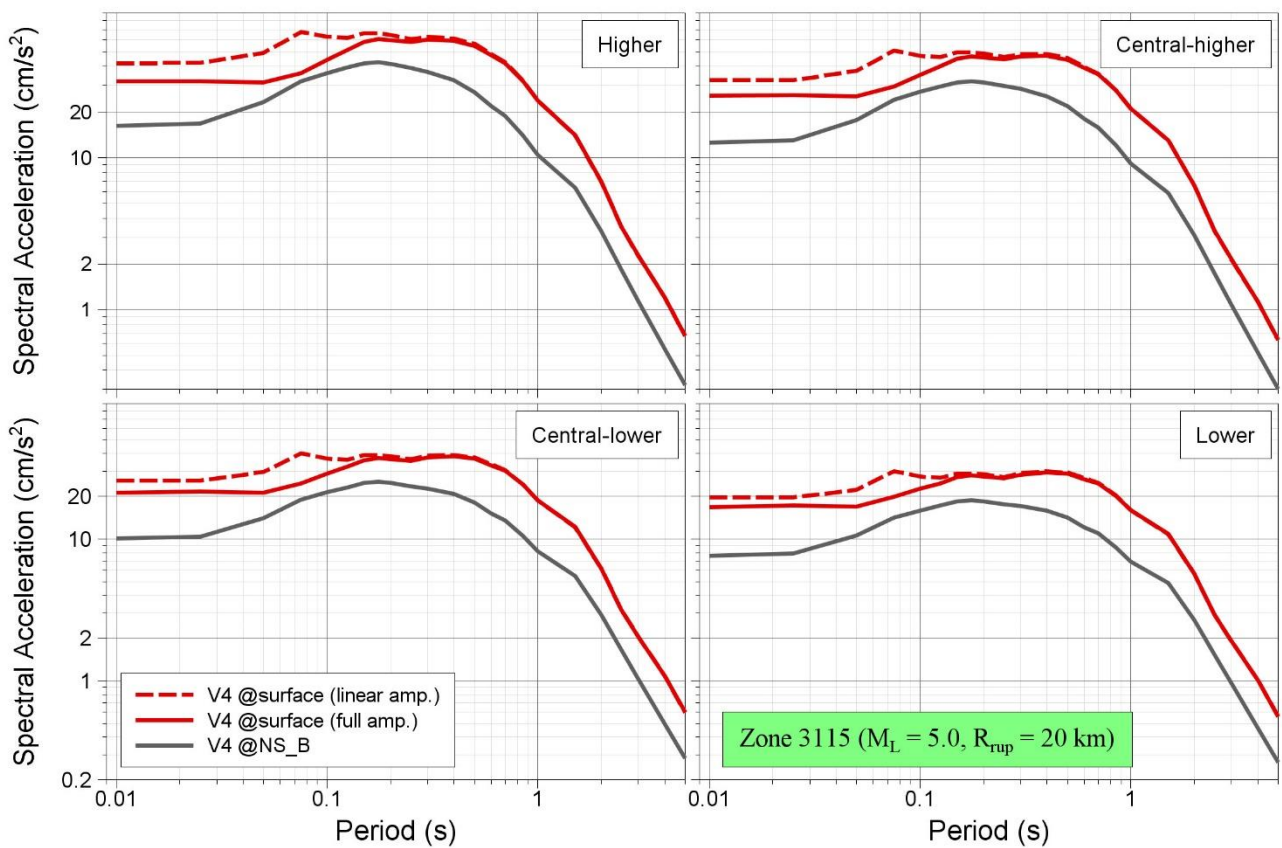


Figure 11.31. Median predicted response spectra in Zone 3115 due to a magnitude M_L 5 earthquake at a rupture distance of 20 km

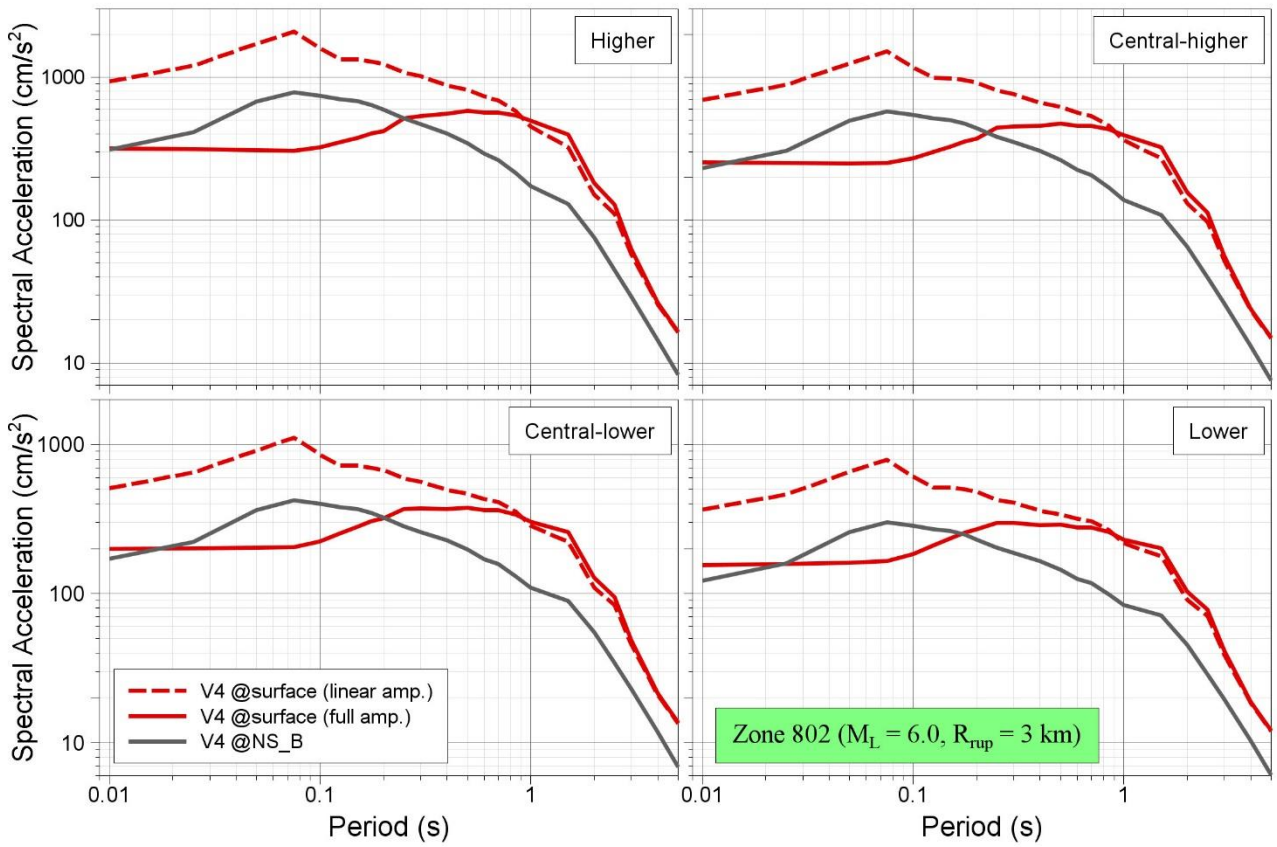


Figure 11.32. Median predicted response spectra in Zone 802 due to a magnitude M_L 6 earthquake at a rupture distance of 3 km

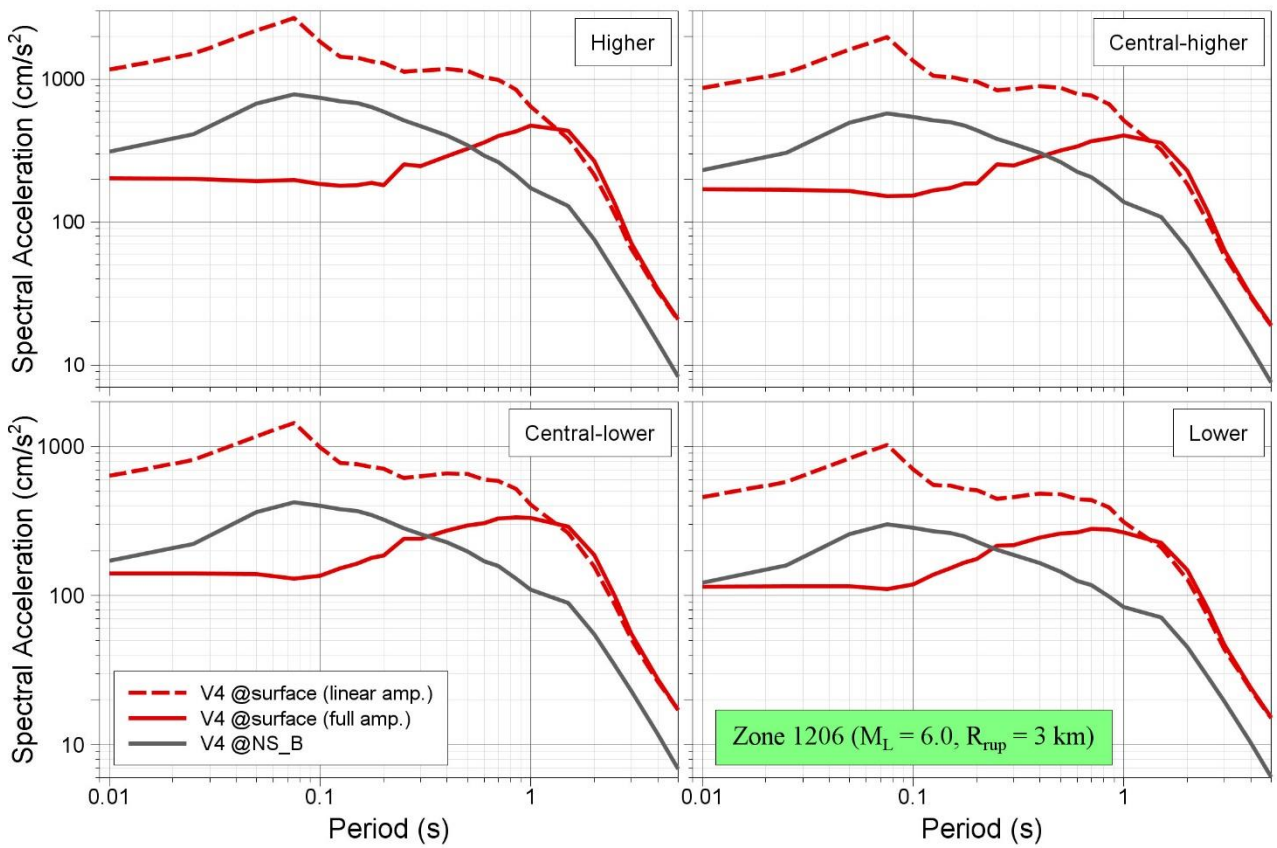


Figure 11.33. Median predicted response spectra in Zone 1206 due to a magnitude M_L 6 earthquake at a rupture distance of 3 km

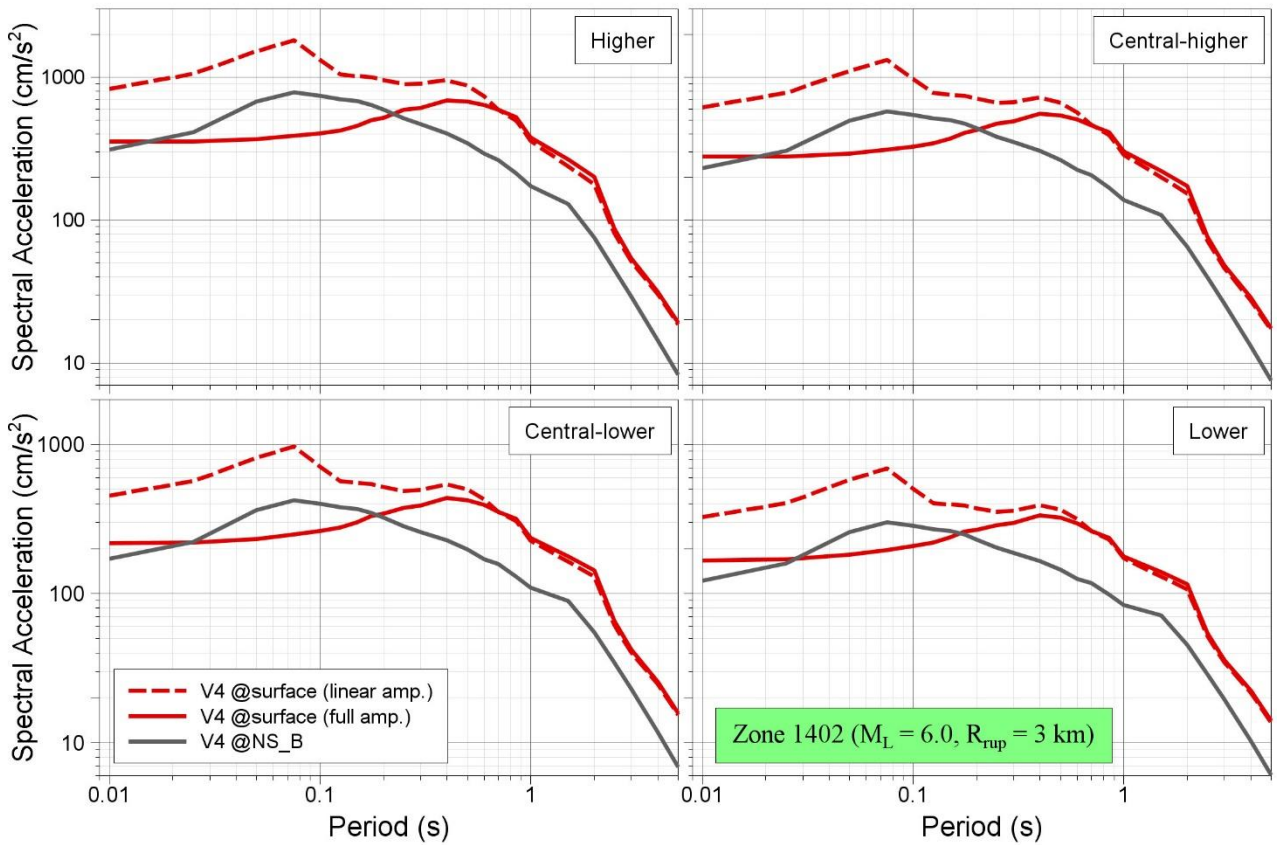


Figure 11.34. Median predicted response spectra in Zone 1402 due to a magnitude M_L 6 earthquake at a rupture distance of 3 km

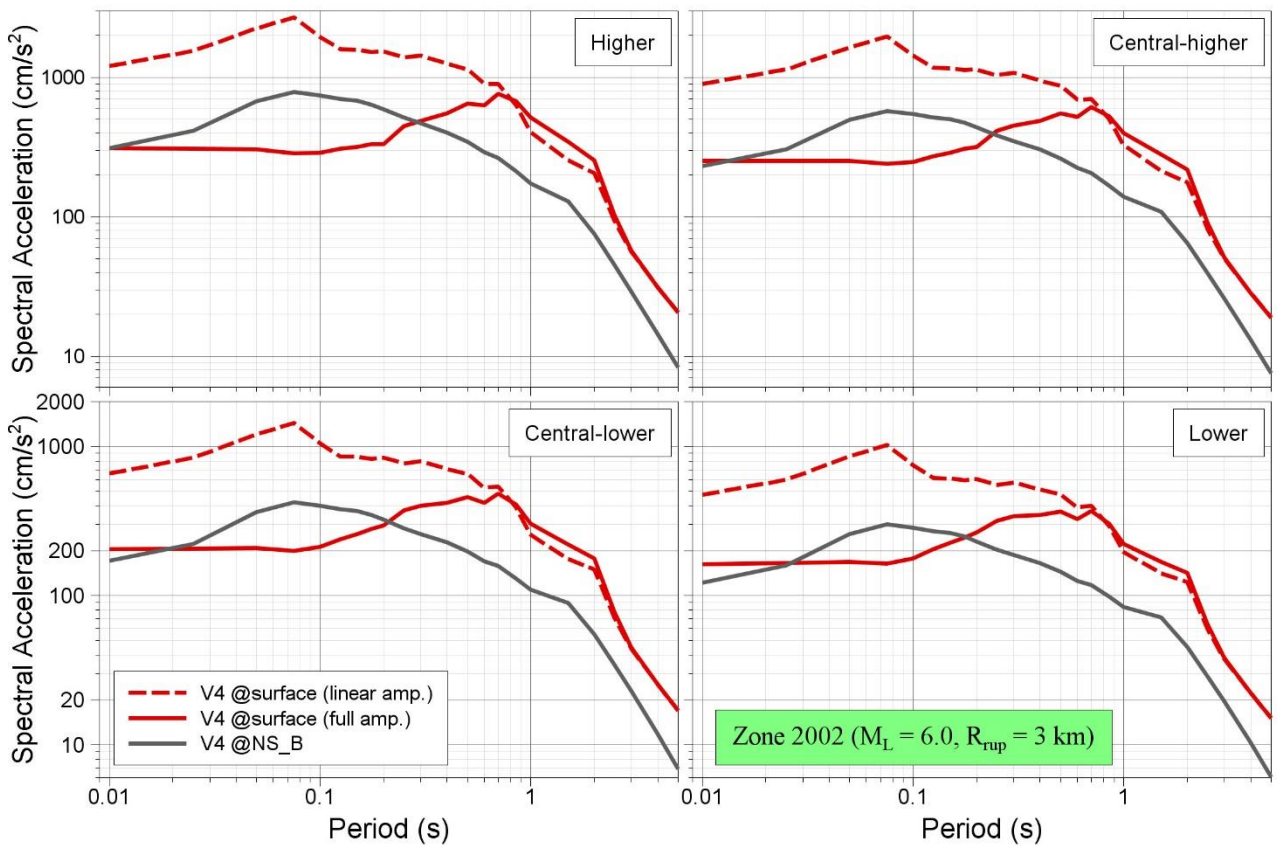


Figure 11.35. Median predicted response spectra in Zone 2002 due to a magnitude M_L 6 earthquake at a rupture distance of 3 km

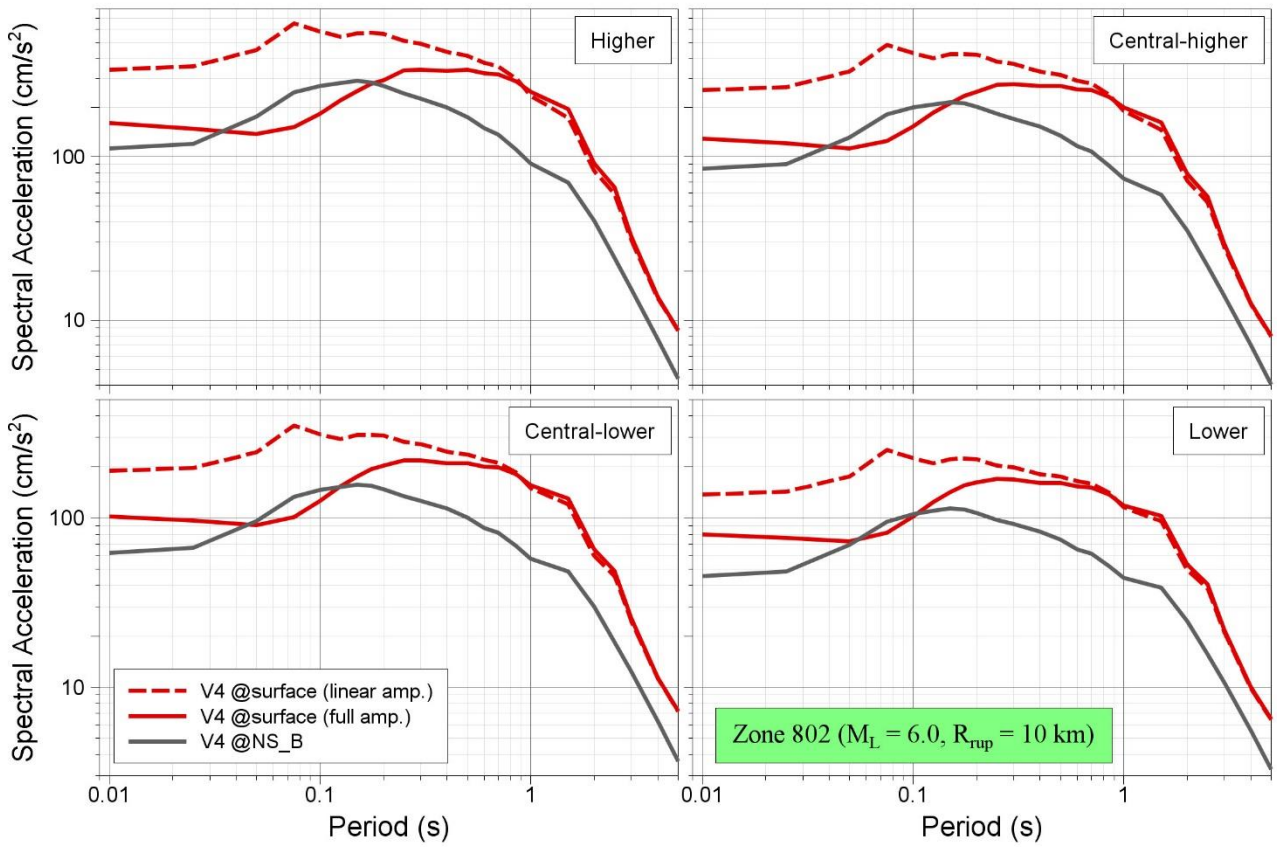


Figure 11.36. Median predicted response spectra in Zone 3115 due to a magnitude M_L 6 earthquake at a rupture distance of 10 km

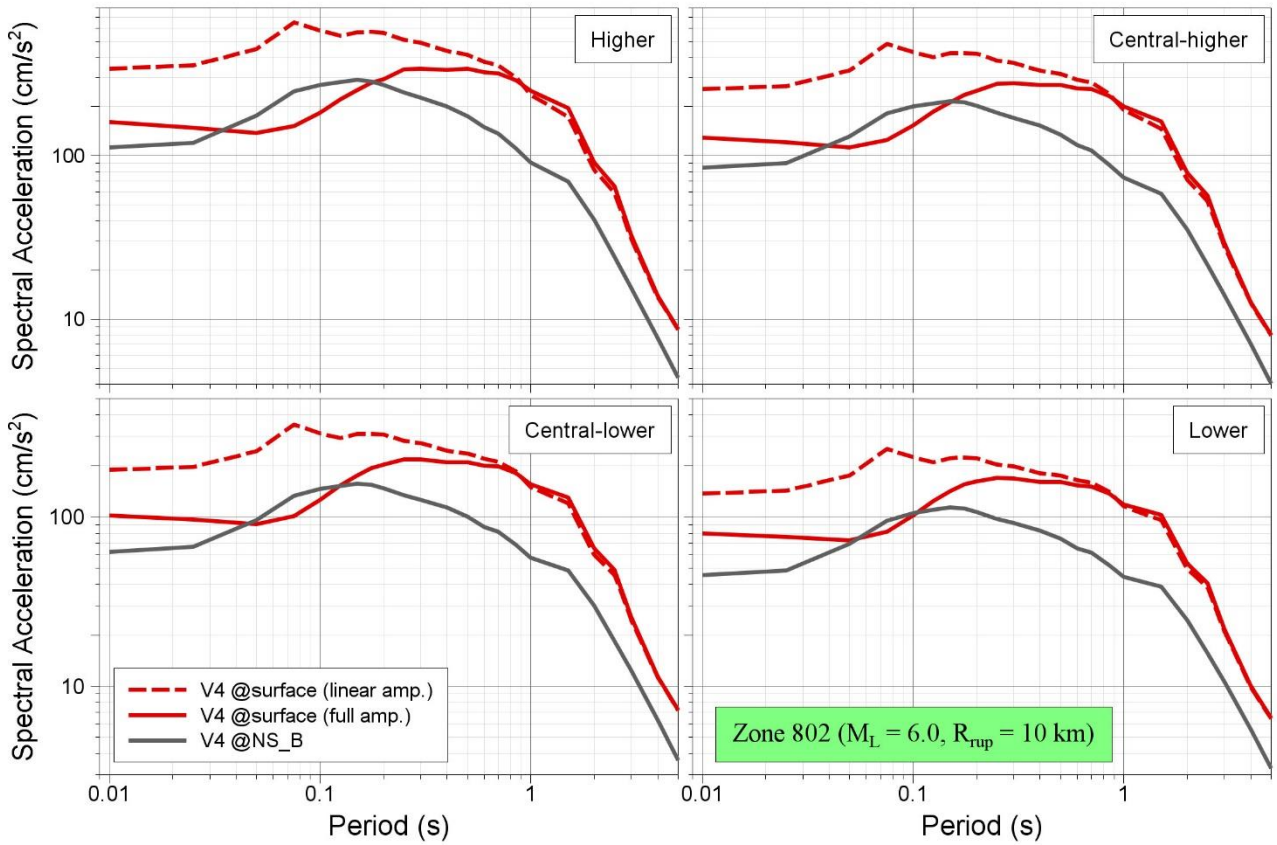


Figure 11.37. Median predicted response spectra in Zone 802 due to a magnitude M_L 6 earthquake at a rupture distance of 10 km

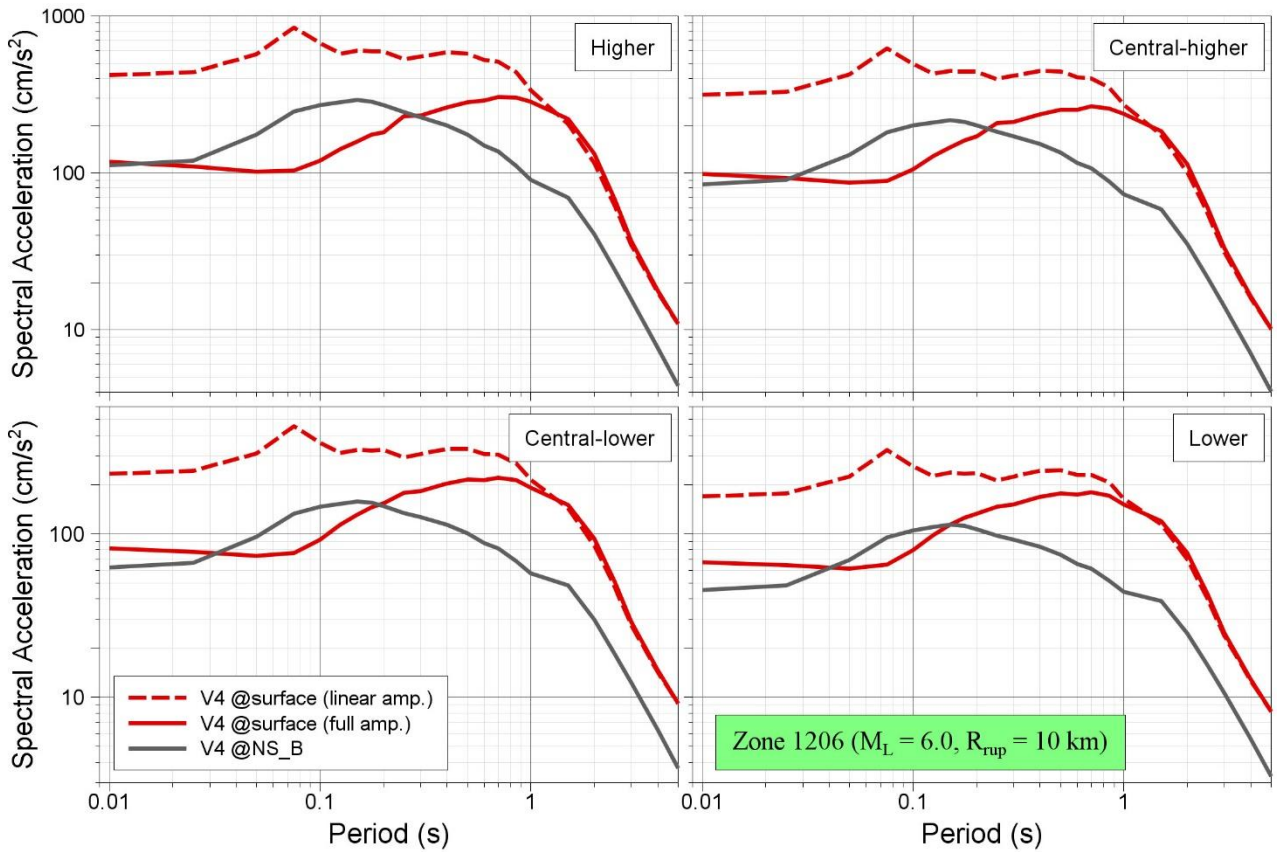


Figure 11.38. Median predicted response spectra in Zone 1206 due to a magnitude M_L 6 earthquake at a rupture distance of 10 km

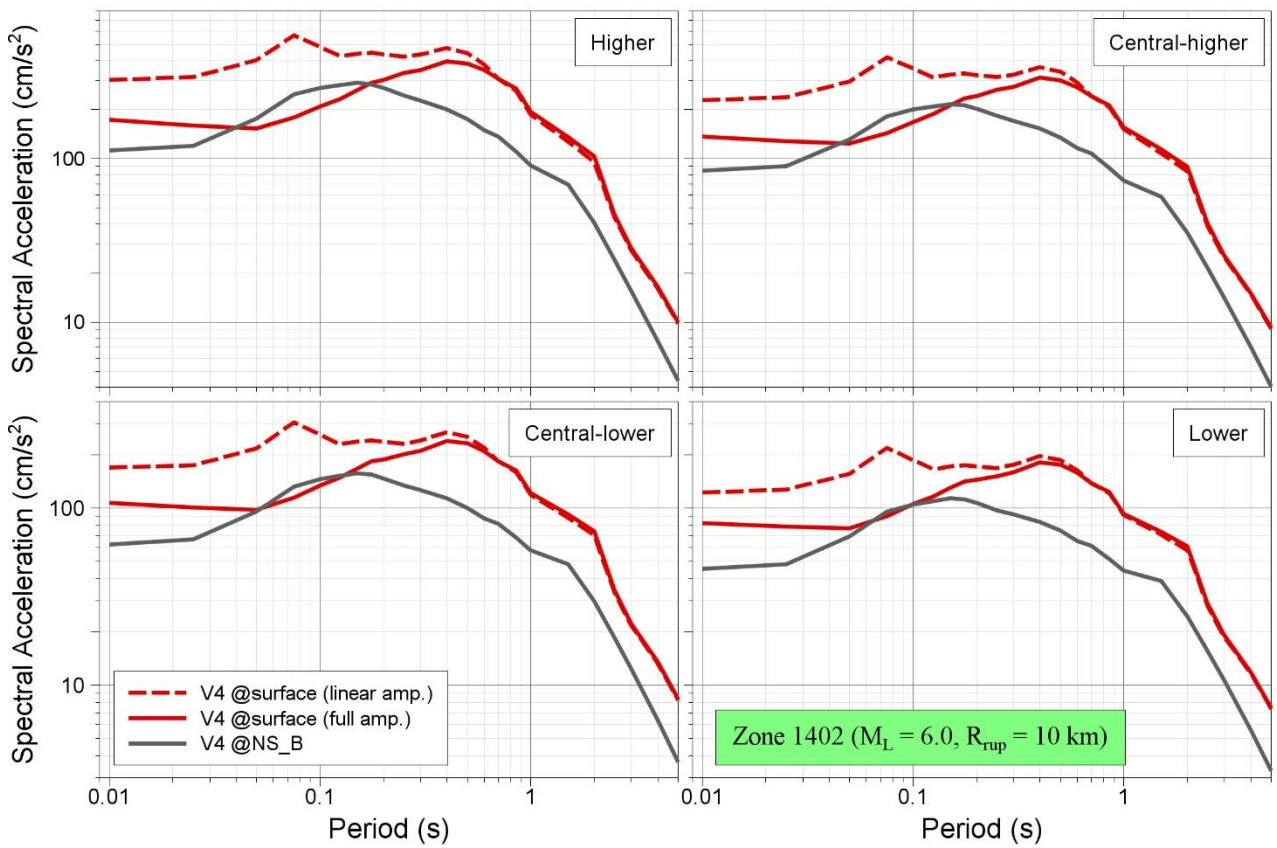


Figure 11.39. Median predicted response spectra in Zone 1402 due to a magnitude M_L 6 earthquake at a rupture distance of 10 km

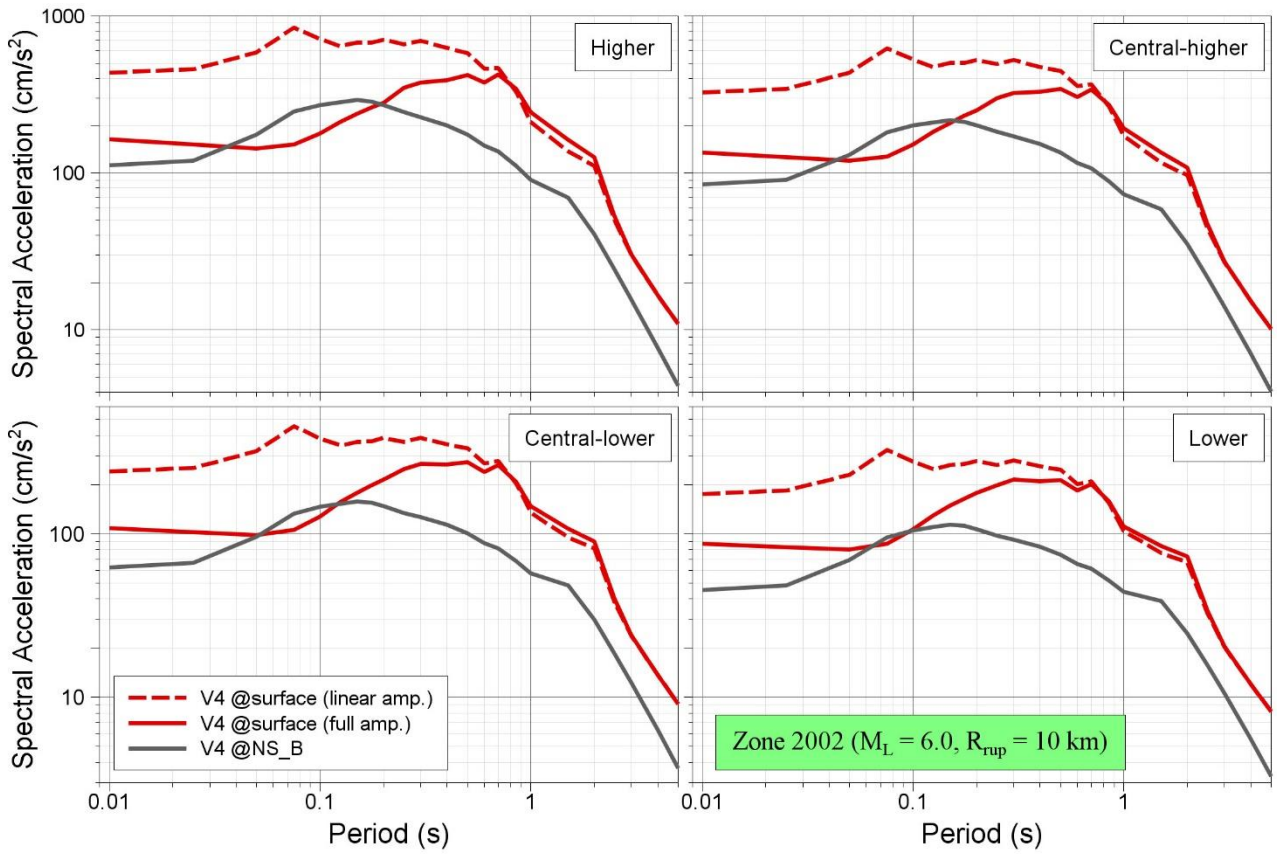


Figure 11.40. Median predicted response spectra in Zone 2002 due to a magnitude M_L 6 earthquake at a rupture distance of 10 km

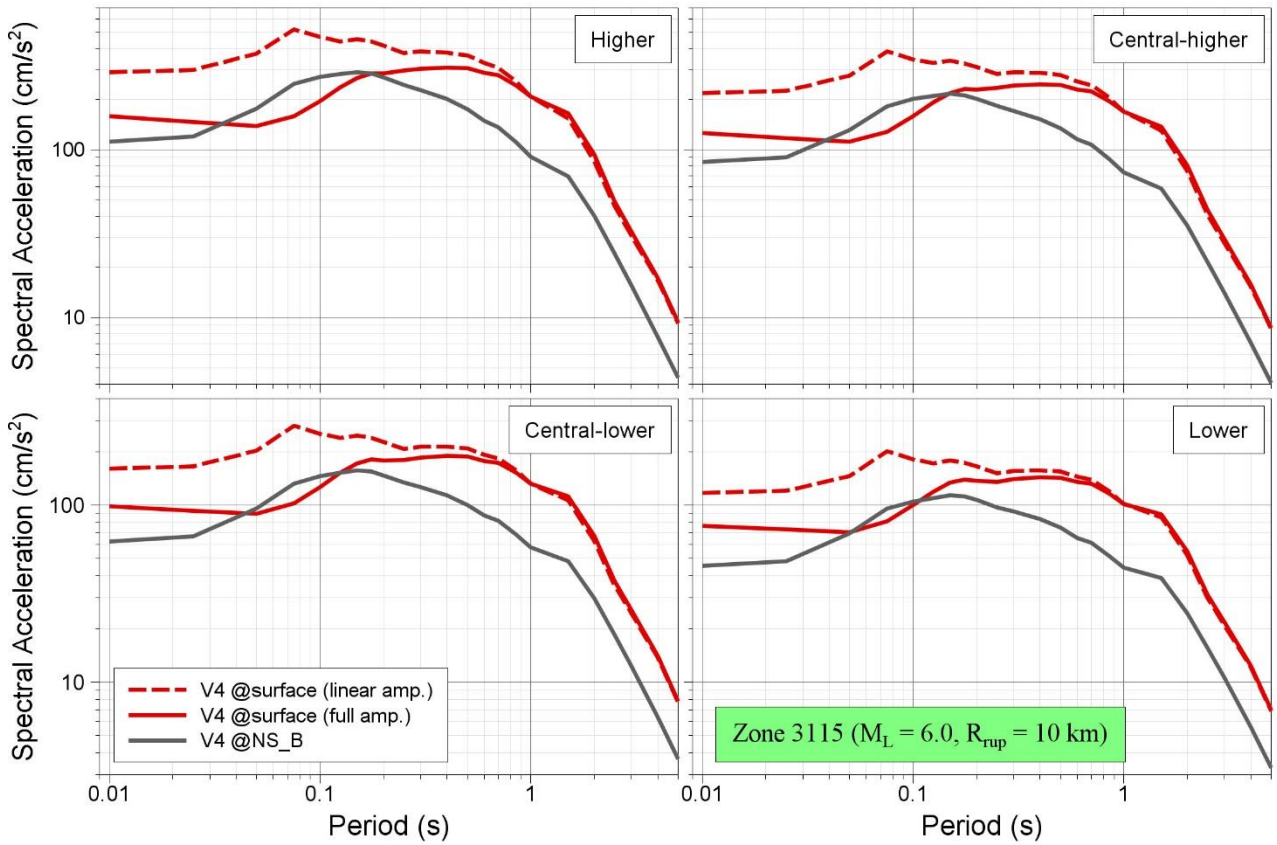


Figure 11.41. Median predicted response spectra in Zone 3115 due to a magnitude M_L 6 earthquake at a rupture distance of 10 km

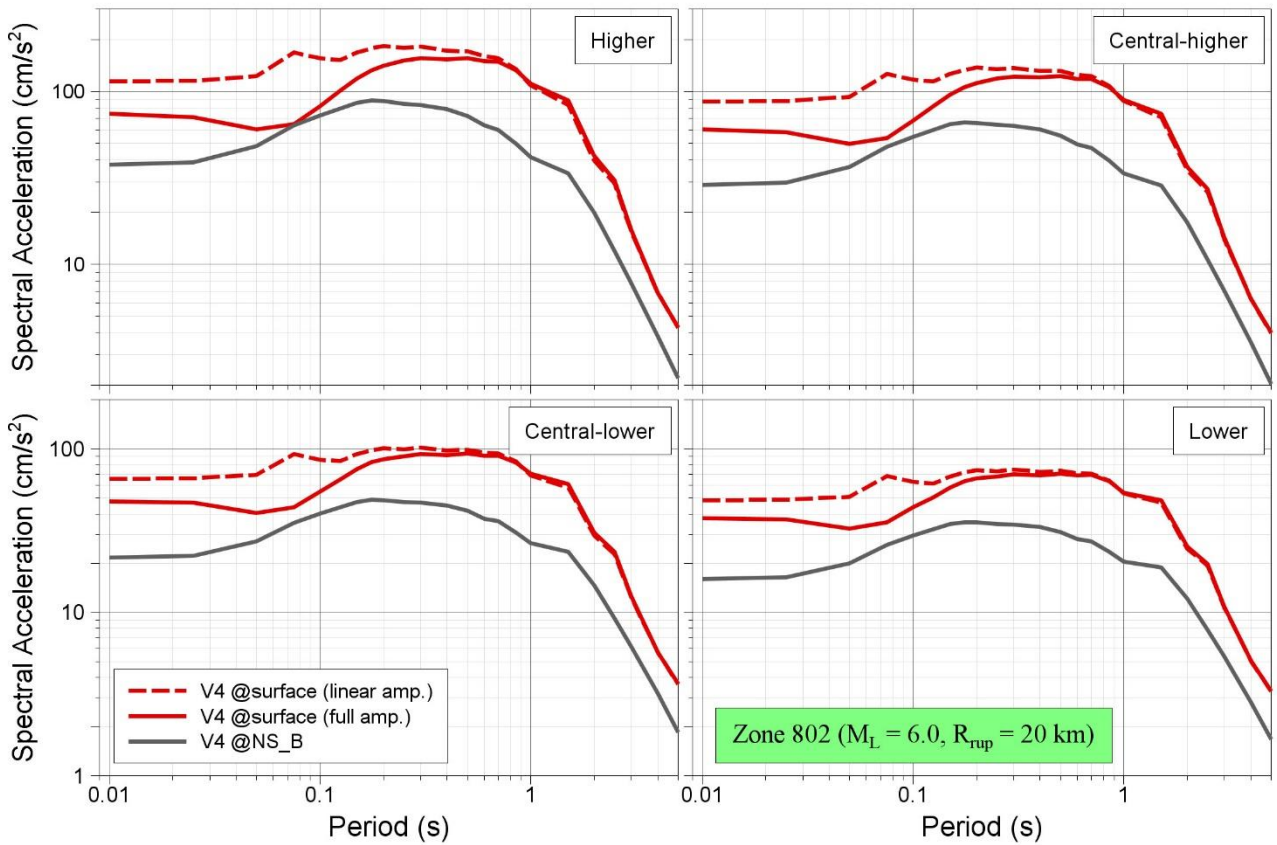


Figure 11.42. Median predicted response spectra in Zone 802 due to a magnitude M_L 6 earthquake at a rupture distance of 20 km

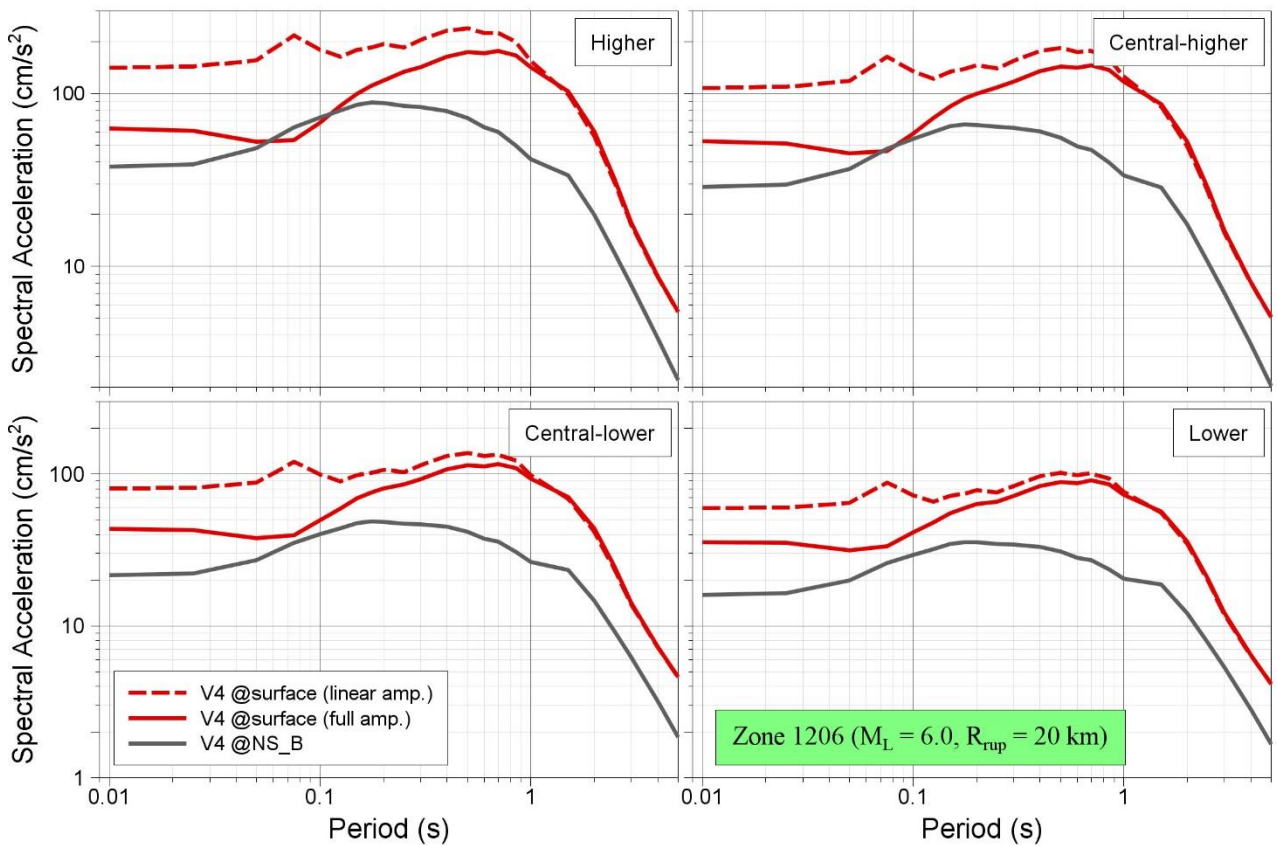


Figure 11.43. Median predicted response spectra in Zone 1206 due to a magnitude M_L 6 earthquake at a rupture distance of 20 km

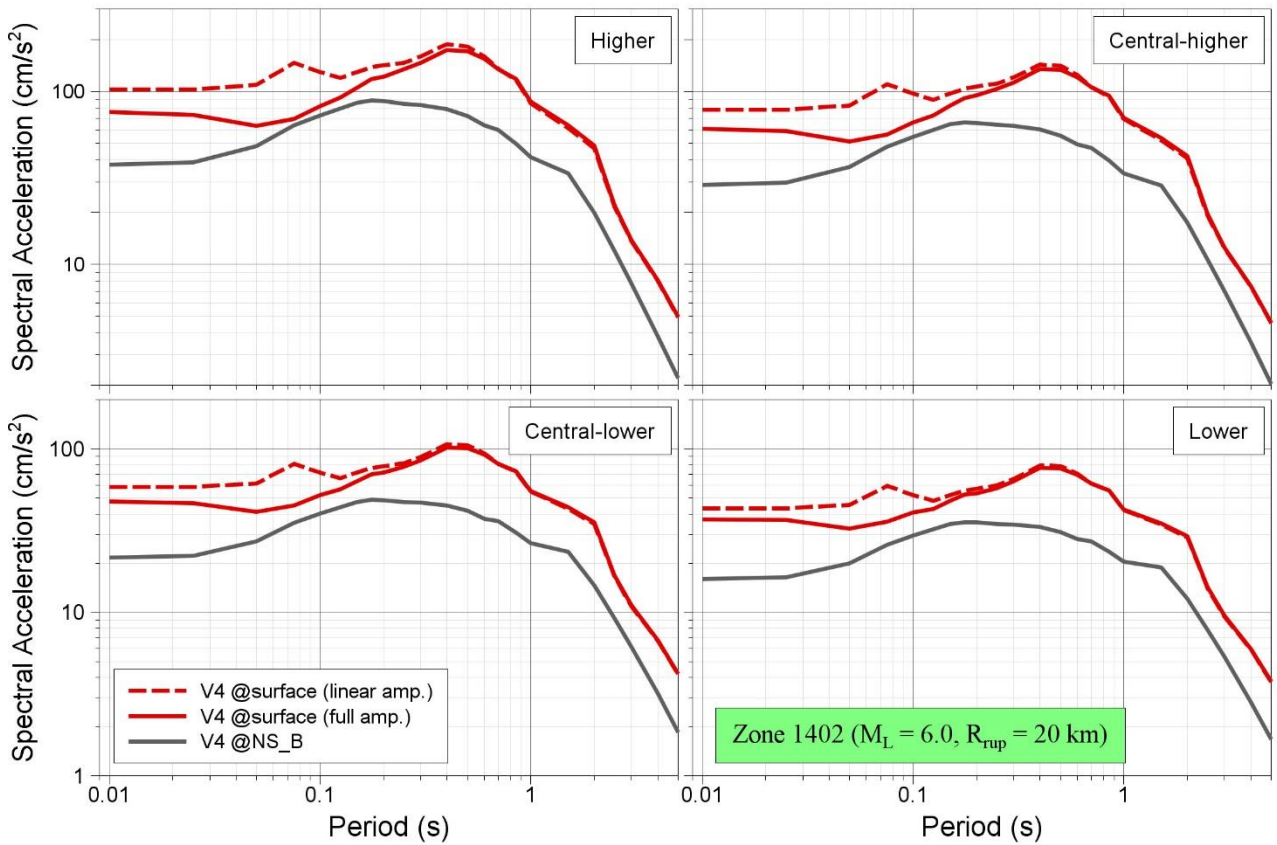


Figure 11.44. Median predicted response spectra in Zone 1402 due to a magnitude M_L 6 earthquake at a rupture distance of 20 km

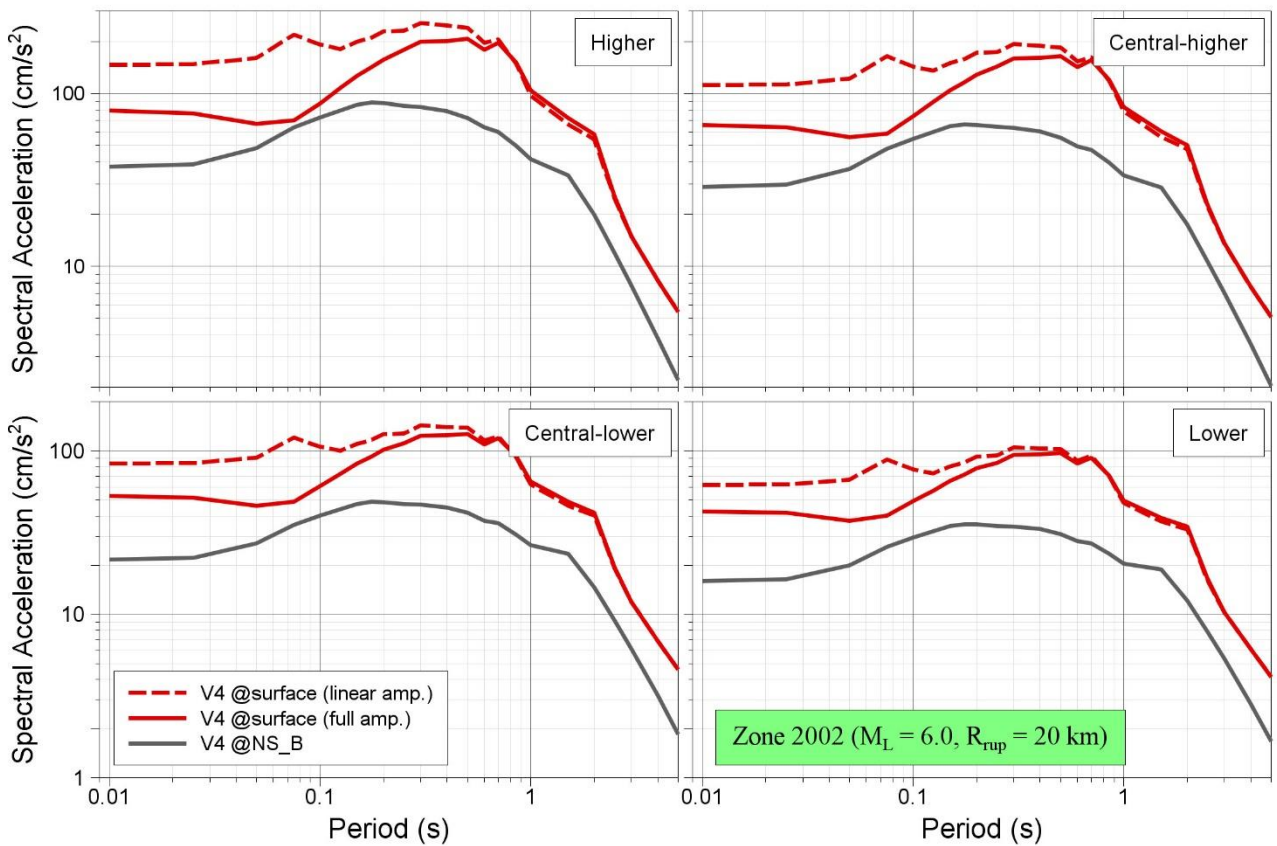


Figure 11.45. Median predicted response spectra in Zone 2002 due to a magnitude M_L 6 earthquake at a rupture distance of 20 km

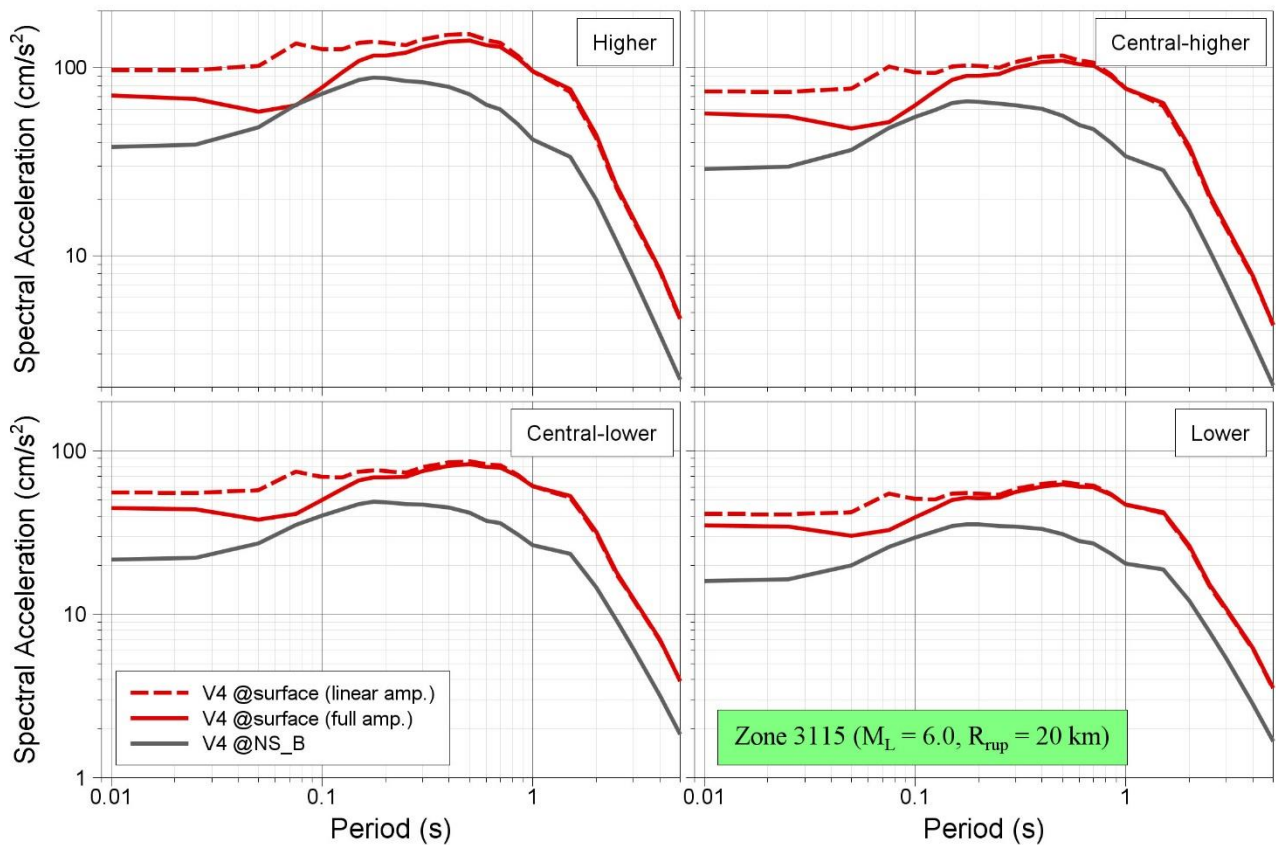


Figure 11.46. Median predicted response spectra in Zone 3115 due to a magnitude M_L 6 earthquake at a rupture distance of 20 km

The comparisons with earlier models in Figures 11.2 to 11.16 show that the models are rather consistent, except that the V1 model yields higher predictions at short distances as a result of only modelling linear site response. Another observation that emerges is that the lower branch in the V2 model was excessively low, a feature that was recognised and addressed in the development of the V3 model. The V3 and V4 models yield comparable median predictions, which is testimony to the stability acquired through the incremental evolution of the models; the differences between the two models are mainly related to the reduced aleatory variability in the current model.

The remaining plots in Figures 11.17 to 11.46 confirm the pronounced effect of the non-linear site response effects under stronger scenarios, reflecting the presence of particularly soft clays and peats in the Groningen field. The plots also display the significant amplification experienced by weaker motions at the NS_B horizon as these propagate to the ground surface through ~800 m of overburden. This is important to note when interpreting the amplitudes of motion leading to non-linear response in the soil layers. The amplitudes of motion on which the AFs are conditioned are referenced to the NS_B horizon, whereas the non-linearity will occur very close to the ground surface where the accelerations will have experienced very considerable amplification as they travel through the many layers between the NS_B rock and the top 10-20 metres of the profile.

11.2. Residuals of surface motions

An important test of the model is whether it produces unbiased predictions of the recorded motions at the ground surface. This can be explored by comparing the recorded surface motions, at both the B and G stations (see Section 3.1), with median predictions from the model in terms of both the NS_B accelerations and the amplification factors corresponding to the zone within which each strong-motion station is located. The differences between the recorded and predicted values—or rather their logarithms—are not strictly residuals since the model was fitted by regression on the surface motions. However, the distribution of these differences, treated in the same way as true residuals, can provide useful insight into how well the model is working, at least in the small-magnitude range represented by the recordings (which is of minor importance to the risk estimates). This is done by calculating the between-event and within-event residuals at the NS_B horizon with respect to the central model (the two alternative versions are identical in the magnitude range of the recordings), as presented in Section 6.5, and then subtracting these residuals from the total surface residuals. The implicit assumption—which is, necessarily, a simplification—is that the remaining residual is related to the site amplification model. Figures 11.47 to 11.65 display the results in the following way: each plot shows the NS_B between-event residuals against magnitude, the NS_B within-event residuals against distance, and the site-response residuals against distance and also against the recording station code.

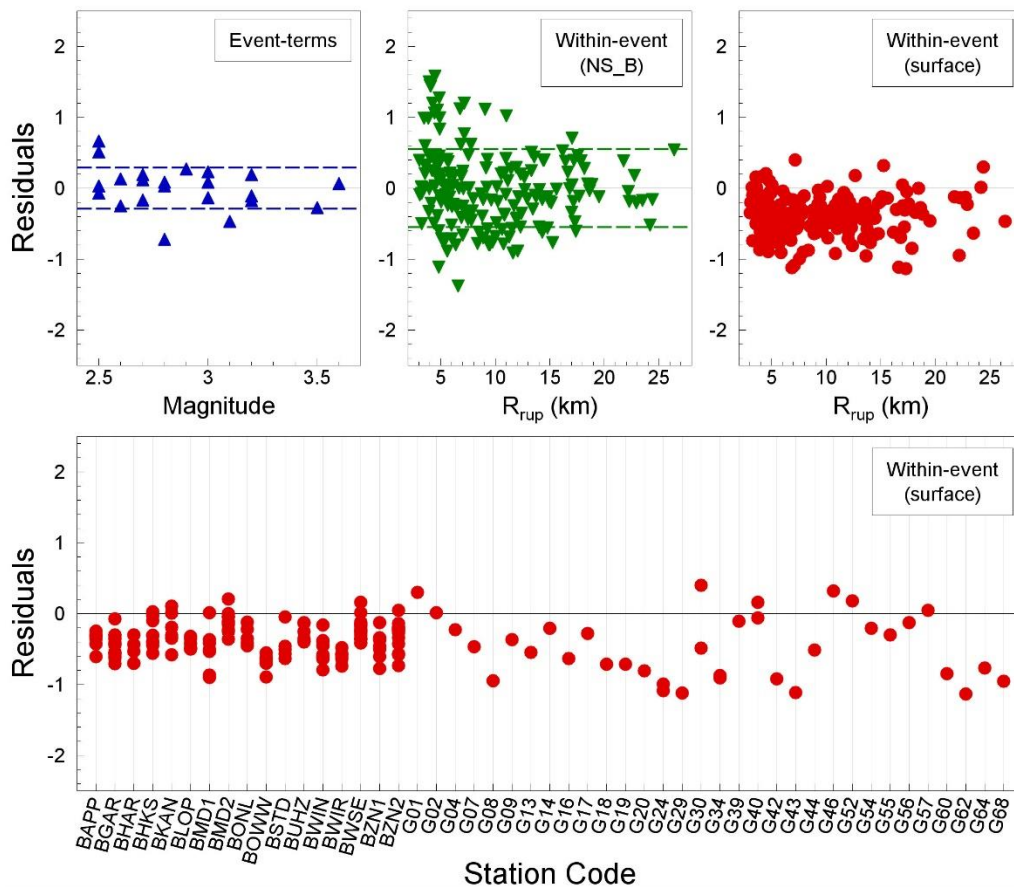


Figure 11.47. De-composed 'residuals' of $S_a(0.01s)$ at the surface (*upper*) and site response 'residuals' against recording station ID code (*lower*)

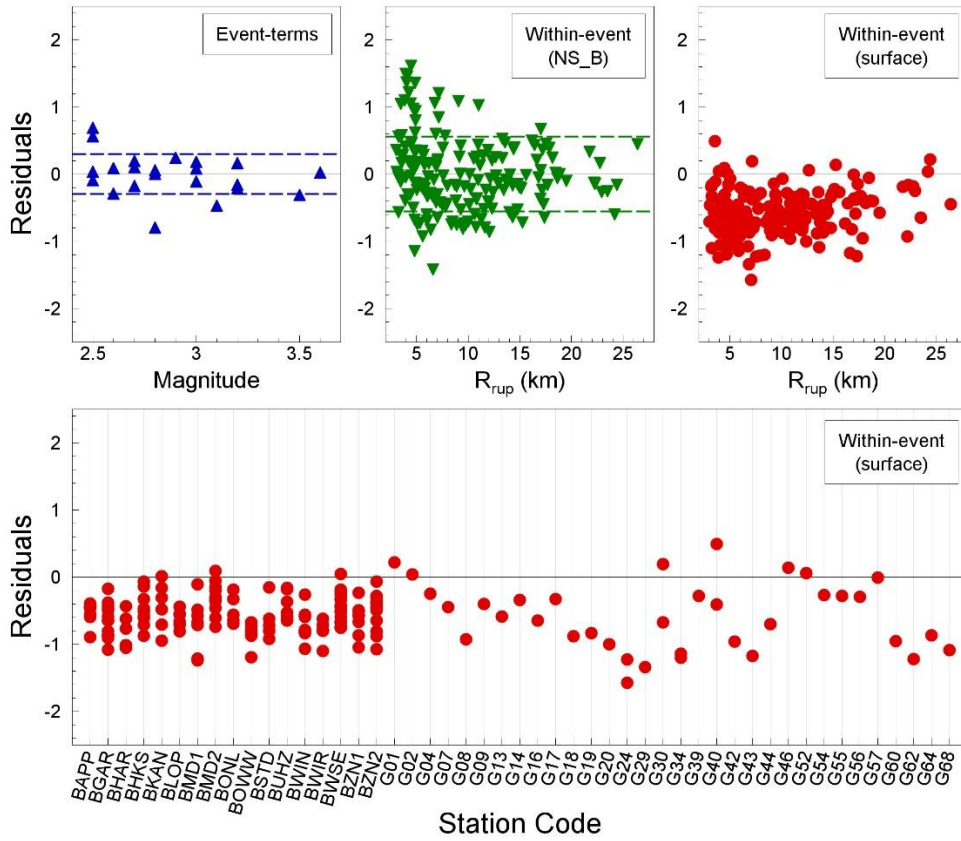


Figure 11.48. De-composed ‘residuals’ of $S_a(0.025s)$ at the surface (*upper*) and site response ‘residuals’ against recording station ID code (*lower*)

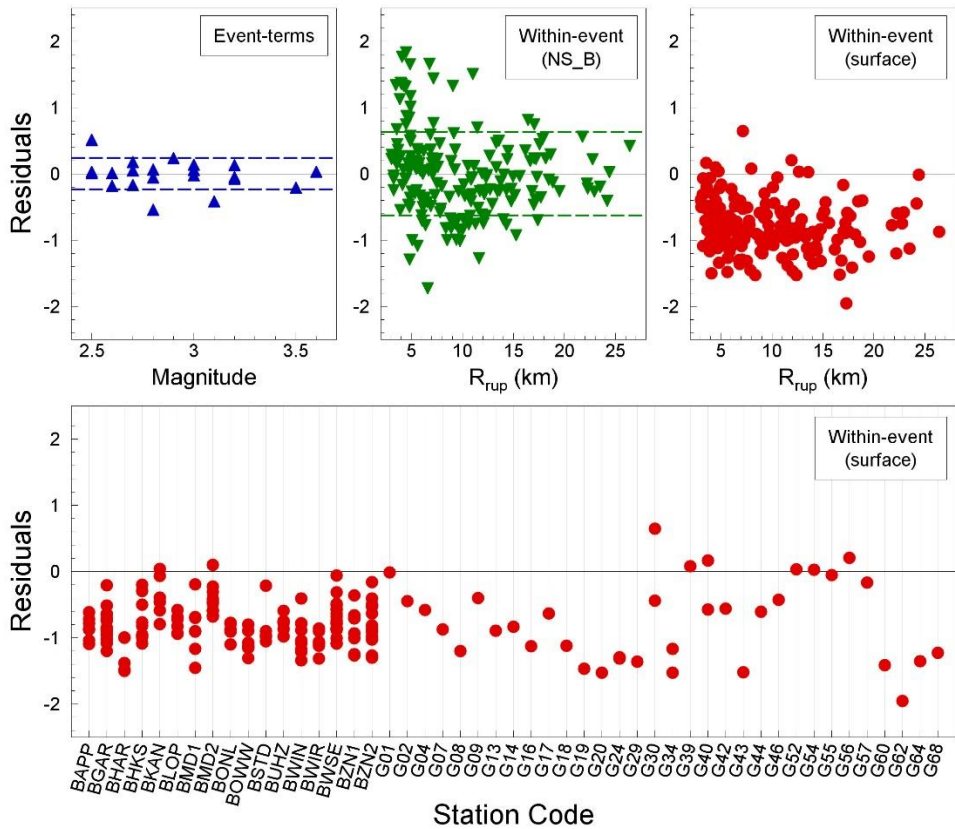


Figure 11.49. De-composed ‘residuals’ of $S_a(0.05s)$ at the surface (*upper*) and site response ‘residuals’ against recording station ID code (*lower*)

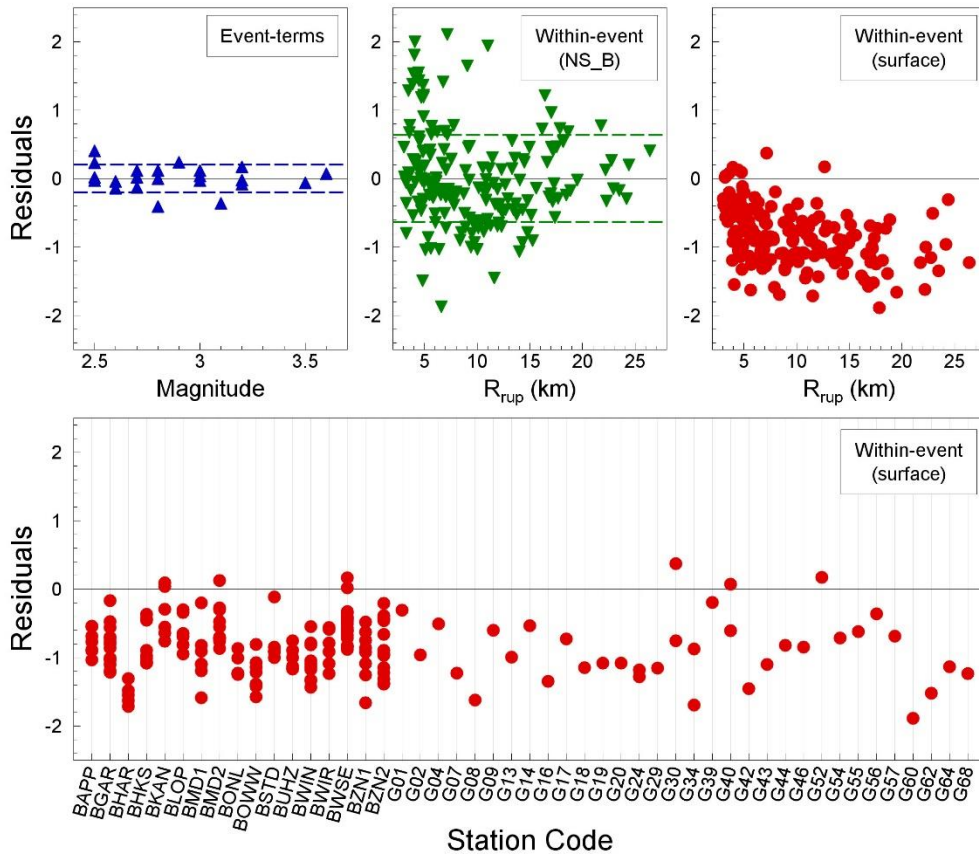


Figure 11.50. De-composed 'residuals' of $Sa(0.075s)$ at the surface (*upper*) and site response 'residuals' against recording station ID code (*lower*)

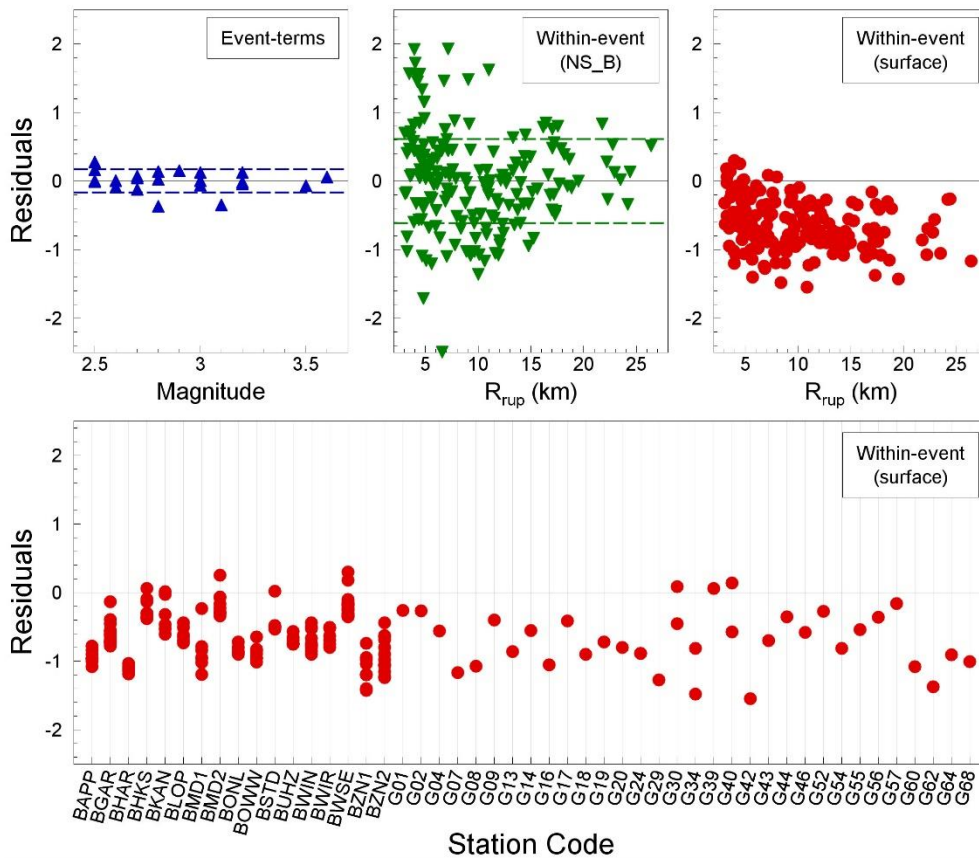


Figure 11.51. De-composed 'residuals' of $Sa(0.10s)$ at the surface (*upper*) and site response 'residuals' against recording station ID code (*lower*)

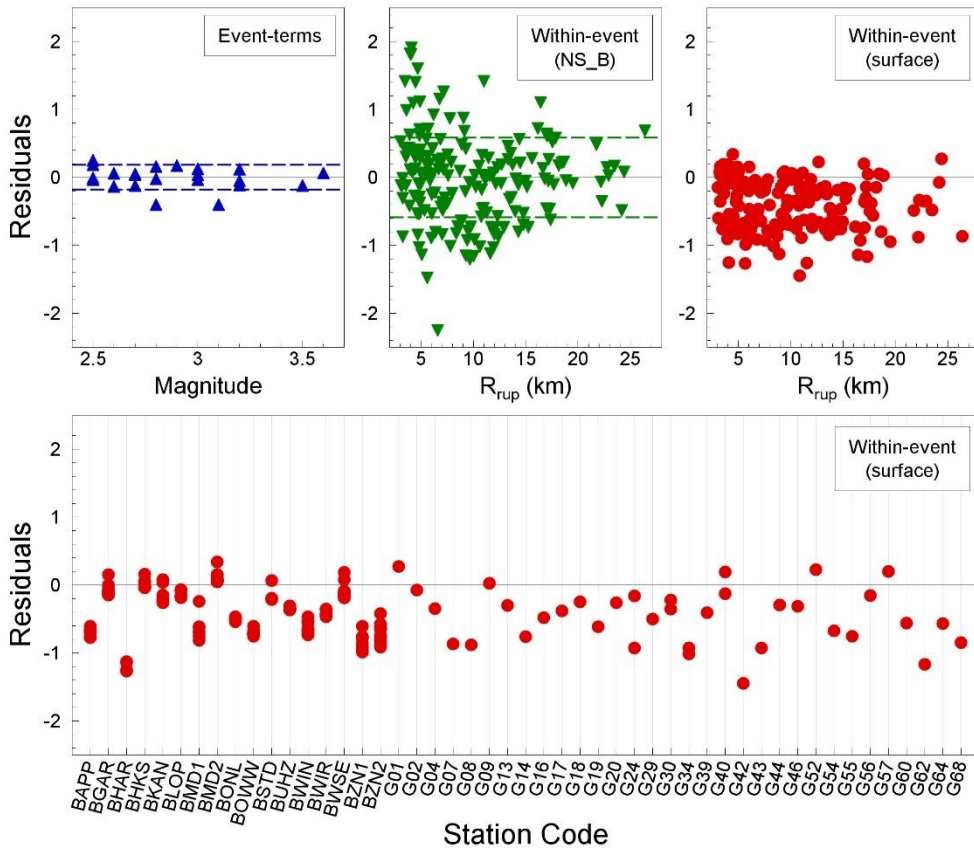


Figure 11.52. De-composed 'residuals' of $Sa(0.125s)$ at the surface (*upper*) and site response 'residuals' against recording station ID code (*lower*)

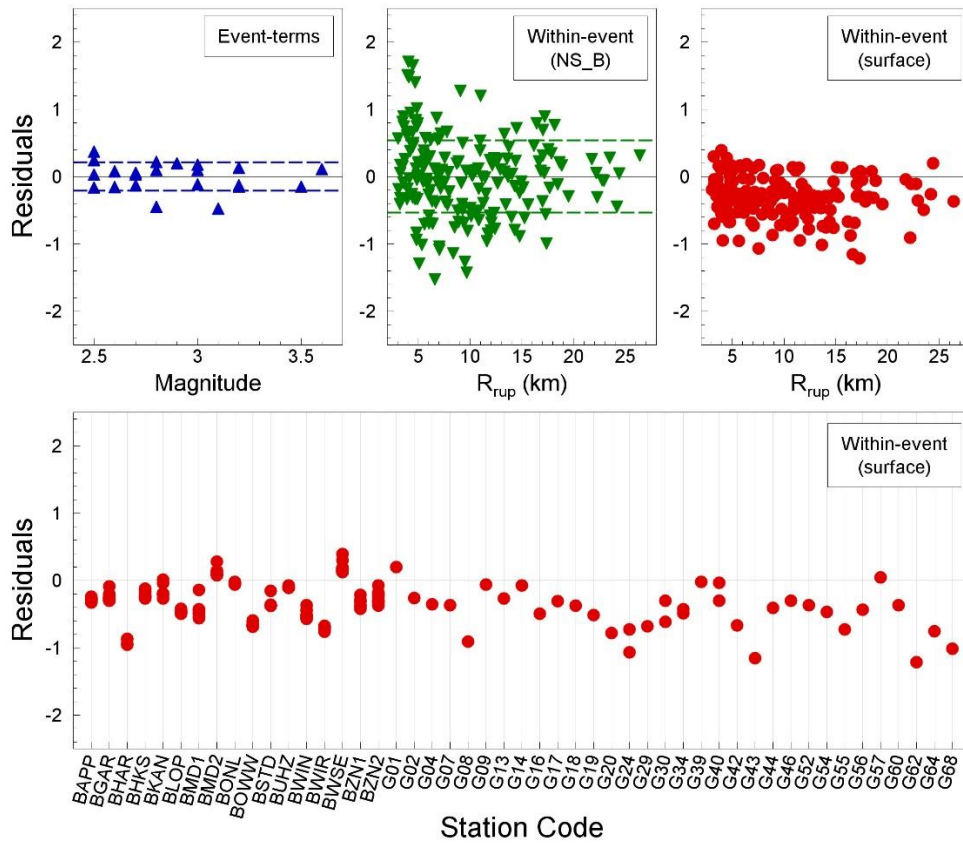


Figure 11.53. De-composed 'residuals' of $Sa(0.15s)$ at the surface (*upper*) and site response 'residuals' against recording station ID code (*lower*)

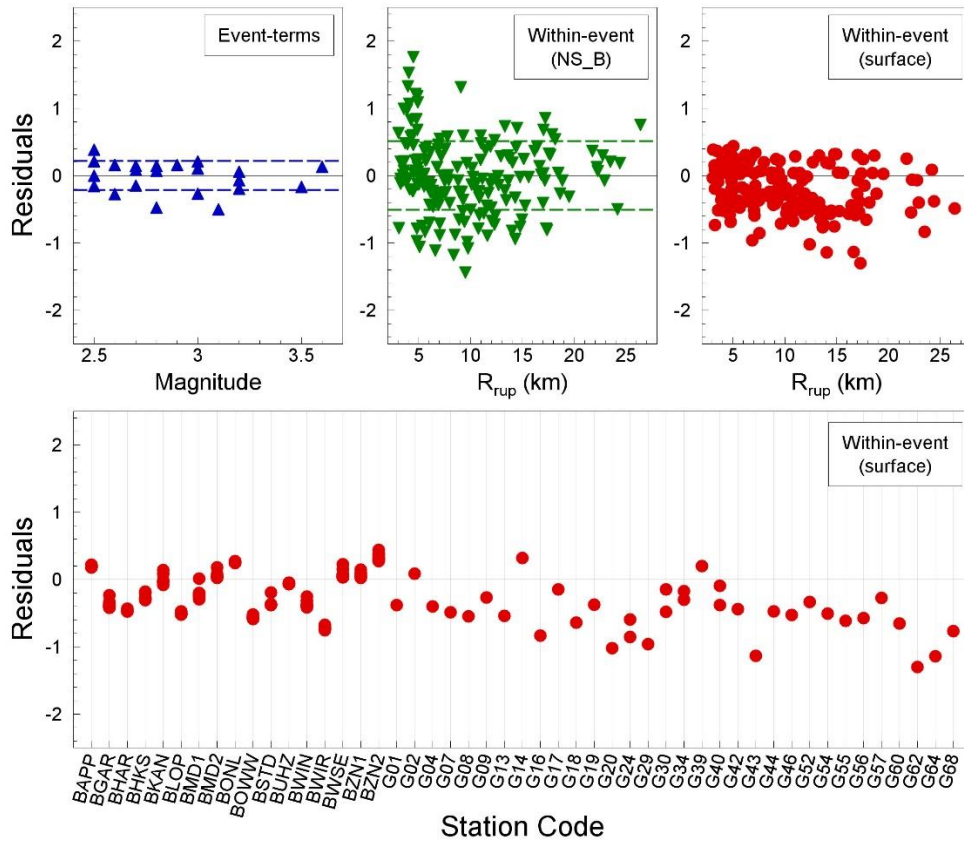


Figure 11.54. De-composed ‘residuals’ of $Sa(0.175s)$ at the surface (*upper*) and site response ‘residuals’ against recording station ID code (*lower*)

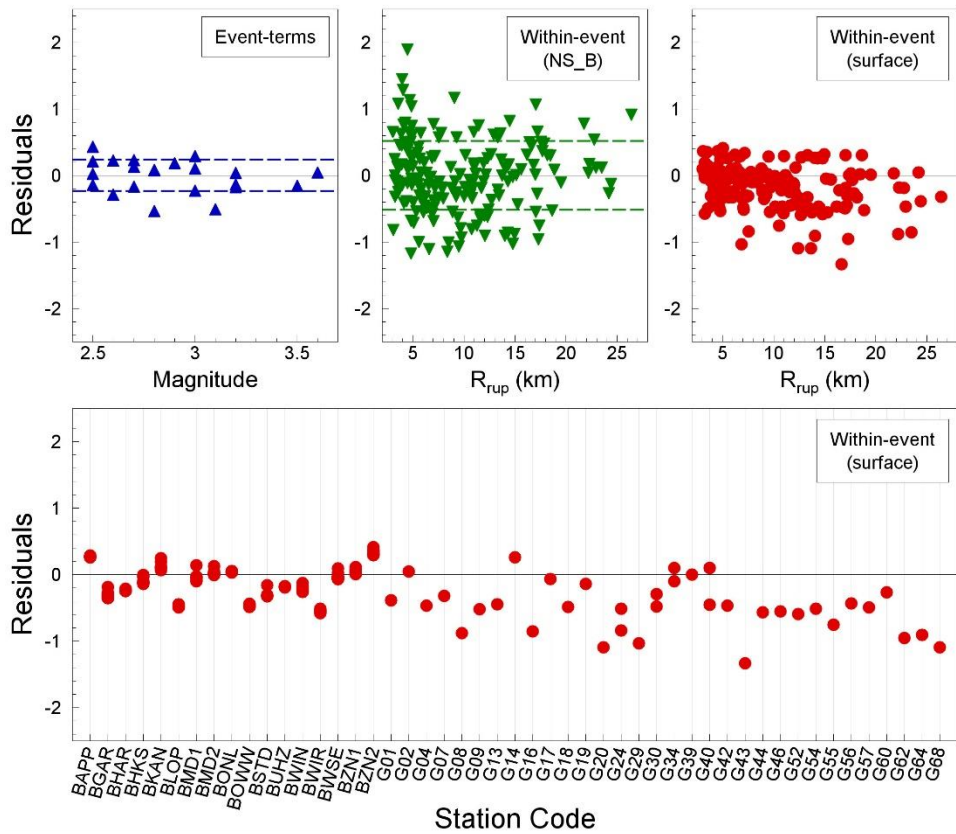


Figure 11.55. De-composed ‘residuals’ of $Sa(0.20s)$ at the surface (*upper*) and site response ‘residuals’ against recording station ID code (*lower*)

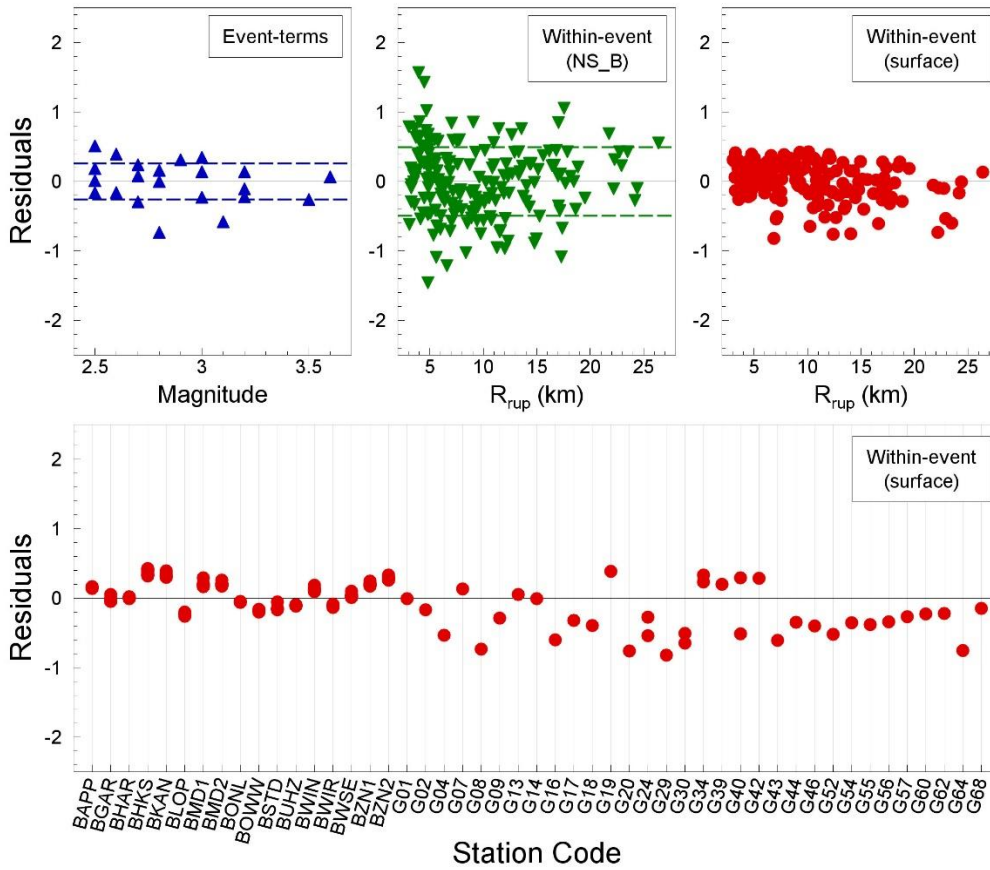


Figure 11.56. De-composed 'residuals' of $S_a(0.25s)$ at the surface (*upper*) and site response 'residuals' against recording station ID code (*lower*)

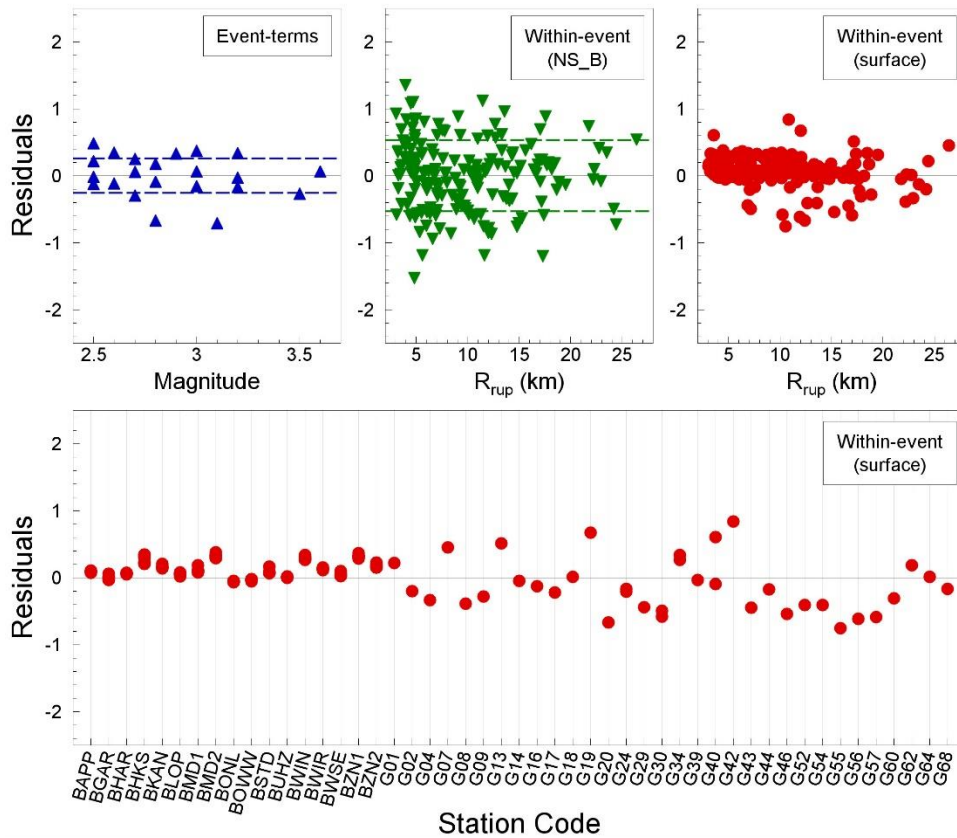


Figure 11.57. De-composed 'residuals' of $S_a(0.30s)$ at the surface (*upper*) and site response 'residuals' against recording station ID code (*lower*)

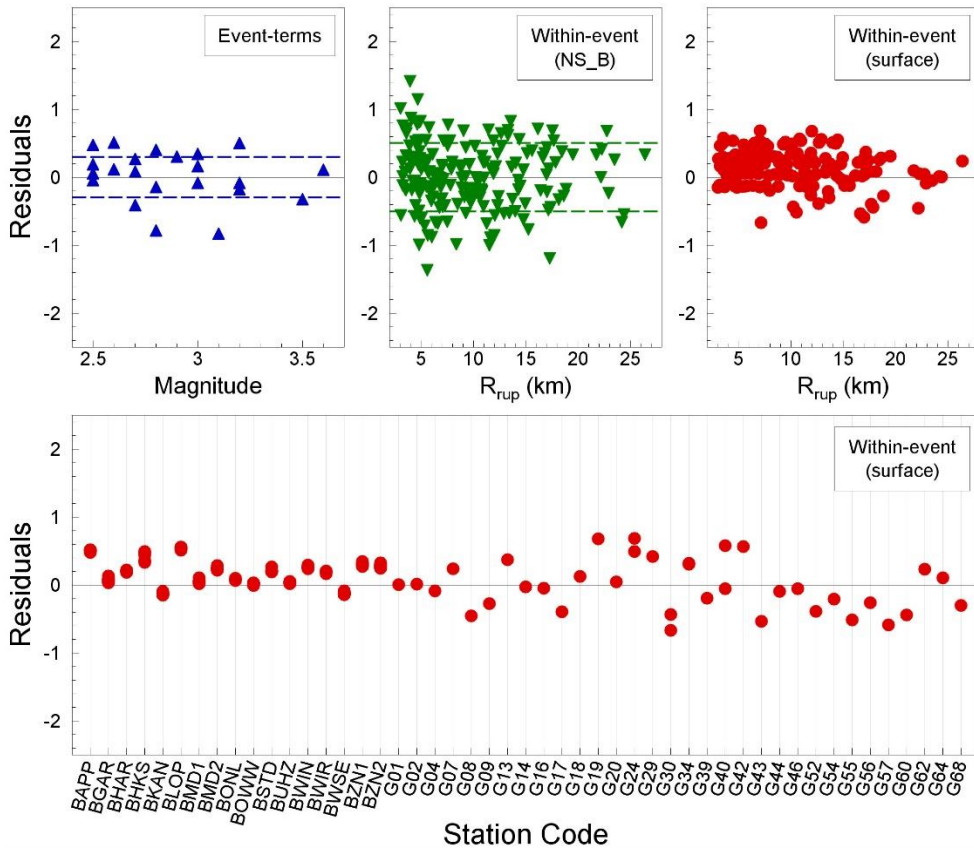


Figure 11.58. De-composed 'residuals' of $Sa(0.40s)$ at the surface (*upper*) and site response 'residuals' against recording station ID code (*lower*)

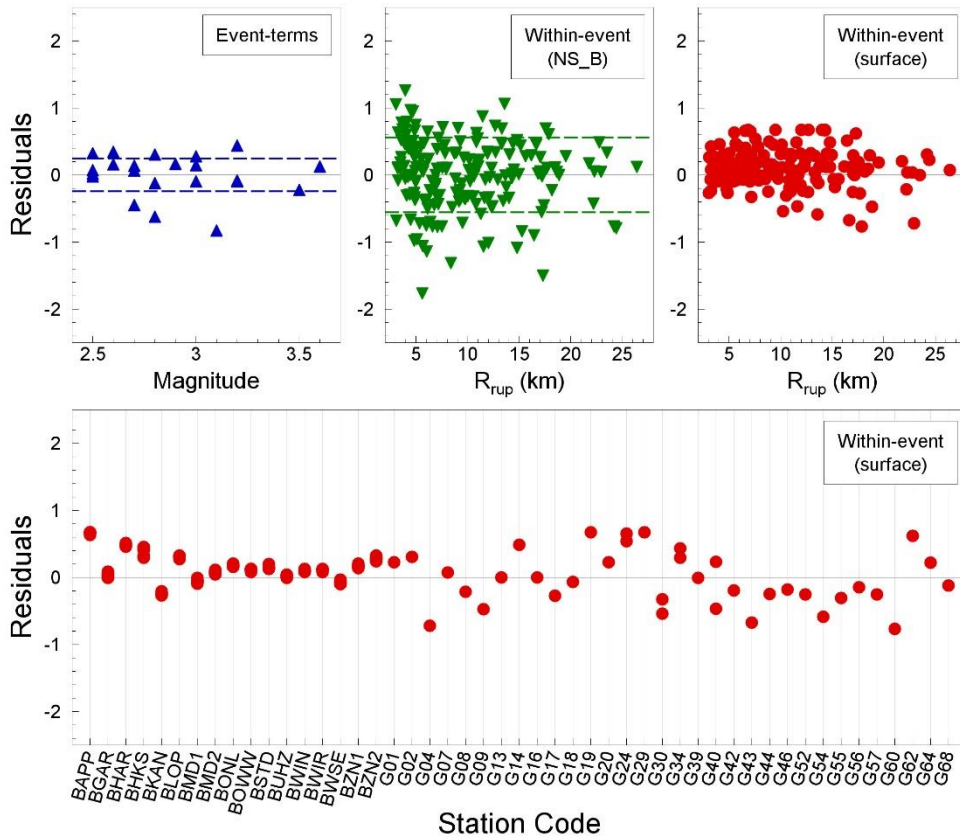


Figure 11.59. De-composed 'residuals' of $Sa(0.50s)$ at the surface (*upper*) and site response 'residuals' against recording station ID code (*lower*)

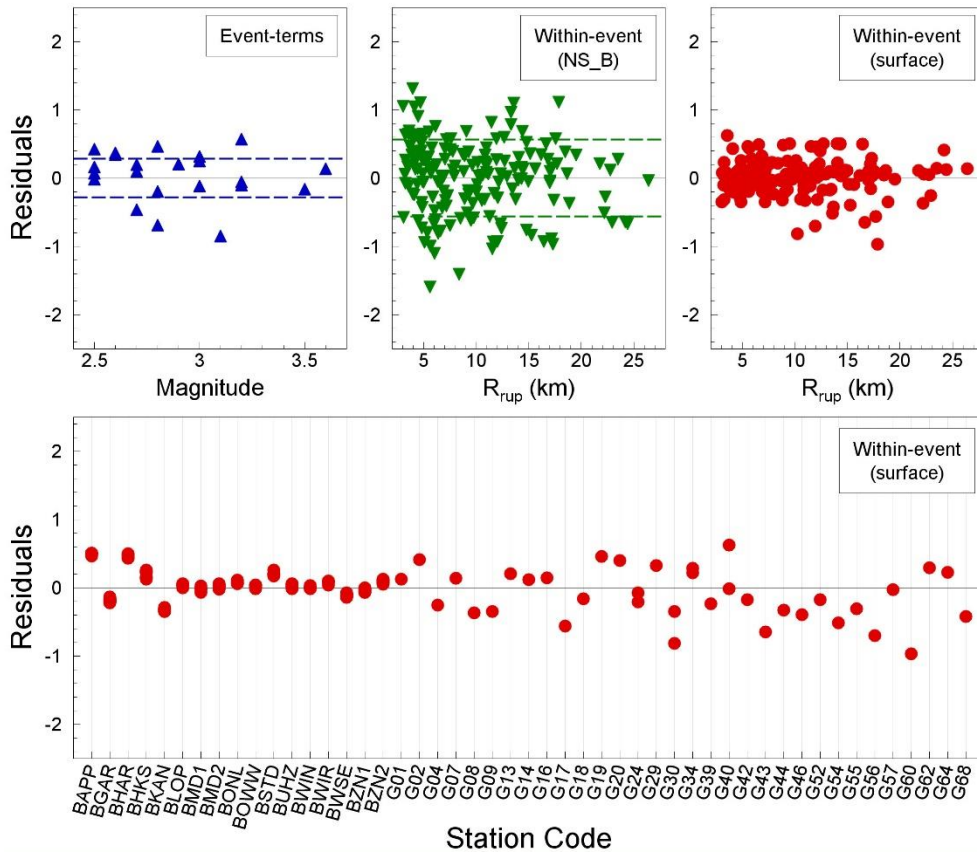


Figure 11.60. De-composed 'residuals' of $S_a(0.60s)$ at the surface (*upper*) and site response 'residuals' against recording station ID code (*lower*)

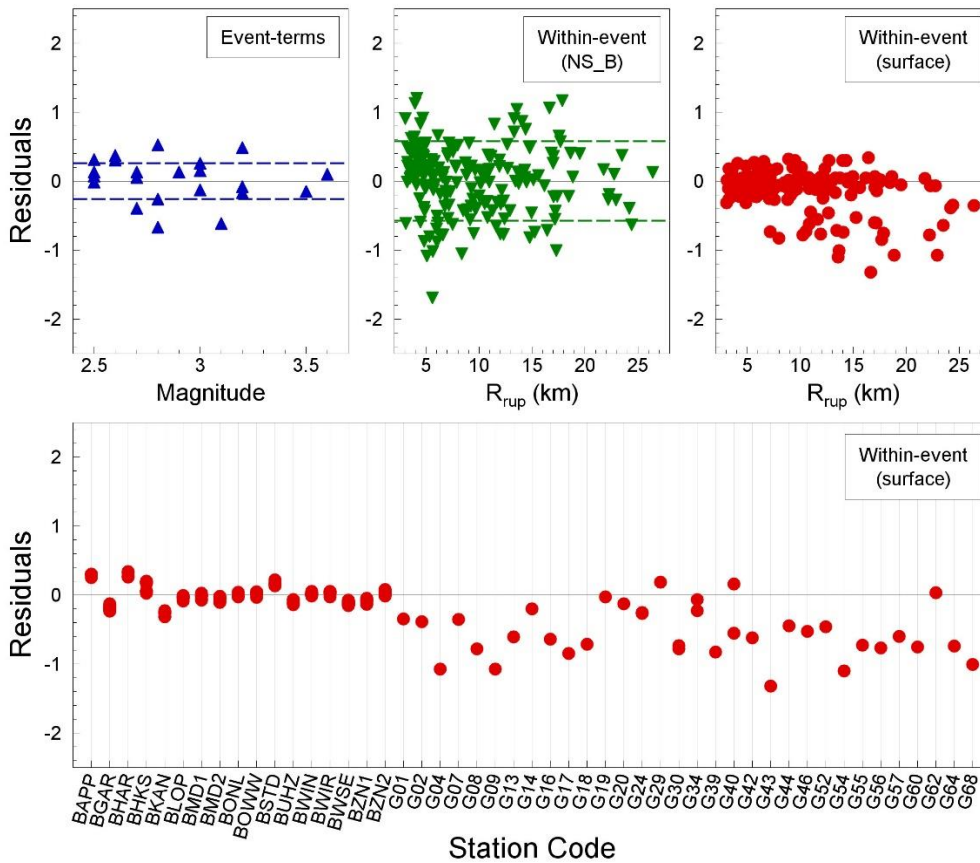


Figure 11.61. De-composed 'residuals' of $S_a(0.70s)$ at the surface (*upper*) and site response 'residuals' against recording station ID code (*lower*)

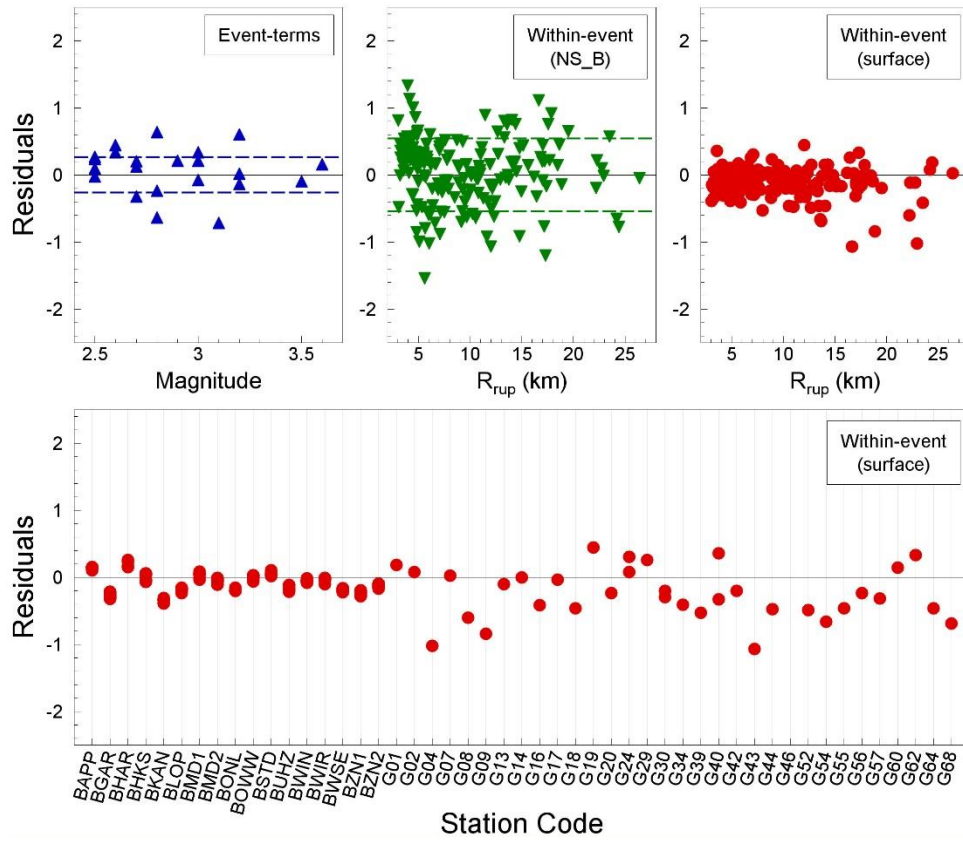


Figure 11.62. De-composed 'residuals' of $Sa(0.85s)$ at the surface (*upper*) and site response 'residuals' against recording station ID code (*lower*)

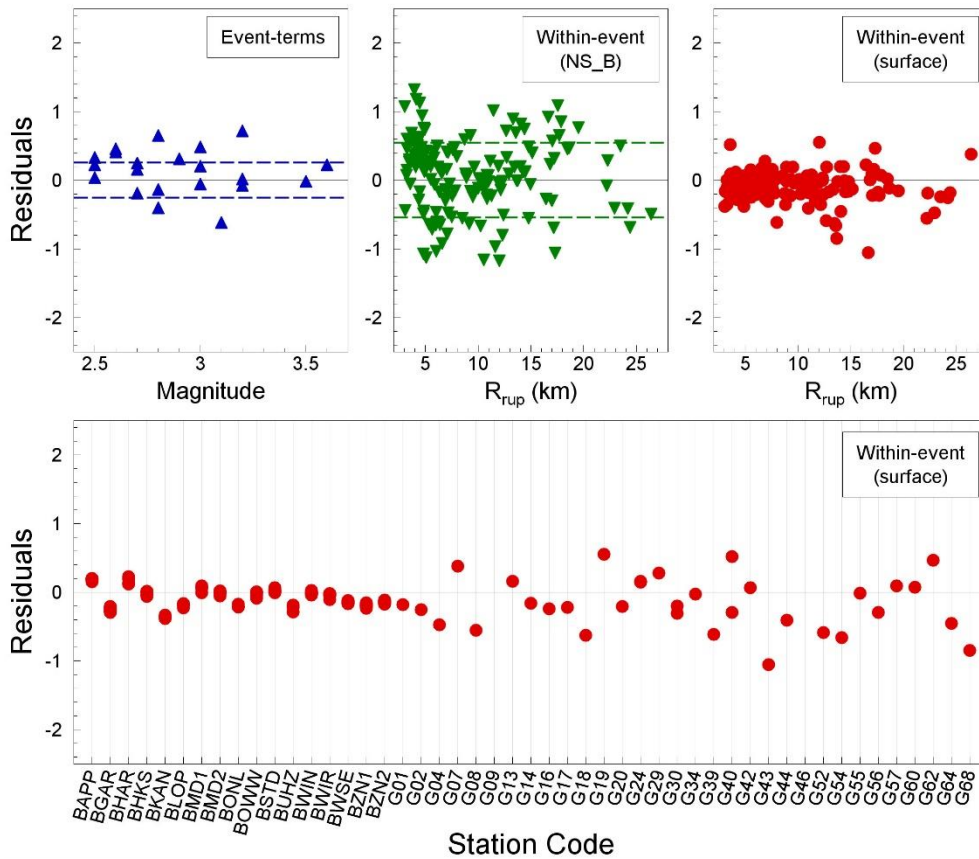


Figure 11.63. De-composed 'residuals' of $Sa(1.0s)$ at the surface (*upper*) and site response 'residuals' against recording station ID code (*lower*)

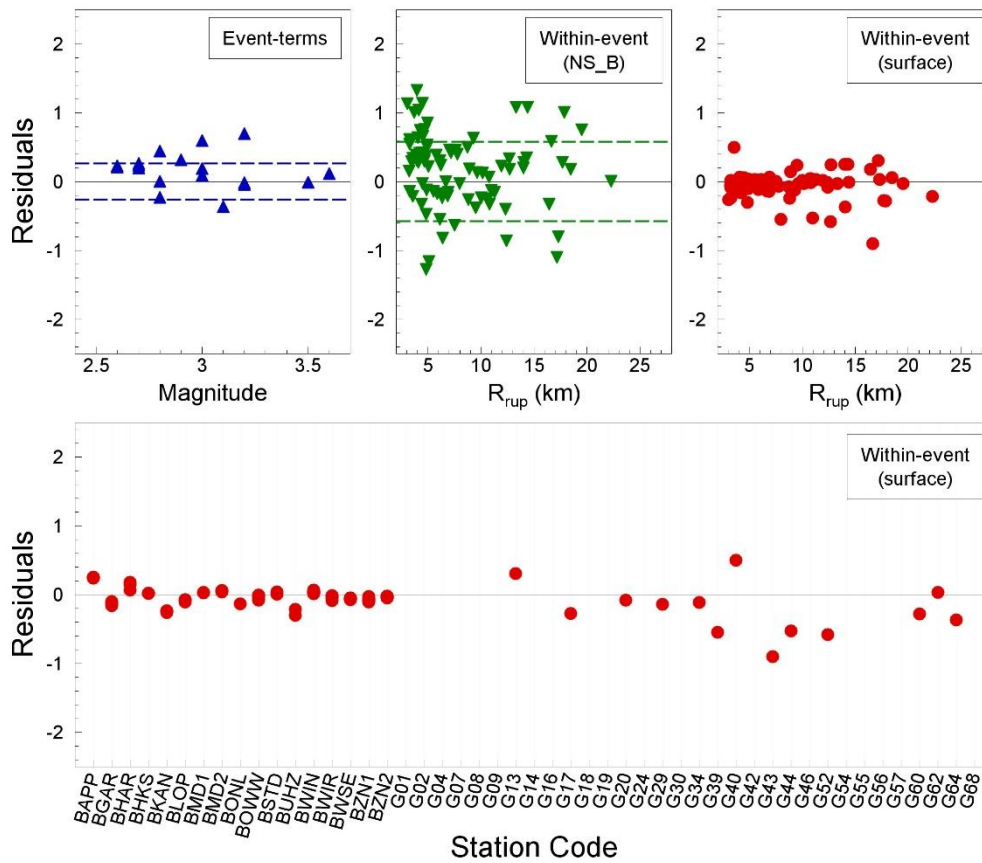


Figure 11.64. De-composed 'residuals' of $S_a(1.5s)$ at the surface (*upper*) and site response 'residuals' against recording station ID code (*lower*)

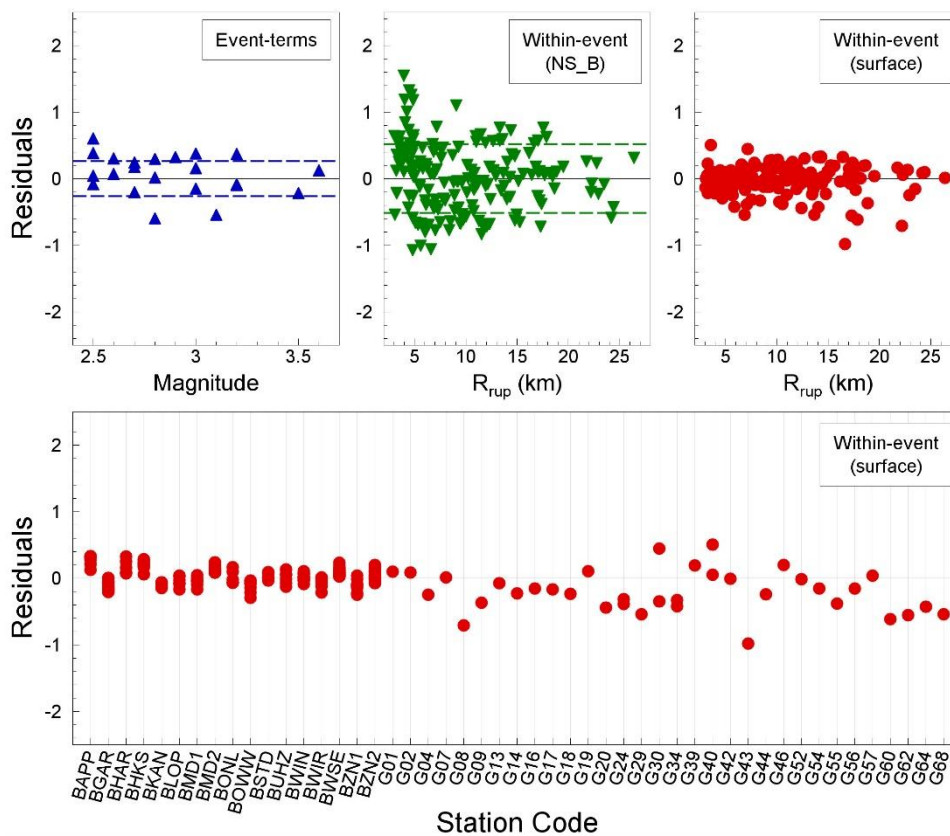


Figure 11.65. De-composed 'residuals' of PGV at the surface (*upper*) and site response 'residuals' against recording station ID code (*lower*)

The patterns that emerge from these figures are very clear and they show that in general the model matches the data very well. The exception is in the period range from 0.01 to 0.2 second, where the site response residuals indicate consistent over-estimation (Figure 11.66). In some cases there is distance dependence of this over-estimation, as can be seen, for example, in Figure 11.50 for $S_a(0.075s)$, which is where the over-estimation is greatest. At longer periods, the model provides a reasonably good fit to the data without any appreciable bias, which is a remarkable result in view of the fact that station-specific profiles were used to deconvolve the recordings to the NS_B horizon and the forward modelling to the surface makes use of representative AFs for large zones. The G-stations exhibit more scatter than the B-stations; the possible reasons for this pattern are being explored as part of the ongoing refinement of the V4 model.

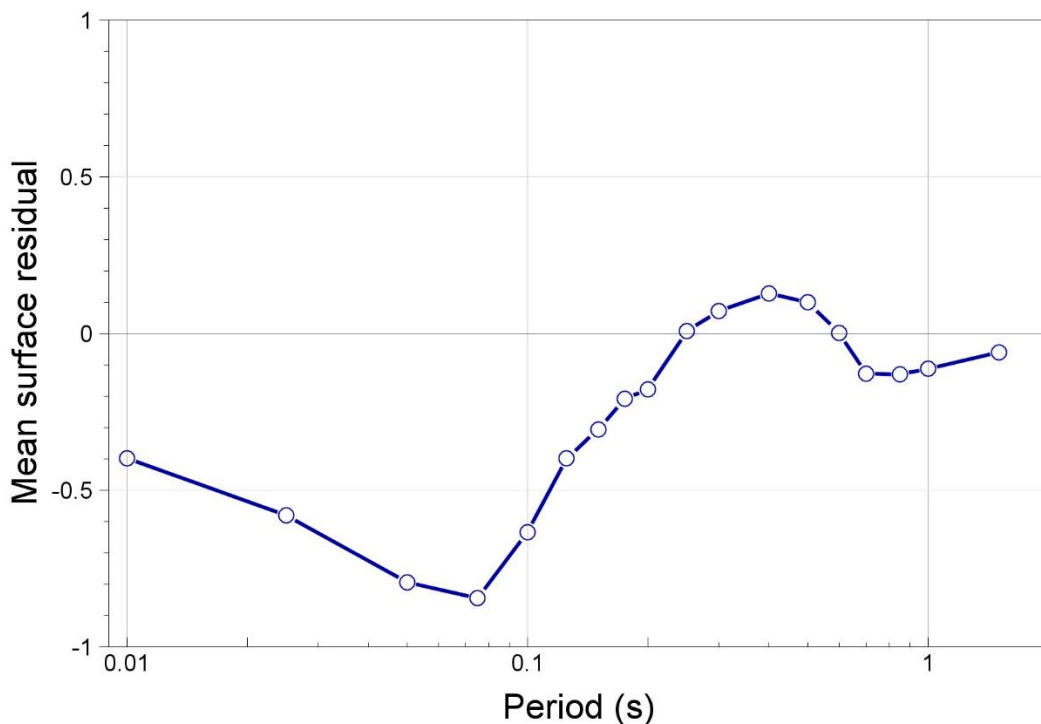


Figure 11.66. Average bias of the central model with respect to the surface data

Returning to the issue of the over-estimation of surface motions at short response periods, the culprit is clearly identified as being the difference between the station-specific amplification functions used to deconvolve the records to NS_B (Section 4.3) and the linear part of the zone-specific amplification factors used in the forward modelling. The latter are consistently larger than the former at short periods across all the recording stations. This issue has been discussed in detail in Section 9.4, where it was also shown that there is a marked magnitude-dependence to this trend as well as some dependence on distance as well. The point can also be illustrated here using examples from a specific station (GARTS/BGAR): Figure 11.67 shows three plots, each displaying the linear AFs for the station and for the host zone (1001), each specific to the magnitude-distance combination of the particular record. All three records are obtained at comparable distances (4.9-5.6 km) but come from earthquakes of different magnitudes.

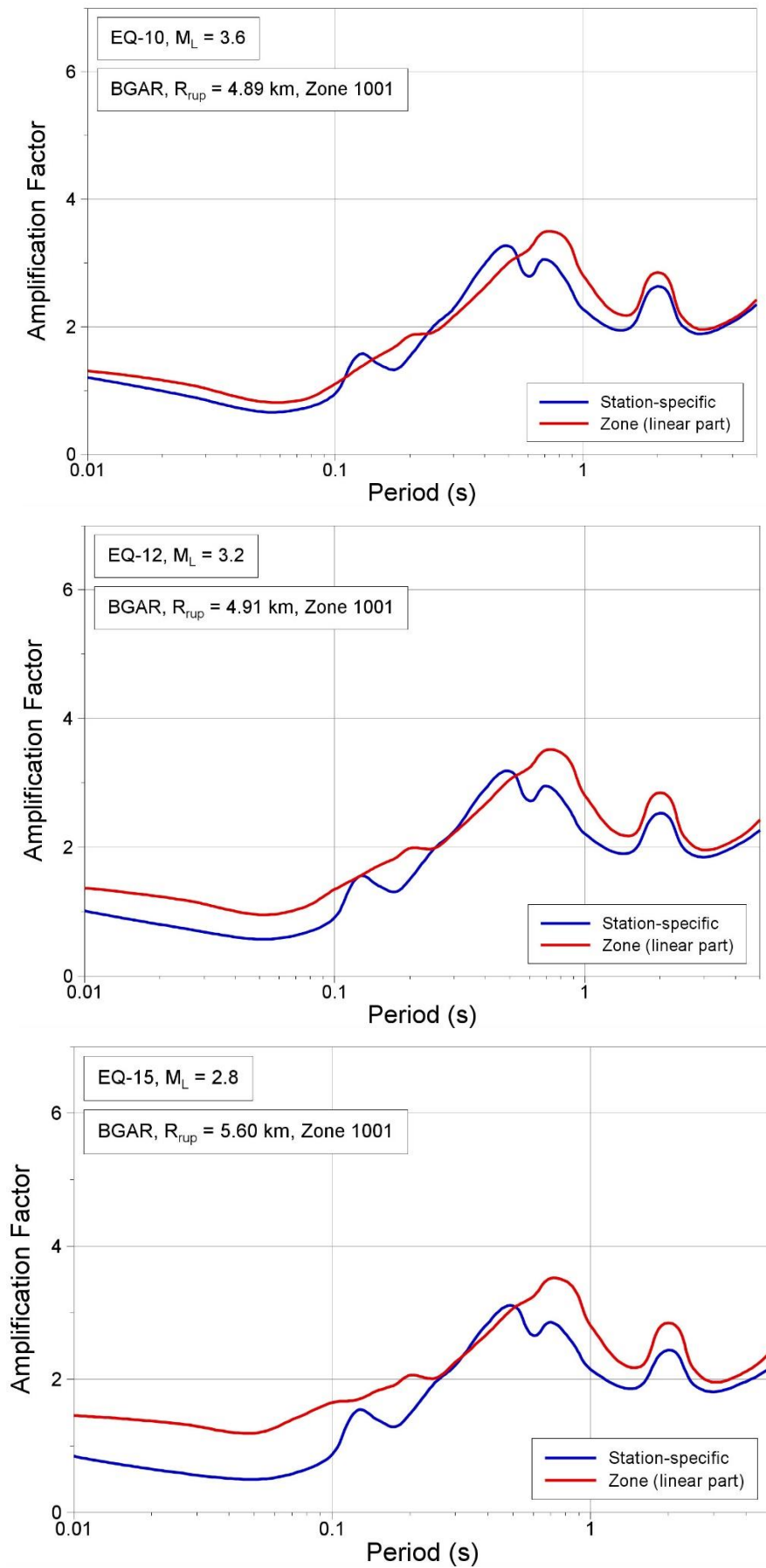


Figure 11.67. Station-specific and zone-specific linear AFs at the GARST/BGAR station, for three records from different magnitude earthquakes.

For the largest event, which is the 2012 Huizinge earthquake of M_L 3.6, the two amplification factors are close, with the zone-specific AF being only very slightly greater. For the earthquake of M_L 3.2, the zone-specific AF is clearly larger than the station-specific value at short periods, and the difference becomes even more pronounced for the smallest event of M_L 2.8. As discussed in Section 9.4, the issue is suspected to have arisen because of the lack of resolution in the magnitude- and distance-dependence of the zone-specific AFs, a consequence simply of not covering the smaller magnitudes in generating the inputs used to perform the field-wide site response analyses on which the zone AFs are based (Section 8.2). The issue is being investigated through some exploratory analyses and it is believed that the over-estimation will be removed in the next version of the GMM (see discussion in Chapter 13). In the meantime, the fact that the model is over- rather than under-estimating the observed ground-motion amplitudes reduces concern over this specific issue since the expectation is that future hazard estimates will be lower in the short-period range. This is consistent with the objective that has guided the GMM development throughout the evolution from V0 to V4, namely that is preferable to err on the side of conservative estimates until there is a secure basis for providing lower estimates as a result of more refined models or reduced uncertainties. Another point worthy of note in this regard is that a large proportion of the exposed building stock is outside the period range affected by this bias (Section 1.3). Moreover, the risk calculations are much more sensitive to the performance of the model in the range of magnitudes above M_L 4, which cannot be tested with the existing data from the field.

11.4. Period-to-period correlations

As explained in Section 1.3, for the risk calculations, spectral ordinates at different response periods often need to be estimated at a single location in the Monte Carlo simulations. This requirement arises because there are building typologies with different characteristic vibration periods and some for which the buildings have different periods of vibration in the two orthogonal directions. Since the risk is being calculated for all buildings simultaneously, the spectral accelerations at each of the target response periods need to be estimated taking account of the correlation of the residuals at different periods. If the accelerations are calculated sampling the variability at each response period with the same epsilon values (*i.e.*, the same number of standard deviations above or below the median predictions for the earthquake scenario in terms of magnitude and distance), this effectively treats the variability at all periods as being perfectly correlated. Various studies have shown that this is not the case and to avoid this unintended conservatism it has been proposed to generate response spectra taking account of the decreasing correlation with increasing separation of the periods (Baker & Cornell, 2006b). For this purpose, a model for the period-to-period correlation of residuals with respect to predicted median spectral accelerations is needed.

For the V2 model, we selected the model of Akkar *et al.* (2014b) derived from accelerograms of tectonic earthquakes in Europe and the Middle East and consistent with the GMPEs of Akkar *et al.* (2014a). The maximum response period for which this model provides coefficients is 4 seconds; for the additional target period considered in the V2 risk model of 5 seconds, the simple assumption was made that the values for 4 seconds can be maintained

constant at longer periods, however this later needed to be modified using extrapolation of the trends in the matrix since the implementation does not work with the same value at two adjacent periods (the identical eigen-values can create difficulties in the matrix inversion).

For the V3 update of the ground-motion model, the response spectral accelerations transformed to the NS_B horizon were used to calculate the period-to-period correlations of the Groningen data, using the total residuals. These are compared in Figure 11.68 with those from the Akkar *et al.* (2014b) model and the models of Baker & Cornell (2006b), Jayaram & Baker (2008) and Abrahamson *et al.* (2014). The main observation is that the four models yield very similar values and the Groningen data generally follow the same trends but do not agree with any of the models perfectly. As has been noted previously in this report, results from the Groningen data at periods beyond 1 second should be treated with caution because of the small number of useable records. In view of these results, we chose to follow the previous practice of adopting another model for application in Groningen. Since the models are rather similar, the choice is not critical but Baker & Jayaram (2008) has the distinct advantage of being a continuous function hence not requiring any interpolation for the correlation coefficients at any of the 23 response periods included in the V3 and V4 models. The corresponding values have been duly generated using the formulation in the paper of Baker & Jayaram (2008) and these are provided in an Excel file as a supplement to this report (see Executive Summary). The size of the correlation matrix precludes presentation of the table in the report without using an almost illegibly small font.

Future refinements of this element of the model may be explored but this is unlikely be to given high priority, not least since the use of the Baker & Jayaram (2008) model is a perfectly reasonable and defensible choice.

11.5. Vertical-to-horizontal ratios

The fragility functions for the Groningen building stock are defined only in terms of horizontal ground motions but for the masonry and pre-cast concrete structures, it is thought that vertical motion may have a significant influence on the response. Therefore, three-dimensional dynamic input to the analyses of the structures will ultimately be required and to this end estimates are required of the vertical motions expected in the Groningen field. In order to ensure that the vertical components are appropriately selected and scaled, V/H (vertical-to-horizontal) response spectral ratios consistent with the seismicity and ground conditions need to be defined. Past practice has often defined the vertical spectrum as simply a scalar product—the factor usually being of the order of $\frac{2}{3}$ —of the horizontal spectrum, but it is now recognised that the V/H ratio varies with response period and that the vertical spectrum has a distinct shape. Moreover, it is recognised that the V/H ratio varies with magnitude, style-of-faulting, distance and site classification. Several of the ground-motion recordings from the Groningen field show high ratios of the vertical to horizontal (geometric mean) components of motion (Figure 11.69). If this pattern persists at large magnitudes, appreciable levels of vertical loading may be expected, for which reason a model for the vertical accelerations is important.

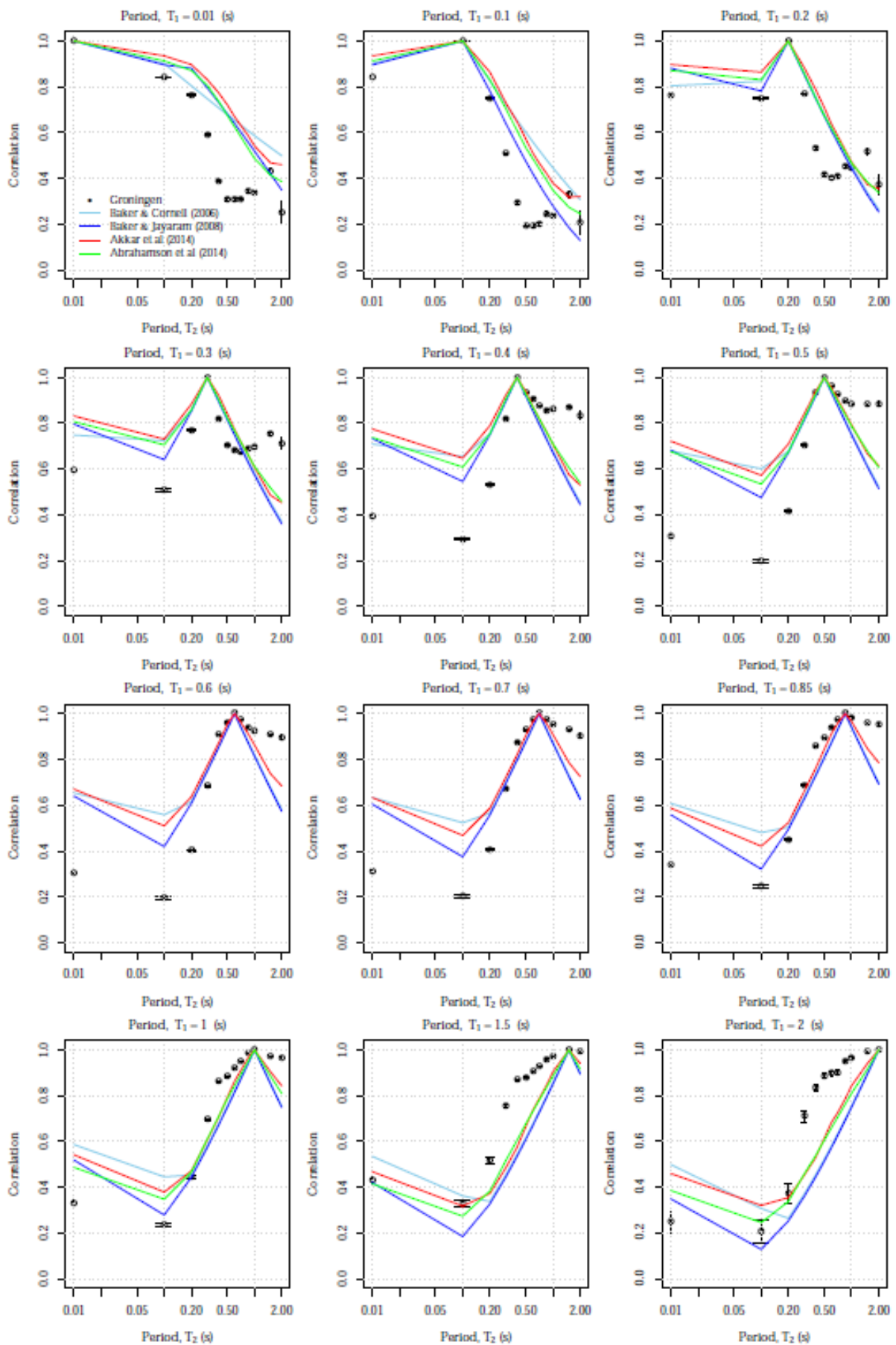


Figure 11.68. Comparison of period-to-period correlations for residuals of response spectral ordinates calculated from the Groningen data (at the NS_B horizon) with four published models

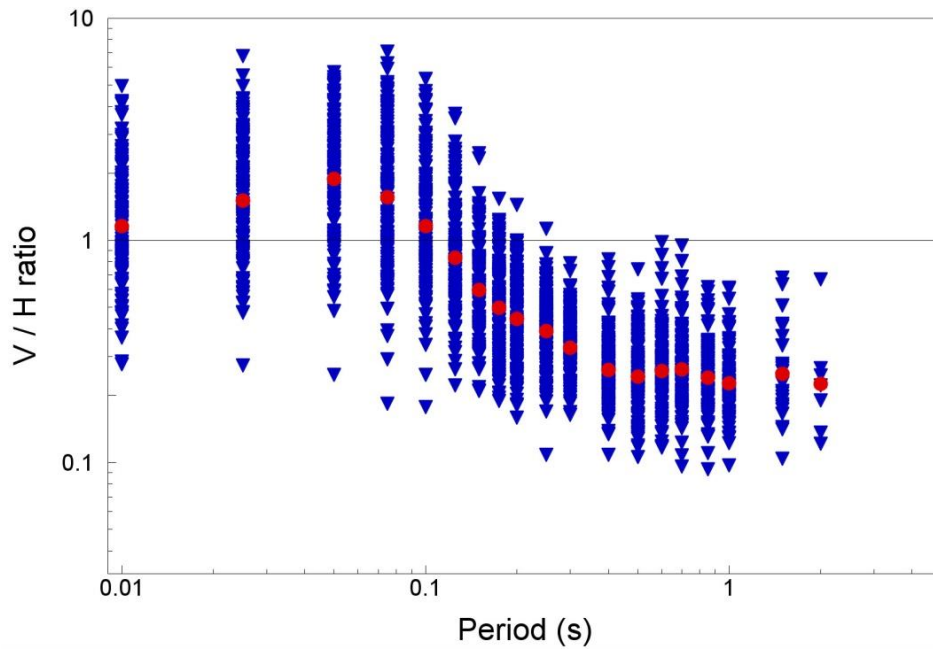


Figure 11.69. Vertical-to-horizontal component ratios against period.

The V/H ratios at a few selected periods are plotted as a function of magnitude and distance in Figures 11.70 and 11.71, from which no clear trend with magnitude can be discerned, although this is not unexpected given the very limited magnitude range covered by the recordings. There are also at best only weak trends with distance: at very short periods, there is a perceptible drop in the largest ratios with increasing distance but this may be partly a result of the limited number of records available at epicentral distances beyond about 20 km.

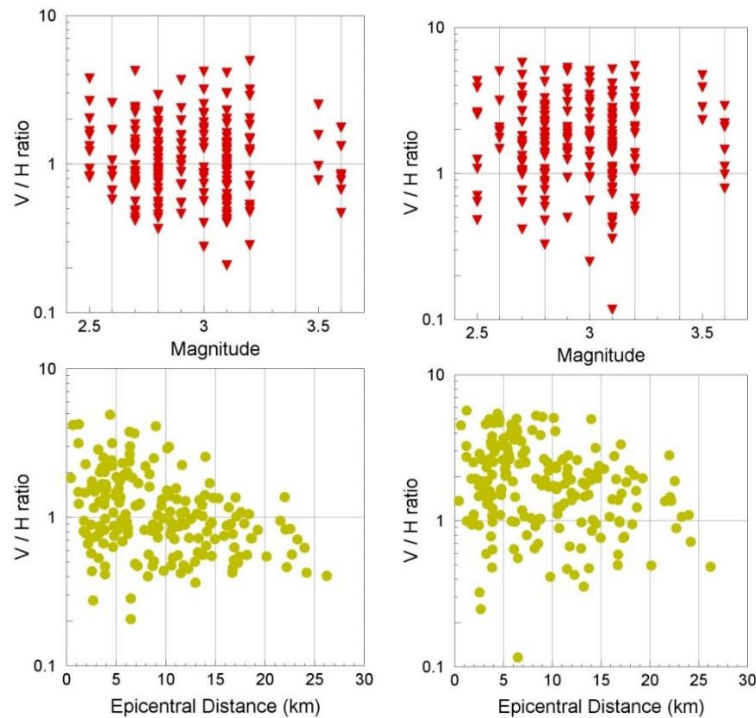


Figure 11.70. Vertical-to-horizontal component ratios against magnitude and distance at $T = 0.01s$ (left) and $T = 0.05s$ (right).

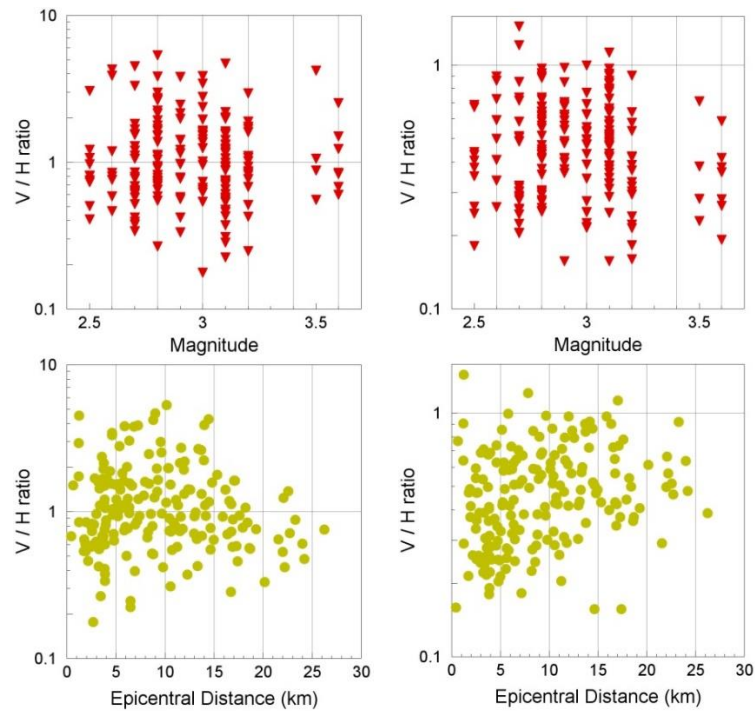


Figure 11.71. Vertical-to-horizontal component ratios against magnitude and distance at $T = 0.1s$ (left) and $T = 0.2s$ (right).

One option for estimating vertical accelerations is to develop GMPEs for the vertical component (e.g., Campbell & Bozorgnia, 2003; Bozorgnia & Campbell, 2016a; Stewart *et al.*, 2015) but conducting PSHA separately for the horizontal and vertical components of motion can lead to different dominant scenarios contributing to the hazard estimates in the two directions (e.g., Bommer *et al.*, 2011). Our preferred approach for generating vertical response spectra is to apply V/H ratios to the horizontal response spectra defined at the ground surface. Given the very limited magnitude range covered by the Groningen recordings, it is unlikely that a usable V/H prediction model could be derived directly from the local data. Therefore, the approach adopted has been to explore the fit of existing models for the prediction of V/H ratios to the Groningen data, and if no model is found to be adequate in its original state, then the possibility of using the local recordings to adjust the equations has been explored. For the V2 model, the final selection was a modified version of the Akkar *et al.* (2014b) equations for predicting V/H ratios, which were modified at period below 0.2 seconds to approximately match the very high ratios observed in the Groningen recordings (Figure 11.72). Since the Akkar *et al.* (2014b) model only extended to 4 seconds, it was decided to maintain the values at this period constant up to 5 seconds, which is the current upper limit of the Groningen GMM.

Since the V2 model was issued, a new model for the prediction of V/H response spectral ratios has been presented by Bozorgnia & Campbell (2016b), using the NGA-West2 database and with the distinct advantage of being valid from a minimum magnitude of M 3.3 (equivalent to M_L 3.5 in the Groningen field). As can be appreciated from Figure 11.73, it provides a better fit to the Groningen data than either of the models previously considered, even though it still underestimates the V/H ratios at short periods by a factor of two on average.

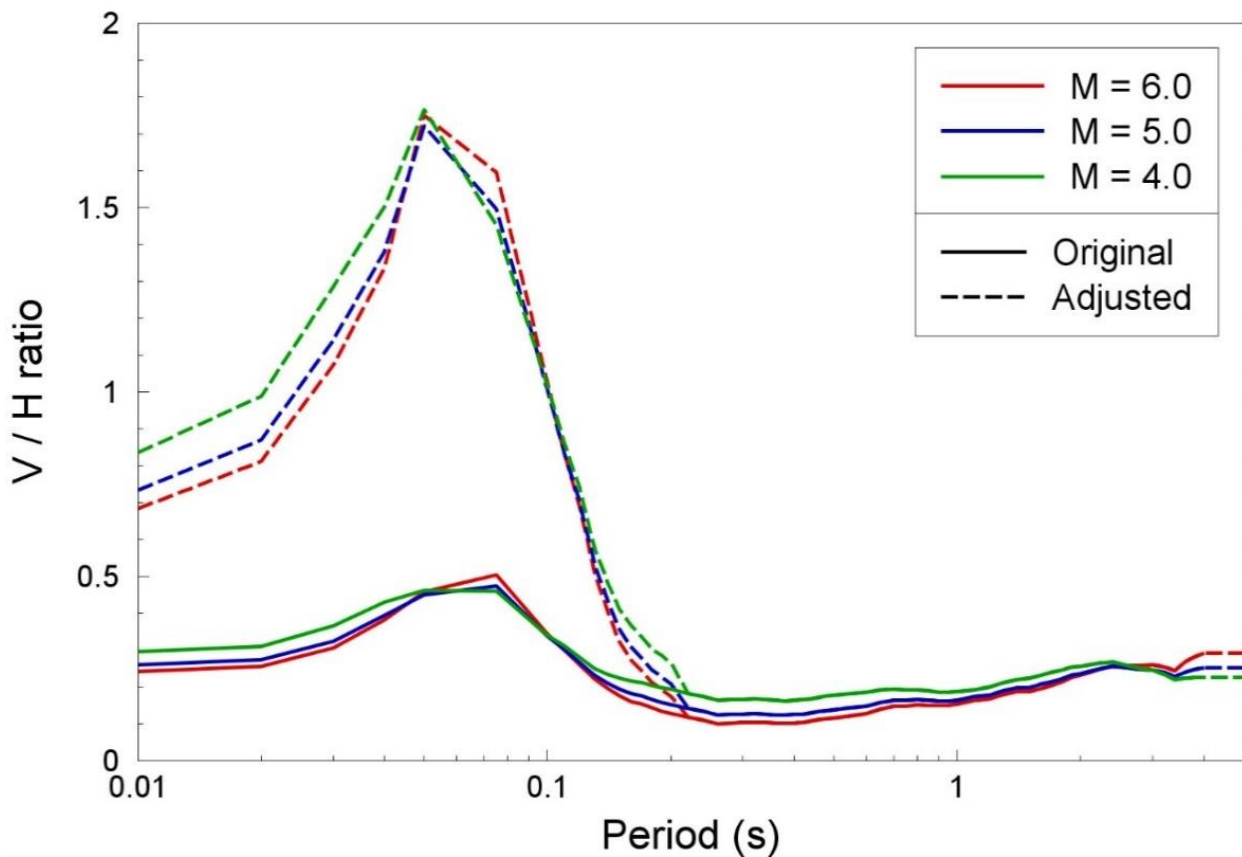


Figure 11.72. Predicted median V/H ratios from the original (*solid*) and Groningen-adjusted (*dashed*) equations of Akkar *et al.* (2014b) for $R_{\text{epi}} = 0$ km; the adjusted model was proposed in V2

At this stage, given that there is not an urgent need to provide a model for the vertical-to-horizontal spectral ratios for Groningen, we refrain from proposing a solution. If a model is to be used as published, then we can clearly recommend the new study by Bozorgnia & Campbell (2016b) but note that it may underestimate the maximum vertical accelerations at short periods. If this is a concern, a simply adjustment of a factor of about 2 could be made to the predictions from this model at short periods. At the same time, it is possible the extremely high vertical-to-horizontal ratios observed in the current Groningen database would not persist at greater magnitudes. Ideas regarding potential further work to derive a more robust model for V/H response spectral ratios are discussed in Chapter 13.

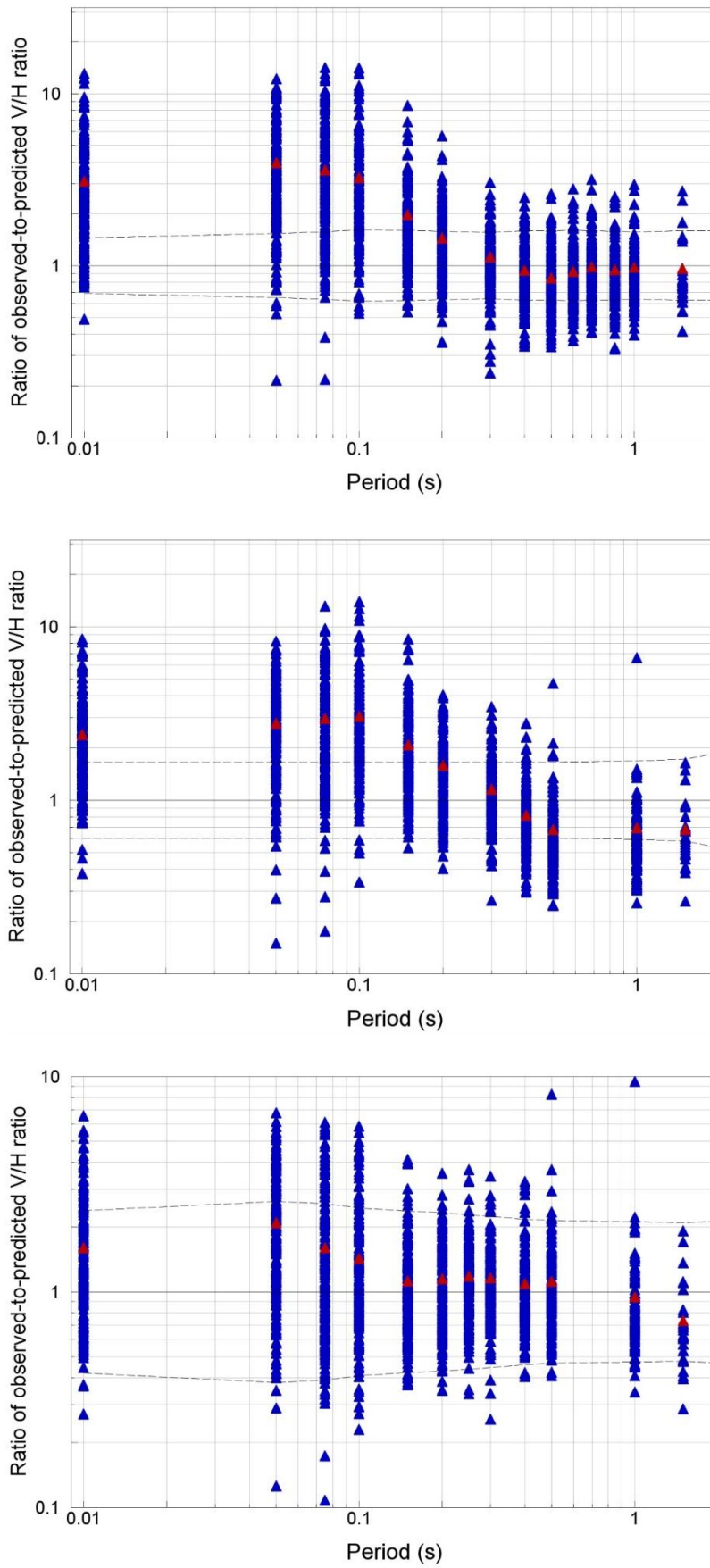


Figure 11.73. Ratios of observed to predicted V/H response spectra ratios for the Groningen data using the models of Akkar *et al.* (2014b) (*top*), Gülerce & Abrahamson (2011) (*middle*) and Bozorgnia & Campbell (2016b) (*bottom*). In each case, the red triangle is the median value and the dashed lines one standard deviation of the GMPE.

12. GMPE for DURATION

The effect of the duration of ground shaking is generally not considered in structural design, other than with regard to its influence on scaling factors to adjust response spectral ordinates to alternative damping ratios (e.g., Stafford *et al.*, 2008). However, the influence of duration has been recognised as being important in the seismic assessment of buildings (e.g., Iervolino *et al.*, 2006; Chandramohan *et al.*, 2016), particularly those constructed from materials such as masonry that is prone to experience degradation of both strength and stiffness under dynamic loading (e.g., Bommer *et al.*, 2004). For this reason, the development of the fragility functions for the buildings in the Groningen field aims to take account of the ground-motion duration, for which reason a predictive equation is required for the chosen definition of the ground-motion duration.

12.1 Durations of Groningen motions

A large number of definitions for the duration of earthquake-induced ground-shaking have been put forward in the technical literature, and application of these definitions to a given accelerogram can produce very different estimates of the duration of strong motion. Bommer & Martínez-Pereira (1999) classified all of the published definitions into three categories:

- Bracketed duration, D_B : defined as the interval between the first and last excursions of a specified threshold of acceleration.
- Uniform duration, D_U : defined as the sum of the intervals during which the acceleration is above a specified threshold.
- Significant duration, D_S : the interval over which some specified portion of the total energy in the record (usually calculated as the integral of the squared acceleration over time) is accumulated.

Each of the definitions can be applied to the actual ground motion or to the response history of an oscillator, or other structure, to that motion. The definitions can also be applied with absolute or relative thresholds: for example, the bracketed duration can be defined by excursions of an absolute acceleration level in excess of, say, $0.1g$, or of a fraction of PGA.

Since duration as a scalar intensity measure has little power when used to predict structural performance, it is usually coupled with a measure of the amplitude of the motion, such as response spectral acceleration. This being the case, it then makes sense to use definitions defined using relative measures (that are independent of the ground-motion amplitude), which will generally result in durations that increase with distance as well as with magnitude. The significant duration is the most widely-used definition, the original interval being that related to the accumulation from 5% to 95% of the total Arias intensity of the record (Trifunac & Brady, 1975). In more recent years, there has been a tendency to move towards using the interval from 5% to 75% of the total energy in the record, which is more likely to isolate the strongest portion of the record that generally corresponds to the arrival of shear waves. However, other variations have been proposed, such as the proposal by Boore & Thompson

(2014) to use a duration that is equal to twice the interval between 20% and 80% of the total energy being accumulated as a surrogate for the 5-95% definition. The motivation for this proposal was an apparently improved ability to identify the window associated with 'strong shaking' when used with smaller earthquakes. Figures 12.1-12.3 show correlations of different duration definitions computed for the entire V4 Groningen database.

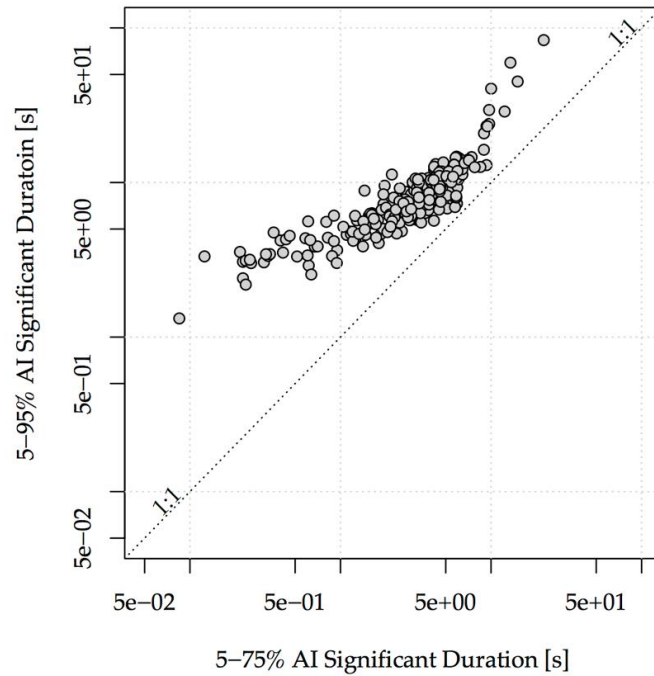


Figure 12.1. Correlation between D_{S5-75} and D_{S5-95} .

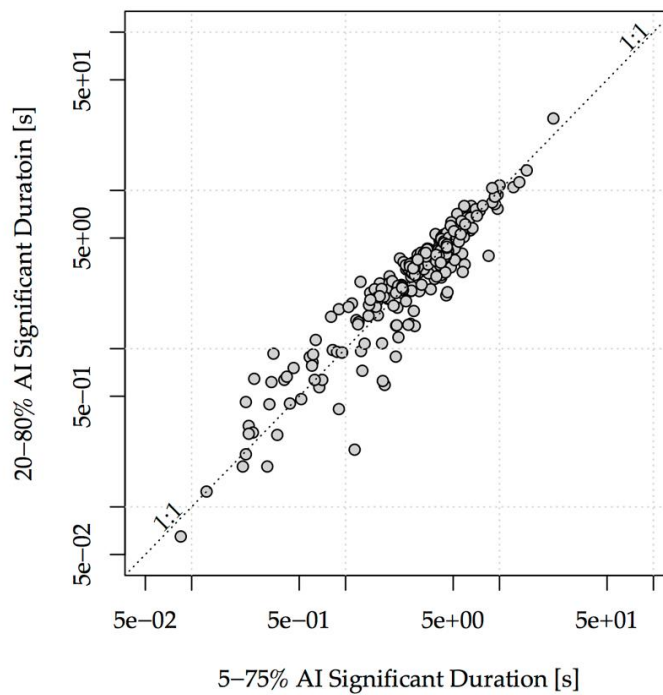


Figure 12.2. Correlation between D_{S5-75} and D_{S20-80} .

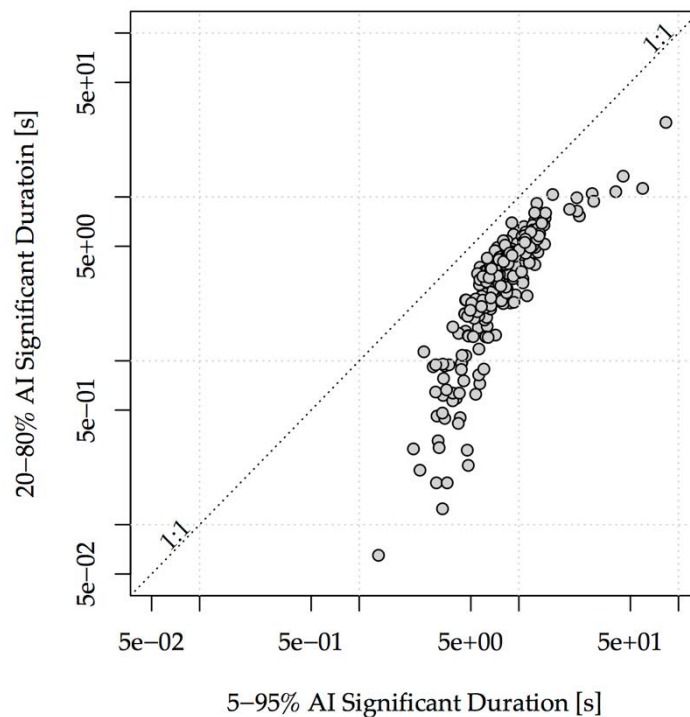


Figure 12.3. Correlation between D_{S5-95} and D_{S20-80} .

As D_{S5-75} is more likely than other metrics to isolate the strongest part of the motion and more prediction equations have been developed for this measure than any other, it has again been selected as the duration measure for which GMPEs have been developed for the Groningen field - consistent with the V1, V2 and V3 GMPEs also. Figure 12.2 indicated that the 20-80% significant duration metric provides durations that are in broad agreement with the 5-75% measure, and Boore & Thompson (2014) suggest that this metric performs well for small magnitude events. However, we ultimately need a prediction equation that will be applied over a broad range of magnitude and distance combinations. Opting for the more common 5-75% measure allows us to gain insight from existing models for the prediction of this measure that would not be possible in the case we selected the 20-80% duration metric.

Figures 12.4 and 12.5 show two cases where D_{S5-75} performs well in terms of its ability to identify the strong portion of the accelerogram where the energy input rate is roughly constant (the steep portions of the Husid plots shown in these figures). The records shown in Figures 12.6-12.9 provide examples of cases where the 5-75% measure is not able to capture this period of 'strong shaking'. The purpose here is to highlight the fact that these duration measures will not always perform well when applied to individual records, even if their performance is reasonably good on average.

For these reasons, work is ongoing to explore which duration definition will work best for the Groningen field. This exploration cannot solely be limited to looking at figures such as those shown in Figures 12.4-12.9, but must also take into consideration how effective these duration measures are when used within the fragility component of the overall risk model. Table 12.1 lists the characteristics of recordings shown in Figures 12.4-12.9.

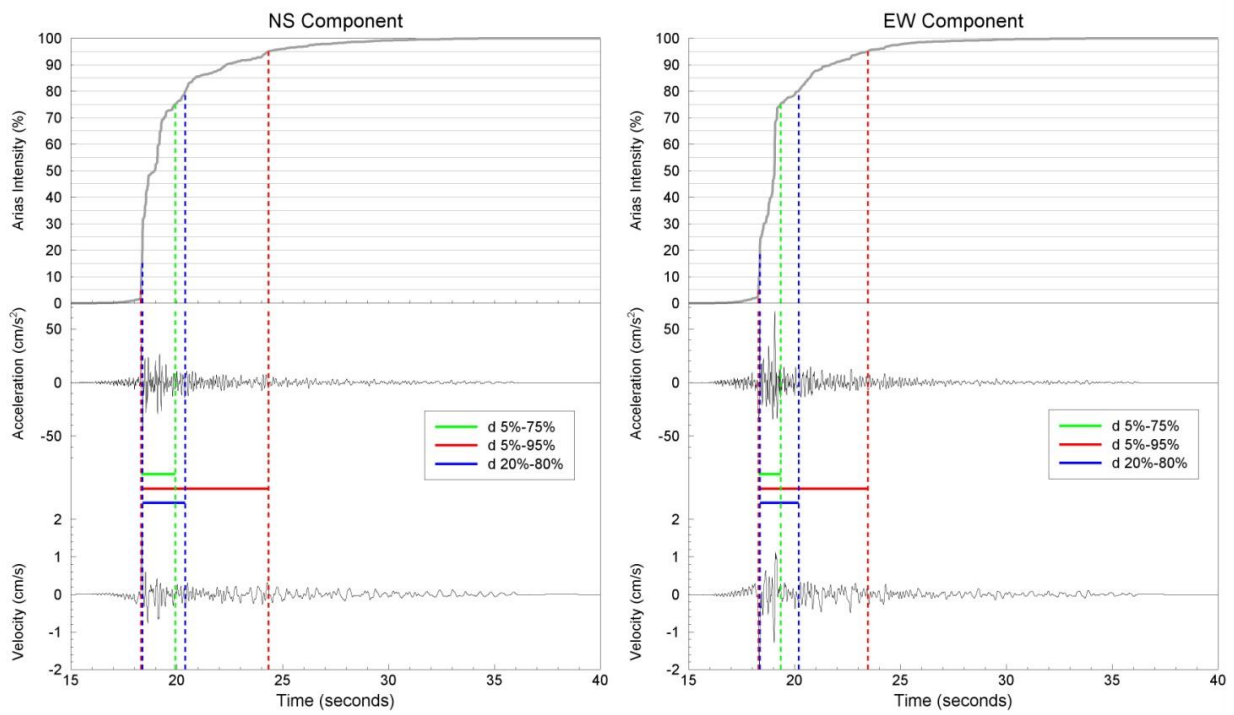


Figure 12.4. Normalised Husid plot, time-series and durations from the GART recording of event ID 10 showing the duration intervals defined by D_S with different starting and finishing percentages of the total Arias intensity.

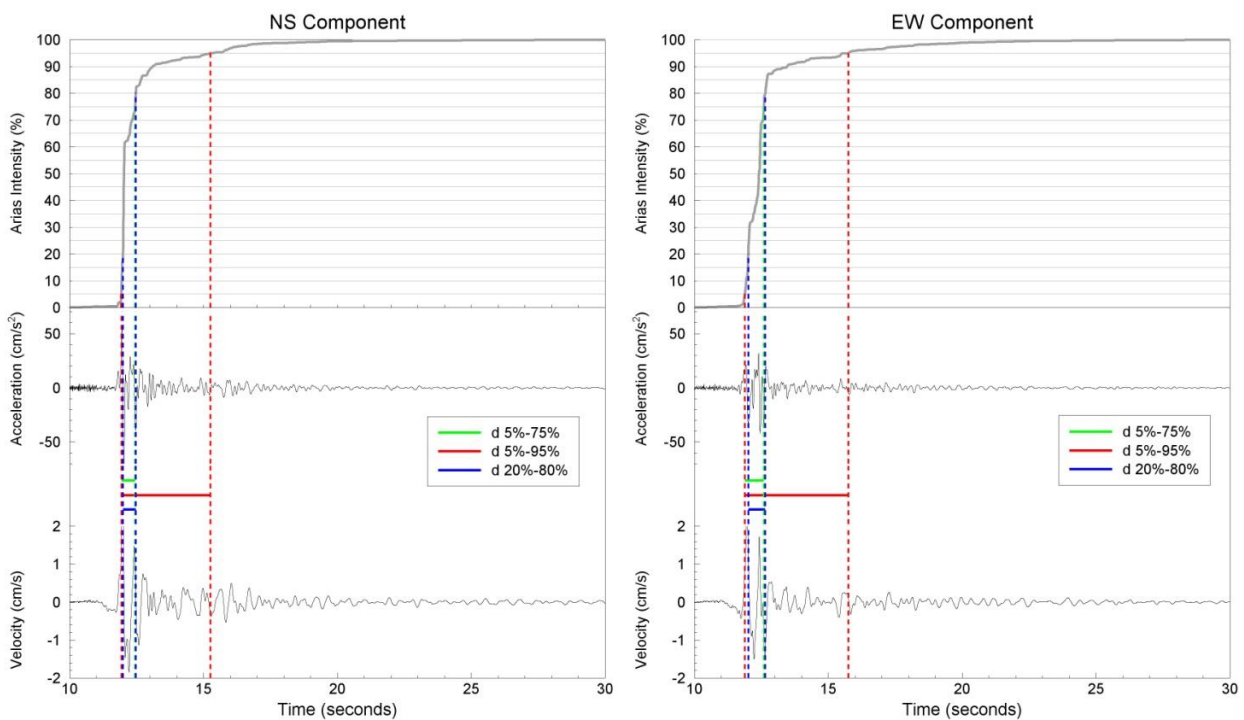


Figure 12.5. Normalised Husid plot, time-series and durations from the MID1 recording of event ID 10 showing the duration intervals defined by D_S with different starting and finishing percentages of the total Arias intensity.

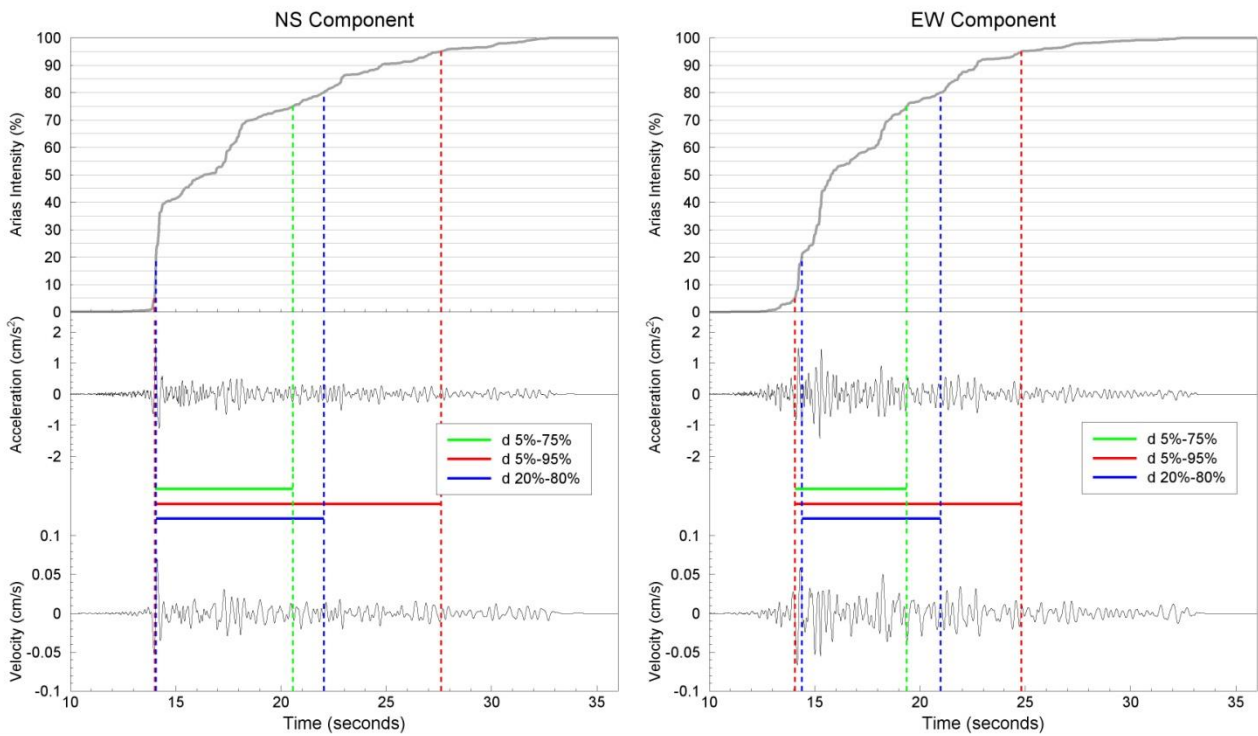


Figure 12.6. Normalised Husid plot, time-series and durations from the MND1 recording of event ID 16 showing the duration intervals defined by D_s with different starting and finishing percentages of the total Arias intensity.

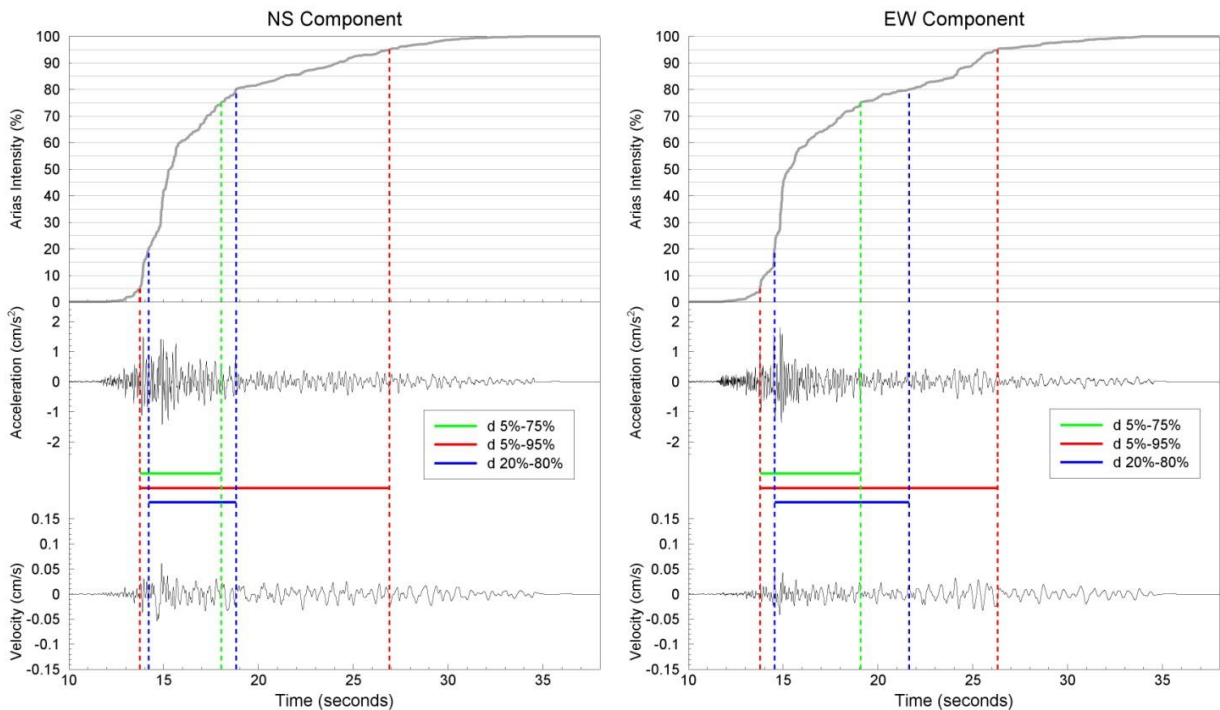


Figure 12.7. Normalised Husid plot, time-series and durations from the BSTD recording of event ID 18 showing the duration intervals defined by D_s with different starting and finishing percentages of the total Arias intensity.

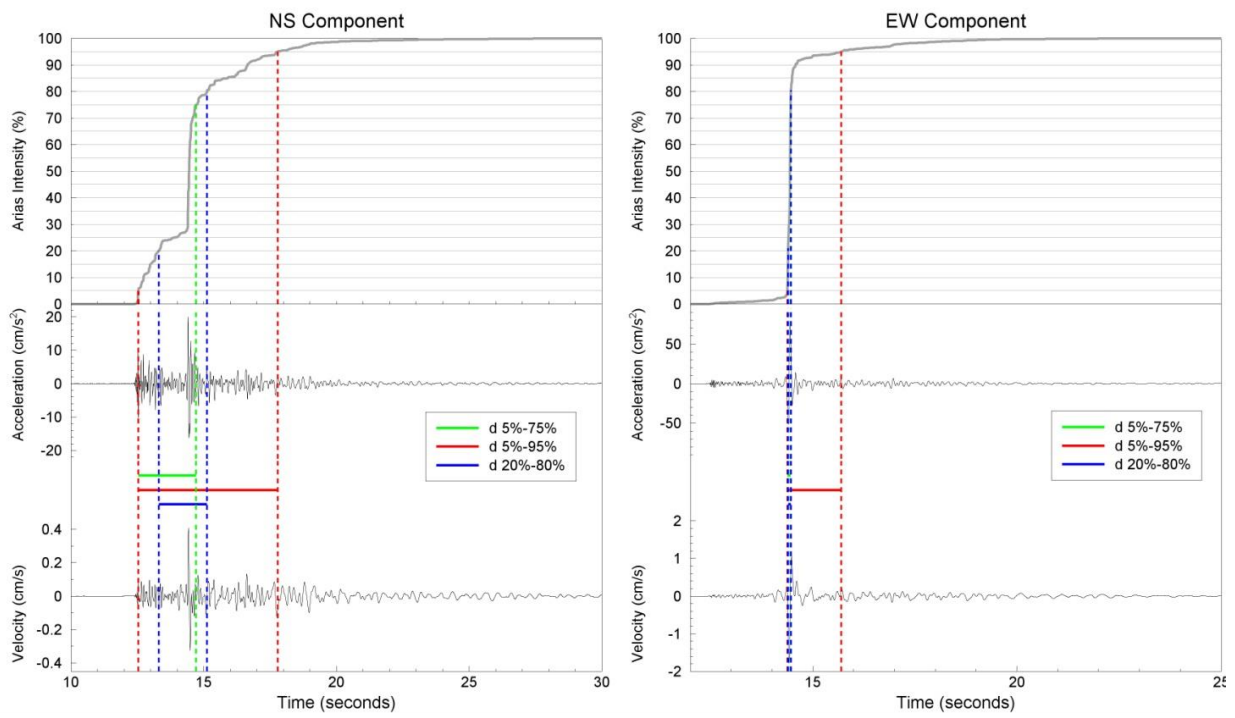


Figure 12.8. Normalised Husid plot, time-series and durations from the BMD2 recording of event ID 19 showing the duration intervals defined by D_S with different starting and finishing percentages of the total Arias intensity.

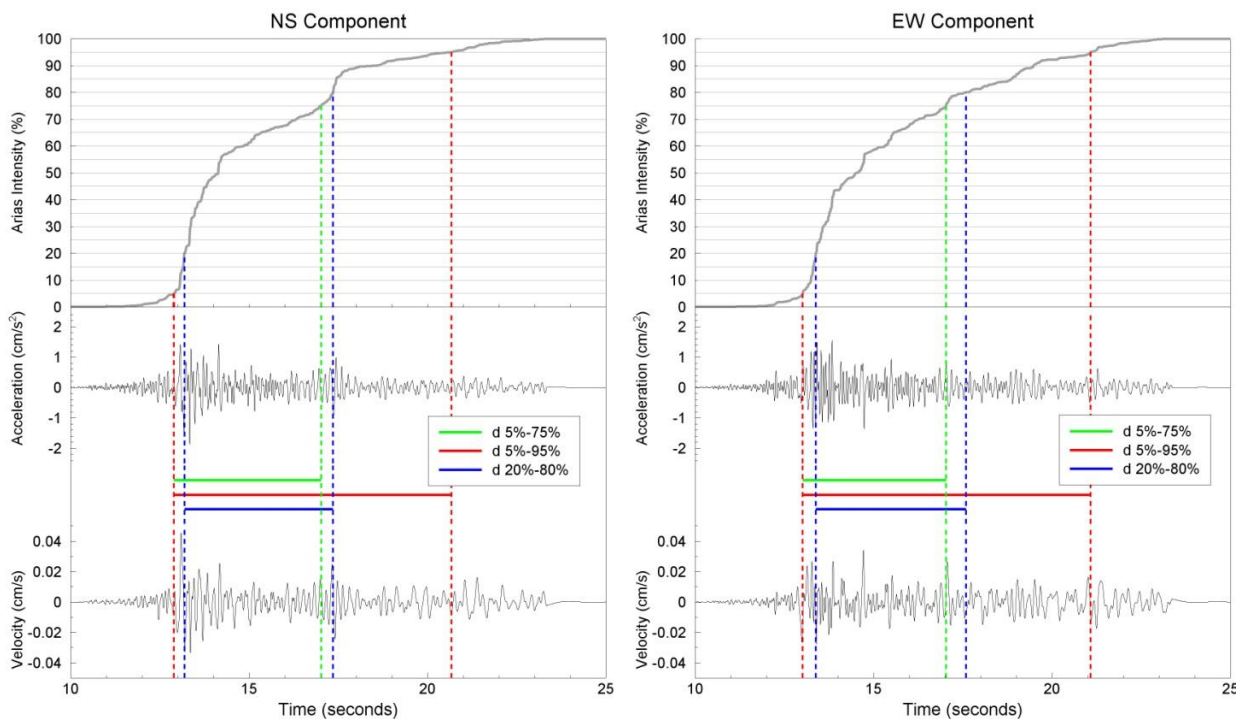


Figure 12.9. Normalised Husid plot, time-series and durations from the BGAR recording of event ID 21 showing the duration intervals defined by D_S with different starting and finishing percentages of the total Arias intensity.

Table 12.1. Characteristics of Groningen recordings shown in Figures 12.4-12.9.

EQ ID	Date	M _L	STAT	R _{epi} (km)	Comp	D _{S5-75} (s)	D _{S5-95} (s)	D _{S20-80} (s)
10	16-VIII-2012	3.6	GARST	3.9	NS	1.615	6.020	2.015
10	16-VIII-2012	3.6	GARST	3.9	EW	1.045	5.170	1.835
10	16-VIII-2012	3.6	MID1	2.0	NS	0.515	3.320	0.480
10	16-VIII-2012	3.6	MID1	2.0	EW	0.705	3.860	0.635
16	13-II-2014	3.0	BMD1	9.3	NS	6.555	13.600	7.975
16	13-II-2014	3.0	BMD1	9.3	EW	5.305	10.760	6.595
18	30-IX-2014	2.8	BSTD	6.7	NS	4.290	13.155	4.600
18	30-IX-2014	2.8	BSTD	6.7	EW	5.310	12.530	7.100
19	05-XI-2014	2.9	BMD2	3.0	NS	2.170	5.250	1.815
19	05-XI-2014	2.9	BMD2	3.0	EW	0.085	1.320	0.065
21	06-I-2015	2.7	BGAR	6.2	NS	4.125	7.780	4.165
21	06-I-2015	2.7	BGAR	6.2	EW	4.015	8.065	4.210

An important issue when including the effects of duration in the risk assessment is to account for the inverse relationship between the duration of the shaking and the amplitude of the acceleration. As shown in Figure 12.10, for the 284 horizontal components in the current Groningen database used for the development of the V4 duration model, there is a clear pattern: components associated with higher levels of acceleration ($> 50 \text{ cm/s}^2$) are associated with durations of 1 second or shorter, whereas all the records with longer durations (longer than, say, 6 seconds) are associated with extremely low amplitudes ($< 5 \text{ cm/s}^2$).

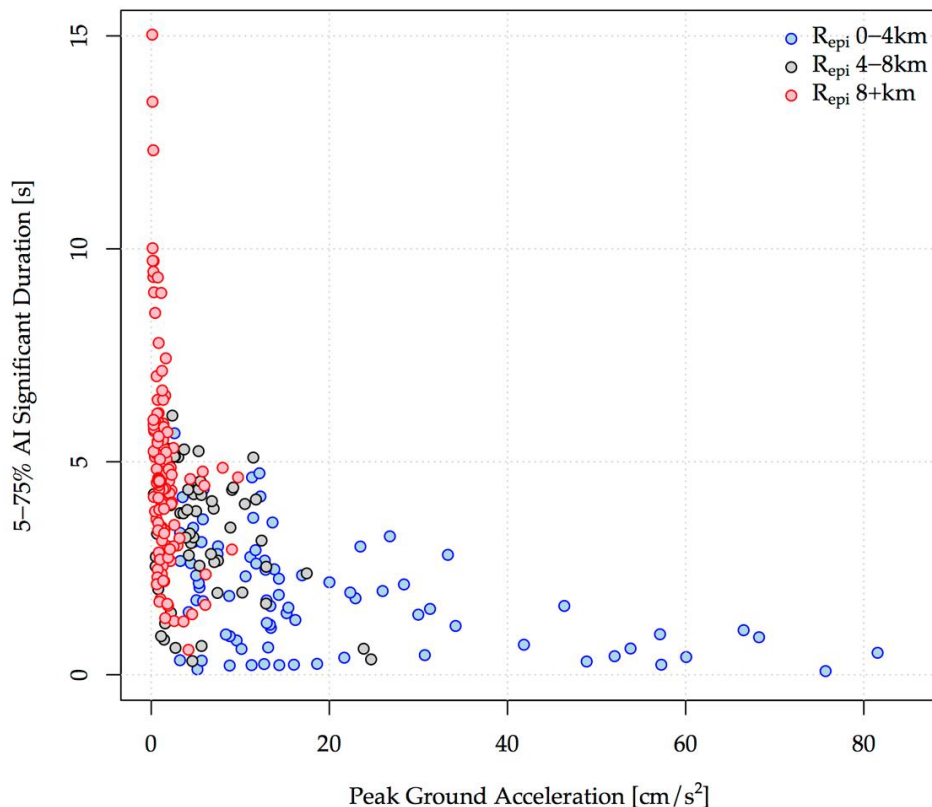


Figure 12.10. Relationship between D_{S5-75} and PGA values in the V3 Groningen database for different distance intervals

The plot also shows that the former type of records (high PGA, short duration) are typically obtained at epicentral distances of less than 4 km, whereas the long-duration, low-amplitude records are generally from recording stations at epicentral distances of at least 8 km. These observations are consistent with the current hypothesis that waves leaving the reservoir at take-off angles that are not nearly vertical are subjected to multiple refractions and reflections by the high-velocity Zechstein salt formation overlying the reservoir—and the even higher velocity anhydrite layers within the Zechstein—leading to signals outside the epicentral area being dominated by multiple indirect arrivals.

12.2 Simulated NS_B durations

The process followed for the development of the V4 GMPE for duration differs significantly from the approaches adopted for the V1-V3 hazard and risk model. For these earlier versions of the model, particularly for the V1 implementation, the existing models of Bommer *et al.* (2009), Kempton & Stewart (2006) and Lee & Green (2014) were considered as options for direct application in Groningen, or as options for starting points that could be adapted to the Groningen field. Ultimately, the model of Kempton & Stewart (2006) was used in V1. Shortly after the development of the V1 model, the Kempton & Stewart (2006) was superseded by the (early) release of the Afshari & Stewart (2016a) model. This updated model that made use of the NGA-West2 ground-motion database (Ancheta *et al.*, 2014) was used as a starting point for the development of the V2 and V3 GMPEs for duration.

The durations within the Groningen field have always presented features that are not typically encountered in other areas. These features are thought to relate to the effect of trapped and refracted waves arising from the particular velocity structure of the Groningen field. The net effect of these phenomena is that durations in the Groningen field appear to increase rapidly with distance within the first several kilometres from the source. Beyond that the durations appear to increase with distance at a rate that is comparable to observations in other regions. However, this is not easy to constrain due to the very limited sampling of distances available in the ground-motion database. Figure 12.11 shows how the durations of the motions in the field differ from the general predictions of the Kempton & Stewart (2006) model. This figure also shows models that were developed to capture this field-specific path scaling in for the V3 model development. The segmented option was considered during the development process, but the smooth line labelled 'Groningen' in Figure 12.11 was ultimately adopted for the V3 model. The V3 duration model was developed in order to make use of the source scaling implied by the Afshari & Stewart (2016a) model, but with path scaling effects calibrated using the small magnitude recordings from the field.

A problem that arises when attempting to make use of the field specific durations is that ground-motion duration does not appear to scale with magnitude for small magnitude events (Afshari & Stewart, 2016a). Although there are theoretical reasons why the source duration will continue to decrease as the magnitude decreases, what happens is that linear site effects cause an essentially constant increment to be added to the source motion. Therefore, even when an impulse is applied to the base of a soil column the various reflections and refractions will cause the energy to be distributed over some finite duration. When the magnitude of the

event decreases to the sorts of levels for which recordings have been made in the field, the source contribution to the observed duration becomes very small and all we observe is this constant increment associated with site effects. This effect can be seen in Figure 12.12 in which the zero-distance durations (observed durations with the field-specific path effects removed) are compared with the predictions of the Kempton & Stewart (2006) and Afshari & Stewart (2016a) models.

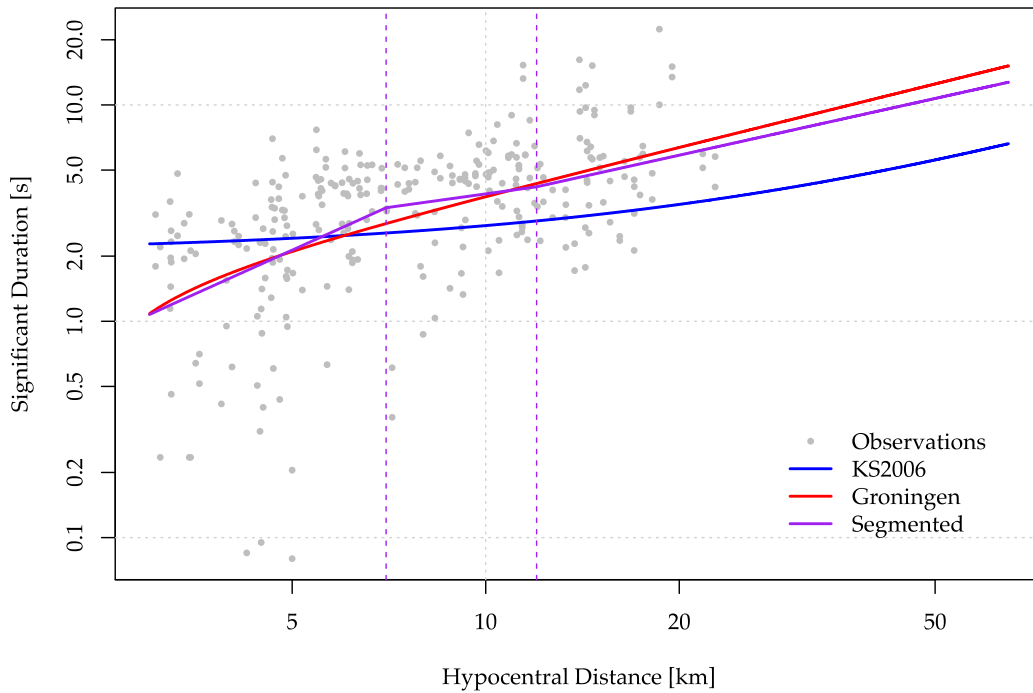


Figure 12.11. Scaling of Groningen durations with hypocentral distance and comparison with the Kempton & Stewart (2006) model.

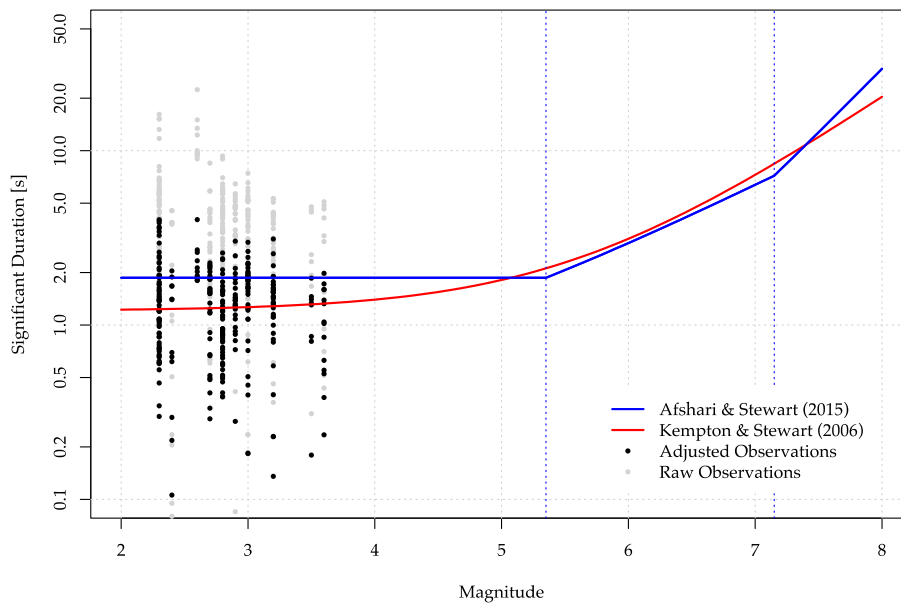


Figure 12.12. Magnitude-independence within the Groningen duration data and comparison with the Kempton & Stewart (2006) and Afshari & Stewart (2016a) predictions.

What is immediately apparent from Figure 12.12 is that it is not possible to infer field-specific magnitude dependence of durations from the observed data. For this reason the magnitude scaling of the Afshari & Stewart (2016a) model was combined with the field-specific path scaling shown in Figure 12.11 in order to obtain the V3 duration model. The parameters of the source-scaling model of Afshari & Stewart (2016a) were adapted to be consistent with the observed durations at small magnitudes and to also enable individual predictions for different levels of the stress parameter. The net result of combining the source and path scaling components in this way was to create a model that agreed very well with the field durations at small magnitudes, and that also agreed very well with the expected levels of source durations from larger magnitude events. However, the V3 model had the distance scaling for small events imposed upon the large magnitudes and this led to unrealistic predictions for the largest scenarios.

This issue can be easily appreciated from Figure 12.13 where the predictions of the Afshari & Stewart (2016a) model are compared to those of the V3 GMPE. At the smallest magnitude shown we can see that the rapid rate of increase that is observed within the Groningen durations is captured in the V3 model, and that the distance scaling at larger distances is reasonably consistent with that of Afshari & Stewart (2016a). As the magnitudes increase the agreement between these models at very short rupture distances continues to be quite good, but clearly the preservation of the distance scaling from the small events leads to extremely long duration predictions for the largest scenarios. The relatively flat scaling of the duration predictions in the Afshari & Stewart (2016a) model is also consistent with other models based upon data from magnitudes of typical engineering interest, e.g., Bommer *et al.* (2006).

The primary objective in moving to the V4 model for duration was to obtain a more realistic model that retained the field-specific features that have been observed in the field, but that reverted to predictions at larger magnitudes that are more consistent with expectations from other regions. The primary issue associated with the V3 model is that the distance scaling was based upon the small magnitude recordings and held fixed when extrapolating to larger magnitudes. Figure 12.13 indicates that durations at a distance of 50km are roughly a factor of 10 greater than those at the source. This is consistent with observations from small events, but what happens for larger events is likely very different.

The factor of 10 that is seen for the small magnitudes represents an increment in duration that is added to some source contribution reflecting the duration of the rupture itself. A large magnitude event can be considered as a combination of many such small events, each triggered at a time that reflects the way that the rupture initiates and propagates over the fault. If the increment in the source duration of each of these fault patches is consistent with the upper left panel of Figure 12.13 then the expected durations from a larger event are really just equal to the time taken for the rupture to propagate over the fault, the rupture duration for individual patches, and the path and site increment seen in this upper left panel. Therefore, rather than taking the overall source duration from the larger event and scaling this by a factor of 10, the only additional contribution to duration for the larger events should

reflect the additional elongation along the travel path from rupture patches distributed over the whole rupture and from the time taken to propagate the rupture over the fault.

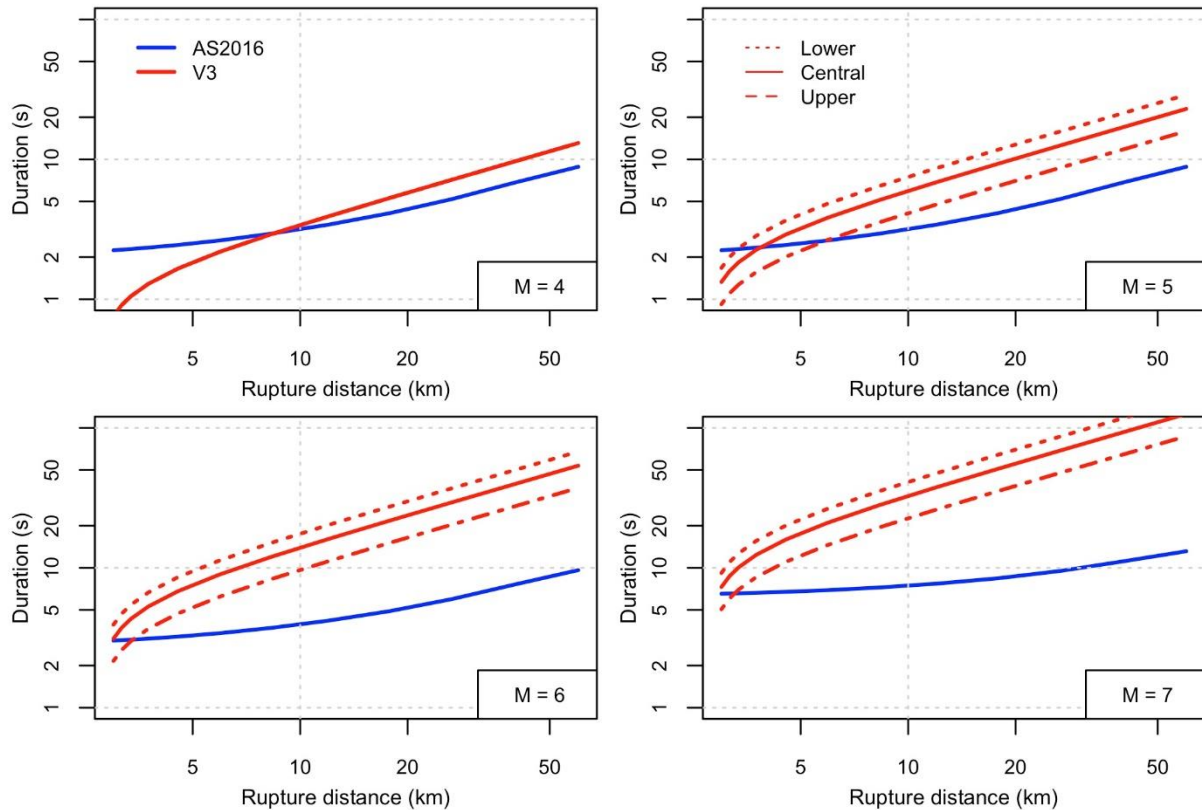


Figure 12.13. Comparison between the predictions of the V3 GMPE for duration and that of the Afshari & Stewart (2016a) model.

This concept of superposition of small ruptures is precisely the basis for the EXSIM approach to ground-motion simulation that was used within the development of the spectral ground-motion model. An input to these EXSIM simulations is a measure of duration, which for the V4 model was taken to be the predictions of the V3 model – but, importantly, only applied to the individual rupture patches within EXSIM. That is, the V3 model, that we believe works well as a field-specific model for small events, was used to model duration contributions from the many small ‘events’ that comprise a larger magnitude scenario. The V4 duration model was therefore based upon the simulations obtained from EXSIM and, just as for the response spectral model, a functional form was developed to capture the scaling of the durations predicted by EXSIM.

A significant advantage of adopting this approach is that the response spectral model and the duration model are now linked together in a more direct manner and the parameterisation of the stress parameter is embedded within the simulations. Therefore, while the V3 model required adjustments for stress parameter to be applied in a rather *ad hoc* manner to the model of Afshari & Stewart (2016a), for the V4 model we have simulations of both response spectral ordinates and duration that are obtained for each of the four stress drop branches.

As with the spectral acceleration model, a total of 436,800 simulations were performed with EXSIM (these are the same simulations used for the generation of the response spectral model). These simulations correspond to the various different finite rupture configurations that are considered for each level of magnitude. For the duration estimates the finite rupture configurations determine where within the overall rupture the process will initiate. This controls the source duration of the rupture as well as the absolute distances between each rupture patch and the recording stations. Figure 12.14 shows examples of the durations that are simulated from EXSIM. As can be appreciated, for any given magnitude and distance combination there will be a range of duration estimates that reflect the variations in hypocentral location and rupture orientation. Figure 12.14 also demonstrates that while the scaling of the durations for the smallest magnitude shown is consistent with the scaling of the V3 model durations shown in the upper left panel of Figure 12.13, there are clear departures for the larger magnitude scenarios. However, the general shape of the duration scaling with respect to distance is far more aligned with that of the Afshari & Stewart (2016a) (and other tectonic models). The EXSIM approach to generating the durations at the NS_B horizon therefore appears to be a realistic option that allows the field specific attributes of the Groningen motions to be captured for the small magnitude events, but to also extrapolate these effects up in a meaningful manner.

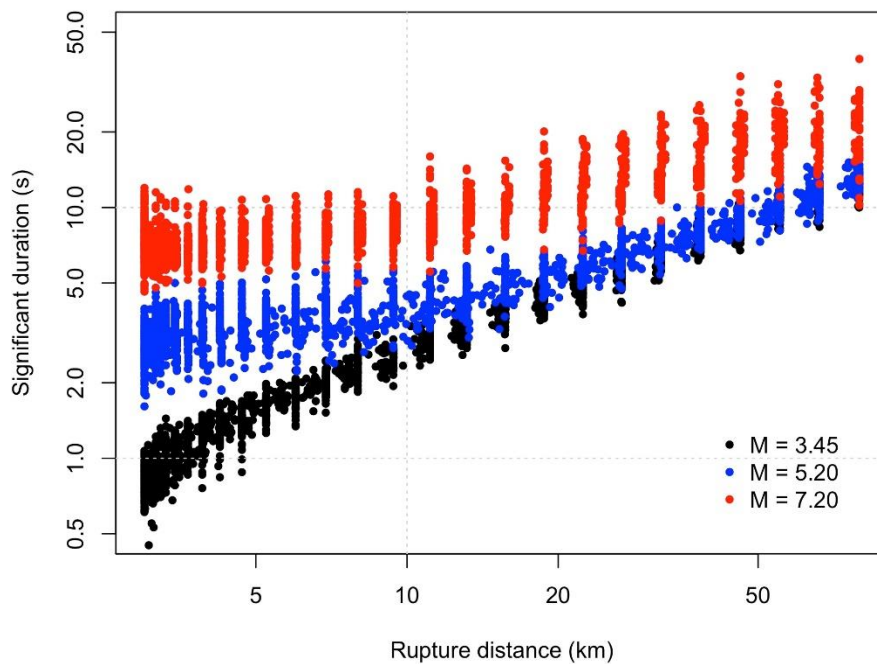


Figure 12.14. Examples of the duration estimates generated by EXSIM for three different magnitudes.

Visual comparison between the EXSIM-predicted durations shown in Figure 12.14 and the median predictions of the Afshari & Stewart (2016a) model in Figure 12.13 suggest that the EXSIM durations are slightly higher for the largest magnitude events. This is true, and can be attributed to two main causes. The first is that the rapid increase with distance that is observed in the field maps across into the EXSIM simulations and so we expect to see higher

than typical durations due to this being a characteristic of the scattering, reflections and refractions in the field.

The second cause is likely to be associated with the observation that seismological models that involve superposition of contributions from discrete patches over the rupture (the vast majority of models) lead to predictions of duration that are slightly higher than empirical observations. This view has recently been proposed by Afshari & Stewart (2016b) who have looked at a number of different seismological simulation approaches. However, while the durations from the large events are still a little longer than those from generic tectonic predictions, what is clear is that the simulations that are used to develop the V4 ground motion model resolve the vast majority of issues that existed with the V3 model. In addition, it remains impossible to assess the extent to which these higher than average predictions are the result of field-specific features of the simulations or are an artefact of the superposition process not adequately capturing effects of interference from source contributions.

12.3 GMPE for surface durations

The EXSIM simulations discussed in the previous section provide estimates of duration at the NS_B horizon, but the GMPE model needs to output surface predictions. Whereas the response spectral model modifies predicted spectral amplitudes at the NS_B horizon via site response, this same approach cannot be applied for the duration predictions. A key reason for this is that the RVT-based site response calculations require a measure of duration as an input, but that approach to site response does not provide predictions of duration as an output.

While site response (both linear and nonlinear) can have an impact upon duration, its effect is relatively weak in comparison with contributions from source and path effects. For that reason, the modification of the NS_B durations to the surface makes use of the generic site response terms within the Afshari & Stewart (2016a) model. This model represents site effects through terms that reflect the near surface velocity profile (via V_{s30}) and the deeper profile using sediment depth terms. These latter terms are extremely weak and are ignored for the V4 model.

The process to develop a functional form for the duration model was similar to the adopted for the response spectral amplitudes. The outputs of the EXSIM simulations were inspected and functional terms that captured the general scaling that was observed were developed. As the breaks in scaling of magnitude and distance that were included within the model for spectral ordinates are related to changes in the stress parameter scaling, rupture geometry scaling and important reflections and refractions along the path, the locations of the breaks in scaling for the duration model are also tied to these.

The overall model for the duration can be written as a combination of source, path and site contributions according to Eq.(12.1).

$$\ln D_{5-75\%} = g_{src}(M) + g_{path}(R_{rup}, M) + g_{site}(V_{S,30}) \quad (12.1)$$

The source contributions are described by two segments with a break in scaling at M 5.45. The form of this function is given in Eq.(12.2).

$$g_{src}(M) = \begin{cases} m_0 + m_1(M - 5.45) & \text{for } M \leq 5.45 \\ m_0 + m_2(M - 5.45) + m_3(M - 5.45)^2 & \text{for } M > 5.45 \end{cases} \quad (12.2)$$

where the magnitude used in Eq.(12.2) is defined as $M \equiv \max(M, 3.5)$. That is, for any event small than magnitude 3.5 the magnitude value is fixed at 3.5. This constraint was imposed in order to reflect the magnitude-independence that is observed in the Groningen duration data over this magnitude range (see Figure 12.12).

The path contribution is segmented about a rupture distance of 12km. For distances shorter than this, the scaling with respect to logarithmic distance is seen to be nonlinear, as can be appreciated from the example data in Figure 12.14. However, for greater distances the scaling of logarithmic duration is essentially linear with logarithmic distance, but with slopes that depend upon the magnitude (again, see the general trends in the data shown in Figure 12.17). The parameterisation of these observations resulted in the functional expressions shown in Eq.(12.3).

$$g_{path}(R_{rup}, M) = \begin{cases} (r_0 + r_1 M) \left[\ln \left(\frac{R_{rup}}{3} \right) \right]^{r_2} & \text{for } R_{rup} \leq 12 \text{ km} \\ (r_0 + r_1 M) \left[\ln \left(\frac{12}{3} \right) \right]^{r_2} + (r_3 + r_4 M) \ln \left(\frac{R_{rup}}{12} \right) & \text{for } R_{rup} > 12 \text{ km} \end{cases} \quad (12.3)$$

Here, the magnitude value that is used within Eq.(12.3) is defined as $M \equiv \min[\max(M, 3.5), 6.0]$. The reason for the bounds being imposed upon the magnitude in this manner is that the magnitude dependence of the distance scaling appears to saturate for larger magnitude events. That is, we observe magnitude dependence in moving from magnitudes 3.5 up to magnitude 6.0, but thereafter the magnitude dependence of the distance scaling is so weak as to be negligible.

As previously mentioned, the site contribution is based upon the model of Afshari & Stewart (2016a). The $V_{S,30}$ scaling of their model is defined in Eq.(12.4) where $V_1 = 600\text{m/s}$, $V_{ref} = 368.2\text{m/s}$ and $\phi_1 = -0.2246$.

$$g_{site,AS16} = \phi_1 \ln \left[\frac{\min(V_{S,30}, V_1)}{V_{ref}} \right] \quad (12.4)$$

In order to make a correction to account for these effects the surface durations are mapped from the EXSIM durations using Eq.(12.5).

$$\ln D_{5-75\%}^{\text{surface}} = \ln D_{5-75\%}^{\text{EXSIM}} + g_{site,AS16}(V_{S,30}^{\text{surface}}) - g_{site,AS16}(V_{S,30}^{\text{NS}_B}) \quad (12.5)$$

However, because the $V_{S,30}$ associated with the NS_B horizon is well above the level of $V_1 = 600\text{m/s}$ then the overall contribution associated with site effects for the V4 model can simply be written as in Eq.(12.6), where $V_1 = 600\text{m/s}$ and $\phi_1 = -0.2246$.

$$g_{site}(V_{S,30}) = \phi_1 \ln \left[\frac{\min(V_{S,30}, V_1)}{V_1} \right] \quad (12.6)$$

To obtain the parameters of the source and path terms a nonlinear least squares regression analysis was conducted using the 436,800 simulated durations from EXSIM. The coefficients from these regressions are presented in Table 12.1. Coefficients are developed for each of the four stress parameter branches discussed in Chapter 6.

The predictions of the V4 duration model are shown with respect to rupture distance for a number of magnitude values in Figure 12.15. This figure shows that the impact of the different stress parameter models is relatively weak in comparison with the impact that was built within the V3 duration model. It is also clear that we have quite strongly nonlinear scaling at close distances and that this scaling also depends significantly upon the magnitude. However, at larger distances it is clear that the magnitude scaling is much weaker. It is also important to note that whereas the V3 model was predicting durations in excess of 100 seconds for the most demanding scenario shown in Figure 12.15, the equivalent durations are now roughly a factor of five smaller for these scenarios.

The magnitude scaling of the V4 duration model is shown in Figure 12.16. This figure clearly shows how the impact of distance diminishes strongly as the magnitude increases. The rapid increase of duration that takes place for small magnitude events shown in Figure 12.16 is similar to the scaling that was embedded within the V3 model for all magnitude events. This can be appreciated in Figure 12.17 where the V3 and V4 model predictions are compared. Clearly, at low magnitudes the model predictions are very similar and are primarily reflecting slight differences in the stress drop (and hence the source scaling). However, while the duration predictions for the larger magnitudes literally go off the scale for the V3 model, the V4 model predictions show that at large distances the durations from magnitude 7 events are actually lower than what was being predicted for magnitude 5 events in the V3 model.

Table 12.2. Coefficients of the V4 duration model

Parameter	Lower (L)	Central (Ca)	Central (Cb)	Upper (U)
m_0	1.0957	1.0418	1.0388	1.0023
m_1	0.7321	0.7089	0.7019	0.6927
m_2	0.7812	0.7455	0.7056	0.7576
m_3	-0.1271	-0.1275	-0.1292	-0.1619
r_0	2.5471	2.5348	2.4949	2.5311
r_1	-0.4075	-0.4016	-0.3931	-0.3982
r_2	0.7338	0.7364	0.7369	0.7319
r_3	1.172	1.1327	1.1216	1.0979
r_4	-0.1176	-0.1073	-0.1044	-0.0978

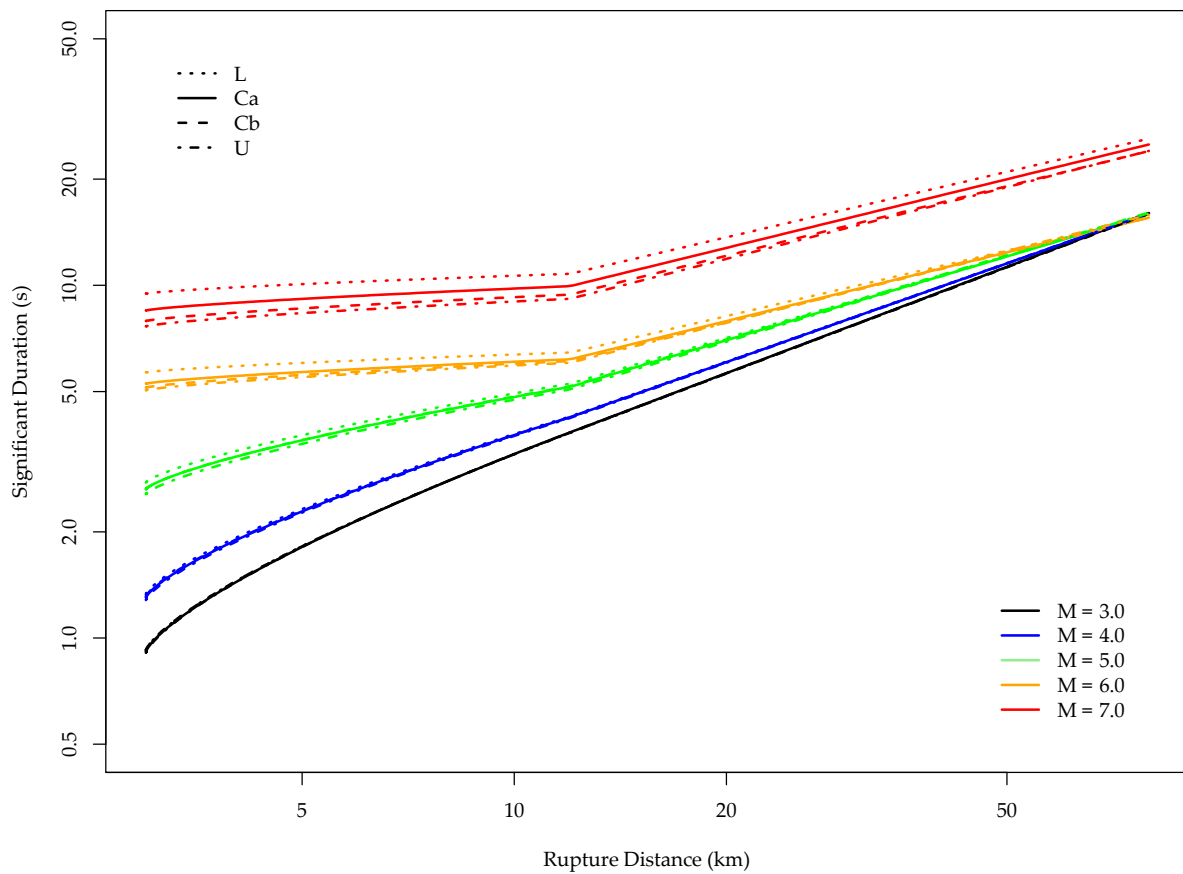


Figure 12.15. Distance scaling of the V4 duration models for a number of different magnitudes.

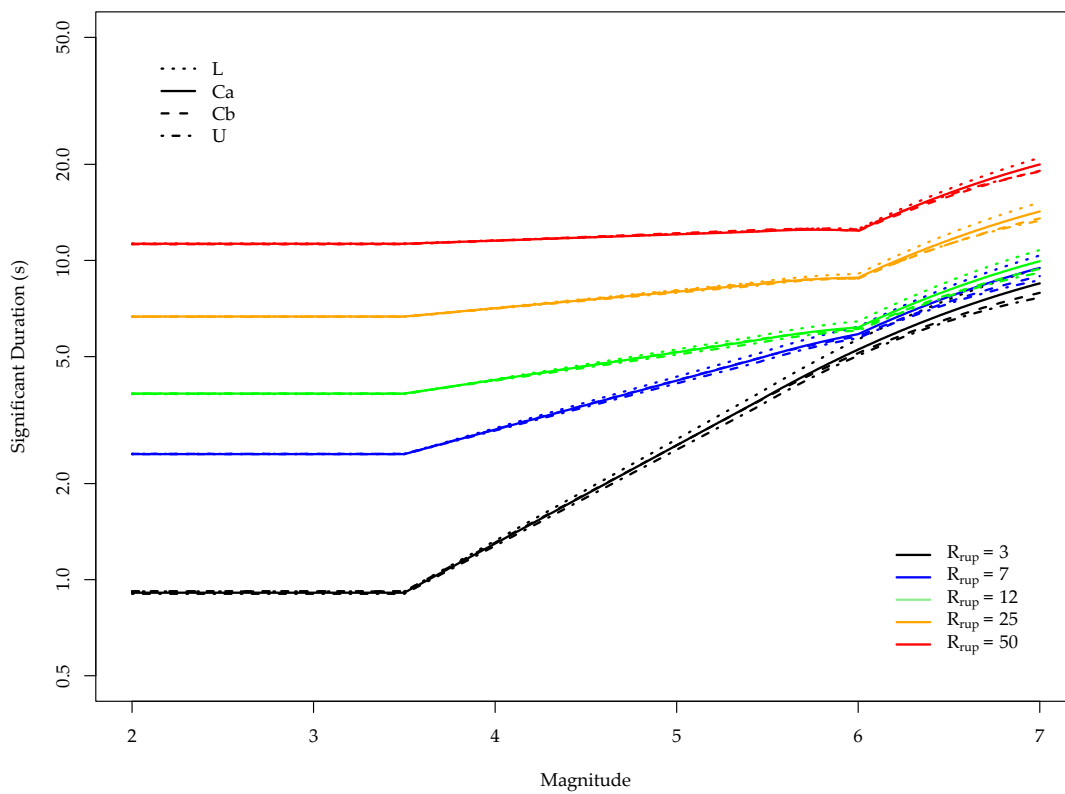


Figure 12.16. Magnitude scaling within the V4 duration model.

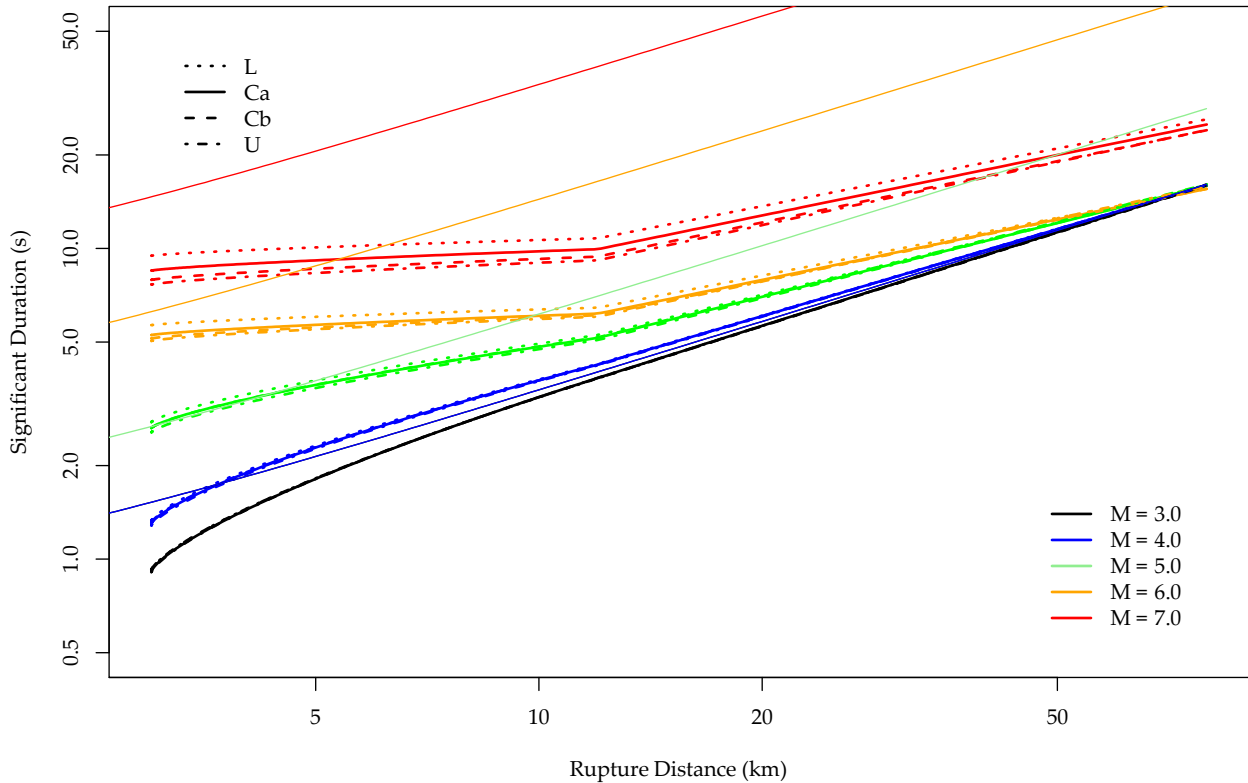


Figure 12.17. Comparison of the distance scaling in the V3 and V4 duration models. Thin lines denote the V3 model, while heavier lines correspond to V4.

Figure 12.18 shows a similar picture, but with durations plotted against the magnitude. As previously discussed, the distance scaling at the small magnitudes is effectively the same in both the V3 and V4 models. This makes perfect sense given that the EXSIM simulations make use of the V3 model to predict durations from small events (or sub-events). For these small events the source size is comparable to, or smaller than, a sub-event contributing to a large magnitude event. Figure 12.18 shows how this agreement between V3 and V4 breaks down as soon as larger magnitudes are considered, with the increase in duration associated with path effects being far more subdued than in the V3 model. Figure 12.19 again compares the V3 and V4 models, but now also includes all three stress drop branches from the V3 model (Figures 12.17 and 12.18 use the central branch from the V3 model) as well as the predictions of Afshari & Stewart (2016a). As noted previously, the stress drop dependence in the V4 model is much subtler than in the V3 model. Also, while the general scaling of the V4 model mirrors that of the Afshari & Stewart (2016a) predictions, there is a noticeable offset. This is due to a combination of field-specific attributes, and the consequence of the superposition approach used within EXSIM – and simulation approaches in general (Afshari & Stewart, 2016b).

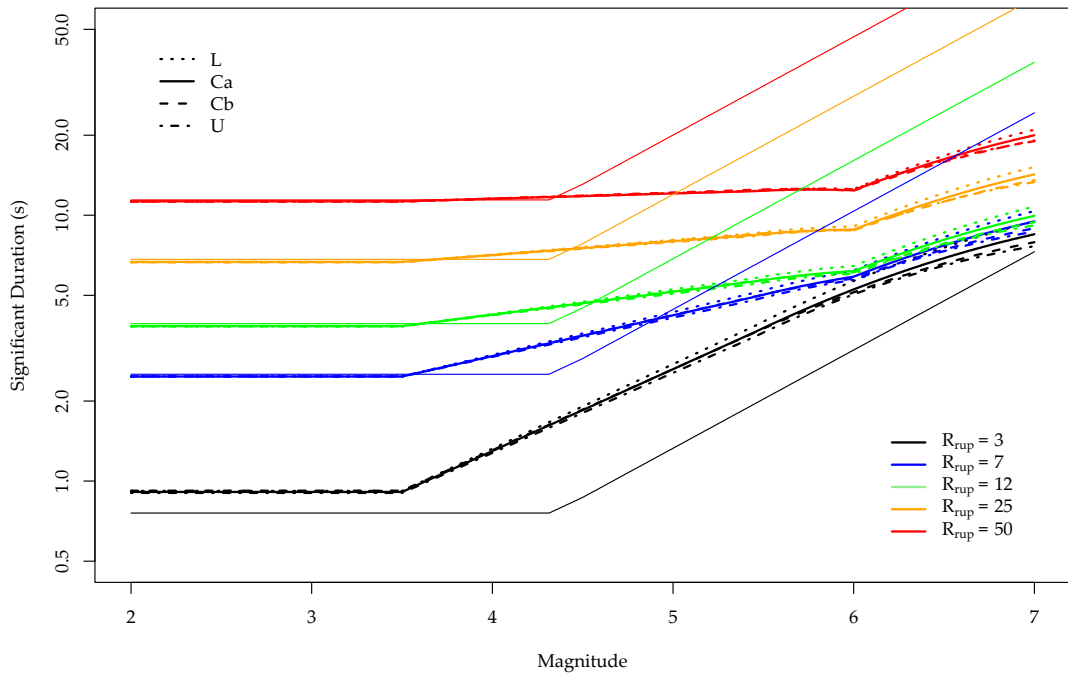


Figure 12.18. Comparison of the magnitude scaling in the V3 and V4 duration models. Thin lines denote the V3 model, while heavier lines correspond to V4.

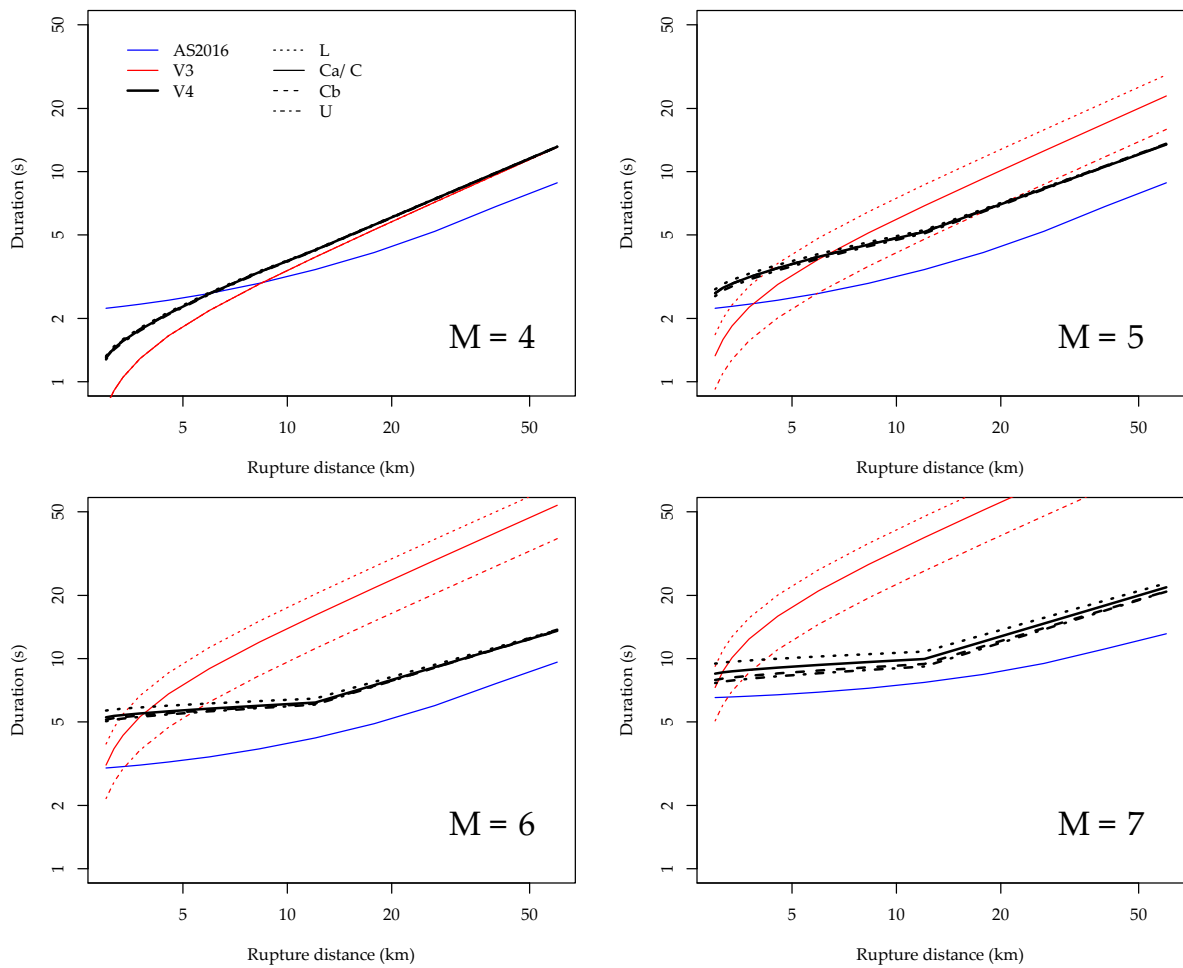


Figure 12.19. Comparison of the V3 and V4 models along with the Afshari & Stewart (2016a) model predictions.

12.4 Residuals and sigma model

As shown in Figure 12.14, for any given combination of magnitude and distance the EXSIM simulations will give a distribution of duration values. Therefore, when developing the duration model the objective is to obtain a relatively simple function—involving a small number of input variables—that can replicate the central values of these distributions. The dispersion around these median predictions is of less importance during the model fitting as this is not the full aleatory variability that needs to be considered within the hazard and risk calculations. The variability arising from EXSIM reflects the stochastic nature of the simulation approach (random phase angles for the various sub-events) and the variation in the properties of the finite source (location of the hypocentre, *etc.*).

In order to provide a sense of how well the V4 model replicates the average behaviour of the EXSIM simulations Figures 12.20 and 12.21 compare the model predictions with the underlying EXSIM data used in the model development.

In Figure 12.20 the duration values are plotted against magnitude in 15 bins of logarithmic distance. The blue dots represent the EXSIM durations while the black dots represent the model predictions. In the vast majority of cases the model that has been developed provides a very good fit to the centre of the data. There are minor departures in some cases, but in order to try to improve the performance of the model the complexity of the model would need to increase significantly. Given that the model is being calibrated to model predictions rather than actual data it is much more preferable to keep the model in its relatively simple form.

In Figure 12.21 one can appreciate that the fitted model is again able to represent the centre of the EXSIM predictions very well. With the durations broken down into specific magnitude bins it is also very clear that the short distance scaling for small events is very different to that for larger events. As with the magnitude scaling, it appears that the relatively simple form adopted for the V4 model is able to do a very good job of representing the centre of the distributions arising from the EXSIM simulations.

It is also clear that the effects of the finite rupture appear more strongly at short distances, and for large magnitudes. This inference can be made from consideration of the degree of variability in the duration predictions for different combinations of magnitude and distance. This makes intuitive sense as the impact of hypocentral position will be more pronounced when one is very close to the rupture (as the difference in the travel paths is a relatively large contributor to the duration) as well as when the source itself is large.

Figure 12.21 also shows that the segmentation of the distance scaling that was based upon a rupture distance of 12km works well for the durations. This distance limit was informed by the full waveform modelling and was used within the inversions as well as for the development of the response spectral model.

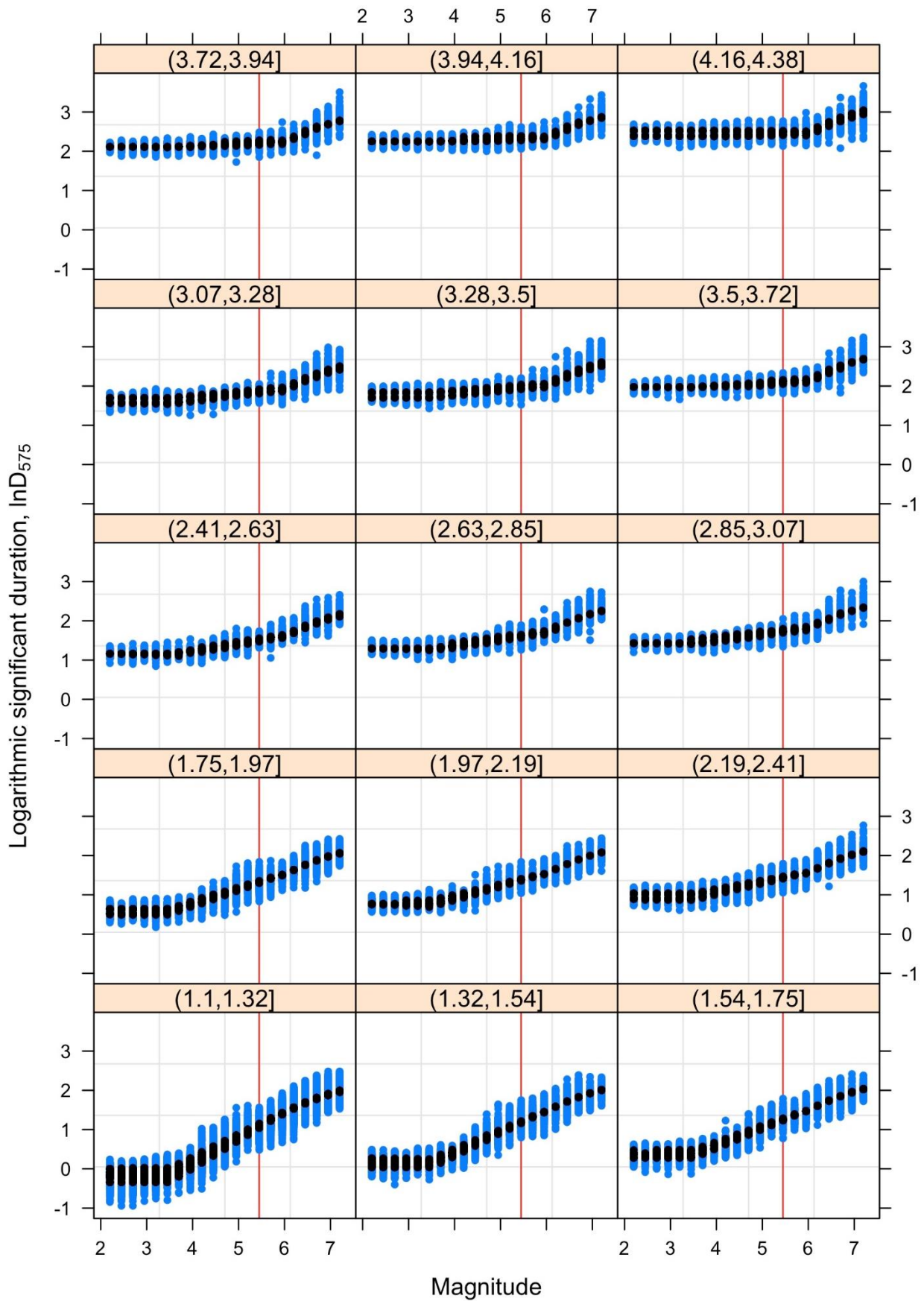


Figure 12.20. Comparison of model predictions (*black*) and EXSIM estimates (*blue*) with respect to magnitude for distance ranges indicated by logarithmic values

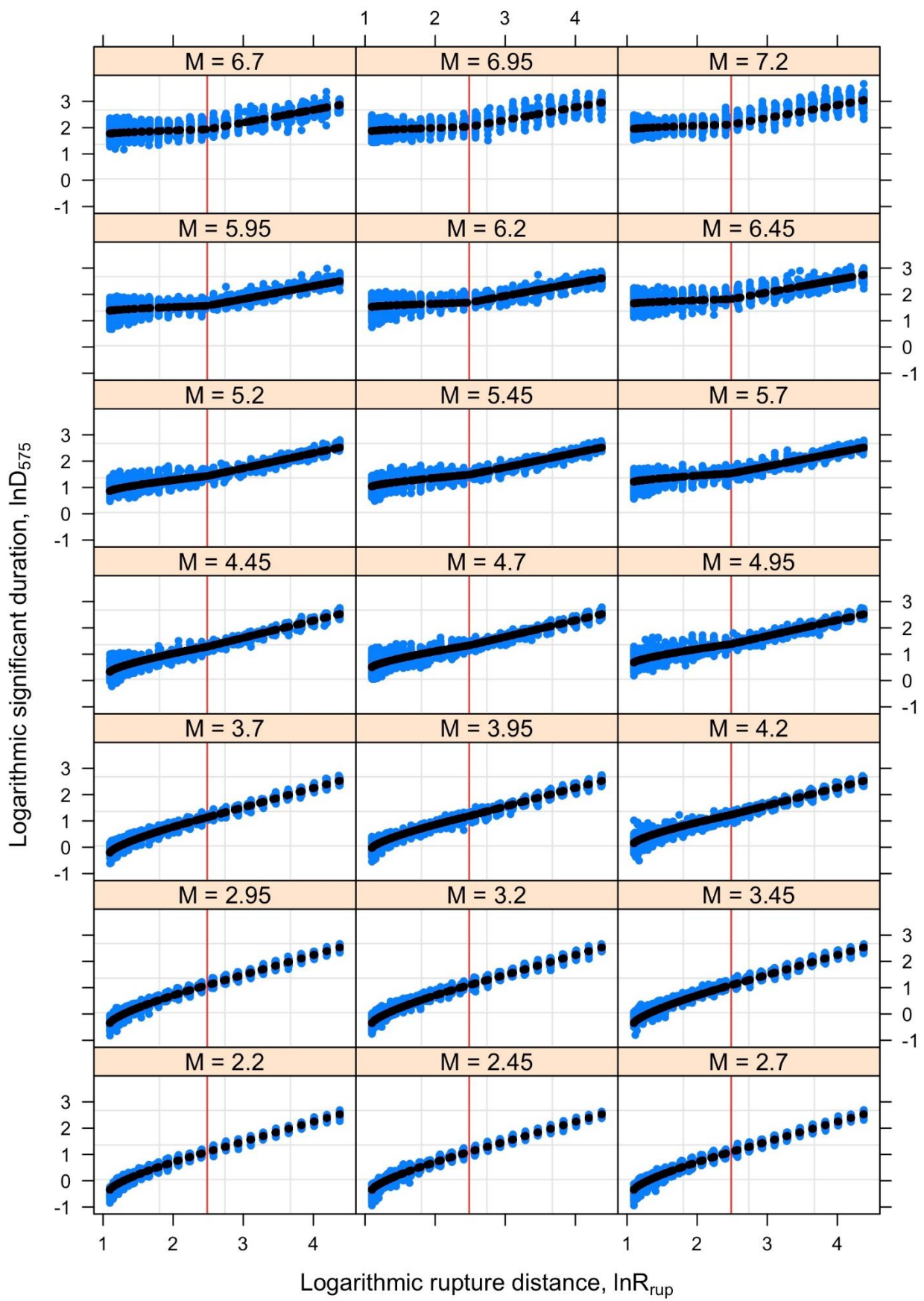


Figure 12.21. Comparison of model predictions and EXSIM estimates with respect to logarithmic distance.

The model for the variance in the duration is not based upon the dispersion seen in Figures 12.20 and 12.21 because this is all conditional upon a model imposing variations in the duration. To obtain the model for the variance of duration the same procedures discussed within Section 6.5 are employed. The residuals of the duration model with respect to the small magnitude field observations are computed and are also partitioned among between event and within event components in order to get the variance components necessary for the hazard and risk calculations. Like in the case of the response spectral model, magnitude uncertainties and spatial correlations were also taken into account in an attempt to refine the estimates of the variance components as much as possible.

Table 12.3 shows the variance components that have been obtained for each of the four stress drop branches. In this table β_0 represents the bias between the developed V4 model (calibrated using the EXSIM results) and the field observations of duration. The bias is very similar for all branches because the stress parameter plays an extremely weak role at low magnitude levels. This bias is computed in logarithmic units because the residuals are computed in logarithmic terms. When viewed as factors these bias values indicate that the field observations are less than 3% higher than the model predictions for these small magnitude events.

The variance components presented in Table 12.3 are lower than those obtained from the V3 model. The difference here is not as striking as for the case of the spectral accelerations and this is due to the fact that magnitude scaling is almost non-existent over the range where field observations have been made. As a result, the adjustments to the dataset and accounting for magnitude errors has a much weaker effect upon the duration model.

Table 12.3. Variance components of the V4 duration model

Branch	β_0	σ_{β_0}	τ	ϕ_{S2S}	ϕ	σ	ρ
Lower (L)	0.0243	0.009	0.3374	0.2815	0.4614	0.6372	1.3891
Central (Ca)	0.0272	0.0101	0.3389	0.2825	0.4585	0.6363	1.3513
Central (Cb)	0.0273	0.0084	0.3245	0.2774	0.4648	0.6311	1.4439
Upper (U)	0.0274	0.0062	0.3397	0.2802	0.4606	0.6372	1.3754

12.5. Correlation of residuals of duration and accelerations

An important aspect of including duration in the risk assessment is to account for the inverse relationship between the duration of the shaking and the amplitude of the acceleration. This general behavior is represented by the scaling of the median prediction models for amplitude and duration. However, for a given scenario there will also be correlations between the duration and amplitude values with respect to their median predictions. This correlation of the residuals with respect to the predicted median values of the two parameters is required in order to properly account for the correlation between these two intensity measures within the risk analyses.

For the previous versions of the duration model for the Groningen field the correlations among spectral amplitudes and duration were taken from Bradley (2011). Recently Baker & Bradley (2017) revisited the Bradley (2011) correlation model using the NGA-West2 database. While they observed that the correlations remained negative at longer periods, they also concluded that the differences have a very weak practical impact. For that reason they did not propose an alternative model to Bradley (2011). For this reason, the Bradley (2011) model is again used to account for the correlation between the D_{S5-75} and $Sa(T)$ as there are still insufficient recordings to warrant the derivation of a Groningen-specific correlation model.

Correlation coefficients (ρ) according to the Bradley (2011) model for the 16 periods of interest are reported in Table 12.4.

Table 12.4. Correlation coefficients according to the Bradley (2011) model.

T [s]	0.01	0.1	0.2	0.3	0.4	0.5	0.6	0.7	0.85	1	1.5	2	2.5	3	4	5
ρ	-0.45	-0.39	-0.39	-0.39	-0.33	-0.28	-0.24	-0.21	-0.17	-0.13	-0.05	-0.01	0.02	0.05	0.09	0.12

13. CONCLUDING REMARKS

In this closing section, we briefly summarise the current state of development of the Groningen ground-motion model (GMM) and discuss options and challenges in the ongoing refinement of this model.

Evolution of the Groningen GMM

The V4 ground-motion model for the Groningen field represents the outcome of several stages of evolutionary development, which began with a very simple model (V0) for PGA and PGV that was constructed for the 2013 Winningsplan. The first bespoke model capturing epistemic uncertainty in a logic-tree formulation and adjusted to local site response characteristics (V1) was issued in March 2015. While the V1 model represented an important starting point for the development of field-specific models, it had two important limitations in terms of not capturing the spatial variation of the site response characteristics and only modelling linear response of the soils covering the field. Both of these shortcomings were addressed in the V2 GMM, issued in October 2015, which comprised a model for the prediction of motions at a buried reference rock horizon with a zonation of the field defining frequency-dependent non-linear amplification factors (AF) to transfer the rock motions to the ground surface. Subsequent developments have essentially focused on refining this framework. In the V3 model, issued in July 2016, the reference rock horizon was moved from the base of the Upper North Sea formation (NU_B) at about 350 m depth to the base of the North Sea supergroup (NS_B) at 800 m, the latter being a much more pronounced impedance contrast and therefore a more suitable elevation to be considered as the top of the elastic half-space in the site response modelling. The V4 model uses the same reference rock horizon but has moved from the representation of earthquake sources as points to modelling extended fault ruptures.

The predicted outputs from the V4 GMM cover all current requirements in terms of hazard and risk estimates for the field, namely horizontal spectral accelerations at a wide range of periods and predictions of duration conditioned on these accelerations. The model also provides guidance on generating conditional spectra that account for period-to-period correlations and vertical response spectra as well. The V4 model additionally includes the prediction of peak ground velocity, which had not been part of the V1-V3 model.

The V4 model captures the nature of seismic wave propagation from the source of the earthquakes in the Rotliegend sandstone that houses the gas reservoir to the ground surface, including the non-linear response of the softer soil deposits under levels of shaking. Through implementation in a Monte Carlo framework, the incorporation of site response effects allows for fully probabilistic estimation of the surface shaking hazard. Moreover, the site amplification effects are conditioned not only on the realisation of motions at the reference rock horizon (the base of the North Sea super group) but also, for short response periods, on magnitude and distance, which is an innovation that has been developed in this project.

The model also reflects other important physical features of induced and triggered earthquake scenarios in the field, including the extended fault ruptures that would necessarily be associated with larger events. In addition, the model captures the uncertainty associated with the extrapolation of the predictions to potential earthquakes of magnitude almost four units greater than the largest earthquake observed to date. Whereas the V1-V3 models used simple 3-branch logic-trees to represent this uncertainty, the V4 GMM logic-tree includes 8 branches, four for median values and two for the associated variability (sigma values).

The hazard results—at least for PGA and a return period of 475 years—obtained with the V3 and V4 GMMs are very similar (Figure 13.1), even though several factors changed in terms of the logic-tree structure and the estimates of associated variability; changes to the site response zonation were very minor. This suggests that the model has reached a certain level of stability and only modest changes are expected in the ongoing development beyond this point. For this reason, we believe that the model can be used with a high degree of confidence for hazard and risk applications in Groningen.

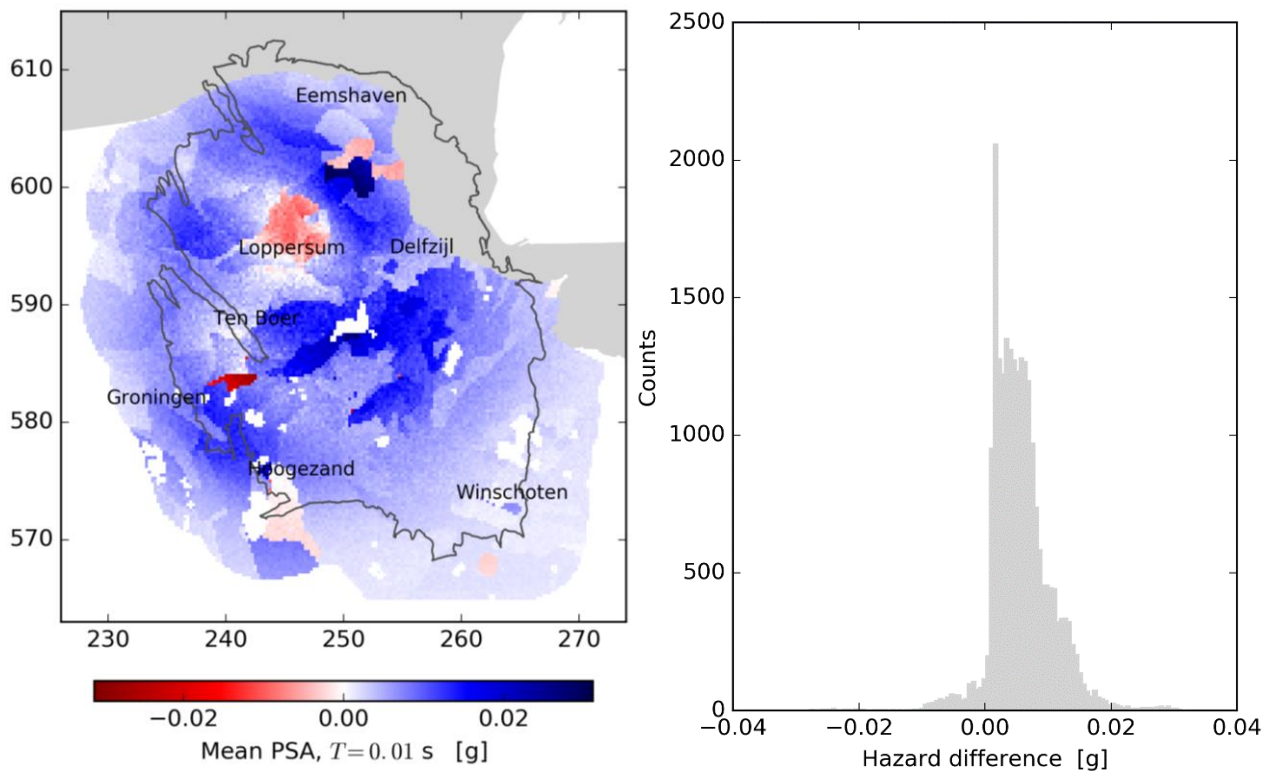


Figure 13.1. Differences in the 475-year PGA hazard estimates obtained using the V4 GMM with respect to those from the V3 model (courtesy of Stephen Bourne and Assaf Mar-Or)

At the same time, it is important to note in passing that Figure 13.1 only shows results for PGA, whereas it is the shape and amplitude of the response spectrum—and not only its zero-period anchor—that determines both seismic risk estimates and the loads to be considered in seismic design.

The V5 Development Stage

While the Groningen ground-motion model has evolved to an advanced state, improvements are of course still possible and another phase of development is now envisaged that will lead to the production of the V5 model in Q3 2017. This will address both issues identified by the authors of this report in the course of the model development and suggestions and challenges from the international expert review panel that undertook a thorough review of the draft version of this report.

One of the features of the Groningen GMM development is that while it has occurred over a period of more than three years, it has occurred as a sequence of fully documented phases rather than as a continuous process allowing for more reflection, iteration and gradual refinement. The requirement to periodically update the hazard and risk estimates has meant that the GMM has had to be developed to state ready for implementation on several occasions (including full documentation: the V1-V3 GMMs reports extend to almost 1,300 pages), and these relatively short developmental phases have obliged us to sometimes be cautious and apply only incremental changes. There have been benefits of the process as well, including opportunities for obtaining insights into the model performance from its implementation in the hazard and risk engine and extensive reviews as well (including the peer review of several journal papers that have summarised different aspects of the work). However, the development in successive ‘sprints’ has also meant that within a given phase of the work, there has rarely been the opportunity to amend any aspect of the model during the course of the work. This has been detrimental since the long sequence of the model-building process (see Figure 2.3) means that several factors must be fixed at an early stage and their subsequent revision would require repetition of the complete sequence of tasks, which has not been possible until the next development stage. Even during the V4 model building, issues came to light—such as the relationship of moment and local magnitudes (see below)—which can only be addressed in the V5 model development.

To meet the target deadlines for an updated seismic risk assessment in November 2017, the V5 GMM needs to be delivered in early September, which means a period of three months from the issue of this report. Once again, therefore, the development will be undertaken at a rapid pace and must therefore be focused on what can be satisfactorily completed within that timeframe. This means that some of the issues that remain to be explored may be addressed in parallel, outside of the actual V5 model development, or else examined in sensitivity studies conducted after delivery of the V5 model summary.

In the remainder of this chapter, the key technical issues that have been identified as warranting further examination are briefly discussed. Some of these will be addressed specifically within V5, others as parallel activities or subsequent sensitivity analyses to be included in the V5 GMM report even if not directly influencing model development (but perhaps having some bearing on the final logic-tree branch weights).

Local and Moment Magnitudes

A fundamentally important issue is the relationship between local magnitudes, M_L , and moment magnitudes, M , in the Groningen field. In early stages of the model development it was simply assumed that the two scales could be considered equivalent in the magnitude range of interest. Subsequent work suggested that the difference between the two scales, for values above M_L 2.5, was a constant offset with M values being consistently 0.2 smaller; this relationship has been employed in the V4 model. The implementation of this conversion relationship between the two magnitude scales affects the model development in two main ways: the inversions of FAS for source and path parameters, and the calibration of the stress parameter scaling of the upper branch of the logic-tree to mimic tectonic GMPEs.

Work on the relationship between the two magnitude scales has continued throughout the V4 development stage and revisions of the seismic moment estimates has finally led to the conclusion that over the magnitude range of interest ($M > 2.5$), the two scales are, on average, equivalent (Figure 13.2.).

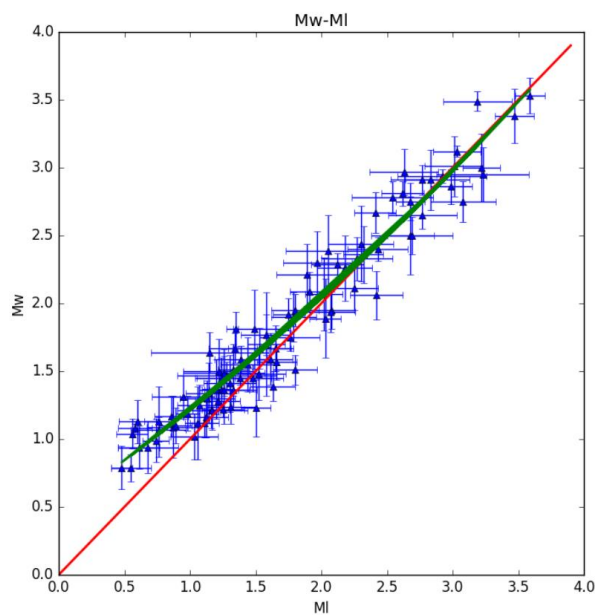


Figure 13.2. Revised M_L - M relationship for Groningen

A journal paper will shortly be submitted summarising the work leading to this conclusion and as the V5 model building progresses, the assumption of $M_L = M$ will be invoked once again.

Inversions of FAS for Source, Path and Site Parameters

As is very well known, and also clearly acknowledged in this report, there are several trade-offs in inversions of FAS of ground motions to estimate source, path and site parameters. The M_L - M relationship is an example of a factor exerting a strong influence on the results of the inversion. In the V3 model derivation, for which it was assumed that the two magnitude

scales are equivalent, a steep near-source decay of $R^{-1.7}$ was found, whereas using the $M = M_L - 0.2$ relationship in V4 changed this to $R^{-1.2}$. As we revert to the original assumption of equivalence of the magnitude, some steepening of the initial segment of geometrical spreading decay can be expected. At the same time, it would be desirable to avoid such strong coupling between these two factors, if possible, and with this in mind options will be explored to constrain the source amplitudes to be consistent with the seismic moment.

Consideration will also be given to the other trade-offs inherent in such inversions, including that between the site amplification and kappa, and also between the stress parameter and kappa. Equally, the extent to which kappa and Q can both be constrained using recordings from a relatively short distance range needs to be considered. While all of these factors will be considered, together with others such as the source velocity (since work is underway by other researchers that may yield improved estimates of the wave velocities in the Carboniferous into which larger ruptures are assumed to propagate), but it is also recognised that the trade-offs cannot be eliminated. Therefore, the objective rather will be to accurately estimate the sensitivity of the results—over the magnitude and distance range of the model application—to these uncertainties and ensure that the logic-tree captures these influences on the range of predicted ground motions.

Calibration of Stress Parameter Models and Magnitude Scaling

The upper branch of the V4 GMM logic-tree was adjusted to provide approximate agreement to three of the NGA-West2 GMPEs, the underlying objective being to have a model that essentially predicts the levels of motion that might be expected from tectonic earthquakes of the same magnitude. In building the V5 model, this same approach will be extended to also include comparisons with GMPEs from other regions, such as Europe and Central and Eastern North America. Comparisons will also be made with GMPEs calibrated over wide ranges of magnitudes—such as Abrahamson *et al.* (2014)—in order to examine the magnitude scaling implied by the Groningen GMM. Similarly, comparison will also be made using the Yenier & Atkinson (2015) model that allows the scaling of the stress parameter with both magnitude and depth. The overall objective will be to provide additional constraint on the spread of predicted amplitudes implied by the final logic-tree.

In parallel with these explorations, we will also explore the origin of the unusually high response spectral ordinates observed at a period of around 1.5 seconds.

Functional Form and Calibration of Reference Rock GMPEs

Following from the previous points, additional topics warranting exploration include the influence of ruptures propagating downwards into the Carboniferous and the nature of the near-source terms, including the magnitude dependence of distance saturation. These are all topics which we hope will be informed by the finite rupture simulations being performed by URC/ExxonMobil (Zucker *et al.*, 2017). The end members of the range of possibilities in terms of near source motions are probably defined by the point source simulations used in

earlier version of the GMM and the EXSIM simulations that essentially assume a heterogeneous fault rupture. The modelling capacity developed by URC/ExxonMobil allows quantitative sensitivity analyses of the effect of differing degrees of source heterogeneity, which could help to inform the range of possible near-source predictions.

Additional Ground-Motion Data

While the final version of this report was being completed, an earthquake of M_L 2.6 occurred towards the south of the field near Solchteren on 27 May 2017 (Figure 13.3). The recorded ground motions from this latest earthquake, at least in terms of PGA, are consistent with the database used to derive the V4 model (Figure 13.4). Nonetheless, the earthquake does include several near-source recordings and provides a valuable addition to the available data hence these recordings will be incorporated into the V5 model derivation.

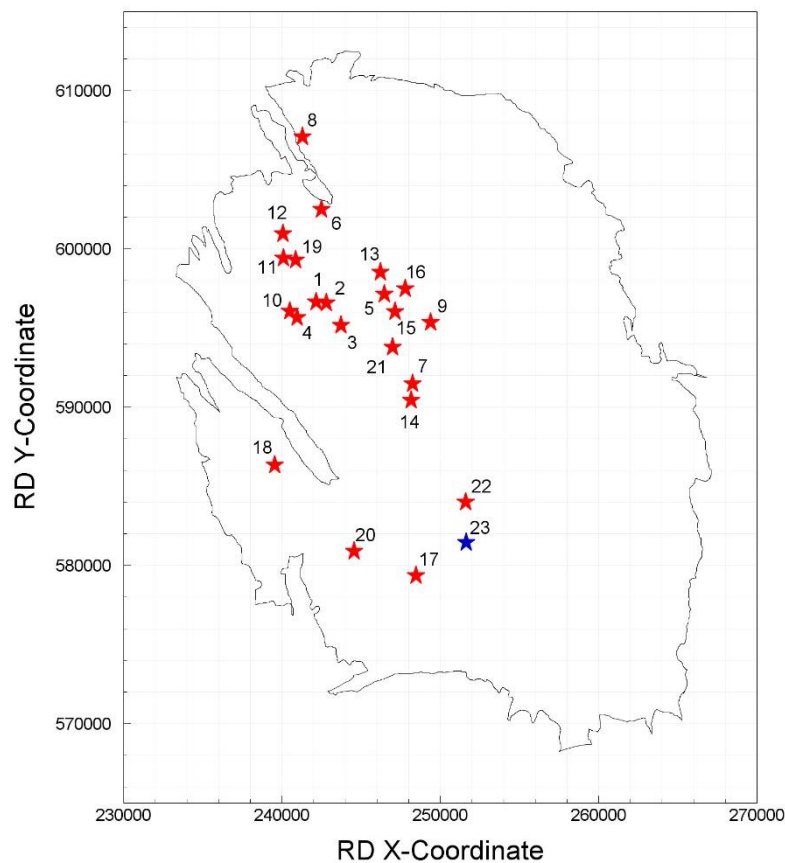


Figure 13.3. Epicentral locations of the 22 earthquakes in the V4 database (*red stars*) and the ML 2.6 Slochteren earthquake of 27 May 2017 (*blue star*)

As explained in Appendix VI, the instrumentation of the building model recently tested to destruction on the shake table at LNEC in Lisbon has yielded records that will provide valuable insight into the usability of the accelerographs installed by TNO in more than 200 houses in the Groningen field. However, the lack of site-specific measures of near-surface

V_s at the locations of these houses limits their use in the model derivation but they will be added to the database used to derive a spatial correlation model (see below).

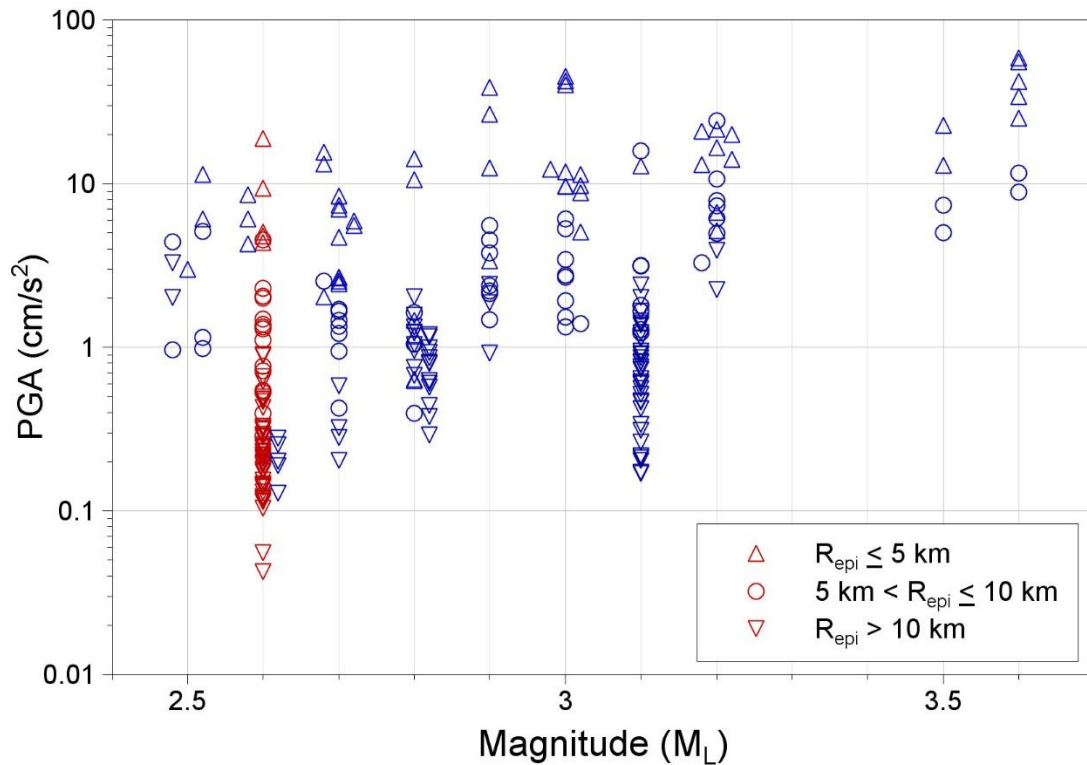


Figure 13.4. Geometric mean PGA values from earthquakes in the database as a function of magnitude; where there are two or more events with the same magnitude, the symbols are displaced left and/or right for greater clarity. The symbols indicate the range of epicentral distance. Blue symbols are the records in the V4 database, the red show those from ML 2.6 Slochteren earthquake of 27 May 2017.

Sigma Model

The inter-event variability represented by the standard deviation τ will be further explored, especially since the current model assumes that the value determined from the small-magnitude recordings applies also at larger magnitudes without modification. Consideration could be given to alternative values at larger magnitudes, informed by other GMMs. In the small-magnitude range, the statistical uncertainty on the estimates of τ from mixed-effects analysis could inform the epistemic uncertainty on this variability independently of the median models.

The current estimates of τ account for the uncertainty in the magnitude estimates. Strictly speaking, the true magnitude of each earthquakes should be the same for all spectral periods and this could be accounted for by expanding the covariance matrix to include all the spectral periods at once. This approach, however, can be very cumbersome, for which reason, the alternative approach proposed by Khuen & Abrahamson (2017) may also be considered.

The intra-event variability in the prediction of the rock motions will also be re-visited. The single-station variability represented by ϕ_{ss} will be re-evaluated, in particular to consider if the short-period increase that was applied at the V3 stage to reflect results emerging from the NGA-East project are really applicable in this case. The issue of whether or not this element of variability may change with independent variables such as magnitude and distance will be addressed.

A Fully Non-Ergodic Model?

The use of single-station sigma, mentioned above, is justified by the inclusion of site-specific amplification effects and their associated uncertainty. This represents a partially non-ergodic model. Since the earthquakes all originate in the gas reservoir and the waves propagate to the NS_B through the same Zechstein and chalk layers, there should be scope for a fully non-ergodic model, and this will continue to be explored. In this direction, reference will be made to recent work on this topic such as that of Landwehr *et al.* (2016).

Component-to-Component Variability

The Groningen data display very large component-to-component variability, which has been shown to be at least partly the result of the records being obtained at short source-to-site distances. However, the influence of the record orientations has so far not been considered in these analyses, and in order to refine the model this will now be taken into account. Consideration will be given to whether the records are exceptionally polarised on the as-recorded orientation, and how the ratio of the horizontal components varies with rotation (and, in particular, the values obtained at the orientation giving median amplitudes of motion).

Period-to-Period Correlation

For the implementation of the GMM in seismic risk calculations, period-to-period correlations of the spectral accelerations need to be considered. The Groningen data are insufficient to allow the derivation of a reliable field-specific model for this correlation across the full range of periods of interest, for which reason published models—shown not to be contradicted by the Groningen recordings—have been adopted. In moving forward, consideration will be given to any new models that have emerged, including the recent proposal by Kotha *et al.* (2017), which suggests that the period-to-period correlation may be magnitude dependent.

Dynamic Soil Properties

An important issue is the low-strain damping used in the site response analyses, which for the V3 and V4 models has been based on analyses of recordings from borehole recordings obtained just outside the limits of the gas field. New work is now underway making use of

the recordings from the extensive array of borehole instruments—the G-stations—and the conclusions from this study may lead to modification of the damping values used in the site response analyses.

Another element of the model that will be updated is the modulus reduction and damping curves applied to the Holland peats encountered at shallow depths in many parts of the study area. Deltares have conducted extensive laboratory testing on samples of the Holland peat, which have led to modification of the MRD curves to be applied to these shallower peat deposits.

HVSR Measurements

A simple exercise that can be conducted to check the site amplification factors calculated for the recording stations (in order to deconvolve the response spectra from the surface to the NS_B horizon) is to estimate horizontal-to-vertical spectral ratios (HVSR) using the records obtained at these locations. These ratios should identify the fundamental periods of the sites, which can then be compared with those implied by the transfer functions calculated using the site profiles.

Non-linear vs Equivalent Linear Site Response Analyses

Although we are satisfied that a robust case has been made for the use of equivalent linear (EQL) site response analyses, it will be valuable to vindicate this modelling choice through some comparisons with fully non-linear (NL) site response analyses. Such comparisons will be made for some selected zones within the field, using common dynamic properties in the two analytical approaches.

Refining the Scenario-Dependence of the Amplification Factors

An important innovation in this work has been the introduction of magnitude- and distance-dependence of the AFs for short response periods. In the forward modelling for the entire field, the small magnitude range was insufficiently sampled by the NS_B input motions used in the site response analyses, leading to poor constraint of the M-R dependence of the AFs at the lower magnitude range. We believe that this is the primary cause of the current bias in the surface predictions at periods of less than 0.25 s with respect to the recorded motions. Consequently, the V5 site response analyses will be run with input motions more carefully sampled in the small-magnitude range and the functional form for the M-R dependence of the AFs may consequently be refined.

While this is expected to remove the bias seen in the V4 predictions of the existing surface motions, it is also recognised that the bias occurs in the period range where EQL site response analysis tends to be problematic. Consequently, the spectral shapes returned by EQL

site response analyses will also be visually examined to judge whether the results are indeed reliable.

Site-to-Site Variability

The basis for the field zonation within the GMM is to refine the initial geological zonation such that within each zone there is a reasonably consistent AF across all locations and across the full range of response periods. The degree to which this has been achieved should be reflected by reduced values of standard deviation of $\ln(AF)$ within the zones. A straightforward exercise to check the degree of benefit added by the zonation will be to calculate the AFs and associated variability for the entire field, and then perhaps for major aggregations of zones (e.g., all those to the north treated as a single group and all the zones to the south as another). The expectation is that the $\sigma[\ln(AF)]$ for the entire field will be appreciably larger than the variability found within the zones.

Vertical-to-Horizontal Ratios

To date, relatively little attention has been paid to the derivation of the V/H ratios, the adopted approach being to simply adapt published models for these ratios to match the Groningen data. Discussions will be held with the structural modelling and fragility teams to ascertain the importance of the vertical motions. If the outcomes of these discussions are that the vertical motions are important, then this issue will be re-visited and explored in greater depth. Possible avenues of investigation including the degree of influence of the site response, as opposed to magnitude and distance, on the ratios.

Duration Model

The predictions of durations has improved significantly during the evolution of the GMM and the V4 model for this parameter produces reasonable results across the magnitude range. Nonetheless, the durations are somewhat longer for larger magnitudes and longer distances than those obtained from empirical GMPEs derived from recordings of tectonic earthquakes. At this time it is not known to what degree this is a genuine feature of the Groningen motions, resulting from the effects of the velocity profile above the reservoir, or whether it is influenced by the tendency of EXSIM to yield long durations. One experiment being designed to explore this issue is to use the full waveform simulations of URC (ExxonMobil) to explore the effect of the Groningen velocity profile on durations when compared with the durations obtained with more typical profiles (i.e., V_s monotonically increasing with depth). Such an exercise would not depend on the capacity of those simulations to accurately predict durations in an absolute sense since the objective would be to quantify the relative path contribution resulting from the specific velocity structure encountered in Groningen.

Attention will also be given to the possible influence of high-frequency noise in the records on the calculated durations. The physical justification for functional form of the duration prediction model will also be explored and strengthened.

Spatial Correlation of Ground Motions

Finally, in parallel with the development of the V5 GMM, an exercise will be conducted to explore the issue of spatial correlation of ground motions in the Groningen field. Using recordings from the B- and G-stations, as well as those from the TNO-installed household accelerographs and the new flexible geophone network that NAM has operated at different locations around the field in recent months (Figure 13.5), an empirical spatial correlation model will be derived. This will then be compared with the effective distances over which full correlation is assumed in the current implementation of the GMM in the hazard and risk model, to assess the degree to which spatial correlation is being adequately accounted for in the hazard and risk calculations.

This exercise will be separate from the V5 model development since spatial correlation only becomes important for spatially aggregated risk metrics (*i.e.*, group risk) and it is yet to be confirmed whether this is a required outcome from the model. This is another area where the URC/ExxonMobil simulations may provide valuable additional constraint.

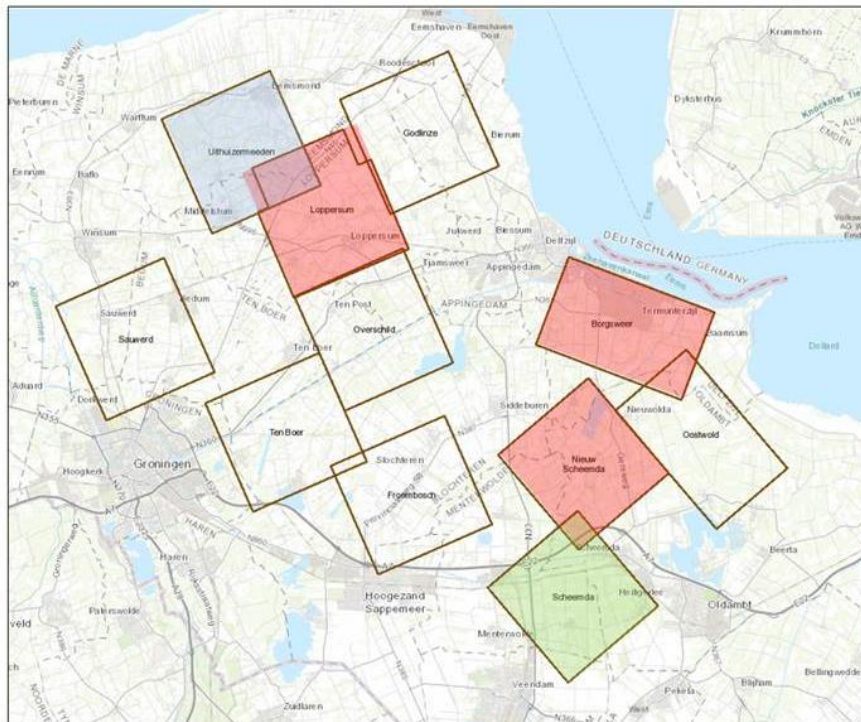


Figure 13.5. Deployment areas (“patches”) for the NAM flexible network of 400 geophones, where the instruments are installed for periods of about 6 weeks. The red areas have already been covered, the green was the most recent area of installation and the blue the next location to be targeted. The blank areas are planned deployment areas. (*Courtesy of Remco Romijn, NAM.*)

REFERENCES

- Abercrombie, R.E. & P.C. Leary (1993). Source parameters of small earthquakes recorded at 2.5 km depth, Cajon Pass, southern California: implications for earthquake scaling. *Geophysical Research Letters* **20**, 1511-1514.
- Abrahamson, N.A. & R.R. Youngs (1992). A stable algorithm for regression analyses using the random effects model. . *Bulletin of the Seismological Society of America* **82**(1), 505-510.
- Abrahamson, N.A., W.J. Silva & R. Kamai (2014). Summary of the ASK14 ground motion relation for active crustal regions. *Earthquake Spectra* **30**(3), 2015-1055.
- Afshari, K. & J.P. Stewart (2015). Effectiveness of 1D ground response analyses at predicting site response at California vertical array sites. *Proceedings, SMIP 15 Seminar on Utilization of Strong-Motion Data*, Davis, CA.
- Afshari, K. & J.P. Stewart (2016a). Physically parameterized prediction equations for significant duration in active crustal regions. *Earthquake Spectra* **32**(4), 2057-2081.
- Afshari, K. & J.P. Stewart (2016b). Validation of duration parameters from SCEC broadband platform simulated ground motions. *Seismological Research Letters* **87**(6), 1355-1362.
- Afshari, K. & J.P. Stewart (2016c). Implications of California Vertical Array data for modeling of non-ergodic site response. *Proceedings of SMIP 2016 Seminar on Utilization of Strong Motion Data*, California Strong Motion Instrumentation Program, Irvine, CA.
- Akkar, S. & J.J. Bommer (2006). Influence of long-period filter cut-off on elastic spectral displacements. *Earthquake Engineering & Structural Dynamics* **35**(9), 1145-1165.
- Akkar, S., M.A. Sandikkaya & J.J. Bommer (2014a). Empirical ground-motion models for point- and extended-source crustal earthquake scenarios in Europe and the Middle East. *Bulletin of Earthquake Engineering* **12**(1), 359-387. *Erratum*: **12**(1), 389-390.
- Akkar, S., M.A. Sandikkaya & B.Ö. Ay (2014b). Compatible ground-motion prediction equations for damping scaling factors and vertical-to-horizontal spectral amplitude ratios for the broader European region. *Bulletin of Earthquake Engineering* **12**(1), 517-547.
- Al Atik, L. (2015). *NGA-East: Ground-motion standard deviation models for central and eastern United States*. PEER Report 2015/07, Pacific Earthquake Engineering Research Center, UC Berkeley, June 2015, 217 pp.
- Al Atik, L., N.A. Abrahamson, J.J. Bommer, F. Scherbaum, F. Cotton & N. Kuehn (2010). The variability of ground-motion prediction models and its components. *Seismological Research Letters* **81**(5), 783-793.
- Ancheta, R.D., R.B. Darragh, J.P. Stewart, E. Seyhan, W.J. Silva, B.S.-J. Chiou, K.E. Wooddell, R.W. Graves, A.R. Kottke, D.M. Boore, T. Kishida & J.L. Donahue (2014). NGA-West2 database. *Earthquake Spectra* **30**(3), 989-1005.
- Anderson, J.G. & J.N. Brune (1999). Probabilistic seismic hazard assessment without the ergodic assumption. *Seismological Research Letters* **70**, 19-28.
- Anderson, J.G. & S.E. Hough (1984). A model for the shape of the Fourier amplitude spectrum of acceleration at high frequencies. *Bulletin of the Seismological Society of America* **74**, 1969-1993.

- Andrus, R.D., N.P. Mohanan, P. Piratheepan, B.S. Ellis, & T.L. Holzer, (2007). Predicting shear-wave velocity from cone penetration resistance. *Proceedings of the 4th International Conference on Earthquake Geotechnical Engineering*, Thessaloniki, Greece, 25-28.
- Ang, A.H-S & W.H. Tang (2007). *Probability Concepts in Engineering*, 2nd Ed. John Wiley & Sons, Inc., Hoboken, NJ.
- Assimaki, D. & E. Kausel (2002). An equivalent linear algorithm with frequency- and pressure-dependent moduli and damping for seismic analysis of deep sites. *Soil Dynamics & Earthquake Engineering*, **22**, 959-965.
- Assimaki D. & W. Li (2012). Site- and ground motion-dependent nonlinear effects in seismological model predictions. *Soil Dynamics & Earthquake Engineering* **32**(1), 143–151.
- Atkinson, G.M. (2006). Single-station sigma. *Bulletin of the Seismological Society of America* **96**, 446-455.
- Atkinson, G.M. (2015). Ground-motion prediction equation for small-to-moderate events at short hypocentral distances, with application to induced-seismicity hazards. *Bulletin of the Seismological Society of America* **105**(2A), 981-992.
- Atkinson, G.M. & D.M. Boore (2014). The attenuation of Fourier amplitudes for rock sites in eastern North America. *Bulletin of the Seismological Society of America* **104**, 513--528.
- Baker, J.W. & B.A. Bradley (2017). Intensity measure correlations observed in the NGA-West2 database, and dependence of correlations on rupture and site parameters. *Earthquake Spectra*, in press. doi: <http://dx.doi.org/10.1193/060716EQS095M>.
- Baker, J.W. & C.A. Cornell (2006a). Which spectral acceleration are you using? *Earthquake Spectra* **22**(2), 293-312.
- Baker, J.W. & C.A. Cornell (2006b). Spectral shape, epsilon and record selection. *Earthquake Engineering & Structural Dynamics* **35**, 1077–1095.
- Baker, J.W. & N. Jayaram (2008). Correlation of spectral acceleration value from NGA ground motion models. *Earthquake Spectra* **24**(1), 299-317.
- Bal, I.E, J.J. Bommer, P.J. Stafford, H. Crowley & R. Pinho (2010). The influence of geographical resolution of urban exposure data in an earthquake loss model for Istanbul. *Earthquake Spectra* **26**(3), 619-634.
- Bala, A., V. Raileanu, I. Zihan, V. Ciugudean & B. Grecu (2006). Physical and dynamic properties of shallow sedimentary rocks in Bucharest metropolitan area. *Romanian Reports in Geophysics* **58**(2), 221-250.
- Baltay, A.S. & T.C. Hanks (2014). Understanding the magnitude dependence of PGA and PGV in NGA-West 2 data. *Bulletin of the Seismological Society of America* **104**(6), 2851-2865.
- Bazzurro, P. & C.A. Cornell (2004a). Ground-motion amplification in nonlinear soil sites with uncertain properties. *Bulletin of the Seismological Society of America* **94**, 2090-2109.
- Bazzurro, P. & C.A. Cornell (2004b). Nonlinear soil-site effects in probabilistic seismic hazard analysis. *Bulletin of the Seismological Society of America* **94**(6), 2110-2123.
- Benjamin, J. R. & A. Cornell, A. (1970). *Probability, statistics, and decision for civil engineers*. McGraw-Hill, New York.

- Boatwright, J. (1978). Detailed spectral analysis of two small New York State earthquakes. *Bulletin of the Seismological Society of America* **68**, 1117-1131.
- Bommer, J. J. & S. Akkar (2012). Consistent source-to-site distance metrics in ground-motion prediction equations and seismic source models for PSHA. *Earthquake Spectra* **28**(1), 1-15.
- Bommer, J.J., S. Akkar & S. Drouet (2012). Extending ground-motion prediction equations for spectral ordinates to higher response frequencies. *Bulletin of Earthquake Engineering* **10**(2), 379-399.
- Bommer, J.J., S. Akkar & Ö. Kale (2011). A model for vertical-to-horizontal response spectral ratios for Europe and the Middle East. *Bulletin of the Seismological Society of America* **101**(4), 1783-1806.
- Bommer, J.J. & J.E. Alarcón (2006). The prediction and use of peak ground velocity. *Journal of Earthquake Engineering* **10**(1), 1-31.
- Bommer, J.J., S.J. Bourne, H. Crowley, B. Edwards, P. Kruiver, S. Oates & A. Rodriguez-Marek (2015b). *Seismic design loads for the Groningen Forum*. A report prepared for NAM, version 3, 26 June 2015, 88 pp.
- Bommer, J.J., K.J. Coppersmith, R.T. Coppersmith, K.L. Hanson, A. Mangongolo, J. Neveling, E.M. Rathje, A. Rodriguez-Marek, F. Scherbaum, R. Shelembe, P.J. Stafford & F.O. Strasser (2015c). A SSHAC Level 3 probabilistic seismic hazard analysis for a new-build nuclear site in South Africa. *Earthquake Spectra* **31**(2), 661-698.
- Bommer J. & B. Dost (2014). *Version 0 ground-motion prediction equations*. 16 June 2014, 17 pp.
- Bommer, J.J., B. Dost, B. Edwards, P.P. Kruiver, P. Meijers, M. Ntinalexis, B. Polidoro, A. Rodriguez-Marek & P.J. Stafford (2015d). *Development of Version 2 GMPEs for response spectral accelerations and significant durations from induced earthquakes in the Groningen field*. Version 2, 29 October 2016, 515 pp.
- Bommer, J.J., B. Dost, B. Edwards, P.J. Stafford, J. van Elk, D. Doornhof & M. Ntinalexis (2016a). Developing an application-specific ground-motion model for induced seismicity. *Bulletin of the Seismological Society of America* **106**(1), 158-173.
- Bommer, J.J., B. Dost, B. Edwards, P.P. Kruiver, P. Meijer, M. Ntinalexis, A. Rodriguez-Marek & P.J. Stafford (2016b). *Development of V3 GMPEs for response spectral accelerations and significant durations from induced earthquakes in the Groningen field*. Version 0, 8 July 2016, 476 pp.
- Bommer, J.J., J. Douglas, F. Scherbaum, F. Cotton, H. Bungum & D. Fäh (2010). On the selection of ground-motion prediction equations for seismic hazard analysis. *Seismological Research Letters* **81**(5), 794-801.
- Bommer, J.J., G. Magenes, J. Hancock & P. Penazzo (2004). The influence of strong-motion duration on the seismic response of masonry structures. *Bulletin of Earthquake Engineering* **2**(1), 1-26.
- Bommer, J.J. & A. Martinez-Pereira (1999). The effective duration of earthquake strong motion. *Journal of Earthquake Engineering* **3**(2), 127-172.
- Bommer, J.J. & R. Mendis (2005). Scaling of displacement spectral ordinates with damping ratios. *Earthquake Engineering & Structural Dynamics* **34**(2), 145-165.

- Bommer, J.J., S. Oates, J.M. Cepeda, C. Lindholm, J.F. Bird, R. Torres, G. Marroquín & J. Rivas (2006). Control of hazard due to seismicity induced by a hot fractured rock geothermal project. *Engineering Geology* **83**(4), 287-306.
- Bommer, J.J., R. Pinho & H. Crowley (2005). Using displacement-based earthquake loss assessment in the selection of seismic code design levels. *Proceeding of ICROSSAR'05 (International Conference on Structural Safety and Reliability)*, Rome, 3567-3574.
- Bommer, J.J., P.J. Stafford & J.E. Alarcón (2009). Empirical equations for the prediction of the significant, bracketed and uniform duration of earthquake ground motion. *Bulletin of the Seismological Society of America* **99**(6), 3217-3233.
- Bommer, J.J., P.J. Stafford, B. Edwards, B. Dost & M. Ntinalexis (2015a). *Development of version 1 GMPEs for response spectral accelerations and for strong-motion durations*. Version 2, 21 June 2015, 304 pp.
- Bommer, J.J., P.J. Stafford, B. Edwards, B. Dost, E. van Dedem, A. Rodriguez-Marek, P. Kruiver, J. van Elk, D. Doornhof & M. Ntinalexis (2017). Framework for a ground-motion model for induced seismic hazard and risk analysis in the Groningen gas field, The Netherlands. *Earthquake Spectra* **33**(2), *in press*.
- Boore, D.M. (2005a). *SMSIM – Fortran programs for simulating ground motions from earthquakes: Version 2.3—A revision of OFR 96-80*. US Geological Survey Open-File Report 00-509, 55 pp.
- Boore, D.M. (2005b). Erratum: Equations for estimating horizontal response spectra and peak acceleration from western north American earthquakes: A summary of recent work, by D.M. Boore, W.B. Joyner and T.E. Fumal. *Seismological Research Letters* **76**(3), 368-369.
- Boore, D. M. (2009). Comparing stochastic point-source and finite-source ground-motion simulations: SMSIM and EXSIM. *Bulletin of the Seismological Society of America* **99**, 3202-3216.
- Boore, D. M. & W. B. Joyner (1984). A note on the use of random vibration theory to predict peak amplitudes of transient signals. *Bulletin of the Seismological Society of America* **74**(5), 2035–2039.
- Boore, D.M., J.P. Stewart, E. Seyhan & G.M. Atkinson (2014). NGA-West2 equations for predicting PGA, PGV, and 5% damped PSA for shallow crustal earthquakes. *Earthquake Spectra* **30**(3).
- Boore, D. M. & E. M. Thompson (2012). Empirical improvements for estimating earthquake response spectra with random vibration theory. *Bulletin of the Seismological Society of America* **102**(2), 761–772.
- Boore, D.M. & E.M. Thompson (2014). Path durations for use in the stochastic-method simulations of ground motions. *Bulletin of the Seismological Society of America* **104**(5), 2541-2552.
- Boore, D.M. (2010). Orientation-independent, nongeometric-mean measures of seismic intensity from two horizontal components of motion. *Bulletin of the Seismological Society of America* **100**(4), 1830-1835.
- Boore, D.M. & J. Boatwright (1984). Average body-wave radiation coefficients. *Bulletin of the Seismological Society of America* **74**, 1615-1621.
- Boore, D.M. & J.J. Bommer (2005). Processing strong-motion accelerograms: needs, options and consequences. *Soil Dynamics & Earthquake Engineering* **25**(2), 93-115.
- Boore, D.M., J.F. Gibbs, W.B. Joyner, J.C. Tinsley & D.J. Ponti (2003). Estimated ground motion from the 1994 Northridge, California, earthquake at the site of the Interstate 10 and La Cienega Boulevard

- bridge collapse, West Los Angeles, California. *Bulletin of the Seismological Society of America* **93**(6), 2737-2751.
- Boore, D.M., J.P. Stewart, M. Seyhan & G.M. Atkinson (2014). NGA-West2 equations for predicting PGA, PGV, and 5% damped PSA for shallow crustal earthquake. *Earthquake Spectra* **30**(3), 1057-1085.
- Boore, D.M. & E.M. Thompson (2014). Path durations for use in the stochastic-method simulations of ground motions. *Bulletin of the Seismological Society of America* **104**(5), 2541-2552.
- Boore, D.M., Watson-Lamprey, J. & Abrahamson, N.A. (2006). Orientation-independent measures of ground motion. *Bulletin of the Seismological Society of America* **94**(4A), 1502-1511.
- Borcherdt, R.D. (1994). Estimates of site-dependent response spectra for design (methodology and justification). *Earthquake Spectra* **10**(4), 617-653.
- Borjse, H. & E. Langius (2015). *Monitoring network building vibrations*. TNO report, 1 April 2015, 133 pp.
- Bosch, J.H.A., R. Harting & J.L. Gunnink (2014). *Lithologische karakterisering van de ondiepe ondergrond van Noord-Nederland (Topsysteem hoofdgebied 5)*. Geological Survey of the Netherlands TNO report 2014-R10680.
- Boulanger, R.W., R. Arulnathan, L.F. Harder, R.A. Torres & M.W. Driller (1997). *Dynamic properties of Sherman Island peat*. Report UCD/CGM-97/01, Department of Civil & Environmental Engineering, University of California, Davis, California.
- Bourne, S.J., S.J. Oates, J. van Elk & D. Doornhof (2014). A seismological model for earthquakes induced by fluid extraction from a subsurface reservoir. *Journal of Geophysical Research Solid Earth* **119**, doi: 10.1002/201JB011663.
- Bourne, S.J., S.J. Oates, J.J. Bommer, B. Dost, J. van Elk & D. Doornhof (2015). A Monte Carlo method for probabilistic hazard assessment of induced seismicity due to conventional natural gas production. *Bulletin of the Seismological Society of America* **105**(3), 1721-1738.
- Bozorgnia, Y. & K.W. Campbell (2016a). Vertical ground motion model for PGA, PGV, and linear response spectra using the NGA-West2 database. *Earthquake Spectra* **32**, 979-1004.
- Bozorgnia, Y. & K.W. Campbell (2016b). Ground motion model for the vertical-to-horizontal (V/H ratios) of PGA, PGV, and response spectra. *Earthquake Spectra* **32**(2), 951-978.
- Bradley, B.A. (2011). Correlation of significant duration with amplitude and cumulative intensity measures and its use in ground motion selection. *Journal of Earthquake Engineering* **15**(6), 809-832.
- Brune, J.N. (1970). Tectonic stress and the spectra of seismic shear waves from earthquakes. *Journal of Geophysical Research* **75**(26), 4997-5009. Correction (1971), **76**(20), 5002.
- Cacace, M. (2008). *Stress and strain modelling of the Central European Basin System*. Dissertation, Free University of Berlin.
- Campbell, K.W. (2009). Estimates of shear-wave Q and κ_0 for unconsolidated and semiconsolidated sediments in Eastern North America. *Bulletin of the Seismological Society of America* **99**(4), 2365-2392.
- Campbell, K.W. & Y. Bozorgnia (2003). Updated near-source ground-motion (attenuation) relations for the horizontal and vertical components of peak ground acceleration and acceleration response spectra. *Bulletin of the Seismological Society of America* **93**(1), 314-331.

Campbell, K.W. & Y. Bozorgnia (2007). *Campbell-Bozorgnia NGA Ground Motion Relations for the Geometric Mean Horizontal Component of Peak and Spectral Ground Motion Parameters*. PEER Report 2007/02, Pacific Earthquake Engineering Research Center, University of California at Berkeley, 240 pp.

Campbell, K.W. & Y. Bozorgnia (2014). NGA-West2 ground motion model for the average horizontal components of PGA, PGV, and 5%-damped elastic pseudo-acceleration response spectra. *Earthquake Spectra* **30**(3), 1087-1115.

Chandramohan, R., J.W. Baker & G.G. Deierlein (2016). Quantifying the influence of ground motion duration on structural collapse capacity using spectrally equivalent records. *Earthquake Spectra* **32**(2), 927-950.

Chiou, B.S.-J. & R.R. Youngs (2008). An NGA model for the average horizontal component of peak ground motion and response spectra. *Earthquake Spectra* **24**(1), 173-215.

Chiou, B.S.J. & R.R. Youngs (2014). Update of the Chiou and Youngs NGA model for the average horizontal component of peak ground motion and response spectra. *Earthquake Spectra* **30**(3), 1117-1153.

Chopra, A.K. (2007). *Dynamics of Structures: Theory and Applications to Earthquake Engineering*. Prentice Hall, Upper Saddle River, New Jersey, third edition.

Clark, D., A. McPherson, T. Allen & M. De Kool (2014). Coseismic surface deformation caused by the 23 March 2012 M_w 5.4 Ernabella (Pukatja) earthquake, central Australia: implications for fault scaling relations in cratonic settings. *Bulletin of the Seismological Society of America* **104**, 24-39.

Cools, R. & O. Rabinowitz (1993). Monomial cubature rules since "Shroud": a compilation. *Journal of Computational and Applied Mathematics* **48**, 309–326.

Cotton, F., R. Archuleta & M. Causse (2013). What is sigma of the stress drop? *Seismological Research Letters* **84**(1), 42-48.

Crowley, H., V. Silva, I.E. Bal & R. Pinho (2012). Calibration of seismic design codes using loss estimation. *Proceedings of 15th World Conference on Earthquake Engineering*, Lisbon, Portugal, Paper no. 4891.

Crowley, H., P.J. Stafford & J.J. Bommer (2008). Can earthquake loss models be validated using field observations? *Journal of Earthquake Engineering* **12**(7), 1078-1104.

Darendeli, M. (2001). *Development of a new family of normalized modulus reduction and material damping curves*. Ph.D. Thesis, Dept. of Civil Eng., University of Texas, Austin, TX.

Dawood, H., A. Rodriguez-Marek, J. Bayless & E.M. Thompson (2016). A flatfile for the KiK-net database processed using an automated protocol. *Earthquake Spectra* **32**(2), 1281-1302.

De Crook, T. & B. Wassing (1996). Opslingering van trillingen bij aardbevingen in Noord-Nederland, *KNMI-RGD interim report*, 14pp.

De Crook, T. & B. Wassing (2001). Voorspelling van de opslingering van trillingen bij aardbevingen, *Geotechniek*, 47-53.

Deichmann, N. (2006). Local magnitude: a moment revisited. *Bulletin of the Seismological Society of America* **96**, 1267-1277

- De Kleine, M.P.E., R.P. Noorlandt, G.L. de lange, M. Karaoulis, & P.P. Kruiver (2016). Geophysical measurements of shear-wave velocity at KNMI accelerograph stations in the Groningen gas field area. Deltares report 1210624-000-BGS-0007.
- Den Haan, E.J. & G.A.M. Kruse (2007). Characteristics and engineering properties of Dutch peats. *Proceedings of 2nd International Workshop on Characterisation and Engineering Properties of Natural Soils*, Singapore, Taylor & Francis, vol. 3, 2108-2133.
- Douglas, J., B. Edwards, V. Convertito, N. Sharma, A. Tramelli, D. Kraaijpoel, B. Mena Cabrera, N. Maercklin & C. Troise (2013). Predicting ground motion from induced earthquakes in geothermal areas. *Bulletin of the Seismological Society of America* **103**(3), 1875–1897.
- Douglas, J. & P. Jousset (2011). Modeling the difference in ground-motion magnitude-scaling in small and large earthquakes. *Seismological Research Letters* **82**(4), 504-508.
- Dost, B., B. Edwards & J.J. Bommer (2016). *Local and moment magnitudes in the Groningen field*. Unpublished report, 4 March 2016, 36 pp.
- Edwards, B., D. Fäh & D. Giardini (2011). Attenuation of seismic shear wave energy in Switzerland. *Geophysical Journal International* **185**, 967-984.
- Edwards, B., A. Rietbrock, J. J. Bommer & B. Baptie (2008). The acquisition of source, path, and site effects from micro-earthquake recordings using *q* tomography: Application to the United Kingdom. *Bulletin of the Seismological Society of America* **98**, 1915-1935.
- EPRI (2013). *Seismic Evaluation Guidance. Screening, Prioritization and Implementation Details (SPID) for the Resolution of Fukushima Near-Term Task Force Recommendation 2.1: Seismic*. EPRI Report No. 1025281, February Electrical Power Research Institute, Palo Alto, California.
- Ernst, F. (2013). Modal Elastic Inversion. *75th EAGE Conference and Exhibition*, London.
- Eshelby, J. D. (1957). The determination of the elastic field of an ellipsoidal inclusion, and related problems. *Proceedings of the Royal Society of London: Series-A* **241**, 376-396.
- Esposito, S. & I. Iervolino (2011). PGA and PGV spatial correlation models based on European multievent datasets. *Bulletin of the Seismological Society of America* **101**(5), 2532-2541.
- Esposito, S. & I. Iervolino (2012). Spatial correlation of spectral acceleration in European data. *Bulletin of the Seismological Society of America* **102**(6), 2781-2788.
- Goda, K. & G.M. Atkinson (2010). Intraevent spatial correlation of ground-motion parameters using SK-net data. *Bulletin of the Seismological Society of America* **100**(6), 3055-3067.
- Grace, H., J.K.M. Henry, A.W. Skempton, R.F. Lloyd Jones, H.Q. Golder, M.S. Millard, M.J. Tomlinson, R. Broadnet, W.R. Rangeley, C.R. Hoare & J. Alston (1957). Discussion on Airport Paper No. 35: "The Planning and Design of the New Hong Kong Airport". In: *Proceedings of Institute of Civil Engineering* **7**, 305–325.
- Grazier, V. (2014). Comment on "Comparison of time series and random vibration theory site-response methods" by Albert R. Kottke and Ellen M. Rathje. *Bulletin of the Seismological Society of America* **104**(1), 540-546.
- Gülerce, Z. & N.A. Abrahamson (2011). Site-specific design spectra for vertical ground motion. *Earthquake Spectra* **27**(4), 1023-1047.
- Hanks, T.C. & H. Kanamori (1979). Moment magnitude scale. *Journal of Geophysical Research* **84**, 2348-2350.

- Hardin, B.O. (1978). The nature of stress-strain behavior for soils. *Proceedings of the ASCE Geotechnical Engineering Division Specialty Conference on Earthquake Engineering and Soil Dynamics*, Pasadena, California, June 19-21, 1978.
- Hashash, Y.M.A., D.R. Groholski & C. Phillips (2010). Recent advances in nonlinear site response analysis. *Proceedings of the 5th International Conference on Recent Advances in Geotechnical Earthquake Engineering and Soil Dynamics and Symposium in honor of Prof. Idriss*, May 24-29 San Diego, California.
- Hashash, Y.M.A., M.I. Musgrove, J.A. Harmon, D.R. Groholski, C.A. Phillips & D. Park (2015). *User Manual for DEEPSOIL 6.0.*, 116 pp.
- Hashash, Y.M.A. & D. Park (2002). Viscous damping formulation and high frequency motion propagation in nonlinear site response analysis. *Soil Dynamics & Earthquake Engineering*, **22**(7), 611–624.
- Hauksson, E., T. Teng & T.L.Henyey (1987). Results from a 1500m deep, three-level downhole seismometer array: site response, low Q values and f_{max} . *Bulletin of the Seismological Society of America* **77**, 1883-1904.
- Hofman, R., E. Ruigrok, B. Dost & H. Paulssen (2017). A shallow velocity model for the Groningen area in the Netherlands. Submitted to *Journal of Geophysical Research*.
- Iervolino, I., G. Manfredi & E. Cosenza (2006). Ground motion duration effects on nonlinear seismic response. *Earthquake Engineering & Structural Dynamics* **35**(1), 21-38.
- Jayaram, N. & J.W. Baker (2009). Correlation model for spatially distributed ground motion intensities. *Earthquake Engineering & Structural Dynamics* **38**(15), 1687-1708.
- Jamiolkowski M., S. Leroueil & D. Lo Presti (1991) Theme lecture: Design parameters from theory to practice. *Proceedings of Geo-Coast 2*, 877-917
- Joyner, W.B., R.E. Warrick & T.E. Fumal, T.E. (1981). The effect of quaternary alluvium on strong ground motion in the Coyote Lake, California, earthquake of 1979. *Bulletin of the Seismological Society of America* **71**(4), 1333-1349.
- Kaklamanos J., B.A. Bradley, E.M. Thompson & L.G. Baise (2013). Critical parameters affecting bias and variability in site-response analyses using KiK-net downhole array data. *Bulletin of the Seismological Society of America* **103**(3), 1733-1749.
- Kaklamanos, J., L.G. Baise, E.M. Thompson & L. Dorfmann (2015). Comparison of 1D linear, equivalent-linear, and nonlinear site response models at six KiK-net validation sites. *Soil Dynamics & Earthquake Engineering* **69**, 207-219.
- Kallioglou, P., T. Tika, G. Koninis, S. Papadopoulos & K. Pitilakis (2009). Shear modulus and damping ratio of organic soils. *Geotechnical and Geological Engineering* **27**(2), 217-235.
- Kempton, J.J. & J.P. Stewart (2006). Prediction equations for significant duration of earthquake ground motions considering site and near-source effects. *Earthquake Spectra* **22**(4), 985-1013.
- Kuehn, N.M. & N.A. Abrahamson (2017). The effect of uncertainty in predictor variables on the estimation of ground-motion prediction equations. Submitted to *Bulletin of the Seismological Society of America*.
- Kim, B. & Y.M.A. Hashash (2013). Site response analysis using downhole array recordings during the March 2011 Tohoku-Oki earthquake and the effect of long-duration ground motions. *Earthquake Spectra* **29**, 37-54.

- Kim B., Y.M.A. Hashash, A. Kottke, D. Assimaki, W. Li, E.M. Rathje, K.W. Campbell, W.J. Silva & J.P. Stewart (2013). A predictive model for the relative differences between nonlinear and equivalent-linear site response analyses. *Transactions, SMiRT-22*, Division IV, San Francisco, CA.
- Kim, B., Y.M.A. Hashash, J.P. Stewart, E.M. Rathje, J.A. Harmon, M.I. Musgrove, K.W. Campbell & W.J. Silva (2016). Relative differences between nonlinear and equivalent-linear 1D site response analyses. *Earthquake Spectra* **32**(3), 1845-1865.
- Kishida, T., R.W. Boulanger, N.A. Abrahamson, M.W. Driller & T.M. Wehling (2009a). Site effects for the Sacramento-San Joaquin delta. *Earthquake Spectra* **25**(2), 301-322.
- Kishida, T., R.W. Boulanger, N.A. Abrahamson, T.W. Wehling & M.W. Driller (2009b). Regression models for dynamic properties of highly organic soils. *Journal of Geotechnical and Geoenvironmental Engineering* **135**(4), 533-543.
- Konno, K. & T. Ohmachi (1998). Ground-motion characteristics estimated from spectral ratio between horizontal and vertical components of microtremor. *Bulletin of the Seismological Society of America* **88**, 228–241.
- Kotha, S.R., D. Bindi & F. Cotton (2017). Site-corrected magnitude and region dependent correlations of horizontal peak spectral amplitudes. *Submitted to Earthquake Spectra*.
- Kottke, A.R. & E.M. Rathje (2013). Comparisons of time series and random-vibration theory site-response methods. *Bulletin of the Seismological Society of America* **103**(3), 2111-2127.
- Kottke, A. (2010). *A Comparison of Seismic Site Response Methods*. Ph.D. Thesis, Dept. of Civil Eng., University of Texas, Austin, TX.
- Kottke, A.R. & E.M. Rathje (2008). *Technical Manual for Strata*. PEER Report 2008/10, Pacific Earthquake Engineering Research Center, University of California at Berkeley, February, 84 pp.
- Kramer, S.L. (1996). *Dynamic response of peat*. Washington State Department of Transportation, Report WA-RD 412.2, November 1996, 55 pp.
- Kramer S.L. (2000). Dynamic response of Mercer Slough peat. *Journal of Geotechnical and Geoenvironmental Engineering* **126**(6), 504-510.
- Kramer, S. L. & S. B. Paulsen (2004). Practical use of geotechnical site response models. *Proceedings of the International Workshop on Uncertainties in Nonlinear Soil Properties and their Impact on Modeling Dynamic Soil Response*, University of California, Berkeley.
- Kruiver, P.P., G. de Lange, A. Wiersma, P. Meijers, M. Korff, J. Peeters, J. Stafleu, R. Harting, R. Dambrink, F. Busschers, J. Gunnink (2015). *Geological schematisation of the shallow subsurface of Groningen - For site response to earthquakes for the Groningen gas field*. Deltares Report No. 1209862-005-GEO-0004-v5-r, 16 March 2015.
- Kruiver, P. P., E. van Dedem, E. Romijn, G. de Lange, M. Korff, J. Stafleu, J.L. Gunnink., A. Rodriguez-Marek, J.J. Bommer, J.J. van Elk & D. Doornhof (2017). An integrated shear-wave velocity model for the Groningen gas field, The Netherlands. *Bulletin of Earthquake Engineering*, DOI: 10.1007/s10518-017-0105-y.
- Kruiver, P.P. & A. Wiersma (2016). *Modifications of the Geological model for Site response at the Groningen Field - For GMPE version 3*. Deltares report 1209862-005-GEO-0009.
- Kulhawy, F.H. & P.H. Mayne (1990). *Manual on estimating soil properties for foundation design*, Report EPRI-EL-6800, Electric Power Research Institute, Palo Alto, California.

- Kwok A.O.L., J.P. Stewart & Y.M.A Hashash (2008). Nonlinear ground-response analysis of Turkey Flat shallow stiff-soil site to strong ground motion. *Bulletin of the Seismological Society of America* **98**(1), 331-343.
- Landwehr, N, N.M. Kuehn, T. Scheffer & N.A. Abrahamson (2016). A nonergodic ground-motion model for California with spatially varying coefficients. *Bulletin of the Seismological Society of America* **106**, 2574-2583.
- Lee, J. & R.A. Green (2014). An empirical significant duration relationship for stable continental regions. *Bulletin of Earthquake Engineering* **12**(1), 217-235.
- Lefebvre, G., & D. LeBoeuf (1987). Rate effects and cyclic loading of sensitive clays. *Journal of Geotechnical Engineering* **113**(5), 476-489.
- Leonard, M. (2014). Self-consistent earthquake fault-scaling relations: Update and extension to stable continental strike-slip faults. *Bulletin of the Seismological Society of America* **104**(6), 2953-2965.
- Li W. & D. Assimaki (2010). Site and ground motion dependent parametric uncertainty of nonlinear site response analyses in earthquake simulations. *Bulletin of the Seismological Society of America* **100**(3), 954-968.
- Li, X.S., Z. Wang, & C.K. Shen (1992). *SUMDES: a nonlinear procedure for response analysis of horizontally-layered sites subjected to multidirectional earthquake loading*, User's Manual, Department of Civil Engineering, University of California, Davis.
- Lin, P.-S., B.S.-J. Chiou, N.A. Abrahamson, M. Walling, C.-T. Lee & C.-T. Cheng (2011). Repeatable source, site, and path effects on the standard deviation for empirical ground-motion prediction models. *Bulletin of the Seismological Society of America* **101**, 2281-2295.
- Lui, L. & S. Pezeshk (1999). An improvement on the estimation of pseudoresponse spectral velocity using RVT method. *Bulletin of the Seismological Society of America* **89**(5), 1384-1389.
- Lunne, T., P.K. Robertson, & J.J.M. Powell (1997). *Cone Penetration Testing in Geotechnical Practice*. EF Spon/Blackie Academic, Routledge Publishers, London, 312 pp.
- Madariaga, R. (1976). Dynamics of an expanding circular fault. *Bulletin of the Seismological Society of America* **66**, 639-666.
- Matasovic, N. (2006). *D-MOD_2: a computer program for seismic response analysis of horizontally layered soil deposits, earthfill dams, and solid waste landfills*, User's Manual, GeoMotions, LLC, Lacey, Washington.
- Matasovic, N. & Y. Hashash (2012). *NCHRP428: Practices and procedures for site-specific evaluations of earthquake ground motions (A synthesis of highway practice)*. National Cooperative Highway Research Program, Transportation Research Board: 78 pages. Washington, D.C.
- Matasovic, N. & M. Vucetic (1993). Cyclic characterization of liquefiable sands. *ASCE Journal of Geotechnical Engineering* **119**(11), 1805-1822.
- McKenna, F. & G. L. Fenves (2001). *The OpenSees command language manual*, version 1.2. Pacific Earthquake Engineering Research Center, University of California at Berkeley, available at <http://opensees.berkeley.edu>.
- Menq, F.Y. (2003). *Dynamic Properties of Sandy and Gravelly Soils*, PhD Thesis, Department of Civil Engineering, University of Texas, Austin, TX.

- Motazedian, D. & G.M. Aktinson (2005). Stochastic finite-fault modelling based on a dynamic corner frequency. *Bulletin of the Seismological Society of America* **95**, 995-1010.
- NCHRP (2012). *Practices and Procedures for Site-Specific Evaluations of Earthquake Ground Motions*, Synthesis 428 (N. Matasovic and Y.M.A. Hashash). National Cooperative Highway Research Program, Transportation Research Board, Washington D.C.
- NEN (2006). NEN 6740:2006 nl, *Geotechnics - TGB 1990 - Basic requirements and loads*. Nederlands Normalisatie-instituut, Delft.
- NEN (2015). *Assessment of buildings in case of erection, reconstruction and disapproval - Basic rules for seismic actions; Induced earthquakes*. Draft NPR 9998, Nederlands Normalisatie-instituut, Delft.
- Ntinalexis, M., B. Polidoro, J.J. Bommer & B. Edwards (2015). *Selection of processing procedures for the accelerograph recordings of induced seismicity in Groningen*. Report prepared for NAM, 24 August 2015, 169 pp.
- Ntinalexis, M., J.J. Bommer & B. Dost (2016). *A database of ground-motion records from the Groningen field designated for the development of the Groningen V3 GMPEs*. Report prepared for NAM, 14 March 2016, 709 pp.
- Papaspiliou M., S. Kontoe & J.J. Bommer (2012). An exploration of incorporating site response into PSHA-part II: Sensitivity of hazard estimates to Site Response Approaches. *Journal of Soil Dynamics & Earthquake Engineering* **42**, 316–330.
- Pehlivan M. (2013). *Incorporating site response analysis and associated uncertainties into the seismic hazard assessment of nuclear facilities*. Ph.D. Thesis, Dept. of Civil Eng., University of Texas, Austin, TX.
- Pehlivan, M., E.M. Rathje & R.B. Gilbert (2012). Incorporating site-specific site response analysis into PSHA. *Second International Conference on Performance-Based Design in Earthquake Geotechnical Engineering*, Taormina, Italy.
- Phillips, C. & Y. Hashash (2009). Damping formulation for non-linear 1D site response analyses. *Soil Dynamics & Earthquake Engineering* **29**, 1143–1158.
- Pruiksma, J.P. (2016). *Nonlinear and equivalent linear site response analysis for the Groningen area*. TNO Report TNO 2016 R10460. 25 March.
- Pyke, R.M. (1979). Nonlinear soil models for irregular cyclic loadings. *ASCE Journal of Geotechnical Engineering* **105**(GT6), 715–726.
- Rathje, E.M. & A.R. Kottke (2011). Relative differences between equivalent-linear and nonlinear site response methods. *Proceedings of 5th International Conference on Earthquake Geotechnical Engineering*, Santiago, Chile.
- Rathje, E.M. & M.C. Ozbey (2006). Site-specific validation of random vibration theory-based seismic site response analysis. *ASCE Journal of Geotechnical & Geoenvironmental Engineering* **132**(7), 911–922.
- Rathje, E.M. & A.R. Kottke (2014). Reply to ‘Comment on ‘Comparison of Time Series and Random-Vibration Theory Site-Response Methods’ by V. Graizer’. *Bulletin of the Seismological Society of America* **104**(1), 547–550.
- Rathje, E.M., A.R. Kottke & W.L. Trent (2010). Influence of input motion and site property variabilities on seismic site response analysis. *Journal of Geotechnical and Geoenvironmental Engineering* **136**(4), 607-619.

- Régnier, J., L.F. Bonilla, P.-Y. Bard, E. Bertrand, F. Hollander, H. Kawase, D. Sicilia, & 47 others (2016). International benchmark on numerical simulations for 1D, nonlinear site response (PRENOLIN): verification phase based on canonical cases. *Bulletin of the Seismological Society of America* **106**(5), 2112-2135.
- Régnier, J., H. Cadet, L.F. Bonilla, E. Bertrand & J.-F. Semblat (2013). Assessing nonlinear behavior of soils in seismic site response: Statistical analysis on KiK-net strong-motion data. *Bulletin of the Seismological Society of America* **103**(3), 1750–1770.
- Rhoades, D.A. (1997). Estimation of attenuation relations for strong-motion data allowing for individual magnitude uncertainties. *Bulletin of the Seismological Society of America* **87**(6), 1674-1678.
- Rijkers, R.H.B., D.J. Huisman, G. de Lange, J.P. Weijers, & N. Witmans-Parker (1998). *Inventarisatie geomechanische, geochemische en geohydrologische eigenschappen van Tertiaire kleipakketten - CAR Fase II*. TNO report NITG 98-90-B, 167 p.
- Robertson, P.K. (1990). Soil classification using the cone penetration test. *Canadian Geotechnical Journal* **27**(1), 151-158.
- Robertson, P.K. & K.L. Cabal (2015). *Guide to Cone Penetration Testing*, 6th edition, Gregg Drilling & Testing, Inc.
- Rodriguez-Marek, A., F. Cotton, N.A. Abrahamson, S. Akkar, L. Al Atik, B. Edwards, G.A. Montalva & H. Dawood (2013). A model for single-station standard deviation using data from various tectonic regions, *Bulletin of the Seismological Society of America* **103**, 3149-3163.
- Rodriguez-Marek, A., G.A. Montalva, F. Cotton & F. Bonilla (2011). Analysis of single-station standard deviation using the KiK-net data. *Bulletin of the Seismological Society of America* **101**, 1242-1258.
- Rodriguez-Marek, A., E.M. Rathje, J.J. Bommer, F. Scherbaum & P.J. Stafford (2014). Application of single-station sigma and site response characterization in a probabilistic seismic hazard analysis for a new nuclear site. *Bulletin of the Seismological Society of America* **104**(4), 1601-1619.
- Sandikkaya, M.A., S. Akkar & P.-Y. Bard (2013). A nonlinear site-amplification model for the next pan-European ground-motion prediction equations. *Bulletin of the Seismological Society of America* **103**(1), 19-32.
- Scandella, L. & R. Paolucci (2010). Earthquake induced ground strains in the presence of strong lateral soil heterogeneities. *Bulletin of Earthquake Engineering* **8**, 1527-1546.
- Scherbaum, F. (1990). Combined inversion for the three-dimensional q structure and source parameters using microearthquake spectra. *Journal of Geophysical Research: Solid Earth* **95**, 12423-12438.
- Schnabel, P.B., J. Lysmer, & H.B. Seed (1972). *SHAKE, a Computer Program for Earthquake Response*. Earthquake Engineering Research Center Report EERC 72-12, University of California at Berkeley.
- Seed, H.B. & I.M. Idriss (1970). Analysis of ground motions at Union Bay, Seattle, during earthquakes and distant nuclear blasts. *Bulletin Seismological Society of America* **60**(1), 135-136.
- Sorensen, K. K., & N. Okkels (2013). Correlation between drained shear strength and plasticity index of undisturbed overconsolidated clays. *Proceedings of the 18th International Conference on Soil Mechanics and Geotechnical Engineering*, Paris, France, 423-428.

- Spetzler, J. & B. Dost (2017). Hypocentre estimation of induced earthquakes in Groningen. *Geophysical Journal International* **209**, 453-465.
- Stafford, P.J. (2014). Source-scaling relationships for the simulation of rupture geometry within probabilistic seismic-hazard analysis. *Bulletin of the Seismological Society of America* **104**(4), 1620-1634.
- Stafford, P.J., R. Mendis & J.J. Bommer (2008). The dependence of spectral damping ratios on duration and number of cycles. *ASCE Journal of Structural Engineering* **134**(8), 1364-1373.
- Stafford, P.J., A. Rodriguez-Marek, B. Edwards, P.P. Kruiver & J.J. Bommer (2017). Scenario dependence of linear site effect factors for short-period response spectral ordinates, submitted to the *Bulletin of the Seismological Society of America*.
- Stewart, J.P., K. Afshari & Y.M.A. Hashash (2014). *Guidelines for Performing Hazard-Consistent One-Dimensional Ground Response Analysis for Ground Motion Prediction*. PEER Report 2014/16, Pacific Earthquake Engineering Research Center, University of California, Berkeley, CA.
- Stewart, J.P., D.M. Boore, E. Seyhan & G.M. Atkinson (2015). NGA-West2 equations for predicting vertical-component PGA, PGV, and 5%-damped PSA from shallow crustal earthquakes. *Earthquake Spectra*, doi: <http://dx.doi.org/10.1193/072114EQS116M>
- Stewart J.P., A.O. Kwok, Y.M.A. Hashash, N. Matasovic, R. Pyke, Z. Wang & Z. Yang (2008). *Benchmarking of nonlinear geotechnical ground response analysis procedures*. PEER Report No. 2008/04, Pacific Earthquake Engineering Research Center, University of California, Berkeley, CA.
- Stewart, J.P. & A.O. Kwok (2008). Nonlinear seismic ground response analysis: code usage protocols and verification against vertical array data. *Geotechnical Engineering and Soil Dynamics IV*, May 18-22, 2008, Sacramento, CA. *ASCE Geotechnical Special Publication* **181**, D. Zeng, M.T. Manzari, and D.R. Hiltunen (eds.), 24 pages (electronic file).
- Stokoe, K. H., J.A. Bay, B.L. Rosenbald, S.K. Hwang & M.R. Twede (1994). *In situ seismic and dynamic laboratory measurements of geotechnical materials at Queensboro Bridge and Roosevelt Island*. Geotech. Engineering Report GR 94-5, Civil Engineering Department, University of Texas at Austin, Texas.
- Strasser, F.O., N.A. Abrahamson & J.J. Bommer (2009). Sigma: issues, insights, and challenges. *Seismological Research Letters* **80**(1), 40-56.
- Sykora D.W. (1987) *Examination of existing shear wave velocity and shear modulus correlations in soils*. US Army Corps of Engineers, Vicksburg, MS.
- Tokimatsu, K. & T. Sekiguchi (2006a). Effects of nonlinear dynamic soil properties on strong Motions at Ojiya K-Net and JMA Stations during 2004 Mid Niigata Prefecture Earthquake. *Proceedings of the 8th U.S. National Conf. on Earthquake Engineering*, San Francisco, California, USA, April 18-22.
- Tokimatsu, K & T. Sekiguchi (2006b). Effects of nonlinear properties of surface soils on strong ground motions recorded in Ojiya during 2004 mid Niigata Prefecture earthquake. *Soils and Foundations* **46**(6), 765-775.
- Tokimatsu, K. & T. Sekiguchi (2007). Effects of Dynamic Properties of Peat on Strong Ground Motions during 2004 Mid Niigata Prefecture Earthquake. *4th International Conference on Earthquake Geotechnical Engineering* June 25-28, Paper No. 1531.
- Toro, G. (1995). *Probabilistic models of site velocity profiles for generic and site-specific ground motion amplification studies*. Department of Nuclear Energy Brookhaven National Laboratory, Upton, New York.

- Trifunac, M.D. & A.G. Brady (1975). A study on duration of earthquake ground motion. *Bulletin of the Seismological Society of America* **65**, 581-626.
- Tsai, C.-C. & C.-W. Chen (2016). Comparison study of one-dimensional site response analysis methods. *Earthquake Spectra* **32**(2), 1075-1095.
- Vanmarcke, E.H. & S.P. Lai, (1980). Strong-motion duration of earthquakes. *Bulletin of the Seismological Society of America* **70**, 1293- 1307.
- Villani, M. & N.A. Abrahamson (2015). Repeatable path and site effects on the ground-motion sigma based on empirical data from southern California and simulated waveforms from the CyberShake platform. *Bulletin of the Seismological Society of America* **105**(5), 2681-2695.
- Wang, M. & T. Takada (2005). Macrospatial correlation model of seismic ground motions. *Earthquake Spectra* **21**(4), 1137-1156.
- Wassing, B.B.T., D. Malers, R.S. Westerhoff, J.H.A. Bosch, & H.J.T. Weerts (2003). *Seismisch hazard van geïnduceerde aardbevingen - Rapportage fase 1*, TNO Geological Survey of the Netherlands report NITG-03-185-C-def, 77 pp.
- Wehling, T.M., R.W. Boulanger, L.F. Harder & M.W. Driller (2001). *Dynamic Properties of Sherman Island Peat: Phase II Study*. Department of Civil & Environmental Engineering, College of Engineering, University of California at Davis. Report No. UCD/CGM-01/05, March 2001, 130 pp.
- Wehling, T.M., R.W. Boulanger, R. Arulnathan, L.F. Harder, & M.W. Driller (2003). Nonlinear dynamic properties of a fibrous organic soil. *Journal of Geotechnical and Geoenvironmental Engineering* **129**(10), 929-939.
- Wells, D. L. & K. J. Coppersmith (1994). New empirical relationships among magnitude, rupture length, rupture width, rupture area, and surface displacement. *Bulletin of the Seismological Society of America* **84**, 974-1002.
- Yamada, S., M. Hyodo, R.P. Orense & S. Dinesh (2008). Initial shear modulus of remolded sand-clay mixtures. *ASCE Journal of Geotechnical and Geoenvironmental Engineering* **134**, 960-971
- Yee, E., J.P. Stewart & K. Tokimatsu (2013). Elastic and large-strain nonlinear seismic site response from analysis of vertical array recordings. *Journal of Geotechnical and Geoenvironmental Engineering*, **139**(10), 1789-1801.
- Yenier, E. & G.M. Atkinson (2014). Equivalent point-source modeling of moderate-to-large magnitude earthquakes and associated ground-motion saturation effects. *Bulletin of the Seismological Society of America* **104**(3), 1458-1478.
- Yenier, E. & G.M. Atkinson (2015). Regionally adjustable generic ground-motion prediction equation based on equivalent point-source simulations: Application to central and eastern North America. *Bulletin of the Seismological Society of America* **105**, 1989-2009.
- Youngs, R.R. (2004). *Software validation report for SHAKE04*, Geomatrix Consultants, Oakland, California.
- Yudistira, T. (2015). *The crustal structure beneath the Netherlands inferred from ambient seismic noise*. PhD Thesis, Utrecht University.
- Zalachoris, G. & E.M. Rathje (2015). Evaluation of one-dimensional site response techniques using borehole arrays. *Journal of Geotechnical and Geoenvironmental Engineering* **141**(12), 04015053-1-15.

Zurek, B., W. Burnett, D. DeDontney, D. & G. Gist (2017). The effect of modeling kinematic finite faults on deterministic formulation of ground motion prediction equations – Groningen: an induced seismicity case study. *87th Annual Meeting of the Society of Exploration Geophysicists*, 24-29 September 2017, Houston, TX, extended abstract.

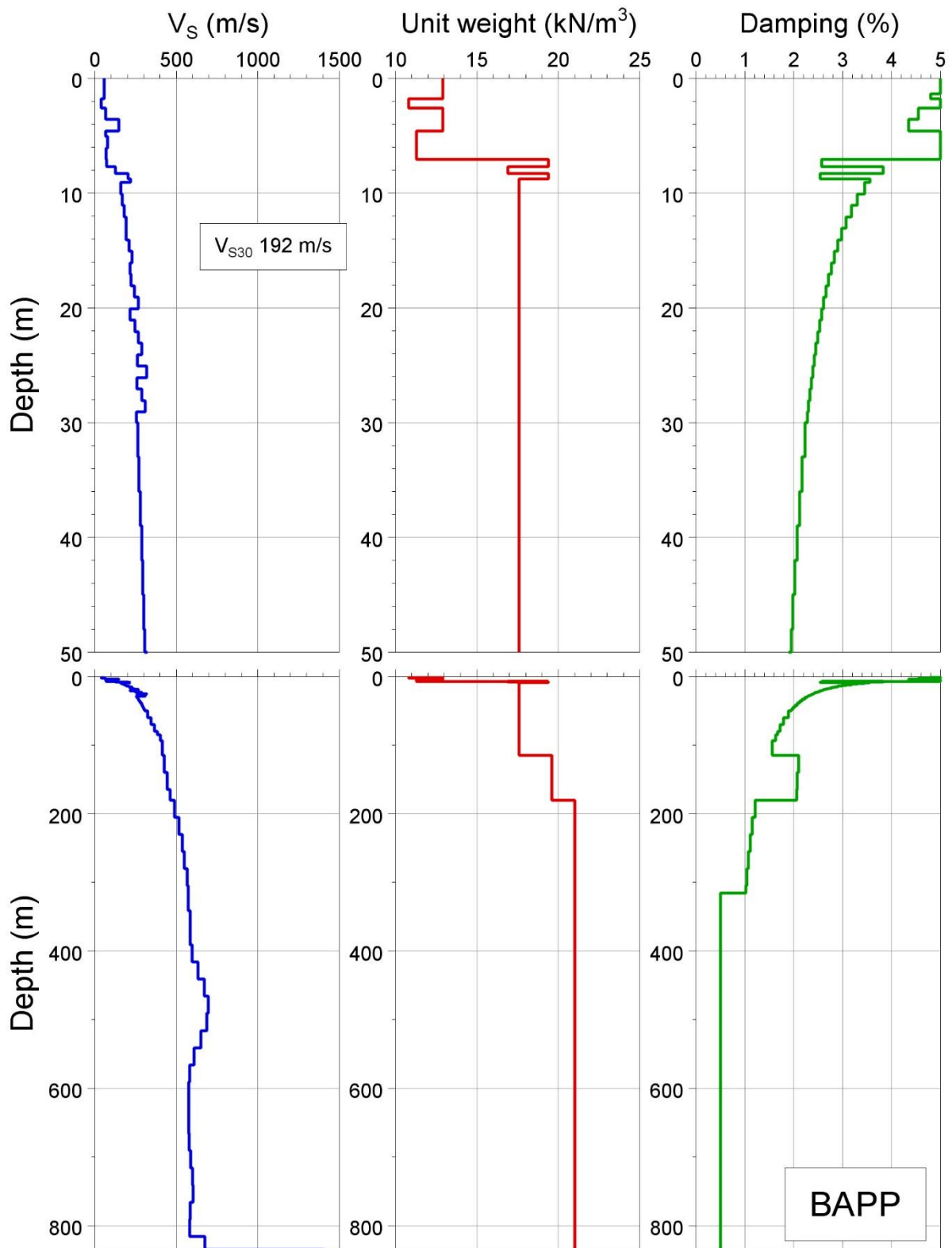
Zwanenburg, C. (2005). *The influence of anisotropy on the consolidation behaviour of peat*, Ph.D thesis Delft University of Technology, October 2005.

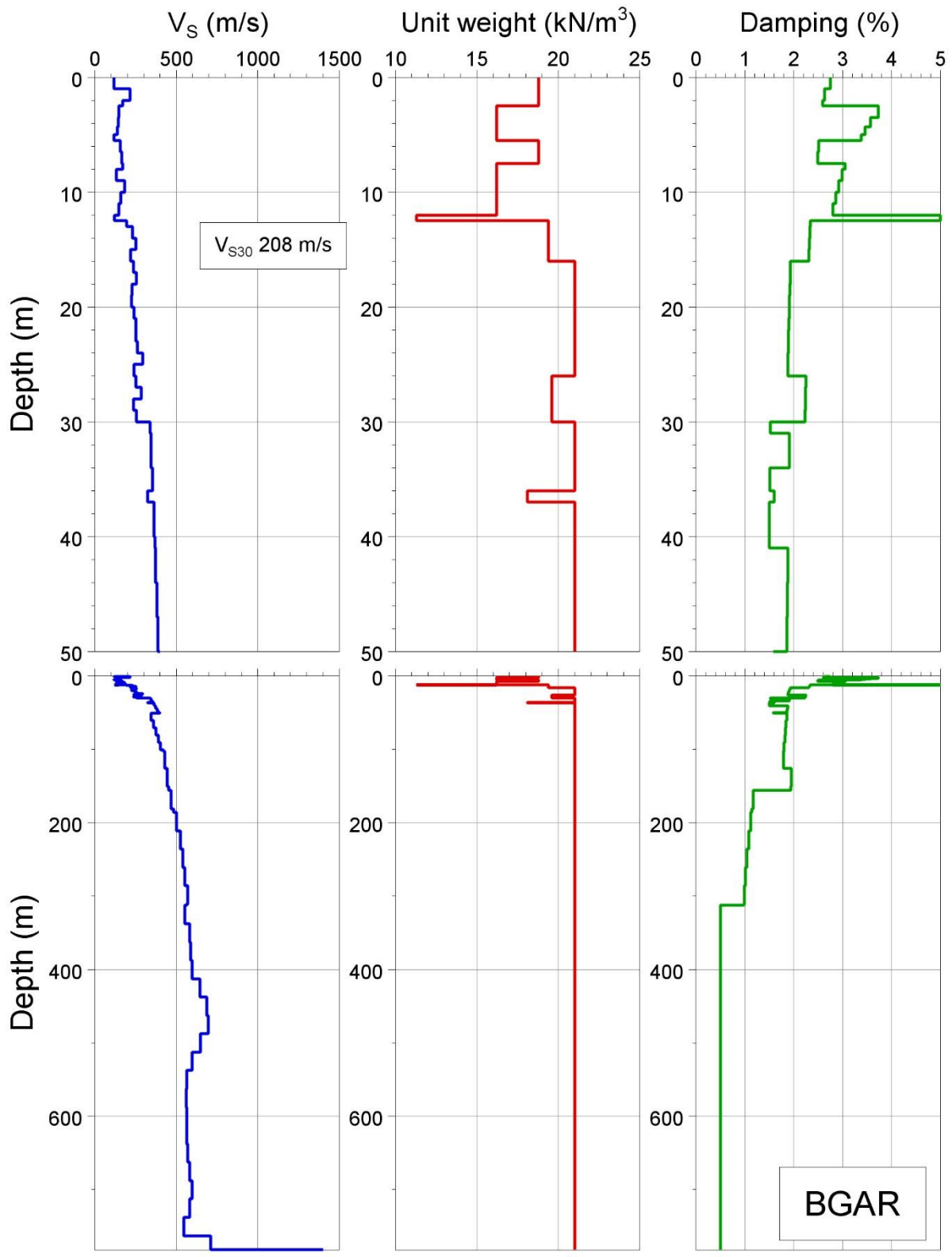
Zwanenburg, C., M. Konstantinou & P. Meijers (2017). *Dynamic behaviour of Groningen peat - Analysis and parameter assessment*. Deltares report 1209862-011-GEO-0005.

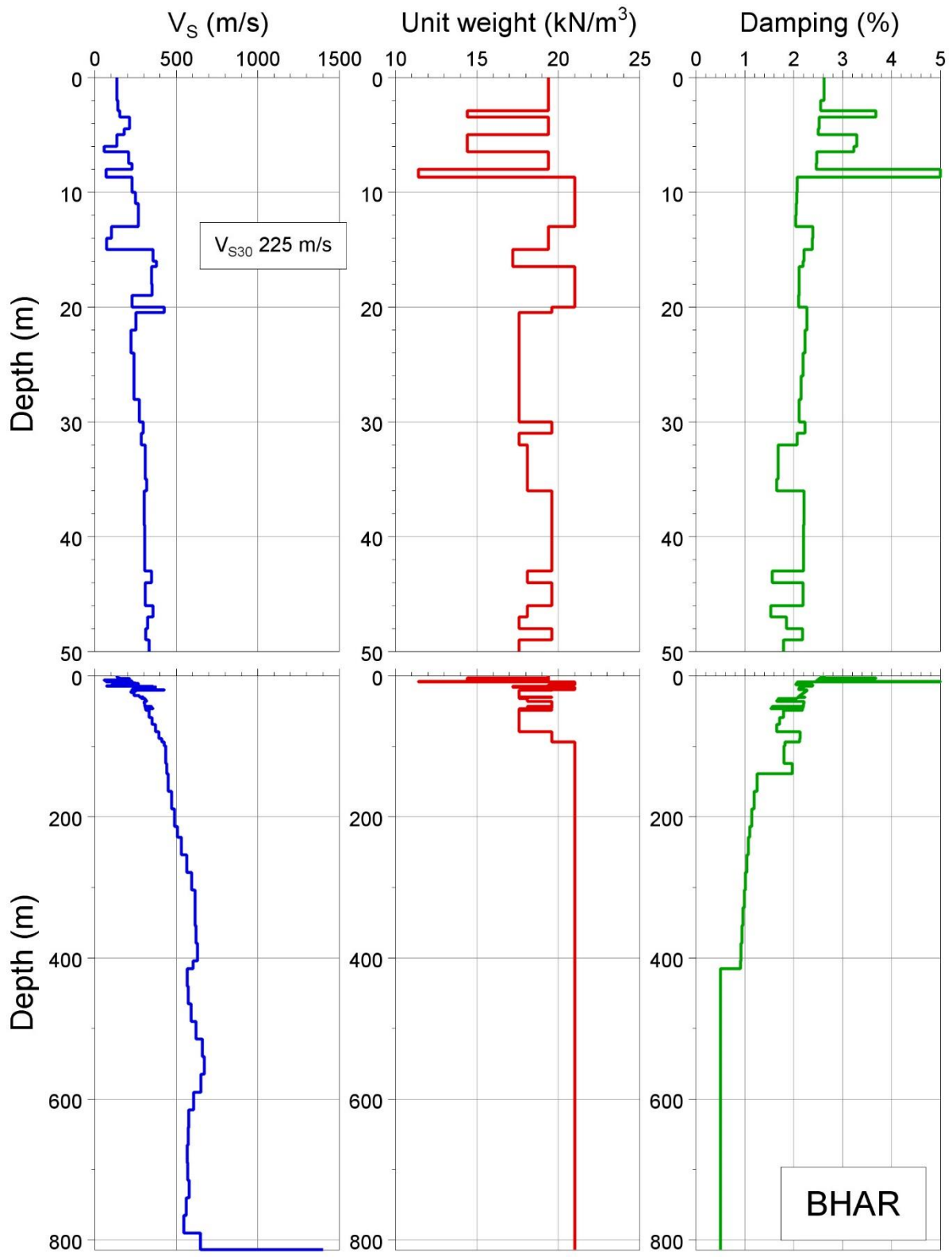
APPENDIX I

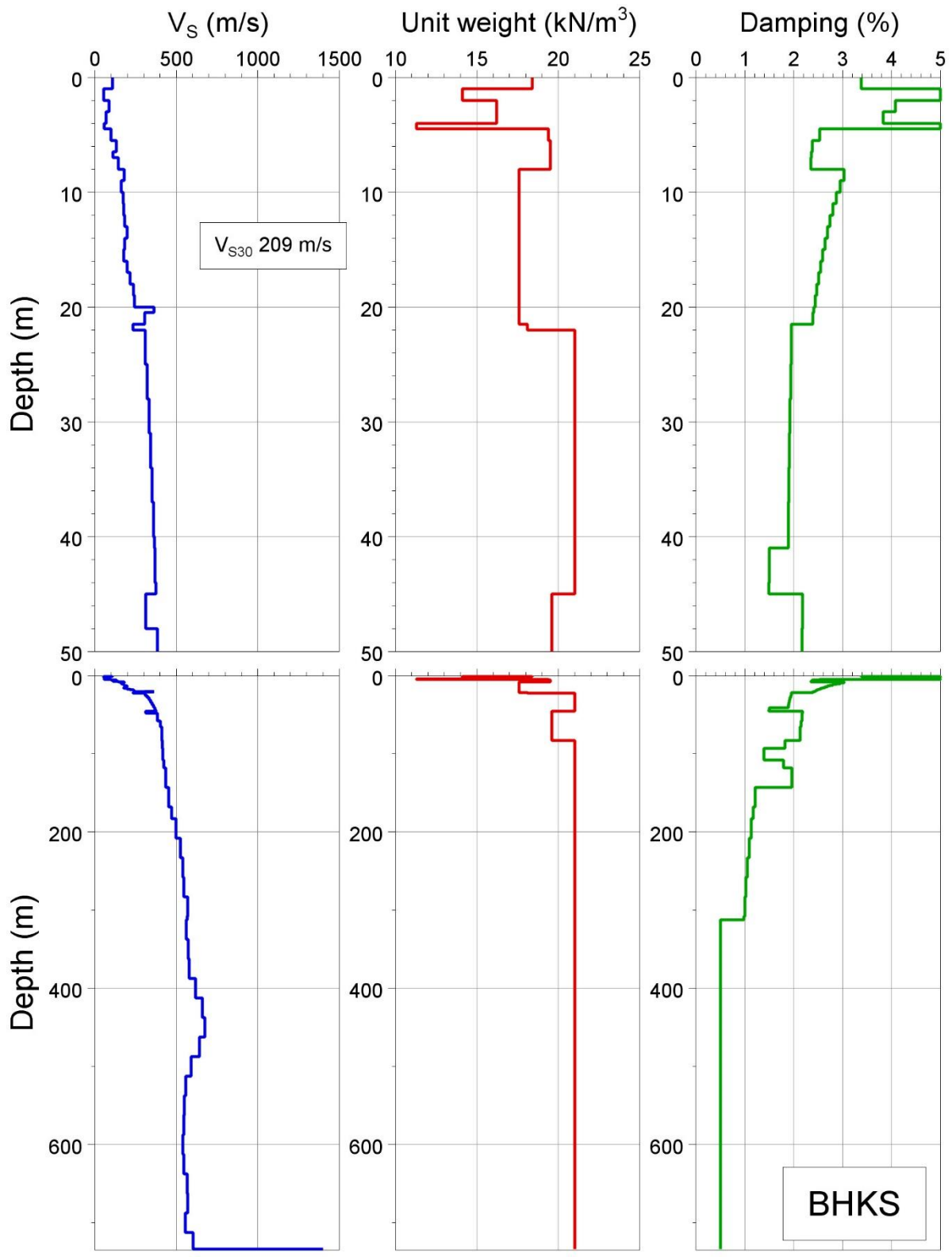
Station V_s , density and damping profiles

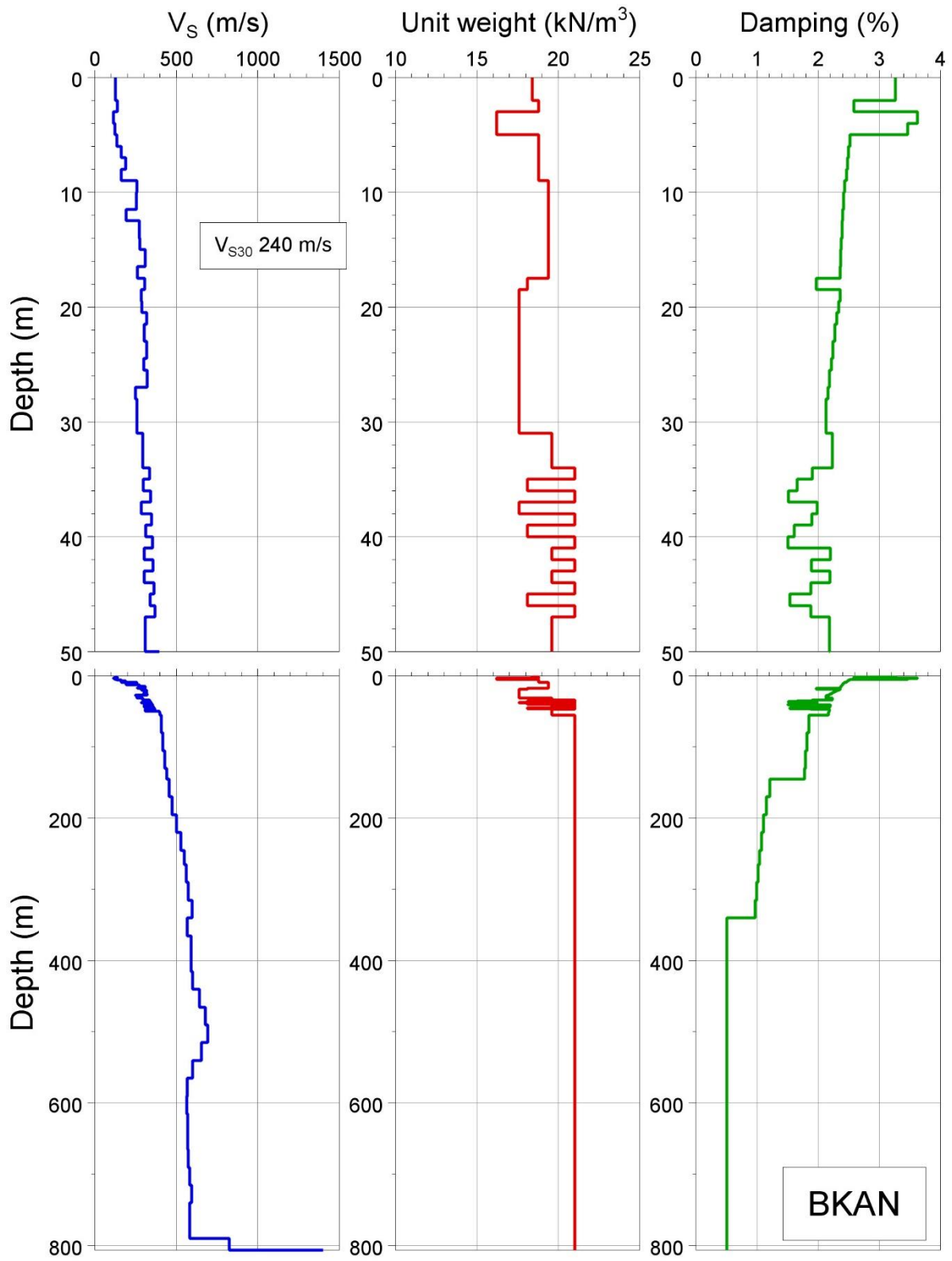
In the following pages, plots are shown for profiles of V_s , unit weight and damping for each of the recording stations, as generated from the field-wide velocity model and the Deltares look-up tables; for the B-stations, the uppermost part of the V_s profile is from in situ measurements conducted by Deltares. For each station, the full profile down to the NS_B horizon is shown, together with an additional plot of the top 50 m in order to provide images with greater resolution for the uppermost part of the profile that is likely to have the largest influence on the site response characteristics.

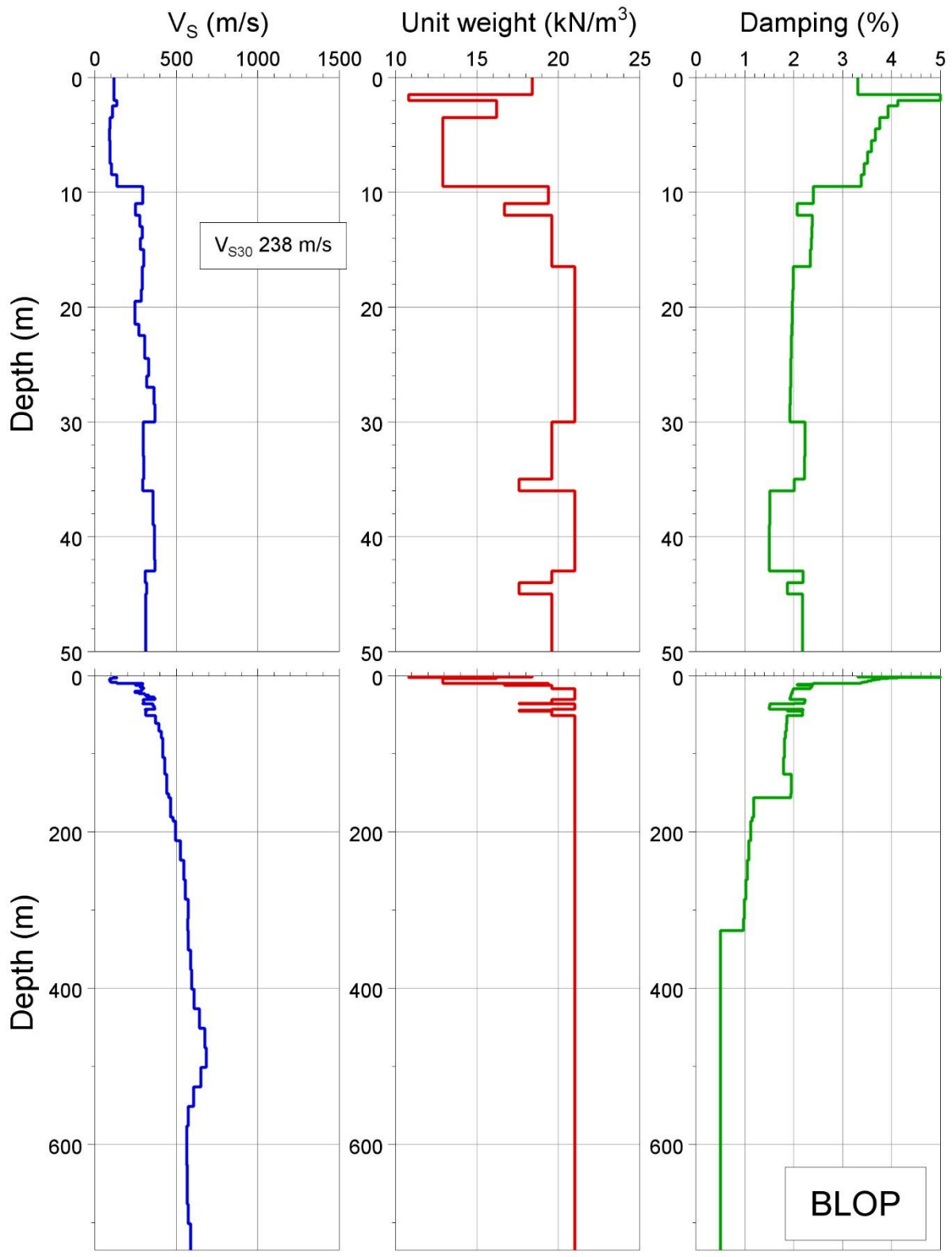


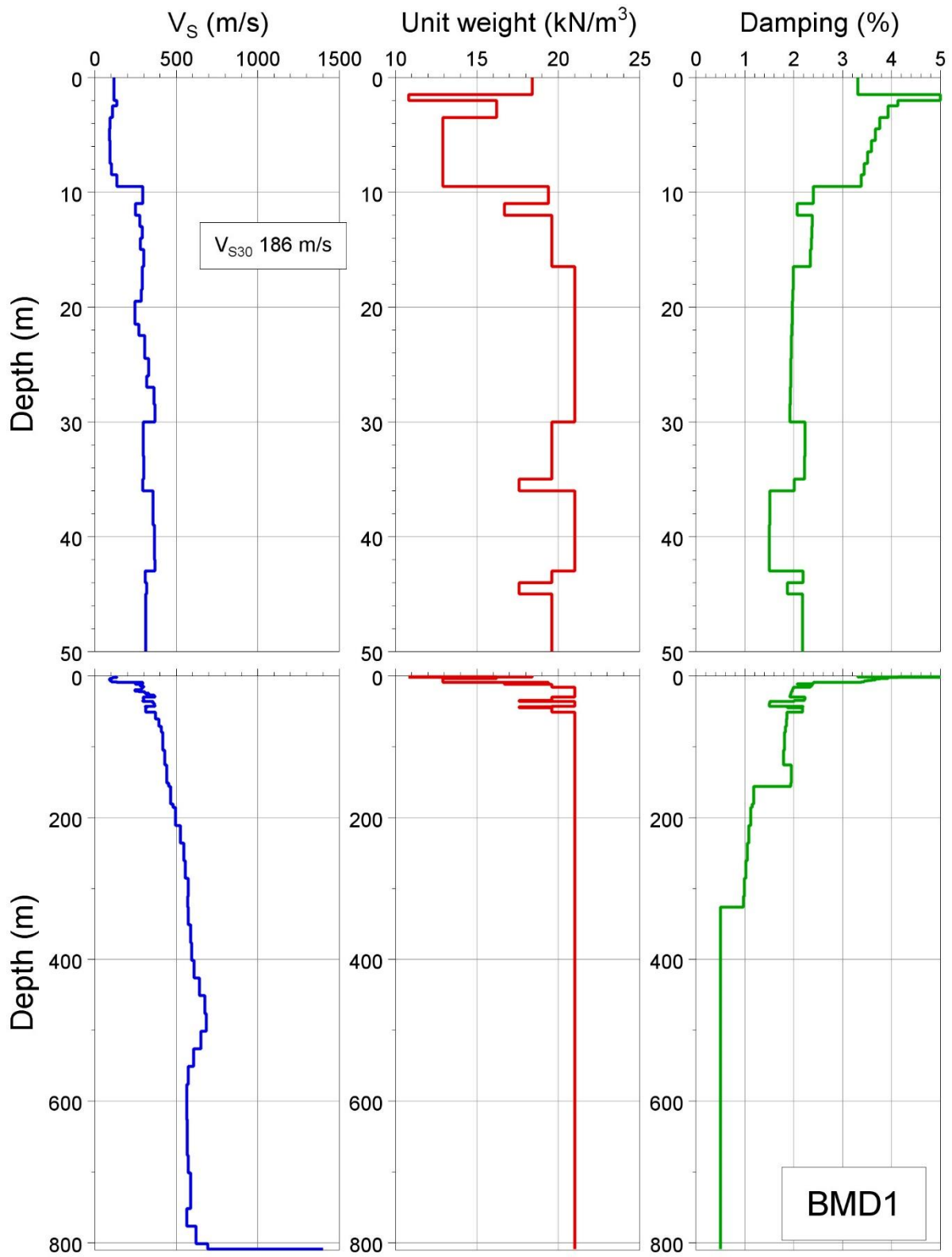


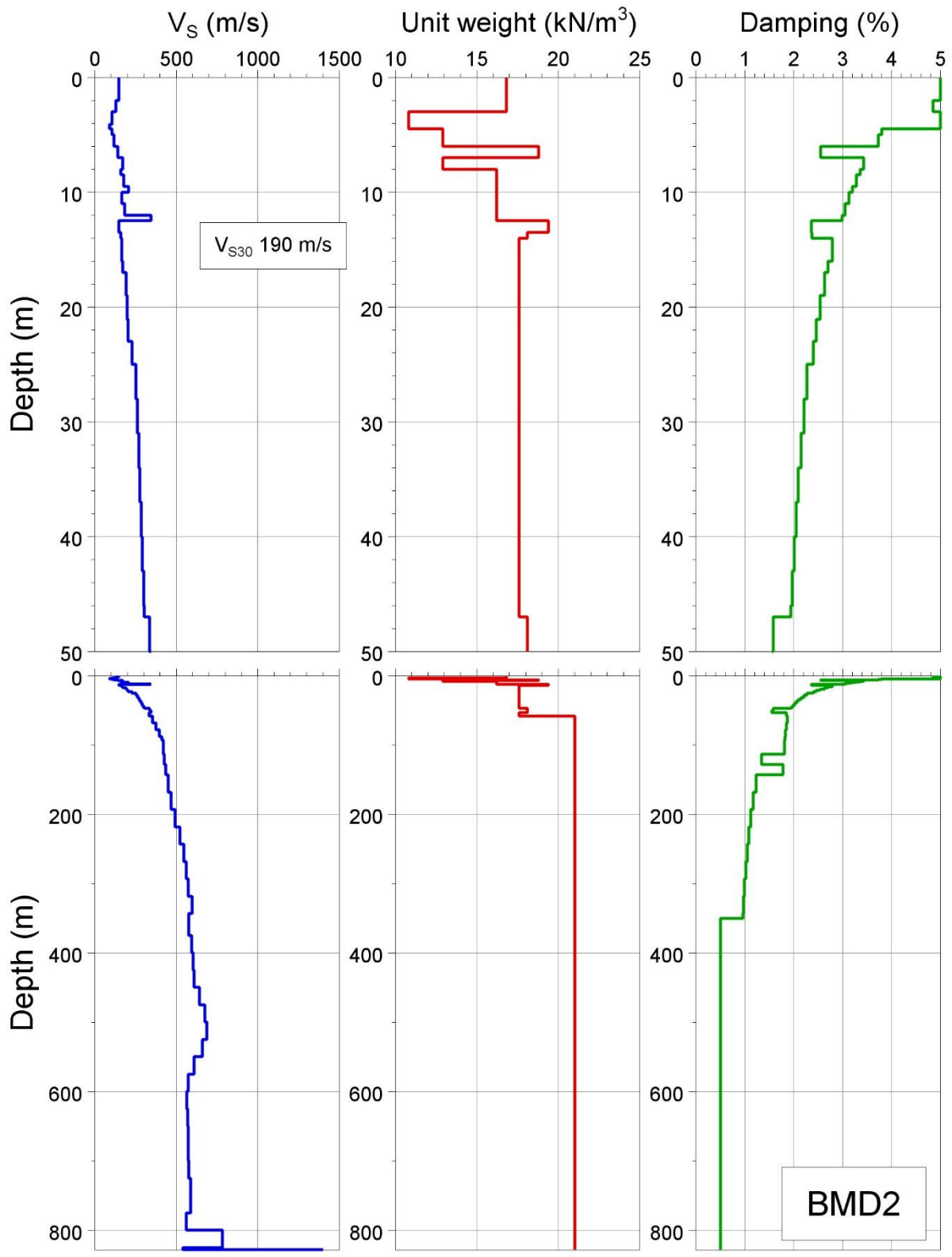


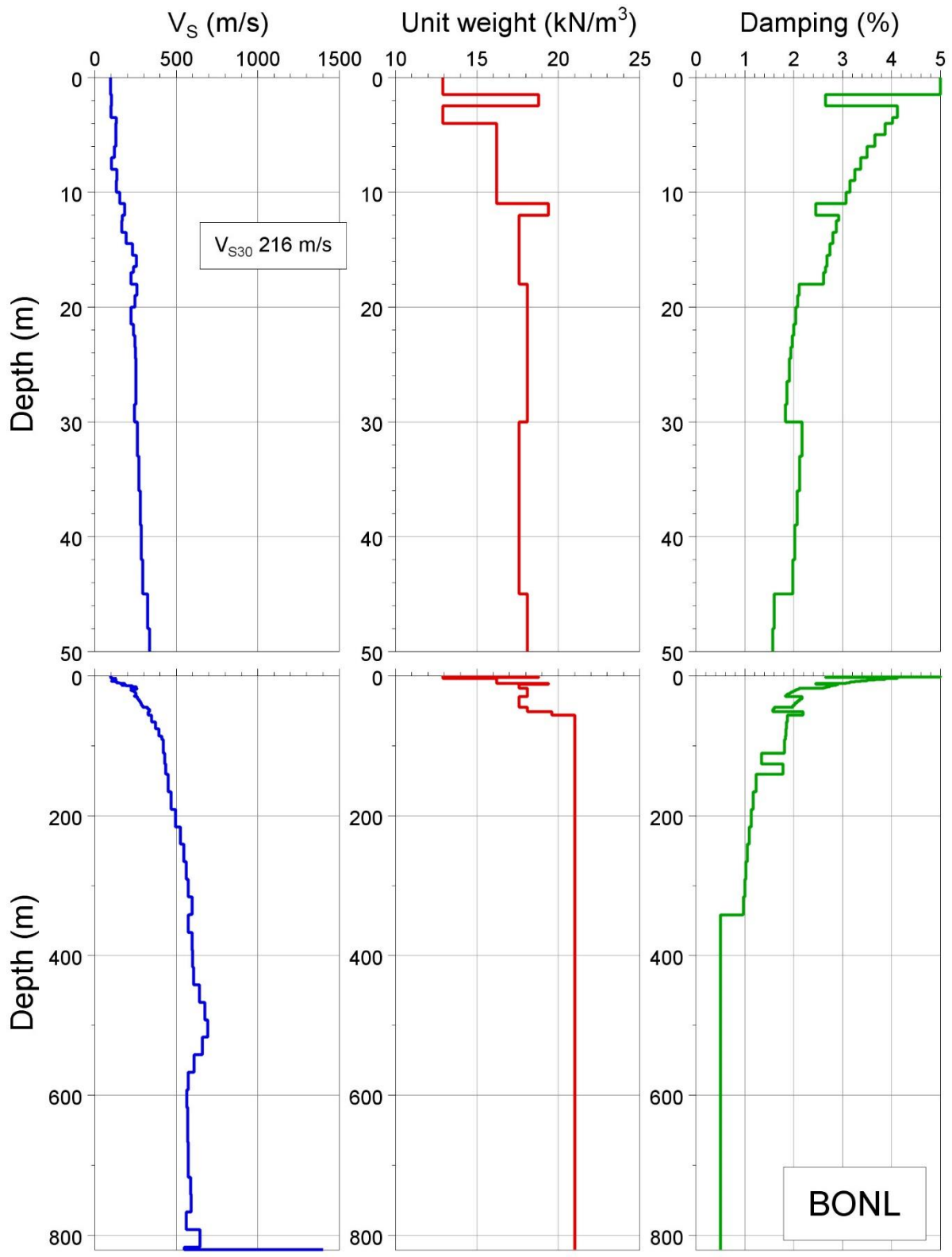


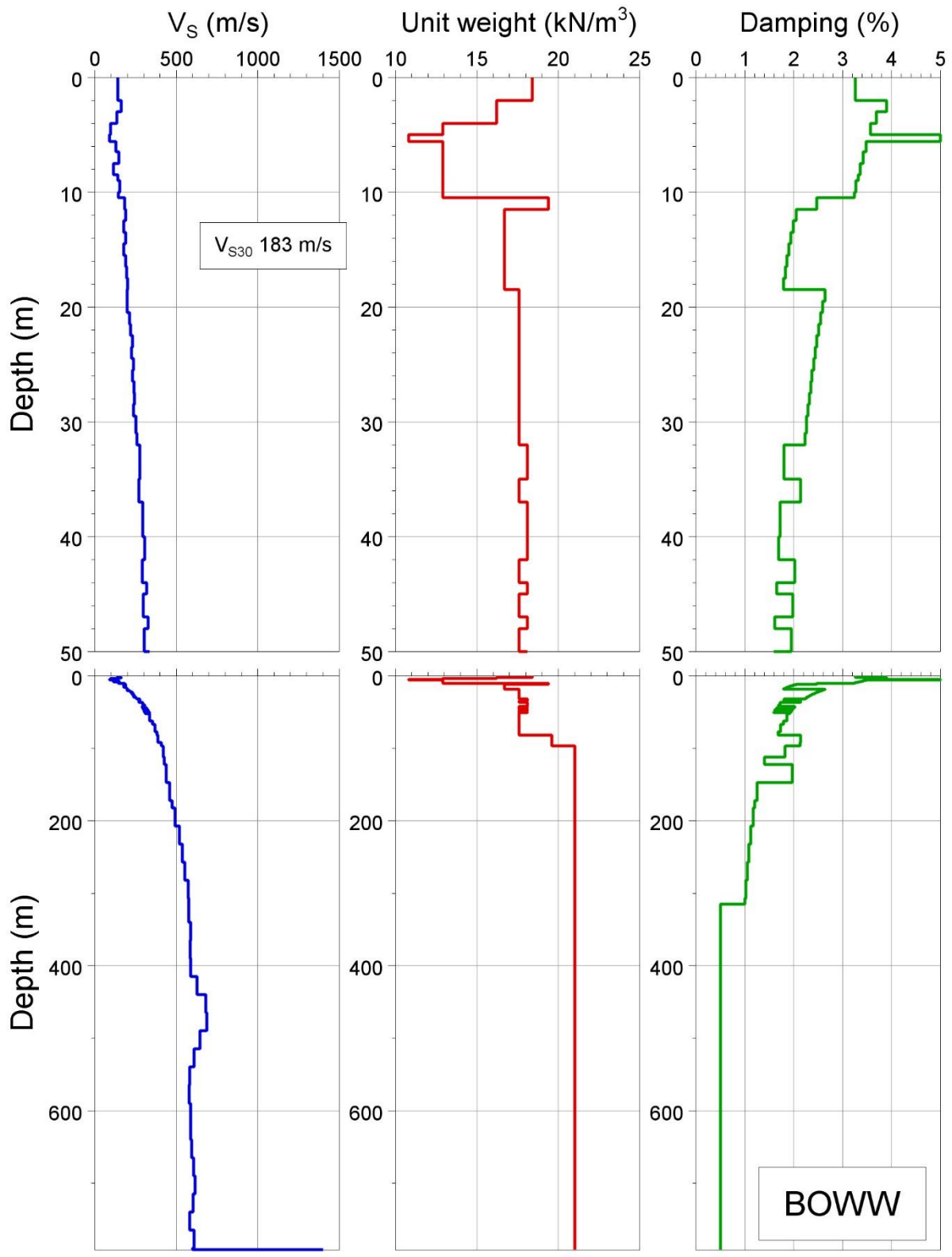


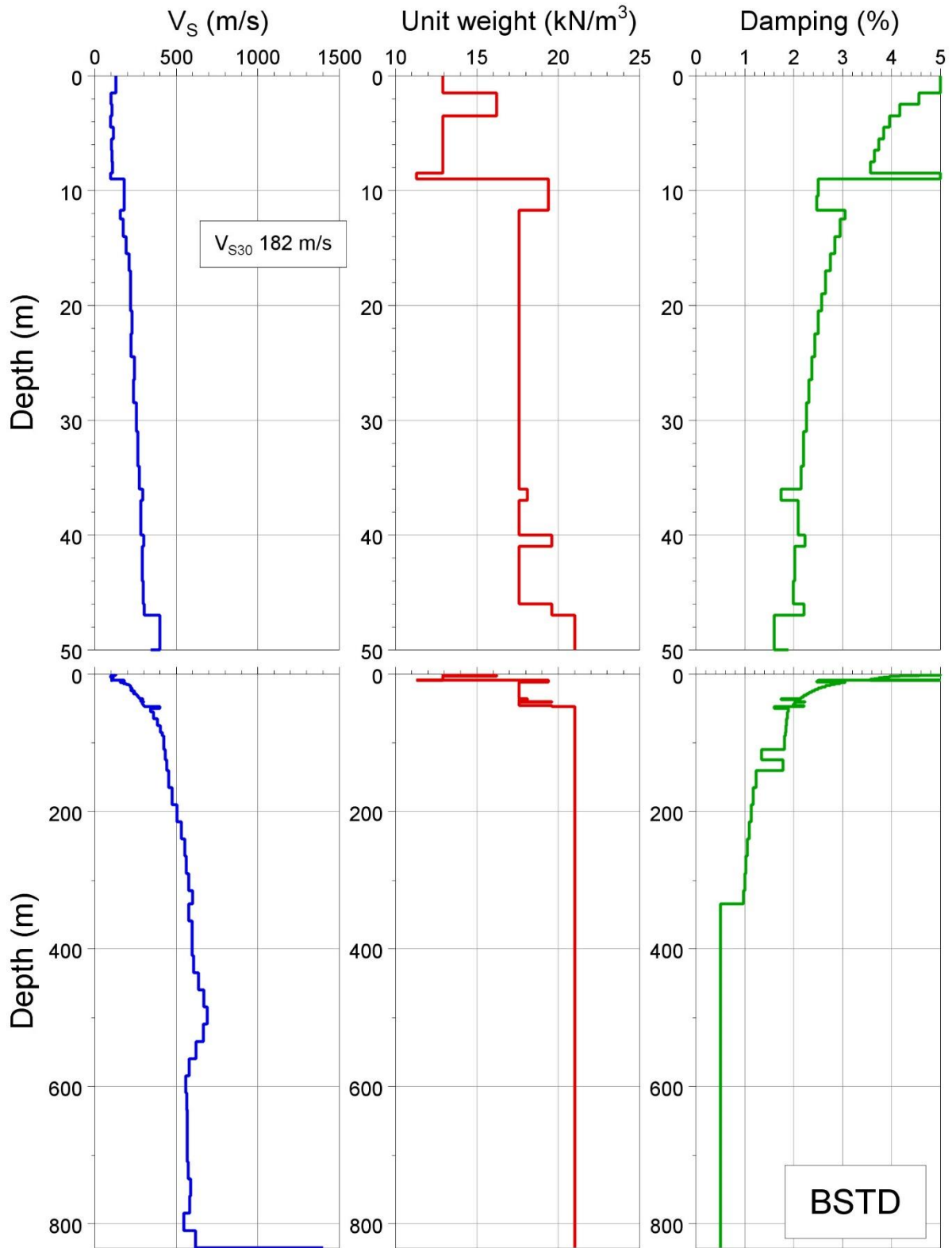


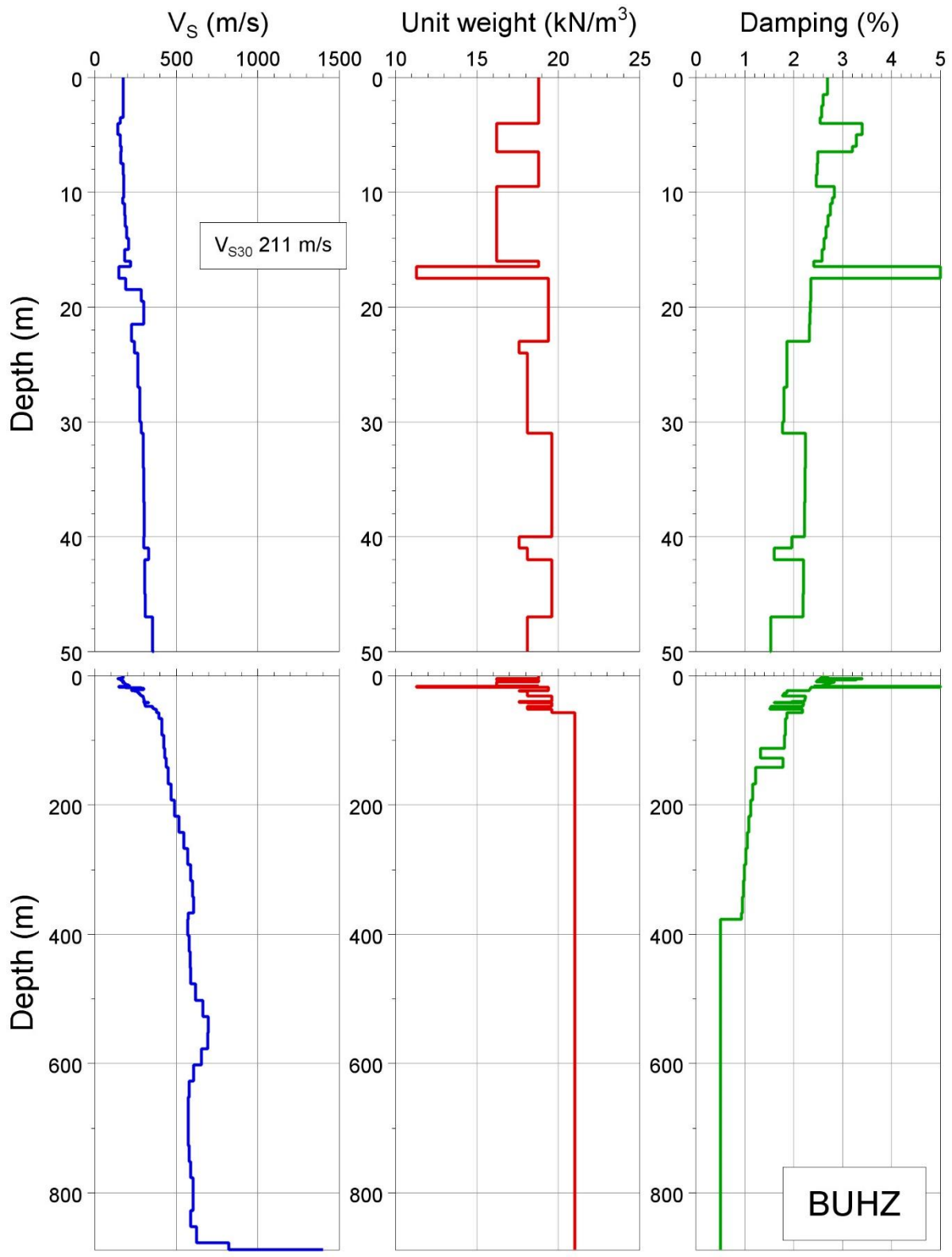


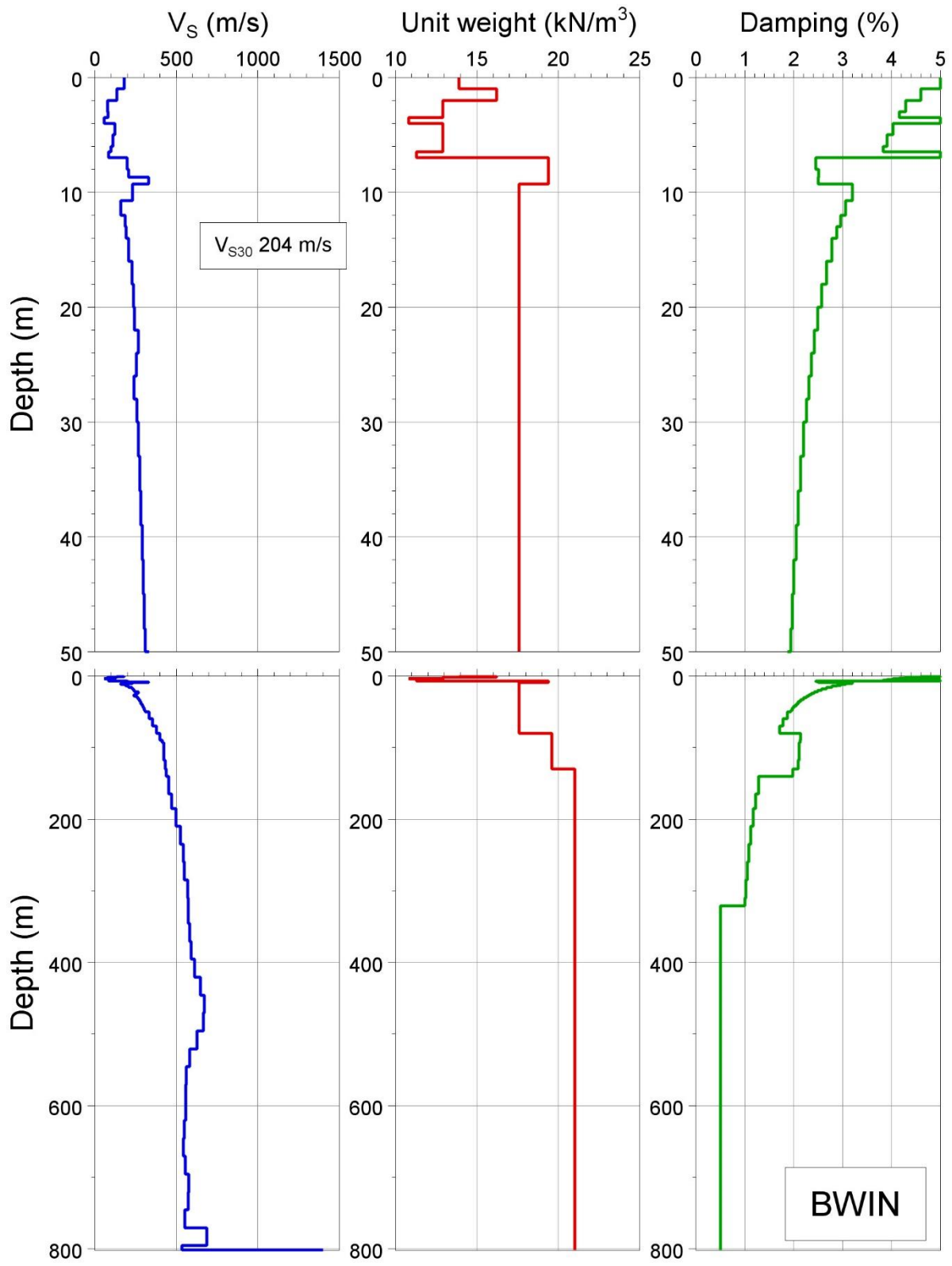


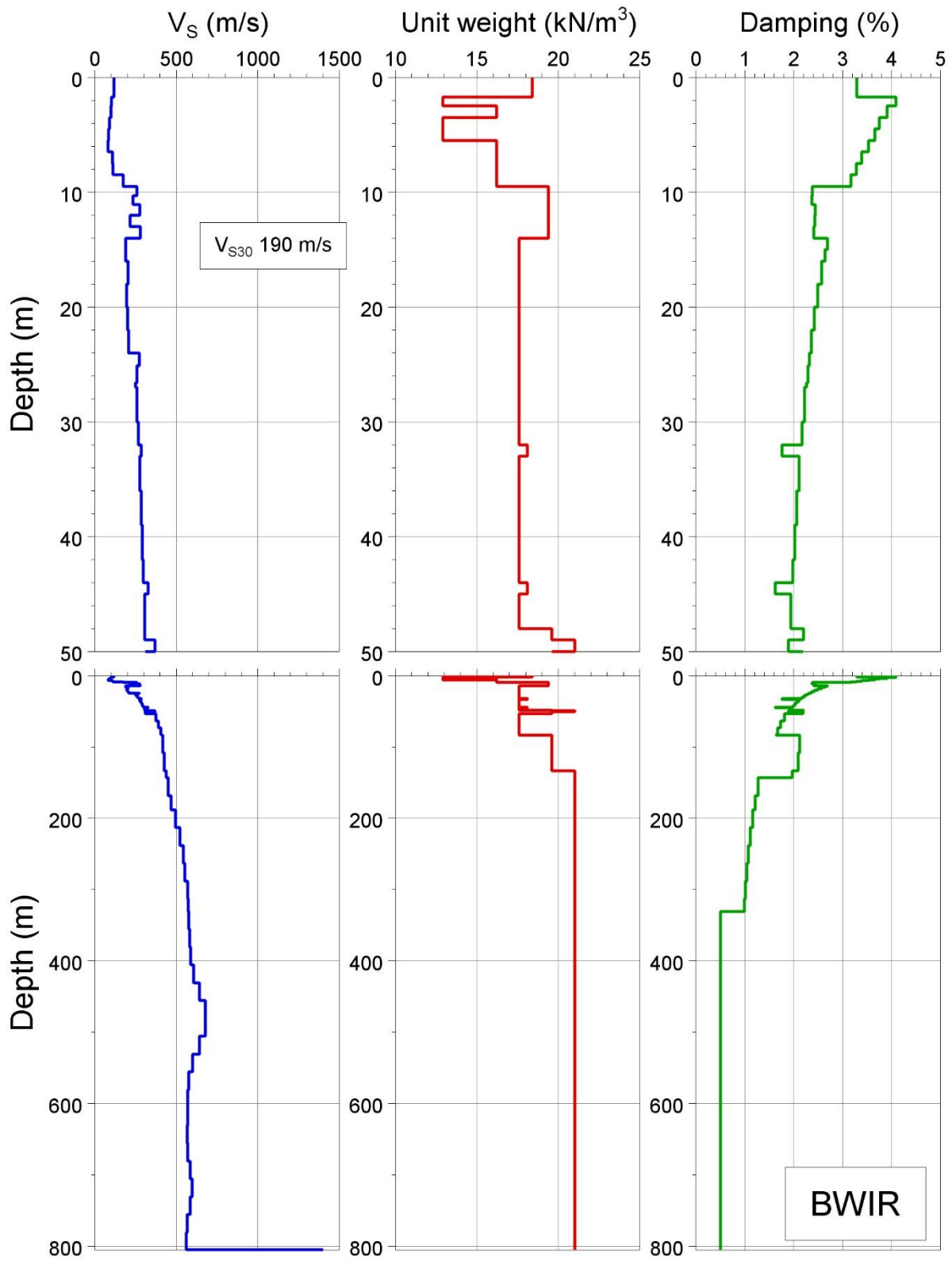


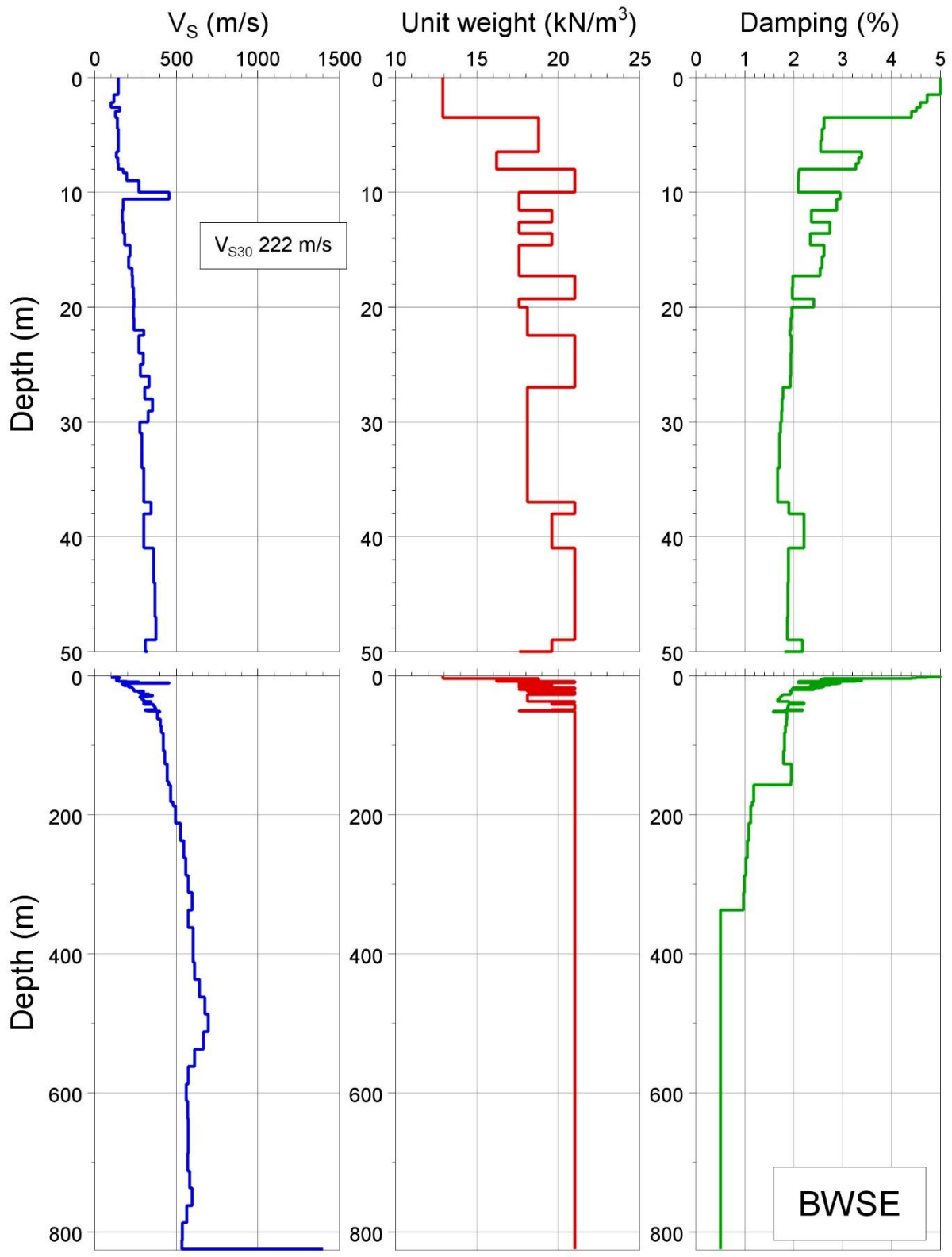


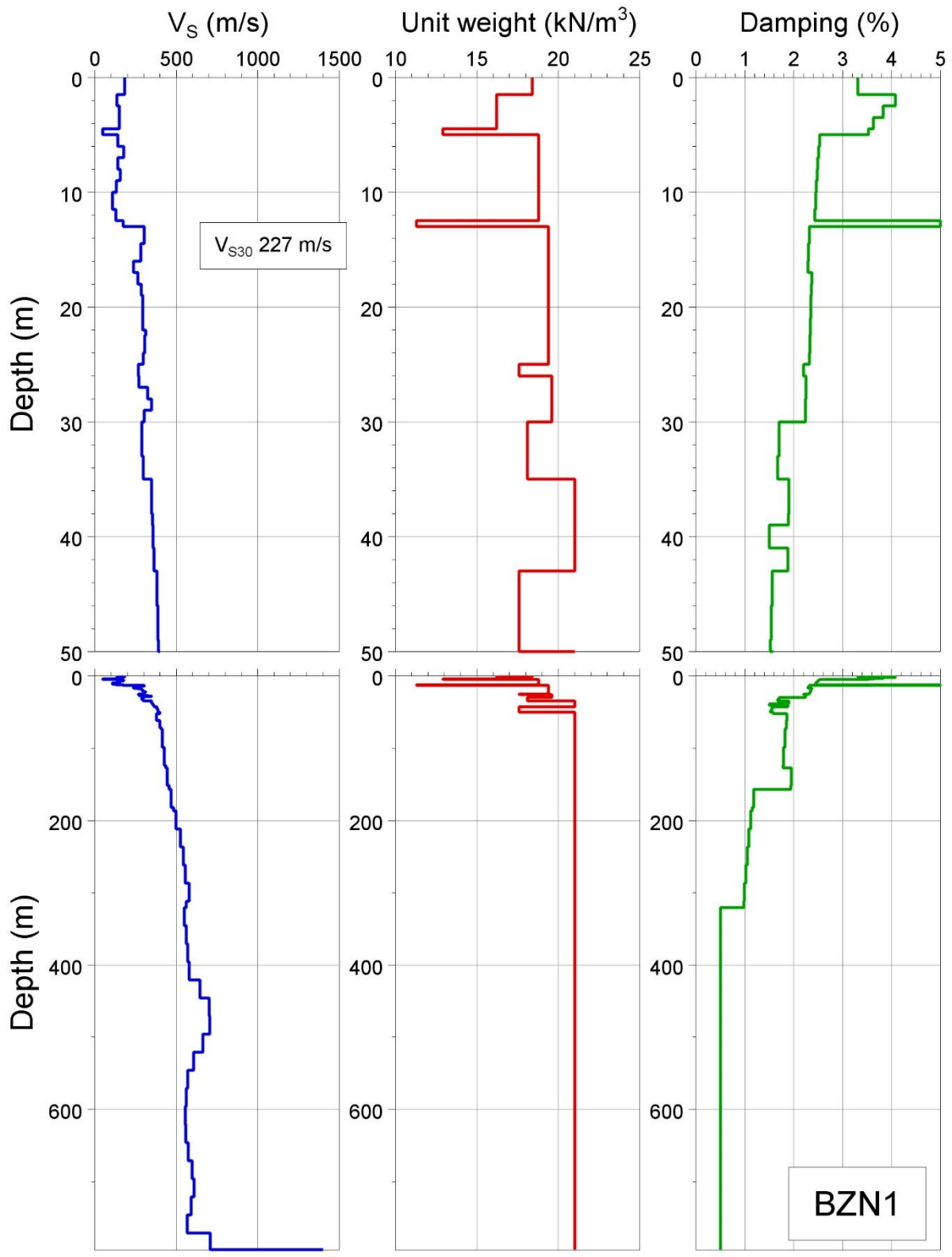


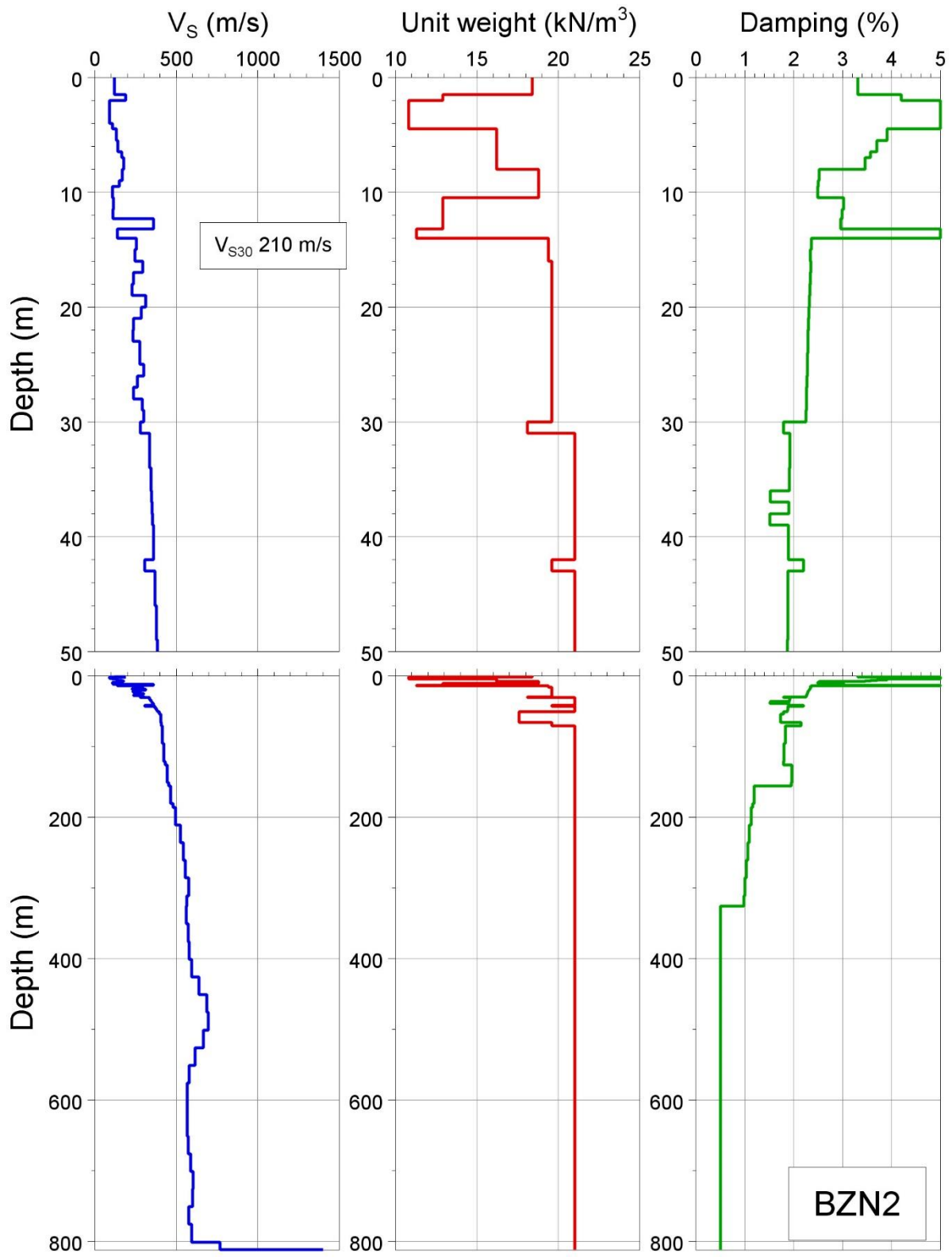


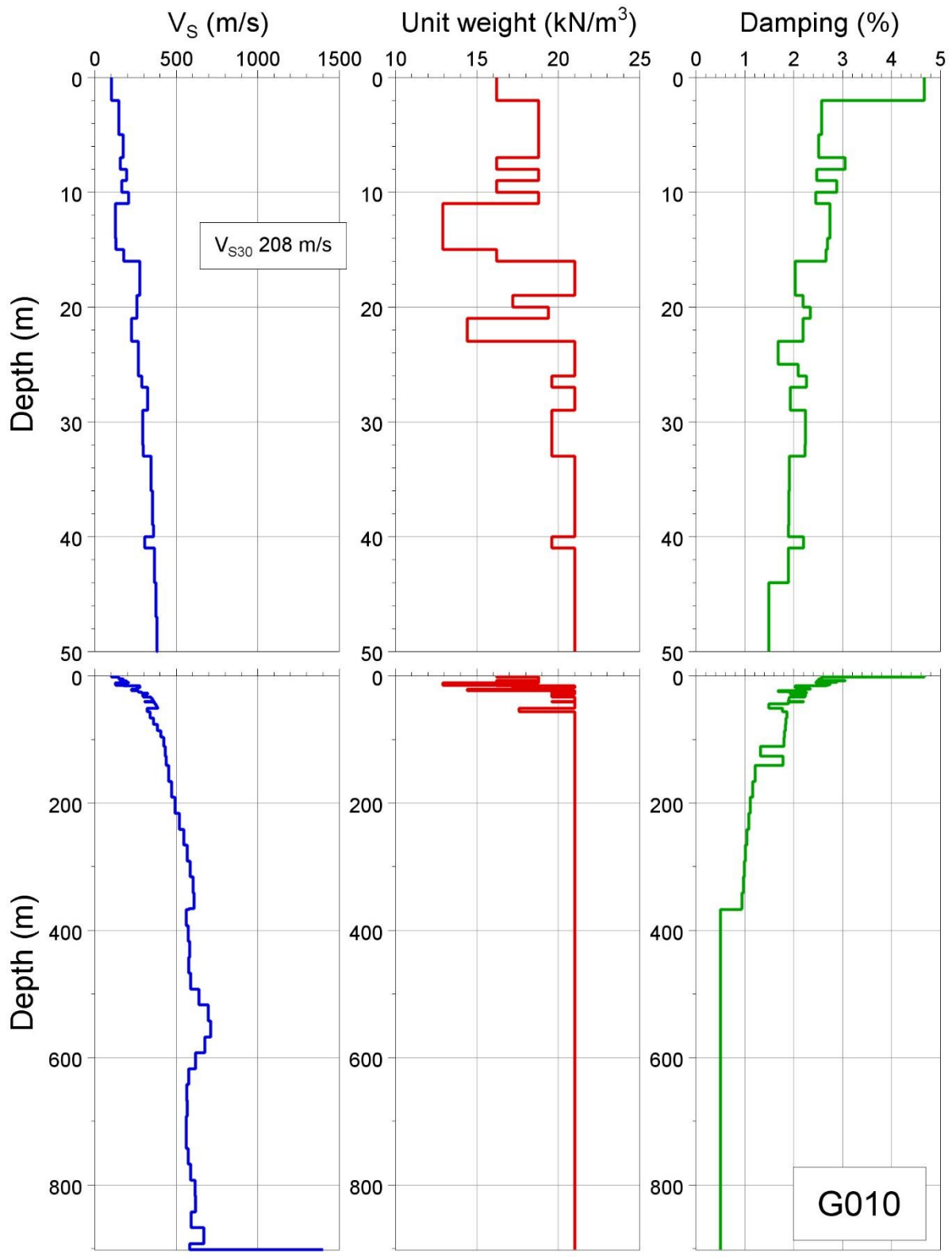


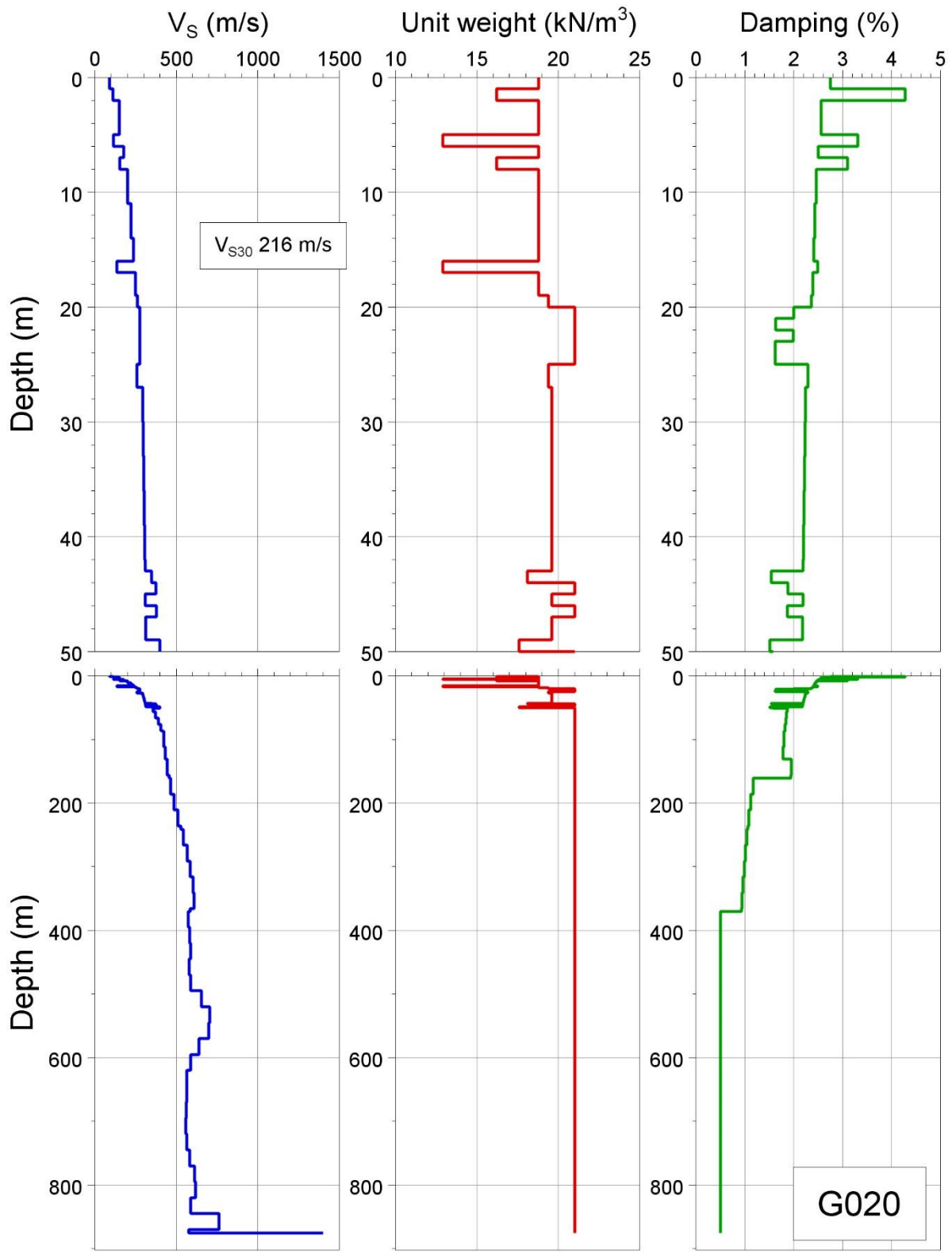


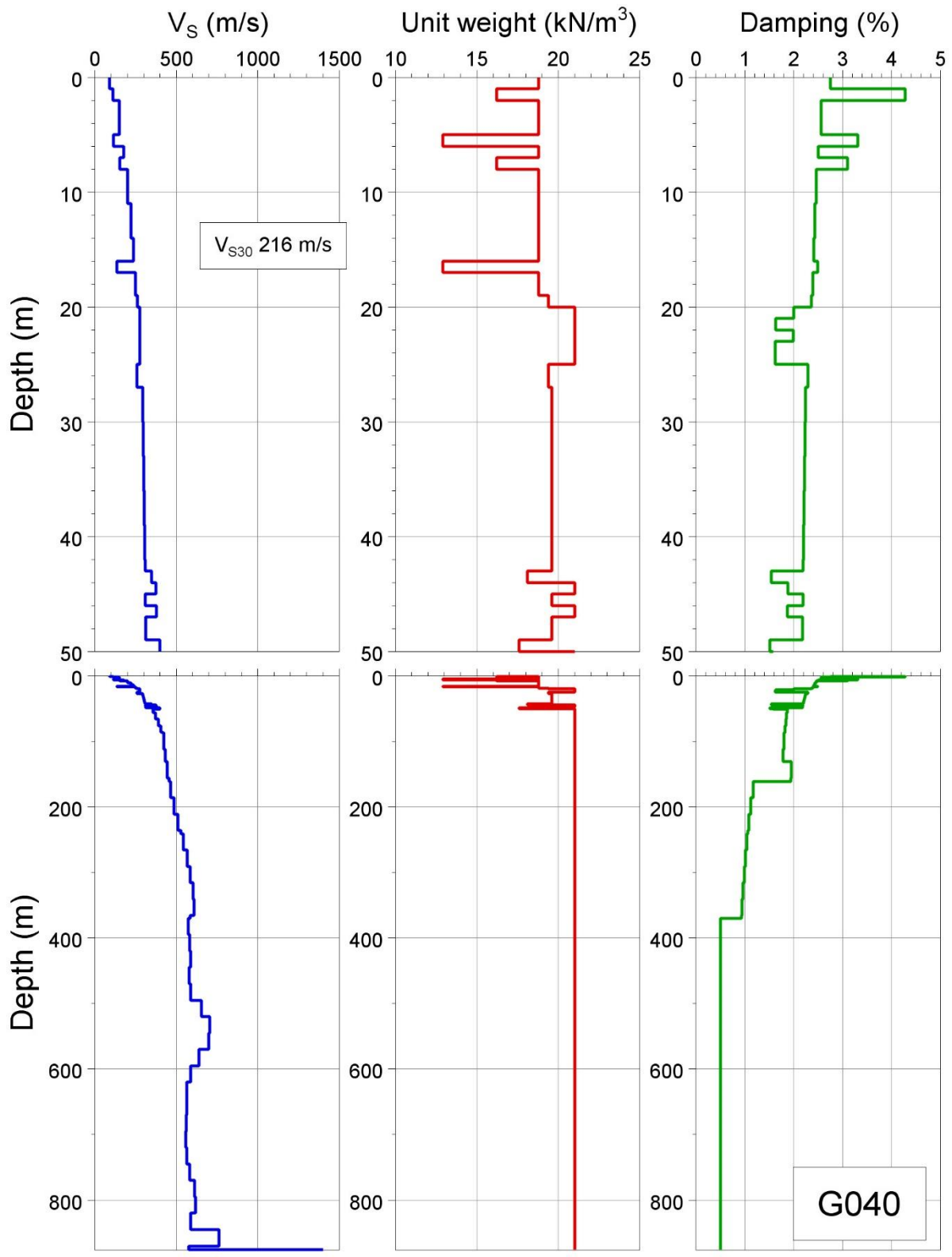


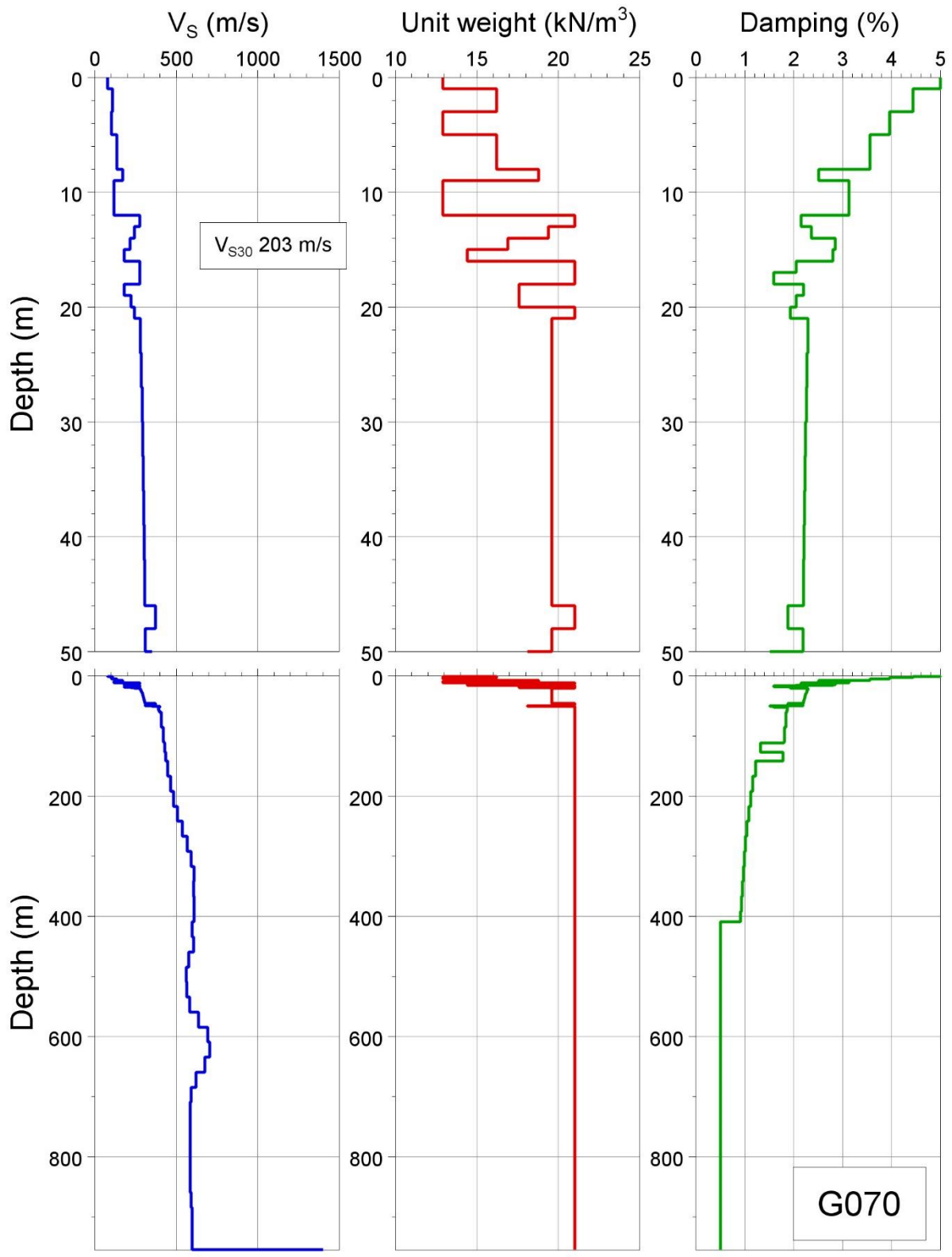


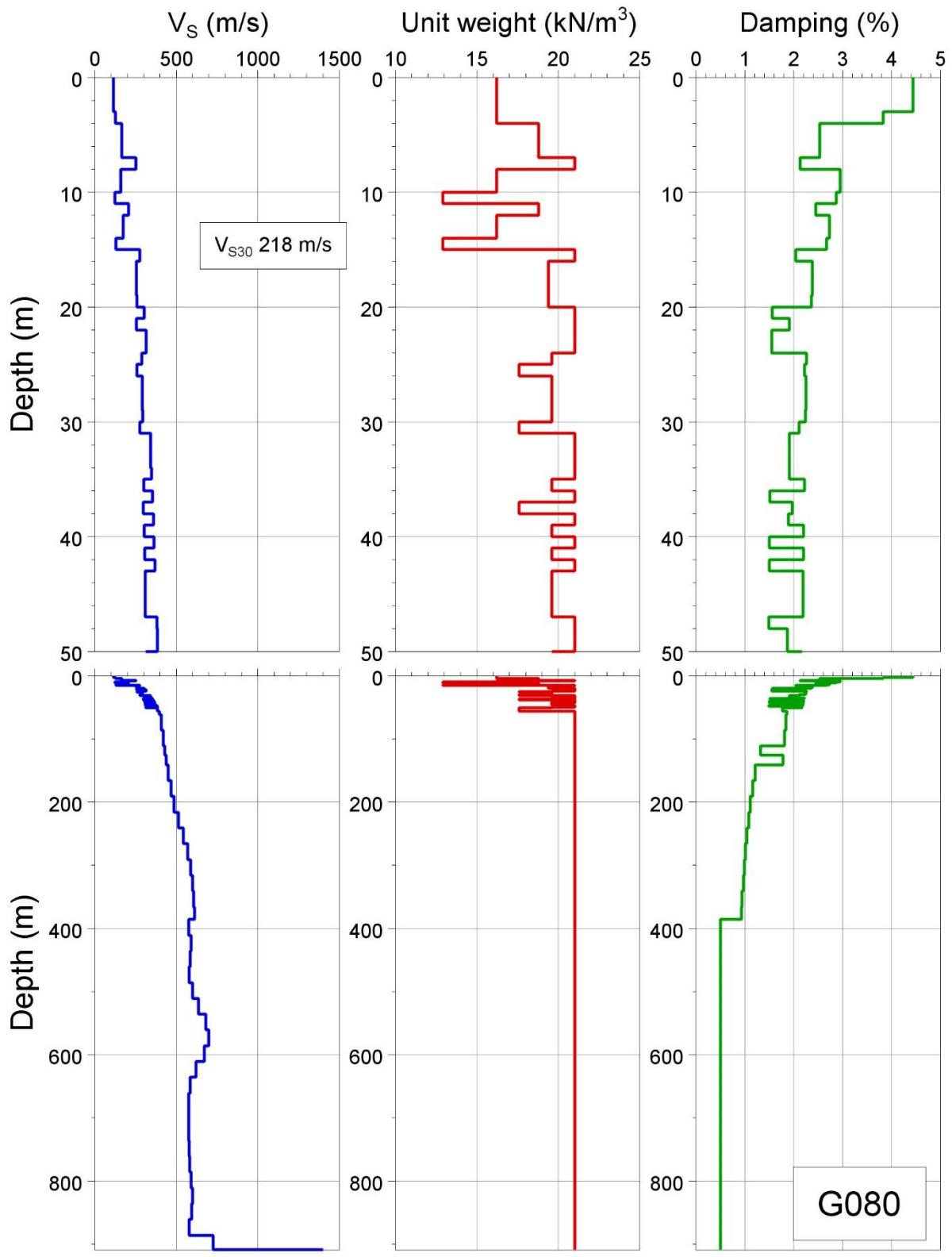


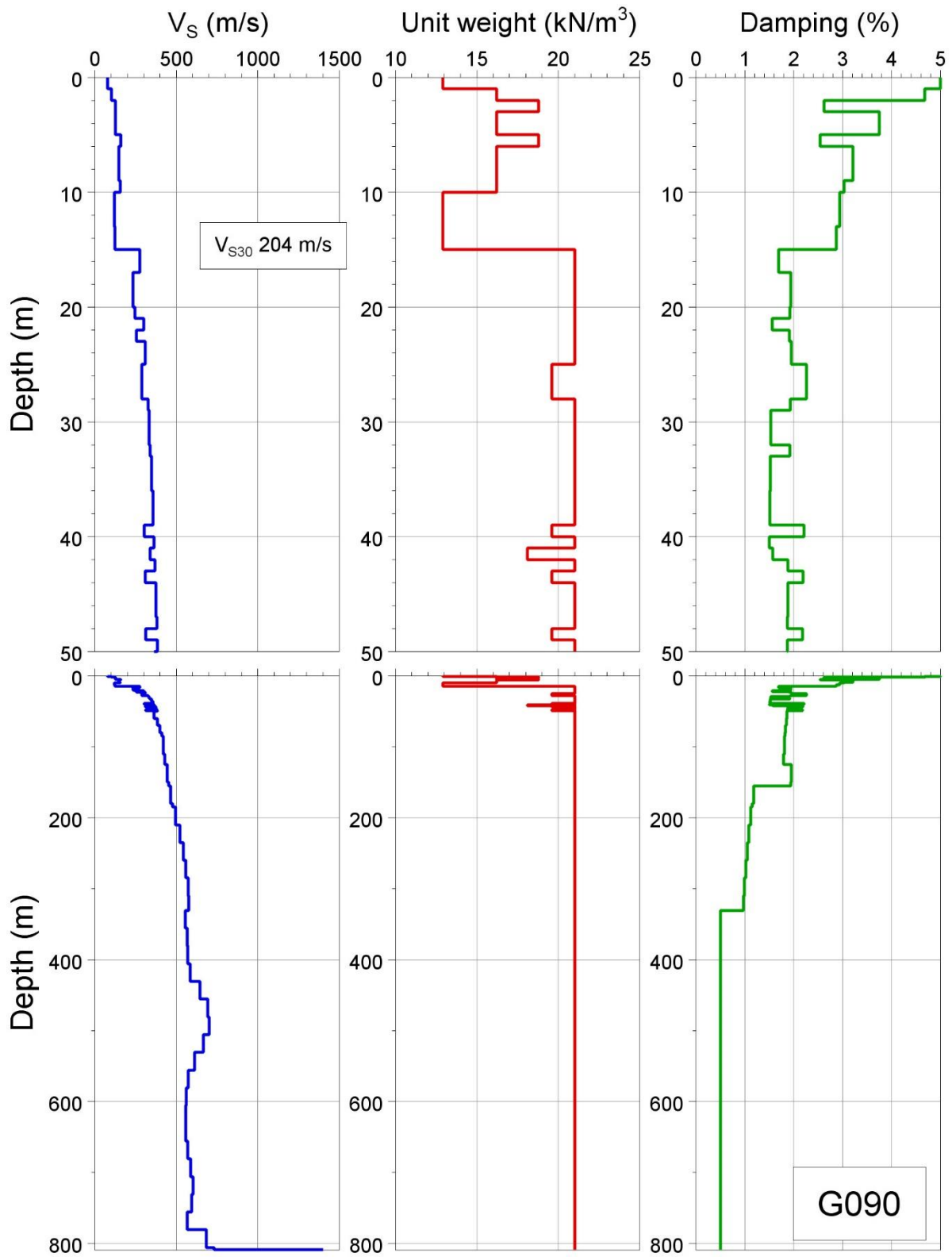


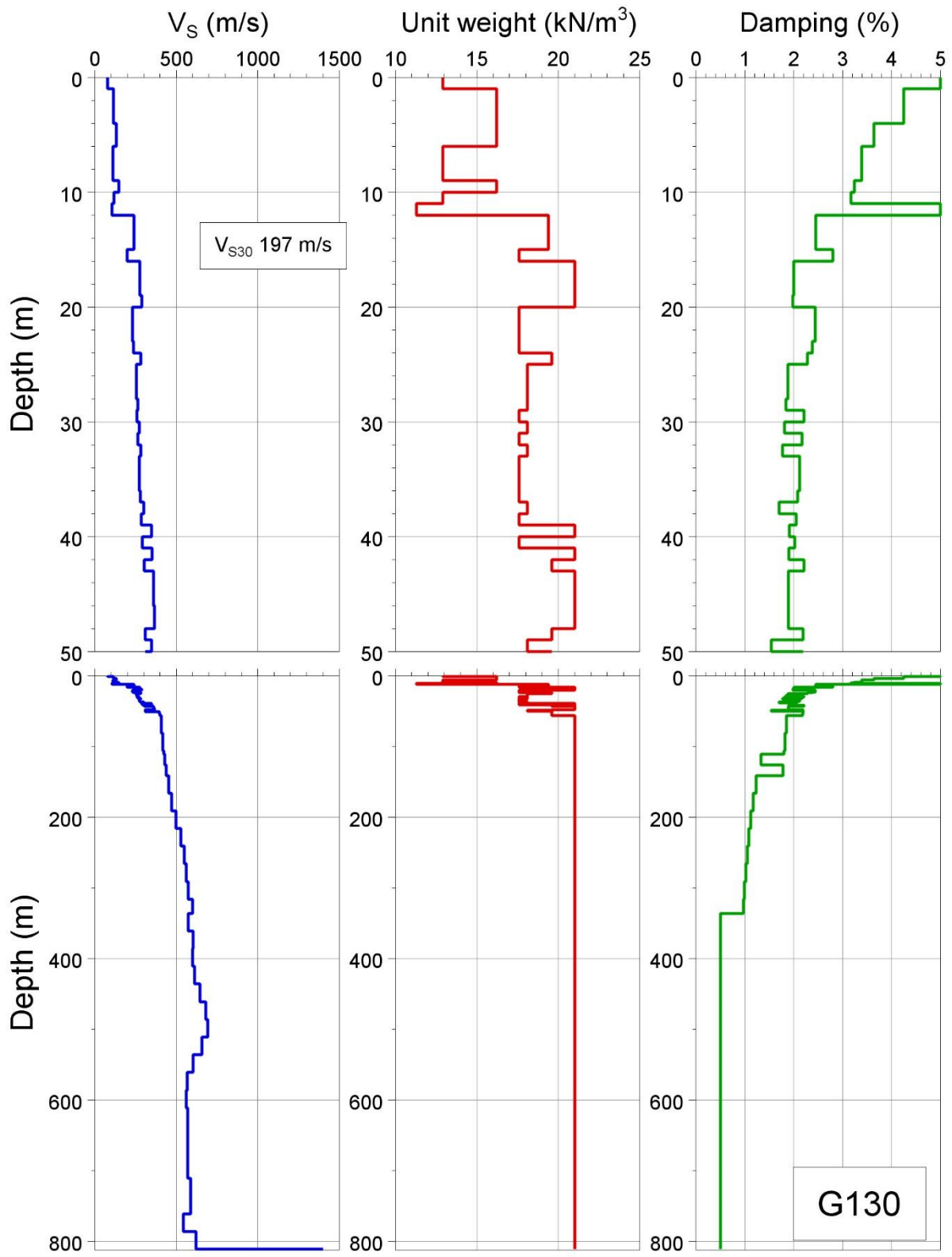


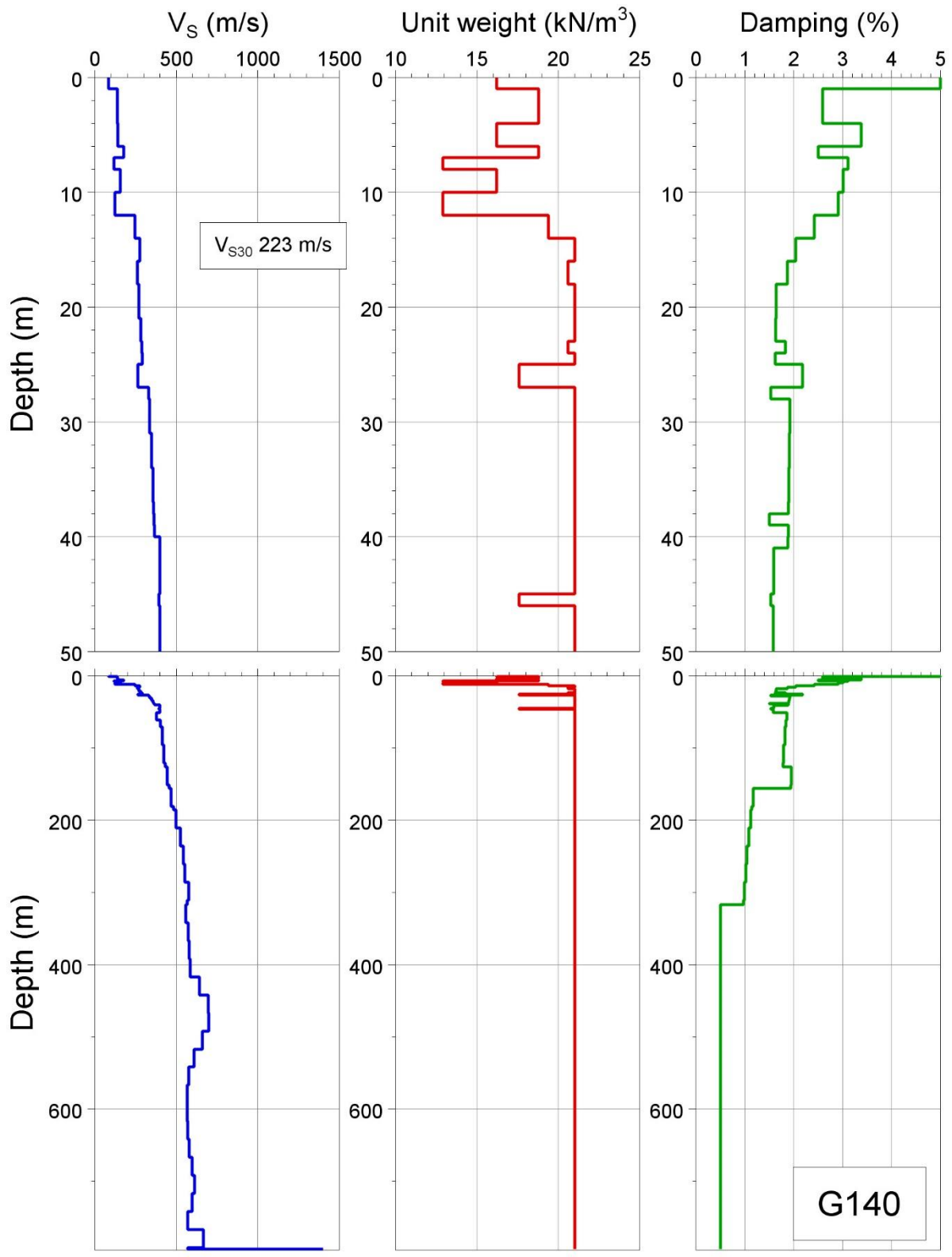


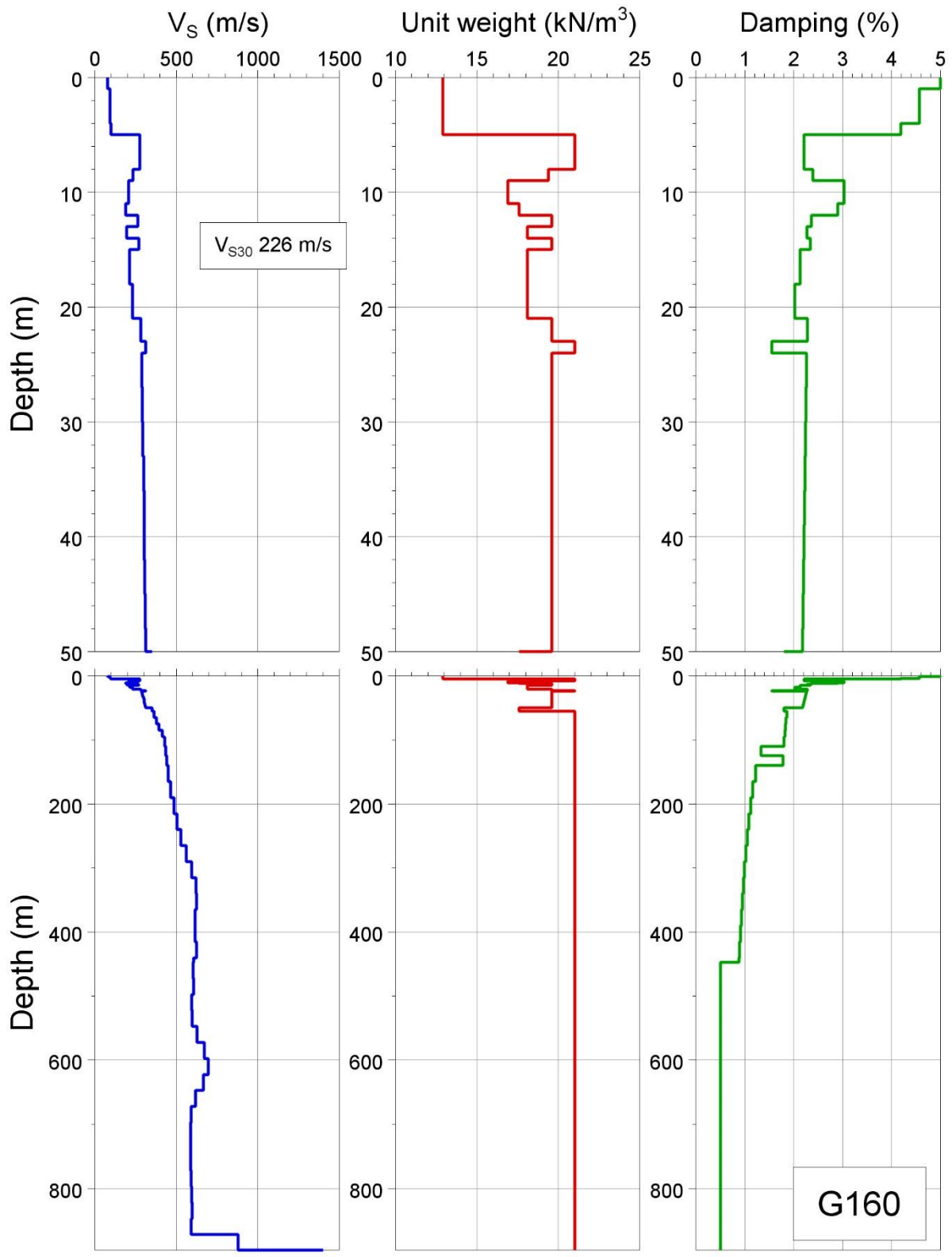


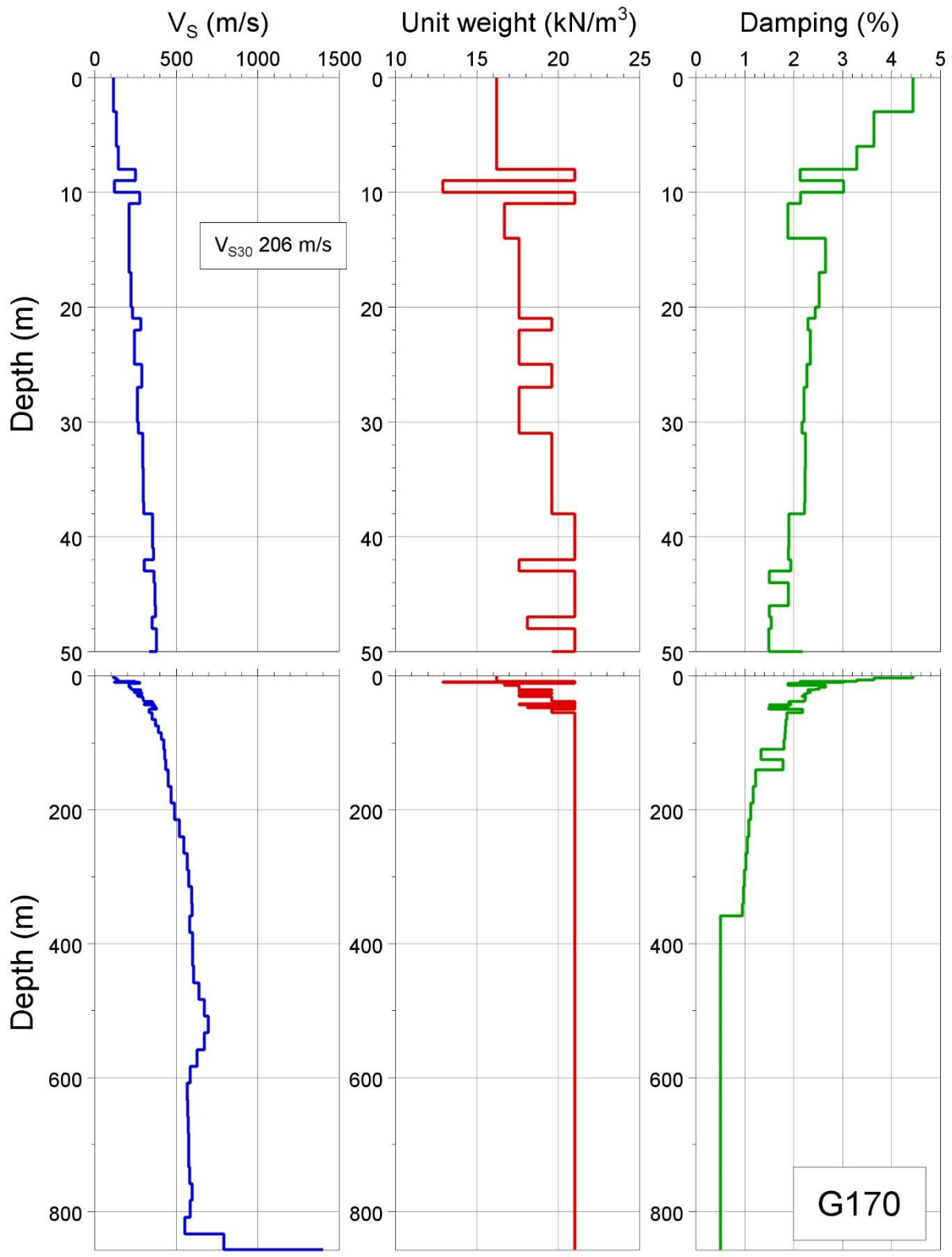


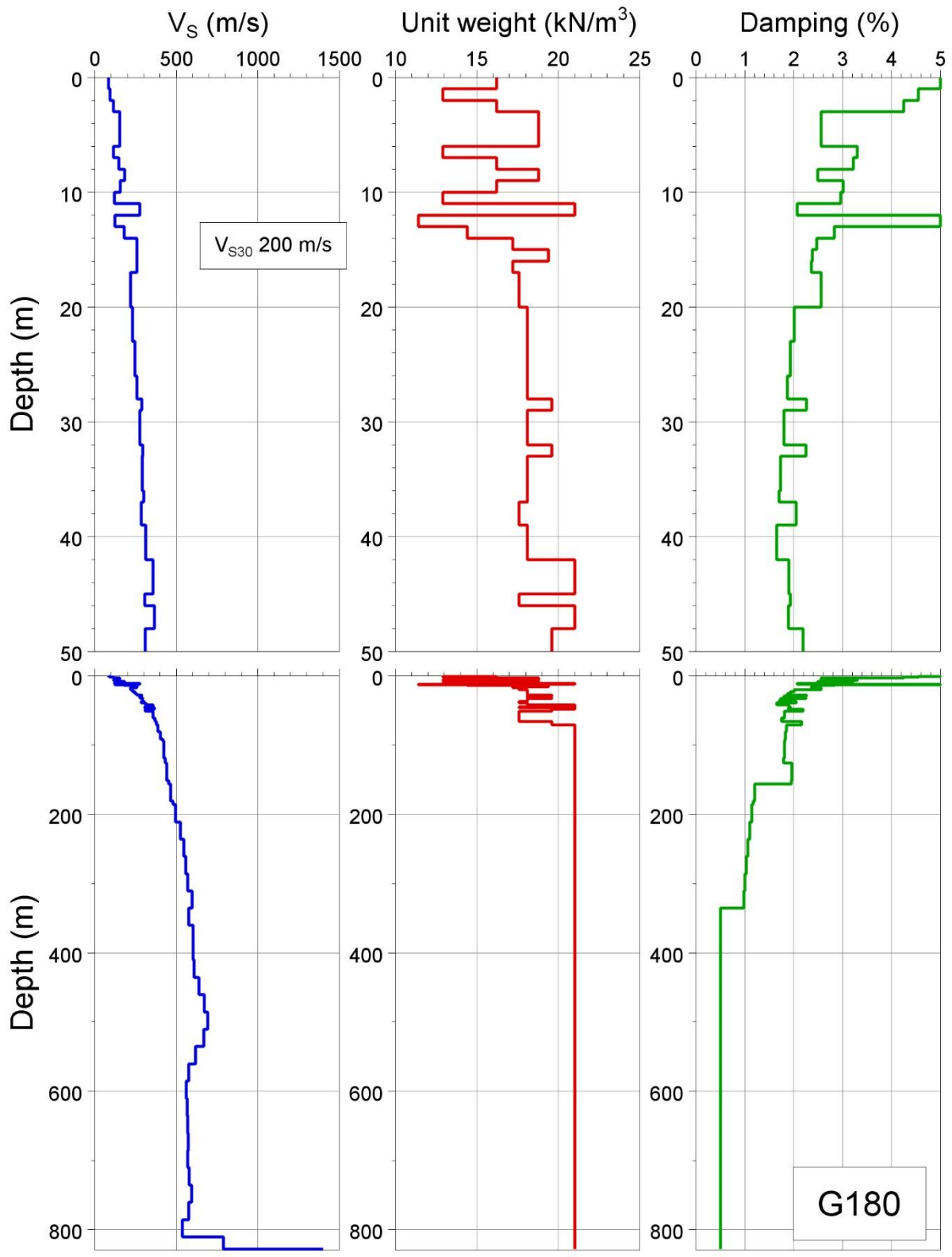


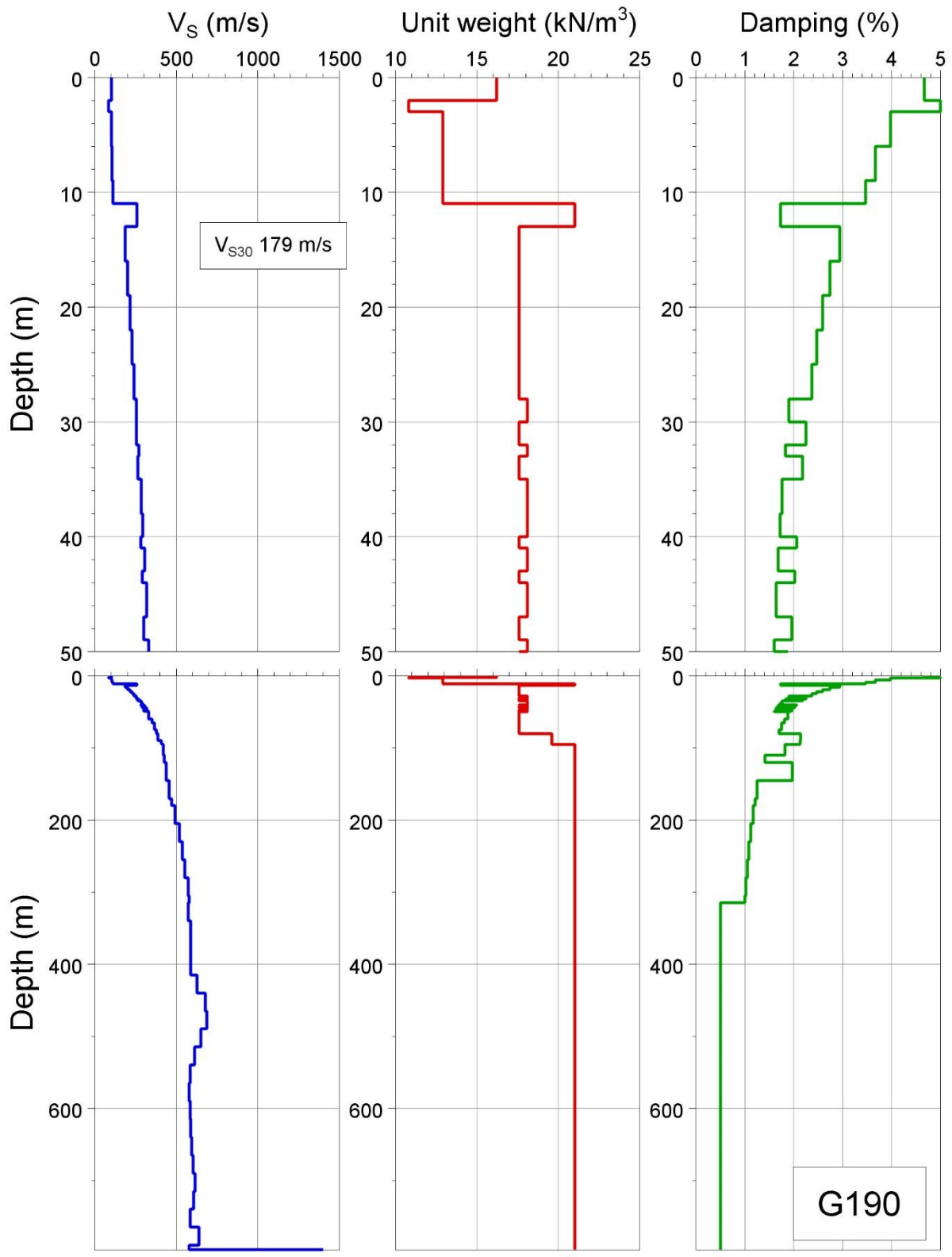


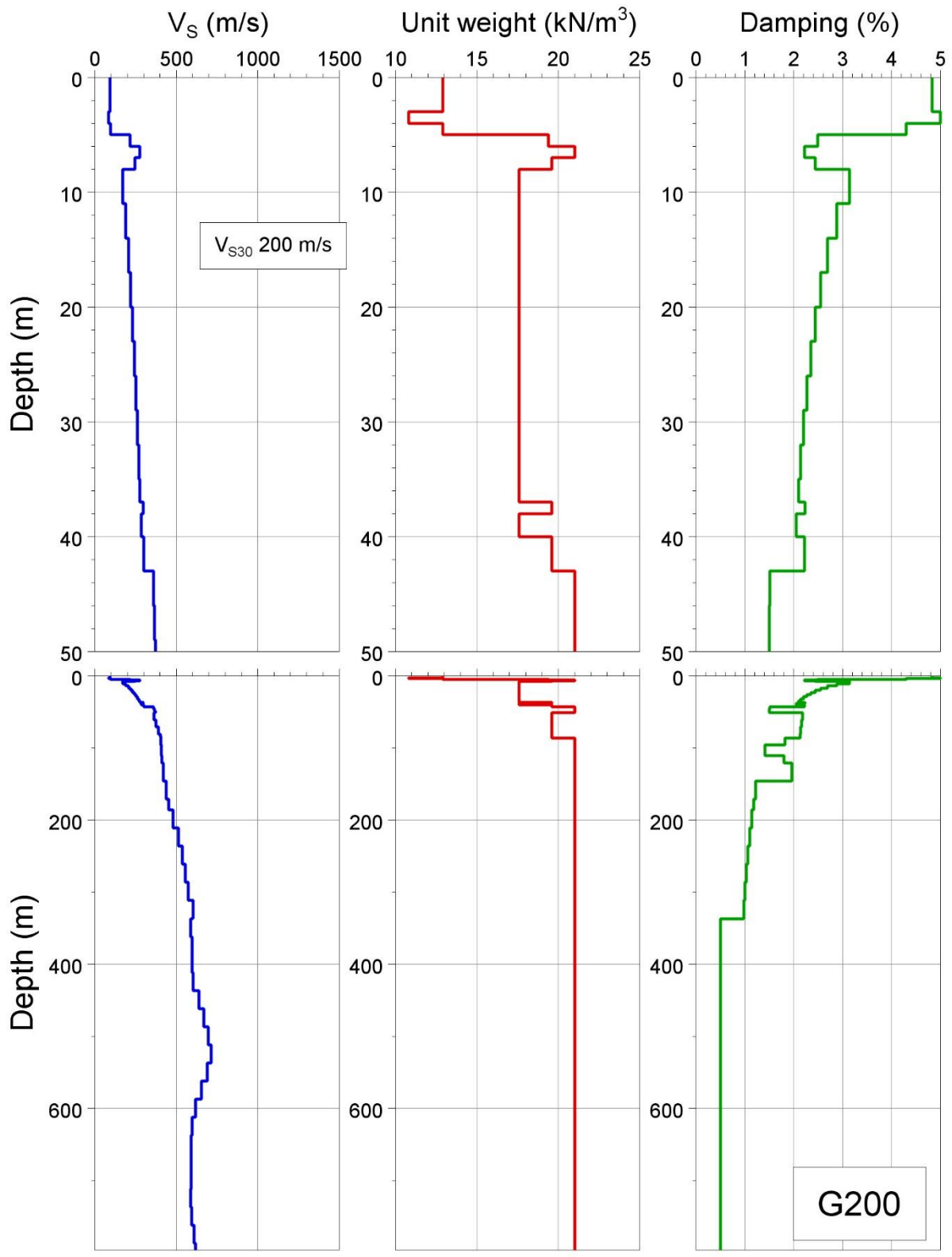


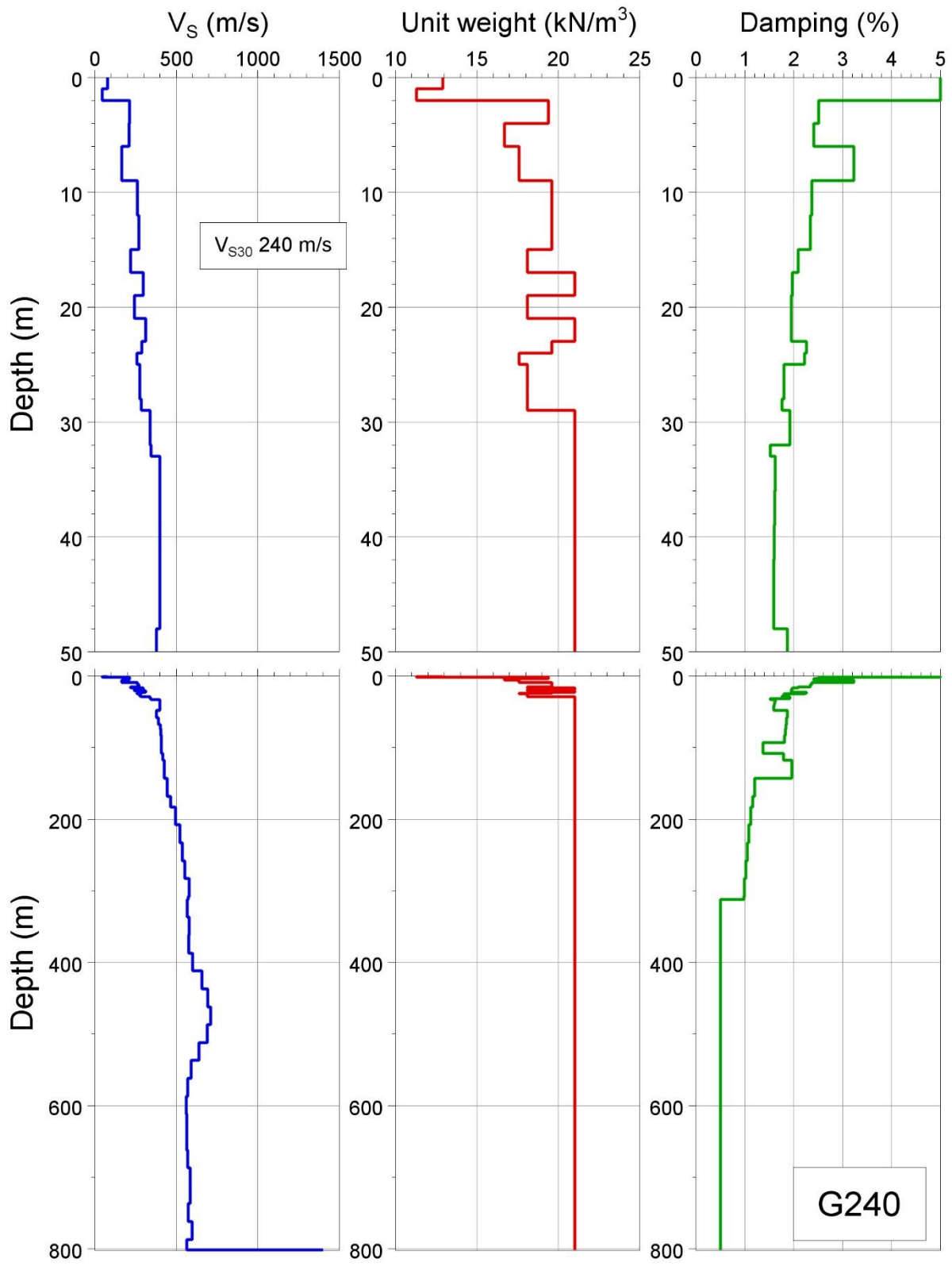


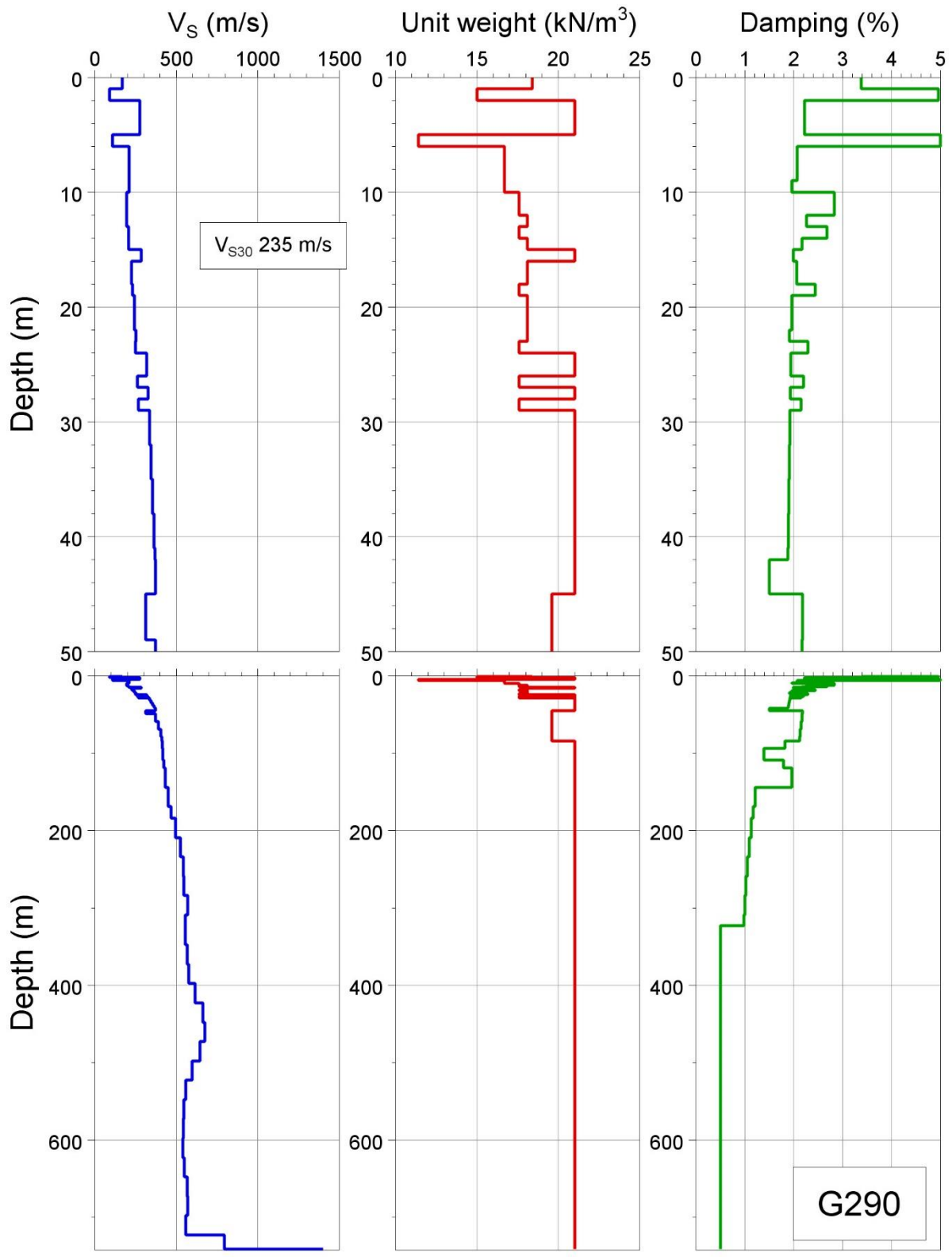


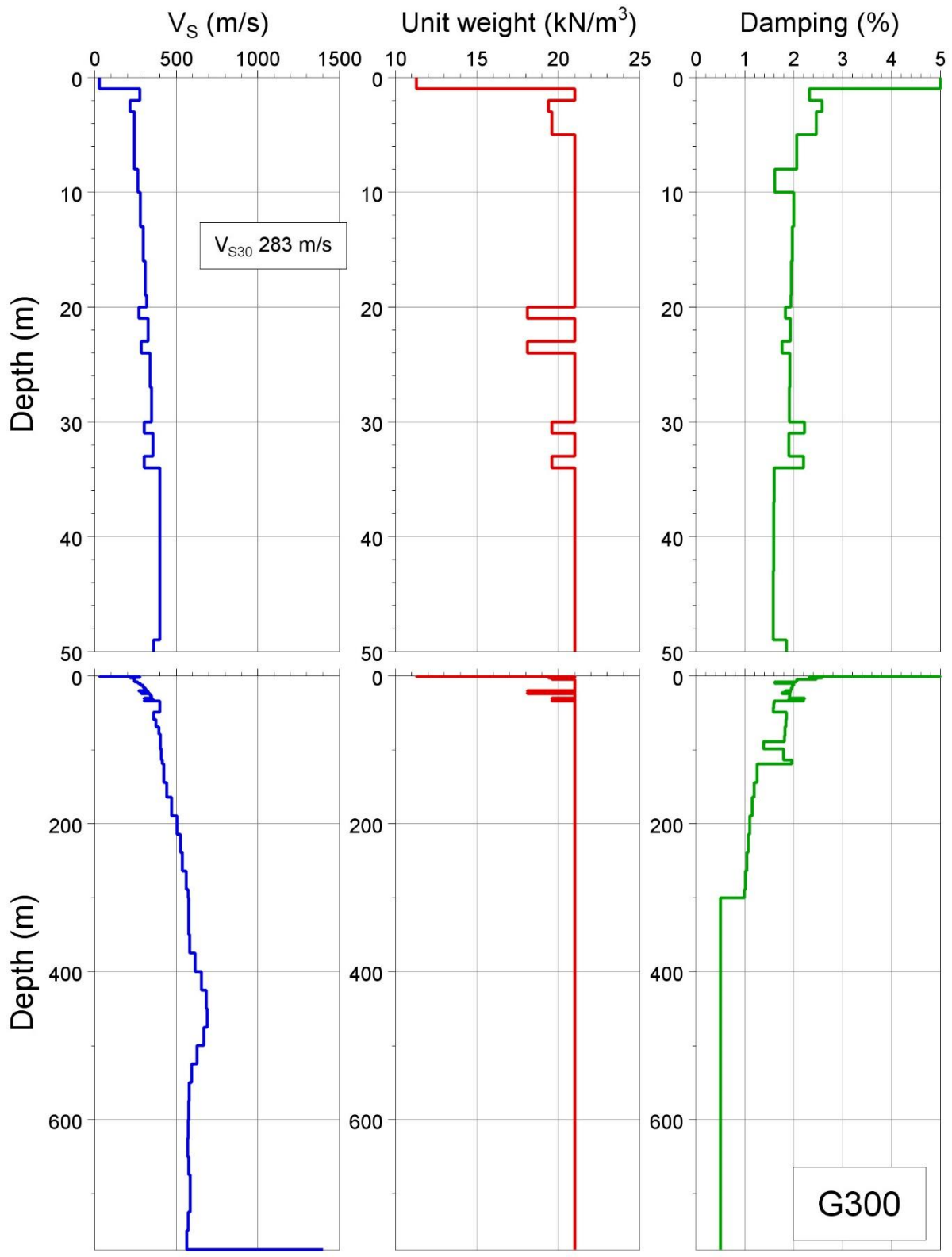


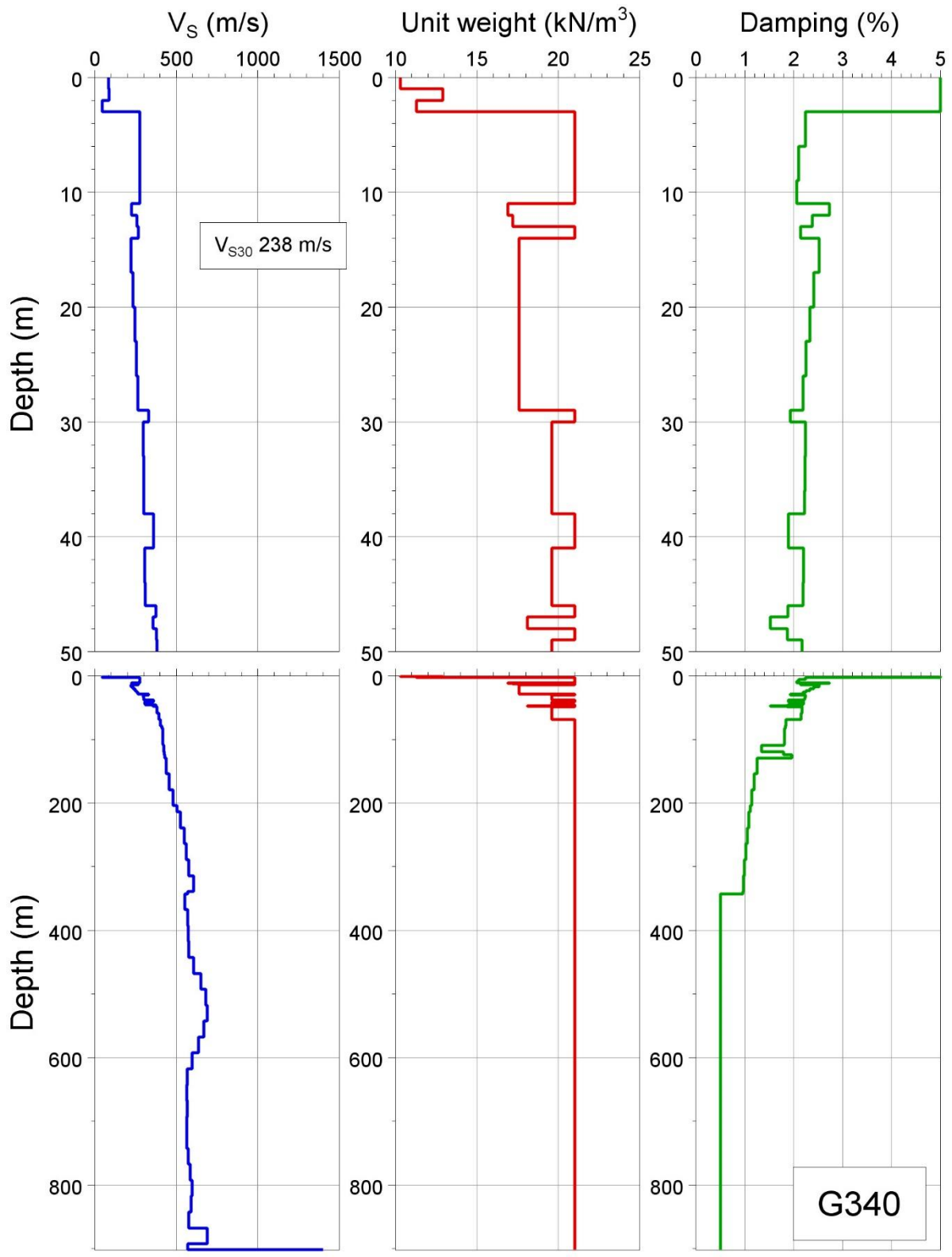


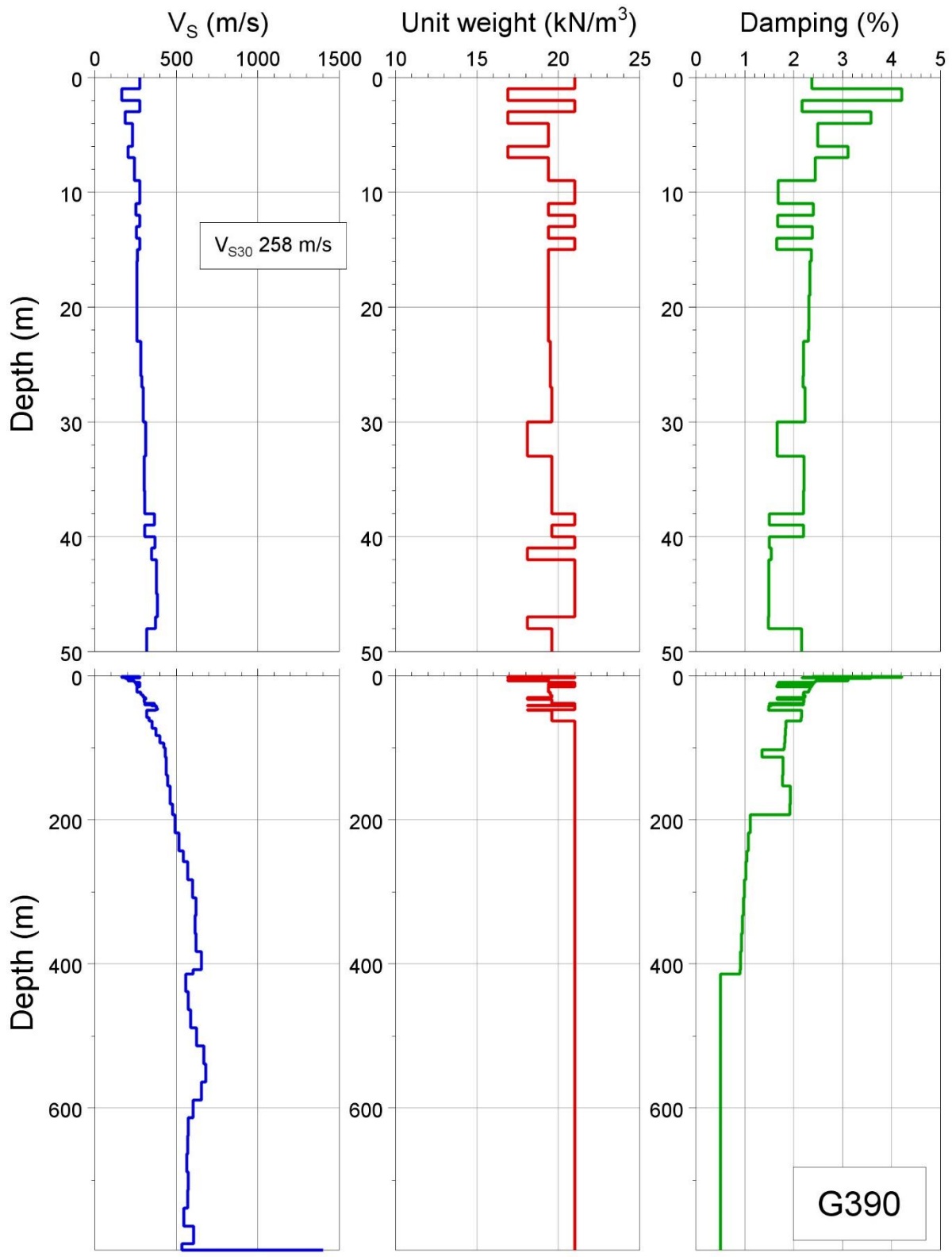


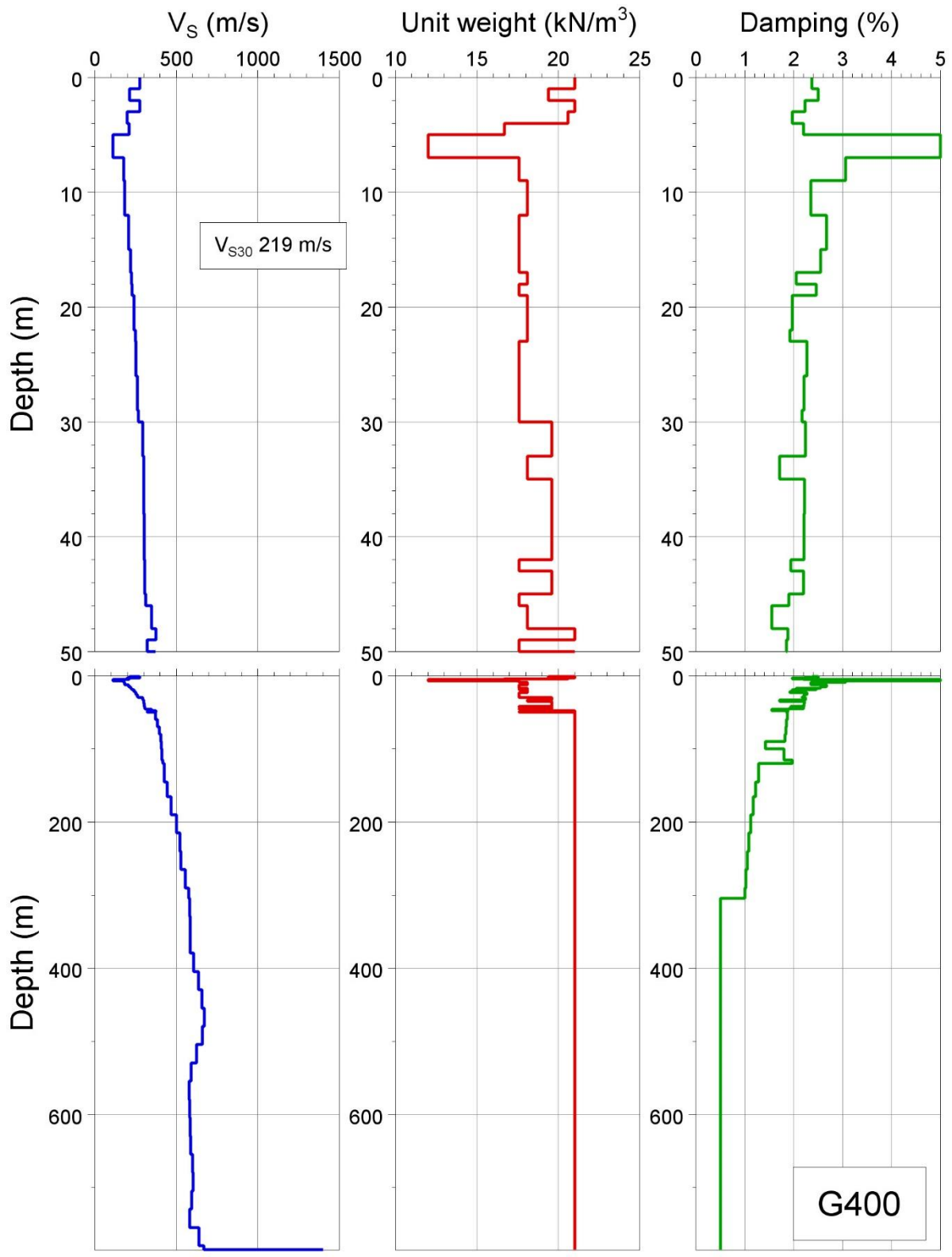


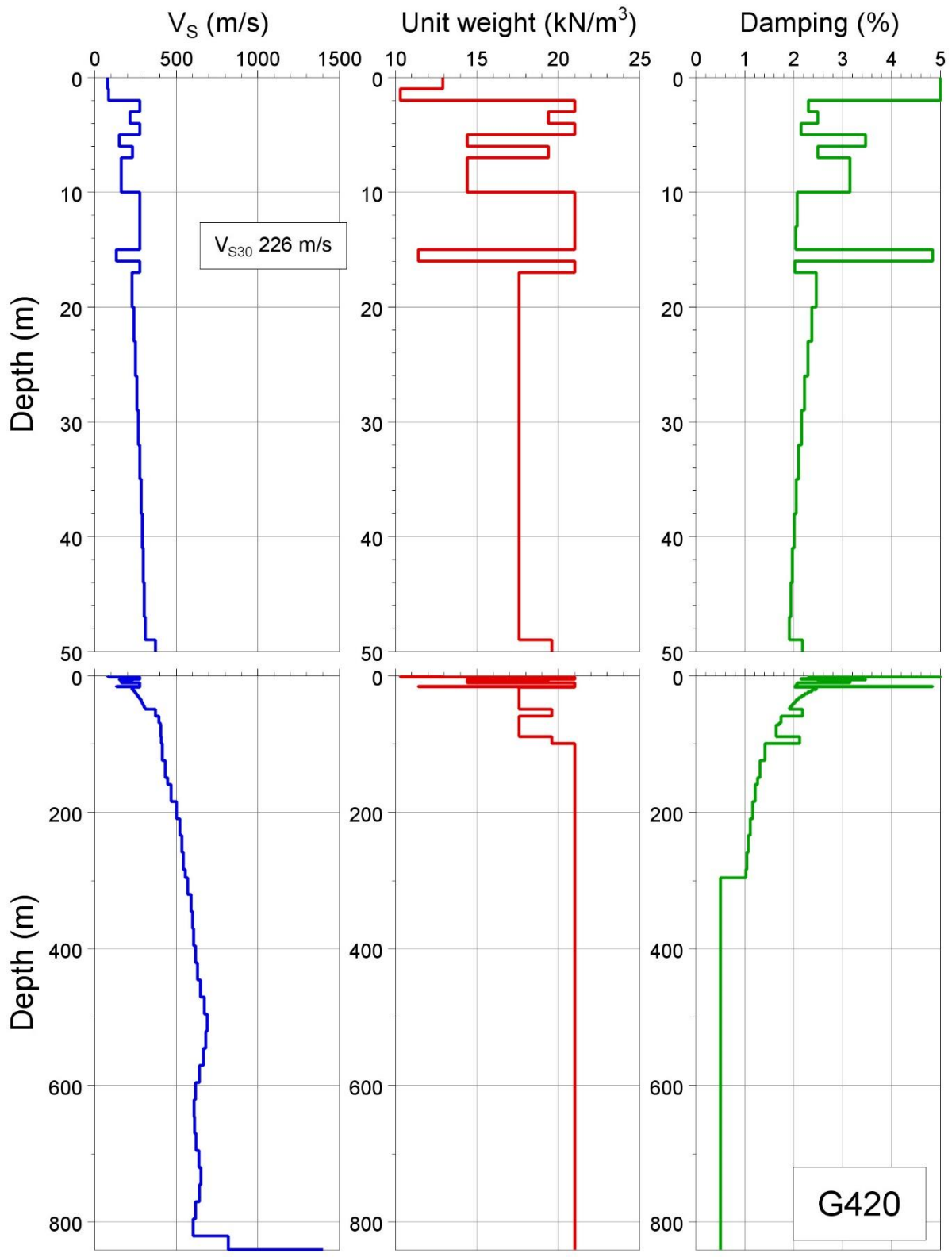


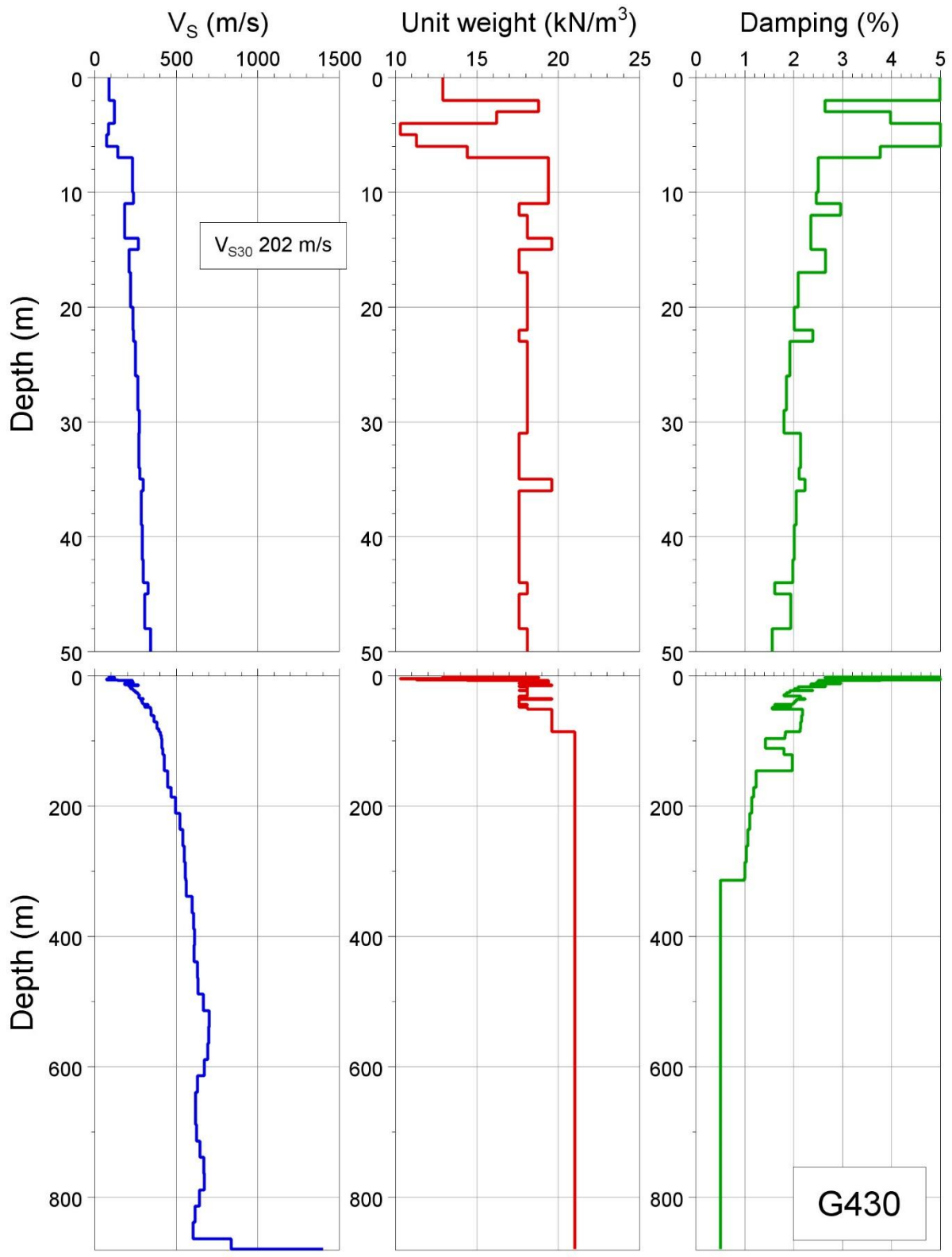


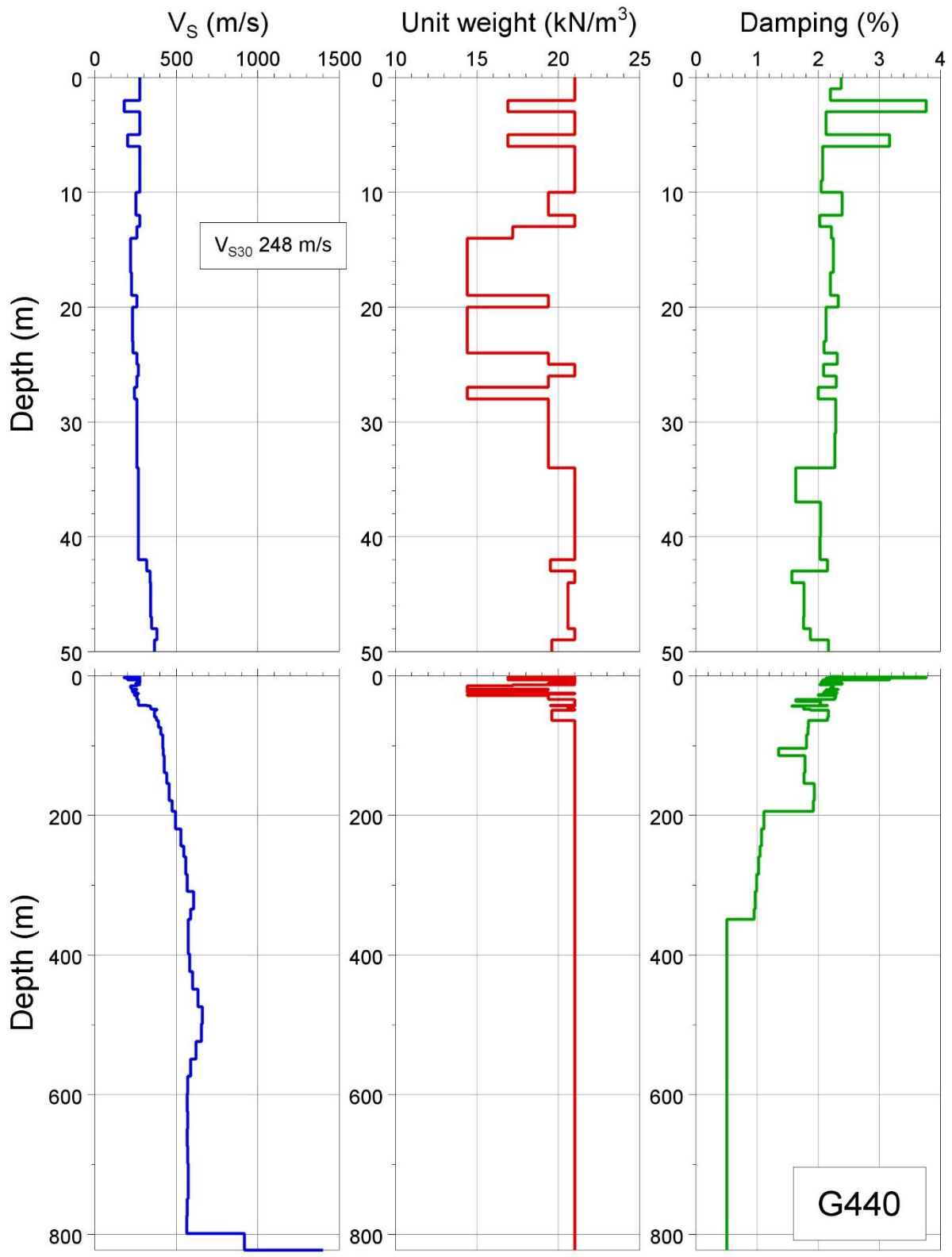


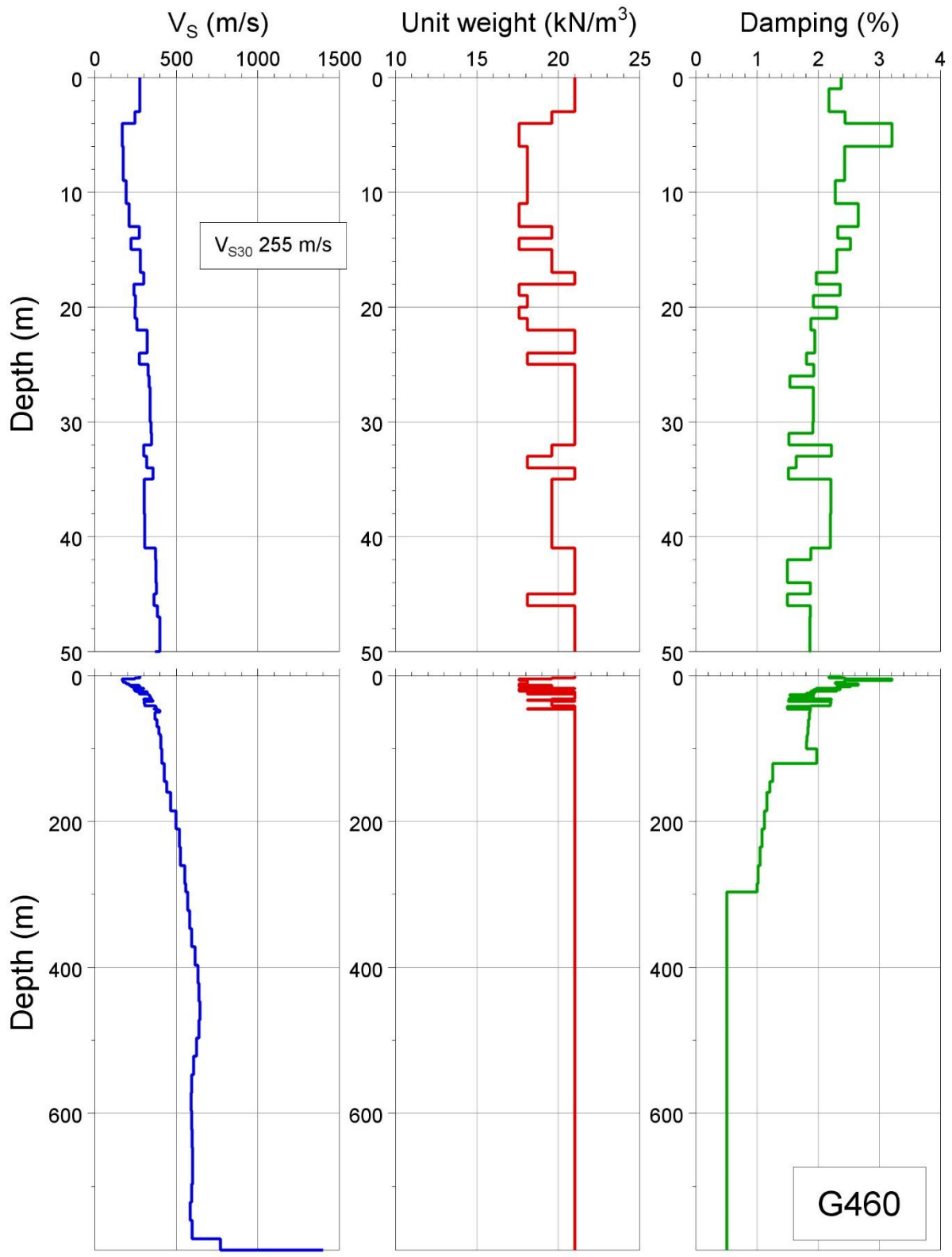


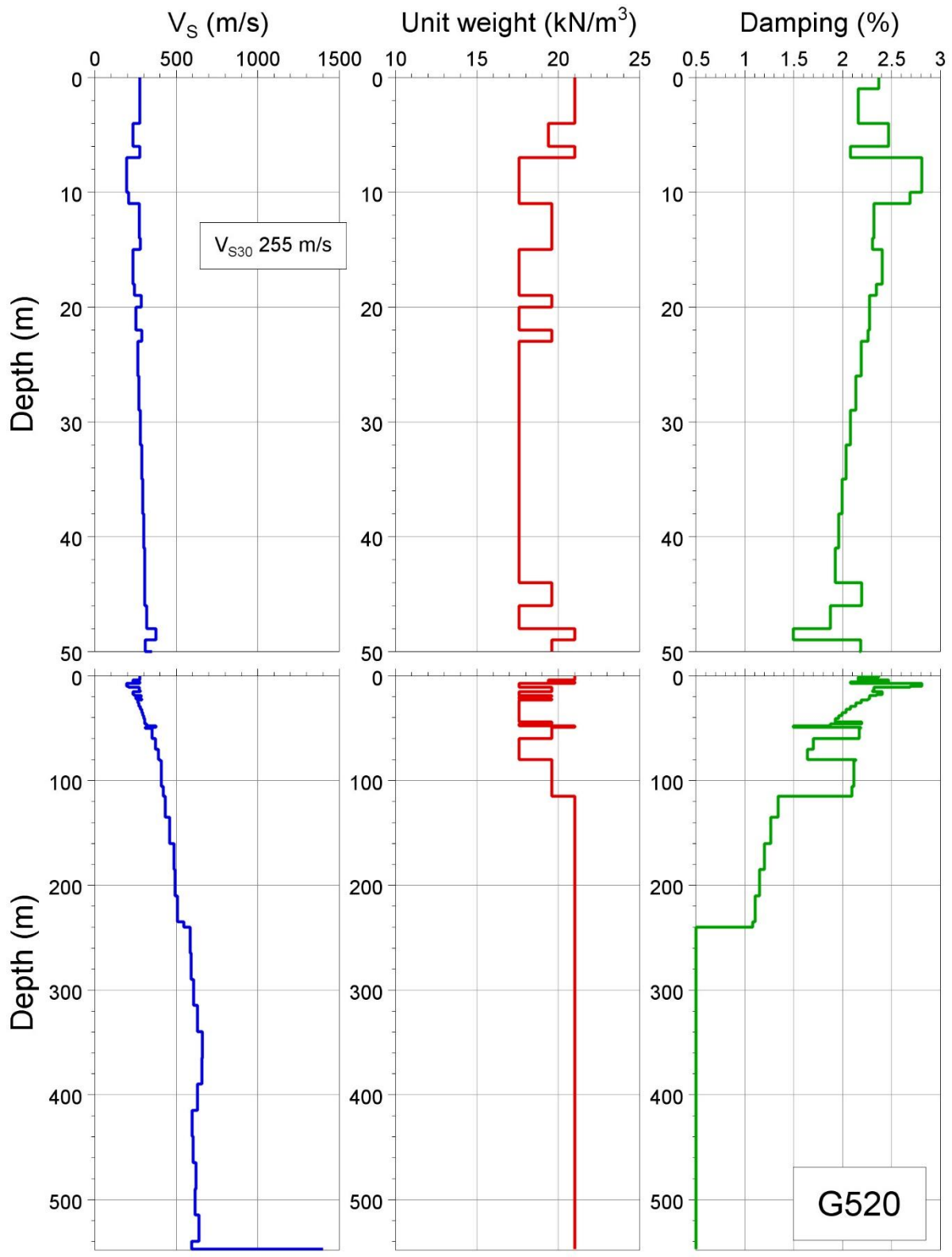


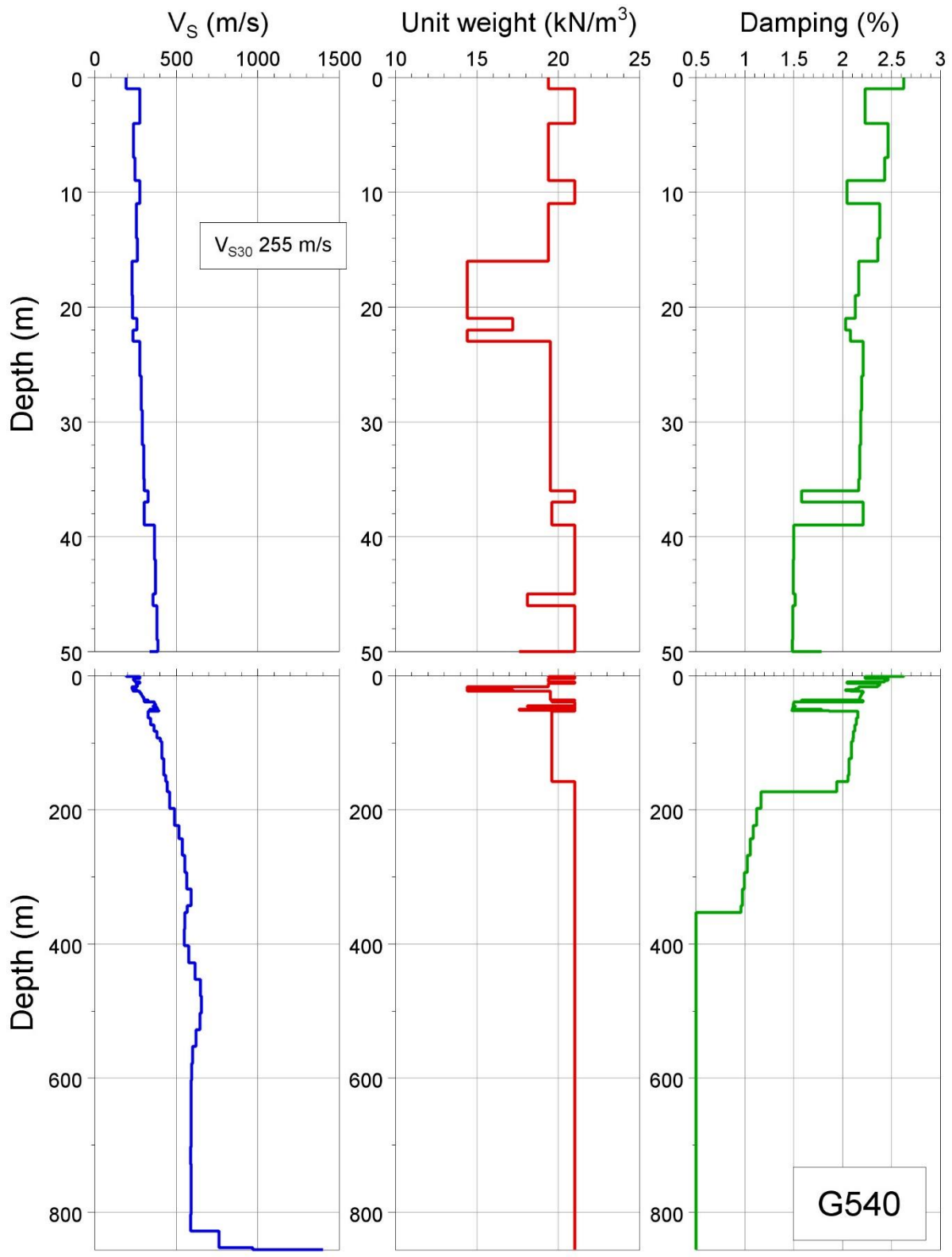


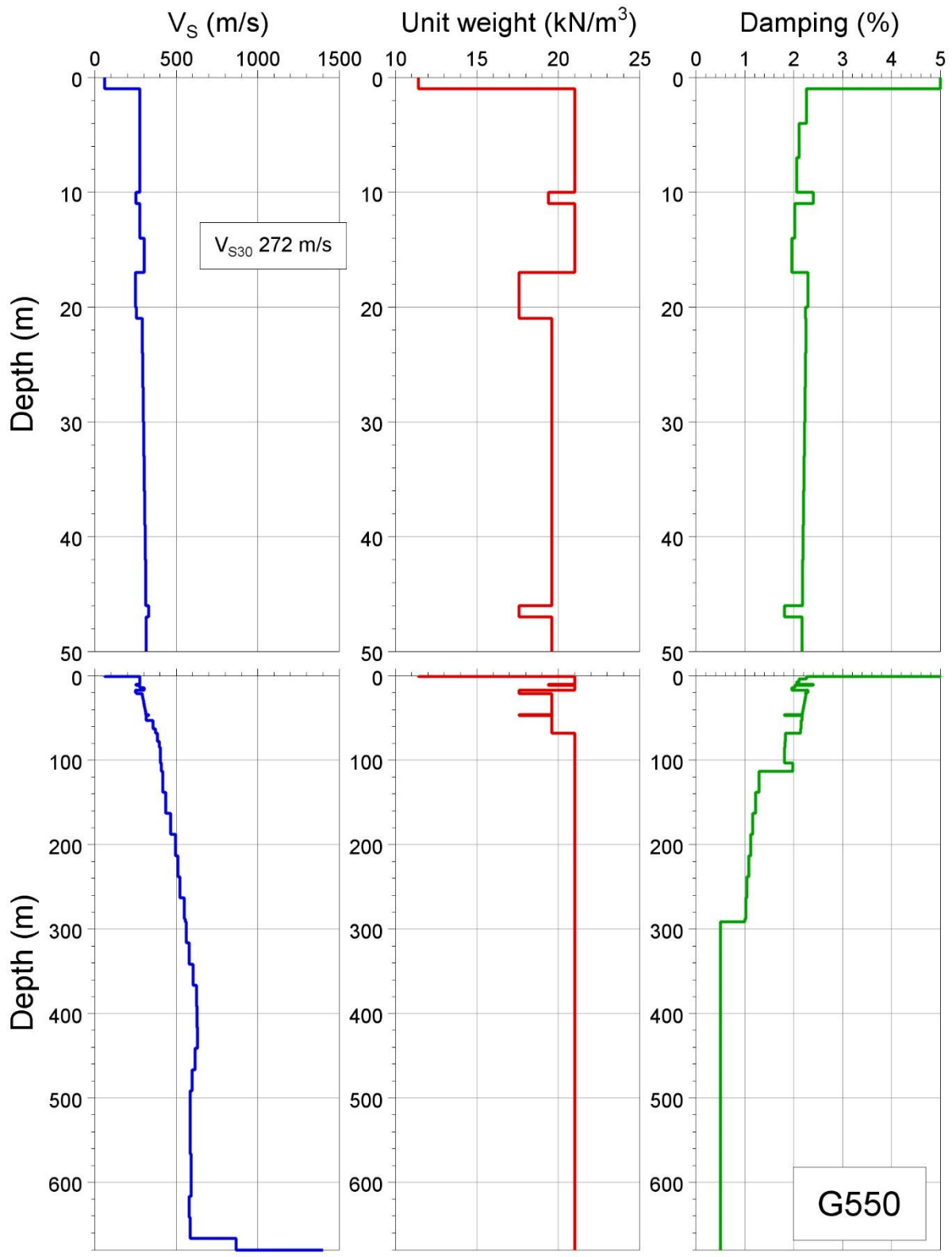


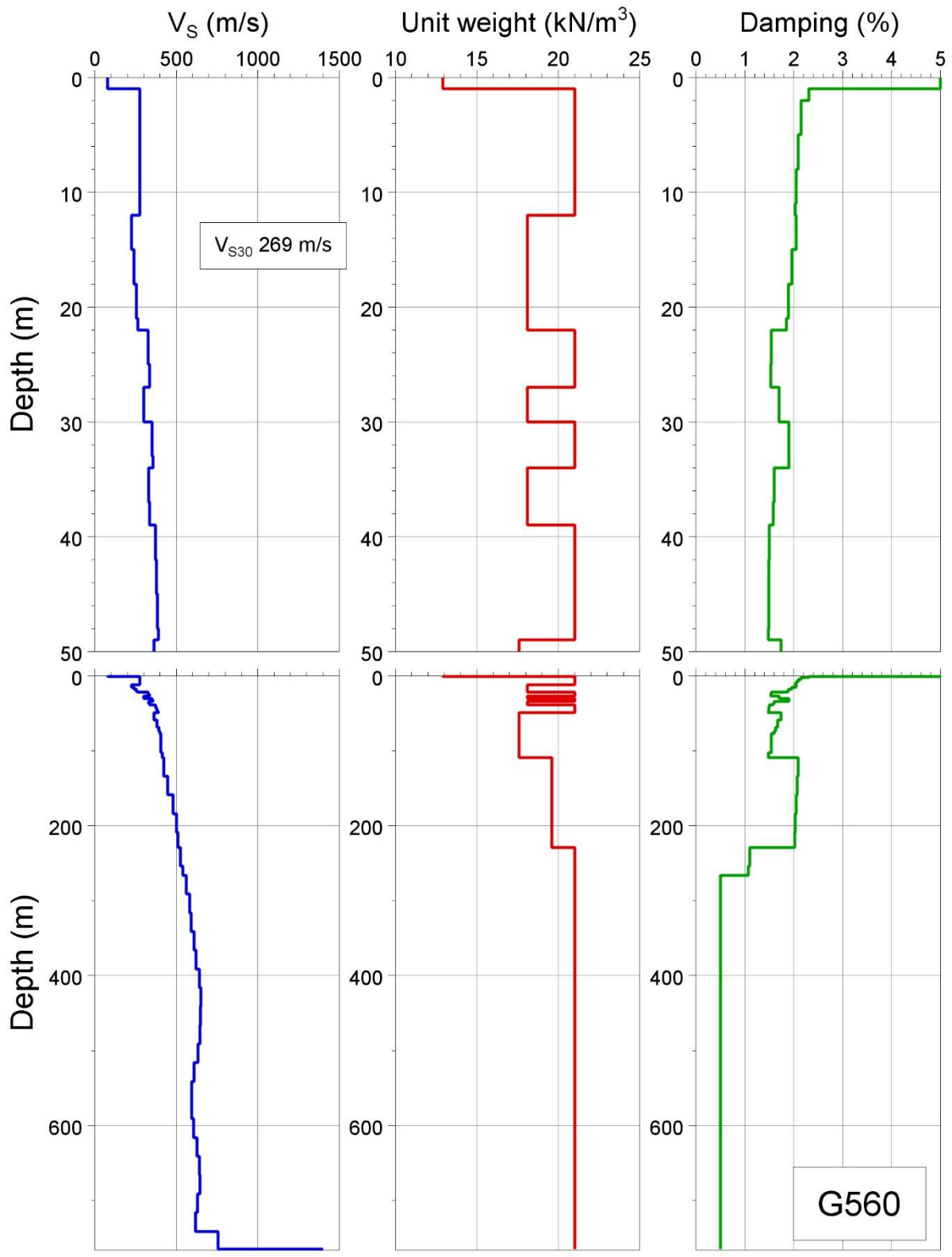


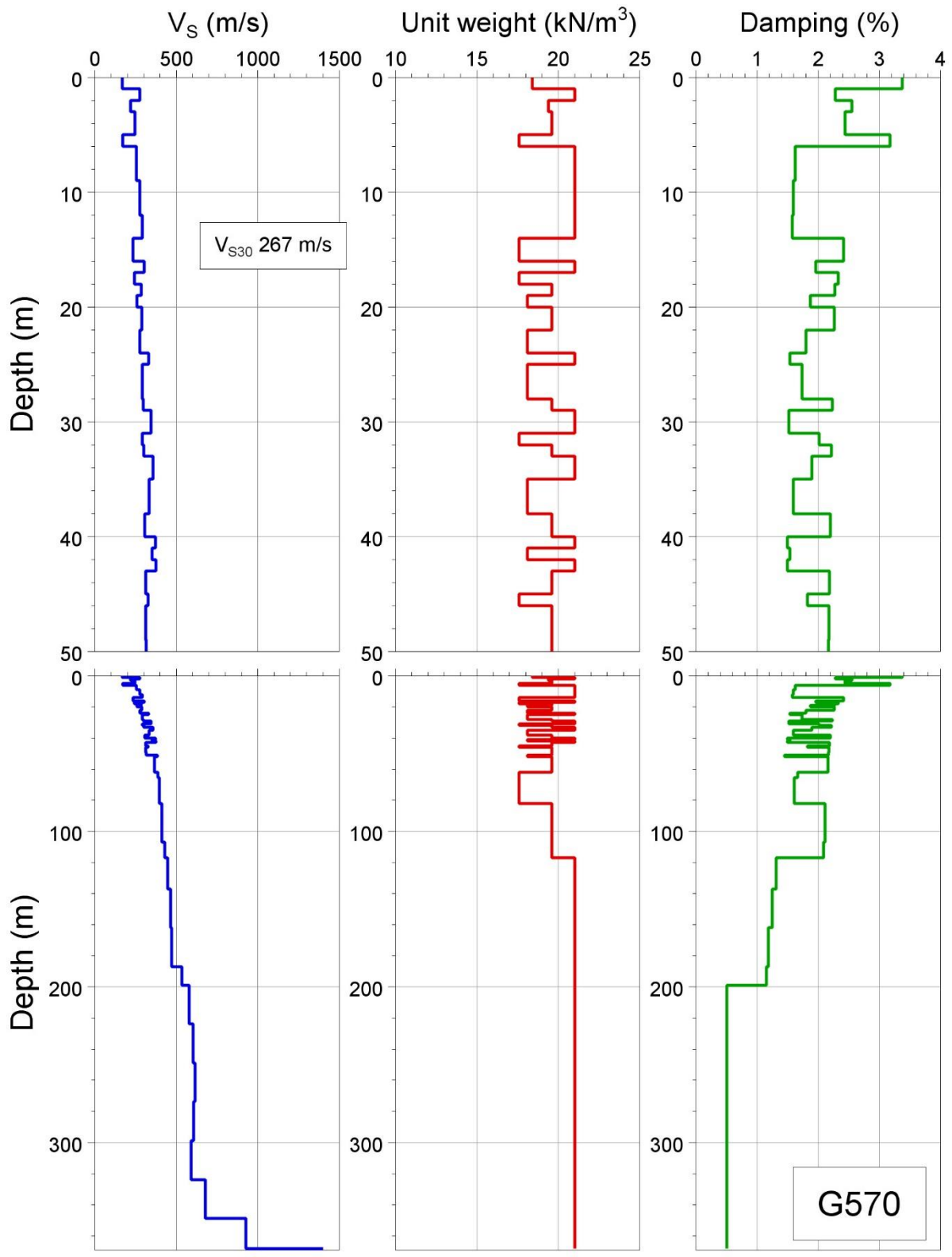


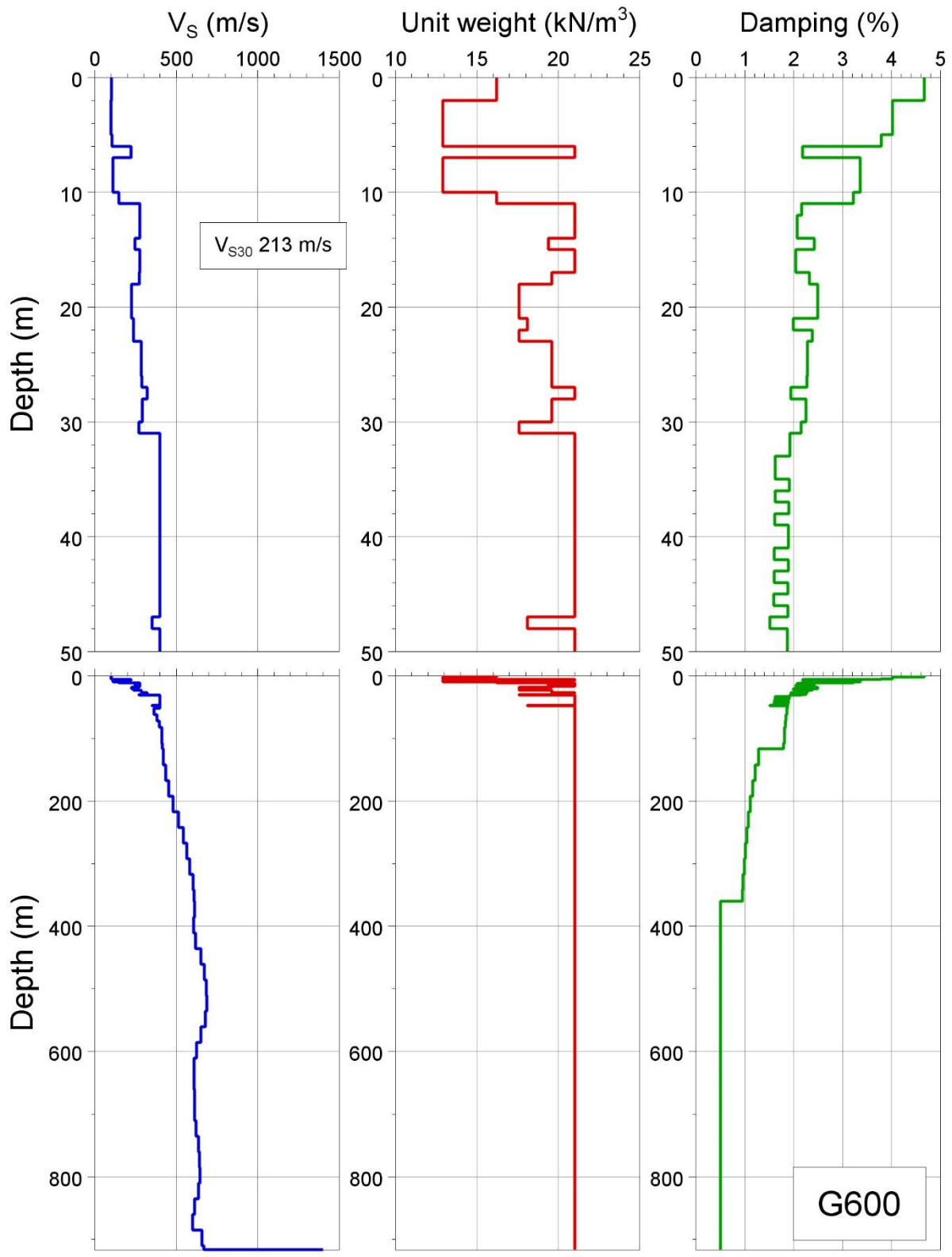


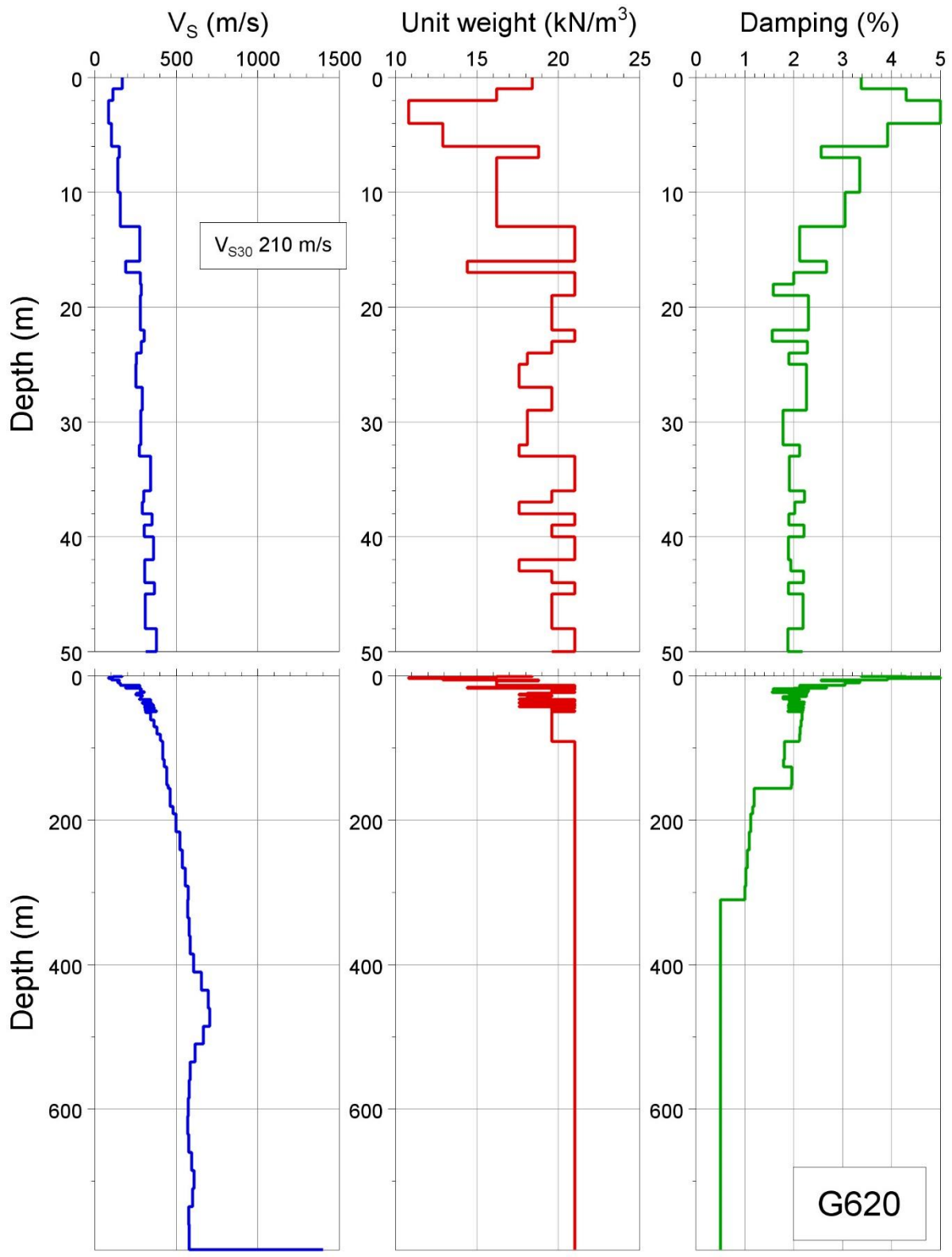


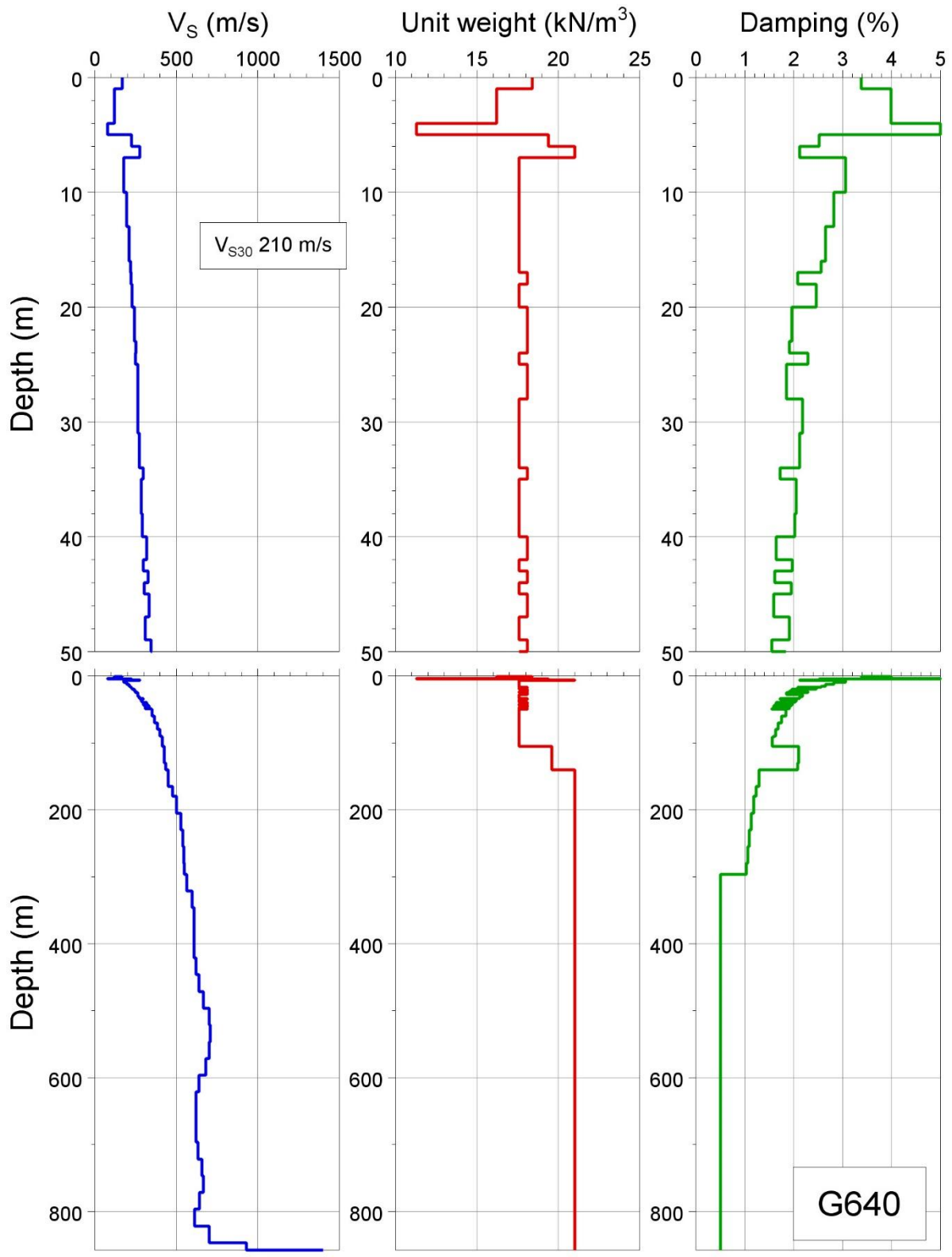


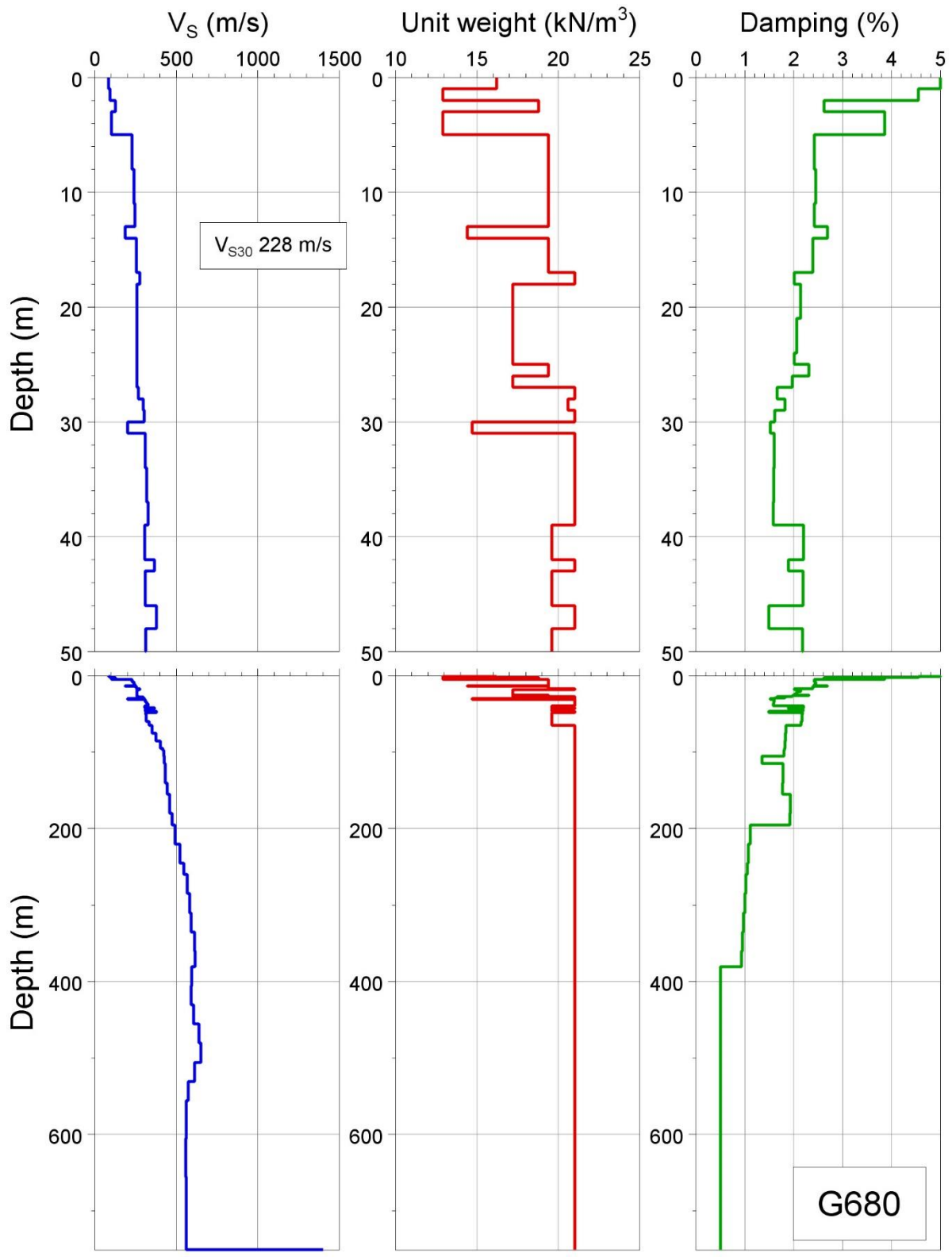








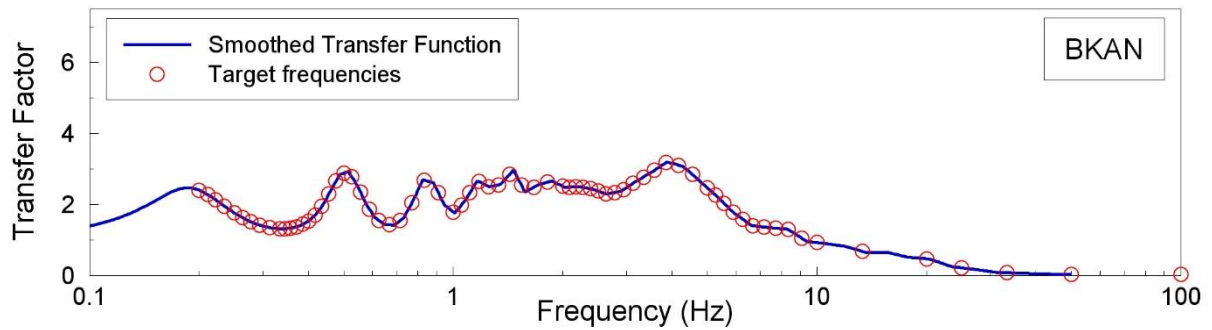
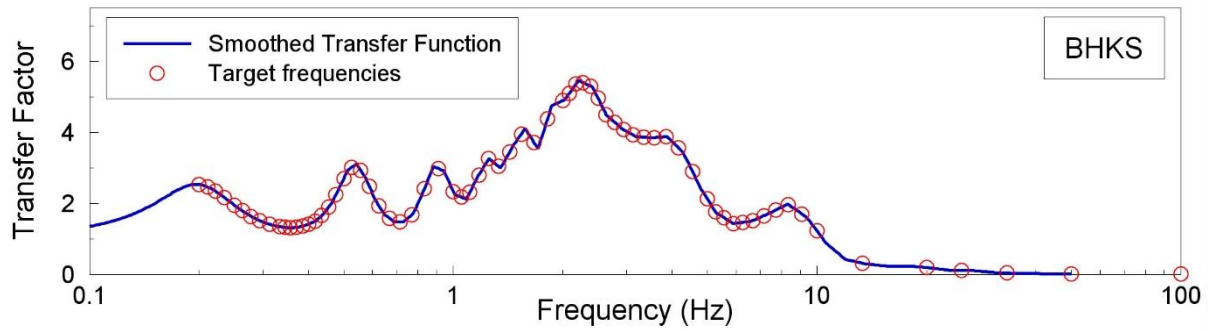
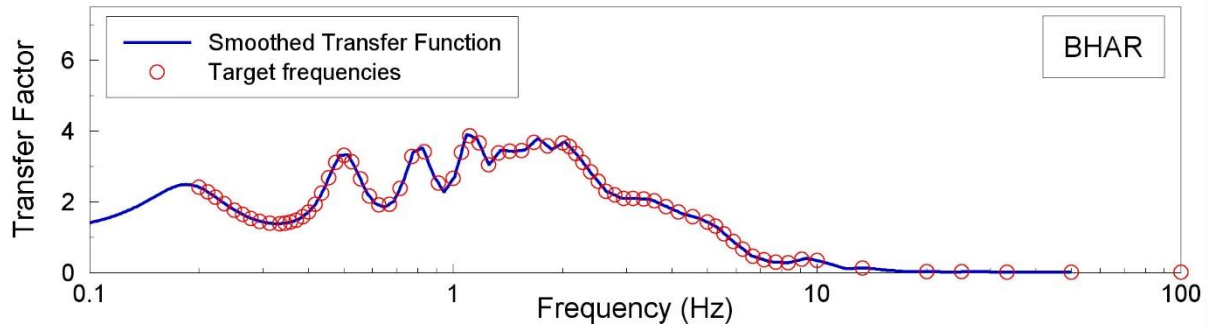
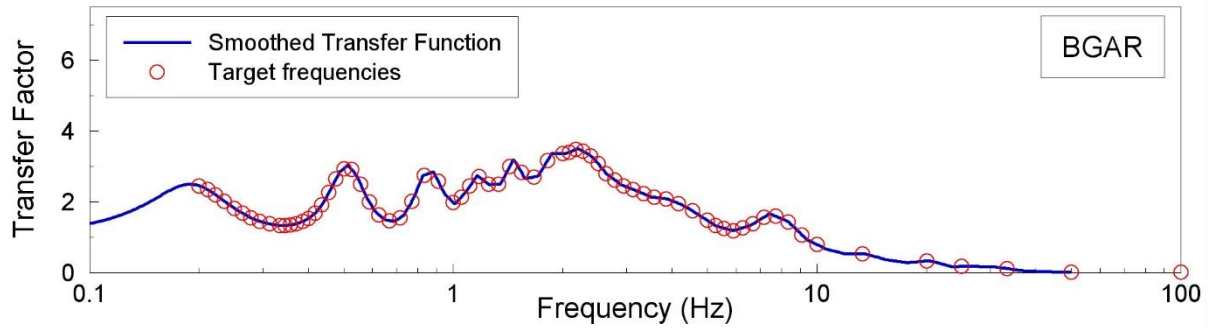
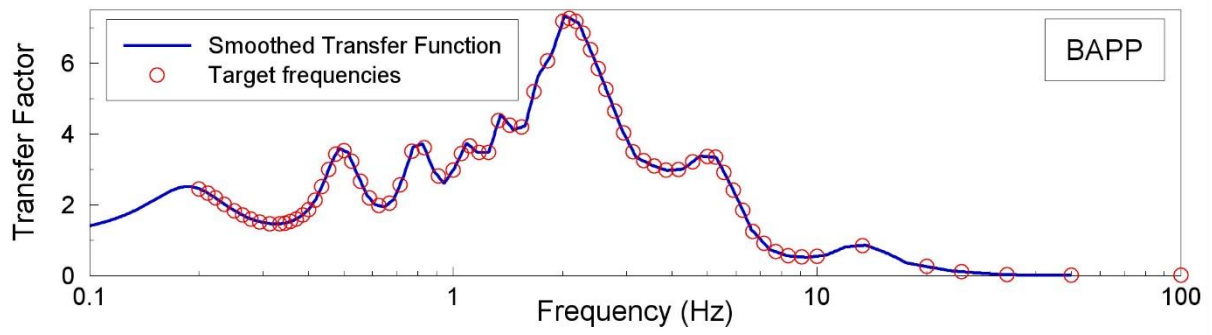


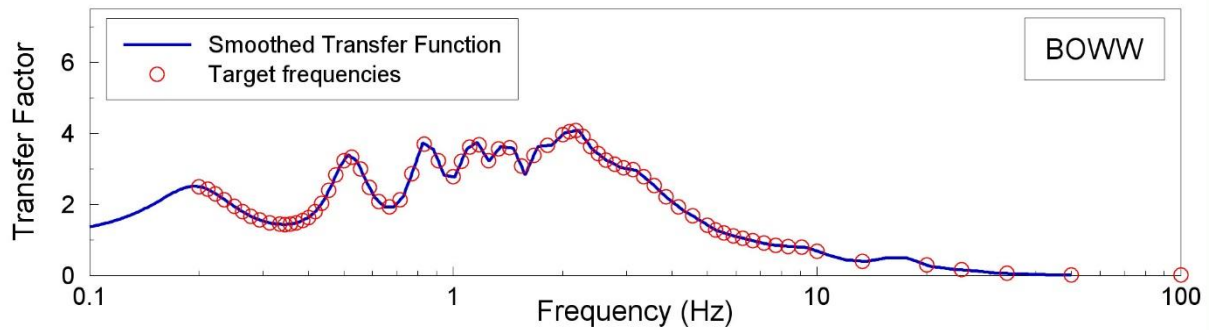
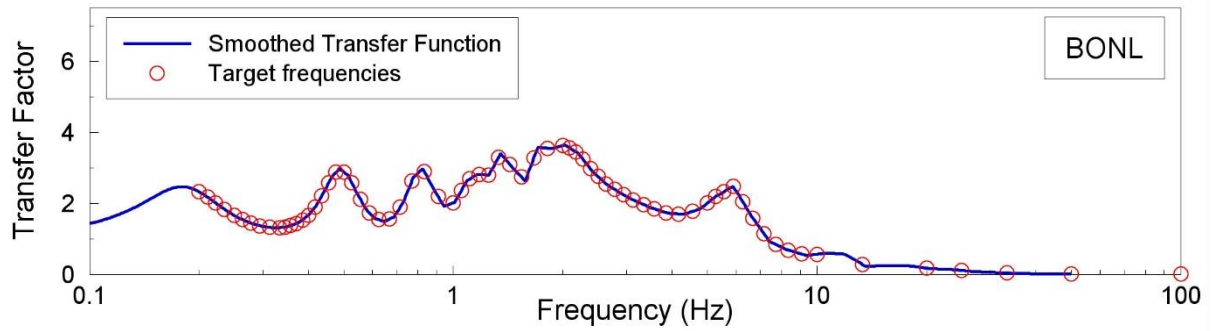
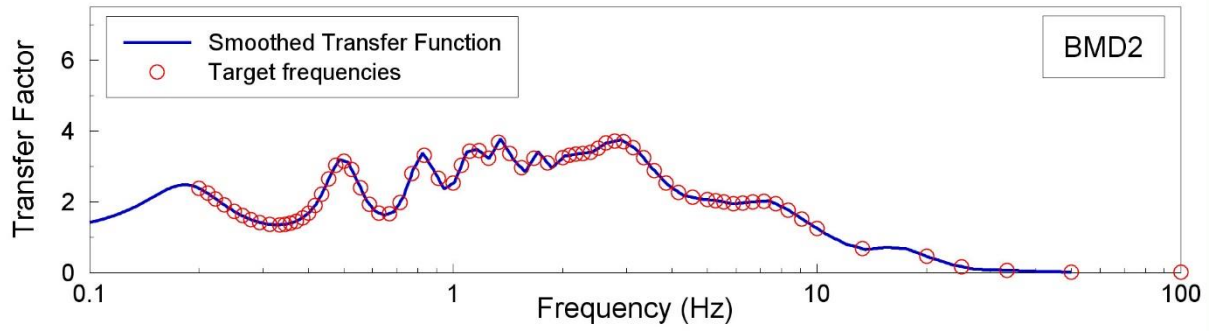
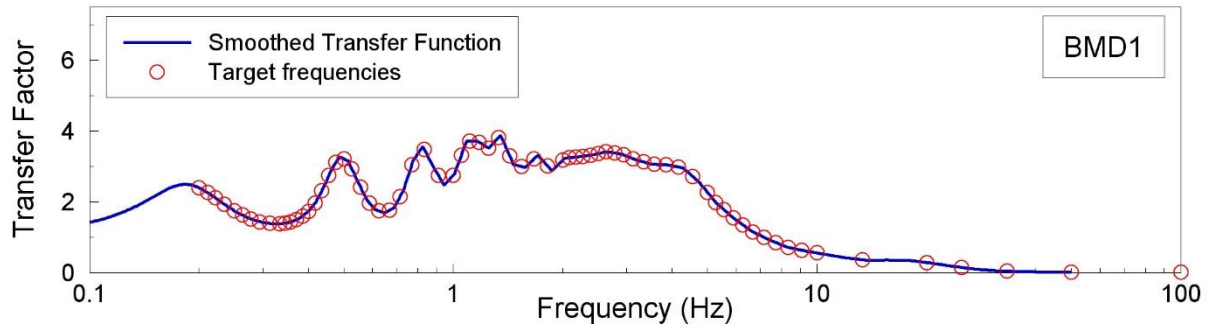
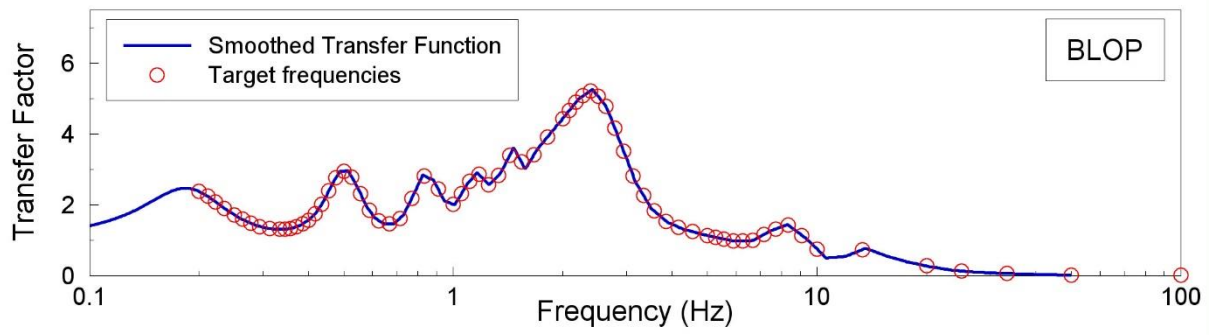


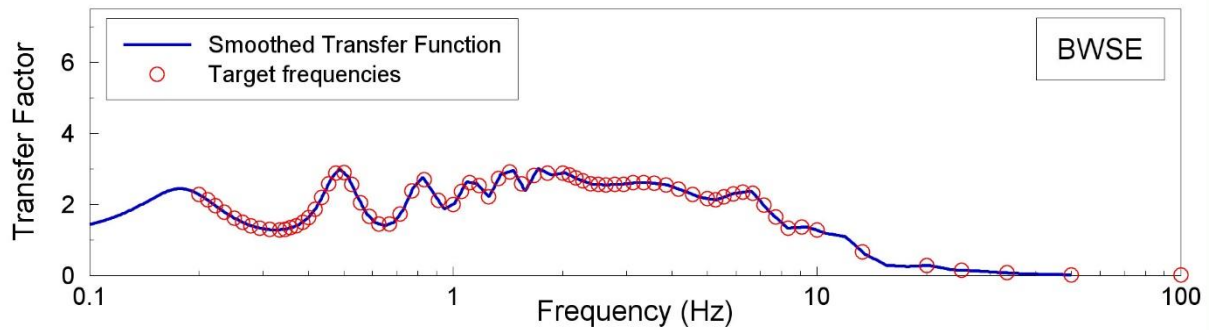
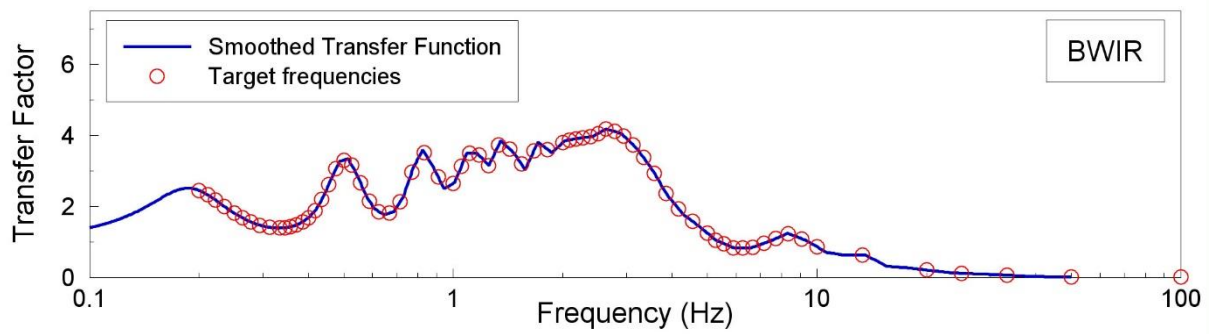
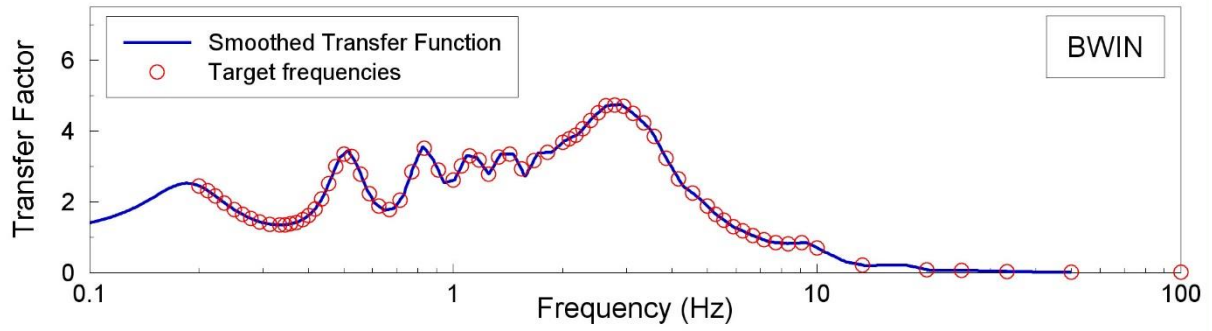
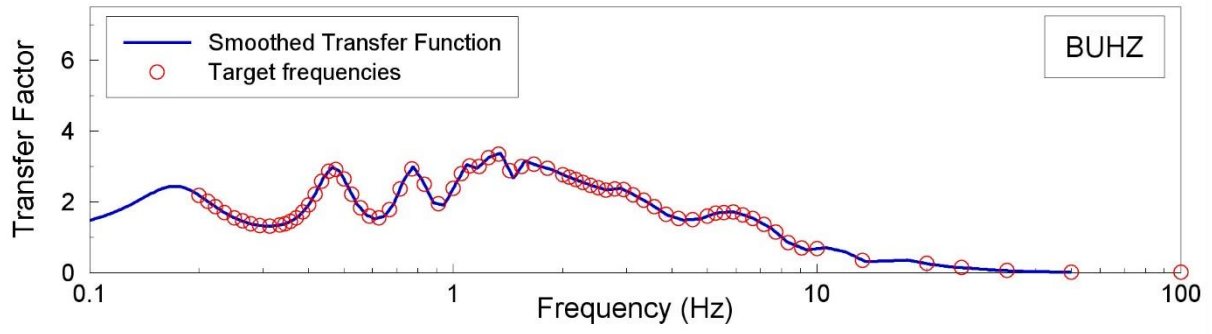
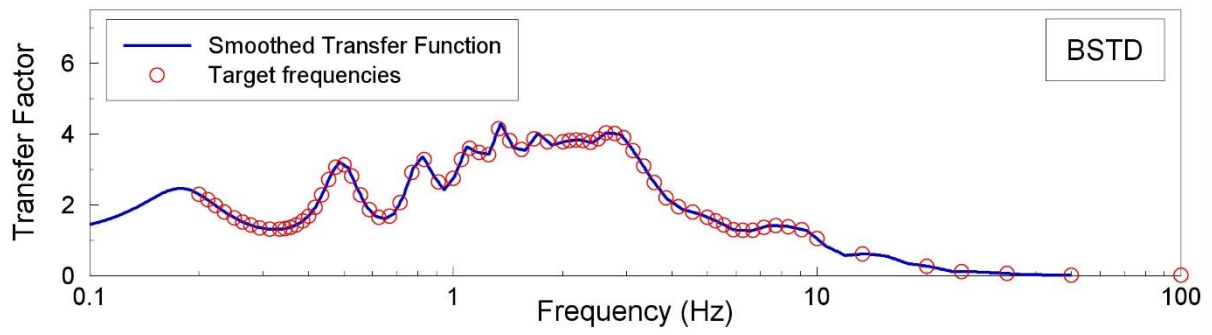
APPENDIX II

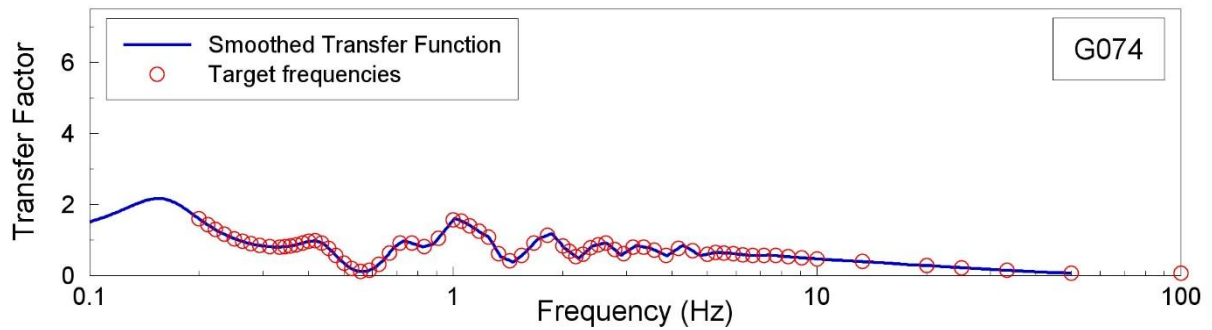
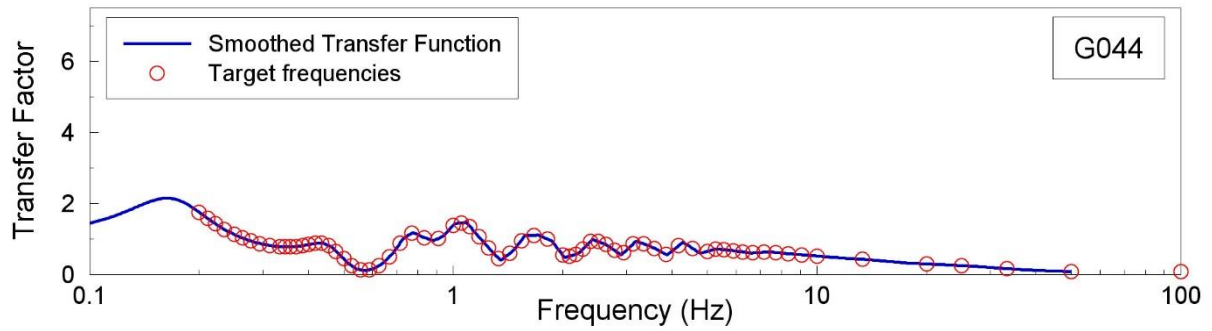
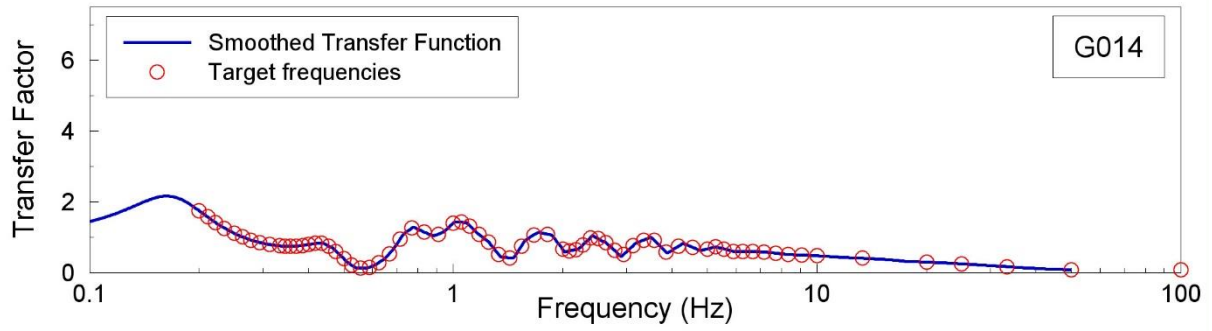
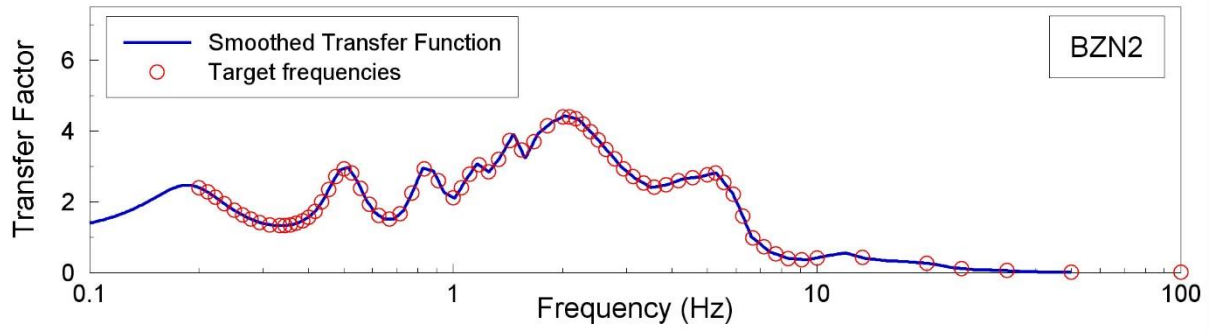
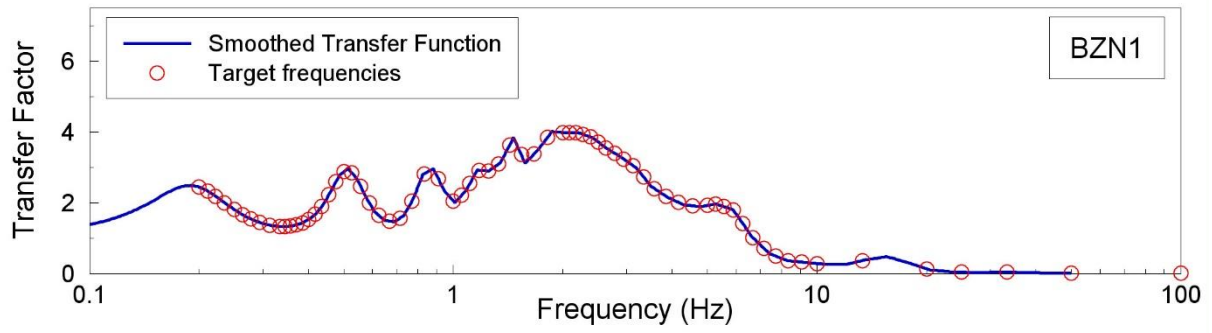
Transfer functions for recording stations

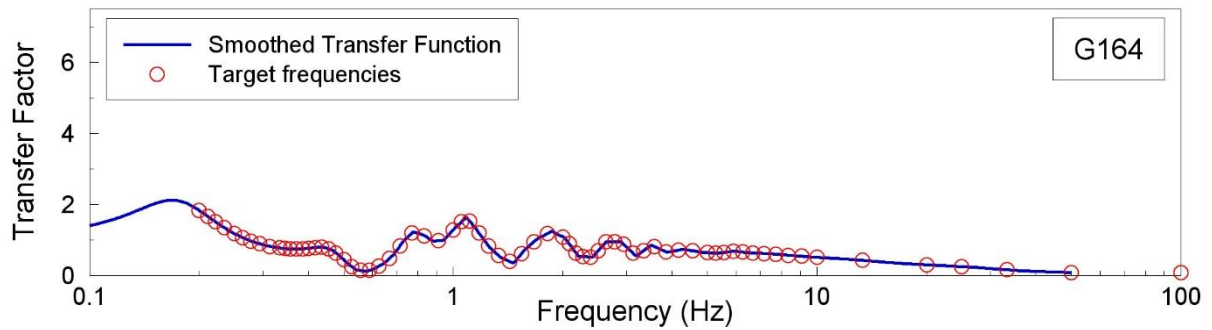
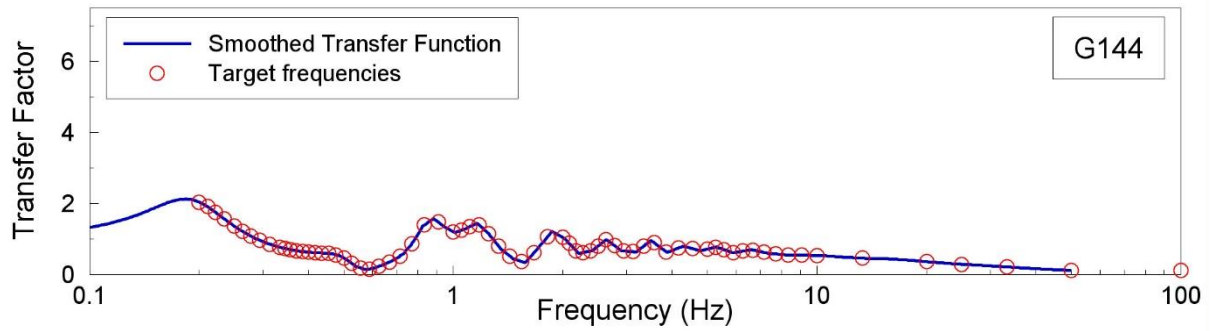
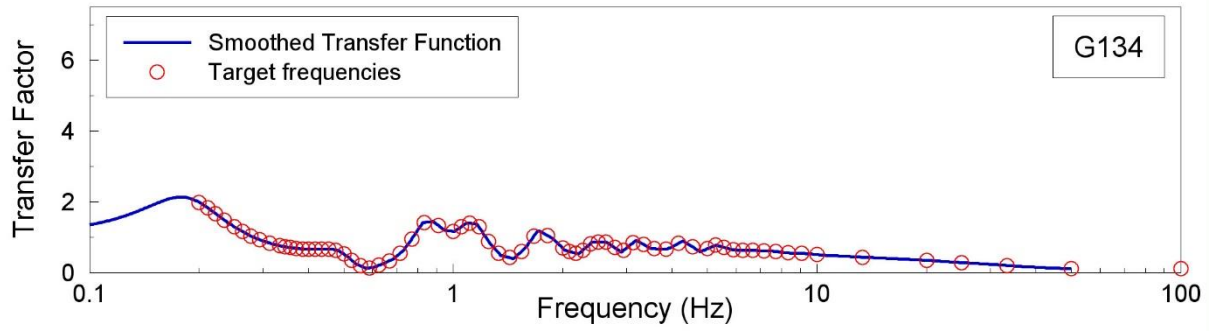
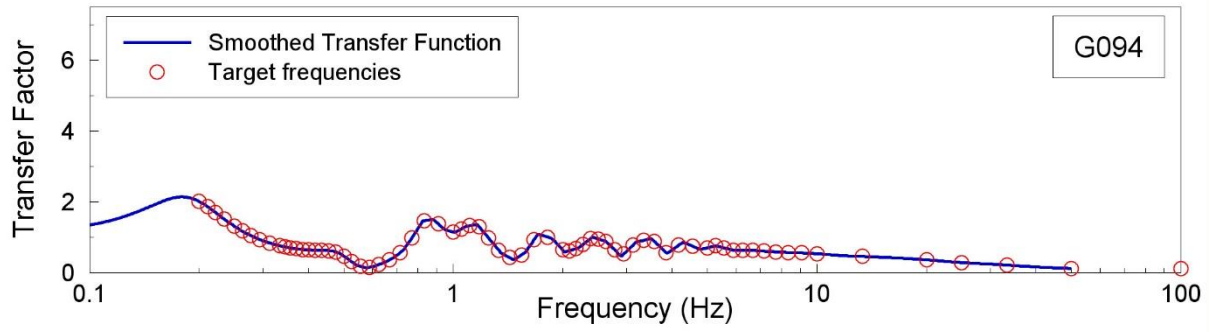
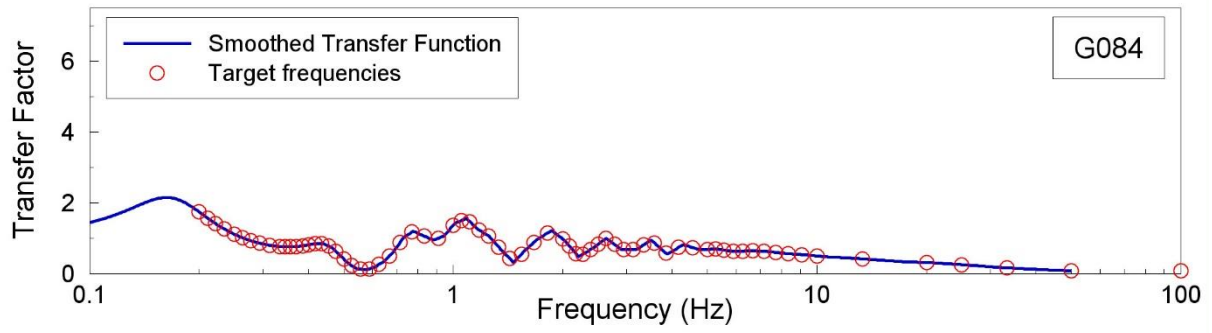
In the following pages plots of the Transfer Functions—in terms of Fourier Amplitude Spectra (FAS) of accelerations—are presented for the recording stations, as calculated using the profiles shown in Appendix I. For the B-stations, the transfer functions are from the surface to NS_B, whereas for the G-stations the transfer functions are from 200 m depth to the NS_B horizon. In each case, the blue line shows the smoothed Transfer Function and the red circles the target frequencies for the simulations of FAS, as listed in Table 1.2.

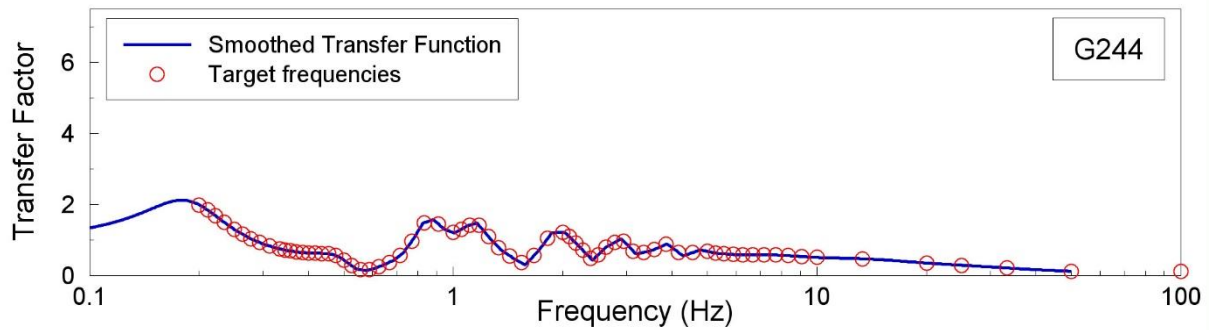
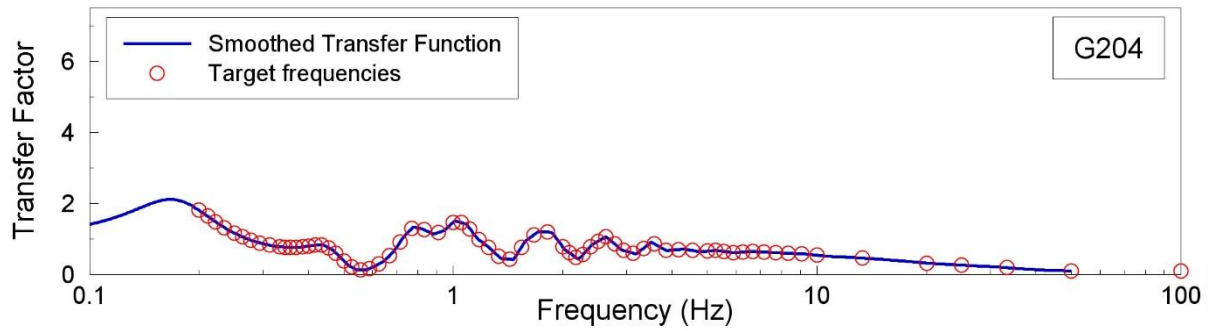
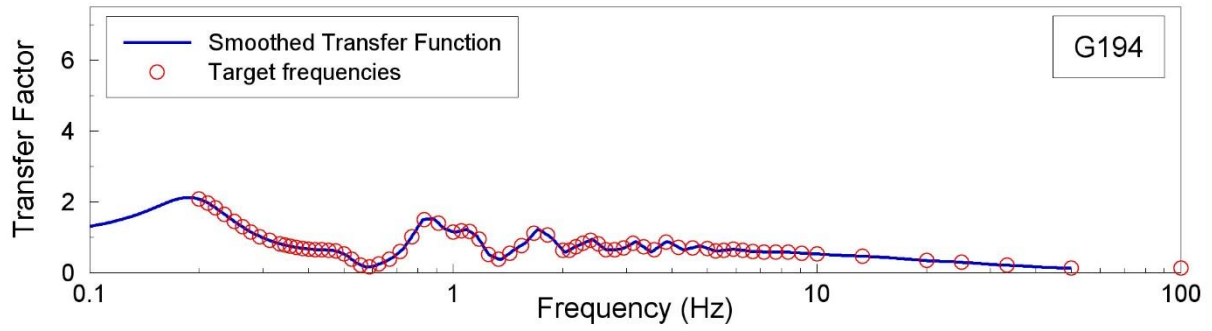
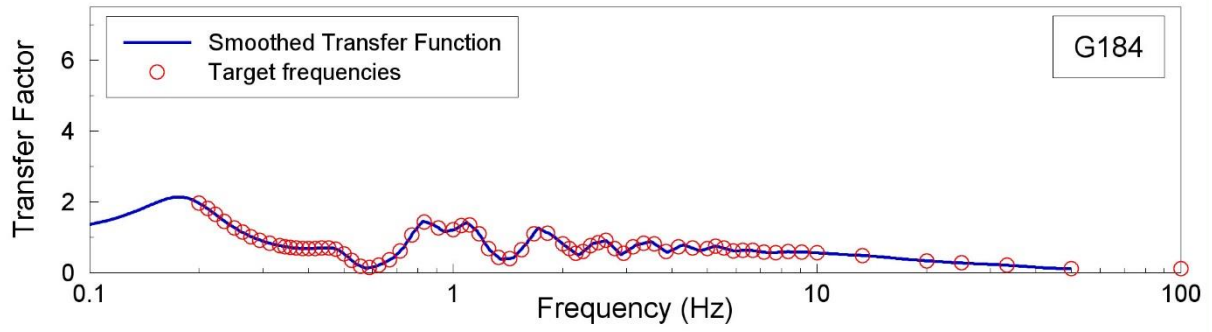
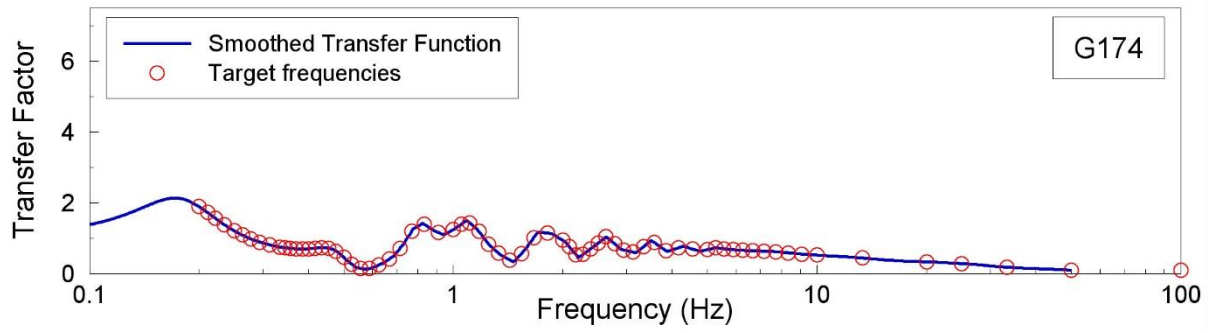


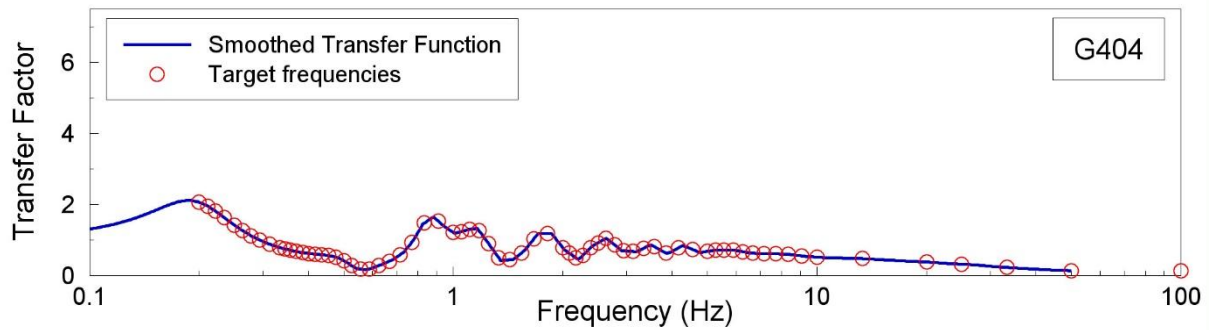
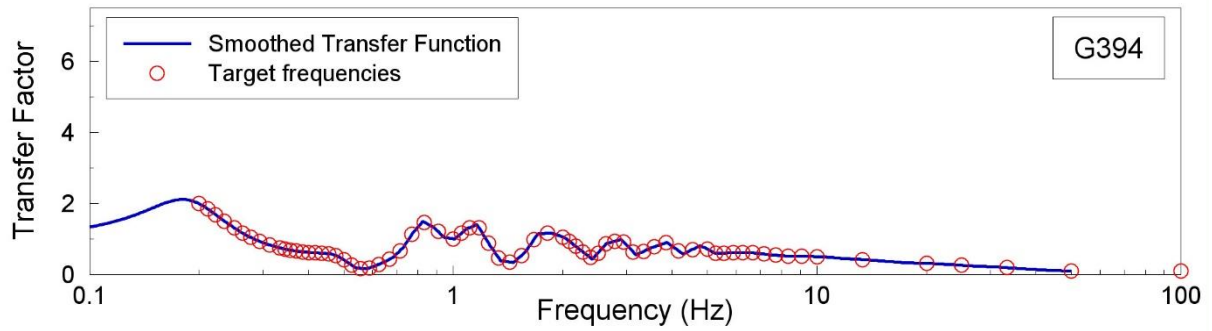
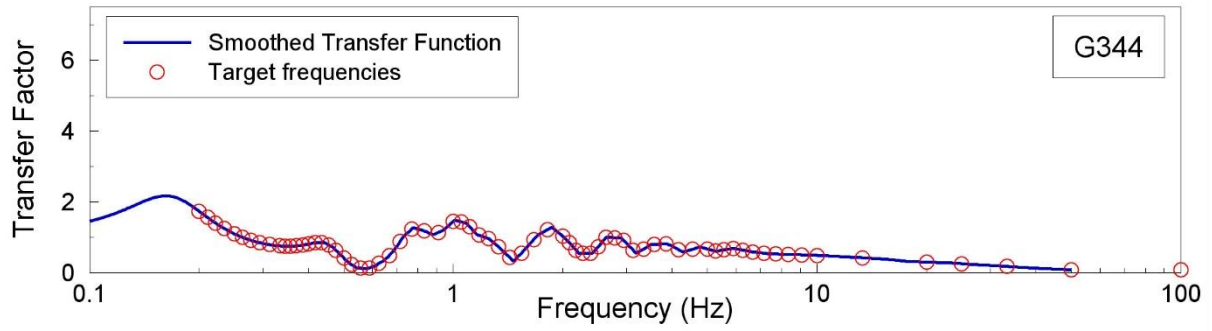
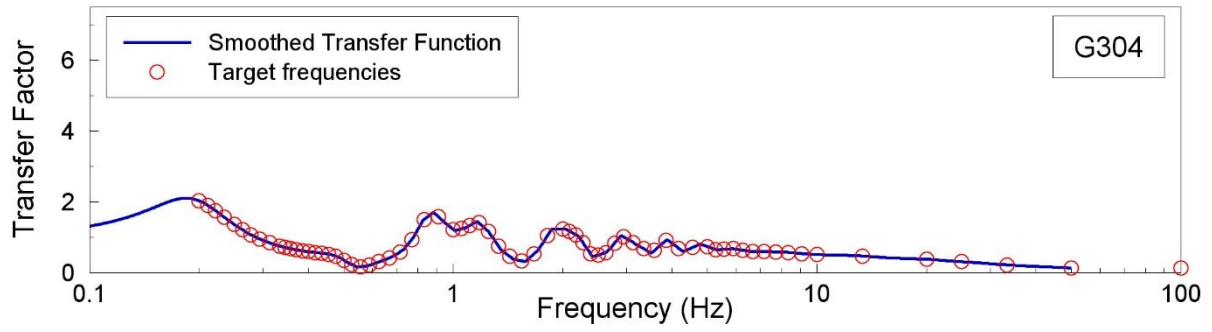
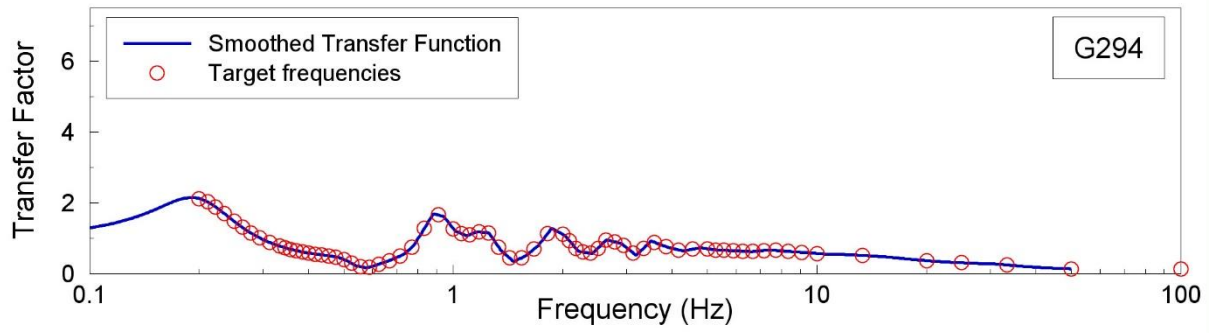


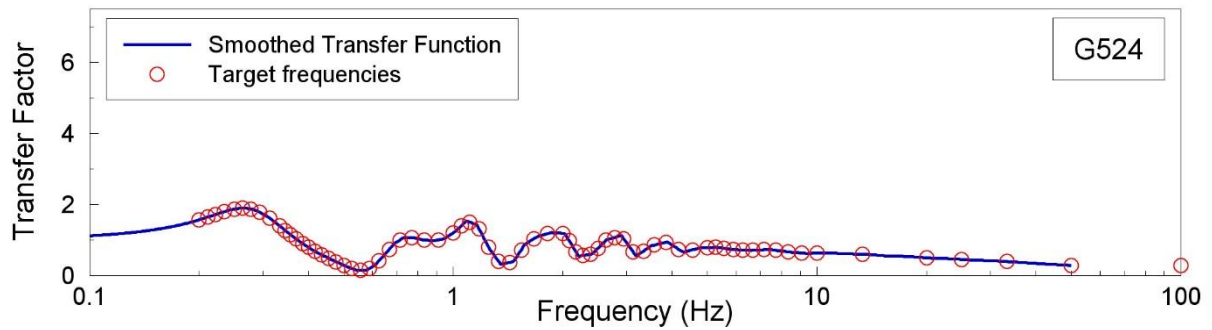
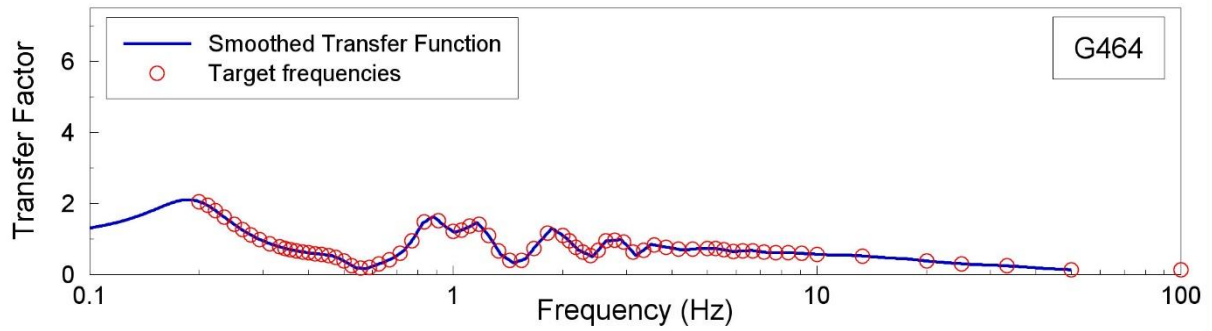
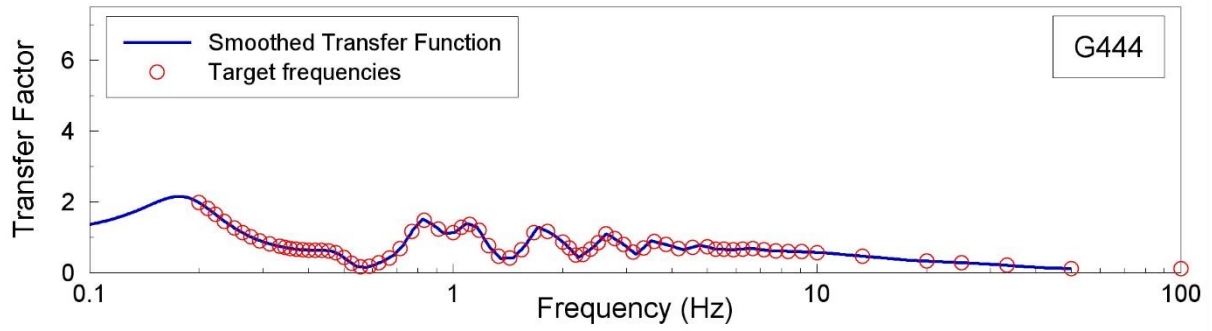
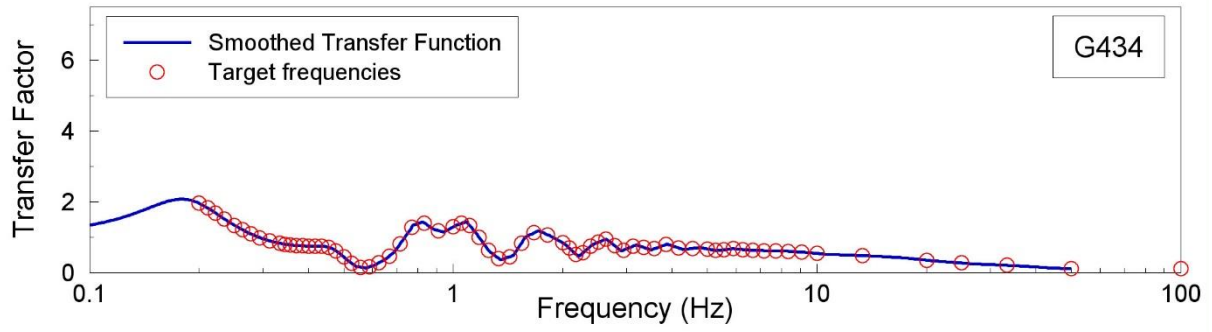
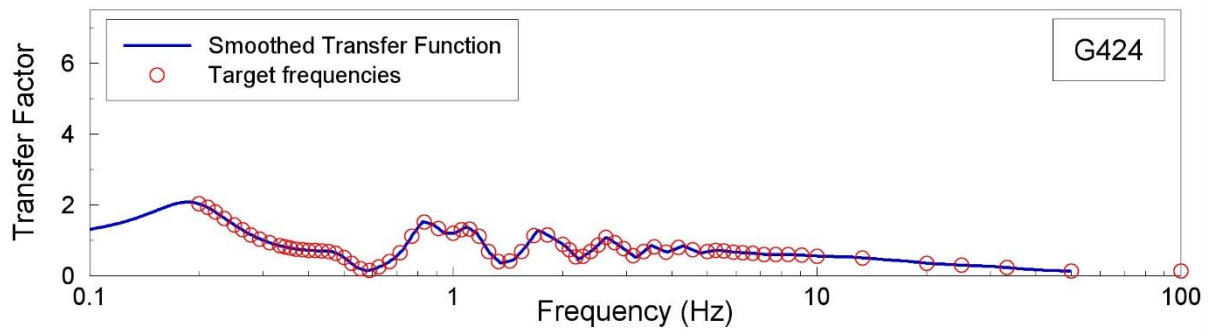


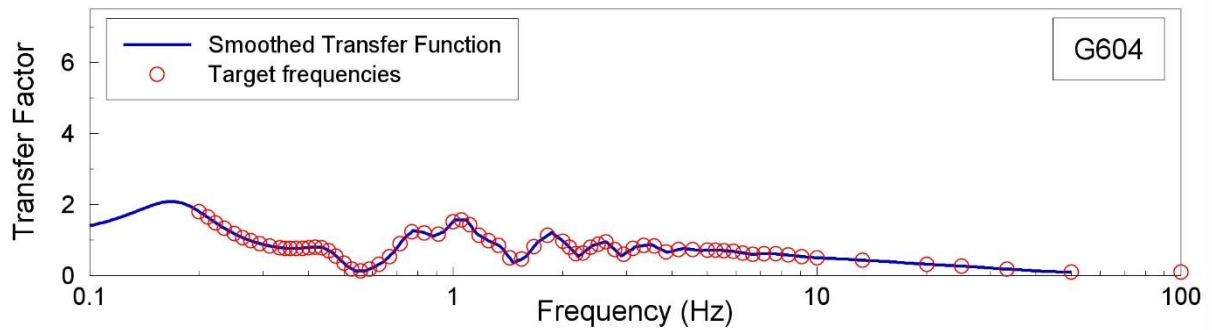
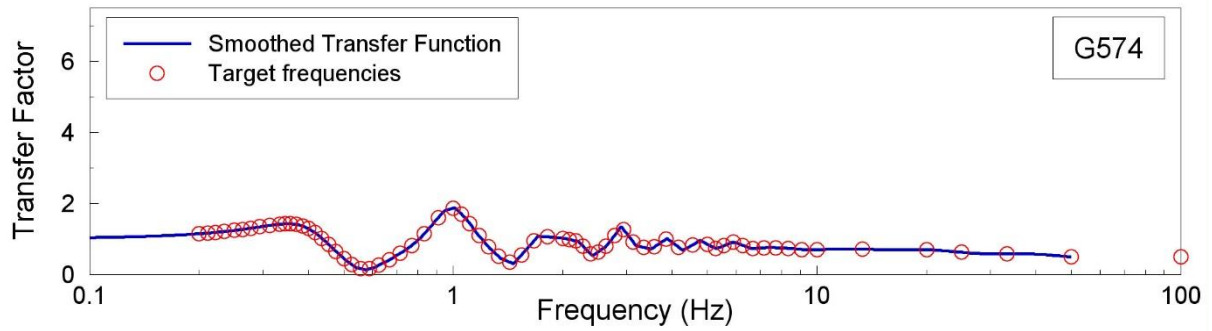
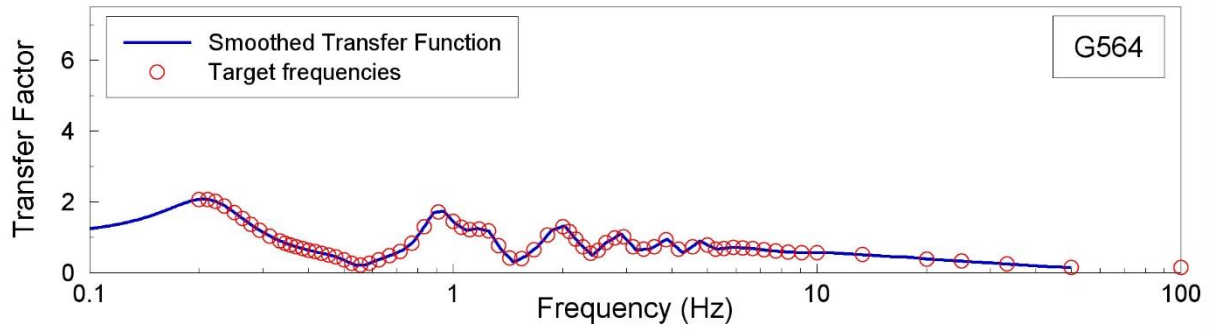
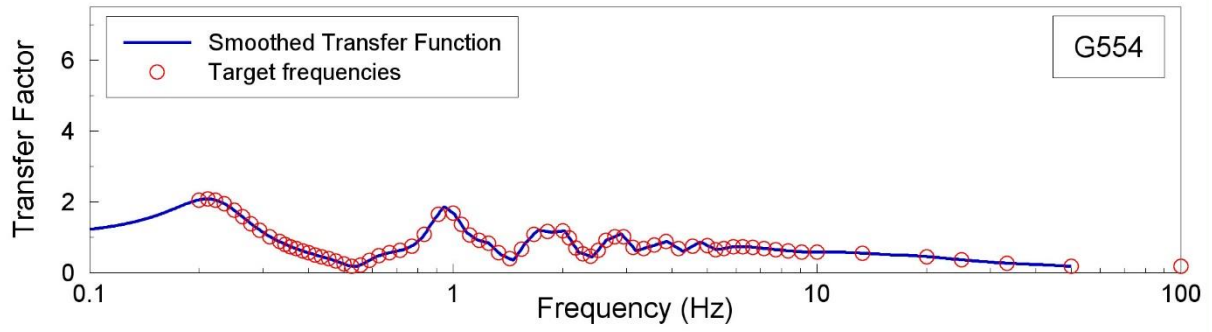
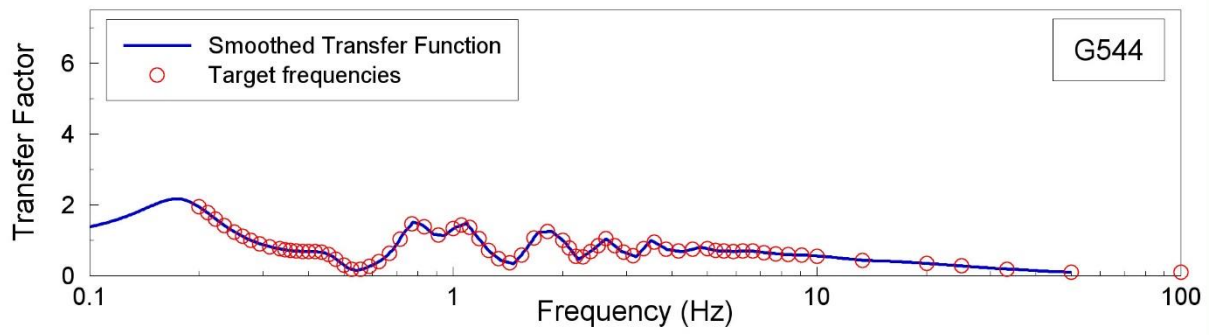


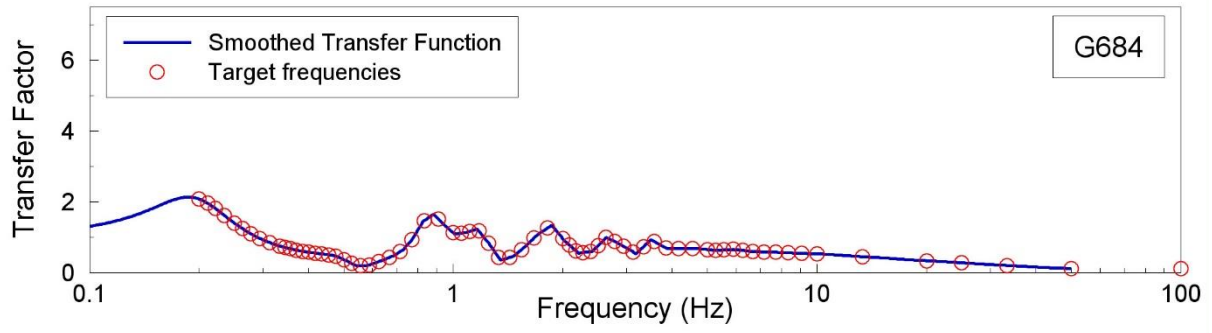
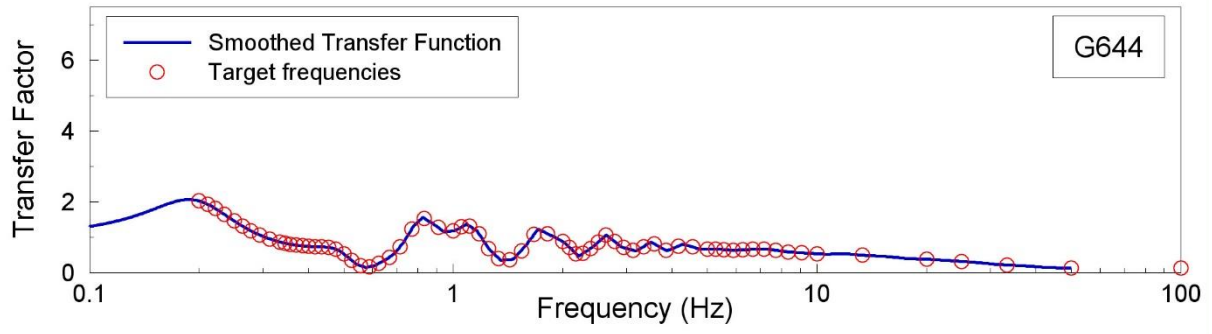
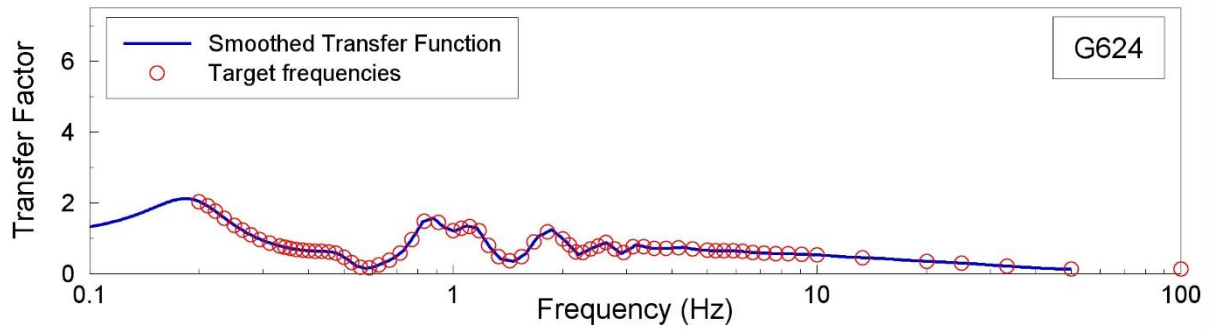










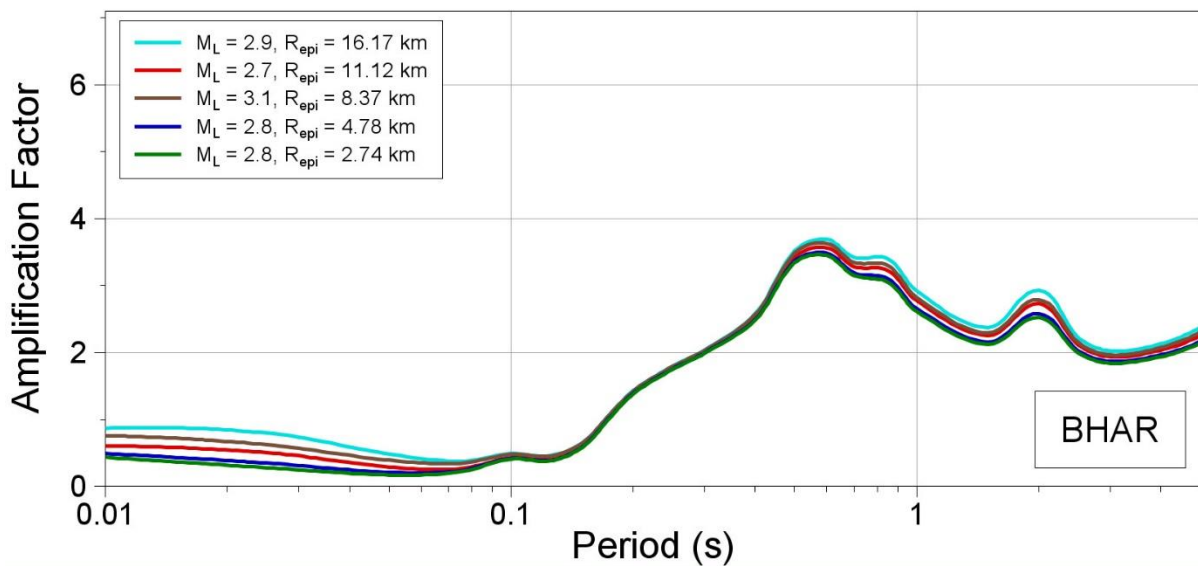
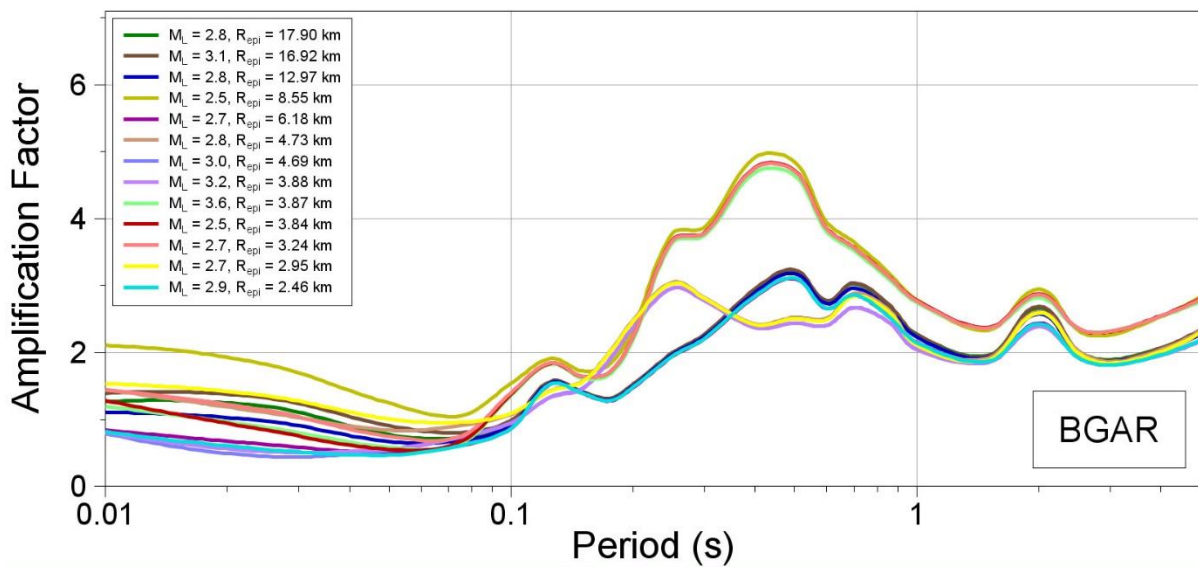
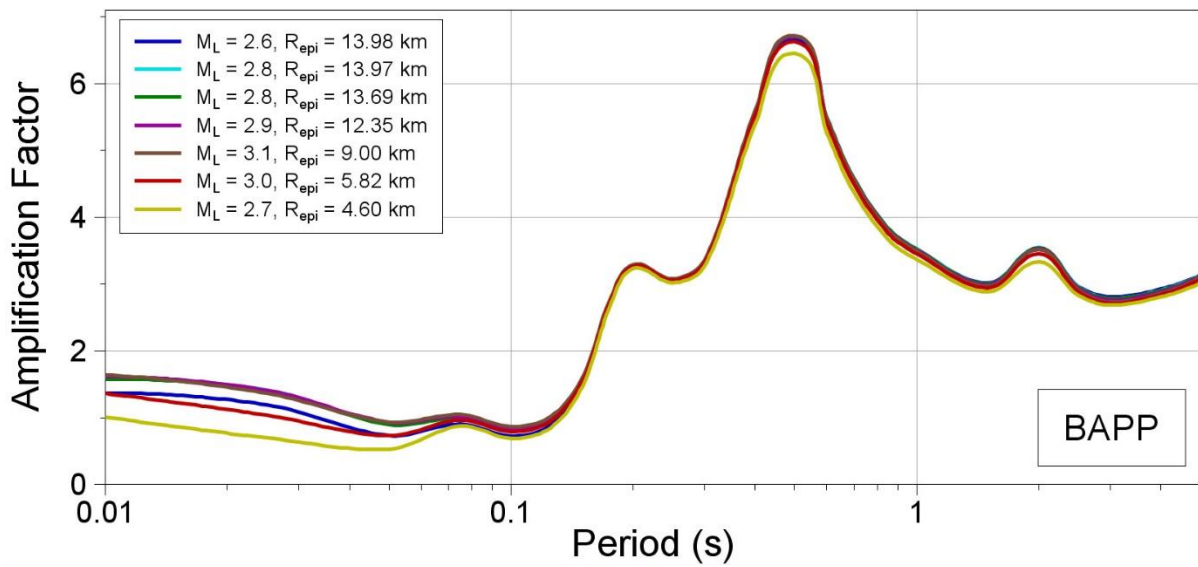


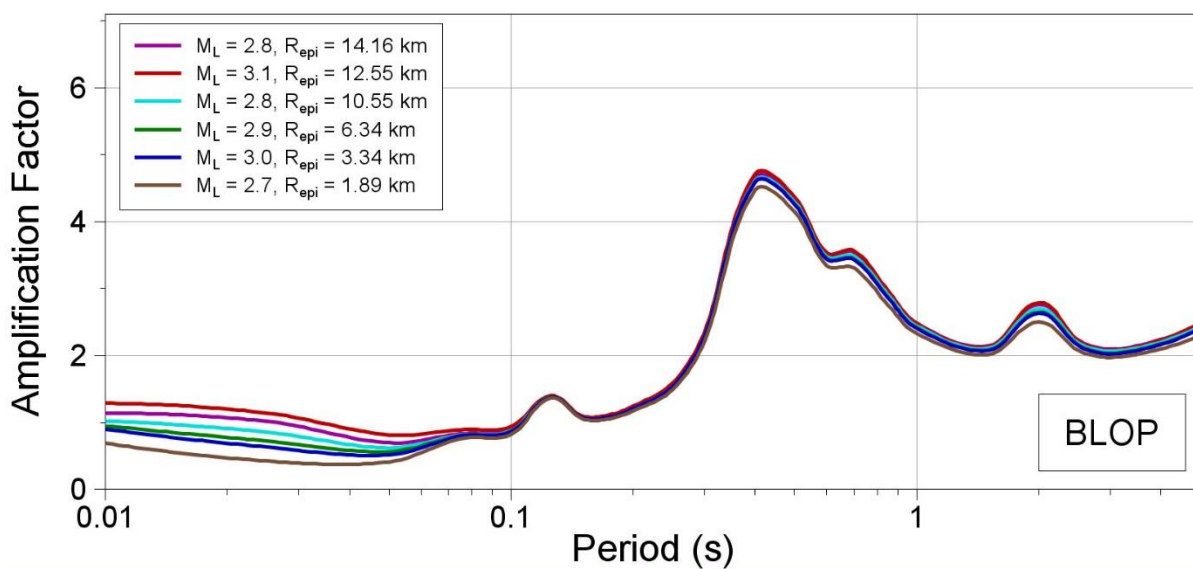
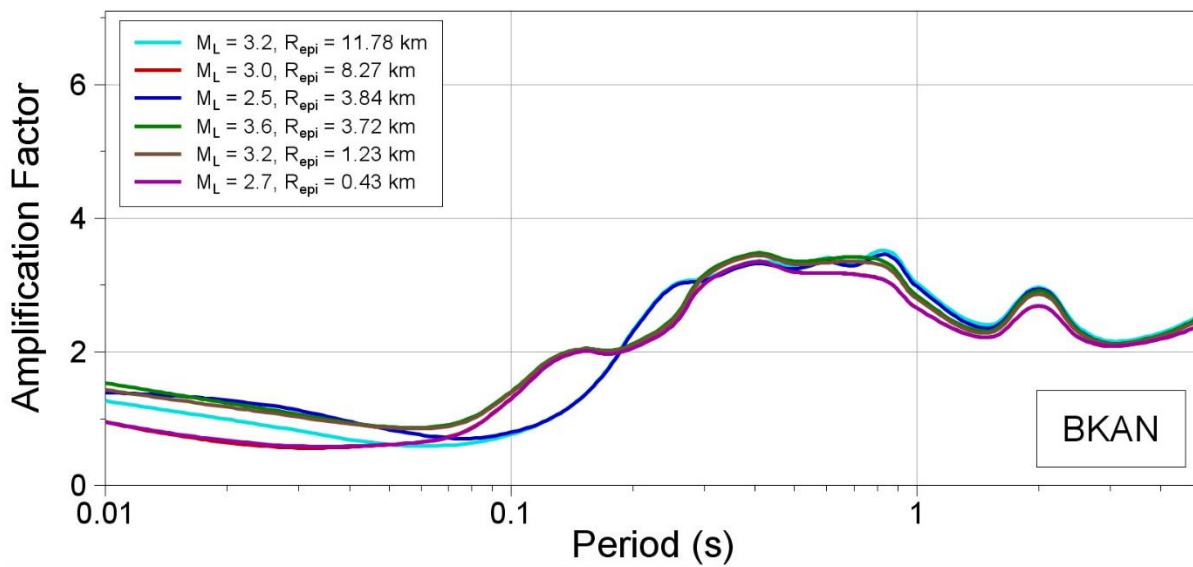
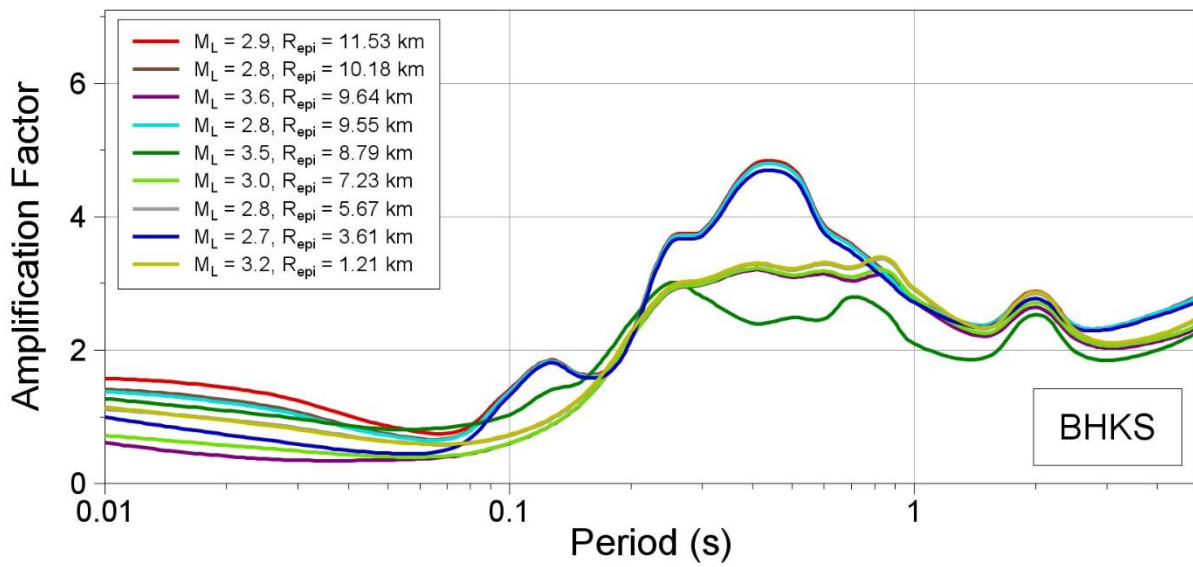
APPENDIX III

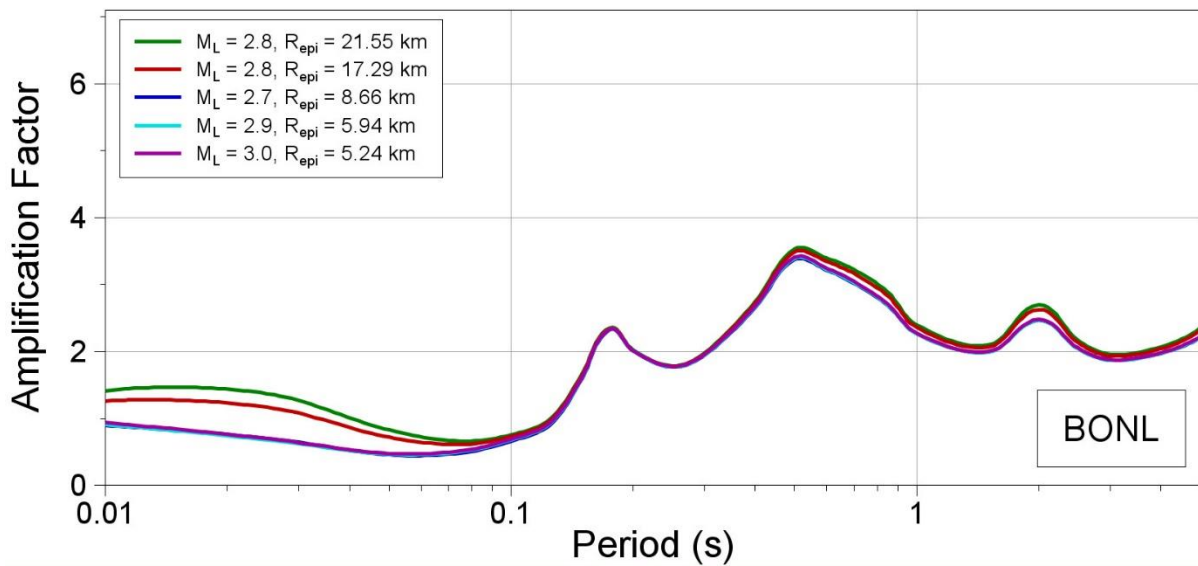
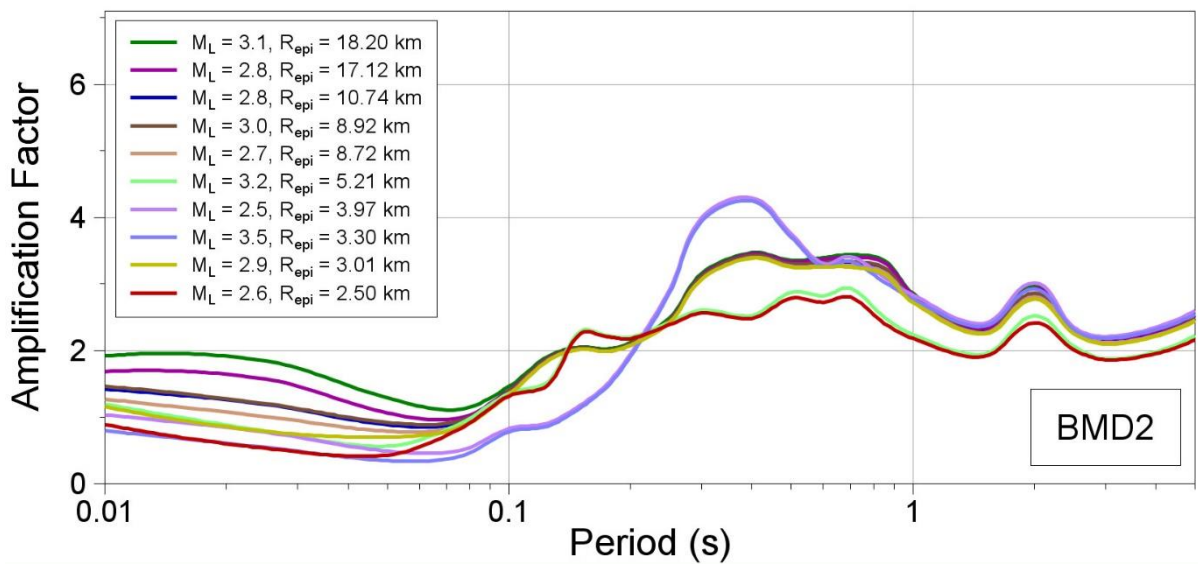
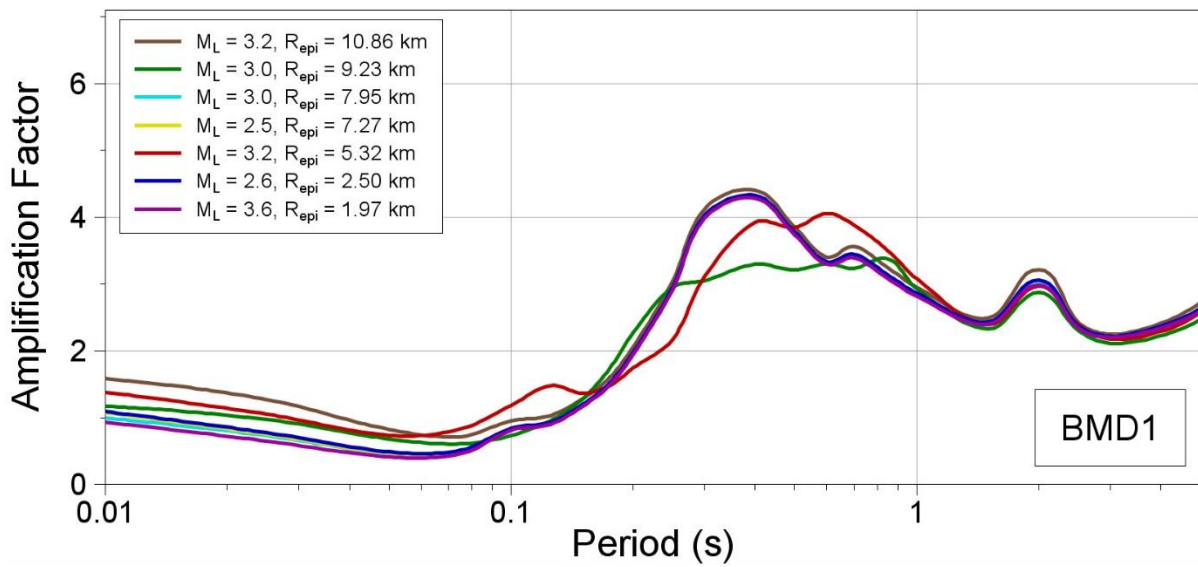
Linear amplification functions for $S_a(T)$ at recording stations

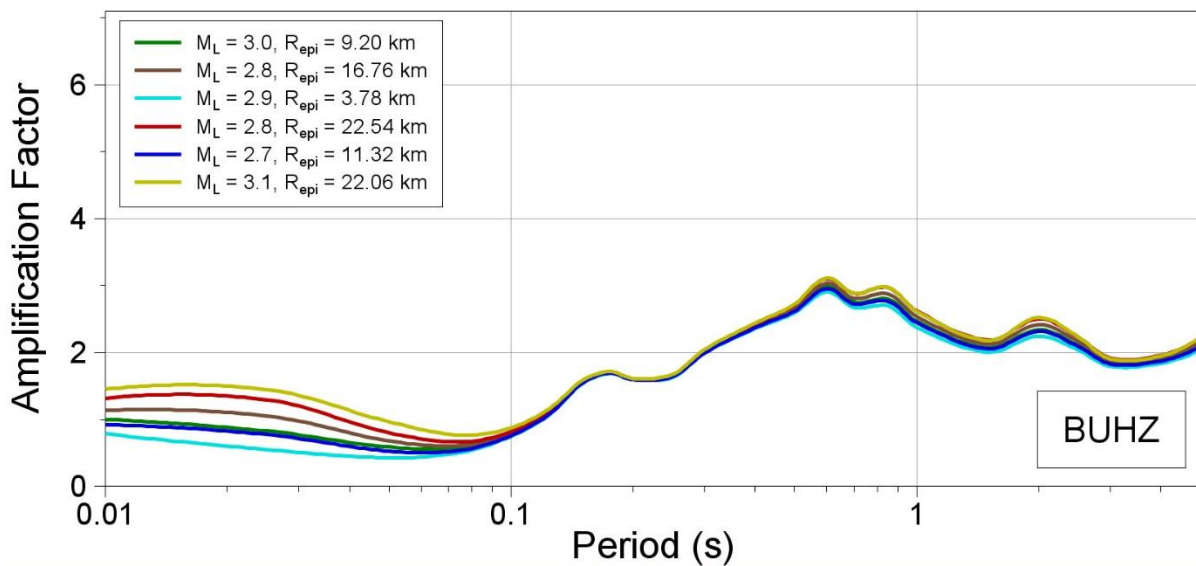
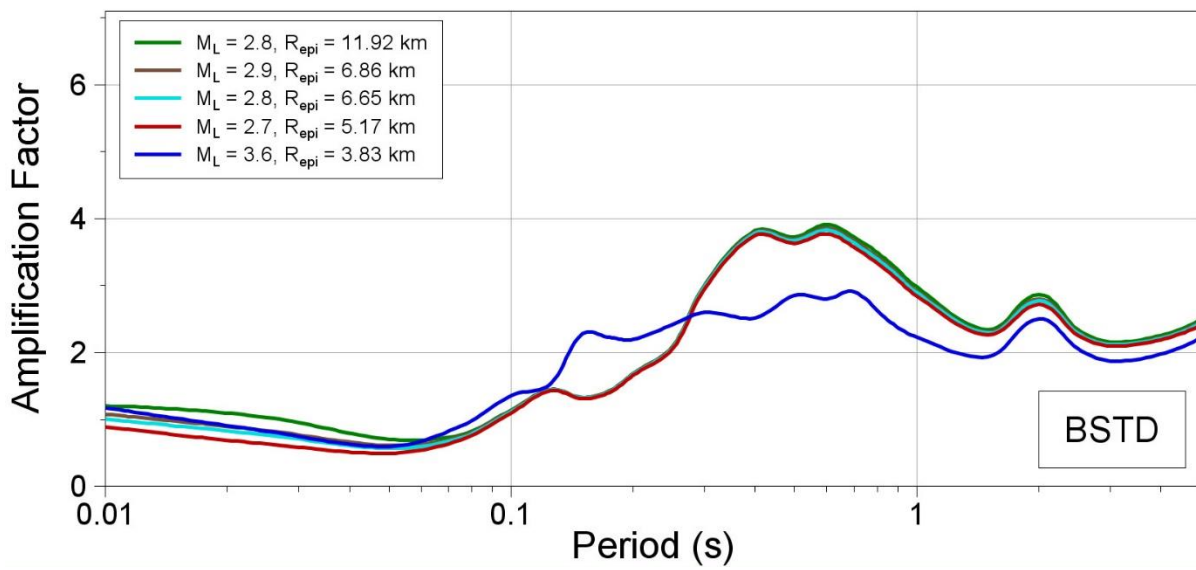
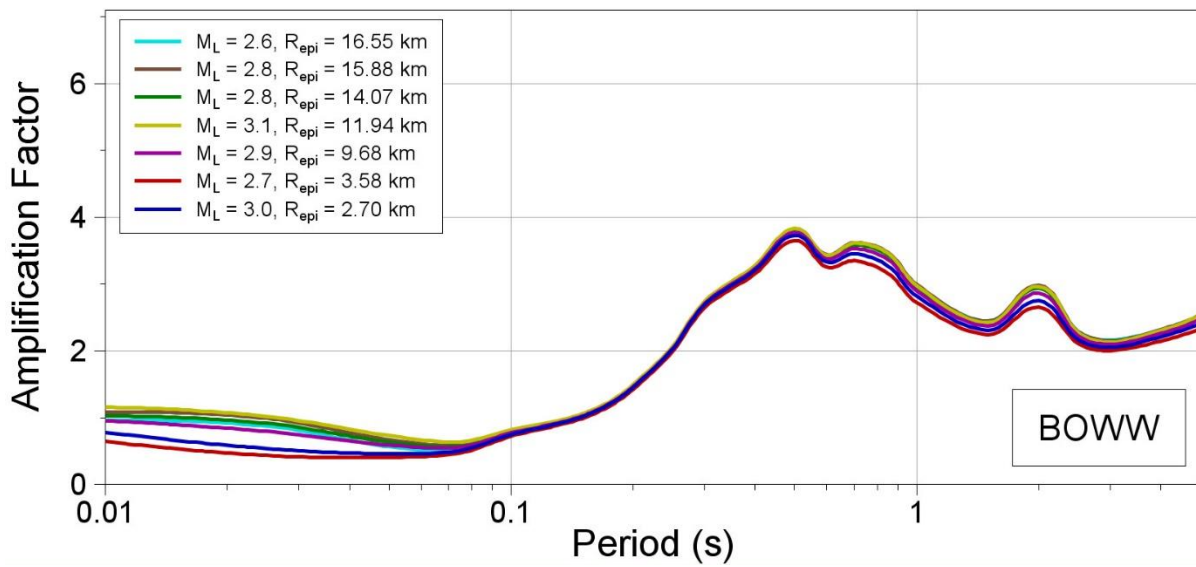
The following pages show plots of the linear amplification functions for response spectral ordinates calculated for the recording stations..

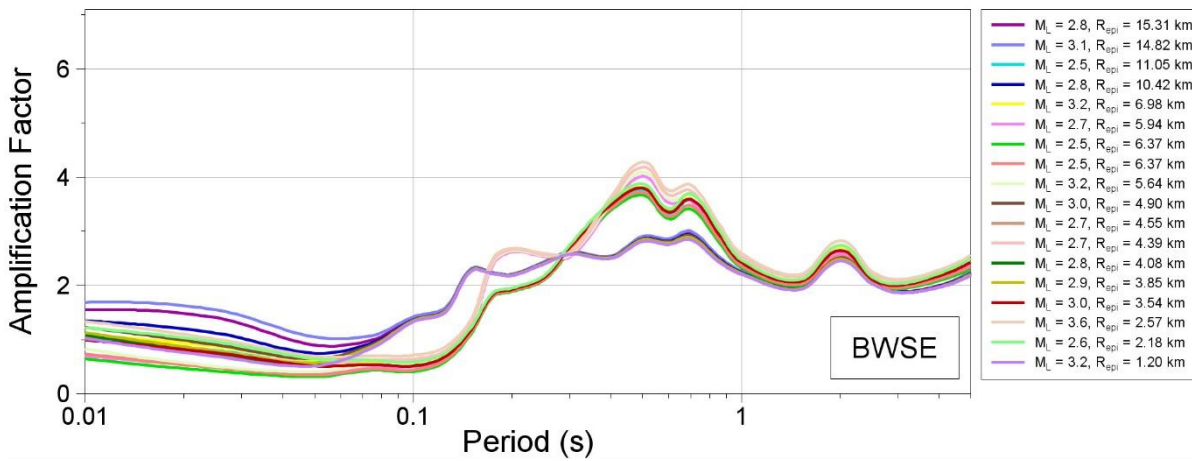
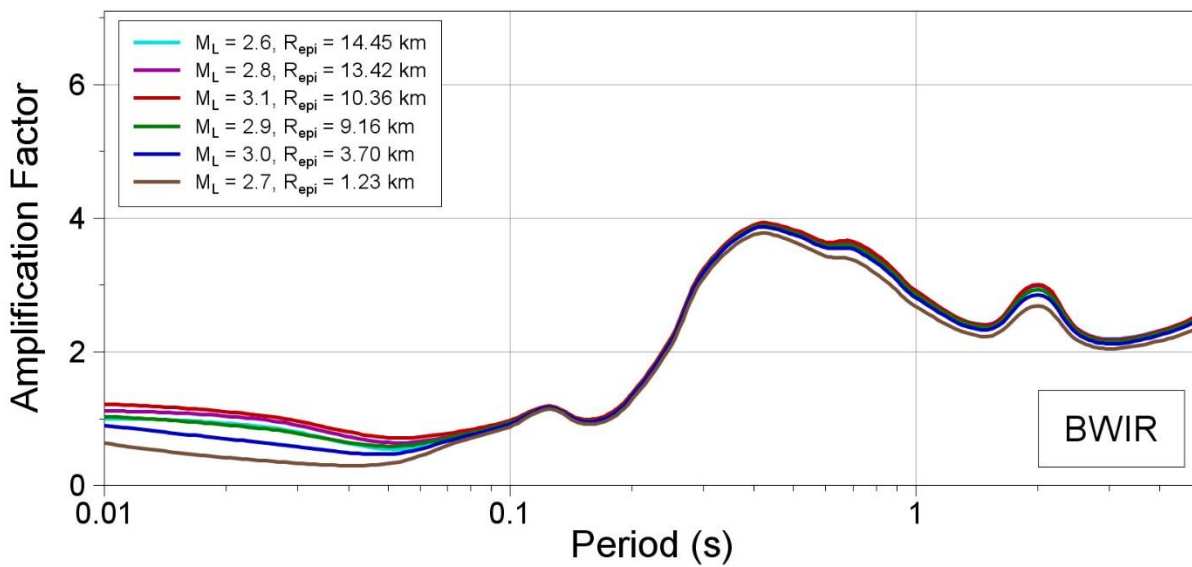
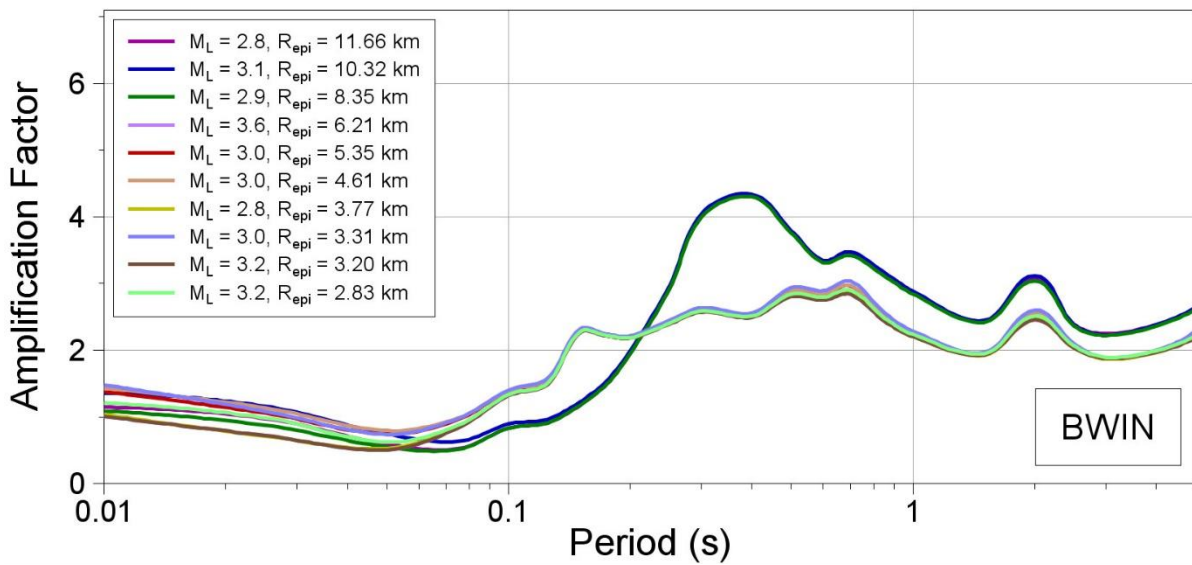
For B-stations, the amplification factors refer to the NS_B horizon and the ground surface, whereas for the G-stations, the reference is from NS_B to 200 m depth; these are calculated as 'within' rather than 'outcrop' response since account is taken of the overlying layers. Since the factors are a function of magnitude and distance, at short periods, they are shown for each record in the first set of plots for the corresponding M-R pair. The second set of plots shows the amplification factor for each station over a range of magnitudes (M_L 2.5 to 3.6 in 0.1 unit increments) and epicentral distances (0 to 20 km in logarithmic increments), with the mean factor highlighted.

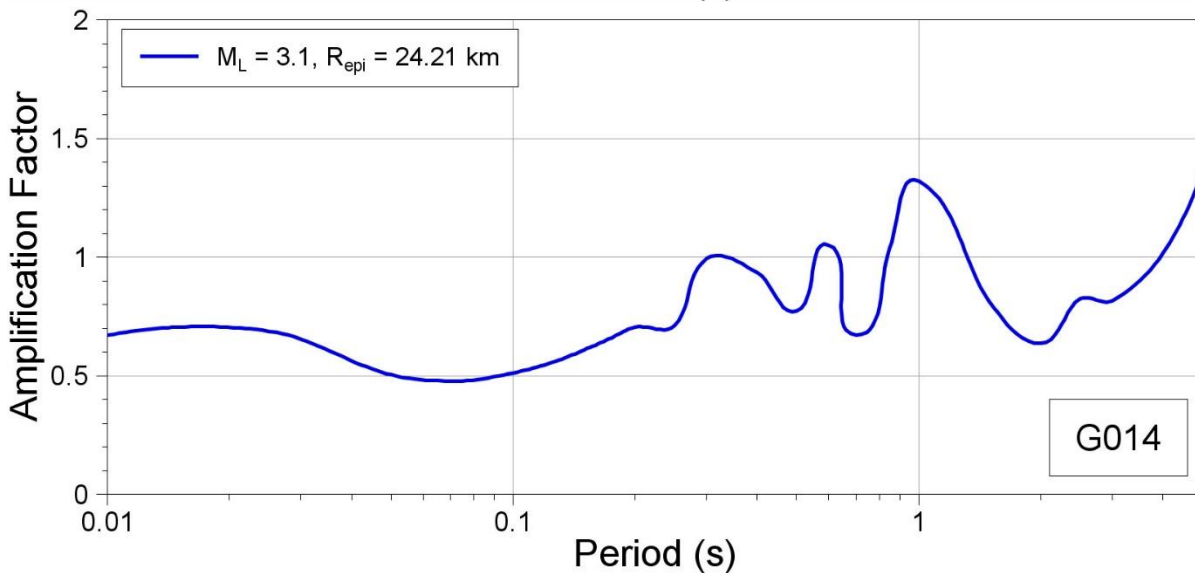
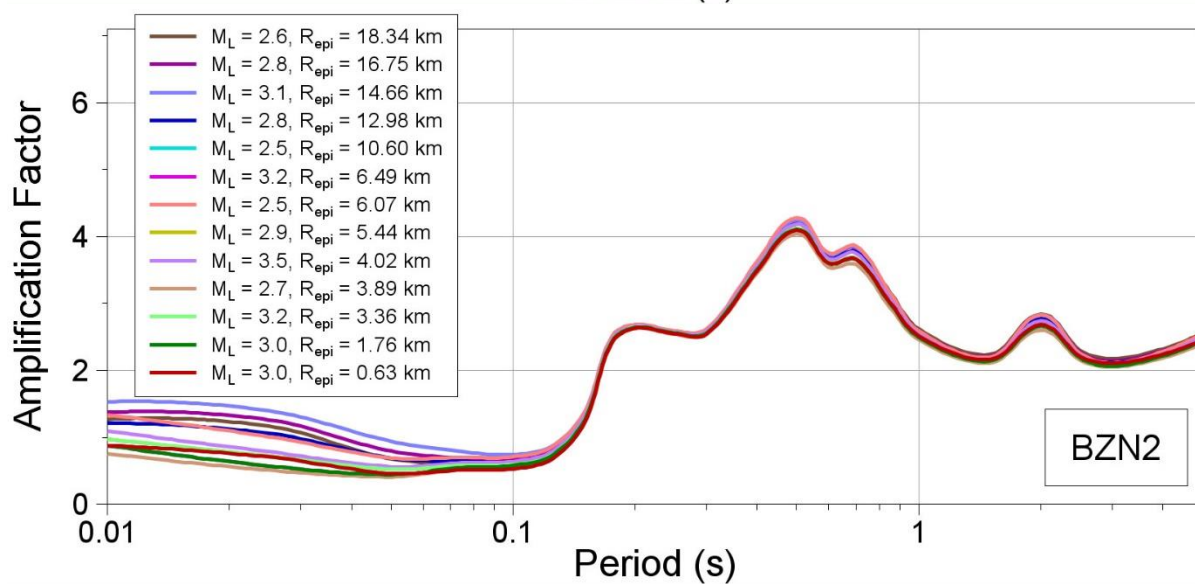
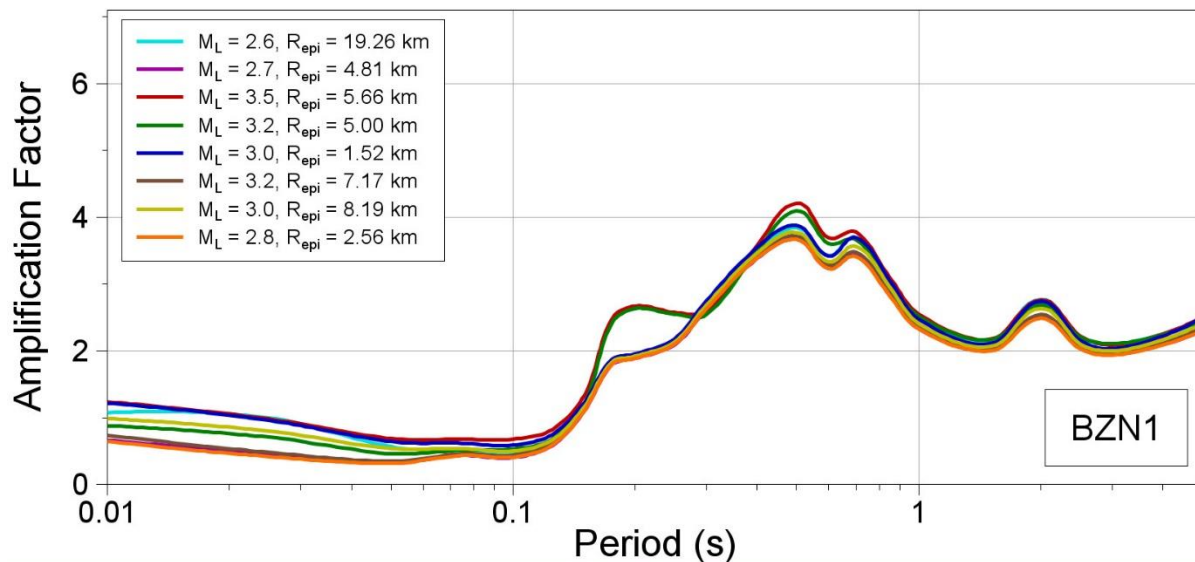


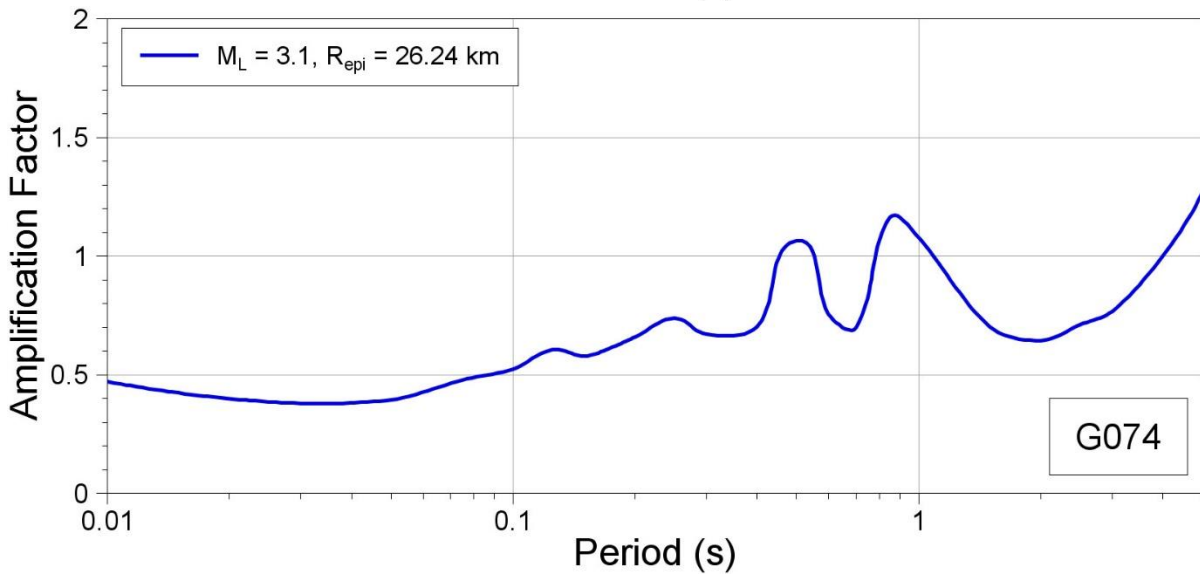
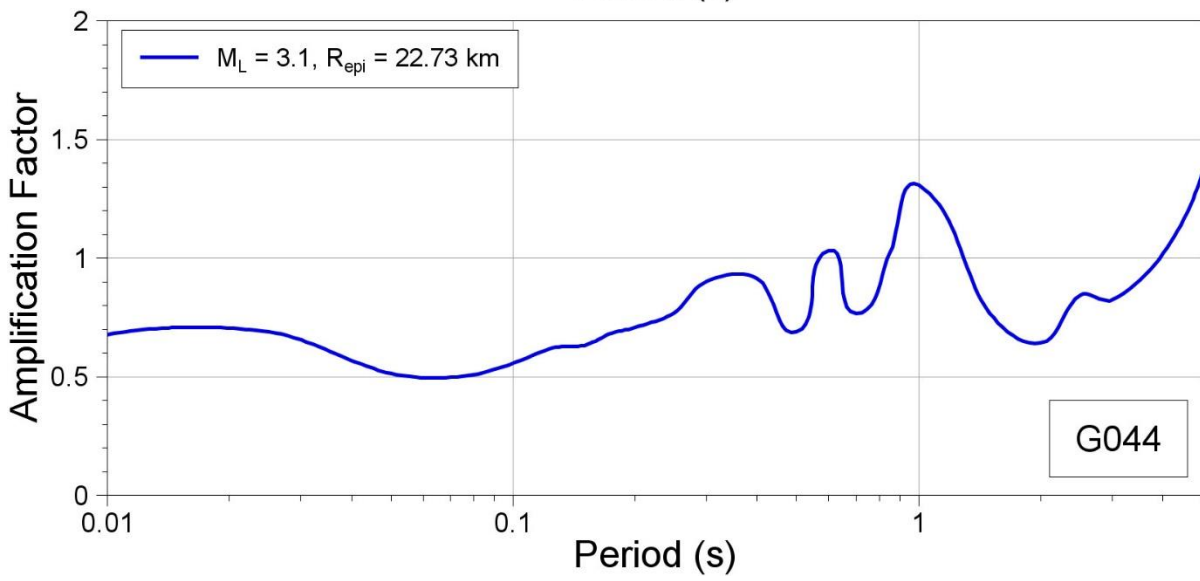
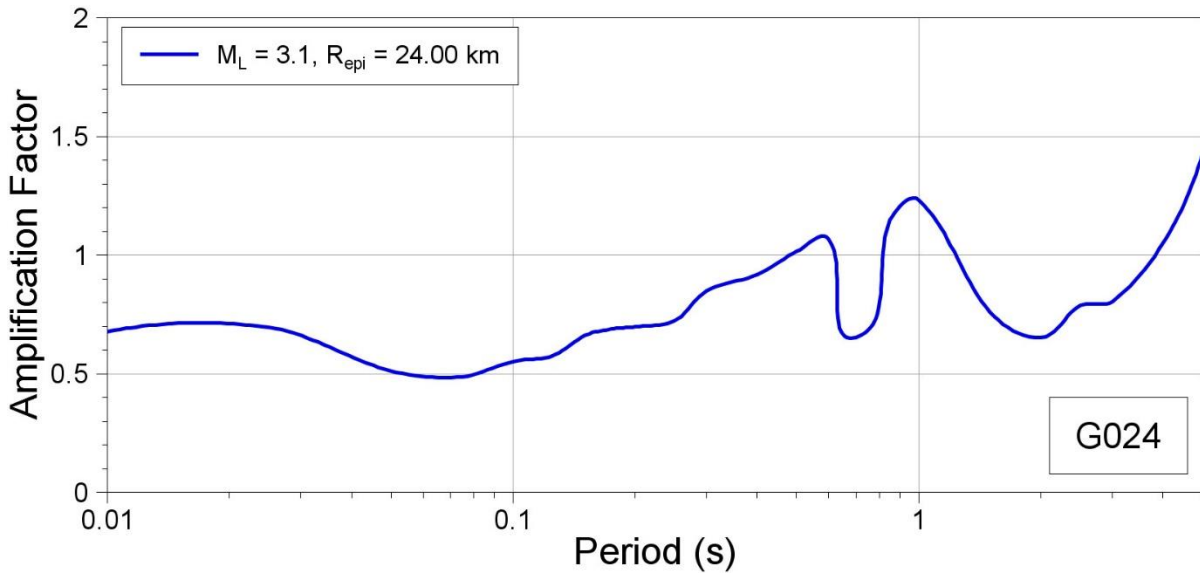


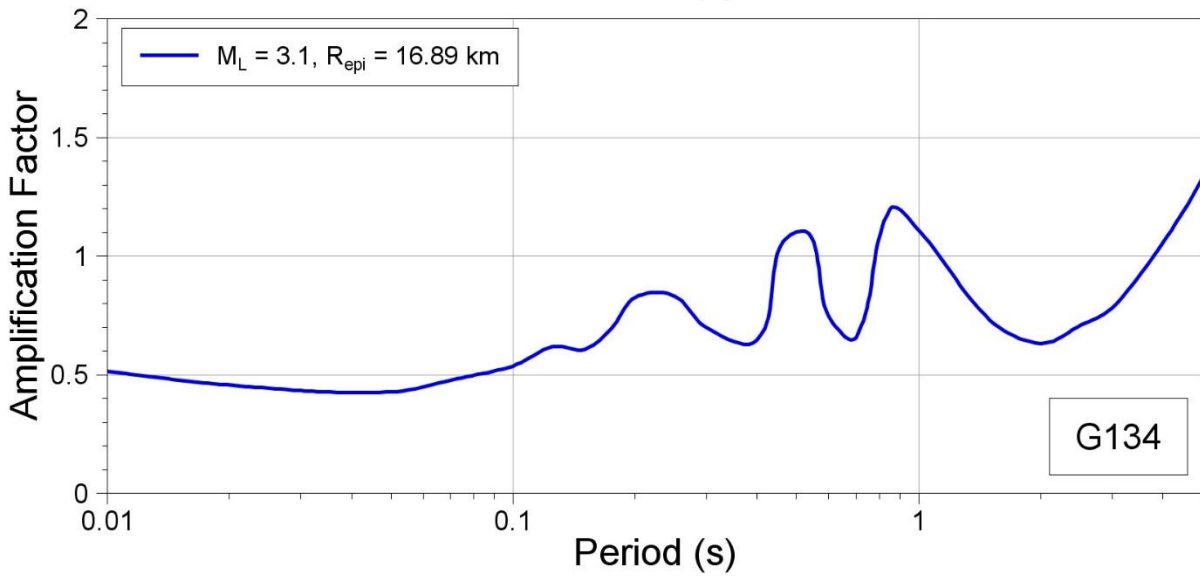
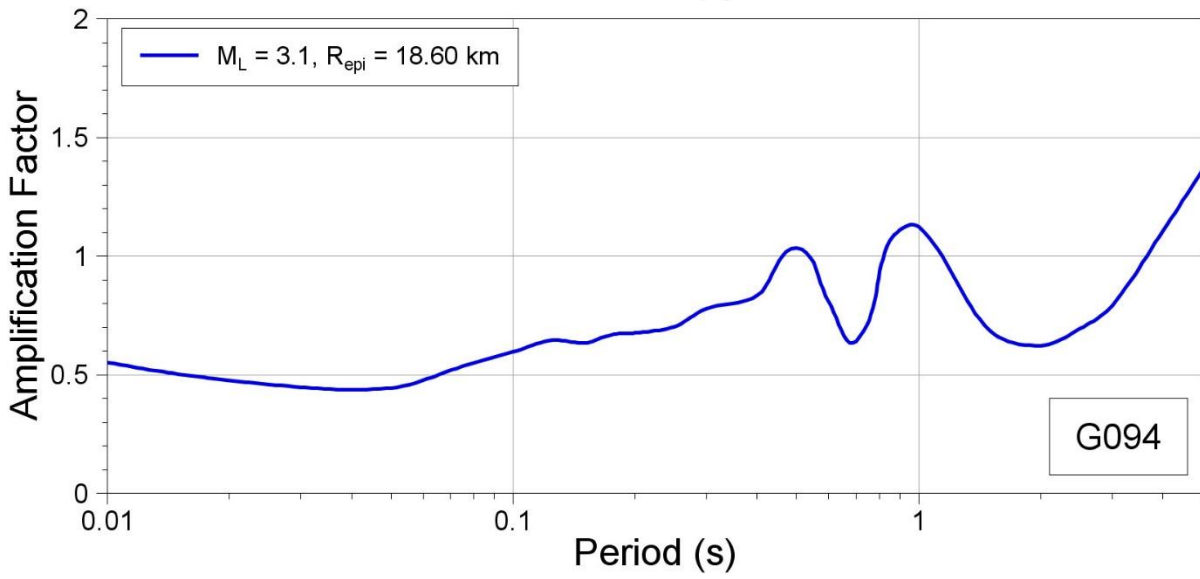
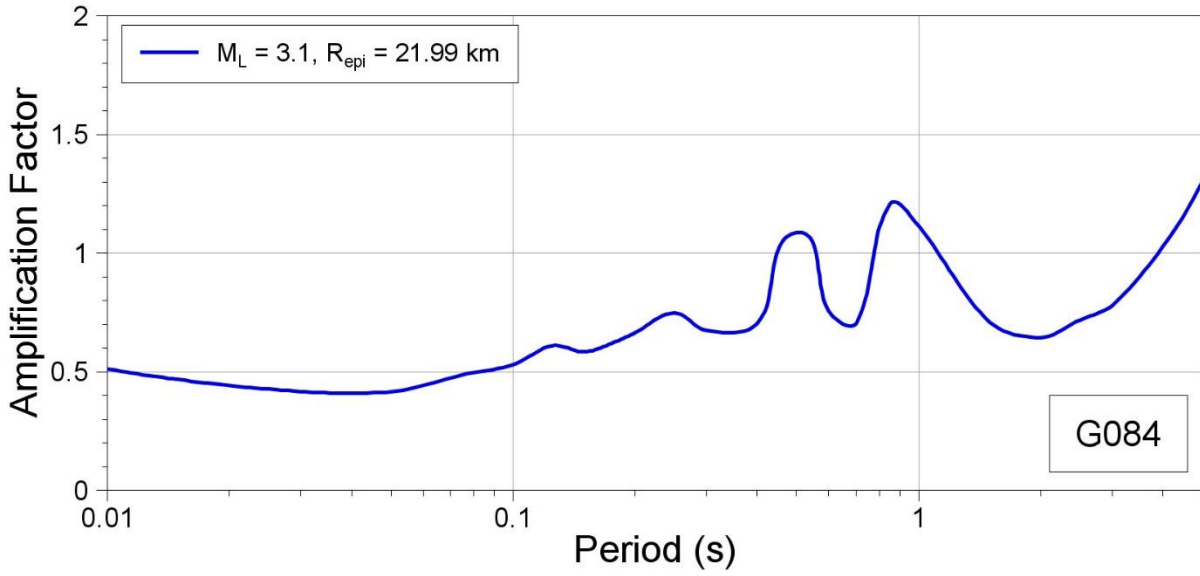


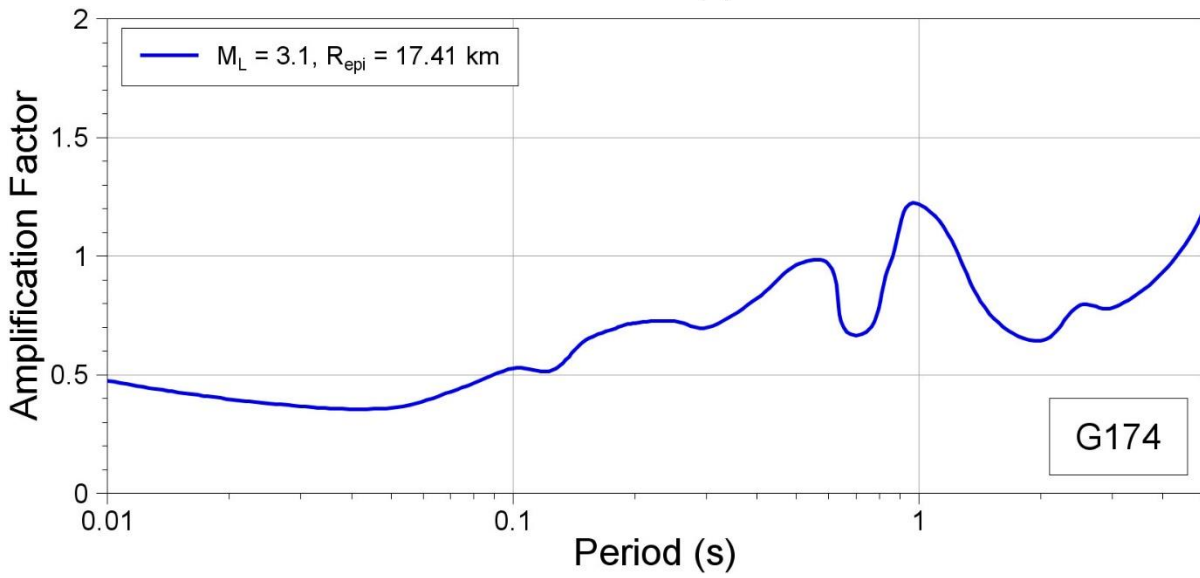
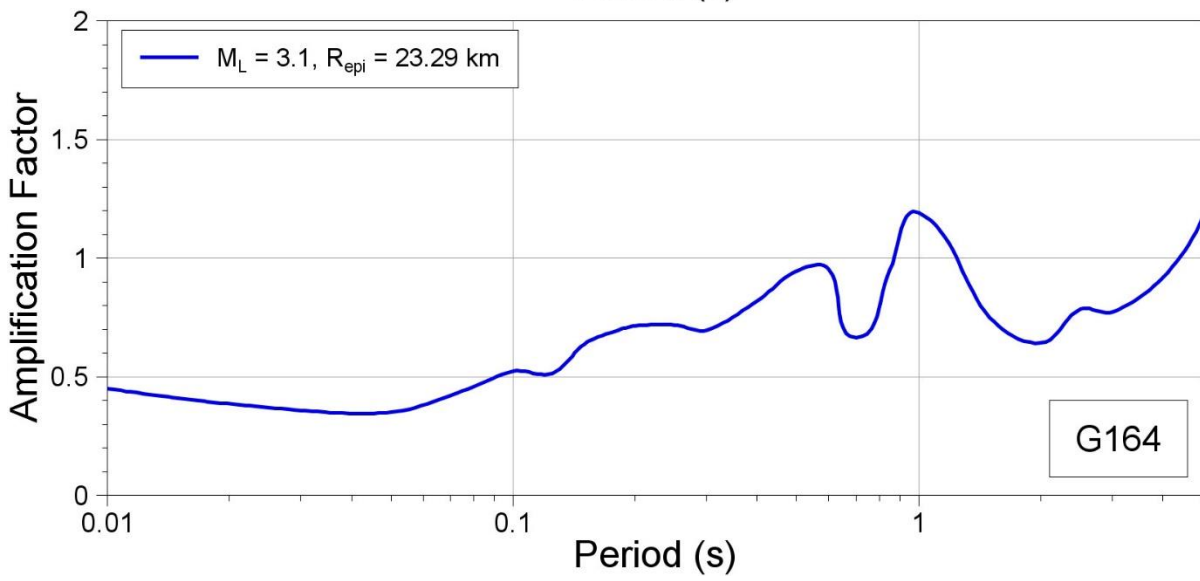
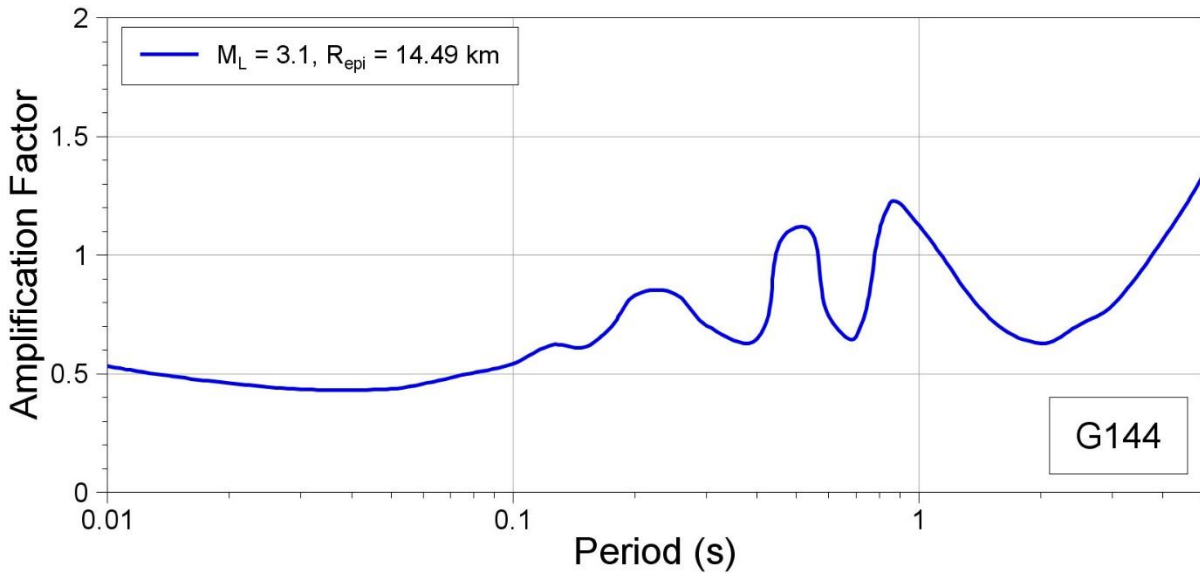


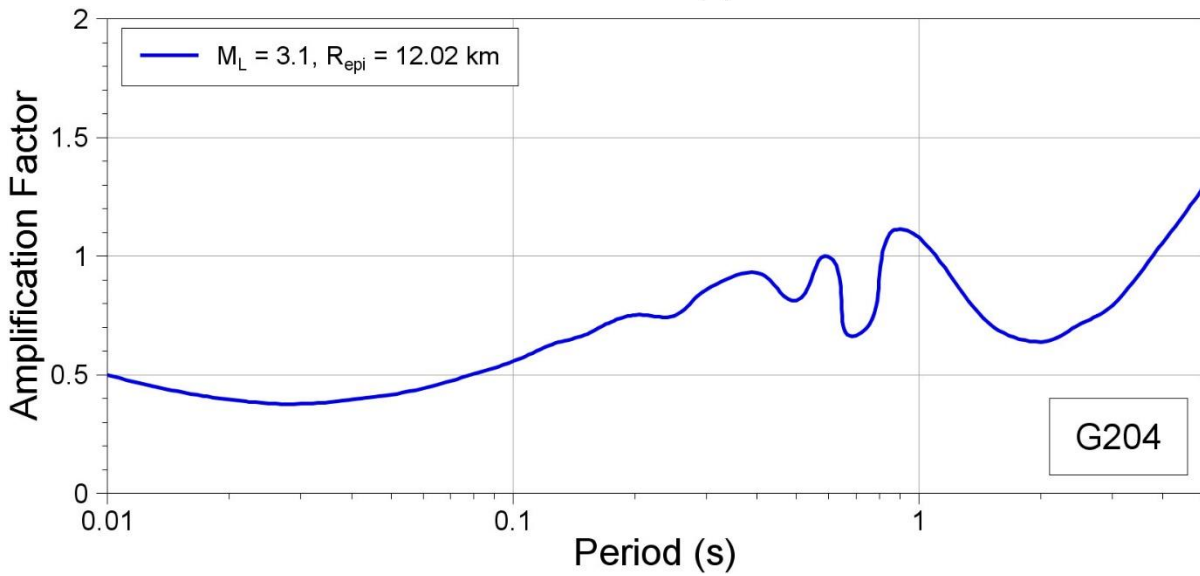
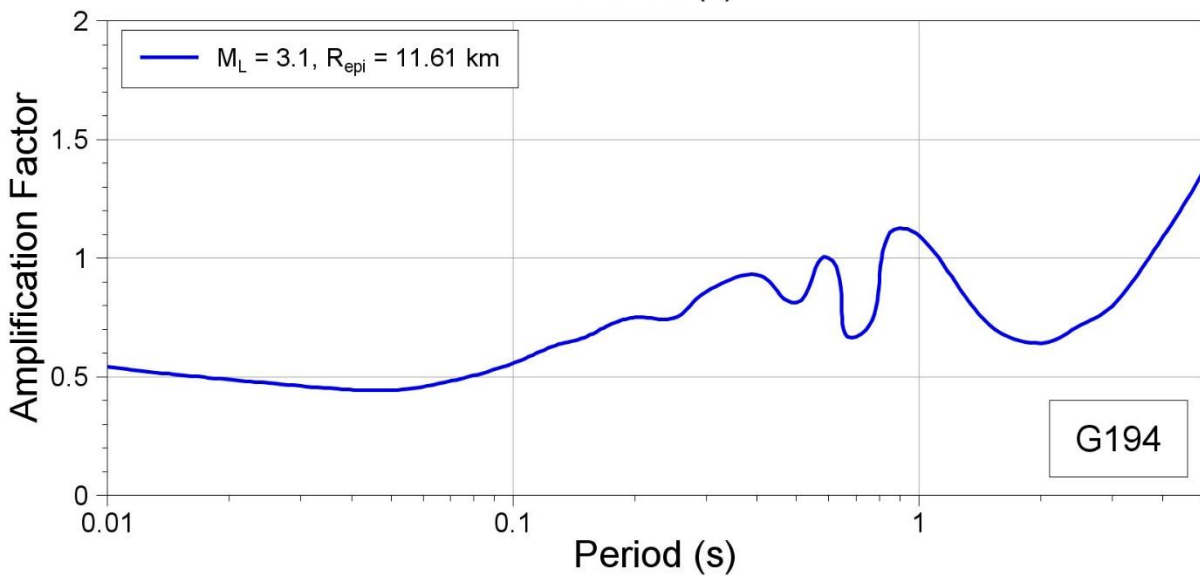
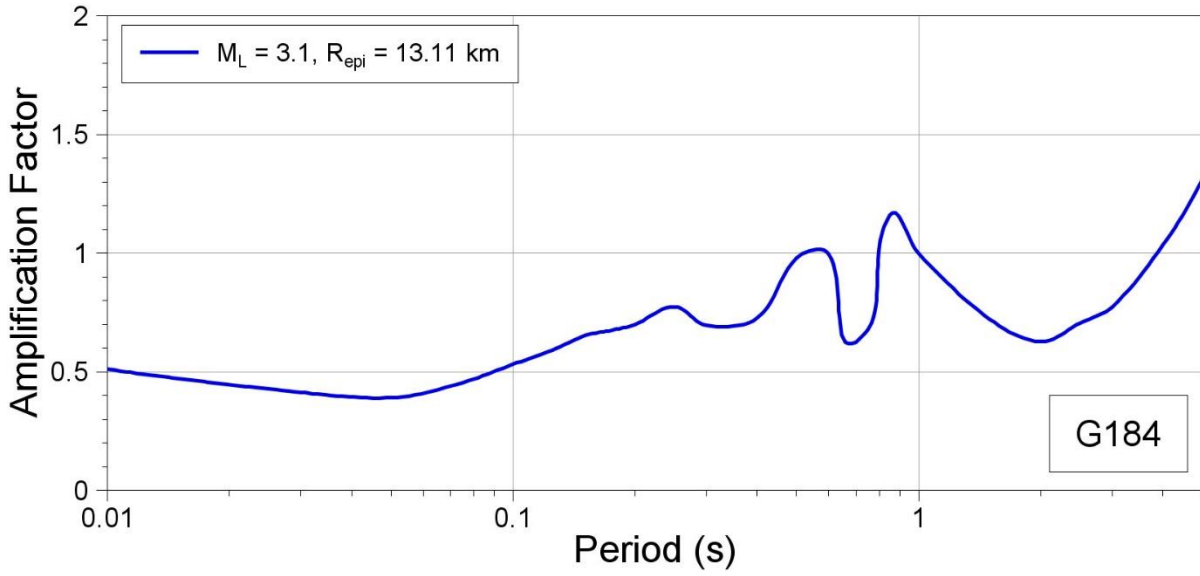


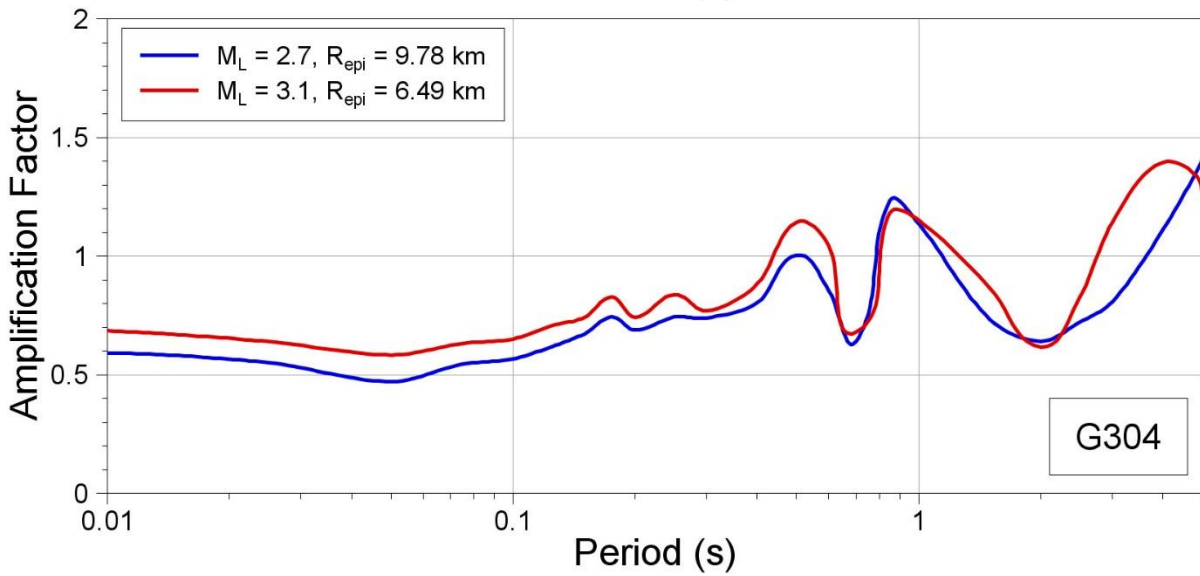
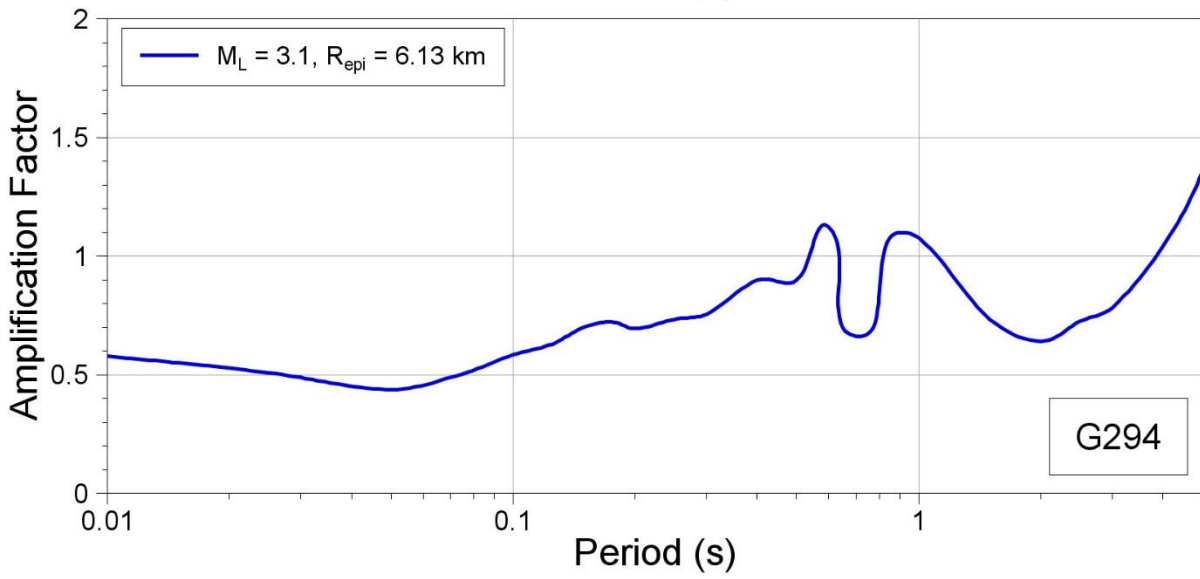
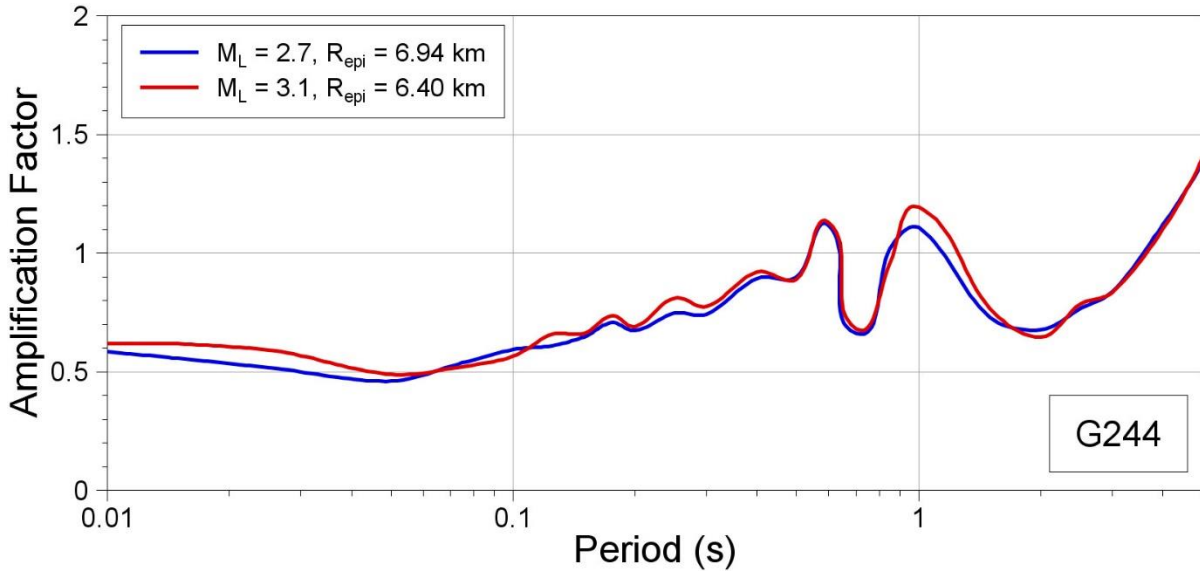


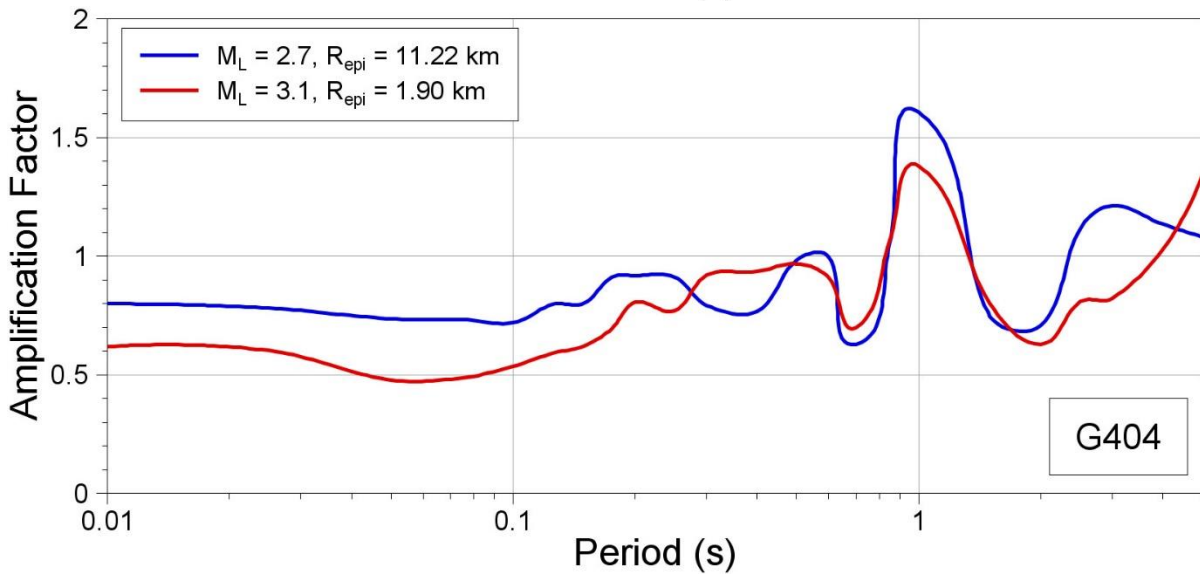
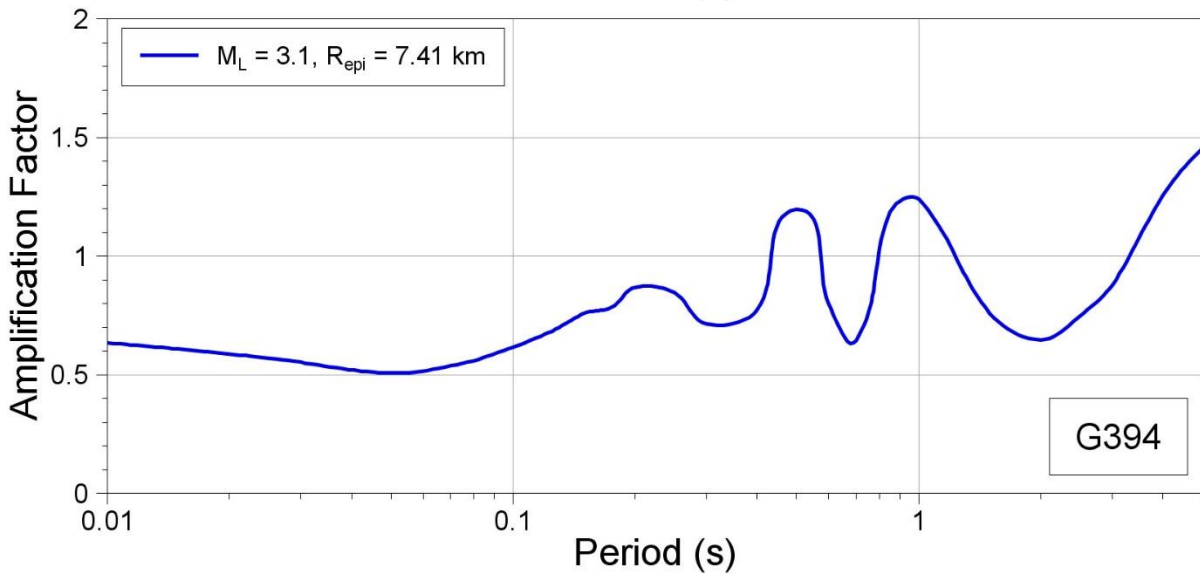
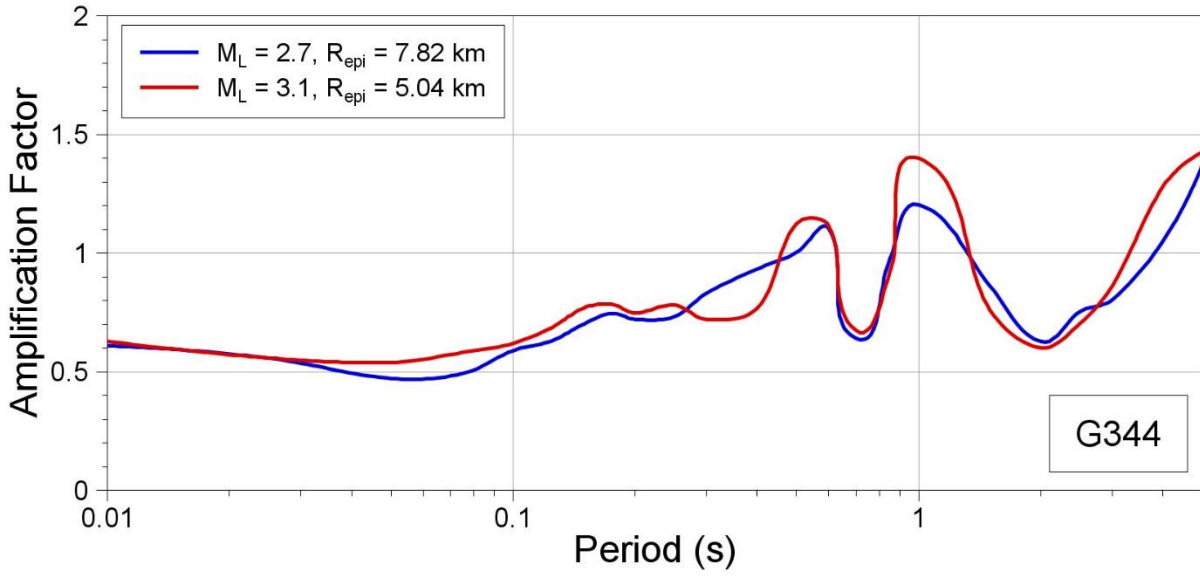


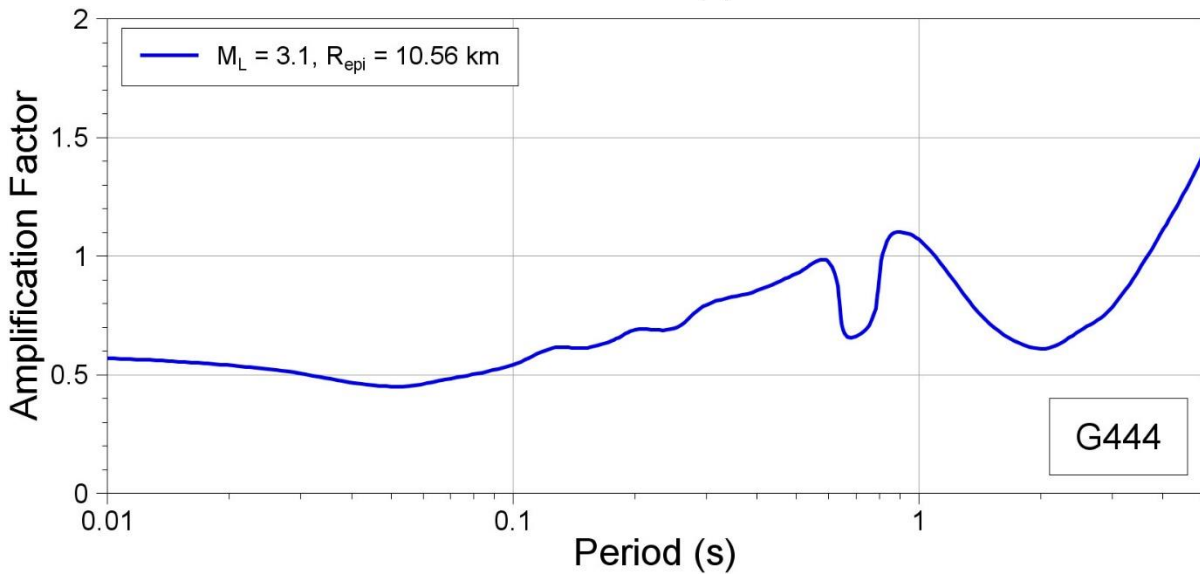
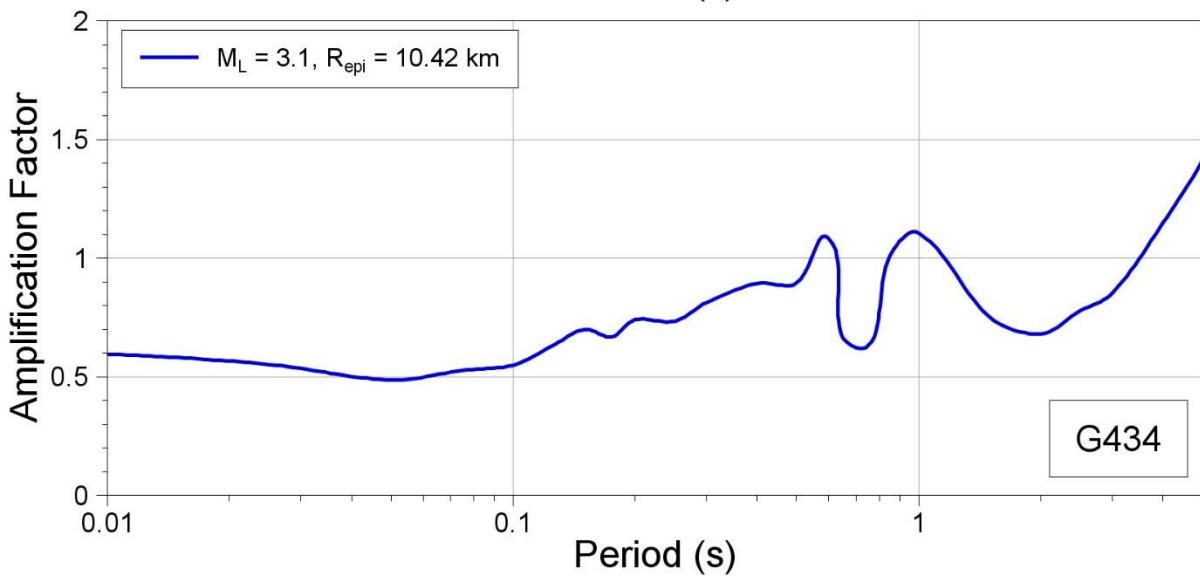
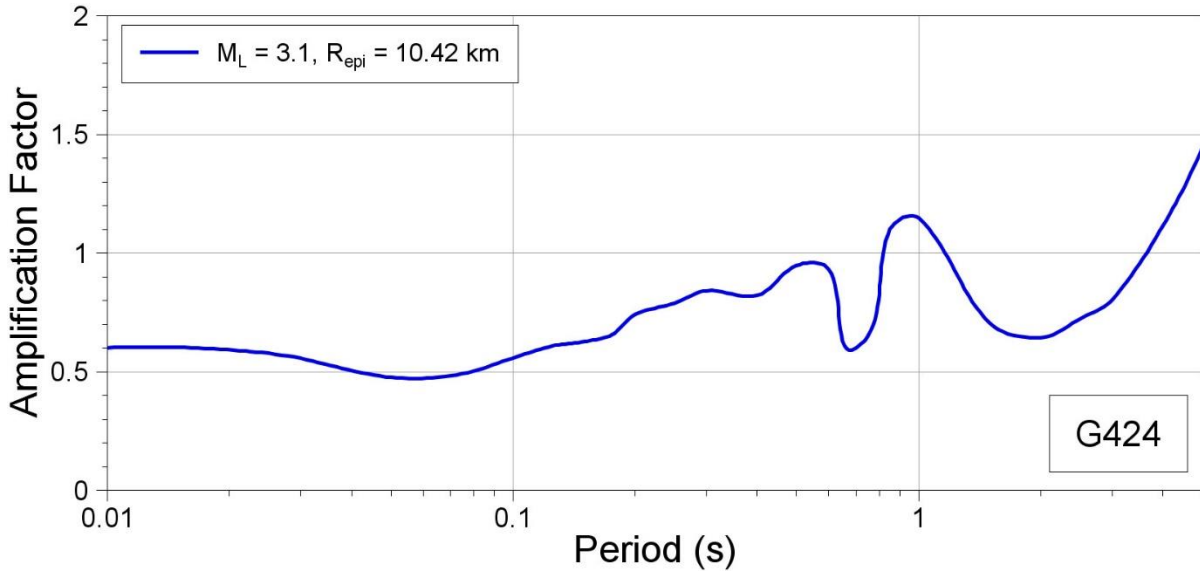


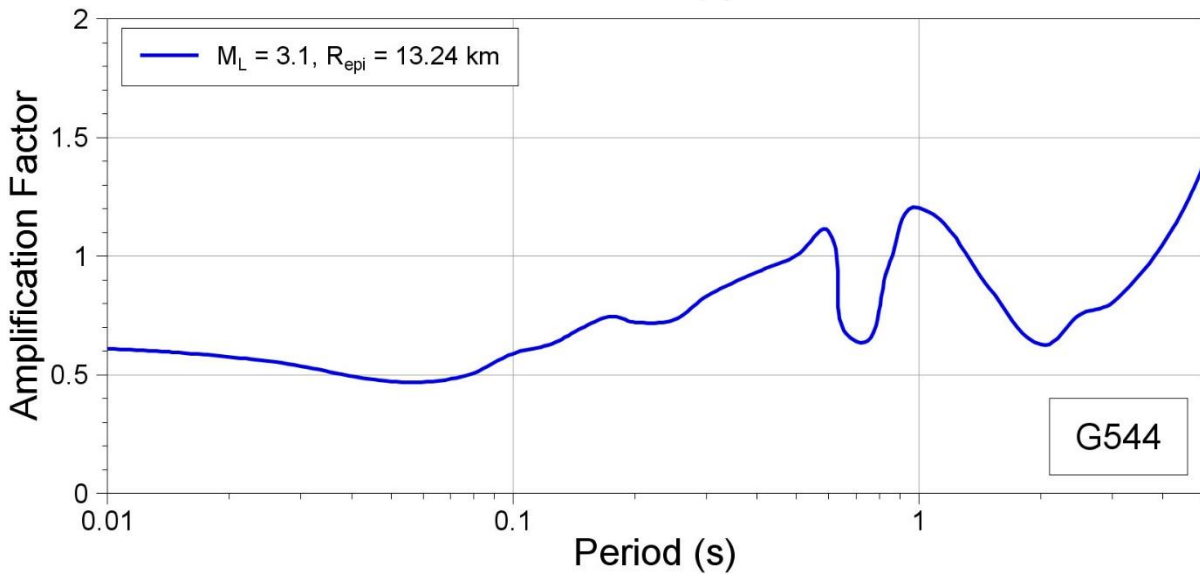
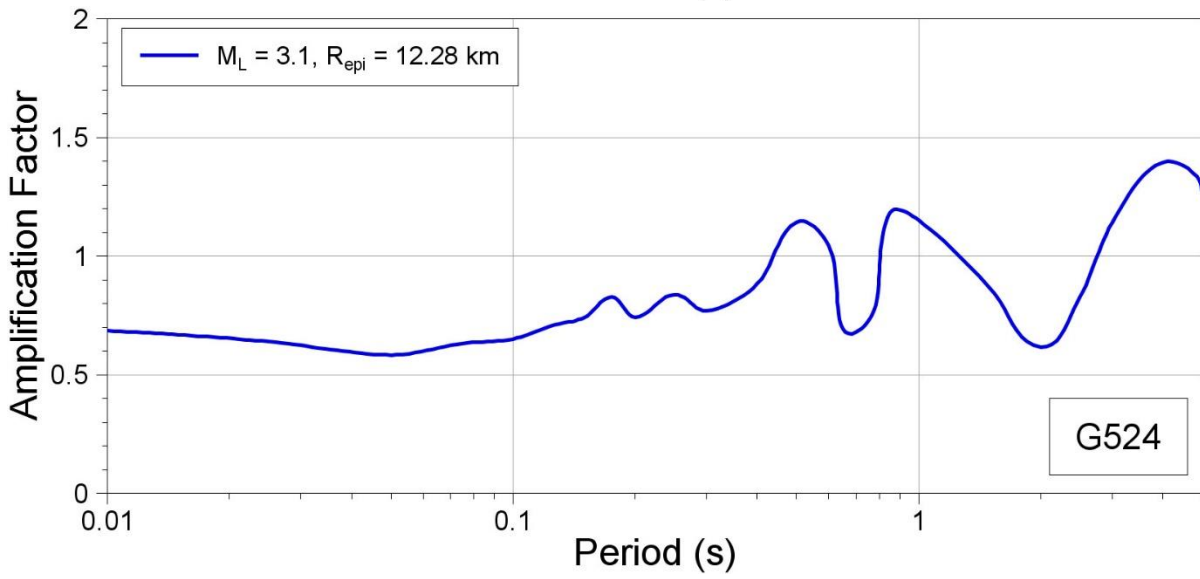
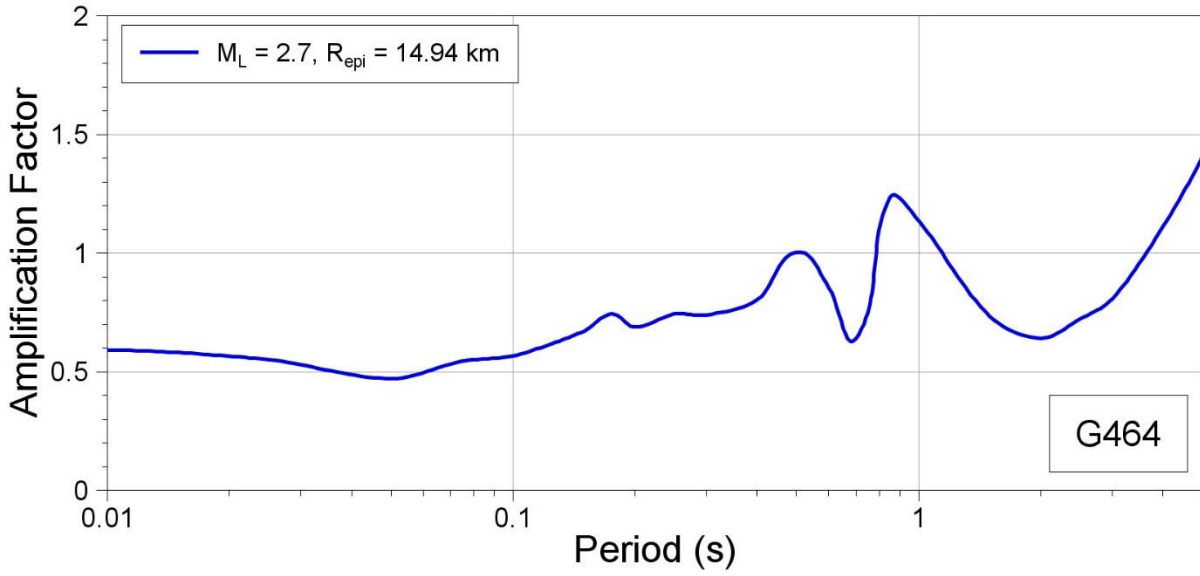


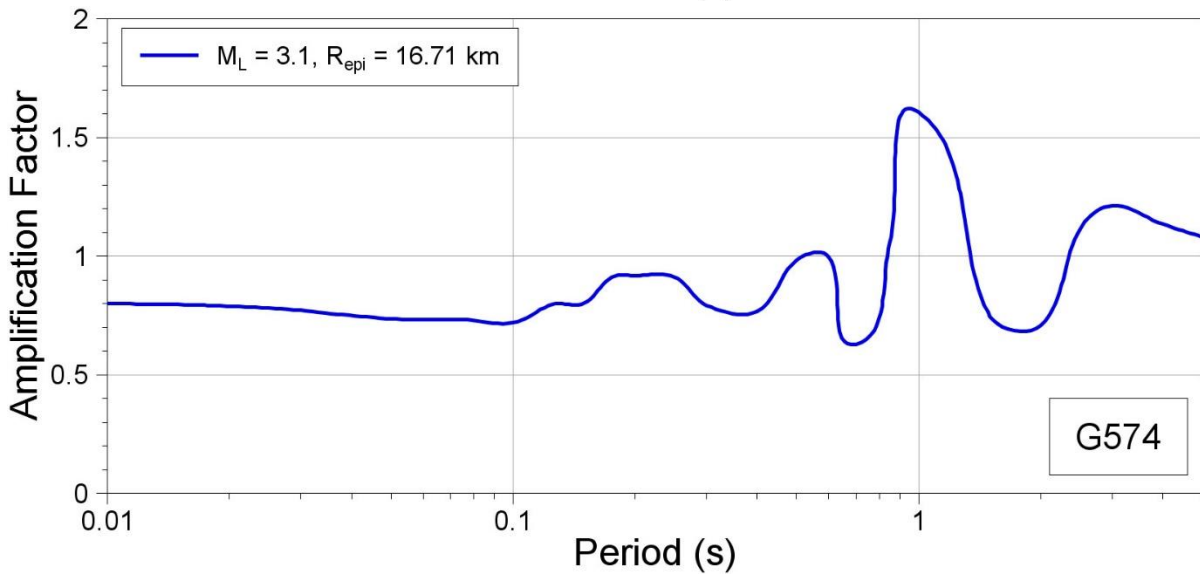
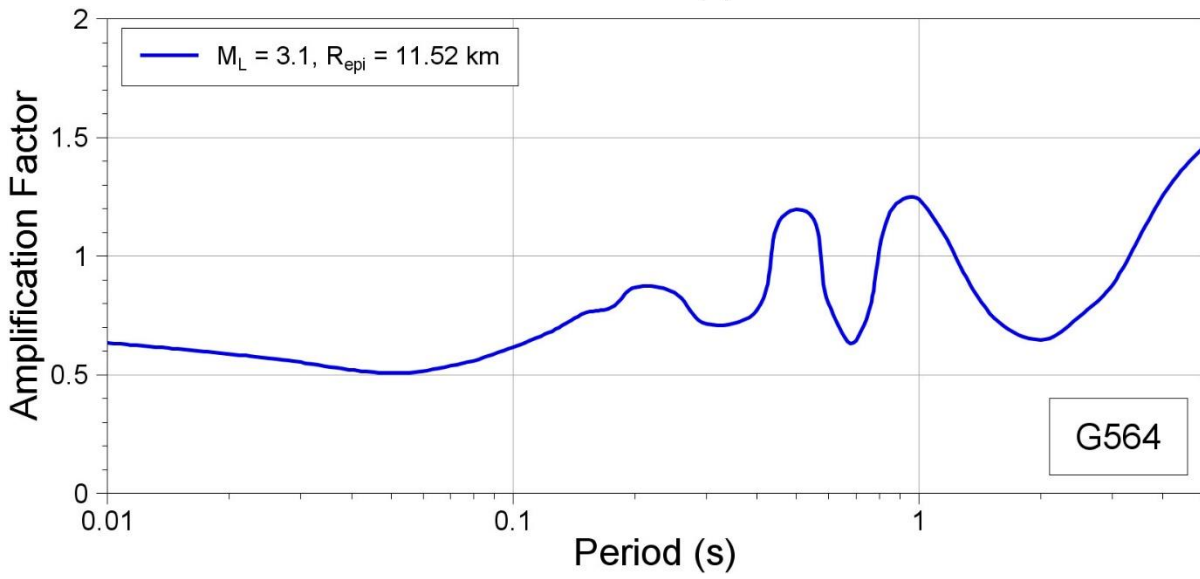
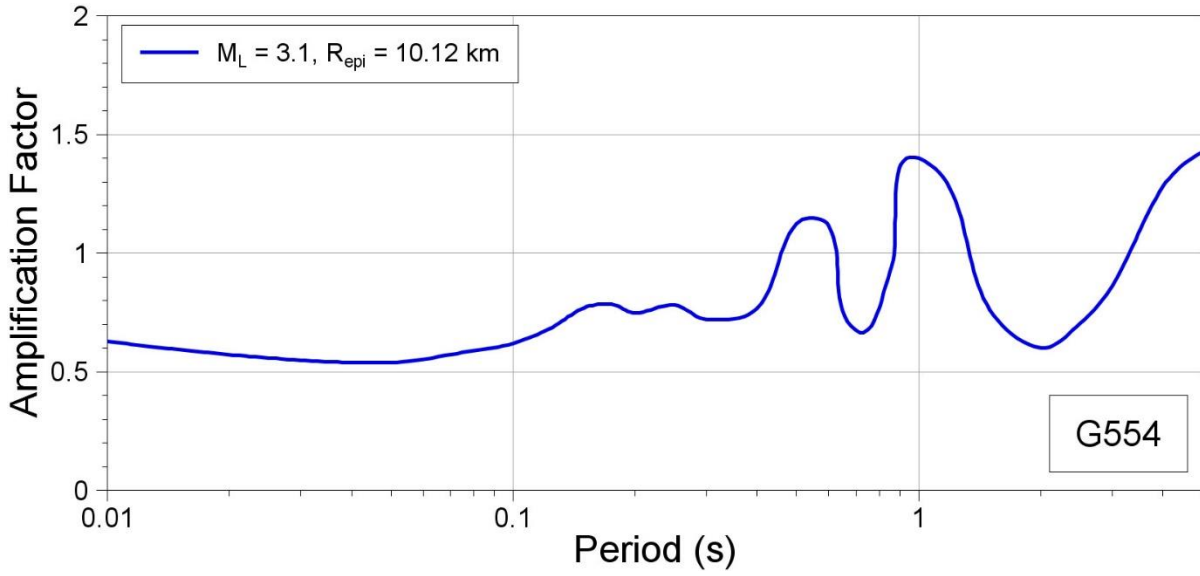


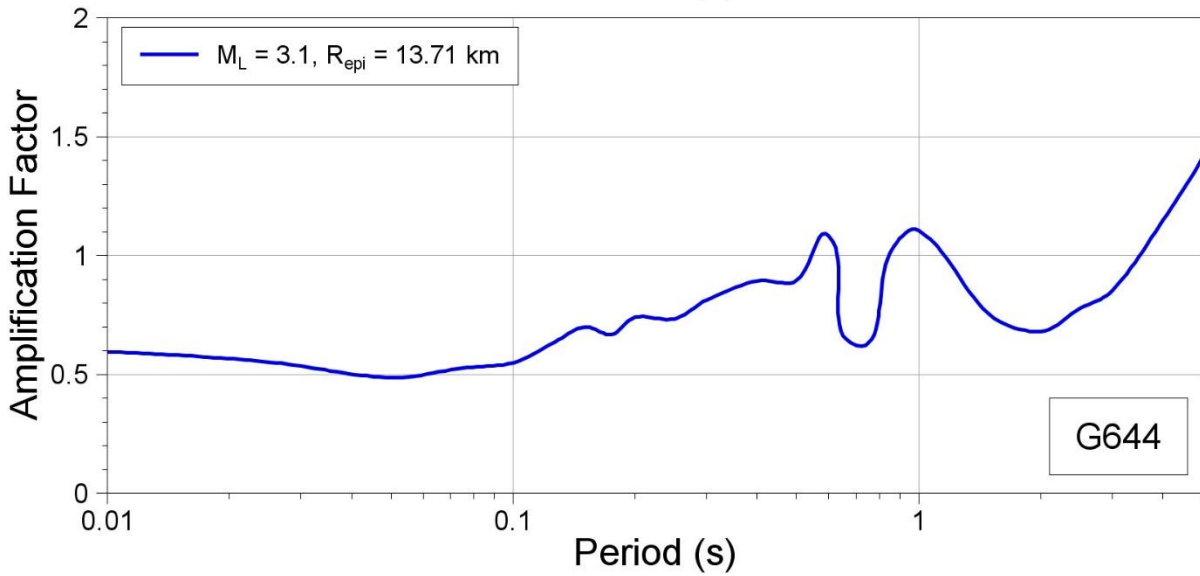
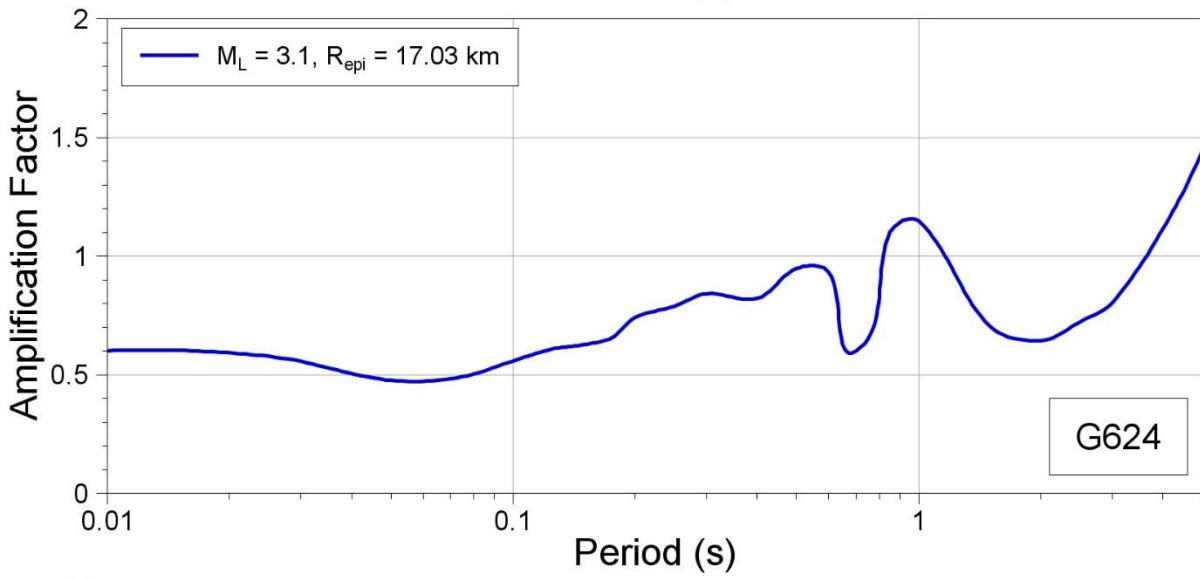
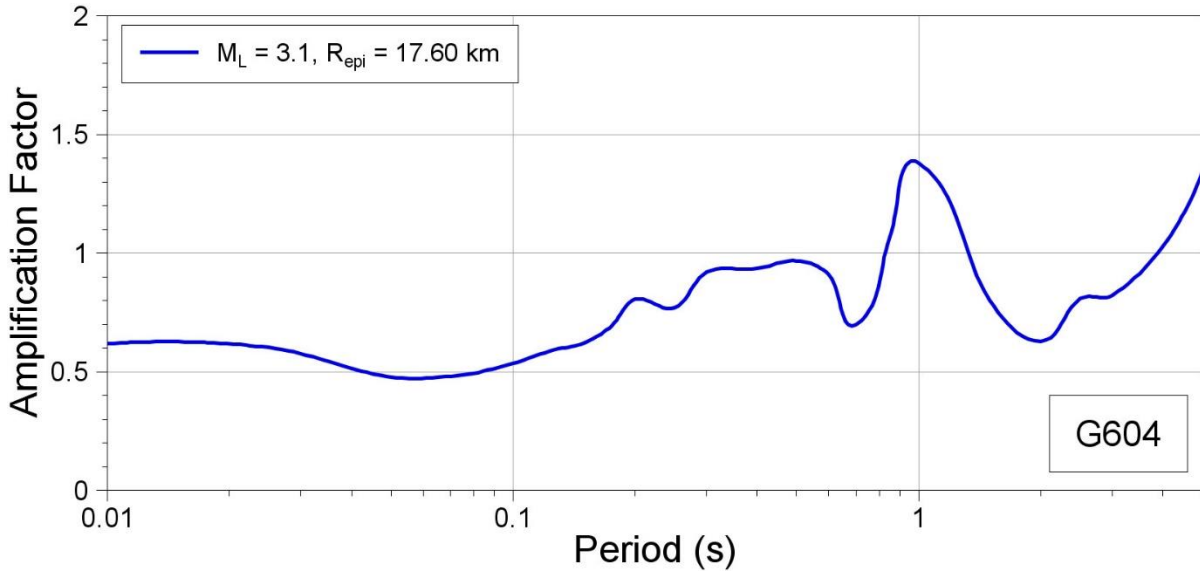


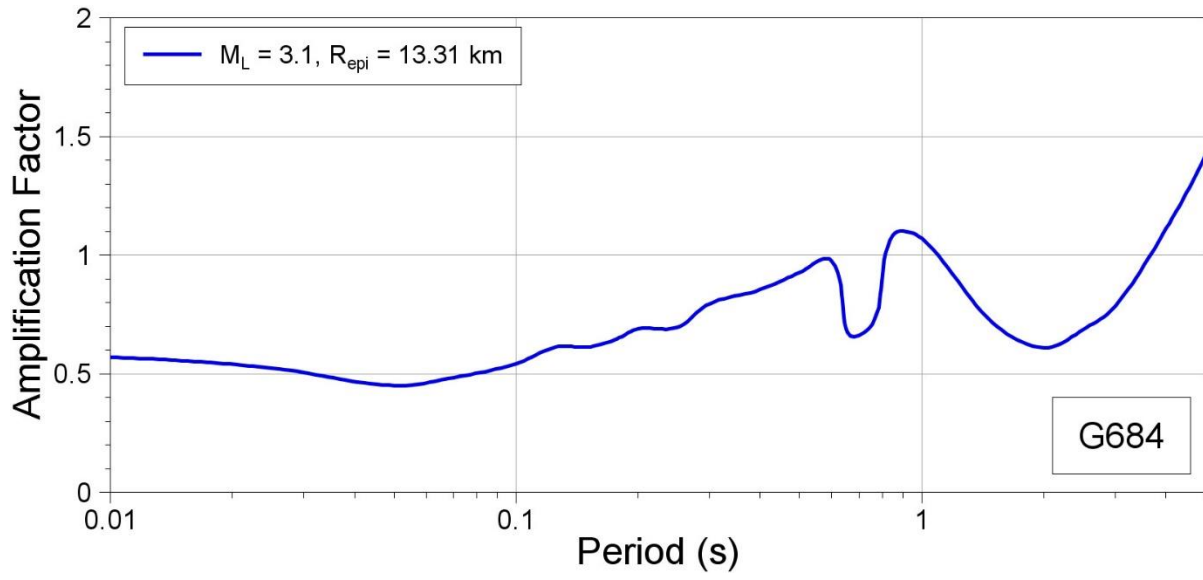


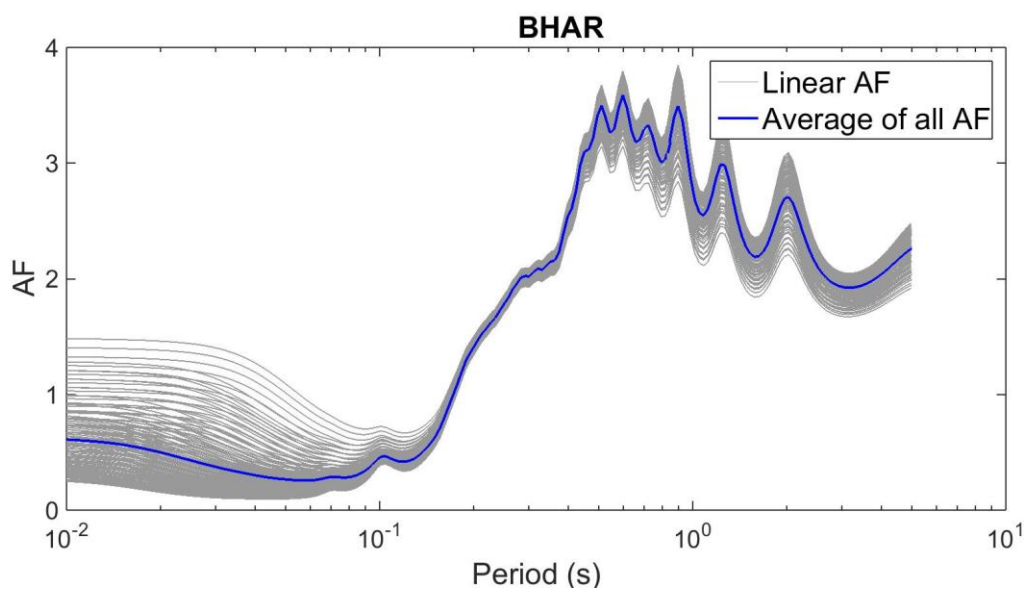
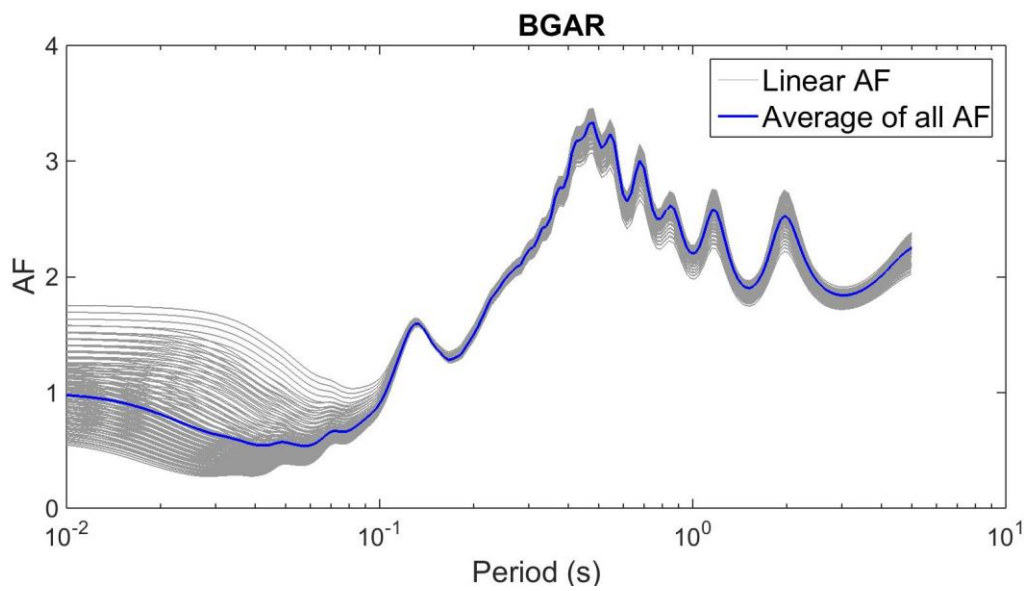
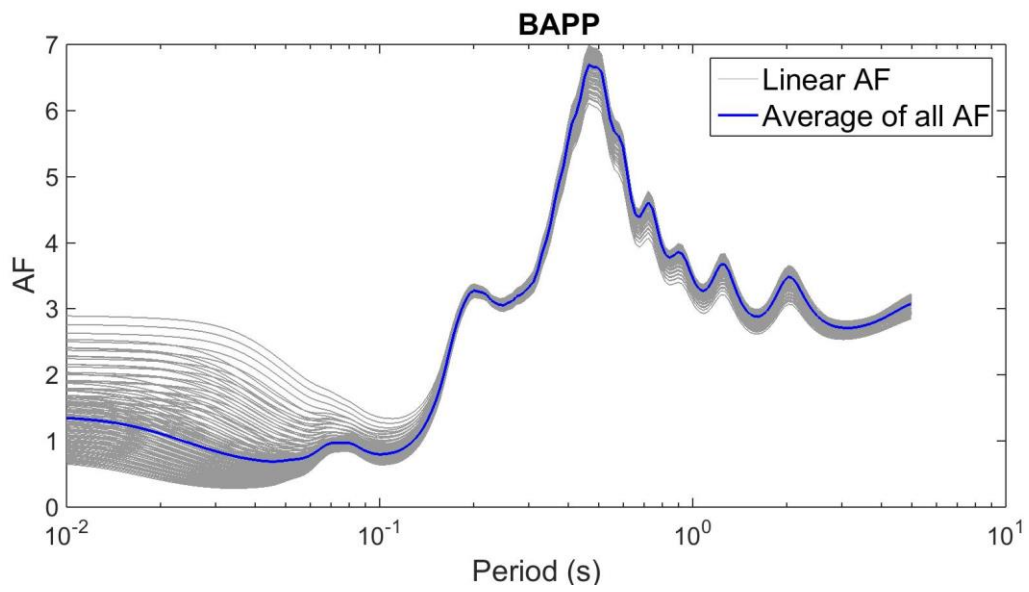


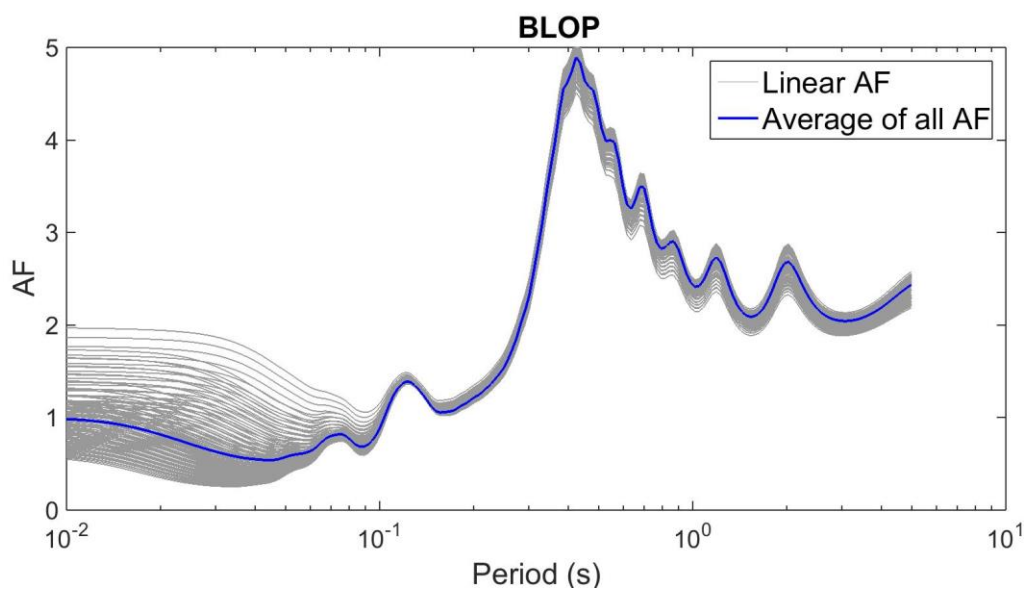
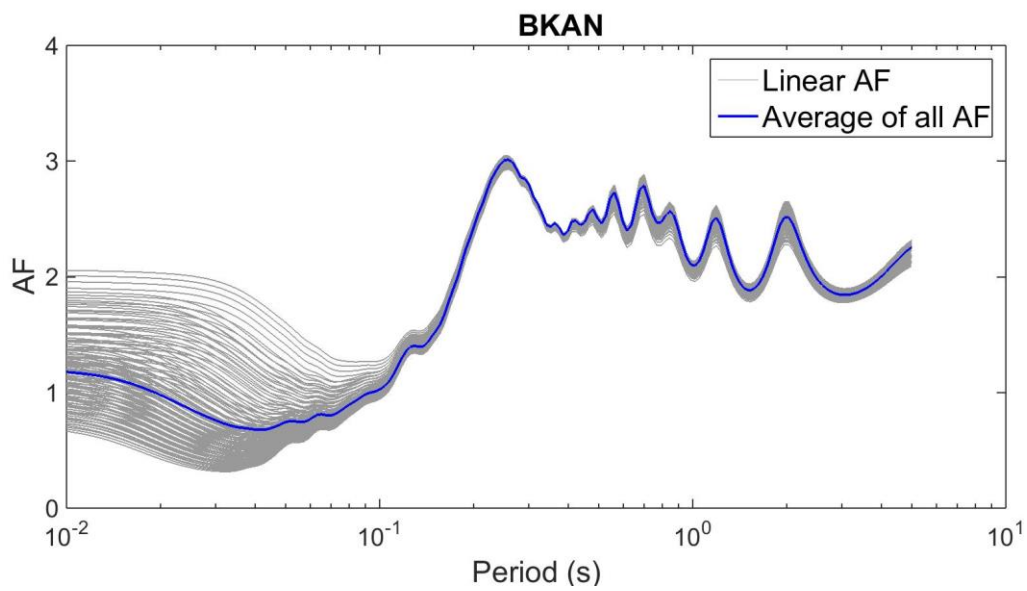
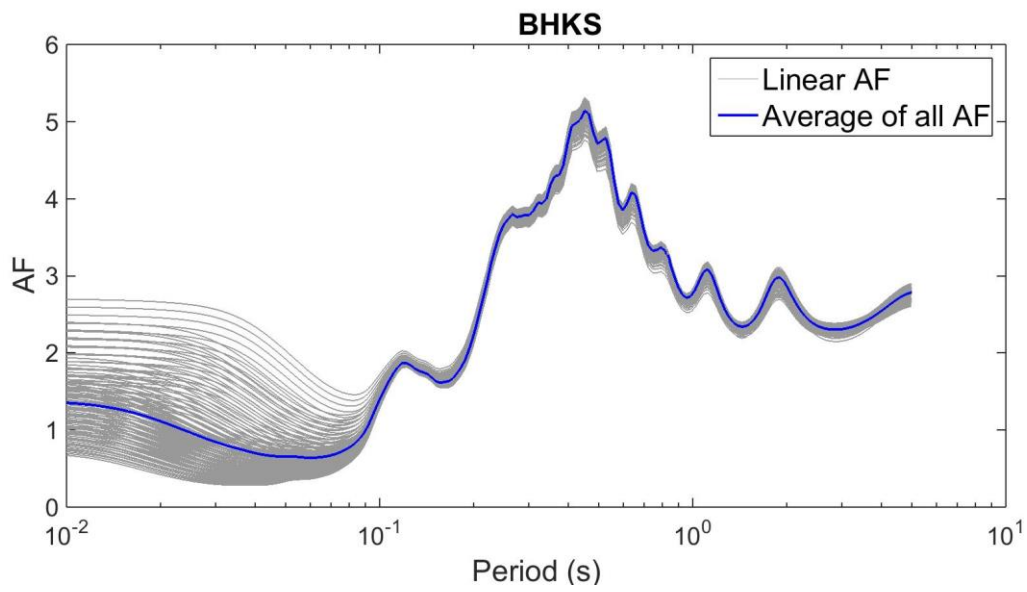


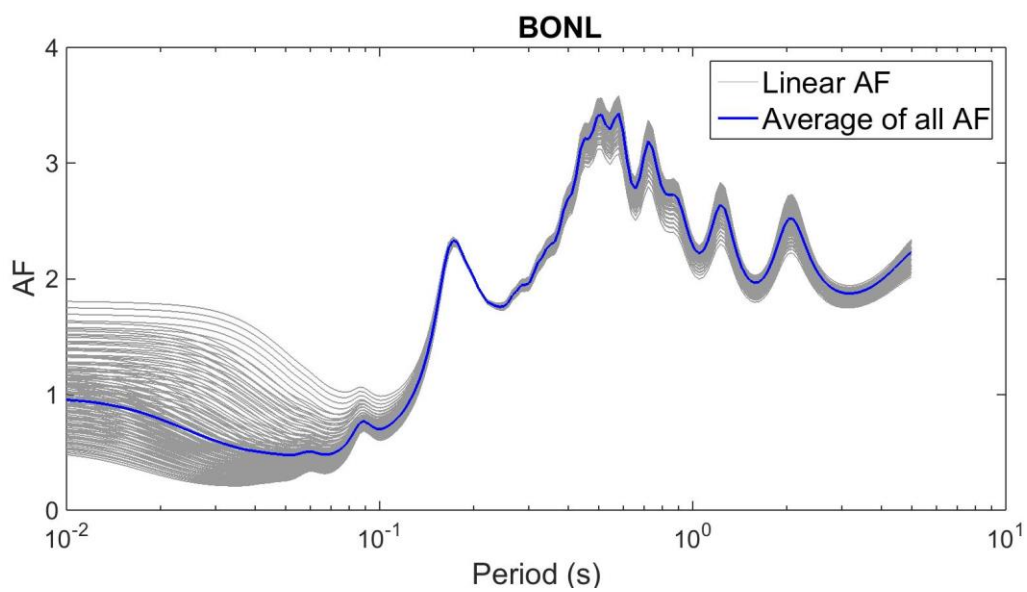
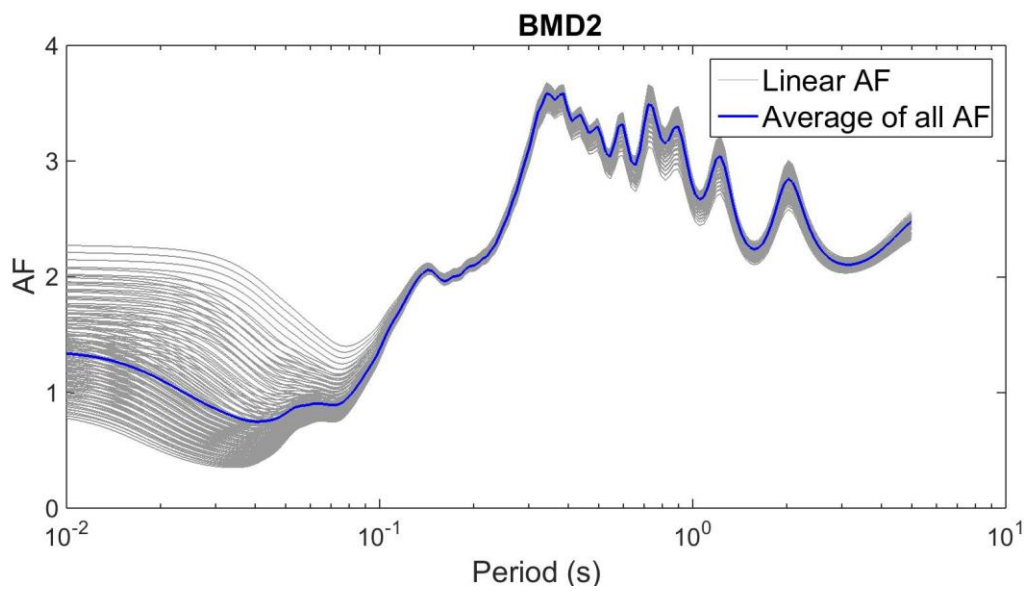
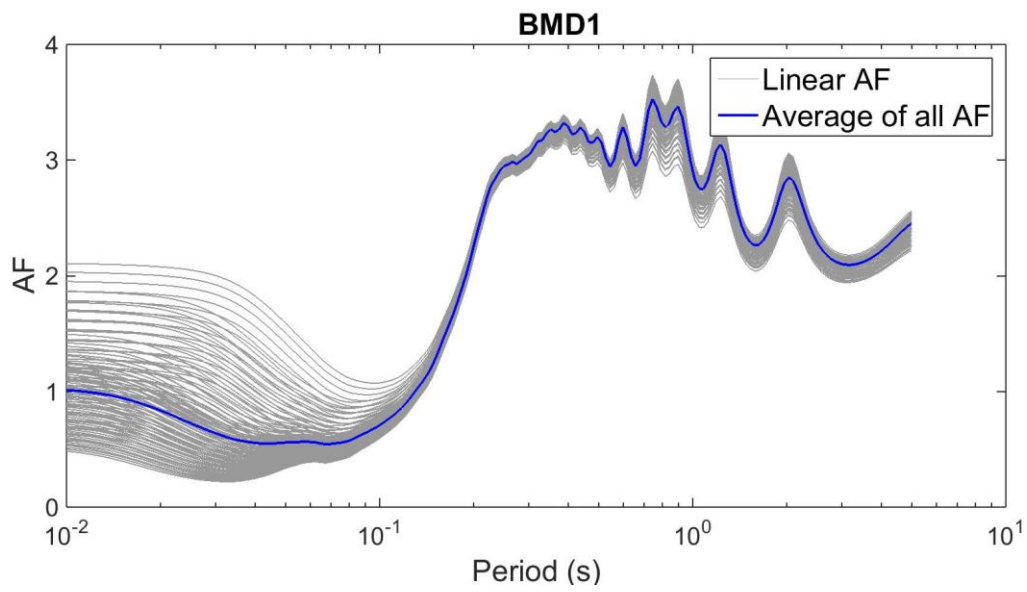


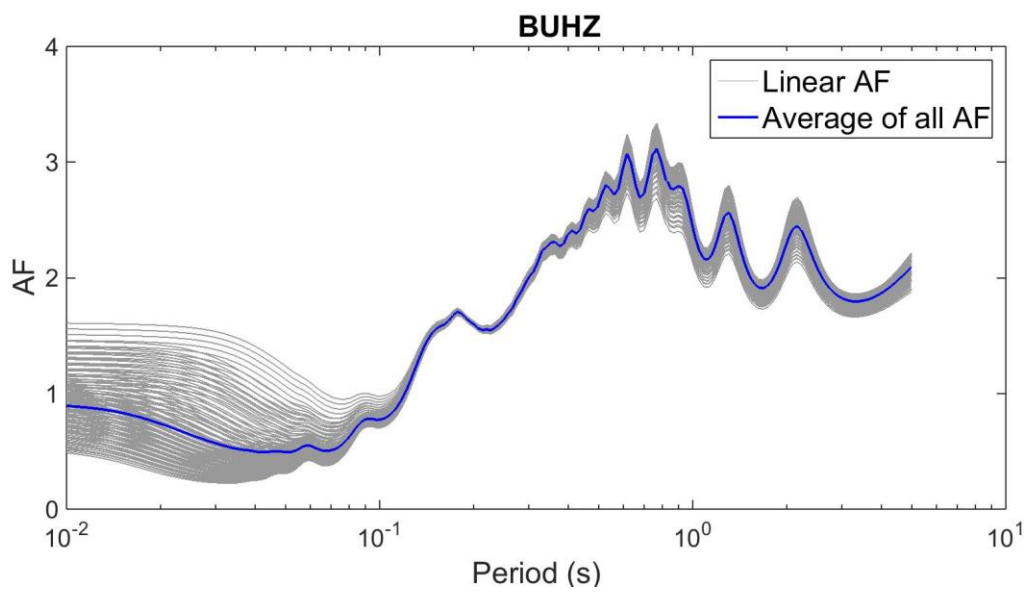
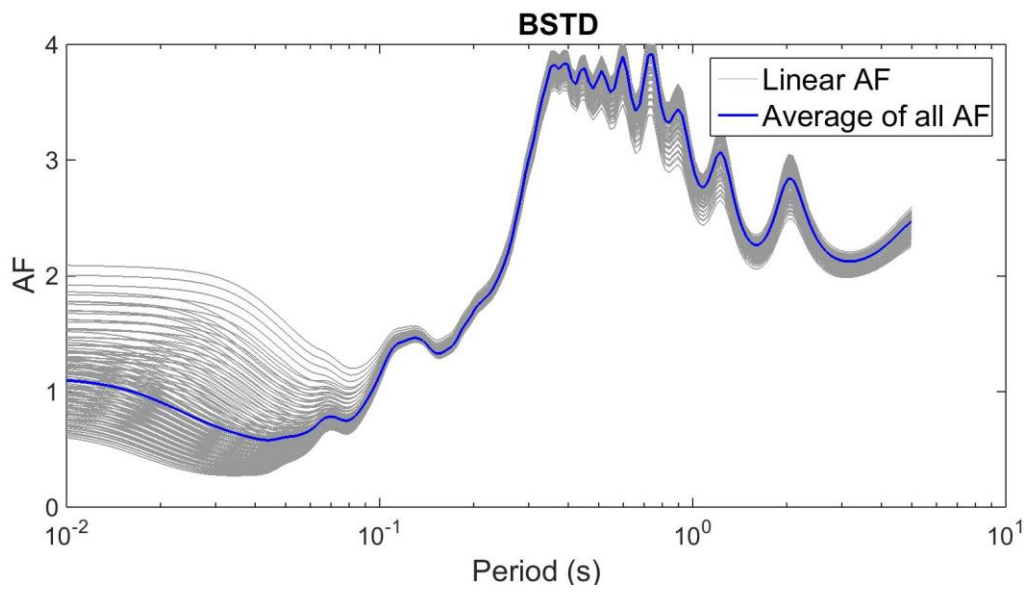
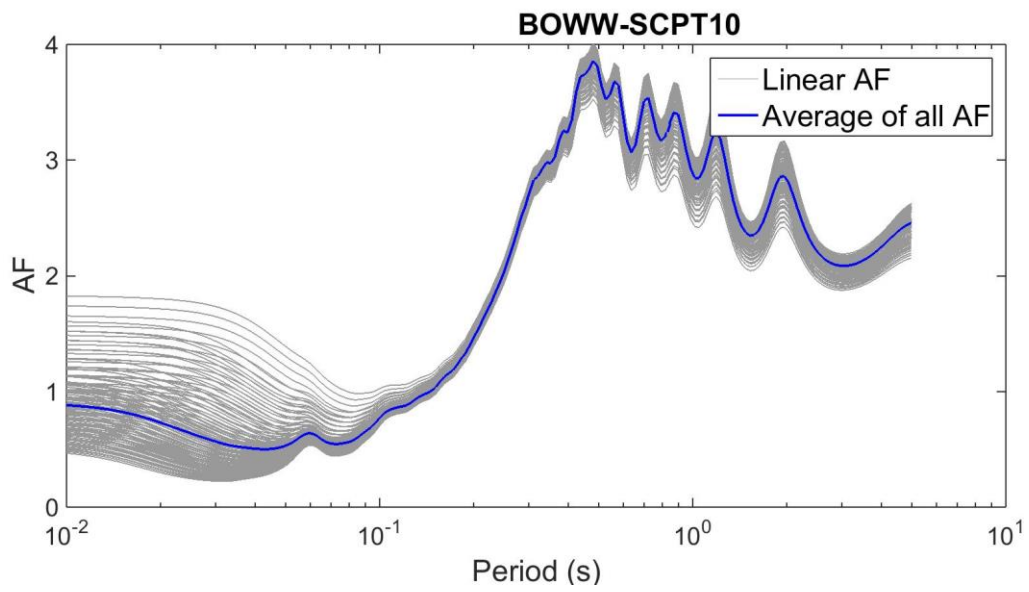


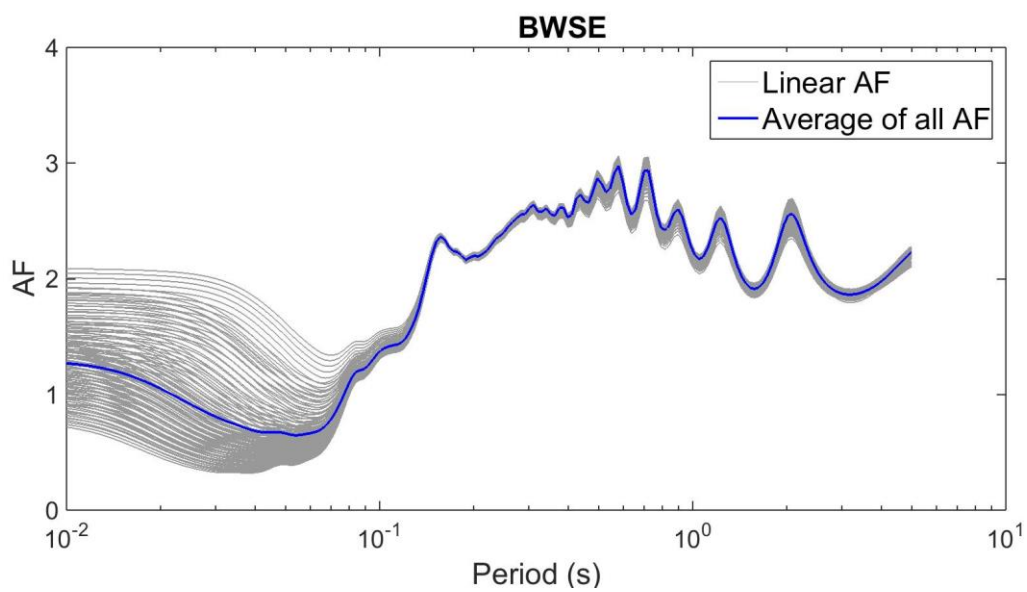
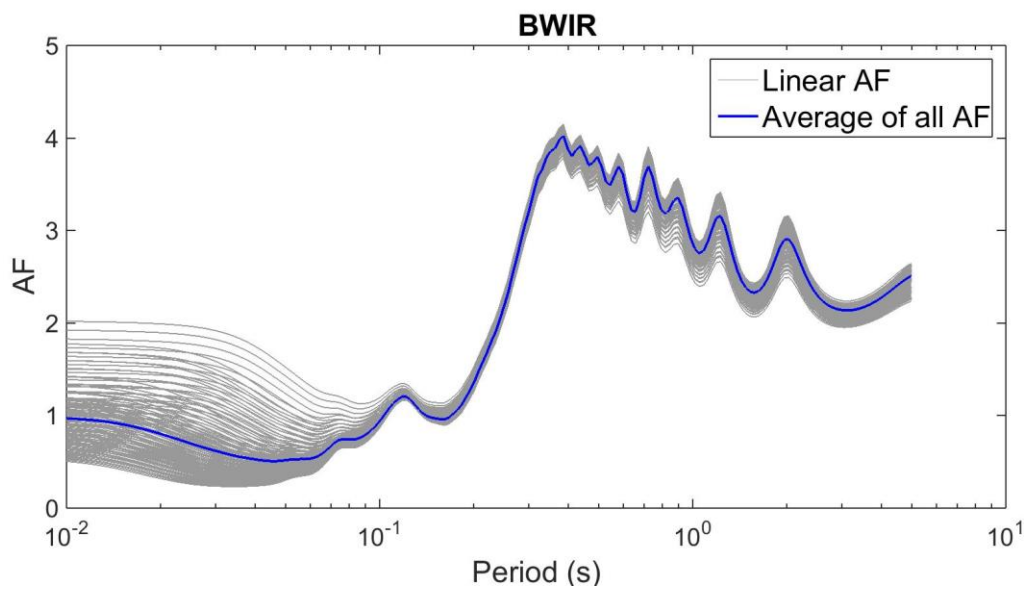
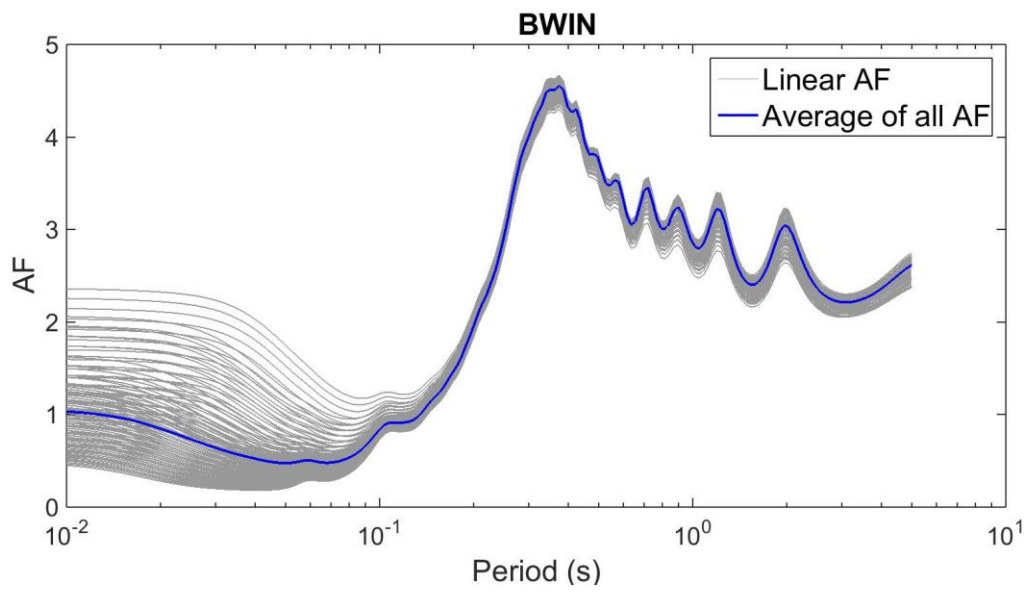


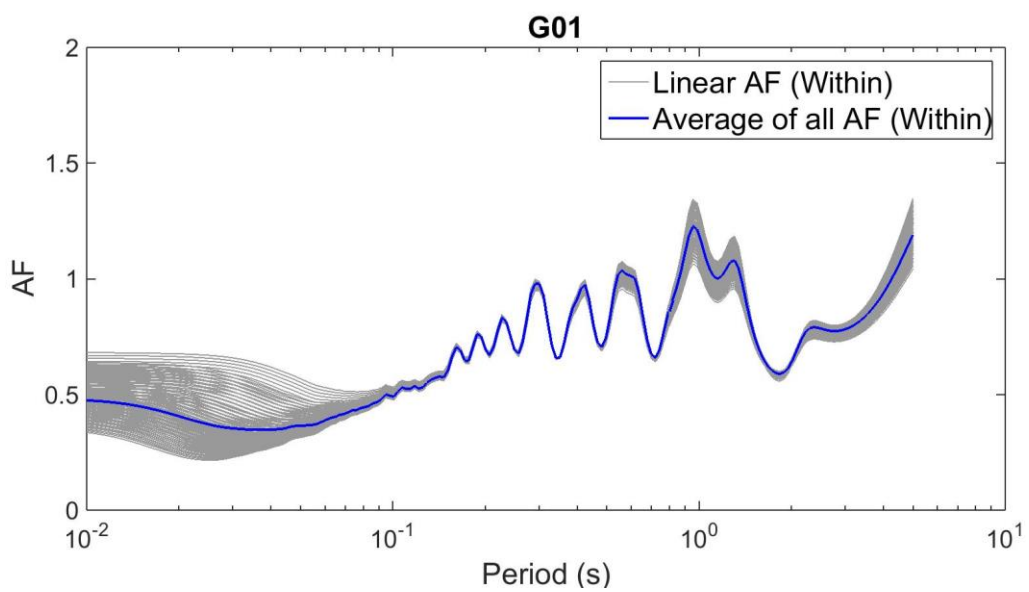
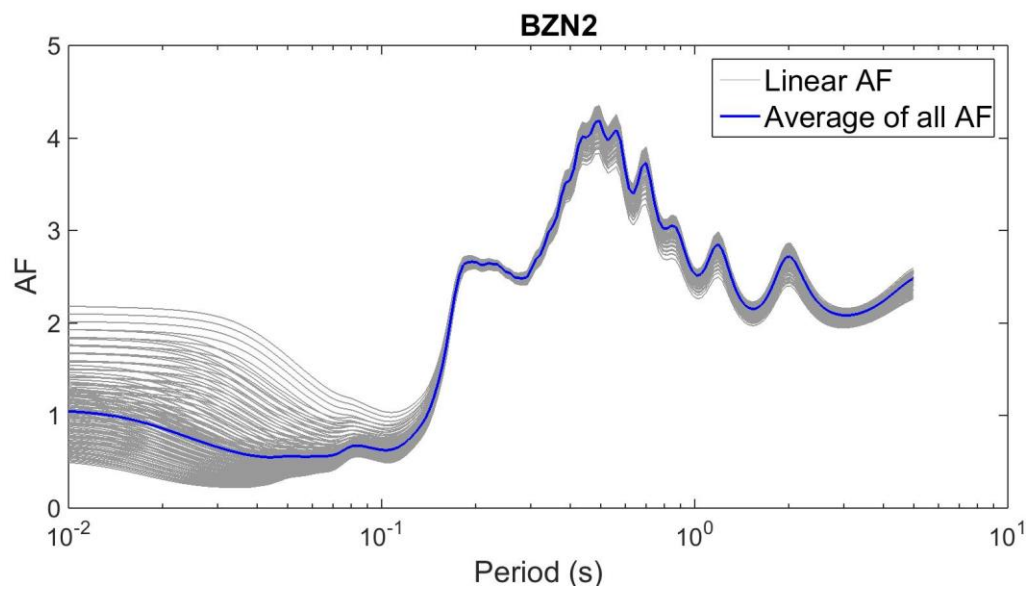
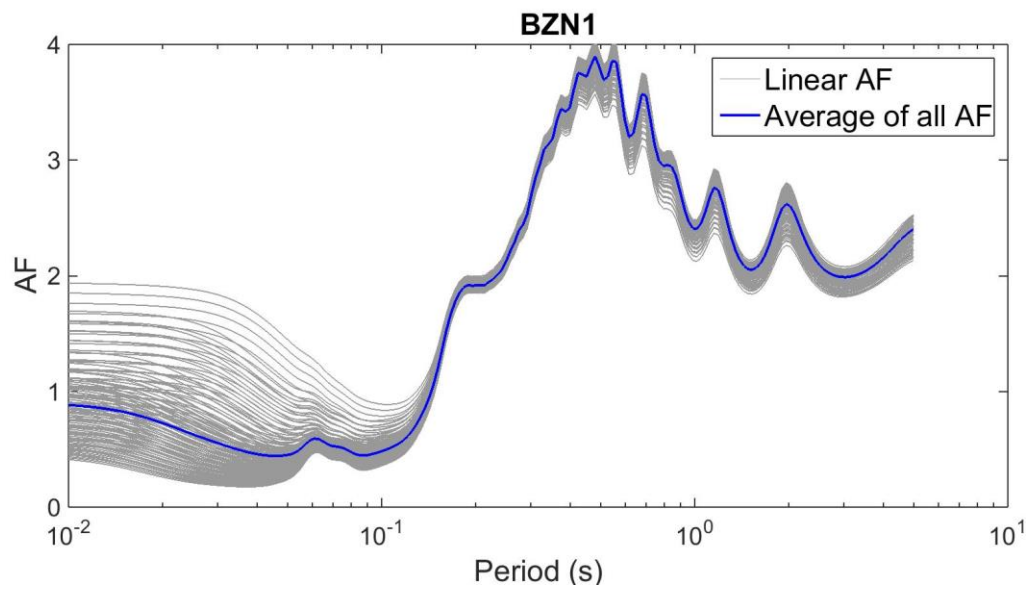


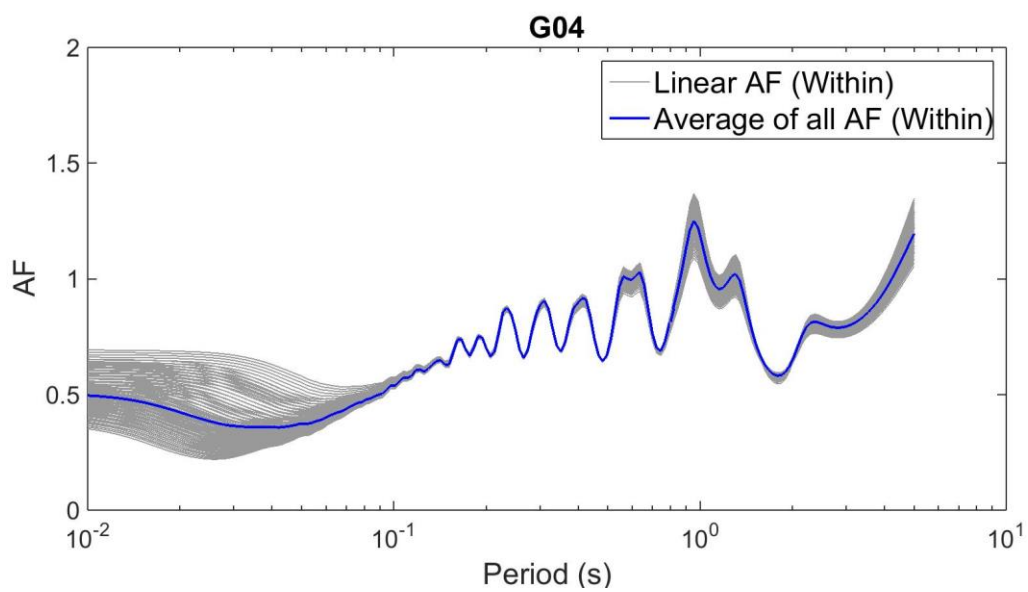
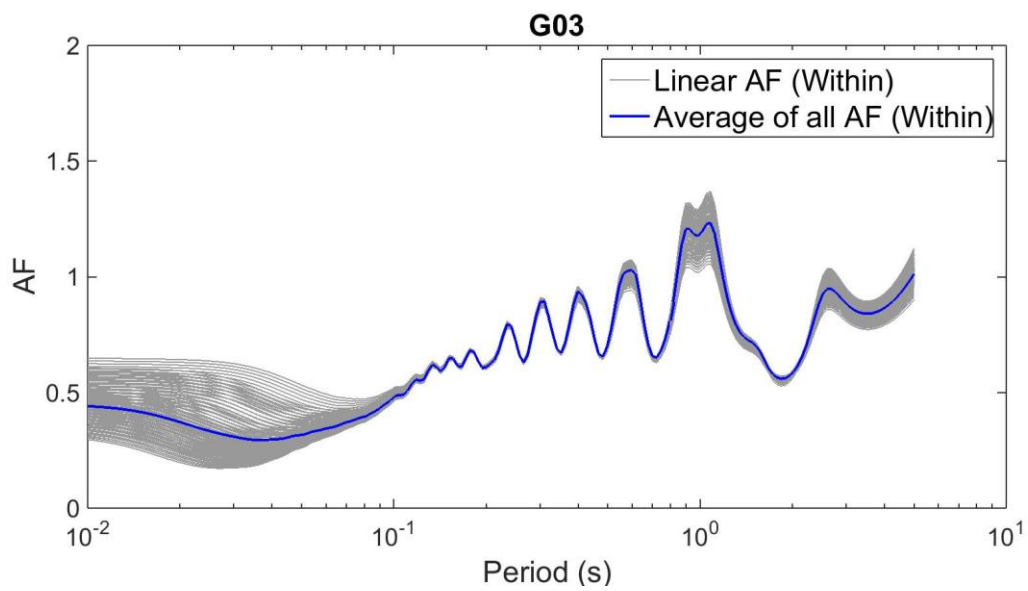
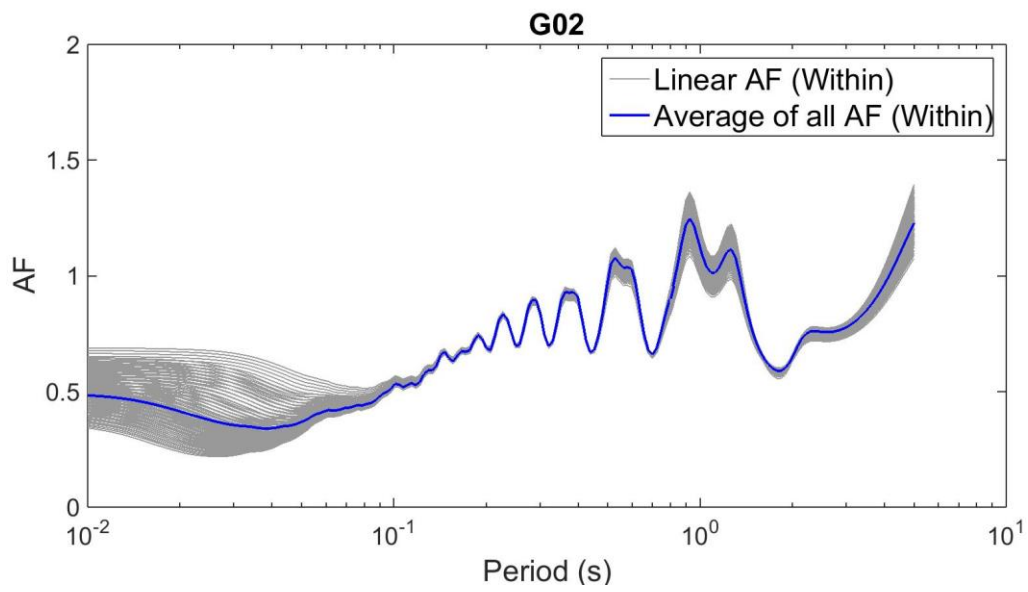


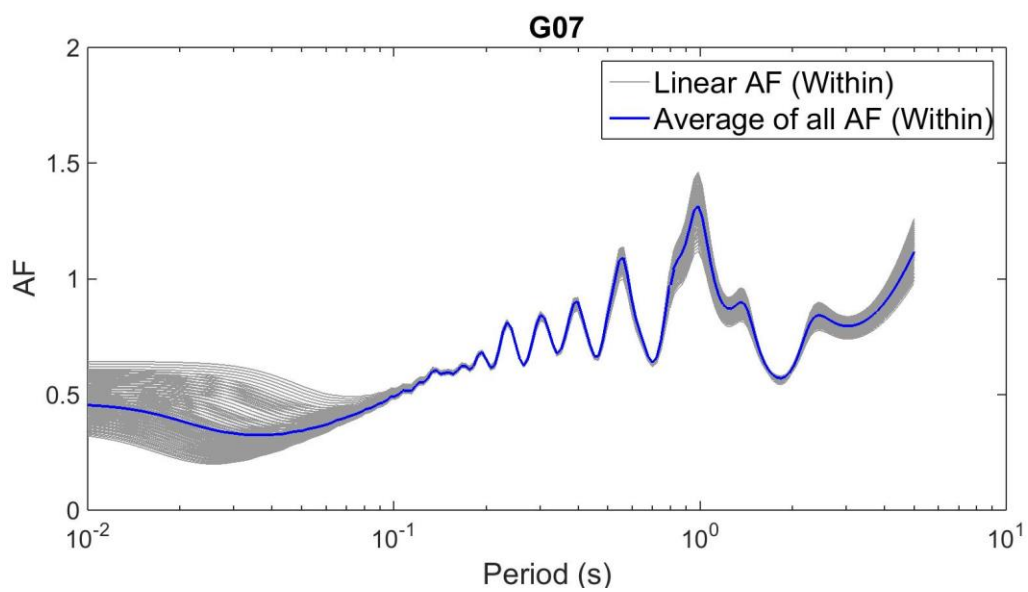
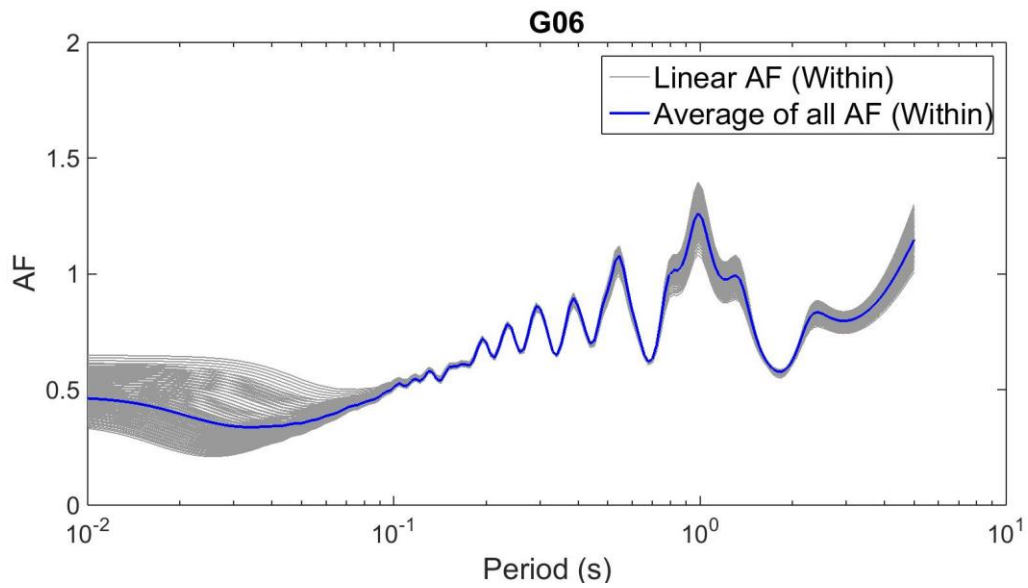
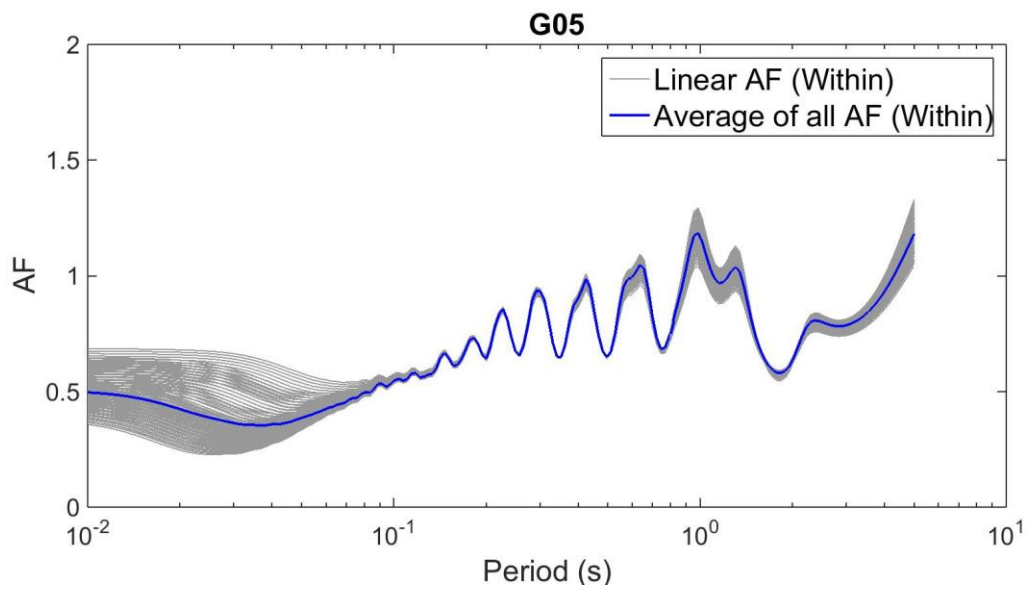


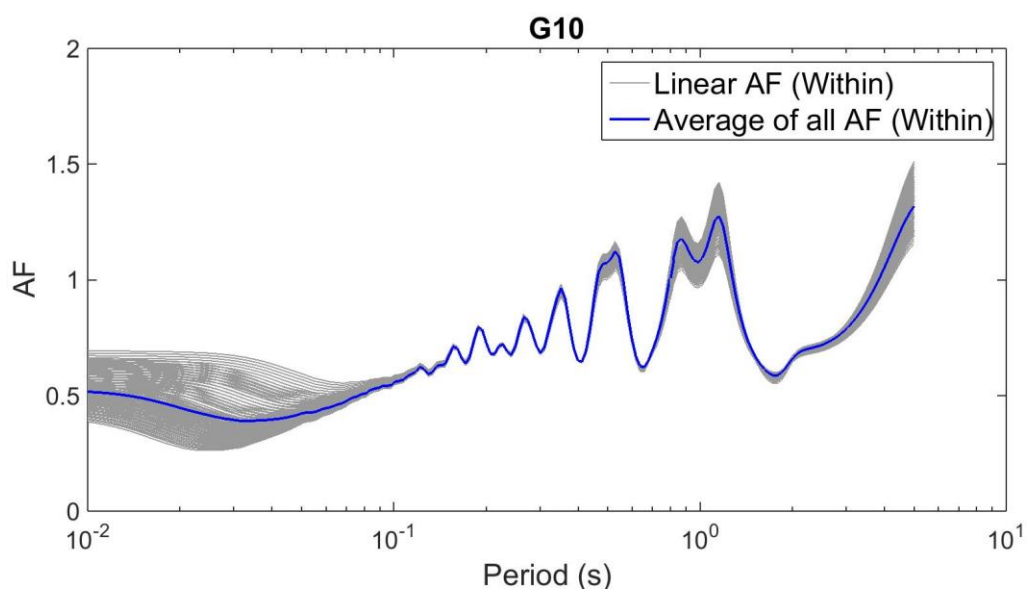
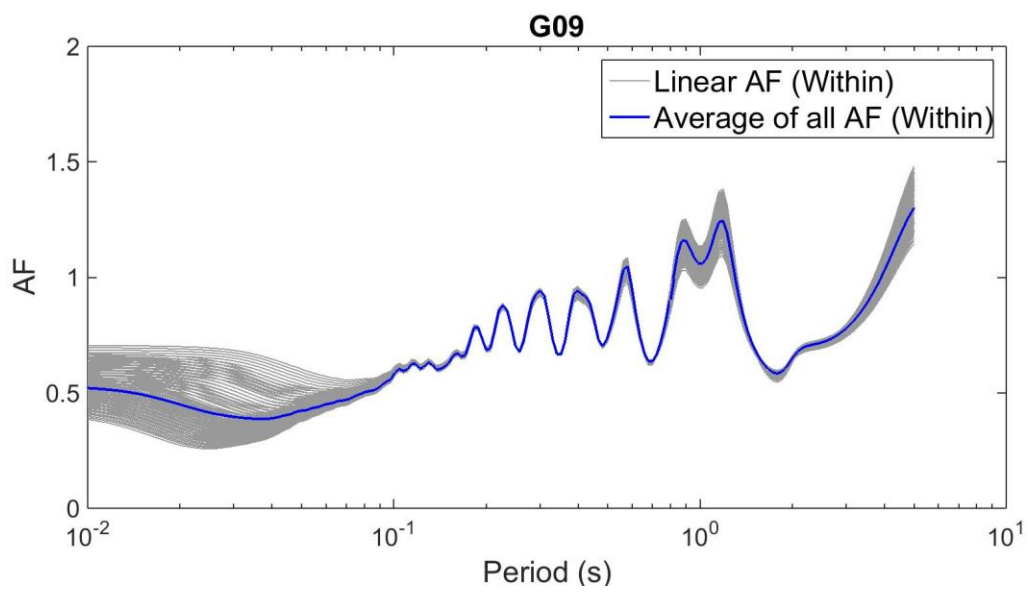
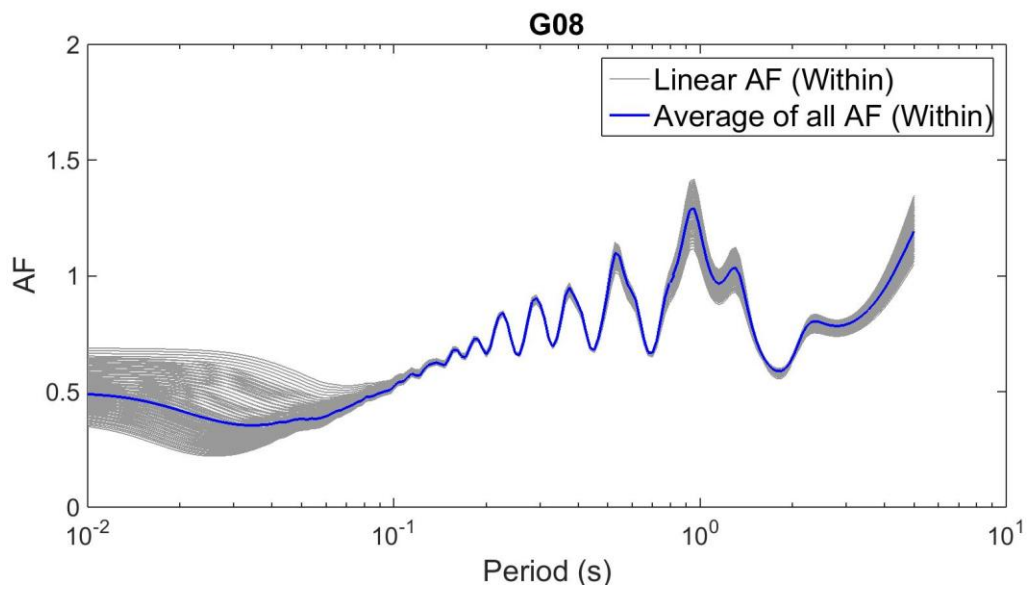


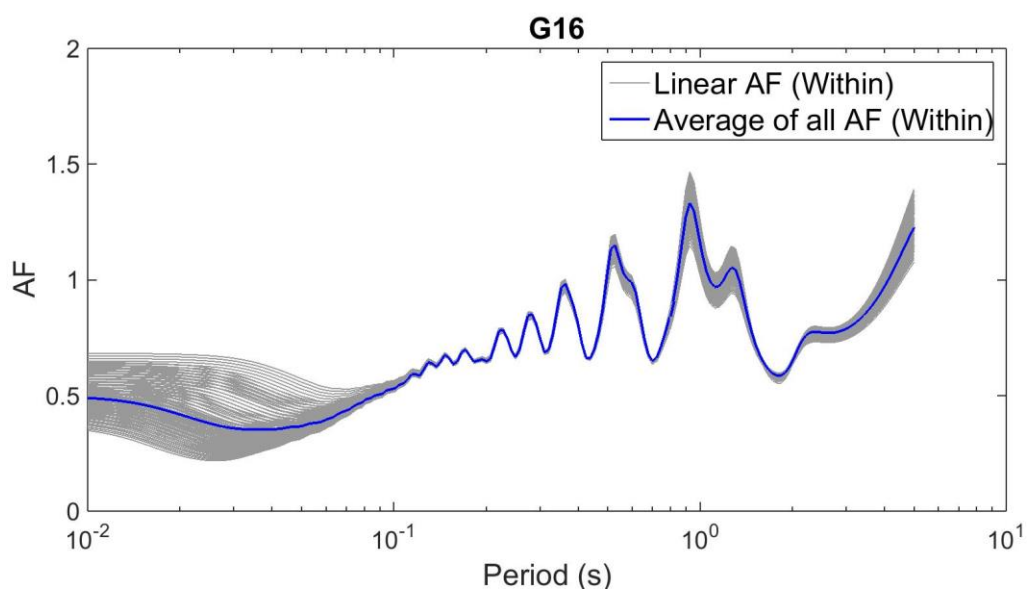
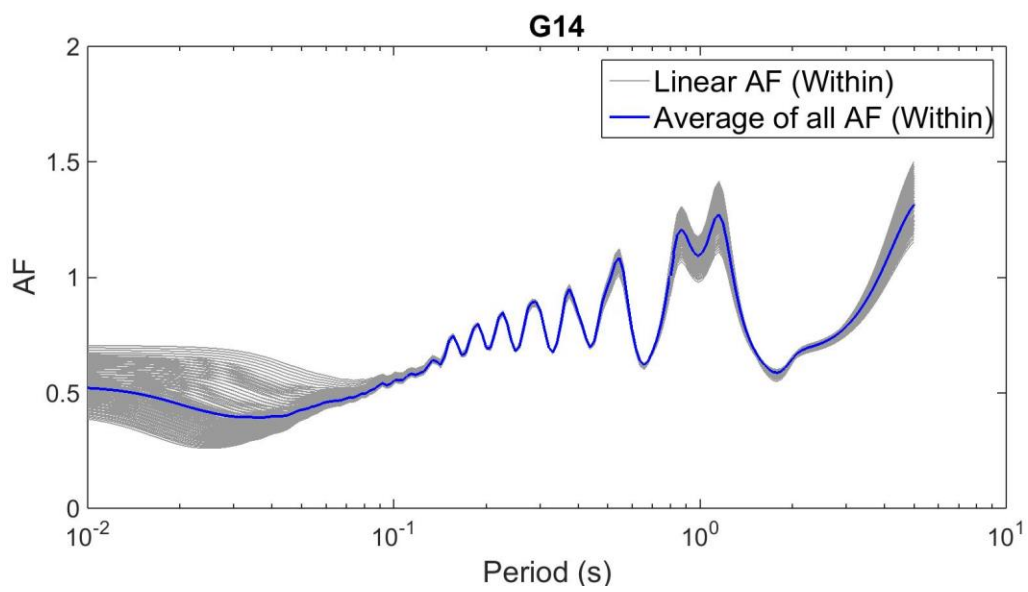
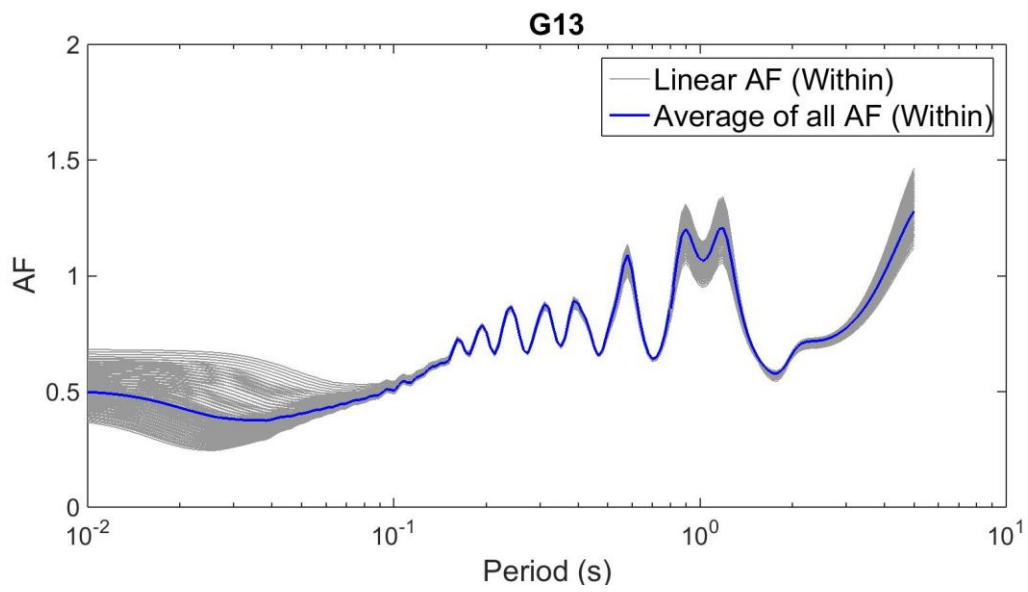


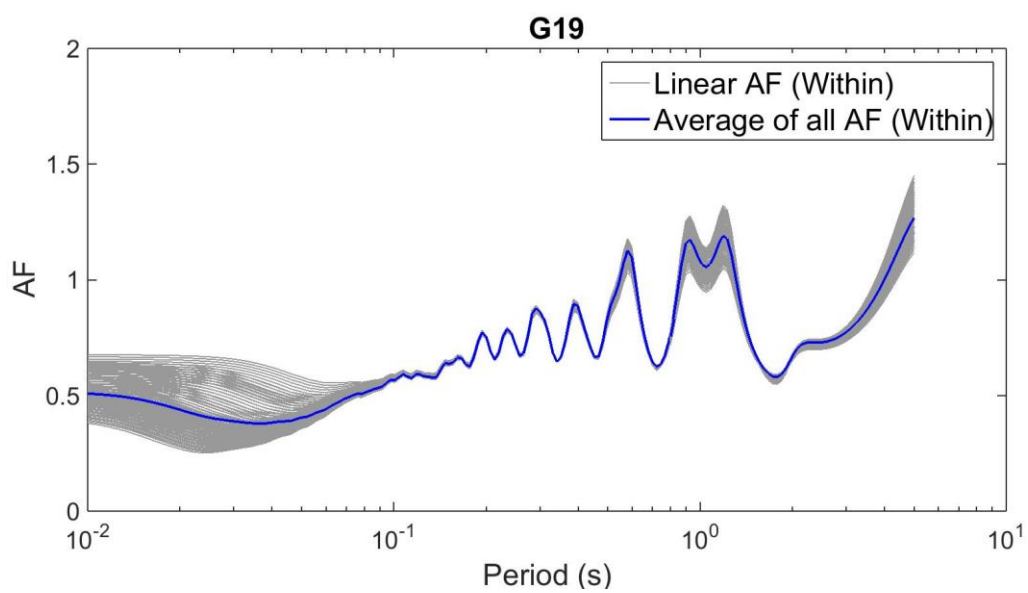
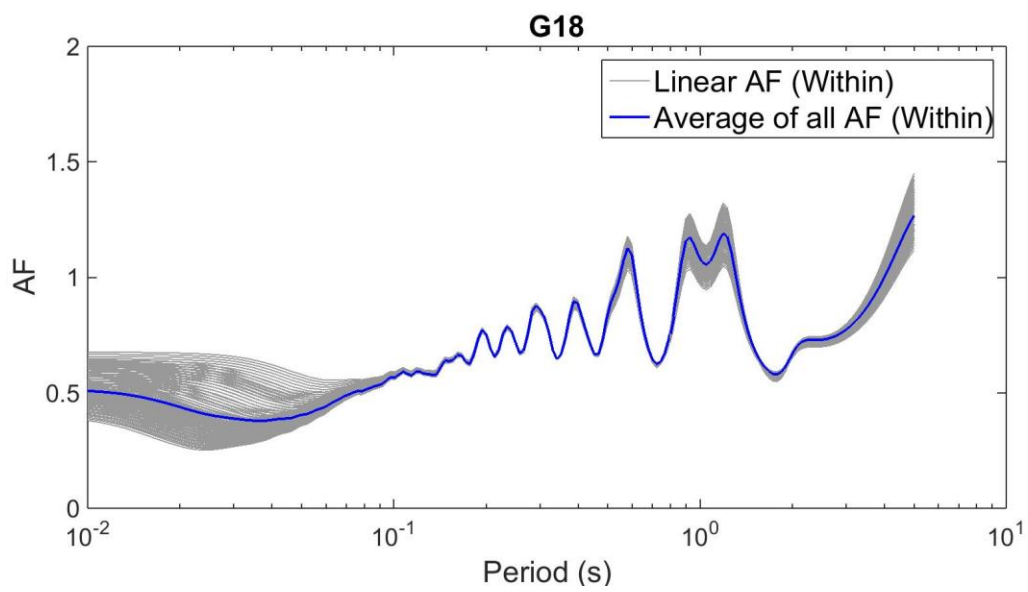
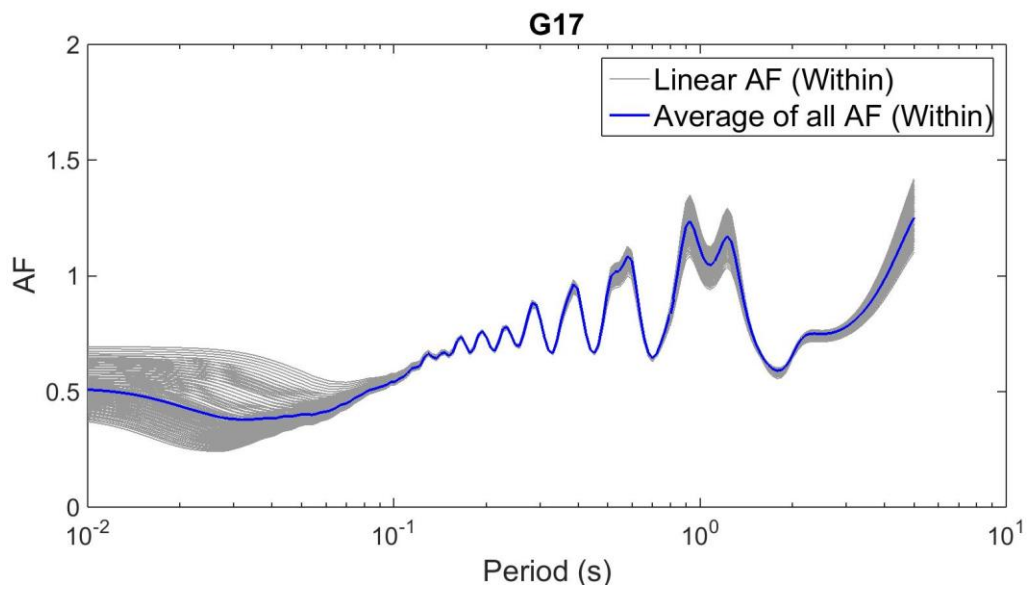


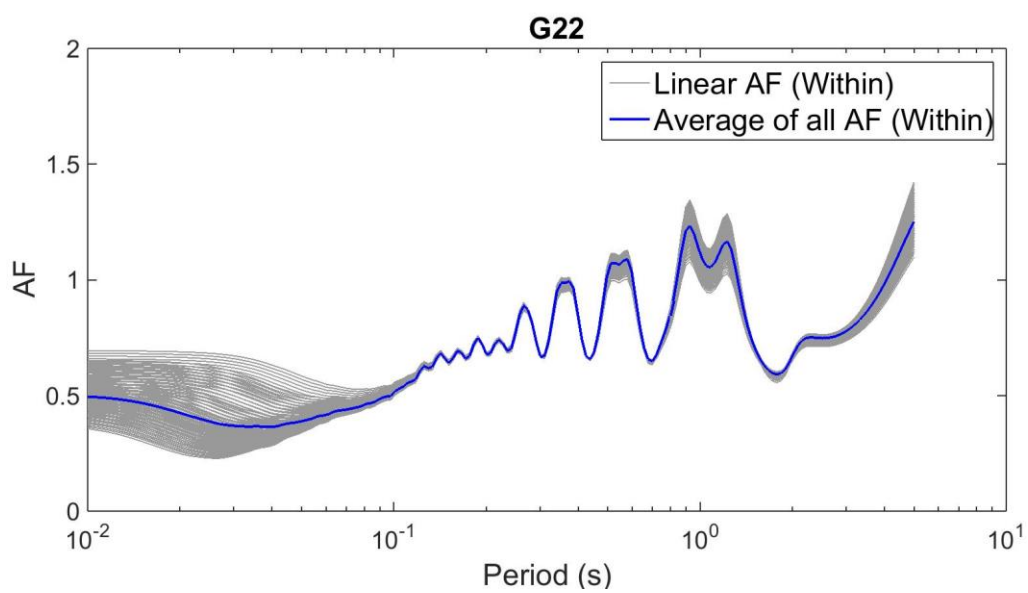
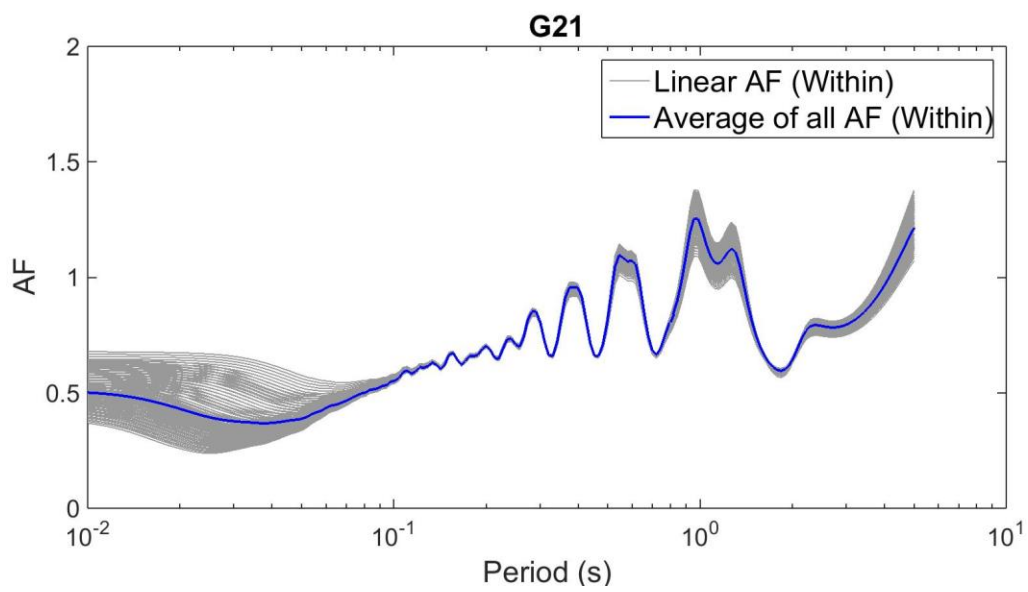
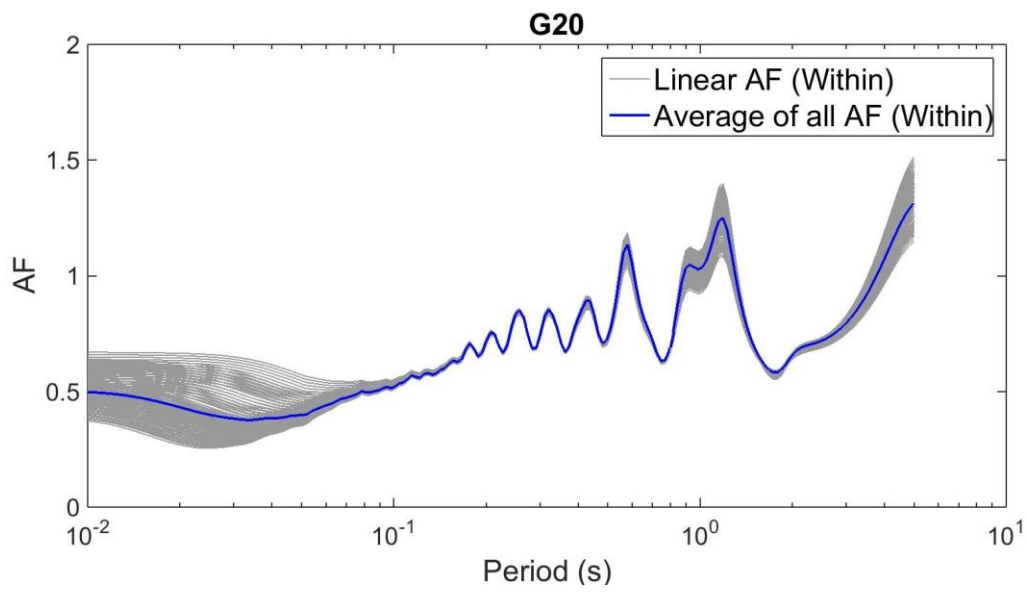


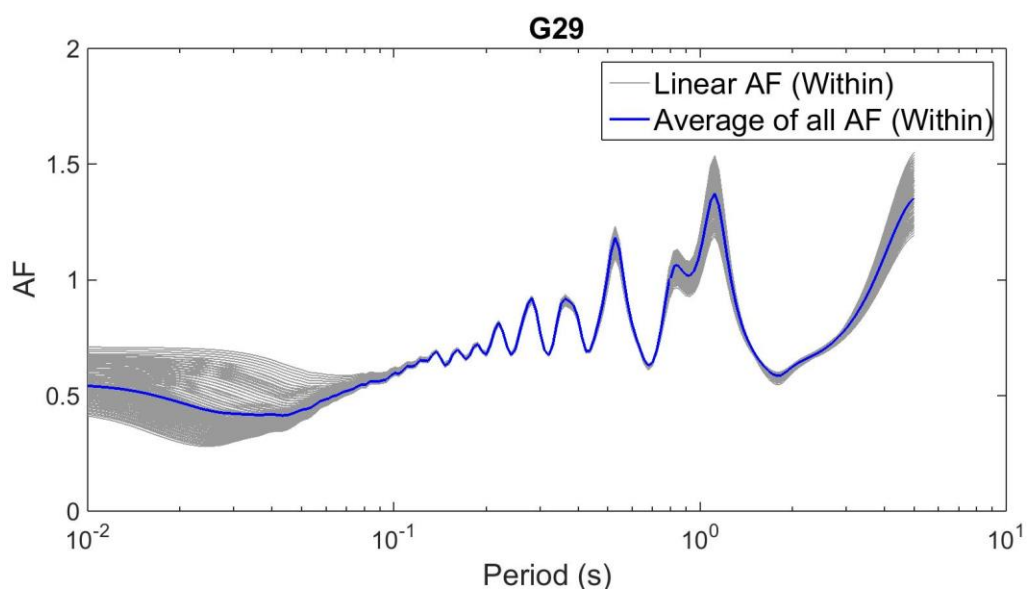
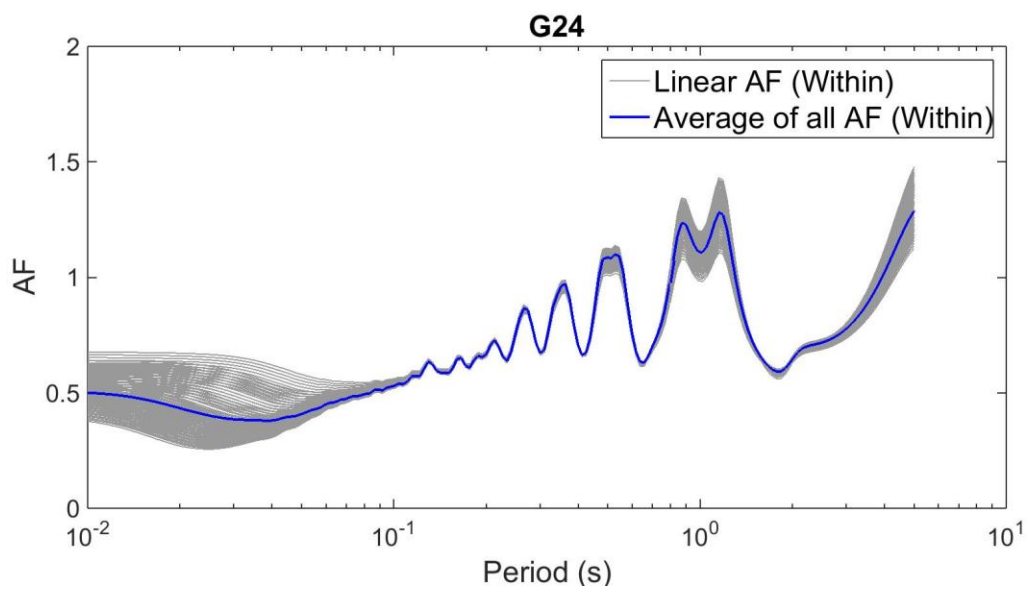
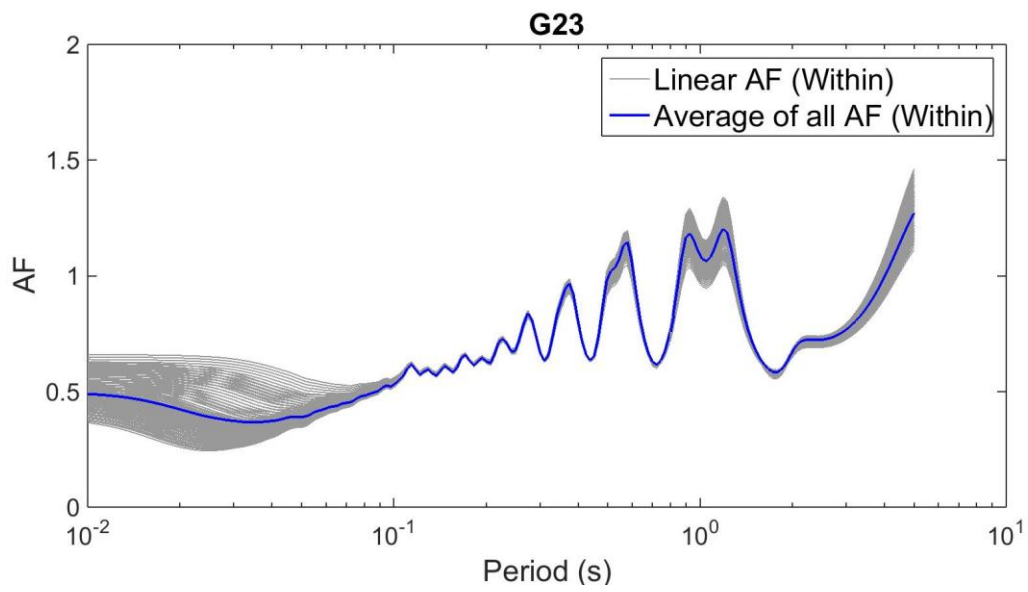


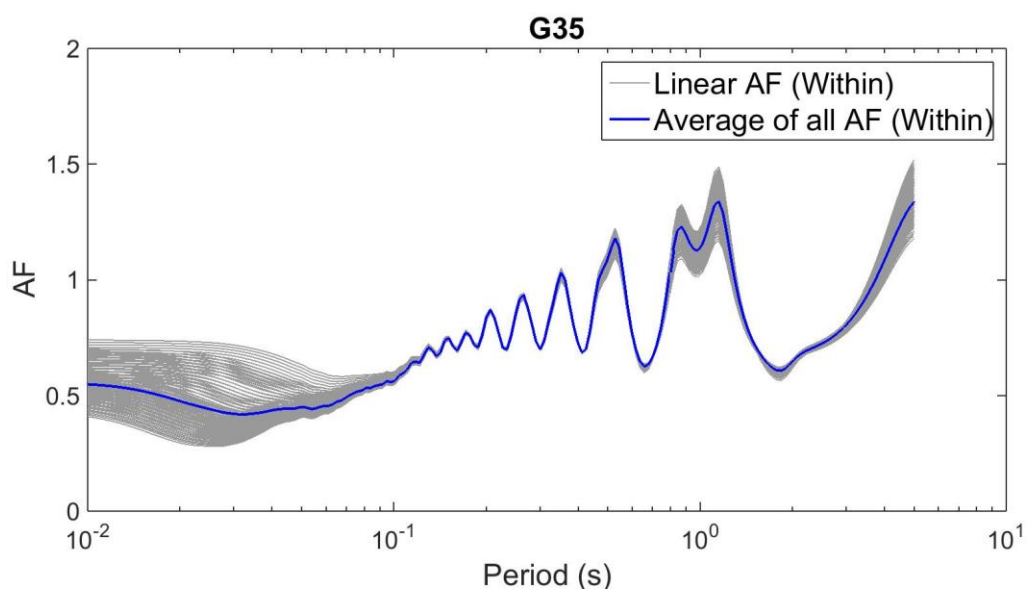
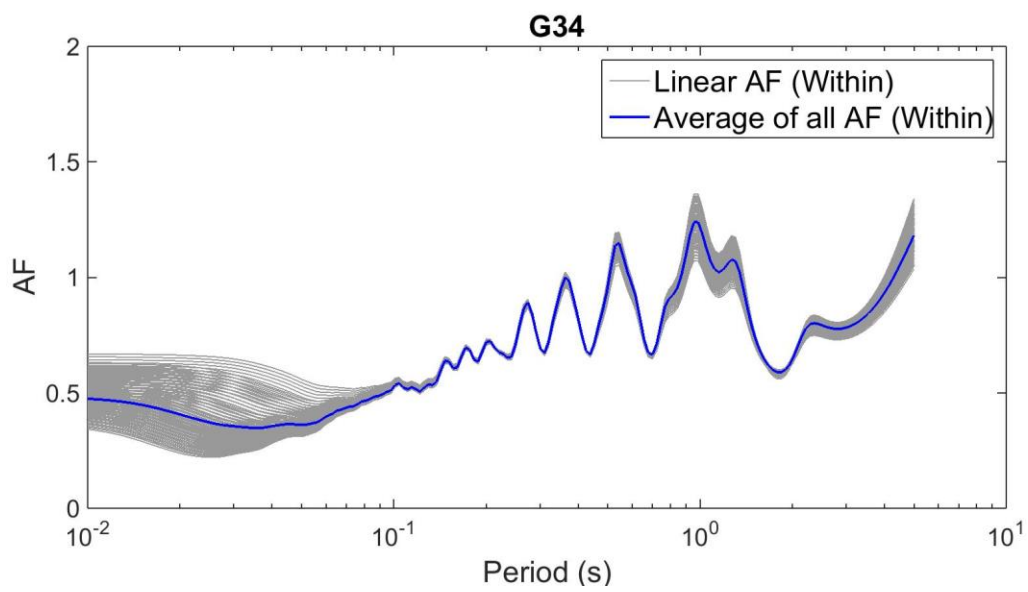
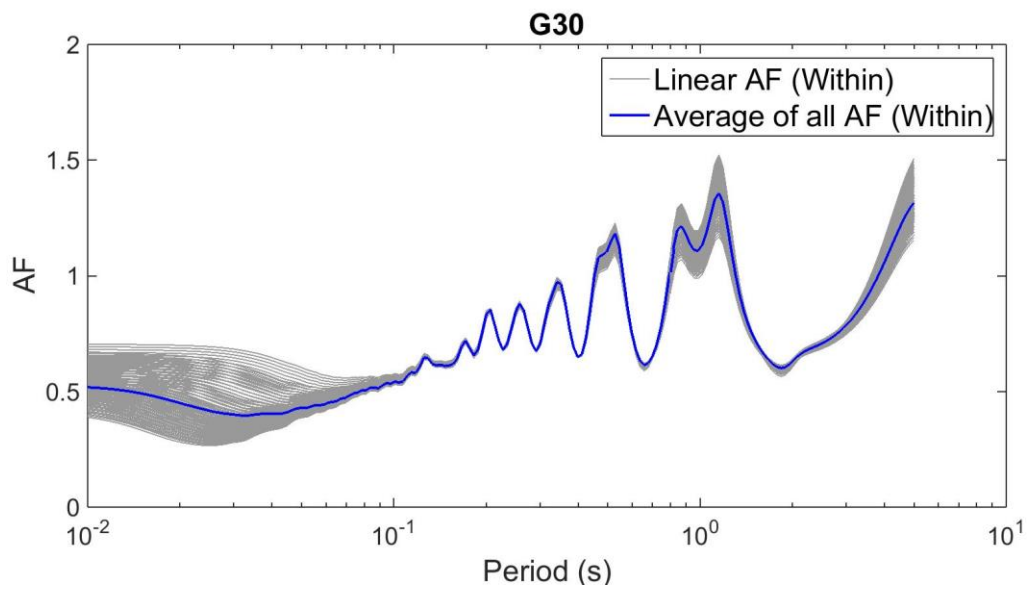


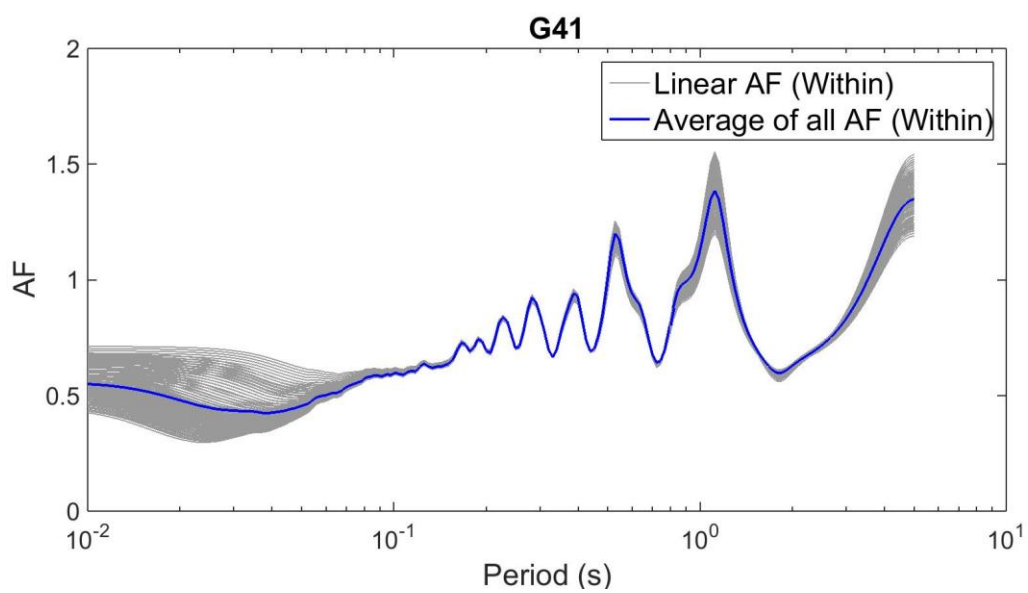
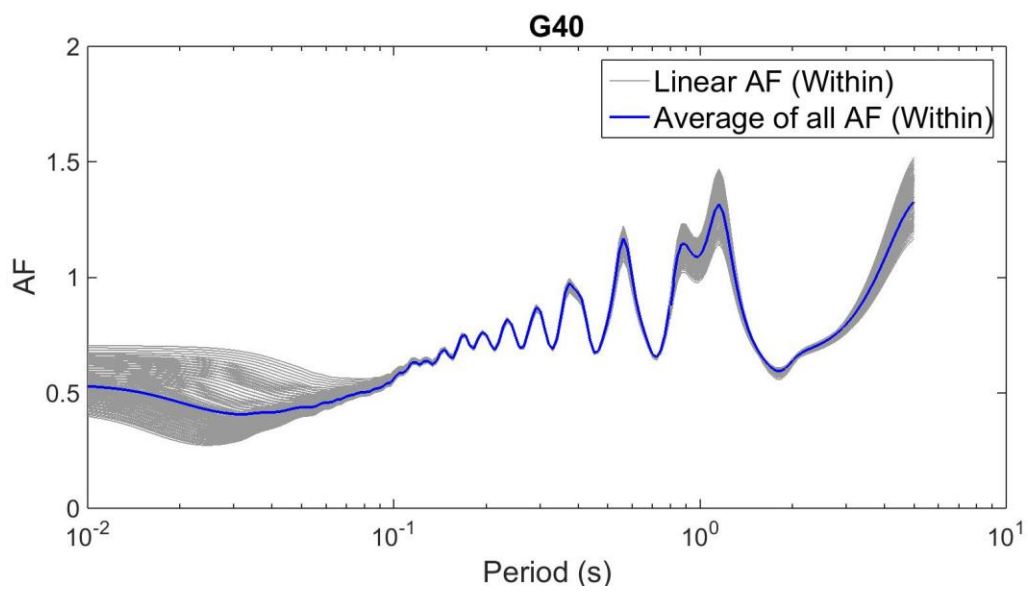
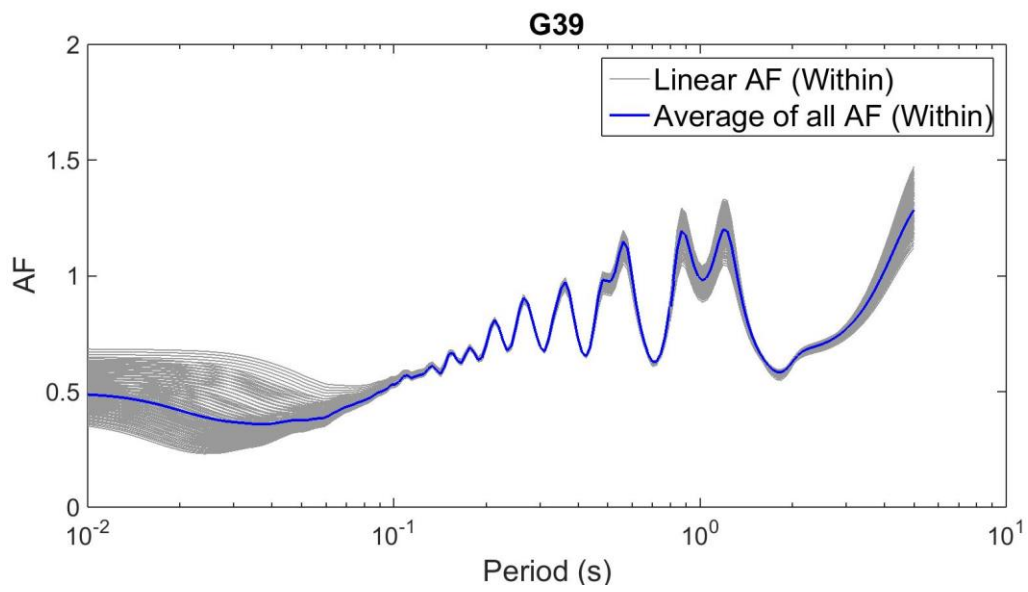


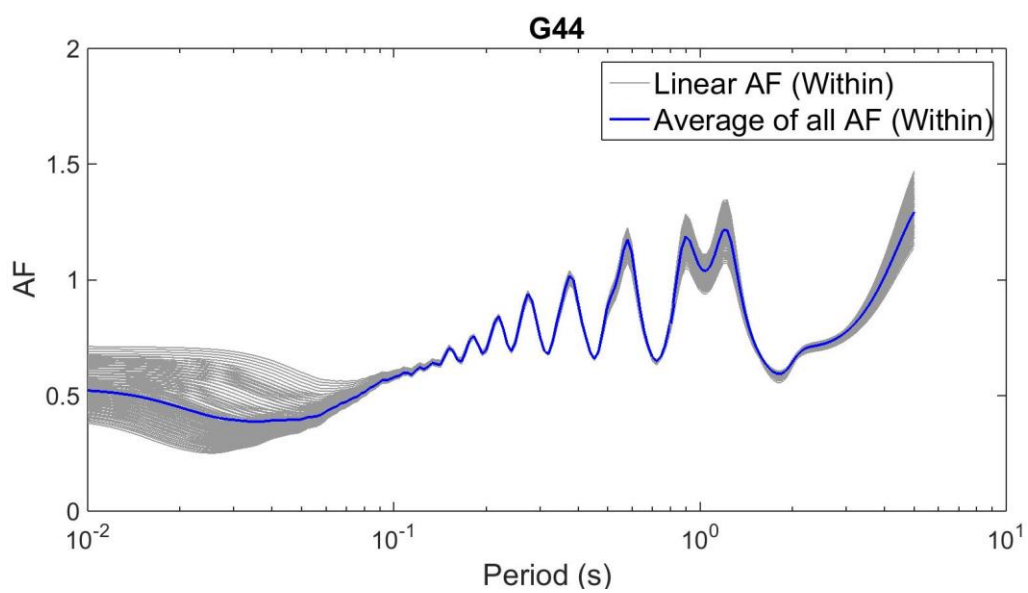
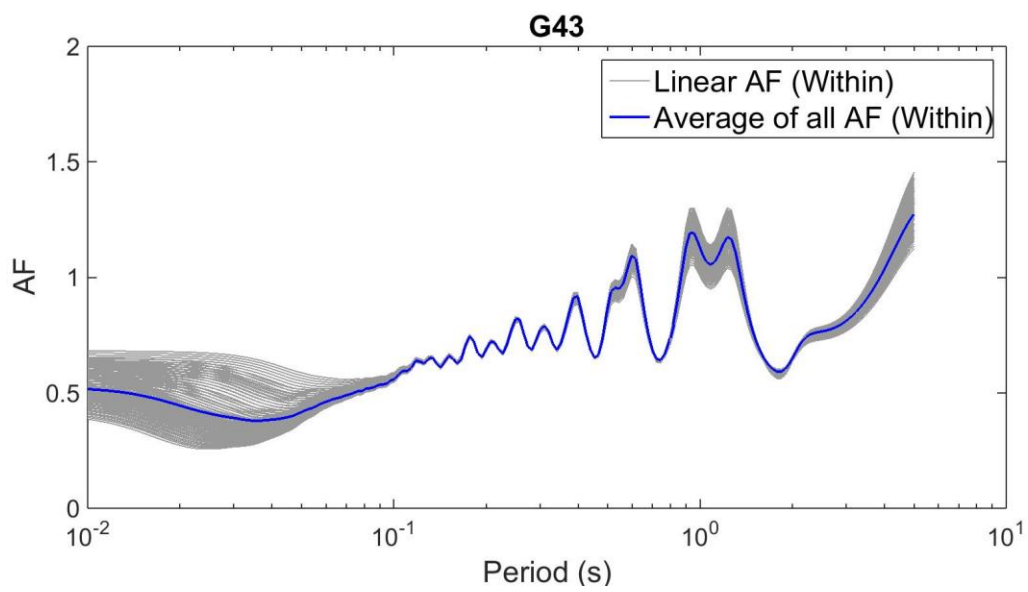
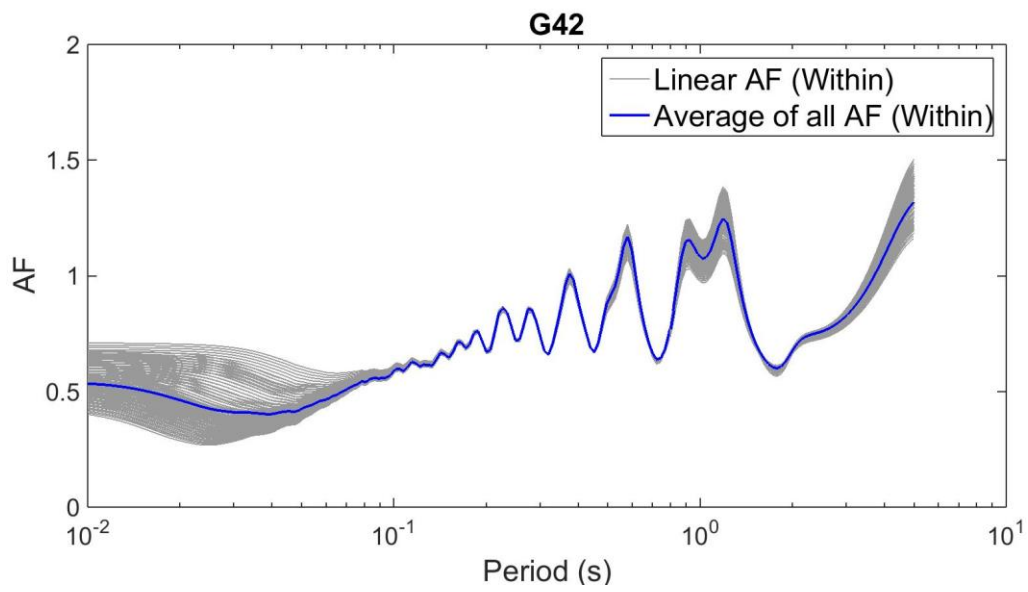


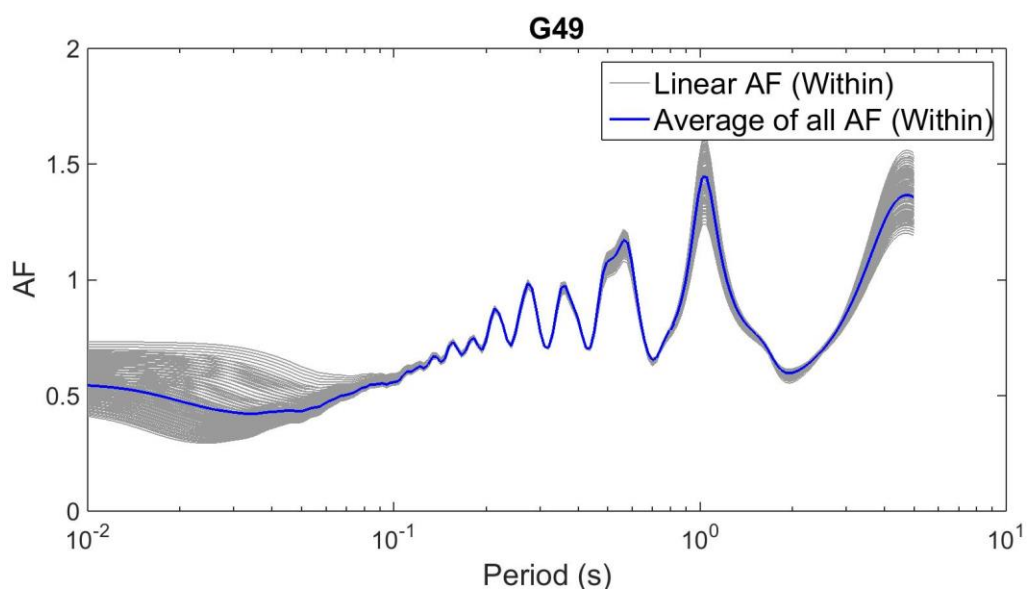
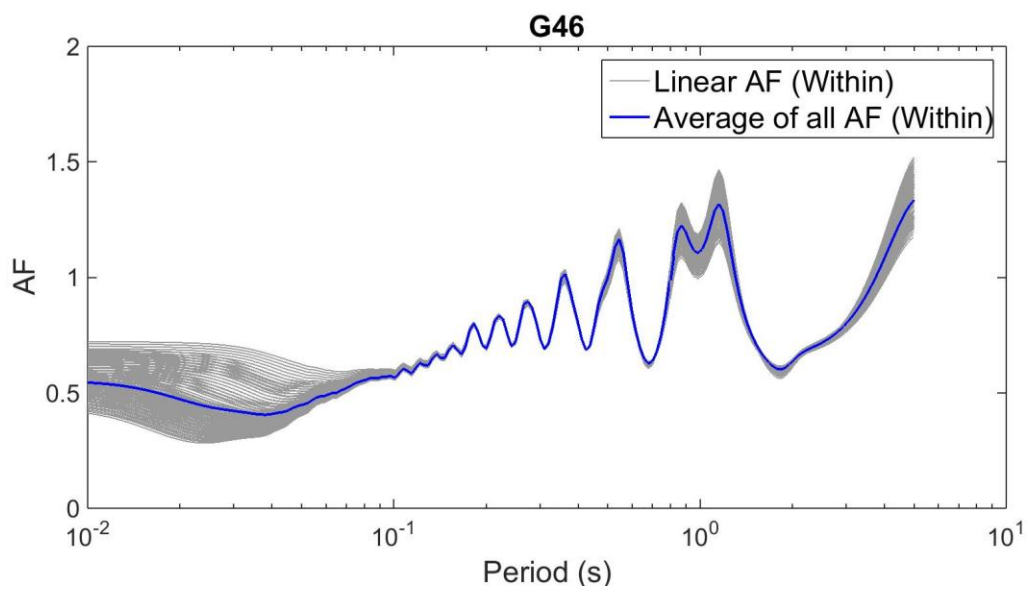
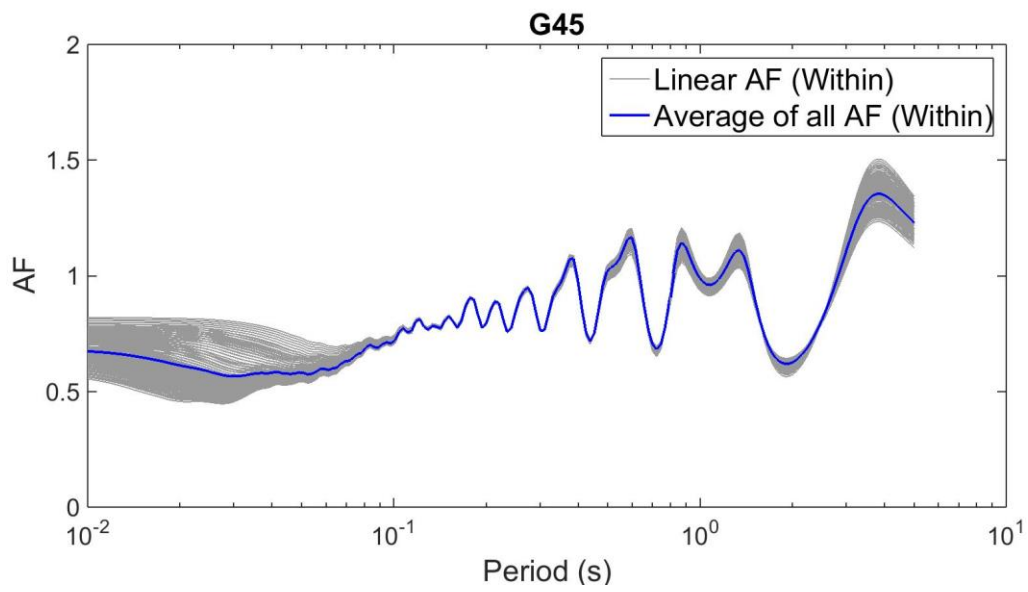


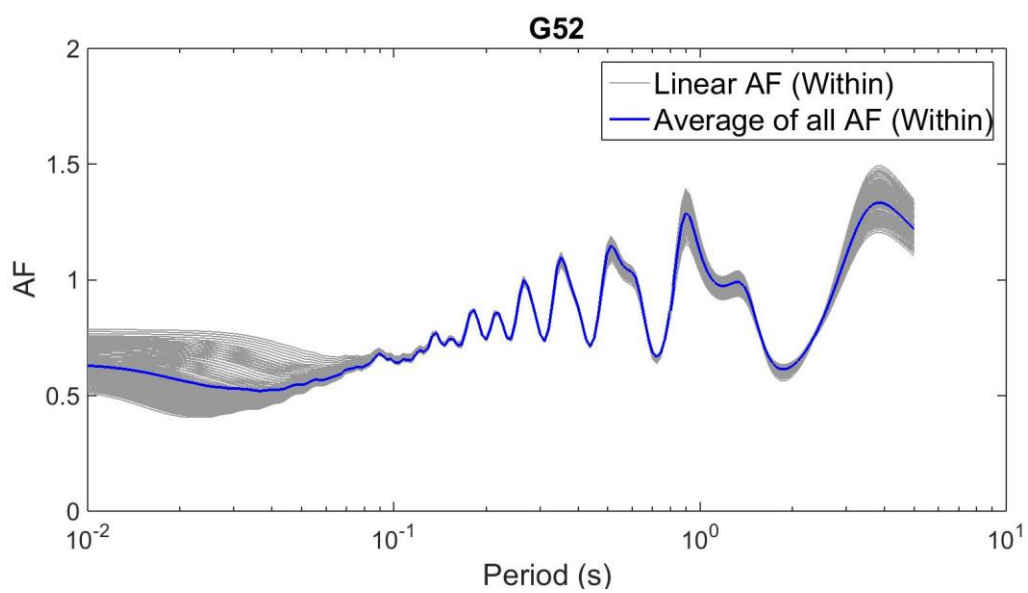
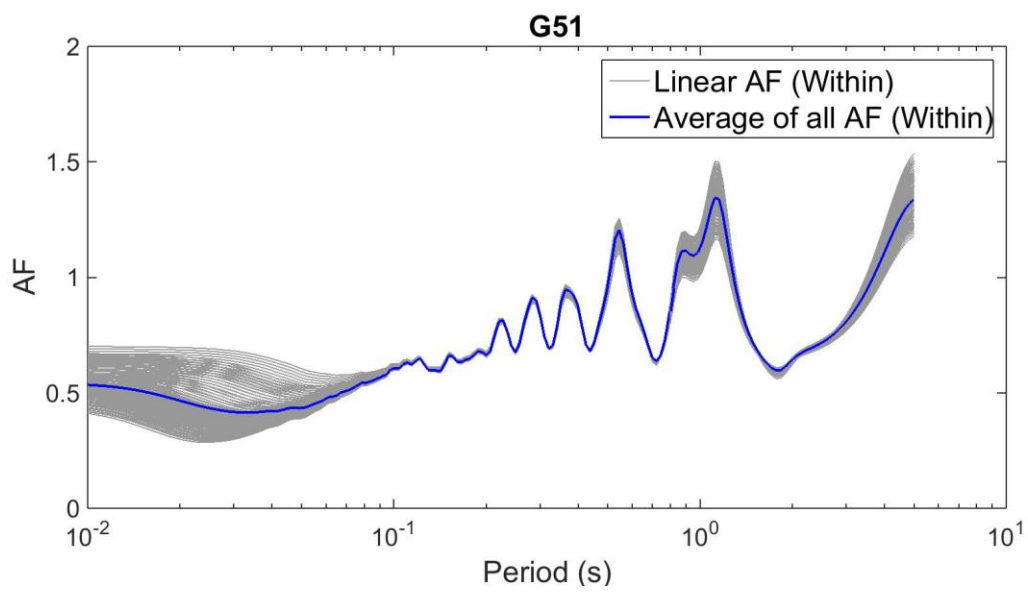
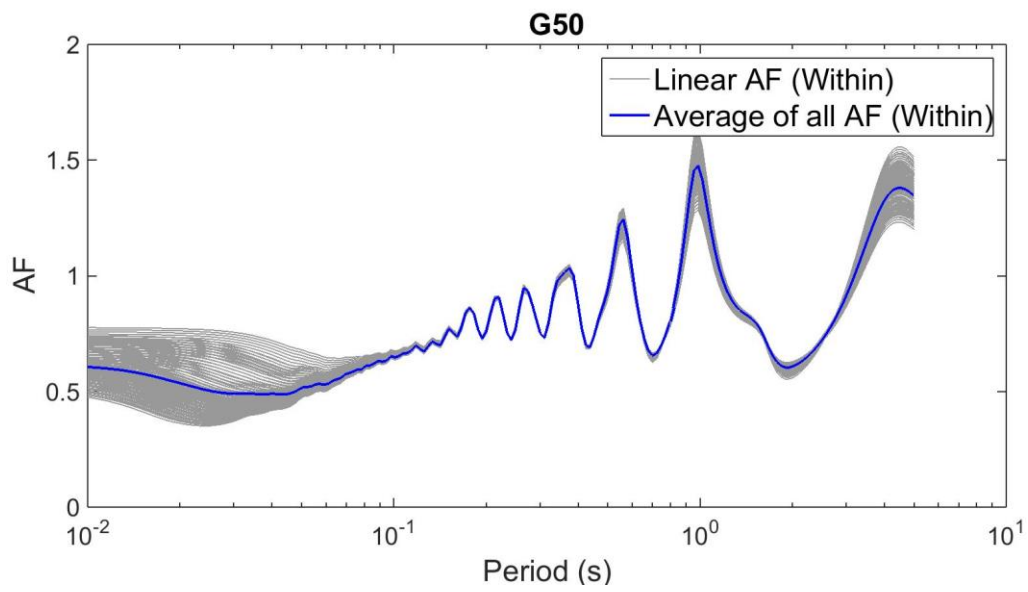


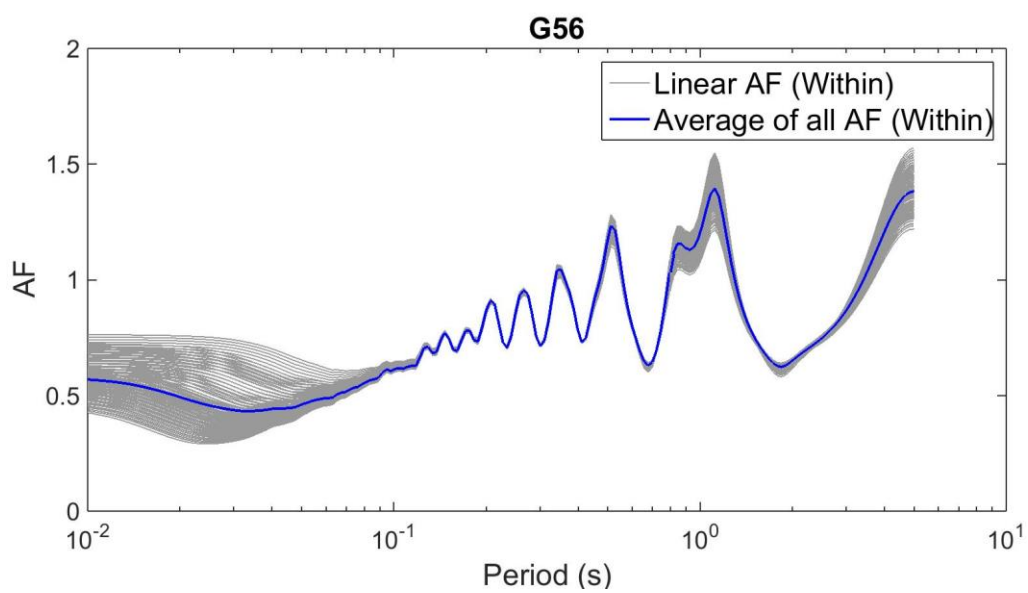
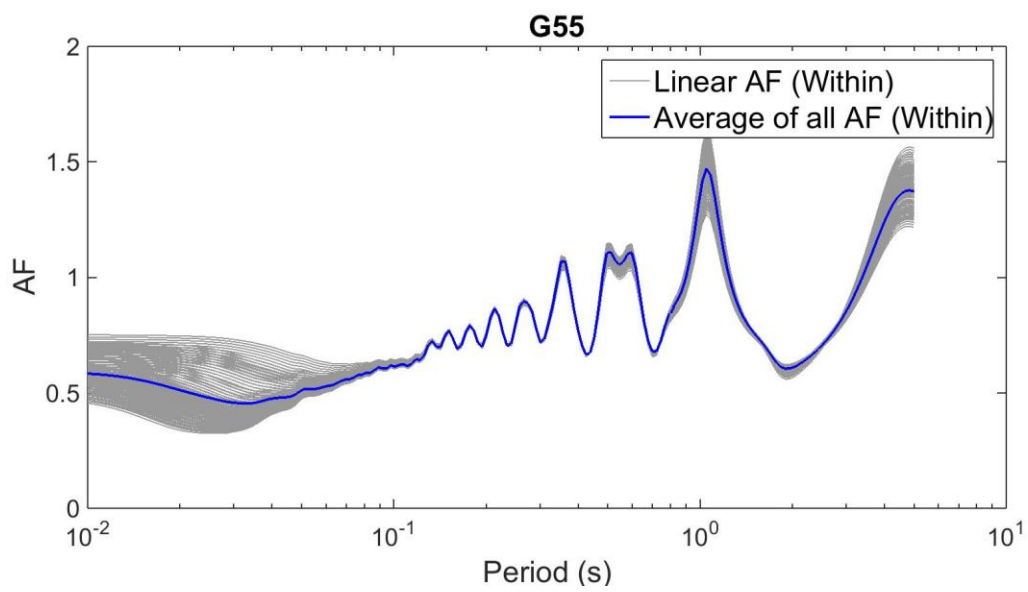
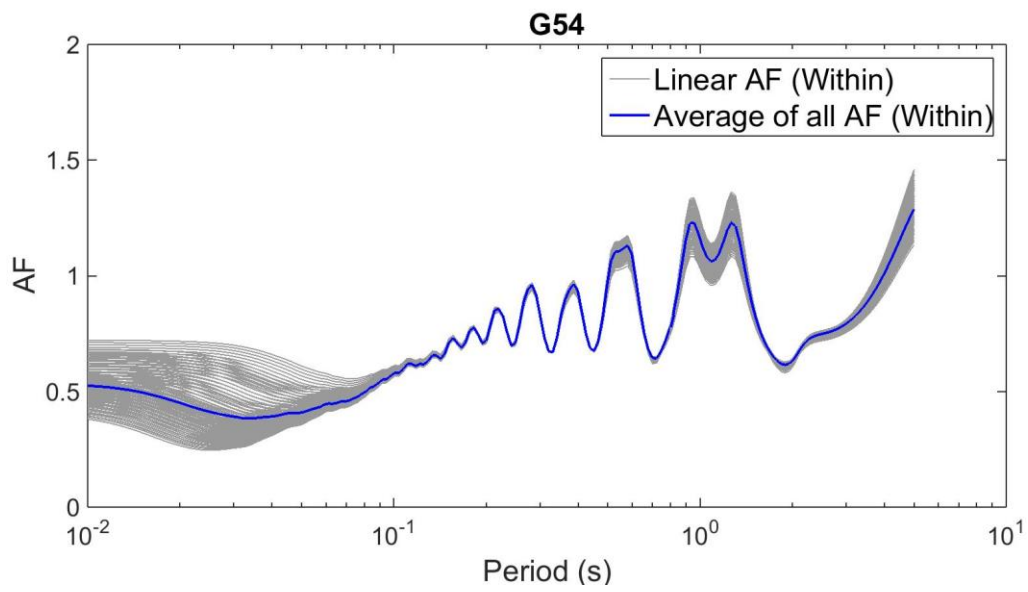


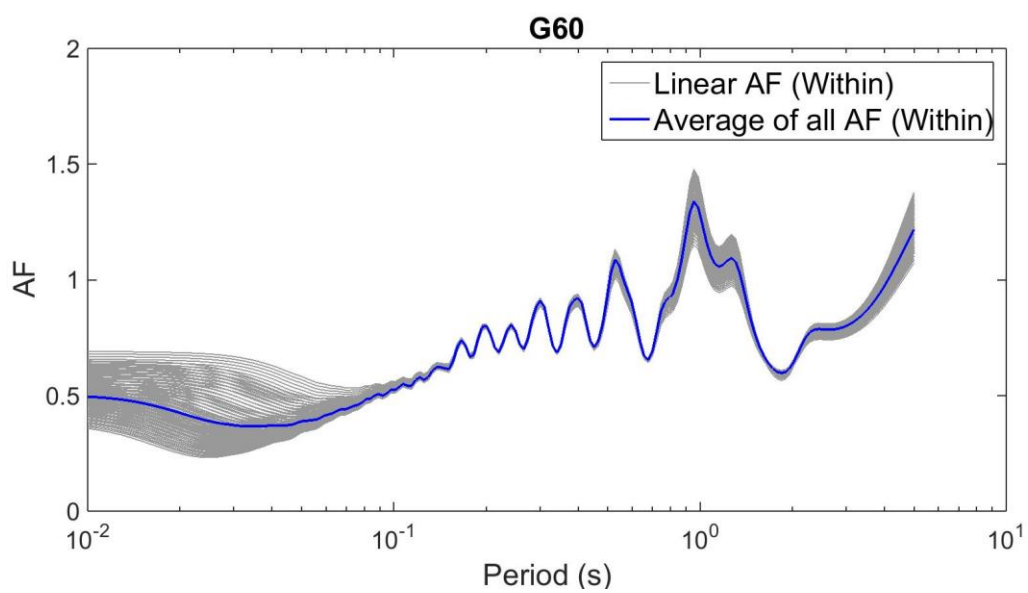
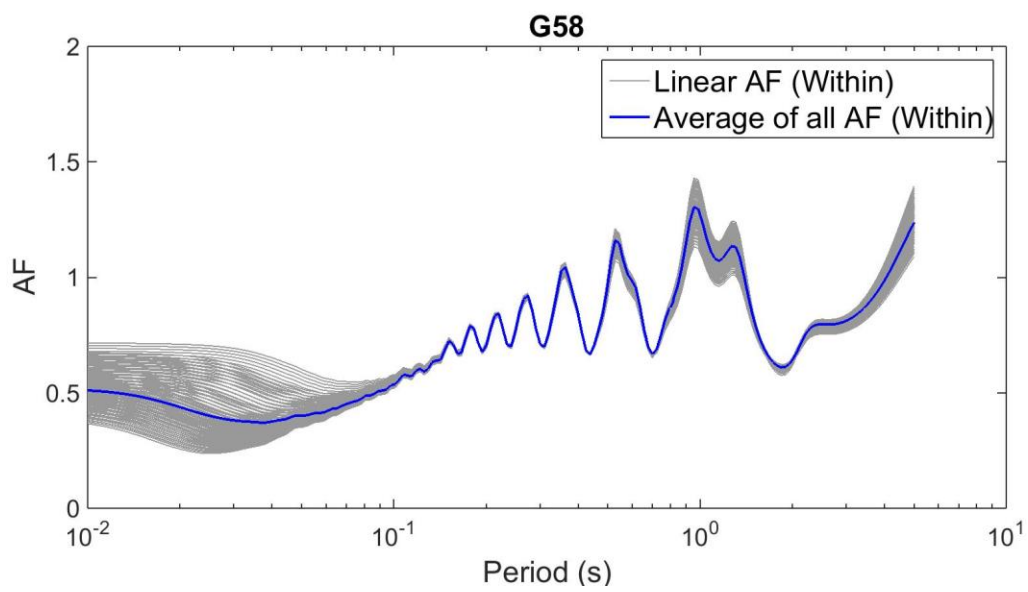
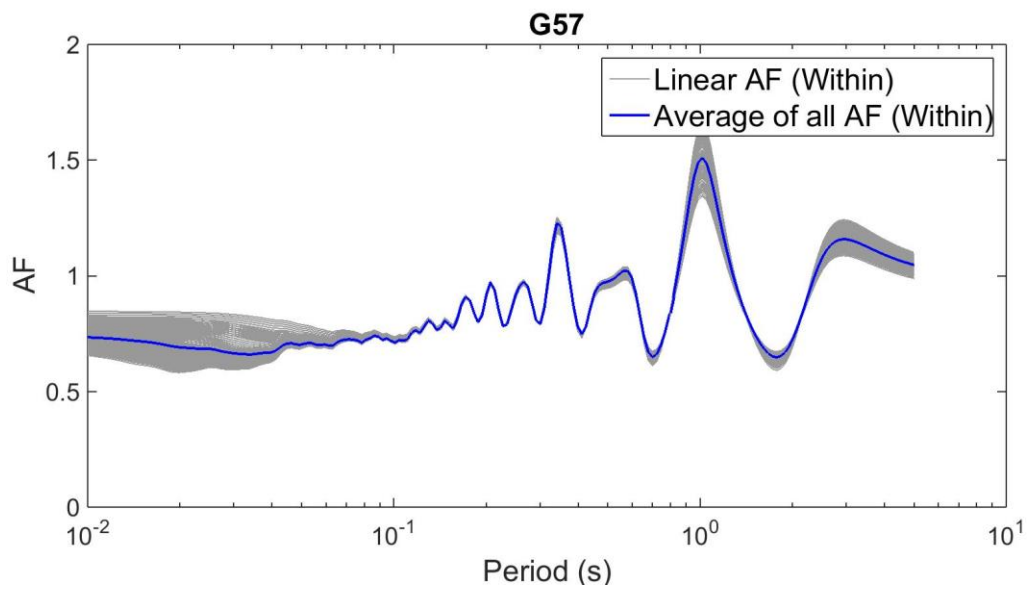


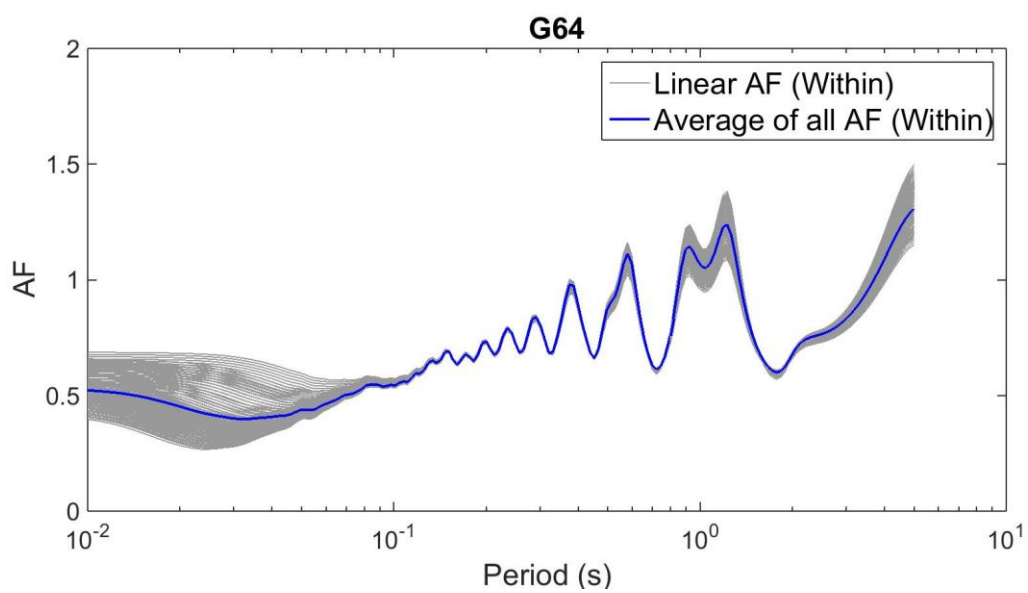
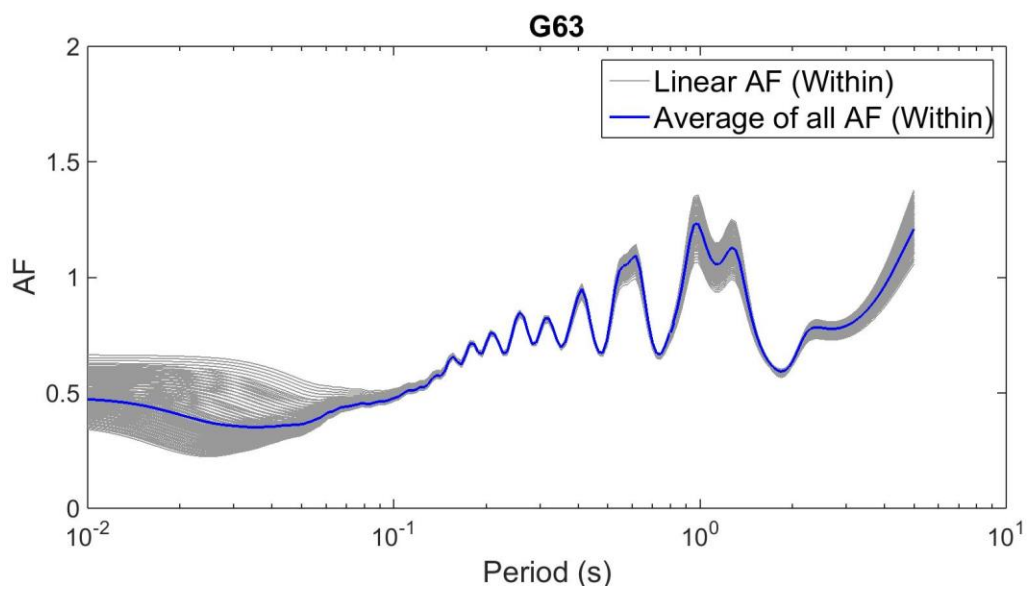
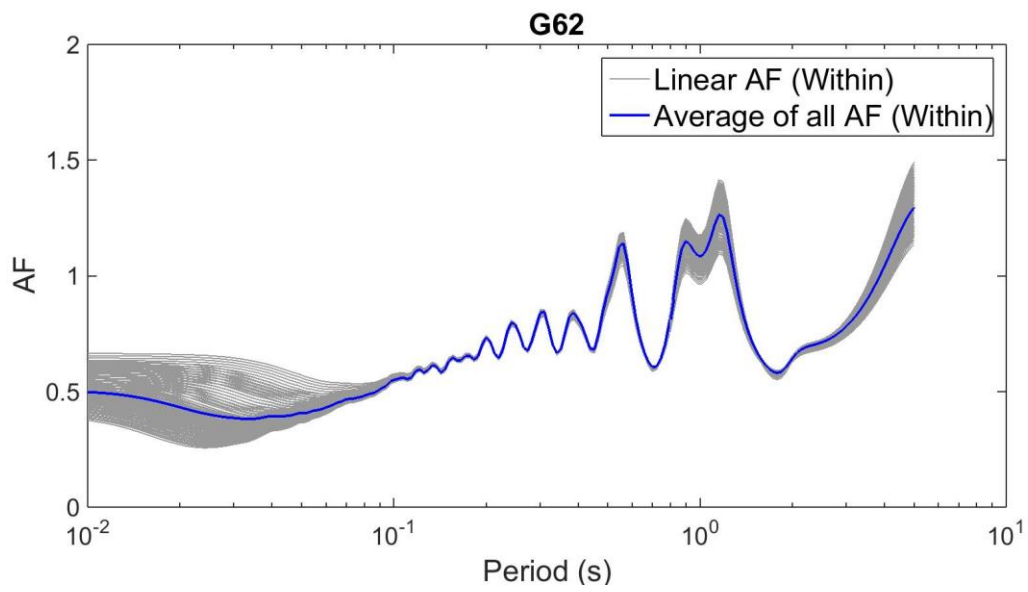


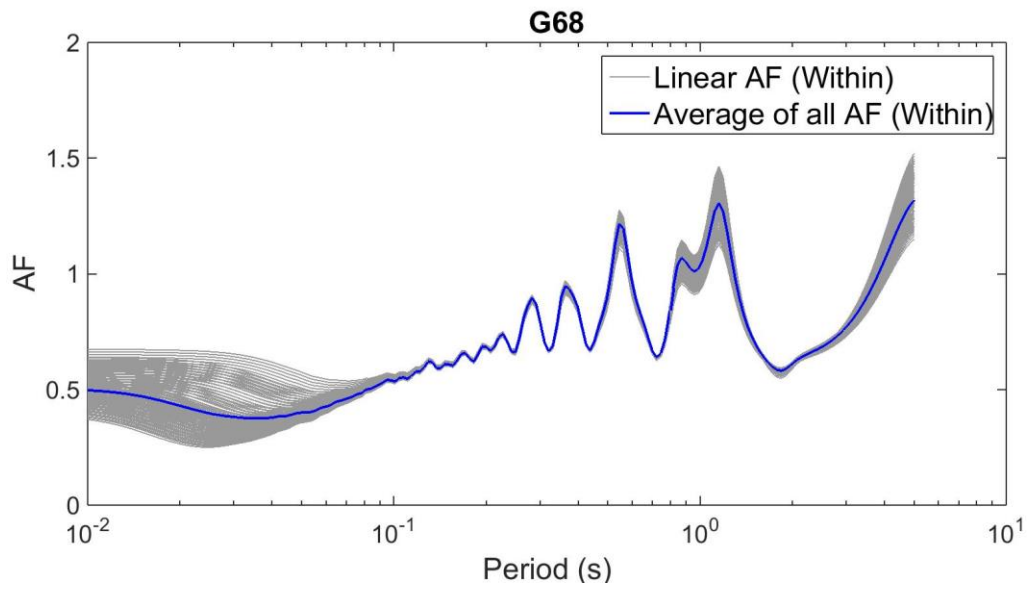








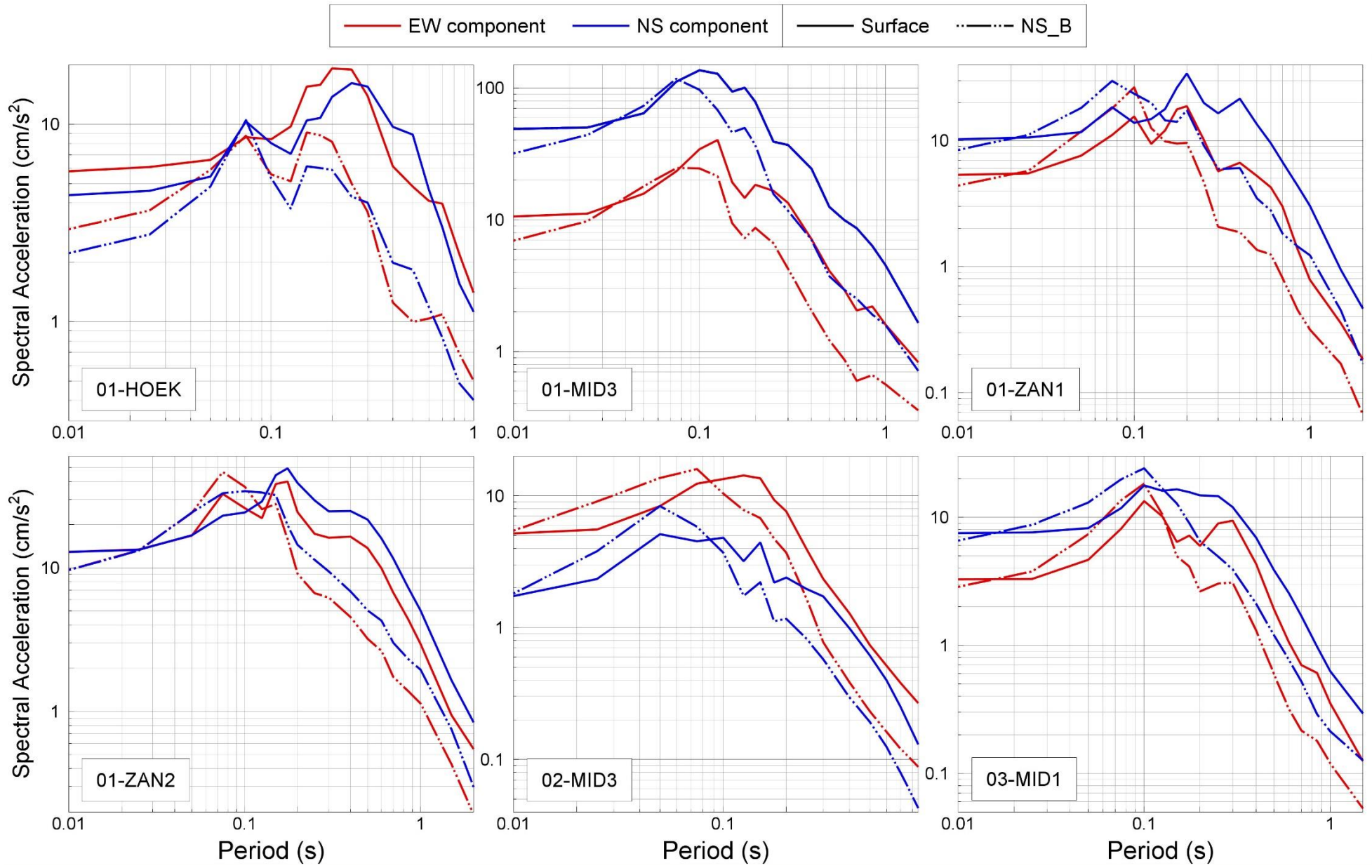


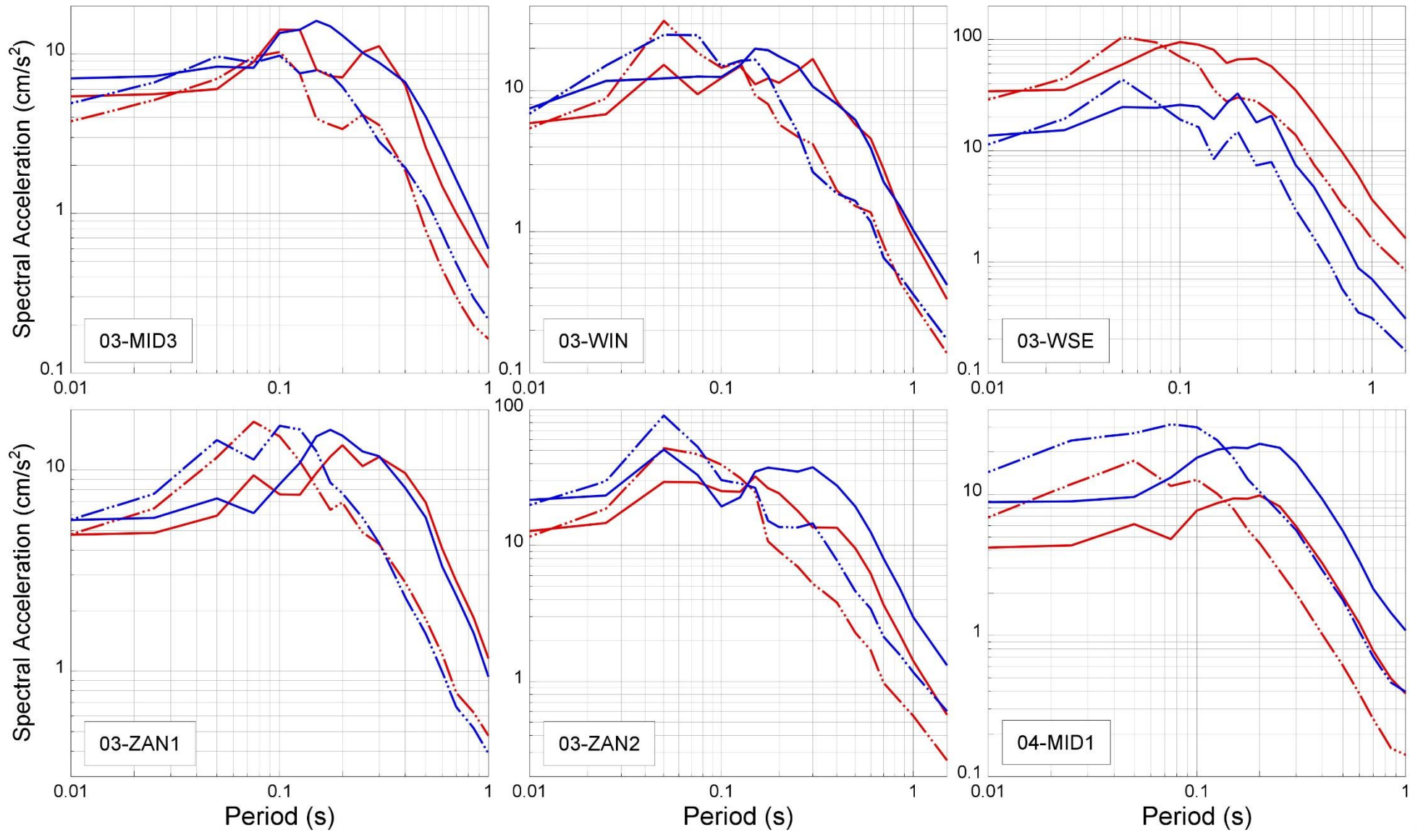


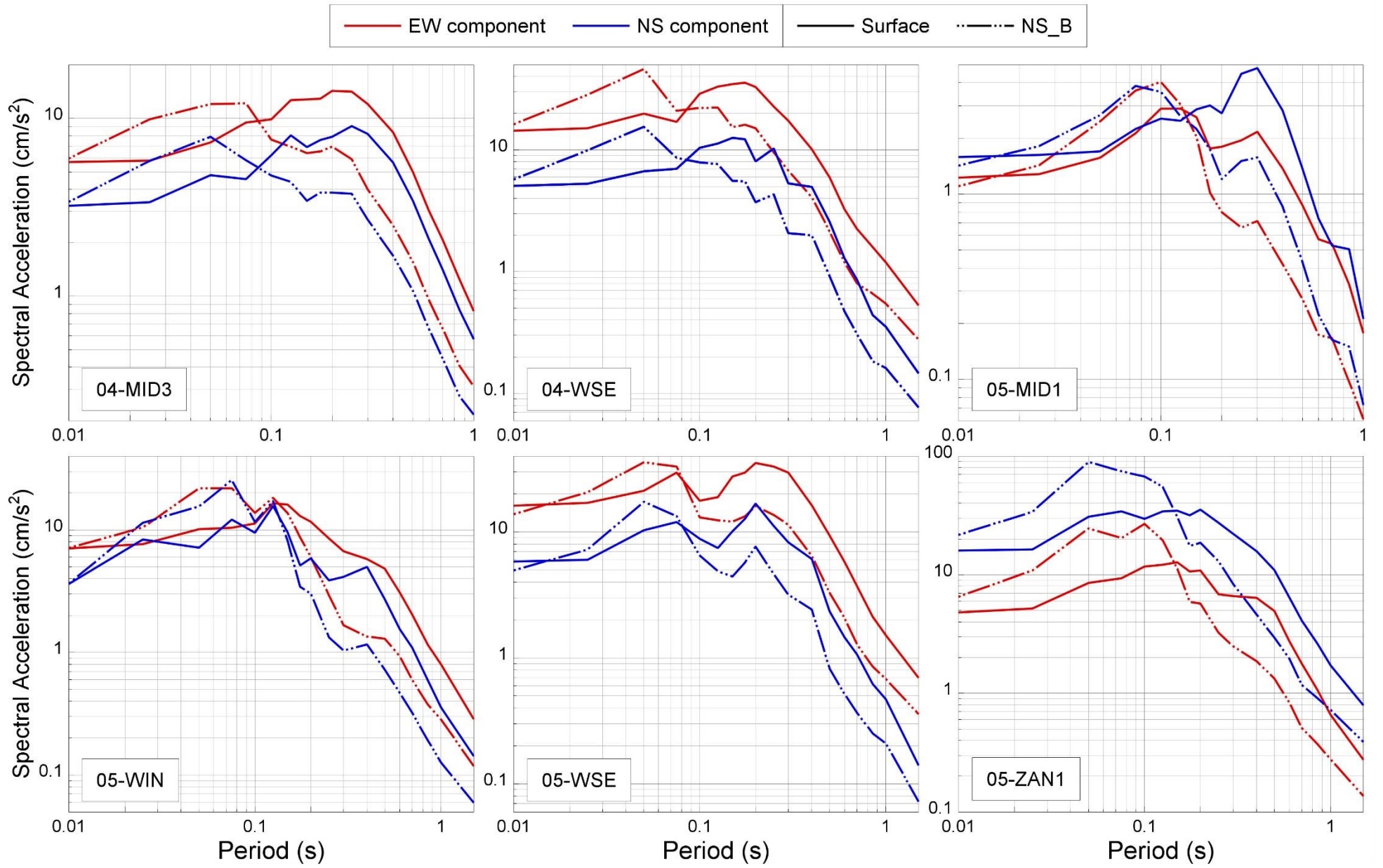
APPENDIX IV

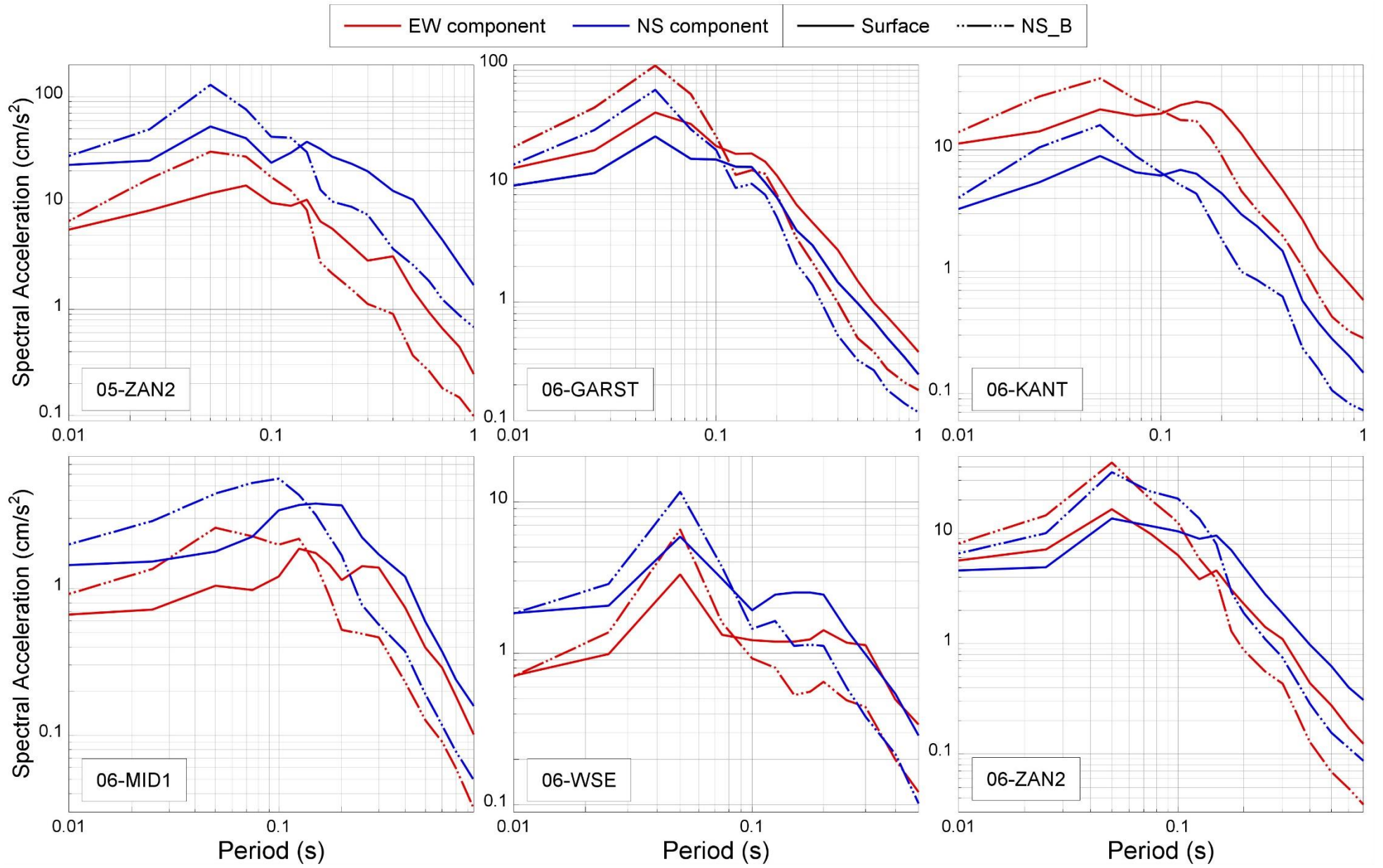
Response spectra at surface (or 200 m borehole) and at the reference rock horizon

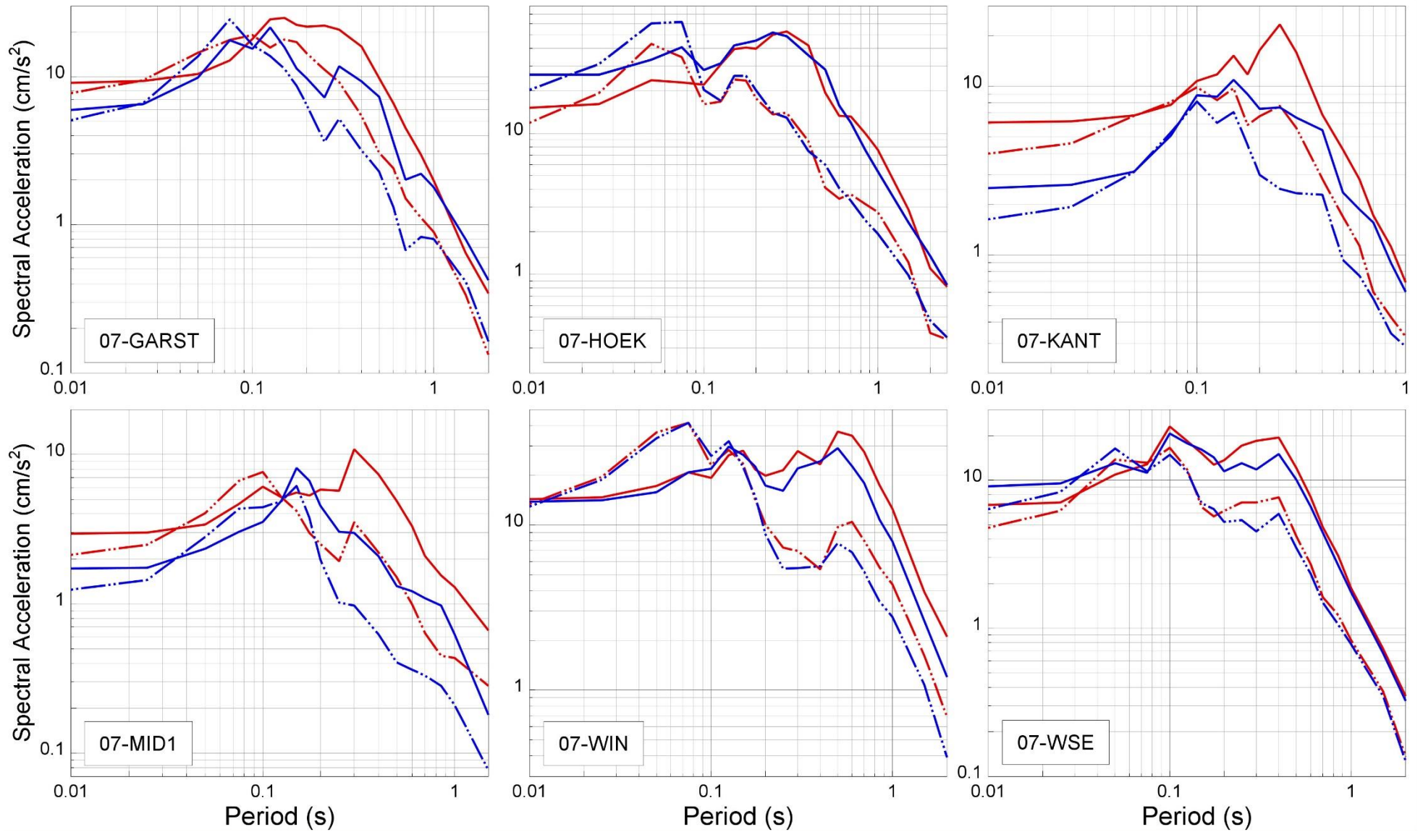
In the following pages plots are shown of the response spectra of the horizontal components from each recording in the database, and on the same axes the spectra as transformed either from the ground surface (for the B stations) or from 200 m depth (for the G stations). These comparisons directly reflect the amplification factors presented in Appendix III. Each record is identified by an earthquake code (Table 3.1) and the station code.

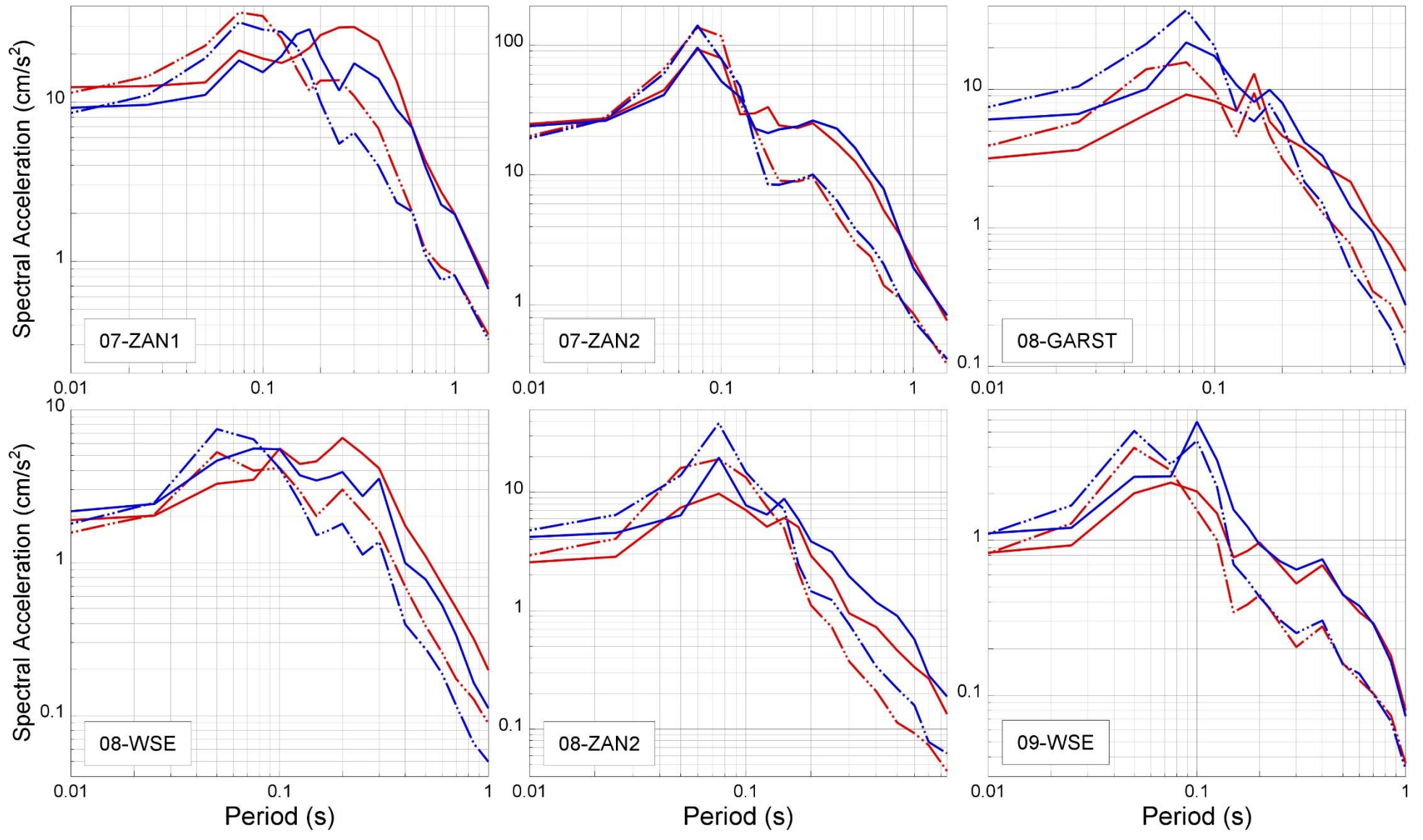


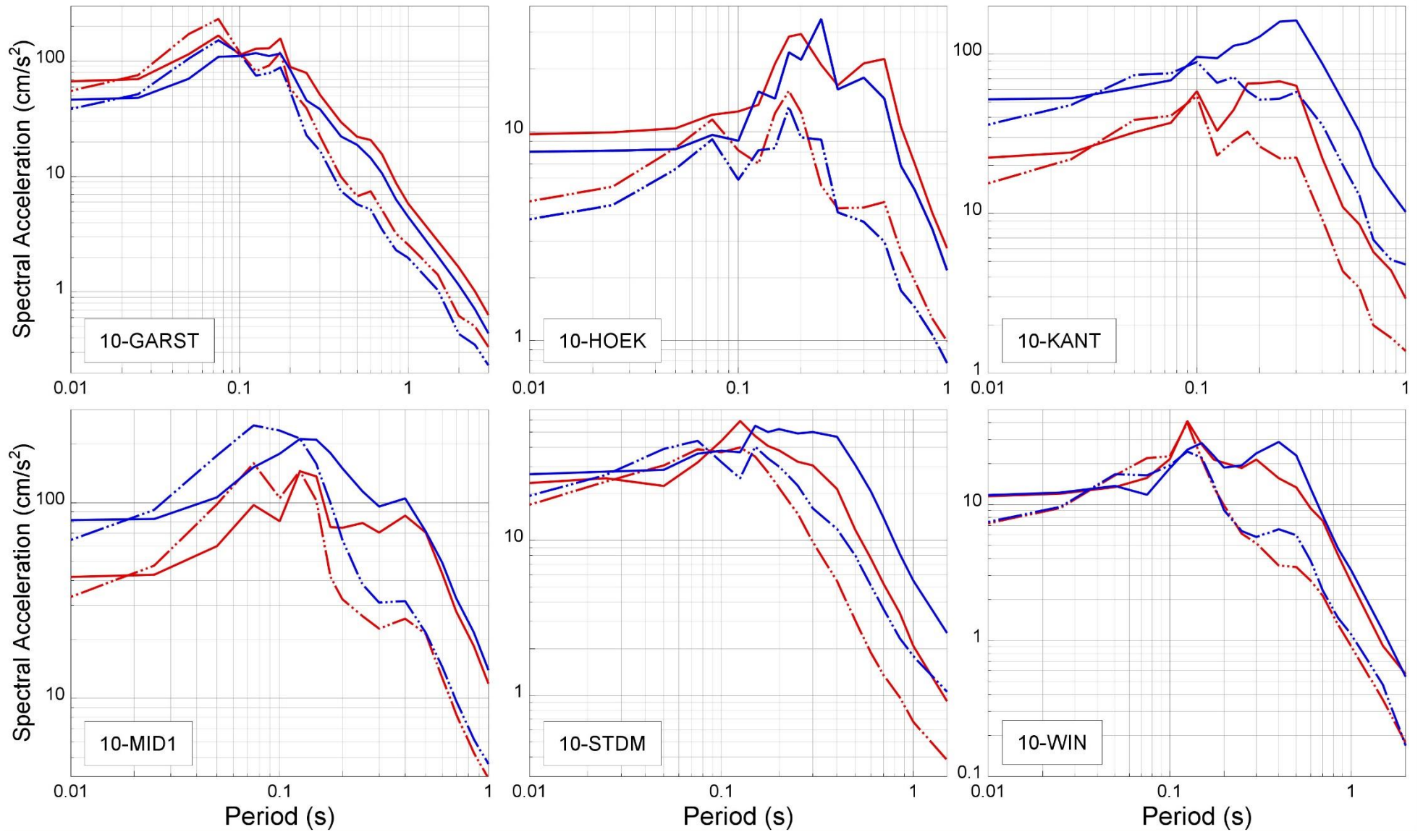


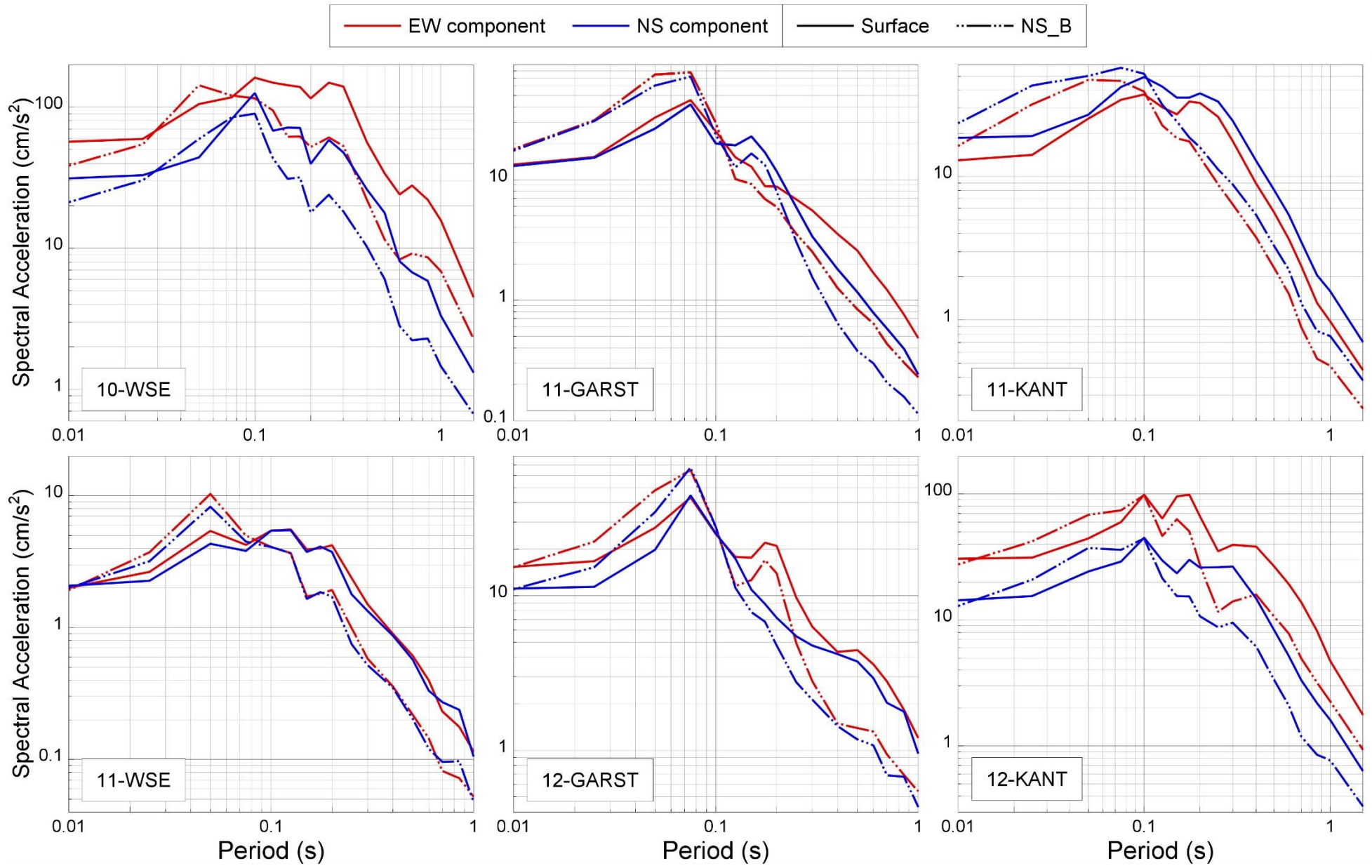


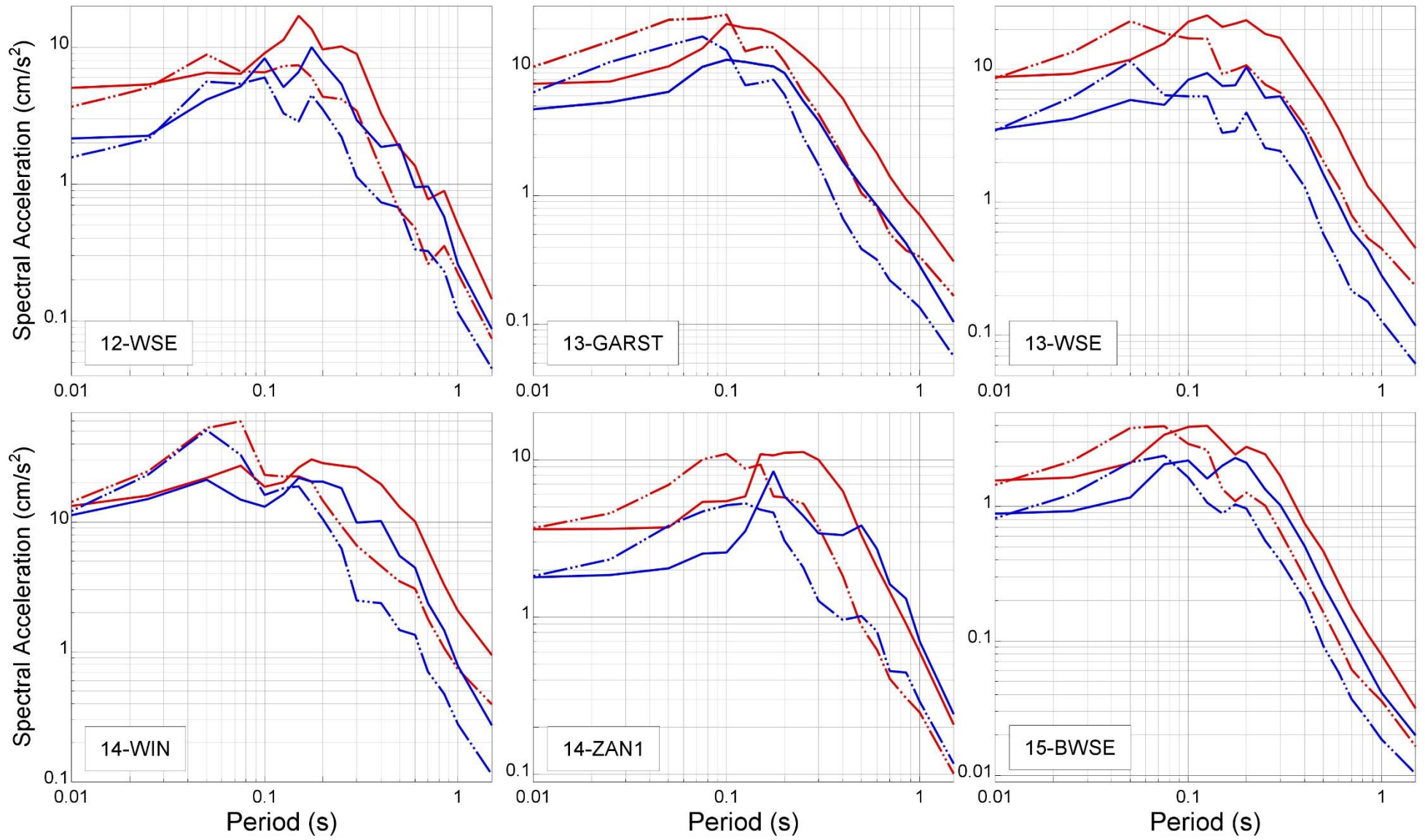


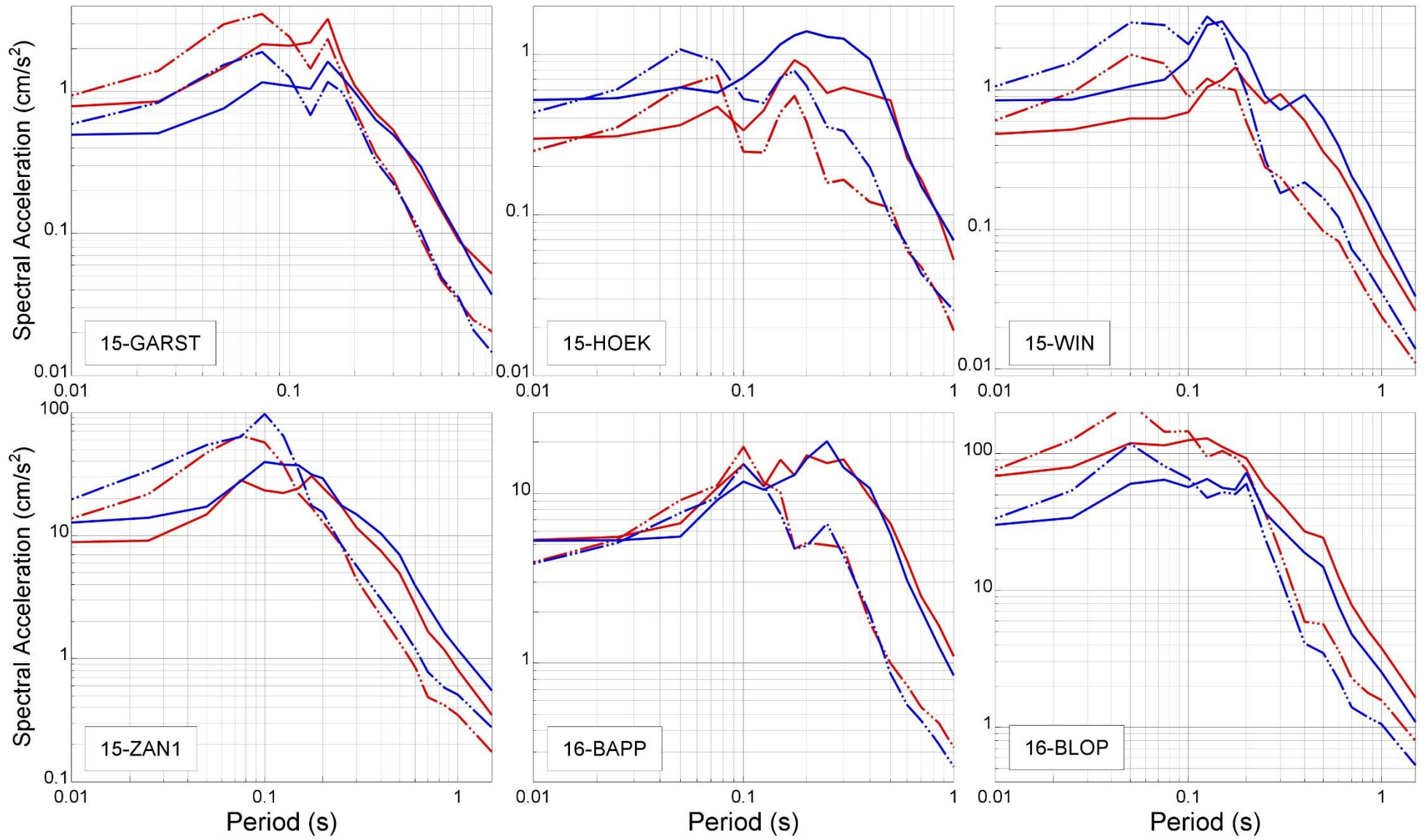


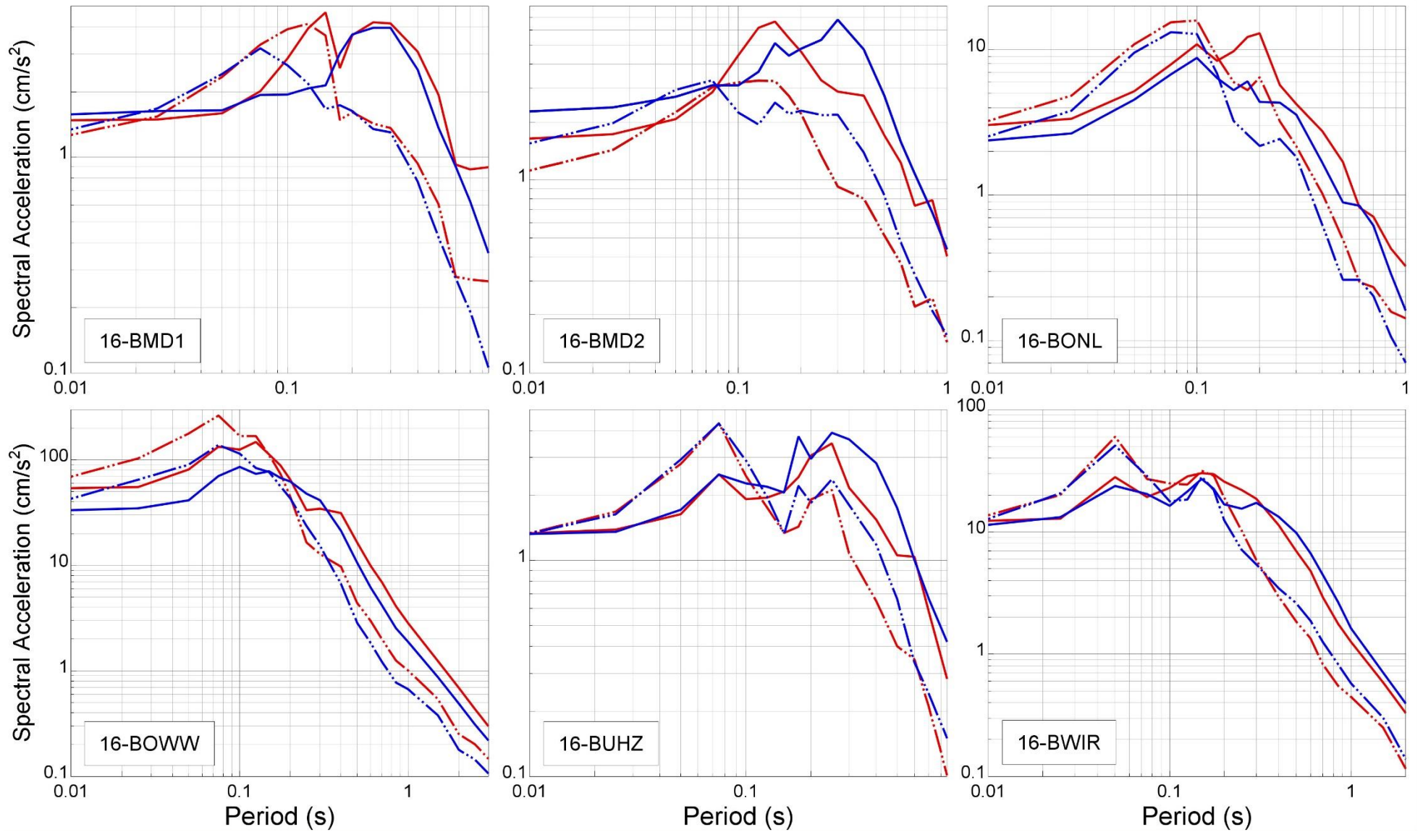


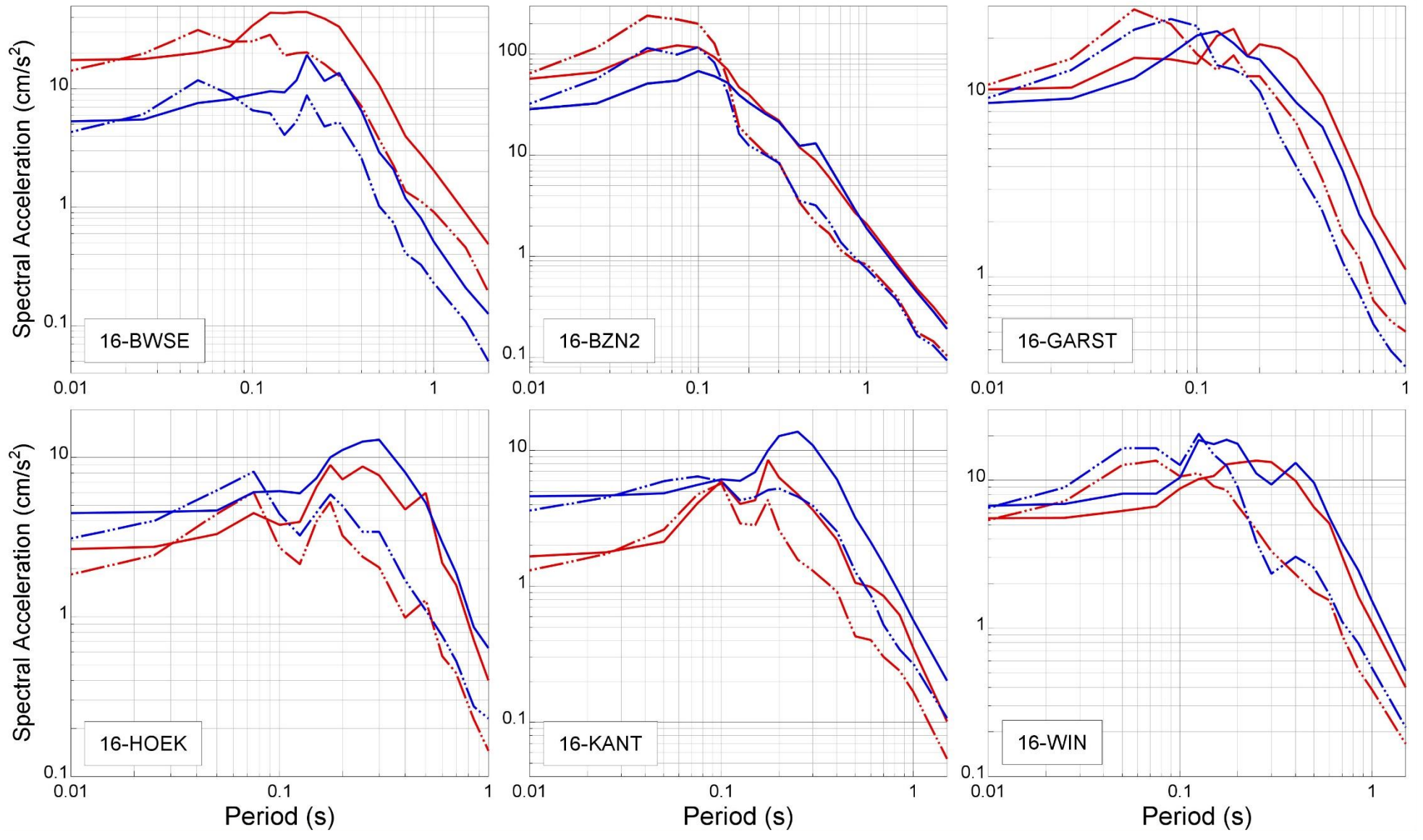


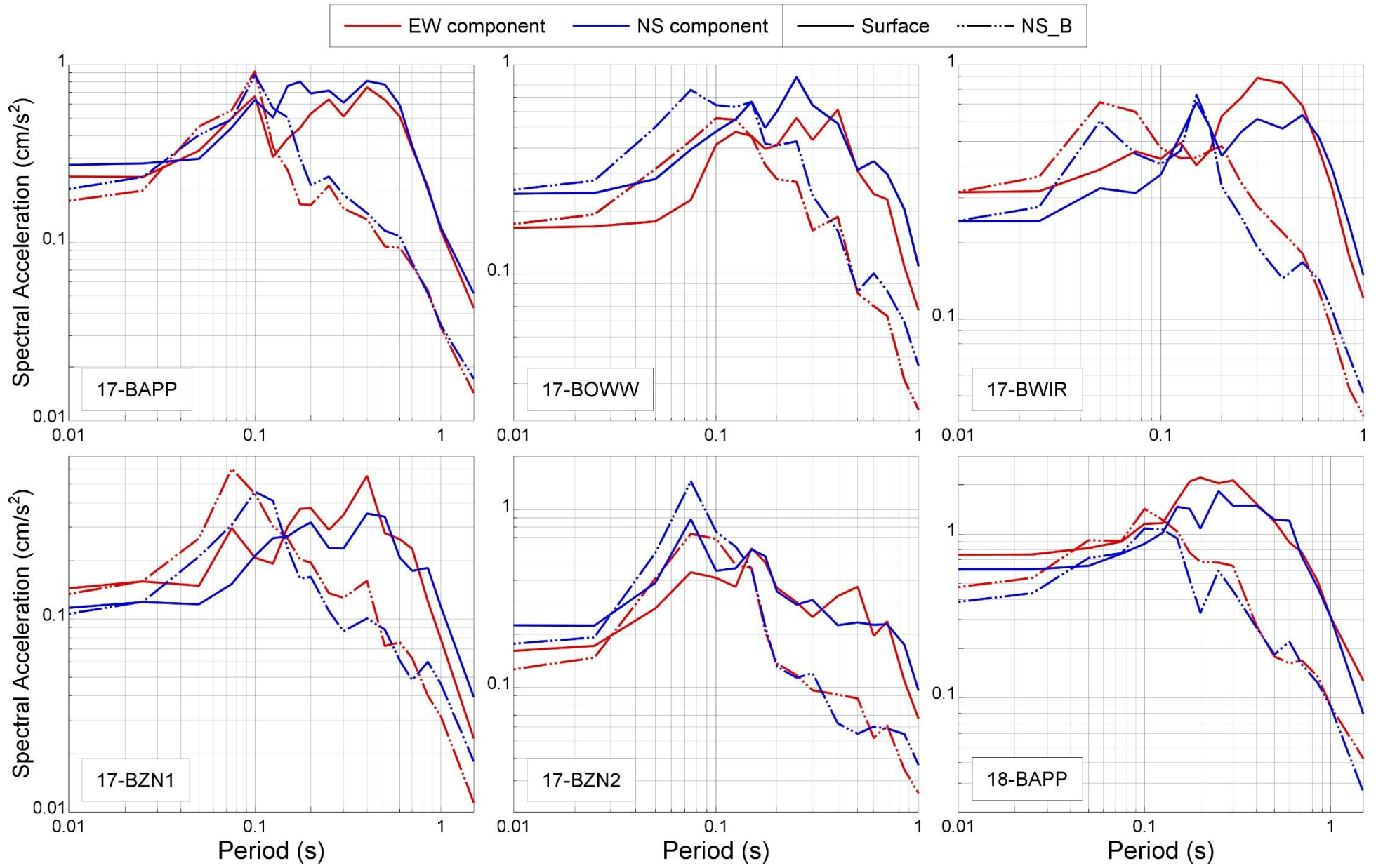


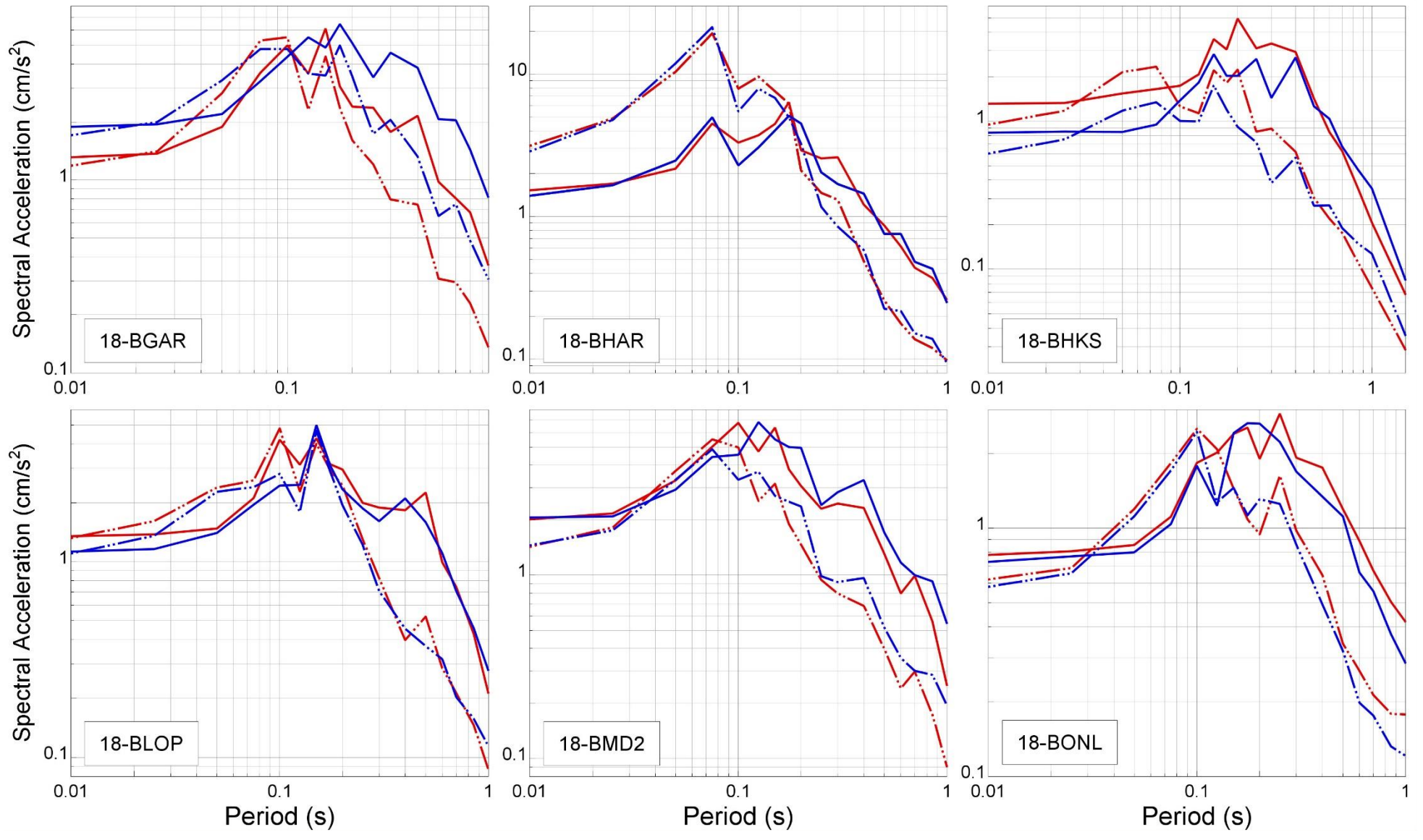


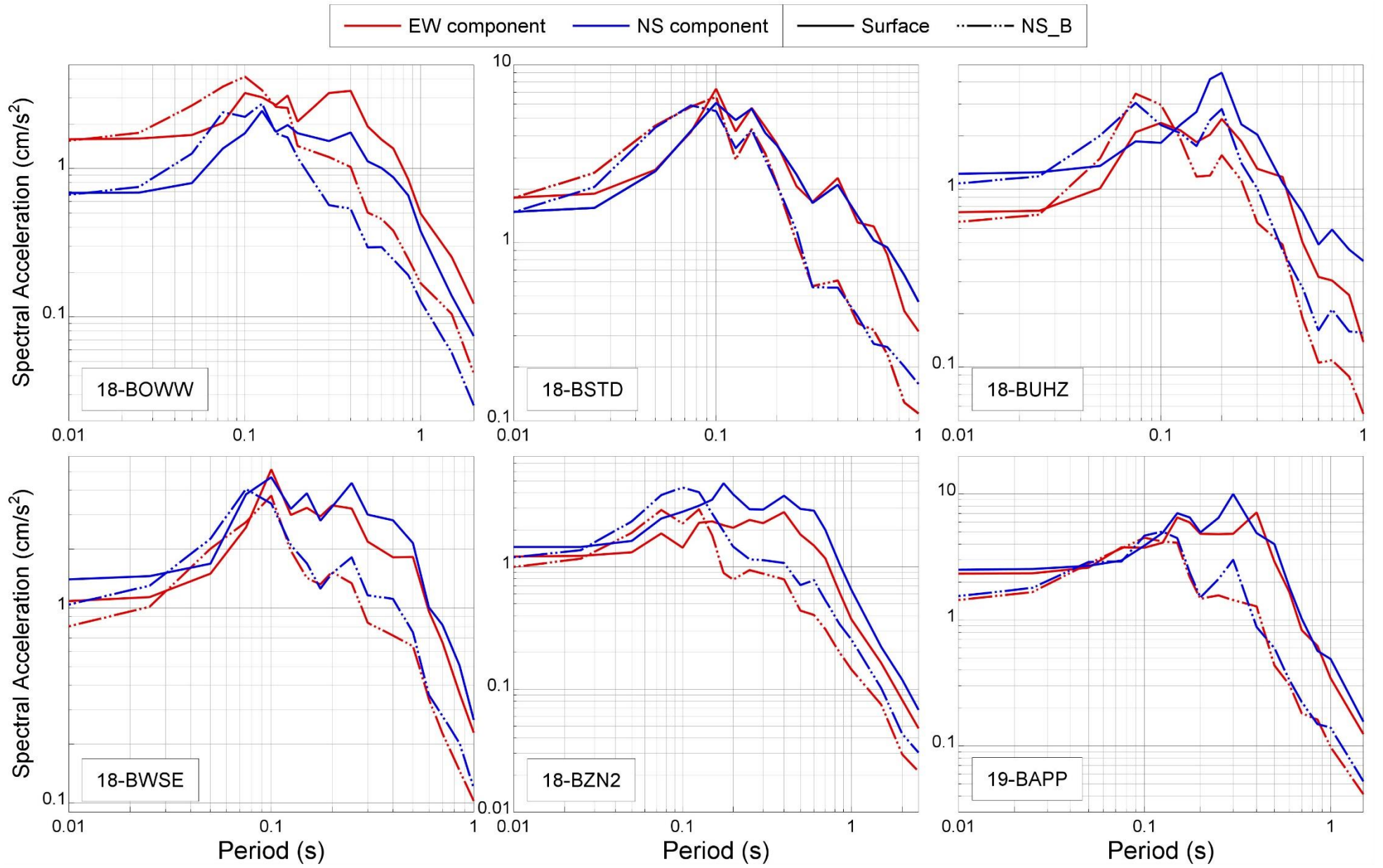


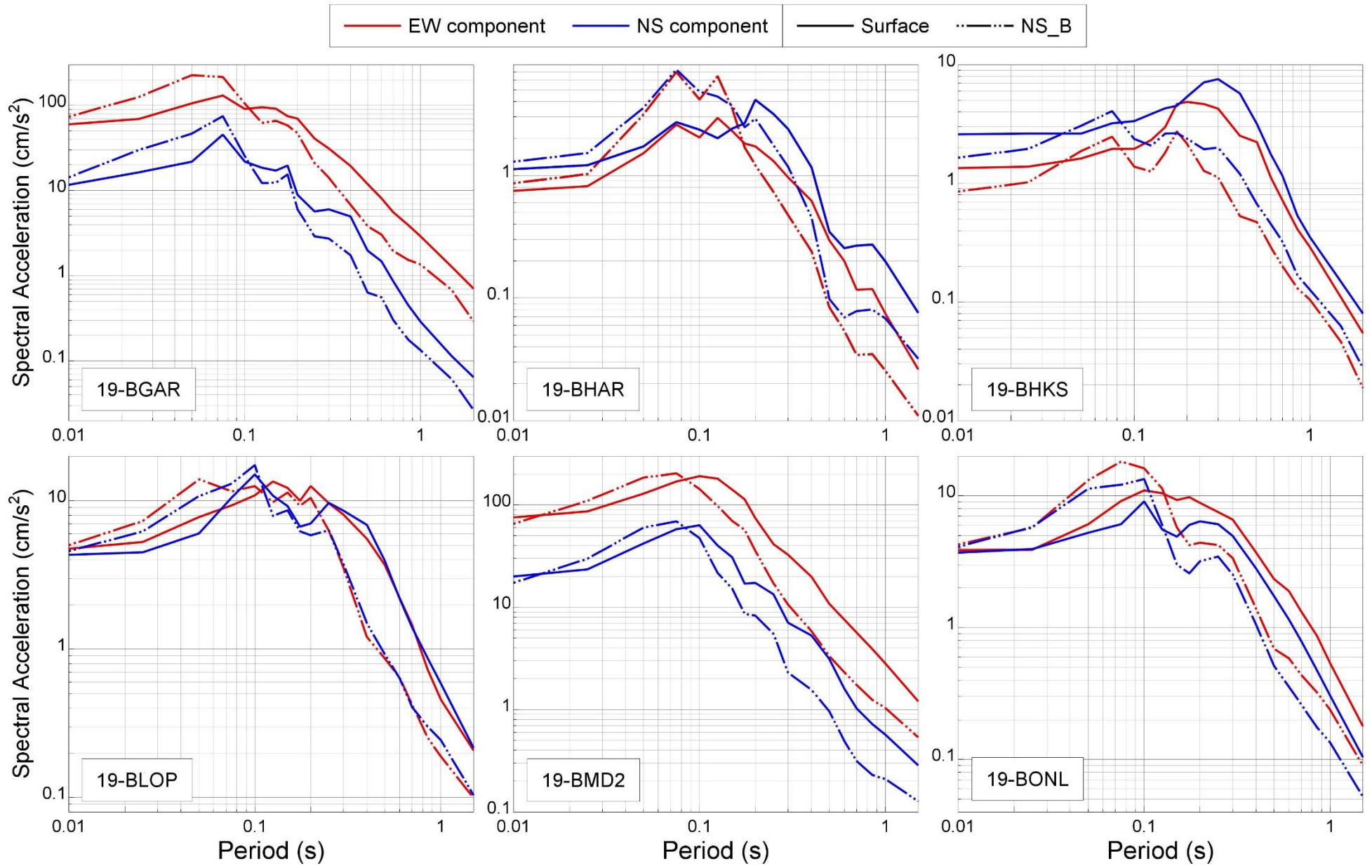


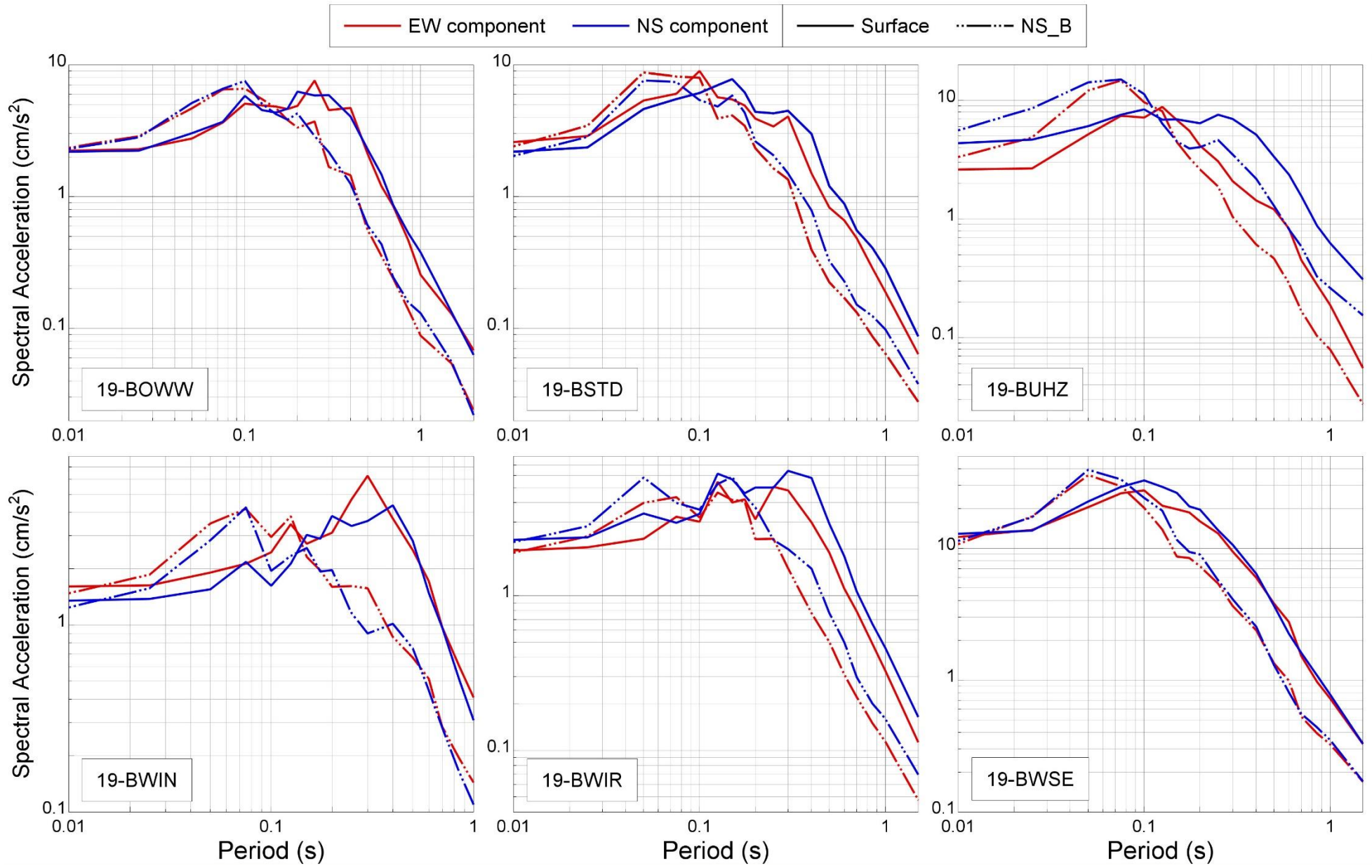


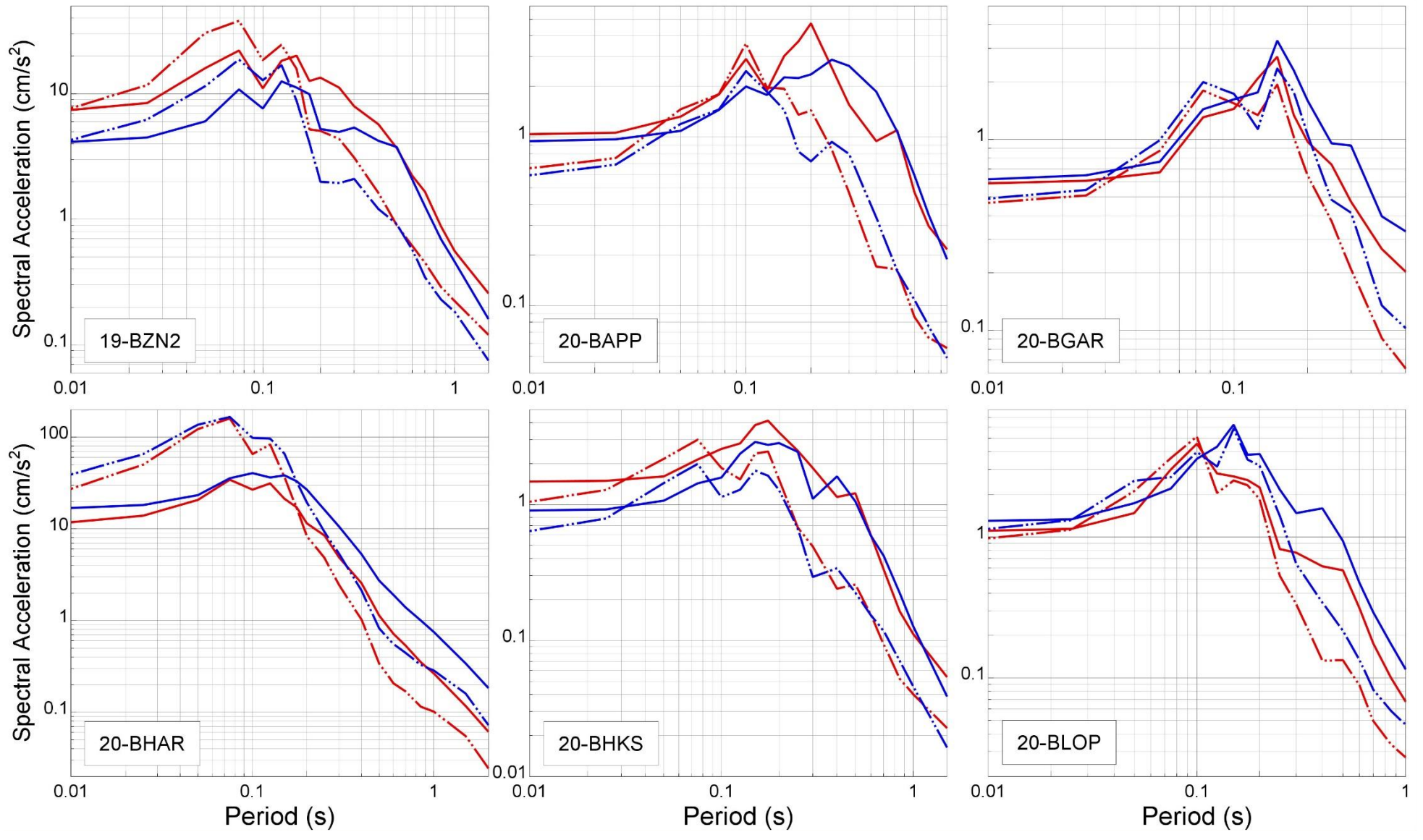


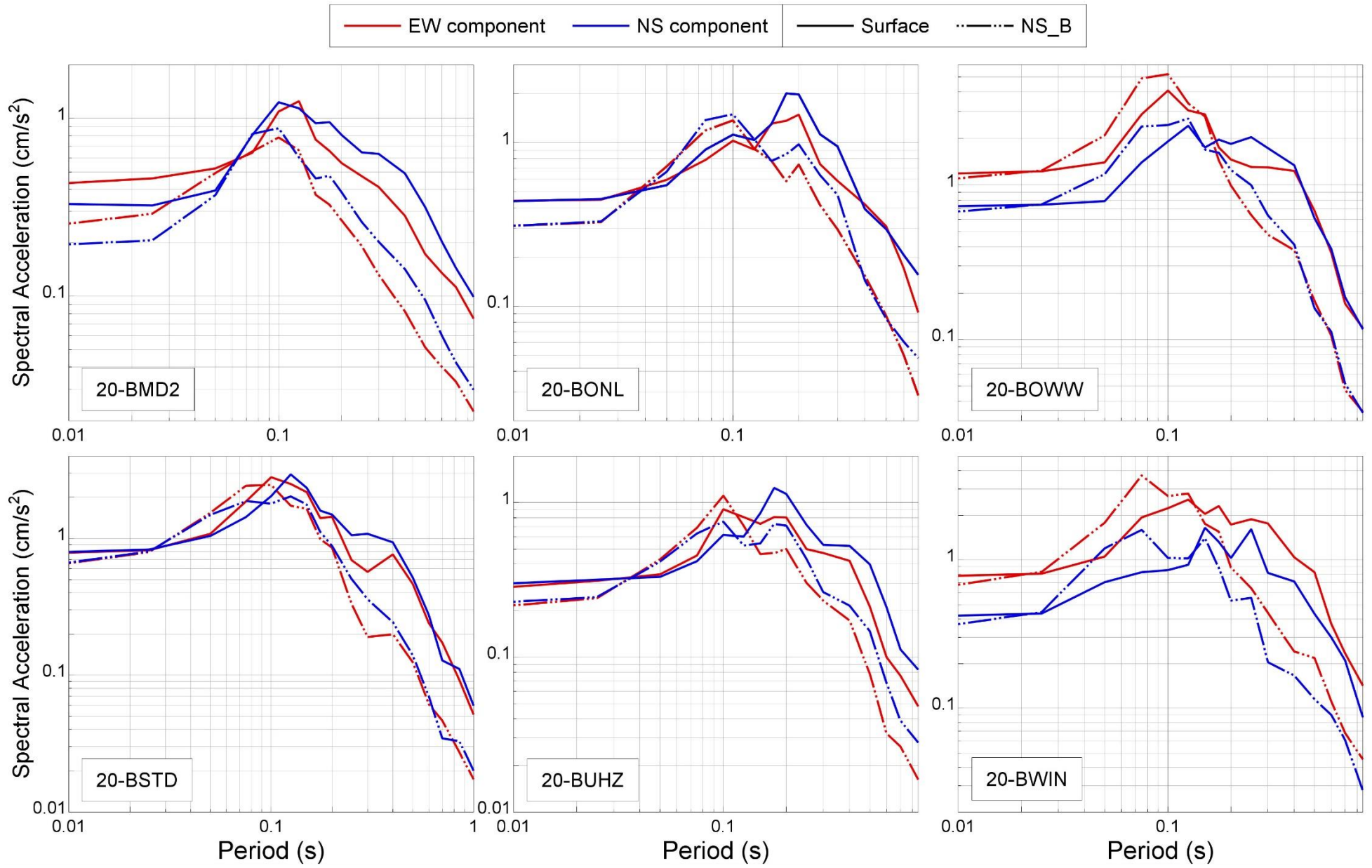


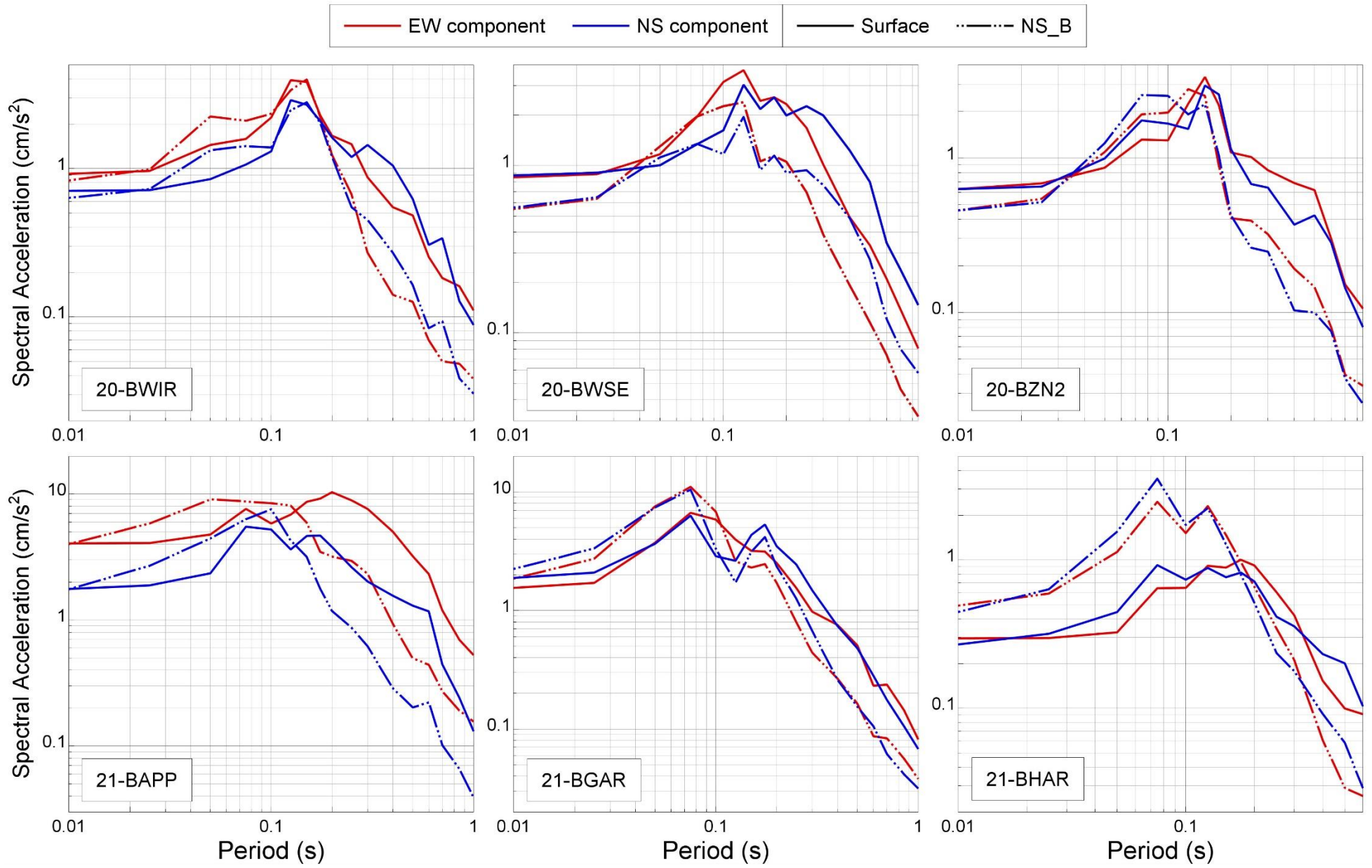


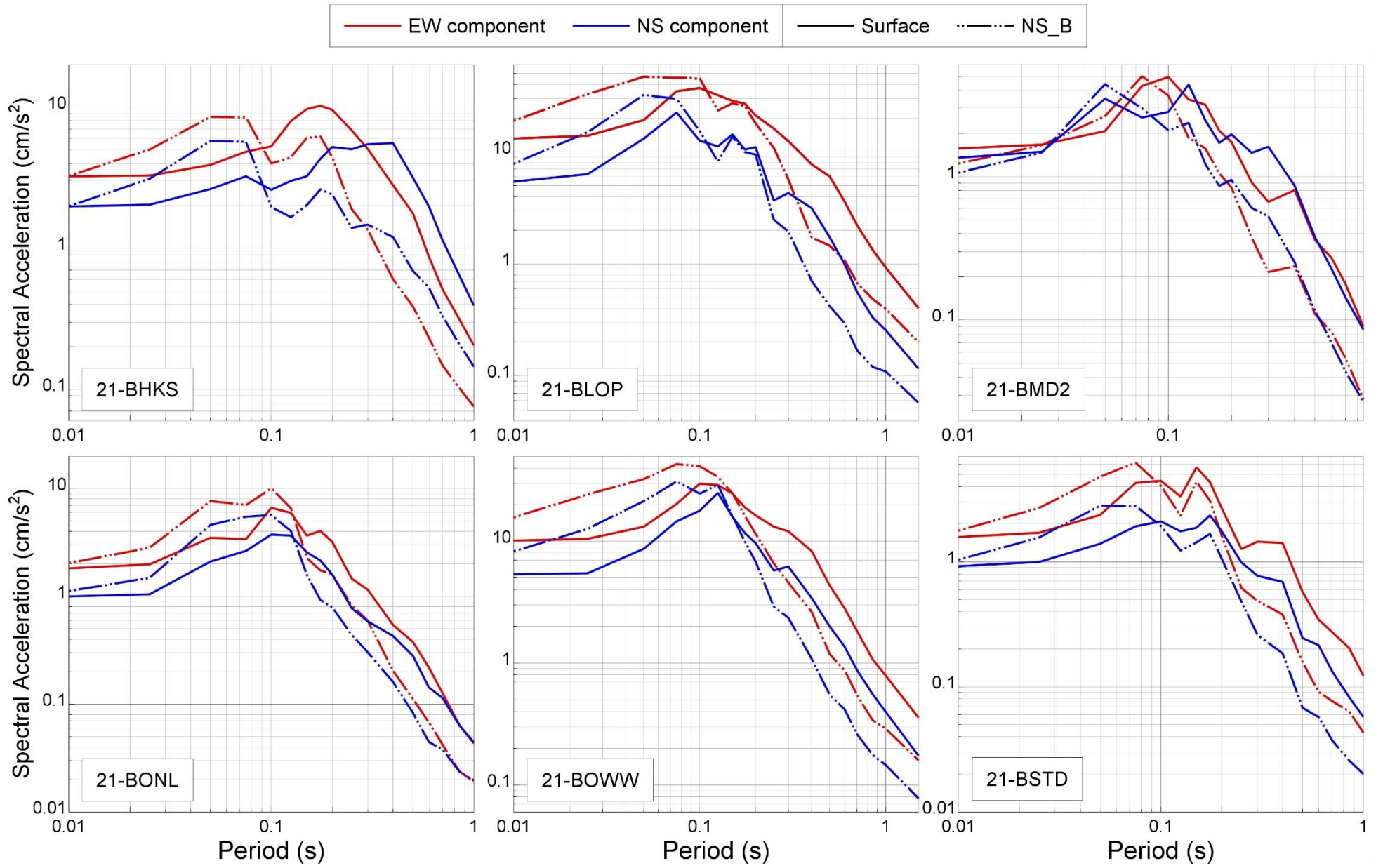


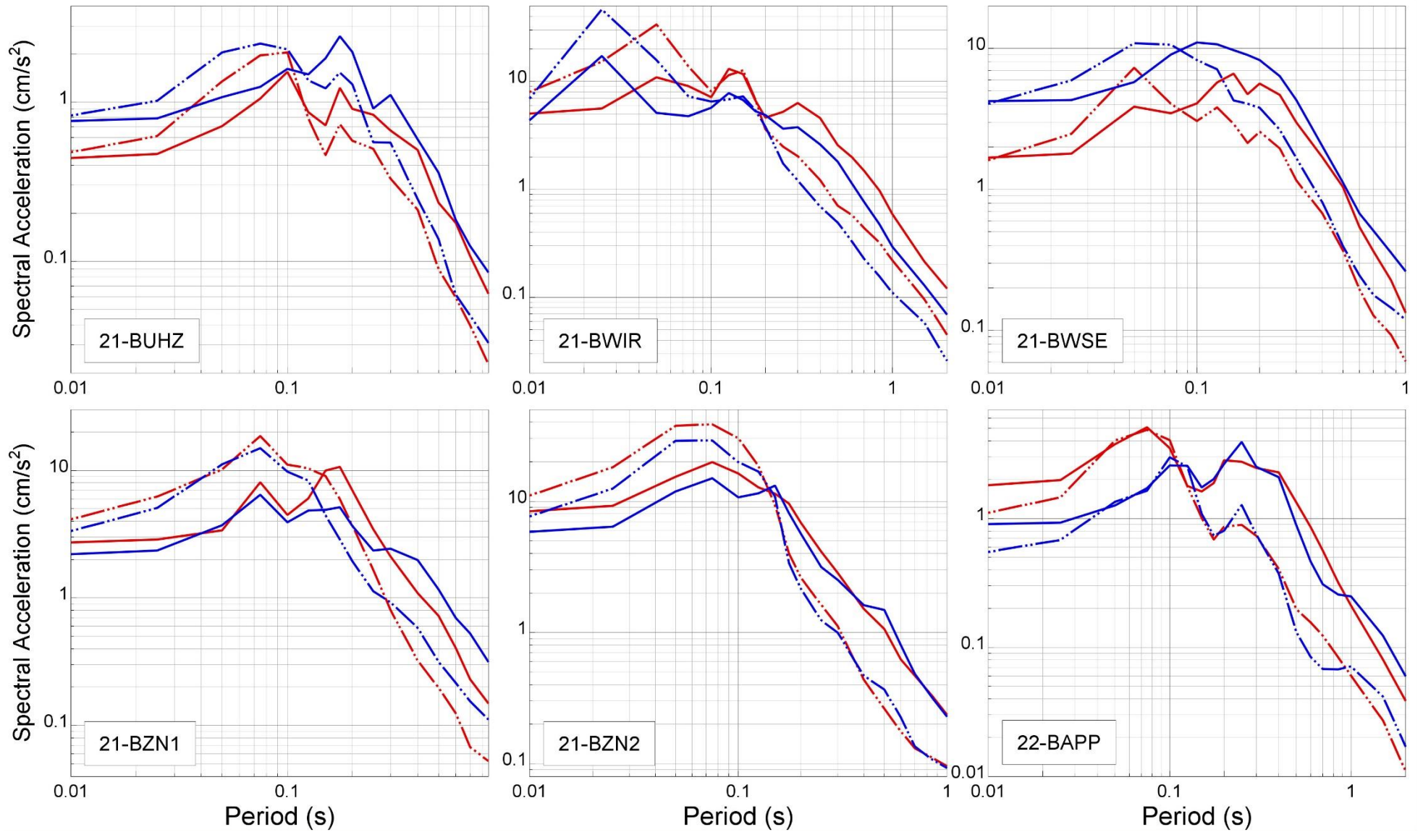


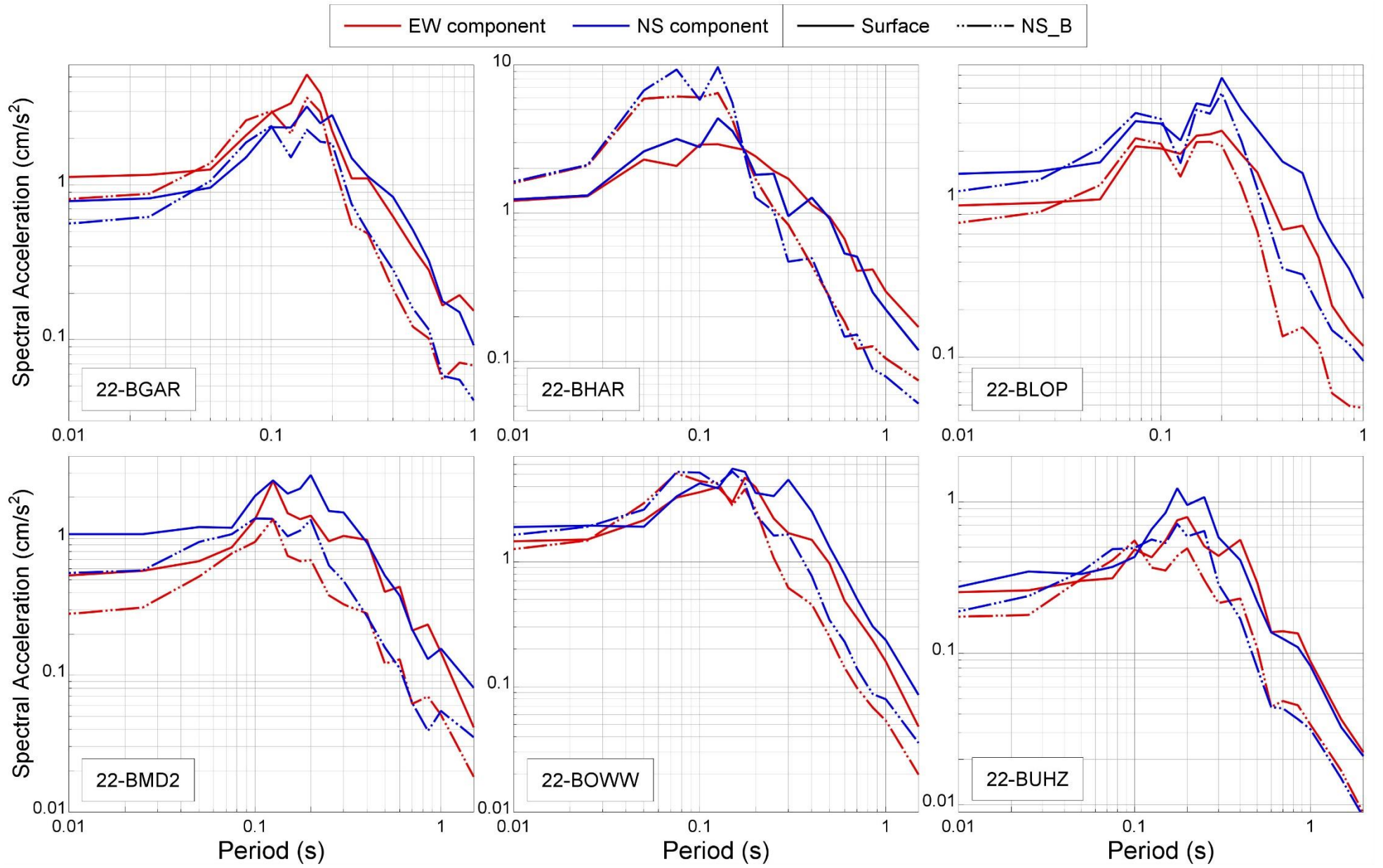


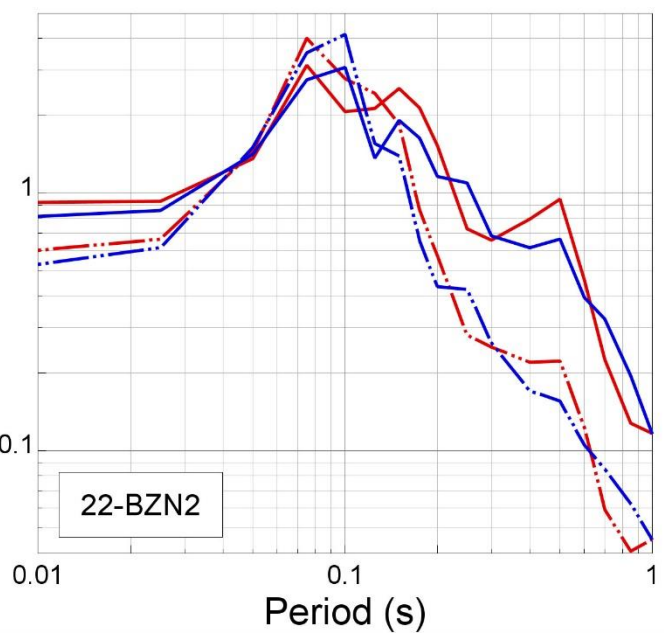
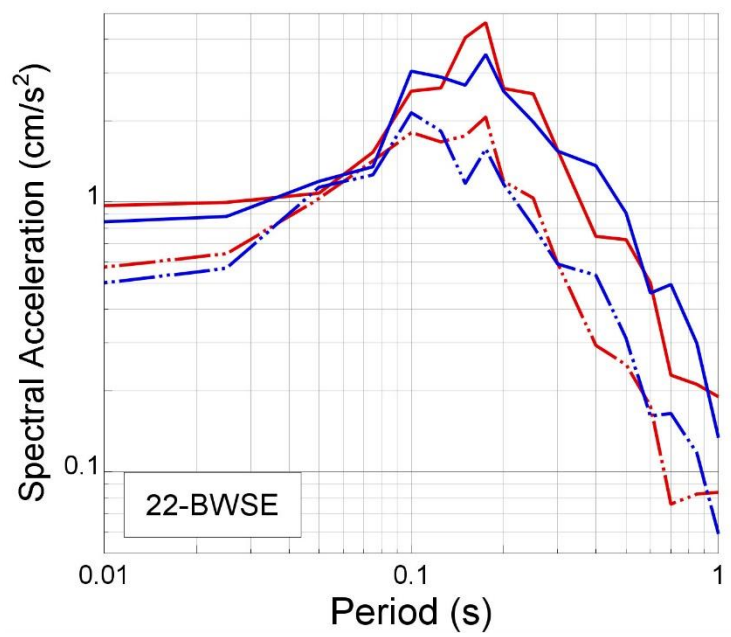
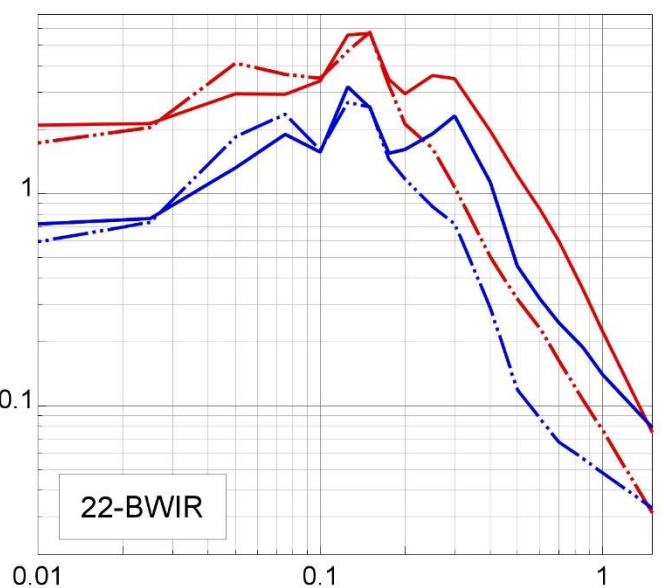
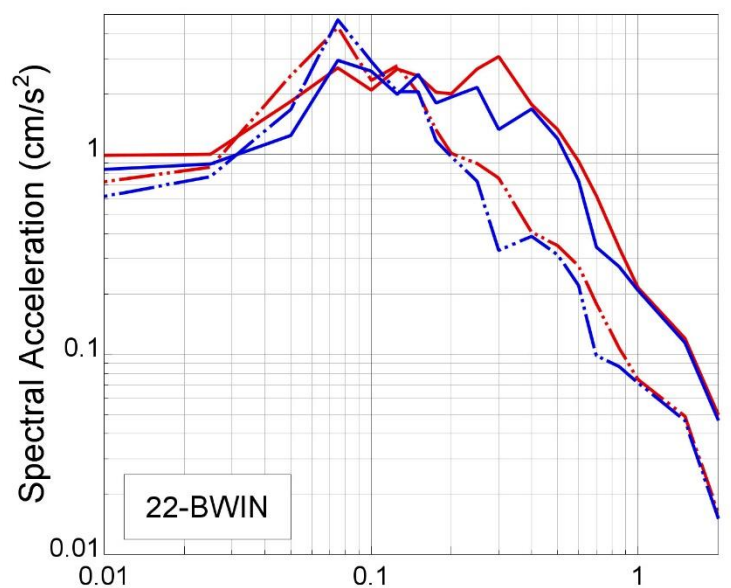
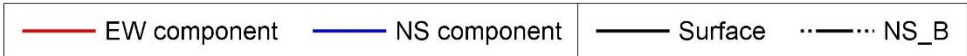


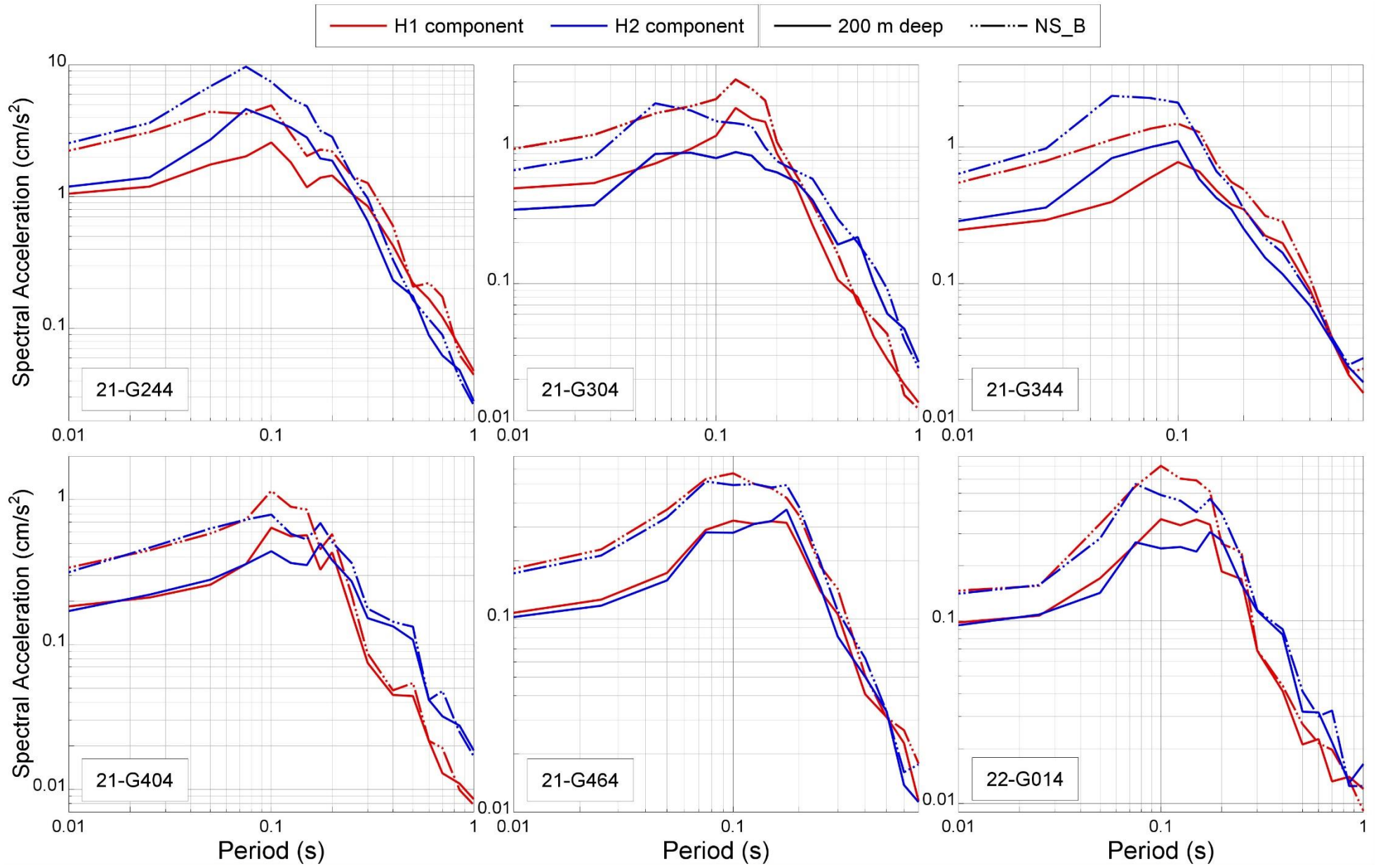


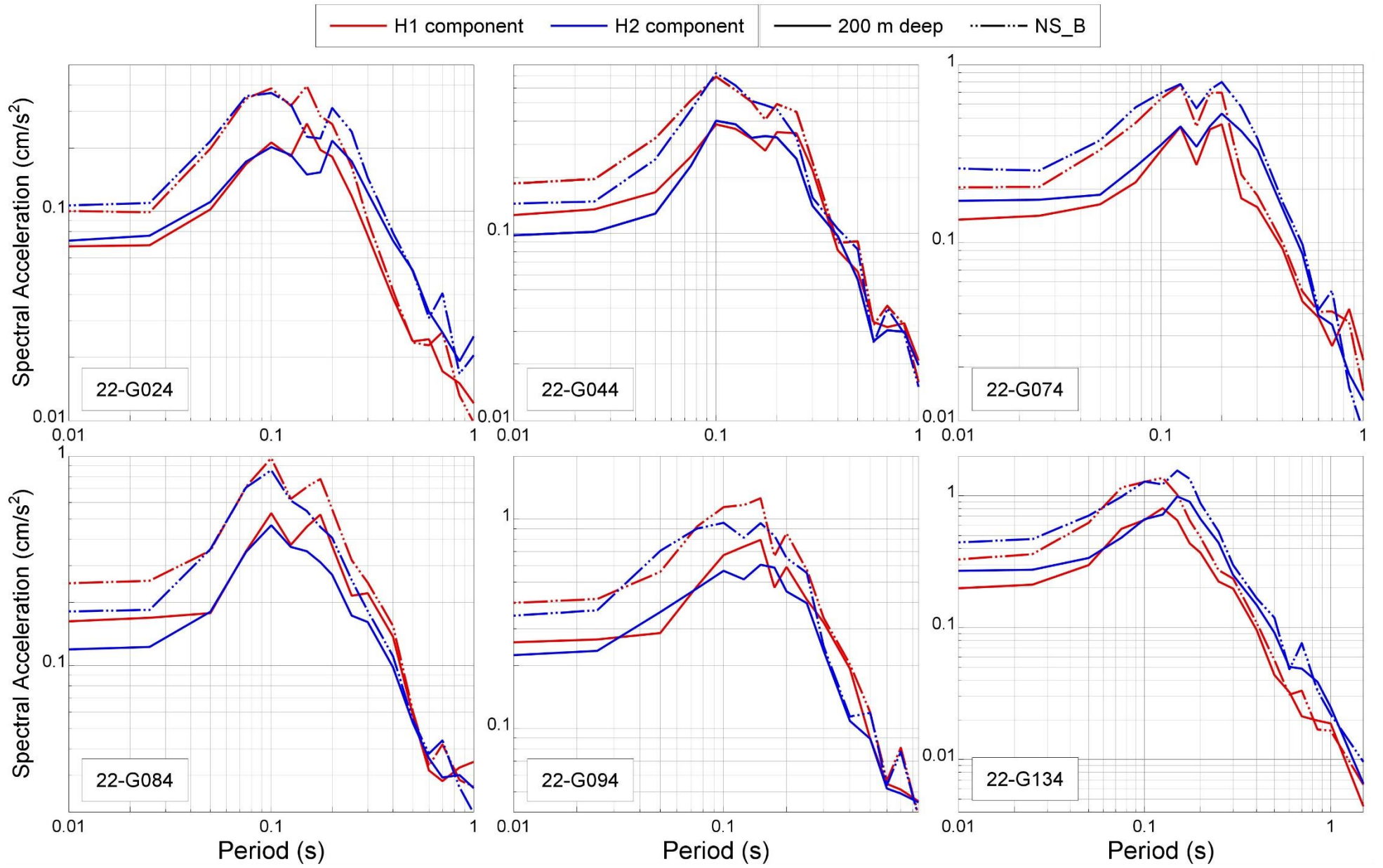


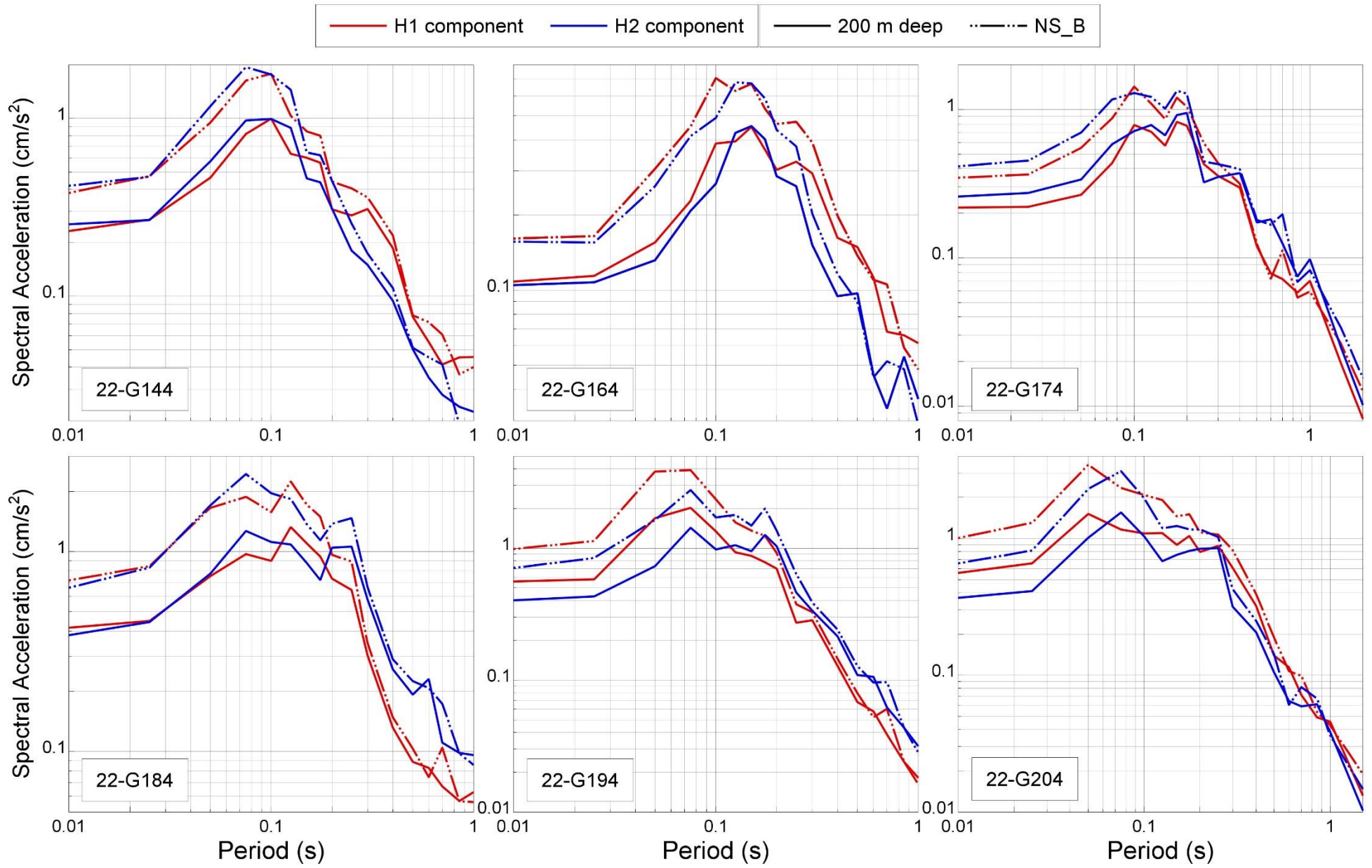


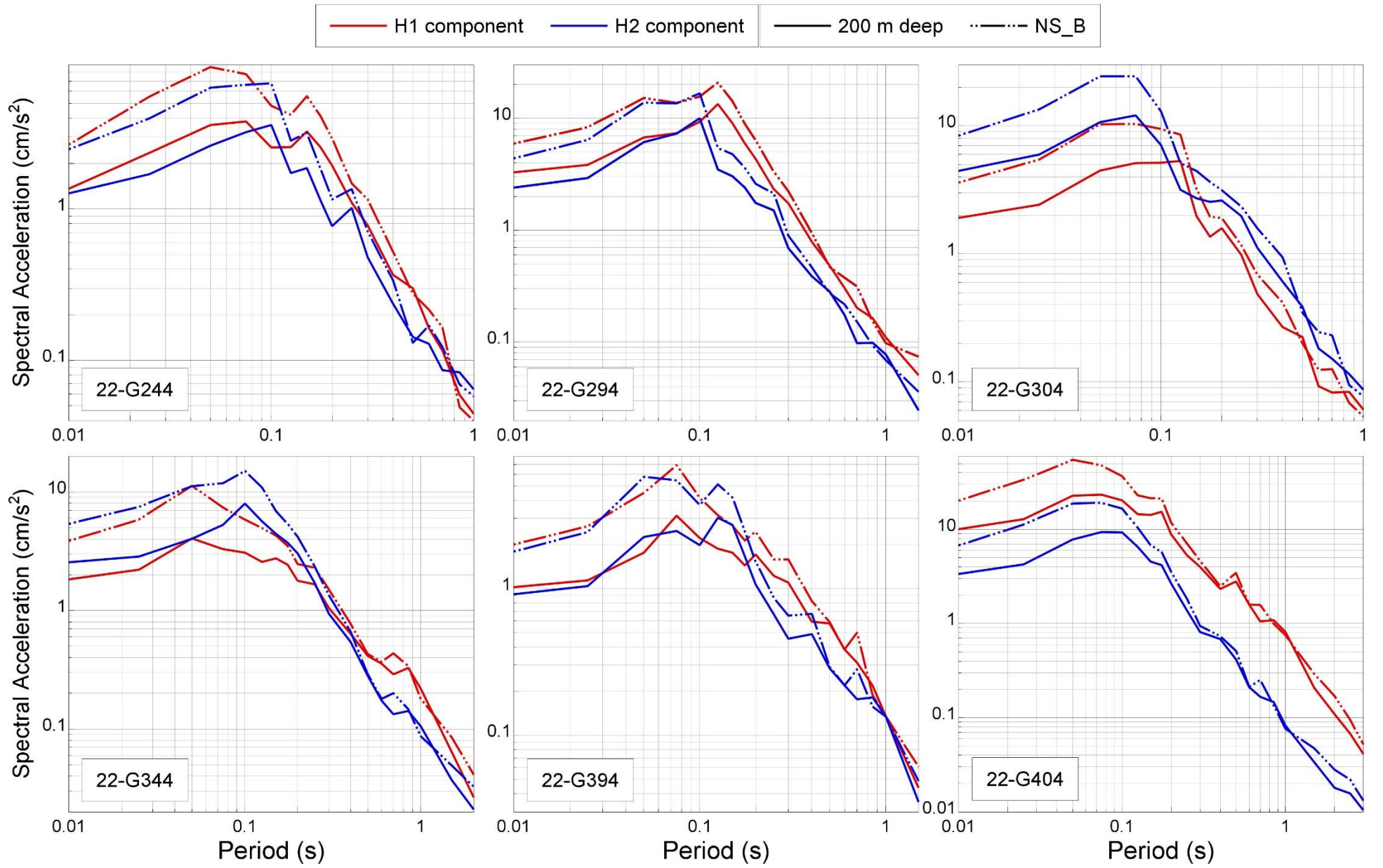


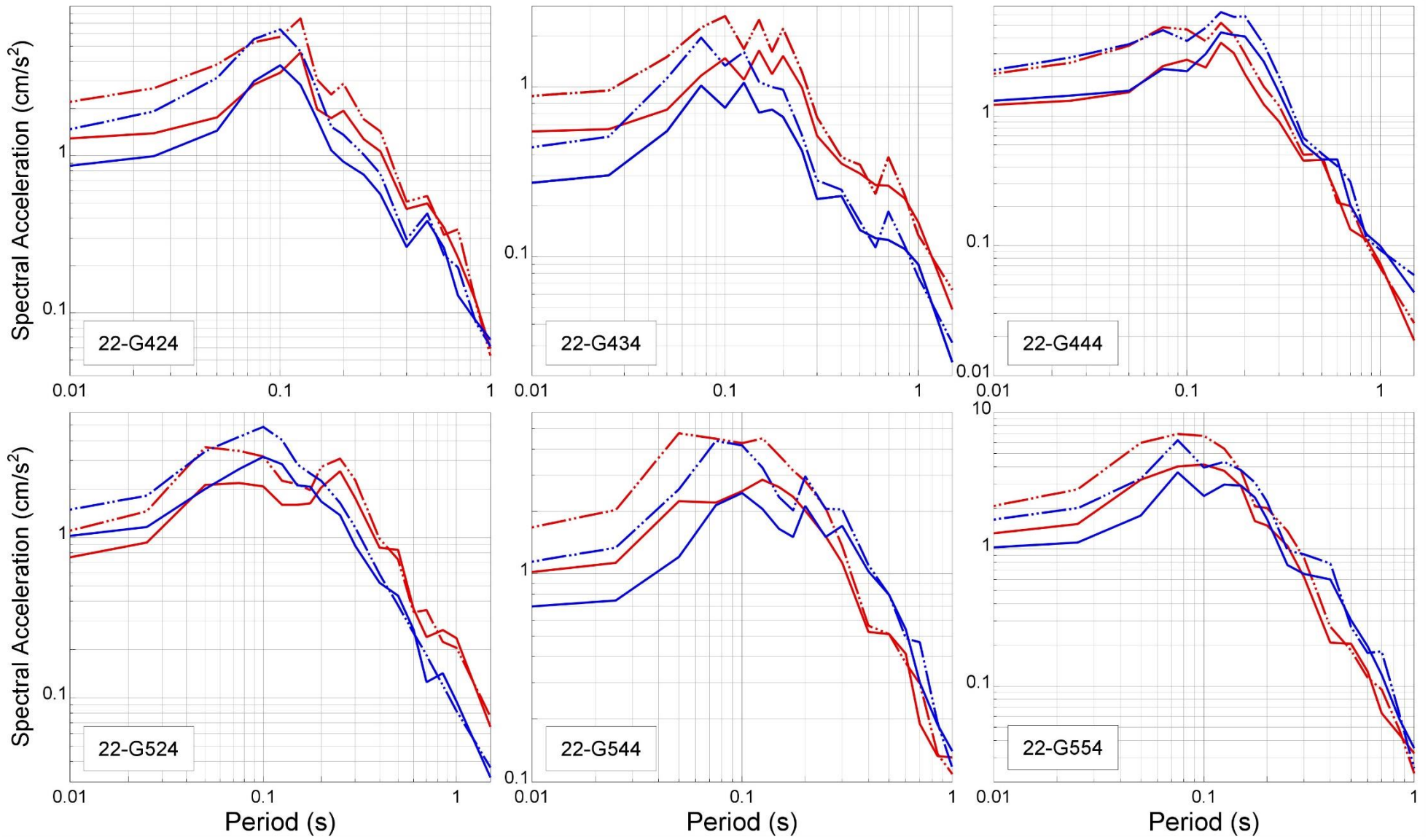


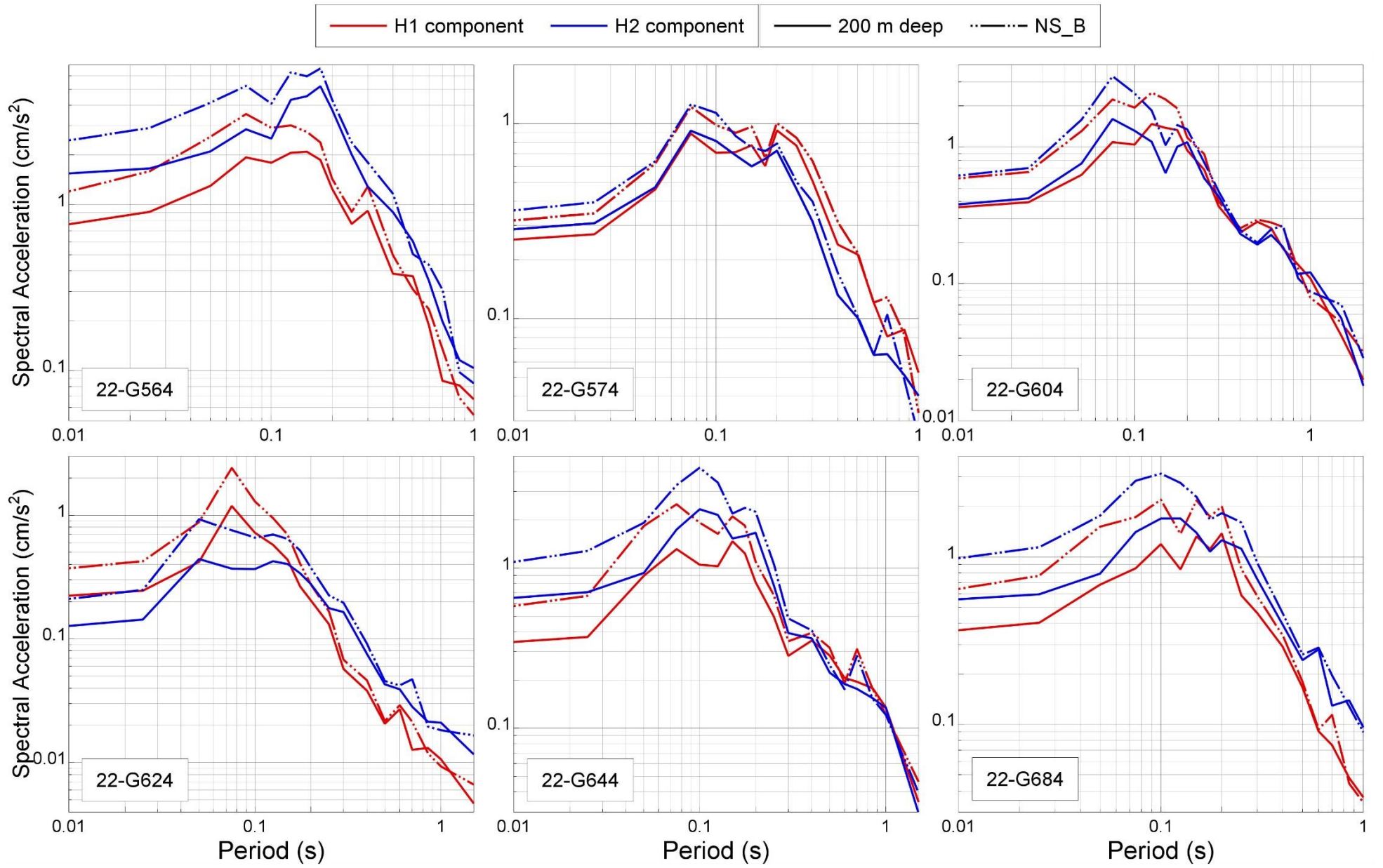












APPENDIX V

Groningen soil characteristics

Table V.1. Codes for stratigraphic units

Code	Formation - Member
AAOP	Anthropogenic
AP	Appelscha
BX	Boxtel
BXKO	Boxtel
BXSI1	Boxtel - Singraven 1
BXSI2	Boxtel - Singraven 2
BXWI	Boxtel - Wierden
DN	Drachten
DR	Drente
DRGI	Drente - Gieten
EE	Eem
NA	Naaldwijk
NASC	Naaldwijk - Schoorl
NAWA	Naaldwijk - Walcheren
NAWO	Naaldwijk - Wormer
NAZA	Naaldwijk - Zandvoort
NIBA	Nieuwkoop - Basal peat
NIGR	Nieuwkoop - Griendtsveen
NIHO	Nieuwkoop - Holland peat
NINB	Nieuwkoop - Nij Beets
PE	Peelo
UR	Urk
URTY	Urk - Tynje

Table V.2. Groningen specific V_s relationships for Eq. (7.1) for V4 GMM

Formation (see Table V.1)	Lithology	Depth dependence *)	# observations	Mean $\ln(V_s)$	Standard deviation $\ln(V_s)$	Coefficient of variance	Slope n	Intercept $\ln V_{s1}$	Mean $\ln(\sigma'_{0}/pa)$	Sum of squares $\ln(\sigma'_{0}/pa)$	Variance regression	Variance velocity (not used)	Source **)	Remark
AAOP	peat	2	87	5.12	0.43	0.08	--	--	--	--	--	--	1	All combined in one lithoclass - no depth dependence because of presence in shallow top only
AAOP	clay	2	87	5.12	0.43	0.08	--	--	--	--	--	--	1	All combined in one lithoclass - no depth dependence because of presence in shallow top only
AAOP	sandy clayey and clayey sand	2	87	5.12	0.43	0.08	--	--	--	--	--	--	1	All combined in one lithoclass - no depth dependence because of presence in shallow top only
AAOP	fine sand	2	87	5.12	0.43	0.08	--	--	--	--	--	--	1	All combined in one lithoclass - no depth dependence because of presence in shallow top only
AAOP	medium sand	2	87	5.12	0.43	0.08	--	--	--	--	--	--	1	All combined in one lithoclass - no depth dependence because of presence in shallow top only
AAOP	coarse sand, gravel and shells	2	87	5.12	0.43	0.08	--	--	--	--	--	--	1	All combined in one lithoclass - no depth dependence because of presence in shallow top only
AP	peat	3	0	--	0.27	--	0.25	4.81	--	--	--	--	3	n from clay literature - intercept consistent with NIBA - $\sigma \ln V_s$ increased to 0.27 for peat
AP	clay	3	0	--	0.20	--	0.25	5.59	--	--	--	--	3	n from clay literature - $V_s=350$ at average depth of 40 m below surface
AP	sandy clayey and clayey sand	2	0	5.86	0.20	0.03	--	--	--	--	--	--	3	Similar to EE so no depth dependence - different average $\ln V_s$
AP	fine sand	2	0	5.86	0.20	0.03	--	--	--	--	--	--	3	Similar to EE so no depth dependence - different average $\ln V_s$
AP	medium sand	2	0	5.99	0.20	0.03	--	--	--	--	--	--	3	Similar to EE so no depth dependence - different average $\ln V_s$ - Medium & coarse sand combined in one V_s class
AP	coarse sand, gravel and shells	2	0	5.99	0.20	0.03	--	--	--	--	--	--	3	Similar to EE so no depth dependence - Medium & coarse sand combined in one V_s class
BX	peat	3	0	--	0.27	--	0.25	4.81	--	--	--	--	3	n from clay literature - intercept consistent with NIBA - $\sigma \ln V_s$ increased to 0.27 for peat
BX	clay	3	0	--	0.20	--	0.25	5.18	--	--	--	--	3	n from clay literature (not enough data) - average V_s from 8 datapoints - in agreement with expert knowledge

Formation (see Table V.1)	Lithology	Depth dependence *)	# observations	Mean ln(Vs)	Standard deviation ln(Vs)	Coefficient of variance	Slope n	Intercept lnVs1	Mean ln(σ' /pa)	Sum of squares ln(σ' /pa)	Variance regression	Variance velocity (not used)	Source **)	Remark
BX	sandy clayey and clayey sand	1	43	--	--	--	0.20	5.38	0.10	5.67	0.04	0.04	1	sufficient data from SCPT data set - depth dependence
BX	fine sand	1	260	--	--	--	0.11	5.51	-0.06	64.41	0.05	0.05	1	sufficient data from SCPT data set - depth dependence
BX	medium sand	2	67	5.62	0.20	0.04	--	--	--	--	--	--	1	No depth dependence in data - σ lnVs increased to 0.2 - Medium & coarse sand combined in one Vs class
BX	coarse sand, gravel and shells	2	67	5.62	0.20	0.04	--	--	--	--	--	--	1	No depth dependence in data - σ lnVs increased to 0.2 - Medium & coarse sand combined in one Vs class
BXKO	peat	3	0	--	0.27	--	0.25	4.81	--	--	--	--	3	n from clay literature - intercept consistent with NIBA - σ lnVs increased to 0.27 for peat
BXKO	clay	3	0	--	0.20	--	0.25	5.18	--	--	--	--	3	From BX
BXKO	sandy clayey and clayey sand	1	43	--	--	--	0.20	5.38	0.10	5.67	0.04	0.04	3	From BX
BXKO	fine sand	1	260	--	--	--	0.11	5.51	-0.06	64.41	0.05	0.05	3	From BX
BXKO	medium sand	2	0	5.62	0.20	0.04	--	--	--	--	--	--	3	From BX - Medium & coarse sand combined in one Vs class
BXKO	coarse sand, gravel and shells	2	0	5.62	0.20	0.04	--	--	--	--	--	--	3	From BX - Medium & coarse sand combined in one Vs class
BXSI1	peat	2	0	4.43	0.27	0.06	--	--	--	--	--	--	3	From NIHO
BXSI1	clay	2	0	4.44	0.27	0.06	--	--	--	--	--	--	3	From NIHO
BXSI1	sandy clayey and clayey sand	2	0	4.70	0.27	0.06	--	--	--	--	--	--	3	From NIHO
BXSI1	fine sand	2	0	4.93	0.27	0.05	--	--	--	--	--	--	3	From NIHO - all sand combined in one Vs class
BXSI1	medium sand	2	0	4.93	0.27	0.05	--	--	--	--	--	--	3	From NIHO - all sand combined in one Vs class
BXSI1	coarse sand, gravel and shells	2	0	4.93	0.27	0.05	--	--	--	--	--	--	3	From NIHO - all sand combined in one Vs class
BXSI2	peat	3	0	--	0.27	--	0.25	4.81	--	--	--	--	3	n from clay literature - intercept consistent with NIBA - σ lnVs increased to 0.27 for peat
BXSI2	clay	3	0	--	0.20	--	0.25	5.18	--	--	--	--	3	From BX

Formation (see Table V.1)	Lithology	Depth dependence *)	# observations	Mean ln(Vs)	Standard deviation ln(Vs)	Coefficient of variance	Slope n	Intercept lnVs ₁	Mean ln(σ ₀ /pa)	Sum of squares ln(σ ₀ /pa)	Variance regression	Variance velocity (not used)	Source **)	Remark
BXSI2	sandy clayey and clayey sand	1	43	--	--	--	0.20	5.38	0.10	5.67	0.04	0.04	3	From BX
BXSI2	fine sand	1	260	--	--	--	0.11	5.51	-0.06	64.41	0.05	0.05	3	From BX
BXSI2	medium sand	2	0	5.62	0.20	0.04	--	--	--	--	--	--	3	From BX - Medium & coarse sand combined in one Vs class
BXSI2	coarse sand, gravel and shells	2	0	5.62	0.20	0.04	--	--	--	--	--	--	3	From BX - Medium & coarse sand combined in one Vs class
BXWI	peat	3	0	--	0.27	--	0.25	4.81	--	--	--	--	3	n from clay literature - intercept consistent with NIBA - σlnVs increased to 0.27 for peat
BXWI	clay	3	0	--	0.20	--	0.25	5.18	--	--	--	--	3	From BX
BXWI	sandy clayey and clayey sand	1	43	--	--	--	0.20	5.38	0.10	5.67	0.04	0.04	3	From BX
BXWI	fine sand	1	260	--	--	--	0.11	5.51	-0.06	64.41	0.05	0.05	3	From BX
BXWI	medium sand	2	0	5.62	0.20	0.04	--	--	--	--	--	--	3	From BX - Medium & coarse sand combined in one Vs class
BXWI	coarse sand, gravel and shells	2	0	5.62	0.20	0.04	--	--	--	--	--	--	3	From BX - Medium & coarse sand combined in one Vs class
DN	peat	3	0	--	0.27	--	0.25	4.81	--	--	--	--	3	n from clay literature - intercept consistent with NIBA - σlnVs increased to 0.27 for peat
DN	clay	3	0	--	0.20	--	0.25	4.99	--	--	--	--	3	n from clay literature - Vs = 150 m/s at average depth of 15 m below surface
DN	sandy clayey and clayey sand	3	0	--	0.20	--	0.25	5.40	--	--	--	--	3	n from clay literature - Vs = 226 m/s at average depth of 15 m below surface
DN	fine sand	2	0	5.87	0.20	0.03	--	--	--	--	--	--	2	No depth dependence for sands
DN	medium sand	2	0	6.11	0.20	0.03	--	--	--	--	--	--	3	No depth dependence for sands - Medium & coarse sand combined in one Vs class
DN	coarse sand, gravel and shells	2	0	6.11	0.20	0.03	--	--	--	--	--	--	3	No depth dependence for sands - Medium & coarse sand combined in one Vs class

Formation (see Table V.1)	Lithology	Depth dependence *)	# observations	Mean ln(Vs)	Standard deviation ln(Vs)	Coefficient of variance	Slope n	Intercept lnVs1	Mean ln(σ_0' /pa)	Sum of squares ln(σ_0' /pa)	Variance regression	Variance velocity (not used)	Source **)	Remark
DR	peat	2	0	5.43	0.27	0.05	--	--	--	--	--	--	3	No depth dependence due to varying glacial conditions - σ lnVs increased to 0.27 for peat
DR	clay	2	0	5.30	0.20	0.04	--	--	--	--	--	--	3	No depth dependence due to varying glacial conditions
DR	sandy clayey and clayey sand	2	0	5.35	0.20	0.04	--	--	--	--	--	--	3	From DRGI - No depth dependence due to varying glacial conditions
DR	fine sand	3	0	--	0.20	--	0.25	5.42	--	--	--	--	3	n from Menq, not enough data, Vs = 285 m/s at average depth of 29 m below surface
DR	medium sand	3	0	--	0.20	--	0.25	5.48	--	--	--	--	3	n from Menq, not enough data, Vs = 300 m/s at average depth of 29 m below surface
DR	coarse sand, gravel and shells	3	0	--	0.20	--	0.26	5.47	--	--	--	--	3	n from Menq, not enough data, Vs = 300 m/s at average depth of 29 m below surface
DRGI	peat	2	0	5.43	0.27	0.05	--	--	--	--	--	--	3	No depth dependence due to varying glacial conditions - σ lnVs increased to 0.27 for peat
DRGI	clay	2	0	5.30	0.20	0.03	--	--	--	--	--	--	3	No depth dependence due to varying glacial conditions
DRGI	sandy clayey and clayey sand	2	33	5.35	0.20	0.04	--	--	--	--	--	--	1	No depth dependence in data - in agreement with to be expected due to varying glacial conditions - σ lnVs increased to 0.2
DRGI	fine sand	3	0	--	0.20	--	0.25	5.63	--	--	--	--	3	n from Menq, not enough data, Vs = 285 m/s at average depth of 15 m below surface
DRGI	medium sand	3	0	--	0.20	--	0.29	5.69	--	--	--	--	3	n from Menq, not enough data, Vs = 300 m/s at average depth of 15 m below surface
DRGI	coarse sand, gravel and shells	3	0	--	0.20	--	0.26	5.69	--	--	--	--	3	n from Menq, not enough data, Vs = 300 m/s at average depth of 15 m below surface
EE	peat	3	0	--	0.27	--	0.25	4.81	--	--	--	--	3	n from clay literature - intercept consistent with NIBA - σ lnVs increased to 0.27 for peat
EE	clay	3	0	--	0.20	--	0.25	5.27	--	--	--	--	3	n from clay literature - Vs = 225 m/s at average depth of 23 m below surface
EE	sandy clayey and clayey sand	2	24	5.56	0.20	0.04	--	--	--	--	--	--	1	No depth dependence according to data (lot of scatter) - σ lnVs increased to 0.2

Formation (see Table V.1)	Lithology	Depth dependence *)	# observations	Mean ln(Vs)	Standard deviation ln(Vs)	Coefficient of variance	Slope n	Intercept lnVs1	Mean ln(σ_0' /pa)	Sum of squares ln(σ_0' /pa)	Variance regression	Variance velocity (not used)	Source **)	Remark
EE	fine sand	2	31	5.55	0.20	0.04	--	--	--	--	--	--	1	No depth dependence for sand according to data - σ_0 lnVs increased to 0.2
EE	medium sand	2	7	5.59	0.20	0.04	--	--	--	--	--	--	1	No depth dependence for sand according to data, average Vs based on 7 points = in good agreement with expert knowlegde - σ_0 lnVs increased to 0.2 - Medium & coarse sand combined in one Vs class
EE	coarse sand, gravel and shells	2	7	5.59	0.20	0.04	--	--	--	--	--	--	1	No depth dependence for sand according to data, average Vs based on 7 points = in good agreement with expert knowlegde - σ_0 lnVs increased to 0.2 - Medium & coarse sand combined in one Vs class
NA	peat	2	0	4.43	0.27	0.06	--	--	--	--	--	--	3	From NIHO, no depth dependence
NA	clay	1	303	--	--	--	0.18	4.91	-1.20	107.49	0.11	0.11	1	sufficient data from SCPT data set - depth dependence
NA	sandy clayey and clayey sand	1	245	--	--	--	0.28	5.25	-0.98	59.65	0.07	0.06	1	sufficient data from SCPT data set - depth dependence
NA	fine sand	1	166	--	--	--	0.36	5.51	-0.78	34.05	0.10	0.10	1	sufficient data from SCPT data set - depth dependence
NA	medium sand	3	0	--	0.20	--	0.25	5.73	--	--	--	--	3	n from Menq, Vs = 250 m/s at average depth of 8 m below surface
NA	coarse sand, gravel and shells	3	0	--	0.20	--	0.25	5.73	--	--	--	--	3	n from Menq, Vs = 250 m/s at average depth of 8 m below surface
NASC	peat	2	0	4.43	0.27	0.06	--	--	--	--	--	--	3	From NIHO, no depth dependence
NASC	clay	1	303	--	--	--	0.18	4.91	-1.20	107.49	0.11	0.11	3	From NA
NASC	sandy clayey and clayey sand	1	245	--	--	--	0.28	5.25	-0.98	59.65	0.07	0.06	3	From NA
NASC	fine sand	1	166	--	--	--	0.36	5.51	-0.78	34.05	0.10	0.10	3	From NA
NASC	medium sand	3	0	--	0.20	--	0.25	5.73	--	--	--	--	3	From NA - Medium & coarse sand combined in one Vs class
NASC	coarse sand, gravel and shells	3	0	--	0.20	--	0.25	5.73	--	--	--	--	3	From NA - Medium & coarse sand combined in one Vs class
NAWA	peat	2	0	4.43	0.27	0.06	--	--	--	--	--	--	3	From NIHO, no depth dependence
NAWA	clay	1	303	--	--	--	0.18	4.91	-1.20	107.49	0.11	0.11	3	From NA

Formation (see Table V.1)	Lithology	Depth dependence *)	# observations	Mean ln(Vs)	Standard deviation ln(Vs)	Coefficient of variance	Slope n	Intercept lnVs1	Mean ln(σ' /pa)	Sum of squares ln(σ' /pa)	Variance regression	Variance velocity (not used)	Source **)	Remark
NAWA	sandy clayey and clayey sand	1	245	--	--	--	0.28	5.25	-0.98	59.65	0.07	0.06	3	From NA
NAWA	fine sand	1	166	--	--	--	0.36	5.51	-0.78	34.05	0.10	0.10	3	From NA
NAWA	medium sand	3	0	--	0.20	--	0.25	5.73	--	--	--	--	3	From NA - Medium & coarse sand combined in one Vs class
NAWA	coarse sand, gravel and shells	3	0	--	0.20	--	0.25	5.73	--	--	--	--	3	From NA - Medium & coarse sand combined in one Vs class
NAWO	peat	2	0	4.43	0.27	0.06	--	--	--	--	--	--	3	From NIHO, no depth dependence
NAWO	clay	1	303	--	--	--	0.18	4.91	-1.20	107.49	0.11	0.11	3	From NA
NAWO	sandy clayey and clayey sand	1	245	--	--	--	0.28	5.25	-0.98	59.65	0.07	0.06	3	From NA
NAWO	fine sand	1	166	--	--	--	0.36	5.51	-0.78	34.05	0.10	0.10	3	From NA
NAWO	medium sand	3	0	--	0.20	--	0.25	5.73	--	--	--	--	3	From NA - Medium & coarse sand combined in one Vs class
NAWO	coarse sand, gravel and shells	3	0	--	0.20	--	0.25	5.73	--	--	--	--	3	From NA - Medium & coarse sand combined in one Vs class
NAZA	peat	2	0	4.43	0.27	0.06	--	--	--	--	--	--	3	From NIHO, no depth dependence
NAZA	clay	1	303	--	--	--	0.18	4.91	-1.20	107.49	0.11	0.11	3	From NA
NAZA	sandy clayey and clayey sand	1	245	--	--	--	0.28	5.25	-0.98	59.65	0.07	0.06	3	From NA
NAZA	fine sand	1	166	--	--	--	0.36	5.51	-0.78	34.05	0.10	0.10	3	From NA
NAZA	medium sand	3	0	--	0.20	--	0.25	5.73	--	--	--	--	3	From NA - Medium & coarse sand combined in one Vs class
NAZA	coarse sand, gravel and shells	3	0	--	0.20	--	0.25	5.73	--	--	--	--	3	From NA - Medium & coarse sand combined in one Vs class
NIBA	peat	1	22	--	--	--	0.57	5.05	-0.77	3.70	0.19	0.15	1	sufficient data from SCPT data set - depth dependence
NIBA	clay	3	0	--	0.27	--	0.25	4.95	--	--	--	--	3	n from clay literature - Vs = 125 m/s at average depth of 10 m - σ lnVs increased to 0.27 for peat

Formation (see Table V.1)	Lithology	Depth dependence *)	# observations	Mean ln(Vs)	Standard deviation ln(Vs)	Coefficient of variance	Slope n	Intercept lnVs ₁	Mean ln(σ ₀ /pa)	Sum of squares ln(σ ₀ /pa)	Variance regression	Variance velocity (not used)	Source **)	Remark
NIBA	sandy clayey and clayey sand	3	0	--	0.27	--	0.25	5.14	--	--	--	--	3	n from clay literature - Vs = 150 m/s at average depth of 10 m - σlnVs increased to 0.27 for peat
NIBA	fine sand	3	0	--	0.27	--	0.25	5.14	--	--	--	--	3	n from clay literature - Vs = 150 m/s at average depth of 10 m - σlnVs increased to 0.27 for peat
NIBA	medium sand	3	0	--	0.27	--	0.25	5.14	--	--	--	--	3	n from clay literature - Vs = 150 m/s at average depth of 10 m - σlnVs increased to 0.27 for peat
NIBA	coarse sand, gravel and shells	3	0	--	0.27	--	0.25	5.14	--	--	--	--	3	n from clay literature - Vs = 150 m/s at average depth of 10 m - σlnVs increased to 0.27 for peat
NIGR	peat	2	0	4.43	0.27	0.06	--	--	--	--	--	--	3	From NIHO
NIGR	clay	2	0	4.44	0.27	0.06	--	--	--	--	--	--	3	From NIHO
NIGR	sandy clayey and clayey sand	2	0	4.70	0.27	0.06	--	--	--	--	--	--	3	From NIHO
NIGR	fine sand	2	0	4.93	0.27	0.05	--	--	--	--	--	--	3	From NIHO - all sand combined in one Vs class
NIGR	medium sand	2	0	4.93	0.27	0.05	--	--	--	--	--	--	3	From NIHO - all sand combined in one Vs class
NIGR	coarse sand, gravel and shells	2	0	4.93	0.27	0.05	--	--	--	--	--	--	3	From NIHO - all sand combined in one Vs class
NIHO	peat	2	13	4.43	0.27	0.06	--	--	--	--	--	--	1	No depth dependence in SCPT data - average Vs in agreement with expert knowledge
NIHO	clay	2	0	4.44	0.27	0.06	--	--	--	--	--	--	3	σlnVs increased to 0.27 for peat
NIHO	sandy clayey and clayey sand	2	0	4.70	0.27	0.06	--	--	--	--	--	--	3	σlnVs increased to 0.27 for peat
NIHO	fine sand	2	0	4.93	0.27	0.05	--	--	--	--	--	--	3	σlnVs increased to 0.27 for peat - all sand in one combined Vs class
NIHO	medium sand	2	0	4.93	0.27	0.05	--	--	--	--	--	--	3	σlnVs increased to 0.27 for peat - all sand in one combined Vs class
NIHO	coarse sand, gravel and shells	2	0	4.93	0.27	0.05	--	--	--	--	--	--	3	σlnVs increased to 0.27 for peat - all sand in one combined Vs class
NINB	peat	2	0	4.43	0.27	0.06	--	--	--	--	--	--	3	From NIHO

Formation (see Table V.1)	Lithology	Depth dependence *)	# observations	Mean ln(Vs)	Standard deviation ln(Vs)	Coefficient of variance	Slope n	Intercept lnVs ₁	Mean ln(σ ₀ /pa)	Sum of squares ln(σ ₀ /pa)	Variance regression	Variance velocity (not used)	Source **)	Remark
NINB	clay	2	0	4.44	0.27	0.06	--	--	--	--	--	--	3	From NIHO
NINB	sandy clayey and clayey sand	2	0	4.70	0.27	0.06	--	--	--	--	--	--	3	From NIHO
NINB	fine sand	2	0	4.93	0.27	0.05	--	--	--	--	--	--	3	From NIHO - all sand combined in one Vs class
NINB	medium sand	2	0	4.93	0.27	0.05	--	--	--	--	--	--	3	From NIHO - all sand combined in one Vs class
NINB	coarse sand, gravel and shells	2	0	4.93	0.27	0.05	--	--	--	--	--	--	3	From NIHO - all sand combined in one Vs class
PE	peat	3	0	--	0.27	--	0.25	4.81	--	--	--	--	3	n from clay literature - intercept consistent with NIBA - σlnVs increased to 0.27 for peat
PE	clay	1	455	--	--	--	0.33	5.27	0.39	41.89	0.03	0.03	1	sufficient data from SCPT data set - depth dependence
PE	sandy clayey and clayey sand	1	41	--	--	--	0.43	5.20	0.66	2.59	0.03	0.03	1	sufficient data from SCPT data set - depth dependence
PE	fine sand	1	222	--	--	--	0.10	5.58	0.54	16.26	0.02	0.02	1	sufficient data from SCPT data set - depth dependence
PE	medium sand	1	72	--	--	--	0.24	5.58	0.61	3.04	0.02	0.02	1	sufficient data from SCPT data set - depth dependence - Medium & coarse sand combined in one Vs class
PE	coarse sand, gravel and shells	1	72	--	--	--	0.24	5.58	0.61	3.04	0.02	0.02	1	sufficient data from SCPT data set - depth dependence - Medium & coarse sand combined in one Vs class
UR	peat	3	0	--	0.27	--	0.25	4.81	--	--	--	--	3	from URTY
UR	clay	3	0	--	0.20	--	0.25	5.12	--	--	--	--	2	from URTY
UR	sandy clayey and clayey sand	3	0	--	0.20	--	0.25	5.27	--	--	--	--	3	from URTY
UR	fine sand	3	0	--	0.20	--	0.26	5.39	--	--	--	--	2	from URTY
UR	medium sand	3	0	--	0.20	--	0.26	5.39	--	--	--	--	3	from URTY
UR	coarse sand, gravel and shells	3	0	--	0.20	--	0.26	5.58	--	--	--	--	3	from URTY
URTY	peat	3	0	--	0.27	--	0.25	4.81	--	--	--	--	3	n from clay literature - intercept consistent with NIBA - σlnVs increased to 0.27 for peat
URTY	clay	3	0	--	0.20	--	0.25	5.12	--	--	--	--	3	n from clay - Vs=190 m/s at average depth of 20 m

Formation (see Table V.1)	Lithology	Depth dependence *)	# observations	Mean $\ln(V_s)$	Standard deviation $\ln(V_s)$	Coefficient of variance	Slope n	Intercept $\ln V_{s1}$	Mean $\ln(\sigma'_{0'}/pa)$	Sum of squares $\ln(\sigma'_{0'}/pa)$	Variance regression	Variance velocity (not used)	Source **)	Remark
URTY	sandy clayey and clayey sand	3	0	--	0.20	--	0.25	5.27	--	--	--	--	3	n from clay - $V_s=220$ m/s at average depth of 20 m
URTY	fine sand	3	0	--	0.20	--	0.26	5.39	--	--	--	--	3	n from Menq (not enough data in SCPT data set) - $V_s=235$ m/s at average depth of 20 m
URTY	medium sand	3	0	--	0.20	--	0.26	5.39	--	--	--	--	3	n from Menq (not enough data in SCPT data set) - $V_s=250$ m/s at average depth of 20 m
URTY	coarse sand, gravel and shells	3	0	--	0.20	--	0.26	5.58	--	--	--	--	3	n from Menq (not enough data in SCPT data set) - $V_s=300$ m/s at average depth of 20 m

Notes on Table V.2:

*) Depth dependence:

1. Depth dependence according to Eq. (7.1) based on data.
2. No depth dependence for V_s .
3. Depth dependence according to Eq. (7.1) based on data based on literature and expert judgement.

***) Source:

1. SCPT data set
2. Wassing *et al.* (2003)
3. Expert estimate

Table V.3. Geomechanical parameters for organic deposits (peat). OCR = over-consolidation ratio; Su = undrained shear strength.
(see Table V.1 for codes of stratigraphic units).

Strat. unit GeoTOP	Average unit weight wet (kN/m ³)	Based on	Average OCR	Based on Kulhawy & Mayne (1990) on CPT dataset & remark	Average Su (kPa)	Based on	K0	Based on
AAOP	12	Expert judgement	2	From NA	22.2	CPT dataset and adjusted Su = qnet/17	0.35	Holocene peat
AP	12	Expert judgement	4	Value for Peelo at 30 m depth	60	Maximum value for NIBA at ~ 20 m depth	1.1	Clay
BX	11.4	CPT dataset	$4.5+0.005*\sigma'_{v0}$	Maximum OCR = 6	$0.25*\sigma'_{v0}+13$	From NIBA	1.1	Clay
BXKO	11.4	CPT dataset	$4.5+0.005*\sigma'_{v0}$	Maximum OCR = 6	$0.25*\sigma'_{v0}+13$	From NIBA	1.1	Clay
BXSI1	10.8	CPT dataset	2	From NA	12.5	From NIHO	0.5	Clay
BXSI2	11.4	CPT dataset	$4.5+0.005*\sigma'_{v0}$	Maximum OCR = 6	$0.25*\sigma'_{v0}+13$	From NIBA	1.1	Clay
BXWI	11.4	CPT dataset	$4.5+0.005*\sigma'_{v0}$	Maximum OCR = 6	$0.25*\sigma'_{v0}+13$	From NIBA	1.1	Clay
DN	12	Expert judgement	4	Value for Peelo at 30 m depth	60	Maximum value for NIBA at ~ 20 m depth	1.1	Clay
DR	12	CPT dataset	$4.5+0.005*\sigma'_{v0}$	Maximum OCR = 6	60	Maximum value for NIBA at ~ 20 m depth	1.1	Clay
DRGI	12	CPT dataset	$4.5+0.005*\sigma'_{v0}$	Maximum OCR = 6	60	Maximum value for NIBA at ~ 20 m depth	1.1	Clay
EE	11.4	CPT dataset	$4.5+0.005*\sigma'_{v0}$	Maximum OCR = 6	$0.25*\sigma'_{v0}+13$	From NIBA	1.1	Clay
NA	10.3	CPT dataset	2	Median value	12.5	From NIHO	0.35	Holocene peat
NASC	10.3	CPT dataset	2	Median value	12.5	From NIHO	0.35	Holocene peat
NAWA	10.3	CPT dataset	2	Median value	12.5	From NIHO	0.35	Holocene peat
NAWO	10.3	CPT dataset	2	Median value	12.5	From NIHO	0.35	Holocene peat
NAZA	10.3	CPT dataset	2	Median value	12.5	From NIHO	0.35	Holocene peat
NIBA	11.3	CPT dataset	2	Median value	$0.25*\sigma'_{v0}+13$	CPT dataset and adjusted Su = qnet/17	0.7	NIBA special case K0=0.7 for all lithologies
NIGR	10.8	CPT dataset	2	Median value	12.5	From NIHO	0.35	Holocene peat
NIHO	10.8	CPT dataset	2	Median value	12.5	CPT dataset and adjusted Su = qnet/17	0.35	Holocene peat
NINB	10.8	CPT dataset	2	Median value	12.5	From NIHO	0.35	Holocene peat
PE	12	Expert judgement	$6-0.005*\sigma'_{v0}$	Minimum OCR = 4	60	Maximum value for NIBA at ~ 20 m depth	1.1	Clay
UR	12	Expert judgement	4	Value for Peelo at 30 m depth	60	Maximum value for NIBA at ~ 20 m depth	1.1	Clay
URTY	12	Expert judgement	4	Value for Peelo at 30 m depth	60	Maximum value for NIBA at ~ 20 m depth	1.1	Clay

Table V.4. Geomechanical parameters for clays. Ip = plasticity index; OCR = overconsolidation ratio; Su = undrained shear strength. (see Table V.1 for codes of stratigraphic units)

Strat. unit GeoTOP	Lith. class	Average unit weight wet (kN/m ³)	Based on	Ip	Based on	Average OCR	Based on Kulhawy & Mayne (1990) on CPT dataset & remark	Average Su (kPa)	Based on <i>et al.</i> (1997) & remark	K0	Based on
AAOP	Clay	13.9	CPT dataset	50	From PE clay used for dike studies	2	From NA	20		0.5	Holocene clay
AAOP	Clayey sand and sandy clay	16.8	CPT dataset	50	From AAOP clay	2	From NA	55		0.5	Clay
AP	Clay	17.6	CPT dataset	30	Sorensen&Okkels (2013)	4	Value for Peelo at 30 m depth	$0.88 \cdot \sigma'_{v0} + 26$	From PE	1.1	Depends on OCR for Pleistocene clay
AP	Clayey sand and sandy clay	18.1	CPT dataset	30	Sorensen&Okkels (2013)	4	Value for Peelo at 30 m depth	$0.60 \cdot \sigma'_{v0} + 55$	From PE	1.2	Clay
BX	Clay	14.4	CPT dataset	50	Sorensen&Okkels (2013) and expert judgement	$4.5 + 0.005 \cdot \sigma'_{v0}$	Maximum OCR = 6	$1.15 \cdot \sigma'_{v0}$		1.1	Depends on OCR for Pleistocene clay
BX	Clayey sand and sandy clay	16.9	CPT dataset	50	Sorensen&Okkels (2013) and expert judgement	$4.5 + 0.005 \cdot \sigma'_{v0}$	Maximum OCR = 6	$0.97 \cdot \sigma'_{v0} + 30$		1.1	Clay
BXKO	Clay	14.4	CPT dataset	50	Sorensen&Okkels (2013) and expert judgement	$4.5 + 0.005 \cdot \sigma'_{v0}$	Maximum OCR = 6	$1.15 \cdot \sigma'_{v0}$		1.1	Depends on OCR for Pleistocene clay
BXKO	Clayey sand and sandy clay	16.9	CPT dataset	50	Sorensen&Okkels (2013) and expert judgement	$4.5 + 0.005 \cdot \sigma'_{v0}$	Maximum OCR = 6	$0.97 \cdot \sigma'_{v0} + 30$		1.1	Clay
BXS11	Clay	14.1	CPT dataset	50	Sorensen&Okkels (2013) and expert judgement	2	From NA	$0.38 \cdot \sigma'_{v0} + 12$	From NA	0.5	From NIHO
BXS11	Clayey sand and sandy clay	16	CPT dataset	50	Sorensen&Okkels (2013) and expert judgement	2	From NA	$0.49 \cdot \sigma'_{v0} + 44$	From NA	0.5	Clay from NIHO
BXS12	Clay	14.4	CPT dataset	50	Sorensen&Okkels (2013) and expert judgement	$4.5 + 0.005 \cdot \sigma'_{v0}$	Maximum OCR = 6	$1.15 \cdot \sigma'_{v0}$		1.1	Depends on OCR for Pleistocene clay
BXS12	Clayey sand and sandy clay	16.9	CPT dataset	50	Sorensen&Okkels (2013) and expert judgement	$4.5 + 0.005 \cdot \sigma'_{v0}$	Maximum OCR = 6	$0.97 \cdot \sigma'_{v0} + 30$		1.1	Clay

Strat. unit GeoTOP	Lith. class	Average unit weight wet (kN/m ³)	Based on	Ip	Based on	Average OCR	Based on Kulhawy & Mayne (1990) on CPT dataset & remark	Average Su (kPa)	Based on	K0	Based on
BXWI	Clay	14.4	CPT dataset	50	Sorensen&Okkels (2013) and expert judgement	$4.5+0.005*\sigma'_{v0}$	Maximum OCR = 6	$1.15*\sigma'_{v0}$		1.1	Depends on OCR for Pleistocene clay
BXWI	Clayey sand and sandy clay	16.9	CPT dataset	50	Sorensen&Okkels (2013) and expert judgement	$4.5+0.005*\sigma'_{v0}$	Maximum OCR = 6	$0.97*\sigma'_{v0}+30$		1.1	Clay
DN	Clay	17.6	CPT dataset	30	Sorensen&Okkels (2013)	4	Value for Peelo at 30 m depth	$0.88*\sigma'_{v0}+26$	From PE	1.1	Depends on OCR for Pleistocene clay
DN	Clayey sand and sandy clay	18.1	CPT dataset	30	Sorensen&Okkels (2013)	4	Value for Peelo at 30 m depth	$0.60*\sigma'_{v0}+55$	From PE	1.2	Clay
DR	Clay	14.7	CPT dataset	15	Sorensen&Okkels (2013)	$4.5+0.005*\sigma'_{v0}$	Maximum OCR = 6	$1.15*\sigma'_{v0}$		1.1	Depends on OCR for Pleistocene clay
DR	Clayey sand and sandy clay	16.7	CPT dataset	15	Sorensen&Okkels (2013)	$4.5+0.005*\sigma'_{v0}$	Maximum OCR = 6	$0.97*\sigma'_{v0}+30$		1.2	Clay
DRGI	Clay	14.7	CPT dataset	15	Sorensen&Okkels (2013)	$4.5+0.005*\sigma'_{v0}$	Maximum OCR = 6	$1.15*\sigma'_{v0}$		1.1	Depends on OCR for Pleistocene clay
DRGI	Clayey sand and sandy clay	16.7	CPT dataset	10	TNO-data	$4.5+0.005*\sigma'_{v0}$	Maximum OCR = 6	$0.97*\sigma'_{v0}+30$		1.2	Clay
EE	Clay	14.4	CPT dataset	40	TNO-data	$4.5+0.005*\sigma'_{v0}$	Maximum OCR = 6	$1.15*\sigma'_{v0}$		1.1	Depends on OCR for Pleistocene clay
EE	Clayey sand and sandy clay	17.2	CPT dataset	40	From EE clay	$4.5+0.005*\sigma'_{v0}$	Maximum OCR = 6	$0.97*\sigma'_{v0}+30$		1.3	Clay
NA	Clay	12.9	CPT dataset	30	Skempton and expert judgement	2	Median value	$0.38*\sigma'_{v0}+12$	For all NA	0.5	Constant 0.5 for Holocene clay
NA	Clayey sand and sandy clay	16.2	CPT dataset	30	From NA clay	2	Median value	$0.49*\sigma'_{v0}+44$	For all NA	0.5	Clay
NASC	Clay	12.9	CPT dataset	30	From NA clay	2	Median value	$0.38*\sigma'_{v0}+12$	For all NA	0.5	Constant 0.5 for Holocene clay
NASC	Clayey sand and sandy clay	16.2	CPT dataset	30	From NA clay	2	Median value	$0.49*\sigma'_{v0}+44$	For all NA	0.5	Clay
NAWA	Clay	12.9	CPT dataset	30	From NA clay	2	Median value	$0.38*\sigma'_{v0}+12$	For all NA	0.5	Constant 0.5 for Holocene clay
NAWA	Clayey sand and sandy clay	16.2	CPT dataset	30	From NA clay	2	Median value	$0.49*\sigma'_{v0}+44$	For all NA	0.5	Clay
NAWO	Clay	12.9	CPT dataset	30	From NA clay	2	Median value	$0.38*\sigma'_{v0}+12$	For all NA	0.5	Constant 0.5 for Holocene clay

Strat. unit GeoTOP	Lith. class	Average unit weight wet (kN/m ³)	Based on	Ip	Based on	Average OCR	Based on Kulhawy & Mayne (1990) on CPT dataset & remark	Average Su (kPa)	Based on	K0	Based on
NAWO	Clayey sand and sandy clay	16.2	CPT dataset	30	From NA clay	2	Median value	$0.49 \cdot \sigma'_{v0} + 44$	For all NA	0.5	Clay
NAZA	Clay	12.9	CPT dataset	30	From NA clay	2	Median value	$0.38 \cdot \sigma'_{v0} + 12$	For all NA	0.5	Holocene clay
NAZA	Clayey sand and sandy clay	16.2	CPT dataset	30	From NA clay	2	Median value	$0.49 \cdot \sigma'_{v0} + 44$	For all NA	0.5	Clay
NIBA	Clay	15	CPT dataset	50	From NIHO clay	2	Median value	$0.38 \cdot \sigma'_{v0} + 12$	From NA	0.7	NIBA special case $k_0=0.7$ for all lithologies
NIBA	Clayey sand and sandy clay	17	CPT dataset	50	From NIBA clay	2	Median value	$0.49 \cdot \sigma'_{v0} + 44$	From NA	0.7	NIBA special case $k_0=0.7$ for all lithologies
NIGR	Clay	14.1	CPT dataset	50	From NIHO clay	2	Median value	$0.38 \cdot \sigma'_{v0} + 12$	From NA	0.5	Holocene clay
NIGR	Clayey sand and sandy clay	16	CPT dataset	50	From NIHO clay	2	Median value	$0.49 \cdot \sigma'_{v0} + 44$	From NA	0.5	Clay
NIHO	Clay	14.1	CPT dataset	50	Skempton and expert judgement	2	Median value	$0.38 \cdot \sigma'_{v0} + 12$	From NA	0.5	Holocene clay
NIHO	Clayey sand and sandy clay	16	CPT dataset	50	From NIHO clay	2	Median value	$0.49 \cdot \sigma'_{v0} + 44$	From NA	0.5	Clay
NINB	Clay	14.1	CPT dataset	50	From NIHO clay	2	Median value	$0.38 \cdot \sigma'_{v0} + 12$	From NA	0.5	Holocene clay
NINB	Clayey sand and sandy clay	16	CPT dataset	50	From NIHO clay	2	Median value	$0.49 \cdot \sigma'_{v0} + 44$	From NA	0.5	Clay
PE	Clay	17.6	CPT dataset	50	Sorensen&Okkels (2013) and TNO-Data	$6-0.005 \cdot \sigma'_{v00}$	Minimum OCR = 4	$0.88 \cdot \sigma'_{v0} + 26$		1.1	Depends on OCR for Pleistocene clay
PE	Clayey sand and sandy clay	18.1	CPT dataset	30	Sorensen&Okkels (2013)	$6-0.005 \cdot \sigma'_{v00}$	Minimum OCR = 4	$0.60 \cdot \sigma'_{v0} + 55$		1.2	Clay
UR	Clay	17.6	CPT dataset	30	Sorensen&Okkels (2013) and TNO-Data	4	Value for Peelo at 30 m depth	$0.88 \cdot \sigma'_{v0} + 26$	From PE	1.1	Depends on OCR for Pleistocene clay
UR	Clayey sand and sandy clay	17.6	CPT dataset	30	Sorensen&Okkels (2013)	4	Value for Peelo at 30 m depth	$0.60 \cdot \sigma'_{v0} + 55$	From PE	1.4	Clay
URTY	Clay	17.6	CPT dataset	30	Sorensen&Okkels (2013) and TNO-Data	4	Value for Peelo at 30 m depth	$0.88 \cdot \sigma'_{v0} + 26$	From PE	1.1	Depends on OCR for Pleistocene clay

Strat. unit GeoTOP	Lith. class	Average unit weight wet (kN/m ³)	Based on	Ip	Based on	Average OCR	Based on Kulhawy & Mayne (1990) on CPT dataset & remark	Average Su (kPa)	Based on	K0	Based on
URTY	Clayey sand and sandy clay	17.6	CPT dataset	30	Sorensen&Okkels (2013)	4	Value for Peelo at 30 m depth	$0.60 \cdot \sigma'_{v0} + 55$	From PE	1.4	Clay
PZ	Clay deep	21	Expert judgement	30	Sorensen&Okkels (2013)	2	Expert judgement	$0.88 \cdot \sigma'_{v0} + 26$	From PE	1	Uncertain for deep clay, assume K0=1
PZWA	Clay deep	21	Expert judgement	30	Sorensen&Okkels (2013)	2	Expert judgement	$0.88 \cdot \sigma'_{v0} + 26$	From PE	1	Uncertain for deep clay, assume K0=1
NUOT	Clay deep	21	Expert judgement	40	Sorensen&Okkels (2013) and Rijkers <i>et al.</i> (1998)	2	Expert judgement	$0.88 \cdot \sigma'_{v0} + 26$	From PE	1	Uncertain for deep clay, assume K0=1
NUOT	Clayey sand deep	21	Expert judgement	40	Sorensen&Okkels (2013) and Rijkers <i>et al.</i> (1998)	2	Expert judgement	325	Rijkers <i>et al.</i> (1998)	1	Uncertain for deep clay, assume K0=1
NUBA	Clayey sand deep	21	Expert judgement	40	Sorensen&Okkels (2013) and Rijkers <i>et al.</i> (1998)	2	Expert judgement	325	Rijkers <i>et al.</i> (1998)	1	Uncertain for deep clay, assume K0=1

Table V.5. Geomechanical parameters for sand. D50 = median grain size; Cu =coefficient of uniformity.
(see Table V.1 for codes of stratigraphic units).

Strat. unit GeoTOP	Lith. Class	Average unit weight wet (kN/m ³)	Based on	K0	Based on	Whole sample D50 (mm)	Whole sample Median Cu	Based on
AAOP	Fine sand	18.4	CPT dataset	0.5	Holocene sand	0.0803	5.53	Bosch <i>et al.</i> (2014)
AAOP	Medium coarse sand	21	Expert judgement	0.5	Holocene sand	0.18818	3.71	Bosch <i>et al.</i> (2014)
AAOP	Coarse sand gravel and shells	21	Expert judgement	0.5	Holocene sand	0.23233	12.34	Bosch <i>et al.</i> (2014)
AP	Fine sand	19.6	CPT dataset	1	Older than Holocene sand	0.11474	1.86	From PE
AP	Medium coarse sand	21	Expert judgement	1	Older than Holocene sand	0.19803	1.94	From PE
AP	Coarse sand gravel and shells	21	Expert judgement	1	Older than Holocene sand	0.5283	7.14	Estimate from deep drillings in Groningen
BX	Fine sand	19.4	CPT dataset	1	Older than Holocene sand	0.11524	2.34	Bosch <i>et al.</i> (2014)
BX	Medium coarse sand	21	Expert judgement	1	Older than Holocene sand	0.19477	2.23	Bosch <i>et al.</i> (2014)
BX	Coarse sand gravel and shells	21	Expert judgement	1	Older than Holocene sand	0.36272	1.99	Bosch <i>et al.</i> (2014)
BXKO	Fine sand	19.4	CPT dataset	1	Older than Holocene sand	0.11524	2.34	From BX
BXKO	Medium coarse sand	21	Expert judgement	1	Older than Holocene sand	0.19477	2.23	From BX
BXKO	Coarse sand gravel and shells	21	Expert judgement	1	Older than Holocene sand	0.36272	1.99	From BX
BXSI1	Fine sand	18.8	CPT dataset	1	Older than Holocene sand	0.11399	2.03	From NA
BXSI1	Medium coarse sand	21	Expert judgement	1	Older than Holocene sand	0.18347	1.75	From NA
BXSI1	Coarse sand gravel and shells	21	Expert judgement	1	Older than Holocene sand	0.30837	1.74	From NA
BXSI2	Fine sand	19.4	CPT dataset	1	Older than Holocene sand	0.11524	2.34	From BX
BXSI2	Medium coarse sand	21	Expert judgement	1	Older than Holocene sand	0.19477	2.23	From BX
BXSI2	Coarse sand gravel and shells	21	Expert judgement	1	Older than Holocene sand	0.36272	1.99	From BX
BXWI	Fine sand	19.4	CPT dataset	1	Older than Holocene sand	0.12113	1.94	Bosch <i>et al.</i> (2014)
BXWI	Medium coarse sand	21	Expert judgement	1	Older than Holocene sand	0.18135	2.44	Bosch <i>et al.</i> (2014)
BXWI	Coarse sand gravel and shells	21	Expert judgement	1	Older than Holocene sand	0.36272	1.99	From BX
DN	Fine sand	19.6	CPT dataset	1	Older than Holocene sand	0.13223	2.27	Bosch <i>et al.</i> (2014)
DN	Medium coarse sand	21	Expert judgement	1	Older than Holocene sand	0.19647	2.21	Bosch <i>et al.</i> (2014)
DN	Coarse sand gravel and shells	21	Expert judgement	1	Older than Holocene sand	0.33565	1.88	Bosch <i>et al.</i> (2014)
DR	Fine sand	19.5	CPT dataset	1	Older than Holocene sand	0.13163	2.11	From DRSC
DR	Medium coarse sand	20.6	CPT dataset	1	Older than Holocene sand	0.2387	1.86	From DRSC
DR	Coarse sand gravel and shells	21	Expert judgement	1	Older than Holocene sand	0.38726	2.35	From DRSC

Strat. unit GeoTOP	Lith. Class	Average unit weight wet (kN/m ³)	Based on	K0	Based on	Whole sample D50 (mm)	Whole sample Median Cu	Based on
DRGI	Fine sand	19.5	CPT dataset	1	Older than Holocene sand	0.13163	2.11	From DRSC
DRGI	Medium coarse sand	20.6	CPT dataset	1	Older than Holocene sand	0.1743	8.85	Only medium sand known for DRGI
DRGI	Coarse sand gravel and shells	21	Expert judgement	1	Older than Holocene sand	0.38726	2.35	From DRSC
EE	Fine sand	19.4	CPT dataset	1	Older than Holocene sand	0.10824	1.76	Bosch <i>et al.</i> (2014)
EE	Medium coarse sand	21	Expert judgement	1	Older than Holocene sand	0.17146	2.57	Bosch <i>et al.</i> (2014)
EE	Coarse sand gravel and shells	21	Expert judgement	1	Older than Holocene sand	0.37613	2.88	Bosch <i>et al.</i> (2014)
NA	Fine sand	18.8	CPT dataset	0.5	Holocene sand	0.11399	2.03	Bosch <i>et al.</i> (2014)
NA	Medium coarse sand	21	Expert judgement	0.5	Holocene sand	0.18347	1.75	Bosch <i>et al.</i> (2014)
NA	Coarse sand gravel and shells	21	Expert judgement	0.5	Holocene sand	0.30837	1.74	Bosch <i>et al.</i> (2014)
NASC	Fine sand	18.8	CPT dataset	0.5	Holocene sand	0.11399	2.03	From NA
NASC	Medium coarse sand	21	Expert judgement	0.5	Holocene sand	0.18347	1.75	From NA
NASC	Coarse sand gravel and shells	21	Expert judgement	0.5	Holocene sand	0.30837	1.74	From NA
NAWA	Fine sand	18.8	CPT dataset	0.5	Holocene sand	0.11399	2.03	From NA
NAWA	Medium coarse sand	21	Expert judgement	0.5	Holocene sand	0.18347	1.75	From NA
NAWA	Coarse sand gravel and shells	21	Expert judgement	0.5	Holocene sand	0.30837	1.74	From NA
NAWO	Fine sand	18.8	CPT dataset	0.5	Holocene sand	0.11399	2.03	From NA
NAWO	Medium coarse sand	21	Expert judgement	0.5	Holocene sand	0.18347	1.75	From NA
NAWO	Coarse sand gravel and shells	21	Expert judgement	0.5	Holocene sand	0.30837	1.74	From NA
NAZA	Fine sand	18.8	CPT dataset	0.5	Holocene sand	0.11399	2.03	From NA
NAZA	Medium coarse sand	21	Expert judgement	0.5	Holocene sand	0.18347	1.75	From NA
NAZA	Coarse sand gravel and shells	21	Expert judgement	0.5	Holocene sand	0.30837	1.74	From NA
NIBA	Fine sand	18.3	CPT dataset	0.7	NIBA special case K0=0.7 for all lithologies	0.11399	2.03	From NA
NIBA	Medium coarse sand	20	CPT dataset	0.7	NIBA special case K0=0.7 for all lithologies	0.18347	1.75	From NA
NIBA	Coarse sand gravel and shells	20	CPT dataset	0.7	NIBA special case K0=0.7 for all lithologies	0.30837	1.74	From NA
NIGR	Fine sand	18.8	CPT dataset	0.5	Holocene sand	0.11399	2.03	From NA
NIGR	Medium coarse sand	21	Expert judgement	0.5	Holocene sand	0.18347	1.75	From NA
NIGR	Coarse sand gravel and shells	21	Expert judgement	0.5	Holocene sand	0.30837	1.74	From NA
NIHO	Fine sand	18.8	CPT dataset	0.5	Holocene sand	0.11399	2.03	From NA

Strat. unit GeoTOP	Lith. Class	Average unit weight wet (kN/m ³)	Based on	K0	Based on	Whole sample D50 (mm)	Whole sample Median Cu	Based on
NIHO	Medium coarse sand	21	Expert judgement	0.5	Holocene sand	0.18347	1.75	From NA
NIHO	Coarse sand gravel and shells	21	Expert judgement	0.5	Holocene sand	0.30837	1.74	From NA
NINB	Fine sand	18.8	CPT dataset	0.5	Holocene sand	0.11399	2.03	From NA
NINB	Medium coarse sand	21	Expert judgement	0.5	Holocene sand	0.18347	1.75	From NA
NINB	Coarse sand gravel and shells	21	Expert judgement	0.5	Holocene sand	0.30837	1.74	From NA
PE	Fine sand	19.6	CPT dataset	1	Older than Holocene sand	0.11674	1.84	Bosch <i>et al.</i> (2014)
PE	Medium coarse sand	21	Expert judgement	1	Older than Holocene sand	0.19803	1.94	Bosch <i>et al.</i> (2014)
PE	Coarse sand gravel and shells	21	Expert judgement	1	Older than Holocene sand	0.46823	2.62	Bosch <i>et al.</i> (2014)
UR	Fine sand	19.7	CPT dataset	1	Older than Holocene sand	0.11674	1.84	From PE
UR	Medium coarse sand	21	Expert judgement	1	Older than Holocene sand	0.19803	1.94	From PE
UR	Coarse sand gravel and shells	21	Expert judgement	1	Older than Holocene sand	0.46823	2.62	From PE
URTY	Fine sand	19.7	CPT dataset	1	Older than Holocene sand	0.11961	2.14	Bosch <i>et al.</i> (2014)
URTY	Medium coarse sand	21	Expert judgement	1	Older than Holocene sand	0.22028	2.04	Bosch <i>et al.</i> (2014)
URTY	Coarse sand gravel and shells	21	Expert judgement	1	Older than Holocene sand	0.43259	1.98	Bosch <i>et al.</i> (2014)
PZWA	Sand deep	21	Expert judgement	1	Older than Holocene sand	0.25	4.08	Estimate from deep drillings in Groningen
NUOT	Sand deep	21	Expert judgement	1	Older than Holocene sand	0.156	2.61	Estimate from deep drillings in Groningen

APPENDIX VI

Analysis of TNO accelerograph recordings

VI.1 Introduction

A large network of digital accelerographs has been installed in the Groningen gas field region by TNO on behalf of NAM. The instruments are mainly installed in private houses with a few more in public buildings. The network now comprises of nearly 400 instruments and hence potentially could provide an extremely valuable database for the derivation of GMMs. However, most of the instruments are not installed at ground-level but rather mounted on brackets on walls and may therefore be influenced by structural response. Additionally, an operator-imposed PGV threshold of 0.1 cm/s has limited significantly the availability of records so far. Work is now underway to ascertain with what degree of confidence the recorded data can be assumed to represent the actual ground-motions, as well as to ensure that the PGV threshold will not restrict the production of records during future earthquakes.

VI.2. Accelerograph network

VI.2.1 Accelerograph locations and characteristics

The operation of the first NAM-TNO instruments started in 2014. Initially, 200 accelerometers were installed, 180 in homes and 20 in public buildings, followed by another 100 installed in houses in 2015. By October of 2016, 53 more had been installed, with plans to raise the total number of installed sensors to 400 in the subsequent months. All sensors are installed after an open public invitation by NAM, under which Groningen province residents volunteer to have a sensor installed in their own house, in exchange for having unique access to the real-time recording streams of that sensor.

The locations of the 353 instruments from which records have been obtained to date are shown in Figure VI.1, but the exact coordinates cannot be disclosed in order to protect the confidentiality of the participants of the program. The network consists of GeoSig digital accelerographs, mounted on metal brackets which are pinned on walls in either the ground floor, the basement or the crawl space that exists just underneath the ground floor slab. Examples are shown in Figure VI.2. Each accelerograph is always connected to a recorder installed nearby.

The accelerographs are set up so that they record motions continuously and transmit them to their recorder. At the end of every minute of the hour, for each of the three components, the recorder performs a series of operations on the acceleration trace recorded in that minute, including, a baseline correction, filtering with a low-cut frequency of 0.8 Hz and integration, so that the velocity trace is obtained. Then, the PGV value is recorded and sent to the central network monitoring system. These minutely reported PGV values are often referred to by the network operator as “heartbeats”.

If any of the three PGV values obtained at each station exceed the threshold of 0.1 cm/s, the 10s preceding and the 20s following the time at which the largest of the three PGV values was recorded, are saved as a record and transmitted to the operator, TNO. The triggering of

three sensors is then flagged as the occurrence of an event. In the case that a recording is not triggered, the acceleration traces are stored in the recorder buffer for a period of a few days and then deleted. They can, however, be retrieved manually by accessing the data stored in each recorder. In that case, the record consists of the accelerations recorded in the minute of the hour in which peak acceleration occurred, irrespective of the moment it occurred within that minute.

Records are available by TNO in CSV format. The sampling rate is 250 Hz, which corresponds to time steps of 0.004s. More information on how the network operation is available from Borsje & Langius (2015).

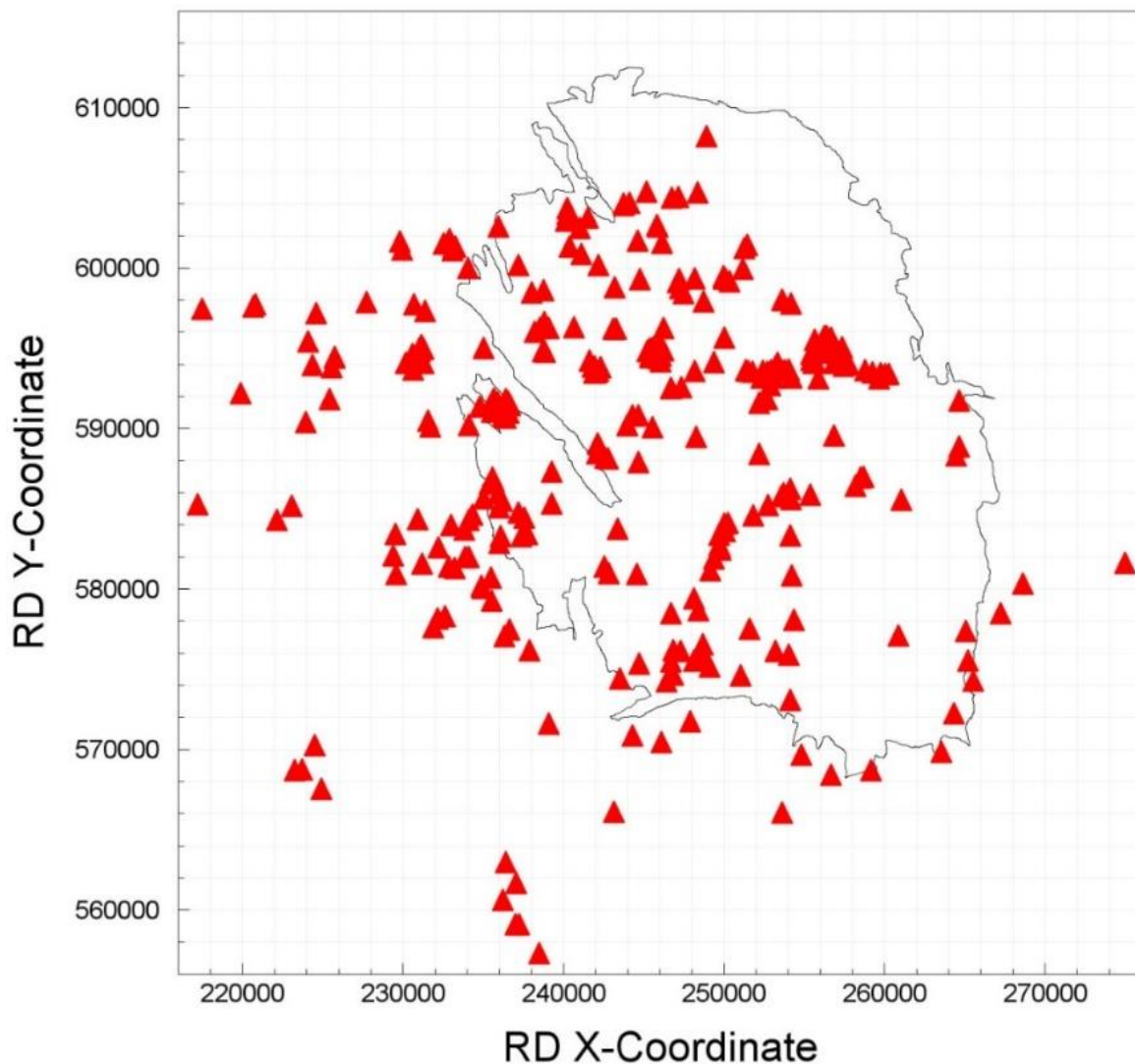


Figure VI.1 Location of the TNO sensors in and around the Groningen field.



Figure VI.2 Sensors installed on the walls at: crawl space level (top), basement level (middle) and ground floor level (bottom). The large blue box of the lowermost figure is the recorder.

VI.2.2 Events recorded to date

A total of five earthquakes of M_L greater than 2.5 have occurred while the network has been operational, listed in Table VI.1. The first event recorded was the 30 September 2014 M_L 2.8 Garmerwolde earthquake (EQ-18). Table VI.2 reports the number of stations from which accelerograms were obtained in each earthquake, as well as the distances of the closest and most distant recording for each event. The ID numbers match those used for the same earthquakes by Ntinalexis *et al.* (2016).

Table VI.1. Earthquakes of $M_L > 2.5$ producing records from the household network

EQ ID	Date			Time		M	WGS84		RD Coordinates		Location
	Y	M	D	H	M		N°	E°	X (m)	Y (m)	
18	2014	IX	30	11	42	2.8	53.258	6.655	239,565	586,336	Garmerwolde
19	2014	XI	5	1	12	2.9	53.374	6.678	240,890	599,307	Zandeweer
20	2014	XII	30	2	37	2.8	53.208	6.728	244,561	580,898	Woudbloem
21	2015	I	6	6	55	2.7	53.324	6.678	246,987	593,800	Wirdum
22	2015	IX	30	05	51	3.1	53.258	6.800	251,603	584,016	Hellum

Table VI.2 Numbers and features of records from each earthquake

EQ ID	M	Recs	Tot	Min. R_{epi} (km)	Max. R_{epi} (km)
18	2.8	42	42	1.14	12.07
19	2.9	89	131	1.38	16.50
20	2.8	22	153	1.75	14.10
21	2.7	37	190	0.93	6.25
22	3.1	36	216	0.63	13.55

Additionally, for the purposes of the comparisons presented in Section VI.3.3, the records from three smaller events that occurred in September and November of 2016 have been retrieved manually from the recorders (as very few of them triggered a recording). These earthquakes, as well as the locations and magnitudes of each, are listed in Table VI.3. Table VI.4 reports the number of stations from which accelerograms were retrieved in each earthquake.

Table VI.3. Earthquakes of $M_L < 2.5$ from which records have been manually retrieved

EQ ID	Date			Time		M	WGS84		RD Coordinates		Location
	Y	M	D	H	M		N°	E°	X (m)	Y (m)	
C1	2016	IX	02	13	16	2.1	53.218	6.844	252,307	582,249	Schilwolde
C2	2016	XI	01	00	12	1.9	53.301	6.807	249,653	591,435	Wirdum
C3	2016	XI	01	00	57	2.2	53.306	6.809	249,776	591,994	Wirdum

Table VI.4. Numbers and features of records from each earthquake

EQ ID	M	Recs	Tot	Min. R_{epi} (km)	Max. R_{epi} (km)
C1	2.1	297	297	2.11	49.35
C2	1.9	302	599	2.40	58.52
C3	2.2	301	900	2.18	59.07

The locations of the epicentres of all eight earthquakes are shown in Figure VI.3. The corresponding magnitude-distance distributions are presented in Figure VI.4. The locations of the stations from which records have been obtained for each earthquake are presented in Figures VI.5-12. A distinction is made in Figures VI.5-9 (corresponding to the five $M_L > 2.5$ earthquakes) between the stations where a recording was triggered and those where it was not. All records from the smaller earthquakes were retrieved manually, so the same

distinction is not made in Figures VI.10-12. In general, for each earthquake, stations from which there are no available records are marked in green. The increasing number of operational stations from 2014 and over time, in both the KNMI and the household network, can also be observed in Figures VI.5-12.

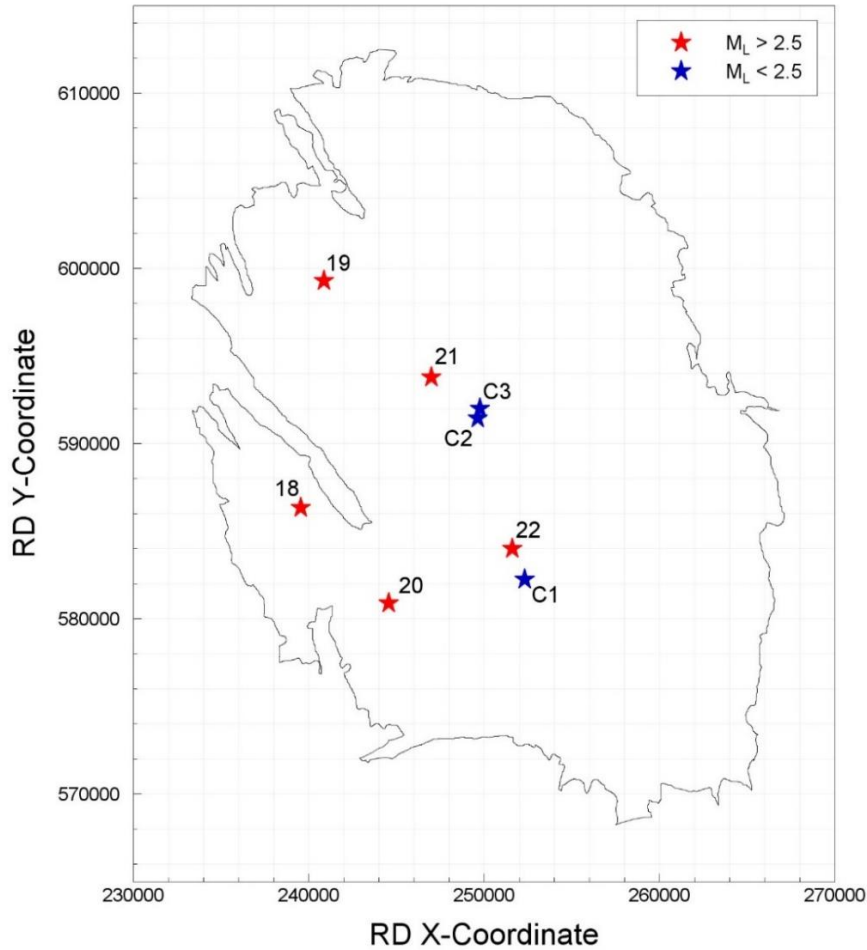


Figure VI.3 Epicentres (*stars*) of the eight earthquakes recorded by the household network

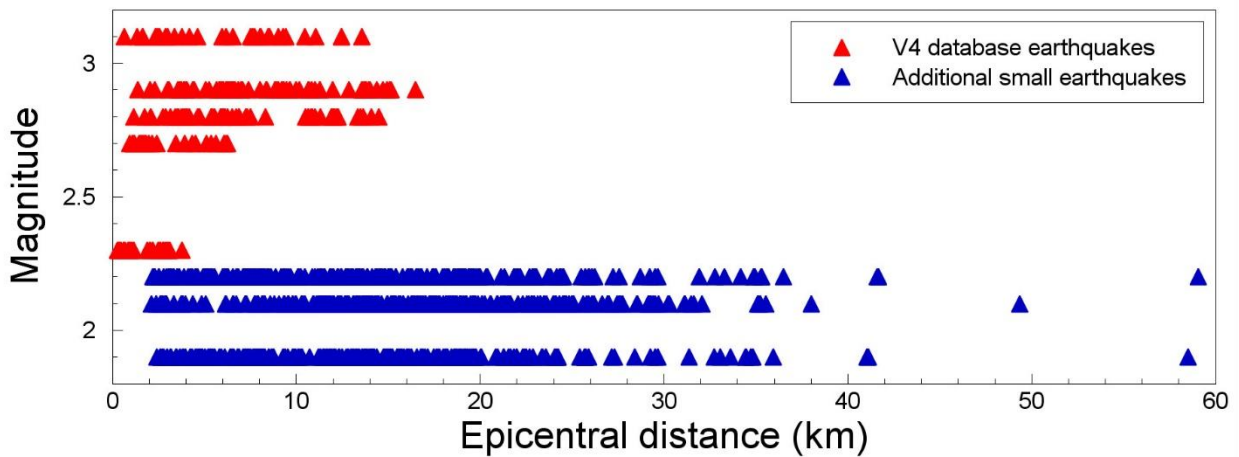


Figure VI.4 Magnitude-distance distribution of the eight earthquakes recorded by the household network

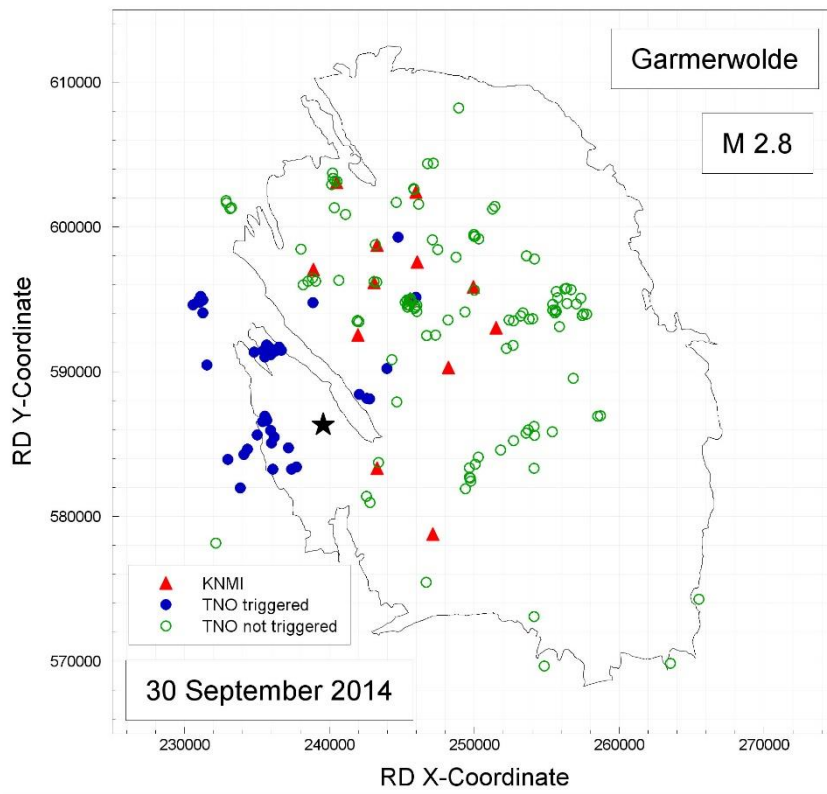


Figure VI.5. Epicentre (*star*) and stations recording EQ-18.

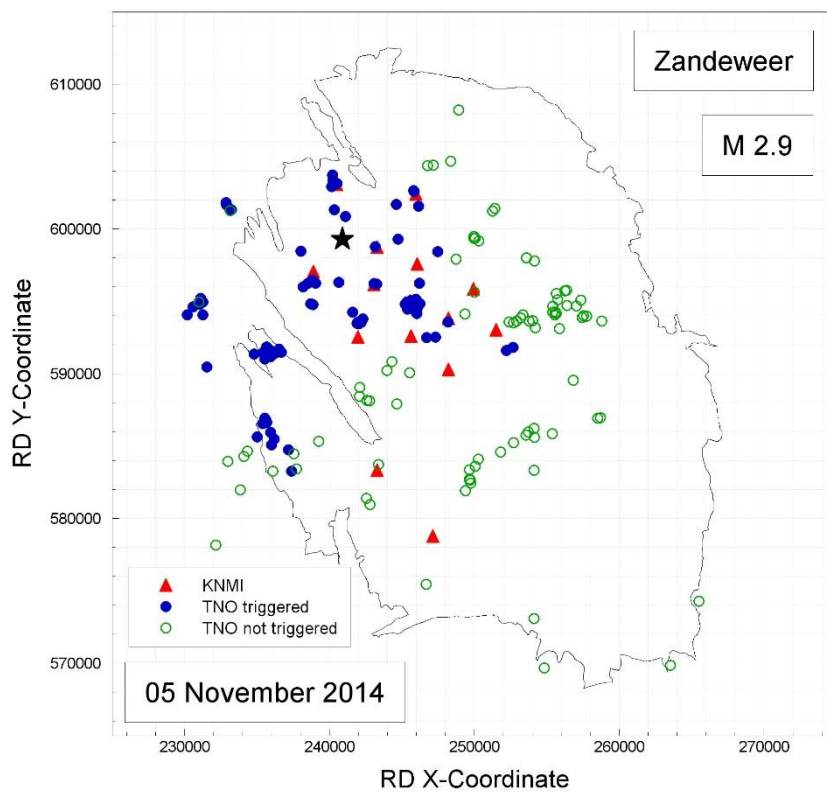


Figure VI.6. Epicentre (*star*) and stations recording EQ-19.

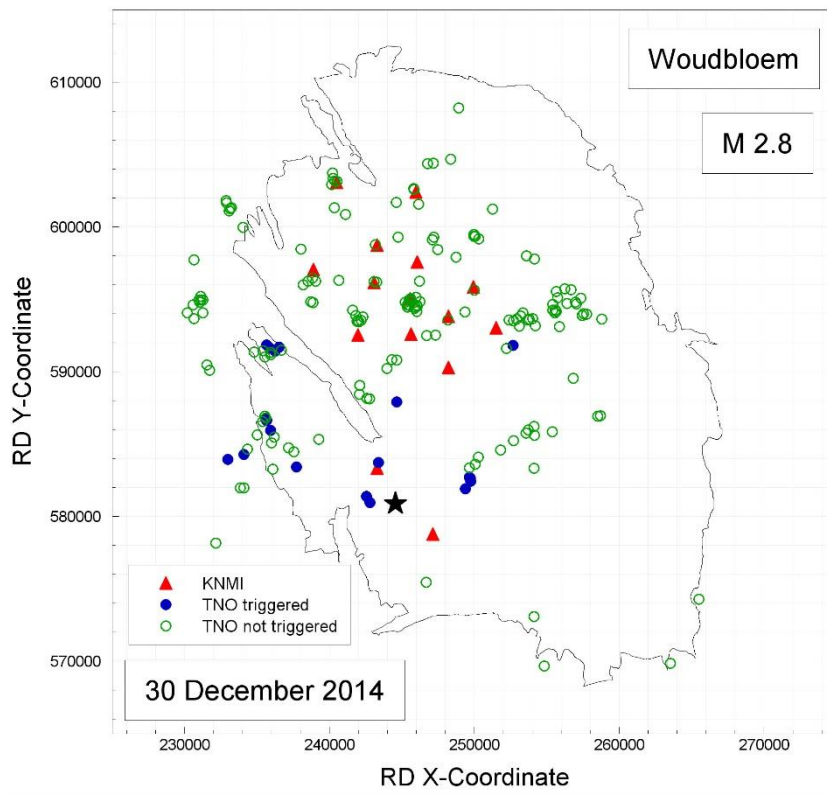


Figure VI.7. Epicentre (*star*) and stations recording EQ-20.

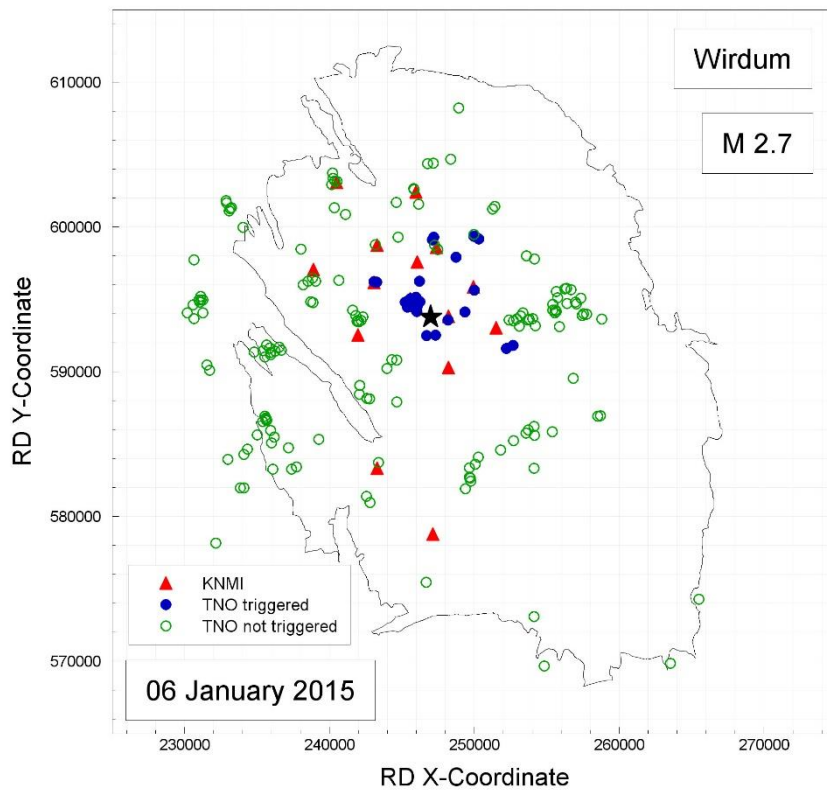


Figure VI.8. Epicentre (*star*) and stations recording EQ-21.

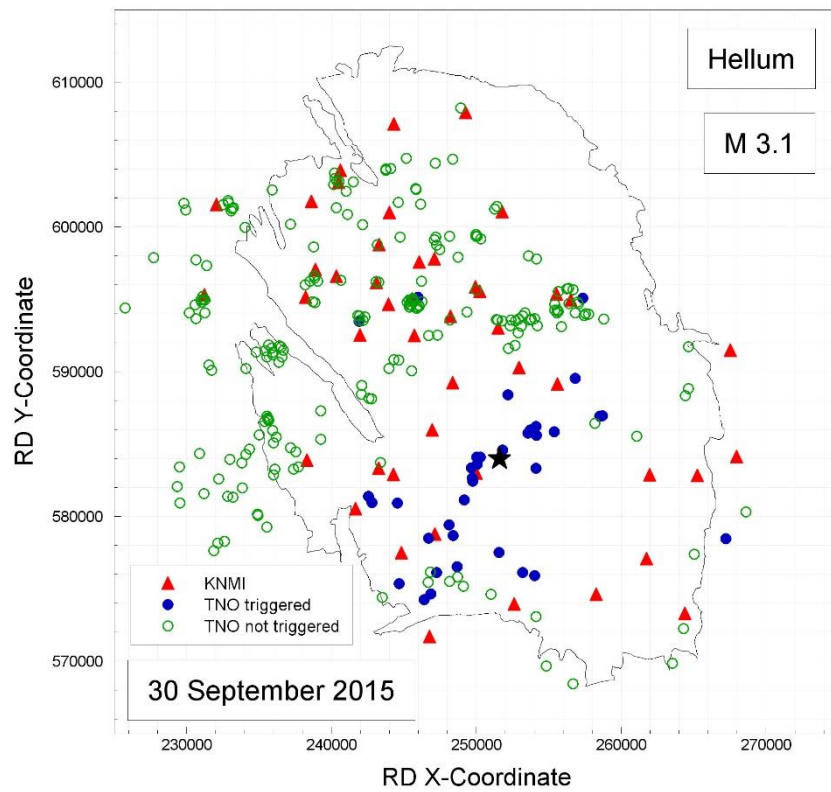


Figure VI.9. Epicentre (*star*) and stations recording EQ-22.

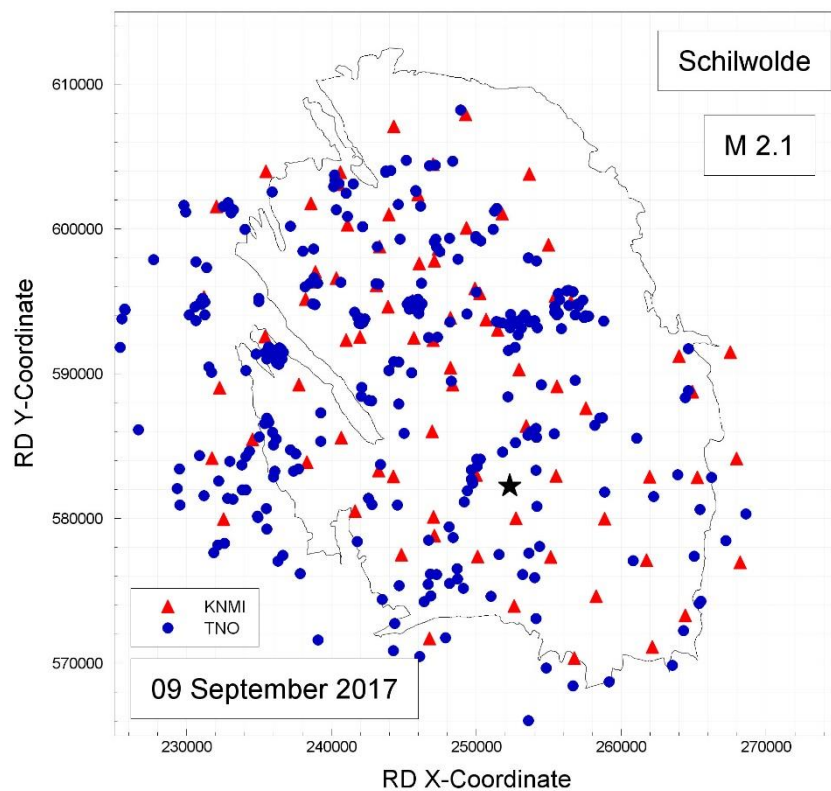


Figure VI.10. Epicentre (*star*) and stations recording EQ-C1. The records from the household network (TNO) were retrieved manually hence the records from the entire network are available.

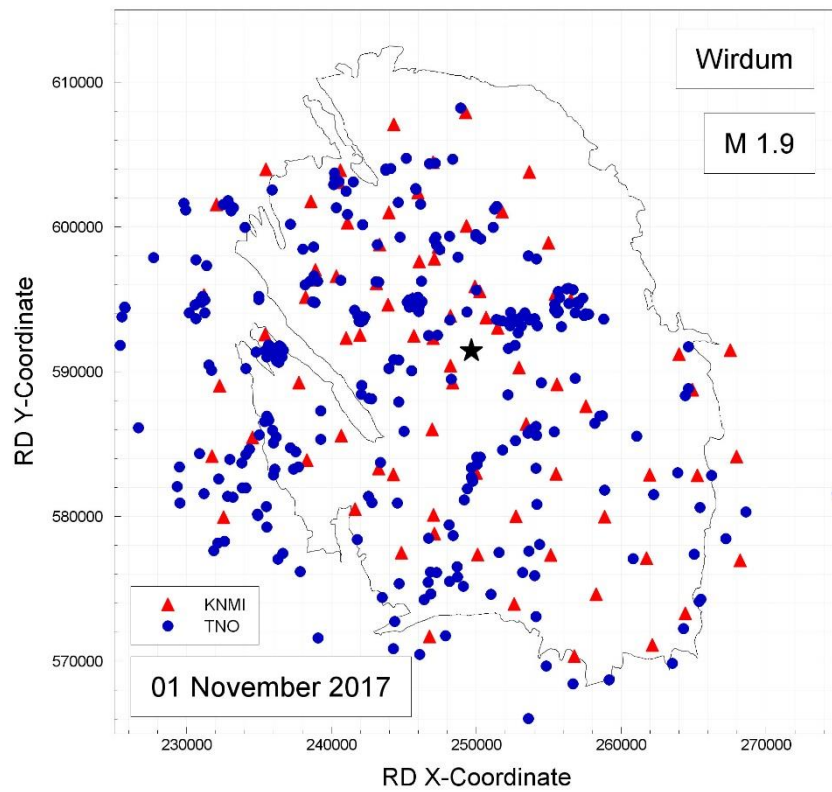


Figure VI.11. Epicentre (*star*) and stations recording EQ-C2. The records from the household network (TNO) were retrieved manually hence the records from the entire network are available.

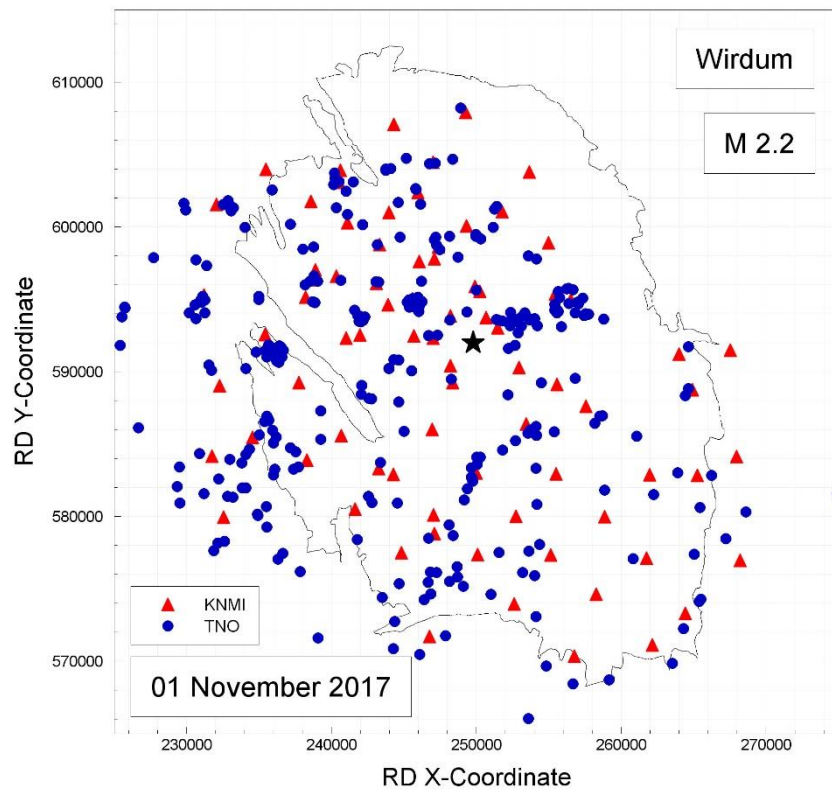


Figure VI.12. Epicentre (*star*) and stations recording EQ-C3. The records from the household network (TNO) were retrieved manually hence the records from the entire network are available.

VI.3. Uncertainty concerning usability

The first household network records started becoming available at the end of 2014, during the development of the V1 Groningen GMPEs, although it was decided not to incorporate these records in the database used for the GMPE derivation (Bommer *et al.*, 2015a). The spectral accelerations recorded were compared to the V0 predictions and to the available spectral accelerations recorded by the KNMI network (Figure VI.13), in order to examine the compatibility of the household network recordings to the KNMI recordings. At the time, the records available from the household network were already twice as many as those available from the KNMI network, with ten times more accelerographs in operation. Therefore, the use of the household network could already provide a significant increase in the data available for GMPE/GMM development for Groningen.

However, the comparison shows that the motions recorded by the household network are significantly stronger than the KNMI-recorded motions, particularly in longer distances. Two features of the instrument installations, shown in Figure VI.2, have been identified as possible causes of this difference namely (a), the robustness of the connection of the brackets to the walls and most importantly (b), the height at which the bracket-sensor set is placed on the wall which could introduce influence of structural response in the records (Bommer *et al.*, 2015a).

Subsequently, the existence of the PGV threshold of 0.1 cm/s was made known and identified as another important reason for the difference observed in Figure VI.13, since, due to the threshold, intermediate and weaker records from epicentral distances further than 5 km were lost. Even in this case, however, the installation features of the household network remain very different from the international standards on ground-motion recording and therefore the usability of the records must be confirmed before they are incorporated in future GMPE/GMM databases.

Two lines of work are currently underway to examine the usability of the records and the extent to which their installation characteristics influence them. The first, discussed in Sections VI.3.1 and VI.3.2, involves the installation of additional sensors in close proximity to existing ones albeit in a manner following more closely the international ground-motion recording standards and the installation of sensors in the LNEC shake table test that will take place in early May. Records obtained from these exercises will then be compared and the degree of structural influence will be identified. The second line of work, discussed in Section VI.3.3, involves the comparison of the patterns of the ground-motions recorded by the two networks with respect to epicentral distance and the removal of the 0.1 cm/s PGV threshold which is limiting the available number of records.

VI.3.1 Additional installations on houses

The first exercise that was proposed to determine the usability of the household network recordings involved installing two additional accelerographs in a sample of houses of the

network. The first new accelerograph would be installed firmly on the floor as close as possible to the existing one, while the second one would be placed on a small concrete slab in the garden, resembling free-field conditions more closely, all three in the same orientation. The accelerographs installed would be identical to those used in the household network.

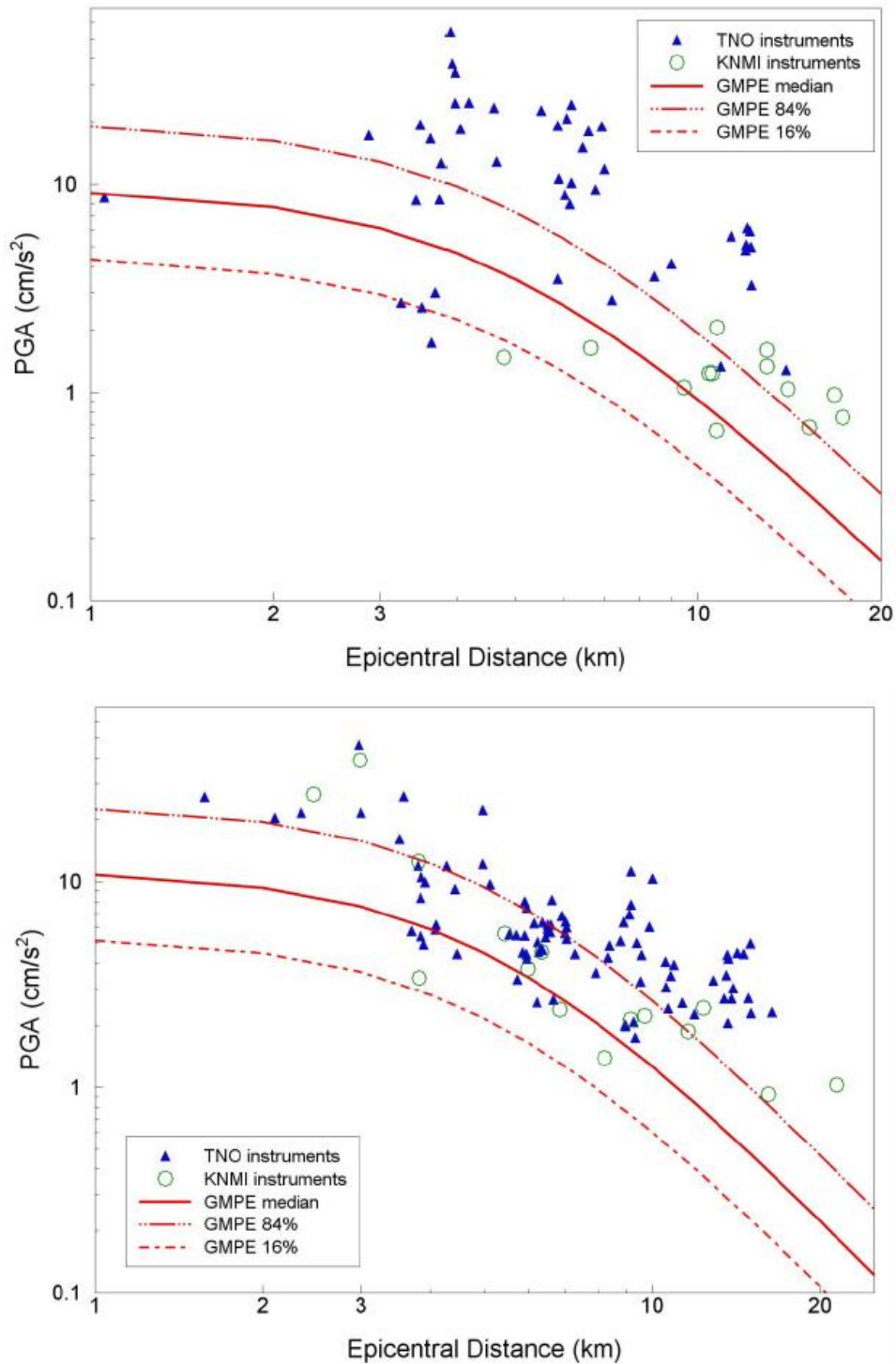


Figure VI.13. Comparison of the geometric mean PGA values recorded by the TNO and the KNMI networks from the M_L 2.8 Garmerwolde (EQ-18, upper) and the M_L 2.9 Zandweer (EQ-19, lower) earthquakes and the median, 16-percentile, and 84-percentile predictions from the Version 0 GMPEs of Bommer & Dost (2014), as a function of epicentral distance (Bommer *et al.*, 2015a)

Then, records produced by the three accelerographs during a future earthquake would be compared; the comparison of the records from the sensor that is on the wall with those from the sensor that is on the floor would lead to identifying the effect of the wall, while comparing the latter records to records from the sensor in the garden would in turn lead to identifying the effect of the house itself. Thus, it would be possible to establish a connection between the records made in the conditions of the household network to free-field records.

Extensive work has been carried out between NAM and TNO in selecting a sample of houses for this exercise; 20 houses were finally selected in July of 2016. The criteria for the selection include house type (terrace, semi-terrace and detached) and part of the structure where the sensor is located (basement, ground floor crawl space and ground floor) so that the possible effect of these conditions can be studied as well. The sample of stations has been selected in the vicinity of Loppersum, which is the centre of the compaction bowl in the Groningen field and the area in the field where greatest seismicity is expected and has been observed to be more frequent. This choice was made in order to increase the probability that recordings of larger amplitudes and good quality will be obtained from the sample during future events.

A similar exercise has already been conducted in the United States. In order to allow development of fully non-ergodic ground-motion models, the necessary spatial density of recorded ground-motions will be obtained by embedding accelerographs in energy smart meters. This is a faster, cheaper and legally easier way to install a large array of accelerographs than installing them as a separate instrument set. Similarly to the household network sensors, however, smart meters are not located on the ground but at a height on walls. In order to perform the same test, the team supervising the program, which includes Professor Norm Abrahamson and Professor Richard Nigbor (to both of whom we are very grateful for providing this information) have installed a pair of these accelerographs (Figure VI.14), at the height of a smart meter and on the ground below. The differences in the Fourier spectral frequency content of what is being recorded are shown in Figure VI.15 and are significant for all frequencies greater than 10 Hz.

A crucial factor to the success of this installation program is the cooperativeness of residents and their willingness to participate and allow the installations of more sensors in their houses. There have been concerns that residents would be hesitant to agree to those installations, particularly concerning the placement of a sensor on a concrete slab on their garden. This exercise has therefore been frozen and an alternative exercise is proceeding, whereby the sensors installed will be much smaller geophones from the new portable geophone network that NAM is using.

The details and goals remain identical to those of the original plan, with only two differences. The first difference is that 25 houses were selected instead of 20, and the second difference is that a three geophones must be installed instead of the two. The third geophone must be installed next to the existing GeoSig accelerograph on the wall, so that the differences in the records due to the difference in the sensors can be accounted for as well. This installation program is, to this date, proceeding and in the stage where residents are being contacted and installation permits are being secured, with the geophones being ready for installation.



Figure VI.14. Installation of an EpiSensor accelerograph (*black*) at smart meter height and on the ground below (*image courtesy of Professor Norm Abrahamson and Professor Richard Nigbor*)

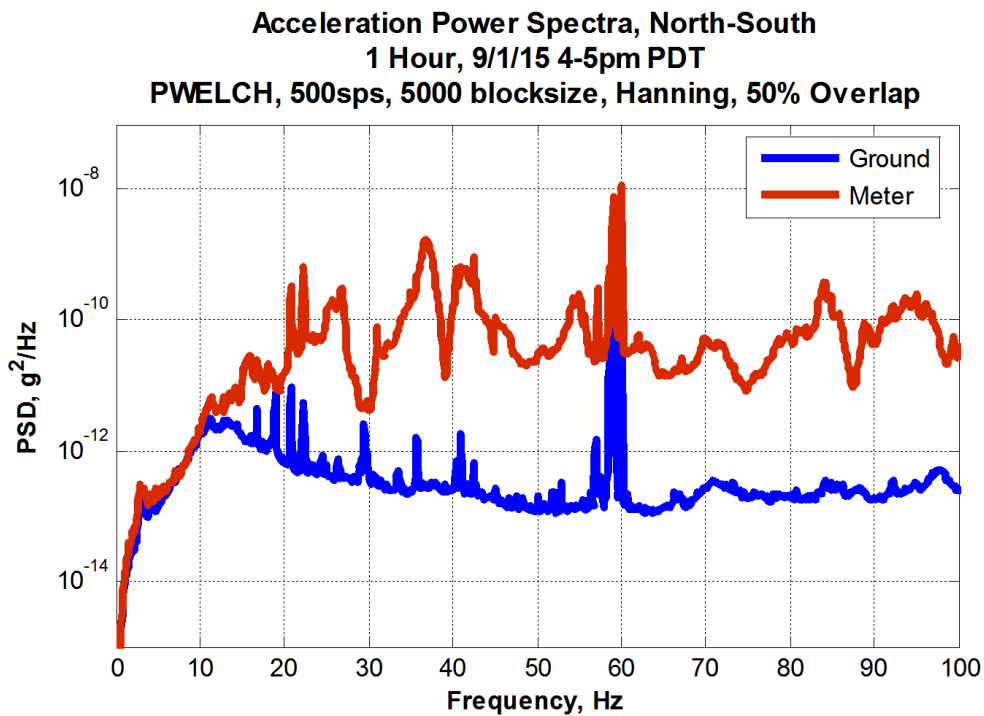


Figure VI.15. Comparison of the Fourier Spectra of the sensor that is installed on the wall to the sensor that is installed on the ground underneath (*image courtesy of Professor Norm Abrahamson and Professor Richard Nigbor*)

VI.3.2 Installations on shake table test houses

Results from this exercise will be available only after the installation is completed and an earthquake which produces significant records of good quality occurs. As significant seismicity in the Groningen field has been less frequent in the last two years, it is unknown how long the waiting period will be.

A shorter term solution is to take advantage of the shaking table tests that take place a few times every year using test houses identical to those built in Groningen. Therefore, in parallel with the installations that will take place in the field, four GeoSig accelerographs and four portable geophones were installed on the LNEC test house (Figure VI.16) during the tests that took place in Lisbon on the 5th and the 8th May of 2017.



Figure VI.16. The specimen house during the shake table test in LNEC on the 5th of May 2017. Six sensors are visible: two installed at a height of 0.5m on the eastern wall (*made by white bricks*), two installed on the eastern wall's foundation beams and two on the northern wall's foundation beams. The remaining pair is installed at 0.5m on the northern internal wall, to the right of the door. The blue sensors are the Geosig accelerographs and the orange sensors are the Geospace geophones.

As observed in Figure VI.16, four of the sensors were installed on the eastern wall, whereas the other four sensors were installed on the northern wall. On each wall, there was an

accelerograph and a geophone at a height of approximately 0.5m and another one of each bolted on the foundation beams directly underneath. The reason for installing sensors on both walls is that under the uni-axial loading on the tables, the test houses may respond very differently in the two orthogonal directions, with the one wall deforming in-plane and the other out-of-plane; therefore, installing sensors on both walls is a way to sample both types of response. Analyses using the data from this exercise are in progress and will be presented in a separate study.

VI.3.3 Comparisons with the KNMI network and loss of data due to PGV threshold

The existence of a PGV threshold of 0.1 cm/s (with records producing smaller PGV values being discarded), was made known through discussions with TNO staff Carine van Bentum in November of 2015 and Erik Langius and Jitse Pruiksma in April of 2016. The reason for the existence of the triggering threshold is so that recordings containing information from non-seismic sources are avoided, and especially triggering from the activity of the house residents, in order to protect their privacy. It is clear that this threshold is the main reason for the difference shown in Figure VI.13. as it means that a dataset of only the strongest motions is produced, thus giving the impression that the network overall records stronger motions.

A request was been made within NAM towards TNO in April of 2016 that the network system configurations are changed so that whenever an earthquake of magnitude greater than 2.5 is announced by the KNMI, the threshold is by-passed and all accelerations recorded by the sensors at the time of the event are transmitted to the central system. The implementation of this system update by TNO is pending, but TNO has agreed to provide all records requested from NAM for any earthquake that occurs until the update, by retrieving the records manually from the recorders before they are deleted.

All earthquakes with M_L greater than 2.5 occurred before this process was put in place and therefore most of the records produced during them were eliminated by the PGV threshold and had been deleted by the recorders by April of 2016. However, the PGV values of all records were broadcast by the recorders to the central network monitoring system in real time (as the PGV values reported for that minute of the hour). This available information provides an opportunity to compare data recorded from the entire household network with the KNMI network data for at least a single ground-motion parameter for the five $M_L > 2.5$ earthquakes which both recorded. These comparisons are presented in Figures VI.17-21.

It can be observed that the values plotted for the KNMI network for earthquakes 19, 21 and 22 are generally slightly below those of the TNO network. A possible cause for this difference could be the processing performed by the recorders before the “heartbeats” are reported. Low-cut filtering at the arbitrary frequency of 0.8 Hz is most likely insufficient for the weaker motions recorded, resulting in higher PGV values which contain noise.

No earthquakes of magnitude greater than 2.5 have occurred since the agreement to retrieve the records manually was put in place. However, three earthquakes of magnitude close to

2.0 occurred in Autumn of 2016, listed in Table VI.3, and it was decided to use spectral accelerations recorded during these events to conduct a preliminary comparison until larger events occur. As these records are fully available, they have undergone high-quality processing following the standards described in Ntinalexis *et al.* (2015) and the response spectral accelerations derived from them can be used for valid comparisons. The comparisons are displayed in Figures VI.22-24 for PGV and spectral accelerations at the periods of 1, 0.1 and 0.01 seconds. The patterns observed with epicentral distance are very similar for both networks, with the spectral accelerations appearing only marginally higher. The existence and nature of outliers in the records is still to be investigated as part of planned work.

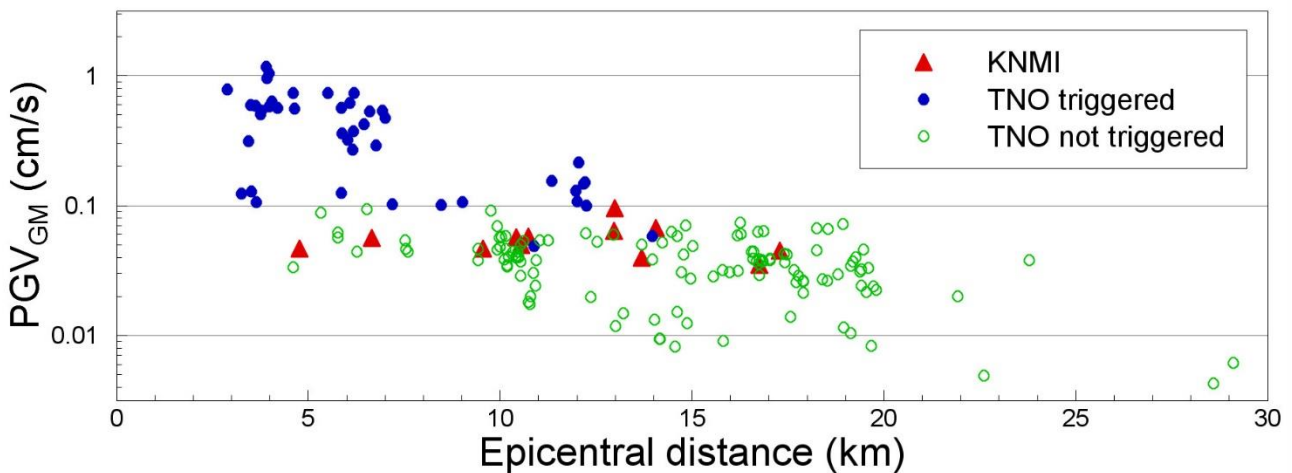


Figure VI.17. Geometric mean PGV values recorded during EQ-18 plotted against distance

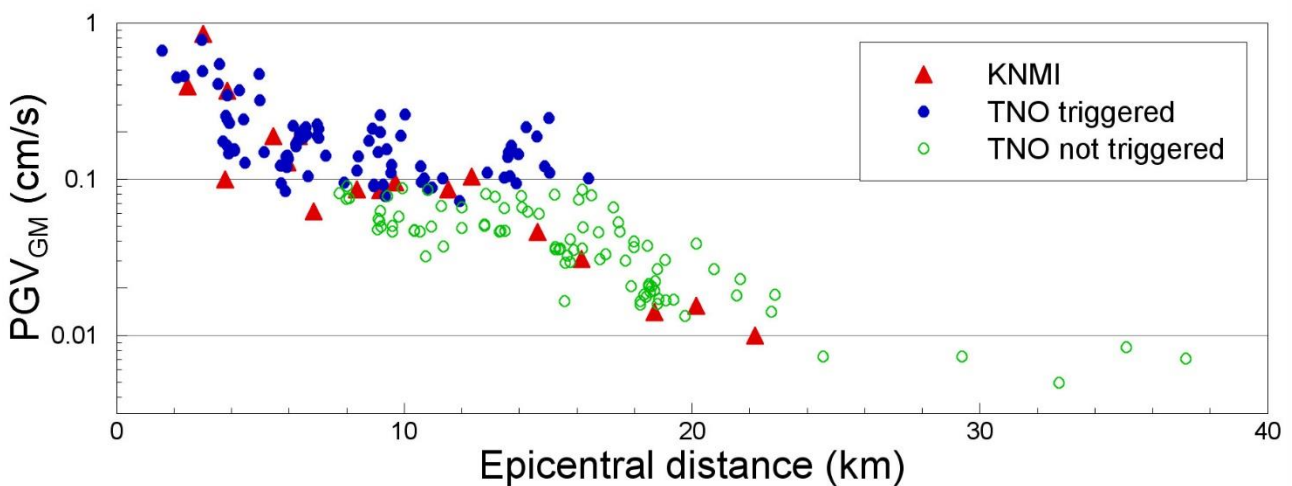


Figure VI.18. Geometric mean PGV values recorded during EQ-19 plotted against distance

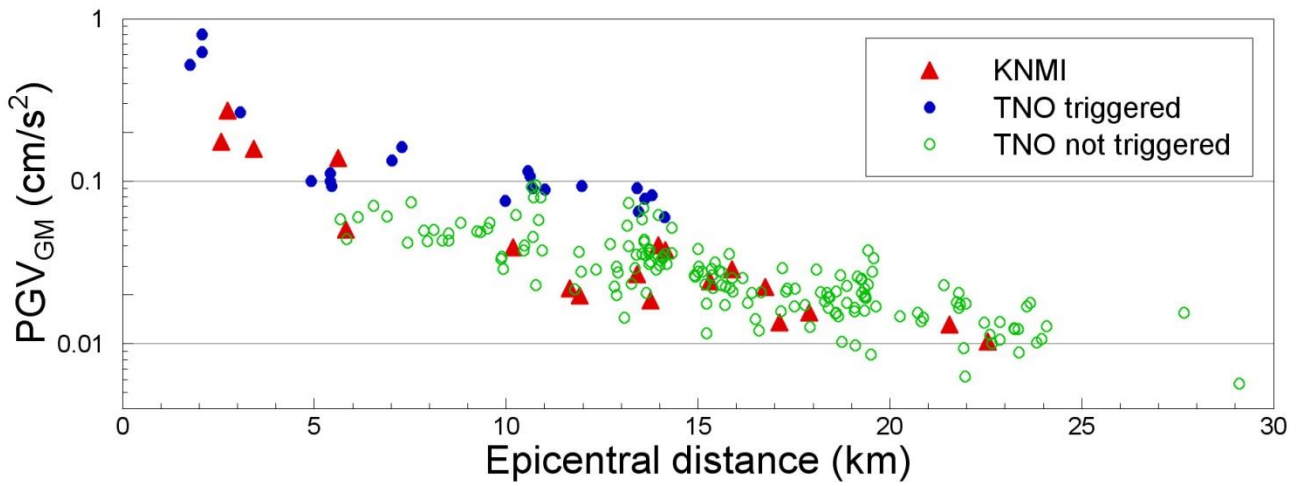


Figure VI.19. Geometric mean PGV values recorded during EQ-20 plotted against distance

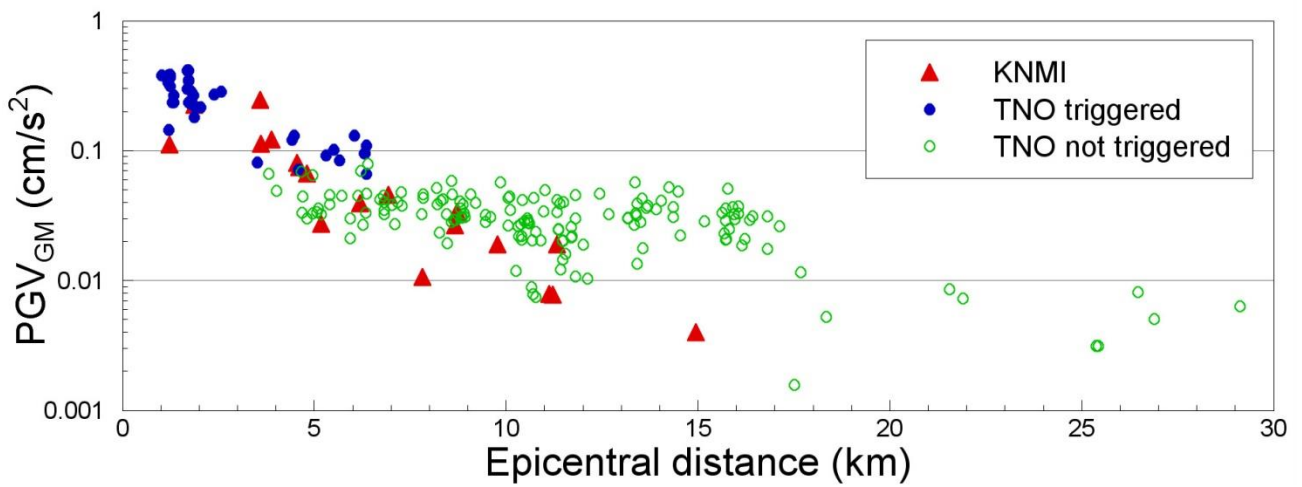


Figure VI.20. Geometric mean PGV values recorded during EQ-21 plotted against distance

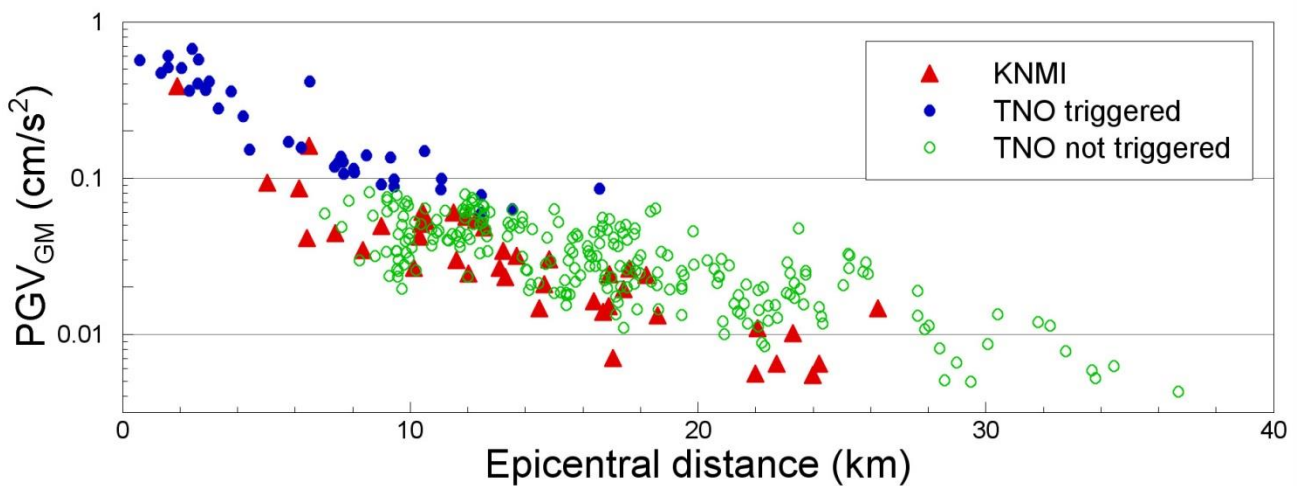


Figure VI.21. Geometric mean PGV values recorded during EQ-22 plotted against distance

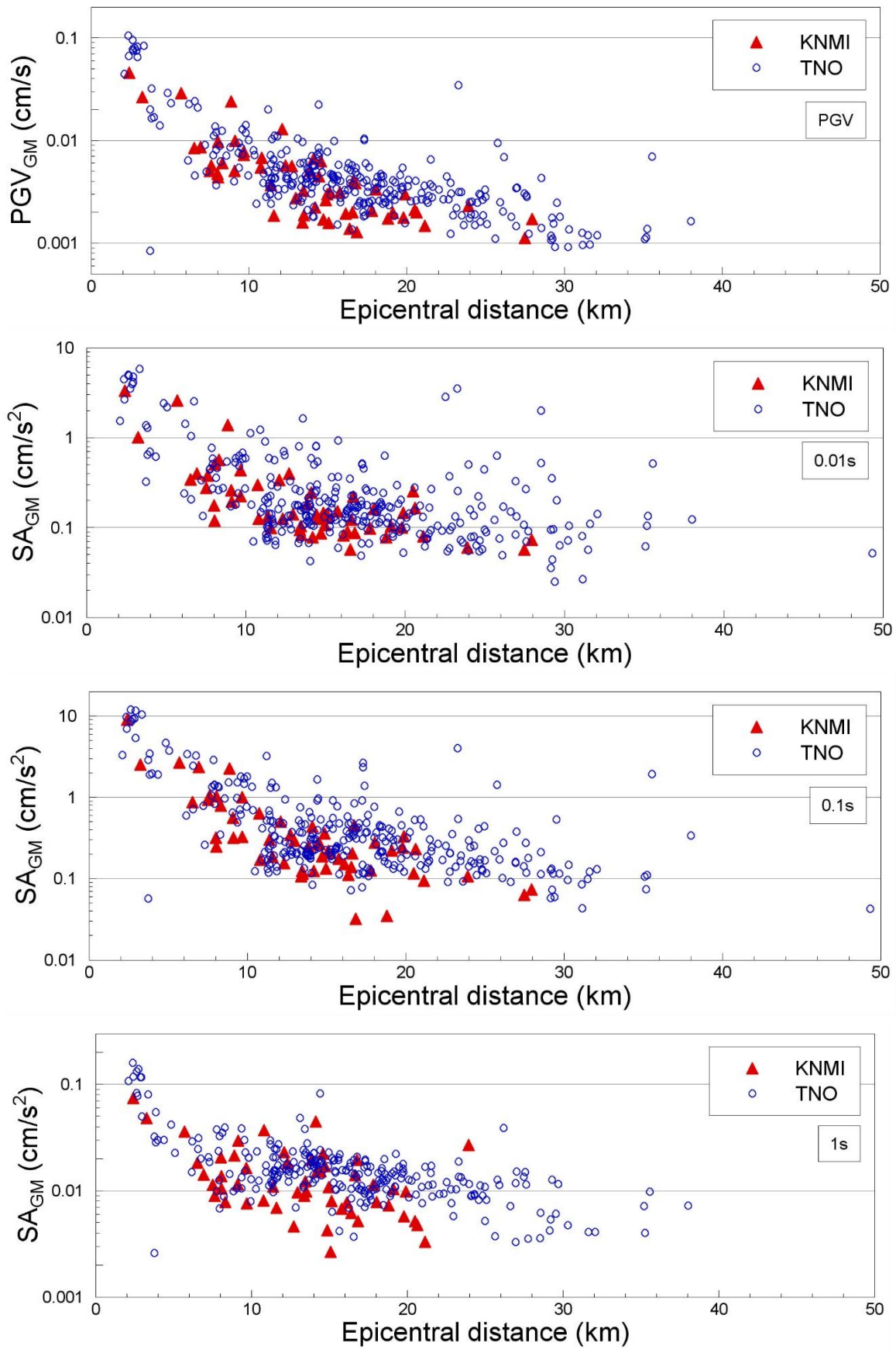


Figure VI.22. Geometric mean PGV and spectral acceleration values recorded during EQ-C1 (M_L 2.1) plotted against distance

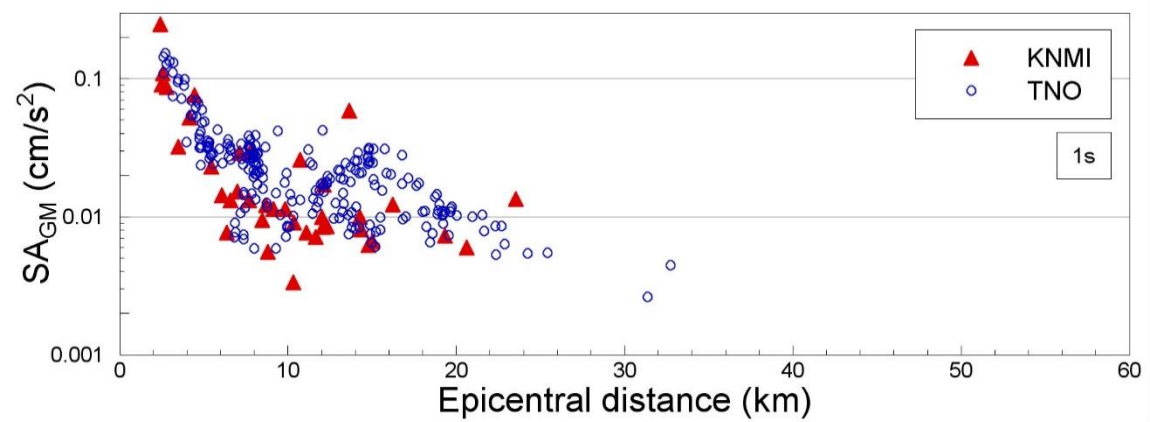
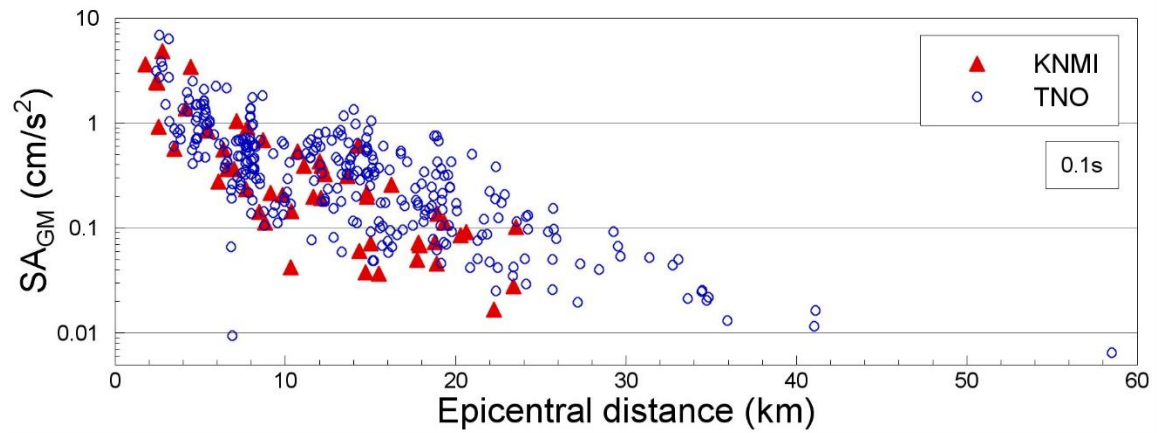
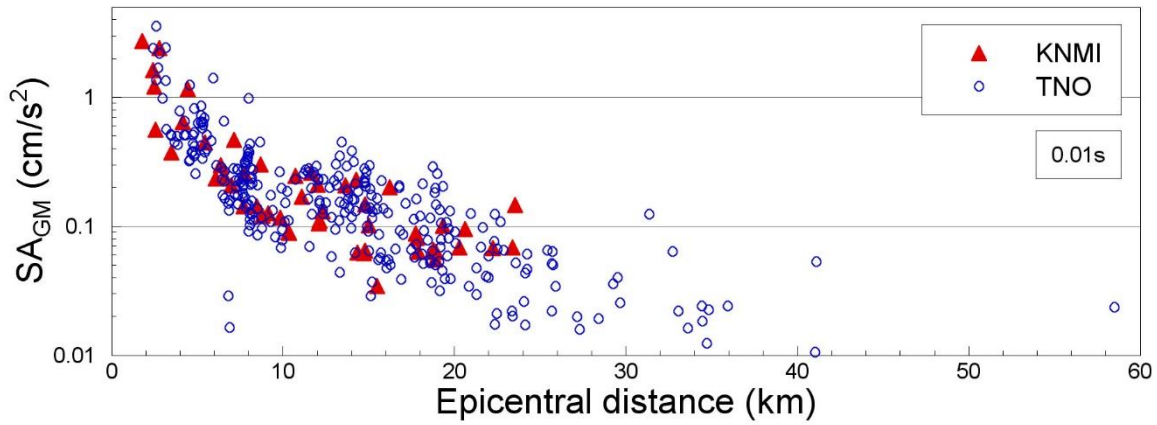
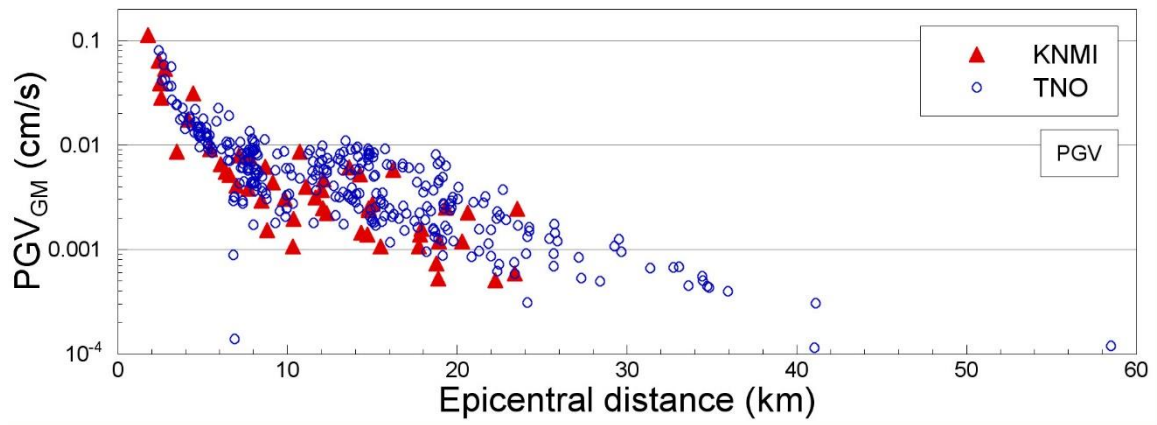


Figure VI.23. Geometric mean PGV and spectral acceleration values recorded during EQ-C2 (M_L 1.9) plotted against distance

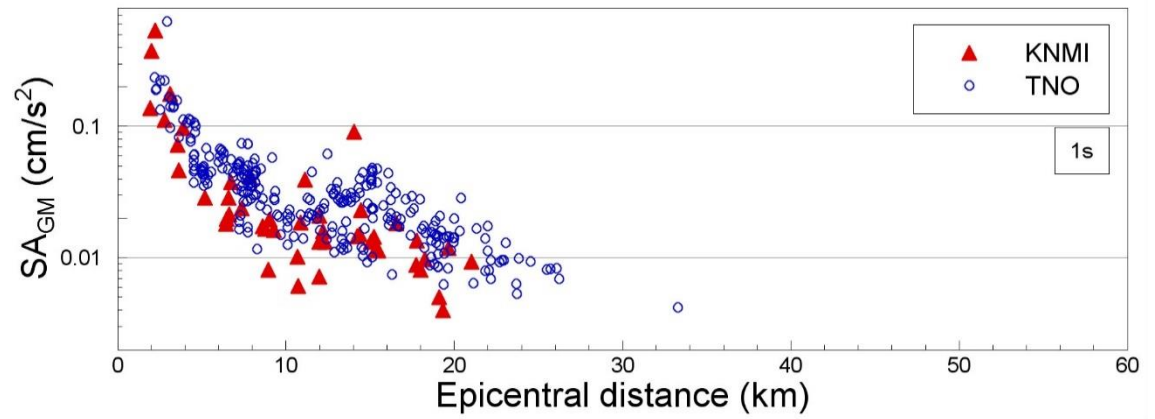
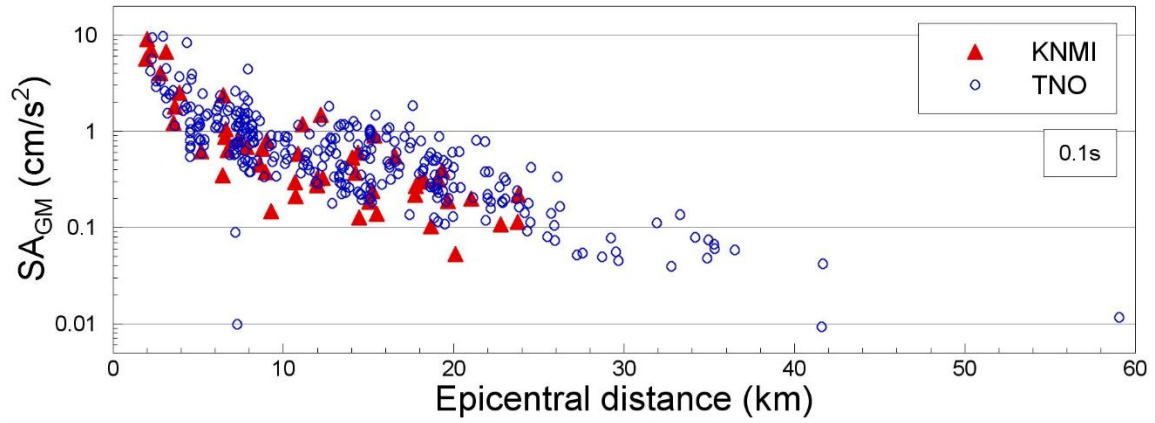
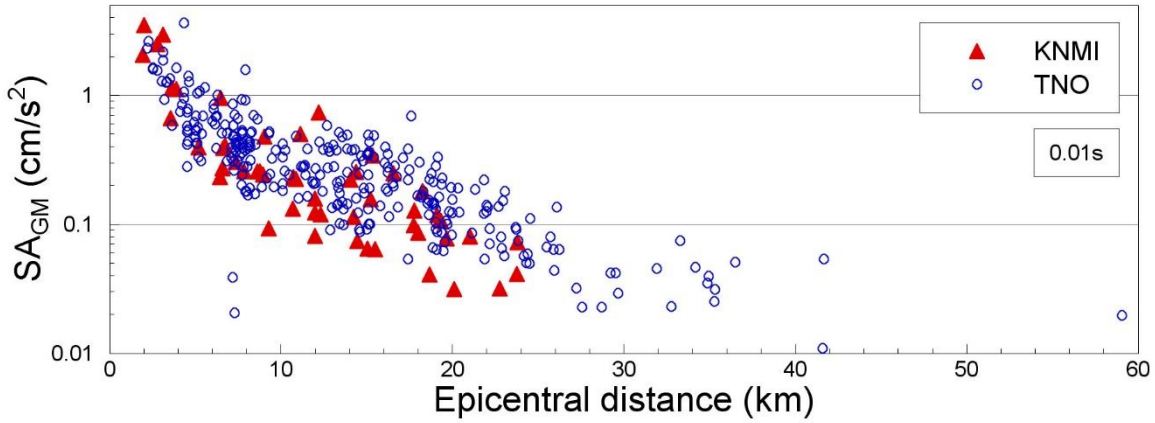
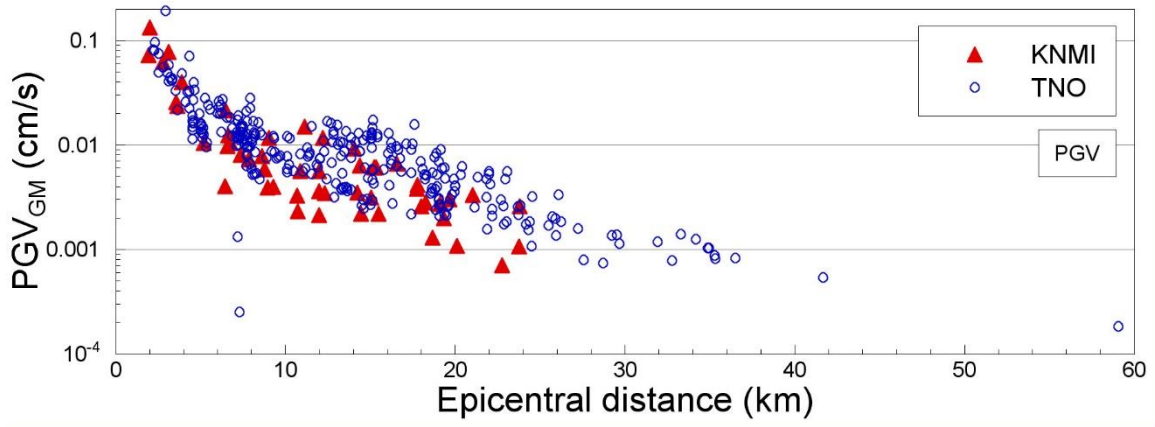


Figure VI.24. Geometric mean PGV and spectral acceleration values recorded during EQ-C3 (M_L 2.2) plotted against distance